Woodhead Publishing Series in Welding and Other Joining Technologies



Advances in Laser Materials Processing

Technology, Research and Applications

Second Edition

Edited by Jonathan Lawrence

WP
Woodhead Publishing

ADVANCES IN LASER MATERIALS PROCESSING

Related titles

Handbook of Laser Welding Technologies
(ISBN 978-0-85709-264-9)

Laser Spectroscopy for Sensing
(ISBN 978-0-85709-273-1)

Laser Surface Engineering
(ISBN 978-1-78242-074-3)

Laser Additive Manufacturing
(ISBN 978-0-08-100433-3)

Woodhead Publishing Series in Welding and Other Joining Technologies

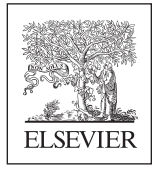
ADVANCES IN LASER MATERIALS PROCESSING

Technology, Research and Applications

Second Edition

Edited by

JONATHAN LAWRENCE



WP
WOODHEAD PUBLISHING
An imprint of Elsevier

Woodhead Publishing is an imprint of Elsevier
The Officers' Mess Business Centre, Royston Road, Duxford, CB22 4QH, United Kingdom
50 Hampshire Street, 5th Floor, Cambridge, MA 02139, United States
The Boulevard, Langford Lane, Kidlington, OX5 1GB, United Kingdom

Copyright © 2018 Elsevier Ltd. All rights reserved.
Chapter 16, Crown Copyright © 2018. Published by Elsevier Ltd. All rights reserved.

No part of this publication may be reproduced or transmitted in any form or by any means, electronic or mechanical, including photocopying, recording, or any information storage and retrieval system, without permission in writing from the publisher. Details on how to seek permission, further information about the Publisher's permissions policies and our arrangements with organizations such as the Copyright Clearance Center and the Copyright Licensing Agency, can be found at our website: www.elsevier.com/permissions.

This book and the individual contributions contained in it are protected under copyright by the Publisher (other than as may be noted herein).

Notices

Knowledge and best practice in this field are constantly changing. As new research and experience broaden our understanding, changes in research methods, professional practices, or medical treatment may become necessary.

Practitioners and researchers must always rely on their own experience and knowledge in evaluating and using any information, methods, compounds, or experiments described herein. In using such information or methods they should be mindful of their own safety and the safety of others, including parties for whom they have a professional responsibility.

To the fullest extent of the law, neither the Publisher nor the authors, contributors, or editors, assume any liability for any injury and/or damage to persons or property as a matter of products liability, negligence or otherwise, or from any use or operation of any methods, products, instructions, or ideas contained in the material herein.

Library of Congress Cataloging-in-Publication Data
A catalog record for this book is available from the Library of Congress

British Library Cataloguing-in-Publication Data
A catalogue record for this book is available from the British Library

ISBN: 978-0-08-101252-9 (print)
ISBN: 978-0-08-101253-6 (online)

For information on all Woodhead publications
visit our website at https://www.elsevier.com/books-and-journals



Publisher: Matthew Deans
Acquisition Editor: Kayla Dos Santos
Editorial Project Manager: Jennifer Pierce
Production Project Manager: Omer Mukthar
Cover Designer: Greg Harris

Typeset by SPi Global, India

To Louise, Ethan, and Lydia
You make it all worthwhile. *Always there; beyond compare*.

This page intentionally left blank

CONTENTS

Contributors *xv*
Preface *xix*

1. "Light" Industry: An Overview of the Impact of Lasers on Manufacturing **1**

M. Sparkes, W.M. Steen

1.1 The Laser, and the Generation of a Mature Industry 1
1.2 Economic Impact of Laser Materials Processing 7
1.3 The Developing Application Space 8
1.4 Future Predictions 17
References 19

2. The Challenges Ahead for Laser Macro, Micro and Nano Manufacturing **23**

J. Lawrence, L. Li

2.1 Introduction 23
2.2 Laser Cutting 23
2.3 Laser Welding 29
2.4 Laser Drilling 32
2.5 Laser Surface Engineering 34
2.6 Additive Multiple Layer Manufacturing 35
2.7 Micro/Nano Fabrication 36
2.8 Fundamental Beam/Material Interactions and Process Modeling 40
2.9 Laser Systems 41
2.10 Conclusions 41
References 42

3. Laser Fusion Cutting of Difficult Materials **43**

J. Lawrence, A. Riveiro, F. Quintero, J. Pou

3.1 Introduction 43
3.2 Principles Involved in Fusion Laser Cutting 44
3.3 Experiences in Laser Cutting of Difficult Materials 45
3.4 Attempts to Improve Cutting Process 50
3.5 Conclusions 62
Acknowledgments 62
References 62

4. Laser-Assisted Glass Cleaving **69**
J. Lawrence, Y.L. Kuo, J. Lin

4.1 Introduction 69
4.2 The Multiple Laser System 70
4.3 Numerical Simulation 71
4.4 Numerical Results and Discussions 74
4.5 Crack Propagation in Laser Cleaving 81
4.6 Conclusions 85
Acknowledgments 86
References 86
Further Reading 87

5. Laser Dicing of Silicon and Electronics Substrates **89**
I. Mingareev, C. Fornaroli, A. Gillner

5.1 Introduction 89
5.2 Industrial Dicing Processes for Silicon and Electronic Substrates 90
5.3 Dicing of Silicon With Ultra-Fast Laser Radiation 96
5.4 Explanation of Surface Phenomena During Laser Dicing Processes 103
5.5 Factors Influencing the Aspect Ratio During Laser Dicing Processes 105
5.6 Increasing Dicing Modification Depth Using High-Repetition-Rate Femtosecond Laser Radiation and Spatial Beam Shaping 115
References 118

6. Laser Machining of Carbon Fiber-Reinforced Plastic Composites **121**
P. Jäschke, V. Wippo, S. Bluemel, R. Staehr, H. Dittmar

6.1 Introduction 121
6.2 Welding of Thermoplastic Composites 124
6.3 Cutting of Composite Structures 132
6.4 Repair Preparation for Composites 140
6.5 Process Emissions 147
References 149

7. Understanding and Improving Process Control in Pulsed and Continuous Wave Laser Welding **153**
J. Lawrence, S. Katayama

7.1 Introduction 153
7.2 Laser Spot Welding Results, and Formation Mechanisms and Suppression Procedures of Welding Defects 154

7.3 CW Laser Welding Results, and Formation Mechanisms and Suppression Procedures of Welding Defects 166
7.4 Conclusions 180
References 181

8. Laser Microspot Welding in Electronics Production 185
J. Lawrence, I. Mys, M. Schmidt

8.1 Introduction 185
8.2 State-Of-The-Art 186
8.3 Micro Welding of Copper and Aluminum 189
8.4 Reliability of Copper-Aluminum Welded Joints 197
8.5 Conclusions 201
References 201

9. Laser Arc Hybrid Welding 203
B. Acherjee

9.1 Introduction 203
9.2 Laser MIG/MAG Hybrid Welding 210
9.3 Laser TIG Hybrid Welding 211
9.4 Laser PAW Hybrid Welding 213
9.5 Laser Arc Hybrid Welding Parameters 214
9.6 Improvements of Performance Characteristics and Weld Quality 221
9.7 Industrial Applications 224
9.8 Safety 227
9.9 Conclusion 229
References 231

10. Influencing the Weld Pool During Laser Welding 235
S. Nothdurft, A. Springer, S. Kaierle

10.1 Introduction 235
10.2 Approaches and Methods for Manipulating Weld-Pool Dynamics 238
10.3 Ultrasound-Assisted Laser-Beam Welding 244
Acknowledgments 254
References 255

11. Laser Transformation Hardening of Steel 257
A.K. Nath, S. Sarkar

11.1 Introduction 257
11.2 Recent Developments 268

11.3 Future Trends 291
11.4 Conclusion 293
References 293

12. Pulsed Laser Annealing Technology for Nano-Scale Fabrication of Silicon-Based Devices in Semiconductors 299
J. Lawrence, K.L. Pey, P.S. Lee

12.1 Introduction 299
12.2 Laser-Induced Formation of p/n Junction 300
12.3 Laser-Induced Formation of Silicide 322
12.4 Conclusions and Future Trends 334
References 335

13. Laser-Induced Forward Transfer Techniques and Applications 339
M. Morales, D. Munoz-Martin, A. Marquez, S. Lauzurica, C. Molpeceres

13.1 Introduction 339
13.2 LIFT Experimental Setup 341
13.3 LIFT Physical Processes 344
13.4 Variations of LIFT 352
13.5 Applications of LIFT 357
13.6 Conclusions 370
Acknowledgments 371
References 371

14. Production of Biomaterial Coatings by Laser-Assisted Processes 381
J. Lawrence, J. Pou, F. Lusquiños, R. Comesaña, M. Boutinguiza

14.1 Introduction 381
14.2 The Laser Way to Produce Coatings 382
14.3 Pulsed Laser Deposition of Bioceramics 383
14.4 Laser Cladding of Bioceramics 394
14.5 Conclusions 406
References 406

15. Thick Metallic Coatings Produced by Coaxial and Side Laser Cladding: Processing and Properties 413
J. Lawrence, V. Ocelík, J.T.M. De Hosson

15.1 Introduction 413
15.2 Coaxial Laser Cladding Geometry and Theoretical Calculations 428

15.3 Experimental Evaluation of Coaxial and Side Cladding Processes 432
15.4 Statistical Relations Between Processing Parameters and Laser Track Geometry 435
15.5 Microstructural Characteristics and Properties of Thick Metallic Coatings 444
15.6 Conclusions 455
Acknowledgments 457
References 457

16. Laser Consolidation—A Rapid Manufacturing Process for Making Net-Shape Functional Components 461
L. Xue

16.1 Introduction 461
16.2 Process Description 462
16.3 Microstructure and Mechanical Properties of Laser-Consolidated (LC) Materials 463
16.4 Case Studies of Various Industrial Applications 484
16.5 Future Trend of the Technology 501
Acknowledgments 502
References 502

17. Laser-Based Additive Manufacturing Processes 507
H. Sahasrabudhe, S. Bose, A. Bandyopadhyay

17.1 Introduction 507
17.2 Techniques 509
17.3 Materials Processed Using Laser-Based Additive Manufacturing Techniques 514
17.4 Materials Used in Laser-Based Additive Manufacturing Techniques 518
17.5 Applications 526
17.6 Summary and Future Trends 532
References 535

18. Direct Infrared Laser Machining of Semiconductors for Electronics Applications 541
I. Mingareev, L. Shah, M. Richardson, M. Ramme

18.1 Introduction 541
18.2 Main Principles of Laser-Matter Interactions 543
18.3 Infrared Ultrashort Pulse Laser Processing 550
18.4 Infrared Nanosecond Pulse Laser Processing 557
18.5 Summary 567
References 569

19. Laser Processing of Direct-Write Nano-Sized Materials 571
J. Lawrence, O.F. Swenson, V. Marinov

19.1 Introduction 571
19.2 Direct-Write Deposition of Nano-Sized Materials 572
19.3 Background of Nano-Sized Materials Sintering 576
19.4 Laser Sintering of Direct-Write Nano-Sized Materials 580
19.5 Future Trends 590
19.6 Sources of Further Information and Advice 591
Acknowledgments 592
References 592

20. Micro- and Nano-Parts Generated by Laser-Based Solid Freeform Fabrication 595
J. Lawrence, A. Ostendorf, A. Neumeister, S. Dudziak, S. Passinger, J. Stampfl

20.1 Introduction 595
20.2 Manufacturing Based on Photopolymerization 598
20.3 Materials for Micro Stereolithography and Two-Photon Laser Lithography 614
20.4 Manufacturing Based on Sintering, Melting, and Cladding 618
20.5 Materials for Micro Sintering, Melting, and Cladding 628
20.6 Conclusions 630
References 630
Further Reading 633

21. Laser-Assisted Additive Fabrication of Micro-Sized Coatings 635
R.M. Mahamood, E.T. Akinlabi

21.1 Introduction 635
21.2 Types of Micro-Sized Coatings and Their Areas of Applications 637
21.3 Laser Based Additive Manufacturing for Micro-Sized Coatings 638
21.4 Case Studies: Fabrication of Ti6Al4V and TiC/Ti6Al4V Composite on Ti6Al4V Substrate Using Laser Metal Deposition Process 646
21.5 Summary 661
Acknowledgments 661
References 661
Further Reading 664

22. Multiphysics Modelling of Laser Solid Freeform Fabrication Techniques 665
J. Lawrence, M. Alimardani, C.P. Paul, E. Toyserkani, A. Khajepour

22.1 Introduction 665
22.2 Physics of LSFF 668

22.3 Multiphysics Modelling of LSFF Processes 672
22.4 Numerical Multiphysics Modelling—A Case Study 677
22.5 Conclusions 689
References 690

23. Process Control of Laser Materials Processing 693
J. Lawrence, R.T. Deam

23.1 Introduction 693
23.2 Theory 694
23.3 Experiments 699
23.4 Experimental Results 700
23.5 Discussion 703
23.6 Conclusions 705
Acknowledgments 706
References 706

24. Development of Laser Processing Technologies via Experimental Design 707
H. Sohrabpoor, A. Issa, A. Al Hamaoy, I.U. Ahad, E. Chikarakara, K. Bagga, D. Brabazon

24.1 Introduction 707
24.2 Design of Experiments (DoE) Methods 709
24.3 Modeling and Optimization of Laser Processes With Nonconventional Approaches 716
24.4 Experimental Analysis of Laser Processing 718
24.5 Conclusion 726
References 727

25. Microstructural Characterization and Mechanical Reliability of Laser-Machined Structures 731
M. Mehrpouya, H. Lavvafi, A. Darafsheh

25.1 Introduction 731
25.2 Laser Micromachining and Its Features 732
25.3 Laser Sources for Laser Machining 736
25.4 Methods of Microstructure and Surface Evaluation 742
25.5 Mechanical Characteristics and Laser-Induced Thermal Effects 746
25.6 Summary 756
References 757

Index 763

This page intentionally left blank

CONTRIBUTORS

B. Acherjee
Birla Institute of Technology, Mesra, India

I.U. Ahad
Dublin City University, Dublin Ireland

E.T. Akinlabi
University of Johannesburg, Auckland Park Kingsway Campus, Johannesburg, South Africa

A. Al Hamaoy
Al-Nahrain University, Baghdad, Iraq

M. Alimardani
University of Waterloo, Waterloo, ON, Canada

K. Bagga
Dublin City University, Dublin Ireland

A. Bandyopadhyay
Washington State University, Pullman, WA, United States

S. Bluemel
Laser Zentrum Hannover e.V., Hannover, Germany

S. Bose
Washington State University, Pullman, WA, United States

M. Boutinguiza
University of Vigo, Vigo, Spain

D. Brabazon
Dublin City University, Dublin Ireland

E. Chikarakara
Dublin City University, Dublin Ireland

R. Comesaña
University of Vigo, Vigo, Spain

A. Darafsheh
Washington University School of Medicine, St. Louis, MO, United States

J.T.M. De Hosson
University of Groningen, Groningen, The Netherlands

R.T. Deam
Swinburne University of Technology, Hawthorn, VIC, Australia

H. Dittmar
Laser Zentrum Hannover e.V., Hannover, Germany

S. Dudziak
Laser Center, Hannover, Germany

C. Fornaroli
Florida Institute of Technology, Melbourne, FL, United States

A. Gillner
Florida Institute of Technology, Melbourne, FL, United States

A. Issa
Al Azhar University, Gaza, Palestine

P. Jäschke
Laser Zentrum Hannover e.V., Hannover, Germany

S. Kaierle
Laser Zentrum Hannover e.V., Hannover, Germany

S. Katayama
Osaka University, Suita, Japan

A. Khajepour
University of Waterloo, Waterloo, ON, Canada

Y.L. Kuo
National Cheng Kung University, Tainan, Taiwan

S. Lauzurica
Universidad Politécnica de Madrid, Madrid, Spain

H. Lavvafi
Loyola University Medical Center, Maywood, IL, United States

J. Lawrence
University of Chester, Chester, United Kingdom

P.S. Lee
Nanyang Technological University, Singapore, Singapore

L. Li
The University of Manchester, Manchester, United Kingdom

J. Lin
National Cheng Kung University, Tainan, Taiwan

F. Lusquiños
University of Vigo, Vigo, Spain

R.M. Mahamood
University of Johannesburg, Auckland Park Kingsway Campus, Johannesburg, South Africa;
University of Ilorin, Ilorin, Nigeria

V. Marinov
North Dakota State University, Fargo, ND, United States

A. Marquez
Universidad Politécnica de Madrid, Madrid, Spain

M. Mehrpouya
Sapienza University of Rome, Rome, Italy

I. Mingareev
Florida Institute of Technology, Melbourne, FL, United States

C. Molpeceres
Universidad Politécnica de Madrid, Madrid, Spain

M. Morales
Universidad Politécnica de Madrid, Madrid, Spain

D. Munoz-Martin
Universidad Politécnica de Madrid, Madrid, Spain

I. Mys
Bayerisches Laserzentrum Gmbh, Erlangen, Germany

A.K. Nath
Indian Institute of Technology, Kharagpur, India

A. Neumeister
Laser Center, Hannover, Germany

S. Nothdurft
Laser Zentrum Hannover e.V., Hannover, Germany

V. Ocelík
University of Groningen, Groningen, The Netherlands

A. Ostendorf
Ruhr University, Bochum, Germany

S. Passinger
Leuze electronic GmbH & CoKG, Owen, Germany

C.P. Paul
University of Waterloo, Waterloo, ON, Canada

K.L. Pey
Nanyang Technological University, Singapore, Singapore

J. Pou
University of Vigo, Vigo, Spain

F. Quintero
University of Vigo, Vigo, Spain

M. Ramme
TRUMPF North America, Farmington, CT, United States

M. Richardson
University of Central Florida, Orlando, FL, United States

A. Riveiro
University of Vigo, Vigo, Spain

H. Sahasrabudhe
LENS Applications Engineer, Optomec Inc., Albuquerque, NM, United States

S. Sarkar
Indian Institute of Technology, Kharagpur, India

M. Schmidt
Bayerisches Laserzentrum Gmbh, Erlangen, Germany

L. Shah
University of Central Florida, Orlando, FL, United States

H. Sohrabpoor
Dublin City University, Dublin Ireland

M. Sparkes
Cambridge University, Cambridge, United Kingdom

A. Springer
Laser Zentrum Hannover e.V., Hannover, Germany

R. Staehr
Laser Zentrum Hannover e.V., Hannover, Germany

J. Stampfl
TU Wien, Vienna, Austria

W.M. Steen
Cambridge University, Cambridge, United Kingdom

O.F. Swenson
North Dakota State University, Fargo, ND, United States

E. Toyserkani
University of Waterloo, Waterloo, ON, Canada

V. Wippo
Laser Zentrum Hannover e.V., Hannover, Germany

L. Xue
National Research Council of Canada, London, ON, Canada

PREFACE

In March 1800 Alessandro Volta constructed the voltaic pile and, for the first time, mankind could reliably generate electricity at will. A laser beam was first emitted in May 1960 from a solid-state ruby laser designed and constructed by Theodore Maiman. In December 1960 laser light was emitted from the first helium and neon gas laser designed and constructed by Ali Javan, William Bennett, and Donald Herriot. It took 71 years for electrical energy to be harnessed for industrial use, when in 1871 the Nollet generator was used commercially for electroplating. This triggered the Second Industrial Revolution and brought about the incredible improvements to the global quality of life that we enjoy today. Optical energy is considerably more versatile than electricity as a source of energy, and with the ability to generate it in large and controllable quantities, only five short years were needed from its birth for the first commercial laser materials processing task to take root: the drilling of holes through diamonds for wire dies using a ruby laser beam, in 1965, by engineers at Western Electric.

Optical energy and lasers will provide a tremendous boost to our future quality of life. This is clearly evident in the adoption of lasers for materials processing in the last 52 years, which has been rapid and continues apace. Rather than simply acting as a replacement energy source in an existing materials processing technology or process the laser has, in most cases, provided a unique solution. This has opened up completely new avenues of laser materials processing research, delivered brand new processes and products, and let us not forget—new science. Laser materials processing will continue to challenge mainstream manufacturing processes because it offers unique advantages for manufacturing and especially high value manufacturing. Added to this is the intrinsic ability for continuous development and the flexibility of use of lasers, which leads to new and unique materials processing applications continuously arising.

Laser materials processing is such an intense and productive area of academic and industrial research that it is beginning to form into an interdisciplinary branch of science and engineering in its own right. The second edition of this book is, therefore, timely as it reflects this new form of laser materials processing science and engineering. The contributions from renowned researchers working in every corner of the globe has resulted in this comprehensive, yet detailed, book on the many topics that comprise

the field. The book serves as both a practitioner's guide and a medium to high-level reference textbook. As such, it will prove useful to the scientist or engineer practicing in, or anticipating the need to move into, the field of laser materials processing; undergraduate and post-graduate students; and with those conducting laser materials processing-related research in either academia or industry.

J. Lawrence

CHAPTER 1

"Light" Industry: An Overview of the Impact of Lasers on Manufacturing

M. Sparkes, W.M. Steen
Cambridge University, Cambridge, United Kingdom

This revised edition seeks to communicate a glimpse of how laser materials processing has evolved since the first 2010 publication. Instead of simply summarizing what is to follow, this introduction aims to place the laser and associated technologies in context with other manufacturing methods using electricity as a comparative benchmark before looking at the state of the art and future of industry based on optical energy. Finally predictions from the previous edition will be reviewed, and we will speculate on the future.

By the early 1990s there was enough commercial activity to warrant the first dedicated book on the subject of laser material processing [1], which presented the reader with a basic introduction to the bulk of the industrialized applications while still having space to describe the workings of the laser, basic optics, and process modelling. Now in its fourth edition, the book's basic principles form part of courses taught in schools and colleges. Today the field of laser applications has expanded so far it is hard to see the boundaries of the subject. The application of optical energy goes from atomic fusion through material processing and photochemistry to the remote sensing of planets. The ready availability of high levels of optical energy (with ever increasing efficiency) in a myriad of wavelengths, pulse lengths/shapes, and physical compactness without the need for huge cooling facilities (or patient staff to align the optics) is now a reality, leading to the growing relevance of the subject of lasers in manufacturing.

1.1 THE LASER, AND THE GENERATION OF A MATURE INDUSTRY

Key technologies fundamentally change manufacturing. Traditionally we start our numbering with the Stone Age, with the last mature development

Advances in Laser Materials Processing
https://doi.org/10.1016/B978-0-08-101252-9.00001-7
Copyright © 2018 Elsevier Ltd.
All rights reserved.

being the Electric Age. With respect to manufacturing, the Optical Age is finally blossoming and has taken its place as an essential tool that is set to dominate developments in this century.

There are many parallels between the dynamo and the laser: one produces large and controllable quantities of electricity, the other the same for electromagnetic radiation. Since the late 19th century, electricity has dominated many developments with astounding results, so much so that it is hard to imagine a world without electricity. We have become dependent upon it. While some might think it strange to write a chapter on the generation of electricity, the electricity produced is being applied in ever more imaginative applications. Optical energy could be considered a progression from electricity as there are many similarities but also additional "knobs to turn," making it an even more versatile energy source (Table 1.1).

Table 1.1 Properties of a laser beam as an industrial power source compared to electricity and other forms of industrial power

Power intensity *Electricity and laser*	A focused laser beam can be one of the most intense power sources available to industry today. A 4 kW laser beam for thick section cutting focused to a 0.2 mm spot size is around 40,000 times more intense than an electric arc [1]
Power transmission *Electricity and laser*	Optical energy is one of the few forms of energy that can be transmitted through a vacuum or air, making it almost uniquely flexible. But it can also be transmitted down optical fibers making it similar to electricity for ease of distribution
Automation *Electricity and laser*	Laser processing can be a non-contact process that creates relatively little noise compared to electric arcs, induction, or flames. Thus laser processes are more open to examination by a variety of in-process sensors offering the possibility of adaptive control and "intelligent" processing
Power shaping *Ion beam and laser*	No other form of energy can be shaped with the precision of optical energy without being in a vacuum. Examples range from photography and holography, to simple point focus or interference fringes
Spectral purity *Electricity and laser*	A laser beam is usually of a single frequency ± dispersion effects around a central value. They can only be tuned within small ranges. A range of processes based on resonant absorption are possible. These photolytic processes include cold cutting with ultraviolet light; photodynamic therapy (PDT), which involves breaking of photosensitive molecules; isotope separation (selective ionisation); and fluorescence analysis. Developments in optical computing will soon be using this property

Table 1.1 Properties of a laser beam as an industrial power source compared to electricity and other forms of industrial power—cont'd

Coherence *Laser*	The stream of electromagnetic waves from a laser is often a single continuous wave stream over measurable distances unlike, for example, radiation from an incandescent bulb. This property has been used for distance measurement and the generation of Bessel beams for low diffraction propagation [2] as well as beam shaping with spatial light modulators (SLM) [3]
Polarization *Laser*	Controlling the direction of the electric field oscillation through polarization effects can influence the absorption of light by materials leading to more efficient processing [4] or fast switching of optical transmission in electro-optic materials [5]
Pulse length	Bursts of laser light can provide additional capabilities for controlling laser-matter interactions, such as increased precision when machining or hole drilling by ablation processes, with limited collateral thermal effects. Taken to the extreme, high-intensity short laser pulses (≈<15 ps) are capable of having multi-photon interactions with the photons arriving simultaneously [6,7]. Examples of manufacturing applications are "transparent" material processing, precision ablation [8], and two photon precision additive manufacturing [9,10]

One common misconception is that the laser is powerful, but truthfully, laser beams are only just moving into the realms of being high powered. A 6 kW laser, which could be considered to be the workhorse for laser cutting job shops over the last 20 years, is about as powerful as two UK domestic electric kettles. The power of the laser comes with its focusability. An industrial 1 kW single mode CW fiber laser can easily be focused to diameters below 7.5 μm, giving a power density of 22.6×10^9 kW/m^2. If this energy density were extended over the entire 1 m^2 it would be more than the equivalent of the entire electrical production of the world! The International Energy Outlook [11] estimates 2016 global electricity generation to be around 23×10^{12} kWh ($\approx 6.3 \times 10^9$ kW).

But first let's consider what a laser can do. It produces a coherent, near parallel beam of electromagnetic radiation. The distribution of power within the beam can be readily manipulated and the range of power can be from μW to PW (Peta 10^{15}) with a range of wavelengths from radio through infrared to ultraviolet or even x-rays (if we include MASERs as a form of laser).

What happens when the radiation strikes the material? For the bulk of laser processes the beam interacts with the electric field within the material causing the structure to vibrate, which is sensed as heating leading to melting and boiling as the structure shakes apart. Looking in more detail, and considering just a single pulse, the interactions are complex. Initially electromagnetic radiation interacts with the electric field of the material's atomic structure (the electron clouds and phonon bonding) and energy is absorbed with characteristic electron-photon interaction timescales of 10^{-15} s (femtosecond). Plasma is formed after around 10^{-12} s (picosecond), vaporization and melting being limited by the material's thermal response rate. Shockwave emission of the plasma has been shown to operate in timescales from the picosecond regime to beyond the millisecond [12]. The material interaction then moves to the more understood "classic phenomena" with vapor and plasma ejection and melt propagation within the material followed by melt/particle ejection depending upon the material and energy input (Fig. 1.1).

To add additional complexity, with the exception of single ultrafast pulses, each of these interactions continues under the influence of additional laser energy being absorbed by the ejected material (Fig. 1.2). It is not therefore sufficient to analyze the response of materials to single pulse interactions because industrial processing relies on multiple pulses in order to increase the rate of the particular process.

For practical applications a laser can be considered a chemically pure form of heat energy that can be placed with great accuracy (while not necessarily affecting the surrounding material), which is not dependent on a thermal gradient for energy transfer. But that is not all that a laser beam can do. The radiation has a particular frequency and is therefore able to interact with specific chemical bonds that are of similar quantum energies, resonant

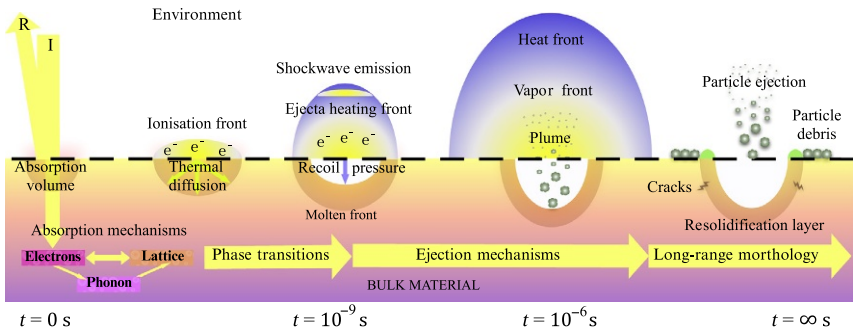


Fig. 1.1 Laser-matter interaction mechanisms and range of time scales [13].



Fig. 1.2 Titanium plume growth during multiple laser pulse interactions [14].

absorption leading to flourescence specific bond breaking (photodynamic therapy, polymerization of dental resins, gene surgery). Even further, the laser beam has other properties that are just beginning to be utilized in industry, such as polarization, phase, pulse length, and coherence. Consider as an example the frequency comb (which may be generated by an ultrafast laser), a broad-spectrum source that looks to have a promising future within precision metrology offering what is effectively an absolute optical encoder. Fringe counting may soon be obsolete [15]. There will no doubt be many more applications from these parameters as the years roll by.

The principal early industrial lasers were the CO_2 and Nd:YAG from which the present applications have been developed. Progress at first was slow due to the unreliability of the equipment and the learning curve of industry, held further back by the James Bond film "Goldfinger" showing Bond being threatened with a laser while strapped to a conveyor belt. This image caught the imagination of the trade unions, preventing some applications from even being tried. Those days are now long past and the laser is an enabler for many growth industries.

Commercial implementation of the laser went through distinct phases. It started with the over-quoted aphorism, "The laser is a solution looking for a problem," which was the case for many years. The early adopters were typically highly qualified laser scientists and engineers who were the only ones capable of keeping those machines functioning. Applications were those that could not be achieved using conventional technologies, or small batch productions such as wooden die board cutting for the packaging industry, drilling holes in cigarette paper, or welding aluminum spacer bars for double-glazed window assemblies. There was no attempt to use the laser as a

competitive technology, so it was therefore necessary to develop new niche applications. The 1980s and 1990s witnessed the push of technology from laser providers as they increased power, improved reliability, and offered new tools to industry. This period saw the creep of laser implementation into mainstream manufacturing such as car production with sheet cutting and laser-welded tailored blanks. The authors still know Tier 1 automotive suppliers scarred by their experience during this time who resist all possible laser implementation as a result of production problems. With the advent of the diffusion cooled CO_2 laser or the DPSS YAG high power laser technology (Diode Pumped Solid State), a point was reached when it could be considered as a mature and reliable technology for many industries. It was then that the dynamics changed and industrialists started to make demands of the laser manufacturer: more power, higher beam quality, more pulsing parameters. The laser became the limiting factor—more power was needed! Then in the 2000s the disc laser, and particularly the fiber laser, arrived with reduced optical alignment problems, a small footprint, high power, and superb beam quality. Many of the previous laser implementation problems were no more as we finally had industrially viable tools.

In 1963, Elias Snitzer [16] invented the fibre laser, just a few years after the invention of the original laser in 1960. Snitzer demonstrated gains of 5×10^4 in 1 m long Nd doped amplifiers. During the 1970s and 1980s a range of doping, pulsing, pumping options, and mode-control techniques were developed, driven by the needs of the optical communication industry for fiber amplifiers. However, powers were still well below a Watt, Wyatt [17] boasting 270 mW from a 540 mW pump in 1989. The 1990s were a race for power between the likes of Polaroid, Spectra Diode Labs, and IPG Photonics, who brought a 100W laser to the market in 2000. The immense cost of these lasers could have stifled the speed of development, but the burst of the dot-com bubble in 2001 lead to a surplus of telecommunications technology, which had relied on fiber laser amplifiers. An industry that had hundreds of millions of pounds in investment to develop laser systems that were highly focused on reliability, and with a readymade supply chain for many kWs of photons, found it had no market to supply. The rest, as they say, is history. The surplus capacity coupled with a need in the industrial sector resulted in the rapid technical and cost reductions that we, the industrial laser user, can benefit from today in both diode and fiber laser sources.

Where does this leave us now? We have had a breakthrough in equipment cost, size, and maintenance that gives almost unlimited optical energy. We also have imaginative and striving industries with laser experience

wishing to optimize their processes and develop novel applications such as those suggested below. This is the description of a launching pad for a spurt in manufacturing technology, of which we are at the threshold.

1.2 ECONOMIC IMPACT OF LASER MATERIALS PROCESSING

It was the original intention of the authors to look at the current state of the laser materials processing industry and its effect upon the global economy. Analysis of the primary, secondary and tertiary global GDP markets would at first glance seem to offer some way to begin to identify the amount of the nearly $74 trillion (2015) [18] underpinned by laser-based manufacturing. Our initial strategy was to break down the areas of application into significant subdomains: transport, energy generation, defense, consumer goods, marking, packaging, semiconductors, etc. Once listed, the problem presents itself: lasers are used throughout the manufacturing chain, so where do you draw the line? Virtually every product currently manufactured benefits in at least one part of its manufacturing cycle from the use of a laser-based process. Consider semiconductor manufacturing, where lasers are used to generate UV, drill via holes, mark both ICs and wire, temper and anneal and weld and trim components. How can this fiscal value be assessed? What is the contribution to the world electronics market? Remove the laser and the chain collapses.

It is simpler to look directly at the market for laser material processing equipment, which can be divided into two distinct areas: laser sales and laser systems. In 2015, typical estimations for laser sales were $3.2 billion while laser systems were $11.8 billion [19]. One key feature in the future of this market is the move from Europe to the Far East. Over the last couple of years China has become the largest consumer of laser systems [20], and perhaps more worrying for the European machine suppliers is that they are losing market share. In China during 2016, Trumpf's sales declined while IPG grew by 4%. In comparison, Han's Laser had the same turnover as Trumpf and IPG combined, coupled with nearly 23% growth [20] as well as with aggressive international acquisition to broaden its geographic impact [21].

In this vast and growing market the conclusion has to be that the laser industry is now a strategic part of global manufacturing. Many products, such as stents, simply could not exist without the laser. The laser is rapidly on the way to being integrated within factories in the same way as electricity. Unlike electricity, optical energy cannot be stored and "pulled" on demand meaning the concept of a plug on the wall as part of a distributed

optic feed, an energy source for many applications, is not possible in the same way. What is possible and is already here are lasers with internal beam sharing and switching capabilities. It is the authors' opinion that this is a solution that will only ever be installed in a few large manufacturing environments, such as one very high-power laser supplying multiple welding stations for automotive fabrication. Process sensitivity and miniaturization makes it more likely that an optimized low-cost laser will be manufactured for specific applications (There is some similarity here with the growth of computers from mainframe to PCs).

1.3 THE DEVELOPING APPLICATION SPACE

1.3.1 Driving Forces

How is cost assessed? The original metrics for laser selection were cost/Watt (at purchase) and running costs, namely wall plug efficiency (including chilling costs) and gas consumption (if appropriate). With the advent of the fiber laser this was superseded by a more complex calculation, the cost of ownership, which considered the lifetime costs of the system (e.g., maintenance and floor space). Common to both of these is the concept of cost per photon while ignoring the efficiency of the process. Most industrial laser users will attest that their lasers are run at only a small percentage of their full capability when working on a dedicated application. In glass processing, for example, picosecond laser pulses are often used to scribe the surface or to create various structures inside the bulk material. However, to prevent a build-up of thermal effects the systems are run at low repetition rates with significantly reduced pulse energy. This is directly in opposition to modern industrial laser design, which is consistently striving for ever-higher peak/average power and higher rep rates. That invariably manifests itself as increased capital cost. The massive productivity gains that can be achieved by moving to more optimized laser parameters demand that application be considered within the calculation. As an example consider laser cutting of mild steel, taking a simplistic approach looking at the Fresnel absorption of iron normal to the surface moving from $C0_2$ 10.6 μm infra-red to fiber (≈1 μm) to blue (≈0.45 μm). The absorption changes from <5%, 30%, to ≈50% [22]. The second principal component, plasma absorption, will limit the amount and quality of the incident energy utilized, again favoring shorter wavelengths [23].

The industrial user demands minimum capital cost, running costs and, perhaps most importantly, low energy consumption. In order for this to be achieved, a shift to process-specific tailored laser sources, optimized for

specific applications, is needed. This is possible through an in-depth understanding of the process, through a shift towards a material-centric approach to process design. The days of buying the most expensive high-power laser you can afford and seeing what it can do are over. Direct diodes, high power ultrafast lasers, and further developments of the fiber laser will lead the source developments for the next 10 years.

1.3.2 Application Trends

The standard laser processes of basic cutting, welding and drilling in established areas like the welding of tailored blanks in the automotive industry, or turbine blade drilling, are now part of a mature and ruthlessly competitive market. While these are substantial commercial applications, they are now mainstream enough to be in the realm of in-house industrial development rather than academic research (the one major exception being the comparatively poor performance of fiber lasers to CO_2 in thick section cutting). These established applications have international commercial vendors vying for business, where reliability or support is frequently the deciding factor for a sale as opposed to performance.

Manufacturing developments are driven by a range of forces, most noticeably the development of new products, reduction in cost, and/or reduced energy consumption. Examples include laser annealing of dopants in CMOS circuitry, trimming Gorilla glass and sapphire for portable device screens security marking, and LIFT (Laser-Induced Forward Transfer) for plastic electronics fabrication. Additionally conformation with legislation, such as the cost of disposal, makes processes like laser cladding economically viable for applications such as both increasing tool life and repair.

New applications are being continually developed or refined to be robust enough for industry. Metal-based laser additive manufacturing is one of the obvious examples of a technology on the brink of mainstream implementation. This process took an unusual route for development. After the initial proof of concept in the 1980s [24], at which time the technology was being hailed in the press as a replacement for all other manufacturing processes, it has taken significant investment in machinery and instrumentation to get the process reliable enough for more widespread application. What is unusual is that the primary driving force behind the development of the technology has been the medical sector for dental [25] and implant [26] components. Typically, aerospace and medical companies are the ones least likely to drive a process. Both academic and commercial research will undoubtedly be looking to reduce the cost of this technology and broaden the implementation space, such as replacing the laser with laser

diodes as the energy source [27], a solution in which technology is finally catching up. One surprise for most observers, considering how the drive for research has been focused on metals, is that metals represent <2% of the estimated $600 million of materials supplied in 2017 for additive manufacturing processes [28].

The processing of plastic, transparent, or brittle materials is becoming more industrially relevant as the consumer electronics market continues to grow. Touchscreens on smart phones, tablets, and e-readers are examples of products that require both cutting and welding. Initially this was approached by the addition of absorbing lower layers or additives [29] to the interface. More recent developments are specialised lasers, including Spectra physics ClearShape [30] (Fig. 1.3) for glass and 2 μm sources with high absorption in plastics for clear-to-clear welding. Plastic applications are particularly relevant to the medical industry where polymers like PET have a heavy usage. The lack of additional chemicals in the join makes biocompatibility testing considerably simpler.

Oil drilling and exploration is one of the few industries still craving an increase in laser power. One of the earliest proposals for the use of high-power lasers was mining in the 1960s, but it was not until the arrival of the high-power fiber laser that any real consideration could be given to its application. Foro Energy used the laser to heat and soften the rock before mechanical drilling, thus reducing the tool wear and increasing the rate of material removal [31]. That is particularly impressive given that the laser has to be operated in such a hostile environment and propagate past opaque mud!

Aerospace still continues to be a challenge for the laser industry due to that community's resistance to change, where they typically only embrace a technology when there is no alternative, e.g., laser turbine drilling. Headline applications include welding or surface treatments but the unsung applications are in the wiring/electronics of an airliner. All wire has to be identifiable every 3 in. (7.6 cm) (SAE AS50881) and be

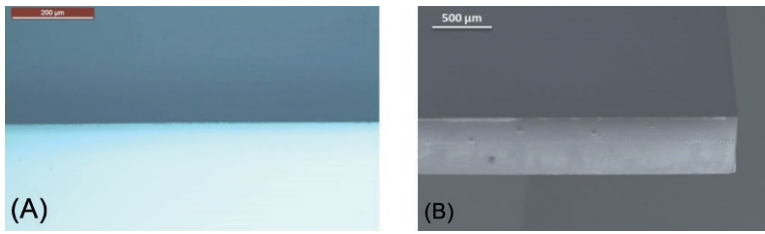


Fig. 1.3 Laser-cut glass suitable for smart device applications. Straight line cut in chemicaly strengthened glass with ClearShape process. (A) Top view. (B) Edge view.

robust enough to withstand mechanical and chemical abuse. Couple this with laser wire stripping and that is a lot of laser processes in one commercial plane. For example, a brief Internet search typically quotes a 747 as having 171 miles of wiring and 3.6 million laser marks. Paint removal is a commercially available application [32] with surprising economic benefits. The weight of paint on a fully painted 747 is 251.7 kg, which represented an increase of up to $138,000 in annual operating costs based on 1998 fuel costs [33].

Direct application of laser technology in medicine was reported as early as 1961 [34], though such uses admittedly caused damage to eye tissue. Low-intensity dermal applications can be used for hair, tattoo, wrinkle, and strawberry birthmark removal. Higher intensities are used for surgery and a range of therapies. One of the most advanced applications of the laser is refractive eye surgery in ophthalmology, which includes a number of forms [35]. The most common are PRK (Photo Refractive Keratectomy) and LASIK (Laser-Assisted In-Situ Keratomileusis) with the recently developed ultrafast process of LIRIC (Laser-Induced Refractive Index Change) [36,37] (Fig. 1.4) offering the potential for repeat procedures. In 2014 it was estimated that just in the United States, nearly 1 million people underwent this type of surgery [38]. It is always interesting to see the high proportion of laser academics and workers wearing glasses. Do we consider the risks differently? Further biological applications are numerous and include surgery with self-cauterization in prostate treatment, urology, and endoscopic micro-surgery: cardiology; orthopedics, as in machining and smoothing of cartilage by photothermolysis; dentistry; photodynamic therapies using optically switchable

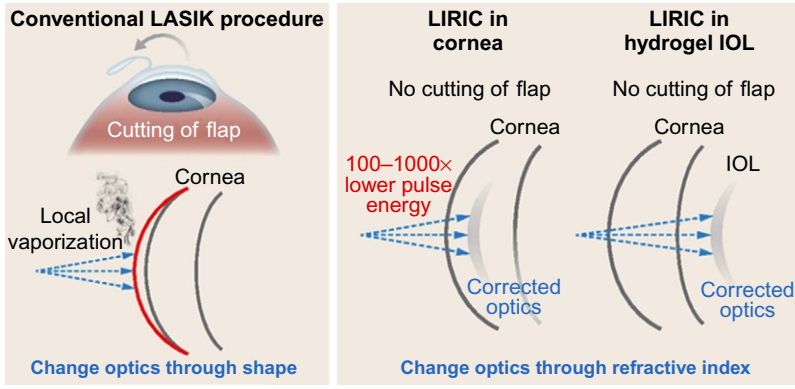


Fig. 1.4 LIRIC eye surgery, minimally invasive and repeatable unlike LASIK.

drugs; biostimulation for arthritis and rheumatism; tissue welding by enhanced healing rates; and diagnostics through fluorescence, spectroscopy and endoscopic viewing.

Laser based surface/material modification is an area gaining real traction. Surface treatment applications have developed over an expanding technological landscape including precision bending with no spring back, cleaning, annealing, transformation hardening with reduced distortion, surface alloying and melting for improved wear or corrosion properties, and laser peening and texturing, the latter two processes taking the place of traditional shot blasting or chemical etching. The latest trend is towards nanotechnology and the creation of laser-induced periodic surface structures (LIPSS) of sub 100 nm on metals, plastics and/or silicon. Potential applications are enhanced light absorption in silicon [39], self-cleaning materials [40], and biomaterials [41]. Ultrafast laser technology ($\approx 10^{-14}$ s pulses) is also being looked at for the healing and addition of defects in single-walled carbon nanotubes [42] and to trim and add functionalization to graphene [43,44].

The mention of lasers within the military is almost a taboo subject, despite being mentioned in article 1 of protocol IV of the Geneva Convention (1995 and agreed to by 107 states in 2016):

> *It is prohibited to employ laser weapons specifically designed, as their sole combat function or as one of their combat functions, to cause permanent blindness to unenhanced vision, that is to the naked eye or to the eye with corrective eyesight devices.*

High-power laser programs have looked at missile (ADAM) and satellite (MIRACL) destruction, mine clearance (ZEUS-HLONS), and drone and boat protection (LAWS). Low-power applications include temporary blindness (PHaSR), targeting, and imaging. The irony for laser weapons is that with modern warfare being more information-based, we now have low-speed unmanned drones that would be prime targets for the science-fiction laser gun. Why does this have a position within a book on materials processing? Simple. Significant developments can only be funded through the military. Just refer back to the levels of fiber-laser funding through the Defence Advanced Research Projects Agency (DARPA). Looking at the equipment being funded for the military now will give an indication of what is to come in industry. It should be remembered that it was defense needs that drove the original invention of the laser.

With the continuing reduction in source [cost/performance] and the rise in quality, reliability, control, and safety, it is not a great leap to suspect

that machining systems will continue the move to the user and away from outsourced services. As examples, low-cost desktop laser cutting systems are now below £500 [45] while welding [46] systems (which are still lagging in terms of hobby penetration) will continue to gain functionality and market penetration. Additive manufacturing systems with many "bedroom" offerings will make the move towards metal. The recent announcement of a <€20,000 metal SLM (Selective Laser Melting) system [47] demonstrates a common movement towards lower costs.

1.3.3 Source Development and Deployment

1.3.3.1 The Technology

There are two facets to the evolution of the processing laser: making the perfect optical source for a given application, and then delivering this to the workpiece. Considering source developments, there is an ever-increasing range of laser wavelengths, mode shapes, and pulse profiles that give the industrial user many opportunities for optimization. Why is this important? From a historical point of view lasers of sufficient power were limited to a choice of two wavelengths (10.6 μm or 1.06 μm) and there was little the operator could do to optimize the process except tweak power focal position and speed. A much wider range of high power wavelengths have become available. For example if you were to look for a 500W source today considering only a single supplier, IPG Photonics, you would additionally have solid state lasers ranging from ≈400 to 900 nm, fiber lasers 532 nm, 1.07 μm, 1.1 μm tuneable to 1.8 and 1.9 μm. Each of these would provide different options for material absorption and plasma transmission. An additional feature, pulsing, has become significantly more flexible and its benefits more understood over recent years. Coupled with pulse shaping (from ≈5 kHz for modulated multi-kilowatt lasers to extremely fast (GHz) with structure within each pulse), new light-matter interactions can be achieved. One of the initial processes that benefited from pulse shape control was lap welding of zinc-coated steel. By tuning pulse profiles, zinc could be vaporized before the melting steel caused an explosive vaporization that would spoil the weld. This leads into the new processing area that uses multiple laser beams simultaneously or in sequence. The idea was mooted in 1987 for stabilizing the keyhole during welding but it was a clumsy arrangement [48]. Fiber delivery overcomes the problem of inserting multiple beams and allows the possibility of a single cable with multi-fiber content for cleaning just prior to brazing or welding all in one process pass [49]. The removal of protective films of either zinc or Al/Si by laser ablation just prior to processing is a

radical innovation. Another example of multibeam processing is a UV pulse prior to heating with infrared that will greatly reduce reflectivity problems during laser surface heat treatment. This area of multibeam/wavelength processing has hardly been investigated yet since it only makes sense to try with the availability of reliable small lasers (Fig. 1.5).

Another level of understanding comes when one looks at materials performance dynamically during processing. For example, who would have predicted high-speed plasma-assisted cutting [50] (where a reliable plasma-assisted coupling mechanism increases cutting speeds by up to 40%) that starts at speeds above those where conventional cutting has failed? Or Si drilling using 1 μm lasers [51]—virtually a transparent material at this wavelength—until the Si becomes heated? The challenge for the optimum selection of equipment for the industrial user is daunting.

With laser design striving towards higher peak power, shorter pulses, and shorter wavelengths, there is a growing problem with transmission within glass or other fiber materials. Photonic bandgap fibers and photonic crystal fibers (fibers with special cladding such as a Bragg reflector or bubbles; the core may be an empty hole) look to be promising technologies that may soon permit not only the delivery of the laser energy, but also the potential for optimization such as pulse compression control [52] and hybrid lasers where wavelength conversion in sealed "gas tubes" within the fiber allow a new range of wavelengths [53].

Processing heads are also evolving, as Trumpf and Amada both have integrated systems for beam size control to optimize laser cutting parameters for different thickness sheets. The next generation may see something like the tuneable acoustic gradient lenses [54] offering high-speed focal shift also being implemented. Optics are continually being developed with ever-higher damage thresholds. Typically this is a coating evolution but other options are being found. In one example surface-structured optics

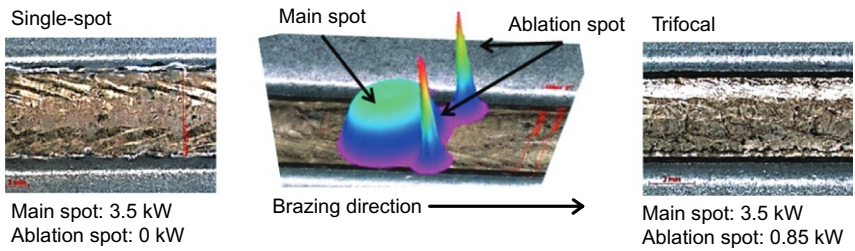


Fig. 1.5 Multiple spot laser brazing.

based upon the moth's eye are being used as an anti-reflection coating on CO_2 laser optics [55]. If this proves successful it will likely be a precursor to a revolution in thinking about optical coatings. Are we moving towards the dismissal of the diffractive limit? The superlens has been demonstrated for a range of wavelengths [56] but not yet for the principal laser wavelengths or powers.

Safety has always been a significant challenge for the introduction and acceptance of laser-based processes. In fact, fear of the technology has been reduced as exposure to laser technologies becomes commonplace. Containment became a bigger issue as fiber laser power levels increased. No longer was a passive metal or concrete wall adequate protection; active monitoring [57] was required. The next significant safety drive for laser materials processing will be lasers in the "eye safe" regions, 1.4–1.8 μm. At these wavelengths the laser is absorbed by the water in the eye, preventing retinal damage, and not strongly absorbed in the cornea (as is the case for the CO_2 laser). It should be noted that the maximum permissible exposure limit still only increased by an order of magnitude for a high rep/CW laser due to heat dissipation limits within the eye. Regardless of wavelength, multiwatt laser beams must be kept away from the eye. There is no "eye-safe" wavelength with multiwatt beams!

1.3.3.2 In-Process Analysis and Control

For many applications, such as precision milling, it would be inconceivable that the system would operate without integrated measurement of the tools to compensate for wear. Industrial laser processing is still at a level that lacks even basic measurements, as a matter of course, for nearly all implementations. How many systems come with integrated measurement of the laser (beam position, diameter, power at the workpiece and spot size)? Let alone measurement of the process! As noted at the beginning of this article, one of the advantages of laser processing is the comparative openness to in-process inspection and analysis. That leads to a potential for automation and intelligent control that will be essential in transferring laboratory science in controlled conditions to real-world applications. It is amazing the number of times the authors have been asked to advise on manufacturing problems only to find out that the equipment supplier had actively prevented the machine operator from determining machine parameters, frequently even keeping the name of the laser manufacturer a secret. It is hoped that books like this will educate the operator to a level where the correct questions are asked.

Fundamentally we still lack real understanding of light–matter interaction in an industrial context. We ensure process stability by keeping within conservative process parameters. Without control we must purchase expensive uniform materials, like laser steel, or live in blissful ignorance and hope that all will be well. In the first instance (ideally in real time), we need quantitative analysis tools that can look at the material interaction at high speed and, through such understanding, offer optimization systems. Considering the fact that just one analysis tool, the high speed holographic camera [58], has been used to observe the timescales of various ejection mechanisms and their relative contributions to the ablation process. Results generated have been used to optimize energy coupling for complex temporal beam profiles, increasing efficiency and quality [59]. As more tools are developed our understanding will progress and processes will become more efficient.

Industrial systems are being developed, but are now far behind their needs. As an example, one of the early applications for monitoring and control was an independent camera seam-tracking system for getting the laser to the correct location, and spectroscopic analysis for later quality assurance. These are being improved and integrated to make more robust systems. One of these is the Weldeye [60], which integrates precision optical coherence tomography (OCT) for part position and in-line weld monitoring by measuring depth/weld development, giving "real time" information to facilitate repair before leaving the tool. It will not be long before computing processing power permits real-time control. Machine Vision Control (MVC) by RAYLASE is a combined camera, scanning unit, and laser beam delivery optics that can inspect a part, identify its type, and accurately position the laser for processing and subsequent inspection and documentation [61].

One industry already looking carefully at the implementation of active quality assurance is additive manufacturing of biomedical devices. For example, Concept Laser has systems that monitor the melt pool size and intensity during manufacturing, then produce 3D tomographic data of the part highlighting potential manufacturing defects. Active control of the process is as yet unreported.

Addition of feedback control and quality assurance systems is continuing to make unstable/precision applications viable and could be a singular advantage to laser processing, differentiating it within the manufacturing process market. There will be a range of directions needed to continue this disruptive push into both established and new markets.

1.4 FUTURE PREDICTIONS

1.4.1 Previous Reflections

The growing importance of optical energy in manufacturing and technology development is such that there will be a demand by students to be able to study optical engineering in the same way that they do electrical or mechanical engineering. This review has only touched upon the huge engineering area opened by the application of this new form of industrial energy. More universities will respond to this need by having dedicated departments for optical engineering or photonics.

In the previous edition we predicted:

> *Handheld laser tools with short focal lengths, for safety reasons, will feed into the craft industry. Such equipment would remove much of the time consuming work in programming CNC equipment when only one or two pieces are to be made.*

Handheld systems exist within industry for marking [62] and paint removal [63]. In cutting, low-power versions have yet to be implemented due to safety constraints, though perversely multi-kilowatt units have been made for specialist application [64]. There are now many desktop systems being offered with low-power lasers for cutting and engraving (principally CO_2, with basic systems approaching ≈£1000). Complete 20W fiber-laser based galvanometer marking systems can now be purchased for £3000!

> *Powerful lasers will be used for deep penetration welding as in ship building, boiler making and pipelines, etc. This process is likely to be a hybrid laser/arc process which will ensure a wider weld pool and hence fewer problems with alignment with the joint line.*

Despite being in European shipyards since 2000, and offering significant improvements over welding or laser-only based processes, the process seems still to be implemented in few key areas. As a technology it is still under the radar for many users, perhaps due to the limited application of thick section welding in most industries. A close cousin, hybrid laser brazing, where resistance is used in place of the arc, operates at speeds >5 m/min and is implemented in the automotive industry in areas that are painted, e.g. roof ditch welds.

> *Micro-nano manufacturing based on ultrafast lasers and powerful femto second pulses will create many ultra small devices for medical and control purposes, slowly simulating our way towards what nature has been doing all along. Glass computers and 'laboratories on chips' are attractive goals which are attracting considerable research interest at present.*

Perhaps it was a little optimistic, expecting a glass computer to be here so soon, but optical interconnects are becoming ever more commonplace, pushing the maximum data communication speeds while reducing power consumption. One estimate of the optical interconnect market expects an increase from its 2015 value of $3.66 billion to $10.03 billion by 2022 [65].

1.4.2 Coming Soon?

In the research domain, advances in fiber laser design mean that it is now possible to deliver almost any beam profile while also being widely tuneable in the temporal, polarization, and wavelength domains. This tool will drive our understanding of fundamental process interactions, paving the way for tailored, low-cost application specific sources.

For industry the switch from subtractive to additive processing will cause significant disruption to established manufacturing processes and design procedures. In the same way as has already happened to plastic-based additive manufacturing, there will be a concerted push to higher resolution, low-cost metal-based manufacture driven amongst other solutions by the further development of direct diode systems. This will continue to service the high-end medical consumers, offering cost reduction and creating a new market for less-premium products.

Moving further into the future, extreme high-power lasers offer the potential of a controllable heat source for chemical refineries where currently massive heaters are used to heat not only the process but all of the surrounding metal and refractories. If this could be taken further, UV irradiation of polymers can be used to break them down into their elements, and could then be recombined into another structure, marking the start of chemical additive manufacturing technology.

The application of lasers has so far focused on the processing of materials through thermal energy generation for cutting, welding, machining, and surface structuring; all techniques commonly employed in manufacturing industries. With materials being the highest cost of most manufacturing operations, and the promise of higher laser powers at greater efficiencies, how soon will it be before we see lasers being used to reverse the manufacturing process by disassembling products and materials back to their constituent components for the recycling of costly micro gadgets? Localized energy generation and improved additive manufacturing could offer a new vision of local cradle-to-cradle manufacturing that is more economic than transportation from globalized factories.

The laser is set to play a major role in ever more obscure areas of our lives and industry. As a final pause for thought, Boeing has patented a range of laser-based jet engine concepts, one being laser detonation of radioactive material such as deuterium to generate a thermonuclear explosion. How keen would you be to get on that plane [66]?

REFERENCES

[1] W. Steen, J. Mazumder, Laser Material Processing, fourth ed., Springer, London, 2010 558 pages.
[2] M. Duocastella, C.B. Arnold, Bessel and annular beams for materials processing, Laser Photonics Rev. 6 (5) (2012) 607–621.
[3] S. Hasegawa, Y. Hayasaki, N. Nishida, Holographic femtosecond laser processing with multiplexed phase Fresnel lenses, Opt. Lett. 31 (11) (2006) 1705–1707.
[4] V. Niziev, A. Nesterov, Influence of beam polarization on laser cutting efficiency, J. Phys. D Appl. Phys. 32 (13) (1999) 1455.
[5] F. McClung, R. Hellwarth, Giant optical pulsations from ruby, J. Appl. Phys. 33 (3) (1962) 828–829.
[6] M. Göppert-Mayer, Über elementarakte mit zwei quantensprüngen, Ann. Phys. 401 (3) (1931) 273–294.
[7] W. Kaiser, C.G. Garrett, Two-photon excitation in CaF2: Eu2+, Phys. Rev. Lett. 7 (1961) 229–231.
[8] K.C. Phillips, H.H. Gandhi, E. Mazur, S. Sundaram, Ultrafast laser processing of materials: a review, Adv. Opt. Photonics 7 (4) (2015) 684–712.
[9] S. Maruo, S. Kawata, Two-photon-absorbed near-infrared photopolymerization for three-dimensional microfabrication, J. Microelectromech. Syst. 7 (4) (1998) 411–415.
[10] Technology—Nanoscribe GmbH [Internet]. 2016 [cited 2016 Dec 19]. Available from: http://www.nanoscribe.de/en/technology/.
[11] International Energy Outlook 2016 [Internet]. U.S. Energy Information Administration; 2016 May. Report No.: DOE/EIA-0484. Available from: http://www.eia.gov/outlooks/ieo/pdf/0484(2016).pdf.
[12] P. French, D. Hand, C. Peters, G. Shannon, P. Byrd, W. Steen, Investigation of the Nd: YAG laser percussion drilling process using high speed filming, in: ICALEO'98 Proceedings LIA, Orlando, FL, 1998, pp. 1–10.
[13] K. Pangovski, Temporal Pulse Design and Analysis of Silicon Ablation Using Advanced Pulse Shaping and Digital Holography in the Nanosecond Domain. PhD Thesis. The University of Cambridge, Cambridge, 2014.
[14] K. Pangovski, M. Sparkes, W. O'Neill, A holographic method for optimisation of laser-based production processes, Adv. Opt. Technol. 5 (2) (2016) 177–186.
[15] T.R. Schibli, K. Minoshima, Y. Bitou, F.-L. Hong, H. Inaba, A. Onae, et al., Displacement metrology with sub-pm resolution in air based on a fs-comb wavelength synthesizer, Opt. Express 14 (13) (2006) 5984–5993.
[16] C.J. Koester, E. Snitzer, Amplification in a fiber laser, Appl. Opt. 3 (10) (1964) 1182–1186.
[17] R. Wyatt, High-power broadly tunable erbium-doped silica fibre laser, Electron. Lett. 25 (1989) 1498.
[18] Gross Domestic Product 2015. World Bank; 2016 Dec p. 4.
[19] Global Demand for Industrial Lasers Reaches $3.2 Billion [Internet]. Optech Consulting; 2016 Mar [cited 2016 Dec 21]. Available from: http://www.optech-consulting.com/html/latest_press_release.html.

[20] Mayer A. China surpasses Europe as largest laser systems consumer [Internet]. Laser Systems Europe. 2016 [cited 2016 Dec 22]. Available from: http://www.lasersystemseurope.com/news/story/chinese-laser-firms-outperform-european-and-us-brands-china.
[21] Chinese laser giant Han's Laser acquires fibre specialist CorActive High-Tech | Laser Systems Europe [Internet]. CorActive High-Tech. 2016 [cited 2016 Dec 22]. Available from: http://www.lasersystemseurope.com/news/story/chinese-laser-giant-hans-laser-acquires-fibre-specialist-coractive-high-tech.
[22] D. Schuöcker, Handbook of the Eurolaser Academy, vol. 2, Chapman & Hall, London, 1998.
[23] J. Greses, P. Hilton, C. Barlow, W. Steen, Plume attenuation under high power Nd: yttritium–aluminum–garnet laser welding, J. Laser Appl. 16 (1) (2004) 9–15.
[24] Deckard CR. Method and apparatus for producing parts by selective sintering [Internet]. Google Patents; 1989. Available from: https://www.google.com/patents/US4863538.
[25] A. Dawood, B.M. Marti, V. Sauret-Jackson, A. Darwood, 3D printing in dentistry, Br. Dent. J. 219 (11) (2015) 521–529.
[26] B. Berman, 3-D printing: the new industrial revolution, Bus. Horiz. 55 (2) (2012) 155–162.
[27] L. Li, K.L. Ng, A. Slocombe, Diode laser sintering of compacted metallic powders for desktop rapid prototyping, in: Proceedings of the 7th European Conference on Rapid Prototyping and Manufacturing, Aachen, 1998, pp. 281–296.
[28] R. Gordon, J. Harrop, 3D Printing Materials 2016-2026: Status, Opportunities, Market Forecasts, IDTechEx, 2016. Market Research Company: http://www.idtechex.com/.
[29] Jones IA, Wise RJ. Welding method [Internet]. Google Patents; 2003. Available from: https://www.google.com/patents/EP1117502B1?cl=en.
[30] J. Bovatsek, R. Patel, Method and Apparatus for Laser Cutting Transparent and Semitransparent Substrates, WO Patent: 2014121261, International Application No.: PCT/US2014/014620, 2014.
[31] M. Zediker, High-power fiber lasers for geothermal, oil, and gas industries, in: SPIE, 2014Available from: http://spie.org/newsroom/5288-high-power-fiber-lasers-for-geothermal-oil-and-gas-industries.
[32] The Products | LCR [Internet]. [cited 2016 Dec 20]. Available from: http://www.mowarped.com/lcr/the-products/.
[33] Painting versus Polishing of Airplane Exterior Surfaces [Internet]. Boeing; 1999 Q1. (Aero). Report No.: 5. Available from: http://www.boeing.com/commercial/aeromagazine/aero_05/textonly/fo01txt.html.
[34] M.M. Zaret, G.M. Breinin, H. Schmidt, H. Ripps, I.M. Siegel, L.R. Solon, Ocular lesions produced by an optical maser (laser), Science 134 (3489) (1961) 1525–1526.
[35] T. Sakimoto, M.I. Rosenblatt, D.T. Azar, Laser eye surgery for refractive errors, Lancet 367 (9520) (2006) 1432–1447.
[36] Zheleznyak L. Ophthalmology/Femtosecond Lasers: LIRIC: Next-generation refractive laser surgery [Internet]. Bioptics World. 2016 [cited 2016 Dec 22]. Available from: http://www.bioopticsworld.com/articles/print/volume-9/issue-11/ophthalmology-femtosecond-lasers-liric-next-generation-refractive-laser-surgery.html.
[37] D.E. Savage, D.R. Brooks, M. DeMagistris, L. Xu, S. MacRae, J.D. Ellis, et al., First demonstration of ocular refractive change using blue-IRIS in live cats, Invest. Ophthalmol. Vis. Sci. 55 (7) (2014) 4603–4612.
[38] T.A. Pasquali, D. Smadja, M.J. Savetsky, G.H.R. Mello, F. Alkhawaldeh, R.R. Krueger, Long-term follow-up after laser vision correction in physicians: quality of life and patient satisfaction, J Cataract Refract Surg 40 (3) (2014) 395–402.
[39] A. Vorobyev, C. Guo, Direct creation of black silicon using femtosecond laser pulses, Appl. Surf. Sci. 257 (16) (2011) 7291–7294.
[40] M. Barberoglou, V. Zorba, E. Stratakis, E. Spanakis, P. Tzanetakis, S.H. Anastasiadis, et al., Bio-inspired water repellent surfaces produced by ultrafast laser structuring of silicon, Appl. Surf. Sci. 255 (10) (2009) 5425–5429.

[41] R. Vilar (Ed.), Laser Surface Modification of Biomaterials: Techniques and Applications, 1st edition, Woodhead Publishing, Sawston, United Kingdom, 2016.
[42] A.H. Romero, M.E. Garcia, F. Valencia, H. Terrones, M. Terrones, H.O. Jeschke, Femtosecond laser nanosurgery of defects in carbon nanotubes, Nano Lett. 5 (7) (2005) 1361–1365.
[43] I. Bobrinetskiy, A. Emelianov, N. Otero, P. Romero, Patterned graphene ablation and two-photon functionalization by picosecond laser pulses in ambient conditions, Appl. Phys. Lett. 107 (4) (2015) 43104.
[44] H. Liu, S. Ryu, Z. Chen, M.L. Steigerwald, C. Nuckolls, L.E. Brus, Photochemical reactivity of graphene, J. Am. Chem. Soc. 131 (47) (2009) 17099–17101.
[45] Desktop Laser cutter & engraver—'FABOOL Laser Mini' [Internet]. [cited 2016 Dec 21]. Available from: http://www.smartdiys.cc/fabool-laser-mini/.
[46] Desktop Manual Welding Laser, Tabletop Laser Welding System [Internet]. [cited 2016 Dec 21]. Available from: https://www.rofin.com/en/products/systems-and-solutions/manual-welding-lasers/desktop/.
[47] Low-cost SLM unit with production costs below 20,000 euros [Internet]. Fraunhofer Institute For Laser Technology ILT; 2016 Nov p. 3. Available from: http://www.ilt.fraunhofer.de/content/dam/ilt/en/documents/Publication-and-Press/press_release/pr2016/PR_Low_Cost_SLM_System_formnext_2016.pdf.
[48] Y. Arata, Challenge of laser advanced material processing, in: Proc. LAMP'87 Conf., Osaka, High Temperature Society of Japan, 1987, pp. 3–11.
[49] M. Thompson, A. Gusenko, M. Grupp, T. Strite, T. Hoult, Improving materials processing with static beam forming, The Laser User 82 (Autumn) (2016) 24–25.
[50] Cutting with light. In: Fascination of sheet metal [Internet]. Trumpf; p. 72–3. Available from: http://www.trumpf.com/fileadmin/DAM/trumpf.com/Innovation/Fascination-of-SheetMetal_Chapter4.pdf.
[51] W. O'Neill, K. Li, High-quality micromachining of silicon at 1064 nm using a high-brightness MOPA-based 20-W Yb fiber laser, IEEE J. Sel. Top. Quantum Electron. 15 (2) (2009) 462–470.
[52] J. Limpert, T. Schreiber, S. Nolte, H. Zellmer, A. Tünnermann, All fiber chirped-pulse amplification system based on compression in air-guiding photonic bandgap fiber, Opt. Express 11 (24) (2003) 3332–3337.
[53] M.R.A. Hassan, F. Yu, W.J. Wadsworth, J.C. Knight, Cavity-based mid-IR fiber gas laser pumped by a diode laser, Optica 3 (3) (2016) 218–221.
[54] J. Yan, A. Mermillod-Blondin, E. McLeod, C.B. Arnold, Rapidly tunable acoustic gradient index lenses for pulsed imaging and laser processing, in: Conference on Lasers and Electro-Optics/International Quantum Electronics Conference [Internet], Optical Society of America, 2009, p. CFI4. Available from: http://www.osapublishing.org/abstract.cfm?URI=CLEO-2009-CFI4, .
[55] Twitchen D, Bennett AM, Anoikin YV, DeWit HGM. Synthetic diamond optical elements [Internet]. US20160003981 A1, 2016. Available from: https://www.google.com/patents/US20160003981.
[56] X. Zhang, Z. Liu, Superlenses to overcome the diffraction limit, Nat. Mater. 7 (6) (2008) 435–441.
[57] Ward S. Active laser guarding system [Internet]. US8416820 B1, 2013. Available from: https://www.google.co.uk/patents/US8416820.
[58] E. Amer, P. Gren, A.F.H. Kaplan, M. Sjödahl, M. El Shaer, Comparison of the laser ablation process on Zn and Ti using pulsed digital holographic interferometry, Appl. Surf. Sci. 256 (14) (2010) 4633–4641.
[59] K. Pangovski, M. Sparkes, A. Cockburn, W. O'Neill, P.S. Teh, D. Lin, et al., Control of material transport through pulse shape manipulation—a development toward designer pulses, IEEE J. Sel. Top. Quantum Electron. 20 (5) (2014) 51–63.
[60] Process visualization and monitoring for laser remote welding [Internet]. [cited 2016 Dec 19]. Available from: http://www.lessmueller.de/en/products/weldeye.

[61] W. Lehmann, Laser + Camera = Innovation, The Industrial Laser User 82 (Autumn) (2016) 28–29.
[62] Handheld Fiber Laser Marking System [Internet]. [cited 2016 Dec 19]. Available from: http://www.fonon.us/fiber-laser-marking-system/handheld-fiber-laser-marking-system/.
[63] Low Power CL 20 portable Backpack-Laser with handheld optic-cleanLASER [Internet]. [cited 2016 Dec 19]. Available from: http://www.cleanlaser.de/wEnglish/produkte/backpack.php?navanchor=2110028.
[64] Laser gun makes the cut in decommissioning. World Nuclear News [Internet]. 2013 Oct 4; Available from: http://www.world-nuclear-news.org/WR-Laser_gun_makes_the_cut_in_decommissioning-0410134.html.
[65] Optical Interconnect Market by Interconnect Level (Chip Level, Rack & Board to Board, Metro & Long haul), Fiber Mode (Single Mode, Multi-Mode), Product Category, Application, and Geography—Global Forecast to 2022 [Internet]. marketsandmarkets.com; 2016 Oct. Report No.: SE 4656. Available from: http://www.marketsandmarkets.com/Market-Reports/optical-interconnect-market-89222473.html.
[66] Budica RJ, Herzberg JS, Chandler FO. Laser-powered propulsion system. US patent 9,068,562 B1, 2015.

CHAPTER 2

The Challenges Ahead for Laser Macro, Micro and Nano Manufacturing

J. Lawrence*, L. Li†
*University of Chester, Chester, United Kingdom
†The University of Manchester, Manchester, United Kingdom

2.1 INTRODUCTION

Laser materials processing has been practiced for more than four decades and is playing an important role in the modern manufacturing industry and the economy. While laser cutting, welding, marking, and drilling processes have reached maturity with wide industrial acceptance, new developments in recent years in additive manufacturing and micro/nano fabrication have enabled new capabilities that lasers can bring to the manufacturing industry. With the availability of high-brightness lasers such as fiber and disk lasers as well as ultra-fast lasers such as femto- and pico-second lasers, new beam-material interaction phenomena appear. Research in new technology development, optimization, modeling/simulation, and understanding the basic science (beam-material interactions, material characteristics and new material properties generated by lasers) involved in laser processing all play critical roles in advancing laser materials processing science and technology. This chapter gives the author's view (based on 25 years of research and development in laser processing) on the challenges and future prospects of laser materials processing research.

2.2 LASER CUTTING

2.2.1 Fiber/Disk Laser Versus CO_2 Laser Cutting

While CO_2 laser cutting still dominates sheet metal profiling (as the equipment manufacturers and their customers understand the processes and cutting parameters very well for various materials), high-power fiber and disk lasers start to compete in the cutting market. The advantages of high-power fiber/disk lasers over the CO_2 lasers include higher energy efficiency

Advances in Laser Materials Processing
https://doi.org/10.1016/B978-0-08-101252-9.00002-9
Copyright © 2018 Elsevier Ltd.
All rights reserved.

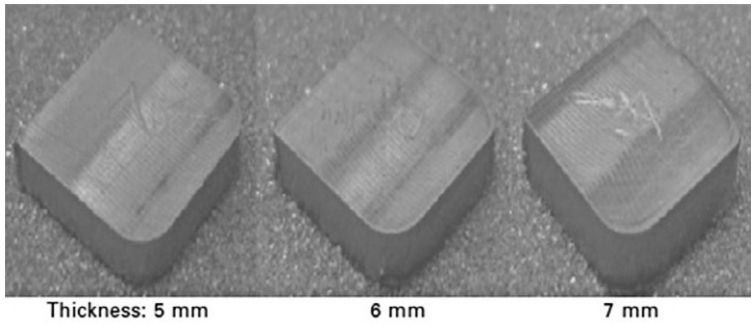


Fig. 2.1 An example of single mode fiber laser cutting of Ti-6Al-4V by the University of Manchester.

(electrical to optical conversion), smaller footprint, and flexibility in beam delivery through optical fibers. However, little is understood about the basic characteristics of fiber/disk laser cutting of various engineering materials. For cutting thin metallic materials (<5 mm), fiber lasers have been found to be faster than CO_2 lasers with comparable or better cut quality. However, for cutting thick metallic materials (>5 mm), CO_2 lasers have been found to be superior to fiber lasers in terms of quality and even speed. Therefore much research is needed to fully understand fiber/disk laser cutting and beam-material interactions. For example, fiber/disk lasers may not have higher beam absorption than CO_2 lasers for thicker metallic materials due to the effect of incident beam angle caused by the cutting front geometry. In addition, Gaussian beam may not be the ideal beam profile for laser cutting as up to 50% of the laser beam may escape from the cut kerf. Top-hat beam and radically polarized beam are being studied for cutting materials. The optimum cutting parameters are needed for various materials at various thicknesses so that these can be used by the laser manufacturers as a database in their provision of the fiber/ disk laser cutting machines. Fig. 2.1 shows an example of fiber laser cut Ti-6Al-4V sheets of 5–7 mm thickness with a 1 kW single mode fiber laser at the University of Manchester.

2.2.2 Cutting Brittle Materials

Laser cutting of brittle materials such as ceramics, semiconductors, and glasses overcomes the difficulties of mechanical machining in terms of tool wear and cutting speed. However, laser cutting of brittle materials can often result in micro-cracking, cut path deviation, and undesirable heat effects such as recasts, spatter, and debris. Numerous techniques have been employed in laser cutting of brittle materials, including thermal vaporization/melt

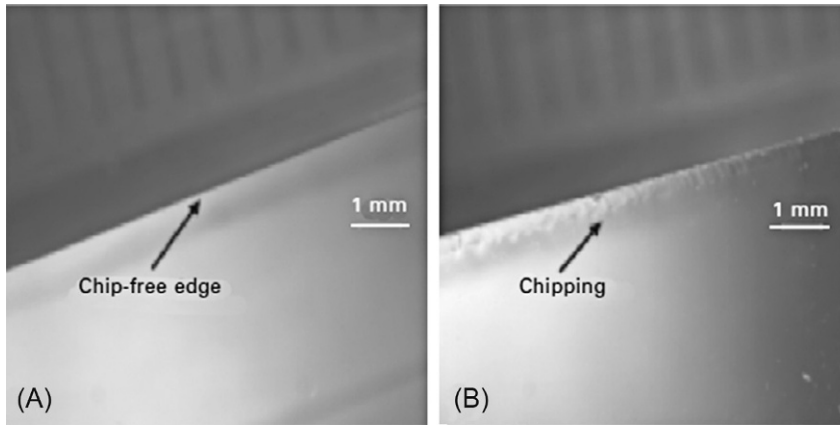


Fig. 2.2 Comparison between a diode laser cut soda-lime glass edges (A) and mechanical cut edges (B), by the University of Manchester [1].

ejection and controlled fracture.Volume absorption (using a laser beam that is partially transparent to the material to be cut) has been found to enable rapid cutting of transparent and semi-transparent materials by the generation of a single crack at temperatures well below the melting or phase transition temperatures. As a result, "stealth" cutting with high-quality cuts without debris and chips (shown in Fig. 2.2) can be achieved. High thermal gradients in laser cutting of brittle and low thermal conduction materials generate thermal stresses that can sometimes lead to undesirable micro-cracks and cut deviation. Control of thermal inputs in cutting ceramic/semiconductor/glass materials is therefore critical to the success of the cutting process. Modeling the stress development and thermal field management is critical to the success of laser cutting brittle materials.

2.2.3 Cutting Composite and Inhomogeneous Materials

Carbon or glass composite materials are becoming more used in the aerospace, energy, automotive, and sport industries due to their light weight and acceptable strengths. Laser cutting of carbon and glass composite materials is complicated by the large difference in material properties between the carbon or glass fibers and their polymer binders. Excessive heat conducted through the fibers often causes the polymer binder to disintegrate. This results in fiber pull-out and large heat-affected zones, as shown in Fig. 2.3. Short pulse, high-speed cutting can minimize the heat effect, but material removal rate is not yet commercially competitive. Research is therefore needed to develop laser-cutting technology that is better in quality and

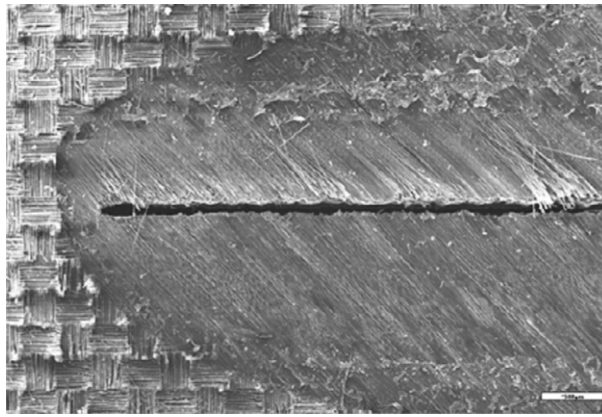


Fig. 2.3 An example of a fiber pull out problem when cutting carbon composite using a continuous wave fiber laser.

faster in speed compared with mechanical and water jet cutting techniques. Modeling of such a process is also challenging as the material property is anisotropic. Wood is another material that has anisotropic material properties. Cutting wood also has a problem of direction dependence and cut quality deviation at the grain boundaries (Fig. 2.4).

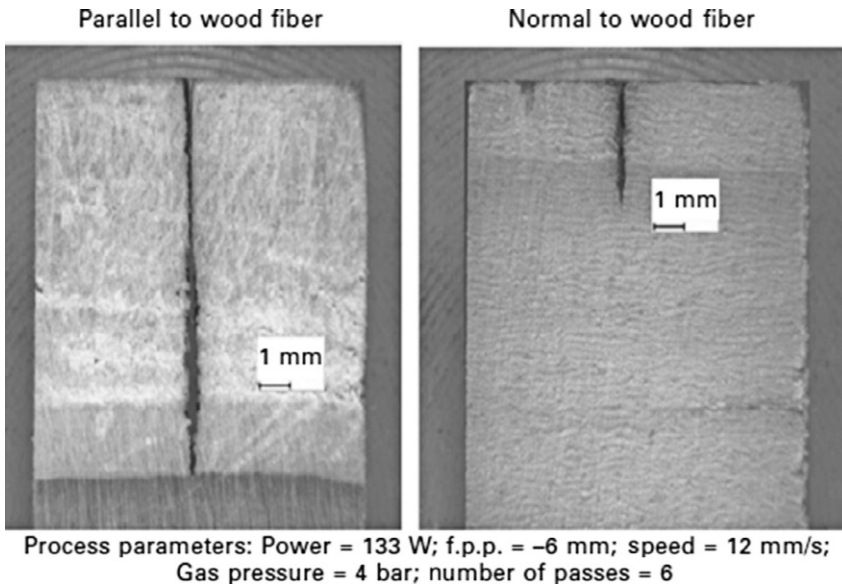


Fig. 2.4 An example showing the direction-dependent laser cutting of wood under the same cutting conditions (cross-section of the cuts showing the cutting depth differences).

2.2.4 Cutting Variable Thickness Materials

Laser cutting has so far been applied successfully for cutting materials with uniform thickness. Cutting variable thickness materials is a new challenge. Sometimes sheet materials supplied from different batches may not have exactly the same thickness. How sensitive and critical the cutting performance is to the material thickness variations is not fully understood. Although some preliminary studies have been carried out on laser cutting of variable thickness steels (shown in Fig. 2.5), much research is needed to provide fundamental understanding of the sensitivity of cutting performance to variations in material thickness when laser parameters are kept constant. In some area of applications such as laser-based decommissioning of buildings and nuclear installations, laser cutting of materials with variable thickness may be required, such as cutting a T-bar and pipes from one side. In these applications, however, cut quality may not be an important factor to be considered. Challenges exist on designing suitable cutting optics (e.g., to control beam divergence), gas delivery, and cutting parameters.

2.2.5 Cutting Thick-Section Materials

Laser cutting is best for material thicknesses of less than 20 mm. As the material thickness further increases, cut quality becomes poorer and cutting speed becomes too low. This is largely due to the problem of material removal, and guiding the laser beam through the kerf. For cutting metallic materials, the role of a laser is to melt the material, and a coaxial gas jet is used to remove the molten material. As the material thickness increases, the laser energy reaching the bottom part reduces and the gas pressure drops. Material removal efficiency therefore drops. Numerous specific techniques have been developed to enable thick section cutting of materials. These include "LASOX" and multiple pass laser cutting. An example is shown for cutting a concrete block of 500 mm thickness (Fig. 2.6) by the University of Manchester. Much research is needed to understand the material, gas, and laser interactions for cutting thick section materials. Competition in cutting thick-section materials comes from wire electro-discharge machining (EDM) and water jet techniques.

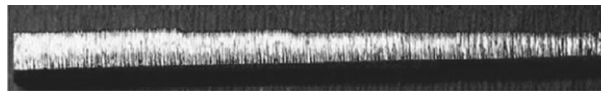


Fig. 2.5 An example of laser cutting of variable thickness materials: EN43 mild steel with a thickness 2–3 mm, by the University of Manchester [2].

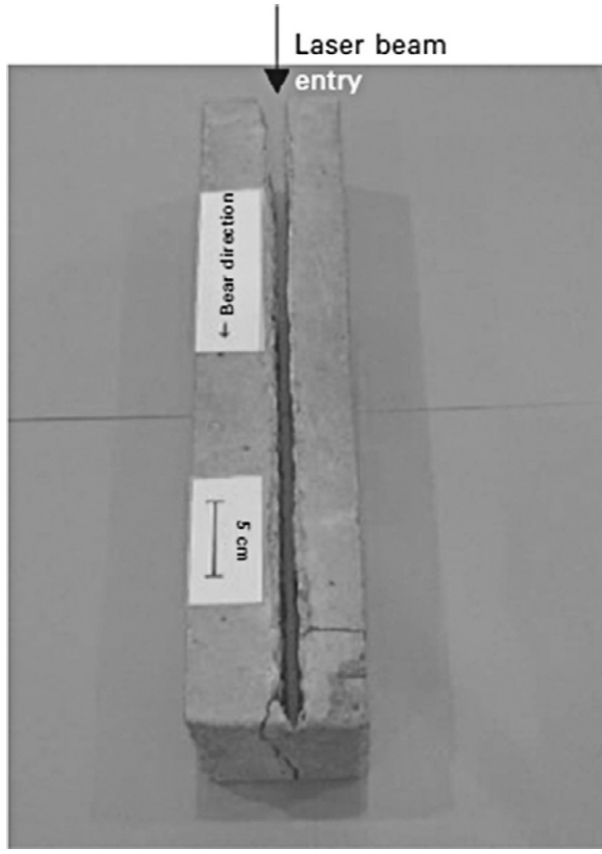


Fig. 2.6 A 500 mm thick concrete cut with a 1 kW laser, by the University of Manchester [3].

2.2.6 Striation-Free and Recast-Free Cutting

Laser cutting results in striation formation, recast, and heat-affected zones. For many applications these can be accepted. For certain applications, such as aerospace and medical industries, material integrity is critical and surface finish is important. Recent research has shown that it is possible to produce cuts with a laser without generating striation (Fig. 2.7). Super quality cutting includes striation-free, recast-free, and minimum heat-affected zone.

2.2.7 Super-High Speed Remote Cutting and Vapor Pressure Cutting

For thin materials (<300 μm), the use of a galvanometer scanning head for high-speed multiple pass machining/cutting based on vapor recoil pressure

melt removal can avoid the use of process gas, and the cutting speed can be extremely high if a high-brightness laser is used. Sharp corners can be cut due to the excellent dynamic properties of the galvanometers. Material removal is not dependent on the assist (as no gas is supplied) and it is closer to drilling and micro-machining processes. Although the cut quality is not as good as gas assisted cutting, when speed and gas consumption are considered, this method would have an advantage. Very little is known about this cutting technique and thus more research is needed to understand the effect of vapor, plume, and their interactions with the laser beam and various engineering materials to be cut, as well as improvements in cut quality. The availability of high average power (>300W average power) and high repetition rate pico-second and femto-second lasers in the near future would provide new opportunities for high-quality and high-speed cutting based on this method.

2.3 LASER WELDING

The main driver for laser welding technology development is the automotive industry where significant welding applications are based on laser technology. Laser welding of zinc-coated steels, aluminum alloys and Mg alloys have been well studied over a few decades. In the aerospace industry, welding of Ti alloys and Ni super-alloys have also been well studied, although welding TiAl is still a problem that has not been solved. The oil and gas industry requires portable laser welding techniques for joining large pipelines. It requires high quality orbital welding techniques and net shape welding (for the internal wall). Nuclear and shipbuilding also requires laser welding technology. However, the thickness of the materials in these industries is

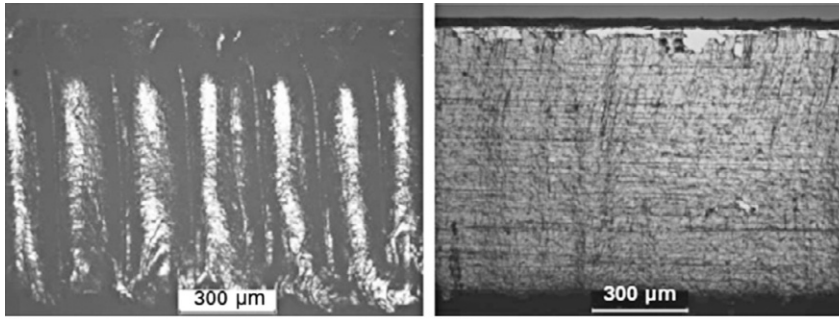


Fig. 2.7 Striation free cutting of mild steel sheets (B) compared with striations shown in (A), by the University of Manchester [4,5].

beyond the current capability of lasers. Thus new developments are needed for welding thicker materials.

2.3.1 Hybrid Laser Arc Welding

There have been rapid increases in the R&D activities of hybrid laser and arc (TIG/MIG/MAG/GMAW, plasma) welding owing to its specific advantages of deep penetration and better gap tolerances. As two different energy sources interact with each other in the welding process, it is more complicated than laser beam welding. The interaction of a laser beam with the electrical arc has been found to be able to stabilize the arc. The current studies are mainly on welding steels and Al alloys. Although arc welding and laser welding are well established, new knowledge is being created on hybrid laser arc welding. Future challenges include the understanding of the process parameter interactions, optimization and weld qualification (including microstructure, porosity, weld geometry, tensile and fatigue strengths, corrosion, and residual stresses) as well as process modeling, monitoring, and control techniques.

2.3.2 Welding Thick-Section Materials

Under the standard conditions, laser welding depth for metallic materials is below 25 mm, at an approximate relationship of 1 mm/kW for a CO_2 laser and 2 mm/kW for a fiber laser. Over the last few years, fiber laser-based welding has enabled the weld penetration of up to 50 mm in steels, at 15–30 kW power, with unusual welding conditions. For certain applications, such as nuclear power and shipbuilding, thick-section welding (>100 mm) is required that is normally beyond the current capability of the lasers. Challenges remain in developing laser welding techniques that can directly compete with conventional welding techniques for thick-section >50 mm welding.

2.3.3 Welding Ultra-Thin-Section Materials

Lasers have unique advantages in welding thin materials (<200 μm) owing to their precise energy delivery. However, surface tension effects become important in thin film welding, as there is very little melt material in the weld zone, which could result in cutting instead of welding. In addition, good contact between the two sheets to be welded is extremely important. Fig. 2.8 shows an example of welding thin-section stainless steel on a thicker stainless steel substrate for pharmaceutical applications. A special patented technique was used to enable such welding to be carried out successfully with tight contact control. Challenges remain for welding materials with thickness <10 μm.

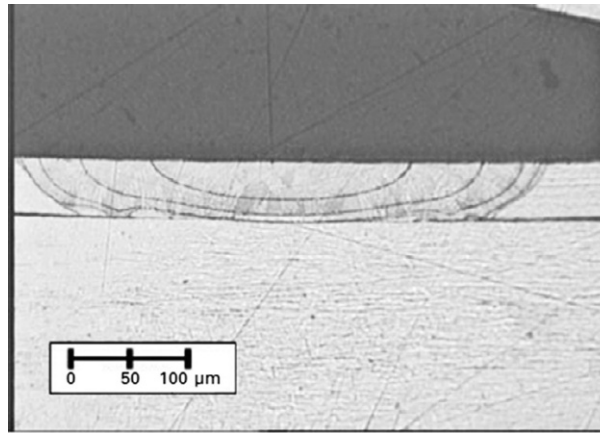


Fig. 2.8 An example (cross-section of the weld) of laser welding of 50 µm stainless steel sheet on a bulk stainless steel substrate, by the University of Manchester.

2.3.4 Welding Dissimilar Materials

Research in laser welding of dissimilar materials has been going on for several decades, yet there are still many problems that remain unsolved. Particular difficulty lies in the formation of brittle intermetallics in the weld zones. A further complication is the formation of galvanic cells between the two materials that promotes corrosion. Special surface protection is needed after the laser welding. Fig. 2.9 shows an example of laser butt welding of Ti-6Al-4V with In718 super alloy for potential applications in

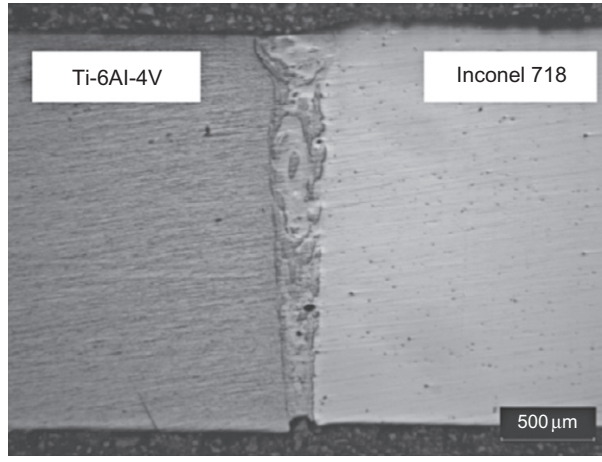


Fig. 2.9 Cross-section of fiber laser butt welded Ti and Ni alloys, by the University of Manchester.

the aerospace industry. Only under very specific operating conditions can cracks in the weld zone be avoided. Understanding of material behavior in welding dissimilar materials is more complicated than welding a single material, particularly when there is a large difference in the properties of the two materials and intermetallics are likely to be formed. Specific thermal management in the welding process is required and sometimes a third material may be needed to modify the weld zone properties.

2.3.5 Porosity Control

Porosity often occurs in laser welding of light alloys, e.g., Al alloys and Ti alloys. The material strength and integrity are affected by the presence of porosity in the welds. Surface oxide layer, plasma/plume generation, and shroud gas moisture could all contribute to porosity in the welds. With better control of these factors, e.g., using an off-axis gas jet to blow away the plume, porosity can be significantly reduced and even weld spatter could be reduced. Further research is needed to reduce porosity in welding various materials.

2.3.6 Net-Shape Welding

Owing to surface tension and rapid melt flow and rapid solidification in laser welding, the resulting weld beads can have sections above or below the original surface of the material. Furthermore, distortion to the weld sheets (particularly for thin sections) can occur. For most applications, this may not be a problem and until now these have not been well studied. However, for applications where fluid flow is affected by surface topographical characteristics and for precision post-weld assembly, net-shape welding is desirable. Recent research work at the University of Manchester has demonstrated the feasibility of achieving net-shape welding for mild steel sheets (Fig. 2.10). Challenges remain to achieve net shape welding for different materials while maintaining high tensile/shear strengths and theoretical prediction of welding conditions for net-shape welding.

2.4 LASER DRILLING

The industrial driver for laser drilling technology is the aerospace industry (e.g., cooling holes in nozzle guide veins and gas turbines), automotive industry (fuel injection nozzles), and electronics industry (e.g., circuit boards). The main advantage of laser drilling over other drilling techniques is the high speed (several orders of magnitude higher drilling speed than mechanical

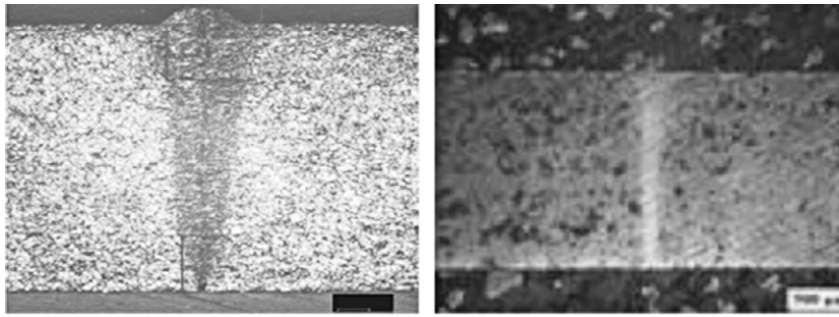


Fig. 2.10 Cross-section of net-shape fiber laser welded mild steel (beam-on-plate) using a single mode fiber laser, by the University of Manchester. (A) One side net-shape welding. (B) Both sides net-shape welding.

and electrical discharge machining) and there is no tool breakage problem. However, laser drilling has inherent problems of poor quality (recast, debris, hole tapering, heat-affected zones). Therefore, research has been carried out over the last few decades to improve quality in laser drilling.

2.4.1 Hybrid Laser Drilling

Laser drilling can be carried out in a number of ways including single pulse drilling, percussion drilling, trepanning, and helical drilling. Trepanning and helical drilling usually provide higher quality holes at the cost of drilling time. While percussion drilling provides the advantages of higher drilling speed, the quality of the holes is usually poorer than trepanning. Although conventional drilling techniques such as electro-discharge machining (EDM) and mechanical micro drilling produce high-quality holes, tool breakage is often a problem (more severe as the hole sizes reduce) that makes them difficult for very small holes, particularly at acute angles to the surface. The combination of laser and EDM or mechanical drilling would provide new opportunities for utilizing the advantages of both laser and EDM or mechanical drilling. Fig. 2.11 compares laser percussion drilled and sequential laser and EDM drilled holes in steel (laser drilling of a pilot hole followed by EDM finishing). In this case drilling time has been reduced compared with EDM drilling and tool breakages have been significantly decreased. From this example, it is clear that "hybrid" drilling would offer benefits in providing both quality and speed in hole production. Challenges remain for drilling at low angles, precise alignment of the laser drilled pilot holes, and EDM electrodes or mechanical drilling tools.

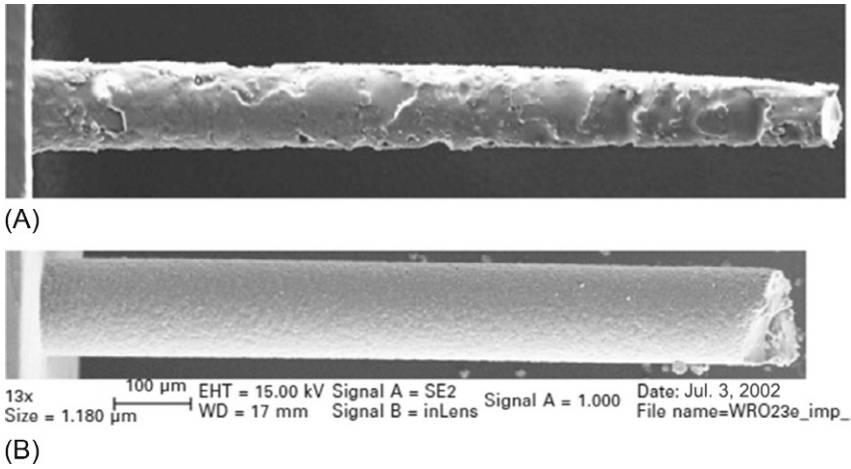


Fig. 2.11 Comparison of laser drilled hole (A) and laser-EDM drilled hole (B) in steel for fuel injection nozzle manufacture [6], by the University of Manchester.

2.4.2 Ultra-Short Pulse Laser Drilling

Femto- and pico-second lasers (commonly known as ultra-fast or ultra-short pulse lasers) are now available at average powers suitable for drilling both metallic and ceramic materials (e.g., ps lasers at 50W average power and fs lasers at 400W average power) at competing drilling speed with longer pulse lasers. Owing to the short pulses of ultra-fast lasers, debris can normally be reduced if drilling at high repetition rate and lower fluence (just above the ablation threshold) and surface finish can be much improved compared with longer pulse lasers. Much research is needed, however, to understand the beam-material interactions as non-linear, multi-photon absorption may occur.

2.5 LASER SURFACE ENGINEERING

The purpose of laser surface engineering is to provide superior surface properties by laser heating, melting, cladding, alloying, glazing, shock peening, and generation of metal matrix composites (MMC) or ceramic matrix composites (CMM). Novel surface properties (e.g., optical, chemical, electrical, and magnetic properties) can be generated by laser-induced surface chemical changes on polymer, ceramic, and semiconductor materials. Considerable research and practical industrial applications have been carried out over the last 40 years, and have intensified recently, particularly

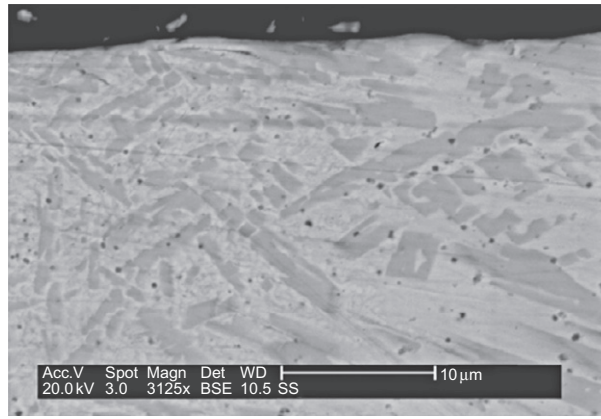


Fig. 2.12 TiB, FeB, Fe2B micro/nano particles imbedded in Fe matrix by diode laser sol-gel surface deposition technique, produced at the University of Manchester [7].

in China. By combining a laser beam with sol-gel slurry, various micro or nano metal matrix composites can be synthesized on a metallic substrate as a coating. An example is shown in Fig. 2.12 for the production of a surface MMC coating with TiB micro/nano particles in the Fe by laser-sol-gel surface coating technique to improve wear resistance. Although CO_2 and Nd:YAG lasers are still widely used, high-power diode, diode-pumped solid state lasers, and excimer lasers are increasingly used for surface engineering due to their capability of delivering rectangular beams. New research in laser surface engineering involving nano-materials and nano-structures is becoming more noticed.

2.6 ADDITIVE MULTIPLE LAYER MANUFACTURING

Although there are many names and terminologies used for additive layer manufacturing using lasers, as far as fully dense metallic parts are concerned, there are two main additive manufacturing processes: blown powder metal deposition orientated from laser cladding, and powder bed or selective laser melting process originated from selective laser sintering process. The blown powder process can deposit fully dense metallic materials both on flat and curved surfaces, making it ideal for repair and hybrid (additive and subtractive) manufacturing processes. The powder bed selective laser melting process is ideal for the production of 3D metallic parts with complicated geometry, especially with complicated internal structures. These processes are used in practical industrial applications such

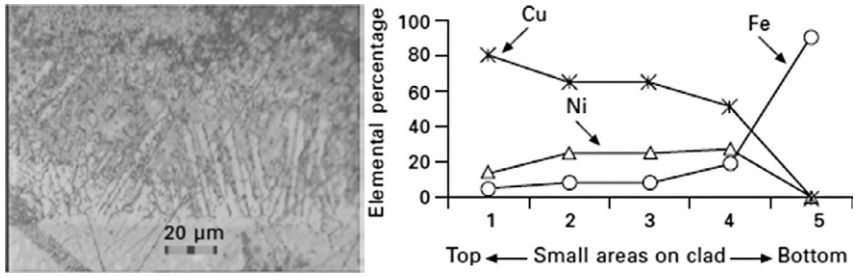


Fig. 2.13 Functionally graded deposition Fe-Ni-Cu using hybrid wire/powder feeding direct laser deposition, by the University of Manchester [8].

as medical implants and aero-engine component repairs. An example is shown in Fig. 2.13 using hybrid wire (Ni)/powder (Cu) laser deposition on a steel substrate to produce functionally grated layers. There are still many problems unresolved in multiple layer additive manufacturing processes. For example, for selective laser melting, the material build-up rate is very slow, typically at 10 cm^3/h, thus it is only suitable for building small components. The blown powder process has a typical problem of poor geometry definition and poor surface finish, thus post process machining is necessary. Substrate distortion is another issue to be resolved for deposition materials on thin-walled components.

2.7 MICRO/NANO FABRICATION

Micro/nano fabrication has been one of the most important developments in laser processing over the last 10 years. Physicists dominate research in this area although more and more engineers are becoming involved. The drivers for micro/nano fabrication research are mainly the demand for laser-based technologies in the renewable energy field (e.g., solar panels, fuel cells), semiconductor industry (photolithography), electronic industry (e.g., display panels), data storage (nano-bumps for hard disks, multi-dimensional data storage), biomedical (e.g., stents, implants, micro-fluidics), and photonic/telecom industries.

2.7.1 Precision Micro-Cutting

Research in fine cutting of thin materials and tubular materials for the medical industry has become intensified over the last 10 years. The high-quality cutting in medical stent production demands improved laser-cutting technology that can minimize the requirement for post-processing. Although

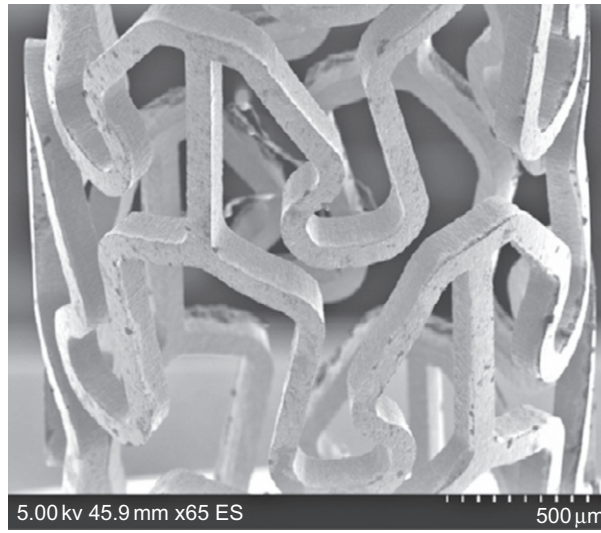


Fig. 2.14 A stainless steel stent cut by a single mode fiber laser, by the University of Manchester.

the industrial stent cutting systems are still mainly based on Nd:YAG lasers, research in the use of fiber lasers and ps/fs lasers for stent cutting is starting to show benefits. Fig. 2.14 shows an example of a stainless steel medical stent cut by a single mode fiber laser. The cutting speed is well above that achieved by Nd:YAG lasers. High-precision cutting with a small heat-affected zone can be achieved. The research in fiber laser and fs/ps lasers for precision cutting will continue while cut quality and cutting speed would expect further improvement.

2.7.2 Laser Surface Micro-Texturing

Laser generation of periodical structures has been studied for more than three decades. Most earlier studies were for the improvement of tribological characteristics. Recent research has intensified in applying laser surface micro/nano-texturing for changing the wettability (e.g., super-hydrophobic and super-hydrophilic surface), optical characteristics (e.g., optical reflection/ absorption control), and other physical/chemical characteristics. Fig. 2.15 shows an example of a nanosecond pulsed laser micro-textured stainless steel surface that has close to super-hydrophobic characteristics, similar to lotus leaf surfaces that possess self-cleaning capability. The use of fs lasers for the generation of periodic ripples (perpendicular to the E-field of the laser beam polarization) has also been investigated by several research

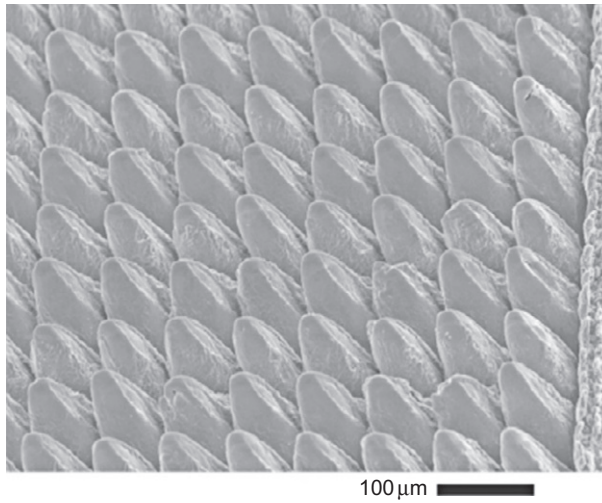


Fig. 2.15 Angled (60 degree) micro-cones produced on stainless steel surfaces for wettability and optical property control, by the University of Manchester [9].

groups. Laser interference photolithography has been well established for producing lines and other patterns. The main challenge is to improve the surface coverage rate.

2.7.3 Direct-Write Micro-Deposition

Laser-based forward and backward transfers have been investigated for several decades. Well-established techniques include laser-induced forward transfer (LIFT) and matrix-assisted pulsed laser evaporation (MAPLE) that can deposit various materials including heat-sensitive bio-materials and cells on 2D and 3D surfaces. Micro-cladding has also been shown to be able to achieve micro-scale resolutions. For producing 3D micro-scale parts, micro-stereolithography, laser PVD, laser CVD, and fs laser two photon polymerization have shown promise. The challenge is to rapidly produce deposited patterns on various substrate surfaces with good adhesion, resolution, and the use of functional materials [10]. The industrial driver for laser direct writing technology is mainly for printed circuits (2D and 3D), sensors, and biomedical research.

2.7.4 Nano-Fabrication

Due to diffraction limits, the standard far field laser beam fabrication resolution is at half of the laser beam wavelength. Thus one way to reduce feature

sizes is to reduce laser wavelength. The development of EUV laser systems has been intensified over the last few years driven by the electronics industry for producing features below 30 nm in lithography. On the other hand, diffraction limits can be overcome using near field effects (e.g., evanescent waves) of optics and plasmonic effects of nanostructured materials. The use of metamaterials as super-lenses and the use of laser tweezers combined with microspheres have demonstrated the capability of writing nano-scale features. For multiple repeating pattern production, laser interference lithography and microlens arrays have shown great promise.

Self-assembled particle lenses have demonstrated high efficiency. Fig. 2.16 shows an example of producing a large number (100 million) of user-defined patterns with a single laser beam by scanning the laser beam at an angle to the self-assembled microspheres. Recent development has enabled the use of the laser tweezers to hold a single or an array of spheres in liquid to enable direct writing of continuous nano-patterns. The challenge in laser nano-fabrication is to enable far field super-resolution and high-efficiency multiple surface patterning. The industrial driver for the nano-fabrication is mainly from the electronic, biomedical, and photonic industries.

The other area of nano fabrication is the production of nano-materials such as nano-tubes, nano-wires and nano-particles. Owing to low efficiency of laser techniques, the nano-material market is dominated by the wet-chemical, electric-discharge, and sol-gel techniques. There is, however,

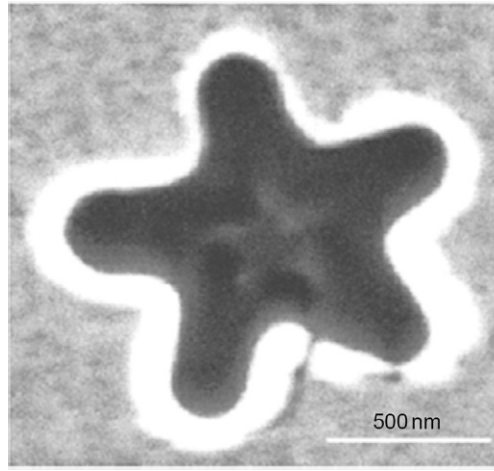


Fig. 2.16 Nano-stars produced using particle lens technique with 100 million similar patterns produced at the same time with a single laser beam, by the University of Manchester [11].

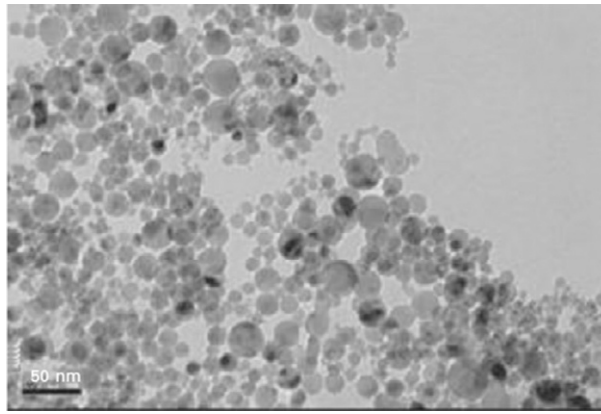


Fig. 2.17 TiO_2 nano particles generated by continuous wave laser ablation in liquid, by the University of Manchester [12].

growing development in laser-based nano-material fabrication. Fig. 2.17 shows an example of nano-TiO_2 particle generation by continuous wave laser ablation in liquid. The challenge is to produce nano-materials that cannot easily be produced with other techniques and with high efficiency and process control (e.g., size, phase, morphology).

2.8 FUNDAMENTAL BEAM/MATERIAL INTERACTIONS AND PROCESS MODELING

Owing to the introduction of new high-power lasers such as fiber lasers, slab lasers, and disk lasers as well as ultra-fast lasers, much research is needed to understand the interaction of these lasers with various materials. In addition, laser interaction with inhomogeneous materials, plasma/plume interaction with the laser beams in remote welding and remote cutting remain to be investigated. Modeling of material solidification including porosity and crack formation and microstructure formation are still challenges not yet fully met. Modeling of laser materials processing can involve multiple phases (solid, liquid, vapor, plasma), multiple scales (macro, micro, and nano) and rapid heating/cooling. Finite element or finite volume (e.g., computational fluid dynamics, or CFD) alone may not be sufficient. Plate I [13] (between pages 428 and 429) shows an example for CFD modeling of laser drilling process. Future development in modeling of laser processing may require combined finite element (mainly suitable for solid phase) and CFD modeling. Molecular dynamics and smooth-particle hydrodynamics modeling are beginning to show benefits in modeling of laser materials processing.

Modeling of material behaviors in laser processing of composite materials and multiple dissimilar materials can be very challenging as the material properties in the interaction zone can be very difficult to define.

2.9 LASER SYSTEMS

CO_2 laser cutting systems, and fiber laser, CO_2 laser, Nd:YAG and DPSS laser-based marking systems and industrial Nd:YAG laser-based drilling systems are mature. The introduction of high-power fiber, disk lasers is beginning to challenge traditional CO_2 lasers for cutting and welding. There are, however, many challenges. For example, focus shift has been found to be one of the main problems for fiber lasers. Internal optic correction is needed to overcome this. Processing heads with built-in sensors are also needed and currently supplied by many manufacturers. Challenges remain for real-time process NDT, monitoring of porosity and microstructure/crack formation, and for reducing power loss in the cutting and welding processes. Beam-shaping for different applications has shown benefits. Gas and electricity savings would be another challenge in nozzle design and laser efficiency improvements. Near field optical systems development for nano-fabrication are closer to becoming accepted by the industries. Special optical designs for the far field super-resolution (beyond diffraction limit) would be a challenge for future research.

2.10 CONCLUSIONS

Laser materials processing plays an important role in modern society. Although laser processing has been practiced for more than 40 years, there are still many scientific, technological, and engineering challenges at both the macro and nano scales. Industrial demand for higher precision, higher speed, and higher energy efficiency has driven the laser technology development, including fiber lasers, disk lasers, diode lasers, and ps/fs lasers over the last two decades. These new laser sources bring new opportunities in materials processing and also new challenges in understanding their interactions with materials. The research in effectively utilizing these new laser sources and finding new capabilities with these lasers will continue to attract research interests. Applications of lasers in solar cell manufacture, electronic systems (ICs and displays), medical products, and aerospace/automotive industries will be the main driver for laser processing research and technical innovations.

REFERENCES

[1] S. Nisar, M.A. Sheikh, L. Li, S. Safdar, Effect of thermal stresses on chip-free diode laser cutting of glass, Opt. Laser Technol. 41 (3) (2009) 318–327.
[2] M. Sobih, P. Crouse, L. Li, Laser cutting of variable thickness materials—understanding the problem, in: 25th International Congress on Applications of Lasers & Electro-Optics (ICALEO'06), 30 October–2 November 2006, Scottsdale, AZ, Laser Institute of America, 2006.
[3] P. Crouse, L. Li, J.T. Spencer, Cutting 500 mm thick concrete using high power lasers below 2 kW, in: Proc. of 22nd International Congress on Application of Lasers & Electro-Optics (ICALEO'03), 13–16 October 2003, Jacksonville, FL, Laser Institute of America, 2003.
[4] L. Li, M. Sobih, P. Crouse, Striation-free laser cutting of mild steel sheets, CIRP Ann. Manuf. Technol. 56 (1) (2007) 193–196.
[5] M. Sobih, P.I. Crouse, L. Li, Elimination of striation in laser cutting of mild steel, J. Phys. D. Appl. Phys. 40 (22) (2007) 6908–6916.
[6] L. Li, C. Diver, J. Atkinson, R. Fiedle-Wangner, H.J. Holml, Sequential laser and EDM micro-drilling for next generation fuel injection nozzle manufacture, CIRP Ann. Manuf. Technol. 55 (1) (2006) 179–182.
[7] A.R. Choudhury, T. Ezz, L. Li, Synthesis of hard nano-structured metal matrix composite boride coatings using combined laser and sol-gel technology, Mater. Sci. Eng. A 445 (2007) 193–202.
[8] L. Li, W.U.H. Syed, A.J. Pinkerton, Rapid additive manufacturing of functionally graded structures using simultaneous wire and powder laser deposition, Virtual Phys. Prototyp. 1 (4) (2006) 217–225.
[9] R. Lloyd, A. Abdolvand, M. Schmidt, P. Crouse, D. Whitehead, L. Li, Z. Liu, Laser-assisted generation of self-assembled microstructures on stainless steel, Appl. Phys. A 93 (1) (2008) 117–122.
[10] K.K.B. Hon, L. Li, I.M. Hutchings, Direct writing technology—advances and developments, CIRP Ann. Manuf. Technol. 57 (2) (2008) 601–620 (Keynote paper at 58th CIRP General Assembly, Manchester).
[11] W. Guo, Z.B. Wang, L. Li, Z. Liu, Near-field laser parallel nanofabrication of arbitrary-shaped patterns, Appl. Phys. Lett. 90 (2007) 243101.
[12] A. Abdolvand, S.Z. Khan, Y. Yuan, P.L. Crouse, M.J.J. Schmidt, M. Sharp, Z. Liu, L. Li, Generation of titanium-oxide nanoparticles in liquid using a high-power, high-brightness continuous-wave fibre laser, Appl. Phys. A 91 (3) (2008) 365–368.
[13] H.K. Sezer, A. Pinkerton, L. Li, P. Byrd, An investigation into delamination mechanisms in inclined laser drilling of thermal barrier coated aerospace superalloys, J. Laser Appl. 17 (4) (2005) 225–234.

CHAPTER 3

Laser Fusion Cutting of Difficult Materials

J. Lawrence*, A. Riveiro†, F. Quintero†, J. Pou†
*University of Chester, Chester, United Kingdom
†University of Vigo, Vigo, Spain

3.1 INTRODUCTION

Laser cutting is traditionally the most common laser manufacturing technology, solidly well established in the majority of industrial sectors. The market share of laser cutting was 23% of worldwide industrial laser applications in 2007, confirming it as one of the most firmly established laser techniques [1]. Nowadays, this is a routine technique for cutting different materials, mainly metallic sheets for different industries.

Laser cutting can be accomplished through different techniques that involve different laser operating modes (pulsed or CW), energy level and whether an assist gas is used. Those techniques are vaporization cutting, fusion cutting, reactive fusion cutting, thermal stress cracking, scribing, and cold cutting. The optimum choice of one of these techniques depends on the physical properties of the material to be cut, the thickness of the workpiece and the selected laser source [2,3].

There are some limitations, mainly concentrated in the maximum possible cut thickness and in the nature of the material. Obviating the clear drawback of the maximum possible cut thickness, some materials can be designed as difficult to cut for different reasons, including the process cannot be properly established, the processing rate is too low, and/or the cut quality is undesirable for the later application of them. Although we will not present an exhaustive description of materials classified as difficult to cut, some examples are:

- Metallic materials: high reflectivity and/or conductive materials (e.g., aluminum or copper, alloys)
- Non-metallic materials:
  - *Ceramics:* Thick structural ceramics (e.g., silicon carbide or Mullite-alumina)

Advances in Laser Materials Processing
https://doi.org/10.1016/B978-0-08-101252-9.00003-0
Copyright © 2018 Elsevier Ltd.
All rights reserved.

- *Composites:* composite materials with extremely different physical properties (e.g., carbon fiber or glass fiber)
- *Stony materials:* inhomogeneous rocks such as some granites.

This chapter will mainly focus on laser cutting of aluminum and its alloys and ceramics, because of the industrial significance of these materials. On one hand, aluminum is the most widely used non-ferrous metal with a current annual consumption of 24 million tons [4]. Aluminum is used in five major areas: building and construction, containers and packaging, transportation, electrical conductors, and machinery and equipment, taking advantage of an excellent weight/strength ratio, high corrosion resistance, or high electrical and thermal conductivities.

On the other hand, ceramic materials are also highly valued. The bonding in ceramics is ionic and/or covalent, and there are no "free electrons." Traditionally this property makes them excellent candidates as electrical insulators. Today, the so-called electrical or electronic ceramics are vital in the modern technological society. Moreover, the rigid bond confers on them high temperature stability and resistance to chemical attack. Mechanical applications of ceramics especially exploit hardness, wear, and corrosion resistance. In summary, the excellent thermal, electrical and dielectric, magnetic and superconductive, optical, chemical, and mechanical properties of ceramics are the main reasons for their wide use [5].

3.2 PRINCIPLES INVOLVED IN FUSION LASER CUTTING

The technique of fusion laser cutting is the most widely used because the energy requirements are substantially less compared to other laser-assisted cutting techniques [3].

The basics of fusion laser cutting are very simple [6,7]. A high-intensity laser beam is focalized by means of transmissive or reflective optics onto or underneath the surface of the workpiece to be cut, Consequently, the material is heated locally in the interaction zone up to the melting point or even to the boiling point throughout the depth of the workpiece, depending on the degree of coupling of the radiation with the workpiece. Therefore a cut slot, commonly called a kerf, is established and a high-pressure gas jet is injected into the slot in order to remove the material melted by the laser beam. In some cases, the high-pressure assist gas not only acts to remove the molten material but also can add more energy to the process when it reacts exothermically with the material.

Production rate and cut quality are defined by different physical mechanisms involved in laser cutting. The most relevant physical mechanisms can be grouped under the following tags [8]:

- Optical mechanisms, namely the absorption of radiation [9,10].
- Thermodynamic mechanisms, namely heat conduction, convective or radiative losses, and phase transitions [11,12].
- Fluidmechanic mechanisms, namely dragging of molten material by assist gas [13]
- Chemical mechanisms, namely oxidation [14]

3.3 EXPERIENCES IN LASER CUTTING OF DIFFICULT MATERIALS

Experimental tests of laser cutting in difficult material were conducted in parallel to the development of laser sources in order to continuously improve finishing and production rates. We will present those results related to the processing of metals and then those related to the cutting of ceramics.

3.3.1 Cutting of Metals, Aluminum, and Alloys

Earliest publications dealing with laser cutting of aluminum and alloys were carried out in order to investigate the cutting process of most industrially used materials. High power requirements limited earliest research in cutting thin sheets, such as for microelectronic applications. Several works were concentrated on the possibility of cutting using a CO_2 laser working in CW and by means of Nd:YAG [15,16].

Consecutive improvements in power and beam quality allowed processing materials with thicker sections. Locke and Hella [17] showed the possibility of cutting thick-sectioned aluminum alloy, namely 6061 alloy at 12.5 mm in thickness. Quality parameters, namely squareness of cut edges and planarity of surfaces, were maintained within acceptable values. However, processing rates were low and required high laser power. Dell'Erba et al. [18] also processed thick-sectioned aluminum by means of a CO_2 laser. Results were compared by means of the moving line-heat source model.

Other investigations were conducted in order to understand problems related to the processing of aluminum. The first problem observed was the high reflectivity to the laser radiation due to the high electrical conductivity of these materials. In this way, work performed by Murakawa et al. [19] exposed the limitations of the cutting process when high reflectivity materials such as aluminum sheets are cut by a CO_2 laser.

Another problem is the high thermal conductivity of these materials. The absorbed energy during laser processing is rapidly dissipated away from the interaction zone. Dell'Erba et al. [18] pointed out the fundamental role of this parameter. Jiang et al. [20] showed that the focal spot position should be 1–2 mm under the material surface while cutting aluminum sheets in order to obtain maximum depth of cut, probably due to the high thermal conductivity of this material. On the other hand, high conduction losses during cutting due to the high thermal conductivity produce a large heat-affected zone (HAZ) in the material surrounding the cutting edge. In summary, high reflectivity and conductivity of these materials come together to frustrate the cutting process [2].

Utilization of reactive gases like compressed air does not allow a substantial advantage in cutting because cutting speed is not significantly higher than with nitrogen as compared to cutting mild steel, for example Locke and Hella [17] and Ketting et al. [21]. During the processing of aluminum alloys, a layer of Al_2O_3 oxide is formed in the cut front. This film prevents the subsequent oxidation of the molten material underneath. Kar and Migliore [22] showed that while using air during cutting of 6061-T6 and 7075-O alloys, cut edges are oxidized and exhibit a higher tendency for recast formation while being more uneven in profile (which promotes fatigue cracking).

Finally, the cutting process is frustrated in obtaining dross-free edges and smooth finishing due to the high viscosity of the molten material, which is hardly dragged by the assist gas. Moreover, viscosity is increased by the presence of aluminum oxides in the molten material because the melting point of Al_2O_3 is much higher than that of aluminum (namely, $T_m(Al) = 660°C$ and $T_m(Al_2O_3) = 2054°C$, respectively) [23,24]. Rapid cooling of molten material due to the high conduction losses during the cutting process also increases the viscosity. High viscosity promotes the formation of large amounts of dross, which must be mechanically removed. In order to reduce the level of dross, Masumoto et al. [23] proposed using argon instead of oxygen or nitrogen to avoid the formation of Al_2O_3 or Aln on the molten material into the kerf. Mostafa et al. [24] evaluated the possibility of using anti-slagging agents to reduce the viscosity of the molten material as proposed by Arata et al. in the pile cutting technique of stainless steel [25]. They verified the possibility of obtaining dross-free edges using alkali and alkali-earth halides after painting the rear surface of the workpiece. Studies conducted by Aritoshi et al. [26] during cutting thin sheets of different aluminum alloys, namely 1050, 2017, 5052, and 7075 alloys by means of a CO_2

laser showed that the height of dross was dependent on the surface tension of the molten material.

Metallurgical characteristics of cuts were assessed by different authors (see Fig. 3.1). Kar and Migliore [22] performed microhardness measurements in the cross-section of a 6061-T6 alloy. Decrease in hardness was observed up to 300 mm into the material due to the destruction of the thermal treatment prior to the processing, as a consequence of the thermal input during cutting. Scavino et al. [28] also performed microhardness measurements on the same alloy and detected a lower reduction in hardness after cutting. Araújo et al. [27] performed a study on the HAZ formed during CO_2 laser cutting of the 2024-T3 alloy. Mechanical properties of machined workpieces were also evaluated. Carpio et al. [29] conducted fatigue tests on 2024-T3 aluminum sheets in order to estimate the possible certification of this machining procedure for aerospace applications. Fatigue behavior of samples was found to be lower than aeronautic requirements. This was attributed to the roughness of the cutting edge, which promotes crack initiation. Scavino et al. [28] also performed an evaluation of the mechanical properties of machined samples of 6061-T6 and 6082-T6 alloys. Tensile and bearing tests showed that mechanical properties were found in the range of international design standards. Unlike studies conducted by Carpio et al.,

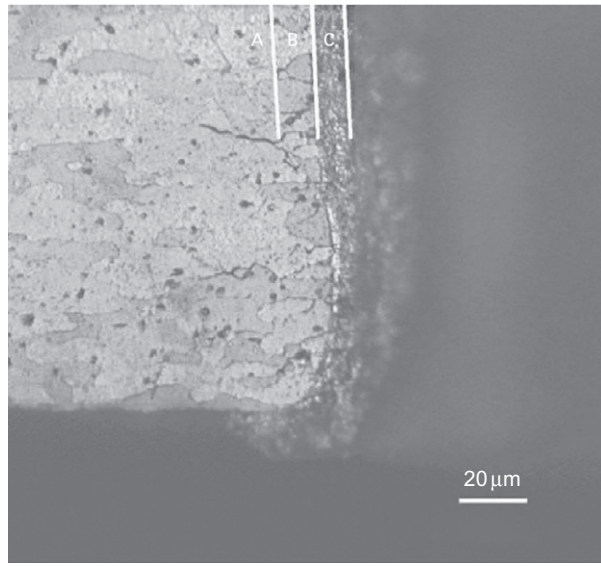


Fig. 3.1 Cross-section micrograph of an Al-Cu alloy 1.6 mm in thickness cut by means of a 2 kW continuous CO_2 laser [27].

axial fatigue tests were found to exhibit a similar response compared to mechanically machined samples.

With regard to the high corrosion resistance of this material, some works evaluated the effects on corrosion resistance in the cut edges after cutting. Tests were performed on cut edges of pure aluminum and an AlMg alloy [21,30] and corrosion resistance was found to be unaffected by the laser cutting process.

3.3.2 Cutting of Ceramics

Simultaneous to the development of cutting metals, some researchers focused on the potential applicability of lasers in the manufacturing processes of ceramic materials, in view of the associated difficulty during the conventional machining as a consequence of their high hardness and fragility.

The first experiences on laser machining of ceramics were focused on the scribing and controlled fracturing techniques [31,32]. Fusion and vaporization laser-cutting techniques using a CO_2 laser were developed simultaneously. Earliest works were focused on processing in CW mode and also for microelectronic applications [33]. Research work conducted by Copley and Bass [34] and Copley et al. [35] analyzed the applicability of vaporization machining of alumina, silicon nitride, and silicon carbide. The influence of laser power, processing speed, and overlapping on grooving depth and obtained roughness were evaluated. Several attempts were performed in order to obtain a comprehensive understanding of the process of cutting. Naeem et al. [36] explored the cutting process of ionic and covalent ceramics with thicknesses ranging from 2–10 mm. Three-dimensional capabilities of laser cutting were demonstrated on silicon carbide [37]. On the other hand, several works expanded the capabilities of CO_2 in cutting of ceramics of a different nature [38,39].

The principal drawback of fusion laser cutting of ceramics is the formation of cracks, microcracks, and fractures due to the high sensitivity to cracking resulting from thermal stresses caused by the localized heating as shown in Fig. 3.2. The mechanical strength is severely affected by microcracks. Several works were conducted to understand the operating conditions that led to its formation and procedures to quantify them. Zhang et al. [40] addressed the effects of laser cutting on ceramic workpieces by evaluating the surface integrity of machined samples under different processing conditions. Also, Lu et al. [41] obtained an equation based on dimensional analysis of the processing parameters relevant to crack formation safe operating regime against plate cracking. They observed that utilization of high

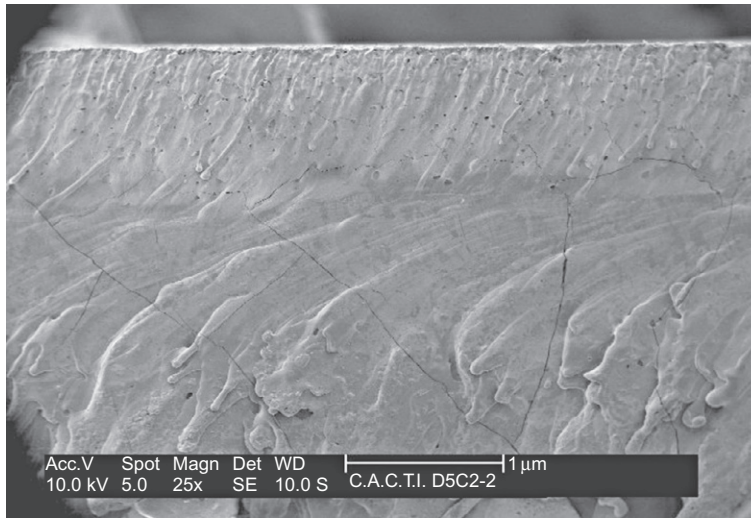


Fig. 3.2 SEM image of the cutting edge of a mullite-alumina composite 4 mm in thickness cut by Nd:YAG laser. Presence of microcracks is evident in the resulting cutting edge.

laser powers and less feed rate decreased the tendency to cracking. However, the thermal load is more rapidly applied if the cutting speed is increased and consequently the higher temperature gradient led to higher thermal stresses increasing the tendency toward cracking. Simultaneously, Modest [42] and Modest and Mallison [43] theoretically studied the circumstances and process of thermal stresses generation caused by laser cutting in order to predict the temporal temperature fields, the receding solid surface, and elastic and viscoelastic stresses during CW or pulsed laser drilling of thin ceramic. Black [44], Black and Chua [45], and Black et al. [46] revisited the different processing parameters affecting the CO_2 laser cutting of ceramic tiles in order to perform a minimal post-treatment. Attention was paid to the effects of various shielding gases and the utilization of multipass cutting and underwater cutting. Also, a theoretical approach was taken in order to correlate the influence of the thickness on the optimum cutting speed, obtaining an inversely proportional dependence.

In order to assess the cut quality, several works were conducted. Quantifiable parameters such as roughness were used in order to characterize the cutting edge of processed samples [47,48]. Other authors have used the crack length or the density of cracks in order to quantify the severity of thermal processing [49–51].

3.4 ATTEMPTS TO IMPROVE CUTTING PROCESS

3.4.1 Processing in Pulsed Mode

3.4.1.1 Processing Ceramics in Pulsed Mode to Avoid Thermal Cracking

An attempt to reduce the tendency to thermal cracking and improving the cut quality at the same time is through pulsed laser processing. The temporal limitation of the laser-matter interaction leads to a decrease of the thermal load suffered by the workpiece [52]. Thermal stresses on the ceramic workpieces are limited by means of processing in pulsed mode, and the appearance of cracks and final fracture of machined samples can be avoided. Most theoretical works have concluded the higher tendency to thermal cracking after the processing in CW mode. Tönshoff and Gonschior [53] validated this hypothesis after CW and pulsed-CO_2 laser cutting of alumina plates 4 mm in thickness. After the experimental and theoretical work, they found that crack length is substantially reduced by means of pulsed processing. In the same sense, works published by Livingstone et al. [54], Black [55,56] also confirm the reduction of cracking during processing in pulsed mode, after studying the CO_2 cutting process in CW, pulsed and super-pulsed mode of ceramic tiles with thicknesses ranging from 3.7 to 9.2 mm. Shigematsu et al. [57] found after CO_2 pulsed laser cutting that cordierite ceramics sintered with an addition of aluminum titanate can be cut without serious failures.

Based on the availability of pulsed Nd:YAG laser sources, several works were published related to pulsed processing in order to reduce the tendency toward cracking. In this way, it is worth highlighting works performed on Nd:YAG laser cutting on several ceramic materials, including silicon nitride, alumina, silicon carbide, zirconia and boron carbide [58–63].

3.4.1.2 Processing Aluminum Alloys in Pulsed Mode to Improve Cutting Efficiency

Processing in pulsed mode has been reported to improve cut quality and performance as a consequence of the more efficient laser radiation coupled with the workpiece and reduced heat input [52]. These advantages are exploited during cutting of aluminum and alloys.

Similar processing rates to CW cutting were found by Olsen et al. during cutting in both CW and pulsed mode [52,64]. Good quality cuts were only obtained in pulsed mode for 4 mm in thickness. Stournaras et al. [65] conducted a study to clarify the influence of pulsed mode processing parameters on cut quality of 5083 alloy 2 mm in thickness. Kerf width, extension of HAZ, and roughness of cutting edge were the selected quality parameters. They found that kerf width and HAZ are mainly influenced by the cutting

speed and laser power respectively. The pulsing frequency and gas pressure are the two major influencing parameters affecting roughness. Masumoto et al. [23] and Stournaras et al. [65] showed that a critical duty cycle exists that allows dross-free cuts to be obtained. Dross weight was found to decrease linearly with the duty cycle for cutting 1 mm of 5052 aluminum alloy. However, roughness was observed to increase with the reduction in duty cycle. They proposed an empirical relation to obtain the critical duty cycle that produces dross-free cuts under different cutting speeds. Dross-free cuts were not obtained for thicker sections.

Implementation of Taguchi methodology performed by Dubey and Yadava [66,67] during Nd:YAG laser cutting of 8011-H14 aluminum alloy with 0.9 mm in thickness allowed the optimum processing conditions in pulsed mode to optimize the quality characteristics to be found. They showed that material removal rate is primarily determined by the cutting speed but the kerf taper is only determined by the pulse frequency. Also, pulse frequency and assist gas pressure are the most significant parameters affecting kerf quality.

Application of super-pulsed modes was also tested in order to process aluminum alloys (see Fig. 3.3). Work performed by Michaelis et al. [69] and Uhlenbusch et al. [70] using a Q-Switch CO_2 laser showed the possibility of processing aluminum plates more than 3 mm in thickness because laser-induced plasma ignited between pulses absorbs the laser radiation very efficiently and transfers it to the workpiece. Moreover, plasma induces a high pressure on the molten material and helps to eject it. Dross-free cuts with good surface roughness were obtained. The same approach was conducted by Maher [68] during Nd:YAG laser cutting of 6061-T6 sheets with 750–1500 mm thickness using high repetition rate pulses. HAZ was found to have a small extension although uneven edges were obtained.

3.4.2 Miscellaneous Methods to Improve Cutting Process

3.4.2.1 Methods to Reduce Cracking Formation in Cutting of Ceramics

Apart from processing in pulsed mode, which was assessed in order to avoid fractures and thermal cracking, other methods have been proposed in order to obtain cuts free of these machining defects.

One of them is the preheating of the workpiece in order to reduce the thermal gradient imposed in the cutting edge to reduce the severity of the damage. Tönshoff and Gonschior [50,53] assessed this technique during the Co_2 laser cutting of Al_2O_3, avoiding the formation of microcracks. The principal drawback of this approach is the necessity of a furnace to heat the ceramic up to 1000°C. A possible solution was proposed by Modest

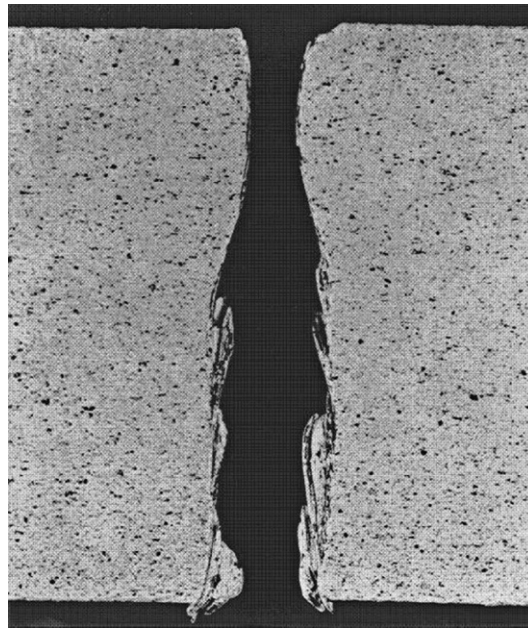


Fig. 3.3 Aluminum sheet with 940 mm in thickness cut by means of a diode-pumped Nd:YAG laser working at up to 220 kHz repetition rates. Cutting speed was adjusted at 5 cm/s. The assist gas flow is not able to remove completely the molten material from the rear part of the cut [68].

[71]. He pointed out the utilization of two superimposed laser beams, one focalized in order to generate the cut slot and the second one defocused in order to preheat the workpiece. An analogous approach was followed by Bernstein et al. [72] during the surface processing of high alumina refractory ceramics in order to control the thermal gradients and cooling rates with the objective of eliminating crack formation during solidification.

Another approach to avoid thermal cracking is cutting by multiple passes. Material is eliminated by means of successive passes to cut the workpiece entirely in depth. Thermal load applied to the ceramic in the cutting edge is reduced in this way. This approach was conducted by Black and Chua [45] during Co_2 laser cutting of ceramic tiles. Quintero et al. [73] followed this technique during Nd:YAG laser cutting of thick silicon infiltrated silicon carbide obtaining crack-free cuts and compared results with single-pass cutting. Multipass cutting has the distinct disadvantage of being a very time-consuming process.

A different approach to avoid microcracks is the technique of underwater cutting conducted with the objective of reducing the influence of heat

around the cut area, because heat will be rapidly dissipated to water. This approach was assessed by several authors [45,46,53,74]. While burnout was noted to be reduced, the intensity of thermal gradient was increased.

An innovative method to reduce thermal stresses is the utilization of a water jet, which guides the laser beam due to the difference in the refractive indices of air and water. This technique called water jet guide laser was assessed in ceramics as alumina or low temperature Co fired ceramic obtaining good quality results as depicted in Fig. 3.4 [75].

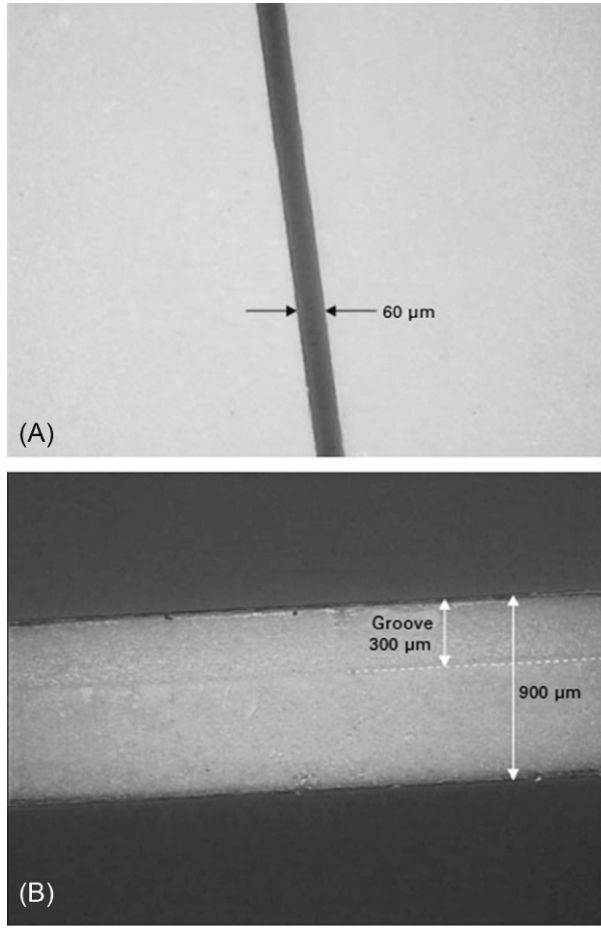


Fig. 3.4 (A) Top and (B) side view of a groove performed on Al_2O_3 ceramic. Experiments were performed with a high power frequency doubled Nd:YAG laser. *(Reprinted from P. Ogawa, D. Perrottet, F. Wagner, R. Housh, B. Richerzhagen, Fast cutting of ceramics with the water jet guided Nd:YAG Laser. The 5th International Symposium on Laser Precision Microfabrication, Nara, 2004, with permission of Synova SA.)*

3.4.2.2 Methods to Improve Cutting Process in Aluminum and Alloys

Some proposals were found to improve cutting process of aluminum and alloys primarily focused in the reduction of the high reflectivity of them. Surface treatments are the most common way to reduce this drawback. In this way, studies conducted by Arata and Miyamoto [76] and Arata et al. [25] allowed the absorption of aluminum under polished conditions to be obtained and compared the results with different surface treatments applied on aluminum such as roughened or anodized. They showed the extremely low absorption of aluminum at room temperature. This work showed the possibility of increasing absorption of these materials by means of surface treatments. Absorption was found to be larger by nearly a factor of 20 after roughening with sandpaper than under polished conditions, although it seems that fine sand particles on the surface of aluminum can be a consequence of the increment in absorption. On the other hand, it was confirmed that the presence of a non-metallic film such as Al_2O_3 after anodizing surfaces extremely increases the values of absorption. Anodizing can increase the cutting speed up to 30% [2]. Work performed by Hoult et al. [77] confirmed the improvement in cutting speed up to 2.5 times during CO_2 cutting when the surface of an AlMgSi alloy 1.2 mm in thickness was anodized. Results showed a significant increase in maximum speed with the thickness of the Al_2O_3 layer. Another approach to improve cutting efficiency is the utilization of paints on the surface of workpieces. Ketting et al. [21] painted the surface of pure aluminum and an AlMg alloy. Painting was seen to increase only cutting speed during processing pure aluminum. Utilization of paint was noted to produce more uneven surfaces. Coating with carbon was also applied. Although the cutting speed was not improved as compared to painted and untreated surfaces, the surface quality remained under conditions similar to an untreated surface. Masumoto et al. [23] showed that in coating with graphite dross is reduced. An original proposal to reduce reflectivity and increase processing rate is the application of ultraviolet radiation on the surface prior to or combined with infrared lasers [78,79]. The reduction in reflectivity was associated with the formation of an absorbing layer on the surface or with the roughening of the sample's surface.

Another approach to cut thick aluminum alloys free of dross was proposed by Masumoto et al. and also conducted by Masumoto et al. [23] and Dabezies and Alarcon [80] (see Fig. 3.5). This approach consisted of performing a first cut and then a following second cutting pass in which the location of the laser beam is shifted into the workpiece to remove the dross generated during the first pass. This approach has the inconvenience of a

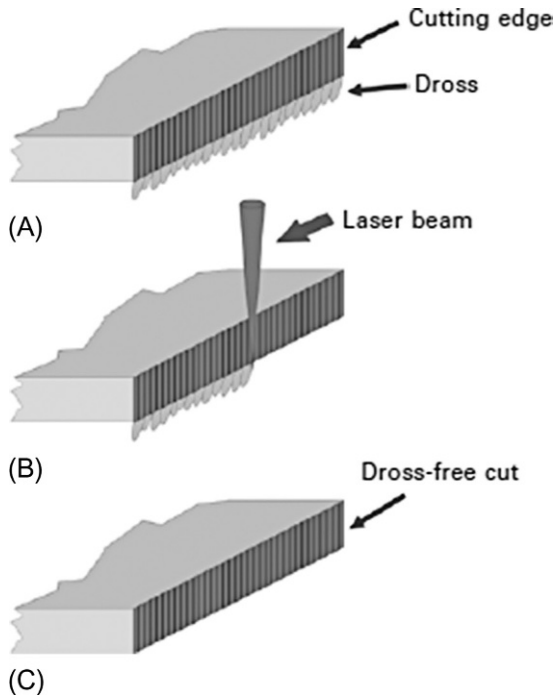


Fig. 3.5 Scheme of the dual cutting technique for thick aluminum sheet [23].

higher release of heat into the workpiece being counter-productive when thermally sensitive aluminum alloys are processed.

3.4.3 Role of the Assist Gas in Traditional Laser Cutting Process

Fusion laser cutting is strongly influenced by the dynamics of the assist gas jet. All studies devoted to the role of the assist gas during cutting agree that this is the main factor influencing the production rate and cut quality [47,81–85]. The assist gas exerts a thrust over the molten material to accelerate and eject it from the cutting front. Olsen demonstrated theoretically that the limiting factor affecting the maximum cutting rate is not the laser power but is instead the average pressure of the assist gas inside the cutting kerf [86].

The main parameters affecting the dynamics of the assist gas jet during cutting are assist gas pressure [82,87,88], standoff distance [82,83,88], gas jet-laser beam relative position [89,90], internal geometry of the nozzle [91], purity, and the nature of the assist gas [84,92].

Commonly, nozzles used to exhaust the assist gas have conical or cylindrical internal geometry [93]. These nozzles exhaust the assist gas in a coaxial manner with regard to the laser beam.

Maximization of momentum transfer from the gas flow to the molten material in order to efficiently extract the molten material [94] requires the development of a laminar boundary layer along the cutting front. Two driving forces—the gradient pressure and viscous friction—come into play to drag the molten material [13,95]. Both factors are increased with increasing gas velocity. Thus, to increase the removal of the molten material it is necessary to increase the gas velocity keeping a laminar boundary layer coupled to the molten material [96]. The easiest way to increase the gas velocity is to increase the supplying pressure. However, sonic coaxial nozzles can only expand the gas flow up to the sonic regime being the assist gas jet underexpanded if the supplying pressure is approximately increased up to two times the ambient pressure [87,97]. Underexpansion of jets after emerging from sonic nozzles produces a Prandtl-Meyer wave pattern (see Fig. 3.6) [94,97]. Reinforcement of shock waves when a gas jet impacts perpendicularly to the workpiece produces a normal shock wave called Mach shock disk (MSD) [81,98]. The strength of the jet is strongly dependent on the supplying pressure and the standoff distance [81]. MSD irreversibly decelerates the flow up to subsonic regime, dramatically reducing the velocity of the jet and momentum transfer from the gas to the molten material. On the other hand, the flow after passing the MSD suffers a strong compression, which increases its static pressure and induces a density gradient, locally changing the refractive index and acting as a lens defocusing the laser beam [99,100].

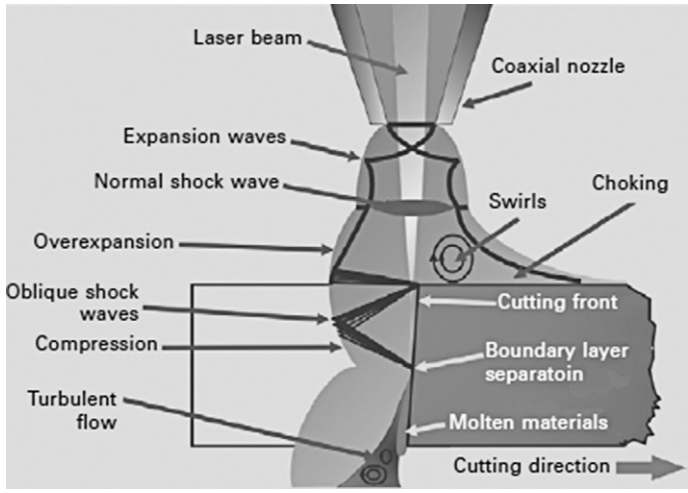


Fig. 3.6 Aerodynamic interactions during laser cutting using a conical sonic nozzle.

Another important outcome is the severe choking suffered by the assist gas jet when impinging on the entry cut kerf, which induces swirls and destabilizing the gas jet into the kerf [91,98]. After crossing the MSD, expansion waves are formed in the jet, being subsequently transformed into compression waves after being reflected in the jet boundaries. The coalescence of these compression waves leads to the formation of an oblique shock wave. The negative gradient pressure produced by the impact of this wave can produce the separation of the boundary layer formed by the assist gas and the molten material and the transformation into turbulence [94]. Then, removal capability of molten material is severely affected. Several investigations were conducted in order to determine the influence of operating parameters on the boundary layer separation and the relation with regard to the cut quality. Man et al. [101] and Duan et al. [102] studied the influence of the supplying pressure, standoff distance, kerf width, and material thickness by means of Shadowgraph technique on a simulated kerf. Highly underexpanded jets as a consequence of high supplying pressures were found to deteriorate the capability of dragging molten material. Also, standoff distance was found to be a relevant parameter affecting the final cut quality of the workpiece [82,88]. Leidinger et al. [103] also found the extreme dependence of cut quality with the standoff distance for highly underexpanded jets by means of numerical simulations and Schlieren photographs.

In summary, these aerodynamic interactions lead to the separation of the boundary layer, reducing the penetration of the assist gas into the kerf and finally leading to the decrease of dragging capabilities and worsening of the cut quality after the boundary layer separation. Therefore, two zones can be distinguished in the final cutting edges: a very smooth upper part and a rough lower part with the presence of a large amount of dross [47]. Detachment of the boundary layer affects both the finishing and the extension of the heat-affected zone in the cutting edge. HAZ is increased due to the additional release of heat from the solidification of the recast layer, a consequence of the non-removal of the molten material after the boundary layer separation.

3.4.3.1 Supersonic Nozzles

In accordance with the previous point, the improvement in the performance of the assist gas jet will lead to a substantial improvement of the cutting quality and processing rate. Several works were performed in order to avoid the MSD and reduce choking. Under these assumptions, a laminar

boundary layer attached to the cutting front will be formed. Consequently, assist gas inside the kerf has a uniform pressure and velocity, maximizing the momentum transfer to the molten material [96]. Rand [104] assessed the dependence of the boundary layer separation with regard to the supply pressure when cutting with a cutting head assisted by a conical-coaxial nozzle. Therefore, it is possible to improve the cut quality by means of the increment in supply pressure if the point of boundary layer separation is located out of the cutting front. However, thick-sectioned materials require using very high pressures and the assist gas consumption is greatly increased too.

In order to increase the gas velocity and maximize the momentum transfer to the molten material, supersonic nozzles with a converging-diverging internal geometry were assessed. Several authors conducted experimental plans to analyze the gas flow by means of numerical or visualization techniques such as Shadowgraph or Schlieren [101,103,105]. Cutting experiments were performed on several materials from mild steel to wood, detecting an improvement in cutting quality and processing rate [106,107]. Gas flow into the kerf was noted to be less sensitive to standoff and workpiece thickness when using supersonic nozzles instead of coaxial nozzles.

Other authors such as Hsu and Molian [108] and Ilavarasan and Molian [109] explored the performance of noncoaxial nozzles in conjunction with conical coaxial nozzles to improve material removal and cut quality. Analytical and experimental studies were performed in order to study the influence of the nozzle angle. Brandt and Settles [89] conducted an experimental plan to visualize the gas dynamics into the kerf for different nozzle angles and standoffs and supplying pressure. Off-axis nozzles at 35–40 degrees with regard to the laser beam substantially improved the cutting speed without deterioration of cut quality due to the most favorable shock wave-boundary layer interaction. Ketting and olsen [110] found during high-pressure laser cutting of an Al-Mg aluminum alloy the enlargement of the parameter range to obtain dross-free cuts when the laser beam is placed in front of the center of the nozzle as compared to on-axis cutting. The improvement is a consequence of the higher penetration of assist gas flow into the kerf.

Quintero et al. [96] performed experiments on laser cutting of advanced oxide ceramics by means of the combination of previously cited works in a self-designed experimental setup. Fig. 3.7 shows a scheme of the self-designed cutting head. Cut quality was found to be strongly dependent on the incidence point of the supersonic jet [85]. By means of the new injection system a complete removal of the molten material from the cutting front

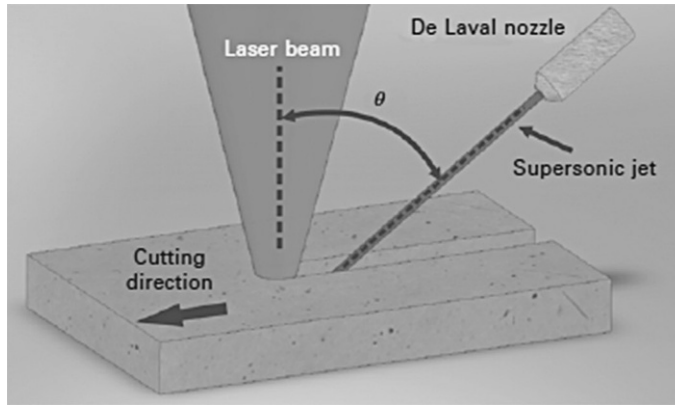


Fig. 3.7 Scheme of the off-axis cutting head incorporating a convergingdiverging nozzle [111].

during Nd:YAG and CO_2 laser cutting of thick-sectioned mullite-alumina workpieces was verified [47,96]. The elimination of the recast layer as compared to processing using conical coaxial nozzles led to the elimination of additional release of heat during solidification and consequently the HAZ is extremely reduced. Microcracks and fractures were avoided by means of this processing methodology. Fig. 3.8 depicts a comparison of the cutting results by means of the new injection system in comparison with those obtained through a conventional cutting head.

Riveiro et al. [111,112] experimentally assessed the performance of the previously cited new injection system in CO_2 laser cutting of 2024-T3 and 7075-T6 aluminum alloys. Processing of both materials by means of the optimized gas-injection system was found to exhibit a superior performance. Dross-free and smooth cut walls were obtained with a superior processing rate as compared to conventional cutting heads. Fig. 3.9 shows a comparison of cut profiles obtained in CW mode with a conventional cutting head and with the optimized assist gas-injection system. Also a noticeable reduction of the HAZ can be noted when using the new cutting head. Superior finishing makes it possible to use this technology to cut these materials for applications in severe working conditions due to the reduced HAZ and absence of cracks and microcracks.

3.4.3.2 High-Pressure Laser Cutting

As shown by Rand [104], the increment of the assist-gas pressure produces a boundary layer separation in a lower position of the cutting edge. Therefore, smooth cuts with a low level of dross can be obtained by increasing the

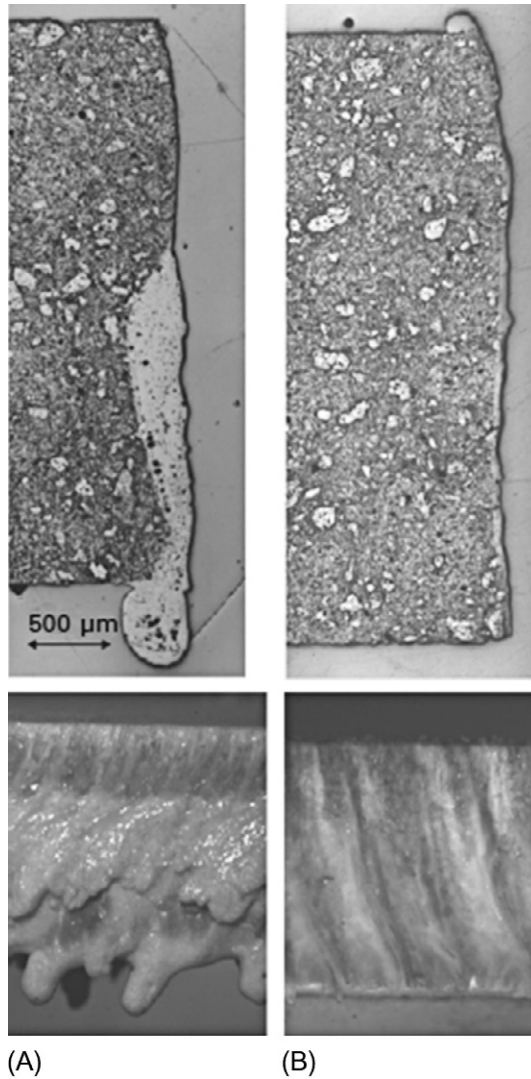


Fig. 3.8 Micrographs of the cross-section and cutting edge obtained during processing by means of different injection systems of assist gas of a mullite-alumina composite 5 mm in thickness. (A) Cutting head assisted by a sonic coaxial nozzle. (B) Cutting head assisted by a supersonic off-axial nozzle [96].

assist gas consumption. Lower detachment of the boundary layer during Co_2 laser cutting of the 2024-T3 alloy as a consequence of the increment in the assist-gas pressure from 3 to 8 bar was assessed by Riveiro et al. [111]. Aluminum alloys have been processed under this approach to improve the cutting process in terms of production rate and quality. Anon [113] has

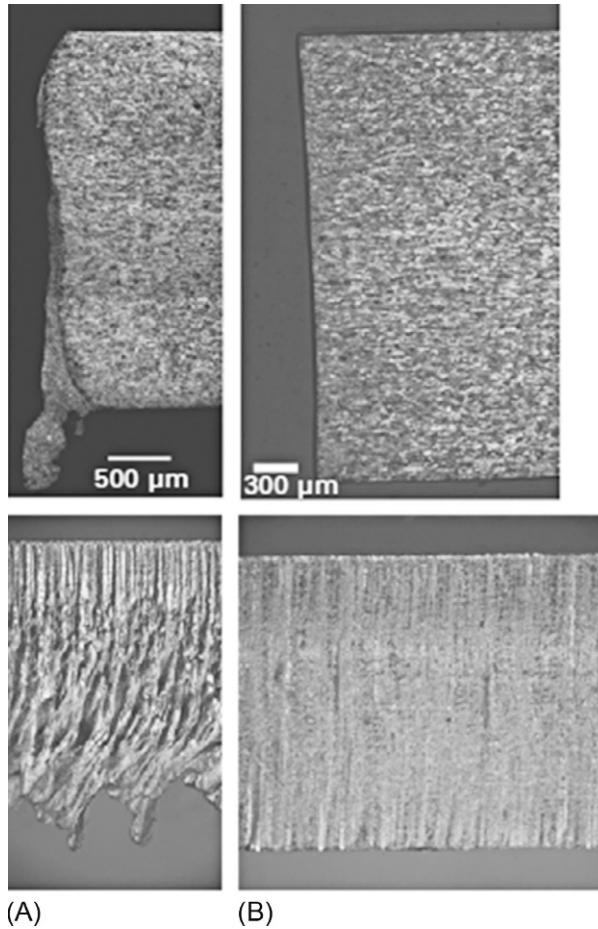


Fig. 3.9 Micrographs of the cross-section and cutting edge obtained during processing by means of different injection systems of assist gas of an AlCu alloy 3 mm in thickness. (A) Cutting head assisted by a sonic coaxial nozzle. (B) Cutting head assisted by a supersonic offaxial nozzle.

shown the possibility of cutting sheet metal of up to 3 mm thick using inert gases at high pressure. Also, Biermann et al. [114] processed aluminum alloys at high pressure and examined cuts from a quality point of view. The same approach was conducted by Ketting and Olsen [110] and Ketting et al. [21] during cutting pure aluminum and an AlMg alloy. Dross-free cuts or cuts with small and easily removable dross were obtained during cutting sheets with 1–2 mm in thickness using n_2 at pressures from 5 to 15 bar. Results were improved if the assist gas jet was moved away with regard to the laser beam as previously mentioned.

3.5 CONCLUSIONS

This chapter summarizes those works dealing with laser cutting of difficult materials. Works performed on laser cutting of two selected groups of materials, namely ceramics and aluminum alloys, were presented. This chapter shows the problems related with this kind of machining technique and the attempts to solve them from different perspectives, namely improving the assist gas dynamics, optimizing the laser beam management, or varying the method of processing.

Although many works have been carried out, several improvements are necessary to transform laser-cutting techniques of these materials and others as composite materials in a routine machining technique from an industrial point of view. New developments, such as those performed on the high-brightness laser sources, open new possibilities for laser-assisted cutting of difficult materials, expanding the processing limits.

ACKNOWLEDGMENTS

This work has been partially financed by different grants from the European Union, the Spanish government, Xunta de Galicia and the University of Vigo.

REFERENCES

[1] D. Belforte, Economic review and forecast, Industr. Laser Solut. 23 (2008) 8–14.
[2] J. Powell, CO_2 Laser Cutting, Springer, London; New York, 1998.
[3] W.M. Steen, Laser Material Processing, Springer, London; New York, 2003.
[4] G.E. Totten, D.S. Mackenzie, Handbook of Aluminum, Marcel-Dekker, New York; Basel, 2003.
[5] M.W. Barsoum, Fundamentals of Ceramics, McGraw Hill, New York, 1997.
[6] I. Miyamoto, H. Maruo, Mechanism of laser cutting, Welding in the World, Le Soudage Dans Le Monde 29 (1991) 283–294.
[7] F.O. Olsen, Fundamental mechanisms of cutting front formation in laser cutting, in: Laser Materials Processing: Industrial and Microelectronics Applications, first ed., SPIE, Vienna, 1994.
[8] A.F.H. Kaplan, Theoretical Analysis of Laser Beam Cutting, Shaker Verlag GmbH, Aachen, 2002.
[9] D. Bäuerle, Laser Processing and Chemistry, Springer-Verlag, Berlin; New York, 2000.
[10] M. Von Allmen, A. Blatter, Laser-beam interactions with materials: physical principles and applications, Springer, Berlin; New York, 1995.
[11] W. Schulz, D. Becker, J. Franke, R. Kemmerling, G. Herziger, Heat conduction losses in laser cutting of metals, J. Phys. D. Appl. Phys. 26 (1993) 1357–1363.
[12] V. Semak, A. Matsunawa, The role of recoil pressure in energy balance during laser materials processing, J. Phys. D. Appl. Phys. 30 (1997) 2541–2552.
[13] M. Vicanek, G. Simon, Momentum and heat transfer of an inert gas jet to the melt in laser cutting, J. Phys. D. Appl. Phys. 20 (1987) 1191–1196.

[14] A. Ivarson, J. Powell, J. Kamalu, C. Magnusson, The oxidation dynamics of laser cutting of mild steel and the generation of striations on the cut edge, J. Mater. Process. Technol. 40 (1994) 359–374.
[15] J.G. Siekman, Cutting of thin metal films with a CO_2-gas laser beam, Microelectron. Reliab. 7 (1968) 305.
[16] R.L. Waters, M.J. Weiner, Resistor trimming and other micromachining with a YAG laser, Solid State Technol. 13 (4) (1970) 43–49.
[17] E.V. Locke, R.A. Hella, Metal processing with a high-power CO_2 laser, IEEE J. Quantum Electron. QE-10 (1974) 179–185.
[18] M. Dell'erba, G. Daurelio, M. Ferrara, CO_2 laser cutting process of thick aluminium, Appl. Phys. Commun. 5 (1985) 23–35.
[19] M. Murakawa, H. Miyazawa, S. Sakai, K. Ohkawa, Cutting of aluminium plate with medium output CO_2 laser, Bull. Jpn. Soc. Prec. Eng. 19 (1985) 223–224.
[20] C.Y. Jiang, W.S. Lau, T.M. Yue, L. Chiang, On the maximum depth and profile of cut in pulsed Nd:YAG laser machining, CIRP Ann. Manuf. Technol. 42 (1993) 223–226.
[21] H.-O. Ketting, K. Schwendner, G. Bech-Nielsen, I. Chorkendorff, F.O. Olsen, Advanced surface analysis on high-pressure CO_2 laser cut test pieces in pure and alloyed aluminum, Laser Materials Processing: Industrial and Microelectronics Applications, first ed., SPIE, Vienna, 1994.
[22] J.K. Kar, L. Migliore, Metallurgical characteristics of laser cut aerospace alloys, in: Proceedings of ICALEO'90, Boston, MA, 1990.
[23] I. Masumoto, M. Kutsuna, K. Ichikawa, Relation between process parameters and cut quality in laser cutting of aluminum alloys, Trans. Jpn. Weld. Soc. 23 (1992) 38–45.
[24] A. Mostafa, Z. Kalazi, J. Takacs, Slag-free laser cutting for aluminum, in: Laser Materials Processing: Industrial and Microelectronics Applications, 1, SPIE, Vienna, 1994.
[25] Y. Arata, H. Maruo, I. Miyamoto, S. Takeuchi, Quality in laser-gas-cutting stainless steel and its improvement, Trans. JWRI 10 (1981) 129–139.
[26] M. Aritoshi, K. Okita, K. Yasuda, N. Arai, I. Takai, S. Funai, Study on cutting of thin aluminum alloy plates by CO_2 laser, Nippon Kikai Gakkai Ronbunshu, C Hen/Trans. Jpn. Soc. Mech. Eng. C 54 (1988) 2794–2801.
[27] D. Araújo, F.J. Carpio, D. Méndez, A.J. García, M.P. Villar, R. García, D. Jiménez, L. Rubio, Microstructural study of CO_2 laser machined heat affected zone of 2024 aluminum alloy, Appl. Surf. Sci. 208–209 (2003) 210–217.
[28] G. Scavino, S. Guelfo, F. D'aiuto, M. Rosso, Laser cutting effects on aluminium sheets mechanical properties, Metall. Ital. 99 (2007) 33–42.
[29] F.J. Carpio, D. Araújo, F.J. Pacheco, D. Méndez, A.J. García, M.P. Villar, R. García, D. Jiménez, L. Rubio, Fatigue behaviour of laser machined 2024T3 aeronautic aluminium alloy, Appl. Surf. Sci. 208–209 (2003) 194–198.
[30] G. Bech-Nielsen, M. Kjaer Larsen, H.O. Ketting, I. Chorkendorff, A corrosion study of laser-cut edges of aluminium and Al_3Mg alloy using CMT (corrosion measurement by titration) and EC (electrochemical) measurements, Corros. Sci. 36 (1994) 759–771.
[31] R. Belland, Laser scribing and drilling of ceramic substrates, Electron. Packag. Prod. 15 (1975) 56–58.
[32] D.J. Garibotti, Dicing of Micro-Semiconductors, United Aircraft Corp, 1963.
[33] J. Longfellow, Sawing alumina substrates with a CO_2 laser, Am. Ceram. Soc. Bull. 52 (1973) 513–515.
[34] S.M. Copley, M. Bass, Shaping materials with a continuous wave carbon dioxide laser, Highw. Eng. 26 (1979) 121–134.
[35] S.W. Copley, R.J. Wallace, M. Bass, Laser shaping of materials, in: Proceedings of ASM Conference on Lasers in Materials Processing, Los Angeles, CA, 1983, pp. 82–92.
[36] M. Naeem, M.E. Preston, J.R. Tyrer, Processing of engineering ceramics with high power CO_2 lasers, Mater. Des. 10 (1989) 281–285.

[37] A. Kitagawa, A. Matsunawa, Three-Dimensional Shaping of Ceramics by Using CO_2 Laser and Its Optimum Processing Condition, Laser Institute of America, Boston, MA, 1991.
[38] S.A.J. Livingstone, I. Black, CO_2 laser cutting of ceramic tile, Lasers Eng. 5 (1996) 127.
[39] R.N. Smith, R.T. Surprenant, D.A. Kaminshki, Fracture characteristics of an aluminum oxide ceramic during continuous wave carbon dioxide laser cutting, J. Laser Appl. 4 (1992) 25–32.
[40] J.H. Zhang, T.C. Lee, X. Ai, W.S. Lau, Investigation of the surface integrity of laser-cut ceramic, J. Mater. Process. Technol. 57 (1996) 304–310.
[41] G. Lu, E. Siores, B. Wang, An empirical equation for crack formation in the laser cutting of ceramic plates, J. Mater. Process. Technol. 88 (1999) 154–158.
[42] M.F. Modest, Transient elastic and viscoelastic thermal stresses during laser drilling of ceramics, J. Heat Transf. 120 (1998) 892–898.
[43] M.F. Modest, T.M. Mallison, Transient elastic thermal stress development during laser scribing of ceramics, J. Heat Trans. T. ASME 123 (2001) 171–177.
[44] I. Black, Laser cutting speeds for ceramic tile: a theoretical-empirical comparison, Opt. Laser Technol. 30 (1998) 95–101.
[45] I. Black, K.L. Chua, Laser cutting of thick ceramic tile, Opt. Lasers Technol. 29 (1997) 193–205.
[46] I. Black, S.A.J. Livingstone, K.L. Chua, A laser beam machining (LBM) database for the cutting of ceramic tile, J. Mater. Process. Technol. 84 (1998) 47–55.
[47] F. Quintero, J. Pou, F. Lusquiños, M. Boutinguiza, R. Soto, M. Pérez-Amor, F. Wagner, Comprehensive assessment of the CO_2 laser cut quality of ceramics with different assist gas injection systems, J. Laser Appl. 16 (2004) 212–220.
[48] X.Y. Wang, W.J. Xu, R.K. Kang, Y.D. Liang, Laser cutting quality of the ceramic slabs, Prog. Adv. Manuf. Micro/Nano Technol. 2005 (Pt 1 and 2) (2006) 505–507. 847–852.
[49] A.J. Murray, J.R. Tyrer, Nd :YAG laser cutting and drilling of PSTZ—influence of substrate heating temperature on recast layer microcracking, J. Laser Appl. 11 (1999) 128–135.
[50] H.K. Tönshoff, M. Gonschior, Ceramics processing with laser radiation, in: Proceedings del ICALEO'93, Laser Materials Processing, Orlando, FL, Laser Institute of America, 1993.
[51] M.F. Trubelja, S. Ramanathan, M.F. Modest, V.S. Stubican, Carbon dioxide laser cutting of a carbon-fiber-silicon carbide-matrix composite, J. Am. Ceram. Soc. 77 (1994) 89–96.
[52] F.O. Olsen, L. Alting, Pulsed laser materials processing, Nd:YAG versus CO_2 Lasers, CIRP Ann. Manuf. Technol. 44 (1995) 141–145.
[53] H.K. Tönshoff, M. Gonschior, Reduction of crack damage in laser cutting of ceramics, in: Proceedings of the LAMP '92, Laser Advanced Materials Processing, 2, 1992, pp. 645–650.
[54] S.A.J. Livingstone, K.L. Chua, I. Black, Experimental development of a machining database for the CO_2 laser cutting of ceramic tile, J. Laser Appl. 9 (1997) 233–241.
[55] I. Black, Laser cutting decorative glass, ceramic tile, Am. Ceram. Soc. Bull. 77 (1998) 53–57.
[56] I. Black, Severance energies for non-metallic materials: part 2—decorative glass and ceramic tile, Lasers Eng. 11 (2001) 165–172.
[57] I. Shigematsu, K. Kanayama, Y. Hirai, M. Nakamura, Machining of cordierite ceramics by CO_2-laser, J. Ceram. Soc. Jpn. 101 (1993) 604–606.
[58] P. Burck, K. Wiegel, Laser machining of Si3N4 ceramics, Opt. Quant. Electron. 27 (1995) 1349–1358.
[59] C. Durand, M. Ramulu, R. St Pierre, J. Machan, An experimental analysis of a Nd:YAG laser cutting process for machining silicon nitride, Int. J. Prod. Res. 34 (1996) 1417–1428.

[60] A.S. Kuar, B. Doloi, B. Bhattacharyya, Experimental investigations on Nd:YAG laser cutting of silicon nitride, Int. J. Manuf. Technol. Manag. 7 (2005) 181–191.
[61] K. Ogata, N. Miyanagi, K. Suzuki, Y. Shimomura, Ceramics Cutting With Pulsed Nd:YAG Laser, LIA (Laser Institute of America), 1991.
[62] I.P. Tuersley, T.P. Hoult, I.R. Pashby, Nd-YAG laser machining of SiC fibre/borosilicate glass composites. Part II. The effect of process variables, Compos. A: Appl. Sci. Manuf. 29 (1998) 955–964.
[63] I.P. Tuersley, T.P. Hoult, L.R. Pashby, Nd-YAG laser machining of SiC fibre borosilicate glass composites. Part I. Optimisation of laser pulse parameters, Compos. A: Appl. Sci. Manuf. 29 (1998) 947–954.
[64] T. Kristensen, F. Olsen, Investigation of cutting of Al alloys with pulsed and CW CO_2 lasers, Welding in the World, Le Soudage Dans Le Monde 33 (1994) 355–361.
[65] A. Stournaras, P. Stavropoulos, G. Chryssolouris, Investigation of laser cutting quality of aluminium, in: Lia (Eds.), Proceedings of ICALEO'06, Scottsdale, 2006.
[66] A. Dubey, V. Yadava, Robust parameter design and multi-objective optimization of laser beam cutting for aluminium alloy sheet, Int. J. Adv. Manuf. Technol. 38 (2008) 268–277.
[67] A.K. Dubey, V. Yadava, Optimization of kerf quality during pulsed laser cutting of aluminium alloy sheet, J. Mater. Process. Technol. 204 (2008) 412–418.
[68] W. Maher, Laser cutting of aluminum with high-repetition-rate pulses, in: Lasers as Tools for Manufacturing II, first ed., SPIE, San Jose, CA, 1997.
[69] A. Michaelis, J.H. Schaefer, J. Uhlenbusch, W. Vioel, Cutting and welding of aluminum with a high-repetition-rate pulsed CO_2 laser, in: CO_2 Lasers and Applications II, first ed., SPIE, The Hague, 1990.
[70] J. Uhlenbusch, U. Bielesch, S. Klein, M. Napp, J.H. Schäfer, Recent developments in metal processing with pulsed laser technology, Appl. Surf. Sci. 106 (1996) 228–234.
[71] M.F. Modest, Minimization of elastic thermal stresses during laser machining of ceramics using a dual-beam arrangement, J. Laser Appl. 13 (2001) 111–117.
[72] J.R. Bernstein, D. Triantafyllidis, L. Li, F.H. Stott, Characterization of high alumina refractory ceramics treated with combined two laser surface processing, in: W.J. Meng, A. Kumar, G.L. Doll, Y.T. Doll, S. Veprek, Y.W. Chung (Eds.), Materials Research Society Symposium—Proceedings, Boston, MA, 2002.
[73] F. Quintero, J. Pou, F. Lusquiños, A. Riveiro, M. Pérez-Amor, A.J.S. Fernandes, Single-pass and multi-pass laser cutting of Si-SiC: assessment of the cut quality and microstructure in the heat affected zone, J. Laser Appl. 19 (2007) 170–176.
[74] N. Morita, S. Ishida, Y. Fujimori, K. Ishikawa, Pulsed laser processing of ceramics in water, Appl. Phys. Lett. 52 (1988) 1965–1966.
[75] P. Ogawa, D. Perrottet, F. Wagner, R. Housh, B. Richerzhagen, Fast cutting of ceramics with the water jet guided Nd:YAG Laser, in: The 5th International Symposium on Laser Precision Microfabrication, Nara, 2004.
[76] Y. Arata, I. Miyamoto, Some fundamental properties of high power laser beam as a heat source (report 2): CO_2 laser absorption characteristics of metal, Trans. Jpn. Weld. Soc. 3 (1972) 152–162.
[77] A.P. Hoult, M.Y. Shan, B. Bryden, I.R. Pashby, Semiquantitative approach to the effect of anodized layer thickness on laser cutting of an aluminium alloy, in: XI International Symposium on Gas Flow and Chemical Lasers and High-Power Laser Conference, first ed., SPIE, Edinburgh, 1997.
[78] G. Kinsman, W.W. Duley, Enhancing the 10.6 μm absorptivity of copper and aluminum using excimer laser radiation, Appl. Phys. Lett. 54 (1989) 7–9.
[79] G. Scott, S.W. Williams, P.C. Morgan, M. Dempster, Enhancing the absorption of aluminum alloys by irradiation with an excimer laser, Laser Materials Processing: Industrial and Microelectronics Applications, first ed., SPIE, Vienna, 1994.

[80] B. Dabezies, C. Alarcon, Laser cutting of aluminium alloys, in: Conference on Lasers and Electro-Optics Europe—Technical Digest, IEEE, Amsterdam, 1994.
[81] K. Chen, Y.L. Yao, V. Modi, Gas jet-workpiece interactions in laser machining, J. Manuf. Sci. E. T. ASME 122 (2000) 429–438.
[82] J. Fieret, M.J. Terry, B.A. Ward, Aerodynamic interactions during laser cutting, in: Proceedings of SPIE—The International Society for Optical Engineering, Quebec City, vol. 668, 1986, pp. 53–62.
[83] H.C. Man, J. Duan, T.M. Yue, Behaviour of supersonic and subsonic gas jets inside laser cut kerfs, in: Laser Institute of America, Proceedings, Pt. 1, Laser Inst of America, San Diego, CA, 1997.
[84] J. Powell, A. Ivarson, J. Kamalu, G. Broden, C. Magnusson, Role of oxygen purity in laser cutting of mild steel, in: D. Farson, W. Steen, I. Miyamoto (Eds.), Proceedings of SPIE—The International Society for Optical Engineering, Orlando, FL, Society of Photo-Optical Instrumentation Engineers, 1993.
[85] F. Quintero, J. Pou, J.L. Fernández, A.F. Doval, F. Lusquiños, M. Boutinguiza, R. Soto, M. Pérez-Amor, Optimization of an off-axis nozzle for assist gas injection in laser fusion cutting, Opt. Lasers Eng. 44 (2006) 1158–1171.
[86] F. Olsen, An evaluation of the cutting potential of different types of high power lasers, in: Proceedings of ICALEO'06, LIA, Scottsdale, 2006.
[87] H.C. Man, J. Duan, T.M. Yue, Dynamic characteristics of gas jets from subsonic and supersonic nozzles for high pressure gas laser cutting, Opt. Laser Technol. 30 (1998) 497–509.
[88] B.A. Ward, Supersonic Characteristics of Nozzles Used With Lasers for Cutting, Laser Inst of America, Boston, MA, 1985.
[89] A.D. Brandt, G.S. Settles, Effect of nozzle orientation on the gas dynamics of inert-gas laser cutting of mild steel, J. Laser Appl. 9 (1997) 269–277.
[90] H. Zefferer, D. Petring, E. Beyer, Investigations of the Gas Flow in Laser Beam Cutting, DVS-Verlag, 1991.
[91] A.V. La Rocca, L. Borsati, M. Cantello, Nozzle design to control fluid-dynamics effects in laser cutting, in: Laser Materials Processing: Industrial and Microelectronics Applications, first ed., SPIE, Vienna, 1994.
[92] J.T. Gabzdyl, D.A. Morgan, Assist gases for laser cutting of steels, in: D. Farson, W. Steen, I. Miyamoto (Eds.), Proceedings of SPIE—The International Society for Optical Engineering, Orlando, FL, Society of Photo-Optical Instrumentation Engineers, 1993.
[93] J.F. Ready, D.F. Farson, T. Feeley, LIA Handbook of Laser Materials Processing, Laser Institute of America, Orlando, FL, 2001.
[94] M.J. Zucrow, J.D. Hoffman, Gas Dynamics, John Wiley & Sons, New York, 1976.
[95] B. Rao, A. Nath, Melt flow characteristics in gas-assisted laser cutting, Sadhana 27 (2002) 569–575.
[96] F. Quintero, J. Pou, F. Lusquiños, M. Boutinguiza, R. Soto, M. Pérez-Amor, Comparative study of the influence of the gas injection system on the Nd: yttrium-aluminum-garnet laser cutting of advanced oxide ceramics, Rev. Sci. Instrum. 74 (2003) 4199–4205.
[97] A.H. Shapiro, The dynamics and thermodynamics of compressible fluid flow, Ronald Press Co, New York, 1953.
[98] J.C. Carling, B.L. Hunt, The near wall jet of a normally impinging, uniform, axisymmetric, supersonic jet, J. Fluid Mech. 66 (1974) 159–176.
[99] J.N. Kamalu, W.M. Steen, Importance of Gas Flow Parameters in Laser Cutting, Metall Soc of AIME, Chicago, IL, 1981.
[100] H.C. Man, J. Duan, T.M. Yue, Design and characteristic analysis of supersonic nozzles for high gas pressure laser cutting, J. Mater. Process. Technol. 63 (1997) 217–222.

[101] H.C. Man, J. Duan, T.M. Yue, Analysis of the dynamic characteristics of gas flow inside a laser cut kerf under high cut-assist gas pressure, J. Phys. D. Appl. Phys. 32 (1999) 1469–1477.
[102] J. Duan, H.C. Man, T.M. Yue, Three-dimensional modelling of the gas field distribution of a high-pressure gas jet used in laser fusion cutting, J. Laser Appl. 13 (2001) 239–246.
[103] D. Leidinger, D. Schuöcker, Investigations of the gas flow of conic-cylindrical and supersonic nozzles in a laser cut kerf, in: Gas Flow and Chemical Lasers: Tenth International Symposium, first ed., SPIE, Friedrichshafen, 1995.
[104] C. Rand, The study of sonic and supersonic jet-kerf dynamics in optimised laser cutting, PhD Thesis, The University of Liverpool, 2004.
[105] F.B. Thomassen, F.O. Olsen, Experimental studies in nozzle design for laser cutting, in: Proceedings of the 1st International Conference on Lasers in Manufacturing, Brighton, East Sussex, England, IFS (Publ) Ltd, 1983.
[106] K. Mukherjee, T. Grendzwell, P.A.A. Khan, C.W. Mcmillin, Gas flow parameters in laser cutting of wood—nozzle design, For. Prod. J. 40 (1990) 39–42.
[107] H. Semrau, H.K. Tönshoff, Laser gas cutting using Laval nozzles, Proc. SPIE 1988 (1990) 449–458.
[108] M.J. Hsu, P.A. Molian, Off-axial, gas-jet-assisted, laser cutting of 6.35-mm thick stainless steel, J. Eng. Ind. 117 (1995) 272–276.
[109] P.M. Ilavarasan, P.A. Molian, Laser cutting of thick sectioned steels using gas flow impingement on the erosion front, J. Laser Appl. 7 (1995) 199–209.
[110] H.O. Ketting, F. Olsen, High pressure off-axis laser cutting of stainless steel and aluminium, in: Proceedings of LAMP'92, Nagaoka, 1992.
[111] A. Riveiro, F. Quintero, F. Lusquiños, J. Pou, M. Pérez-Amor, Laser cutting of 2024-T3 aeronautic aluminum alloy, J. Laser Appl. 20 (2008) 230–235.
[112] A. Riveiro, B. Davila, F. Quintero, F. Lusquiños, R. Comesaña, J. Pou, An outlook into the laser cutting of aeronautic aluminium alloys, in: V. Kujanpää, A. Salminem (Eds.), 11th NOLAMP Conference in Laser Processing of Materials, Lappeenranta University of Technology, Lappeenranta, 2007.
[113] Anon, Burr-free laser cutting of aluminium materials, Gratfreies Laserschneiden von Al-Werkstoffen 31 (1990) 151–152.
[114] B. Biermann, S. Biermann, H.W. Bergmann, Cutting of Al-alloys using high-pressure coaxial nozzle, J. Laser Appl. 3 (1991) 13–20.

This page intentionally left blank

CHAPTER 4

Laser-Assisted Glass Cleaving

J. Lawrence*, Y.L. Kuo†, J. Lin†
*University of Chester, Chester, United Kingdom
†National Cheng Kung University, Tainan, Taiwan

4.1 INTRODUCTION

In the past decades, ever since laser machining became popular in the manufacturing industries, new processes such as laser marking and laser engraving have been fully developed. Recently laser machining has been developed rapidly for intensive application to nonmetals. One of the new technologies is laser cleaving, which finds many applications in machining glass, ceramic, and many other brittle materials [1,2]. The conventional laser machining methods for glass are mostly based on the thermal breaking mechanism. The melting zone with side cracking is significantly large in the full body cutting for the glass thickness from 30 μm to 1 mm. Alternatively the laser scribing method by focused/defocused laser beams has been proposed to cleave the glass with the thickness from 200 to 10 mm. Recently the laser system with multiple beam refection for the near infrared laser has been successfully applied to separate glass with a thickness larger than 10 mm. However, the above method is limited to practical applications due to the difficulties of the implementation of the beam reflector for the poor environment in the job shops.

The laser cleaving processes with the thermal shock effects have been applied to separate the brittle materials without the removal of the substrate materials. Because of the extraordinary cutting performance of the brittle materials by a focused laser beam, many studies have been carried out in literature. The main concerns in laser cleaving are the machined surface characteristics and cleaving efficiency, both of which are dramatically influenced by the laser beam mode. The thermal cleaving process is based on the fracture mechanism of the brittle substrates caused by a large temperature gradient. Using one or several laser beams to generate a steep temperature gradient near the heating zone, the thermal shock wave could propagate and coincide with the laser beam path in a controllable situation [3]. For example, Lumley et al. [4] have successfully applied CO_2 laser in the cleaving of alumina and glass.

Advances in Laser Materials Processing
https://doi.org/10.1016/B978-0-08-101252-9.00004-2
Copyright © 2018 Elsevier Ltd.
All rights reserved.

Paterson et al. [5] found that a tremendous tensile stress state was generated to cleave the glass sheets by a line-shaped laser beam due to a high temperature gradient on the glass substrate. The mechanism of controlling the fracture mode in the laser cleaving has also been studied recently by other researchers [3]. Accordingly, the shape of the beam spot is a key issue to dominate the heat diffusion, temperature, and stress distributions on the cleaving area. However, very few studies have been made to investigate the effects of the intensity profile of the laser beam in the cleaving process [5], and it can be found that the fracture of the substrate is merely initiated on the surface irradiated with a laser beam. Since the most important need is for a deep and clean cut for the glass substrate at high speed, especially for the LCD panel industries, the control of the thermal stress profiles in the depth of the substrate is an important task. It has only been the subject of limited investigation by Kuo and Lin [6] with multiple laser sources in laser cleaving.

4.2 THE MULTIPLE LASER SYSTEM

The proposed innovative technology consists of a line-shaped CO_2 laser beam (10.6 μm) to preheat the glass surface, a pulsed Nd:YAG laser beam (1.06 μm) to penetrate the thermal cracking, and a cooling air stream to build a steep temperature gradient. Owing to high absorption of the Nd:YAG laser at a wavelength of 1.06 μm at an elevated temperature state of the soda-lime glass [7], a pulsed Nd:YAG laser beam was imposed along the cleaving path preheated by the CO_2 laser beam in order to generate an intensive stress state inside the glass substrate. Fig. 4.1 is an illustration of the arrangements of the multiple laser beam system used in glass cleaving.

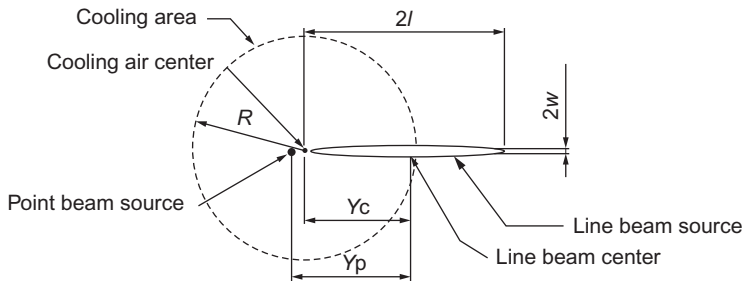


Fig. 4.1 Locations of the line-shaped beam, pulsed laser beam, and the cooling air stream in the laser cleaving process.

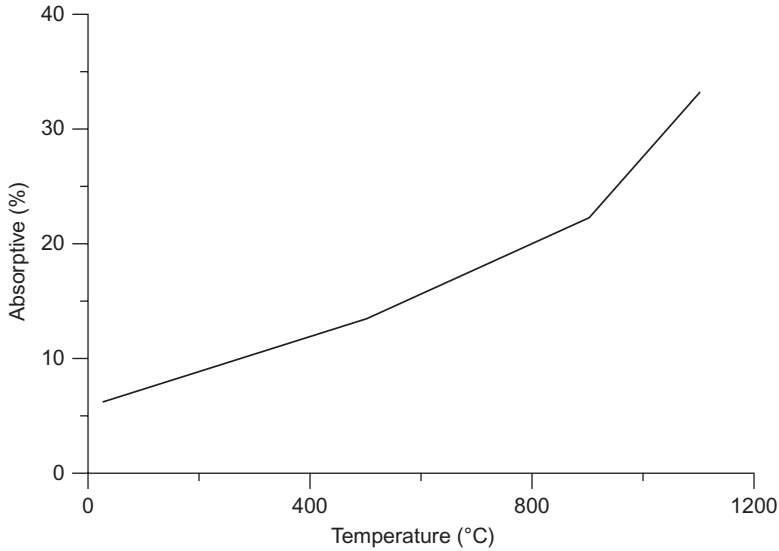


Fig. 4.2 Relationship between the absorption coefficient and temperature of soda-lime glass for Nd:YAG laser radiation (wavelength of 1.06 μm).

Fig. 4.2 shows the relationship between the absorption coefficient and the temperature of the soda-lime glass for the Nd:YAG laser radiation (wavelength of 1.06 μm) [2,7]. It can be seen that the absorption coefficient increases with the temperature; the value is up to 35% at the glass temperature of 1200°C. According to a significant change of the absorption in the near infrared radiation, the wavelength of 1.06 mm of the pulsed Nd:YAG laser beam makes it possible to partially transmit into the glass substrate and heat up the glass sheet as an internal heat source. In comparison with the laser scribing by the CO_2 laser radiating on the surface of the glass sheet, the multiple laser system would provide a deep and intense stress state due to the implementation of the pulsed Nd:YAG laser.

4.3 NUMERICAL SIMULATION

With the proposed multiple laser system, the cleaving mechanism on the glass substrate has not yet been fully investigated. The stress fields of the glass sheets in the line-shaped laser combined with pulsed laser need to be analyzed in detail. The phenomenon of crack propagation in the cleaving path caused by a multiple laser beam system has been observed in this research. Laser cleaving includes temperature distribution, stress field and property variation, all of which are significantly interrelated. In order to simplify

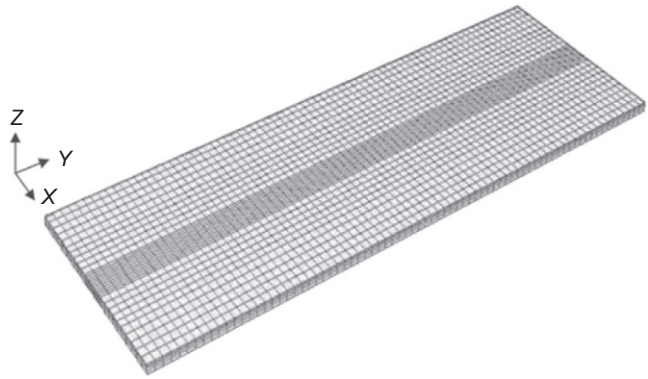


Fig. 4.3 Geometry and grid structure of the glass substrate in the numerical analysis.

the analysis, the problem of the laser cleaving on glass sheets herein will be decoupled by two distinct analytical models: the thermal model and the mechanical model in the thermal-elastic numerical analysis.

A soda-lime glass specimen was selected with the dimensions of $76 \times 26 \times 1\,mm^3$ as illustrated in Fig. 4.3. Using the software ABAQUS [8], the element was adopted in the thermal analysis and the computational domain with the meshes shown in Fig. 4.3, where a fine meshing around the laser beam was applied to simulate the steep temperature gradients around the heating zone. The domain meshes used for the stress analysis are the same, but an alternative element type was replaced to calculate the stress and displacement.

4.3.1 Assumptions and Boundary Conditions

The following assumptions are made in the thermal and stress analyses:

(1) The mechanical and thermal properties are isotropic.
(2) The laser intensity distribution is Gaussian mode.
(3) The thermal boundaries with free convection and thermal radiation in the surrounding air are considered.
(4) There is no phase change during laser heating.
(5) The specimen is assumed to be annealed before laser cleaving, and its initial condition is free of stress.
(6) The stress-strain relationship of the glass substrate is perfectly elastic.
(7) Body force has been ignored.

The temperature-dependent properties such as the thermal conductivity, specific heat, Poisson's ratio, and Young's modulus of soda-lime glass have been considered in the simulation and the relationships at various temperatures can be found in Ref. [9].

Numerous factors affect the reflectivity [7]. For simplification, the initial temperature of the specimen is assumed to be the ambient temperature $T_\infty = 25°C$. The thermal radiation has been considered, therefore the heat of radiation is $q = \varepsilon\sigma\left(T^4 - T_\infty^4\right)$, where the surface emissivity is $\varepsilon = 0.8$ [10] and the Stefan-Boltzmann constant is $\sigma = 5.670 \times 10^{-8} \mathrm{W/m^2 K^4}$. The heat convection from the surface of the specimen to the surrounding air is expressed as $-k\dfrac{\partial T}{\partial n} = h\left(T - T_\infty\right)$, where the coefficient of the heat convection is quoted as $h = 21 \mathrm{W/m^2\,°C}$ [10] at the cooling area on the upper surface as illustrated in Fig. 4.1 with $R = 9.5$ mm. Furthermore $h = 191 \mathrm{W/m^2\,°C}$ [11] is on the other surfaces including the lower surface of the substrate. The threshold of stress required to initiate cracks in the soda-lime glass is given as the fracture strength of approximately 70 MPa for practical applications [9]. As the specimen was clamped at one side and the other surfaces are free of stress, the boundary conditions of the stress analysis are expressed as follows:

$$u_x\left(x,,,y,,,z,,,t\right) = 0 \quad x = 0 \tag{4.1}$$

$$u_y\left(x,,,y,,,z,,,t\right) = 0 \quad y = 0 \tag{4.2}$$

$$u_z\left(x,,,y,,,z,,,t\right) = 0 \quad z = 0 \tag{4.3}$$

4.3.2 The Beam Mode of the Continuous-Wave CO_2 Laser

The line-shaped (ellipse) beam mode as illustrated in Fig. 4.1 is transformed from a circular Co_2 laser beam with the Gaussian mode passing through a cylindrical lens. The intensity profile is expressed [10] as

$$I_{\text{line}}\left(x',y'\right) = \frac{PL_a}{\pi wl}\exp\left[-\left(\frac{x'^2}{w^2} + \frac{y'^2}{l^2}\right)\right] \tag{4.4}$$

where

$I_{\text{line}}(x', y')$ is the laser intensity absorbed by the substrate.

L_a is the absorption coefficient of the material under laser radiation, the absorption coefficient is taken as an average value of 0.9 for the soda-lime glass with Co_2 laser [9].

P is the laser power.

w is the radius of the minor axis of the ellipse.

l is the radius of the major axis of the ellipse.

4.3.3 The Beam Mode of the Pulsed Nd:YAG Laser

A circular pulsed Nd:YAG laser beam with the Gaussian mode intensity as illustrated in Fig. 4.1 is expressed as

$$I_{\text{pulse}}\left(x',y'\right)=\frac{PL_{\text{a}}}{\pi r^2}\exp\left[-\left(\frac{x'^2+y'^2}{r^2}\right)\right] \tag{4.5}$$

where L_{a} is the absorption coefficient of the material under laser radiation, the absorption coefficient is taken as an average value of 0.2 for the soda-lime glass with Nd:YAG laser [7] and r is the radius of the laser spot.

A new coordinate system (x', y') of the moving laser beam at a cutting speed v is expressed by $x'=x$, $y'=y(v,t)$, where (x, y) is the original coordinate system and t is the time of the traveling beam.

4.4 NUMERICAL RESULTS AND DISCUSSIONS

4.4.1 Cleaving Temperatures

In order to verify the numerical results for a moving heat source problem on the meshed domain and boundary conditions discussed above, the Rosenthal's solution of the point heat source on a thick plate [12] was applied and the results are shown in Fig. 4.4. The thermal cycles of the

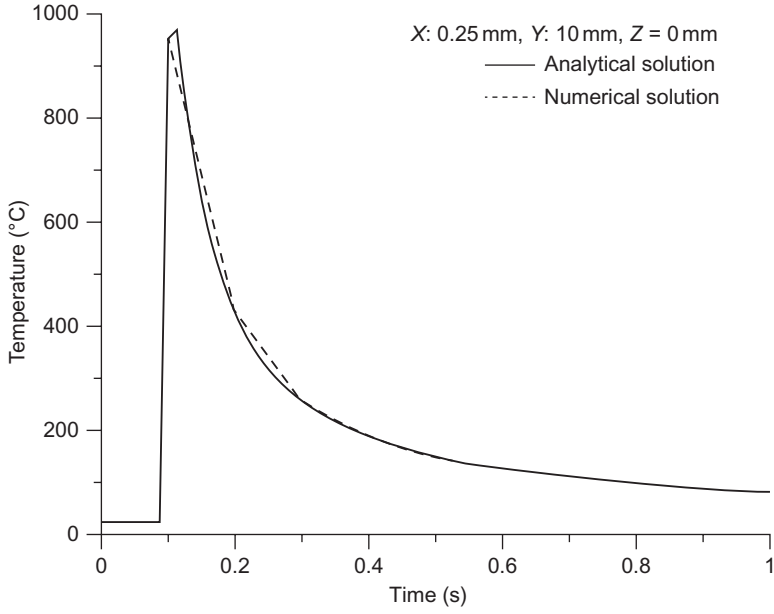


Fig. 4.4 Numerical results and analytical solutions of the thermal cycles at a specific position for a moving point laser beam spot on the glass substrate.

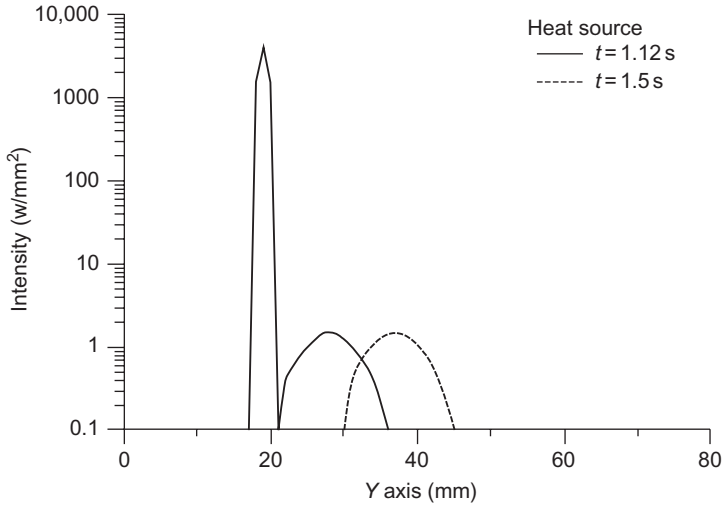


Fig. 4.5 Intensity profiles of the multiple laser beams.

analytical and numerical solutions at the interior point of the glass sheet are approximately identical.

In the laser cleaving on the glass substrate, the intensity profile of the multiple laser system is shown in Fig. 4.5. The pulse duration time is 0.5 ms in the present experiment. Since the brittle fracture phenomenon dominates the cleaving process due to the thermal shock effects on the glass, the temperature profiles in the center of the substrate at various depths with a time step of 1.12 s for multiple laser beams cleaving is shown in Fig. 4.6. Owing to the heating of the pulsed laser, a peak temperature of 1016°C was found at the location of the pulse. However, the heating effect is not significant at the depth of the substrate as shown in Fig. 4.6. As the laser beam moves forwards, the temperature profiles at various time steps are shown in Fig. 4.7, where the peak temperatures at the center of the line-shaped laser beam are equivalent in the cleaving conditions with and without a pulsed laser beam.

4.4.2 Stress Profiles

As the line-shaped laser beam moves along the center line of the substrate at various time steps, the stress profiles of σ_{xx} on the upper surface are shown in Fig. 4.8. It can be seen that the maximum tensile stresses σ_{xx} on the upper surface along the Y axis are located at the starting point of the cleaving path at various time steps. Since the thermal expansion of the glass substrate causes a compressive stress state in the heat-affected zone of the

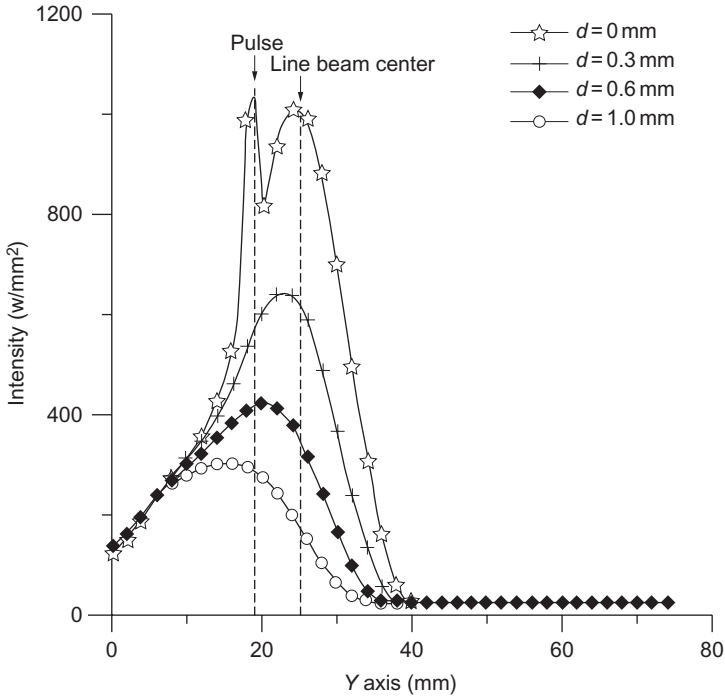


Fig. 4.6 Profiles of the temperature along the *Y* axis at the center of the substrate with various depths at the time step of 1.12 s in multiple laser beam cleaving.

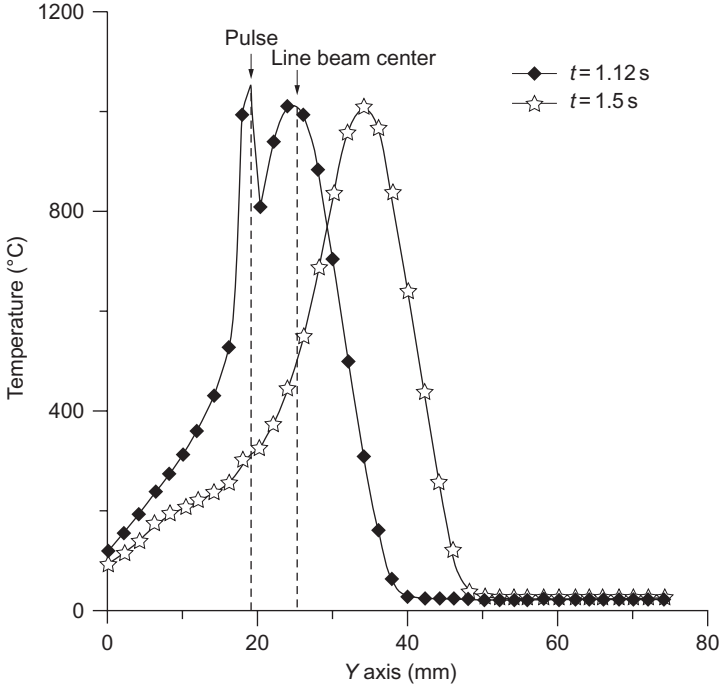


Fig. 4.7 Profiles of the surface temperature along the *Y* axis at the center of the substrate at various time steps of 1.12 and 1.50 s in multiple laser beam cleaving.

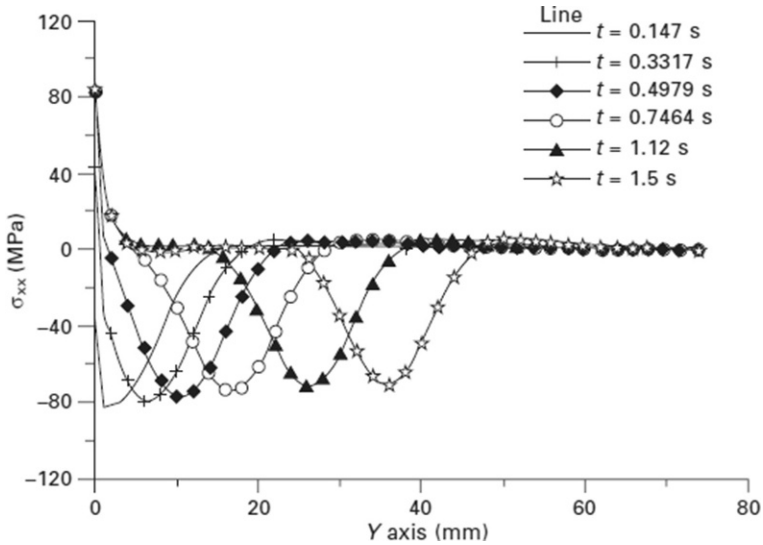


Fig. 4.8 Profiles of the stress σ_{xx} on the upper surface along the *Y* axis at the center of the substrate with various time steps in laser cleaving without the pulsed laser.

laser interaction, the stress field changes to the tensile stress state during the cooling stage. The heat of the laser beam has been accumulated at the laser interaction zone, therefore the compressive stress occurs at the front of the cutting edge and the crack due to the thermal shock propagating along the cleaving direction. A compressive stress of σ_{yy} occurs at the interaction zone of the laser beam. Based on the findings from the other study for laser cleaving [5], a stable crack will be formed under a condition of surrounding compressive stress during the heating stage. then transferred to a tensile stress state in the cooling stage in laser cleaving. It means that the side cracking could be prevented by a large compressive stress state.

As shown in Fig. 4.9, with a pulsed laser beam, the stress profiles of σ_{xx} on the upper surface at the center of the glass substrate are not affected by the pulsed laser. The amounts of the maximum tensile stress are close to the case without a pulsed laser beam at various time steps as shown in Fig. 4.8.

Fig. 4.10 shows the stress profiles of σ_{xx} at the center of the glass substrate at various substrate depths in laser cleaving by the multiple laser system at the time step of 1.12 s. Fig. 4.11 is the case of the time step of 1.50 s. It can be found that the stress field caused by the pulsed laser irradiation is dependent on the time steps. The instant response of the stress σ_{xx} is not noticeable due to the time lag of the thermal diffusion in the pulse laser irradiation at the time step of 1.12 s as shown in Fig. 4.10. However, at the

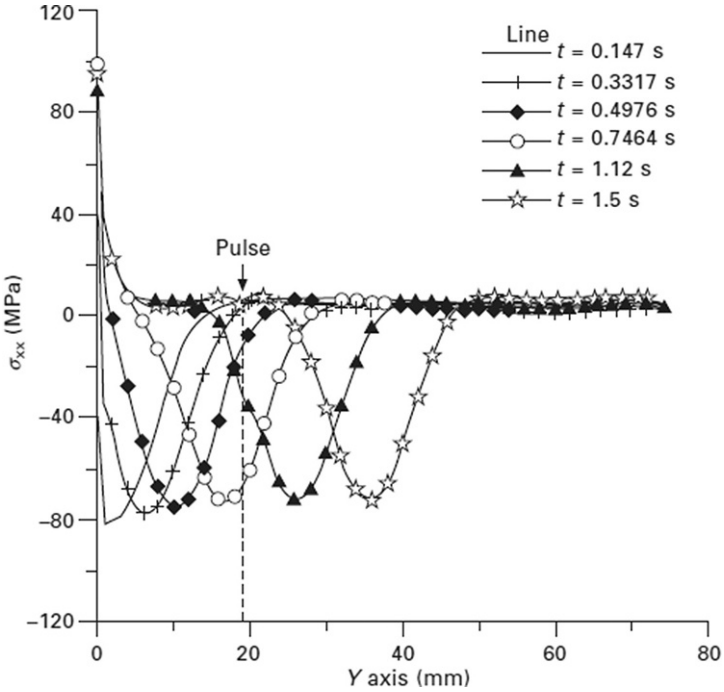


Fig. 4.9 Profiles of the stress σ_{xx} on the upper surface along the *Y* axis at the center of the substrate with various time steps in laser cleaving with the pulsed laser.

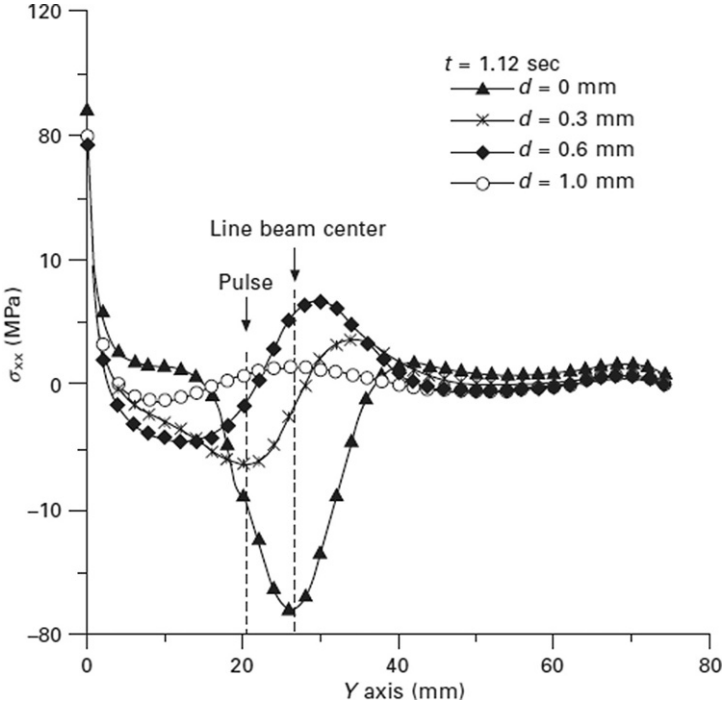


Fig. 4.10 Profiles of the stress σ_{xx} along the *Y* axis at the center of the substrate at the time step of 1.12 s with various substrate depths in laser cleaving with the pulsed laser.

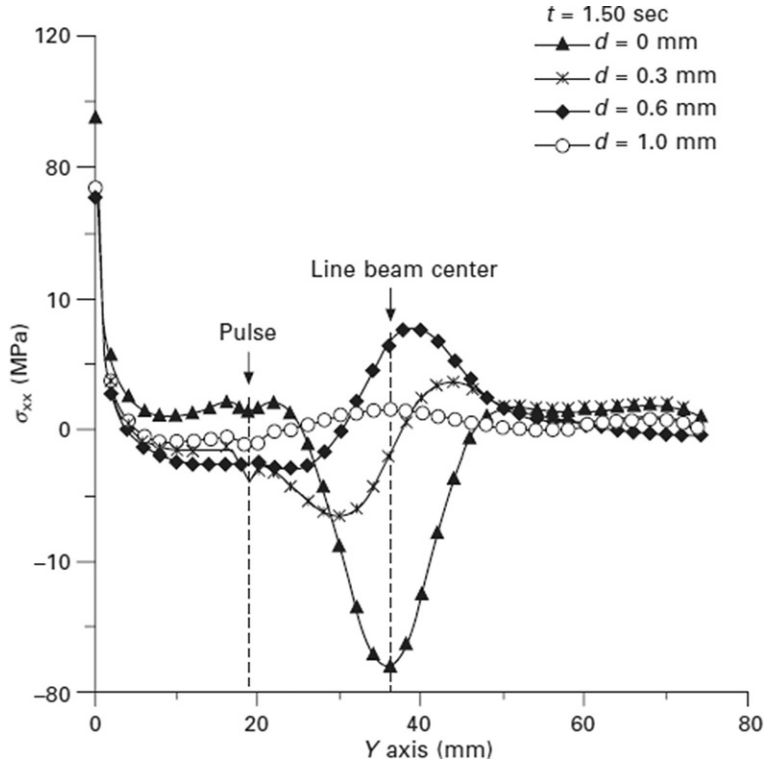


Fig. 4.11 Profiles of the stress σ_{xx} along the *Y* axis at the center of the substrate at the time step of 1.50 s with various depths in laser cleaving with the pulsed laser.

location of the pulse irradiation as shown in Fig. 4.11, it can be found that there are little increments of the stress σ_{xx} at various depths at the time step of 1.50 s. It also can be seen that the upper surface is in the compressive stress state and the interior of the substrate is in the tensile stress state near the region of the line-shaped beam center.

From the aspect of the shear stress such as τ_{xy} causing the cracking phenomenon in the laser cleaving, the stress profiles are shown in Figs. 4.12 and 4.13 at different settings of the lasers and cooling systems. At the same time step of 1.12 s, with the pulsed laser irradiating, the shear stress states increase with the pulse imposing and the average increment of approximately 20% of the peak shear stress at various depths. The influence of the shear stress is instantaneous. Furthermore, at the time step of 1.5 s, in the cooling stage after the laser pulse, the shear stress increases dramatically on the upper surface. According to the findings in Figs. 4.12–4.14, the shear stresses are effectively distributed into the substrate due to the imposing of the pulsed

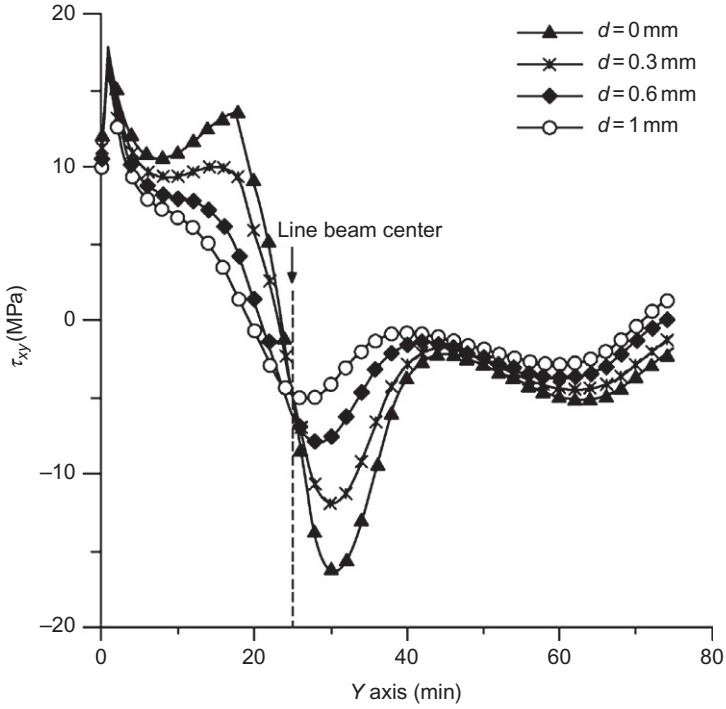


Fig. 4.12 Profiles of the stress τ_{xy} along the *Y* axis at the center of the substrate at the time step of 1.12 s with various depths in laser cleaving without the pulsed laser.

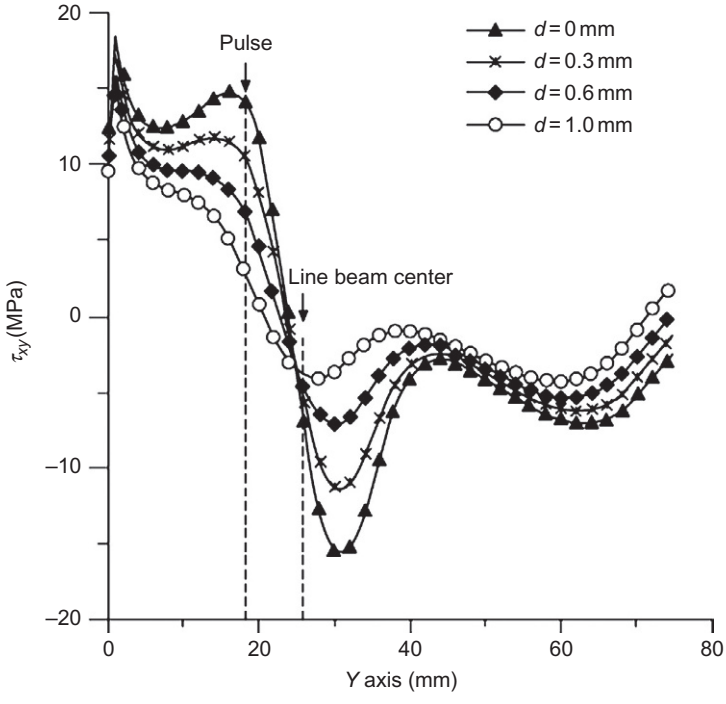


Fig. 4.13 Profiles of the stress τ_{xy} along the *Y* axis at the center of the substrate at the time step of 1.12 s and various depths in laser cleaving with the pulsed laser.

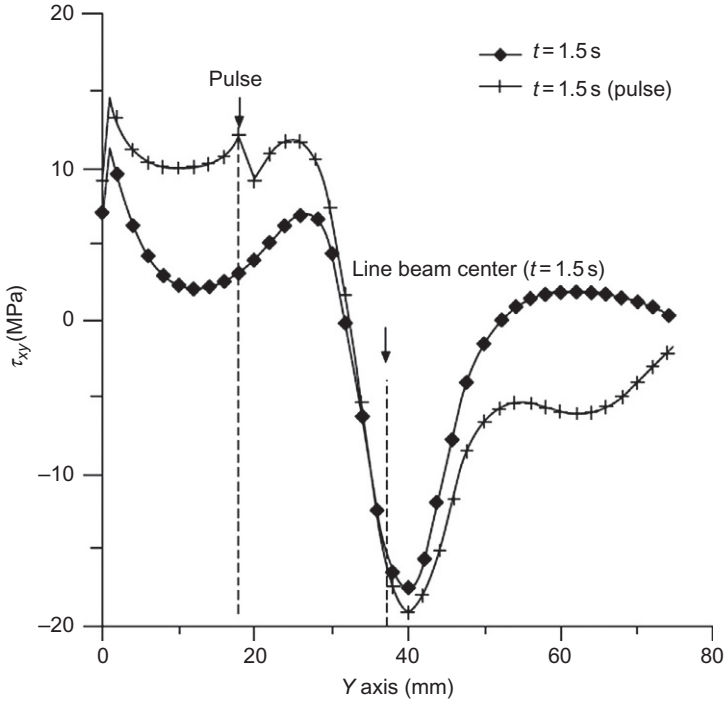


Fig. 4.14 Profiles of the stress τ_{xy} along the *Y* axis at the center of the substrate at the time step of 1.5 s with different settings in laser cleaving.

laser. Accordingly, in comparison with the stress states in tension as shown in Figs. 4.10 and 4.11, the crack propagation due to the shearing mechanism is much deeper in the glass substrate.

4.5 CRACK PROPAGATION IN LASER CLEAVING

The experimental arrangement of the multiple laser cleaving system is illustrated in Fig. 4.1. A CO_2 (10.6 μm) laser and a pulsed Nd:YAG (1.06 μm) laser were used as the heat sources and the CO_2 beam spot was transformed through a cylindrical lens to form an elliptic beam spot with a radius of the major axis of 15 mm and a radius of the minor axis of 0.7 mm, respectively. The pulsed Nd:YAG laser spot following the CO_2 line-shaped laser beam with a cooling air jet was adopted to enhance the thermal stress at the cleaving depth. Owing to an increase of the absorptivity of soda-lime glass for the 1.06 μm wavelength of the Nd:YAG laser, the heating effect of the pulsed Nd:YAG laser beam is significant on the glass preheated by the CO_2 laser in the cleaving. In the cleaving conditions of the CO_2 laser energy of

50W, the peak power of the pulsed Nd:YAG laser of 3400W, the cooling air flow velocity of 2.8 m/s, and the cutting speed of 1500 mm/min, the locations of the lasers and the cooling air are illustrated in Fig. 4.1, where a soda-lime glass sheet ($76 \times 26 \times 1\,mm^3$) was used as the substrate material in the experiment. The cracking surface has been photographed by a CCD camera and examined by an optical microscope.

The cleaving process has been visualized experimentally at various settings of the laser beam with cooling jet implementation. As shown in Figs. 4.15–4.18, the edge of the crack formation was denoted as point F and the center of the line-shaped laser beam was denoted as point C. The distances between the crack edge and the laser beam center have been measured at various settings of the laser cleaving process. As shown in Figs. 4.15 and 4.16, the crack propagation at the time steps of 1.0 and 2.0 s, respectively,

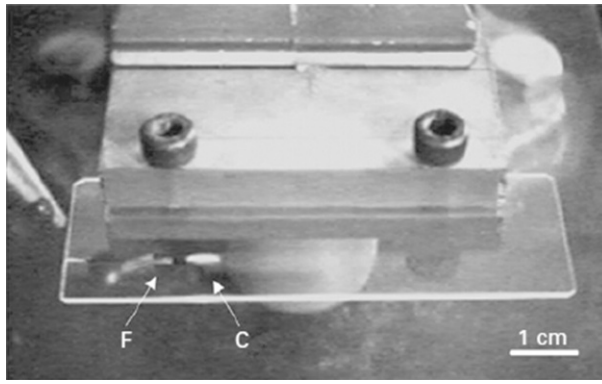


Fig. 4.15 Crack propagating at the time step of 1.0 s in line-shaped laser cleaving.

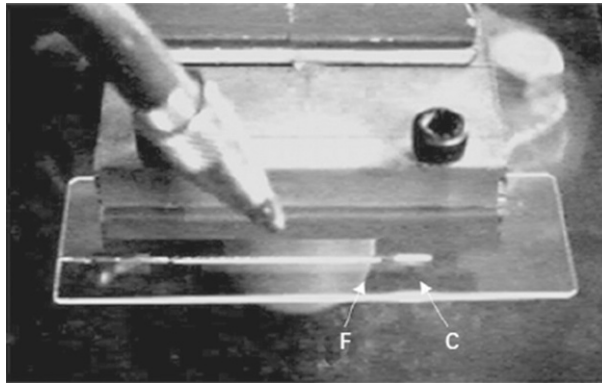


Fig. 4.16 Crack propagating at the time step of 2.0 s in line-shaped laser cleaving.

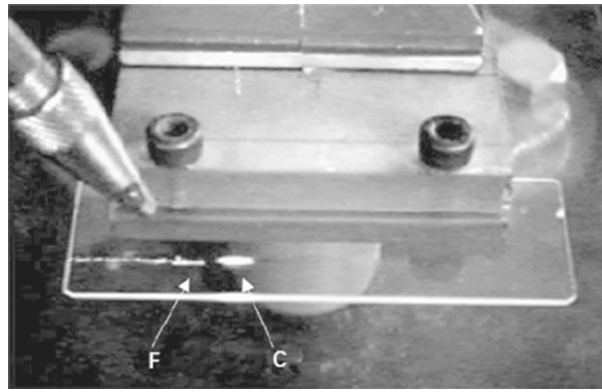


Fig. 4.17 Crack propagating at the time step of 0.09 s after the pulse in multiple laser beam cleaving.

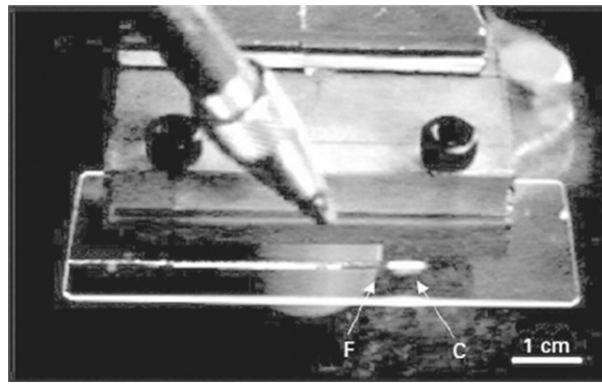


Fig. 4.18 Crack propagating at the location of the laser pulse in multiple laser beam cleaving.

in the line-shaped laser cleaving. With the pulsed laser irradiation, Fig. 4.17 shows the crack propagation at a time lag of 0.09 s after the laser pulse and Fig. 4.18 is the instantaneous response of the crack formation with the multiple laser beams cleaving.

As shown in Figs. 4.19–4.21, the typical patterns of crack propagation in laser cleaving are similar at various laser beam settings. However, a straight and fat cleavage surface without surface melting could be generated at the cleaving condition in the present experiment. As denoted in Fig. 4.21A the width of the cut, t_c, is about 0.77 mm, which is larger than the length of the minor axis of 0.7 mm of the laser beam. The upper surface was fractured at the front of the laser beam and the cleaving process was seized. Due to the numerical results as discussed, this type of fracture mode

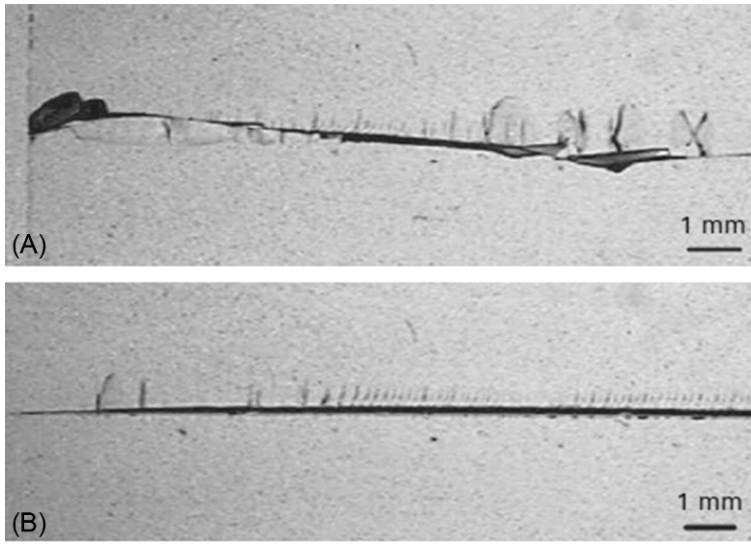


Fig. 4.19 Crack pattern at the front edge (A) 0–15 mm, and (B) 15–30 mm of the glass substrate in line-shaped laser cleaving without cooling air.

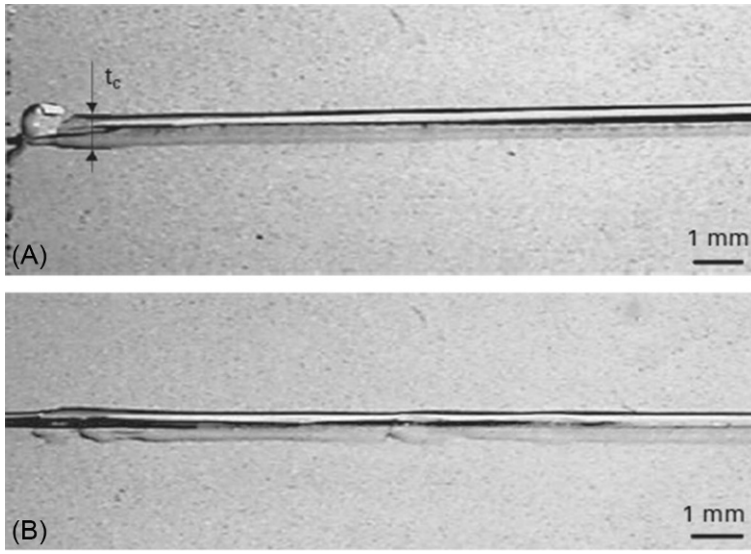


Fig. 4.20 Crack pattern at the front edge (A) 0–15 mm, and (B) 15–30 mm of the glass substrate in line-shaped laser cleaving with cooling air.

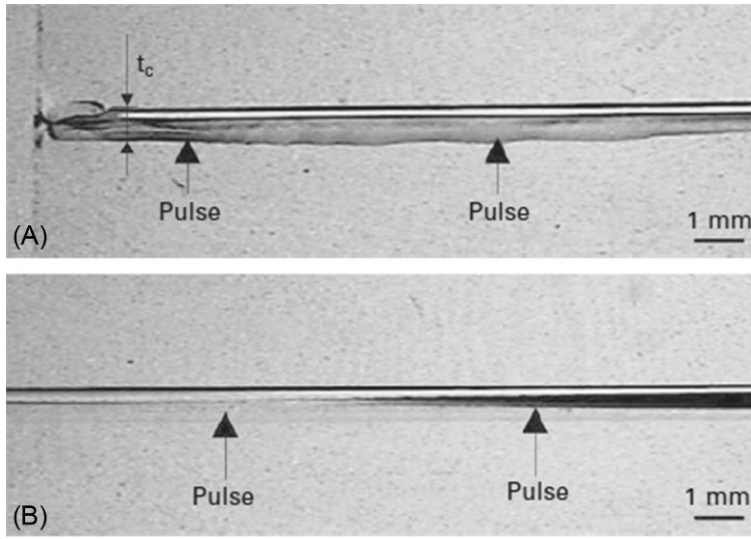


Fig. 4.21 Crack pattern at the front edge (A) 0–15 mm, and (B) 15–30 mm of the glass substrate in multiple laser beams cleaving.

was mainly generated by the shearing stresses at the depth of the substrate during the laser heating.

In comparison with other studies by laser machining method for glass sheets, it can be clearly found that there are many advantages of the proposed technique. Except for the good surface quality, excellent cracking controllability, and the high efficiency of the removal rate for deep cracking, the penetration effects of the pulsed laser beam can provide outstanding characteristics similar to the technique with multiple beam reflection. Furthermore, it is flexible in the system implementation for the practical applications.

4.6 CONCLUSIONS

Since the glass substrate heated by a line-shaped laser beam is difficult to break through deeply with the thermal expansion effects on the glass surface, this drawback could be overcome by adopting a pulsed Nd:YAG laser beam with a line-shaped CO_2 laser beam to generate a significant shear stress state on the cracking surface to form a mixture fracture mode with tensile and shear stress states in the interior of the glass substrate. With this innovative method of dual laser beams, the results show that the speed of cracking propagation will be increased by imposing the pulsed laser after

the line-shaped laser beam. As the line-shaped laser beam was followed with a pulsed Nd:YAG laser beam in the cleaving process, the shear stress was dramatically increased at the cleaving depth. The stress state in front of the cracking edge changes from compressive to tensile stress. Thus the propagation of the crack is aligned with the beam direction, and it caused a stable fracture on the surrounding region of the cleaving path. With a pulsed laser, the shearing mechanism dominates the crack propagation in the substrate depth with a clear fracture surface along the beam path. In comparison with the laser cleaving case, straightness and fatness of the cleaving surface have been significantly improved in the present study with the proposed multiple-laser system. According to the feasibility in the applications, surface quality, cracking controllability, and the efficiency of the removal rate for deep cracking on glass sheets, the implementation of the pulsed laser beam can perform dramatically for glass cutting in comparison with other existing laser machining techniques.

ACKNOWLEDGMENTS

This work is supported by the National Science Council under the grant number: NSC 94-2622-E-006-037-CC3. The authors would like to express the thanks to *Optics and Lasers in Engineering*, Elsevier, for the original publication of the portions in this work.

REFERENCES

[1] M. Morita, Generation and propagation behavior of laser induced thermal cracks, J. Ceram. Soc. Jpn. 101 (1993) 510–515.
[2] W.M. Steen, Laser Material Processing, Springer-Verlag, 1991.
[3] C.H. Tsai, C.S. Liou, Fracture mechanism of laser cutting with controlled fracture, J. Manuf. Sci. Eng. Trans. ASME 125 (2003) 519–528.
[4] R.M. Lumley, et al., Controlled separation of brittle materials using a laser, Am. Ceram. Soc. Bull. 48 (1969) 850–854.
[5] N. Paterson, T. Tawn, K. Williams, A.D. Nurse, On the numerical modeling of laser shearing of glass sheets used to optimize production methods, Proc. Inst. Mech. Eng. C J. Mech. Eng. Sci. 218 (2004) 1–11.
[6] Y.-L. Kuo, J.-M. Lin, Laser cleaving on glass sheets with multiple laser beams, Opt. Lasers Eng. 46 (2008) 388–395.
[7] J.E. Ready, Industrial Applications of Lasers, Academic Press, Cambridge, MA, 1978.
[8] ABAQUS, ABAQUS User's Manual Volume II, HKS Inc., Pawtuckett, RI, 1998. G.K. Chui, Laser cutting of hot glass, Am. Ceram. Soc. Bull. 54 (1975) 514–518.
[9] P.B. Narottam, R.H. Doremus, Handbook of Glass Properties, Academic Press, Cambridge, MA, 1986.
[10] Y.Z. Wang, J. Lin, Characterization of the laser cleaving on glass sheets with a line-shape laser beam, Opt. Laser Technol. 39 (2007) 892–899.
[11] F.P. Incropera, D.P. DeWitt, Fundamentals of Heat and Mass Transfer, Wiley, 1996.
[12] S. Kou, Welding Metallurgy, Wiley, 1987.

FURTHER READING

[1] M.A. Finucane, I. Back, CO_2 laser cutting of stained glass, Int. J. Adv. Manuf. Technol. 12 (1996) 47–59.
[2] A. Helebrant, C. Buerhop, R. Weißmann, Mathematical modeling of temperature distribution during CO_2 laser irradiation of glass, Glass Technol. 34 (1993) 154–158.
[3] M. Ikeda, T. Shibata, E. Makino, Y. Takahashi, A. Ono, F. Matsumoto, Study on laser breaking of glass plate (1st report)—generation and growth of vertical cracks by scribing, Int. J. Jpn Soc. Precis. Eng. 62 (1996) 413–417.
[4] M.A. Saifi, U.C. Paek, Scribing glass with pulsed and Q-switched CO_2 laser, Am. Ceram. Soc. Bull. 52 (1973) 838–841.
[5] W. Unger, W. Wittenbecher, The cutting edge of laser technology, Glass Process. 75 (1998) 101–102.
[6] Y.C. Zhou, Z.M. Zhu, Thermal fracture characteristics induced by laser beam, Int. J. Solids Struct. 38 (2001) 5647–5660.

This page intentionally left blank

CHAPTER 5

Laser Dicing of Silicon and Electronics Substrates

I. Mingareev, C. Fornaroli, A. Gillner
Florida Institute of Technology, Melbourne, FL, United States

5.1 INTRODUCTION

As the demand for high performance portable electronic products increases, so too does the need for micro electronical components, such as integrated circuits or diodes; for example, electroluminescent diodes [1]. Due to ongoing miniaturization, not only do these components have to be more powerful with every new generation, but also more compact, more delicate, and thus more complex. As expected, producing and processing these products pose a huge challenge for conventional manufacturing technologies [2–4]. Usually, micro electronical components are made out of a semiconducting material such as silicon. For transistors, on the one hand, the electronical characteristics are directly exploited through the use of local doping gradients. Silicon, on the other hand, is mainly chosen for electroluminescent diodes on account of its outstanding mechanical characteristics. Thanks to their crystalline grid structure, semiconductors are very stiff even when minimal material thicknesses amount to only a few 100 μm.

Since silicon is found all over the earth and, therefore affordable, it is the most important element primarily used for manufacturing semiconductor elements [5]. In several process steps raw silicon is manufactured into flat disks with a diameter of 100–200 mm and a thickness of 0.1–0.5 mm. In a batch process a large number of components are applied on these wafers in parallel [6]. The components are separated in the final processing step so that they can be manufactured as chips later on [6,7]. The separation constitutes the last and most important processing step within the processing chain. Costly and complexly produced components can be damaged at this point if process control is inadequate, which obviously decreases productivity significantly. In addition the separation process determines the wafer efficiency; in other words, the output of chips per wafer. This output is influenced by the cutting width, which always includes a safety distance to the active components and, thus

Advances in Laser Materials Processing
https://doi.org/10.1016/B978-0-08-101252-9.00005-4
Copyright © 2018 Elsevier Ltd.
All rights reserved.

absorbs micro-cracks or thermal damage. Since the thickness of the components cannot be infinitesimally small, due to the requirement specifications of the mechanical load capacity, a small decrease in the cutting width automatically leads to an increased aspect ratio—the ratio between the cutting depth and cutting width. The accessible aspect ratio of the separation technology has to be maximized in order to optimally utilize the wafer surface and therefore reach the highest possible process efficiency.

Nowadays, although several alternative manufacturing processes for wafer separation are available, the classical method—mechanical sawing with a diamond cutting disk—is widespread and still considered the state of the art [8,9]. Nonetheless, two-step procedures, like scribe and break, waterjet-, or laser-beam based processes can be used as alternatives [10–14]. Indeed, separation through laser ablation has several advantages: tool wear does not have to be considered, the sensitive substrate will not be mechanically burdened during cutting, and the cutting width can be reduced due to the microscopic tool size. Depending on the kind of laser procedure used, however, thermal damage of the material can occur. And yet, when ultrashort pulsed laser radiation is applied, thermal damage can be avoided almost completely and the wafer efficiency, therefore, increases significantly [15–17].

5.2 INDUSTRIAL DICING PROCESSES FOR SILICON AND ELECTRONIC SUBSTRATES

5.2.1 Mechanical Dicing With Diamond Saws

Wafer dicing using diamond saw has been the state of the art in wafer processing industry for decades, as the technology is well established and sufficiently tested [8,9]. In this mechanical abrasive manufacturing process, a rapidly rotating disk saw (up to 60,000 rpm) with defined immersion depth is guided vertically through the wafer. The circumference of the saw is studded with abrasive diamond particles. To reduce frictional heat and to remove ablation particles, cooling lubricant is continuously added during the cutting process. The wafer is fixed on a carrier foil, on which the chips remain after separation. Usually, the material is separated at a feed rate of ~100 mm/s [10]. Due to the mechanical load and vibrations, damages such as cracks, fractures, and scratches might occur. A security zone has to be maintained to keep these defects away from the electronic component itself. The minimum achievable cutting width is set by the geometrical tool size and is in the range of ~50 μm [18,19]. The tool wear has to be constantly monitored so that constant process quality can be guaranteed.

5.2.2 Mechanical Scribe and Break

In this two-stage procedure, a notch is first scribed into the silicon substrate to weaken the material at a specific location. Then it is cleaved along this weakened area. A distinction is made here between the placement of a notch with a diamond tip and the cutting of a groove with a diamond disk saw. In contrast to cutting through the material completely, here the saw is adjusted to cut through approximately half of the material thickness [11]. The increased cutting velocity and the decreased mechanical weakening are advantageous compared to a full cut. Due to the two-stage procedure however, the processing is more complex and thus failure-prone. Additionally, the separation is limited to linear cutting patterns. A two-stage separation through scribe and break will fail if functional layers are applied to the upper or lower side of the wafer. Moreover, in the mechanical separation process, functional layers can delaminate from the substrate.

5.2.3 Water Jet Dicing

Instead of cutting mechanically, water jet cutting deploys a fine water jet with an extremely high pressure of up to 6000 bar. So that the process can cut at velocities relevant to the industry, the water is mixed with abrasive particles [20,21]. These particles accelerate the material ablation in the cutting line, but inevitably damage the wafer surface. Furthermore, a water-based manufacturing process like this one generally requires cleaning and drying steps after the separation. Unlike in the mechanical process, there is no significant heating of the substrate. Achievable cutting widths are around 100 µm and are limited by the nozzle geometry and the resulting water jet diameter [20,21].

5.2.4 Water Jet Hybrid Dicing With Laser Radiation

In water-jet hybrid cutting with laser radiation, the laser beam is coupled into a fine water jet and propagates in this water jet similar to an optical fiber. The water jet fulfills several tasks: it guides the laser radiation, cools the cut kerf, and removes the ablation particles. In the water jet, the laser beam remains virtually collimated for several centimeters since the laser beam is completely reflected in the transition between water and air. In contrast to the conventional laser cutting, this approach can generate kerfs with straight walls.

The laser beam sources used are pulsed at a duration from nanoseconds (ns) to microseconds (µs) [12,22]. The coupling between ultra-short pulse lasers with a water jet is not yet possible. The high intensities lead to nonlinear absorption within the water jet. However precise injection

of the focused laser beam into the water jet nozzle is challenging, and an insufficient calibration can quickly damage the nozzle. This leads to the circumstance that neither the nozzle diameter nor the resulting water jet can be dimensioned as small as desired. Typical minimal nozzle diameters are in the range of 50 µm [22]. Like water jet cutting, the water jet hybrid cutting with laser radiation is also a manufacturing process that needs a cleaning- and drying-process after the separation.

5.2.5 Laser-Based Scribe and Break

In this technology, laser structuring initially weakens the material. Subsequently, fine kerfs are applied to the surface to separate the chips from one another. Laser-based scribing can be used to produce significantly smaller kerfs within a shorter period of time than would be possible with mechanical processing [23]. Just as with the mechanical scribe and break process, the disadvantages are mainly the two-step process and the reduced flexibility with regard to the cutting pattern and the materials that can be processed, including potential functional layers.

5.2.6 Stealth Dicing

Similar to laser-based scribe and break, stealth dicing first weakens the substrate, which is then afterwards separated into individual chips. In this process, the material is invisibly modified, or weakened in the volume of the material itself, which is where the term "stealth dicing" stems from [24,25]; the laser radiation largely penetrates the material and is sharply focused into its center. This works because the laser radiation wavelength used is in the range of 1 µm—in which silicon is mostly transparent—and focused with a high numerical aperture [13,26,27]. The chips are separated when the carrier foil is stretched in the x and y directions. Not only does stealth dicing reach high cutting speeds, but it also has a nearly nonexistent cutting kerf, two main advantages. Since there is neither mechanical nor thermal ablation of the material, no ablation particles occur. A disadvantage of the process is that the material has to be transparent for the incident laser light. Processing of semiconductor components with metallic functional layers is thus not possible [13]. Moreover, there is a potential danger in the mechanical separation process, as the functional layers could delaminate.

5.2.7 Laser Dicing (Short Pulse Laser)

Short pulsed laser beam sources that have a pulse duration in the range of 10–100 ns are often used to cut silicon. The wavelength is mostly in the UV

range of ~355 nm. Besides cutting complex patterns, these sources can also be used to label semiconductor components [14,28,29]. Furthermore, the technology is less complex than water jet-based separation processes and more universal than two-stage processes. Short focusing optics beams allow diameters in the range of 10 µm to be used. Since the ablation is dominated by melting, the process generates heat-affected zones of up to 30 micrometers around the cutting kerf. Overall, a cutting width of ~50 µm can be reached [14].

5.2.8 Overview and Conclusions

Table 5.1 shows the separation technologies described above and their respective limitations.

5.2.9 Scientific Publications on the Material Processing of Silicon With Ultra-Short Pulsed Laser Radiation

To date, several scientific papers have been published about sublimation cutting of silicon with ultra-fast lasers. Table 5.2 summarizes relevant publications with their respective research focus and main insights.

Table 5.1 Overview of the separation technologies and their limitations

Technology	Limitation
Mechanical separation through diamond sawing	The high load upon the substrate leads to a decreasing wafer efficiency. Not applicable for material thickness in the range of 100 µm
Mechanical scribe and break	Complex and failure-prone processing. Materials with functional layers can scarcely be processed
Water-jet cutting	Contamination and impairment of the surface through abrasive particles. Cleaning and drying steps are necessary. The minimal cutting kerf width cannot be reduced at will
Water-jet hybrid cutting with laser radiation	The minimal cutting kerf width cannot be reduced at will. Cleaning and drying steps are necessary
Laser-based scribe and break	Only suitable for thin substrates. Materials with functional layer can scarcely be processed
Stealth dicing	Materials with metallic functional layers cannot be processed since they are not transparent
Laser-beam cutting (short pulse laser)	Thermal damage occurs around the cutting kerf and leads to a smaller process efficiency

Table 5.2 Overview of scientific publications in the field of sublimation cutting of silicon with ultra-fast lasers

Research Focus	Insights	Source
Examination of the sublimation cutting of silicon having a material thickness of 100 µm at a laser wavelength of 780 nm and pulse duration of 150 fs	The quality of the cut is mainly influenced by pulse energy and polarization direction. Effective cutting velocities up to 550 mm/min can be reached by focusing the laser radiation upon a line instead of a dot	[30]
Examination of the modification threshold of silicon and the morphology of the ablation process at a laser wavelength of 780 nm and pulse duration range from 5 to 400 fs	Independent of the pulse duration, the ablation threshold is 0.2 J/cm^2. Following modification mechanisms can be identified: oxidation, amorphization, recrystallization, bubble formation, ablation, and ripple formation	[13]
Examination of the process efficiency of silicon micro processing at a wavelength of 800 nm and pulse duration of 83 fs	Depending on the laser fluence, two ablation regimes have been identified. The ablation close to the ablation threshold is dominated by two-photon absorption. In the case of fluences, which are significantly higher than the ablation threshold, the absorption takes place via free electrons. The ablation efficiency in this area is decreased due to plasma shielding, redeposition, and resolidification of melting particles	[31]
Examination of the ablation process of silicon at a laser wavelength of 266 nm and pulse duration of 60 ps	At laser fluences above 100 J/cm^2, the ablation rate increases but cracks form at the entry of the ablation geometry. The adjusted laser fluence and the amount of laser pulses needed to generate a through hole are logarithmically connected for the percussion drilling of silicon wafers with material thicknesses of 260, 380, and 550 µm	[32]
Examination of sublimation cutting of silicon and metals at a laser wavelength of 780 nm and pulse duration of 150 fs	The quality of the ablation can be improved by reducing the fluence and the pulse-to-pulse overlap and simultaneously increasing the amount of passes in view of the surface roughness and the minimal cut width. The optimal beam deflection velocity is in the range of 100 m/min	[33]

Examination of the separation process of silicon having a material thickness of 220 µm with different laser-based procedures, among others at a laser wavelength of 1064 nm and pulse duration of 12 ps	Approximately the same breaking strength can be attained with sublimation cutting of silicon with ultra-short pulsed laser radiation as with the separation with the diamond cutting disc. The breaking strength is lower due to edge defects with higher pulse durations in the nanosecond and microsecond range. The highest strength can be achieved when thermal induced stress is used for separation. Here, a continuous wave laser at a wavelength of 1075 nm is used	[34]
Examination of the temporal development of the hole depth and geometry during laser-beam drilling of silicon at a laser wavelength of 1030 nm and pulse duration of 8 ps	The development of the hole geometry can be divided into three phases. During the first phase, a straight hole geometry develops without deviations from the beam propagation direction. After ~40% of the depth has been attained, the second phase starts. Here, first ablation channels branch off the main direction. In the third phase, although the drilling depth stagnates, the hole's volume keeps on growing with each laser impulse because massive sideways ablation channels form. The attainable drilling depth essentially depends on the pulse energy applied	[35]
Examination of the separation process of silicon having a material thickness of 250 µm processed using high performance ultra-short pulsed lasers at a laser wave length of 1030 nm and pulse duration in the range of femtoseconds	An effective cutting velocity of 40 mm/s is demonstrated with a repetition rate of 13 MHz and laser power of 11W at beam deviation velocities of 3 m/s. In this case the cutting width is 16.5 µm and the cutting depth lies in the range of 75 µm	[36]
Examination of the separation process of silicon with a material thickness of 50 µm processed at a laser wavelength of 780 nm and pulse duration in the range of 150–200 fs	Photographs of the ablation process—taken with a high speed camera—show that the rise time for an enlargement of the hole diameter correlates with the pulse energy. The rise time amounts to 10 ns for pulse energies of 30 and 180 µJ and 30 ns for pulse energies of 350 and 500 µJ. The rise time can be correlated with the thermal impairment of the ablation geometry	[37]

5.3 DICING OF SILICON WITH ULTRA-FAST LASER RADIATION

5.3.1 Theoretical Analysis of the Development of the Ablation Geometry

Already at an early stage of the ablation process, large kerf angles above 70 degrees occur (see Fig. 5.1, right). A kerf angle of 72 degrees and an aspect ratio of 1.6 result from an ablation depth of 35 µm and a width of 22 µm. As shown in Fig. 5.1 on the left side, projection effects of the incident laser radiation have to be considered due to the steep kerf walls. Ensuing from the initial peak intensity I_0, the effective intensity I_{eff} declines with increasing projection angle and falls below the ablation threshold at the critical projection angle $\alpha_{\text{krit.}}$ When both effects are taken into account, the following equation results:

$$I_{\text{eff}} = I_{\text{o}} \cdot A\left(\text{Polarization}\left(\alpha_{\text{proj.}}\right)\right) \cdot \cos\left(\alpha_{\text{proj.}}\right). \tag{5.1}$$

How this typical ablation geometry develops can be explained by a geometrical model based on calculations done by Urs Eppelt [38]. He specifies the fundamental equations to compute an asymptotic ablation contour and derives, furthermore, an approximate solution on the basis of the complementary error function [38]. Fig. 5.2 illustrates the geometrical model and the basics for calculating the ablation geometry. An incoming laser beam is projected on the wall of the ablation geometry and the projection angle α_{proj} forms between the perpendicular vector of the wall and the vector of incidence.

The following equation can be derived from Fig. 5.2:

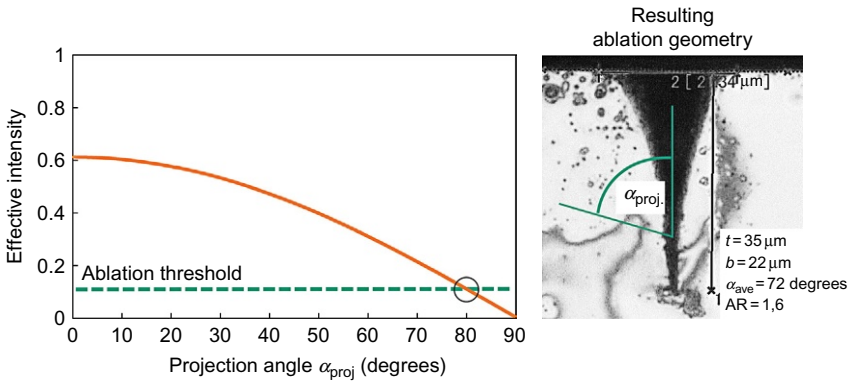


Fig. 5.1 Effective intensity depending on the projection angle and an exemplary ablation threshold (left). Resulting ablation geometry with a depth of 35 µm, width of 22 µm, average kerf angle of 72 degrees, and aspect ratio of 1.6 (right).

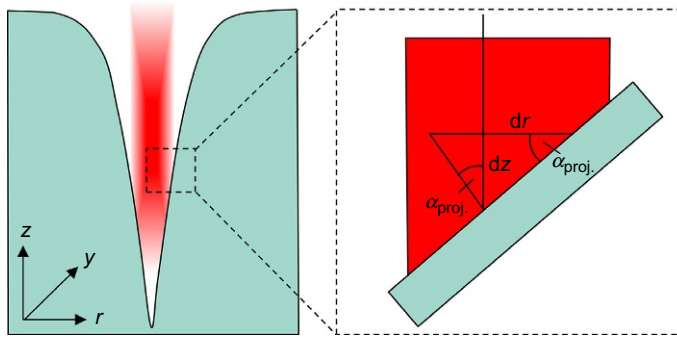


Fig. 5.2 Incoming laser beam and its interaction with the angled walls of the ablation geometry.

$$\frac{dz}{dr} = \tan\left(\alpha_{proj.}\right). \tag{5.2}$$

Eq. (5.5) results when the fundamental associations of Eqs. (5.3), (5.4) are inserted into Eq. (5.2):

$$\tan\left(\alpha_{proj.}\right) = \frac{\sin\left(\alpha_{proj.}\right)}{\cos\left(\alpha_{proj.}\right)}, \tag{5.3}$$

$$\sin^2\left(\alpha_{proj.}\right) + \cos^2\left(\alpha_{proj.}\right) = 1, \tag{5.4}$$

and

$$\frac{dz}{dr} = \frac{\sqrt{1-\cos^2\left(\alpha_{proj.}\right)}}{\cos\left(\alpha_{proj.}\right)}. \tag{5.5}$$

Eq. (5.6) follows from transforming and simplifying:

$$\frac{dz}{dr} = \frac{\sqrt{\cos^2\left(\alpha_{proj.}\right)\left(\frac{1}{\cos^2\left(\alpha_{proj.}\right)} - 1\right)}}{\cos\left(\alpha_{proj.}\right)}, \tag{5.6}$$

and

$$\frac{dz}{dr} = \sqrt{\left(\frac{1}{\cos^2\left(\alpha_{proj.}\right)} - 1\right)}. \tag{5.7}$$

In the asymptotic limiting case and maximum kerf depth, Eq. (5.8) is valid with $l(r)$ as intensity at the position r and I_s as a threshold intensity for material ablation.

$$\cos\left(\alpha_{\text{proj.}}\right)\cdot I\left(r\right)=I_{\text{S}}. \tag{5.8}$$

Eq. (5.9) follows from inserting Eq. (5.8) into Eq. (5.7):

$$\frac{\mathrm{d}z}{\mathrm{d}r}=\sqrt{\left(\frac{I\left(r\right)^{2}}{I_{\text{S}}{}^{2}}-1\right)}. \tag{5.9}$$

Since $I(r)$ is typically significantly larger than I_s the term in the square root can be simplified to Eq. (5.10):

$$\frac{\mathrm{d}z}{\mathrm{d}r}=\sqrt{\left(\frac{I\left(r\right)^{2}}{I_{\text{S}}{}^{2}}\right)}\rightarrow\frac{\mathrm{d}z}{\mathrm{d}r}=\frac{I\left(r\right)}{I_{\text{S}}}. \tag{5.10}$$

In case of a Gaussian intensity distribution, the following is valid:

$$I\left(r,z=0\right)=I_{0}\exp\left(-\frac{2r^{2}}{w_{0}^{2}}\right). \tag{5.11}$$

When Eq. (5.11) is inserted into Eq. (5.10); Eq. (5.12) can be derived:

$$\frac{\mathrm{d}z}{\mathrm{d}r}=\frac{I_{0}}{I_{\text{s}}}\exp\left(-\frac{2r^{2}}{w_{0}^{2}}\right)\quad\text{and}\quad\mathrm{d}z=\frac{I_{0}}{I_{\text{s}}}\exp\left(-\frac{2r^{2}}{w_{0}^{2}}\right)\mathrm{d}r. \tag{5.12}$$

Transformation of Eq. (5.12) and integral notation leads to Eq. (5.13):

$$z\left(r\right)=\frac{I_{0}}{I_{\text{s}}}\int_{-r}^{r}\exp\left(-\frac{2r^{2}}{w_{0}^{2}}\right)\mathrm{d}r. \tag{5.13}$$

Eq. (5.16) follows when the solution of the integral (complementary error function) from Eq. (5.14) and the substitution from Eq. (5.15) are taken into account:

$$\operatorname{erfc}\left(z\right)=\frac{2}{\sqrt{\pi}}\int_{z}^{\infty}\exp\left(-\eta^{2}\right)\mathrm{d}\eta, \tag{5.14}$$

$$\eta=\sqrt{2}\,\frac{r}{w_{0}},\quad\mathrm{d}\eta=\sqrt{2}\,\frac{\mathrm{d}r}{w_{0}}, \tag{5.15}$$

and

$$z\left(r\right)=\frac{I_{0}w_{0}}{I_{\text{s}}\sqrt{2}}\int_{\sqrt{2}\frac{r}{w_{0}}}^{\infty}\exp\left(-\eta^{2}\right)\mathrm{d}\eta. \tag{5.16}$$

The final correlation between the attainable depth z and the radial coordinate r follows from solving the integral:

$$z(r) = -\frac{I_0}{I_s}\sqrt{\frac{\pi}{2}}w_0 \operatorname{erfc}\left(\sqrt{2}\frac{r}{w_0}\right), \tag{5.17}$$

and

$$\alpha_{\text{krit}} = \arccos\left(\frac{I_s}{I_0}\right). \tag{5.18}$$

Eq. (5.17) shows that depth z qualitatively depends on the complementary error function at r and scales quantitatively with the threshold intensity, the effective peak intensity at hand, and the radiation radius. At the given threshold and peak intensity, the maximum attainable depth can be calculated. The model is based on the projection of incident laser radiation on the walls of the ablation geometry and enables ablation up to a maximum angle—the so-called critical angle—which can be calculated from Eq. (5.18).

5.3.2 Validation of the Ablation Model Through Experimental Results

In this section, the previously found ablation model will be validated with chosen experimental results in terms of the attained ablation depth. The pulse peak power can be calculated based on the pulse energy, focus diameter, and pulse duration. Table 5.3 illustrates the three chosen pulse energies, pulse peak power, and peak intensities at a pulse duration of 10 ps and a focus diameter of 11 µm.

The left side of Fig. 5.3 depicts the development of the ablation depth as it depends on the number of passes for pulse energies of 2, 4, and 6 µJ. On the right side of Fig. 5.3, the cross-section of the ablation geometry after 1000 passes can be seen. The incident laser radiation has a wavelength of 532 nm, pulse duration of 10 ps, focus diameter of 11 µm, is *p*-polarized,

Table 5.3 Correlation between pulse energy, pulse peak power, and peak intensity at a pulse duration of 10 ps and focus diameter of 11 µm

Pulse energy (J)	Pulse peak power (W)	Peak intensity (W/cm^2)
2×10^{-6}	2×10^{5}	4.2×10^{11}
4×10^{-6}	4×10^{5}	8.4×10^{11}
6×10^{-6}	6×10^{5}	1.3×10^{12}

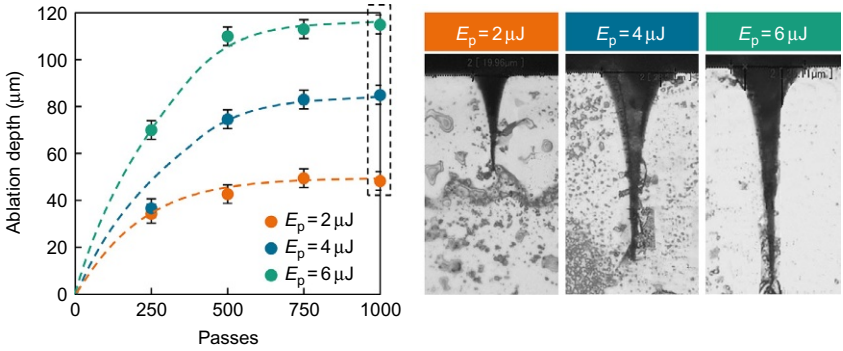


Fig. 5.3 Development of the ablation depth depending on the number of passes from 100 to 1000 and pulse energies of 2, 4, 6 µJ. Further experimental parameters: wavelength 532 nm, pulse duration 10 ps, repetition rate 400 kHz, pulse distance 5 µm, focus diameter 11 µm, p-polarization.

and the pulse distance is 5 µm. The largest ablation depth can be attained at the highest pulse energy of 6 µJ, which adds up to 118 µm in this case. The application of a pulse energy of 4 µJ reduces the depth to 90 µm, which eventually amounts to merely 50 µm at a pulse energy of 2 µJ. The development of the ablation depth proceeds for all pulse energies asymptotically when plotted against a threshold value. With an increasing numbers of passes, the ablation depth per pass declines. This effect can be explained by the ongoing declining effective intensity. Moreover, the cross-sections on the right side qualitatively confirm the curve of the complementary error function thanks to their funnel-like contour.

According to the same system, the ablation depth was analyzed after 1000 passes at a pulse distance of 1.3 µm in otherwise identical test conditions. The pulse distance was reduced by lowering the beam deflection velocity, which amounts to 0.5 m/s in this case, instead of 2 m/s previously. With such a small pulse distance—in relation to the focus diameter—thermal accumulation effects occur in the ablation kerf due to pulse-to-pulse interaction. Resulting from this are ablation depths of 67, 110, and 138 µm at pulse energies of 2, 4, and 6 µJ. The number of applied pulses correlates reciprocally with the pulse distance. So that the ablation depths can be compared on the basis of the ablation per single pulse, the number of passes with which the ablation depths are determined has to be adjusted by the differences of the pulse distances. At a pulse distance of 1.3 µm, a scale factor of 4 arises in relation to a pulse distance of 5 µm. Thus ablation depths of 60, 95, and 115 µm result. Fig. 5.4 shows a comparison between the experimental ablation geometries in cross-sections and the predicted theoretical ablation

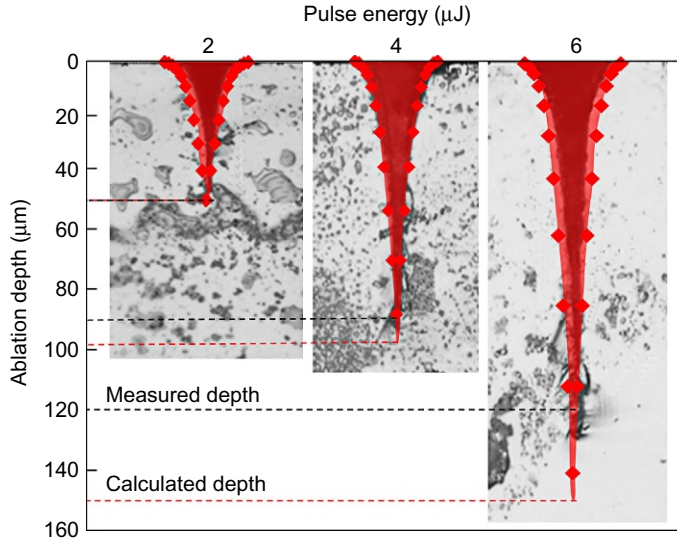


Fig. 5.4 Comparison of experimentally obtained ablation geometries and the theoretical values at the following experimental conditions: wavelength 532 nm, pulse duration 10 ps, repetition rate 400 kHz, pulse distance 5 µm, focus diameter 11 µm, p-polarization.

geometries. The test conditions are identical to those from Fig. 5.3. The theoretical ablation geometries are calculated with the data from Table 5.3 and the threshold intensity of 3×10^{10} W / cm^2, which was previously determined at a wavelength of 532 nm and pulse duration of 10 ps. Prior to this, the peak intensities from Table 5.3 were multiplied with the absorption factor of 0.5. This absorbance is used as an average value to simplify the calculation and contains the overlapping of reverse effects, such as the projection angle, the variable temperature, and changes in the surface structure.

When the calculated contours are directly compared with the cross-section images, the depth at 2 µJ pulse energy is in very good accordance with the calculated depth. Deviations of 10% and 26% can be seen at pulse energies of 4 and of 6 µJ, respectively. Both of the testing points mentioned last show a smaller depth, just as the model predicts. The form of the ablation geometry for all three pulse energies is consistent with the calculated shape.

Fig. 5.5 shows the comparison between the simulations and experiments summarized for the pulse distances of 5 and 1.3 µm. While the calculated ablation depth does not deviate from the experimental value at a pulse energy of 2 µJ and pulse distance of 5 µm, there are deviations from the experimental value at the same pulse energy and a pulse distance of 1.3 µm. In this case the ablation depth lies at 60 µm, which amounts to ~18% more

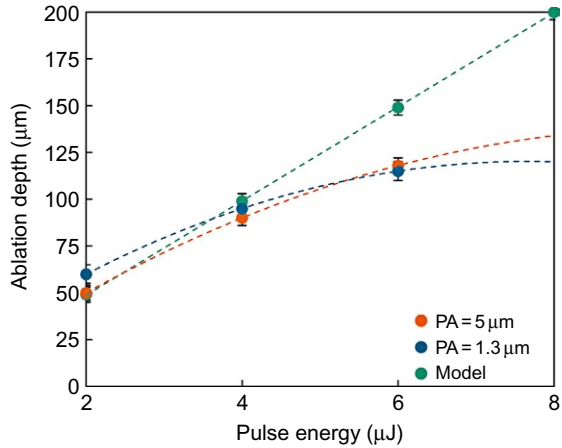


Fig. 5.5 Comparison of the calculated ablation depth with the experimentally derived values at pulse distance of 1.3 and 5 µm after 250 and 1000 passes. Further experimental parameters: wavelength 532 nm, pulse duration 10 ps, repetition rate 400 kHz, focus diameter 11 µm, p-polarization.

than the 50 µm predicted. Thermal interaction occurs between the laser pulses and the material at a small pulse distance. The material is heated up in an area of several square micrometers where the laser beam hits the surface, which leads to a higher degree of absorbance and, therefore, higher ablation per pulse.

At a pulse distance of 5 µm, a pulse energy of 4 µJ and 1000 passes, an ablation depth of 90 µm can be seen, which is equivalent to a percentile deviation of 10% to the calculated depth. Greater differences appear between the modeled and the actual value at a pulse energy of 6 µJ and an identical pulse distance. The results deviate from the calculated depth of 149 µm by up to 30%. Clearly, the calculated ablation depth is systematically higher than the experimentally determined ablation depth—especially with high pulse energies. This effect can be traced back to the fact that Eq. (5.17) implies the peak intensity—which contains the pulse energy—is directly and proportionally correlated with the resulting ablation depth. This in turn, suggests that infinite pulse energy can generate an infinite ablation depth, which is not the case for real ablation processes. In fact, a logarithmic correlation exists between the predominant peak intensity and the ablation depth. Because the intensity is not completely available for the ablation process, but is reduced by heat diffusion into the surrounding material, an increase of the peak intensity does not lead to an enlargement of the cutting kerf depth in the same manner. Instead of creating a deeper cutting kerf, thermal

effects, combined with a greater effective diameter of the laser beam, cause the ablation width to increase. Thus to maximize the aspect ratio, particular attention has to be paid to the intensity of the incoming laser pulses.

The influence of the pulse distance declines as peak intensities increase because a thermal load already occurs during the single-pulse ablation. Furthermore, other influential factors can lead to deviations between model and experiment, that is, polarization-dependent energy coupling with a nonperpendicular laser beam incidence, nano- and micro-scale surface effects, a difficult material removal out of the kerf with increasing cutting depth, and temperature-dependent absorption effects, all of which can lead to varying threshold intensities.

5.4 EXPLANATION OF SURFACE PHENOMENA DURING LASER DICING PROCESSES

In the previous chapters, we explained the development of ablation geometry and compared model and experiment in a qualitative and qualitative manner. This chapter will deal with the explanation of ablation phenomena. To begin with, the varying ablation depth will be the focus of attention; this depth is displayed based on longitudinal cuts seen in Fig. 5.6. After 250 passes, single peaks with increased ablation depth can already be seen on the bottom of the ablation geometry. At this point, the depth of the peaks amounts to ~5 µm. A periodic distribution at an interval of 5 µm predominates except for some areas, which were probably influenced by the sample preparation.

The magnification illustrates that the surface structure not only occurs at the bottom of the kerf but also on the walls, and that the structure obviously expands with each pass. The extremely rough surface resembles so-called LIPPS (Laser-Induced Periodic Surface Structure), which appears on several materials when irradiated with ultra-short pulsed laser radiation. The dimension and periodicity depend mostly on the wavelength, the polarization, and the intensity, where there have been several attempts to explain how these self-organizing structures develop. Most, however, assume they arise when surface effects and the interference of laser radiation interact with the micro- and nano-roughness [39,40]. Usually, the periodic structure is in the magnitude of the wavelength and thus deviates from the present experimental result. Many conditions can be held accountable for this. On the one hand, the peak intensity is more than five times higher than the threshold intensity and, on the other hand, the laser radiation strikes the

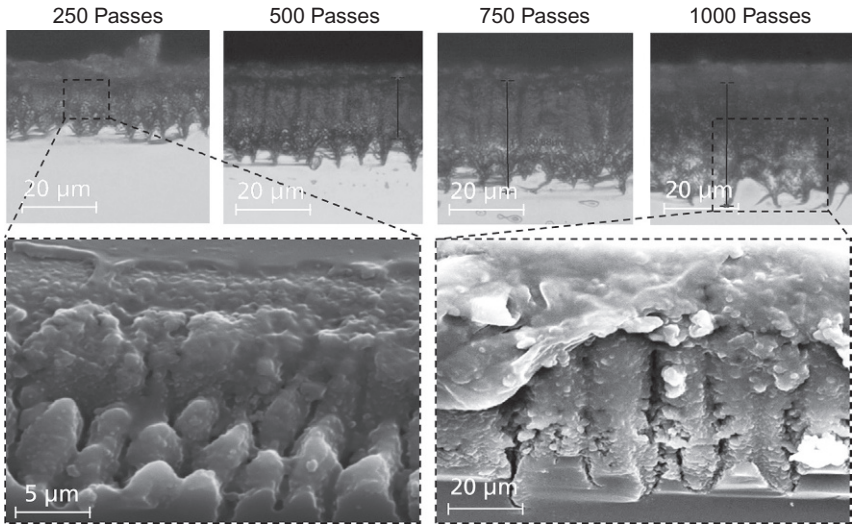


Fig. 5.6 Light-microscope and SEM pictures of ablation geometries in longitudinal section with increasing number of passes from 250, 500, 750, and 1000. Further experimental parameters: wave length 532 nm, pulse duration 10 ps, peak intensity 4.2×10^{11} W/cm^2, repetition rate 400 kHz, pulse distance 5 µm, focus diameter 11 µm, p-polarization.

sample at a constantly increasing angle of projection. The structure, which already exists after 250 passes, remains the same after additional passes and is still visible after 1000 passes. There are no essential changes to the periodic structure and the dimension. It is, however, noticeable that the ablation channels, to some extent, do not run symmetrically in the z-direction, but branch off to the left or to the right. Fig. 5.7 displays the structure of the ablation kerf for different pulse distances of 5, 3.8, 2.5, and 1.3 µm.

The green lines indicate the pulse distance. The periodic structure for all constellations amounts to ~5 µm and is, therefore independent of the pulse to pulse distance. In addition, some ablation channels branch off laterally since a great number of pulses hit the same spot for the pulse distances of 2.5 and 1.3 µm, which presumably results in a variety of polarization-dependent reflections in the ablation channel. As already discussed in the previous passage, the varying depth is likely a consequence of LIPPS formation, which presets a preferred direction for ablation. The incident laser beam is deflected on these structures and, therefore the surface structures, initially only several 100 nm deep, are further deepened to form ablation channels several micrometers deep.

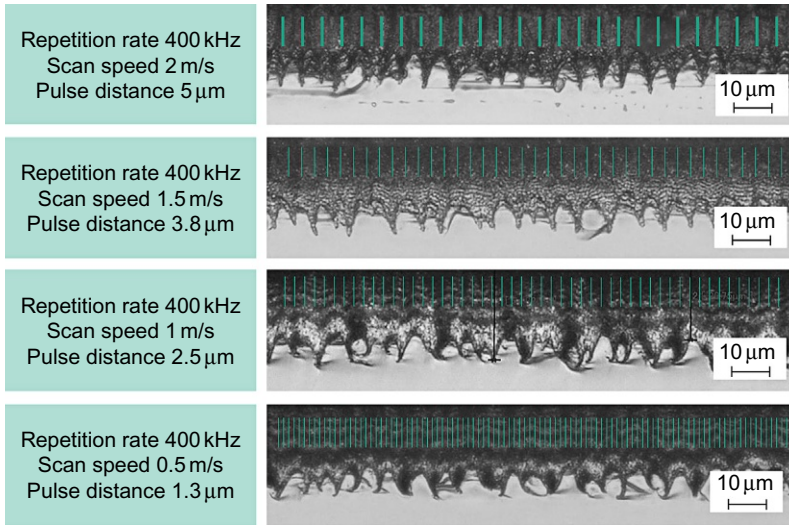


Fig. 5.7 Light-microscope measurements of the cutting kerf in longitudinal view at different pulse distances of 1.3, 2.5, 3.8, and 5 µm and 500 passes. Further experimental parameters: wavelength 532 nm, pulse duration 10 ps, peak intensity 4.2×10^{11} W/cm^2, repetition rate 400 kHz, focus diameter 11 µm, p-polarization.

5.5 FACTORS INFLUENCING THE ASPECT RATIO DURING LASER DICING PROCESSES

5.5.1 Peak Intensity

While we have partially already discussed the influence of the peak intensity on the aspect ratio in previous chapters, this section will present the correlation between the peak intensity and the attainable aspect ratio in a detailed manner and furthermore determines an optimal peak intensity. This correlation is shown in Fig. 5.8 for a wavelength of 532 nm, pulse duration of 10 ps, repetition rate of 400 kHz, focus diameter of 11 µm, p-polarization, and 1000 passes. Whereas the ablation depth initially rises linearly as the incidental laser intensity increases, the ablation depth drifts asymptotically towards a threshold value of 175 µm. Due to the high peak intensity, persistent plasma clouds form. Since the incoming energy cannot be transformed into material ablation, it has to be assumed that a majority is transformed into heating and melting. While the ablation width initially increases very little and remains in the range of under 30 µm up to an intensity of 20×10^{11} W / cm^2, it increases continuously afterwards and finally amounts to more than 50 µm at the maximum inserted peak intensity of 100×10^{11} W / cm^2. The relation

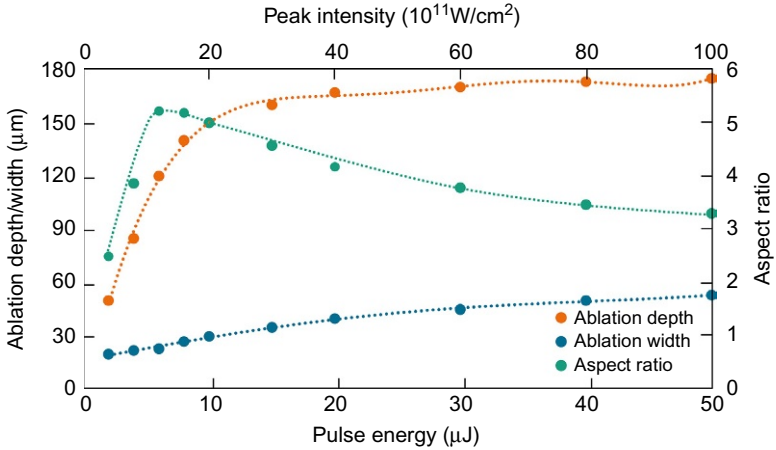


Fig. 5.8 Ablation depth, width, and the resulting aspect ratio at different pulse energies and thus peak intensities. Further experimental parameters: wavelength 532 nm, pulse duration 10 ps, repetition rate 400 kHz, focus diameter 11 µm, p-polarization, 1000 passes.

between the peak intensity and the aspect ratio can be extrapolated from the superposition of these two developments and consequently results in the optimal range of intensities of 10×10^{11} W / cm^2 up to 15×10^{11} W / cm^2. In this particular field, the maximum aspect ratio is 5.2.

5.5.2 Wavelength

Fig. 5.9 shows the ablation depth and width for the three wavelengths (355, 532, and 1064 nm) as the amount of passes increases from 100 up to 1000, at a pulse energy of 2 µJ and, consequently, a peak intensity of 4.2×10^{11} W/cm^2. As before, the pulse duration is 10 ps, the focus diameter 11 µm, the pulse distance 5 µm, and the incidental laser radiation is p-polarized. After 100 passes, the wavelength already influences the ablation depth noticeably. At a wavelength of 355 nm, the depth amounts to 32 µm, at 532 nm to 20 µm, and at a wavelength of 1064 nm, the ablation depth is 15 µm. At approximately this distance, all three curves then run asymptotically towards their particular threshold values of the ablation depth. After 1000 passes and a wavelength of 355 nm, this depth amounts to 61 µm, at 532 nm to 51 µm, and at 1064 nm, the asymptotic ablation depth amounts to 45 µm. Although there are significant differences in the depths, these results are not reflected in the proportions of the threshold intensities. This is due to the fact that

the ablation threshold is only valid for discrete single pulse ablation and that no incubation effects are taken into account. Incubation effects are responsible for different ablation properties of material in dependence on the number of laser pulses that strike the same spot. In addition, the ablation threshold was determined for the straight incidence on a surface and not for the ablation in a prestructured kerf. The right side of Fig. 5.9 shows the development of the ablation width from 100 up to 1000 passes for all three wavelengths (355, 532, and 1064 nm). Similar to the ablation depth, a clear scaling is recognizable. After several hundred passes, three ablation widths can already be seen: 22 µm at a wavelength of 355 nm, 20 µm at a wavelength of 532 nm, and 18.5 µm at a wavelength of 1064 nm. The ablation width is at its highest at 355 nm because the threshold intensity for ablation is at its lowest due to the direct band gap. Therefore, a higher amount of the Gaussian intensity allocation lies above the ablation threshold and is available for the ablation process.

The maximum aspect ratio is 2.77 for a wavelength of 355 nm, 2.55 for a wavelength of 532 nm, and 2.43 for a wavelength of 1064 nm. In terms of the attainable aspect ratio, the ablation at a wavelength of 1064 nm is more effective than at a wavelength of 355 nm. The various absorption mechanisms can be held accountable for these ratios in connection with a high share of reflections at a wavelength of 1064 nm. Fig. 5.10 shows a qualitative comparison of the ablation results with various wavelengths—355, 532, and 1064 nm—based on light-microscopic pictures of the ablation cross-section.

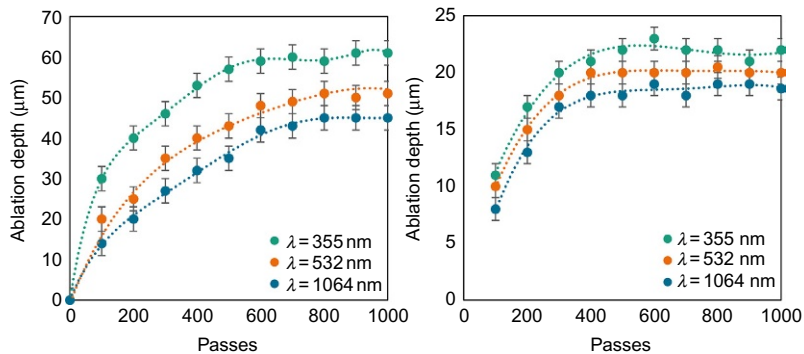


Fig. 5.9 Ablation depth and width at different wavelengths—355, 532, and 1064 nm—depending on the number of passes—from 100 to 1000. Further experimental parameters: pulse duration 10 ps, peak intensity 4.2×10^{11} W/cm^2, repetition rate 400 kHz, pulse energy 2 µJ, focus diameter 11 µm, pulse distance 5 µm, p-polarization.

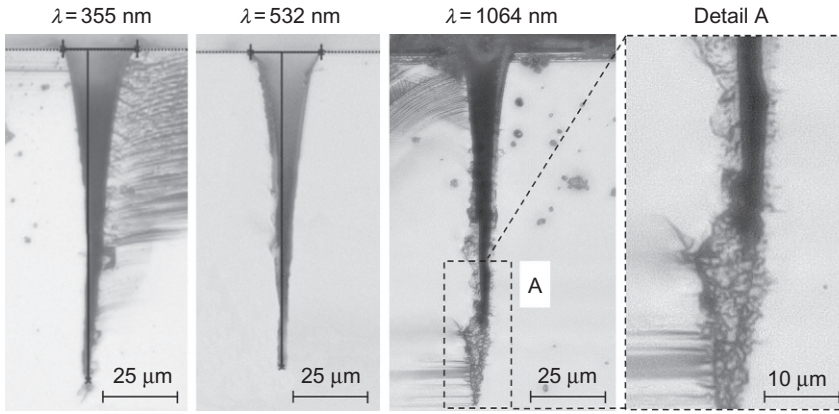


Fig. 5.10 Qualitative comparison of the ablation geometry in a cross-section at different wavelength of 355, 532, and 1064 nm. Further experimental parameters: pulse duration 10 ps, peak intensity 1.3×10^{12} W/cm^2, repetition rate 400 kHz, pulse energy 6 µJ, focus diameter 11 µm, pulse distance 5 µm, p-polarization, 1000 passes.

For all wavelengths, the ablation contour is straight and free of ablation particles. At a wavelength of 1064 nm, micro cracks appear around the cutting kerf. These micro cracks can possibly be traced back to deeply penetrating radiation of previous passes or a high amount of reflections in the cutting kerf. Throughout each reflection, a small part of the incident laser radiation is absorbed; under certain circumstances this can lead to this microscopic damage.

5.5.3 Direction of Polarization

The direction of polarization determines how much of the incident laser radiation is absorbed in the ablation geometry and, therefore, has an influence on the aspect ratio. Fig. 5.11 shows the two ablation geometries with perpendicular laser radiation after 600 and 1000 passes.

The cutting kerf does not run symmetrically to the beam propagation direction, but branches to the left and to the right. This phenomenon can be explained by the high amount of reflected laser radiation that is not absorbed at first, but rather reflected on the opposite side. As a result, some projection angles deviate greatly from the optical axis. Once the ablation geometry has begun moving in a direction deviating from the z-axis, the reflection effects increase and the direction can no longer be reversed. To some extent, a minor bending of the ablation geometry can also be noted with p-polarized laser radiation. This is due to the fact that a perfect polarization contrast ratio cannot be achieved with a real laser beam.

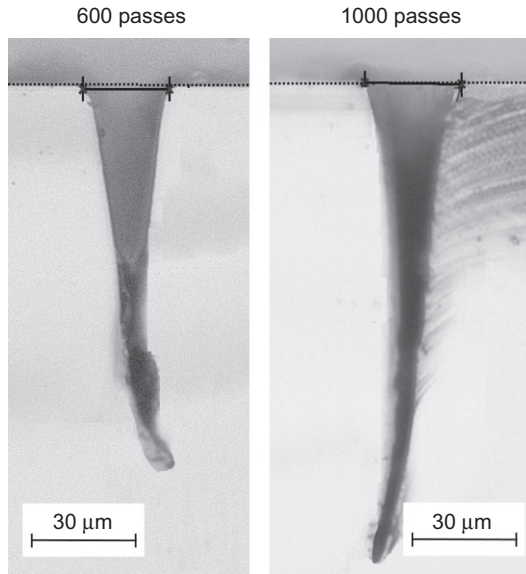


Fig. 5.11 Ablation geometries after 600 and 1000 passes for perpendicularly polarized laser radiation. Further experimental parameters are as follows: wavelength 532 nm, pulse duration 10 ps, peak intensity 1.7×10^{12} W/cm^2, repetition rate 400 kHz, pulse energy 8 µJ, focus diameter 11 µm, pulse distance 5 µm.

Typically, the contrast is in the range of 100:1. With each reflection in the ablation geometry, the p-polarized amount will mainly be absorbed and the s-polarized amount reflected. Therefore, the ratio of the polarization amount changes with each absorption process. This process is highly likely with high aspect ratios and many reflections. The formation of preferred directions even with p-polarized laser radiation can be explained if the following are also taken into consideration: material inhomogeneity, local different surface topographies, and changing thermal edge conditions—which can lead to different absorption ratios. Fig. 5.12 shows pictures of the back of a complete severed silicon sample with a material strength of 120 µm. The previously described effect—the bending of ablation channels with s-polarization—can be seen in an inhomogeneous cutting kerf that has, as a result, a cutting edge with lateral variations of up to 40 µm.

The cutting edge with parallel polarized radiation is straight and ~15 µm wide, although a minor modulation of the cutting edge process is visible. Hence the ablation with p-polarized radiation attains higher aspect ratios, higher ablation rates, and also proves to be advantageous in terms of the cutting-edge quality.

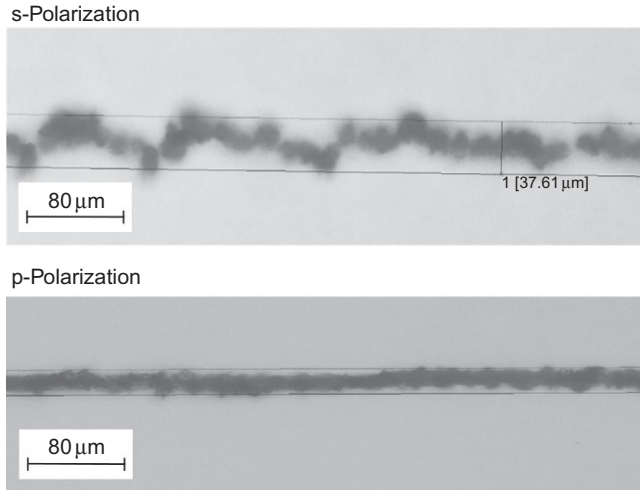


Fig. 5.12 Back view of a completely cut silicon sample with a material thickness of 120 µm for s-polarization (top picture) and p-polarization (bottom picture). Further experimental parameters: wavelength 532 nm, pulse duration 10 ps, peak intensity 1.7×10^{12} W/cm^2, repetition rate 400 kHz, pulse energy 8 µJ, focus diameter 11 µm, pulse distance 5 µm, 1000 passes.

5.5.4 Hybrid Experiments With Local Increase of the Substrate Temperature in the Cutting Kerf by Means of Coaxial Incidental Continuous Wave Laser Radiation

5.5.4.1 Experimental Setup

The experimental setup differs from those in the previously conducted experiments in that a second laser beam is directed at the silicon sample by means of a wavelength independent semipermeable mirror (see left side of Fig. 5.13).

For the investigations in this work, the focal diameter of the coaxially coupled continuous wave laser has been selected which is at least two times larger than the focal diameter of the ultra-fast laser beam; this larger diameter eases the installation and alignment of the setup and guarantees stability and reproducibility of the experimental results throughout the process. The hybrid operation for the local thermal pretreatment is shown on the right side of Fig. 5.13. The cw laser is used to place a local temperature gradient into the cutting kerf—the maximum temperature is always obtained in its center. At this point the maximum projection angle of the ablation process is reached as well. As the distance from the center of the cutting kerf increases, the temperature declines. Both laser beams are coaxially aligned via process control that uses a CMOS beam detector camera (see Fig. 5.14).

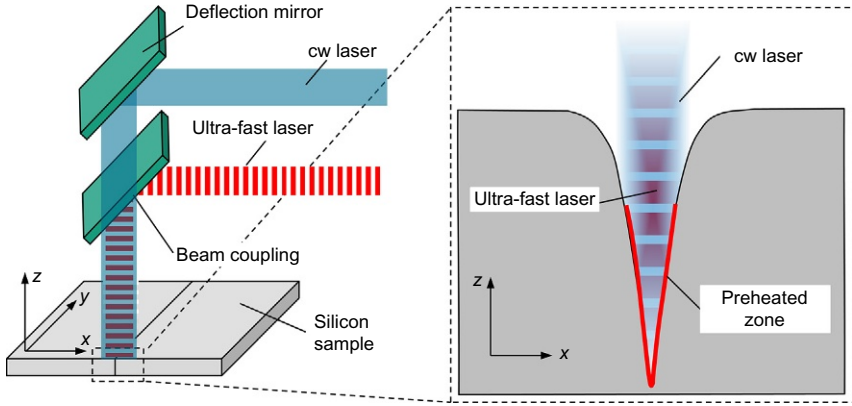


Fig. 5.13 Experimental setup for the hybrid ablation experiments with ultra-fast and cw laser radiation and locally preheated substrate temperatures.

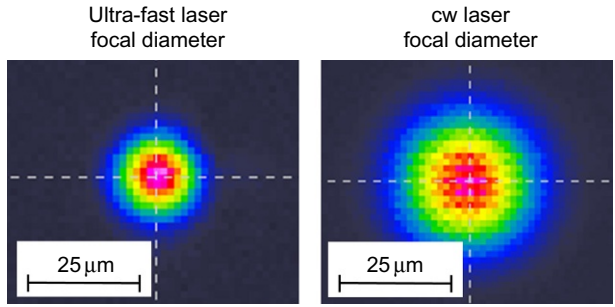


Fig. 5.14 Beam diagnostics and alignment of the ultra-fast and cw lasers.

On the left side, Fig. 5.14 shows the beam cross-section of the ultra-fast laser with a focal diameter of 20 µm. The beam cross-section of the cw laser with an identical focal plane is illustrated on the right side of Fig. 5.14. The focal diameter is 40 µm. The laser beams are aligned laterally in the focal plane with an accuracy of 2 µm. The pixel size of the CMOS beam detector camera is 1.7 µm.

5.5.4.2 Examinations of the Aspect Ratio

Fig. 5.15 illustrates the development of the ablation depth and width at various sample temperatures over an increasing number of passes (from 100 up to 1000) and a focal diameter of the cw laser of 40 µm. The process parameters of the ultra-fast laser are set as follows: 6 µJ pulse energy, 20 µm focal diameter, 200 kHz repetition rate, 8 µm pulse distance, and 3.8×10^{11} W / cm^2 peak intensity. A positive correlation can be seen between ablation depth and increasing depth.

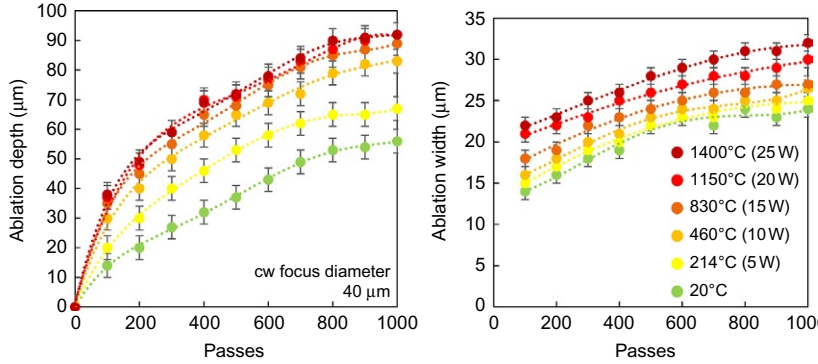


Fig. 5.15 Ablation depth and width at different substrate temperatures of 20°C, 214°C, 460°C, 830°C, 1150°C, and 1400°C resulting from heating with a coaxial cw laser at an average power of 5–30 W and a beam deflection speed of 1.5 m/s. Further experimental parameters: wavelength 1064 nm, pulse duration 10 ps, peak intensity 3.8×10^{11} W/cm^2, repetition rate 200 kHz, pulse energy 6 µJ, focus diameter 20 µm, pulse distance 8 µm, p-polarization. Parameters of the cw laser: wavelength 1070 nm, focus diameter 40 µm, p-polarized.

After 1000 passes, the respective ablation depths amount to 56 µm at a temperature of 20°C, 67 µm at a temperature of 214°C (5W), 83 µm at a temperature of 460°C (10W), 89 µm at a temperature of 830°C (15W), 92 µm at a temperature of 1150°C (20W), and 92 µm at a temperature of 1400°C (25W). Since the melting temperature of silicon is reached at an output power of 25W, the power does not need to be increased any further. A strong correlation of the ablation depths attainable can be seen when the substrate temperature is increased up to 830°C. Temperatures beyond this only lead to a marginal increase of the ablation depth.

For all substrate temperatures, the width increases approximately linearly as the number of passes increases. The higher the output of the preheat laser, the wider the ablation geometry. In particular, after 1000 passes, the ablation width amounts to 24 µm at 20°C, 25 µm at 214°C (5W), 26.5 µm at 460°C (10W), 27 µm at 830°C (15W), 30 µm at 1150°C (20W), and finally 32 µm at 1400°C (25W). Initially, the resulting aspect ratio profits greatly from the increasing sample temperature, and at a temperature of 214°C (5W) it amounts to 2.7. This corresponds to an increase of 17% in comparison with the aspect ratio of 2.3 at a temperature of 20°C. A further increase of the temperature of 460°C (10W) leads to an aspect ratio of 3.1 (+34%). The maximum aspect ratio of 3.3 (+43%) is reached at a substrate temperature of 830°C (15W). Therefore, the increasing ablation width impinges upon

the resulting aspect ratio, which measures up to 2.9 at a substrate temperature of 1400°C (25W). Compared to a 100 µm focal diameter of the cw laser, a diameter of 40 µm can be used to generate greater increases of the aspect ratios. This can be traced back to the radiated area and the different steep temperature gradients, which are directly proportional to the focal diameter used.

5.5.4.3 Qualitative Evaluation of the Ablation Geometry

After the correlation between the substrate temperature, the ablation threshold, and the resulting aspect ratios has been examined, the quality of the ablation geometry must be considered regarding thermal damage, crack formations, or the formation and precipitation of melting particles. In this context, Fig. 5.16 illustrates ablation geometries after 500, 800, and 1000 passes at a substrate temperature of 460°C and after metallographic sample preparation. The temperature was generated by a cw laser with a focal diameter of 40 µm and laser power of 10W at a beam deflection speed of 1.5 m/s. The process parameters of the ultra-fast laser are as follows: pulse duration 10 ps, focal diameter 20 µm, peak intensity 1.3×10^{12} W / cm^2, pulse distance 8 µm, repetition rate 200 kHz, p-polarization. After 500, 800, and

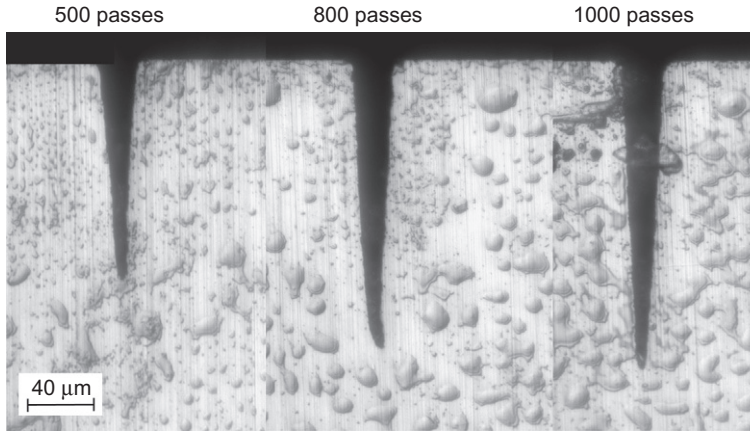


Fig. 5.16 Ablation geometries in cross-sectional view after 500, 800, and 1000 passes at a substrate temperature of 460°C through irradiation with a coaxial cw laser at an average power of 10°W and a beam deflection speed of 1.5 m/s. Further experimental parameters: wavelength 1064 nm, pulse duration 10 ps, peak intensity 1.3×10^{12}W/cm^2, repetition rate 200 kHz, pulse energy 20 µJ, focus diameter 20 µm, pulse distance 8 µm, p-polarization. Parameters of the cw laser: wavelength 1070 nm, focus diameter 40 µm, p-polarization.

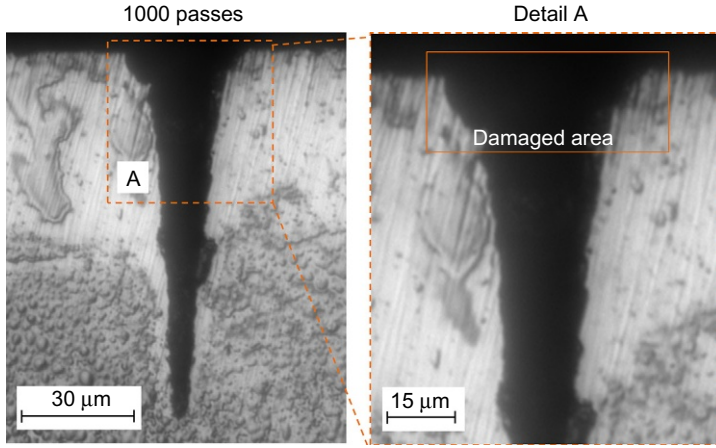


Fig. 5.17 Ablation geometry in cross-sectional view after 1000 passes at a substrate temperature of 1150°C through irradiation with a coaxial cw laser at an average power of 20°W and a deflection speed of 1.5 m/s. Further experimental parameters: wavelength 1064 nm, pulse duration 10 ps, peak intensity 3.8×10^{11} W/cm^2, repetition rate 200 kHz, pulse energy 6 µJ, focus diameter 20 µm, pulse distance 8 µm, p-polarization. Experimental parameters of the cw laser: wavelength 1070 nm, focus diameter 40 µm, p-polarization.

1000 passes, the ablation geometry shows a sharp profile without cracks. Neither thermal damages nor precipitate of melt or ablation particles can be seen at the laser radiation entrance surface. An aspect ratio of 4.3 results after 500 passes. After 800 passes, an aspect ratio of 5.3 results and after 1000 passes, the aspect ratio finally amounts to 5.4.

Fig. 5.17 illustrates cross-sections of metallographically prepared ablation geometries resulting from a substrate temperature of 1150°C (20W) after 1000 passes. The temperature is generated by a cw laser beam with a focal diameter of 40 µm and a laser power of 20W at a beam deflection speed of 1.5 m/s. The process parameters of the ultra-fast laser are as follows: pulse duration 10 ps, focal diameter 20 µm, pulse energy 6 µJ, peak intensity 3.8×10^{11} W / cm^2, pulse distance 8 µm, repetition rate 200 kHz, p-polarization. No significant thermal damage in form of excessive melt formation can be detected as with the process at a substrate temperature of 460°C. However, it is conspicuous that the course of the ablation geometry is not constant at the junction to the wafer surface. The ablation width grows dramatically (see the framed area in the enlargement on the ride side of Fig. 5.17). This enlargement causes the aspect ratio to fall and amounts to 3.1 after 1000 passes. It is highly likely that the unsteady enlargement of

the ablation width can be traced back to the overexposure of the ablation contour by the cw laser with a 40 μm focal diameter. Consequently, the surrounding material around the cutting kerf heats up, which lowers the ablation threshold and increases the ablation width.

5.6 INCREASING DICING MODIFICATION DEPTH USING HIGH-REPETITION-RATE FEMTOSECOND LASER RADIATION AND SPATIAL BEAM SHAPING

Interaction of subpicosecond pulsed laser radiation with semiconductor materials can lead to nonlinear propagation phenomena resulting in deep material modifications along the optical propagation axis. Femtosecond laser-produced groove depths considerably exceeding the dimensions of the high-intensity focal volume that is assumed for linearly propagating light can be achieved in semiconductors like silicon. Therefore, nonlinear light propagation and heat accumulation effects must be considered as import factors influencing the kerf geometry. A series of Si scribing/dicing experiments were performed utilizing laser radiation produced by an Amplitude Satsuma femtosecond fiber laser (wavelength $\lambda = 1030$ nm, pulse duration of $t_p = 350$ fs, repetition rate $f_{rep} = 500$ kHz, and pulse energies up to $E_p = 10$ μJ). Linearly polarized laser radiation was focused onto the surface of intrinsic and doped <100>-Si wafers using a 5×/NA = 0.1 microscope objective resulting in sub 10 μm modification spot size measured using the 1/e2 metric. In addition, spatial beam shaping was adopted to create elliptical energy distributions using a set of two positive and one negative cylindrical lenses (see Fig. 5.18A). Process parameter studies were performed by varying the scan speed, the pulse energy, the number of scan repetitions, and

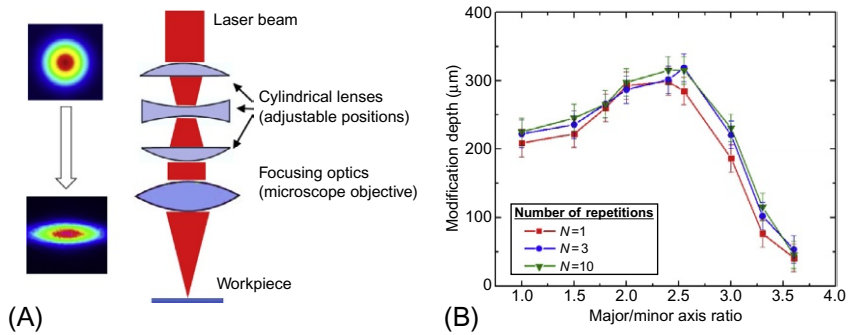


Fig. 5.18 (A) Adjustable spatial beam shaping using cylindrical lenses, and (B) Experimental results for modification depths obtained in Si at different ratios of major and minor ellipse axes, at a constant translation speed $v = 0.5$ mm/s, and $E_p = 8.5$ μJ.

the major/minor axis ratio of the elliptical energy distribution. The major axis of the ellipse was oriented in the direction of the laser beam translation, while laser polarization was perpendicular to the translation direction. Modifications were investigated using optical microscopy and SEM by producing cross-sections, as well as by mechanical separation of irradiated wafers along the modification tracks. Chemical wet etching was applied to reveal the modification morphology.

Fig. 5.18B shows the experimentally obtained data for modification depths achieved for different ratios of the major and minor ellipse axes, and varying number of passes. For the ratio value of 1.0, which corresponds to nearly circular beam profile, modification depths up to $d = 227\,\mu m$ were achieved. Increasing the major/minor ratio to 2.6 resulted in maximum modification depths of $d = 314\,\mu m$ (see Fig. 5.19). The cross-sections of the modified areas revealed a conical crater shape along ~150 μm depth of the channel, and afterwards the channel width was nearly constant at $w = 8.9\,\mu m$. The crater width at the surface was approximately $w = 18.22\,\mu m$, resulting in the maximum aspect ratio of the channel of $d/w = 15.20$.

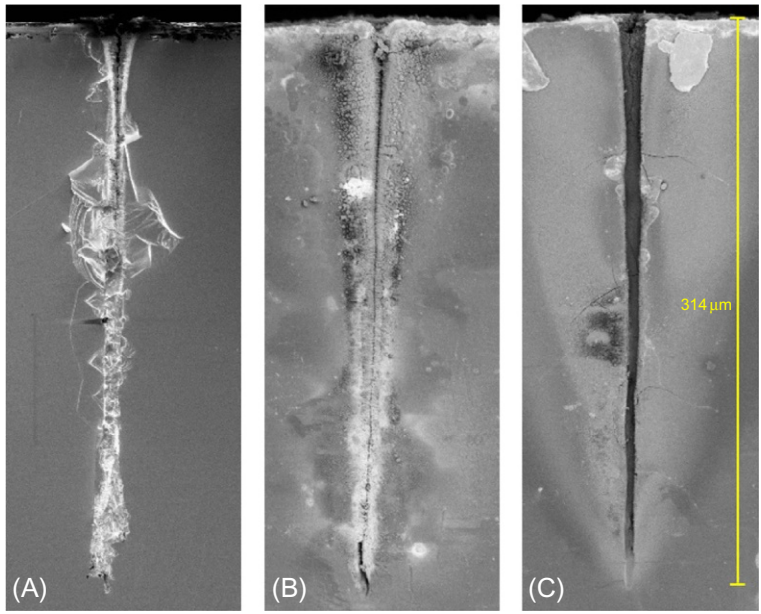


Fig.5.19 Cross-sections of laser-processed Si wafer: (A) As-cleaved surface, (B) after etching for 30 min in 5:1 buffered oxide etch solution, and (C) after etching for 40 min in 20 wt% HF solution.

Further process parameter studies were performed using the ellipse axis ratio of 2.6 and by varying the translation speed. At smaller translation speeds of $v = 0.1$ mm/s, modification depths of over $d = 410$ µm were achieved. However, the modification morphology revealed a large heat-affected volume at the bottom of the channel, as well as its bending towards the end. Processing at slower translation speeds results effectively in a large energy dosage (optical energy deposited per time and groove length unit) applied. The excessive heat is accumulated at the bottom of the channel, which causes melting and material structure changes, potentially promoting crack formation and degrading the quality of laser processing. Longitudinal sections show large regions in the central part of the modification, where the material appears less affected by the processing than the regions near the substrate surface and the bottom of the channel.

Formation of very deep channels could be potentially caused by a variety of linear and nonlinear light propagation and laser-semiconductor interaction phenomena. First, especially at slow translation speeds, light propagation inside the laser-induced channel is similar to a drilling process with ultrafast lasers. Due to the sharply defined material modification thresholds, interaction of laser radiation with the channel walls is limited once an initial surface crater is created. However, for subsequent pulses, the laser beam is

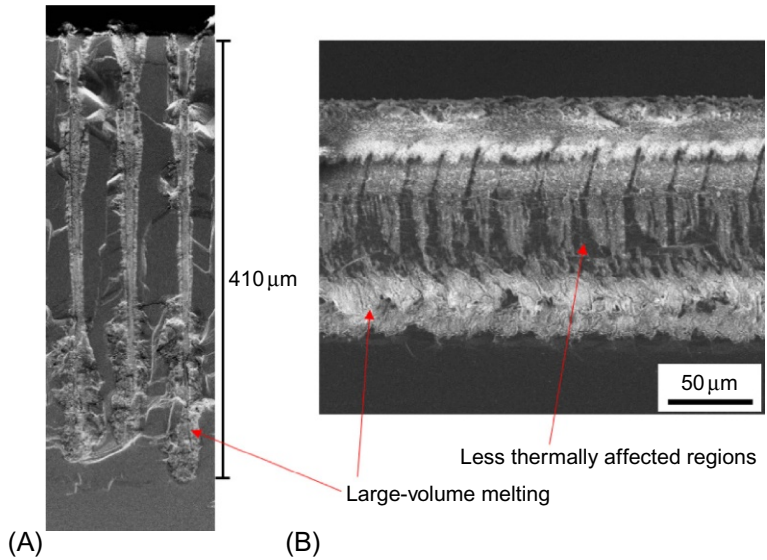


Fig. 5.20 (A) Cross-sections of laser-induced grooves produced at $v = 0.1$ mm/s and (B) longitudinal section of the groove.

subject to multiple reflections resulting in optical energy reaching deep into the wafer. Second, the applied laser wavelength (1.03 μm) is very close to the band edge gap of Si (~1.1 μm at room temperature), the optical penetration depth can reach ~200 μm, resulting in "semitransparency" of the material. Therefore, both linear and nonlinear, i.e. two-photon absorption, are possible in Si. Nonlinear propagation effects similar to filamentation in dielectrics [41] can occur, e.g., periodic Kerr-induced self-focusing of the laser beam and subsequent defocusing due to the negative refractive index of laser-induced plasmas (Fig. 5.20).

REFERENCES

[1] B. McClean, IC Insights Research Bulletin, Arizona, 2014.
[2] G. Kucera, Miniaturisierung und Mechatronics stehen im Mittelpunkt, Elektronik Praxis, Würzburg, 2014.
[3] P. Russer, P. Lugli, M. Weitze, Elektronik im Kleinen—Gestern und Heute: Begriffsdefinition und Hintergründe zur Nanoelektronik, Springer, Heidelberg, 2013.
[4] S. Endler, E.A. Angelopoulos, S. Ferwana, C. Harendt, M.-U. Hassan, J.N. Burghartz, Ultradünne Chips in flexibler Elektronik, in: Proceedings Elektronische Baugruppen und Leiterplatten—EBL (GMM-FB 71), Stuttgart, 2012.
[5] R. Sauer, Halbleiterphysik: Lehrbuch für Physiker und Ingenieure, Oldenbourg Verlag, München, 2010.
[6] R. Hull, Properties of Crystalline Silicon, INSPEC The Institution of Electrical Engineers, London, 1999.
[7] J.E. Ayers, Digital Integrated Circuits: Analysis and Design, McGraw-Hill Higher Education, Maidenhead, UK, ISBN: 0071181644, 2003 . S. 31 ff.
[8] S. Takyu, T. Kurosawa, N. Shimizu, S. Harada, Novel wafer dicing and chip thinning technologies realizing high chip strength, in: IEEE (Hg.): 56th Electronic Components and Technology Conference 2006, San Diego, CA, USA, May 30–June 2, 2006 (IEEE Proceedings), 2006, pp. 1623–1627.
[9] S.Y. Luo, Z.W. Wang, Studies of chipping mechanisms for dicing silicon wafers, Int. J Adv. Manuf. Technol. 35 (11–12) (2008) 1206–1218.
[10] H. Beneking, Halbleiter-Technologie : eine Einführung in die Prozesstechnik von Silizium und III-V-Verbindungen, Teubner, Stuttgart, 1991.
[11] R. Doering, Y. Nishi, Handbook of Semiconductor Manufacturing Technology, 2. Aufl., CRC Press, Boca Raton, FL, 2008.
[12] B. Richerzhagen, Wasserstrahlgeführtes Laserschneiden von Wafern, in: S.A. Synova, C.H. Lausanne (Eds.), 2014. verfügbar unter: http://www.synova.ch/fileadmin/user_upload/conferences/2000_LEF.pdf.
[13] M. Kumagai, N. Uchiyama, E. Ohmura, Ryuji Sugiura, A. Kazuhiro, F. Kenshi, Advanced dicing technology for semiconductor wafer—stealth dicing, IEEE Trans. Semicond. Manuf. 20 (3) (2007) 259–265.
[14] J. Ren, S. Orlov, L. Hesselink, H. Howard, J. Conneely, P. Herman, et al., Nanosecond laser silicon micromachining, in: SPIE (Eds.), Lasers and Applications in Science and Engineering. Photon Processing in Microelectronics and Photonics III, SPIE (SPIE Proceedings, 5339) San Jose, CA, 25 January 2004, 2004, pp. 382–393.
[15] R. Poprawe, Lasertechnik für die Fertigung, Springer Verlag, Heidelberg, 2005. pp. 309–313.

[16] C. Kulik, Short and ultrashort laser pulses: an upcoming tool for processing optical and semiconductor materials, Proc. SPIE 5339 (2004) 35–48.
[17] H. Hügel, T. Graf, Laser in der Fertigung: Grundlagen der Strahlquellen, Systeme, Fertigungsverfahren, 3. Auflage, Springer Verlag, Heidelberg, 2014.
[18] N. Bärsch, K. Körber, A. Ostendorf, K.H. Tönshoff, Ablation and cutting of planar silicon devices using femtosecond laser pulses, Appl. Phys. A 77 (2003) 237–242.
[19] J. Bonse, S. Baudach, J. Krüger, W. Kautek, M. Lenzner, Femtosecond laser ablation of silicon-modification thresholds and morphology, Appl. Phys. A 74 (2002) 19–25.
[20] D. Hwang, C. Grigoropoulos, Efficiency of silicon micromachining by femtosecond laser pulses in ambient air, Appl. Phys. 99 (2006) 083101.
[21] G. Raciukaitis, V. Kazlauskiene, J. Miskinis, Ablation of silicon by picosecond pulses of laser radiation, in: Proceedings of the 23rd ICALEO, Orlando, FL, 2004.
[22] A. Ostendorf, C. Kulik, T. Bauer, N. Bärsch, Ablation of metals and semiconductors with ultrashort-pulsed lasers: improving surface qualities of microcuts and grooves, Proc. SPIE 5340 (2004) 153–163.
[23] R. Zengerle, Mikrosystemtechnik 2: Aufbau- und Verbindungstechnik 1, Universität Freiburg, Mikrosystemtechnik, Vorlesungsskript, Freiburg, 2002.
[24] U. Efrat, Optimizing the wafer dicing process, in: IEEE (Hg.): 15th IEEE/CHMT International Electronic Manufacturing Technology Symposium. Santa Clara, CA, USA, 4-6 Oktober 1993 (IEEE Proceedings), 1993, pp. 245–253.
[25] Internet: http://www.microwaterjet.com/technology/the-advantages/.
[26] Internet: http://www.incodema.com/processes/MicroCut-Cutting.aspx.
[27] B. Richerzhagen, Industrial applications of the water-jet guided laser, Ind. Laser User 28 (2002) 28–30.
[28] E. Gu, C.W. Jeon, H.W. Choi, Micromachining and dicing of sapphire, gallium nitride and micro LED devices with UV copper vapour laser, in: Proceedings of Symposium H on Photonic Processing of Surfaces, Thin Films and Devices, of the E-MRS 2003 Spring Conference, Glasgow, 2004.
[29] F. Fukuyo, K. Fukumitsu, N. Uchiyama, Stealth dicing technology and applications, in: Japan Laser Processing Society (JLPS) (Eds.), The 6th International Symposium on Laser Precision Microfabrication, Williamsburg, VA, 4-8 April 2005 (Proceedings of LPM2005), 2005.
[30] Hamamatsu (Eds.), Laser Advanced Materials Processing, 2014. Online verfügbar unter http://www.hamamatsu.com/resources/pdf/etd/SD_tech_TLAS9004E01.pdf.
[31] K. Fukumitsu, M. Kumagai, E. Ohmura, H. Morita, K. Atsumi, N. Uchiyama, The mechanism of semiconductor wafer dicing by stealth dicing technology, in: Japan Laser Processing Society (JLPS) (Eds.), The 4th International Congress on Laser Advanced Materials Processing, Kyoto, Japan, 16-19 May 2006 (Proceedings of LAMP2006), 2006.
[32] O. Haupt, F. Siegel, A. Schoonderbeek, L. Richter, R. Kling, A. Ostendorf, Laser dicing of silicon: comparison of ablation mechanisms with a novel technology of thermally induced stress, J. Laser Micro/Nanoeng. 3 (3) (2008) 135–140.
[33] S. Schoenfelder, M. Ebert, C. Landesberger, K. Bock, J. Bagdahn, Investigations of the influence of dicing techniques on the strength properties of thin silicon, Microelectron. Reliab. 47 (2006) 168–178.
[34] O. Haupt, et al., Laser dicing of silicon: comparison of ablation mechanisms with a novel technology of thermally induced stress, J. Laser Micro/Nanoeng. 3 (3) (2008).
[35] S. Döring, et al., Evolution of hole depth and shape in ultrashort pulse deep drilling in silicon, Appl. Phys. A 105 (2011) 69–74.
[36] K. Venkatakrishnan, A high-repetition-rate femtosecond laser for thin silicon wafer dicing, J. Micromech. Microeng. 18 (7) (2008) 075032.

[37] A. Yokotani, Development of dicing technique for thin semiconductor substrates with femtosecond laser ablation, in: Photon Processing in Microelectronics and Photonics III, Proc. of SPIE, vol. 5339, 2004.
[38] U. Eppelt, Simulation des Abtragsverhaltens von Dielektrika und Halbleitern bei der UKP-Laserbearbeitung, RWTH Aachen. Dissertation in Vorbereitung, Aachen, 2015.
[39] B. Tan, K. Venkatakrishnan, A femtosecond laser-induced periodical surface structure on crystalline silicon, J. Micromech. Microeng. 16 (5) (2006) 1080.
[40] R. Wagner, et al., Subwavelength ripple formation induced by tightly focused femtosecond laser radiation, Appl. Surf. Sci. 252 (24) (2006) 8576–8579.
[41] D. Esser, S. Rezaei, J. Li, P.R. Herman, J. Gottmann, Time dynamics of burst-train filamentation assisted femtosecond laser machining in glasses, Opt. Exp. 19 (25) (2011) 25632–25642.

CHAPTER 6

Laser Machining of Carbon Fiber-Reinforced Plastic Composites

P. Jäschke, V. Wippo, S. Bluemel, R. Staehr, H. Dittmar
Laser Zentrum Hannover e.V., Hannover, Germany

6.1 INTRODUCTION

Composites based on carbon fiber reinforced plastics (CFRPs) show great potential for lightweight constructions in many industrial fields. The main reason for this arises from the high achievable strength-to-weight ratio that is produced when a composite is created using the combination of either a thermoset or thermoplastic as the polymer matrix, with a continuous carbon fiber arrangement as reinforcement. For the high-grade composite construction materials used today, the use of both noncrimp fabrics (typically applied as tapes within fiber placement processes) and fabrics (e.g., for use in resin transfer molding (RTM) processes and in organic sheets for thermoforming steps) have become well established in industry. In addition, for parts and components made of CFRP, a greater design freedom exists compared to classic metal constructions. The use of this class of composite material allows for significant reductions in carbon dioxide emissions due to its high strength to weight ratio and as a result, it has been heavily utilized by the aerospace industry for the development of new components. The use of CFRP is not limited to just the aerospace industry; there has been an increased interest for its use in infrastructural parts in automotive, railway, and marine applications as well within the sports and leisure sector.

For the majority of CFRP composites produced today, the matrix material is based on thermoset plastics (as opposed to thermoplastics) such as epoxy resins or polyurethane. Thermoplastic based CFRP composites are of rising interest not only for their exceptional impact tolerances, but also due to the other favorable properties they exhibit such as chemical resistance, recyclability, and relative ease of production for advanced parts. This class of material exhibits other outstanding properties such as weldability and

Advances in Laser Materials Processing
https://doi.org/10.1016/B978-0-08-101252-9.00006-6
Copyright © 2018 Elsevier Ltd.
All rights reserved.

the possibility of applying thermoforming steps. In terms of the economic aspects of their use, they also have a nearly unlimited storage time without the need for cooling. Different thermoplastic composites are available on the market. For high-performance applications, the materials mainly used for the polymeric matrix material are polyetheretherketone (PEEK), polyetherketoneketone (PEKK), polyphenylene sulfide (PPS), or polyetherimide (PEI).

In order for high production rates with short cycle times to be achievable for the manufacturing of composite parts, with regards to repair, maintenance, and assembly of parts, the use of automated process chains becomes a requirement. In this context, trimming, drilling, composite layer removal, and joining processes are of primary importance. Composite materials typically are cut using mechanical processes such as abrasive waterjet techniques, milling, or grinding. These processing options all have similarly unattractive deficiencies—be it the necessity of a complex water circuit required for water jet cutting, or high tool wear for milling and grinding. Moreover, since the operating principles for these methods are not free of forces, they can produce varying results in terms of processing quality as the tools can be pushed aside or deformation of treated parts can occur.

Unlike the fabrication of CFRP composites, laser processes are used for the machining of metal parts on a large scale. The use of lasers in production cycles is promoted by their inherent ability to be a noncontact operation and their flexibility for use in three-dimensional machining. In that regard, applied tool wear is no longer an issue and a process free of forces can be utilized. Already used for the processing of metals, high feed rates can also be realized in composite processing through the use of high power laser systems such as CO_2, fiber, or disk lasers in the multi-kW range. With this cutting strategy, there will be heat induced damage at the cutting edge, typically referred to as the heat affected zone (HAZ), due to the thermal impact of the process. The HAZ is influenced by the thermal characteristics of the polymeric matrix material and the carbon fiber reinforcement. Laser radiation is absorbed in the CFRP part and transferred as process heat throughout the laser-material interaction. This promotes localized overheating in the polymer matrix, as the carbon fibers have a much higher thermal conductivity than that of the surrounding plastics and as a result, heat transfer mainly occurs in the fiber direction. This can also result in degradation of the polymer material and evaporation, causing reduced adhesion between the reinforcing fibers and the matrix material, affecting the overall mechanical performance of the processed part. These effects are mainly determined

by the orientation and type of carbon fibers used, as well as the applied cutting strategy.

In addition to cutting, laser based ablation processes can be used for the repair of composite structures. Compared to the more conventional construction materials, significantly more complex repair strategies are required to assure continuing usability for CFRP composites. In composites repair, damaged areas within laminate structures are comprehensively extracted by a selective removal of single carbon fiber plies. These layers can be eliminated using pulsed laser processing in the UV or NIR range or by applying cw lasers at very high feed rates by use of fast scanners, e.g., polygon-based systems. With laser processing it becomes possible to realize a scarfed structure within the composite part. This stepped structure forms the basis for the following refill step, typically consisting of a vacuum process, allowing new fiber plies in conjunction with new resins to be consolidated. There is currently great interest in the thermal impact of laser processing regarding the influence of the laser-material interaction and its correlation to HAZ formation on the potential modification of mechanical properties. In order to determine the influence the use of lasers has on mechanical properties adequate testing programs need to be run to generate applicable test data to form a basis for composite construction guidelines.

The use of thermoplastics in the construction of CFRP composites gives the material the ability to be welded. For the construction of structural and interior parts in a range of industries, it requires that different components be joined together in complex assemblies. Today, the use of rivets and the application of adhesive bonding techniques are wide spread for this purpose. However, in attempt to reduce the weight and cycle times of these assemblies, efforts have been made to forgo the use of filler and additional materials in the joining process. To employ an adhesive bonding technique for PPS-, PEEK-, or PEKK-matrix based composites, extensive surface preparation needs to be done as high-performance polymers are characterized by their high chemical resistance. In addition to the manufacturing of carbon fiber based composite materials, there is also interest in using glass fiber reinforced composite material combinations.

For the joining of unreinforced and short glass fiber reinforced thermoplastics, laser transmission welding (LTW) is accepted as an industrially established technology. This technology exhibits outstanding properties such as excellent reproducibility and high flexibility. The application involves a localized energy input and lack of flash melt in the matrix material. Adaptation and transfer of LTW to the joining of combinations containing

CFRP composites would be of interest, especially if continuous glass fiber reinforced structures are involved. Diode lasers are typically the laser source used for this application, emitting in the NIR range.

If LTW is to be applied as a processing technology for the reliable welding of composites in an industrial environment, the process specific characteristics such as beam guidance, shaping, and deflection must be considered. Furthermore, process temperatures and optical properties also must be monitored and controlled when using lasers. Welding connections must be evaluated regarding the quality of the weld seam and the achievable joint strengths for both static and fatigue testing. The latest developments focus on the welding of structural parts comprised of CFRP-CFRP-connections for both fabric and noncrimp fabric reinforcements. As a result, the welding technique used has shifted from the more traditional transmission welding configuration to heat conduction welding, providing remarkably high joint strengths.

This chapter gives an overview of the latest findings in laser processing of CFRP composites and focuses on several subtopics within it. It outlines the various configurations for welding composites, including both transmission and heat conduction welding. It also describes the various cutting strategies important for trimming and drilling as well as ablation and its role as an essential part of the composite repair chain. Finally, it outlines the analysis and handling of process emission, both generated and released during the cutting process.

6.2 WELDING OF THERMOPLASTIC COMPOSITES

Thermoplastic parts are commonly used in the automotive and aerospace industry. Their use in these industries often requires them to be joined to other thermoplastic parts to generate complex structures. The joining can be done with adhesive bonding, bolting, or welding. Different welding techniques can be applied such as vibration, ultrasonic, induction, resistance, and laser welding [1]. Laser welding is an established joining technique to weld unreinforced or short glass fiber reinforced thermoplastics. Its advantages are the local heat input, 3D-capability, high flexibility, and reproducibility [2]. Due to the absence of mechanical vibrations in the welding process as is characteristic of other welding techniques, such as ultrasonic welding, medical and electronic devices can be welded by laser radiation [3]. Diode lasers are often used for welding processes due to their high degree of efficiency and their low investment cost compared to other laser types. In the

last couple of years, LTW has been further developed to be applied for long fiber reinforced plastics.

6.2.1 Influences on Laser Transmission Welding

LTW is based on the partial optical transparency of natural thermoplastics in the NIR range. This transparency of the upper part allows the NIR laser radiation to pass through it and be absorbed by the part underneath (absorbing part) when the bottom part contains materials such as carbon black or carbon fibers. Radiation is then converted into heat in the absorbing part. The absorbing characteristics are affected by the kind and amount of additive. The developed process heat conducts to the transparent part, which then in turn becomes molten as well. In order to support the heat conduction, a constant clamping pressure along the weld seam needs to be applied [4,5] (Fig. 6.1).

The LTW is divided into four different basic types:contour, quasisimultaneous, mask, and simultaneous welding (Fig. 6.1). For contour welding, the weld seam is created with one pass of the laser beam. This welding technique can be applied to generate long and three-dimensional weld seams [4,6]. In contrast to contour welding, the process for quasisimultaneous welding involves multiple passes of the laser beam over the joining area guided by a scanner optic. This technique has the advantage of a high

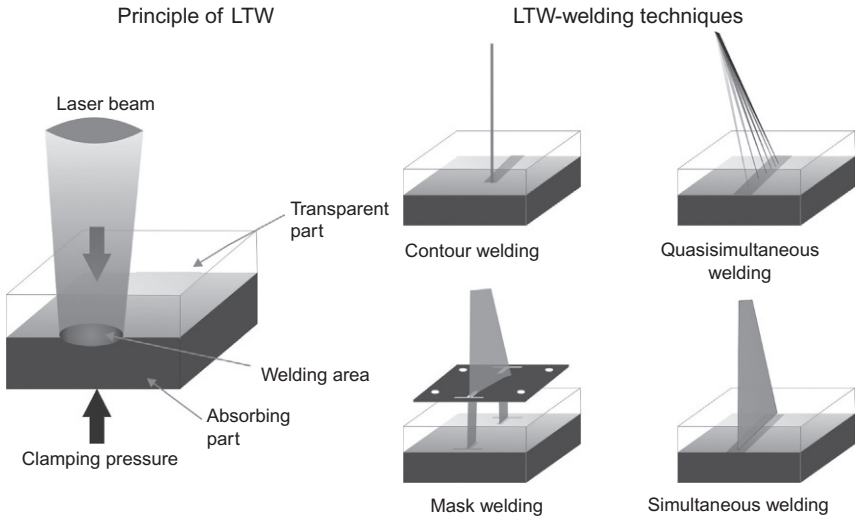


Fig. 6.1 Principle of laser transmission welding (left), and basic laser transmission welding techniques (right).

gap bridge capability, but the disadvantage of limited weld seam lengths. The amount of applied energy (energy per unit length E_s) is the reference value E_s, which allows comparing contour and quasisimultaneous welding to each other. It is calculated by:

$$E_s = \frac{N \times P_L}{v} \tag{6.1}$$

with the number of laser beam passes over the weld seam N, the laser output power P_L and welding speed v. For mask welding, the laser beam is widened or shaped to a line and moved over a mask.

The mask is a negative of the weld seam and is placed above the work piece. With this joining technique, complex contours with small dimensions can be realized [4,7]. For simultaneous welding, the laser beam is shaped analog to the weld seam geometry and the whole weld seam becomes liquefied at the same time [2,8].

As was discussed earlier, the capability of the LTW process is affected by the material of the joining parts. When the laser radiation hits the transparent part, part of the radiation is absorbed by the thermoplastic material. Radiation can be scattered due to glass fibers, additives, etc. as well as reflected on surfaces. The remaining radiation, which passes through the transparent part, will contribute to the actual welding process [9,2,8].

The absorbing part also influences the welding process as it dictates how much of the electromagnetic radiation is absorbed and transferred into heat. The absorption of radiation depends, for example, on the amount of carbon black in the material.

If heat is developed, it is not only conducted to the transparent joining part, but also inside the absorbing part. If the absorbing part contains carbon fibers, process heat conducts along these fibers. Carbon fibers have high heat conductivity along the fibers, but a low heat conductivity perpendicular to the fiber orientation. This results in a weld seam development, which depends on the carbon fiber orientation within the weld seam.

Fig. 6.2 shows the fraction pattern of unmodified PPS (PPS nat.) welded to PPS containing carbon black (PPS c.b.) and welded to carbon fiber fabric reinforced PPS (CF/PPS). The fraction pattern of the PPS nat./PPS c.b. combination shows a homogeneous joining area. Compared to this, the fraction pattern for the combination of PPS nat./CF/PPS is irregularly shaped, as the enclosing angle between weld seam orientation and carbon fiber roving orientation changes between 0° and 90°. If the fiber orientation is 90°, the process heat conducts out of the weld seam and in the

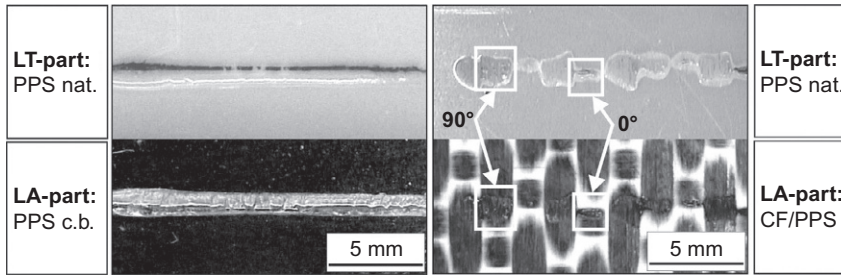


Fig. 6.2 Fraction pattern of PPS nat./PPS c.b. (left) and PPS nat./CF/PPS (right) [8].

process, increases the weld seam width for higher applied energy. If a low amount of energy is applied, the heat conducts out of the welding area and less energy is available for the actual welding process, resulting in a smaller weld seam. When the enclosing angle is 0°, the process heat remains in the weld seam [8].

Fig. 6.3 shows how the process temperature difference varies with the kind of absorbing member used. The temperatures were detected using a pyrometer outputting a voltage signal. Due to the transparent part, in this case the glass fiber fabric reinforced PPS, thermal radiation out of the weld

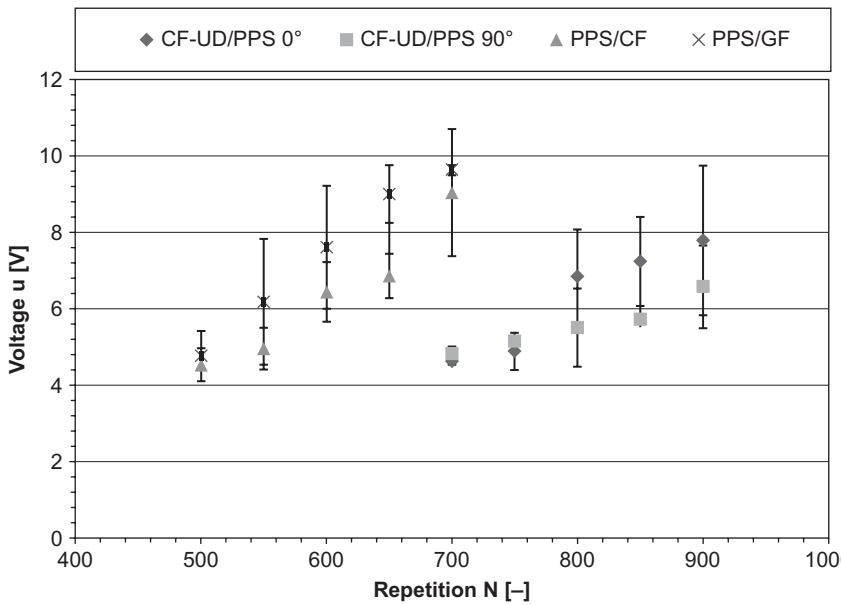


Fig. 6.3 Temperature signal during quasisimultaneous welding of different absorbing parts with GF/PPS as the laser transparent part [10].

seam is partially shielded. As a result, only a reference value can be detected. The absorbing parts consisted of unidirectional PPS (CF-UD/PPS), short carbon fiber (PPS/CF), and short glass fiber reinforced PPS with the additive carbon black (PPS/GF c.b.).

The applied welding technique was quasisimultaneous welding with a constant welding speed of $v = 5000\,\text{mm/s}$ and a constant laser power of $P = 130\,\text{W}$. In order to increase E_s only the number of repetitions was increased. For the short fiber reinforced material, a first weld seam was obtained for $N = 500$ repetitions with a temperature signal of $u = 4.7\,\text{V}$. For the CF-UD/PPS material, about $N = 700$ repetitions were needed to generate a weld seam with a similar temperature signal. Therefore, about 1.4 times more energy is necessary to generate a weld seam on endless carbon fiber reinforced PPS than on short fiber reinforced PPS. This is due to the difference in heat conduction within the material as well as a different absorbing behavior of the materials. Furthermore, for CF-UD/PPS, the difference in the temperature signal increases with increasing number of repetitions due to the carbon fiber orientation within the weld seam. So, the weld seam temperature is lower for CF-UD/PPS with a fiber orientation of 90° to the weld seam due to the conductive heat loss compared to the orientation of 0° [10].

The influence of the heat conduction along the carbon fibers on the weld seam width for contour © and quasisimultaneous welding (QS) is shown in Fig. 6.4. The CFRP used consists of unidirectional PPS. In order to determine the influence of heat conduction on the absorbing part, experiments were carried out without the transparent part by doing bead on plate welding on the absorbing part. In these investigations, the welding speed and the number of repetitions were kept constant while the laser power was varied in order to obtain different energy per unit length [8].

Fig. 6.4 shows that the average weld seam width w increases with increasing E_s as there is more energy available to melt the matrix material. The highest weld seam width increase was detected for contour welding with a fiber orientation of 90° relative to the weld seam orientation. This is about 1.7 times higher than for contour welding of CF-UD/PPS with an enclosing angle of 0° and clarifies the influence of the heat conduction on the weld seam development.

For quasisimultaneous welding, the energy is applied by multiple passes of the laser beam. Between each pass, the material starts to cool down leading to heat loss. This results in quasisimultaneous welding having smaller weld seam widths than contour welding because there is less heat available for melting the matrix material [10].

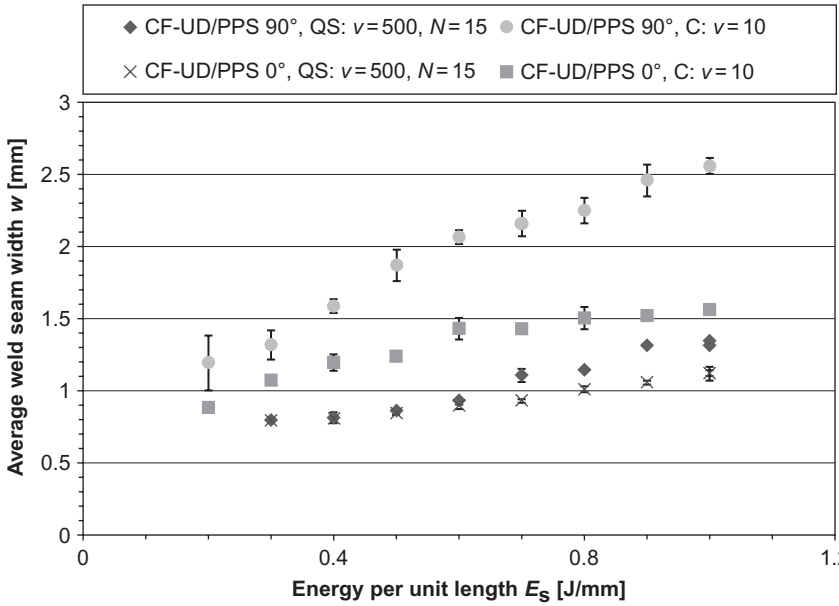


Fig. 6.4 Weld seam width for bead on plate welding with different welding techniques [10].

As was previously discussed, the weld seam widths and process temperatures are influenced by the welding technique used and the high heat conductivity of carbon fibers. As a result, these parameters also influence the strength of the weld seam produced. Fig. 6.5 depicts the lap shear strength for two different sets of quasisimultaneous welding parameters. The absorbing part used was CF/PPS, consisting of a carbon fiber fabric welded to GF/PPS. The GF/PPS had a low transparency for the wavelength of the diode laser used and as a result, it was not possible to use contour welding to weld this material combination. Thus the joining process was conducted by quasisimultaneous welding, which generates the process heat slower than contour welding and in doing so avoids damaging the transparent part. Compared to the parameter set with $v = 4000\,\text{mm/s}$ (A), the parameter set with $v = 2000\,\text{mm/s}$ (B) required more energy per unit length to generate a first reliable weld seam. The maximum lap shear strength σ was obtained with parameter set B. Increasing the number of welding cycles, a higher energy per unit length was applied in order to compensate for the heat loss in the welding zone. This led to an increase in the weld seam width and in turn to a higher lap shear strength. It was also found that with increasing energy per unit lengh above $E_s = 850\,\text{J/cm}$, the lap shear strength for parameter set B started to decrease, which is seen in Fig. 6.5. This indicates that the

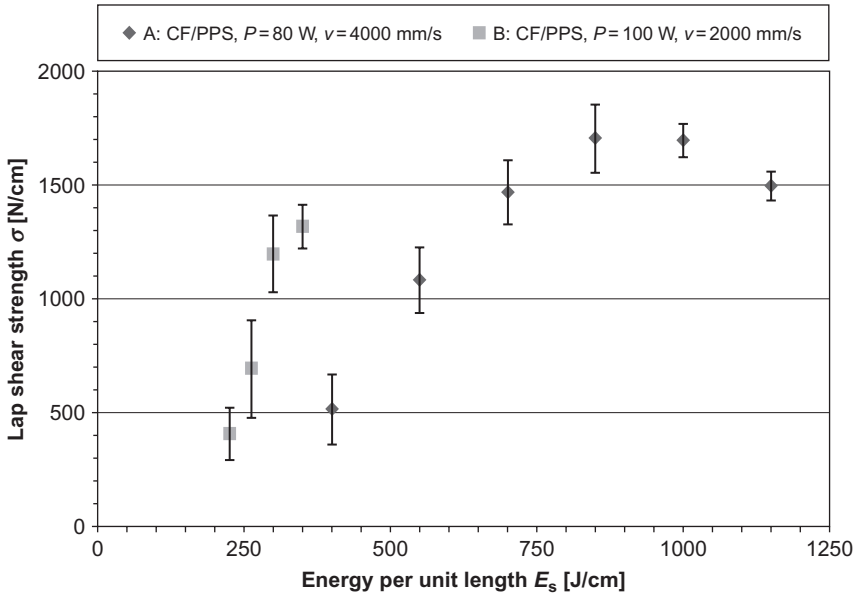


Fig. 6.5 Lap shear strength for different applied energy per unit length of quasisimultaneous welded CF/PPS to GF/PPS [8].

temperatures in the joining area are so high, that the matrix material starts to degenerate, resulting in the generation of cavities in the joining area. It also shows that moving forward, the loss in strength cannot be compensated by increasing the weld seam width [8].

6.2.2 Examples for Laser Transmission Welded Parts

One application of LTW is the welding of isolation pins to a CFRP plate (Fig. 6.6). These pins are used to fix isolation material in an aircraft. Traditionally, they are attached to the fuselage by means of adhesive bonding. This joining method takes a long time as the adhesive has to harden before any loads can be applied. To demonstrate a faster joining method, a LTW process was developed. A weld seam was generated by contour welding on the base of the pin. The pin consists of Polyamide 6.6 and the CFRP base plate was made with a copolyamide matrix and a carbon fiber fabric. In order to compensate for the inhomogeneous heat development due to the varying fiber orientation within the weld seam, a process control was applied. This process control adapted the laser power depending on the reference temperature detected by a pyrometer within the laser-material-interaction area [11].

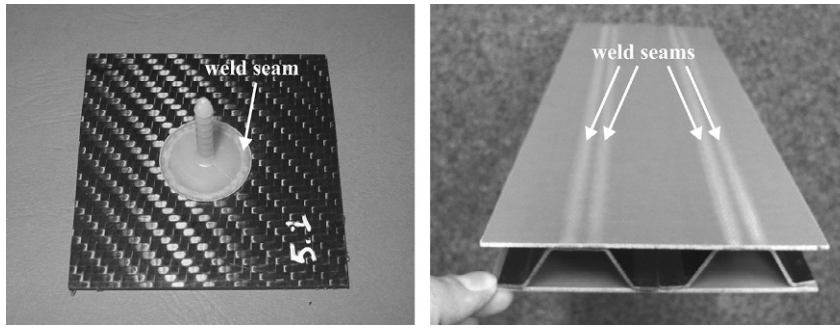


Fig. 6.6 Laser welded isolation pin (left), stiffener panel with Ω-profiles made by AGC AeroComposites Yeovil (right) [12].

Another example is a stiffener panel (Fig. 6.6). This panel consists of two face sheets, which are welded to two Ω-profiles. The Ω-profiles consist of glass fiber fabric reinforced PEI containing carbon black. The face sheets are the same material, but without the carbon black and are partially transparent for the laser radiation. The transmissivity of the face sheets was about 17% [12].

6.2.3 Further Laser Based Welding Techniques for Composites

For some applications it is necessary to join CFRP-parts to CFRP-parts. This is not possible with the classical LTW due to the absence of transparency of the material. In order to overcome this limitation, laser heat conduction welding was introduced. For this welding technique, the process heat is developed on the surface of the upper part. Due to heat conduction, the lower part becomes molten too. After solidification, a reliable weld seam is generated. In order to support the heat conduction between both parts, they have to be pressed together. First experiments were conducted with CF/PPS and the applied welding technique used was contour welding. To evaluate this welding technique, lap shear samples were produced. These samples obtained a maximum lap shear strength of $\sigma = 44.4\,\mathrm{N/mm^2}$ [13].

The joining of composite structures to metal parts presents another application for laser joining. To do so, the surface of the metal part has to be pretreated, e.g., by sand blasting or laser structuring. Afterwards, the metal part is pressed together with the thermoplastic composite part and then heated up by laser radiation. Due to heat conduction through the metal part, the composite become molten and the liquid thermoplastic is pressed into the surface structuring of the metal. Once cooled, the thermoplastic will have solidified, leaving the parts connected to each other. Another option when the composite part shows sufficient transparency for the laser radiation

is to apply transmission joining. The transmission joining is conducted analog to transmission welding, but the absorbing plastic part is replaced by a pretreated metal part. The connection strength depends on the structuring type of the metal. Common structures are grids and craters, which can vary in depth, distance to each other, and the existence of undercuts. [14,15].

6.3 CUTTING OF COMPOSITE STRUCTURES

Laser cutting setups and strategies originally evolved from the field of metal machining. Hence, early cutting experiments were conducted using cutting heads and contour cutting strategies so that the process is able to cut through the full material thickness in one pass on a defined contour. In order to achieve sufficient feed rates for thicker materials with this technique, it requires laser systems with several kilowatts of power. This approach is limited by its movement dynamics and as a result suffers from the effects of high thermal load due to the long laser-material interaction times. Compared to alternative cutting techniques for CFRP material, the resulting HAZ from the increased thermal load in the contour cut is found to be quite high ($\beta > 150\,\mu m$). An exemplary cross section micrograph of a contour cut 4-layer CF/PPS specimen of $d = 1.24\,mm$ thickness with accentuated HAZ is shown in Fig. 6.7A).

The quality of a laser cut can be assessed in great depths by measuring the HAZ using a cross-section micrograph as demonstrated by Staehr et al. [16], by SEM microscopy [17], by dye penetrant tests [17], and by Raman spectroscopy [18]. Cross-section micrographs are a widely-used analysis technique, as they enable the measurement of both kerf width and cutting edge angles. With the use of an SEM equipped with EDX or conducting

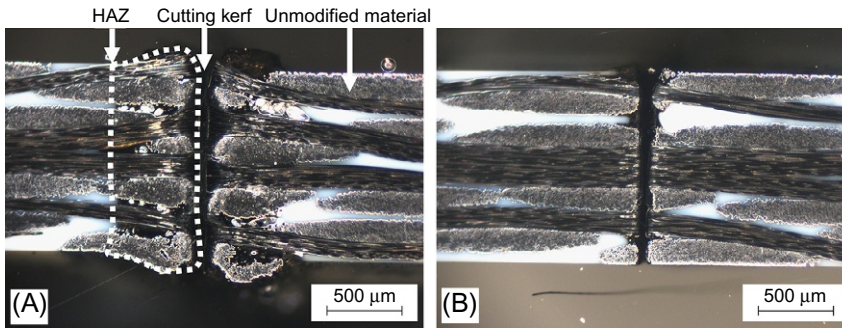


Fig. 6.7 Cross-section micrograph of a laser cut CF/PPS specimens using (A) a contour cutting strategy, (B) Multipass cutting strategy.

Raman spectroscopy, it is possible to investigate the composition of the cutting edge to further analyze the ablation process.

The cutting-edge quality can dramatically be increased by applying cutting strategies with a short laser-material interaction time such as multipass cutting (also referred to as remote cutting). With this technique, a galvanometer scanner system is used for the deflection of the laser beam within a defined working field (Fig. 6.8). The mirrors used for deflection are very light, and as a result the beam can be accelerated to very high scanning speeds v_s of several m/s. In turn, increasing the scanning speed v_s allows for the minimization of the laser-material interaction time and thus the thermal load, which results in a reduced HAZ (see Fig. 6.7B).

Increasing the scanning speed v_s also reduces the amount of material ablated with each pass, and as a result, multiple passes on the same geometry are therefore required to achieve a full cut. The main parameter influencing the HAZ is the scanning speed v_s, which in turn affects the number of passes needed and the period of time elapsed before the laser passes the same point of the path again. This period of time is identical to the scanning time for one path and directly depends on the scanning length l and the scanning speed v_s [20]. A longer scanning length l increases the time period

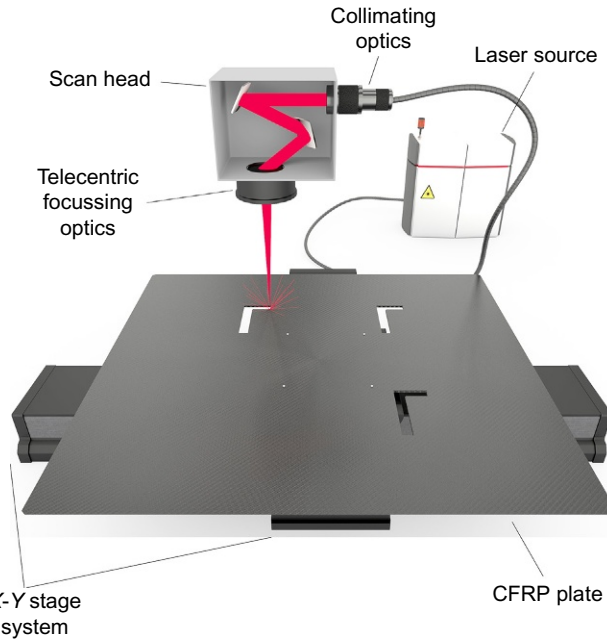


Fig. 6.8 Schematic laser cutting setup for multipass cutting [19].

between two passes and therefore reduces the HAZ (Fig. 6.9). Although the time between passes gives the material time to dissipate the introduced thermal energy, depending on factors such as the material characteristics, scanning geometry, and material thickness, the scanning time may not be long enough on its own for adequate heat dissipation. Of these factors, the material thickness has a significant influence on the required delay time, as both heat conduction and accumulation vary with material thickness and with thicker materials, the efficiency of surface losses due to convection cooling decreases. By implementing a pause or time delay between passes, it allows the material to cool and dissipate the head introduced in each pass, and in doing so reduce the HAZ further, thus improving the achievable cutting quality. The length of the delay time, which is necessary for a minimized HAZ, depends on many different factors.

For high quality near-net-shaped cutting, one major quality aspect is the cutting edge angle. This cutting edge angle can be adjusted to orthogonal orientations by using telecentric lenses. In addition to the lenses, the beam quality and spot size both have been identified to affect the cutting kerf angle. In Staehr et al. it was shown that the use of brilliant laser sources can produce very high aspect ratios between the cutting kerf width and cutting depth while at the same time still maintaining nearly rectangular cutting kerfs (Fig. 6.10) [19].

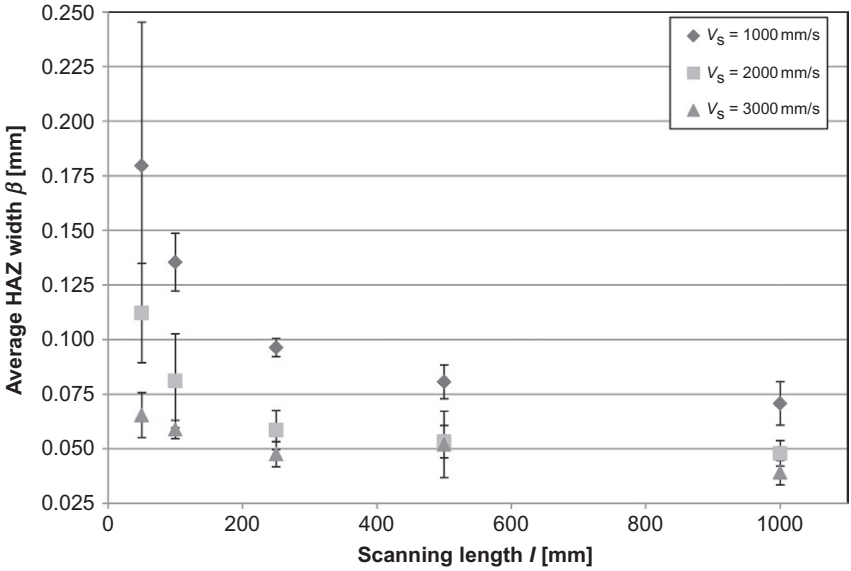


Fig. 6.9 Average HAZ width depending on scanning length *l* and scanning speed v_s. [19]

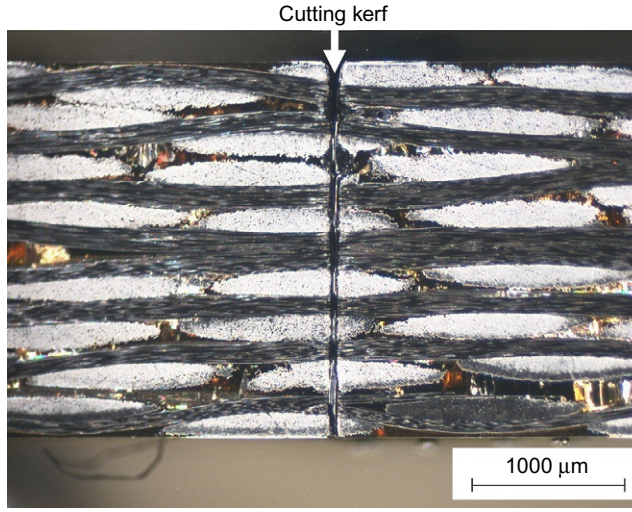


Fig. 6.10 Micrograph of cutting kerf with aspect ratio of 40 between kerf width and material thickness.

The large variety of polymers predominantly used in reinforced composites can generally be categorized into two classes, thermoplastics and thermosets, each with its own unique functionality. In contrast to thermosets, thermoplastics have the inherent ability to melt. Within this melting phase it has been shown that the outgassing of volatile components (mostly water absorbed in the polymer) might cause porosity and swelling in the HAZ. This behavior was successfully suppressed by drying materials prior to the cutting process or by applying cutting strategies with low heat input [16].

Currently, there is significant research in the field of laser of cutting of CFRP investigating the use of a wide variety of laser sources. In terms of optimized cutting edge quality, many experiments refer to pulsed laser sources emitting in the ultra-violet range or to ultra-short pulsed laser emitting pulses in the range of picoseconds or femtoseconds. While with the ablation mechanism, high quality cuts without noticeable HAZ can be realized, the achievable cutting velocities for this technique are comparably slow [21,22]. This is due in part because of the low average laser power available on the market today. Experiments performed with a unique laboratory scale picosecond pulsed laser with an average laser power of $P_L = 1.1\,\text{kW}$ were able to achieve an effective cutting speed of $v_{eff} = 0.9\,\text{m/min}$ [23]. The experiment also revealed that even with a

picosecond system, such high laser power can lead to heat accumulation, so that a pause was necessary. In recent experiments, it has been shown that with a continuous wave laser with good beam quality or high power nanosecond pulsed laser sources it is possible to achieve good quality cuts and a high effective cutting speed v_{eff} of several m/min [18].

As a final qualification for the cut quality using lasers, mechanical testing of a laser cut coupon is often required by the end customer, allowing for a comparison of results between the various other cutting techniques such as milling, drilling, or waterjet cutting. Initial investigations on this topic revealed that the load bearing area is reduced by the HAZ which in turn is directly linked to reduced mechanical properties [24]. The deviation from strength values achieved by conventional techniques was shown to increase with increasing HAZ. With the evolution of laser cutting strategies from contour cutting towards high quality multipass cutting, the influence on the mechanical properties was shown to have only reduced effects on the mechanical properties [25,26]. This has been proven true in not only static tests, but also in a range of other testing conditions such as fatigue testing, testing after exposure of specimens to thermocycling, testing after immersion in water, oil, and high humidity environment at different temperatures, and testing on demonstration parts as shown in Fig. 6.11 [18,27]. In an effort to identify significant deviations, the applied testing methods used a very high ratio between cutting edge length and sample volume or incorporated strongly modified specimen geometries [25,28].

As described previously, break times between two successive passes directly increase the quality of the cutting edge and minimize the HAZ. For thicker materials, where larger numbers of repetitions are required for a complete cut, the break time is one of the main influences for the resulting process times. The overall process efficiency can be improved by structuring the break time such that other areas of the same big part or multiple parts of the same plate get processed in the delay. For example, to cut out multiple shapes on one sheet of CFRP, the break time needed for each pass of one shape could be better utilized by repositioning the scanner to start cutting the next shape. For this the working field of the scanning optic has to be enlarged with the use of additional handling systems. The most common solutions are 3D linear stage systems or six-axis industrial robots. The former is applicable for the processing of 2D plates or 3D parts with simple geometries. Due to their high precision, linear stages are more applicable for laser set ups utilizing/making use of a small focal diameter. Furthermore, linear stages can be used with mirror guided laser sources such as ultra-short pulsed lasers or lasers emitting in the ultra-violet range.

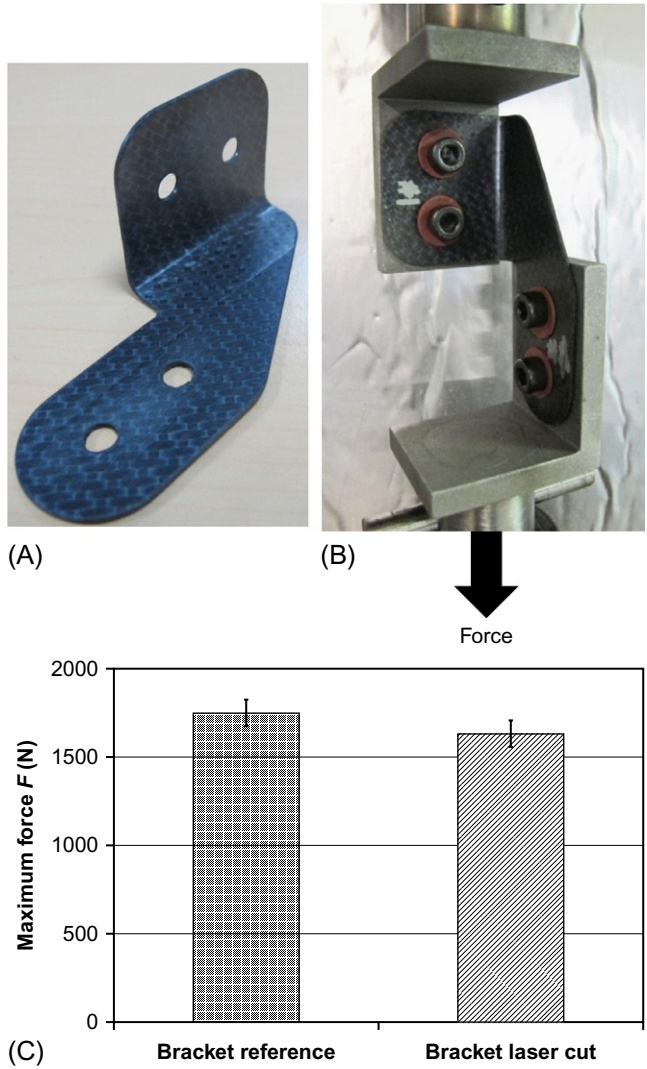


Fig. 6.11 (A) 3D Laser machined CF/PPS bracket, (B) test setup, and (C) maximum force F results for laser machined and milled reference part [18,27].

A robot cell with a scanning system equipped to the end effector of the robot enables the processing of big and complex shaped CFRP parts. As the robot process is less accurate than that of the linear stage setup, its use is often limited by a given job's accuracy requirements or the intended focal diameter to be used. Although the reduced accuracy is limiting in some regards, this set up offers maximized 3D capabilities, especially when equipped with a scanning optic enabling focal adjustment.

Staehr et al. performed a study comparing a linear stage system with a six-axis robot system. The linear stage system used a single-mode fiber laser setup with a small resulting focal diameter, whereas the robot system utilized a nanosecond pulsed disk laser with a bigger focal diameter. Although each handling system used a different laser source, both laser sources operated with an average power of $P_L = 1500$W. Staehr et al. stated that the characteristics and complexity of the positioning systems were adapted to the unique requirements of the laser source. A dynamic high precision option is achieved by a linear stage and rotary axis assembly. A system offering a larger working range and maximized 3D capability is represented by a robot system carrying a 3D scanning optic [19].

Two kinds of cutting strategies can be used in combination with such handling systems. The first strategy is "step-and-repeat" cutting, where the handling system stops while the scanning optic is cutting and then moves to the next desired position. This strategy is especially useful for cutting thin parts or if many cutting geometries are placed compactly within the scanning field of the optic. Additionally, the programming effort is comparably low.

The second strategy is the "cutting-on-the-fly" method. Here the handling system is continuously moving over the workpiece while the scanning optic is cutting the programmed geometries. As a result, this strategy is often more complex in terms of the programming since the scanning optic has to compensate for both moving speed and direction of the handling system while cutting. While this complicates the programming, it allows the handling system to follow a more simplified path along the cutting geometries, as the only requirement of the system is that all the geometries must fall within the scanning field along the path at an appropriate speed. The scenarios where this strategy is most efficient would be for long continuous cutting paths, if many small geometries need to be cut out, or if the break time between two paths would be too long compared to one continuous movement.

Since laser cutting is a thermally sensitive process, another important factor to consider for automated setups is the monitoring and control system used to regulate the temperature. Several works have shown the potential of in-process thermography imaging for both monitoring and control [25,27]. The noncontact thermography measurements can be supported by preceding temperature measurements within the material volume to relate the noncontact surface temperature measurement to the internal temperatures and the resulting HAZ [29,30]. Although multipass cutting strategies

offer reduced heat input, heat accumulation can be observed by thermal monitoring, reaching critical temperature values in areas with a high density of cutting contours [27]. To meet the requirements of end users and to sustain efficient processing, material cooling options can be designed to speed up the process and to comply with material specific threshold temperatures. A very effective way shown was the use of water cooled fixtures providing a maximized contact area between material and fixture and thus leading to high heat dissipation, reducing the temperature value level by more than 40% while maintaining the process duration (see Fig. 6.12) [31].

For thin materials and cutting geometries less prone to heat accumulation forced convection at the material surface reduce the HAZ as well. As for the active control of machining parameters, thermography can be implemented in the manipulation of delay times to maintain exact thermal load levels as shown in Fig. 6.13 [25]. In these expermients, the threshold temperature was set to $T_{th} = 28°C$. As a result of the heat dissipation time needed, the overall process time is extended, especially for threshold temperatures close to the ambient temperature. As explained before, an efficient solution for enhanced heat dissipation can be found in active cooling options, e.g., water cooled fixtures.

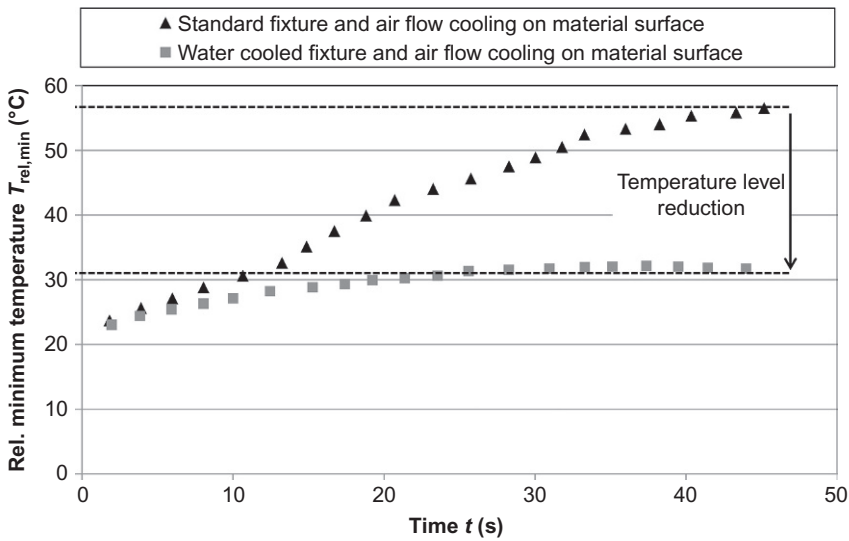


Fig. 6.12 In-process temperature monitoring while multipass-cutting of CFRP on a standard fixture versus water cooled fixture; the temperature values show the minimum temperature during the constant delay time of $t_d = 2$ s between consecutive passes [31].

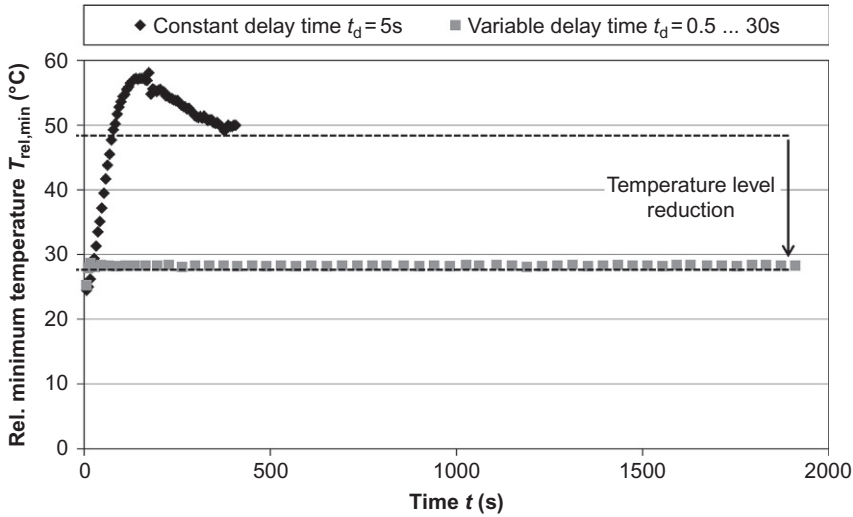


Fig. 6.13 In-process temperature monitoring for a cutting process with uncontrolled constant delay time and temperature controlled variable delay time; the threshold temperature was set to T_{th} = 28°C; the temperature values show the minimum temperature during the delay time between consecutive passes [25].

6.4 REPAIR PREPARATION FOR COMPOSITES

The use of CFRP has increased for applications that benefit from the use of strong, lightweight materials in industries like aviation, automotive, and energy generation. Due to issues with cost, a long service time is desired, as it is very expensive to produce parts from CFRP. Furthermore, applications that rely on CFRP are often strenuous and damage may occur due to fatigue, inappropriate handling, or accidents. The ability to repair parts and machines made of CFRP requires great precision, but would help to improve the service life and the cost of using CFRP for these applications [32]. A process called scarfing is used to restore affected parts (Fig. 6.14).

6.4.1 Composite Repair: A Challenging Procedure

The challenge of repairing composites begins with the comprehensive inspection of the part, which is required to determine the extent of the damage. There are several inspection techniques, each with varying degrees of complexity, e.g., knock tests, thermographic inspection, x-ray tomography to name a few [33,34]. The type of damage can vary a lot and as a result, using a single detection technique is not adequate to characterize all of them. Thus, in order identify and analyze all the damage in a composite material, a multidevice damage detection system is required. Following damage

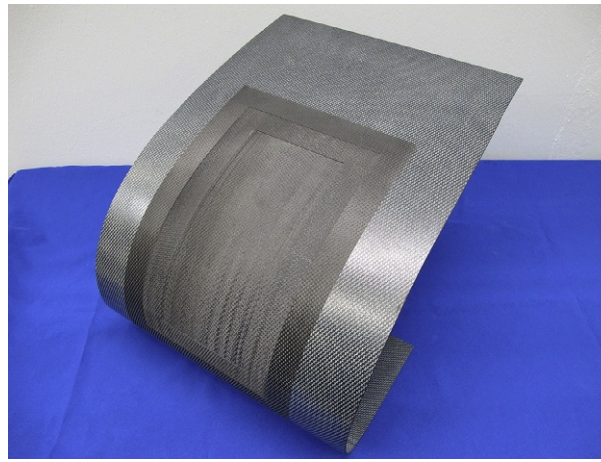


Fig. 6.14 Slat made of CFRP showing scarfed damage zone.

detection, the next step is to completely remove (scarf) the affected region of the part, which in most cases is done by manually grinding [35]. Before inserting the repair patches, the built up dust and particles often need to be removed after the damaged material section has been scarfed. In general, there are two common methods used to replace the scarfed damaged material, these being the use of prepreg patches or a wet-layup technique [36]. Prepreg patches consist of a layer of fibers, which are already covered by a polymer matrix, attached to a carrier sheet. These sheets are then removed and the prepregs are placed into the scarf zone. For wet lay-up, the dry reinforcing fibers are initially anointed with resin to produce the patches. After the patches have been placed in the scarf zone, the resin needs to be cured. This requires the application of a vacuum in order to generate enough pressure to compress the single patches into the scarf zone. With the damaged material replaced, the repaired section must be cured to consolidate with the native part. The curing conditions can vary drastically; from curing at room temperature, with heating mats, in an autoclave, or to using circulating air ovens, the curing conditions used depends on several factors. The type of material, size of the repair, and desired process time all heavily influence and dictate what curing parameters are selected [37]. Successful curing concludes the repair, which is usually succeeded by reapplying protective coatings.

Laser technology can be used for both the scarfing process as well as for the steps involved in surface preparation done prior to applying the patches such as cleaning or surface activation [38].

6.4.2 Laser Processing as a Promising Solution Towards Automation

Laser technology offers some significant advantages for CFRP repair preparation in comparison to alternative tooling strategies like conventional milling, sandblasting, or water jet processing [39]. Due to its contact-free working principle it neither induces forces into the part's structure nor is it prone to the excessive tool-wear caused by the carbon fibers. Therefore, parts do not become distorted during machining and frequent changing of tools is also unnecessary. In addition, laser processing is usually performed without any cooling liquids and as a result, the part does not need to be rinsed following processing to remove any residues from the parts surface as is with other processes.

Another advantage specific to the task of laser scarfing is the laser process's high geometrical resolution. It allows the laser process to react to imperfections in the CFRP's fiber lay-up. Two common examples of imperfections resulting from the CFRP production process are undulation in the CFRP surface and waviness of individual fiber layers [40]. Waviness in particular poses an almost unsolvable challenge for conventional tools, as cutting through these wavy fibers would affect the distribution of forces. The use of a laser process however can react to these sporadic imperfections and make adjustments accordingly.

The difficulty in designing an effective laser based process for repair preparation stems largely from the composite's heterogeneous heat conduction properties that must be considered and accounted for [41]. For most composites, the reinforcing fibers have a higher heat conduction coefficient than the polymer matrix, but for carbon fibers this difference is much more significant (Table 6.1). Thus, in order to ablate both fibers and

Table 6.1 Heat conductivity coefficients for composite related materials [42–44].

Material	Heat conductivity c_H ($Wm^{-1}K^{-1}$)
Carbaon fiber (unidirectional tape) [42]	50 (in fiber direction), 1 (perpendicular to fiber direction)
Glass fiber (unidirectional tape) [42]	0.4 (in fiber direction), 0.2 (perpendicular to fiber direction)
Epoxy [42]	0.2
PEEK [42]	0.25
Polyethylene (low density) [43]	0.33
Polypropylene [43]	0.1–0.22
Carbon fiber in epoxy [44]	5–7 (in plane), 0.5–0.8 (traverse)
Glass fiber in epoxy [43]	0.23

polymer matrix material without causing severe damage to the material, proper hardware and adapted process strategies must be chosen.

6.4.3 Laser Sources Used

Due to the thermal and optical properties of composites, use of lasers for scarfing can be quite challenging. As a result, choosing the optimal laser source for the given material properties of the composite is a crucial step in the process.

The optical characteristics of the composite influence the choice of wavelength that needs to be selected. Most polymer materials have high optical transmissivity unless they are artificially blackened. However, in composite material the fiber volume content is usually greater than 50%. Therefore, regarding the absorption of laser energy, the optical spectrum of the reinforcing fibers is a key characteristic and determines the potential laser wavelength suitable for the process. Glass fiber reinforced plastics (GFRP) show rather high reflection and transmissivity rates over large parts of the optical spectrum (Fig. 6.15), whereas CFRP show a constant low reflection and almost no transmissivity (Fig. 6.16).

The transmissivity for a material is largely dependent on the material's thickness as light traversing through matter is constantly attenuated. Thus the amount of light transmitted decreases with increasing material thickness.

The transmissivity of GFRP is such that the use of lasers operating with wavelengths in the range of $\lambda = 400\,\text{nm}$ to $\lambda = 5000\,\text{nm}$ is not suitable for

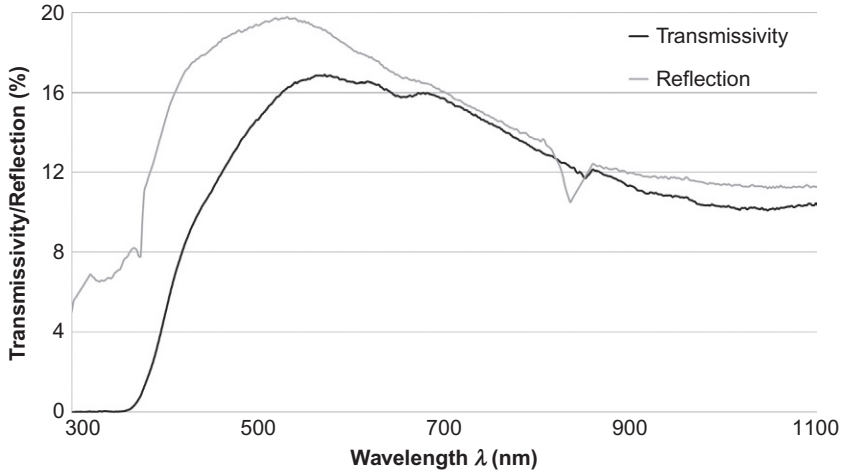


Fig. 6.15 Optical spectrum for GFRP ($d = 10\,\text{mm}$).

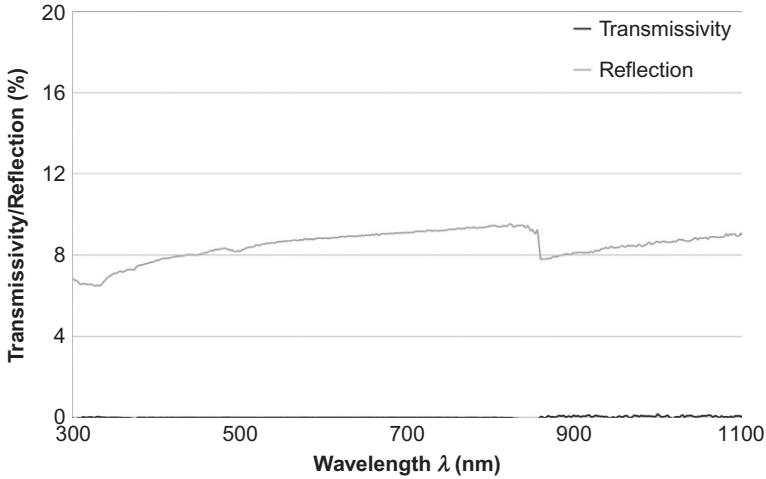


Fig. 6.16 Optical spectrum for CFRP ($d = 4$ mm).

laser processing, but is instead more optimized to use lasers operating in UV range (below $\lambda = 400$ nm). CFRP on the other hand shows constant characteristics over most of the transmissivity spectrum from UV to NIR, allowing for very effective near-infrared lasers to perform the laser scarfing.

As mentioned earlier, the thermal properties of the material also need to be considered when determining the laser source. In order to limit the thermal load induced by the laser, short or ultra-short pulsed laser sources provide significant advantages over long pulsed or continuously emitting lasers. Short pulse lasers reduce the material-laser interaction time allowing the fibers to conduct surplus energy, present as heat, out of the processing area between two consecutive pulses [45]. However, a mismatch between processing strategy and utilized system technology may still cause unintentional thermal damages to the composite material.

6.4.4 System Technology for Laser Based Composite Repair

Apart from the laser source, additional system technology is needed to realize an automated laser scarfing process to repair fiber reinforced composite parts. In order to achieve this, implementation of a sufficiently fast and precise laser system becomes paramount. This becomes especially important when lasers with very high pulse repetition rates ($f \gg 100$ kHz) are in use, as a high scanning velocity is needed to be able to restrict the pulse overlap [46]. Axes or robotic systems assist the process when areas that need to be scarfed are larger than the scanner's working field. Various measuring

techniques help to increase the level of automation, e.g., thermography or pyrometry to monitor thermal stress on the composite part [47], triangulation to keep the focal distance constant, interferometry to measure the depth of the scarfing [48], and fiber orientation analysis to detect the fiber layer currently in process.

6.4.5 Laser Ablation of CFRP Structures for Composites Patch Repair

In composite patch repair, scarfing is used in the preliminary preparation steps to remove the damaged material from the section to be repaired. To do so, laser ablation has been identified as a viable approach with three different techniques in development so far.

Heat-and-brush is a two-step process utilising a low pulse energy fluence move over the surface in a wobbling mode. Although the energy applied to the surface is enough to sufficiently vaporize the matrix material, it is not enough to ablate the fibers. Therefore, the laser process is interrupted and the fibers are mechanically brushed off, before the process is repeated for the next composite layer [49].

Groove-and-remove also is a two-step procedure, but does not require changing the tool. The first step involves establishing the contour of the region to be ablated and cutting it to the desired depth, effectively severing the reinforcing fibers of the damaged zone from the intact material. Similar to the heat-and-brush-approach, the area contained within the contour is then scanned merely vaporizing the top resin layer. With the top resin layer removed, the adjoined carbon fiber layer can now be removed by using a powerful exhaust system or by applying a gas stream [50].

Full ablation uses high pulse energy fluencies (approx. $H_P > 40\,J/cm^2$) to ablate both fibers and matrix material at the same time. While this procedure is less time-efficient than the first two approaches, it provides full control over the depth of ablation thus allowing for more precision in removing the layers of the damaged composite material as it utilizes online measuring techniques. In both the heat-and-brush as well as the groove-and-remove procedures, the measuring techniques would be interfered by the fibers still present in the working field [15].

The scarf itself can be realized either as a continuous ramp or in defined steps with various scarf ratios (Fig. 6.17). Also, the scarf geometry is dependent on the scanner system, fully flexible, and can be programmed to change the scarf geometry from layer to layer. It is possible to program unique scarf geometries for individual damage and composite lay-ups.

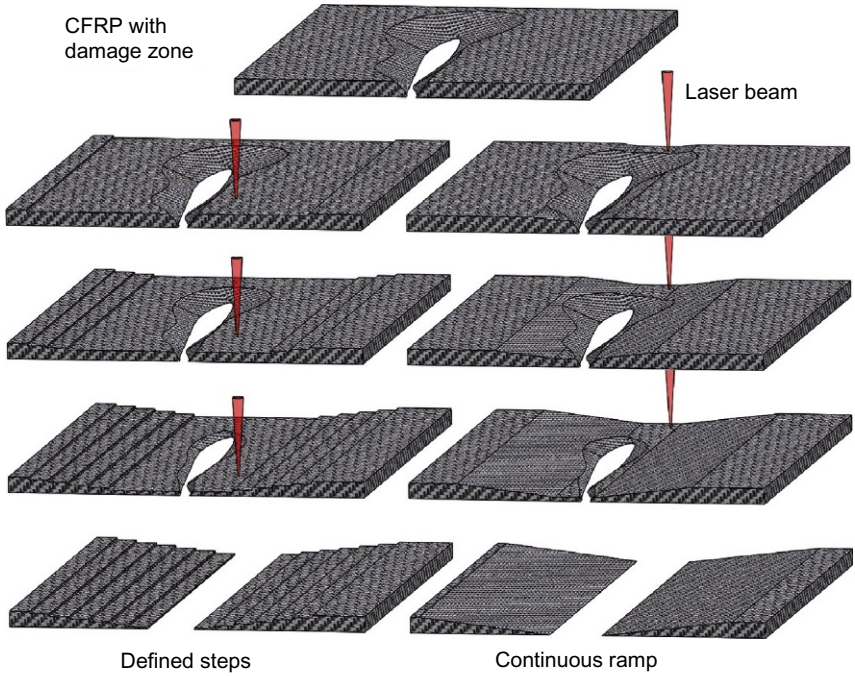


Fig. 6.17 Scarf schematics.

The most important processing parameters for laser ablation are pulse energy fluence, line distance, and scanning velocity, as they determine the amount of energy induced into the composite's surface. It was noticed that the dominant fiber orientation in the current layer that is ablated, also influences the process result [51]. Laser scanning performed in the same direction as the fibers' orientation will accumulate a heat wave in front of the laser beam. This leads to a higher amount of the matrix material being vaporized, partially freeing some of the fibers from the matrix, and resulting in a rougher and less defined surface, similar to that of the heat-and-brush process. Guiding the laser beam perpendicular to the fiber orientation will allow the heat to dissipate without intense heat accumulation, producing a smoother surface.

Currently, laser scarfing is an open-loop controlled process. The development of online measuring techniques plays a crucial role in the advancement to automatically controlled processes as there are multiple variants in fiber lay-up, some of which may not be disclosed by the manufacturers, coupled with the potential for localized lay-up deviations resulting from undulation or waviness. Online depth measuring and fiber orientation

analysis are both technologies that are able to assist in the laser scarfing process. Depth measurements are taken to determine the current fiber layer that is processed in crimped-fabric and single-axial unidirectional composites. Fiber orientation analysis however, could be used to precisely identify the interfaces between individual layers in multiaxial composite systems. This would enable the laser scarfing process to ablate single layers with a high degree of precision and to react to local changes in the fiber lay-up due to waviness.

6.4.6 A Glimpse on Other Related Laser Based Surface Treatments

Due to its versatility, laser technology can be used for several other composite material surface treatment applications beyond just surface preparation for repairs, which are also applicable in the entire composite repair procedure.

Composite repair of structural parts might require removing paint or protective coatings from a damaged zone prior to laser scarfing. Lasers have been used by the aviation industry to strip off paint [52,53] but could also be used to remove dirt or other surface contaminants before subsequent processing steps. This is especially important if composite parts are assembled by adhesive bonding. The low surface energies of most polymers will often lead to a reduced bonding strength unless the surface is treated to improve its bonding behavior. Lasers can be used for surface structuring [54,55] (e.g., to increase the size of the contact area between the composite material and the applied adhesive) as well as for enabling mechanical interlocking.

The use of lasers with high photonic energies allows for even more surface structuring capabilities, as they could crack molecular chains on the polymer surface, leaving open bonds in a process called photochemical activation. These open bonds are very reactive and are able to form stronger connections with applied adhesives [56,57].

6.5 PROCESS EMISSIONS

The erosive laser processing of CFRP causes considerable emissions of fumes, organic gases, and particles. The latest investigations show the dependency of composition and release rate on the cutting strategies and the processed material. The emissions are analyzed in terms of the total concentration of organic gases (volatile organic compounds—VOCs), inorganic gases, and emitted particles. Experiments revealed that relevant amounts of

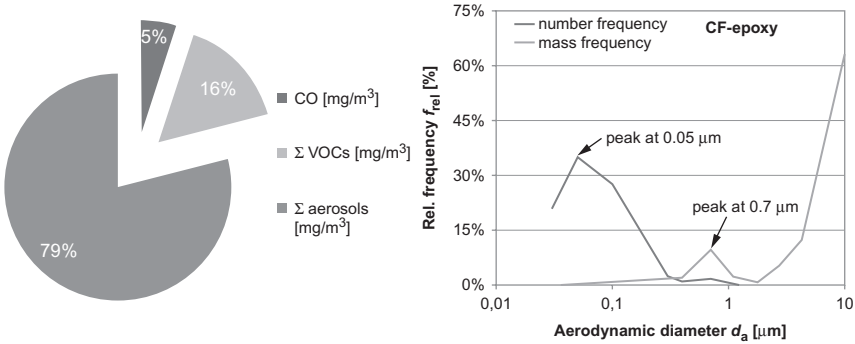


Fig. 6.18 Potential composition of process emissions during ablation of CFRP [58] and particle size distribution of aerosols [59].

VOCs and carbon monoxide (CO) as well as spherical and fibrous particles are released during laser cutting of CFRP materials (Fig. 6.18) [58]. In terms of the aerosols released, it can be stated that the highest mass of particle is captured with an aerodynamic diameter in the range of $d_a = 0.7\,\mu m$, while the highest number of particles is captured with a diameter in the range of $d_a = 0.05\,\mu m$ [59]. This is made evident in Fig. 6.18, which shows the particle size distribution during laser cutting of CF/Epoxy.

Furthermore, it has been presented that adapted and optimized process strategies, such as multipass cutting, decrease not only the heat input and therefore the quality of the cutting edge, but also have a direct influence on the amount of hazardous emissions emitted [60].

There are three basic steps useful for developing both the analysis of potential emission as well as defining the required emission safety measures with regards to emission capture and treatment, protection of workers, and the environment [58]. In the first step, an emission prognosis, based on a pyrolysis, can be performed for new materials to determine lead components which can be expected within the process emissions. This step should be performed at an early stage, so that the results can be used to design the required capture and filtration systems. In the second step, the process emissions in the exhaust air are analyzed quantitatively, during real process conditions, using optimized parameters. In the third step, once the process emission capture system in the workspace has been optimized, the air in the workspace can then be analyzed. The latest research in process emissions for laser cutting of CFRP has shown that no so called WHO-Fibers have been found to be emitted thus far [59]. WHO-fibers are defined by the World Health Organization (WHO) as respirable and critical hazardous

fibers which have a length $l > 5\,\mu m$, a diameter $d < 3\,\mu m$, and a ratio between length and diameter >3:1. The experiments cited within this section reveal that process emissions have to be captured in an adequate manner during the erosive laser processing of CFRP. At the same time, all measured emission rates were below the limit threshold values according to German regulations dealing with emission limits. The treatment of the process emissions with surface filters and activated charcoal is adequate to filter the aerosols, VOCs, and CO and ensures protection of the environment. Such filter systems are well established in industry. Alternative filtration techniques, which are suitable for CFRP processing, are filter systems based on a catalytic cleaning.

REFERENCES

[1] D. Grewell, A. Benatar, Welding of plastics: fundamentals and new developments, Int. Polym. Process. 22 (2007) 43–60.

[2] T. Frick, Untersuchung der prozessbestimmenden Strahl-Stoff-Wechselwirkungen beim Laserschweißen von Kunststoffen, Dissertation Friedrich-Alexander-Universität Erlangen-Nürnberg, Bamberg: Meisenbach, 2007.

[3] V.A. Kagan, R.G. Bray, W.P. Kuhn, Laser transmission welding of semi-crystalline thermoplastics. Part I. Optical characterization of nylon based plastics, J. Reinf. Plast. Compos. 21 (2002) 1101–1122.

[4] R. Klein, Laser Welding of Plastics, Wiley-VCH, Weinheim, 2012.

[5] M. Chen, G. Zak, P.J. Bates, Effect of carbon black on light transmission in laser welding of thermoplastics, J. Mater. Process. Technol. 211 (2011) 43–47.

[6] G. Fiegler, Ein Beitrag zum Prozessverständnis des Laserdurchstrahlschweißens von Kunststoffen anhand der Verfahrensvarianten Quasi-Simultan- und Simultanschweißen, Shaker Verlag, Aachen, 2007.

[7] U.A. Russek, Laserschweißen von Kunststoffen, Süddeutscher Verlag, München, 2009.

[8] P. Jaeschke, Laser transmission welding of continuous carbon fiber reinforced plastics and thermoplastic polymers, PhD Thesis, Leibniz University Hanover, Germany. Hanover: PZH Produktionstechnisches Zentrum, 2012.

[9] J. Bliedtner, H. Mueller, A. Barz, Lasermaterialbearbeitung: Grundlagen-Verfahren-Anwendungen-Beispiele, Hanser Verlag, München, 2013.

[10] V. Wippo, P. Jaeschke, U. Stute, D. Kracht, H. Haferkamp, The influence of carbon fibers on the temperature distribution during the laser transmission welding process, in: 15th European Conference on Composite Materials (ECCM15), Venice, Italy, 2012.

[11] P. Hansen, C. Jeenjitkaew, V. Wippo, P. Jaeschke, Laser transmission welding of thermoplastic composite structures, in: SAMPE Europe Conference & Exhibition—SEICO14, Paris, France, 2014.

[12] P. Hansen, V. Wippo, S. Cooper, D. Conway, C. Jeenjitkaew, P. Jaeschke, Mechanical performance of long fiber reinforced stiffener panels manufactured using laser welding, in: 17TH European Conference on Composite Materials, ECCM17, Munich, Germany, 2016.

[13] V. Wippo, J. Ihde, P. Jaeschke, P. Linde, O. Suttmann, L. Overmeyer, Laser heat conduction welding of inline cleaned endless carbon fiber reinforced thermoplastics, in: 17th European Conference on Composite Materials, Munich, Germany, 2016.

[14] P. Amend, C. Mohr, S. Roth, Experimental investigations of thermal joining of polyamide aluminum hybrids using a combination of mono- and polychromatic radiation, Phys. Procedia 56 (2014) 824–834.
[15] P. Amend, S. Pfindel, M. Schmidt, Thermal joining of thermoplastic metal hybrids by means of mono- and polychromatic radiation, Phys. Procedia 41 (2013) 98–105.
[16] R. Staehr, S. Bluemel, P. Hansen, P. Jaeschke, O. Suttmann, L. Overmeyer, The influence of moisture content on the heat affected zone and the resulting in-plane shear strength of laser cut thermoplastic CFRP, Plast. Rubber Compos. 44 (3) (2015) 111–116.
[17] F. Fischer, S. Kreling, D. Blass, R. Staehr, S. Bluemel, P. Jaeschke, K. Dilger, Laser material machining of CFRP—an option for damage-free and flexible CFRP processing, in: J.P. Davim (Ed.), Machinability of Fibre-Reinforced Plastics, Advanced Composites, vol. 4, De Gruyter, Berlin, 2015, pp. 1–29.
[18] S. Royo Pérez, P. Hansen, R. Staehr, S. Bluemel, V. Wippo, S. Bastick, P. Jaeschke, Laser cutting and the influence on the mechanical properties of long fibre reinforced CF-PPS and CF-PEI, in: Proceedings of the 17th European Conference on Composite Materials, 2016.
[19] R. Staehr, S. Bluemel, P. Jaeschke, O. Suttmann, L. Overmeyer, Laser cutting of composites—two approaches toward an industrial establishment, J. Laser Appl. 28 (2) (2016) 22203.
[20] S. Bluemel, V. Angrick, S. Bastick, P. Jaeschke, O. Suttmann, L. Overmeyer, Remote laser cutting of composites with a fibre guided thin-disk nanosecond high power laser, in: Proceedings of Lasers in Manufacturing, 2015.
[21] Y. Sato, M. Tsukamoto, K. Nakai, T. Nariyama, K. Takahashi, S. Masuno, H. Nakano, Experimental investigation of CFRP ablation with UV and N-IR nanosecond lasers, in: Proceedings of ICALEO 2013, 32nd International Congress on Applications of Lasers & Electro-Optics, 2013, pp. 758–762.
[22] A. Wolynski, T. Herrmann, P. Mucha, H. Haloui, J. L'huillier, Laser ablation of CFRP using picosecond laser pulses at different wavelengths from UV to IR, Phys. Procedia 12 (2011) 292–301.
[23] C. Freitag, M. Wiedenmann, J.-P. Negel, A. Loescher, V. Onuseit, R. Weber, M.A. Ahmed, T. Graf, High-quality processing of CFRP with a 1.1-kW picosecond laser, Appl. Phys. A 119 (4) (2015) 1237–1243.
[24] P. Jaeschke, F. Fischer, M. Kern, U. Stute, D. Kracht, Laser cutting of CETEX thermoplastic composites using high-power multimode fibre laser, in: Proceedings of Sampe 2011, 2011.
[25] P. Hansen, S. Royo Pérez, R. Staehr, P. Jaeschke, Quasi-static and fatigue evaluation of laser machined CF-PPS and CF-PEI composites, in: Proceedings of the 20th International Conference on Composite Materials; ICCM 20, 2015.
[26] W.V. Bestenbostel, M. Kolb, A. Fürst, A. Wetzig, Damage-property correlation after laser cutting of CFRP, in: Proceedings of the 16th European Conference on Composite Materials (ECCM16), 2014.
[27] O. Meier, P. Hansen, R. Staehr, S. Bluemel, S. Royo Pérez, J. Lindner, P. Jaeschke, Efficient laser cutting of high-performance thermoplastic composites, in: Proceedings of International Conference & Exhibition on Thermoplastic Composites, 2016.
[28] A. Fürst, M. Rose, A. Klotzbach, J. Hauptmann, T. Heber, E. Beyer, Influence of laser irradiation on the failure behavior of uniderectional fibre reinforced polymers, in: Proceedings of the 16th European Conference on Composite Materials (ECCM16), 2014.
[29] S. Bluemel, R. Staehr, P. Jaeschke, U. Stute, Determination of corresponding temperature distribution within CFRP during laser cutting, Phys. Procedia 41 (2013) 408–414.
[30] S. Bluemel, R. Staehr, P. Jaeschke, O. Suttmann, L. Overmeyer, Correlation of internal and surface temperatures during laser cutting of epoxy-based carbon fibre reinforced plastics, J. Reinf. Plast. Compos. 34 (8) (2015) 662–671.

[31] R. Staehr, J. Lindner, S. Bluemel, O. Meier, P. Jaeschke, O. Suttmann, L. Overmeyer, The impact of cooling strategies and fixture options on the thermal load during laser processing of carbon fibre reinforced thermoplastics, in: Proceedings of the 17th European Conference on Composite Materials, 2016.
[32] R.B. Heslehurst, Structural repair methodology for wind turbine blades, in: Proceeding of SAMPE Tech 2012, 2012.
[33] V. Munoz, B. Valès, M. Perrin, M.L. Pastor, H. Welemane, A. Cantarel, M. Karama, Damage detection in CFRP by coupling acoustic emission and infrared thermography. Compos. Part B 85 (2016) 68–75, https://doi.org/10.1016/j.compositesb.2015.09.011.
[34] M. Mieloszyk, M. Krawczuk, P.H. Malinowski, T. Wandowski, W.M. Ostachowicz, Active thermography method for delamination detection and localisation in composite structures, in: Proceeding of European Workshop on Structural Health Monitoring 6, 2012.
[35] K.B. Katnam, L.F.M. Da Silva, T.M. Young, Bonded repair of composite aircraft structures: a review of scientific challenges and opportunities, Prog. Aerosp. Sci. 61 (2013) 26–42.
[36] M.S. Found, M.J. Friend, Evaluation of CFRP panels with scarf repair patches. Compos. Struct. 32 (1–4) (1995) 115–122, https://doi.org/10.1016/0263-8223(95)00045-3.
[37] M. Kaden, R. Keck, Repair concept supported by laser removal and inductive heating, in: Proceeding of International Congress of the Aeronautical Sciences (ICAS) 28, 2012.
[38] F. Fischer, L. Romoli, R. Kling, Laser-based repair of carbon fiber reinforced plastics, CIRP Ann. Manuf. Technol. 59 (2010) 203–206.
[39] D. Herzog, P. Jaeschke, O. Meier, H. Haferkamp, Investigations on the thermal effect caused by laser cutting with respect to static strength of CFRP. Int. J. Mach. Tools Manuf. 48 (2008) 1464–1473, https://doi.org/10.1016/j.ijmachtools.2008.04.007.
[40] S. Hörrmann, C. Viechtbauer, A. Adumitroaie, M. Schagerl, The effect of fiber waviness as manufacturing defect on the fatigue life of CFRP materials, in: Proceeding of International Conference on Composite Materials 20, 2015.
[41] R. Joven, R. Das, A. Ahmed, P. Roozbehjavan, B. Minaie, Thermal properties of carbon fiber-epoxy composites with different fabric weaves, in: Proceeding of SAMPE Tech 2012, 2012.
[42] M. Biron, Thermoplastics and thermoplastic composites, second ed., Elsevier/WA, Amsterdam, Boston, 2013.
[43] N.N.: Thermal Conductivity of common Materials and Gases, The Engineering ToolBox, Web 25 Feb. 2017, http://www.engineeringtoolbox.com/thermal-conductivity-d_429.html.
[44] T. Tian, Anisotropic thermal property measurement of carbon-fiber/epoxy composite materials, Mechanical (and Materials) Engineering—Dissertations, Theses, and Student Research. Paper 27, 2011 http://digitalcommons.unl.edu/mechengdiss/27.
[45] R. Weber, C. Freitag, T.V. Kononenko, M. Hafner, V. Onuseit, P. Berger, T. Graf, Short-pulse laser processing of CFRP, Phys. Procedia 39 (2012) 137–146.
[46] H. Dittmar, F. Gaebler, U. Stute, UV-laser ablation of fibre reinforced composites with ns-pulses, Phys. Procedia 41 (2013) 266–275.
[47] H. Dittmar, P. Herda, P. Jaeschke, O. Suttmann, L. Overmeyer, Optimising process efficiency during remote laser cutting of CFRP by utilisation of a double-scan-head. Phys. Procedia 83 (2016) 1279–1288, https://doi.org/10.1016/j.phpro.2016.08.135.
[48] M. Kogel-Hollacher, M. Schönleber, T. Bautze, M. Strebel, R. Moser, Measurement and closed-loop control of the penetration depth in laser materials processing, in: Proceeding of International Conference on Photonic Technologies (LANE) 9, 2016.
[49] M. Peach, CO_2 laser system treats aircraft composite materials, in: optics.org, 2013, http://optics.org/news/4/10/48.

[50] E. Zahedi, C. Freitag, M. Wiedenmann, V. Onuseit, R. Weber, T. Graf, High ablation rate laser processing of CFRP for repair purpose, in: Proceeding of International Congress on Applications of Lasers & Electro-Optics (ICALEO) 34 (M304), 2015.
[51] F. Voelkermeyer, P. Jaeschke, U. Stute, D. Kracht, Laser-based modification of wettablility for carbon fiber reinforced plastics. Appl. Phys. A (2012) https://doi.org/10.1007/s00339-012-7237-3.
[52] O.G. Schulz, P. Saunders, SLCR laser material processing for controlled removal of CFRP as the first step in the repair chain, in: Proceeding of SAMPE Tech 2012, 2012.
[53] SAE, Paint Stripping of Commercial Aircraft—Evaluation of Materials and Process, SAE International, Warrendale, PA, 1998. http://www.sae.org/. document MA4872.
[54] H. Dittmar, P. Jaeschke, O. Suttmann, L. Overmeyer, Macro-structuring of composite material by UV-laser ablation, in: Proceeding of International Congress on Applications of Lasers & Electro-Optics (ICALEO) 32, 2013.
[55] M.A. Belcher, C.J. Wohl, J.W. Hopkins, J.W. Connell, Laser surface preparation for adhesive bonding of aerospace structural composites, in: Proceeding of European Conference on Composite Materials (ECCM) 14, 2010.
[56] A. Buchman, H. Dodiuk, M. Rotel, J. Zahavi, Laser-induced adhesion enhancement of polymer composites and metal alloys. J. Sci. Technol. 8 (10) (1994) 1211–1224, https://doi.org/10.1163/156856194X01031.
[57] F. Fischer, S. Kreling, K. Dilger, Surface structuring of CFRP by using modern excimer laser sources, Phys. Procedia 39 (2012) 154–160.
[58] J. Walter, C. Hennigs, M. Huse, M. Hustedt, S. Kaierle, L. Overmeyer, Analysis of potentially hazardous substances emitted during laser processing of carbon fiber reinforced plastics, in: Proceedings of Lasers in Manufacturing, 2015.
[59] J. Walter, A. Brodesser, M. Hustedt, S. Bluemel, P. Jaeschke, S. Kaierle, Laser processing of carbon fiber reinforced plastics—release of carbon fiber segments during short-pulsed laser processing of CFRP, Phys. Procedia 83 (2016) 1021–1030.
[60] J. Walter, M. Hustedt, R. Staehr, S. Kaierle, P. Jaeschke, O. Suttmann, L. Overmeyer, Laser cutting of carbon fiber reinforced plastics—investigation of hazardous process emissions, Phys. Procedia 56 (2014) 1153–1164.

CHAPTER 7

Understanding and Improving Process Control in Pulsed and Continuous Wave Laser Welding

J. Lawrence*, S. Katayama†
*University of Chester, Chester, United Kingdom
†Osaka University, Suita, Japan

7.1 INTRODUCTION

Laser welding has gained great popularity as a promising joining technology with high quality, high precision, high performance, high speed, good flexibility, and low deformation or distortion, in addition to its many applications due to ease of use with robots, reduced man-power, full automation, systematization, production lines, etc. Applications of laser welding are also increasing. In order to properly apply pulsed wave (PW) and continuous wave (CW) lasers to welding or joining, it is important to know the specifications and capabilities of laser apparatuses, the factors affecting weld penetration and welding defects, and the mechanisms and behavior of welding, as well as to evaluate weldability and mechanical properties of welds and joints.

In this chapter, in order to understand the fundamentals of PW and CW laser welding and to properly utilize the welding process on the basis of better understanding its phenomena, laser-induced plume behavior, the interaction between a laser beam and its induced plume, melt flows, keyhole behavior, and bubble generation in the molten pool leading to porosity formation in the weld fusion zones will be described and discussed in detail. Concerning spot welding with the PW Nd:YAG laser, the welding conditions affecting weld geometry and penetration, plume behavior, formation mechanisms and suppression procedures of porosity or pores and solidification cracking, in-process monitoring and adaptive control during welding, and so on will be summarized. Concerning bead welding, the factors affecting weld geometry or penetration, plume behavior, interaction between a laser beam and plume or plasma, formation mechanisms and suppression procedures of porosity or pores, in-process monitoring and adaptive control to give a constant bead width in CW welding will be described.

Advances in Laser Materials Processing
https://doi.org/10.1016/B978-0-08-101252-9.00007-8
Copyright © 2018 Elsevier Ltd.
All rights reserved.

7.2 LASER SPOT WELDING RESULTS, AND FORMATION MECHANISMS AND SUPPRESSION PROCEDURES OF WELDING DEFECTS

7.2.1 Factors Affecting Laser Spot-Weld Penetration and Welding Defects

In laser spot welding, weld penetration and geometry are affected by laser (peak) power, focused power density and transverse electromagnetic mode (TEM), beam diameter, defocused distance (laser focusing situation), pulse duration or length, pulsed energy, pulsed shape, material physical properties such as laser beam reflectivity, thermal diffusivity, surface tension, the content of volatile elements, environment such as air, inert shielding gas and vacuum, and so on [1–5]. Welding defects such as porosity, solidification cracks, underfilling (or concave surface), are influenced by joint geometry, keyhole behavior, thermal cycle, a low solidification temperature of liquid extent, spattering, etc., in addition to the above factors [1–5]. The effects of pulse length and defocused distance on the penetration depths of laser spot welds in Type 316 austenitic stainless steel (subjected to a pulsed Nd:YAG laser beam of about 5 kW peak power and ~0.7 mm focused spot diameter through GI fiber of 0.8 mm diameter) are indicated in Figs. 7.13 and 7.23 [4], respectively. In these figures, cross-sectional spot-weld fusion zones and porosity location are shown schematically. The penetration increases rapidly until 5 ms and then gradually from 5 to 20 ms. Deeper penetration and wider melt areas of spot welds are formed at higher pulse energy due to longer pulse duration and at higher power density due to shorter defocused distance. In the case of short pulse length of 1 ms, deep penetration is not obtained even at high power density. This is attributed to a short irradiation period after the formation of a keyhole. In order to produce a deeply penetrated spot weld, a laser beam of high power density should be shot for a longer period. High power density is effective enough to produce a deep keyhole in a formed molten pool [3]. Porosity is formed in shallow weld metals made at high power densities due to short defocused distances as well as in deeply penetrated weld fusion zones due to long laser irradiation duration. It is assumed in all cases that porosity formation takes place as a result of rapid collapse of a keyhole due to the rapid termination of laser irradiation power [1–5]. (Figs. 7.1 and 7.2).

It is generally observed that solidification cracks are formed in pulsed Nd:YAG laser spot weld fusion zones in most aluminum alloys such as A5052, A5083, A6061, A2029, A7075, and fully austenitic stainless steel Type 310S [1,2,4]. It should also be noted that solidification cracking or hot

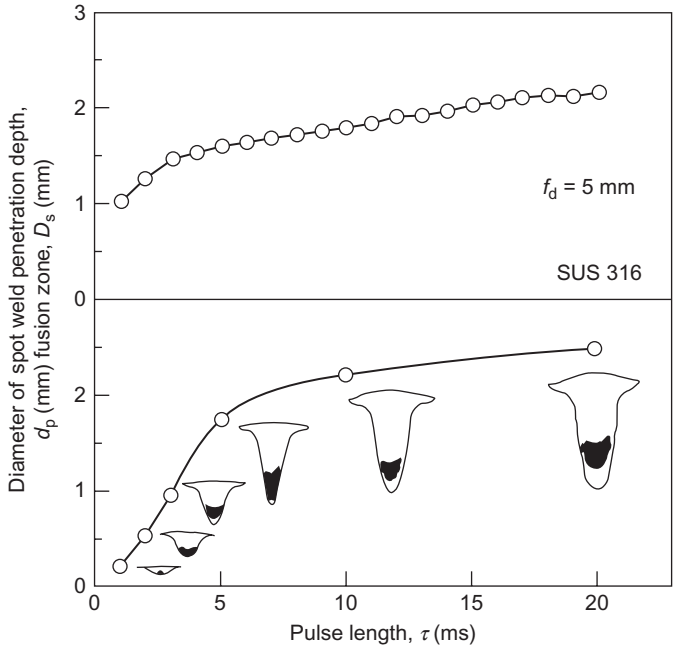


Fig. 7.1 Effect of pulse length on penetration depth and fusion zone diameter of pulsed Nd:YAG laser spot welds in Type 316 austenitic stainless steel.

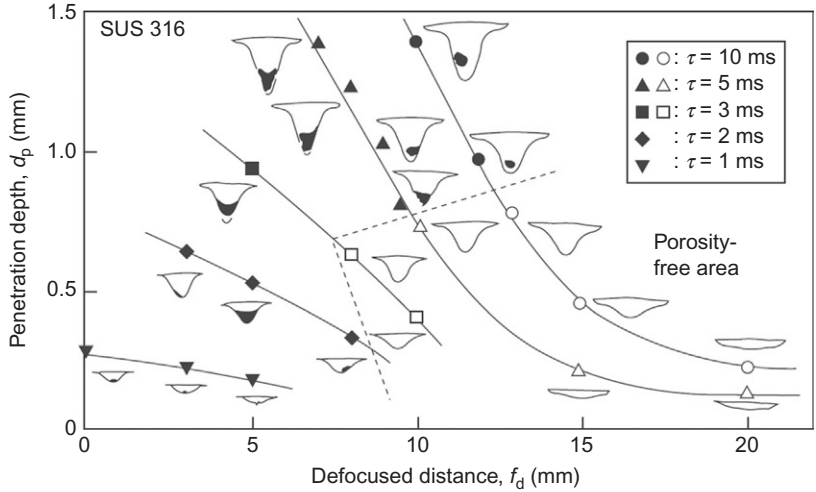


Fig. 7.2 Effects of pulse length and defocused distance on penetration depth of pulsed Nd:YAG laser spot weld in Type 316 steel and porosity formation location and conditions.

cracking occurs easily in pulsed laser spot welding of alloys except pure metals or alloys with a small amount of alloying elements because grain boundaries with a low melting point of liquid form in a wide range due to rapid solidification of dendrite tips.

7.2.2 Phenomena During Spot Welding With Pulsed Laser

Plume behavior was observed during pulsed Nd:YAG laser spot welding of aluminum alloys, stainless steels or commercially pure titanium by high-speed video or streak cameras. The plume was analyzed with spectroscopic measurement, and evaporated particles were observed by transmission electron microscopy (TEM) and analyzed with energy dispersive X-ray spectrometry (EDS) or X-ray diffractometry (XRD) [6–12].

An example of high-speed streak images and frame photographs of laser-induced plumes from Ti plate in air is shown in Fig. 7.3 [6,12]. The streak speed is 86.12 m/s, the slit width is 0.1 mm, and the time resolution is 1.16 μs. The bright light emission (white parts in photos) named "a plume" is generated just after melting and grows upwards smoothly in the initial stage, and fluctuates periodically after the stable growth. In this case, the growth rates of a luminous plume were high, about 20 m/s and 100 to 170 m/s in the initial and periodic stages, and the periodic duration was about 0.21 to 0.32 ms [6,7] These values are different in materials because of different physical properties.

An example of spectroscopic analysis of plume generated from the A5083 aluminum alloy plate subjected to the irradiation of pulsed Nd:YAG laser in air is shown in Fig. 7.4 [6,8,10] In this figure, Mg, AlO and MgO are detected, and Al and AlH are seen in the other wavelengths. The lines of ions such as Al II and Mg II, and Ar I in the case of Ar shielding gas are not detected, and thus the plume temperature is not regarded to be high. The Al and AlO ratio increases with increases in the pulse energy and the consequent peak power density of a laser beam. The ratio of MgO to AlO is high in the initial and last stages where the temperature of molten pool is low. This is attributed to the physical properties that Mg with higher vapor pressure than Al is more easily evaporated at lower temperatures just above the melting point of an alloy.

An example of ultrafine particles produced from the A5083 plate with a pulsed Nd:YAG laser of about 80 J/p energy and 10^{10} W/m^2 peak power density in air is shown in Fig. 7.5 [6,9]. In (C) the element C (peak at 0.3 keV) comes from the supporting film for observation. Ultrafine particles of about 10–150 nm size are observed, consisting of Al, Mg, and O,

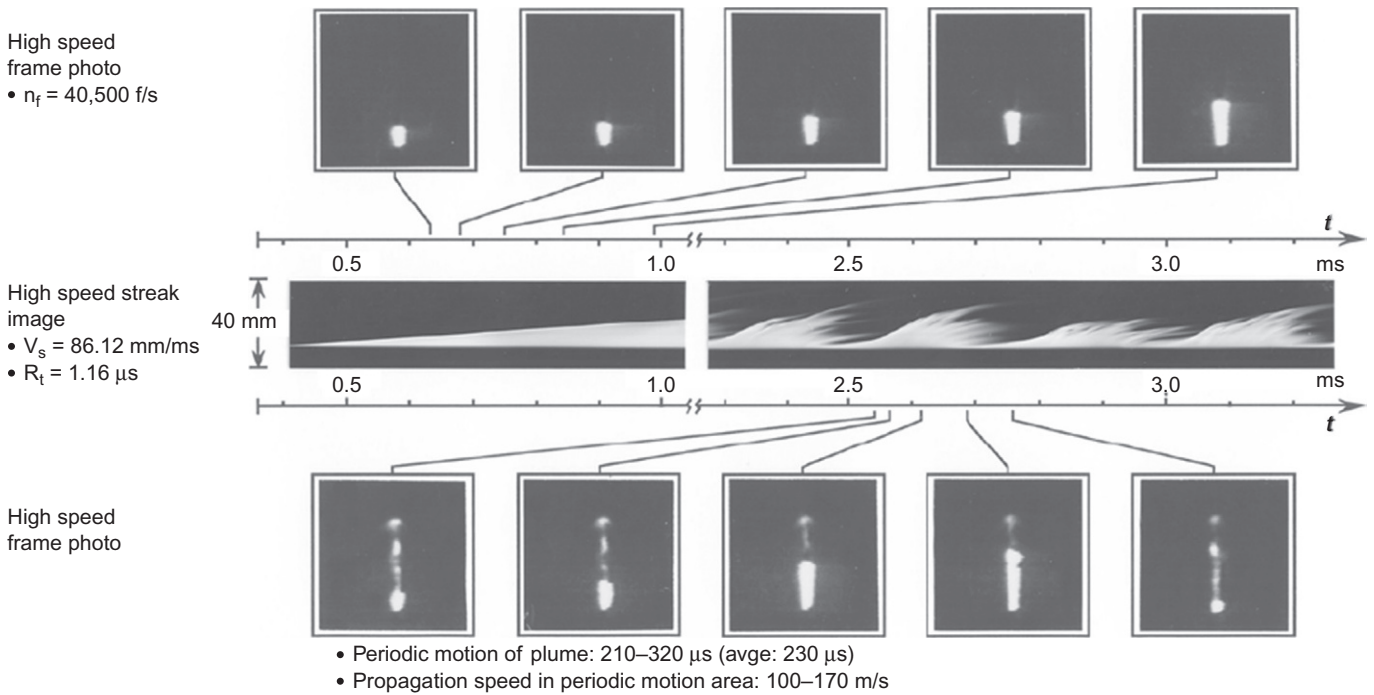


Fig. 7.3 High-speed streak image and frame photographs of plume induced during pulsed Nd:YAG laser spot welding of pure Ti in air (V_s = 86.12 m/s, R_t = 1.16 μs, n_f = 40,500 f/s, α_p = 7 ms, E_0 = 17.3 J/s).

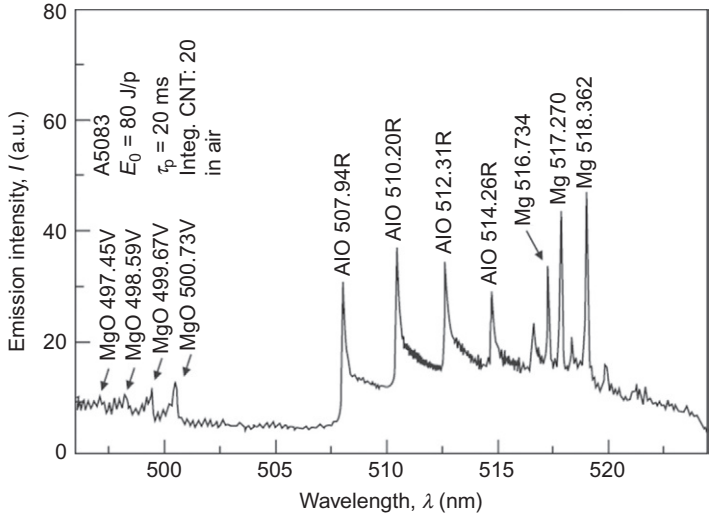


Fig. 7.4 Spectroscopic measurement result of plume induced during pulsed Nd:YAG laser spot welding in air, showing emission from MgO and AlO molecules and Mg neutral atoms near 510 nm.

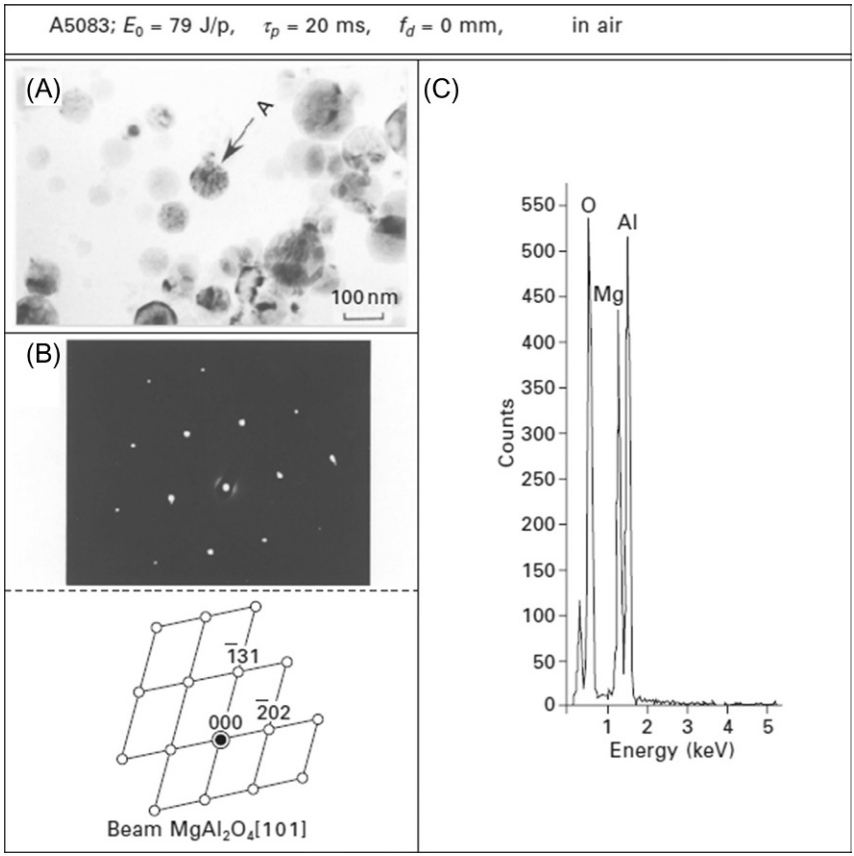


Fig. 7.5 Analytical results of ultrafine particles from A5083 alloy exposed to pulsed Nd:YAG laser in air: (A) TEM photo, (B) electron diffraction pattern and its key diagram, and (C) energy dispersive spectroscopy (EDS) spectra.

and are identified to be $MgAl_2O_4$ oxides. $MgAl_2O_4$ oxide particles are also confirmed by the X-ray diffractometer method. In the air the vaporized particles are easily oxidized, while in Ar shielding atmosphere alloy ultrafine particles of Al and Mg are detected. It is considered that these ultrafine particles exert Rayleigh scattering on the incident laser beam [13,14] The luminous plume is caused by the emission of neutral atoms and partly weakly ionized atoms, and in addition, oxides of alloying elements such as AlO or MgO in air, and these vapors ejected from a keyhole inlet form ultrafine particles during flying.

An example of temporal change of the laser-irradiation area on the A5083 alloy surface in air is exhibited in Fig. 7.6 [6,10], showing melting and keyhole behavior on the molten pool surface. (A photo showing a wide-open keyhole is not selected, since the outline of a keyhole is obscure due to a bright plume.) According to the simultaneous behavior observation results of a plume and a keyhole, a keyhole is always open, and fluctuates to cause a periodic fluctuation of plume growth [6,12]. The keyhole fluctuates and its surface closes in about 0.7 ms after the laser irradiation termination at 10 ms. The quick surface closing of a keyhole results in the formation of a pore or porosity.

Figs. 7.7 and 7.8 show examples of X-ray transmission in situ observation results of keyhole behavior and the variation in keyhole depth in the molten pool of a Type 304 stainless steel plate subjected to rectangular pulse-shaped laser [15]. The keyhole forms after 2 ms, grows at about 0.5 m/s drilling speed (1 m/s at the maximum) until 7 ms, and deepens gradually by repeating the formation of a deeper or shallower keyhole. The deep keyhole exists in 1 ms and partly in 2 ms after laser irradiation termination, and the keyhole with the quickly closed surface results in the formation of a pore (porosity).

7.2.3 Suppression Procedures of Laser Spot Welding Defects

Porosity is formed in deeply penetrated spot welds made with a pulsed laser, as shown in Fig. 7.7. The porosity can be reduced by controlling the laser pulse shape with a tailing power (shown in Fig. 7.9) or saw-like power decrease [1,2,4,7]. The location of a pore moves upwards according to the pulse shape. The rapid increase in the pulse peak power sometimes results in the formation of spatters, resulting in the formation of underfilling or concave spot-weld surface [2,7,16].. The slow increase in laser power during keyhole growth in the initial stage is effective in the suppression of spattering and underfilling [2,7,16]. In other words, the suppression of rapid growth of a keyhole is essential to the reduction in spattering in the small molten pool with a small amount of melt.

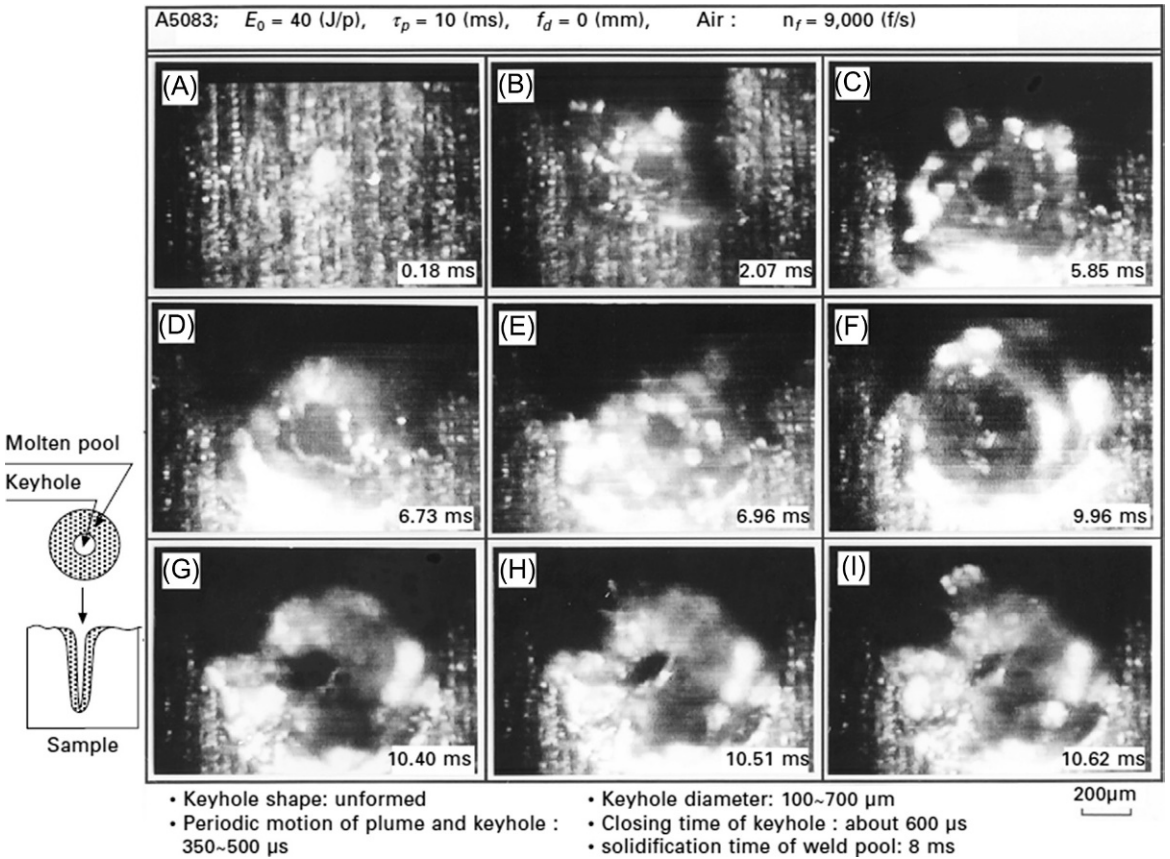


Fig. 7.6 Typical temporal change in keyhole inlet in molten pool during pulsed Nd:YAG laser spot welding of A5083 alloy in air.

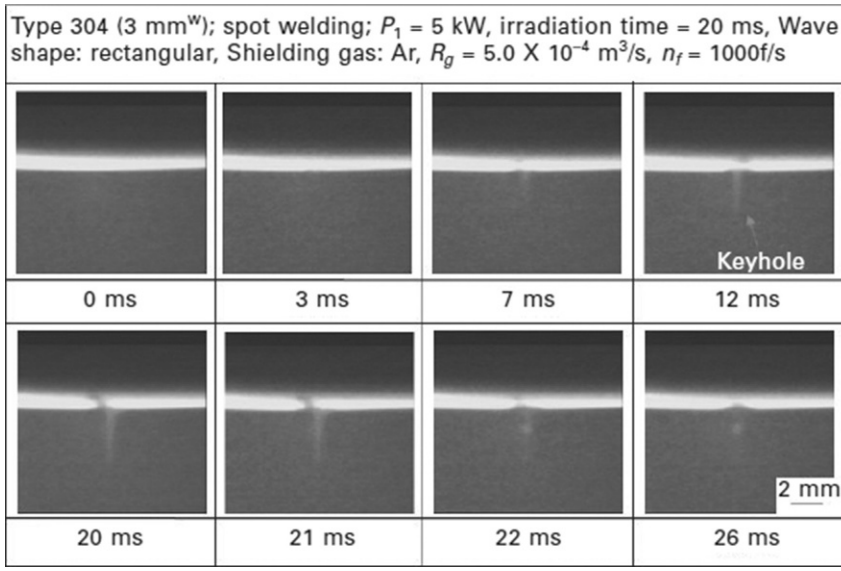


Fig. 7.7 X-ray transmission real-time observation photos of keyhole and porosity formation behavior during spot welding of stainless steel with laser of rectangular pulse shape.

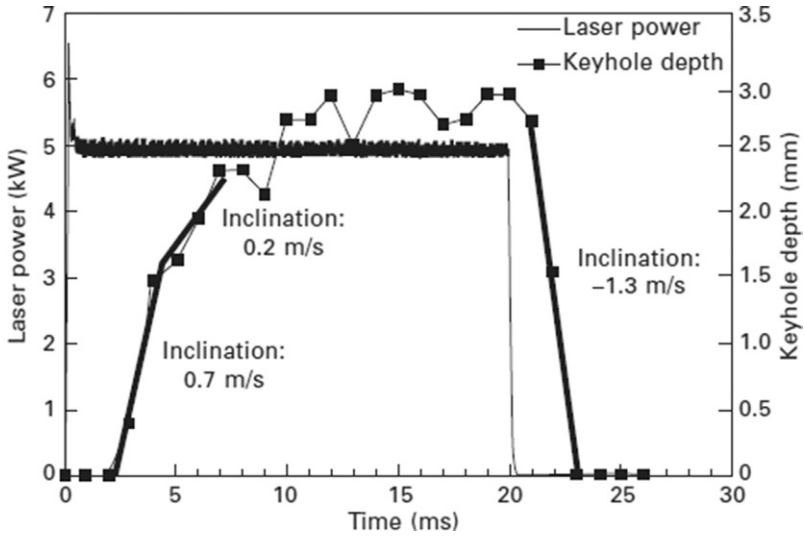


Fig. 7.8 Variation in keyhole depth in Type 304 molten pool subjected to laser of rectangular pulse power.

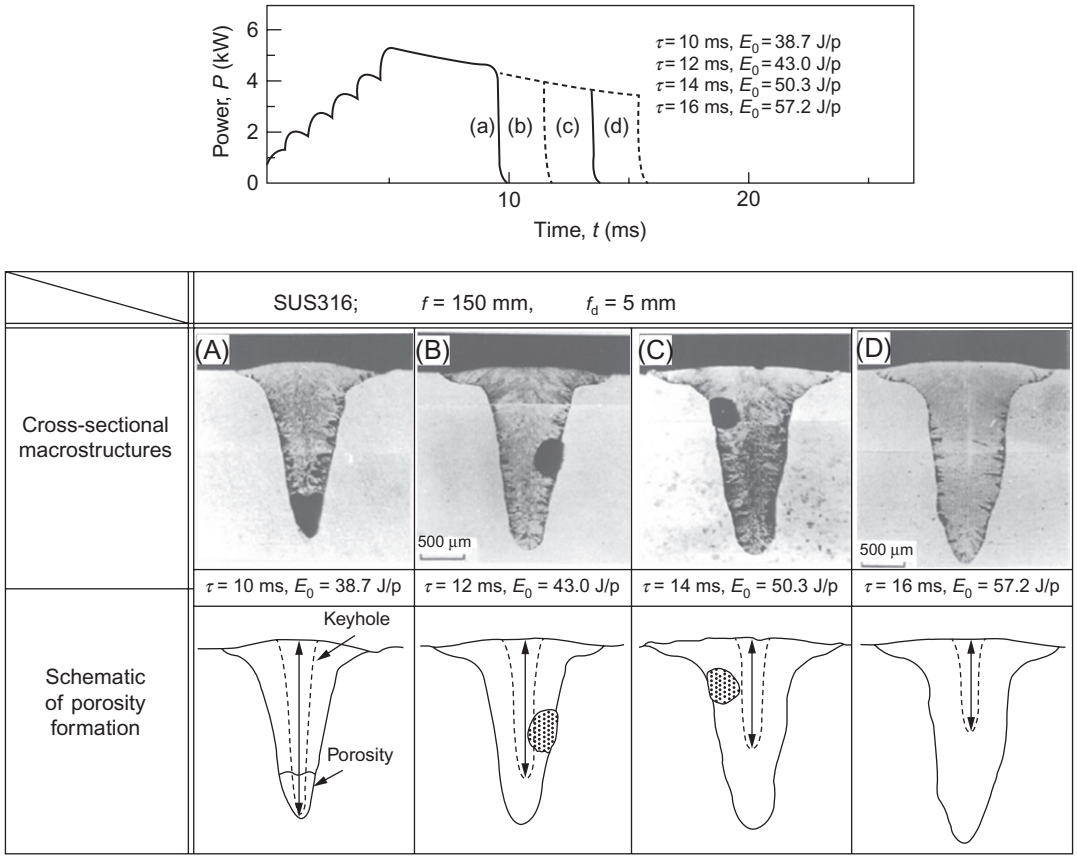


Fig. 7.9 Various laser pulse shapes and obtained laser spot welds with pores, showing effects of controlled pulse shape and proposed mechanism of porosity reduction.

In laser spot welding, solidification cracks are easily formed. Examples of A5083 alloy weld made under the normal and controlled pulse shapes are shown in Fig. 7.10 [2,17]. Cracking is attributed to the formation of low-melting-point liquid along grain boundaries all over the wide areas due to a small heat input and the consequent rapid solidification of cellular dendrite tips. The tailing power can reduce cracking by suppressing the rapid growth of cellular dendrite tips [2,17]. In seam welding, a crack can be removed by melting, but occurs again during solidification in spot welding. Porosity and cracking can be prevented in seam welds (except the last spot weld) by selecting proper repetition rates to produce sound overlapped spot welds, as shown in Fig. 7.11 [2].

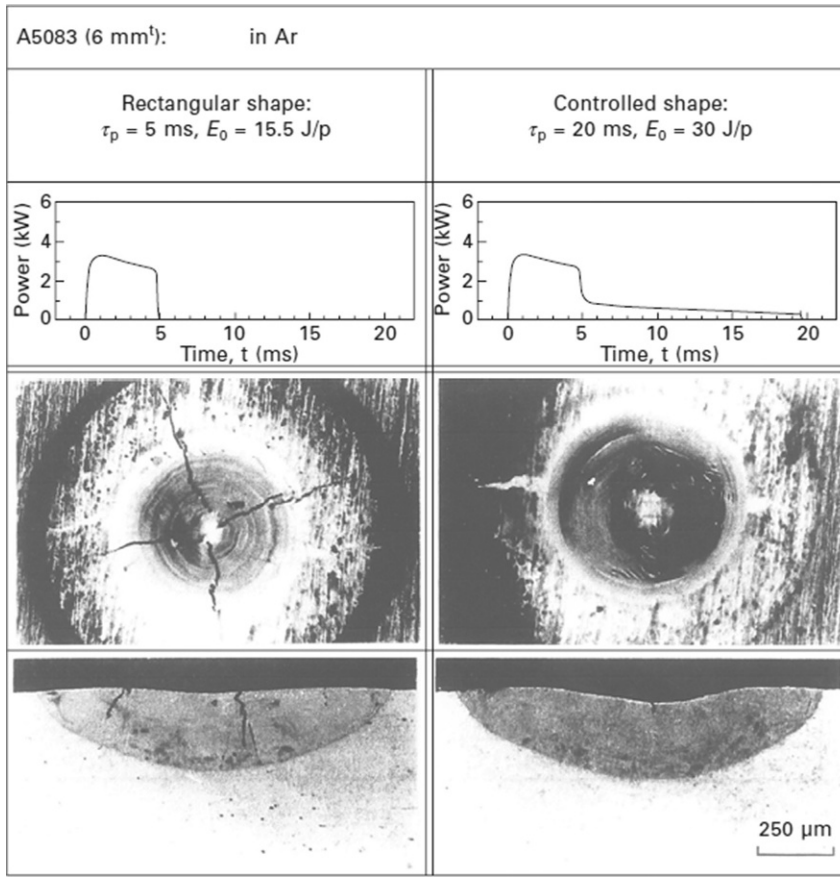


Fig. 7.10 Laser spot welds in A5083 alloy produced under rectangular and controlled shapes.

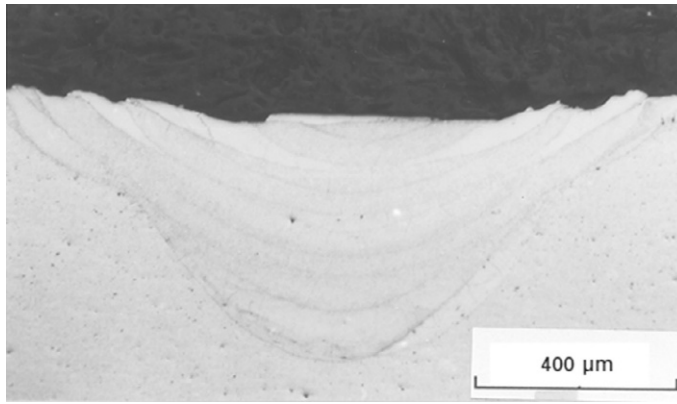


Fig. 7.11 Sound seam weld in A5083 alloy produced under controlled pulse shape, showing no porosity and no cracks.

7.2.4 Monitoring and Adaptive Control During Laser Spot Welding

Monitoring is widely studied to judge the quality of welds. In the last stage of development of the welding process, adaptive control of laser power and irradiation period based upon proper monitoring signals is regarded as ideal technology in laser spot welding. A schematic setup developed for in-process monitoring and adaptive control is shown in Fig. 7.12 [18]. The signals of a vertically reflected laser beam and the heat radiation from the laser-irradiated part can be monitored. Welding phenomena are also interpreted by simultaneously observing plume behavior and variation in the molten pool size in this research [18].

An example of the monitoring results of a reflected laser beam and heat radiation is shown in Fig. 7.13 [18], together with the pulse shape of a Nd:YAG laser beam used and high-speed images of plume behavior (lower) and molten pool surface (upper) observed, where 0.1 and 1.0 mm thick A3003 sheets are subjected to lap welding in air. The reflected laser signal increases with an increase in the laser irradiation power but decreases after the formation of the melted zone, and then is low due to the formation of a keyhole in the time taken to form the flat surface after the laser termination. Small peaks of the reflected laser beam at about 2.7 and 4.5 ms mean the reflection through the keyhole from the underlying sheet surface and from the flat surface during the collapsing of a keyhole, respectively. The heat radiation signal increases gradually, and the period above 1.7 µW is judged as the lap welding process of two sheets. Under the same laser irradiation conditions, a through-hole was formed due to the deformation of 0.1 mm

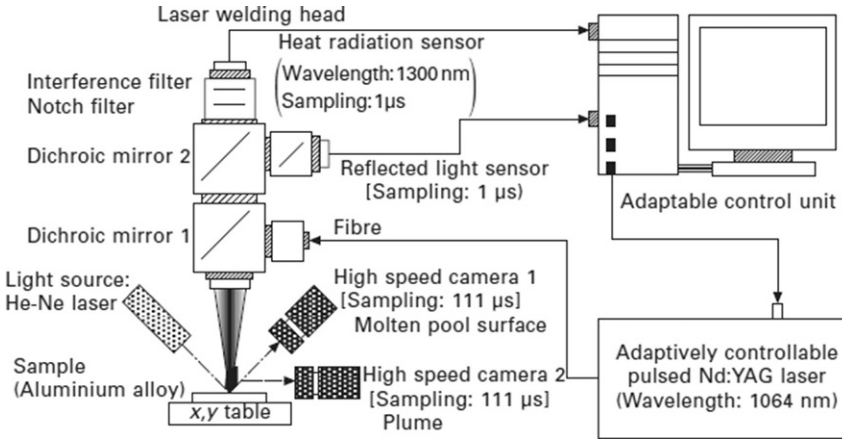


Fig. 7.12 Schematic arrangement of experimental set-up of in-process monitoring and high-speed cameras and laser adaptive control system.

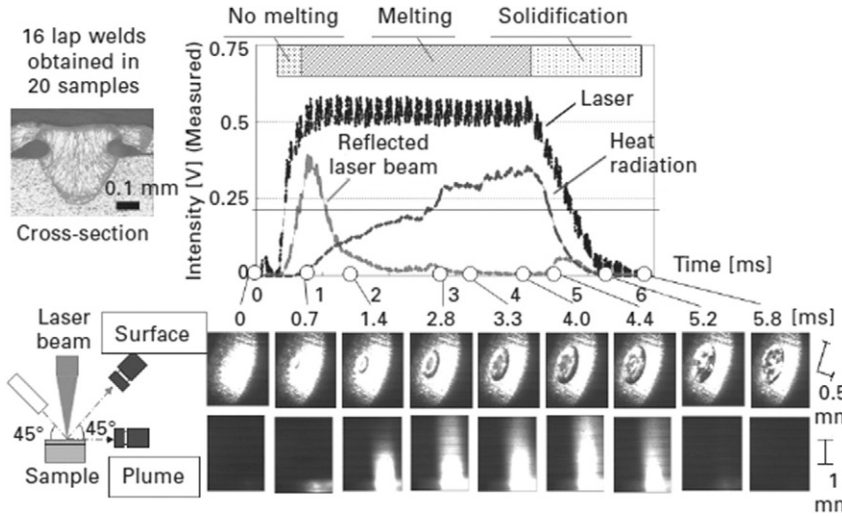


Fig. 7.13 Monitoring results of laser micro-spot lap welding of A3003 sheets, showing laser pulse shape, and reflected laser beam and heat radiation signals, in addition to high-speed observation images.

thick sheet. During hole formation, the reflected laser signal was high and the heat radiation signal was low. In this laser spot welding, therefore, the heat radiation signal is utilized for adaptive control.

It is confirmed that adaptive control is successfully performed even in spot welding during a very short period [18]. An example of the in-process

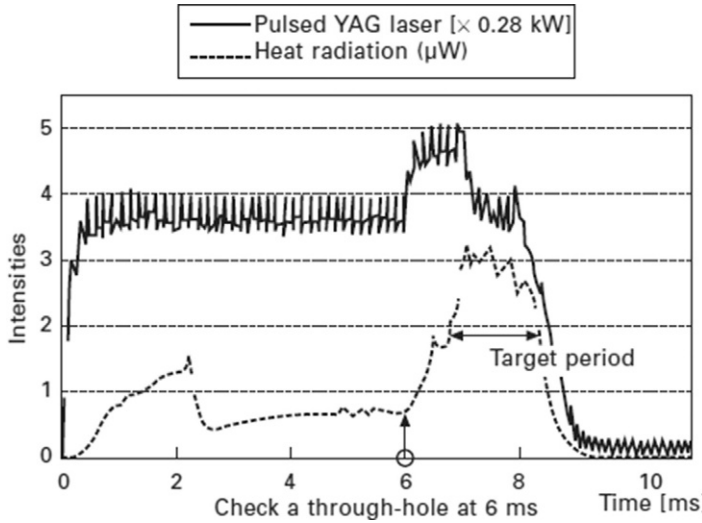


Fig. 7.14 Signal of heat radiation monitored, and adaptively controlled laser power.

repairing during spot welding of A3003 sheets is shown in Fig. 7.14 [18], showing the laser power wave and the heat radiation signal. At 6 ms, the adaptive control unit recognizes the existence of a through-hole by a low level of the signal, and exerts the laser power to increase from 1.07 to 1.39 kW. It is confirmed that laser pulse duration and peak power can be adaptively controlled on the basis of the heat radiation signal at every 0.15 ms interval during irradiation, and consequently stable lapped welds are always produced adaptively or repaired in process [18].

7.3 CW LASER WELDING RESULTS, AND FORMATION MECHANISMS AND SUPPRESSION PROCEDURES OF WELDING DEFECTS

7.3.1 Factors Affecting Laser Weld Bead Penetration

When welding with a CW laser, weld penetration and geometry are affected by laser power, beam diameter, focused power density, TEM (transverse electromagnetic) mode, defocused distance (laser focusing situation), material physical properties, such as laser beam reflectivity, thermal diffusivity, surface tension, and the content of volatile elements, the environment such as air, shielding gas type, gas flow rate, and vacuum, laser-induced plasma and plume, and so on [19–37].

Type 304 welds made with a CO_2 laser of 10 kW power in different shielding gases are exhibited in Fig. 7.15 [23,25], showing the effect of

shielding gas on the penetration. The penetration is deep in He gas, but the depth decreases with an increase in the gas ratio of Ar to He. The penetration is considerably shallower in N_2 gas. The penetration geometries and depths of weld beads made with a fiber laser of 1–10 kW power are indicated in Fig. 7.16 [32]. The penetration increases with an increase in the

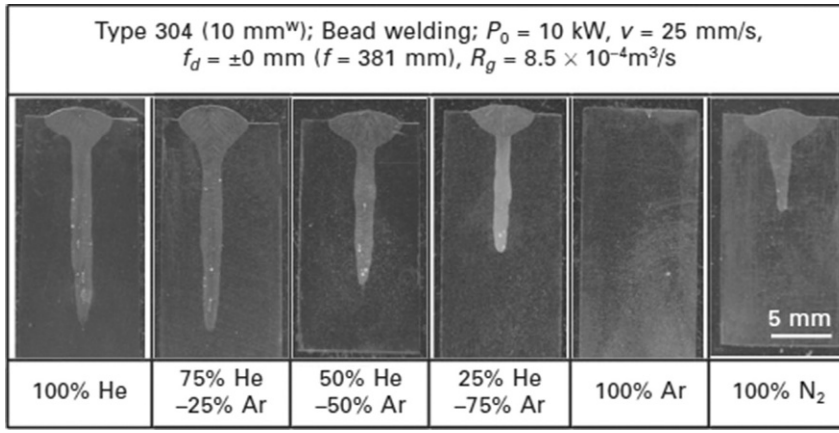


Fig. 7.15 Cross-sections of Type 304 weld beads produced with 10 Kw CO_2 laser in different shielding gases.

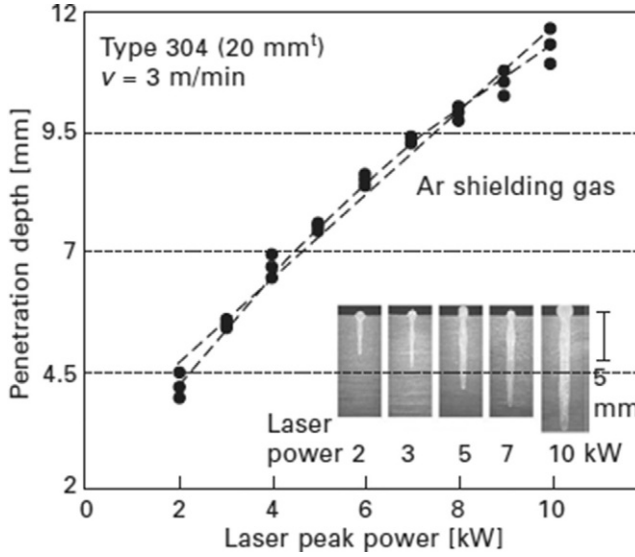


Fig. 7.16 Penetration geometries and depths of Type 304 weld beads made with fiber laser of 1 to 10 kW power.

laser power. Deeply penetrated welds can be produced in fiber laser welding at high powers even in Ar shielding gas. The comparison of these figures demonstrates that the effect of a shielding gas is more noted at higher powers of CO_2 laser, but is not so great in welding with Nd:YAG or fiber laser of about 1.06 μm wavelength.

The penetration depths in various aluminum alloys are shown as a function of defocused distance in Fig. 7.17 [21]. The welds are deep near the focal point because of high power density but become shallow at the longer defocused distance. Deeper penetration can be easily formed in alloys with a larger amount of volatile alloying elements such as Mg and Zn [19–21].

The penetration depths of weld beads produced with a fiber laser of 10 kW power and different beam diameters (and correspondingly different power densities) at the focal point are shown as a function of welding speed in Fig. 7.18 [28]. The weld beads are deeper at the slower welding speeds. It is noted that the higher power densities can produce deeper weld beads

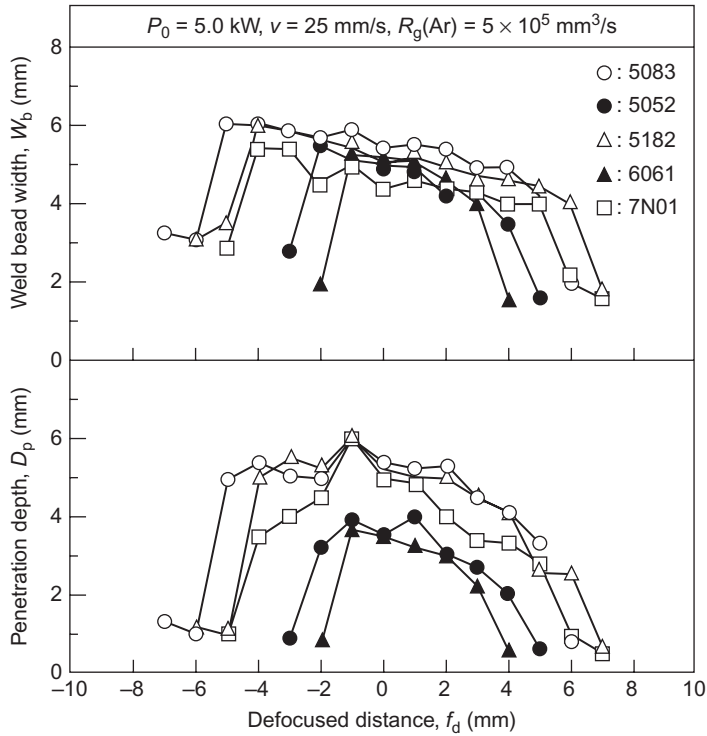


Fig. 7.17 Effect of defocused distance on penetration depths in various aluminum alloys.

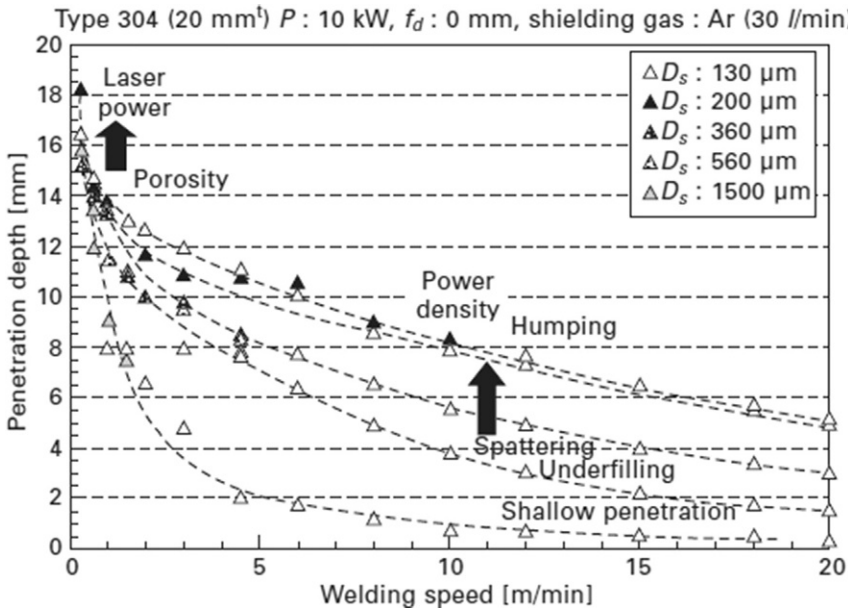


Fig. 7.18 Effect of different beam diameters and welding speeds on penetration depths of weld beads produced in Type 304 steel with fiber laser of 10 kW power.

at high welding speeds, while at low speeds the effect of power density on weld penetration is small, although the power exerts significant effect on the penetration.

7.3.2 Behavior and Characteristics of Laser-Induced Plume, and Interaction Between Laser and Induced Plume During CW Laser Welding

The behavior and characteristics of a laser-induced plume and/or plasma, and the interaction between a laser beam and a plume are observed or measured by using spectroscopic measurement, high-speed video cameras, and a probe laser beam. An example of the observation system for visualization of interaction between the laser beam and the plume during welding is schematically shown in Fig. 7.19 [29,30]. Fiber laser, diode laser, and Helium-Neon laser of 1090, 830, and 633 nm in wavelength, respectively, are used as a probe beam during Nd:YAG or fiber laser welding.

Fig. 7.20 gives examples of induced gas plasma and metal plume observed during CO_2 laser welding of A5083 aluminum alloy under the conditions of 5 kW power, 50 mm/s speed, and 30 L/min coaxial flow of He, Ar, and N_2 shielding gas [12]. In He gas, a plume is only formed by the emission

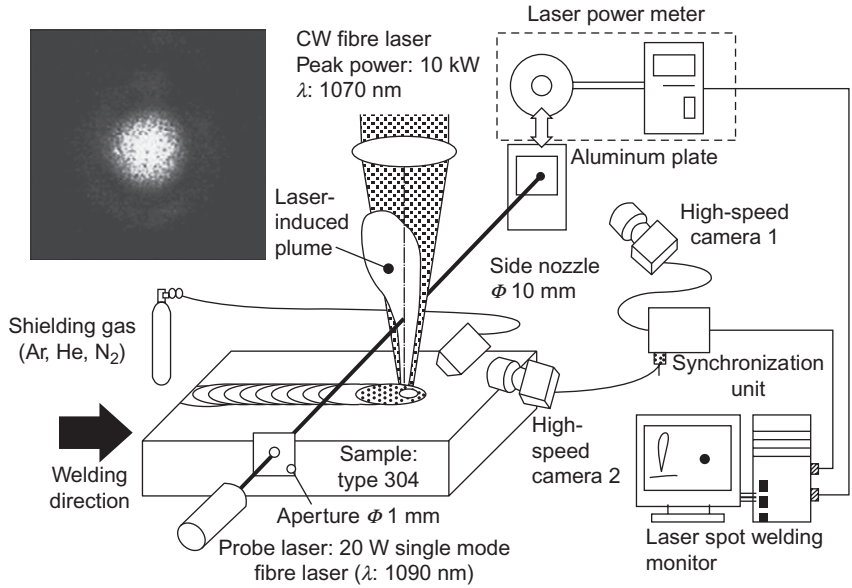


Fig. 7.19 Schematic observation and measurement system for visualization of interaction between probe laser beam and laserinduced plume during welding.

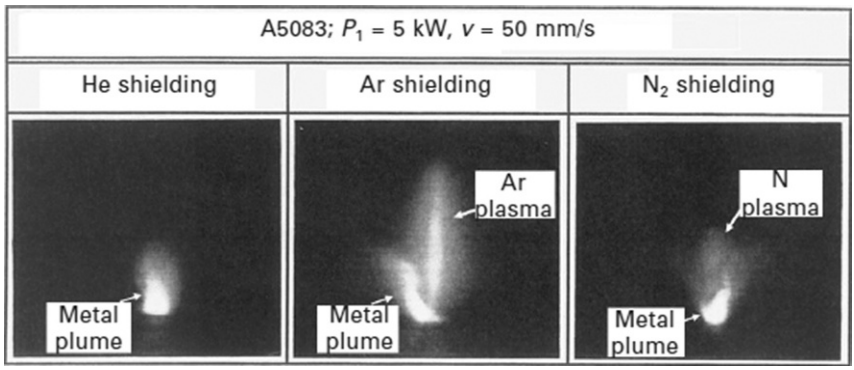


Fig. 7.20 Plasma and plume observed during CO_2 laser welding of A5083 aluminum alloy in He, Ar and N_2 coaxial shielding gas, showing effect of shielding gas kind on plasma formation.

of neutral metal atoms spouting from a keyhole inlet during welding, while in Ar or N_2 gas, gas plasma is always or sometimes formed under the nozzle in addition to the plume from the keyhole. In welding with a CO_2 laser of 10 kW or more in Ar or N_2 side gas, a gas plasma flows up periodically to block an incident laser beam so as to reduce weld penetration A welding example at 15 kW power in N_2 side gas demonstrating the relationship

between gas plasma formation and keyhole behavior is shown in Fig. 7.21 [15,26]. It is assumed that the Ar or N_2 gas plasma is more easily formed because of lower ionization potential in comparison with He gas, and the gas plasma exerts the inverse Bremmstrahlung process on the CO_2 laser beam because the effect is proportional to λ^2, where λ is the wavelength [10,36]

An example of spectroscopic measurement and analysis of a plume during welding of Type 304 stainless steel with a 10 kW fiber laser beam at the ultra-high power density of about 1 MW/mm^2 in Ar shielding gas is shown in Fig. 7.22 [32]. Almost all peaks are detected to come from the emission of neutral atoms, and the emission from Ar gas is not detected. The inverse Bremmstrahlung effect seems to be negligibly weak to a laser beam of about 1 μm wavelength. According to the Saha equation, it is estimated that a plume is in the state of a weakly-ionized plasma (about 6000 K and 2% atomic ions) [32]. Fig. 7.23 shows examples of photos displaying the relationship between plume behavior and probe laser motion [30,32]. It is confirmed that the refraction and attenuation of a probe laser beam exist due to an inclined refraction index profile caused by slanted distribution of vapor density at high temperatures and Rayleigh scattering [29–32]. The interaction of such a small-sized plume on a laser beam of about 1.06 μm wavelength is judged to be small.

The plume and plasma behavior and consequent keyhole are schematically illustrated in Fig. 7.24 [36]. In the case of a CO_2 laser of about 10.6 μm wavelength, Ar gas and N_2 gas forms gas plasma, resulting in the decrease in weld penetration, while in the case of a Nd:YAG, fiber, or disk laser of about 1.0 mm wavelength, the shielding gas effect is small, and laser power and its density exert the penetration [28,32].

7.3.3 Suppression Procedures of Laser Welding Defects

Porosity is easily formed in deeply penetrated weld beads at low welding speeds, as already shown in Figs. 7.15 and 7.18. X-ray transmission observation results confirm that bubbles are generated from a keyhole tip to form porosity at low welding speeds, while bubbles not formed at high welding speeds, resulting in no porosity, as examples of 6 kW fiber laser welding are shown in Fig. 7.25 [27]. From such observation results, plume behavior, keyhole behavior, melt flows, and bubble generation leading to porosity formation in the molten pool are schematically summarized in Fig. 7.26 [36]. At low welding speeds, a deep keyhole is likely to collapse, then a laser beam is irradiated on the collapsed liquid wall of the keyhole, and consequently downward melt flows are caused by the recoil pressure of evaporation from

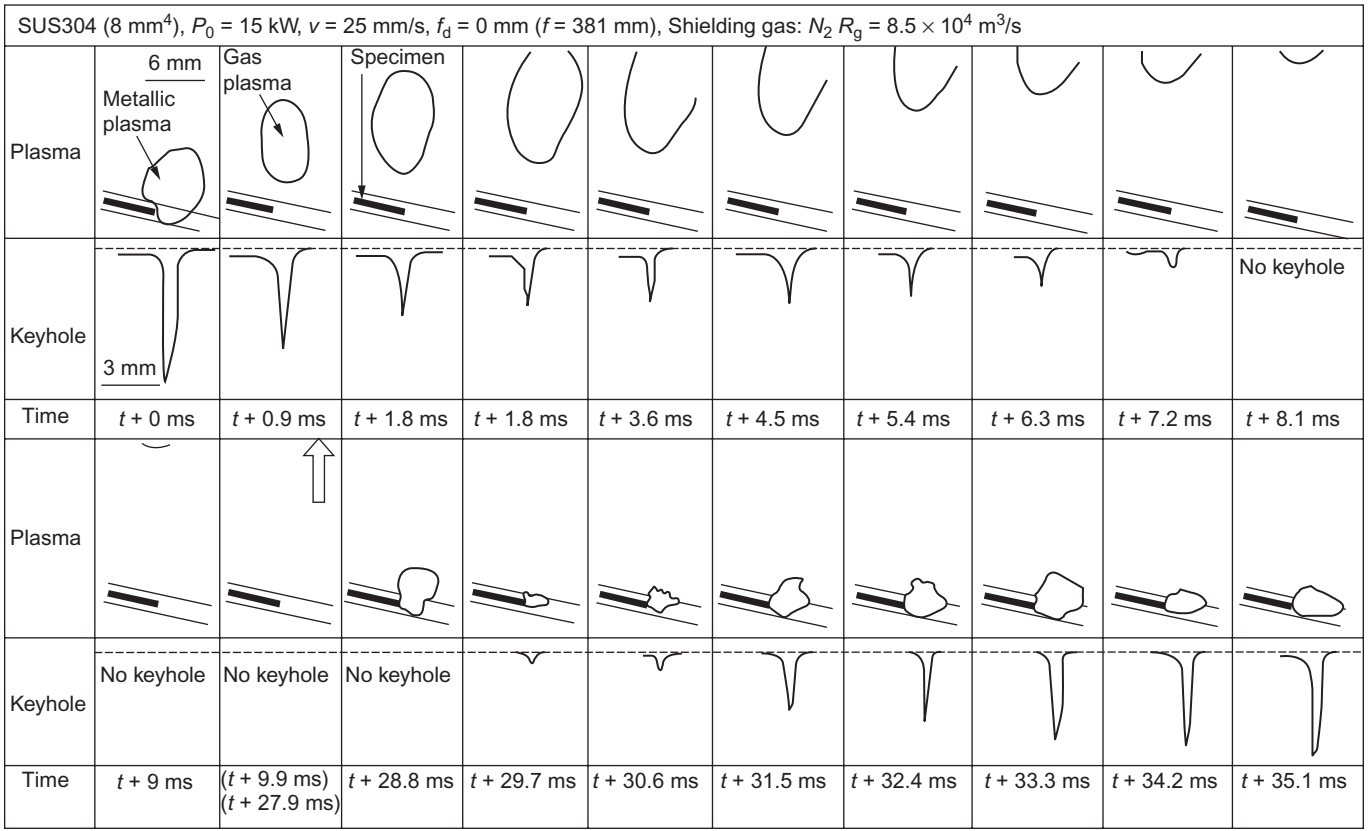


Fig. 7.21 Simultaneous observation result of phenomena during CO_2 laser welding at 15 kW power in N_2 gas, showing relationship between gas plasma formation and keyhole behavior.

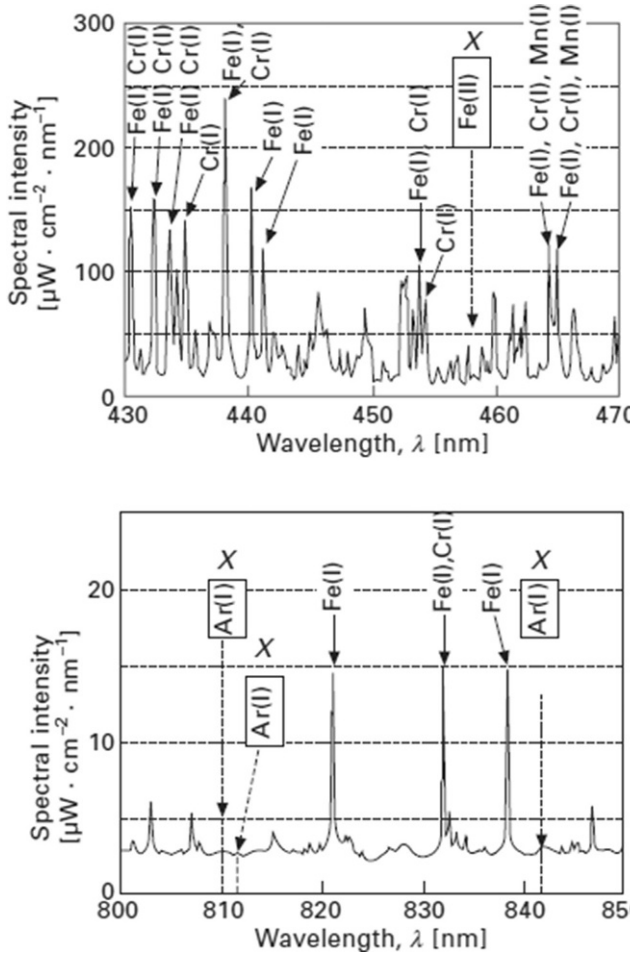


Fig. 7.22 Spectroscopic measurement and analytical result of plume induced during 10 kW fiber laser welding of Type 304 stainless steel.

the collapsed wall. Such phenomena may produce large bubbles leading to pores. As the welding speed is slightly increased, intense evaporation sometimes takes place from the front wall of a keyhole (where the liquid layer is thin) to deform the rear wall of the keyhole (where the liquid is large) to produce a bubble. Under a certain condition, bubbles flow upward to disappear from the molten pool surface. If the material has such a high surface tension to produce a stable keyhole, the vapors are strongly ejected upwards from the keyhole inlet to induce the melt flow near the inlet upwards, and smaller bubbles are formed from the keyhole tip. Consequently, pores are

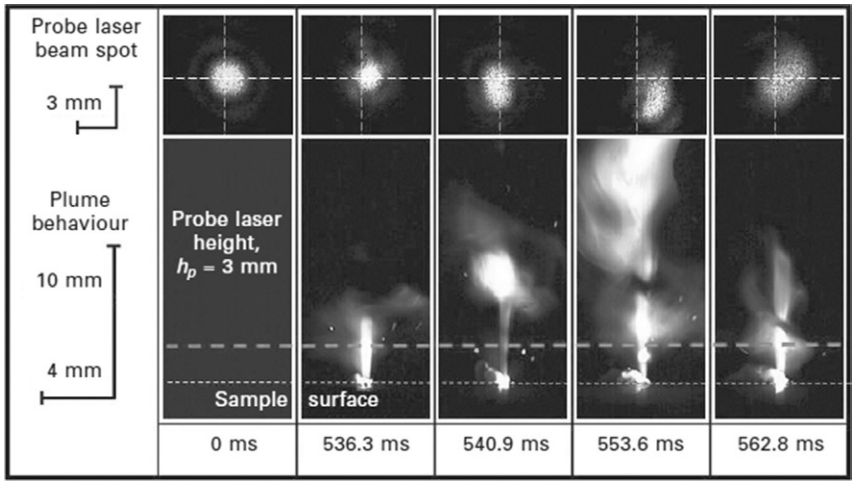


Fig. 7.23 Simultaneous observation results of probe fiber laser behavior (upper) and laser-induced plume (lower), showing visual interaction between laser and plume.

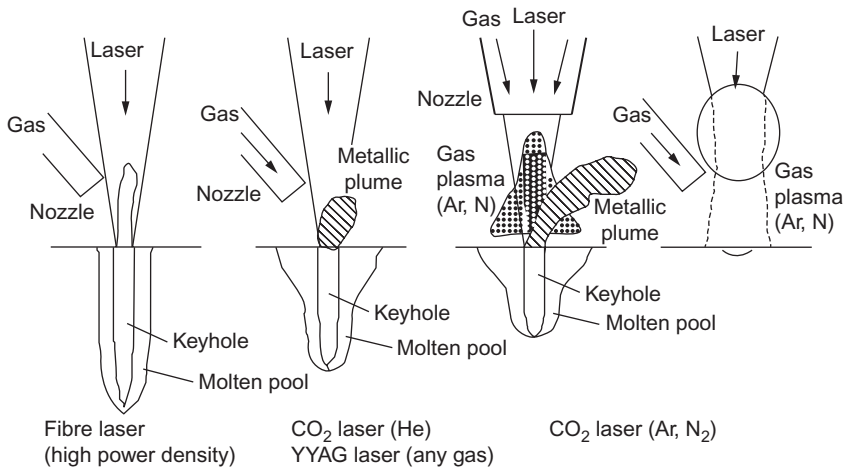
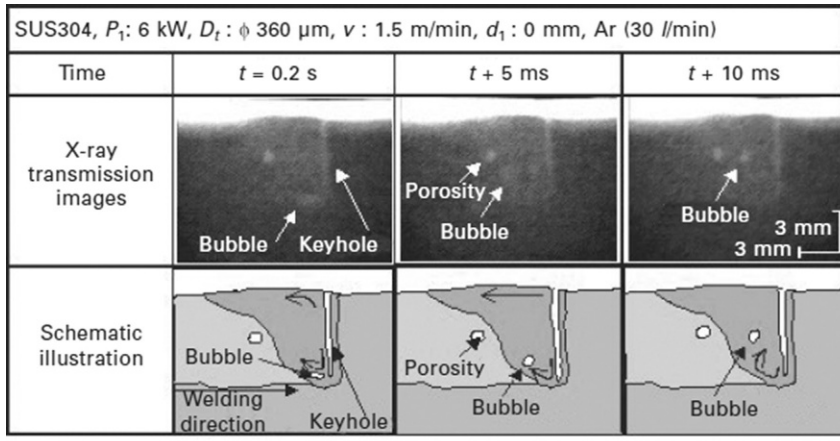
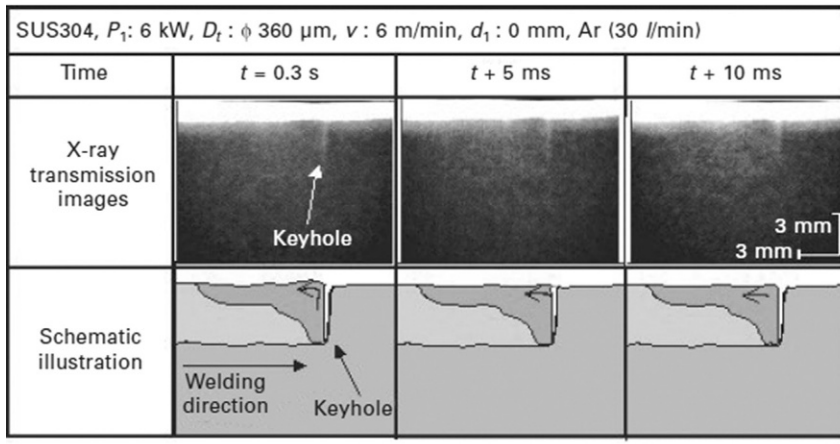


Fig. 7.24 Schematic illustration of plume and plasma behavior and consequent keyhole in laser weld fusion zone.

present near the bottom part of the weld bead. When the welding speed is high enough, a plume ejects upwards, and a keyhole becomes so stable as to suppress or prevent bubble formation, resulting in reduced or no porosity. At high powers such as a 20 to 40 kW CO_2 laser in He shielding gas and/or at high power densities such as a 10 kW fiber laser of 0.2 mm focused beam, bubbles leading to pores are sometimes generated from the middle part of a keyhole.



(A)



(B)

Fig. 7.25 X-ray transmission observation results and schematic representation of keyhole behavior, melt flows, bubble formation and molten pool geometry during welding with 6 kW fiber laser at speeds of (A) 1.5 m/min and (B) 6 m/min.

Examples of X-ray transmission photos during CW Nd:YAG laser welding of Type 304 steel in Ar, He, and N_2 shielding gas are shown in Fig. 7.27 [37]. Bubbles are formed in an inert gas such as Ar and He, but bubbles are hardly seen in N_2. Ar and He gas is generally detected in the pores; therefore, Ar or He gas is involved in an unstable keyhole at lower welding speeds, but a harmful influence of N_2 is reduced by reacting with Cr vapors in the keyhole or being included due to high solubility in the molten pool. N_2 gas is regarded as a proper shielding gas in Nd:YAG, disk or fiber laser welding of austenitic stainless steels.

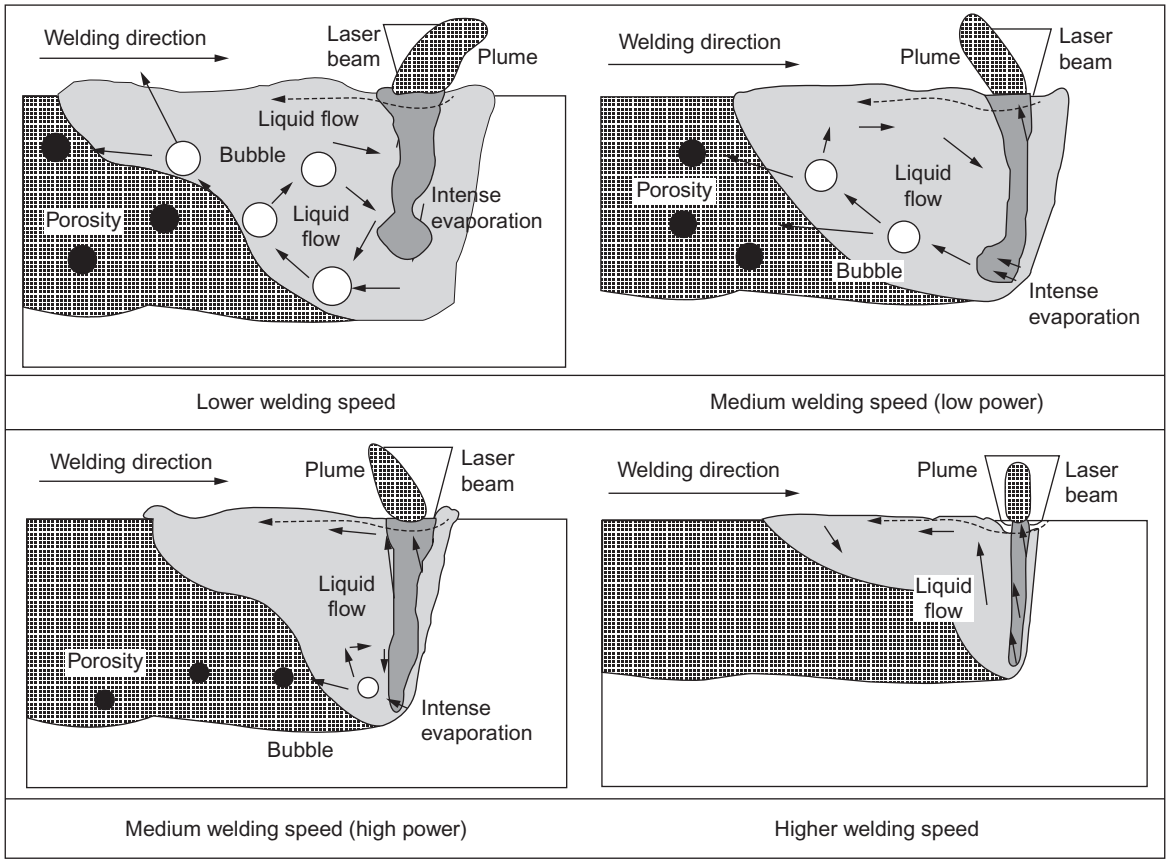


Fig. 7.26 Schematic representation of plume behavior, keyhole behavior, melt flows, and bubble generation leading to porosity formation in molten pool according to respective conditions.

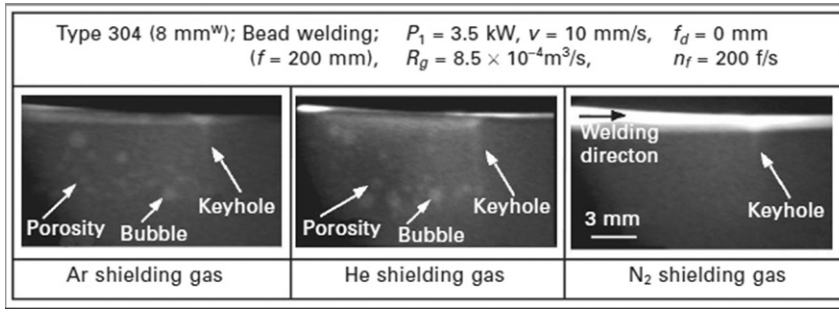


Fig. 7.27 X-ray transmission observation photos of keyhole and/or bubble generation in molten pool during CW Nd:YAG laser welding of Type 304 steel in Ar, He and N_2 co-axial shielding gas.

Bubbles, resulting in pores or porosity, are normally formed from the tip of a keyhole during laser welding, and thus the following procedures for the reduction in porosity are proposed [23–27,34–39], and their effectiveness is confirmed:

(i) full penetration welding
(ii) proper pulse modulation as shown in Fig. 7.28 [35,38]

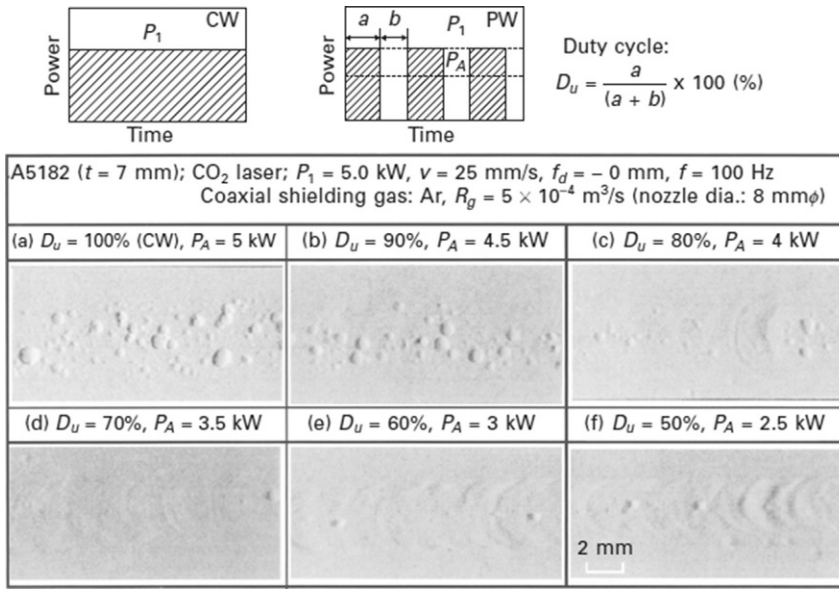


Fig. 7.28 Effect of pulse modulation on porosity in CO_2 laser weld beads of aluminum alloy: (A) D_u = 100% (CW), P_A = 5 kW, (B) D_u = 90%, P_A = 4.5 kW, (C) D_u = 80%, P_A = 4 kW, (D) D_u = 70%, P_A = 3.5 kW, (E) D_u = 60%, P_A = 3 kW, and (F) D_u = 50%, P_A = 2.5 kW.

(iii) forwardly tilted laser beam
(iv) twin-spot laser welding
(v) vacuum welding
(vi) the use of a tornado nozzle
(vii) hybrid welding with laser and TIG or MIG at high arc current
(viii) high speed welding, and so on

In laser welding of Zn-coated steel, it is important to control a gap between lapped sheets to escape vapors and their pressure due to low evaporation temperature and high vaporization pressure of Zn. Laser brazing can be applied to join Zn-coated steel sheets without porosity or pits [39]; moreover, laser welding of die cast alloys or sintering alloys is difficult because pores are inevitably formed in weld fusion zones [39].

In some Al-alloys, for example, cracks occur under some conditions, but do not take place under the other conditions. The experimental results concerning the formation conditions of cracking in A7 N01 aluminum alloy are shown in Fig. 7.29 [38]. It is found that cracking is easily formed at higher welding speeds in thicker plates.

In laser welding of Al-alloys, spattering occurs easily, and consequently an underfilled weld bead can be formed. The surface is modified by applying hybrid welding with MIG arc (as the following heat source) [34,35].

A7N01; P_1 = 5 kW/(CW), f = 254 mm, f_d = 0 mm, Ar ($R_g = 5 \times 10^5$ mm^3/s, ϕ = 8 mm)						
	25 mm/s	50 mm/s	75 mm/s	100 mm/s	125 mm/s	150 mm/s
1 mm^t			○	○	○	○
2 mm^t	○	○	○	○	○	○
3 mm^t	○	○	○	○	▲	▲
4 mm^t	○	○	▲	▲	●	●
5 mm^t	○	○	●	●	●	○
6 mm^t	○	▲	●	●	●	○

○: No cracking ▲: Crack in half sections observed ●: Crack in all sections

Fig. 7.29 Effects of plate thickness and welding speed on cracking in A7 N01 aluminum alloy welded with CO_2 laser.

7.3.4 Monitoring Results and Adaptive Control During Laser Bead Welding

Bead-on-plate welding of a 0.1 mm thick Type 304 stainless steel sheet was carried out on a 1.0 mm thick Al plate with a 2.0 mm diameter through hole (for providing difference in thermal diffusivity or heat transfer) with a 75W fiber laser beam at 10 mm/s welding speed. The obtained weld bead surface appearance is shown in Fig. 7.30 [40,41]. The bead width is 320 μm on the average on the plain plate, while it increases to 790 μm at the maximum on the through-hole position. A typical example of the monitoring results of laser power, heat radiation, and high-speed observation images is shown in Fig. 7.31 [40,41]. A molten pool is observed to grow up to double in size and then decreases into normal size while the laser beam spot passes through the through-hole position. The reflected light is kept almost

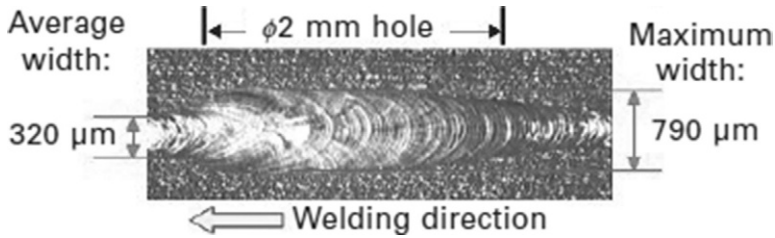


Fig. 7.30 Surface appearance of fiber laser weld bead in Type 304 sheet near through-hole in underlying plate.

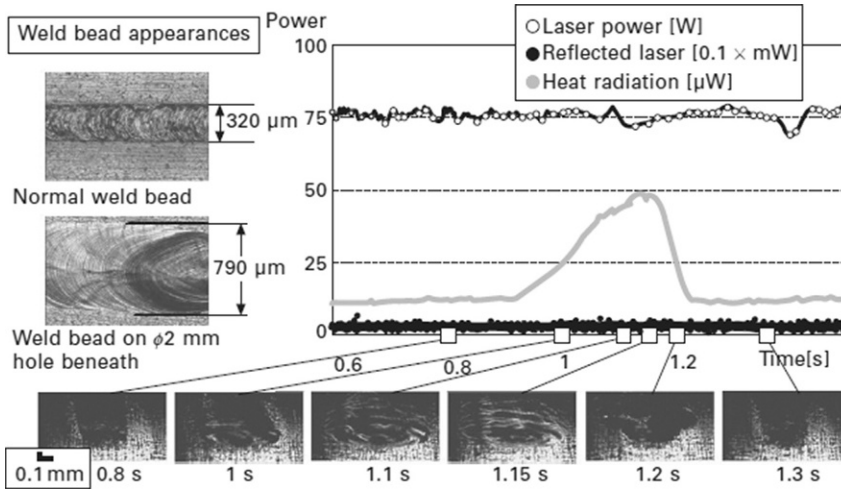


Fig. 7.31 Typical in-process monitoring results of laser power, heat radiation and high-speed observation photos during fiber laser welding of Type 304 sheet set on plate with through-hole.

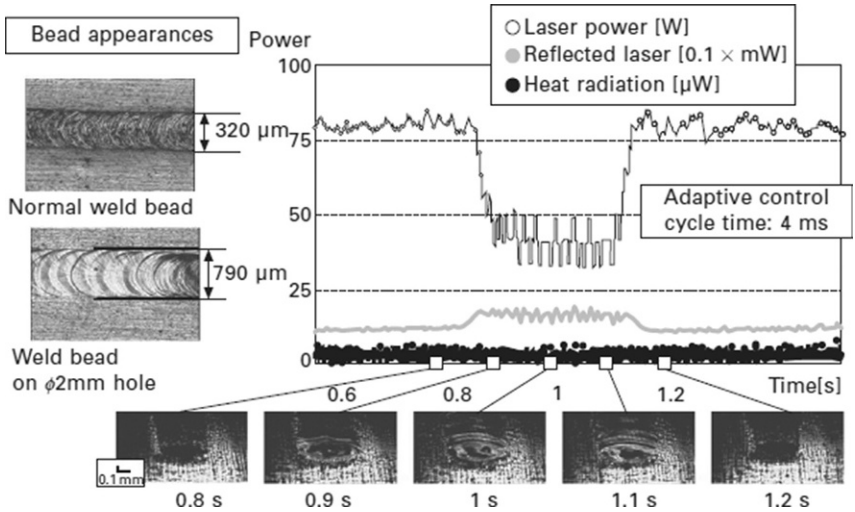


Fig. 7.32 Monitoring result during bead-on-plate welding under adaptive control for suppression of bead expansion induced by surrounding conditions.

constant despite the through-hole. On the other hand, the heat radiation intensity increases more than twice as high as that measured on the Al plate, and then drops down to the normal level measured on the heat sink.

A typical experimental result of monitoring during fiber laser welding under the adaptive control at 4 mscycle time is shown in Fig. 7.32 [40,41]. The lower photos demonstrate that the molten pool size is widely reduced even at the through-hole position in comparison with that without adaptive control as shown in Fig. 7.30. Then the laser peak power showing such rapid and complicated changes is controlled under the adaptive control. Consequently, it is found that adaptively-controlled peak power in micro welding with a CW fiber laser is beneficial to the stable production of a weld bead regardless of the existence of the heat sink area.

7.4 CONCLUSIONS

Important items during PW or CW laser welding was described in detail. Especially in spot welding, the welding conditions affecting weld geometry and penetration, laser-induced plume behavior, the interaction between a laser beam and its induced plume, keyhole behavior, and solidification cracking, bubble generation in the molten pool leading to the porosity formation in the weld fusion zones was summarized. Formation mechanisms and suppression procedures of porosity or pores and solidification cracking,

and in-process monitoring and adaptive control during welding for the prevention of hole was also described. In bead welding, the factors affecting weld geometry or penetration, plume behavior, interaction between laser beam and plume or plasma, formation mechanisms and suppression procedures of porosity or pores, in-process monitoring, and adaptive control was described. This data will be referred to by every person related to lasers and its welding.

REFERENCES

[1] A. Matsunawa, S. Katayama, H. Ikeda, K. Nishizawa, Effect of pulse shaping on reduction in pulsed laser welding, in: Proc. of ICALEO '92, Orlando, LIA, vol. 75, 1992, pp. 547–556.

[2] A. Matsunawa, S. Katayama, M. Mizutani, H. Ikeda, K. Nishizawa, Fusion and solidification characteristics in pulse-shaped Nd:YAG laser welding, in: Proc. of 5th CISFFEL, La Baule, SI, vol. 1, 1993, pp. 219–226.

[3] S. Katayama, T. Takemoto, A. Matsunawa, Effect of pulse shape on melting characteristics in pulsed laser spot welding, in: Proc. of ICALEO '95, San Diego, LIA, vol. 80, 1995, pp. 846–855.

[4] S. Katayama, S. Kohsaka, M. Mizutani, K. Nishizawa, A. Matsunawa, Pulse shape optimization for defect prevention in pulsed laser welding of stainless steel, in: Proc. of ICALEO '93, Orlando, LIA, vol. 77, 1993, pp. 487–497.

[5] S. Katayama, N. Seto, M. Mizutani, A. Matsunawa, X-ray transmission in-situ observation of keyhole during laser spot welding and pulse-shaping for prevention of porosity, in: Proc. of ICALEO 2001, Jacksonville, LIA, 2001 Session C-Welding 804, 2001.

[6] J.D. Kim, Temporal and spatial high-resolution measurement of laser welding phenomena and elucidation of formation mechanisms and development of preventive procedures of welding defects (Doctorate thesis), Osaka University, 1997.

[7] A. Matsunawa, J.D. Kim, S. Katayama, T. Takemoto, Spectroscopic characteristics of pulsed laser-induced plume of aluminum alloys, Rev. Laser Eng. 24-6 (1996) 679–688 (in Japanese).

[8] J.D. Kim, S. Katayama, T. Takemoto, A. Matsunawa, Observation of evaporated particles behaviors and plasma parameters in laser welding, Rev. Laser Eng. 24-9 (1996) 987–995 (in Japanese).

[9] J.D. Kim, S. Katayama, M. Mizutani, T. Takemoto, A. Matsunawa, Structure and composition of evaporated particles and plume in laser welding, Rev. Laser Eng. 24-9 (1996) 996–1005 (in Japanese).

[10] A. Matsunawa, J.D. Kim, S. Katayama, T. Takemoto, Spectroscopic studies on laser-induced plume of aluminum alloys, in: Proc. ICALEO '95, San Diego, LIA, vol. 80, 1995, pp. 719–728.

[11] J.D. Kim, S. Katayama, A. Matsunawa, Plasma diagnostics in pulsed Nd:YAG laser welding, in: Proc. of the 6th Int. Symp., JWS, Nagoya, vol. 1, 1996, pp. 203–208.

[12] A. Matsunawa, N. Seto, J.D. Kim, M. Mizutani, S. Katayama, Observation of keyhole and molten pool behaviour in high power laser welding—mechanism of porosity formation and its suppression method, Trans. JWRI 30-1 (2001) 13–27.

[13] A. Matsunawa, S. Katayama, T. Tokumura, T. Ariyasu, Characteristic of plume induced by pulsed Nd:YAG laser irradiation and their effect on materials processing, Proc. of CISFFEL vol. 1 (1983) 53.

[14] A. Matsunawa, T. Ohnawa, Beam-plume interaction in pulsed YAG laser processing, Trans. JWRI 20-1 (1991) 9–15.

[15] N. Seto, Elucidation of keyhole behaviour and porosity formation mechanism, and porosity prevention procedures (Doctorate thesis), Osaka University, 2000.
[16] M. Mizutani, K. Tanaka, S. Katayama, A. Matsunawa, YAG laser spot welding under microgravity and vacuum, and pulse-shaping for prevention of porosity, in: Proc. of 7th Int. Welding Symposium, JWS, Kobe, 2001, pp. 573–578.
[17] S. Katayama, M. Mizutani, A. Matsunawa, Modelling of melting and solidification behaviour during laser spot welding, Sci. Technol. Weld. Join. 2–1 (1997) 1–9.
[18] Y. Kawahito, S. Katayama, In-process monitoring and adaptive control for stable production of sound welds in laser microspot lap welding of aluminium alloy, J. Laser Appl. 17-1 (2005) 30–37.
[19] S. Katayama, C.D. Lundin, Laser welding of aluminum alloy 5456—laser weldability of aluminum alloys (report I), J. Light Met. Weld. Constr. 29-7 (1991) 295–307 (in Japanese).
[20] S. Katayama, C.D. Lundin, Laser welding of commercial aluminum alloys—laser weldability of aluminum alloys (report II), J. Light Met. Weld. Constr. 29-8 (1991) 349–360 (in Japanese).
[21] A. Matsunawa, K. Kojima, S. Katayama, CO_2 laser weldability of aluminum alloys (report I)—effect of welding conditions on melting characteristics, J. Light Met. Weld. Constr. 35-10 (1997) 461–472 (in Japanese).
[22] S. Katayama, N. Seto, J.D. Kim, A. Matsunawa, Effect of nitrogen on laser weldability of aluminium alloys, IIW, 1999, IIW Doc No. IX-1949–99.
[23] S. Katayama, Y. Kobayashi, N.K. Seto, M. Mizutani, A. Matsunawa, Effect of vacuum on penetration and defects in laser welding, in: Proc. of Laser Materials Processing Conference ICALEO 2000, LIA, USA, 2000 89-Section C, 2000, pp. 182–191.
[24] S. Katayama, N. Seto, J.D. Kim, A. Matsunawa, Formation mechanism and reduction method of porosity in laser welding of stainless steel, in: Proc. of ICALEO '97, San Diego, USA, 1997 83-Part 2-Section G, 1997, pp. 83–92.
[25] S. Katayama, N. Seto, J.D. Kim, A. Matsunawa, Formation mechanism and suppression procedure of porosity in high power laser welding of aluminum alloys, in: Proc. of ICALEO '98, LIA, Orlando, USA, 1998 85-Section C, 1998, pp. 24–33.
[26] N. Seto, S. Katayama, A. Matsunawa, High-speed simultaneous observation of plasma and keyhole behavior during high power CO_2 laser welding: effect of shielding gas on porosity formation, J. Laser Appl. 12-6 (2000) 245–250.
[27] K. Kinoshita, M. Mizutani, Y. Kawahito, S. Katayama, Phenomena of welding with high-power fiber laser, in: ICALEO 2006 Congress Proceedings, (25th International Congress on Applications of Lasers & Electro-Optics), Scottsdale, LIA 2006 99 Paper #902, 2006, pp. 535–542 (CD).
[28] S. Katayama, Y. Kawahito, K. Kinoshita, N. Matsumoto, M. Mizutani, Weld penetration and phenomena in 10 kW fiber laser welding, in: ICALEO 2007 Congress Proceedings (Proc. of 26th International Congress on Applications of Lasers & Electro-Optics), Orlando, LIA, vol. 100, 2007, pp. 353–359 (CD).
[29] Y. Kawahito, K. Kinoshita, S. Katayama, S. Tsubota, T. Ishide, Visualization of interaction between laser beam and YAG-laser-induced plume, in: ICALEO 2005 Congress Proceedings, Miami, LIA (Laser Institute of America), vol. 98, 2005, pp. 920–928 (CD).
[30] Y. Kawahito, M. Mizutani, S. Katayama, Elucidation of high-power fiber laser welding phenomena of stainless steel and effect of factors on weld geometry, J. Phys. D. Appl. Phys. 40 (2007) 5854–5859.
[31] Y. Kawahito, K. Kinoshita, N. Matsumoto, M. Mizutani, S. Katayama, High-speed observation and spectroscopic analysis of laser-induced plume in high-power fiber laser welding of stainless steel, Q. J. Jpn. Weld. Soc. 25-3 (2007) 455–460 (in Japanese).

[32] Y. Kawahito, K. Kinoshita, N. Matsumoto, M. Mizutani, S. Katayama, Interaction between laser beam and plasma/plume induced in welding of stainless steel with ultra-high power density fiber laser, Q. J. Jpn. Weld. Soc. 25 (3) (2007) 461–467 (in Japanese).
[33] S. Katayama, S. Oiwa, H. Ishida, N. Ozawa, M. Mizutani, Y. Kawahito, Effect of laser-induced plume on laser beam focusing during remote welding, 61st Annual Assembly of Int. Inst. Welding (IIW), Graz, IIW Doc. IV-962-08, 2012.
[34] H. Nagayama, M. Mizutani, Y. Kawahito, S. Katayama, Weld penetration and welding phenomena of aluminum alloy with high-power fiber laser, in: CALEO 2007 Congress Proceedings (Proc. of 26th International Congress on Applications of Lasers & Electro-Optics), Orlando, LIA, vol. 100, 2007, pp. 916–924 (CD).
[35] S. Uchiumi, J.B. Wang, S. Katayama, M. Mizutani, T. Hongu, K. Fujii, Penetration and welding phenomena in yag laser-mig hybrid welding of aluminum alloy, in: ICALEO 2004 Congress Proceedings, San Francisco, LIA, 97, 2004, p. 530 (CD).
[36] S. Katayama, Y. Kawahito, M. Mizutani, Collaboration of physical and metallurgical viewpoints for understanding and process development of laser welding, in: ICALEO 2007 Congress Proceedings (Proc. of 26th International Congress on Applications of Lasers & Electro-Optics), Orlando, LIA, vol. 100 #701, 2007, pp. 360–369 (CD).
[37] S. Katayama, Y. Kawahito, M. Mizutani, Effect of gas compositions on laser weldability of stainless steel, in: Proc. of the 69th Laser Materials Processing Conference, vol. 69, 2007, pp. 161–170 (in Japanese).
[38] S. Katayama, A. Matsunawa, Laser weldability of aluminum alloys, in: Proc. of the 69th Laser Materials Processing Conference, vol. 43, 1998, pp. 33–52 (in Japanese).
[39] S. Katayama, Y. Kawahito, M. Mizutani, Welding phenomena and results in laser joining of various materials, in: Proc. of the 66th Laser Materials Processing Conference, vol. 66, 2006, pp. 1–8 (in Japanese).
[40] Y. Kawahito, M. Kawasaki, S. Katayama, In-process monitoring and adaptive control during micro welding with CW fiber laser, Online Proceedings of LPM 2007, #07-39.
[41] Y. Kawahito, M. Kawasaki, S. Katayama, Process monitoring and adaptive control in 100W fiber laser welding, in: ICALEO 2007 Congress Proceedings (Proc. of 26th International Congress on Applications of Lasers & Electro-Optics), Orlando, LIA, vol. 100, 2007, pp. 52–57 (CD).

This page intentionally left blank

CHAPTER 8

Laser Microspot Welding in Electronics Production

J. Lawrence*, I. Mys†, M. Schmidt†
*University of Chester, Chester, United Kingdom
†Bayerisches Laserzentrum Gmbh, Erlangen, Germany

8.1 INTRODUCTION

Modern electronic manufacturing is determined by factors such as reducing product weight and permanently increasing functionality at fixed or even decreased manufacturing costs. The most suitable way to implement these trends is the application of new materials and enhanced material mixing.

Pure Cu and Cu alloys that are traditionally used in electronics stand out through very good electrical and thermal properties, having a large specific weight and relatively high price at the same time. So, a high price in particular is the driving force behind substitution of Cu with more cost-efficient materials. One smart alternative to Cu is the application of pure Al or Al alloys. Al has moderate thermal and electrical conductivity, but it is good enough for a wide range of applications. At the same time, Al possesses more than three times a smaller specific weight compared to Cu (see Table 8.1). Finally, Al is significantly cheaper than Cu, and the price difference between these two metals has constantly increased during recent years. Because of that, rising cost pressures in the manufacturing of electronic products forces the application of more cost-efficient Al and its alloys instead of Cu. Especially when manufacturing large-volume products such as heat sinks, the weight advantages and economic benefits of Al should be exploited to the full extent. Further actual applications of Al are specialized PCBs, light-weight electric motors, sensors, actuators, etc.

The main handicap, however, for widespread use of Cu and Al is the lack of reliable joining techniques for them. Cu and Al are dissimilar materials that show very poor weldability and have numerous limitations when they are joined using conventional welding processes.

Advances in Laser Materials Processing
https://doi.org/10.1016/B978-0-08-101252-9.00008-X
Copyright © 2018 Elsevier Ltd.
All rights reserved.

Table 8.1 Comparison of main technological properties and prices of Cu and Al

Properties	Cu	Al
Thermal conductivity, W/mK	393.6	226
Electrical conductivity, μS	58	37.7
Specific weight, g/cm^2	8.95	2.7
Price, US$/tonne (April 2008)	8740	2948

8.2 STATE-OF-THE-ART

8.2.1 Welding Metallurgy of Copper and Aluminum

From a metallurgical point of view, mating metallic materials to be welded can be divided into similar and dissimilar; however, there is not a distinct line between the meaning of both terms. Generally, the similar joints are prepared on the same materials (pure metals or alloys) or different materials with the same main alloying elements and comparable chemical properties, such as Al-Al, Al-AlMn3, Cu-CuSn0,12, etc. The mating materials in dissimilar joints are composed as a rule of main alloying elements of different groups in the periodic table. The periodic group defines chemical and consequently metallurgical and technological properties of welded joints.

There are different approaches for the estimation of weldability. The most well-known is a Darken-Gurry ellipse that is a further refinement of the Hume-Rothery rules for a formation of solid solutions [1]. It describes a solubility of alloying elements in the matrix depending on atom radius and electronegativity and indicates chemical elements with pure solubility and thus high affinity to formation of brittle intermetallic phases.

In fact, Cu and Al show absolute solubility in liquid state and limited solubility in solid state under equilibrium condition: solubility of Al in Cu is limited to 8 wt.%, while the solubility of Cu in Al is almost close to zero. In both cases the solid solutions take place due to low solubility of both materials in the intermediate range, and the interfacial phase formation can be noted quite early. Especially in the range with high Cu content between 54 and 92 wt.%, several intermetallic phases (cu_2Al, cu_3Al_2, cuAl, $cuAl_2$ etc.) may occur (compare to Fig. 8.1).

Generally, because of their nature, the intermetallic phases are characterized by very high hardness, unsatisfactory ductility, and brittleness as well as a lower electrical conductivity compared to the main materials. So, for example, phases Cu_4Al_3 and cuAl with comparable content on Cu and Al have high hardness up to 700 HV. The electrical conductivity of the Cu-Al phases grows with rising Al content [2].

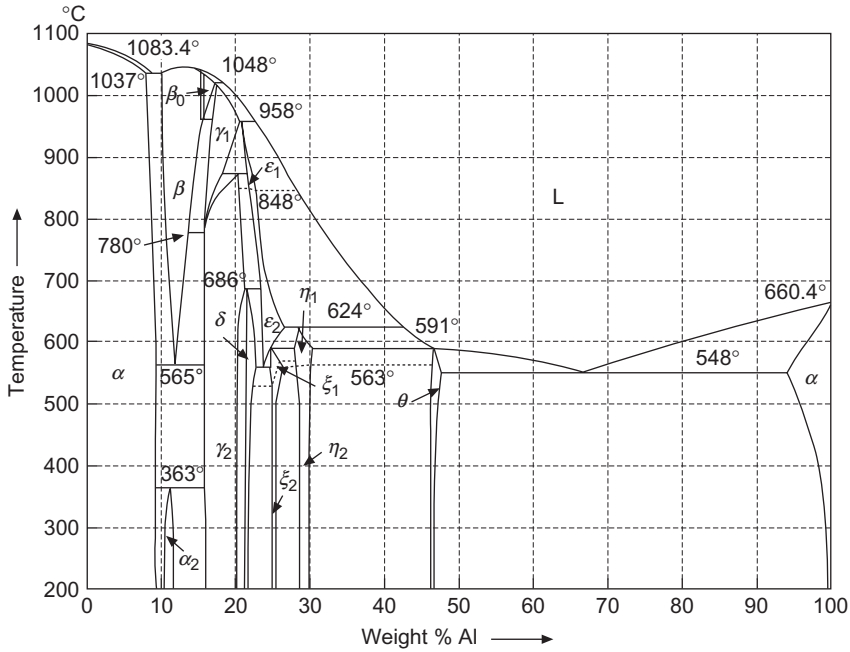


Fig. 8.1 Cu-Al binary phase diagram.

Among poor metallurgical affinity of Cu and Al, both materials show large mismatches in physical properties. A difference in thermal expansion leads to large residual stresses in the joints, and thus causes fatigue problems and reduces joint strength. Different thermal conductivities of two metals increase residual stress due to a large distortion of heat field and nonuniform heat dissipation. A substantial difference in the melting temperature between Cu and Al promotes formation of segregation of low-melting eutectics, especially on grain boundaries. Therefore, the Cu-Al fusion joint is very susceptible to hot crack formation.

8.2.2 Welding of Copper and Aluminum

Cu and Al are essential materials in electrical engineering facilities. In industrial manufacturing, both materials are welded in similar joints with each other; however, there are some applications, for example, current bars or solar thermal collectors, that require dissimilar joints on Cu-Al. Because of the above-mentioned metallurgical incompatibility, such weld joints are made predominantly by means of pressure joint

welding processes. For the welding of large parts, friction stir welding, cold and hot pressure welding, flash butt welding, explosive welding, wedge bonding, rolling plating, etc., are applied. Small parts in micro range are joined mainly by means of ultrasonic welding processes [3,4]. Ultrasonic welding is especially suitable for welding of thin parts such as foils and wires; however, friction and plating welding processes are limited with respect to flexibility and miniaturization and can be applied on only a few joining configurations. As a rule, a fusion joint welding is free of these limitations.

In contrast to pressure joint welding that is widely used in industrial applications, fusion joint welding of Cu and Al is to this day still only a research subject because of the numerous, above-mentioned welding problems. Most research on the welding of Cu and Al are focused on beam welding processes like electron beam welding and laser beam welding because of their low heat input during joining and good controllability. An electron beam welding of a soft-annealed Cu and Al with a thickness of 3.00 mm in a butt joint is considered [5]. To improve the stability and strength of the welded joints, the interlayers of Zn foil (thickness of 0.50 mm) and Ag foil (thickness of 0.20–0.70 mm) has been used. Due to the low boiling temperature of the Zn interlayer and formation of intermetallic phases in a microstructure, only moderate welding quality and poor ductility of joints has been achieved. For homogeneous heating and melting of Cu and Al samples during electron beam welding of butt joints [6], proposes a beam offset in the direction of the Cu sample with higher melting temperature and thermal conductivity.

The first experiments in pulsed laser welding of Cu and Al are described in Ref. [7]. When the proper operating parameters are established, comparable good tensile strength and low electrical resistance of joints has been obtained. With the addition of moderate contact pressure during welding, the stability of Cu-Al welded joints has been improved. In Ref. [8] Cu and Al parts are pulsed laser welded by using Sn as a filler metal. A formation of intermetallic phases in joints was prevented by predominant melting of Sn filler metal with defocused laser beam. Hanebuth and Papperitz [9] introduces continuous wave (CW) welding with CO_2 laser and pulsed welding with a Nd:YAG laser of Cu and Al parts for medical application in overlap and butt joint. In both cases the process parameter and welding conditions were trimmed to obtain a ductile eutectic microstructure with a 33 wt.% Cu; however, the produced joints had a lot of pores and cracks and were of unacceptable quality.

8.3 MICRO WELDING OF COPPER AND ALUMINUM

8.3.1 Strategies for Micro Welding of Copper and Aluminum

To improve the quality of laser welded joints, the total number and volume of intermetallic phases in a weld structure should first be reduced and the thermal expansions of welded materials should be optimally matched. To achieve this, we use the following approaches in our experiments [10]

Reduction of temperature and increase of cooling gradients in the welding zone. Formation and growth of intermetallic phases are the typical diffusion processes that are mainly determined by the heat input and heat affecting time as well as by the cooling gradients. One way to reduce an overall heat input during welding is the use of spot welding with a small spot diameter and short welding time (shorter than 10 ms). T spot welding with several weld spots without overlapping applied instead of CW seam or spot seam welding allows further decreasing of heat input and thus temperature in a fusion zone. Rapid cooling of a welding zone leads to a suppression of the intermetallic phases due to the positive short-term metallurgical effects.

Control of the melting ratio and intermixing of the materials to be welded. To achieve an optimal metallurgical composition in the weld microstructure and to eliminate segregation of high-and low-melting phases, a precise control of the melting ratio of both materials is required. One possibility to implement this is the application of the lateral laser beam offset in the direction of either joining partner. The other way to improve the weld microstructure is reducing melt intermixing in the welding zone—the less melt intermixing that occurs, the fewer intermetallic phases can grow. It can be accomplished by interruption of the flow of melted material in a weld pool using rapid pulse power modulation.

Enhanced alloying of weld microstructure and/or creation of diffusion barrier between material to be welded. As known in macro welding, an application of a filler metal that is metallurgically compatible with welded materials and is applied in the interface zone between the main materials provides successful welding of dissimilar metals; however, due to the restrictions in part dimensions in micro range, the thickness (volume) of the additional materials is also limited, so they can only be used for the alloying of a weld microstructure. As a third material with a large metallurgical affinity to Cu and Al, one of pure Ni, Ag, or Sn can be selected. Furthermore, material such as Ag possesses a thermal expansion that is well matched with Cu and Al and can be used for reduction of residual stress in welded joints.

8.3.2 Process Characterization

The experiments on welding of Cu and Al are carried out on overlap joints with side face weld and fillet welds (see Fig. 8.2). O_2-free Cu (OF-Cu) and pure Al Al-99.5 samples are symmetrically joined with three welding spots on both sides. To improve the mechanical properties of the welded joints the filler materials Ni, Ag, and Sn are investigated. The filler metal is applied in the form of a thin foil or galvanic coating on a Cu sample with thicknesses in the range of 3–100 µm. The foil is placed manually on the interface between the joining partners before the welding process begins. For the welding tests a pulsed, fibre-coupled Nd:YAG laser with maximum pulse duration of 20 ms is used. Using different imaging optics, the spot diameters of 0.28 and 0.40 mm are implemented.

Fig. 8.3 shows a typical process window for welding of overlap joint with side face weld. It describes tensile strength of welded joints and failure

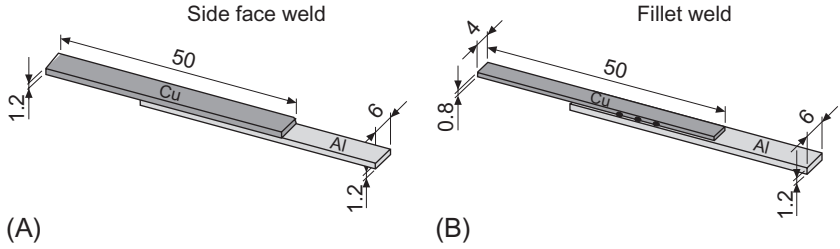


Fig. 8.2 Overlap joint with (A) side face weld and (B) fillet weld.

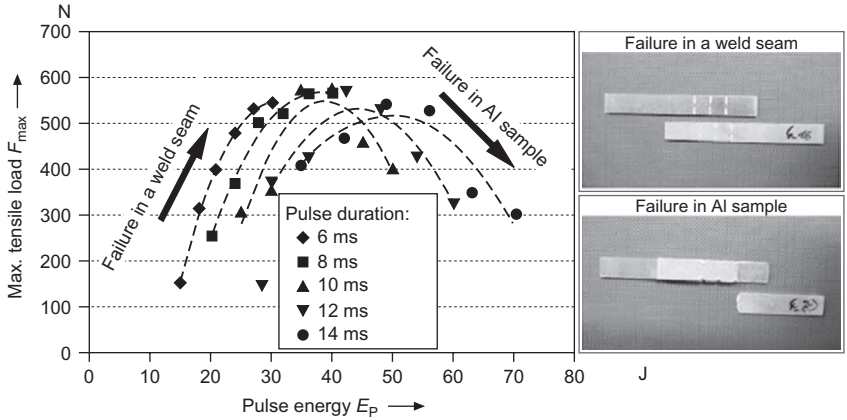


Fig. 8.3 Tensile strength of overlap joint with side face weld as a function of pulse duration and pulse energy.

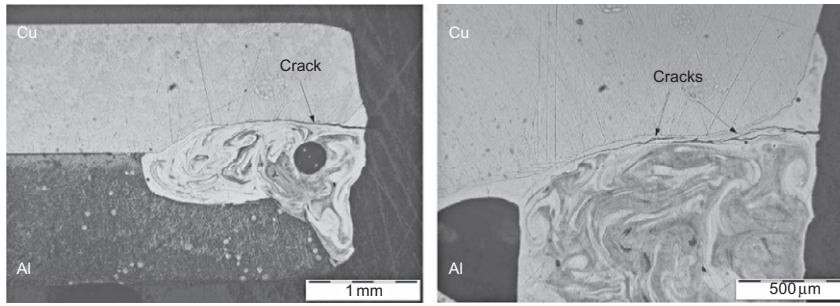


Fig. 8.4 Cross-sections of welding spots of two typical Cu-Al joints ($P_h = 3$ kW, $\tau_h = 9$ ms).

behavior depending on pulse duration and pulse energy for laser spot diameter of 280.00 mm. In the left-hand part of the diagram the tensile load increases because of growth of the joint cross-section at higher pulse energies—samples fail in a weld seam. A joint cross-section expands predominantly in the Al sample due to its lower melting temperature. At further increasing of pulse energy, the cross-section of welded joint reaches the remaining cross-section of the unaffected Al sample and a tensile load achieves a maximal value. From this value, every increase of pulse energy causes a further reduction of the remaining cross-section of the Al sample and therefore reduces joint strength. In this case, the welded joints fail in the Al samples only.

In a range of small pulse energies Cu-Al welded samples fail during tensile testing predominantly in a weld microstructure on the Cu side. As observed when the metallographic specimens and fracture structures are analyzed, such failure behavior is caused by cracks near the interface Cu-solidified melt (see Fig. 8.4). The element analysis of weld microstructure by means of EDX indicates that a large number of intermetallic, Cu-rich phases take place in this area. These brittle phases with restricted ductility were probably led by cooling to high crack susceptibility of the welded joints. It can be also assumed that a large misalignment in thermal expansion of Cu and Al intensifies crack sensitivity.

8.3.3 Effect of Laser Beam Offset

First the effect of beam offset on tensile strength of welded Cu-Al samples is considered (see Fig. 8.5). It shows only beam offset in the direction of the Al sample because the correlation between beam offsets and tensile strength cannot be reliably determined when the beam is offset in the Cu direction. This is caused by higher reflectivity of Cu and strong absorption dependence on the surface conditions of Cu samples—it leads to a large

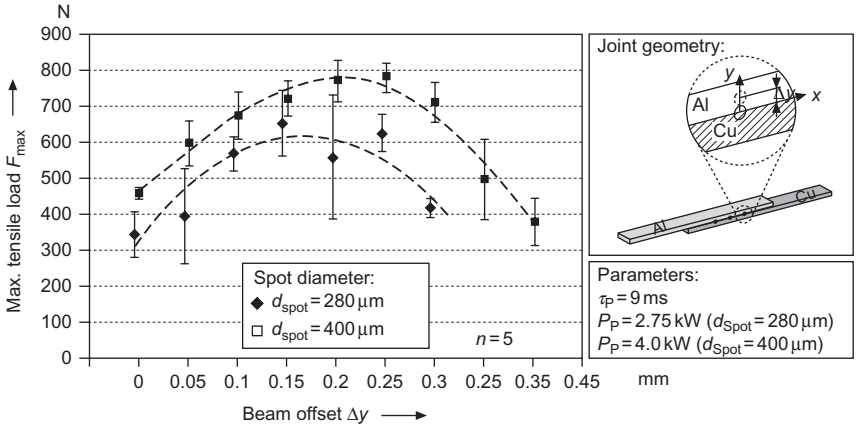


Fig. 8.5 Tensile strength of side face welds as a function of beam offset for different beam diameters.

fluctuation in the tensile strength of welded joints. The tensile load curves have a distinct maximum at 0.15 mm for 280.00 mm beam spot diameter and 0.20–0.25 mm for 400.00 mm beam diameter. A beam offset in the Al sample direction shifts a metallurgical composition of the joint in the Al-rich corner of a binary phase diagram. A cross-section area of welded joints at optimal beam offset is located at 70%–85% in Al and the microstructure corresponds to hypoeutectic alloy, which mainly consists of α-Al and the $AlCu_2$ phase. The weld microstructure becomes more ductile with fewer intermetallic phases. It cannot be ruled out that thermal expansion of the solidified melt is matched better on the thermal expansion of solid materials when welded with beam offset.

Microstructure composition of a fillet weld can be controlled by a beam offset and an incidence angle of laser beam relative to fillet position. Dependence of the weld depth and tensile strength of welded joints on beam offset and incidence angle is shown in Fig. 8.6. An incidence angle is determined between an optical axis of laser beam and normal to sample surfaces. Depth of welded joints is measured in a Cu sample. An increase of incidence angle of laser beam up to 75° causes a growth of weld depth due to an alignment of an optical axis and a plane between Cu and Al samples; however, at a further increase of incidence angle, the laser beam is partly shadowed by a larger Al sample that leads to a reduction of 250 Advances in laser materials processing of the energy density in the fillet and consequently to the reduction of the weld depth. A beam offset in the direction of the Cu sample up to 0.20 mm leads to increasing weld depth. At a beam

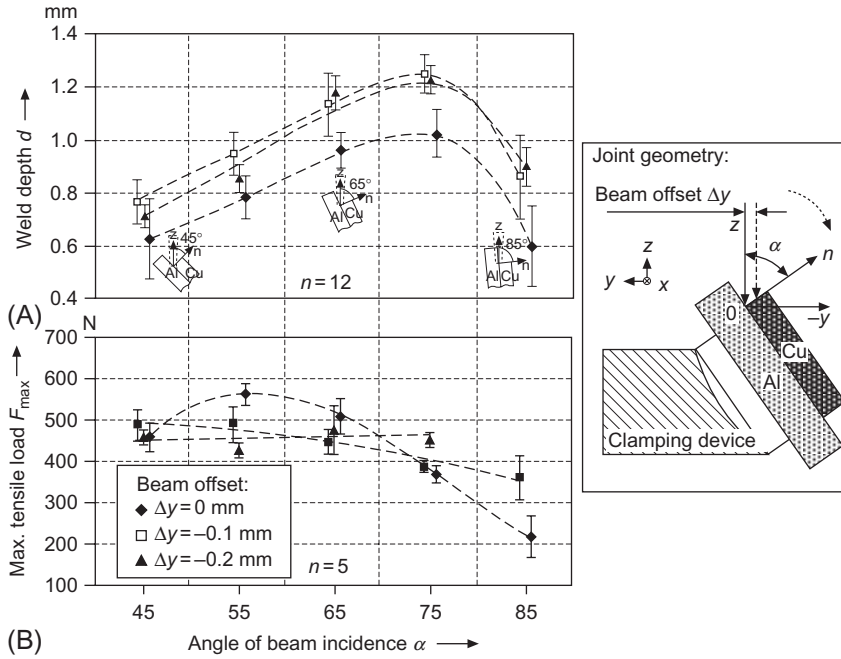


Fig. 8.6 (A) Weld depth and (B) tensile strength of fillet weld as a function of beam offset and angle of beam incidence.

offset of 0.30 mm, the reproducible joints at tested process parameters cannot be welded.

The analysis of the strength of fillet weld joints shows no clear dependence of tensile strength on the angle of beam incidence. Additionally, joint strength did not correlate to weld depth. During welding without beam offset the maximal joint strength is obtained at 55°. A further increase of incidence angle causes a significant reduction of tensile strength. When samples are welded with beam offset, the effect of incidence angle almost disappears. Due to the lack of correlation between incidence angle, tensile strength, and weld depth it can be assumed that the mechanical properties of fillet joints are mainly defined by hooking the melts of Cu and Al into each other and not directly by quality of microstructure.

8.3.4 Effect of Thin Interlayer Filler Materials

The effect of filler materials on mechanical properties is quite distinctive. Fig. 8.7 shows the effect of Ni and Ag of different thicknesses on tensile strengths of side weld joints. A Ni foil yields only a negligible improvement of the tensile strength with a slight reduction of its spreading. In contrast,

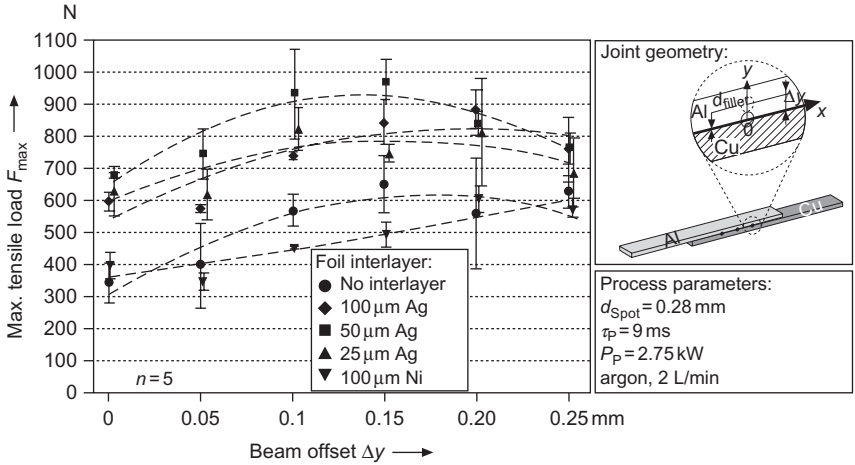


Fig. 8.7 Tensile strength of side face welds at welding with metal foil interlayers.

a Ag filler material improves the welding results significantly. The samples welded with Ag foils with thicknesses of 25, 50, and 100 µm have the maximum, with the above-mentioned beam offset of 0.10–0.20 mm and have narrow tensile strength values of 750–800 N, independent of the thickness of the Ag foil. Most samples welded with optimal beam offset fail in a tensile test in the Al base material (and not in the welded joint). Thus the real tensile strength of the weld seems to be even higher than the measured values.

For a further reduction of thickness of the filler interlayer, the galvanic coatings of the Cu sample are used. This time Ag and Sn coatings are applied with a thickness of 3.00 and 10.00 mm. Results of the tensile test on Cu-Al joints welded with coatings as a function of beam offset are shown in Fig. 8.8. For comparison, the diagram includes the tensile strength of joints welded without interlayer and with a 50 µm Ag foil as well. Application of Sn coatings causes just a slight decrease of tensile strength compared to reference (without interlayer). In contrast the effect of Ag coatings is more distinctive. Increasing the thickness of Ag coating leads to an increase in tensile strength. The mechanical properties of joints welded with 10 µm Ag coating are comparable to joints made with 25 µm Ag foil.

The effect of the foil interlayer on the strength of fillet weld joints depending on angle of beam is shown in Fig. 8.9. Application of Ag foil leads to significant improvement of mechanical properties. At an optimal incidence angle between 65° and 75°, the weld joint strength is equal to the strength of the Cu sample. The load-displacement curve for these joints shows typical progression with large elongation that can be observed during

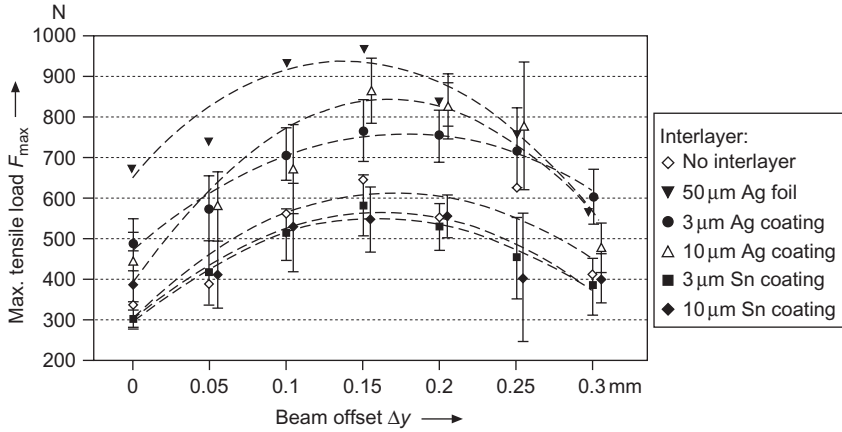


Fig. 8.8 Tensile strength of side face welds at welding with galvanic coating interlayers.

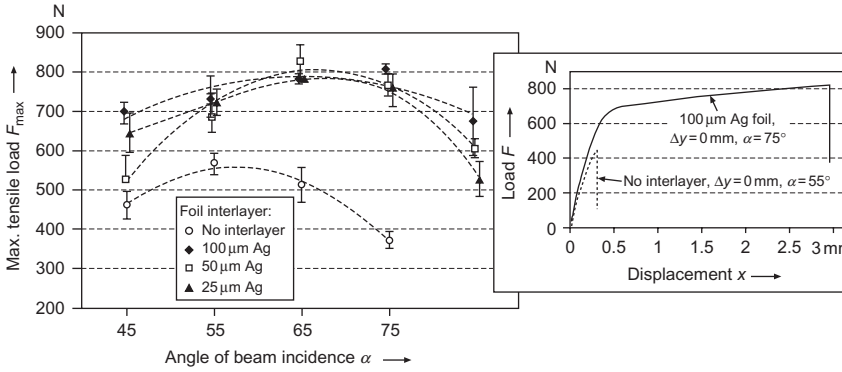
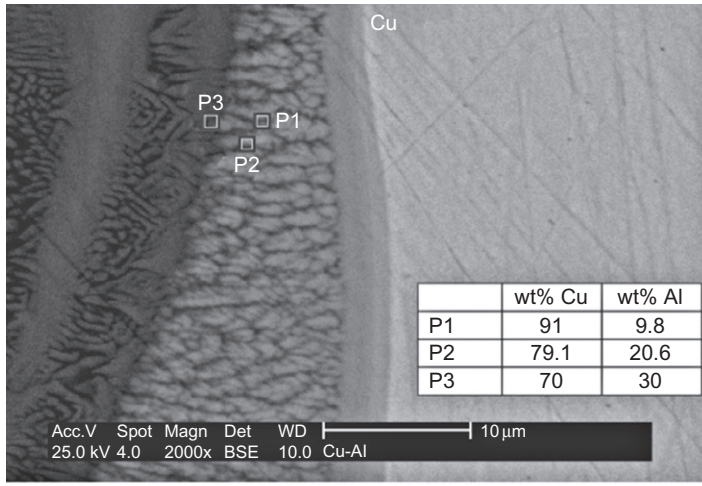


Fig. 8.9 Tensile strength of side fillet welds and load-displacement diagram at welding with metal foil interlayers.

testing of pure Cu samples. Like side face joints, the thickness of interlayer foil is not a crucial factor for the tensile strength of welded joints. At optimal incidence, the angle of the tensile strength of welded joints is located in the small range, independent of foil thickness. The angle dependence of joint strength is comparable to weld depth distribution in Fig. 8.6; however, the weld depth of samples with Ag foil is smaller, at about 0.10–0.30 mm, than when welds are made without interfacial foil.

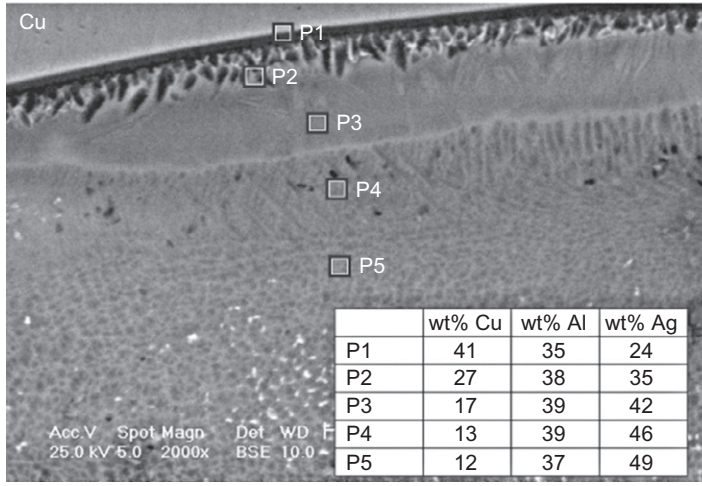
The analysis of microstructure composition by means of EDX helps us to understand the improvement of the mechanical properties of welded

joints when welding with the Ag interlayer. In particular, phase formation on the interface between Cu and weld microstructure is observed and characterized. Two types of samples are examined: welded without interlayer and with 0.10 mm Ag foil. A Cu-Al a-phase (Item P1) follows a very thin recrystallization zone on the Cu (see Fig. 8.10A). The a-phase adjoins a region where the Cu weight concentrations within the range of about 70 and 80 wt.% are measured (P2 and P3). Within this concentration



	wt% Cu	wt% Al
P1	91	9.8
P2	79.1	20.6
P3	70	30

(A)



	wt% Cu	wt% Al	wt% Ag
P1	41	35	24
P2	27	38	35
P3	17	39	42
P4	13	39	46
P5	12	37	49

(B)

Fig. 8.10 EDX analysis of the interface between Cu and microstructure of samples welded: (A) without interlayer and (B) with Ag foil.

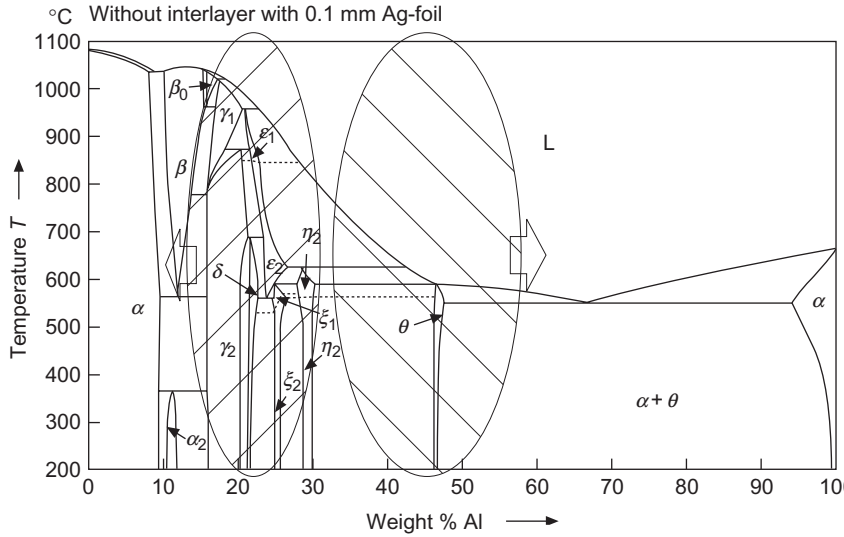


Fig. 8.11 Cu-Al binary phase diagram with microstructure composition range when welding without and with Ag foil interlayer.

range, a number of intermetallic phases may occur, as shown in Fig. 8.11. Considering the excessive hardness (and corresponding restricted ductility) of these phases, the high crack susceptibility of Cu-Al joints without a Ag interlayer can be explained.

The joints made with a Ag interlayer show a relatively uniform distribution of Al particles in a Ag-rich matrix (see Fig. 8.10B). The maximal weight concentration of Cu in the resolidified melt does not exceed 50%, corresponding to the intermetallic-poor region with a α-q-solid solution (see Fig. 8.8). Such microstructure gains good mechanical properties at high cooling gradients—*θ*-inclusions are finely dispersed in a-matrix. This fact, in combination with a relatively high Ag concentration, probably improves ductility of the weld microstructure. Additionally, the pure Ag possesses an optimal thermal expansion exactly in between Cu and Al so that the possible residual stresses during cooling and solidification can be reduced.

8.4 RELIABILITY OF COPPER-ALUMINUM WELDED JOINTS

An important precondition for the application of welded joints in a serial production is their proven reliability. This is especially applicable in automotive manufacturing. To check the mechanical reliability of welded joints we perform dynamic fatigue tests. The samples are tested on self-made

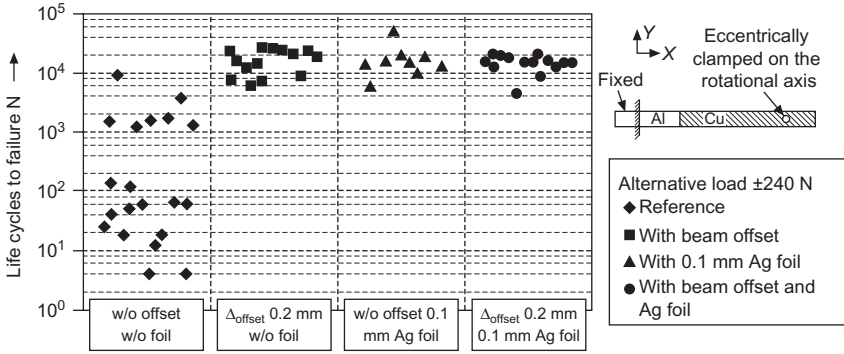


Fig. 8.12 Results of dynamic fatigue test on side face welds at alternate load of ±240 N.

equipment at a sinusoidal load up to ±500 N and a load period of 0.7 s. Fig. 8.12 shows the results of fatigue tests with moderate alternative load of ±240 N on samples, which are welded at different conditions. Every point in the diagram means one tested, welded sample. The nonoptimized samples fail in a wide range between 4 and 10,000 cycles. In contrast, the samples welded with 0.20 mm beam offset and/or 0.10 mm Ag interlayer foil show enhanced stability and fail only after 7000 tests cycles; however, most joints hold for more than 10^4 cycles.

At higher loads of ±360 N, the samples without optimization fail in the first few cycles (see Fig. 8.13). Durability of samples welded with 0.20 mm beam offset or with 0.1 Ag foil spread in a wide range. Samples welded by the combining of beam offset and Ag interlayer show high stability and fail only in the Al sample (and not in the weld joint itself).

A further reliability factor is the thermal stability of the welded joints. The assemblies in modern automotive applications like numerous servomotors or parts of transmission control ran at permanent high temperatures. So, for e.g., engine components in modern cars should run stable at temperatures of 120–140°C. At this condition, the joints should not change their properties.

Fig. 8.14 shows the tensile strength behavior of side face joints depending on a load time of up to 200 h. The welded samples are annealed in a furnace with oxygen atmosphere at a constant temperature of 140°C. The tested samples have been welded at four different conditions by the combination of beam offset and Ag interfacial foil. All four types of welded samples showed almost no changes in tensile strength throughout the time range of 200 h. The strength values scattered in a range of about 10%, which

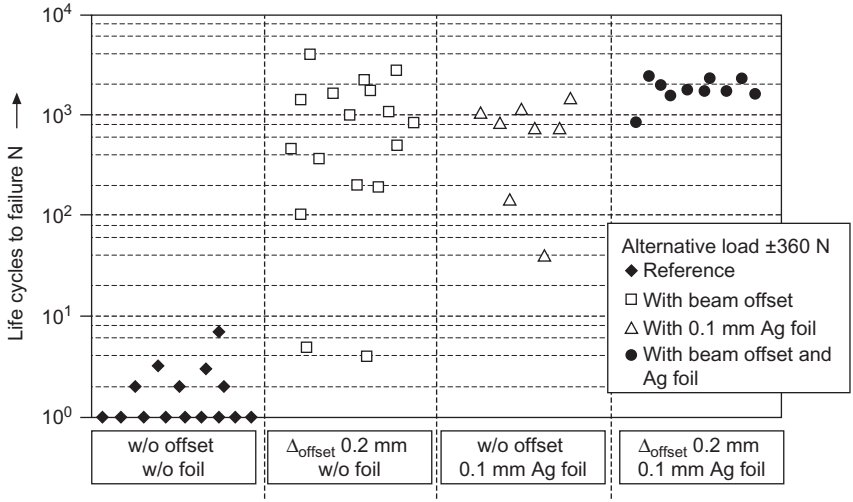


Fig. 8.13 Results of dynamic fatigue test on side face welds at alternate load of ±360 N.

referred to the nonloaded samples. Moreover, no increase in ohmic resistance of the welded joint is observed (not shown in Fig. 8.14).

Similar results were obtained in a climatic test on welded joints with a sinusoidal temperature load in a range between temperatures $T_{min} = -40°C$ and $T_{max} = 140°C$ (according to DIN ISO 16750). After 170 test hours, the tensile strength was in a range of 10% of referred to reference values.

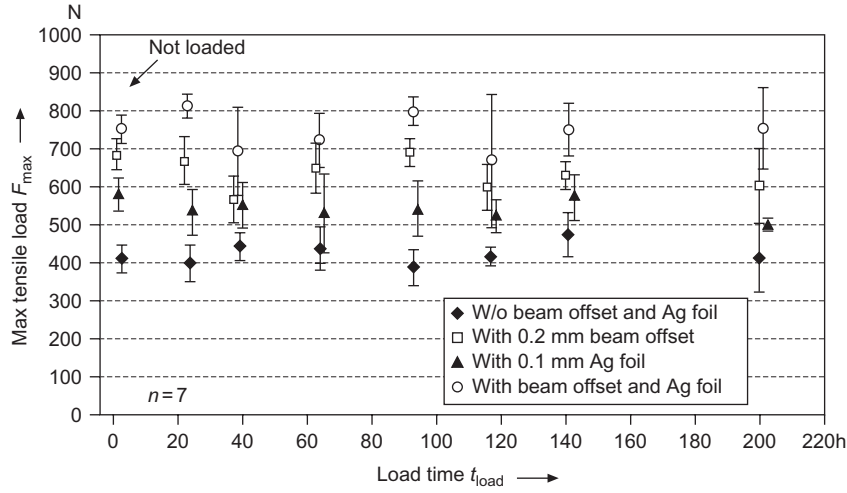


Fig. 8.14 Tensile strength of side weld joints after aging by annealing at a constant temperature of 140°C.

Another important fatigue property is the resistance of welded joints against aggressive chemical agents, especially in automotive applications. According to DIN ISO 16750, an immunity of components or assemblies against chemical agents is defined as no change in properties sufficient to affect material performance over 24 h. The standard defines more than 25 different chemical agents that are relevant for automotive applications.

In experiments, we focus on the most relevant fluids such as different cleaners, salt water, and fluids from the car itself (oil, ethanol, and in extreme cases, battery fluid sulfuric acid). The welded samples are chemically aged in a bath with each fluid for 48 h. After the test, the samples are cleaned and finally electrical conductivity and tensile strength are measured. Fig. 8.15 shows the results of a chemical aging test depending on the tensile strength of a chemical agent for different welded samples. At aging with all chemical agents, except for 30% sulfuric acid, almost no changes of tensile strength are observed. Only samples that are welded with beam offset of 0.20 mm show a slight decrease of tensile strength of about 14%. A significant reduction of tensile strength up to 40% is observed on all samples after aging with 30% sulfuric acid. An optical appraisal of the aged samples shows that an Al-rich material is affected more than Cu. The possible reason for that is a reduction reaction between Al and sulfuric acid with the formation of a Al sulfate and discharge of hydrogen. Additionally, pitting corrosion of an Al-rich material is noticed.

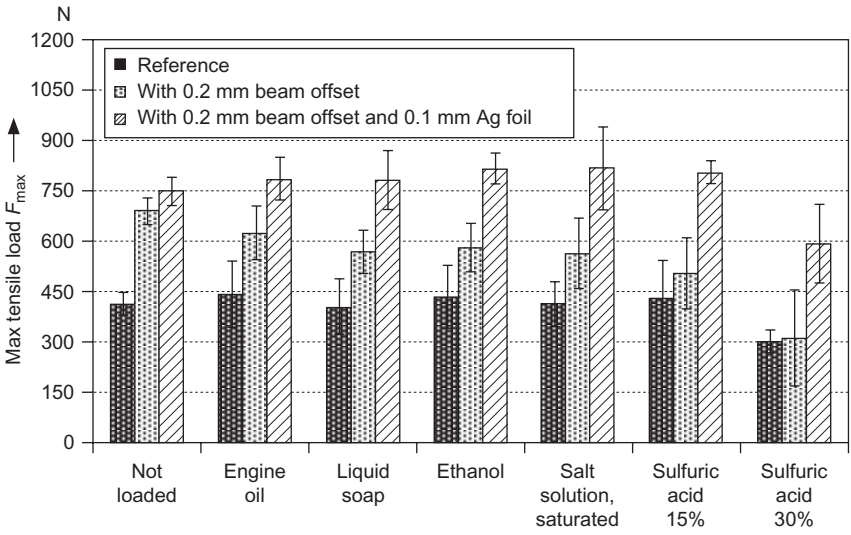


Fig. 8.15 Tensile strength of side weld joints after 48 h aging with selected chemical agents.

Behavior of an electric resistance of welded samples is comparable to tensile strength. After aging with relevant agents, except 30% sulfuric acid, we observe a slight increase in resistance in all samples of a maximum of 10% compared to the nonloaded samples. After loading with 30% sulfuric acid, electric resistance grows to 15%, but only in samples with an Al-rich welding zone. The reason for that should be the formation of a Al sulfate and pitting corrosion in weld joints as described above.

8.5 CONCLUSIONS

Laser spot welding of Cu and Al on overlap joints with side face weld and overlap joints with fillet welds has been investigated. Al-Cu welds that are made with the conventional process show poor mechanical properties and insufficient reliability. The mechanical characteristics of Cu-Al welded joints can be significantly improved by affecting weld microstructure by adjusting Cu and Al content in weld composition (proper laser beam incidence position/beam offset) and micro alloying with suitable interlayer materials. The best performance of welded joints is achieved with Al-rich microstructure made by beam offsetting directed to the Al sample. An optimal beam offset is approximately equal to beam radius; moreover, tensile strength of welded joints can be more than doubled if Ag interfacial foils with a thickness of 25–50 μm are applied. An optimal incidence angle for the welding of fillet weld is between 65° and 75°. In this case, the weld joint strength is equal/better than the strength of the Cu sample. The comprehensive aging experiments show enhanced reliability of optimized Cu-Al welded joints especially concerning their dynamic properties.

REFERENCES

[1] L.S. Darken, R.W. Gurry, Physical Chemistry of Metals, McGraw-Hill Publ. Comp. Ltd, London, New York, Toronto, 1953.
[2] M. Braunovic, N. Aleksandrov, Intermetallic compounds at aluminium-to-copper and copper-to-tin electrical interfaces, in: Proceedings of the Thirty-Eighth IEEE Holm Conference on Electrical Contacts, 25–34, 1992.
[3] C. Pohle, Schweißen von Werkstoffkombinationen: metallkundliche und fertigungstechnische Grundlagen sowie Ausführungsbeispiele, DVS-Verlag, Düsseldorf, 1999.
[4] J. Wodara, Ultraschallfügen und -trennen, DVS-Verlag, Düsseldorf, 2004.
[5] H. Bandow, Beitrag zum Verbinden von aluminium mit Kupfer durch Elektronenstrahlschweißen, Schweißen Schneiden 23 (1971) 274–277.
[6] A. Matting, H. Koch, L. Dorn, Beitrag zum Verschweißen verschiedenartiger Metalle mit dem Elektronenstrahl, in: Metall., Heft 4, 1970, pp. 345–353.
[7] G.J. Marshall, Laser Welding Cu-Cu and Cu-Al Conductors, Ind and Sci Conf Manage Inc, Chicago, 1978, pp. 91–101.

[8] C. Lampa, I. Sarady, J. Powell, J. Mattson, C. Magnuson, Laser welding of dissimilar metals, in: Proceedings of the 4th NOLAMP Conference, 16–18 August 1993, Sonderborg, Denmark, 1993, pp. 215–223.
[9] H. Hanebuth, A. Papperitz, Laserstrahlfügen aus Anwendersicht, in: Laser in der Elektroproduktion und Feinwerktechnik, 2005, pp. 145–154.
[10] G. Eßer, I. Mys, M. Schmidt, Laser micro welding of copper and aluminum using filler materials, in: Laser Precision Microfabrication LPM 2004, Proceedings of SPIE, vol. 5662, SPIE, Belligham, 2004, pp. 337–342.

CHAPTER 9

Laser Arc Hybrid Welding

B. Acherjee
Birla Institute of Technology, Mesra, India

9.1 INTRODUCTION

Laser arc hybrid welding is a fusion welding process that combines the principles of laser welding and arc welding. In this process the laser beam is used as the primary heat source that interacts in the same weld pool created by a secondary heat source, i.e., the arc generated during an electing arc welding process. Laser welding is preferred due to its ability to produce a narrow and deep weld pool, as the laser beam can be focused on a very small area which increases laser power density. This is a noncontact process that is faster, flexible, and cleaner compared to the conventional welding processes. Due to the tight focus and high speed of laser welding, heat input is minimized, which reduces the chances of thermal distortion in welded parts. However, laser sources are costlier and their costs drastically increase with the power requirements. The laser welding process is applicable to limited welding positions only. It has poor gap-bridging ability, thus requiring high precession in workpiece fit-up and edge preparations. Another concern is the electrical efficiency of the laser systems, which is very poor (2%–10%) for most of the laser systems used for welding. Laser welding is also very difficult for materials having high reflectivity, such as aluminum, copper, gold, etc. On the other hand, arc-welding processes have excellent gap-bridging ability, high electrical efficiency (60%–80%) and can weld materials having high reflectivity. Arc welding systems are also much cheaper than the laser systems of equivalent capacity. However, arc-welding processes have some drawbacks such as low energy density which makes the process slower. This induces high heat input at the weld zone which may result in thermal distortion of the welded part. Hybridization of laser welding with arc welding compensates for the drawbacks of both welding processes while also combining the advantageous features of laser welding and arc welding, in a common interaction zone at the same weld pool. The use of a secondary heat source compensates for the requirement of a

Advances in Laser Materials Processing
https://doi.org/10.1016/B978-0-08-101252-9.00009-1
Copyright © 2018 Elsevier Ltd.
All rights reserved.

high-power laser source, which drastically reduces the cost of the set-up. The potential benefits of laser arc hybrid welding can only be achieved if the laser welding and arc welding processes are suitably combined and the parameters are optimized.

In laser arc hybrid welding, the laser beam is focused on the joint while the welding torch is held at a suitable position so that the arc is aimed at the same interaction zone (Fig. 9.1). The laser can be used in two different ways. In the first approach, the laser is used only to preheat the materials that are to be welded by the arc-welding process. This is referred to as the laser-assisted arc-welding process, in which no significant improvement in weld penetration or welding speed is achieved. In this process a low-power laser source is generally used to augment the arc-welding process. This is a conduction-mode welding process that creates a "cup" shaped weld bead, a characteristic feature of high-energy conventional arc welding processes. In the second approach, a high-power laser beam is used to perform a deep penetration welding. This is a penetration mode welding process characterized by the formation of a keyhole at the joint. In this process, the synergic action of a laser beam having high energy density and an electric arc having high energy efficiency is used to heat the weld zone and to melt the workpiece materials to form a weld with deep penetration in a faster way. This process is known as the arc-assisted laser welding process, most commonly known as the laser arc hybrid welding process. The high-power laser beam melts and vaporizes the materials at the joint which form a keyhole as the

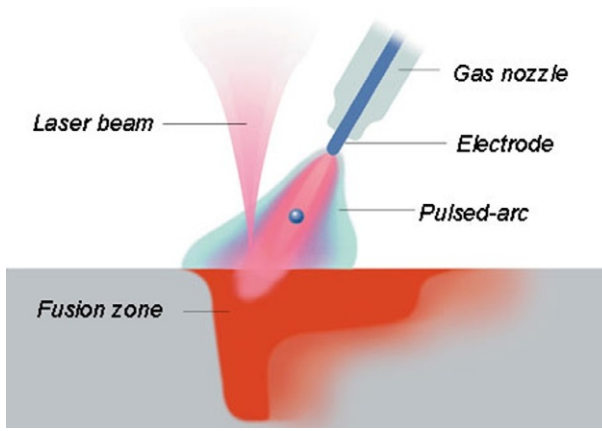


Fig. 9.1 Schematic of laser arc hybrid welding process. *(Courtesy: Fronius International GmbH).*

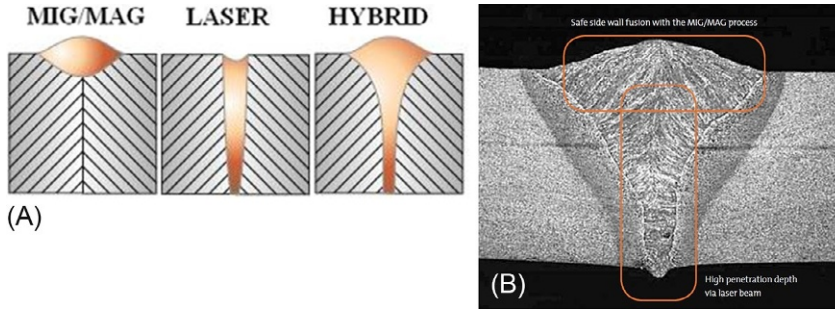


Fig. 9.2 Examples of seam appearances (A) in different welding processes, and (B) in laser arc hybrid welding process. *(Courtesy: Carl Cloos Schweisstechnik GmbH).*

rapid expansion of metal vapors exerts the recoil pressure that pushes the molten material away from the vapor column until a steady state condition is achieved. The keyhole may form partially or fully through the thickness of the base materials. The shape and size of the keyhole is governed by the process parameters and forces such as surface tension, gravity, vapor recoil pressure, etc. The electric arc of the arc welding assists the laser welding process. Both welding processes mutually influence the formation of the weld pool (Fig. 9.2). The electric arc keeps heating and melting the base material along with the melting of electrode or filler rod, which generates the droplets of filler materials. These droplets are detached periodically from the electrode tip and the metal droplet is transferred to the workpiece to fill the joint gap. The dynamic interaction of laser irradiation, electric arc, and the filler droplet govern the formation of shape and size of the weld bead and the strength of the weld. Shielding gas is supplied at the weld zone to protect the weld pool from atmospheric contaminations. The materials are then allowed to cool to solidify the weld pool, which results in a permanent metallurgical bond in the form of a weld.

9.1.1 Historical Developments

Laser arc hybrid welding has been demonstrated as far back as the late 1970s by Prof. W.M. Steen and his coresearchers at Imperial College, London. The research paper published by Steen et al. [1] introduced the concept of "arc-augmented laser welding" that combined laser beam welding with conventional arc welding. Their research showed the clear advantages of combining a laser beam and an electric arc for welding. A drastic increase of welding speed and penetration depth is observed along with increased

process stability. However, the research and development on laser arc hybrid welding experienced slow growth until then. Initially the lack of availability of a high-power reliable laser source and required human skills as well as an incomplete knowledge of the process were the reasons behind its slow progress [2]. The development of a reliable high-power industrial laser in the late 1980s [3] attracted researchers from academic institutions and industry to take up the challenge of improving the process to make it viable for industrial application. Several drawbacks of the individual arc welding and laser welding processes were eliminated, and gap bridgability and reflectivity of the materials were no longer a barrier to a successful welding operation [4–6]. In the 1990s, laser arc hybrid welding saw greater development due to the availability of high-power CO_2 lasers. At that time, the application of CO_2 laser welding was well established in industry. Several studies on the laser arc hybrid welding processes were done, focusing on the economic viability of the process, welding position and preparation of edges, minimization of metallurgical defects, optimization of process parameters, etc [7–10]. However, after reporting several process advantages, its very limited industrial application was due to high equipment cost and the complexity of the process because of a large number of control parameters and the unavailability of an integrated commercial laser arc hybrid welding system. The first industrial laser arc hybrid welding system was introduced in 2000 by Fraunhofer ILT, a Germany-based company, in an oil tank manufacturing industry [11]. This system has been installed in different industries including the automotive industry and the shipbuilding and tube manufacturing industries for welding of metallic sheets [11]. A number of laser arc hybrid welding systems are commercially available now (Make: Fronius [12], ESAB [13], CLOOS [14], Laser Trader [15], etc.). ESAB has introduced a self-adaptive laser arc hybrid welding system, Hybrio, for performing fully automated welding at numerous industries, including rolling stock, containers, shipbuilding, offshore, construction, pipeline production, and the energy sector [13]. The laser MIG/MAG hybrid welding head with the integrated seventh axis has been developed by CLOOS (Fig. 9.3) [14]. Mitsubishi Heavy Industries developed a coaxial laser arc hybrid welding head for welding car bodies [15]. The industrial applications of laser arc hybrid welding have grown in this century not only because of the development of commercially available integrated hybrid welding heads [16], but also due to the availability of cheaper, reliable, and efficient high-power laser systems with the advancement of the instrumentation, automation, and control.



Fig. 9.3 Integrated laser arc hybrid welding head developed by CLOOS. *(Courtesy: Carl Cloos Schweisstechnik GmbH).*

9.1.2 Lasers and Arc Welding Systems

A large variety of laser arc hybrid welding processes has been developed based on the combination of different laser sources and arc-welding systems. Continuous-wave CO_2 lasers and Nd:YAG (neodymium-doped yttrium aluminum garnet) lasers are the most commonly used laser sources. MIG/MAG (metal inert gas/metal active gas) welding, TIG (tungsten inert gas) welding, and PAW (plasma arc welding) are the major arc welding systems used in laser arc hybrid welding processes [16–24]. The CO_2 laser is the highest power continuous wave laser available until now. Because of its high power, the CO_2 lasers are widely used for material processing applications. CO_2 lasers use carbon dioxide, nitrogen, and helium in different proportions as its active medium. CO_2 lasers emit a far-infrared laser beam with a wavelength of 10.6 μm. CO_2 lasers can be operated in continuous mode or in pulse mode. The output power of a continuous wave CO_2 laser ranges from a few watts to 30 kW or more, and in a pulse mode the peak power can reach millions of watts. The Nd:YAG laser is the most widely used solid-state laser for materials processing. In this laser the Nd:$Y_3Al_5O_{12}$ crystal is used as a lasing medium and is optically pumped using a xenon flash lamp or laser diodes. The Nd:YAG laser emits an infrared laser beam having a wavelength of 1.064 μm. Nd:YAG lasers are operated in continuous mode or in pulsed

mode. Pulsed Nd:YAG lasers are typically operated in Q-switch mode. In Q-switch mode the peak power of a Nd:YAG laser can be achieved in the range of gigawatts with a pulse duration in nanoseconds. The maximum available power of a commercially available continuous wave Nd:YAG laser is in the range of a few kilowatts. The main difference between the CO_2 laser and the Nd:YAG laser is their operating wavelengths. The Nd:YAG laser has a shorter wavelength; it also has better beam quality compared to the CO_2 laser. A laser beam with a shorter wavelength is used for welding reflective metals like aluminum, stainless steel, copper, gold, etc. Because of the shorter wavelength of the Nd:YAG laser, the laser beam can be transported from the source to the workstation via optical fiber cables. The weld quality of Nd:YAG laser welding of aluminum and magnesium alloys is superior to CO_2 laser welding, because the use of the Nd:YAG laser reduces the threshold irradiation required for keyhole welding which in turn produces a more stable weld pool [25]. The Nd:YAG laser has greater welding efficiency than the CO_2 laser [25,26]. Due to the longer wavelength of the CO_2 laser, the gas plasma produced during welding absorbs a great proportion of the laser beam, which partially blocks the laser beam reaching the weld pool [1]. This problem can be minimized by the selection of proper shielding gases having high ionization potential. Helium is used as a shielding gas to minimize this effect when welding with the CO_2 laser. However, inert gases such as argon or argon gas mixtures or active gases like CO_2 are generally used as shielding gases for welding with other laser sources [16,27]. The electro-optical efficiency, commonly known as plug efficiency, of both the CO_2 laser and a flash-lamp pumped Nd:YAG laser is very poor, only around 2%–10%. The efficiency of a diode-pumped Nd:YAG laser may reach 20%. Because of this, CO_2 and Nd:YAG lasers require more electrical power to operate. They also require chiller units to take away waste heat from the system. These machines take up a large amount of space while also requiring a great deal of maintenance. Other potential alternatives for CO_2 and Nd:YAG lasers for laser arc hybrid welding are disc and fiber lasers [28–31]. A fiber laser is a diode-pumped solid-state laser in which the active gain medium is an optical fiber doped with rare earth elements. The most commonly used fiber laser is the Yb:YAG (ytterbium-doped yttrium aluminum garnet) laser, which emits a beam with a 1.1-micron wavelength. A disc laser is a diode-pumped solid-state laser in which the lasing medium consists of a disc of ytterbium-doped yttrium aluminum garnet crystal. It produces a laser beam with a 1.03-μm wavelength. The advantages of fiber and disc lasers are their high output power, high optical quality, compact size, high peak power, higher plug efficiency (20%–30%), and low cost per kW as compared to CO_2

and Nd:YAG lasers. They also require less maintenance and have a longer life. The application of fiber lasers in laser arc hybrid welding has gained popularity in recent years with increasing output power and high beam quality and the ability to weld aluminum alloys [28,29] and titanium alloys [30,31] which are difficult to weld with CO_2 lasers. Diode lasers can also be used for welding. The application of diode lasers in laser arc hybrid welding is limited by their inability to form a keyhole because of their relatively low output power and poor beam quality. However, the use of high-power diode lasers in deep penetration welding has been reported in Ref [32]. The diode lasers emit a beam of 0.8–1 micron wavelengths. The plug efficiency of diode lasers is 30%–50%. High-power diode lasers may find their place in the future as the primary heat source in laser arc hybrid welding with technical advancement. The secondary heat source used in the laser arc hybrid welding process is an electric arc. The most common electric arc welding used in laser arc hybrid welding process is the MIG/MAG welding [1,17,18,23,33–37]. In this process a consumable electrode is used and the arc is generated between the metal electrode and the workpiece. The electrode is continuously fed from a spool. This process has very good integration capability as the electrode itself acts as filler material. The welding torch is designed in such a way that it can act as a nozzle for supplying shielding gas at the welding zone. TIG and PAW are also extensively used in laser arc hybrid welding processes [19–22,38–40]. In the TIG welding process the arc is generated between a nonconsumable tungsten electrode and the workpiece. Filler material is supplied externally using a filler rod. TIG welding is generally used for welding hard-to-weld metals such as stainless steel and aluminum-magnesium alloys [41]. In PAW the arc is generated between the nonconsumable tungsten electrode and the nozzle of a specially designed welding torch, and then the arc is transferred to the workpiece. In this process two different gases are used. One of those is used for producing plasma and the other for shielding the welding zone. The submerged arc welding (SAW) process can also be used in laser arc hybrid welding processes [42].

9.1.3 Advantages and Limitations

Because of the synergic action of a laser beam with an electric arc at the same weld pool, the laser arc hybrid welding process offers several advantages over the laser welding and arc weld processes, such as:

(i) Higher welding speed and penetration depth with increased productivity
(ii) Fewer welding passes in a multipass weld joint
(iii) A narrow weld seam with small heat-affected zones
(iv) Improved weld seam stability due to improved side wall fusion

(v) Lower sensitivity to workpiece tolerances
(vi) Better gap-bridging ability
(vii) Access to all welding positions with proper selection of parameters
(viii) Less filler material as compared to arc welding
(ix) Less weld distortion because of lower heat input as compared to arc welding
(x) Addition of filler materials helps to fill the joint gap and adds alloying elements which is not possible in autogenous laser welding
(xi) Can weld a wide variety of metals and alloys including highly reflective materials and reactive metals
(xii) High integration capability and full automation
(xiii) Lower capital costs compared to laser welding, due to the reduction of laser power requirement when hybridized with arc welding
(xiv) Improved plug efficiency due to reduction in power consumption

Although the laser arc hybrid welding process has numerous process advantages, the process has certain limitations too, such as:

(i) Very high capital cost as compared to arc welding
(ii) Accurate positioning and proper part fit-up are required
(iii) Large numbers of process parameters must be controlled
(iv) Additional safety measures must be taken

9.2 LASER MIG/MAG HYBRID WELDING

In the laser MIG/MAG hybrid welding process, a CO_2 laser, Nd:YAG laser, or a fiber laser is used as the primary heat source. The electric arc produced during MIG/MAG welding is used as a secondary heat source. They share a common process zone while having a combined effect on the weld pool formation. The laser generates a keyhole at the weld pool that ensures a deep penetration weld. The molten filler material produced during MIG/MAG welding helps to fill the root gap and permits welding of the parts with higher gaps and fit-up issues [17]. It is observed that the stability of the MIG/MAG arc improves when it is combined with a laser beam [10]. A paraxial arrangement (arc leading or laser lading) of a laser beam and the MIG/MAG welding torch is generally used in laser MIG/MAG hybrid welding. The use of filler materials improves the chemical composition of the weldment by adding alloying elements in the weld pool while also improving the mechanical properties of the weldment. A consumable electrode in the form of a continuously fed filler wire makes the MIG/MAG process more efficient in terms of volume of melt pool than that of TIG and

PAW, where cold wire filler rods are used. The greater volume of melt pool produced during MIG/MAG welding makes this process more efficient for bridging the weld gap than TIG or PAW. Shielding gases are used to protect the molten weld pool from atmospheric contamination. Inert gases such as helium, argon or nitrogen or a mixture of those gases in different proportions are generally used during MIG welding, Active gases such as CO_2 or a mixture of CO_2 with inert gases in different proportions are used as shielding gases during MAG welding. However, the choice of shielding gases also depends on the laser source used in the laser MIG/MAG hybrid welding process. A pulsed mode MIG/MAG power supply is generally used in laser MIG/MAG hybrid welding which enables better control of arc length, formation of metal droplet and its transfer mode, arc stability, and spatter formation during welding. Due to the high welding speed used in laser arc hybrid welding, the wire feed rate is set at a higher value that requires a higher current rating to maintain the arc length at equilibrium. The use of high average current value and the heat radiation from arc and laser material interaction in the laser MIG/MAG hybrid welding process heats up the welding torch. To prevent damage that torch, it is water-cooled. Push- or pull-type wire feeder is used in the MIG/MAG welding process, depending on the wire materials. Though the push-type wire feeder is common in the laser MIG/MAG hybrid welding process because of better control and stability irrespective of materials, pull-type wire feeder is often used for soft materials such as aluminum. The composition of the electrode wire (filler) materials must be chosen based on the compatibility with workpiece materials to achieve desired weld quality. Due to the fast cooling rate of the laser arc hybrid welding process, the electrode wire composition used in MIG/MAG welding may not be acceptable for the laser MIG/MAG hybrid welding process. A very narrow root gap or no gap is used in laser arc hybrid welding, which effects the dilution of filler material into the weld pool. The weld pool formed during laser MIG/MAG hybrid welding has greater proportions of filler material at the top cap part and the base material at the bottom root part. A small joint gap up to 1 mm enables the molten filler to reach to the root of the joint and thus improve the degree of homogeneity by improving dilution in the weld pool.

9.3 LASER TIG HYBRID WELDING

In laser TIG hybrid welding, the electric arc produced during TIG welding is used as the secondary heat source. The arc is established between a nonconsumable tungsten electrode and the workpiece material. Additional

filler materials may or may not be used as per the process requirement. The additional filler material is provided by using filler wire/rod supplied externally. The rate of metal deposition in laser TIG hybrid welding is much less than the laser MIG/MAG hybrid welding, because only a fraction of the heat of the arc is used to melt the filler wire in laser TIG hybrid welding. As the filler wire is separated from the electrical circuit of the laser TIG hybrid welding set up, the welding current and the metal deposition rate during welding can be determined independently. However, the electrode contamination due to hot metal vapor, erosion of the tungsten electrode tip due to use of high frequency arc ignition, and the high affinity of tungsten for oxygen are common problems associated with TIG welding [3]. Shielding gas is used to protect the weld pool while also protecting the electrode from atmospheric contamination or oxide formation. The melting rate of the base material for laser TIG hybrid welding is nearly twice the sum of the melting rate of laser welding and TIG welding, individually [43]. It is reported that when a TIG arc is used with a laser beam in a common interaction zone, the laser energy absorption in the base material is improved due to the preheating of the base material using the leading TIG arc [44]. On the other hand, the use of a laser at the common weld pool stabilizes the TIG arc. Because of the high power density of the laser beam, a part of the base material at the weld zone melts and vaporizes, which provides a conductive path for the arc. The TIG arc follows the shortest conductive path between the electrode and the metal, thus it roots to the laser interaction zone. The rooting and narrowing of the arc-to-laser interaction zone increases electrical conductivity along the arc column and stabilizes the arc [35,45,46]. The coaxial and paraxial arrangements are used for the laser TIG hybrid welding process. In the coaxial arrangement the laser beam is passed through a coaxially placed hollow TIG electrode. This enables the projection of the laser beam on the TIG arc, and both the laser beam and the TIG arc share a common central axis. The change in the distribution of current density due to the use of a hollow electrode makes the focus point of the laser smaller [47]. In this configuration the absorption of laser energy by the arc plasma is more severe, especially for CO_2 laser TIG hybrid welding. Thus a deep penetration welding of thick materials is not possible. However, the use of a laser having high beam quality like the Nd:YAG laser improves the penetration when the same laser power is used. In the paraxial arrangement the arc is placed either at the front or at the back of the laser beam on the weld line along the direction of weld, and they share a common weld pool. During comparative studies between coaxial and paraxial CO_2 laser TIG

hybrid welding configurations, the effect of welding current on the weld penetration and on the hybrid arc is found to be consistent for coaxial laser TIG hybrid welding. However, the maximum weld penetration is achieved for the paraxial configuration, which is approximately 20% more than that for coaxial configuration [38]. In paraxial arrangements, the laser beam and the TIG arc can be placed either on the same side of the workpiece or on the opposite side. An increase of 300% in speed is reported when the laser beam and the TIG arc are placed on the opposite side of the workpiece. However, an increase of 100% in speed is obtained when the laser beam and TIG arc are placed on the same side of the workpiece for the same arc current setting, during welding of 0.8-mm-thick titanium and 2-mm-thick mild steel [45,48]. The laser TIG hybrid welding process is generally used for welding thin gauge materials. The ability of laser TIG hybrid welding for butt welding of very thin austenitic stainless steel sheets has been demonstrated [39].

9.4 LASER PAW HYBRID WELDING

In the laser PAW hybrid welding process, a constricted plasma arc is used as the secondary heat source. Similar to TIG welding, a nonconsumable tungsten or tungsten alloy wire is used as the electrode in plasma arc welding. Filler materials may or may not used. Unlike with TIG, the electrode used in PAW is recessed in the welding torch. A water-cooled constricting nozzle of small diameter is used inside the welding torch to squeeze the arc, which increases its intensity and improves the stability and shape of the arc. The inert gas passed through the constricting nozzle, known as orifice gas, is used to produce plasma. The shielding effect is further enhanced by using another shielding gas, which is passed through the outer ring of the torch. In PAW, the arc is established either between the electrode and the constricting nozzle (nontransfer arc) or between the electrode and the workpiece material (transfer arc). Initially, high-frequency current is used during the ignition of the pilot arc between the electrode and the constricting nozzle, and the current is fixed at a level after the pilot arc is established. During welding, the arc is transferred to the workpiece, which turns into part of the electrical circuit. As compared to the TIG arc, the plasma arc is more stable and pointed. The constricted plasma arc does not deflect easily at the closest point of base metal because of the jet action due to the constriction of the arc plasma. The laser beam and plasma jet are directed at the common interaction zone. The laser beam is either directed perpendicular to the material

surface [21] or it is tilted at a small angle from the perpendicular axis [20]. The PAW torch is generally held at an angle of 35–45 degrees from the laser beam axis in a paraxial arrangement [20]. In a coaxial arrangement, the laser beam is surrounded by the plasma arc [21]. The hybridization effect of laser and plasma arc increases the welding speed and stabilizes the arc plasma. The penetration depth is more for laser PAW hybrid welding than for laser welding for the same energy input per unit length of the weld [20]. As compared to the results of laser TIG hybrid welding, the heat input from the arc can be reduced up to 40% when laser PAW hybrid welding is used [22].

9.5 LASER ARC HYBRID WELDING PARAMETERS

A large number of process parameters are to be controlled during the laser arc hybrid welding process. Both types of processes have a number of control parameters. Hybridization of the processes requires new parameters to be defined in addition to the control parameters of the individual units. The optimum process parameters of the laser arc hybrid welding process cannot simply be determined from the combination of optimum parameters of the individual welding processes. The optimum value of the parameters may change due to the interaction effect of the laser beam with the electric arc. For example, the laser power requirement for laser arc hybrid welding is less than that for the autogenous laser welding process, due to the use of a secondary heat source [49].

9.5.1 Laser Power

In laser arc hybrid welding, the laser power is the main source of the heat that produces the keyhole and ensures the deep penetration welding [50]. Because of the use of the electric arc with the laser at the same weld pool, the laser absorption within the material is also increased. The power density has the greatest effect on welding during welding with a laser. Power density is the ratio of power to beam spot area. Power density increases with power and decreases with an increase of beam spot area. Large beam spots create wider keyholes with less penetration for a given laser power. The weld penetration increases with laser power. The results of bead-on-plate laser MIG/MAG hybrid welding of A5052 and SUS304 aluminum alloys with fiber laser using laser power ranging from 2–10 kW showed the increase of weld penetration with laser power for both alloys [29]. It is also found that the laser absorption increases when the keyhole is formed at the weld zone due to the application of high power density [29].

9.5.2 Welding Speed

Laser arc hybrid welding possesses beneficial characteristics such as a higher welding speed, which increases productivity. However, the weld penetration is inversely affected by the welding speed. At a high welding speed the interaction time is less, thus decreasing the heat input per unit length of the weld, which in turn reduces the weld penetration. To compensate for this, more laser power is required and the filler wire feed rate must be increased to maintain a constant volume of weld pool. The welding speed to filler wire feeding ratio is an important factor for the stability of the keyhole and the entire process. A too-high welding speed may cause improper fusion or lack of penetration of the weld. A too-low welding speed may create a larger weld pool with deep penetration until the limit of the burn through the material and may cause partial decomposition. The fast heating and cooling cycle due to the higher welding speed may result in metallurgical defects within the weldment.

9.5.3 Relative Positioning of the Laser Beam and the Arc Welding Torch

The relative positioning of the laser beam and the arc welding torch is also a factor. The laser beam is always directed perpendicular to the welding direction to get the maximum possible weld penetration. The arc welding torch can be positioned in front of the laser beam (arc leading) or just behind the laser beam (laser leading). During the arc-leading process the torch is positioned at a drag angle. During the laser-leading process the welding torch is positioned at a push angle. Dragging generally produces deeper penetration and a narrower weld width than the pushing technique. In an arc-leading process the weld deposition is narrow and convex as compared to the laser leading process. The effect of leading or trailing arrangements of the arc welding torch was found to be quite insignificant. Only an improvement of 10% weld penetration is observed when the MAG torch is placed behind the CO_2 laser beam [18]. Contrary to this, an improvement of weld penetration is observed when using arc leading configuration during the welding of type 304 stainless steel using the laser TIG hybrid welding process with a 1.8 kW Nd:YAG laser [19].

9.5.4 Relative Distance Between the Laser Beam and the Arc (Lase-to-Electrode Distance)

The relative distance between the laser beam and the electrode of electric arc (laser to electrode distance) is one of the significant control parameters of the laser arc hybrid welding process. The arc must be in close proximity

to the laser beam to ensure their synergic effect in the common weld pool. The laser-to-arc separation distance is typically kept from 0 mm (for coaxial arrangement) to 3 mm (for arc-leading or laser-leading arrangements), depending on the types of laser parameters, arc welding parameters, and materials used [5,18,33]. The best results are obtained for a laser-to-electrode separation distance of 1–2 mm. Increasing the gap between the laser beam and the electrode may result in a loss of the hybridization effect as they act into separate weld pools, which adversely affects the penetration of weld and the stability of the arc. Coaxial arrangement or a very short gap may lead to a problem of absorption of laser energy by the arc plasma, which partially blocks the laser beam resulting in less penetration. Using a Nd:YAG laser TIG hybrid welding set up with coaxial arrangement, a lower weld penetration is observed as compared to a 2-mm laser and electrode gap [16]. The laser-to-arc distance affects the morphological characteristics of the weld pool. The weld pools appear more asymmetrical with the increase of lateral displacement of the MIG torch from the fixed laser source [17].

9.5.5 Focal Point Position

The focal position of the laser beam affects the penetration of the weld. The maximum weld penetration is generally achieved when the focal point of the laser beam lies below the surface of the workpiece [51]. The focus of the laser beam changes when it penetrates the molten pool. The volume of the weld pool in laser arc hybrid welding is much greater than the autogenous laser welding. The formation of cup-shaped weld deposition in laser arc hybrid welding increases the curvature of the top surface of the melt pool, which changes the focus of the interacting laser beam. The focus of the laser beam during CO_2 laser MIG hybrid welding was reduced by 0.7 mm versus autogenous laser welding [52]. The optimum focus of the laser beam is shifted from −2 to −4 mm during the welding of a mild steel plate using CO_2 laser MAG hybrid welding with a 0.6 m/min welding speed [53].

9.5.6 Angle of Electrode

The angle of electrode is controlled by holding the welding torch at an angle measured from the workpiece surface. The electrode angle is provided in such a way that the shielding gas coming from the torch nozzle effectively deflects the laser-induced plasma from the weld zone to increase the laser penetration of the weld. The electrode angle is typically set around 45–65 degrees, [17,49], which reduces the arc length. The laser beam is generally directed normal to the workpiece surface to obtain better penetration.

However, the laser beam is tilted at an angle during the welding of highly reflective materials to avoid any damage of the laser head due to the reflected beam.

9.5.7 Shielding Gas Composition

The shielding gas is generally used during welding to protect the weld zone from the surrounding atmosphere. The use of shielding gas also influences the arc characteristics, the formation of weld profile, and the mode of metal transfer. Inert gases such as helium and argon are the predominant constituents of shielding gases used in laser arc hybrid welding processes. Nitrogen, carbon dioxide, and carbon monoxide (CO) are also used as shielding gas constituents based on the selection of materials, the laser source, and the arc parameters. The arc stability and the plasma shape depend on the composition of the shielding gas used in laser arc hybrid welding, which affects weld penetration [54]. The laser energy absorption by the laser-induced plasma or by gas plume during the CO_2 laser arc hybrid welding process is a well-known problem. This reduces the laser intensity reaching the weld pool, decreasing the weld penetration. The use of a high ionization potential shielding gas such as helium during welding with a CO_2 laser reduces the effect of plasma absorption. A mixture of argon, helium, and CO_2 is also used in the CO_2 laser arc hybrid welding process [17]. The use of helium ensures deeper penetration, whereas the use of argon improves the arc stability. In CO_2 laser welding the optimum percentage of helium proportion varies from 30% to 80%, depending on other parameters and the material used. It is found during welding of high-strength steel using the CO_2 laser MIG/MAG hybrid welding process, that using helium at less than 30% in shielding gas requires an additional source of helium as a secondary plume suppression gas [33]. The use of CO in shielding gas up to 10%, during the CO_2 laser MIG/MAG hybrid welding process, is found to stabilize the arc [33]. The use of a small percentage of oxygen ($\leq$5 %) in the shielding gas reduces the spatter formation and improves the metal transfer during welding. However, no significant vapor plume absorption of laser energy is noticed during the welding with lasers having a shorter wavelength such as Nd:YAG lasers, fiber lasers, disc lasers, etc. Thus, the choice of shielding gas composition during welding with Nd:YAG, fiber, and disc lasers is based mainly on the requirement of shielding and arc stability. The shielding gas delivered through the arc welding torch is generally sufficient to protect the molten weld pool. However, an additional nozzle/torch is used in some cases, such as welding of reactive metals like titanium, to supply shielding

gas, which trails the arc. This provides a shielding atmosphere during the cooling to avoid formation of oxides.

9.5.8 Power Modulation of the Arc Welding Source

A direct-current (DC) power source or an alternating-current (AC) power source is used for arc welding. The electrode is either connected to the positive terminal (DCEP) or to the negative terminal (DCEN) of a DC power source, whereas, due to the cyclic change of polarity in AC supply, no such selection is required. The polarity of an arc welding system is changed to achieve the heat balance between the electrode and the workpiece material, which also defines the shape of the weld bead. A pulse current power source is also used, and is particularly preferred for welding thin parts. The arc power is controlled by the welding current and voltage. Due to the dynamic behavior of the arc, the current and voltage changes continuously during the welding. Current positively affects the rate of melting of the consumable electrode, filler, and base materials. Voltage affects the arc length and the welding current. The increase of arc length increases the voltage, thus reducing the welding current and the melting of the electrode. A constant current or a constant voltage power source is used during welding. A constant current power source keeps the current at a moderately constant level for a reasonable change of voltage. A constant voltage power source keeps the voltage at a moderately constant level for a reasonable change of current. A constant current power source is generally used for the TIG or PAW, whereas a constant voltage power source is used for the MIG/MAG welding. In PAW and TIG welding, the current is preset, and any changes of welding current due to the change of arc length are not critical because of the use of a nonconsumable electrode and separately used filler material. During MIG/MAG welding, the welding current is controlled by the wire feed speed. The change of wire feed speed changes the arc length and arc voltage, which in turn changes the arc current and melting rate of the electrode to maintain an equilibrium arc length. In MIG/MAG welding, voltage and wire feed rates are preset and the current is measured during welding. Multiprocess welding power source is also available, which has the features of both constant current and constant voltage power sources. Conventional TIG welding is generally carried out with an AC power source because it prevents the electrode from overheating, removes oxides during the positive phase, and heats up the workpiece deeply during negative phase. An AC power source is also used in the laser TIG hybrid welding process [49]. The use of a DC power source in CO_2 laser TIG hybrid welding results in

higher energy input and longer electrode life [55]. The DC power source with electrode positive is used in the conventional MIG/MAG welding process as well as in the laser MIG/MAG hybrid welding process, which increases the deposition rate [56]. The use of pulse mode in laser TIG hybrid welding or in laser MIG/MAG hybrid welding reduces the amount of spatter and heat-affected zones. Pulse width and pulse frequency are the additional parameters to be controlled during the use of pulsed current. Pulse width determines the time duration of the pulse (peak current) while also affecting the size of the metal droplet and the width of the arc cone. The pulse frequency controls the overall heat input to the weld zone [17]. The mode of metal transfer is an important factor that is affected by arc power, electrode stick-out, electrode diameter and shielding gas composition and gas pressure. There are three different modes of metal transfer observed during arc welding: projected/spray transfer, gravitational/globular transfer, and short circuit transfer. Spray transfer is much preferred in laser arc hybrid welding to ensure deep penetration due to high heat input per unit length during maintenance of high welding speed. Lower turbulence of the weld puddle is observed during the use of spray mode metal transfer due to the projection of small filler droplets into the weld pool [57]. The use of pulsed current enhances the spray metal mode transfer as the use of peak current for small pulse duration and pulse frequency affects the formation of metal droplets and detaches it frequently, which reduces the possibility of formation of bigger droplets, a characteristic feature of gravitational transfer. The ratio of laser power to arc power is also an important factor for laser arc hybrid welding, which affects the geometry and metallurgical property of the weld. This balances the effects of the laser beam and the arc on the common weld pool. Higher energy ratio ensures a narrow and deep weld while increasing the welding speed. The weld bead size increases with arc power until a steady-state condition is achieved. However, very high arc power causes a reduction in penetration depth because of the change of metal mode transfer from spray transfer to globular transfer.

9.5.9 Wire Feed Rate

The feed rate of the consumable electrode is determined based on the requirement of metal deposition at the weld. In a constant voltage MIG/MAG welding setup, the wire feed rate is preset. The higher wire feed rate enables the operator to join a weld with a higher part gap, also helping to increase the welding speed [17]. The selection of wire feed rate is critical to avoid a lack of deposition or the supply of extra material. With a higher wire

feed rate, the higher current is required to increase the rate of deposition. The increase of the wire diameter also requires higher current to maintain the constant arc length.

9.5.10 Joint Gap

Laser arc hybrid welding has a better ability to join the parts with joint gap than laser welding. The laser beam can weld parts with a gap up to 0.2–0.25 mm only, without visible weld defects like undercut or incomplete weld bead. However, a joint gap of 1 mm can easily be welded with the laser arc hybrid welding process. The joint gap above 1 mm can also be welded, but this requires the proper selection of the process parameters of laser arc hybrid welding. The laser-to-arc energy ratio, laser-arc distance, welding speed, and wire feed rate are the critical parameters that determine the rate of deposition of the filler materials to fill the joint gap. Increasing the joint gap reduces the weld penetration; thus welding speed is to be reduced to obtain a good weld. It is observed during the CO_2 laser MIG hybrid welding of high-strength carbon steel that the wire feed rate is to be increased with the joint gap. The results presented in Ref [17] show that the welding speed can be increased during welding of parts having a joint gap up to 1 mm, because the small joint gap simplifies the penetration as more filler material reaches the root of the joint. However, increasing the joint gap more than 1 mm requires the welding speed to be reduced. A larger joint gap may require multiple weld passes and the use of a backing plate.

9.5.11 Joint Configuration and Edge Preparation

The basic joint configurations used in welding are butt, corner, edge, lap, and tee joints. All these joint configurations are used in the laser arc hybrid welding process. Due to the small spot diameter of the laser beam, the square edges are used for welding, whereas grooves are made at joints when using arc welding, especially for thick sections. For thick materials welding using arc welding V, U, or J grooves are made at joint edges to ensure that the molten filler material can reach the root of the joint. The shape of the groove determines the volume of the materials deposition and the number of weld passes required, which influences joint strength, residual stress distribution, and bead geometry. For heavy sections, double V, double U, or double J grooves are used which reduces the volume of the materials deposition required, produces symmetric welds, and minimizes warpage. The simultaneous action of joint filling by filler deposition using arc welding and deep penetration by laser requires a different joint design for laser

arc hybrid welding. Thin metal sheets or metal plates having a thickness less than 6–8 mm do not require edge preparation for welding using laser arc hybrid welding. For material having a thickness more than 6–8 mm, preparation of edges is required. The grooves used in parts for laser arc hybrid welding generally are smaller, including angle, narrow root opening, and larger land thickness as compared to the grooves used in arc welding. The V groove used for laser arc hybrid welding resembles the shape of a wine glass or a funnel. For a part having a different thickness, the groove is made in such a way that the land thickness of the part should be the same at the joint while the height difference is to be compensated at the cap. The large weld pool at the cap has better tolerance to geometrical mismatch.

9.6 IMPROVEMENTS OF PERFORMANCE CHARACTERISTICS AND WELD QUALITY

The improvement of welding performance due to the use of laser arc hybrid welding techniques can be measured in terms of increase in welding speed, weld penetration, and gap bridging ability while cost is reduced. The enhancement in weld quality can be assessed in terms of the improvement of mechanical properties and morphological characteristics with reduction or elimination of welding defects. As compared to autogenous laser welding, the laser MIG hybrid welding process is 50% faster [17]. The increase of weld speed up to 300% is measured during laser the TIG hybrid welding process, when the laser beam and TIG arc are placed on the opposite sides of the workpiece. With the laser beam and TIG arc on the same side of the workpiece, an increase of 100% in speed is obtained for the same arc current setting, during welding of 0.8-mm thick titanium and 2-mm thick mild steel [45,48]. The use of a plasma arc with a CO_2 laser results in an increase of welding speed of 50–100% and an increase of weld penetration up to 20%, when judged against laser welding [58]. Using the laser arc hybrid welding process, steel and aluminum thin sheets can be welded at high welding speeds ranging between 4 and 14 m/min [59,60]. Emmelmann et al. [20] reported an increase of welding speed up to 100% for welding of 2- and 4-mm thick S235JR steel sheets with a 300W laser 4500W plasma arc hybrid welding system. Kutsuna and Chen [53] compared the CO_2 laser MAG hybrid welding of carbon steels with laser welding and found an increase of welding speed up to 30% for hybrid welding. The results presented by Nielsen et al. [18] show that the welding speed is increased in the range of 30%–100% during CO_2 MAG hybrid welding of C/Mn steel as compared

to laser welding using cold filler wire. The speed can further be increased up to 200% when a joint gap of 0.6 mm is kept between mating parts. Laser arc hybrid welding is used for welding thick as well as thin materials. For welding thick plates, it is generally employed up to a thickness that can be welded in a single pass. Laser arc hybrid welding offers higher weld penetration because of the higher energy deposition due to the use of laser and arc, and better absorption of laser energy into base materials when the arc interacts at the same weld pool. Steel plates of thickness up to 25 mm are successfully welded using a 20 kW laser and a MAG hybrid welding system in a single pass with a welding speed of 1 m/min. Steel plates of 30-mm thickness are also welded in dual passes using a laser dual MAG hybrid system where two MAG torches are placed on two different sides of the plates [34]. Plates with higher thicknesses can also be welded at favorable weld conditions using multiple weld passes and an optimum joint gap. Matsudata et al. [61] reported that the weld penetration obtained by using a 5 kW CO_2 laser 5 kW TIG hybrid welding system is 1.3–2 times deeper than that obtained by laser welding alone. Swanson et al. [37] performed bead-on-plate welds on 6-mm thick low carbon steel plates using laser plasma arc hybrid welding and achieved an increase in welding speed of 100% for full penetration welding, or an increase in penetration depth of 25%–100% compared with the laser alone. Laser arc hybrid welding can bridge a joint gap up to a few millimeters depending on the selection of material thickness, laser power, welding speed, and filler wire feed rate. Shi [36] compared the gap bridging capability of the hybrid coaxial CO_2 laser MAG welding process with autogenous laser welding and laser welding with cold wire. Butt joint welds are made in 8 mm thick C/Mn steel. Hybrid welding has much greater gap bridging capability than autogenous laser welding or laser welding with cold wire. The joint gaps up to 1.4 mm are welded using hybrid welding without adjusting the welding parameters. Wider joint gaps up to 1.6 mm are also welded by regulating the wire feed rate or the welding speed, keeping remaining parameters constant. The work presented by Nilsson et al. [17] shows that a small joint gap is beneficial for hybrid welding. Maximum welding speed of 1.6 m/min is reached with a gap of 1 mm, during welding of 6-mm steel plates using the CO_2 laser MIG hybrid welding process. Butt joints with joint gaps up to 2 mm have been realized by reducing the welding speed and increasing the wire feed rate. Improvement of welding speed due to presence of a joint gap is also reported for welding of a 5-mm thick aluminum alloy sheet by using a Nd:YAG laser MIG hybrid welding. As compared to zero gap, the welding speed can be increased twofold during

welding with a joint gap of 0.6 mm while the number of pores are also significantly reduced [18]. C/Mn steel plates of 2.13-mm thickness with 0.6-mm joint gap can be successfully welded by using CO_2 laser MIG hybrid welding with a welding speed of 3.5 m/min [58]. The T joints with 1-mm parts gap in 2-mm mild steel sheets are welded using Nd:YAG laser MIG hybrid welding with a welding speed of 3 m/min. During Nd:YAG laser MIG hybrid welding of 2-mm thick aluminum alloy in fillet joint with a 0.6-mm parts gap, a welding speed up to 7 m/min is realized [16]. The use of the laser arc hybrid welding process can reduce the cost of the weld and thus the production of the welded parts. The use of a secondary heat source reduces the laser power requirement, therefore reducing the direct cost. High welding speed, better seam quality, and fewer weld passes needed due to deep penetration also make this process more economical than autogenous laser welding. Bayer et al. [40] estimated that the use of a 2 kW Nd:YAG laser along with a 2 kW TIG welding setup may reduce the cost up to 50% while increasing the productivity up to 50%. It would also minimize the effort required for edge preparation and control of seam width. Reduction of 1 kW in laser power requirement approximately reduces the electricity consumption in the order of 35 kVA [62]. It is found that in the use of the Nd:YAG laser MIG hybrid welding system for welding 1–4 mm thick mild steel, stainless steel, and aluminum sheets, the laser power requirement can be reduced by 1 kW, as compared to pure laser welding. The saving of 1 kW in laser power costs around 100,000€. However, the additional cost of the MIG setup around 40,000€ is to be incurred [16]. Reutzl et al. [63] reported that the use of laser MIG/MAG hybrid welding results in a reduction of 93% in man hours, 83% in electrode consumption, and 10% in other consumables such as gas shielding cups and contact tips, as compared to conventional MIG/MAG welding processes. In addition, the volume of harmful fumes also gets reduced when a hybrid system is used. The capital cost of the laser system appears negligible when compared to savings of recurring costs of MIG/MAG welding. Laser arc hybrid welding is able to join a wide variety of metals including highly reflective metals such as alumimum, stainless steel, nickel, etc. and reactive metals like titanium. In all cases, a high-quality weld with perfectly acceptable mechanical properties is obtained. Adequate mechanical properties with improved fatigue strength are achieved for CO_2 laser MIG hybrid welding of aluminum alloy AA6013 [23]. For fiber laser MIG hybrid welding of titanium sheets, the parts with better combinations of strength and ductility are achieved as compared to the fiber laser welded parts [31]. The use of the CO_2 laser

MAG hybrid welding process for welding aluminum alloy sheets results in a considerable reduction of pores as compared to CO_2 laser welding, even with 0.6-mm part gaps [18]. In Nd:YAG laser MAG hybrid welding of zinc-coated steel sheets in lap joint configuration, the creation of blowholes is restrained considerably moreso than in laser welding, even with a 0-mm part gap, which ensures a sound weld [35]. The welding of AISI 304 steel by using Nd:YAG laser TIG hybrid technique results in a significant reduction of pores [19]. As compared to Nd:YAG laser welding of 10-mm A6061 aluminum alloy, the use of Nd:YAG laser TIG hybrid welding results in deeper penetration and complete elimination of cracks [64]. The weld bead formed by using laser arc hybrid techniques has better ductility than that formed by using laser welding. The use of a laser PAW hybrid technique and laser MIG hybrid technique for welding of C/Mn steel result in a reduction of hardness value by 27% and 23%, respectively, as compared to autogenous laser welding [24].

9.7 INDUSTRIAL APPLICATIONS

The concept of a laser arc hybrid welding process has been shaped into a number of industrial applications over the years. Due to its numerous process advantages, higher productivity, and better weld quality as compared to laser welding or arc welding, this process is an attractive alternative for different industries. The capital cost of the welding system can be compensated for by providing faster welding speed and deeper penetration to reduce the cost per unit length of weld. The laser arc hybrid welding can be used to weld a wide variety of metals from ferrous metals such as steels and stainless steels to the nonferrous metals such as aluminum, magnesium, copper, nickel, titanium, and their alloys. This can weld thin sheet metals as well as thick metal plates. The high welding speed and deep penetration allows the welding of thick plates using a fewer number of weld passes, which reduces the weld distortion. The first industrial laser arc hybrid system was deployed by Fraunhofer ILT in an oil tank manufacturing company in 2000. It generated interest among the industries using high-volume welding, which resulted in the installation of a number of laser arc hybrid welding systems in automotive, shipbuilding, and tube-manufacturing industries in the succeeding years [11]. Laser arc hybrid welding also found use in numerous industries, including aerospace, rolling stock, container manufacturing, offshore, construction, pipeline production, heavy engineering, and energy sectors. Different aspects of laser arc hybrid welding such as automation

potential, the reduction in cost per unit length of weld, and weldability of materials have been investigated by several researchers for different industrial applications. [63,65,66]. The major applications of laser arc hybrid welding are found in automobile and shipbuilding industries where a large number of metallic components are welded to build light or heavy vehicles and ships. The gap bridging capability with the faster processing of the laser arc hybrid welding process makes it a competent alternative for the automobile industry. The major automobile industries such as Volkswagen and Audi have implemented laser arc hybrid welding in their production lines [67]. A total of 48 hybrid welds are made in each Volkswagen Phaeton to produce high quality fillet and butt joints for the extruded sections, castings, and aluminum sheets. On an Audi A8, the roof frame and its different parts are welded using laser arc hybrid welding. Daimler also uses the hybrid welding technique for axle production, which results in an increase in productivity by increasing the welding speed and wire efficiency while maintaining good penetration and improved metallurgical properties [59]. The laser arc weldability of high strength TRIP (transformation-induced plasticity) steel for the car industry is investigated using a 2kW Nd:YAG laser and 350A MIG welding system. Improved metal transfer and deep penetration are reported [68]. The Meyer-Werft GmbH, a German shipyard company, introduced laser MIG/MAG hybrid welding in their production line to weld steel panels and stiffeners used for fabrication of ships (Fig. 9.4). By using a 12kW CO_2 laser with a 450A MIG/MAG welding setup, 12-mm thick fillet joints with 20-meter long weld seams are produced successfully. The use of the hybrid welding technique reduced the weld



Fig. 9.4 Laser arc hybrid welded steel panels and stiffeners used for fabrication of ships at Meyer-Werft GmbH. *(Courtesy: Meyer-Werft GmbH).*

distortion and thus, to a large extent, eliminated the reworking required for flattening the parts. The increase in welding speed and the reduction of filler material requirement have also been reported. The performances of the welded sections are characterized by tensile tests, hardness tests, impact tests, bending tests, and fatigue tests. Satisfactory results were found[69]. The Italian shipbuilding company Fincantieri also implemented laser arc hybrid welding using the Nd:YAG laser and MAG welding technique, which makes them able to resolve issues such as weld distortion and joint-gap bridging in an effective way [70]. The laser arc hybrid welding system using a fiber laser has also been developed for the shipbuilding industry [71]. The work published in Ref [72] reported the application of an automated 25 kW CO_2 laser 6kW MIG/MAG hybrid welding setup in shipbuilding and other industries. The setup is integrated with a gantry and controlled online using seam tracking, weld quality monitoring, and process-control software. Materials like ASTM A-36 steel, high-strength alloy steel (HLSA 65), and super austenitic stainless steel (AL6-XN) having a thickness up to 12 mm are successfully welded with full penetration using welding speeds between 1.9 and 2.5 m/min. The aerospace industry uses materials having a high weight-to-strength ratio. Materials such as aluminum, magnesium, titanium, and their alloys are used in aircraft manufacturing. The aircraft structure is mainly tested for strength and fatigue resistance as they are crucial performance characteristics. Satisfactory mechanical properties with improved fatigue strength are achieved for CO_2 laser MIG hybrid welding of aluminum alloy AA6013 [23]. Aluminum alloy plates of 12.7-mm thickness are successfully welded using Nd:YAG laser MIG hybrid welding and fiber laser MIG hybrid welding processes [28]. The commercially pure titanium sheet of 1.5-mm thicknesses was welded at welding speeds up to 9 m/min using a fiber laser MIG welding. The welded parts with better combinations of strength and ductility are achieved with the hybrid welding as compared to fiber laser welded parts [31]. A European project called Economical and Safe Laser Hybrid Welding of Structural Steel (HYBLAS) made use of laser MAG hybrid welding to weld 25-mm thick steel plates in a single pass, using 20 kW laser power and 1 m/min welding speed. The thick steel sections up to 30 mm and fillet welds up to 20-mm thick were successfully welded using dual pass laser MAG hybrid welding, in which both sides of the plates are welded simultaneously with two MAG sources. The laser beam and a MAG welding torch are placed on one side of the plates while another MAG torch is placed on the opposite side of the plates, targeting the same weld line. The weldability of steels having yield strength

from 180 to 690 MPa are examined with the laser MAG hybrid welding system and defect-free joints are obtained for all structural uses with good mechanical properties and better fatigue properties [34]. Fraunhofer ILT expanded the existing state-of-the art of laser MAG hybrid welding of high-strength structural steels regarding welding of thick parts, bridging the joint gaps, prevention of hot cracks, and improvement of fatigue properties. A physical model is also developed to investigate the crucial parameters for welding thick sections with joint gap, without drop-through. Very good weld quality with excellent mechanical properties is achieved using favorable welding conditions with very narrow V or Y groove edge preparation. Using a 20 kW CO_2 laser and up to 7.2 kW Nd:YAG laser with a MAG welding setup, very deep weld penetration with special seam-shaping capability has been demonstrated [73]. The laser arc hybrid welding process is used in the power industry to weld tight wall panels and the ribbed pipes of boilers. The laser MAG hybrid welding technique has been adopted by Energoinstal S.A. for fabrication of wall panels and ribbed pipes of boilers due to process stability, higher joint gap tolerance, deep penetration, and higher efficiency of the hybrid welding technique [74]. The industrial application of the CO_2 laser MIG/MAG hybrid welding system for welding of a telescopic lifter is reported in Ref. [75]. The prime reason for using this system in the production unit was due to its ability to bridge the joint gaps effectively.

9.8 SAFETY

Safety can be considered as a tool for preventing accidents, minimizing risks, and preparing for complications arising out of any changes in the system [76]. Safety hazards can result from optical radiation, electric shock, fire, explosion, and fumes during laser arc hybrid welding. The main safety concerns are from laser systems. IEC 825-1:1993 is the international standard on laser safety, issued by the International Electrotechnical Commission. It is widely followed outside North America for the safe use of lasers. ANSI (American National Standards Institute) Z136.1:1993 [77] is the American standard for the safe use of lasers, which has been revised to bring it close to the international (IEC) standard. This standard provides some mandatory requirements for laser users such as designating a person as the laser safety officer for each laser facility as well as safety training for the personnel using the laser facility. ANSI developed a classification of lasers based on the severity of hazards that may result due to their exposure, which is internationally

adopted. It divides the lasers in terms of class 1, 2, 3A, 3B, and 4. The Class 1 lasers are safe for humans due to their very low radiant energy and output power. Class 2 lasers may cause potential eye hazards, but are safe for accidental momentary viewing, which covers visible emission only. Class 3A lasers are safe for accidental viewing with the unaided eye, which does not cover the lasers whose emission wavelength is above 4000 nm. Class 3B lasers may cause hazards to the unaided eye, but are safe for viewing diffuse reflections only. Class 4 lasers cause eye and skin hazards. All lasers are labeled with their hazard class. The eye hazard or skin injury not only depends on the site of exposure but also on the laser wavelength and the duration of exposure. Protective eyewear is required for Class 3 and 4 lasers to protect from direct or reflected laser radiation. The laser system is to be placed inside a protective enclosure to prevent the operator or any other person from direct exposure to the laser beam radiation. The American Welding Society, in association with the American National Standards Institute, has framed an American National Standard ANSI Z49.1:2005 for safety in welding, cutting, and allied processes. The International Organization for Standardization (ISO) also provided a number of codes related to health and safety in welding and allied processes [78,79]. The Bureau of Indian Standards furnished an Indian code of practice (IS 818:1968) for safety and health requirements in electric and gas welding and cutting operations [80]. The detailed safety rules and precautions can be found in these documents. However, in general some safety precautions are to be taken when using arc welding, such as the use of an eye shield to protect from the intense glare of the electric arc. In laser arc hybrid welding, eye protection is required to protect from exposure to the laser radiation as well from ultraviolet rays produced during arc welding. The spatter and hot metal parts during welding may cause burn hazards. The laser system and the arc welding system use high voltage and current, which may cause life-threatening electric shock hazards. Pulsed lasers often use large capacitor banks that can store large amounts of electric charge even after the system is switched off. Individuals who install and repair the laser arc hybrid welding system must use appropriate procedures, tools, and protective equipment. They may require electric safety-related work practice training. It also must be ensured that the equipment has the correct current capacity. An isolation switch must also be provided to avoid any spark that may cause a fire hazard in the presence of any flammable substance. Fumes are produced during laser arc hybrid welding which may cause discomfort, suffocation, and poisoning depending on the use of shielding gas, work materials composition, atmospheric

condition, generated heat, and any presence of volatile substances, etc. Sometimes depletion of oxygen due to the use of high-pressure shielding gases may cause suffocation, especially in a confined region. Gases produced during welding such as carbon monoxide, ozone, and nitrogen oxides are toxic. The fumes from some metals such as lead, copper, chromium, manganese, zinc, cadmium, and beryllium are toxic [81]. Thus, a proper ventilation system shall be provided with the provision of a local exhaust system to remove the fumes from the working zone to avoid a hazard. Special respiratory protection may be required when welding galvanized metal or when cadmium is present in the welding rod.

9.9 CONCLUSION

The laser arc hybrid welding process combines arc welding with laser welding in the common interaction zone. The synergic effects of the laser beam and the electric arc in the same weld pool results in an increase of welding speed and penetration depth along with the enhancement of gap-bridging capability and process stability. Because of its numerous process advantages, higher productivity, and better weld quality as compared to laser welding or arc welding, it is an attractive alternative for different industries. Laser arc hybrid welding has been demonstrated as far back as the late 1970s, but only received much attention this century. A number of laser arc hybrid welding processes have been developed based on the combination of different laser sources (CO_2 laser, Nd:YAG laser, fiber lasers, etc.) and arc welding (MIG/MAG, TIG, PAW, SAW, etc.) systems. Laser arc hybrid welding can be used to weld a wide variety of metals from ferrous metals such as steels and stainless steels to the nonferrous metals such as aluminum, magnesium, copper, nickel, titanium, and their alloys.

Hybridization of the welding processes results in the evolution of some new parameters in addition to the control parameters of the individual processes. Thus a large number of process parameters must be controlled simultaneously. The desired benefits of hybrid welding can only be achieved if the laser welding and arc welding processes are suitably combined and the parameters are optimized. In laser arc hybrid welding, the laser power is the main source of the heat that produces the keyhole and ensures deep penetration welding. The laser-to-arc separation distance is typically kept from 0 to 3 mm, depending on the types of laser parameters, arc welding parameters, and materials used. The best results are obtained for a laser-to-arc separation distance of 1–2 mm. Due to the high welding speed used in

laser arc hybrid welding, the wire feed rate is set at a higher value which requires a higher current rating to maintain the arc length at equilibrium. The shielding gas composition influences the arc characteristics, the formation of weld profile, and the mode of metal transfer. Laser arc hybrid welding can bridge a joint gap up to a few millimeters depending on the selection of material thickness and welding parameters. The laser-to-arc energy ratio, laser arc distance, welding speed, and wire feed rate are the critical parameters that determine the rate of deposition of the filler materials to fill the joint gap. The simultaneous action of joint filling by filler deposition using arc welding and deep penetration by laser requires a different joint design for laser arc hybrid welding. Metal plates of less than 6–8 mm thickness do not require edge preparation for welding using laser arc hybrid welding. The grooves used in thick metal plates for laser arc hybrid welding generally have a smaller include angle, a narrow root opening, and a larger land thickness as compared to the grooves used in arc welding.

The steel plates of thickness up to 25 mm are successfully welded using laser arc hybrid welding in a single pass with a welding speed of 1 m/min. Plates with higher thicknesses can also be welded at favorable weld conditions using multiple weld passes and optimum joint gap. As compared to autogenous laser welding, the laser arc hybrid welding process is 50%–100% faster. It is observed that a small joint gap is beneficial for hybrid welding, and maximum welding speed is achieved for a gap of 0.6–1 mm. Use of laser arc hybrid welding may reduce the cost of welding up to 50% while increasing productivity up to 50%. It may also minimize the effort required for edge preparation and control of seam width. The use of a secondary heat source reduces the laser power requirement, therefore reducing the direct cost. High welding speed, better seam quality, requirement of fewer weld passes and less filler materials due to deep penetration also make this process more economical than arc welding and laser welding. High quality welds with perfectly acceptable mechanical properties and enhanced fatigue properties are obtained for laser arc hybrid welding. The use of the laser arc hybrid welding process results in considerable reduction of pores, cracks, and other defects in welds. The weld bead formed by using laser arc hybrid techniques has better ductility than that formed by using laser welding.

The growing number of industrial applications proved the potential of this process for commercial use. The major applications of laser arc hybrid welding are found in the automobile and shipbuilding industries. The laser arc hybrid welding process also found its application in these industries:

aerospace, rolling stock, container manufacturing, offshore, construction, pipeline production, heavy engineering, energy sectors, etc.

REFERENCES

[1] W.M. Steen, M. Eboo, J. Clarke, Arc augmented laser welding, in: Proc. of the 4th International Conference on Advances in Welding Processes, 1978, 1, Harrogate, UK, 1978, pp. 257–265.

[2] J.F. Ready, Industrial Applications of Lasers, second ed., Academic Press, London, 1997.

[3] P. Seyffarth, I.V. Krivtsun, Laser-Arc Processes and Their Applications in Welding and Material Treatment, Taylor & Francis, London, 2002.

[4] H. Cui, I. Decker, J. Ruge, Wechselwirkungen zwischen WIGSchweißlichtbogen und fokussiertem Laserstrahl, in: Proc. of the Conference Laser'89, Springer, Berlin, 1989, pp. 577–581.

[5] K.H. Magee, V.E. Merchant, C.V. Hyatt, Laser assisted gas metal arc weld characteristics, in: Proc. of the Laser Materials Processing Conference ICALEO'90, Boston, USA, 1990, pp. 382–389.

[6] B.R. Finke, F. Stern, I. Decker, Auswirkungen eines unterstützenden Laserstrahls auf den WIG-Schweißprozess, DVS-Ber. 135 (1991) 149–152.

[7] U. Dilthey, F. Lüder, A. Wieschemann, Expanded capabilities in the welding of aluminium alloys with the laser-MIG hybrid process, Aluminium 75 (1999) 64–75.

[8] U. Dilthey, A. Wieschemann, Prospects by combining and coupling laser beams and arc welding processes, Riv. Ital. Saldatura 52 (6) (1999) 749–759.

[9] T. Graf, H. Staufer, Laser Hybrid Process at Volkswagen, International Institute of Welding, 1999. IIW-Doc. XII-1730-02.

[10] U. Dilthey, F. Lueder, A. Wieschemann, Technical and economical advantages by synergies in laser arc hybrid welding, Weld. World 43 (1999) 141–152.

[11] D. Petring, C. Fuhrmann, Recent progress and innovative solutions for laser-arc hybrid welding, in: Proc. of the 1st Pacific International Conference on Application of Lasers and Optics, Melbourne, Australia, 2004, pp. 7–10.

[12] Fronius International GmbH, https://www.fronius.com/cps/rde/xchg/SID-F92B902E-920234D8/fronius_international/hs.xsl/79_687_ENG_HTML.htm#.WLQh5dR97Gg.

[13] ESAB, http://www.esab.com/automation/en/process/Hybrid-Laser-Welding.cfm.

[14] Carl Cloos Schweisstechnik GmbH, http://www.cloos.de/de-en/products/qineo/laser-hybrid-weld/.

[15] Laser Trader Limited, http://www.lasertrader.co.uk/index.php/products/precitec-roducts/laser-welding-heads/yh50-hybrid-welding-head/. S. Tsubota T. Ishide M. Watanabe T. Akaba Laser welding system for various 3-d welding—development of coaxial laser welding head, Mitsubishi Heavy Industries Ltd, Tech. Rev.42(2)(2005).https://www.mhi.co.jp/technology/review/pdf/e422/e422086.pdf.

[16] T. Ishide, S. Tsubota, M. Watanabe, Latest MIG, TIG, arc-YAG laser hybrid welding systems for various welding products, in: Proc. of 1st International Symposium on High-Power Laser Macroprocessing, (SPIE 2003), 4831, Osaka, Japan, 2002, pp. 347–352.

[17] K. Nilsson, S. Heimbs, H. Engström, A.F.H. Kaplan, Parameter influence in CO_2-laser/MIG hybrid welding, in: Proc. of 56th Annual Assembly of the International Institute of Welding, 2003, IIW Doc. IV-843-03, Bucharest, Romania, 2003.

[18] S.E. Nielsen, M.M. Andersen, J.K. Kristensen, T.A. Jensen, Hybrid Welding of Thick Section C/Mn Steel and Aluminium, International Institute of Welding, 2002, IIW doc. XII 1731-02.

[19] Y. Naito, S. Katayama, A. Mastsunawa, Keyhole behaviour and liquid flow in molten pool during laser-arc hybrid welding, in: Proc. of 1st International Symposium on

High-Power Laser Macroprocessing, 2002, (SPIE 2003), 4831, Osaka, Japan, 2002, pp. 357–362.
[20] C. Emmelmann, M. Kirchhoff, N. Petri, Development of plasma-laser-hybrid welding process, Phys. Procedia 12 (2011) 194–200.
[21] F. Möller, C. Thomy, Interaction effects between laser beam and plasma arc in hybrid welding of aluminum, Phys. Procedia 41 (2013) 81–89.
[22] C.H. Kim, Y.N. Ahn, J.H. Kim, CO_2 laser micro plasma arc hybrid welding for galvanized steel sheets, Trans. Nonferrous Met. Soc. China 21 (2011) s47–s53.
[23] W.V. Vaidya, K. Angamuthu, M. Koçak, R. Grube, J. Hackius, Strength and fatigue resistance of laser-MIG hybrid butt-welds of an airframe aluminium alloy AA6013, Weld. World 50 (11/12) (2006) 88–97.
[24] C. Bagger, F. Olsen, Comparison of plasma, metal inactive gas (MIG) and tungsten inactive gas (TIG) processes for laser hybrid welding, in: Proc. of the Laser Materials Processing Conference ICALEO 2003, Jacksonville, USA, 2003, pp. 13–17.
[25] P.G. Sanders, J.S. Keske, K.H. Leong, G. Kornecki, High power Nd:YAG and CO_2 laser welding of magnesuim, J. Laser Appl. 2 (11) (1999) 96–103.
[26] K.G. Watkins, Laser welding of magnesuim alloys, magnesuim technology, in: MS Annual Meeting and Exhibition, 2003, San Diego, USA, 2003, pp. 153–156.
[27] T. Ishide, S. Tsubota, M. Watanabe, K. Ueshiro, Development of YAG Laser and Arc Hybrid Welding Method-Development of Various TIG-YAG and MIG-YAG Welding Methods, International Institute of Welding, 2002, IIW doc. XII-1705-02.
[28] C.M. Allen, G. Verhaeghe, P.A. Hilton, C.P. Heason, P.B. Prangnell, Laser and hybrid laser-MIG welding of 6.35 and 12.7 mm thick aluminium aerospace alloy, Mater. Sci. Forum 519–521 (2006) 1139–1144.
[29] S. Katayama, Y. Kawahito, M. Mizutani, Laser welding and hybrid welding of aluminium alloys, in: Proc. of the 12th International Conference on Aluminium Alloys, Yokohama, Japan, 2010, pp. 908–914.
[30] C. Thorny, Application of high power fibre laser in laser and laser-MIG welding of steel and titanium, Weld. World 46 (9s) (2005) 88–98.
[31] C. Li, K. Muneharua, S. Takao, H. Kouji, Fiber laser-GMA hybrid welding of commercially pure titanium, Mater. Des. 30 (2009) 109–114.
[32] C.E.A. Walsh, Characteristics of high-power diode-laser welds for industrial assembly, J. Laser Appl. 15 (2) (2003) 68–76.
[33] A. Fellman, P. Jernstrøm, V. Kujanpää, The effect of shielding gas composition in hybrid welding of carbon steel, in: Proc. of the 9th Nordic Laser Materials Processing Conference, Trondheim, Norway, 2003, pp. 103–112.
[34] S. Webster, J.K. Kristensen, D. Petring, Joining of thick section steels using hybrid laser welding, Ironmak. Steelmak. 35 (7) (2008) 496–504.
[35] M. Ono, Y. Shinbo, A. Yoshitake, M. Ohmura, Development of laser-arc hybrid welding, NKK Tech. Rev. (2002) 70–74.
[36] S. Shi, Laser and hybrid laser MAG welding of thick section C-MN steel, in: Proc. of the 2005 International Forum on Welding Technologies in Energy Engineering, Shanghai, China, 2005.
[37] P.T. Swanson, C.J. Page, E. Read, H.Z. Wu, Plasma augmented laser welding of 6 mm steel plate, Sci. Technol. Weld. Join. 12 (2) (2007) 153–160.
[38] Y. Chen, Z. Lei, L. Li, L. Wu, Experimental study on welding characteristics of CO_2 laser TIG hybrid welding process, Sci. Technol. Weld. Join. 11 (4) (2006) 403–411.
[39] J.L. Arias, A. Vandewynckele, J. Vazquez, P. Romero, Laser TIG hybrid welding of very thin austenitic stainless steel sheet, in: Proc. of the Laser Materials Processing Conference ICALEO 2005, Miami, USA, 2005, pp. 104–107.
[40] E. Bayer, B. Brenner, R. Poprawe, Hybrid laser welding techniques for enhanced welding efficiency, in: Proc. of the Laser Materials Processing Conference ICALEO'96, Detroit, USA, 1996, pp. 157–166.

[41] H.B. Cary, S.C. Helzer, Modern Welding Technology, sixth ed., Pearson, NJ, 2005.
[42] U. Reisgen, S. Olschok, Laser-submerged arc hybrid welding, Paton Weld. J. 4 (2009) 38.
[43] D.M. Gureev, A.E. Zaikin, A.B. Zolotarevsky, Method of laser-arc material processing and its applications, Trans. Phys. Inst. USSR Acad. Sci. 198 (1989) 41–61.
[44] U.A. Dilthey, U. Wiesschemann, Prospective offered by combining and coupling laser beam and arc welding, Weld. Int. 16 (9) (2002) 711–719.
[45] W.M. Steen, M. Eboo, Arc augmented laser welding, Met. Construct. 11 (7) (1979) 332–335.
[46] C. Bagger, F.O. Olsen, Review of laser hybrid welding, J. Laser Appl. 17 (1) (2005) 2–14.
[47] Y. Chen, Q. Xu, Y. Su, Welding application of combined laser coaxial arc heat source, Trans. China Weld. Inst. 16 (4) (1995) 239–242.
[48] W.M. Steen, Arc augmented laser processing of materials, J. Appl. Phys. 51 (11) (1980) 5636–5641.
[49] L. Liu, X. Hao, G. Song, A new laser-arc hybrid welding technique based on energy conservation, Mater. Trans. 47 (6) (2006) 1611–1614.
[50] M. Gao, X.Y. Zeng, Q.W. Hu, Effects of welding parameters on melting energy of CO_2 laser-GMA hybrid welding, Sci. Technol. Weld. Join. 11 (5) (2006) 517–522.
[51] M. El Rayes, C. Walz, G. Sepold, The influence of various hybrid welding parameters on bead geometry, Weld. J. 83 (5) (2004) 147s–153s.
[52] C.V. Hyatt, K.H. Magee, J.F. Porter, V.E. Merchant, J.R. Matthews, Laser-assisted gas metal arc welding of 25-mm-thick HY-80 plate, Weld. J. 80 (7) (2001) 163s–172s.
[53] M. Kutsuna, L. Chen, Interaction of Both Plasma in CO_2 Laser—MAG Hybrid Welding of Carbon Steel, International Institute of Welding, 2002, IIW document, XII 1708-02.
[54] M. Gao, X. Zeng, Q. Hu, Effects of gas shielding parameters on weld penetration of CO_2 laser-TIG hybrid welding, J. Mater. Process. Technol. 184 (2007) 177–183.
[55] E. Beyer, R. Imholff, J. Neuenhahn, K. Behler, New aspects in laser welding with an increased efficiency, in: Proc. of the Laser Materials Processing Conference ICALEO'94, Orlando, USA, 1994, pp. 183–192.
[56] F. Möller, H. Kügler, S.F. Goecke, Laser-GMA-hybrid welding of high strength multimaterial joints, in: Proc. of the 3rd International WLT-Conference on Lasers in Manufacturing Conference 2015, Munich, Germany, 2015.
[57] G. Campana, A. Fortunato, A. Ascari, G. Tani, L. Tomesani, The influence of arc transfer mode in hybrid laser-MIG welding, J. Mater. Process. Technol. 191 (2007) 111–113.
[58] C. Bagger, B.D. Wiwe, N.A. Paulin, F.O. Olsen, Closing the weld gap with laser/MIG hybrid welding process, in: Proc. of the 9th Nordic Laser Materials Processing Conference, Trondheim, Norway, 2003, pp. 113–124.
[59] H. Staufer, Laser hybrid welding in the automotive industry, Weld. J. 86 (2007) 36–40.
[60] D. Petring, C. Fuhrmann, N. Wolf, R. Poprawe, Investigations and applications of laser-arc hybrid welding from thin sheets up to heavy section components, in: Proc. of the Laser Materials Processing Conference ICALEO 2003, Jacksonville, USA, 2003, pp. 1–10.
[61] J. Matsuda, A. Utsumi, M. Katsumura, M. Hamasaki, S. Nagata, TIG or MIG arc augmented laser welding of thick mild steel plate, Join. Mater. 1 (1988) 31–34.
[62] T. Graf, H. Staufer, Laser-hybrid welding drives VW improvements, Weld. J. 82 (2003) 42–48.
[63] E.W. Reutzel, M.J. Sullivan, D.A. Mikesic, Joining pipe with the hybrid laser-GMAW process: weld test results and cost analysis, Weld. J. 85 (6) (2006) 66–71.
[64] S. Fujinaga, R. Ohashi, S. Katayama, A. Matsunawa, Improvements of welding characteristics of aluminum alloys with YAG laser and TIG arc hybrid system, in: Proc. of the 1st International Symposium on High-Power Laser Macroprocessing, (SPIE 2003), 4831, Osaka, Japan, 2002, pp. 301–306.

[65] S. Olschok, U. Reisgen, U. Dilthey, Robot application for laser-GMA hybrid welding in shipbuilding, in: Proc. of the Laser Materials Processing Conference ICALEO 2007, Orlando, USA, 2007, pp. 308–315.
[66] C. Walz, I.S. Springer, M. El Rayes, T. Seefeld, G. Sepold, Hybrid welding of steel for offshore applications, in: Proc. of the 11th International Offshore and Polar Engineering Conference, Stavanger, Norway, 2001.
[67] H. Staufer, Laser hybrid welding and laser brazing: State of the art in technology and practice by the examples of the Audi A8 and VW-Phaeton, in: Proc. of the 3rd International WLT-Conference on Lasers in Manufacturing Conference 2015, Munich, Germany, 2015, pp. 203–208.
[68] M. Lee, W. Chang, Y. Kweon, D. Lee, Laser-MIG hybrid weldability of high strength steel for car industry, in: Proc. of the Laser Materials Processing Conference ICALEO 2005, Miami, USA, 2005, pp. 134–142.
[69] F. Roland, T. Reinert, G. Pethan, Laser welding in ship building—an overview of the activities at Meyer Werft, in: Proc. of the IIW International Conference in Connection with Annual Assembly 2002, Copenhagen, Denmark, 2002, pp. 103–115.
[70] C.H.J. Gerritsen, J. Weldingh, J.K. Kristensen, Development of Nd:Yag laser-MAG hybrid welding of T joints for shipbuilding, in: Proc. of the 10th Nordic Laser Materials Processing Conference, Lulea, Sweden, 2005, pp. 395–406.
[71] U. Jasnau, A. Sumpf, Laser hybrid welding with high power fiber laser—new chances for use of laser technology, in: Proc. of the Nordic Welding Conference 2006, Tampere, Finland, 2006.
[72] N.J. Orozco, Fully integrated hybrid-laser welding control process, processes for laser hybrid welding, in: Proc. of the Laser Materials Processing Conference ICALEO 2003, Jacksonville, USA, 2003, pp. 31–40.
[73] D. Petring, C. Fuhrmann, N. Wolf, R. Poprawe, Progress in laser-MAG hybrid welding of high-strength steels up to 30 mm, in: Proc. of the Laser Materials Processing Conference ICALEO 2007, Orlando, USA, 2007, pp. 300–307.
[74] J. Adamiec, M. Więcek, W. Gawrysiuk, Fibre laser usage in boiler elements' production for the power industry, Weld. Int. 24 (11) (2010) 853–860.
[75] P. Jernstrøm, Hybrid welding of hollow section beams for a telescopic lifter, in: Proc. of the 1st International Symposium on High-Power Laser Macroprocessing, (SPIE 2003), 4831, Osaka, Japan, 2002, pp. 353–356.
[76] D.K. Bandopadhyay, Laser safety, in: Proc. of the Seminar on Application of Laser in Materials Processing (WALMI 2000), Kolkata, India, 2000, pp. 28–45.
[77] ANSI Z136.1:1993, American National Standard for Safe Use of Lasers, 1993.
[78] ISO 10882-1:2011, Health and safety in welding and allied processes—sampling of airborne particles and gases in the operator's breathing zone—Part 1: sampling of airborne particles, 2011.
[79] ISO 10882-2:2011, Health and safety in welding and allied processes—sampling of airborne particles and gases in the operator's breathing zone—Part 1: sampling of gases, 2011.
[80] IS 818:1968, Code of practice for safety and health requirements in electric and gas welding and cutting operations (first revision), 1968.
[81] Department of Labor, Health and Safety in Welding, Department of Labor, Wellington, New Zealand, ISBN: 0-478-28075-0, 2006.

CHAPTER 10

Influencing the Weld Pool During Laser Welding

S. Nothdurft, A. Springer, S. Kaierle
Laser Zentrum Hannover e.V., Hannover, Germany

10.1 INTRODUCTION

The motives for influencing the weld pool during laser-beam welding of metals are numerous: welding dissimilar material joints, influencing the macrostructure, and control over the solidification or grain orientation require intervention in the welding process. In the following chapter, various methods, their motivation, and the results of the relevant research are presented and summarized. This is preceded by a brief introduction to continuous laser-beam welding.

10.1.1 Weld-Pool Flow During Laser-Beam Welding of Metals

The primary flow in the weld pool is produced by the welding process itself. In deep-penetration laser-beam welding of metals with high surface power densities, a keyhole is formed, due to the pressure of the metal vapor that rises (Fig. 10.1). This keyhole is surrounded by the molten mass. At the front of the keyhole, the material melts and then flows around the keyhole on both sides and solidifies behind it. This dynamic process is produced by the movement of the keyhole across the workpiece, whereby the flow velocity can be higher than the welding speed [1], and it sinks at the edge of the weld pool. Furthermore, there are dynamics caused by the friction between the escaping metal vapor and the keyhole wall [2].

A further important dynamic force the Marangoni flow, was initially assigned only to heat-conduction welding. Fuhrich et al. [3] demonstrated in experiments and through simulation that the effect is also important in deep-penetration welding. The thermal energy introduced during the laser-welding process is dissipated by convection and conduction. Conduction is based on the temperature difference in the molten mass, whereby the heat transport is diffusive. The warmest point of the weld pool lies in the middle of the process zone, where the direct entry of the laser

Advances in Laser Materials Processing
https://doi.org/10.1016/B978-0-08-101252-9.00010-8
Copyright © 2018 Elsevier Ltd.
All rights reserved.

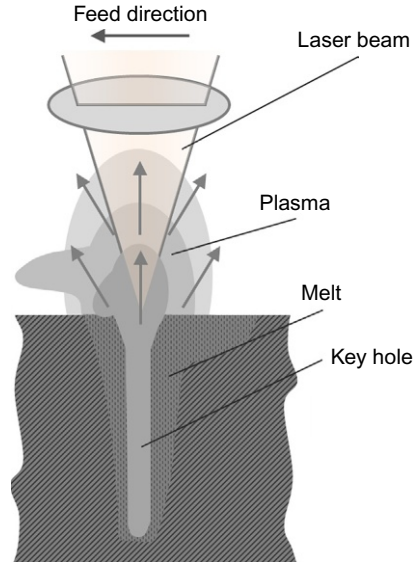


Fig. 10.1 Schematic drawing: laser-beam welding process.

beam is located. The temperature decreases towards the edge, resulting in a thermal gradient. In convective heat transport, due to density differences, the heat is dissipated by a dynamic force that overlays conduction. This causes a change in the temperature distribution, and consequently a change in the gradient. Since the surface temperature has a direct influence on the surface tension and viscosity, a compensation flow is generated here. In this process, the surface tension drops as the temperature rises. The so-called Marangoni convection is induced by the surface tension gradient, and has direct effects on the shape of the weld pool. This can be documented during the welding process by means of the temperature distribution in the weld pool. Fig. 10.2 shows the relationship between the direction of the surface tension gradients and the flow in the weld pool. A negative gradient leads to wide and flat seams, a positive gradient to narrow and deep seams [4].

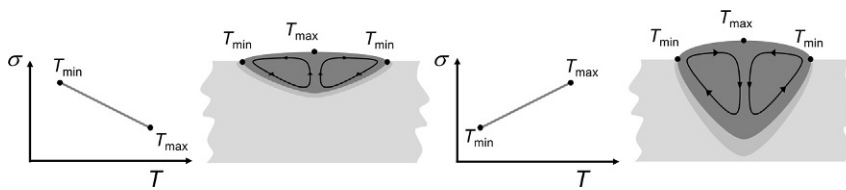


Fig. 10.2 Marangoni convection: relationship between surface tension σ and weld-pool flow direction.

With pure metals, the surface tension usually decreases with the temperature. This means that in the middle around the keyhole there is high surface tension, while it is low around the periphery [5].

The molten mass is a highly dynamic system to be considered as an incompressible fluid in which three (or four) aggregate states are juxtaposed. Depending on the vapor pressure of the capillary, the weld-pool form, gravity, and the surface tension, the keyhole will be constricted without regularly recurring manipulation. A stabilization of the capillary is possible through the deflection of the molten mass from the capillary to the side or backward, in order to avoid constriction [6].

Molten mass ejection and spatter are a result of the weld-pool movement and the resulting upwardly directed pressure from the evaporation of the material. Fluid metal is ejected out of the keyhole, whereby a higher viscosity of the molten mass usually results in an increased spatter tendency.

There is no comprehensive analytical description for the complex flow situation. An overview of the current state of research in the field of laser-beam welding simulation can be found in Dal et al. [7]. A comprehensive overview of keyhole modeling can be found in Svenungsson et al. [8].

Fabbro [9] describes the shape of the weld pool for different welding speeds when using an Nd:YAG solid-state laser ($P = 4\,\text{kW}$, $d_f = 0.6\,\text{mm}$, steel). At welding speeds below 5 m/min, the weld pool is extensive, even in the area in front of the clearly defined cylindrical keyhole. The surface is rather chaotic and is characterized by alternating flow conditions; no clear laminar flow arises. Occurrence of the Marangoni flow is also unlikely. Spatter comes mainly from the keyhole edge due to the limited hydromechanics. If the speed is increased to more than 6 m/min, a single periodic wave (swelling) is formed at the upper end of the keyhole back wall, but here spatter is produced. This oscillating wave is produced by the contradictory effect of the vapor pressure and the weld pool, which attempts to close the keyhole. With a further increase in the speed (9–11 m/min), the expansion of the keyhole is elongated. Vapor is produced in two places. There are also fluctuations in the flow here, but with a lower oscillation of the molten mass, the wave crests are lower. If the feed speed is increased to 12–19 m/min, the keyhole is lengthened, but the overall expansion is less than in the previous case. Only small waves appear in the molten mass. A strong lateral flow arises; the central flow comes from the bottom of the front keyhole wall and is deflected backward. No spatter is discerned. Up to 16 m/min, the seam surface is flush with the surface of the joining partners, since the lateral flows collide with the central flow and push into the center

and upwards. The vapor column is stable and stationary, perpendicular to the front keyhole wall and meeting the upper part of the posterior keyhole wall. At welding speeds of more than 20 m/min, humping occurs behind the keyhole due to instability. The seam is characterized by large ejections and considerable differences between excessively filled and underfilled areas. The flow starts from the floor of the front of the keyhole so that the back-flow velocity is very high.

Other influences on the formation of the weld pool that will not be considered further in the following are, e.g., the beam position and the focus position. The use of different laser beam sources and the amount of power used also have an impact on the shape of the weld pool [10].

10.2 APPROACHES AND METHODS FOR MANIPULATING WELD-POOL DYNAMICS

In the following, various methods, research approaches, and their results for influencing weld-pool dynamics are presented. The sections are subdivided into electromagnetic and vibrational as well as ultrasound manipulation. In addition, the influence on the molten mass through the introduction of alloying elements and the use of process gases will be discussed.

10.2.1 Weld-Pool Manipulation Using Electromagnetic Forces

Electromagnetic forces can influence the quality and stability when welding aluminum using high-power laser beam sources. In this case, a reduction of root sagging [11]and surface roughness as well as a reduction in the number of spatters and pores [12] can be achieved through the removal of the gas bubbles in the molten mass by using electromagnetic separation [13]. The influence of the Lorentz force of the magnetic field on the weld pool is used in this case (see Fig. 10.3). Gatzen [14] has shown that a coaxial magnetic field has an effect on the horizontal component of the weld pool flow by using low-frequency magnetic fields to influence the weld pool mixing in welding tests with filler wire containing silicon.

Magneto fluid dynamics is concerned with the forces and movements of fluids in magnetic fields. Two effects are known: a change in the velocity profile and the reduction of turbulence [15]. When electrically conductive fluid media (molten mass) flow through a magnetic field oriented transversely to the direction of flow, the velocity profile is weakened proportionally to the increasing strength of the magnetic field. This phenomenon is known as the Poiseuille-Hartmann flow. The Lorentz force (a cross product

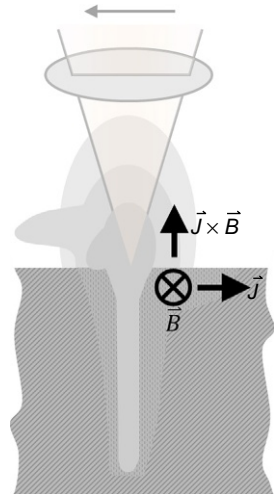


Fig. 10.3 Schematic drawing: electromagnetic weld-pool manipulation (Lorentz force).

of magnetic field and current density $\vec{j}$) acts on moving charge carriers in a magnetic field $\left(\vec{B}\right)$. It achieves its greatest value when the motion is perpendicular to the field lines, and it is 0 when moving along the field lines. In order for the Lorentz force to have a positive effect, the surface tension of the molten mass must be high enough. Otherwise, spatter arises from the detachment of drops [6]. The Hartmann number $Ha = B \cdot l \cdot \sqrt{\frac{\sigma_e}{\eta}}$ can be used as a reference or measure for the influence of the static magnetic field on the flow [16]. σ_e is the electrical conductivity, η is the dynamic viscosity, and l is the characteristic length scale. As the magnetic field increases, the influence increases. The Hartmann number and thus the influence of the magnetic field on the flow are significantly higher for aluminum than for iron [15]. The greatest influence is thus exerted by the magnetic flux density. For oscillating magnetic fields, the frequency and penetration depth are also decisive, whereby direct current achieves positive and alternating current achieves rather negative results [6]. The skin effect for higher-frequency alternating current states that the current density inside the conductor is lower than in the outer regions due to damping. Two different ways of introducing electric current into the weld pool can be distinguished: conduction introduces current and a magnetic field from the outside while induction generates a current in the material through an applied magnetic alternating field [17]. In welding experiments and process simulation with

low-frequency magnetic fields to influence the weld-pool modulation, the dynamics in the weld pool are increased both in the case of the DC field, and in the case of low-frequency AC fields. Frequency has a significant impact. The primary direction of the volume forces remains the same in the process, and dampens the horizontal flow component. Mixing was investigated using a filler material containing silicon. Mixing is also largely determined by the superimposition of process-induced interference [18]. When forming the weld pool using electromagnetic forces, the direction of the magnetic field has a decisive influence on the shape of the weld seam [19]. The flow can be laminarized and the speed distribution can be changed.

Fig. 10.4 shows the influence of electromagnetic weld-pool support. Initially, without support, there is root sagging and a slight seam undercut. In the middle case with optimal parameters, there is no root sagging and a slight weld reinforcement on the upper surface. If the power becomes excessive, a root undercut develops [11].

For aluminum bead-on-plate welds, the surface quality can be improved by 50% and the occurrence of pores reduced by 80% [20]. A magnetic alternating field (up to 0.4T and 10 kHz) suppresses pores and stabilizes the surface (aluminum) [13]. For CO_2 laser beam welding, electric and magnetic fields have an influence on the plasma and its shielding effect, and the welding penetration depth is increased. However, when the magnetic field is too strong, the plasma control becomes again worse [21]. Vollertsen and Thomy [22] use electromagnetic stirring to homogeneously distribute a filler material for hot-crack suppression during laser welding of aluminum without negative influences on the weld seam. A thin copper foil is placed between the materials to be joined (identical aluminum-type joint). The mixing is clearly shown using metallographic preparation. The homogeneity of the seam increases with decreasing welding speed, which is due, inter alia, to

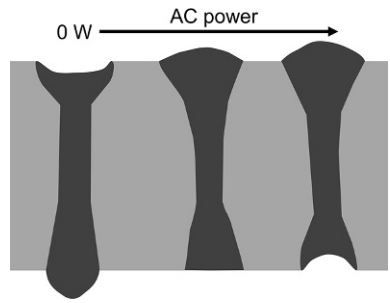


Fig. 10.4 Root formation as a function of AC power according to Fritzsche et al. [11].

the extended time available for mixing. Furthermore, the homogeneity of the molten mass increases with higher frequency and higher flux densities [23]. This introduction of electromagnetic forces using an externally applied current via a filler wire for homogenizing the mixing of the base material and filler material is successful at up to 6 m/min welding speed [2]. Bachmann et al. [24] show in simulations that by inductive support from an AC magnet on the root side in aluminum welds, root sagging is reduced by balancing the hydrostatic pressure, while the convection in the molten mass can be reduced. Here, the magnetic field is at a right angle to the feed direction. The influence of the Marangoni flow is reduced; a vortex formed at the lower rear end of the weld pool counteracts it.

Lindenau assumed why the welding process becomes more "restless" and less stable. Interactions arise within the capillary so that a current flows in the workpiece and in the weld pool. Either the temperature distribution in the plasma or a variably high activation energy (work function) of the electrons at various points of the weld-pool surface is responsible for this current flow. He sees the thermionic discharge as a bonding member, since conductive plasma is necessary for a current flow. When current flows in the molten mass, it can again be influenced by magnetic fields. An interaction of the current with its own magnetic field is also conceivable, and as a result, an electrical vortex flow or an acceleration of the fluid conductor is possible. A current induced by the molten mass movement in the magnetic field has been verified (directionally independent Hartmann effect); its influence is noticeable during welding. Other effects such as grain refinement or improved degassing could not be demonstrated [6].

10.2.2 Weld-Pool Manipulation With Alloying Elements

The molten mass can also be influenced by the addition of alloying elements. Wire-like or powder-like filler materials can be fed during the welding process, or applied as a powder or paste prior to the welding process. The alloying elements present in the material can also have an influence, depending on their concentration. In a hybrid process, wire can be fed through a welding current source. The fusion joining of different materials always results in the formation of a new alloy in the weld pool.

Alloying elements can be divided into three groups: surface active elements, elements that react with surface active elements, and elements that have no significant influence. The surface activity is characterized by

an influence on the surface tension and its gradients, which in turn has an influence on the flow of the molten mass [25]. The silicon content of aluminum materials has an influence on the thickness of the intermetallic phase that forms at the interface between solid aluminum and liquid iron by hot-dip aluminization. As the silicon content increases, the growth rate of the Fe_2Al_5 and $FeAl_3$ phases decreases [26]. Theoretically and experimentally, there is little influence of the sulfur content of a steel base material on the form of the weld pool [27]. A model for gas tungsten arc (GTA) welding, verified by experiments with steel, demonstrates the influence of different alloying elements on the shape of the weld pool. Sulfur, oxygen, selenium, and tellurium are highly surface active elements that increase the weld penetration depth to weld seam width ratio via a positive surface tension. When using elements reacting with surface active elements, the ratio becomes smaller. Aluminum as an alloying element reacts with oxygen and sulfur and produces flatter and wider seams [28].

10.2.3 Weld-pool manipulation via gas feed

The weld pool can also be alloyed with the help of gaseous substances, thus influencing the flow. This includes, for example, the use of an oxygenated shielding gas. For GTA welding of steel, oxygen has a greater impact on the weld depth than the sulfur content of the base material when it is in the weld pool [25]. Experimental studies demonstrate that the width of the weld pool decreases with increasing oxygen and sulfur concentration. The reason for this is the influence on the Marangoni flow, which causes the surface flow to move away from the keyhole. On the keyhole walls, however, this change does not significantly influence the surface flow. Simulations show that the weld penetration depth under O_2 increases, not due to changes in the Marangoni flow, but due to the formation of CO on the keyhole walls, due to the increased pressure in the keyhole [27]. But other influences are also shown by the use of different (shielding) gases. When a surface-active process gas (CO_2) is used, the weld-pool surface becomes oxidized. The Marangoni flow cannot be reversed in this way, but the outflowing component of the flow can be reduced. However, this effect can only be used up to a welding speed of 2–3 m/min [2]. In contrast, Berkmanns et al. explain the modified seam shape when welding with a high-power diode laser as being due to the direction reversal of the flow as a function of the CO_2 content of the ArCO_2 shielding gas [4]. The simulation of a complete through-weld with and without the use of shielding gas shows that the gas supply leads to

a flow of the molten mass toward the rear end of the weld pool. In the process, the weld pool around the keyhole is formed concavely. Thus, the flow generated by the shielding gas assists and enlarges the keyhole, and thereby stabilizes the process. As is also known, this stabilizing effect of the shielding gas also prevents or even suppresses spatters and pores [29].

10.2.4 Weld-Pool Manipulation Through Vibration

A further approach is to introduce vibrations into the weld pool. This method is also used to influence the solidification of castings. When casting an overheated aluminum alloy, excitation with ultrasound (18 kHz) for 15 min demonstrates a positive effect during solidification. The microstructure is finer and degassing is improved [30]. Dommaschk [31] gives a detailed overview of the influence on the structure for the solidification of molten metal by vibration as an alternative to chemical grain refinement. The effect is, on one hand, based on the dynamic nucleation directly from the molten mass, and on the other hand by a multiplication of the nuclei via the breaking off of dendritic branches, which act as nuclei during the solidification process. In pure metals, no distinction can be observed between vibration treated solidified samples and those that have not been manipulated. In the case of eutectic alloys with a considerable rise in temperature in the cooling curve, this can be virtually completely suppressed by vibration. Nucleation is improved as a result of this increase in the supra-cooling. For alloys with a wide solidification interval with a low temperature rise, this is additionally reduced, and the globulitic microstructure is finer. In a red brass alloy (CuSn5Zn5Pb5), acceleration is the most important parameter of the vibration. The casting surface must not be freely accessible. The best properties (mechanical properties and density) can be achieved with a vibration acceleration of $1.5 \times g$ if this is introduced immediately after the mold filling, and is maintained until complete solidification sets in. In lamellar graphite iron, refining of the lamellae and the proliferation of eutectic cells are observed [31]. In aluminum lost-mold casting, when vibrations are introduced, the resulting grains become smaller during acceleration between 1 and $4 \times g$, and the secondary dendrite arms break off. Acceleration of more than $4 \times g$ leads to defects. The probability of the formation of large pores increases, because small pores accumulate through excitation [32]. In a Pb-Sn alloy, the lamellar distance can be increased by 10% during solidification with introduced vibration, but a different growth form of the microstructure was not achieved [33].

In the gas tungsten arc welding process (GTA) of EN AW-7075, a an electric transducer can be used to reduce hot cracking and to improve the microstructure when a frequency of 1000–2050 Hz is introduced. The hardness increases [34]. In contrast, in a nickel alloy (690) Wu [35] generates a reduced number of large dendrites and a randomly distributed grain orientation at a reduced hardness level with vibrations via a vibration system at 48 and 58 Hz.

10.2.5 Weld-Pool Manipulation With Ultrasound

Molten metal can also be influenced with sound frequencies above 20 kHz (ultrasound). Kim et al. introduce ultrasonic vibration laser welding and, using aluminum alloys, show that a better aspect ratio and a higher welding penetration depth can be achieved. The indirect introduction of ultrasound via a piezoelectric transducer improves the quality in terms of cracks and porosity [36]. For bead-on-plate welds in MIG (metal inert gas) welding and GTA welding, the best results were obtained with an excitation of 20 Hz with a ceramic ultrasonic transducer using a λ long waveguide (EN AW-2017A) with a node position at $\frac{3}{4}\lambda$. These include grain refinement and reduced porosity and hardness in the heat-affected zone. An increased amount of precipitates of copper and silicon from the molten mass can be observed, particularly in this position. The seam shape is narrower and deeper for the TIG process and vice versa for the MIG seams. Problems with the supply of shielding gas presumably occurred due to the formation of an air cushion caused by the vibration [37]. For nonvacuum electron beam braze-welding of dissimilar steel-aluminum joints, Jäger [38] uses ultrasound (20 and 40 kHz, indirect coupling via a sonotrode, and direct coupling via a tungsten rod at the sonotrode) to stimulate the weld pool. Influences are clearly detectable as the intermetallic phase is peeled off by cavitation bubbles at interfaces, but immediately forms again. Furthermore, an accumulation of silicon grains in the molten mass can be observed. The mechanical properties are improved, but the binding is worse if the ultrasonic output is too high. Ultrasonic treatment by means of a sonotrode in the casting trough of an aluminum molten mass leads to significantly smaller grain sizes and a refinement of the intermetallic phases (Al_3 (Zr, Ti)) after casting [39].

10.3 ULTRASOUND-ASSISTED LASER-BEAM WELDING

Within the Collaborative Research Centre 1153 ("Process chain to produce hybrid high performance components by Tailored Forming" of the German

Research Association (DFG)), the influence of ultrasonic vibrations on the molten mass during laser beam welding of dissimilar joint materials is investigated in subproject A3.

10.3.1 Motivation

The extent to which indirect ultrasonic coupling into the molten mass is possible, and the influence this ultrasonic excitation has on the weld pool is to be examined with a laser-beam welding device specially developed for this purpose with the possibility of ultrasound coupling into the welding zone. At 20 kHz and small amplitudes in the range of up to 10 µm, altered flow processes should to improve the mixing in the weld pool and the fine-grain formation in steel-steel dissimilar joints. Furthermore, the intermetallic phase formation must be controlled or minimized while the forming phase seams should be dispersed. During the thermal joining of steel and aluminum, these intermetallic phase seams arise in the area of the molten contact zone between the two materials (see Fig. 10.5). Due to their characteristically high hardness values (≥1000 HV) and low ductility, these intermetallic phases, which preferably form at the interfaces, the mechanical properties of the joint despite their small extent.

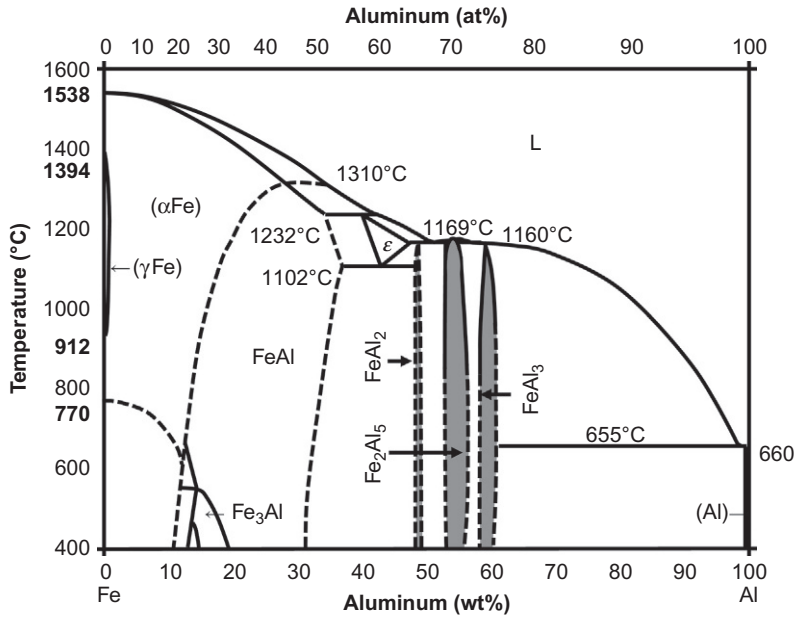


Fig. 10.5 Fe-Al phase diagram based on Baker [40].

10.3.2 Experimental Procedure

In order to couple ultrasound into the weld pool, a device has been developed in which the semi-finished workpieces are part of a vibratory system, see Fig. 10.6. The amplitude of the ultrasonic vibration increases from the converter to the joint. The weld pool is located in the vibration loop so that it is stimulated with the maximum deflection. The position of the laser processing head is fixed, and a motor rotates the oscillating system at welding speed below the processing head, while the focus of the laser beam is on the workpiece surface.

For the tests shown here, steel 20MnCr5 and the aluminum alloy EN AW-6082 in the form of round bars with a diameter of 30 mm and a length of 50 mm were butt welded. For the roughness of the joining surfaces, a mean value of $R_Z = 31.7 \pm 7.3\,\mu m$ was determined for the EN AW-6082 specimens, and $R_Z = 43.3 \pm 12.1\,\mu m$ for the 20MnCr5 steel specimens.

The supply of argon as shielding gas takes place using two shielding gas tubes. The laser beam power ($P_L = 4.5\,kW$), the welding speed ($v_f = 1.5\,m/min$), the focal position ($z = 0$), and the angle of incidence in the welding direction (10 degrees) are constant for all experiments. A first series of experiments (Fig. 10.7) showed the influence of beam displacement (−0.55 to 1.1 mm) on the weld pool formation without using ultrasound. Negative values for the beam displacement mean that the beam is on the aluminum side, at 0 the beam is centered on the joint faces, and positive values indicate displacement towards the 20MnCr5. The welding depth is highest for the centrally positioned case, and decreases in both outward directions. In this case, the good absorption and the high melting point of the steel on one hand, and the lower absorption in combination with a lower melting

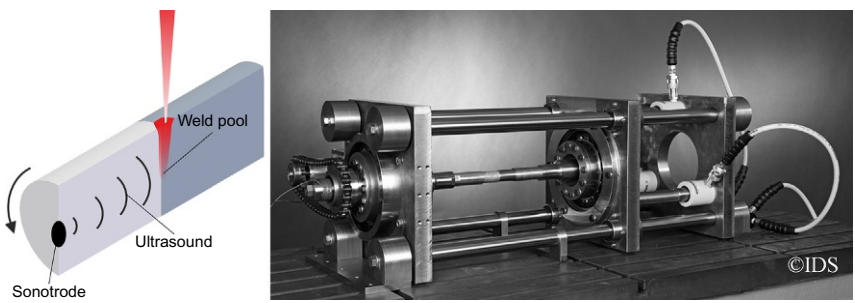


Fig. 10.6 Left: Schematic representation of the principle of the weld-pool influence by means of indirect ultrasonic excitation. Right: Photo of the conversion into an ultrasound-assisted laser welding system (with the kind permission of the Institute of Dynamics and Vibration Research (Hannover, Germany)).

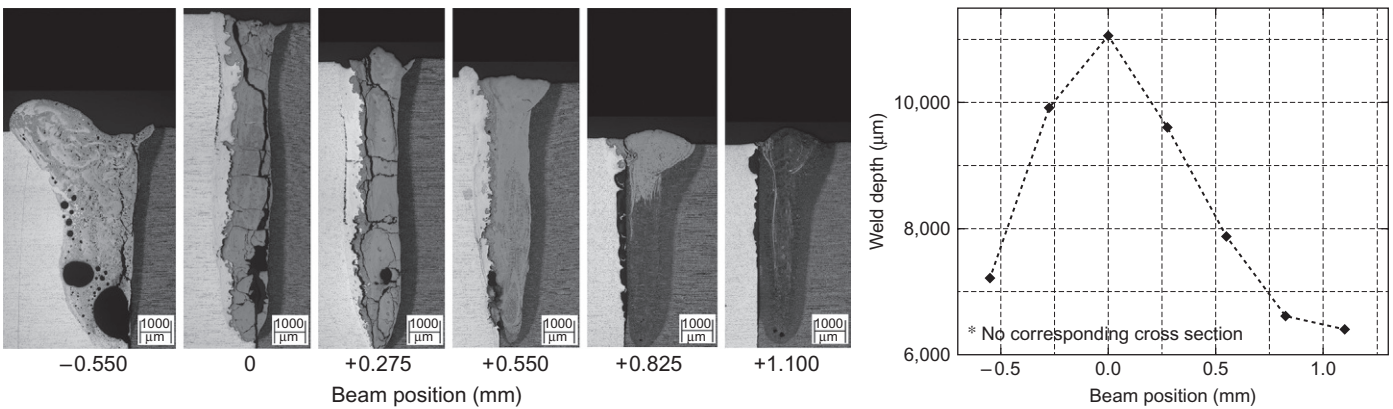


Fig. 10.7 Weld penetration depth as a function of beam displacement: Left: Cross sections, Right: Representation of the weld depth as a diagram; neg. position range: EN AW-6082, pos. position range: 20MnCr5.

point and higher thermal conductivity of the aluminum alloy balance one another out. If the joining zone is moved further towards the steel side, the welding depth decreases, as the energy introduced can only produce a smaller weld pool. The more the displacement to the steel side progresses, the more the amount of the aluminum in the molten mass sinks, simultaneously decreasing the bonding surface. When displaced to the aluminum alloy side, the weld pool is broadened by the horizontal heat dissipation, it is but shallower. The transverse cracking tendency decreases from the central position when it is moved to the steel side. Due to the lowest crack tendency and the best connectivity, the position of 0.55 mm on the steel side was used for subsequent tests. Based on the results of these preliminary tests, the beam was placed 0.55 mm on the steel side for the steel-aluminum dissimilar joints.

Two further test series are shown below. The first is to show the influence of ultrasonic excitation on weld-pool formation for bead-on-plate welds in an aluminum alloy. For the second series, the above mentioned steel-aluminum dissimilar joints were tested in the joining process.

10.3.3 Influence of Ultrasound on the Weld-Pool Formation of Aluminum Bead-on-Plate Welds

First, bead-on-plate welding tests were carried out with EN AW-6082 aluminum alloy in order to consider the influence of ultrasonic excitation on the weld pool isolated in one material without generating a dissimilar joint or the influence of a gap between the joining partners. The excitation is between 0 and 800 mA, which corresponds to a vibration amplitude of 0 µm or approx. 8 µm. The relationship between current intensity and amplitude is to be regarded as linear.

The change in the shape of the welded seam can be clearly seen in the cross sections in Fig. 10.8. The welding penetration depth decreases with an increase of the excitation amplitude. Without ultrasonic excitation and at a lower amplitude, the weld is still uniformly reinforced. As the excitation frequency increases, the weld undercut increases in the middle while material is collected at the edges. The shape of the weld seam changes significantly with high excitation frequencies. The narrow, lower area of the weld seam is missing. The upper part still has a nearly uniform width.

The change in the microstructure of the molten mass is shown in detail in Fig. 10.9. Already in the first line with the least magnification, which is the best overview, there is a clear change in the grain structure. While this is initially rather line-like, it assumes a globulitic shape with increasing

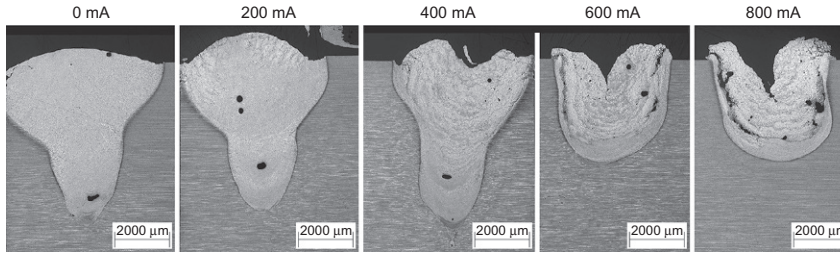


Fig. 10.8 Bead-on-plate welds in EN AW-6082 aluminum with different ultrasonic amplitudes.

amplitude during the welding process. One reason for this is that the solidification is not undisturbed and occurs in a preferential direction to the right and left through heat dissipation. However, when disturbed by oscillation, a constant change of the preferred solidification form or direction is present. The average grain size grows with the increase in amplitude; the size differences of the individual grains also increase significantly. This is especially noticeable in the high magnification in the middle and lower lines.

This shows that ultrasound can be successfully coupled into the molten mass. It has an influence on the resulting microstructure; even small amplitudes of a few microns have an influence on the microstructure.

An examination of the weld seam surface (Fig. 10.10, right), in this case the molten volume measured below the upper edge of the workpiece (Fig. 10.10, left), shows in cross sections that the surface area of the weld metal is reduced with increasing amplitude. Qualitatively, this could be already observed in the seam shape shown in Fig. 10.8.

10.3.4 Influence of Ultrasonic Excitation on the Properties of Steel-Aluminum Dissimilar Joints

In the next step, weld tests were carried out on steel-aluminum dissimilar butt joints (20MnCr5 and EN AW-6082) with different ultrasonic excitation frequencies, in order to study the effects on the mixing of the different materials in the joining zone area. The excitation is also between 0–800 mA; assuming a linear relationship between current intensity and amplitude, this corresponds to an amplitude of 0 µm to approx. 8 µm.

Fig. 10.11 shows, for example, a sample of a welded steel-aluminum dissimilar joint without the use of ultrasound. The welding seam between the two materials can be seen in the center. On the surface there are no cracks. The heat-affected zone of the steel material is visible on the right side.

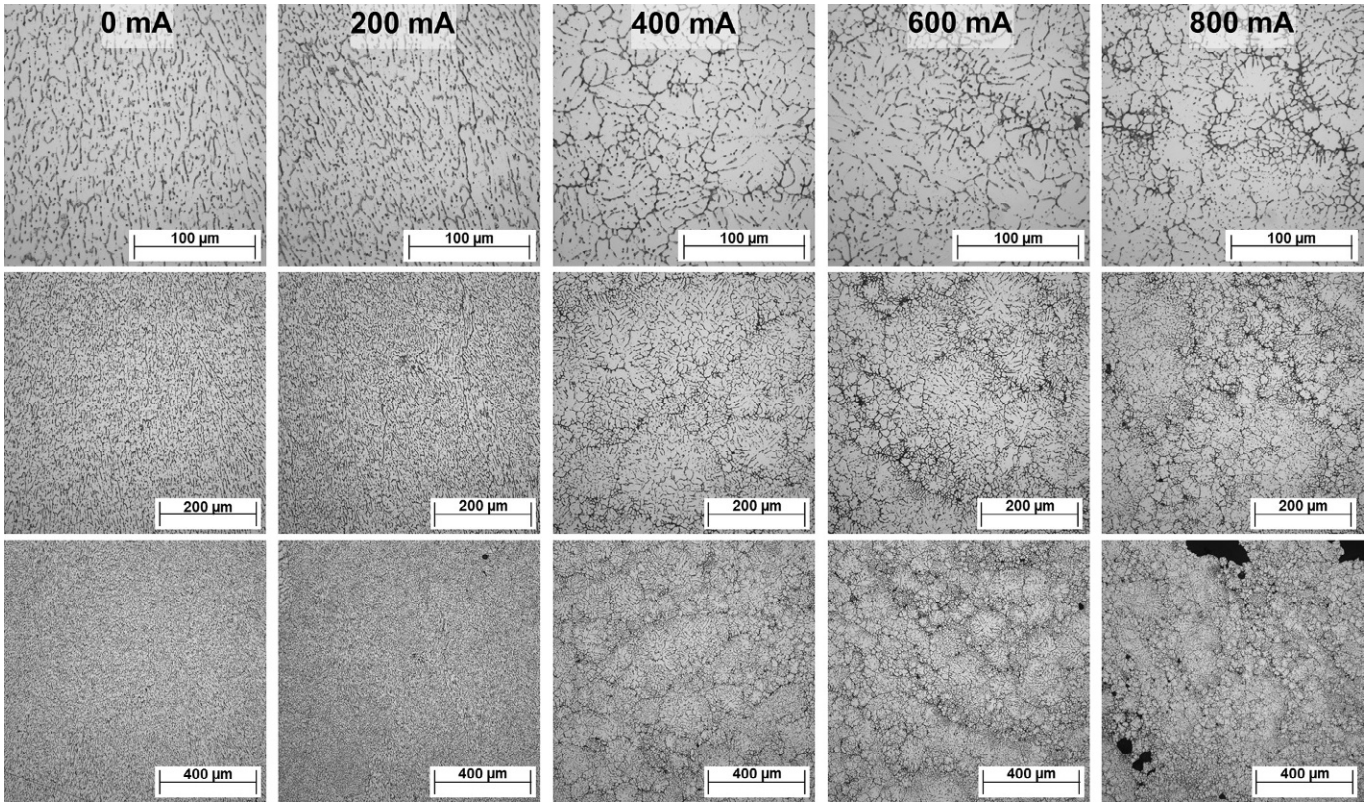


Fig. 10.9 Detailed images of the structure of aluminum bead-on-plate welds in three different magnifications (rising from top to bottom) for five different excitation amplitudes.

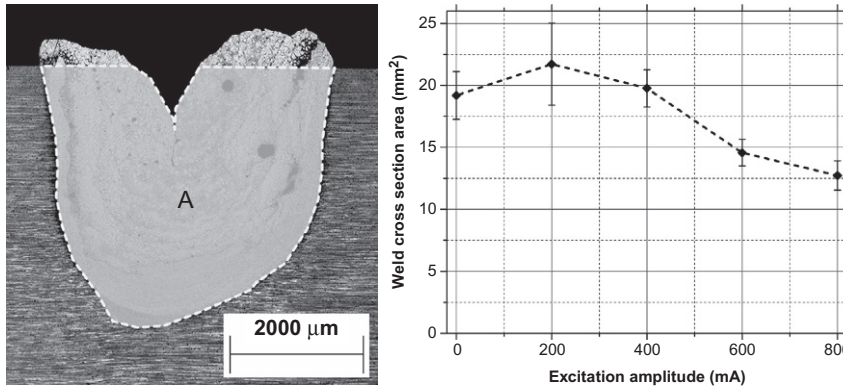


Fig. 10.10 Left: Example of a weld area measurement; Right: Change of the weld surface area as a function of the vibration amplitude in the weld pool.

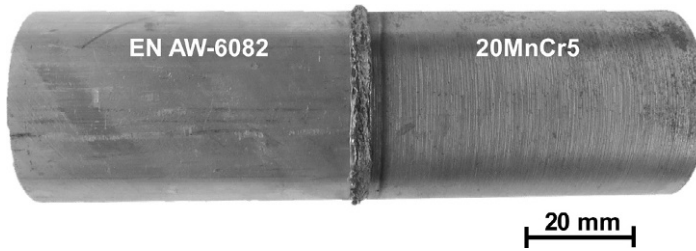


Fig. 10.11 Laser-beam welded joint from EN AW-6082 and 20MnCr5, diameter 30 mm, beam 0.55 mm on the steel side.

Fig. 10.12 shows the effect of the ultrasonic excitation on the weld surface. The weld seam formation without ultrasonic influence (0 mA) can be seen on the left. The volume proportion of the molten mass that is expelled from the welding zone increases as the amplitude increases. The 800 mA sample presents the highest amplitude used. Due to the significantly lower viscosity of the aluminum molten mass compared to the molten steel, this is mostly influenced by this effect. Ultrasonic vibration thus shows a significant influence on weld-pool dynamics.

This statement is supported by the cross sections in Fig. 10.13. Most of the expelled molten mass comes from the aluminum side of the seam. The stronger the excitation, the greater the proportion of the mixed molten mass that is moved. The seam undercut increases with the amplitude. All sections show strong cracking. These are due to the formation of the intermetallic phases which produce cracks via the introduction of stresses.

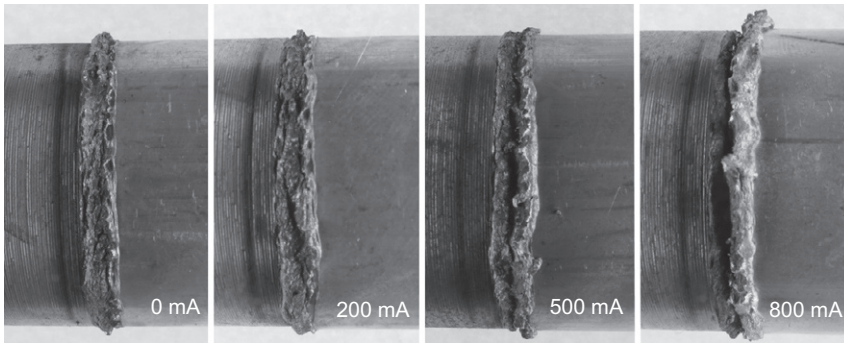


Fig. 10.12 Images of the weld surface with differing ultrasonic excitation.

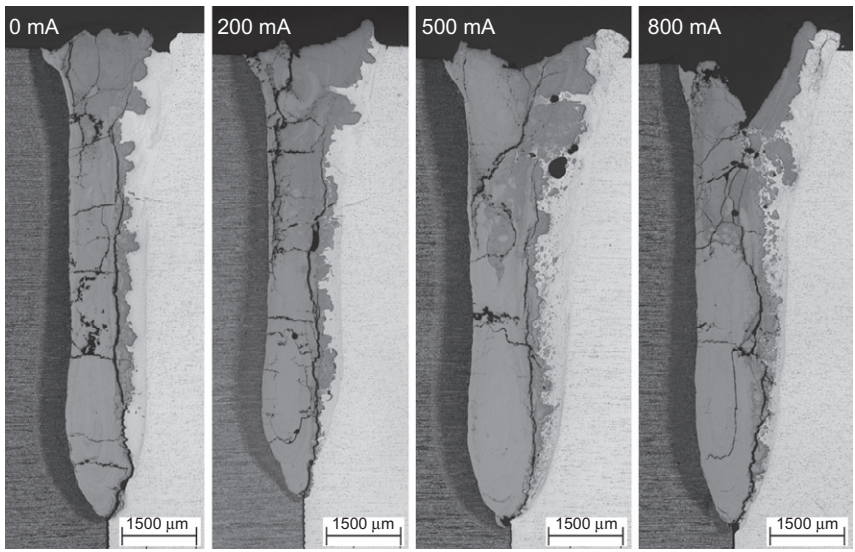


Fig. 10.13 Cross sections of laser beam welded dissimilar material joints with different ultrasonic excitation amplitudes, left steel, right aluminum.

A reduction in crack formation will hopefully be shown in later experiments. Here, only the influence of the ultrasound on the mixing is investigated. Fig. 10.13 also shows the effects of ultrasonic excitation in the molten mass. The stronger the exciting amplitude, the more finely distributed the areas of mixing on the aluminum side. The weld-pool dynamics resulting from this also cause molten mass ejection.

Fig. 10.14 shows enlarged sections of the cross sections from Fig. 10.13, in order to qualitatively show the influence of coupled amplitude on the

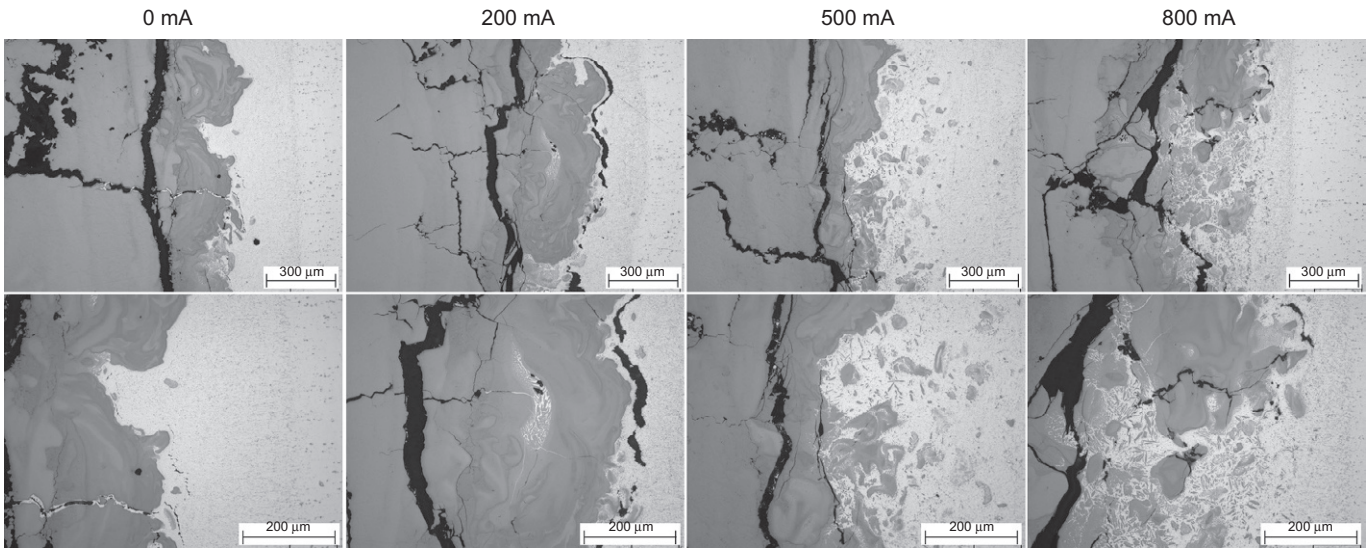


Fig. 10.14 Enlarged sections of the cross sections from Fig. 10.13 with different level ultrasonic excitation ultrasonic excitation amplitudes, left steel, right aluminum.

mixing in the weld pool. As the amplitude increases, the degree of mixing is increased, and the sharp transition between the base material and the mixing area is reduced. Thus, the direct influence of ultrasound on the mixing behavior of the molten mass is hereby verified. The highest amplitude (Fig. 10.14, right) produces, as expected, the highest mixing level. For further experiments, this offers the possibility of reducing the intermetallic phases, and thus reducing the brittleness of the seam and the occurrence of cracks. This could lead to being able to weld dissimilar joints of steel and aluminum in higher material thicknesses, by improving the mechanical properties that can be achieved.

10.3.5 Summary and Outlook

Indirect ultrasonic coupling in the weld pool during laser-beam welding processes on steel-aluminum dissimilar joints has an influence on the seam formation. Weld-pool dynamics are related to the type of vibration. The higher the vibration amplitude, the higher the degree of mixing. When determining suitable amplitude, an average value between (horizontal) deflection and (vertical) expulsion of the molten mass has to be found. With the help of further experiments, in which the relationships between the applied ultrasonic vibration and the degree of mixing and cracking are determined more closely, this approach can lead to an improvement in weldability of dissimilar steel and aluminum joints with high sheet thickness. A scanning electron microscope study will provide further insights into the distribution of the elements and the homogeneity of the distribution as well as the localization of intermetallic phases. The mechanical properties and the distribution and number of cracks and location of crack formation should be determined using a larger number of samples for statistical verification.

The outcome of the larger number of these studies would be an evaluation of the process and a process window in which the properties of the weld can be improved with the support of ultrasonic vibration in the weld pool during laser beam welding of dissimilar joints.

ACKNOWLEDGMENTS

The results presented in Section 10.3 in this chapter were obtained from the Collaborative Research Centre 1153 in subproject A3 "Process chain to produce hybrid high performance components with Tailored Forming." The authors would like to thank the German Research Foundation (DFG) for financial and organizational support of this project.

REFERENCES

[1] M. Beck, P. Berger, F. Dausinger, H. Hügel, Aspects of Keyhole/Melt interaction in high speed laser welding, SPIE 1397 (1990) 769–774.

[2] M. Leimser, F. Dausinger, H. Hügel, Melt pool dynamics and element distribution in laser welding of aluminium alloys with filler wire, in: Proceedings of the 3rd International WLT-Conference on Lasers in Manufacturing, 13–16 June 2005, Munic, 2005, pp. 61–66.

[3] T. Fuhrich, P. Berger, H. Hugel, Marangoni effect in laser deep penetration welding of steel, in: Proceedings of the 18st International Congress on Applications of Lasers & Electro-Optics, ICALEO, 15–18 November 1999, San Diego, CA, 2001, pp. 166–175.

[4] J. Berkmanns, W. Danzer, J. Härtl, Influence of process gases in welding with diode lasers, in: Proceedings of the 21st International Congress on Applications of Lasers & Electro-Optics, ICALEO, 14–17 October 2002, Scottsdale, AZ, 2002.

[5] S. Postma, Weld Pool Control in Nd:YAG Laser Welding, PhD Thesis, Twente, Universiteit Twente, Netherlands, 2003.

[6] D. Lindenau, Magnetisch beeinflusstes Laserstrahlschweißen. (Magnetically assisted laser beam welding), PhD Thesis, Laser in der Materialbearbeitung—Forschungsberichte des IFSW, Utz, 49, 2006 (in German).

[7] M. Dal, R. Fabbro, An overview of the state of art in laser welding simulation, Opt. Laser Technol. 78 (2016) 2–14.

[8] J. Svenungsson, I. Choquet, A.F. Kaplan, Laser welding process: a review of keyhole welding modelling, Phys. Procedia 78 (2015) 182–191.

[9] R. Fabbro, Developments in Nd-Yag laser welding, in: S. Katayama (Ed.), Handbook of Laser Welding Technologies, Woodhead Publishing Limited, Oxford, 2013, pp. 47–72.

[10] M. Sohail, S.-W. Han, S.-J. Na, A. Gumenyuk, M. Rethmeier, Characteristics of weld pool behavior in laser welding with various power inputs, Weld. World 58 (2014) 269–277.

[11] A. Fritzsche, V. Avilov, A. Gumenyuk, K. Hilgenberg, M. Rethmeier, High power laser beam welding of thick-walled ferromagnetic steels with electromagnetic weld pool support, Phys. Procedia 83 (2016) 362–372.

[12] M. Bachmann, V. Avilov, A. Gumenyuk, M. Rethmeier, Experimental and numerical investigation of an electromagnetic weld pool control for laser beam welding, Phys. Procedia 56 (2014) 515–524.

[13] V. Avilov, A. Schneider, M. Lammers, A. Gumenyuk, M. Rethmeier, Electromagnetic control of the weld pool dynamics in partial penetration laser beam welding of aluminium alloys, in: Proceedings of the 31st International Congress on Applications of Lasers & Electro-Optics, ICALEO, 23–27 September 2012, Anaheim, CA, 2012, pp. 250–256.

[14] M. Gatzen, Influence of low-frequency magnetic fields during laser beam welding of aluminium with filler wire, Phys. Procedia 39 (2012) 59–66.

[15] M. Kern, P. Berger, H. Hügel, Magneto-fluid dynamic control of seam quality in CO_2 laser beam welding, Weld. Res. Suppl. (2000) 72s–78s.

[16] H. Yasuda, Applications of high magnetic fields in materials processing, in: S. Molokov, R. Moreau, H.K. Mofatt (Eds.), Magnetohydrodynamics, Springer, Dordrecht, The Netherlands, 2007, pp. 329–344.

[17] G. Ambrosy, P. Berger, V. Avilov, H. Hügel, Reducing porosity in laser welding of aluminium alloys by electromagnetic forces, in: Lasers in Manufacturing 2005, LIM, International WLT-Conference on Lasers in Manufacturing, 3, 2005, pp. 49–54.

[18] M. Gatzen, Durchmischung beim Laserstrahltiefschweißen unter dem Einfluss niederfrequenter Magnetfelder (Dilution in deep-penetration laser beam welding under the influence of low-frequency magnetic fields). Strahltechnik, 55, BIAS Verlag, 2014 (in German).

[19] G. Ambrosy, P. Berger, H. Huegel, D. Lindenau, Improvement of laser beam welding by electromagnetic forces in the weld pool, in: Proceedings of the First International Symposium on High-Power Laser Macroprocessing, 27–31 May 2002, Osaka. Proceedings of SPIE, Bellingham, Washington, 48, 2003, pp. 175–179.

[20] A. Schneider,V. Avilov, A. Gumenyuk, M. Rethmeier, Laser beam welding of aluminium alloys under the influence of an electromagnetic field, Phys. Procedia 41 (2013) 4–11.
[21] H. Tse, H. Man, T. Yue, Effect of electric and magnetic fields on plasma control during CO_2 laser welding, Opt. Lasers Eng. 32 (1999) 55–63.
[22] F. Vollertsen, C. Thomy, Magnetic stirring during laser welding of aluminium, in: Proceedings of the 23rd International Congress on Applications of Lasers & Electro-Optics, ICALEO, 4–7 October 2004, San Francisco, CA, 2004.
[23] C. Thomy, F. Vollertsen, Influence of magnetic fields on dilution during laser welding of aluminium, Adv. Mater. Res. 6–8 (2005) 179–186.
[24] M. Bachmann, V. Avilov, A. Gumenyuk, M. Rethmeier, Numerical simulation of full-penetration laser beam welding of thick aluminium plates with inductive support, J. Phys. D Appl. Phys. 45 (2012).
[25] D. Aidun, S. Martin, Effect of sulfur and oxygen on weld penetration of high-purity austenitic stainless steels, J. Mater. Eng. Perform. 6 (1997) 496–502.
[26] F.-C. Yin, M.-X. Zhao, Y.-X. Liu, W. Han, Z. Li, Effect of Si on growth kinetics of intermetallic compounds during reaction between solid iron and molten aluminum, Trans. Nonferrous Met. Soc. China 23 (2013) 556–561.
[27] B. Ribic, S. Tsukamoto, R. Rai, T. DebRoy, Role of surface-active elements during keyhole-mode laser welding, J. Phys. D Appl. Phys. 44 (2011) 485203.
[28] C.R. Heiple, P. Burgardt, Fluid flow phenomena during welding, ASM Handbook, Vol. 6: Welding, Brazing and Soldering, ASM International, Materials Park, OH, 1993. pp. 19–24.
[29] L. Zhang, J. Zhang, G. Zhang, W. Bo, S. Gong, An investigation on the effects of side assisting gas flow and metallic vapour jet on the stability of keyhole and molten pool during laser full-penetration welding, J. Phys. D Appl. Phys. 44 (2011) 135201.
[30] S. Jia, L. Nastac, The influence of ultrasonic stirring on the solidification microstructure and mechanical properties of A356 alloy, Chem. Mater. Eng. 1 (2013) 69–73.
[31] C. Dommaschk, Beitrag zur Gefügebeeinflussung erstarrender Metallschmelzen durch Vibration (Contribution to the influence of vibration on the microstructure of solidifying molten metals), PhD Thesis, Freiberg, Technische Universität Bergakademie Freiberg, 2003 (in German).
[32] Z. Zhong, F. Zitian, D. Xuanpu, T. Bo, P. Di, L. Jiqiang, Influence of mechanical vibration on the solidification of a lost foam cast 356 alloy, China Foundry 7 (2010) 24–29.
[33] R. Caram, M. Banan, W.R. Wilcox, Applied low frequency axial vibrations to effect textured solidification in a Pb–Sn eutectic alloy, J. Crystal Growth 114 (1991) 249–254.
[34] K. Balasubramanian, D. Kesavan, V. Balusamy, Studies on the effect of vibration on hot cracking and grain size in AA7075 aluminum alloy welding, Int. J. Eng. Sci. Technol. 3 (2011) 681–686.
[35] W. Wu, Influence of vibration frequency on solidification of weldments, Scr. Mater. 42 (2000) 661–665.
[36] J.S. Kim, T. Watanabe, Y. Yoshida, Ultrasonic vibration aided laser welding of Al alloys: improvement of laser welding-quality, J. Laser Appl. 7 (1995) 38–46.
[37] A. Krajewski, W. Włosiński, T. Chmielewski, P. Kołodziejczak, Ultrasonic-vibration assisted arc-welding of aluminum alloys, Bull. Pol. Acad. Sci. Tech. Sci. 60 (2012) 41–852.
[38] S. Jäger, Nonvakuum-Elektronenstrahlschweißen mit gepulstem Strahlstrom und Ultraschallanregung (Non Vacuum Electron Beam Welding with pulsed electron beam and ultrasonic excitation), PhD Thesis, Hannover, Leibniz Universität, 2009 (in German).
[39] L. Zhang, D.G. Eskin, L. Katgerman, Influence of ultrasonic melt treatment on the formation of primary intermetallics and related grain refinement in aluminum alloys, J. Mater. Sci. 46 (2011) 5252–5259.
[40] U.R. Kattner, B.P. Burton, Al-Fe (aluminum-iron), in: H. Baker (Ed.), Binary Alloy Phase Diagrams Volume 3, American Society for Metals, Ohio, OH, 1992.

CHAPTER 11

Laser Transformation Hardening of Steel

A.K. Nath, S. Sarkar
Indian Institute of Technology, Kharagpur, India

11.1 INTRODUCTION

Laser surface transformation hardening is a manufacturing process for improving the mechanical properties of the highly stressed mechanical components, such as enhancing the wear resistance, the cavitation erosion resistance, and under favorable conditions, the fatigue strength of bearings, cams, and gears without melting the surface or adding any external materials. This was first reported in 1973 with the introduction of high-power CO_2 lasers in material processing applications. Since then, because of several attractive features, this has been much researched and adopted in the manufacturing industry [1–15]. Some of those attractive features are:

- Selective and localized heat treatment of engineering parts controlled by the laser beam
- Self-quenching through heat conduction in the cold interior of the part without the requirement of any external quenchant, unlike conventional heat treatment processes
- Minimum heat input energy
- Negligible part distortion, thus applicable on the finished part
- No need of post processing
- Controlled case depth within a mm or so from the surface
- Improved fatigue life

Because of these attractive features, laser hardening is becoming the optimal technological solution for the surface treatment of small and complex engineering components. However, this process has some limitations:

- The oxide-free clean metallic surfaces are highly reflective of laser radiation, requiring the application of absorption coating on the surface being laser heat treated
- Nonavailability of enough high-power lasers to heat-treat large surface areas in a single pass

Advances in Laser Materials Processing
https://doi.org/10.1016/B978-0-08-101252-9.00011-X
Copyright © 2018 Elsevier Ltd.
All rights reserved.

- Tempering of the overlapped zone causing softening of the hardened zone when a large surface area is covered by overlapped laser passes
- Maximum hardness and depth of hardening dependent on temperature rise and cooling rate, predicting them in components of different shapes and mass distribution is an issue. This necessitates online process monitoring with feedback control for reproducibility of results

Laser hardening is usually done in medium carbon steels and low alloy steels having a carbon content of less than 2 wt%. The laser hardening process is fundamentally similar to the conventional hardening process with the difference being that this does not often require an external quenching medium. This involves the following three steps:

1. Heating a top surface layer by laser to a temperature above Ac3 austenitization temperature, but below the melting point.
   The plain carbon steel having a eutectoid carbon percentage of 0.76 wt% has a pearlitic microstructure, which consists of lamellae of two phases: ferrite (α phase) and cementite (Fe_3C). Ferrite has a body centered cubic (BCC) crystal structure and can dissolve a maximum of 0.008 wt% C at room temperature and 0.028 wt% at eutectoid temperature, 727°C (Ac1) and above. Cementite (Fe_3C) is an intermetallic compound consisting of 6.67 wt% carbon. Hypereutectoid steel has more than 0.76 wt% C and it consists of pearlite grains accommodating 0.76% carbon. The remaining carbon in the form of cementite is distributed around pearlite grains. The microstructure of hypo-eutectoid steel, which has less than 0.76 wt% carbon, consists of ferrite grains and pearlite colonies. In laser hardening of hypo-eutectic steel, as the eutectoid temperature, Ac1 (727°C), is reached during laser heating, pearlite colonies transform into austenite (γ phase) (Fig. 11.1).
   This has a face centered cubic (FCC) crystal structure and can dissolve 0.76 wt% C at eutectoid temperature and a maximum of 2.14 wt% C in solid solution at 1147°C. Cemetites (Fe_3C) in pearlite begin dissolving and the carbon starts diffusing into eutectoid ferrite lamellae transformed austenite. Carbon from high-content austenite also diffuses into low-content austenite and proeutectoid ferrite. Proeutectoid ferrite also starts transforming into austenite at the eutectoid temperature, becoming completely transformed when the temperature reaches the Ac3 point.
2. Holding the heated surface layer above the austenitization temperature Ac3 for enough time for the complete transformation of proeutectoid ferrite to austenite, dissolution of cementite (Fe_3C), and diffusion of carbon uniformly in austenite phase. This depends on the prior size of the pearlite colonies and that of the proeutectoid ferrite regions.

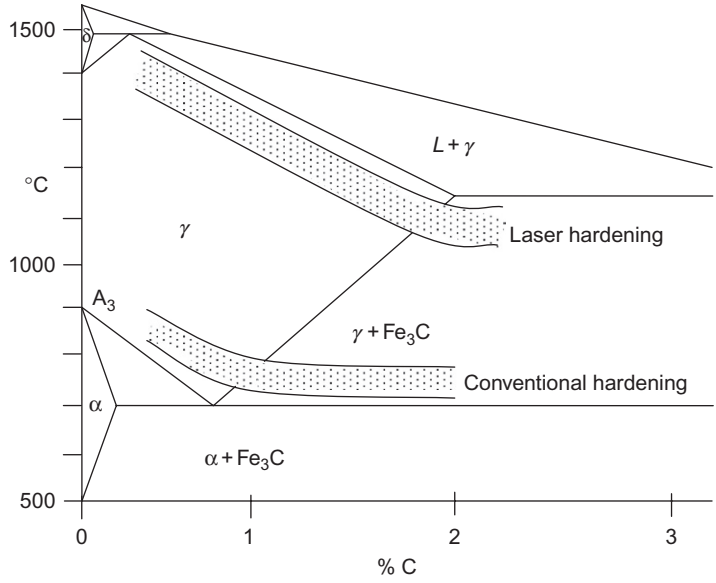


Fig. 11.1 Temperature regions of conventional and laser beam hardening in the iron-carbon diagram [8].

The austenitization temperature Ac3 depends on the composition of steel and varies from 912°C for 0 wt% C to 723°C for 0.76 wt% C. In laser processing the heating rate is usually very high, in the 10^2–10^4 K/s range. The Ac3 temperature increases with an increasing heating rate, tending to saturate at 912°C for a heating time of less than 1 s [8]. Homogeneous distribution of carbon in the austenite phase is diffusion kinetic controlled. It depends on the raised temperature and the lamellae spacing in pearlite colonies and the initial ferrite grain size. Specimens having initial larger ferrite grain size would require longer holding time above the Ac3 temperature for the carbon to diffuse uniformly and form homogeneous austenite. With the typical processing time of one second, an optimum surface temperature above 1200°C is reported [16]. As the temperature below the surface increases due to heat conduction, it is always lower than the surface temperature. Therefore, for maximum hardness and hardening depth the surface temperature should be as high as possible, limited by the melting point.

In the case of eutectic steel having 0.76 wt% C, the homogeneous austenite with uniformly diffused carbon is formed at a relatively lower temperature above the Ac3 point. On the other hand, homogeneous austenite cannot be obtained during the short processing time typical of

laser hardening, because of carbides (Fe_3C) randomly distributed around pearlite grains. Still, maximum hardness can be obtained by heating above the Ac3 point in the area of austenite + carbides [16].

3. Subsequent fast cooling by self-quenching through heat conduction in the rest of the bulk material for FCC austenite phase to transform into tetragonal body centered martensite metastable phase. All austenite material with carbon content more than a critical value C_c (which is usually taken to be 0.05 wt% C) transforms to martensite; the remaining reverts to ferrite [7]. Fig. 11.2 schematically shows the body centered tetragonal unit cell of martensite steel.

   The tetragonality arises from the preferential occupation of octahedral interstitial sites along the *c* axis by carbons. Martensite is a hard and brittle metastable phase. Its hardness depends on the extent of tetragonal distortion as measured by the ratio of the longer *c* axis to the shorter *a* axis (square face), which in turn depends on the carbon content. The higher the carbon content, the higher the c/a ratio (Fig. 11.3).

Fig. 11.3 shows how the degree of tetragonality varies with carbon content and Fig. 11.4 shows the average relationship between carbon content and hardness for steels containing different amounts of martensite.

Austenite to martensite transformation is a diffusionless process. The cooling rate required for martensite transformation depends on the carbon content and other alloying elements present in the steel, which tend to slow

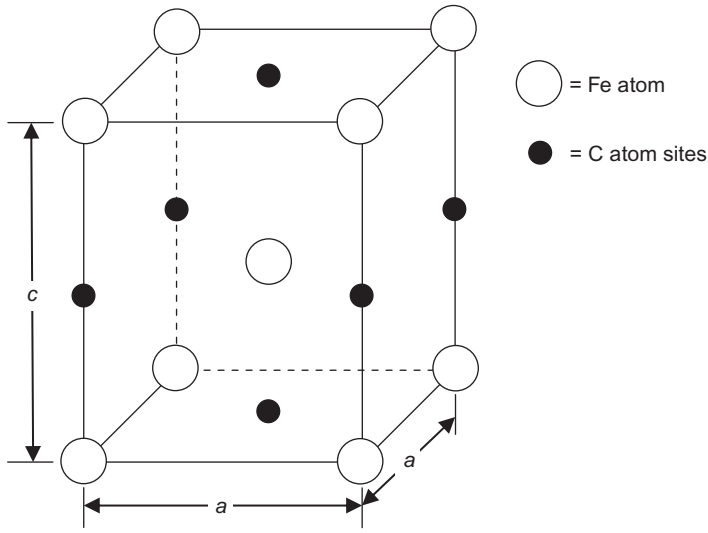


Fig. 11.2 The body-centered tetragonal unit cell of steel martensite [17, p. 382].

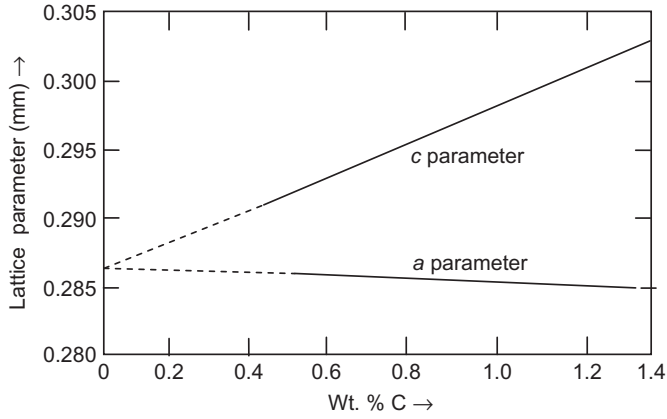


Fig. 11.3 Variation of degree of tetragonality with carbon content for steel martensite [17, p. 382].

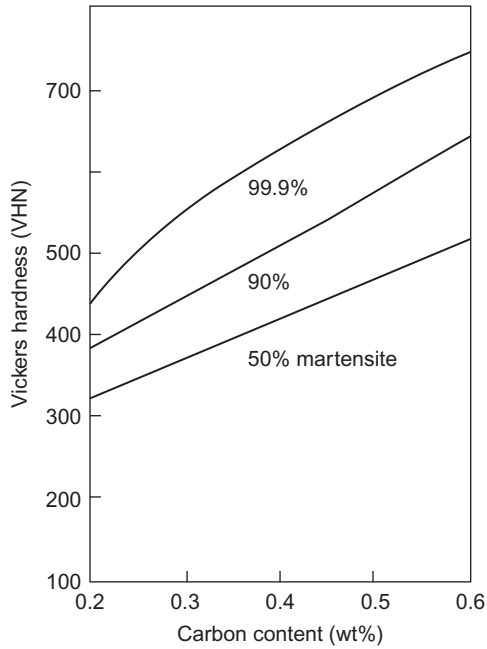


Fig. 11.4 Average relationship between carbon content and hardness for steels containing different amounts of martensite [18, chapter 6, p. 306].

the decomposition of austenite into ferrite and pearlite. This is illustrated in Fig. 11.5A–C which show the time-temperature transformation diagrams of (a) plain carbon steel containing 0.5 wt% C, (b) steel of eutectoid composition (0.8 wt% C), and (c) an alloy containing chromium.

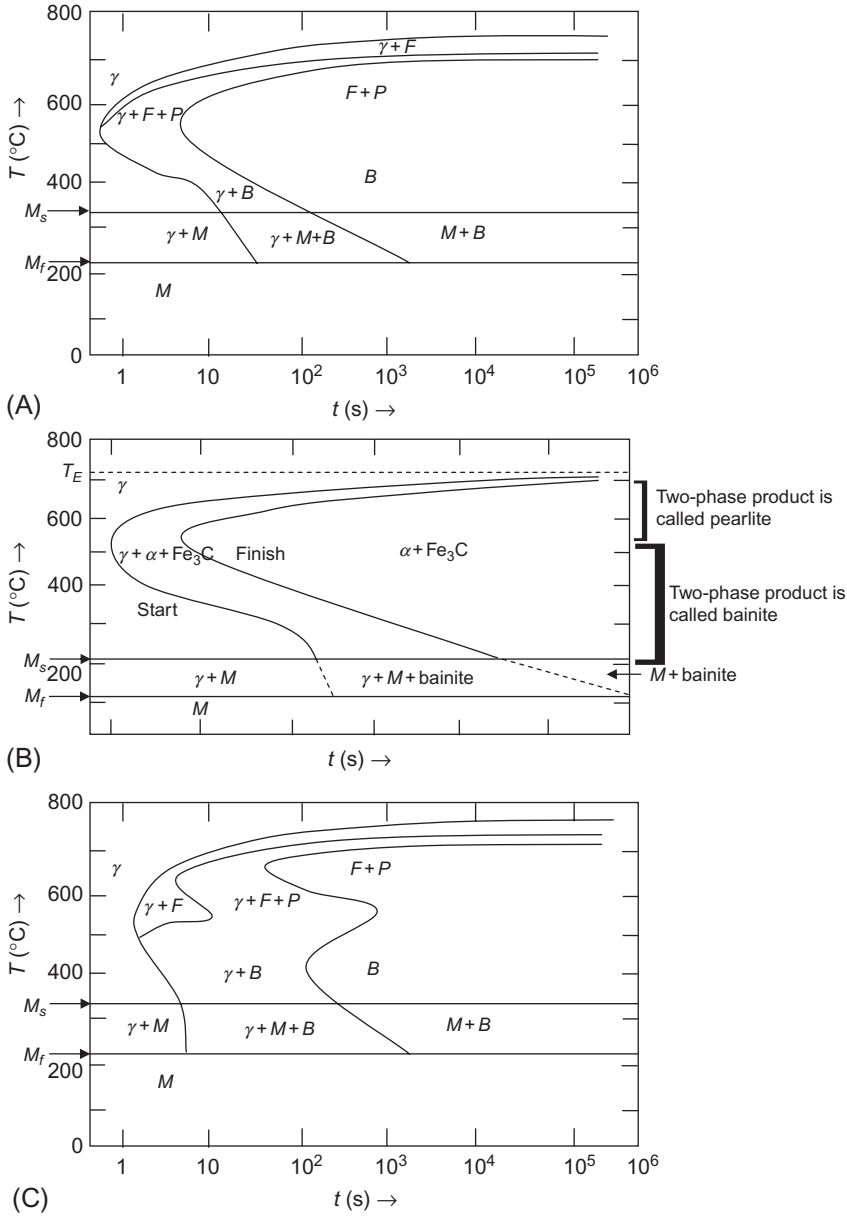


Fig. 11.5 Time-temperature transformation diagrams of (A) plain carbon steel containing 0.5 wt% C [17, p. 380], (B) steel of eutectoid composition (0.8 wt% C) [17, p. 360], and (C) an alloy containing chromium [17, p. 380].

In order to understand the effects of various laser and process parameters on the surface characteristics, microstructure, residual stress, maximum hardness and depth of hardening in various engineering components of different geometries and grades of steels extensive theoretical modeling and experimental studies have been carried out since the first reporting of the process [4–11,19–30].Various online process monitoring methods and feedback control to ensure the desired maximum hardness, depth of hardness, and reproducibility in different engineering components have also been developed for industrial applications [14]. In the following sections brief outlines of the lasers popular in laser hardening, various types of ferrous materials that have been surface-hardened with lasers, and the research work carried out in this area until about 5 years ago are presented.

11.1.1 Lasers in Surface Hardening

Until recently, high-power CW CO_2 lasers operating at ~10 μm wavelength, lasers where the technology was first matured and became commercially available for industrial applications, were mostly used for heat treatment application. With the development of high-power solid-state Nd:YAG, disk and fiber lasers operating at ~1 wavelength and newer high power diode lasers operating in the 0.8–0.9 μm wavelengths, CO_2 lasers are now facing competition due to several advantages of using these lasers. When the CO_2 laser beam is incident on a polished steel surface, more than 70%–80% of the laser power is reflected. Though the absorptivity tends to increase with the increase of surface temperature, absorbing coating of some suitable material, such as magnesium phosphate, zinc phosphate, or colloidal graphite, is usually applied on the surface.This increases the laser power absorption for effective surface hardening, which incurs extra cost to the process for application and removal. Solid-state and diode lasers with wavelengths about one-tenth of the CO_2 laser wavelength have higher absorption than a CO_2 laser due to their shorter wavelengths. This means that the need for surface coating is greatly relaxed. Moreover, low-loss optical fibers are commercially available to transmit and deliver the high-power beam of ~1 μm wavelength from solid-state and diode lasers, but such fibers are not yet available for the ~10 μm wavelength CO_2 laser beam. Among all these lasers, high-power diode lasers are becoming the first choice in industrial laser surface hardening applications because of their flat top intensity distribution, high efficiency, low operation and maintenance costs, and compact size [31–34].

11.1.2 Materials for Laser Surface Hardening

It is mentioned above that ferrous materials like medium carbon steels and low alloy steels are amenable to laser surface hardening. More specifically, this means AISI 1040 [4], 1045 [23], and low alloy steels for dies like AISI 4140 [12] or x40Cr13, 5135 [5], heavy duty and ball bearing steels like 100Cr6, tool steels like X210CrW12, martensitic stainless steel, such as AISI 420 [24] 440C [35], railroad steels [36], and other steels [3–6,16,19–23,37].

11.1.3 Background Information

Since the laser hardening process is a thermal process and depends on carbon diffusion in the austenite phase, many earlier studies on laser hardening involved predicting the temperature distribution in laser heating by solving the heat transfer model. With this knowledge, one could predict the carbon diffusion distance, cooling rates, and microstructure formation [7,18]. Steen and Courtney [4] established an empirical relation between the depth of hardening, z, and the laser processing parameters, namely absorbed laser power, P, laser spot diameter, d, and laser scan speed, v. A linear relationship between the hardening depth, z, and a derived parameter, $P/\sqrt{(dv)}$, was established that fitted well with the experimental results of laser hardening in medium carbon steels (AISI 1040 [4], 1045 steels [23]). Kou and coworkers developed a three-dimensional heat flow model to obtain the temperature distribution in cylindrically shaped parts during laser processing. They also explained the microstructure of a hardened zone in AISI 1018 steel with the help of the calculated peak temperature, heating, and cooling rates [26]. Ashby and Easterling modeled the laser surface hardening process for both hypo- and hyper-eutectoid steels by combining an approximate solution for the temperature field with the equations describing the kinetics of structure changes with diffusion of carbon and the "kinetic strength" of the heating cycle [7,38]. They concluded that the most important parameters controlling the hardening process were the laser energy density and the beam interaction time, besides the composition and initial microstructure of steel. For ensuring homogenization of austenite, Davis et al. estimated the time above the Ac3 temperature that the workpiece must be maintained for carbon to diffuse [28]. Ohmura et al. developed a finite difference model to analyze the changes with the time of heat flow, the carbon redistribution in austenite, and subsequent quenching to martensite during the laser hardening process [29]. Meijer and Sprang showed through their experimental and theoretical study that while the laser hardening process depended on

two independent parameters, namely the absorbed laser power density and the beam interaction time for a given depth of hardening, the maximum surface temperature was the only necessary control parameter to optimize the hardness and residual stress, etc. [8]. Jacot and Rappaz developed a two-dimensional diffusion model for the prediction of phase transformation and subsequently a combined model for describing the dissolution of pearlite, the transformation of pro-eutectoid ferrite to austenite, and the homogenization and grain growth of austenite [9,10]. They found that the finishing temperature of austenitic transformation Ac3 depended on the carbon content and the heating rate. The Ac3 temperature increased with the heating rate between two extreme values, 770°C and 912°C, for medium carbon steel. They calculated the austenite homogenization temperature also, which increased from 800°C to 1200°C with the increase of the heating rate from 0.1 K/s to 1000 K/s [9]. The calculated values compared well with the experimental results reported in the literature [9]. Na and Yang have also shown through their theoretical and experimental studies that the start of the austenization temperature, Ac1, and the finish of the austenitic transformation temperature, Ac3, increase with the heating rate in the laser transformation hardening process [30]. Kommanduri and Hou presented a thermal analysis of the laser hardening process, which facilitated the prediction and optimization of the process parameters for practical applications [11]. The kinetic strength of the heating cycle presented by Ashby and Easterling [7] and the variation of homogenization temperature with heating rate reported by Jacot and Rappaz [9] suggest that a finite soaking time above the phase transformation temperature is necessary to get a uniform distribution of carbon in austenite microstructure. Miokovic et al. presented a detailed analysis of the effects of inhomogeneous austenitic formation as well as heating and cooling rates on the resultant phase formation using a coupled heat conduction and phase transformation model [12]. Shin and coworkers developed a predictive model based on a three-dimensional thermal model coupled to a two-dimensional kinetic model for phase distribution and experimental results on laser hardening of AISI 1516 steel shafts with a complex feature, and also for the residual stress induced in laser hardening and the tempering effect in multi-track processing [31,39,40].

As the laser hardening process got established with a better understanding of the process, several industrial laser systems have been developed for surface hardening of various engineering components in recent times [14,34]. Most of these systems are based on high-power near-infrared (~1 μm) lasers, i.e., Nd:YAG, fiber, or diode lasers. They are often integrated

with online temperature monitoring systems based on either IR pyrometer or CCD camera. In order to treat specific engineering components, suitable beam shaping and scanning systems have been also developed that are integrated with the laser system. The Fraunhofer Institute for Material and Beam Technology (IWS) in Germany has pioneered these developments [14]. In order to make the process more cost effective and reduce overall manufacturing time, laser hardening is also being integrated with other machining processes such as turning, milling, and grinding in the production line. However, this process is still not as popular as other laser applications such as cutting, marking, or welding. Nevertheless, this niche technology has immense potential. Therefore many manufacturing industries have been adopting this process to enhance the surface characteristics of various engineering components, such as the turbine blades, crankshafts, piston ring grooves, and tractor engine parts, etc. [3,14,15,41–46]. A few examples of laser surface hardening with high-power diode lasers are presented in Figs. 11.6–11.8.

While the research and development on some of aspects of laser hardening mentioned above has continued in recent times, investigations of some of the new aspects, such as the hardening of very low carbon steels having less than 0.1 wt% C and thin steel sheets, repetitive laser pulse hardening of different types of steel, the effect of external quenching, online process monitoring and laser beam shaping for hardening engineering parts, have been reported. Hitherto, low carbon steels with a carbon content of less than 0.1 wt% C have seldom been hardened by a laser because of poor



Fig. 11.6 Hardening of a key way on a shaft [34].

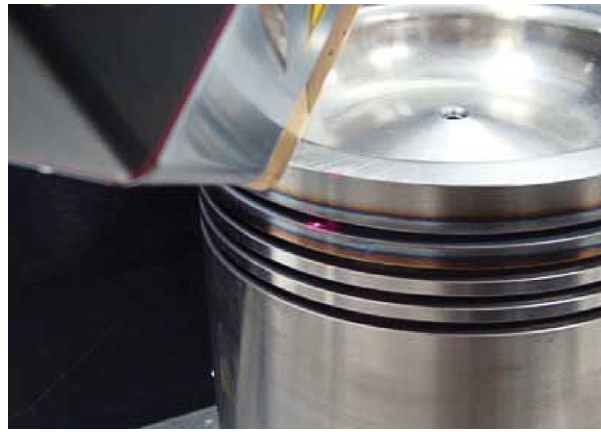


Fig. 11.7 The top and bottom surface of a piston ring groove have been selectively heat treated to enhance wear resistance [34].



Fig. 11.8 Heat treatment of the bearing contact area on a wheel spindle of a large vehicle using a diode laser [34].

hardenability. Recently laser hardening of steel sheets with 0.05–0.07 wt% C has been reported [47,48]. Some of these studies have been reported in steel sheets of thickness comparable to or less than the thermal diffusion length under the typical laser hardening conditions, having insufficient bulk material along depth for self-quenching. The effect of external quenching media on laser hardening has also been reported [49,50]. In the following sections a brief review of these experiments is presented.

11.2 RECENT DEVELOPMENTS

11.2.1 Analytical Modeling of Laser Hardening

Analytical models can be helpful in predicting hardness profile and hardness depth for a set of laser process parameters without performing the actual experiment. Thus, it can save both time and resources. Although, depending on different equations used in developing the model, there will be some limitations of the model. However, a good approximate value can be achieved.

Orazi et al. [51] developed a simplified time-efficient mathematical model to predict the austenization of hypo-eutectoid steel by proposing an austenite transformation time parameter $I_{p\to a}$ (i.e., time for transformation from pearlite to austenite) to take care of the overheating induced in pearlite transformation by the fast heat cycle. They showed that this parameter remains constant for low-medium carbon steel. The main assumption in the model was that the reduction in hardness is primarily because of the partial pearlite transformation during laser heating with a high heating rate and not the partial carbon diffusion into austenite (Fig. 11.9A and B).

The concept of distributed austenization of grains during transformation hardening was introduced. The predicted hardened profile showed a gradual variation of hardness values instead of a steep gradient between the hardened zone and the base material. The model considered the transition zones in the hardened profile that matches experimental results well.

Ahmed et al. [52] developed an analytical model to predict the melt-pool depth and profiles for IN625 using an extended laser source. Multiple Gaussian beam profiles were superimposed to form a rectangular beam. Experiments were done with a diode laser and simulated results matched well with experimental results. Although the model has been developed for melting case, more accuracy of simulated results could be achieved for cases where Marangoni effects are minimum, i.e., no melting cases. Therefore, this model can be used in industrial applications where laser transformation hardening with overlapped tracks is required.

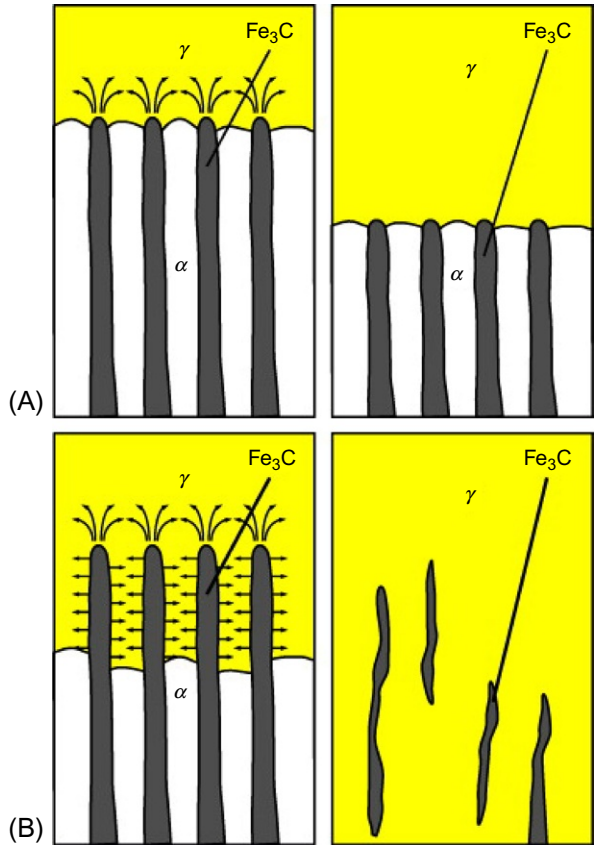


Fig. 11.9 (A) Pearlite dissolution near the equilibrium (overheating <5 < 5°C), (B) Pearlite dissolution with high levels of overheating [51].

Chen et al. [53] proposed an analytical model incorporating the Laplace transform, experimental temperature data, and the sequential-in-time concept to predict surface temperature, surface heat flux, and surface absorptivity during laser irradiation. The model is independent of initial guess value, is not very sensitive to measurement errors, and does not include any iterative steps. Predicted values by the model are in good agreement with the experimental results.

Lee et al. [54] presented a solution method for the inverse laser surface heating problem. The model showed that by minimizing mean square error between the experimental data obtained from inside the body and the estimated data from the derived analytical solution of a laser surface heating problem with time-dependent boundary conditions, it is possible

to predict the temperature function at the laser heating end. Therefore the entire three-dimensional temperature field and heat flux over entire time and space domains could be obtained. The model is simple, efficient, and does not require any integral and time-consuming numerical operations. Conformance between predicted and experimental results shows the accuracy of the proposed model.

Fortunato et al. [55] presented a detailed review of different mathematical models available for laser transformation hardening of hypo-eutectoid carbon steels, then proposed a comprehensive model which is easy to apply and less time consuming. The model considers laser beam characteristics, fast austenization of steel, and effect of tempering on overlapped tracks. The model calculates three-dimensional thermal fields generated in the workpiece and predicts the microstructural evolution of the target material considering thermodynamic thresholds. Results obtained from the proposed model match well with the experimental results of single- and double-pass laser treatment of AISI 1040 steel.

Zhang et al. [56] developed a two-dimensional non-Fourier equation based on a hyperbolic heat conduction equation with thermal relaxation time. Because laser irradiation involves localized heating within a very short time, it creates a very high temperature gradient and the waveform propagation of heat in media becomes dominant. As a result, the nature of heat conduction becomes completely different from classical heat conduction problems and it cannot capture the transient behavior of the medium completely. The present model considers boundary conditions with time-step heating and a uniform temperature distribution at a localized area of the surface. Using different numerical examples, the non-Fourier effect of temperature field over time has been shown to differentiate solutions obtained from the classical heat conduction equation and the proposed model.

One of the major problems in laser surface hardening of an extended surface by multiple overlapping tracks is back tempering. Giorleo et al. [57] proposed a laser surface treatment test to mimic the undesired effect that happens in actual laser treatment. The hardness values were measured. Based on the experimental results, it was assumed that temperature and time are strictly correlated, and a new model based on maximum temperature was developed. With the help of a simple linear formula, the model could predict the loss in hardness values in tempered zones. It has been suggested that, if the model is integrated with numerical codes, it can predict loss in hardness value in a tempered zone as a function of maximum temperature.

That, in turn, can further predict laser process parameters that give a minimum decrease in hardness.

Recently, Winczek et al. [58] proposed a three-dimensional temporary temperature field in a semi-infinite body considering a moving heat source. Complex trajectories were assumed to be combinations of different straight lines. The model considered changes in temperature profiles due to successive passes of the laser beam. The proposed solution can be applied to different laser-material interaction processes that consider a moving laser source. The solution can be further used to analyze different stress states and thermo-mechanical states involving phase changes due to different laser-material processing.

11.2.2 Numerical and FEM Analysis

Although numerical and FEM analyses take a lot of time to run, they can give much more accurate results compared to analytical models.

Sowdari et al. [59] developed an enthalpy-based finite element model to calculate the rate of heating, the heat-affected zone, temperature distribution, solid-liquid interface, and the shape and size of melt pool depth during laser surface treatment for given laser process parameters. Therefore the model can be used to predict the optimal laser process parameters to ensure no melt case, which is undesirable for laser transformation hardening.

Fortunato et al. [60] presented a regression model to measure the reflectivity coefficient in the laser surface hardening process. The proposed model has been numerically calculated using surface temperature measured by a pyrometer and compared with theoretical predictions with the help of process simulations. By varying the input data, a variation in output temperature was calculated, and a comparison between theoretical and experimental hardness values has been reported.

Bojinović et al. [61] made a simulation study on austenite kinetics in laser hardening considering the effects of the temperature change rate. Different sets of laser process parameters were considered to keep the maximum surface temperature the same during laser transformation hardening. Two different approaches were considered to evaluate microstructure and hardness. The first approach considers heating rate dependent austenitisation temperatures that govern the kinetics of microstructure transformation. The second approach neglects the heating rate dependence. Results showed that different laser process parameters leading to the same surface temperature give lesser depth of hardness when the laser is travelling with relatively

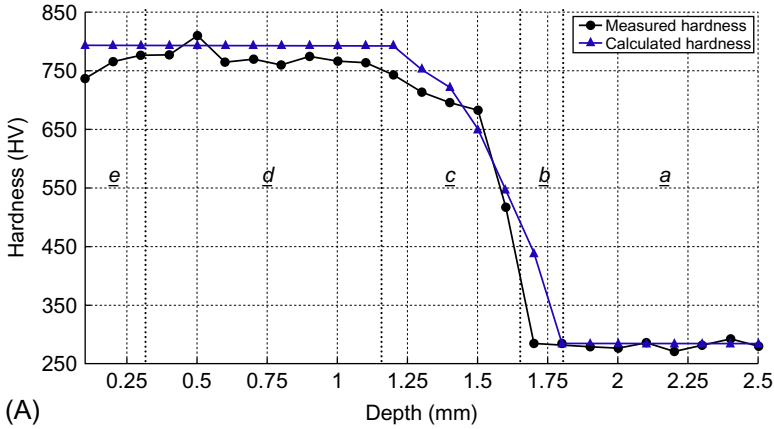


Fig. 11.10 Calculated and measured hardness values vs. depth at $Y = 60$ mm on the *YZ* symmetry plane [61].

higher speeds. The predicted hardened profile is in good agreement with experimental observations (Fig. 11.10).

Since in actual industrial practice one may need to surface harden complex three-dimensional geometry, a better control could be achieved by implementing the proposed model. The model considers maximum surface temperature and laser scan speed to achieve a desired depth of surface modification instead of controlling laser power alone, which may cause melting at some places in complex three-dimensional geometries.

Microstructures play a very important role in the final hardness value. Domański et al. [62] carried out numerical simulations to predict different microstructures for different cooling rates. The Johnson-Mehl Avrami equation and the generalized Kolmogorov equation are commonly applied for evaluating the transformation of austenite into ferrite, bainite, and martensite. The volume fraction of the martensitic phase is generally calculated using the Koistinen-Marburger equation or any of its modified formulas. This kind of numerical study involving cooling rate and microstructure correlation is of utmost importance for industry to obtain the desired microstructure and mechanical properties of any desired part.

Moumni et al. [63] developed an anisothermal model for steel, considering thermo-mechanical and metallurgical aspects. As laser transformation hardening involves localized phase changes and high cooling rates, the generation of stresses around the heat-affected areas is possible. Low temperature phases were considered to be elastoplastic whereas high temperature phases were considered to be viscoplastic in nature. The model was integrated with

the COMSOL Multiphysics software, which can predict phase transformation, inelastic deformation, residual displacements, and stresses due to laser material processing.

Babu et al. [64] used a design of experiment-based approach and developed a quadratic regression model to predict the responses using response surface methodology. The effect of direct and interaction effects of laser process parameters on laser transformation hardening were investigated. Further, the optimal parameter to get the maximum hardened width while minimizing both hardened depth and area were obtained. Predicted results were verified with experimental results.

Pérez et al. [65] developed a multilayer perceptron neural model for laser surface modifications based on Green's function. The model is highly versatile and efficient, and can be used for designing feedback control as well as an expert real-time supervision system for industrial applications.

Lambiase et al. [66] developed an expert system using an artificial neural network to predict the hardness values for given process parameters. The input process parameters were laser power, laser scan speed, number of scans, and percentage of overlaps. Based on the input process parameters, an analytical model was used to generate the temperature profile. This temperature profile, along with the artificial neural network, was used to predict the hardness value. Predicted results matched well with the experimental results. The model can be further used to get desired hardness at a certain depth from the surface.

Li et al. [67] developed a numerical model to study the effects of overlapping ratio on hardness and residual stress distribution for multitrack laser surface melting of steel. Compressive residual stress was found in the melting zone, whereas tensile residual stress was found in the heat-affected and the boundary of overlapped zones. Experimental results were in good agreement with the predicted results by the developed model.

There may be some thermal damages post laser transformation hardening. Zeng et al. [68] developed a quantified damage model that gives a comprehensive description of thermal damage caused by the laser surface transformation process. Using experimental data and finite elemental modeling, different analyses were carried out to evaluate changes in microstructure, microhardness, and residual stress values due to laser irradiation. A scalar, which has value ranges between 0–1, has been described to quantify thermal damage. A future work has been suggested to investigate the detail correlation among microhardness, residual stress, and mechanical properties to develop a coupled model of thermal damage and strength.

Liverani et al. [69] developed a numerical model to predict residual stresses generated after laser transformation hardening by considering deformation from thermal expansion, elastic and plastic deformation, and changes in microstructures for any components with arbitrary geometry. The model can predict depth of hardness and residual stresses as functions of component geometry, laser process parameters, and scanning strategy. Results showed that an increase in laser fluence or exposure velocity leads to an increase in depth of hardness and a reduction in compressive residual stresses and introduction of tensile residual stresses at high laser powers. The model can be used to predict the influential process parameters to get a desired depth of surface modification for any complex geometry within a very short time. Thus, this has very good potential to be used in actual industrial practices.

In order to achieve a uniform microstructure post laser surface hardening, Khajeh et al. [70] used a finite element-based model to develop a power-control-based strategy as a function of maximum surface temperature. The model can be used to reduce the edge effect problem. Using this approach, a more uniform microstructure could be achieved, which subsequently affects different mechanical properties. The approach is suitable in achieving a proper austenization temperature at the start of the track while avoiding surface melting at the end. A combination of higher laser scan speed and larger beam size has been suggested as an alternative in case of constant laser power.

Gupta et al. [71] estimated posteriori error using a dual weighted residual method for an optimal control problem in laser transformation hardening of steel. The problem involving a dynamic system with a semilinear parabolic equation and an ordinary differential equation has been discretized using the finite-element method. The performance of the proposed dual-weighted residual method is found to outperform the result given by residual method.

11.2.3 Phase Transformation Behavior

Gouné et al. [72] presented an overview of the recent advances including their pros and cons in modeling and experimental methods to understand the detailed phase transformation mechanisms involved in high-temperature austenitic phase to the ferrite phase for low alloyed steels. This understating is important because the austenite-to-ferrite microstructure transformation mechanism helps to understand the formation of possible microstructures and their chemistry, which in turn helps to tailor the

mechanical properties as per requirement. Although numerous theoretical models have been developed in this direction, their limitations lie in proper parameter selection such as interface thickness, transinterface diffusivity, and interface binding energy. Though challenging, these limitations can be resolved to a great extent with the help of atomic level models. Nowadays, that is possible with the help of highly sophisticated analytical tools such as SEM-FIB, analytical TEM, 3D atom probe, etc. An atomic-level theoretical model combined with these high spatial resolution techniques is expected to give structural and chemical information to validate experimental data in the near future for a better understanding of austenite-to-ferrite transformation.

Working in the same direction, Aqida et al. [73] studied the laser transformation hardening of H13 tool steel using a CO_2 laser with different laser process parameters (i.e., laser peak power, percentage of overlap, and pulse repetition frequency). XRD analysis of the phases of laser transformation hardened specimens confirmed the presence of the martensite phase in a case of specimens irradiated with a laser spot size of 0.4 mm. However, specimens irradiated with a laser spot size of 0.2 and 0.09 mm do not show any presence of the martensite phase. The combination of low irradiance and longer exposure time helped to initiate the martensite phase transformation for laser spot size of 0.4 mm whereas for the smaller laser spot diameter, more rapid cooling occurred. This limited the heat transfer to the surface, therefore the martensitic phase transformation was skipped. The study reveals a more-than-twofold increase in surface hardness value as compared to base material. Sources of increase in hardness were attributed to different phases formed and grain size after laser irradiation.

11.2.4 Laser Transformation Hardening With Repetitive Laser Pulses

The time duration for which a surface layer could be held at a temperature above Ac3 and the thickness of the hardened layer is usually limited, later one within 1 mm or so by the onset of surface melting, which must be avoided in transformation hardening. This also limits the heating and cooling rates in CW laser hardening, which influence the resulting microstructure and mechanical properties. Several studies had been carried out in the past on the effect of modulated/pulsed laser beams on the hardening process to alleviate these limitations. Danileiko et al. reported that the pulse-periodic laser beam was better suited to produce surface hardening

compared to the CW laser beam. This is because of the additional process controlling parameters, viz. pulse duration and pulse frequency, besides the laser intensity and scan speed, which could ensure better homogenization of the austenitic phase, the microhardness, and the hardening depth [74]. They carried out an experimental investigation with a quasi-CW Nd:YAG laser of 4 ms pulse duration operating at the 50 Hz frequency. They calculated the thermal cycle of pulse-periodic laser interaction by solving the one-dimensional heat-conduction equation with boundary conditions corresponding to irradiating the surface by a series of rectangular laser pulses of equal intensity. From their analysis they concluded that the carbon dissolution was cyclically cumulative. This increased the fraction of martensite in the irradiated region as well as process efficiency. Habedank et al. also established with their experimental simulation study that the pulse laser hardening with low-pulse frequencies (25–100 Hz) enabled a higher hardening depth compared to that of the CW laser, and could generate compressive residual stresses leading to higher endurance limits [75]. Wu et al. developed a three-dimensional model for the pulsed laser transformation hardening considering the spatial and temporal laser intensity distribution, showing that the temporal pulse shape had great effects on surface hardening [76]. Miokovic et al. carried out laser hardening experiments with a different number of heating and cooling cycles at heating rates of 1000 and 10,000 K/s and cooling rates of 1000 and 3000 K/s. They reported an increase in surface hardness and hardening depth with an increasing number of laser pulses in the AISI 4140 workpiece [13]. However, the hardness depth tended to saturate as the number of pulses increased beyond three (Fig. 11.11).

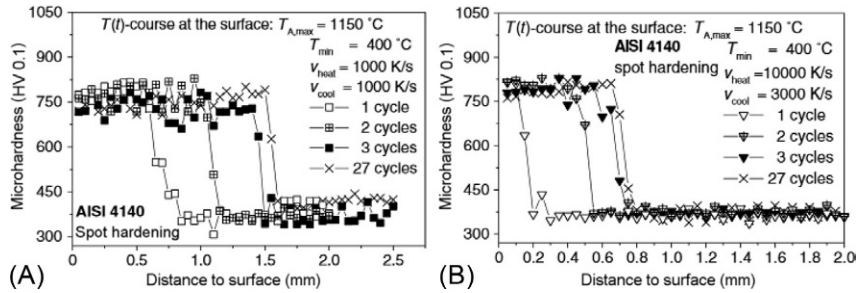


Fig. 11.11 Microhardness vs. distance to the surface after laser surface hardening with heating and cooling rates of 1000 K s^{-1} (A) and a heating rate of 10,000 K s^{-1} and a cooling rate of 3000 K s^{-1} (B) after 1 cycle and after cyclic time-temperature change in the austenite region with 2, 3, and 27 cycles for T_{min} = 400°C (error = ±20 HV0.1) [13].

Recently, Kostov et al. [77] also showed a similar nature of extension of the hardened zone along depth as well as in a lateral direction, and a slight material softening with repeated austenite-martensite transformations induced by laser surface hardening. They also reported the generation of compressive residual stresses at the surface and tensile stresses inside the surface induced by the laser hardening process. The compressive stress zone increased along depth with the number of repetitive laser pulses (Fig. 11.12).

They carried out further experiments on local temporal strain and stress development during laser surface spot hardening in real-time using in-situ synchrotron X-ray diffraction analysis. They could separate thermal and elastic strains and identify contributions from the effects of phase transformation, quenching, and mechanical constraint by the colder material adjacent to the laser-processed zone [78,79].

The temperature history for the cyclic laser heating and cooling was also studied numerically and analytically by several researchers [74,80–82]. Smurove et al. have analyzed the heating, melting, evaporation, and solidification including velocity and position of phase boundaries by numerical modeling [80]. Yilbas and coworkers derived a close-form solution for the temperature during heating and cooling cycles using a Laplace transformation method, then presented results for two laser pulses [81]. They also investigated the laser consecutive pulse heating of a solid surface and the influence of laser pulse parameters on the melting and mushy zone

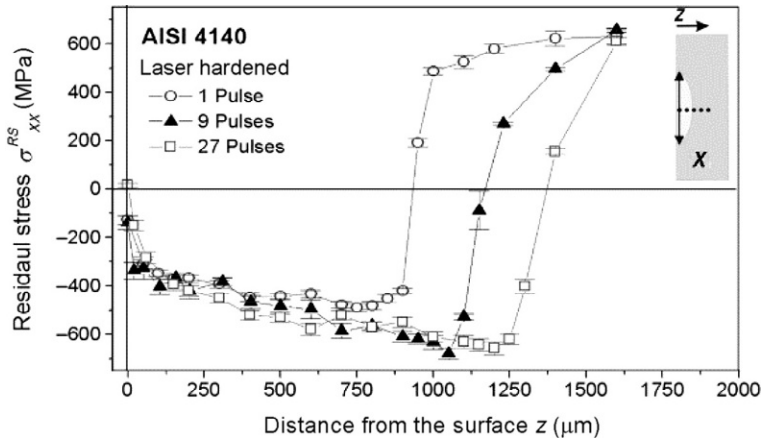


Fig. 11.12 Residual stress distribution in the depth *z* after laser surface hardening by means of 1, 9, and 27 laser pulses [77].

formation in the irradiated region by numerical simulation [82]. More recently, Mahmoudi et al. [83] studied the effects of different laser process parameters such as laser pulse duration, pulse energy, scan speed on hardness value, and depth of hardness of AISI 420 martensitic stainless steel using a pulsed Nd:YAG laser operating at 15 Hz. Further, corrosion resistance of the laser-hardened zone was also studied. Achieved hardness was almost in the same order as that of a conventionally heat-treated specimen. From the metallographic investigations, it was shown that carbides in grain and grain boundaries get discontinuous and spherical after laser heat treatment. Therefore it causes chromium carbides to dissolve and hence increases the corrosion resistance. The overlapping of two subsequent tracks caused a tampering of phase and a deposition of carbide in the overlapping zone. This caused a decrease in corrosion resistance. Therefore with a decrease in percentage of overlap, corrosion resistance increased. A slightly different approach has been followed by Jiang et al. [84]. They made investigations on discrete laser transformation hardening—basically a few discrete hardened spots distributed in a particular fashion over a selected area of the workpiece—of AISI O1 tool steel using a pulsed Nd:YAG laser. It has various triobological applications such as improved lubrication conditions, wear performance, etc. The effect of various laser processing parameters, including laser pulse energy, pulse duration, and defocus distance, on characteristics of the laser-treated spots were studied. They reported that laser pulse durations greater than 8 ms were more effective for achieving higher hardness and that the laser pulse energy was the main parameter affecting the depth and diameter of the spot hardening.

Nath et al. [85] presented analytical solutions for temperature profiles of the heating and cooling cycles in repetitive laser pulse irradiation while also investigating the effects of various process parameters such as laser power, beam diameter, scan speed, pulse duration, repetition frequency, and duty cycle on surface hardening. It has been shown that the average heating rate is lower in repetitive laser pulse irradiation. Also, the soaking time above the phase transformation temperature on which the homogeneity of microstructure and the depth of hardening depends is longer than that of CW laser hardening. This was validated with their experimental results of laser hardening of AISI 1055 steel with a modulated-power fiber laser by demonstrating that the depth of hardness increased with an increase in the number of laser pulses in a low-frequency range (Fig. 11.13). Similar trends followed with a reduction in interpulse duration (Fig. 11.14). A similar result (Fig. 11.15) was obtained by Kostav et al. [77].

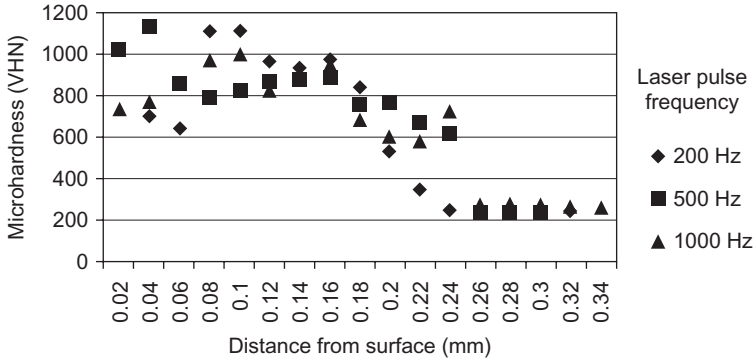


Fig. 11.13 Measured microhardness profiles at different repetition frequencies, laser power = 1080 W, duty cycle = 30%, scan speed = 12 mm/s [85].

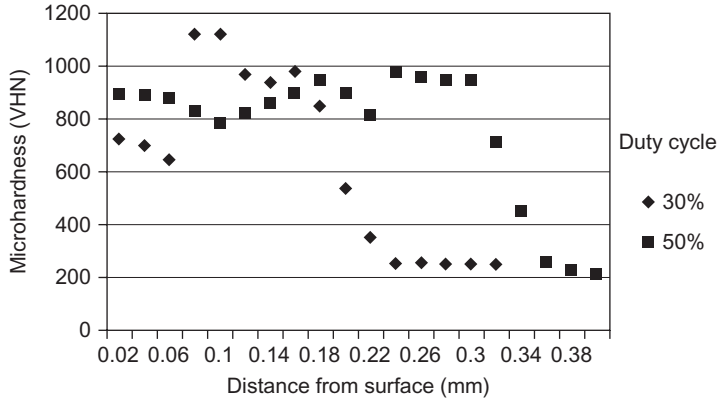


Fig. 11.14 Measured microhardness profiles for 30% and 50% duty cycles, laser power = 1080 W, frequency = 200 Hz, scan speed = 12 mm/s [85].

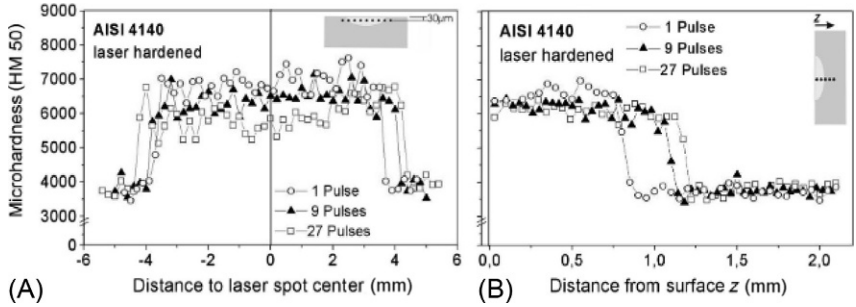


Fig. 11.15 Distribution of microhardness inside and outside the processing zone at the cross-sectional plane (A) in lateral direction in a distance of 30 μm to the surface (B) in the depth *z* [77].

11.2.5 Laser Hardening of Very Low Carbon Steel Thin Sheets

In recent times there has been some interest in laser surface modification of very low carbon steel (C wt% ≪0.1) thin sheets (~1 mm thickness) with a potential application in hardening the surfaces of automobile body parts after forming [47,48]. So and Ki [86] investigated the effects of specimen thickness on hardening performance in the laser heat treatment of carbon steel with a high-power diode laser using a process map approach. The process map of laser intensity and the interaction time for laser hardening of carbon steel up to different depths were determined using a heat-conduction model considering carbon diffusion time in austenite and cooling time [87]. Through their study they showed that as the specimen thickness reduces, the area of heat-treatable regions decreases and it moves toward low laser power. They validated their approach by conducting laser heat treatment on AISI 1020 steel specimens (base material hardness ~130 Hv) using a 3 kW diode laser. They reported that the maximum hardness obtained under optimum laser processing conditions decreased from 350 Hv for a 10-mm thick specimen with the decrease of sheet thickness, approaching 200 Hv for ~1-mm sheet thickness [86]. Sarkar et al. [47] formulated an analytical model to determine heating and cooling thermal cycles in thin sheet considering heat conduction along depth and radial direction with and without heat sink. They showed that cooling rates of more than 1000°C/s could be realized even in thin sheets of thickness comparable to thermal diffusion length, sufficient for self-quenching and austenite-to-martensite transformation. For a laser beam diameter more than ~4 mm the radial heat conduction cooling tends to be rendered ineffective, resulting in initial fast cooling from a temperature above Ac3 to about 500°C followed by very slow surface cooling, a condition conducive for the austenite-bainite transformation [17]. They validated the predictions of the thermocycle with the experimental results on laser surface hardening of ~1-mm thick very low carbon steel sheets containing 0.05% and 0.07% carbon, performed using a high-power fiber laser. The depth of hardness could be controlled almost up to the entire sheet thickness (Fig. 11.16) by laser line energy density, i.e., fluence defined as laser power divided by the product of laser spot diameter and scan speed.

The average microhardness increased by about 80% in both types of steel. The increase was attributed to the austenite-martensite transformation and the formation of iron silicon carbide, silicon carbide, and aluminum nitride. Since martensite formation was one factor among several others

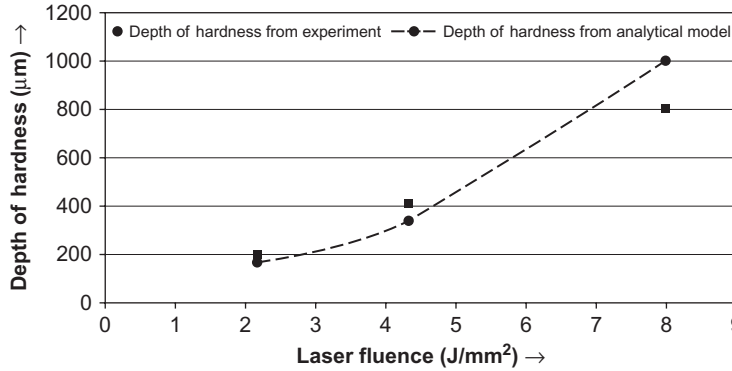


Fig. 11.16 Comparison between depths of hardness obtained from experiment and analytical model [47].

for the improvement of microhardness, its tempering effect was found to contribute only marginally in overall microhardness in overlapped laser hardening. Significant improvement in both yield strength (~60%) and ultimate tensile strength (~30%) with a nearly 30% reduction in percentage elongation was found in both grades of steel laser hardened up to ~300 μm depth. The wear resistance and scratch resistance of the laser-hardened surface also improved significantly. Syed et al. [48] also reported similar improvements in mechanical properties in a C-Mn low carbon (0.05 wt% C) automotive steel sheet of 1-mm thickness, which was surface hardened using a high-power diode laser. They reported an increase in microhardness by 133%–145% as compared to base hardness. The increase of hardness was attributed to the formation of harder phases, identified as a mixture of martensite, bainite, and prior-ferrite. The cooling rate at the laser-treated surface was measured to be in the 600–700°C/s range for a laser beam dimension of 4 mm × 4 mm. They also reported significant improvements in both yield strength (25%–40%) and ultimate tensile strength (20%) due to the sandwich effect of a composite layer constituting hardened layer (thickness ~250–300 μm) and base.

11.2.6 Effect of Heat Sinks

A heat sink in conjunction with a thin steel sheet can be used to increase the hardenability of the thin steel sheet. Ki et al. [88] used four different heat sinks (copper, steel, stainless steel, no heat sink) along with two different grades of steel DP590 and boron steel to study the effect of heat sinks on laser transformation hardening. Thermal conductivity of the heat sink and

thermal contact resistance between steel sheet and heat sinks were found to be two important parameters for the process. The study showed that in presence of heat sinks, both cooling and carbon diffusion are similar to that of the thick plate case whereas the heat-treatable region remains same to that of no heat sink case. The study also showed that the heat sink could enhance the hardenability of the steel sheet. It is also quantatively proportional to thermal conductivity of the heat sink material. A one-dimensional heat-conduction model was used to validate the experimental results. In another study, Kim et al. [89] studied the effects of different heat sink materials (Fig. 11.17) to control the thermal deformation in laser transformation hardening of steel and found that there were two different thermal deformation mechanisms.

One is plastic deformation while the second is deformation due to martensitic phase transformation. A decrease in thermal deformation in the presence of the heat sink was mainly attributed to two facts: a decrease in the heating effect reduced the plastic deformation and the enhancement of the cooling rate led to the formation of the martensitic phase. It was shown that positive deformation took place due to plastic deformation and negative deformation occurred due to the martensite phase formation. A transition zone between these two deflection regions also existed. It contained a

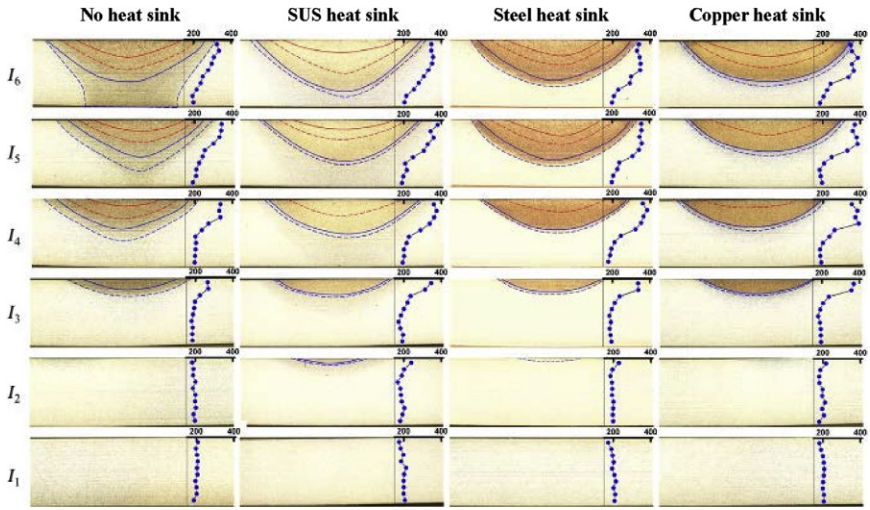


Fig. 11.17 Optical micrographs showing the cross-sections of heat treated DP 590 steel specimens for $t_i = 1.13$ s. From bottom to top, intensity level increases from I_1 to I_6. Micro Vickers hardness values along the center of the heat-treated zones are shown on the right side of the images [89].

bainite/ferrite or pearlite/ferrite microstructure predominantly for higher interaction times. The thermal deformation behavior completely reversed in the presence of the heat sink. Therefore with the proper selection of process parameters it is possible to find zero deflection regime to minimize thermal deformation. This study could be used to effectively control the thermal deformation not only in laser transformation hardening of steel but also for any laser-based sheet metal manufacturing processes.

11.2.7 Water-Assisted Laser Transformation Hardening

Jin et al. [90] carried out a feasibility study on laser surface hardening of tool steel underwater. They found that the depth of penetration and the heat-affected zone of the laser surface hardened area is smaller than that of laser surface hardening done in an argon gas environment. Orazi et al. [50] also used annular water flow simultaneously while hardening AISI 1040 with an Nd-YAG laser and demonstrated uniform hardness over an extended surface (Fig. 11.18).

In a recent study, Sarkar et al. [49] carried out laser hardening of thin AISI 1045 steel sheets with a waterjet assist and compared the hardening results with that of conventional laser hardening. Results presented in

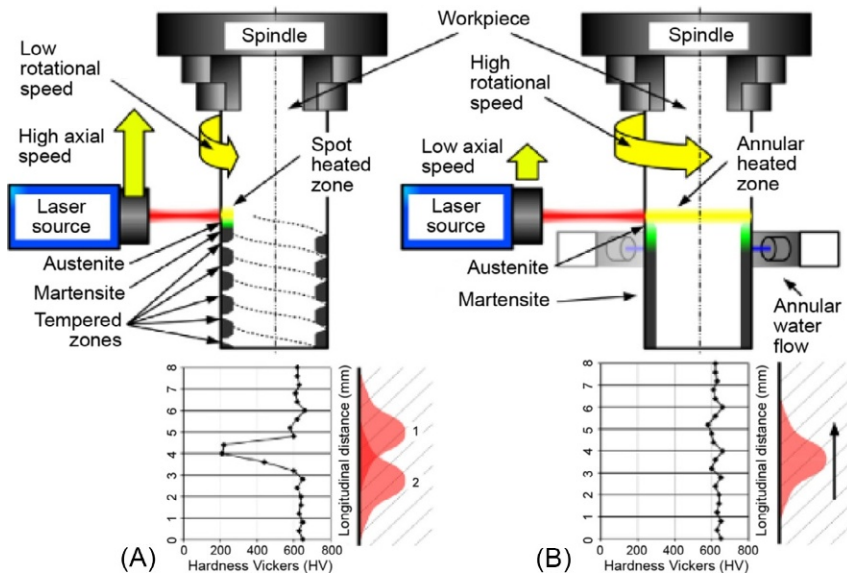


Fig. 11.18 Process setup and kinematics: (A) "classical" laser hardening (B) new process with ring spot [50].

Figs. 11.19 and 11.20 show that, with a judicious selection of process parameters, it is possible to get a similar range of peak microhardness values and depth of surface modification to that of conventional laser surface hardening using water assist.

However, one marked difference is that in this process, peak microhardness values occur at a depth relatively closer to the top surface than that of a conventional laser surface hardening process. This could be due to relatively fast cooling at the top surface due to forced convective heat transfer in the waterjet which could prevent too much diffusion of carbon. Therefore the present process can be used for those cases where high hardness values are required near the top surface, especially for thin sheets and thermally sensitive materials. However, some laser power loss in water due to scattering and

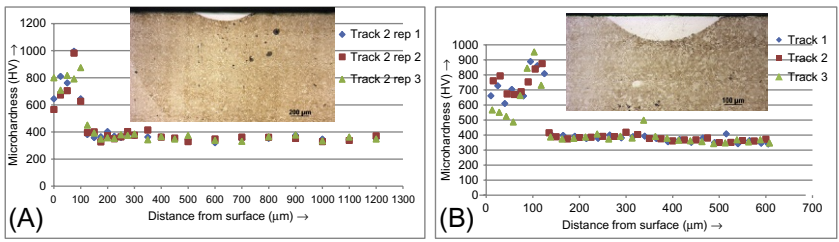


Fig. 11.19 (A) Waterjet-assisted processing condition with specimen thickness 1.2 mm; laser power 600 W and laser scan speed 2500 mm/min; depth of surface modification 120 μm (approx) (B) waterjet-assisted processing condition with specimen thickness 0.6 mm; laser power 600 W and laser scan speed 2500 mm/min; depth of surface modification 146 μm (approx) [47].

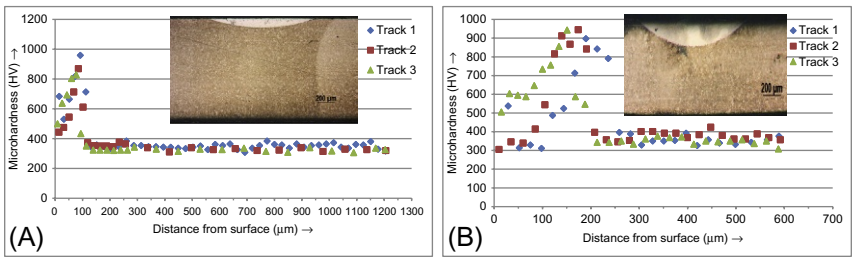


Fig. 11.20 (A) Laser surface hardening in air with specimen thickness 1.2 mm; laser power 500 W and laser scan speed 5000 mm/min; depth of surface modification 128 μm (approx) (B) laser surface hardening in air with specimen thickness 0.6 mm; laser power 500 W and laser scan speed 4000 mm/min; depth of surface modification 170 μm (approx) [47].

absorption would necessitate an increase in power requirement to achieve depth of hardness comparable to that of laser surface hardening in air.

11.2.8 Online Monitoring, Laser Beam Shaping and Scanning for Overlapped Hardening

Online monitoring of temperature signals during laser transformation hardening can predict the depth of surface modification under certain laser process parameters [8]. Online monitoring and feedback control is required in industrial application of this process to ensure the reproducibility of the laser hardening depth in complex engineering parts without doing any metallographic characterization. Bonβ [14] has presented a comprehensive review of different online measuring techniques based on IR pyrometers and a CCD camera as well as of beam-shaping techniques suitable for laser hardening of different engineering parts. He provided a lot of examples (Fig. 11.21) of how laser beam hardening can be applied in production and what parts can be hardened wisely.

Santhanakrishnan et al. [91] developed a process model by correlating laser process parameters such as laser power, scan speed, percentage of overlap, and scan vector length with depth of surface modification and hardness value using data obtained by a pyrometer and an infrared camera (Fig. 11.22).

Depending upon different process parameters, nonuniform depth of hardness with a mixture of austenite and martensite phases or of bainite, pearlite, and ferrite or a uniform depth of hardness with a mixture of austenite and martensite phases was obtained. This process model can come in handy for process engineers to decide process parameters to get a desired depth of hardness for hypo-eutectoid steels.

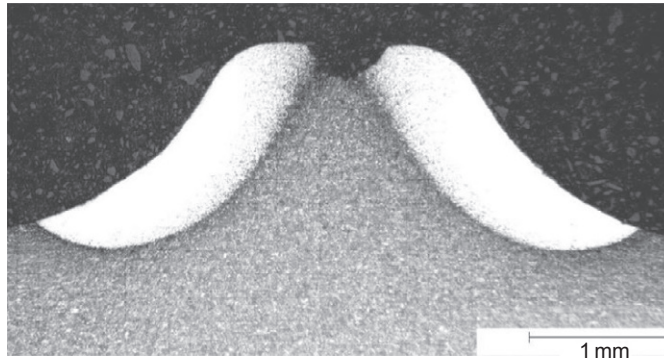


Fig. 11.21 Cross-section of a laser-hardened ball bearing screw, simultaneous application of two laser spots, annealing avoided [14, chapter 11, p. 295].

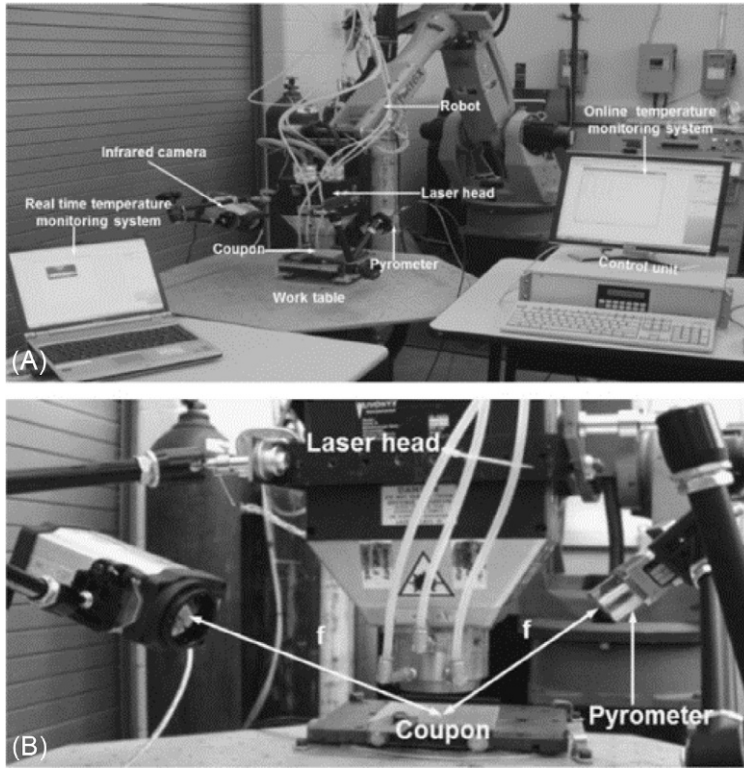


Fig. 11.22 (A) An overall experimental setup of a real-time temperature measurement system, (B) close view of the coupled real time temperature measurement system that consists of a laser-assisted infrared pyrometer and infrared camera [91].

Martinez et al. [92,93] developed a novel method named laser transformation hardening with scanning optics. They studied the effects of laser scan speed, separation between two hardened tracks, and scanning strategy on hardness values and their distribution. Results showed that laser hardening using scanning optics can produce homogenous hardness distribution with less thermal distortion as compared to the conventional laser surface hardening process [92]. Based on the scanning optics, a closed loop PID system was developed (Fig. 11.23) to control process temperature during the laser transformation hardening [93].

The movement of scanning optics allows greater flexibility in hardening variable widths of a component. Bouquet et al. [94] developed a setup to laser harden the surface of a component in the machining center itself after machining is completed. This reduced the setup change over time, logistics, and other idle time to perform laser hardening separately. A thermal model

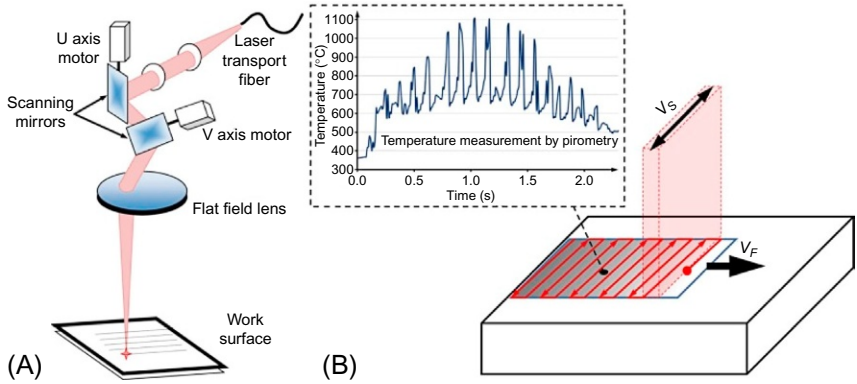


Fig. 11.23 (A) 2D scanner components; (B) thermal field generated in a part point [93].

has been developed and validated experimentally to obtain optimal hardening parameters. Further work to get optimal laser process parameters for desired hardness on the surface while maintaining high toughness values in the core material of the component under consideration, is suggested.

Wellburn et al. [95] used a variable laser beam profile shaper to convert a top hat beam into a thin annular-shaped profile having a uniform central intensity. The power ratio of central-to-annular intensity features could be varied. A 3D Lagrangian type finite-element model incorporating temperature, grain size, and a carbon-content dependent time constant was used to simulate the temperature field during laser irradiation. The resultant martensite fraction in hypo-eutectoid steel was predicted. With subsequent validation of the theoretical model with experimental results (Fig. 11.24),

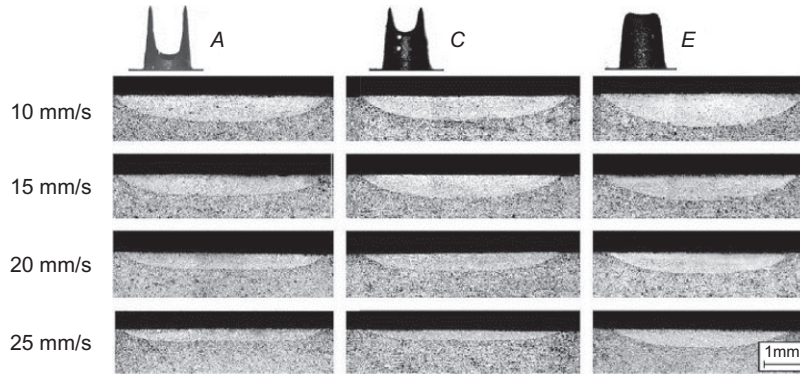


Fig. 11.24 Hardened layer cross-section in AISI 1045 steel, beam profile vs. processing speed [95].

it has been shown that for a given processing speed, the uniformity of the hardened layer is dependent on the power ratio of central-to-annular intensity features and the ratio shifts to higher value as the processing speed increases. The present process reduces the amount of overlapping in two subsequent tracks, thus reducing the effect of tempering as compared to laser surface hardening by a top hat beam profile.

The study shows that with a proper selection of process parameters, it is possible to get a uniform hardened layer using a circular laser beam profile. The achieved uniformity is higher than or comparable to other methods reported to create layer uniformity. Exploiting the capabilities of different profile modulation by the laser beam shaping setup, the present study can be applied for other laser heat treatment processes such as surface remelting, alloying, glazing, etc., to get a uniform layer modification.

Giorleo et al. [96] proposed a technique (Fig. 11.25) to harden the surface of cylindrical surfaces by rotating the job at a very high rotational speed in order to avoid the tempering effect associated with the overlapped zone. The effects of different laser process parameters, workpiece rotational speed, and workpiece diameter on hardened width, depth, and hardness values were studied.

Leonardo et al. [50] have developed a new method to harden the surface of large cylindrical components using lasers. In their experimental setup they used a fixed laser source having a Gaussian beam profile and rotated the workpiece at a very high speed. Thus a ring spot geometry was obtained on the surface of the workpiece. An annular water flow was maintained simultaneously as a quenching medium. This technique does not lead to any



Fig. 11.25 Apparent spot technique applied to a circular laser hardening [96].

tempering effects, therefore producing almost uniform hardness value and depth of hardness along the entire workpiece surface. Also, the process is energy efficient and flexible enough to adopt as compared to conventional induction hardening. However, if the surface geometry of the workpiece is very complex, the proposed technique will be difficult to adopt and may need some modifications in the experimental setup design.

Yao et al. [97] have conducted experiments on softening in an overlapped region (Fig. 11.26) in the multipass laser surface hardening process for three different steels. Softening width varied for different grades of steel (Fig. 11.27) and phases present in the corresponding overlapped zones were analyzed. The study concluded that the activation energy for diffusion of carbon in steel plays a major role in obstructing the decomposition of carbide phases, whereas the cooling rate has a limited role in reducing the temper softening effect in the case of multipass laser surface hardening with overlapped tracks.

Tani et al. [24] carried out the numerical simulation-based approach to correlate different process parameters such as laser power, scan speed, scan strategy, percentage of overlap, energy distribution at the surface, etc., with hardness value and depth of hardness for an AISI 420B martensitic stainless steel hollow axisymmetric cylindrical part. Experimental results match well with the predicted values. The model reduces experimental activities to a great extent while helping to obtain optimum process parameters for the desired hardness value and the depth of hardness for any complex industrial component.

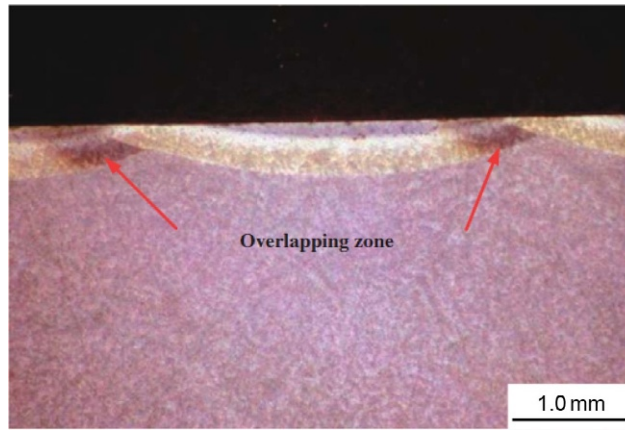


Fig. 11.26 Cross section image of overlapping passes (9Cr2Mo steel) [97].

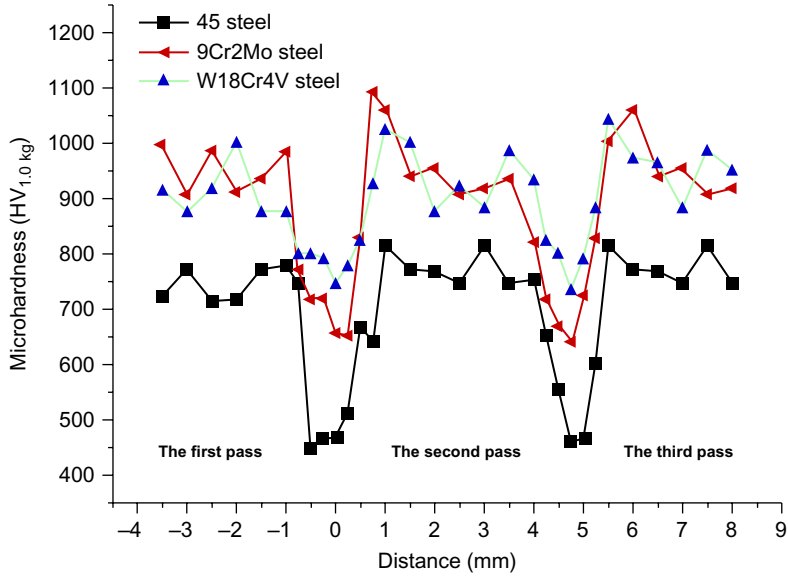


Fig. 11.27 Hardness distribution of the surface treated by laser-overlapping scanning for different steels [97].

More recently Cordovilla et al. [98] carried out an analysis of tempering in case overlapping laser hardening process, extending a laser hardening temperature/oxidation-coupled model developed by them [99] to take into account the tempering of the second track over the martensite of the first one. The predictions of hardness across the two overlapped laser scan tracks by the model were validated with the experimental results of overlapped hardening of 42CrMo4 steel.

A few other aspects also were investigated in recent times. Mahmoudi et al. [100] studied the susceptibility of stress corrosion cracking in the laser-hardened zone of AISI 420 martensitic stainless steel. Hydrogen embrittlement was reported to be the major cause of crack propagation; the preferable site of crack initiation being at the grain boundary and carbide-tempered martensite or ferrite interface. Pellizzari et al. [101] investigated wear properties of laser-hardened forged steel for hot rolls. They found that at a low test temperature, the formation of the martensite phase due to laser hardening hindered wear by adhesive fracture. At higher temperatures, the formation of different microstructures could create wear-protective oxide layers that can further result in better or worse wear resistance compared to the base material. Wang et al. [102] investigated secondary hardening which starts at 450°C and reaches maximum hardness of 672 HV at 560°C, of laser-melted

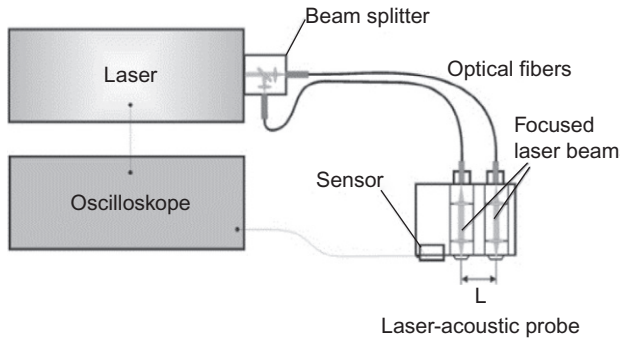


Fig. 11.28 Laser acoustic handheld probe for measuring the velocity of surface acoustic waves [103].

high chromium steel. It was found that the combined effects of martensitic phase transformation, precipitations of ultrafine carbide, and dislocation strengthening result in the secondary hardening of the laser melted layer.

Schneider et al. [103] tried to predict the depth of hardness and hardness value using acoustic waves (Fig. 11.28) for laser surface hardening of different grades of steel. Experimental results (Fig. 11.29) show that the depth of hardening could be predicted closely by the proposed acoustic model.

Lesyk et al. [104] applied an ultrasonic impact load on the surface of the laser-treated tool steel. The study shows that the combination of laser surface treatment along with the ultrasonic impact load can increase the hardness values almost three times that of the base metal while also reducing surface microrelief, waviness, and roughness parameters to a great extent. Sato et al. [105] demonstrated laser hardening of sintered products of different alloy steels, namely Fe-2Cu-0.8C, Fe-2Cu-0.5C, and Fe-4Ni-0.5Mo-1.5Cu-0.5C, fabricated in various shapes that are difficult to harden with other surface-hardening techniques.

11.3 FUTURE TRENDS

The laser surface transformation hardening process is now a well-established manufacturing process to enhance the mechanical properties at selected areas of engineering components made of ferrous materials. However, it requires trained laser material processing personnel to start using the process for any engineering component. It also often requires a series of trial runs, sample preparation, and characterizations. In order to make this process more user friendly and popularize it in the manufacturing industry,

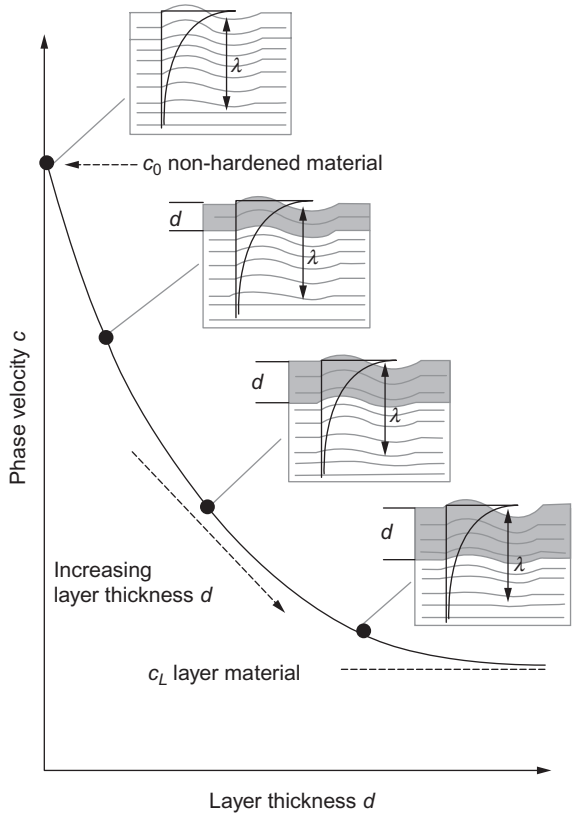


Fig. 11.29 Effect of a surface layer on the material on the propagation velocity of surface acoustic waves [103].

the future trend of research and development is expected to include the following:

- Deeper process understanding and process optimization, e.g., in terms of efficiency and process speed, and a minimum tempering effect in overlapped tracks
- R&D on user-friendly predictive modeling and the development of intelligent software and programs for determining reliable laser processing parameters quickly to surface harden any engineering component with the desired depth of hardening, without requiring a series of initial trials
- Development of online process monitoring and feedback control to ensure reproducibility and uniformity of the desired hardness over the selected processing areas

- R&D to widen the scope of laser treatment of new types of steel including less hardenable steels such as very low carbon steels, sintered products, and jobs with limited bulk material for effective self-quenching
- Development of beam-shaping optics with standard fixed optics and flexible galvanometer-driven scanning mirror systems for adjusting shape, dimensions, and intensity distribution of laser beam for laser treating parts of various shapes and sizes as well as those that are difficult to harden with other surface hardening techniques
- Development of laser hardening integrated with other machines such as turning and milling centers, and a production line to reduce overall processing time and cost

11.4 CONCLUSION

Laser hardening with the development of a better understanding of the process, predictive modeling for fixing optimum laser processing parameters, and online process monitoring and control, is now an established manufacturing process for enhancing the mechanical properties of selected surface areas of engineering parts and is becoming popular in industry. From the above literature review on laser hardening, it is apparent that research and development on its various aspects is still going on abated worldwide even after several decades following its introduction in 1973. This will continue in order to increase its industrial applications even more.

REFERENCES

[1] E. Locke, R. Hella, Metal processing with a high-power CO_2 laser, in: IEEE/OSA Conference on Laser Engineering and Applications, Washington, DC, May 30–June 1, 1973, paper 5.9, 1973, pp. 33.
[2] J.W. Hill, M.J. Lee, I.J. Spalding, Surface treatments by laser, Opt. Laser Technol. 6 (6) (December 1974) 276–278.
[3] K. Sridhar, A.S. Khanna, in: N.B. Dahotre (Ed.), Surface Engineering Series, Lasers in Surface Engineering, vol. 1, ASM International, 1998.
[4] W.M. Steen, C. Courtney, Surface heat treatment of EnS steel using a 2 kW continuous-wave CO2 laser, Metals Technol. 6 (1) (1979) 456–462.
[5] J. Senthil Selvan, K. Subramanian, A.K. Nath, J. Mater. Process. Technol. 91 (1999) 29.
[6] A. Basu, J. Chakraborty, S.M. Shariff, G. Padmanabham, S.V. Joshi, G. Sundararajan, J. Dutta Majumdar, I. Manna, Laser surface hardening of austempered (bainitic) ball bearing steel, Scr. Mater. 56 (10) (May 2007) 887–890.
[7] M.F. Ashby, K.E. Easterling, The transformation hardening of steel surfaces by laser beams—I Hypo-eutectoid steels, Acta Metall. 32 (11) (1984) 1935–1948.
[8] J. Meijer, I. van Sprang, Optimization of laser beam transformation hardening by one single parameter, CIRP Ann. Manuf. Technol. 40 (1) (1991) 183–186.

[9] A. Jacot, M. Rappaz, A two-dimensional diffusion model for the prediction of phase transformations: application to austenitization and homogenization of hypoeutectoid Fe-C steels, Acta Mater. 45 (2) (February 1997) 575–585.
[10] A. Jacot, M. Rappaz, A combined model for the description of austenitization, homogenization and grain growth in hypoeutectoid Fe–C steels during heating, Acta Mater. 47 (5) (1999) 1645–1651. 31 March.
[11] R. Komanduri, Z.B. Hou, Thermal analysis of laser surface transformation hardening—optimization of process parameters, Int. J. Mach. Tools Manuf. 44 (9) (July 2004) 991–1008.
[12] T. Mioković, V. Schulze, O. Vöhringer, D. Löhe, Prediction of phase transformations during laser surface hardening of AISI 4140 including the effects of inhomogeneous austenite formation, Mater. Sci. Eng. A 435–436 (5) (November 2006) 547–555.
[13] T. Mioković, V. Schulze, O. Vöhringer, D. Löhe, Influence of cyclic temperature changes on the microstructure of AISI 4140 after laser surface hardening, Acta Mater. 55 (2) (January 2007) 589–599.
[14] S. Bonß, Advances in Laser Materials Processing, first ed., Chapter 11; 2010, pp. 291–326.
[15] A.N. Safonov, Basic directions of effective use of laser equipment for heat treatment of alloys, proceedings of the 3rd conference of metal scientists of Russia, Met. Sci. Heat Treat. 39 (7–8) (1997) 275–279.
[16] F. Vollertsen, K. Partes, J. Meijer, State of the art of laser hardening and cladding, in: Proceedings of the Third International WLT-Conference on Lasers in Manufacturing 2005, Munich, 2005.
[17] K.M. Ralls, T.H. Courtney, J. Wulff, Introduction to Materials Science and Engineering, Wiley India Pvt. Ltd, New Delhi, India, 2011.
[18] M. Steen, J. Mazumder, Laser Material Processing, fourth ed., Springer, London, 2010.
[19] J.R. Bradley, S. Kim, Laser transformation hardening of iron-carbon and iron-carbon-chromium steels, Metallurgical transactions A, Phys. Metall. Mater. Sci. 19 A (8) (1988) 2013–2025.
[20] M.J. Tobar, C. Álvarez, J.M. Amado, A. Ramil, E. Saavedra, A. Yáñez, Laser transformation hardening of a tool steel: Simulation-based parameter optimization and experimental results, Surf. Coat. Technol. 200 (22–23) (2006) 6362–6367.
[21] H. Pantsar, Relationship between processing parameters, alloy atom diffusion distance and surface hardness in laser hardening of tool steel, J. Mater. Process. Technol. 189 (1–3) (2007) 435–440.
[22] H.J. Shin, Y.T. Yoo, D.G. Ahn, K. Im, Laser surface hardening of S45C medium carbon steel using ND:YAG laser with a continuous wave, J. Mater. Process. Technol. 187–188 (12) (June 2007) 467–470.
[23] F. Lusquiños, J.C. Conde, S. Bonss, A. Riveiro, F. Quintero, R. Comesaña, J. Pou, Theoretical and experimental analysis of high power diode laser (HPDL) hardening of AISI 1045 steel, Appl. Surf. Sci. 254 (4) (2007) 948–954. 15 December.
[24] G. Tani, A. Fortunato, A. Ascari, G. Campana, Laser surface hardening of martensitic stainless steel hollow parts, CIRP Ann. Manuf. Technol. 59 (1) (2010) 207–210.
[25] C. Soriano, J. Leunda, J. Lambarri, V. García Navas, C. Sanz, Effect of laser surface hardening on the microstructure, hardness and residual stresses of austempered ductile iron grades, Appl. Surf. Sci. 257 (16) (2011) 7101–7106. 1 June.
[26] Kou Sindo, D.K. Sun, Y.P. Le, A fundamental study of laser transformation hardening, Metall. Trans. A. 14 (3) (March 1983) 643–653.
[27] H.S. Carslaw, J.C. Jaeger, Conduction of Heat in Solids, second ed., Oxford University Press, London, 1959.
[28] M. Davis, P. Kapadia, J. Dowden, W.M. Steen, C.H.G. Courtney, Heat hardening of metal surfaces with a scanning laser beam, J. Phys. D. Appl. Phys. 19 (10) (1986) 1981–1997, 024.

[29] E. Ohmura, I. Katsunori, H. Koichi, Computer simulation on structural changes of hypoeutectoid steel in laser transformation hardening process, JSME Int. J., Ser. 1: Solid Mech. Strength Mater. 32 (1) (1989) 45–53.
[30] S.-J. Na, Y.-S. Yang, Influence of heating rate on the laser surface hardening of a medium carbon steel, Surf. Coat. Technol. 34 (3) (1988) 319–330.
[31] S. Skvarenina, Y.C. Shin, Predictive modeling and experimental results for laser hardening of AISI 1536 steel with complex geometric features by a high power diode laser, Surf. Coat. Technol. 201 (2006) 2256–2269.
[32] I.R. Pashby, S. Barnes, B.G. Bryden, Surface hardening of steel using a high power diode laser, J. Mater. Process. Technol. 139 (1–3) (2003) 585–588.
[33] E. Kennedy, G. Byrne, D.N. Collins, A review of the use of high power diode lasers in surface hardening, J. Mater. Process. Technol. 155–156 (30) (November 2004) 1855–1860.
[34] http://www.titanovalaser.com/.
[35] K.H. Lo, F.T. Cheng, H.C. Man, Laser transformation hardening of AISI 440C martensitic stainless steel for higher cavitation erosion resistance, Surf. Coat. Technol. 173 (1) (2003) 96–104 1 August.
[36] S.M. Shariff, T.K. Pal, G. Padmanabham, S.V. Joshi, Influence of chemical composition and prior microstructure on diode laser hardening of railroad steels, Surf. Coat. Technol. 228 (15) (August 2013) 14–26.
[37] J.D. Majumdar, I. Manna, Laser processing of materials, Sadhana 28 (3 & 4) (2003) 495–562. June/August.
[38] W.-B. Li, K.E. Easterling, M.F. Ashby, Laser transformation hardening of steel—II. Hypereutectoid steels, Acta Metall. 34 (8) (1986) 1533–1543.
[39] N.S. Bailey, W. Tan, Y.C. Shin, Predictive modeling and experimental results for residual stresses in laser hardening of AISI 4140 steel by a high power diode laser, Surf. Coat. Technol. 203 (14) (2009) 2003–2012.
[40] R.S. Lakhkar, Y.C. Shin, M.J.M. Krane, Predictive modeling of multi-track laser hardening of AISI 4140 steel, Mater. Sci. Eng. A 480 (1–2) (May 2008) 209–217.
[41] D.M. Roessler, Laser processing of materials for automotive applications, Mater. Manuf. Process. 4 (3) (1989) 285–310.
[42] Anon, Gold dredge 8 named ASME historic monument, World Dredging & Marine Construction 22 (7) (1986) 10–11.
[43] Yu.I. Mulin, V.A. Sokolov, Laser hardening of tool and die fixture parts, Sov. Energy Technol. 5 (1989) 44–45.
[44] A.P. Androsov, S.I. Aleksenko, M.V. Boyarkin, V.G. Kusidis, V.I. Petrov, Laser hardening of Diesel engine valve, Met. Sci. Heat Treat. 30 (1) (1988) 67–70.
[45] V.V. Divinskii, L.A. Medvedovskaya, G.A. Rainin, A.V. Sviridov, Laser hardening of tractor-engine components, Sov. Electr. Eng. 59 (11) (1988) 42–44.
[46] A.A. Ablaev, E.M. Birger, V.V. Divinskii, S.G. Drozdov, L.A. Medvedovskaya, Laser hardening of repaired A-41 engine crankshafts, Met. Sci. Heat Treat. 31 (1-2) (1989) 12–15.
[47] S. Sarkar, M. Gopinath, S.S. Chakraborty, B. Syed, A.K. Nath, Analysis of temperature and surface hardening of low carbon thin steel sheets using Yb-fiber laser, Surf. Coat. Technol. 302 (25) (September 2016) 344–358.
[48] B. Syed, S.M. Shariff, G. Padmanabham, S. Lenka, B. Bhattacharya, S. Kundu, Influence of laser surface hardened layer on mechanical properties of re-engineered low carbon steel sheet, Mater. Sci. Eng. A 685 (2017) 168–177.
[49] S. Sarkar and A.K. Nath, Water-jet assisted laser surface hardening of medium carbon steel using fiber laser, In: National Laser Symposium 25, KIIT University, India, 20–23 December 2016.
[50] L. Orazi, E. Liverani, A. Ascari, A. Fortunato, L. Tomesani, Laser surface hardening of large cylindrical components utilizing ring spot geometry, CIRP Ann. Manuf. Technol. 63 (1) (2014) 233–236.

[51] L. Orazi, A. Fortunato, G. Cuccolini, G. Tani, An efficient model for laser surface hardening of hypo-eutectoid steels, Appl. Surf. Sci. 256 (6) (2010) 1913–1919. 1 January.
[52] N. Ahmed, K.T. Voisey, D.G. McCartney, Investigation into the effect of beam shape on melt pool characteristics using analytical modelling, Opt. Lasers Eng. 48 (5) (2010) 548–554.
[53] H.-T. Chen, J.-H. Lin, X.-J. Xu, Analytical estimates of surface conditions in laser surface heating process with experimental data, Int. J. Heat Mass Transf. 67 (December 2013) 936–943.
[54] S.-Y. Lee, T.-W. Huang, A method for inverse analysis of laser surface heating with experimental data, Int. J. Heat Mass Transf. 72 (May 2014) 299–307.
[55] A. Fortunato, A. Ascari, E. Liverani, L. Orazi, G. Cuccolini, A comprehensive model for laser hardening of carbon steels, ASME. J. Manuf. Sci. Eng. 135 (6) (2013) 061002–0610028.
[56] L. Zhang, X. Shang, Analytical solution to non-Fourier heat conduction as a laser beam irradiating on local surface of a semi-infinite medium, Int. J. Heat Mass Transf. 85 (2015) 772–780.
[57] L. Giorleo, B. Previtali, Q. Semeraro, Modelling of back tempering in laser hardening, Int. J. Adv. Manuf. Technol. 54 (9) (2011) 969–977.
[58] J. Winczek, A. Modrzycka, E. Gawrońska, Analytical description of the temperature field induced by laser heat source with any trajectory, Procedia Eng. 149 (2016) 553–558.
[59] D. Sowdari, P. Majumdar, Finite element analysis of laser irradiated metal heating and melting processes, Opt. Laser Technol. 42 (6) (2010) 855–865.
[60] A. Fortunato, A. Ascari, L. Orazi, G. Campana, G. Cuccolini, Numerical evaluation of the reflectivity coefficient in laser surface hardening simulation, Surf. Coat. Technol. 206 (14) (2012) 3179–3185. 15 March.
[61] M. Bojinović, N. Mole, B. Štok, A computer simulation study of the effects of temperature change rate on austenite kinetics in laser hardening, Surf. Coat. Technol. 273 (15) (July 2015) 60–76.
[62] T. Domański, W. Piekarska, M. Kubiak, Z. Saternus, Determination of the final microstructure during processing carbon steel hardening, Procedia Eng. 136 (2016) 77–81.
[63] Z. Moumni, F. Roger, N. Thuy Trinh, Theoretical and numerical modeling of the thermomechanical and metallurgical behavior of steel, Int. J. Plast. 27 (3) (2011) 414–439.
[64] P. Dinesh Babu, G. Buvanashekaran, K.R. Balasubramanian, Experimental investigation of laser transformation hardening of low alloy steel using response surface methodology, Int. J. Adv. Manuf. Technol. 67 (5) (July 2013) 1883–1897.
[65] J. Antonio Pérez, J. Antonio Orosa, Neural modeling of laser surface treatments, Int. J. Adv. Manuf. Technol. 46 (5) (2010) 605–610. January.
[66] F. Lambiase, A.M. Di Ilio, A. Paoletti, Prediction of laser hardening by means of neural network, Procedia CIRP 12 (2013) 181–186.
[67] C. Li, Y. Wang, Z. Zhang, B. Han, T. Han, Influence of overlapping ratio on hardness and residual stress distributions in multi-track laser surface melting roller steel, Opt. Lasers Eng. 48 (12) (December 2010) 1224–1230.
[68] C. Zeng, W. Tian, H. Liang, A comprehensive study of thermal damage consequent to laser surface treatment, Mater. Sci. Eng. A 564 (1) (March 2013) 381–388.
[69] E. Liverani, A.H.A. Lutey, A. Ascari, A. Fortunato, L. Tomesani, A complete residual stress model for laser surface hardening of complex medium carbon steel components, Surf. Coat. Technol. 302 (2016) 100–106. 25 September.
[70] A. Khajeh, S.A.J. Jahromi, The finite element analysis of the surface transformation hardening process using the power control strategy in order to reduce edge effect problems, Comput. Mater. Sci. 88 (1) (June 2014) 151–155.
[71] N. Gupta, N. Nataraj, A dual weighted residual method for an optimal control problem of laser surface hardening of steel, Math. Comput. Simul. 103 (September 2014) 12–32.

[72] M. Gouné, F. Danoix, J. Ågren, Y. Bréchet, C.R. Hutchinson, M. Militzer, G. Purdy, S. van der Zwaag, H. Zurob, Overview of the current issues in austenite to ferrite transformation and the role of migrating interfaces therein for low alloyed steels, Mater. Sci. Eng. R Rep. 92 (June 2015) 1–38.
[73] S.N. Aqida, D. Brabazon, S. Naher, An investigation of phase transformation and crystallinity in laser surface modified H13 steel, Appl. Phys. A 110 (3) (March 2013) 673–678.
[74] Y.K. Danileoko, A.M. Prokhorov, A.I. Pchelintsev, A.V. Sidorin, Heat hardening of steel by pulse-periodic laser radiation, Sov. J. Quantum Electron. 16 (12) (1986) 1611.
[75] G. Habedank, J. Woitschig, T. Seefeld, W. Juptner, F. Vollertsen, R. Baierl, H. Bonas, P. Mayr, R. Schroder, F. Jablonski, R. Kienzler, Endurance limit of pulsed laser hardened component-like specimens—experiment and simulation, Mater. Sci. Eng. A 488 (2008) 358–371.
[76] W. Wu, N.G. Liang, C.H. Gan, G. Yu, Numerical investigation on laser transformation hardening with different temporal pulse shapes, Surf. Coat. Technol. 200 (2006) 2686–2694.
[77] V. Kostov, J. Gibmeier, A. Wanner, Local residual stress distributions induced by repeated austenite-martensite transformation via laser surface hardening of steel AISI 4140, Mater. Sci. Forum 681 (March 2011) 321–326.
[78] V. Kostov, J. Gibmeier, F. Wilde, P. Staron, R. Rössler, A. Wanner, Fast in situ phase and stress analysis during laser surface treatment: a synchrotron x-ray diffraction approach, AIP Rev. Sci. Instr. 83 (11) (November 2012) 115101-1–115101-11.
[79] V. Kostov, J. Gibmeier, A. Wanner, Spatially resolved temporal stress evolution during laser surface spot hardening of steel, J. Mater. Process. Technol. 239 (January 2017) 326–335.
[80] I.Yu. Smurov, A.A. Uglov, A.M. Lashyn, P. Matteazzi, L. Covelli, V. Tagliaferri, Modelling of pulse-periodic energy flow action on metallic materials, Int. J. Heat Mass Transf. 34 (4–5) (1991) 961–971.
[81] M. Kalyon, B.S. Yilbas, Repetitive laser pulse heating analysis: pulse parameter variation effects on closed form solution, Appl. Surf. Sci. 252 (6) (2006) 2242–2250. 15 January.
[82] S.Z. Shuja, B.S. Yilbas, S.M.A. Khan, Laser consecutive pulse heating and phase change: influence of spatial distribution of laser pulse intensity on melting, Int. J. Therm. Sci. 48 (10) (2009) 1960–1966.
[83] B. Mahmoudi, M.J. Torkamany, A.R. Sabour Rouh Aghdam, J. Sabbaghzade, Laser surface hardening of AISI 420 stainless steel treated by pulsed Nd:YAG laser, Mater. Des. (1980-2015) 31 (5) (May 2010) 2553–2560.
[84] J. Jiang, L. Xue, S. Wang, Discrete laser spot transformation hardening of AISI O1 tool steel using pulsed Nd:YAG laser, Surf. Coat. Technol. 205 (21–22) (2011) 5156–5164.
[85] A.K. Nath, A. Gupta, F. Benny, Theoretical and experimental study on laser surface hardening by repetitive laser pulses, Surf. Coat. Technol. 206 (8–9) (2012) 2602–2615.
[86] S. So, H. Ki, Effect of specimen thickness on heat treatability in laser transformation hardening, Int. J. Heat Mass Transf. 61 (June 2013) 266–276.
[87] H. Ki, S. So, Process map for laser heat treatment of carbon steels, Opt. Laser Technol. 44 (7) (2012) 2106–2114.
[88] H. Ki, S. So, S. Kim, Laser transformation hardening of carbon steel sheets using a heat sink, J. Mater. Process. Technol. 214 (11) (2014) 2693–2705.
[89] S. Kim, S. So, H. Ki, Controlling thermal deformation using a heat sink in laser transformation hardening of steel sheets, J. Mater. Process. Technol. 216 (2015) 455–462.
[90] B. Jin, M. Li, T. Woo Hwang, Y. Hoon Moon, Feasibility studies on underwater laser surface hardening process. Adv. Mater. Sci. Eng. 2015 (2015) 6, 845273. https://doi.org/10.1155/2015/845273. Hindawi Publishing Corporation.

[91] S. Santhanakrishnan, R. Kovacevic, Hardness prediction in multi-pass direct diode laser heat treatment by on-line surface temperature monitoring, J. Mater. Process. Technol. 212 (11) (November 2012) 2261–2271.
[92] S. Martínez, A. Lamikiz, I. Tabernero, E. Ukar, Laser hardening process with 2D scanning optics, Phys. Procedia 39 (2012) 309–317.
[93] S. Martínez, A. Lamikiz, E. Ukar, I. Tabernero, I. Arrizubieta, Control loop tuning by thermal simulation applied to the laser transformation hardening with scanning optics process, Appl. Therm. Eng. 98 (5) (April 2016) 49–60.
[94] J. Bouquet, D. Van Camp, O. Malek, P. Ten Haaf, K. Vanmeensel, B. Lauwers, Aiming for improved lifetime of die and mold components through an integrated laser hardening operation combining machining and a selective heat treatment in one setup, Procedia CIRP 46 (2016) 541–544.
[95] D. Wellburn, S. Shang, S.Y. Wang, Y.Z. Sun, J. Cheng, J. Liang, C.S. Liu, Variable beam intensity profile shaping for layer uniformity control in laser hardening applications, Int. J. Heat Mass Transf. 79 (2014) 189–200.
[96] L. Giorleo, A. Liu, B. Previtali, Apparent spot in circular laser hardening: effect of process parameters, Int. J. Mater. Form. 3 (1) (2010) 1119–1122.
[97] C. Yao, B. Xu, J. Huang, P. Zhang, Y. Wu, Study on the softening in overlapping zone by laser-overlapping scanning surface hardening for carbon and alloyed steel, Opt. Lasers Eng. 48 (1) (January 2010) 20–26.
[98] F. Cordovilla, Á. García-Beltrán, P. Sancho, J. Domínguez, L. Ruiz-de-Lara, J.L. Ocaña, Numerical/experimental analysis of the laser surface hardening with overlapped tracks to design the configuration of the process for Cr-Mo steels, Mater. Des. 102 (15) (July 2016) 225–237.
[99] F. Cordovilla, Á. García-Beltrán, J. Dominguez, P. Sancho, J.L. Ocaña, Numerical-experimental analysis of the effect of surface oxidation on the laser transformation hardening of Cr–Mo steels, Appl. Surf. Sci. 357 (Part A) (2015) 1236–1243. 1 December.
[100] B. Mahmoudi, M.J. Torkamany, A.R. Sabour Aghdam, J. Sabbaghzadeh, Effect of laser surface hardening on the hydrogen embrittlement of AISI 420: martensitic stainless steel, Mater. Des. 32 (5) (May 2011) 2621–2627.
[101] M. Pellizzari, M.G. De Flora, Influence of laser hardening on the tribological properties of forged steel for hot rolls, Wear 271 (9–10) (2011) 2402–2411.
[102] Y. Wang, M.Y. Li, B. Han, T. Han, Y.Y. Cheng, Influence of secondary carbides precipitation and transformation on the secondary hardening of laser melted high chromium steel, J. Mater. Sci. 45 (13) (2010) 3442–3447.
[103] D. Schneider, R. Hofmann, T. Schwarz, T. Grosser, E. Hensel, Evaluating surface hardened steels by laser-acoustics, Surf. Coat. Technol. 206 (8–9) (2012) 2079–2088.
[104] D.A. Lesyk, S. Martinez, V.V. Dzhemelinskyy, A. Lamikiz, B.N. Mordyuk, G.I. Prokopenko, Surface microrelief and hardness of laser hardened and ultrasonically peened AISI D2 tool steel, Surf. Coat. Technol. 278 (25) (September 2015) 108–120.
[105] M. Sato, Y. Adachi, H. Motoyama, Application of laser hardening technology to sintered parts, SEI Tech. Rev. 82 (2016) 66–69.

CHAPTER 12

Pulsed Laser Annealing Technology for Nano-Scale Fabrication of Silicon-Based Devices in Semiconductors

J. Lawrence*, K.L. Pey†, P.S. Lee†
*University of Chester, Chester, United Kingdom
†Nanyang Technological University, Singapore, Singapore

12.1 INTRODUCTION

Highly doped and very shallow p/n junctions are semiconductor diodes that form the basic building blocks in semiconductor devices. It is one of the most important technologies in integration devices that are ultra large. The stringent requirements of ultrashallow junction of source and drain terminals in complementary metal-oxide-silicon (CMOS) to reduce short channel effects have led to the development of new dopant activation and defect annealing processes such as laser thermal processing (LTP) [1–4]. On the other hand, silicides are metal-silicon compounds acting as Ohmic or Schottky contacts in semiconductor devices. They are usually formed using conventional thermal treatment or rapid thermal processing to induce a solid-state reaction between the metal overlayer on a silicon substrate, typically a p/n junction.

In part one of this chapter, various methods for the formation of ultrashallow p^+/n junctions using an excimer pulsed laser annealing technique of 248.0 nm wavelength will be presented. The characteristics of junctions formed using single- and multiple-pulse shallow melt and nonmelt laser annealing on amorphous and single crystalline Si substrate will be compared. The effect of the type of substrates, (i.e., Si, SiGe, and SOI) on the formation of the nano-scale p-type junctions for device process integration will be discussed. To overcome the defect-related enhanced diffusion during pulsed laser annealing, a novel junction engineering methodology using laser-generated defects such as vacancies is illustrated.

Advances in Laser Materials Processing
https://doi.org/10.1016/B978-0-08-101252-9.00012-1
Copyright © 2018 Elsevier Ltd.
All rights reserved.

In part two the formation of silicide and germanosilicide using excimer pulsed laser annealing will be covered. In particular, the formation of Ni- and Ni(Pt)Si/SiGe using single- and multiple-pulse laser annealing is demonstrated.

12.2 LASER-INDUCED FORMATION OF P/N JUNCTION

Pulsed laser annealing is a transient annealing and the quenching rates of pulsed laser processing are of the order of 10^{10} K/s, which enables the extension of solid solubility, induces a reaction in the solid or liquid phase, and leads to the formation of metastable crystalline or amorphous phases of the annealed layers. LTP of ultrashallow junctions typically involves preamorphization of the silicon surface and dopant implantation followed by melting of the amorphized and implanted regions (and the substrate) using a pulsed excimer laser. The advantages of LTP are: a "near-zero" thermal budget (since laser pulses last only for tens of nanoseconds); the extent of dopant diffusion is controlled by the melt depth (with negligible diffusion in the adjacent solid substrate); and the rapid quench rate (metastable process). This allows active dopant concentrations to exceed the solid solubility limit [3,4].

In general, the structural changes induced by laser irradiation of an amorphized silicon (a-Si) layer on crystalline silicon (c-Si) can be characterized by three cases:

Case I: The laser fluence is only slightly greater than the threshold fluence for melting a-Si. In this case, the primary melt (molten layer produced directly by laser irradiation) does not penetrate through the entire a-Si layer. Typically, large-grained (LG) polycrystalline silicon (poly-Si) will be formed near the surface region followed by fine-grained (FG) poly-Si in the underlying region (Fig. 12.1B). The fraction of the LG region will increase at the expense of the FG region with increasing fluence—a result of explosive crystallization [5,6].

Case II: The laser fluence is just sufficient for the primary melt front to reach the a/c interface without melting the underlying c-Si substrate (Fig. 12.1C). Single-crystalline silicon is thus formed via liquid phase epitaxy (LPE), using the underlying substrate as a template [7]. In theory, this regrowth process should produce crystals with reasonably good quality [5]; however, it has been reported that residual defects such as microtwins and stacking faults exist in the crystallized layer [8].

Case III: At even higher energy densities, the primary melt front penetrates beyond the amorphous/crystalline (a/c) interface (Fig. 12.1D). In this

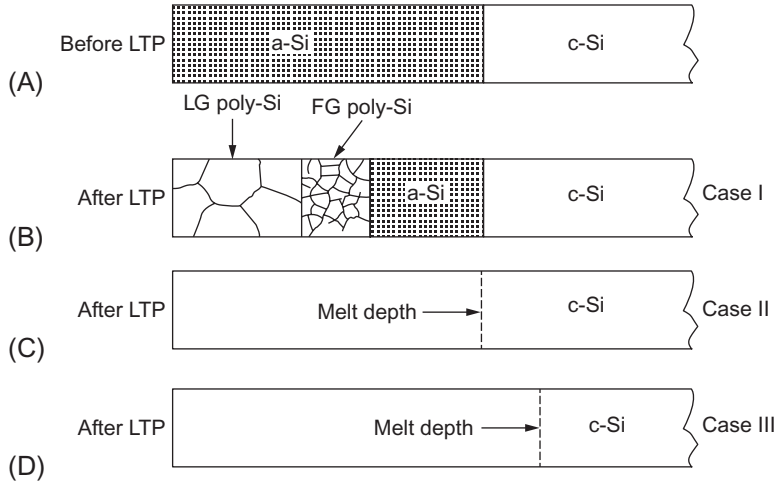


Fig. 12.1 Illustration of the structural changes induced by laser irradiation of an a-Si overlayer on c-Si.

case, single-crystalline silicon is also formed upon solidification [7,9]. The melting of a part of the crystalline substrate adjacent to the amorphous layer ensures the epitaxial growth of a nearly defect-free crystal with minimum "quenched-in" interstitials [10].

The main advantage of LTP is that it offers the feasibility of forming abrupt, highly activated, and ultrashallow junctions due to its extremely rapid heating and cooling rates in the nanosecond regime [3,4,11–14]. Thus, the thermal budget is minimized (near zero) while providing proper dopant activation for the implanted species. Since the process does not reach thermal equilibrium, the concentration of electrically active dopants can actually exceed the solid solubility limit [4,12]. If the Si substrate is melted to a depth greater than the range of the implanted ion, the dopant atoms will be incorporated substitutionally into the regrown epitaxial Si lattice. As a result, the sheet resistance decreases significantly [9,14]. Dopant incorporation into the lattice at high concentrations is proven to be a direct result of solute trapping during solidification [7,15]. This means that if the time required to regrow one or more monolayer of atoms during solidification is significantly shorter than the residence time of the impurity at the interface, the dopant has a high probability of being incorporated into the growing solid [7].

Another factor that contributes to the high degree of dopant activation upon laser melting is the near-unity interface segregation coefficient, k_i of the common dopants, such as B, P, and As during LTP [12,16]. In the

theory of crystal growth, k_i is defined as the ratio of the solute concentration in the growing solid to that in the liquid at the liquid/solid interface. If $k_i = 1$, the solute is entirely incorporated into the bulk solid and no segregation to the surface occurs. When k_i deviates from unity, segregation effects begin to manifest themselves by an accumulation of impurities in front of the advancing liquid/solid interface [7,17]. Since the equilibrium k_i values of these common dopants are lower than 1 (equilibrium k_i of B, P, and As is 0.8, 0.35, and 0.3, respectively [7]), these observations provide evidence of the highly nonequilibrium crystallization process of LTP.

12.2.1 Effect of Laser Fluence

Fig. 12.2 shows the sheet resistance of a 1 keV boron-implanted sample (preamorphized with a 5 keV, $1 \times 10^{15}/cm^2$ Ge^+) as a function of laser fluence. The samples were subjected to a single-pulse irradiation from a 248.0 nm KrF laser. It is observed that the sheet resistance decreases as fluence increases, indicating an increase in dopant activation and possibly an increase in junction depth with increasing fluence. However, the R_s remains virtually unchanged (at approximately 200 Ω/sq) when the fluence is increased to a value above $0.52 J/cm^2$. This implies that the dopants are almost fully activated at such high fluence levels. The high degree of dopant activation

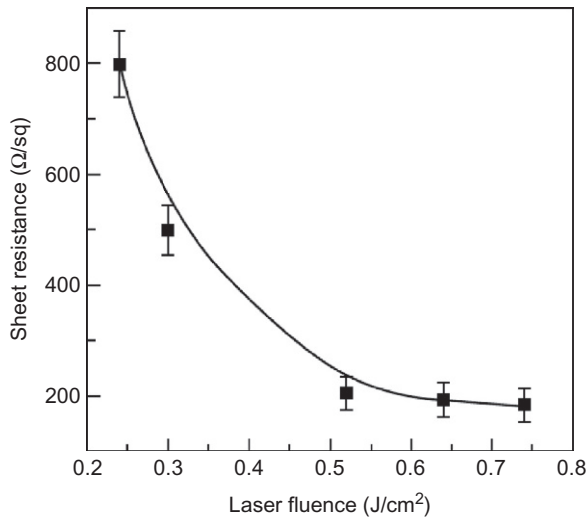


Fig. 12.2 Sheet resistance of a 1 keV boron-implanted sample as a function of laser fluence. *(Reused with permission from Y.F. Chong, K.L. Pey, A.T.S. Wee, A. See, C.-H. Tung, R. Gopalakrishnan, Y.F.Lu, Proc. of Adv. MicroE. Proc. Tech. SPIE, vol. 4227, 2000, p. 124. Copyright 2000, Conference of SPIE.)*

is attributed to the extremely high heating ($>1\times10^{10}$ °C/s) and quenching rates of the laser process. As a consequence, the dopants are engulfed in the substitutional sites during crystallization (solute trapping), with dopant concentrations that can exceed the equilibrium solid solubility limit in silicon.

The effect of single-pulsed laser irradiation on the redistribution of boron atoms is illustrated in Fig. 12.3. The most prominent feature in Fig. 12.3 is the presence of step-like dopant profiles following laser annealing. For example, the junction abruptness, defined as the slope of the abrupt SIMS trailing profile, of the 0.52 J/cm^2 laser-annealed sample is less than 4 nm/decade. These profiles are in sharp contrast to those obtained after spike RTA, where those samples exhibit graded concentration profiles. For advanced CMOS technologies, a nearly fat and abrupt profile is desired for the source/drain extension junctions to confine the electric field in the channel region under the gate and to reduce the subthreshold leakage current. In order to achieve a reasonably high degree of dopant activation for the laser-annealed samples, the melt depth should be large enough to encompass the boron profile at 1×10^{18} atoms/cm^3.

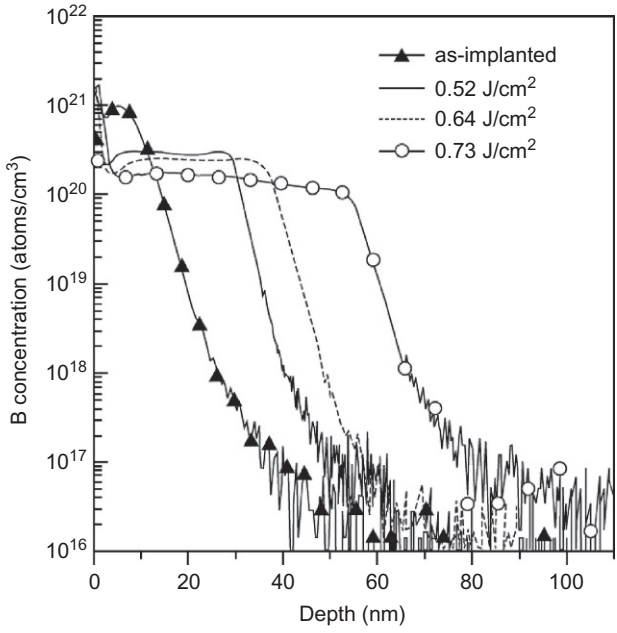


Fig. 12.3 SIMS depth profiles showing the effect of single-pulsed 248.0 nm laser irradiation on the redistribution of boron atoms.

The formation of the abrupt junction can be explained as follows. During laser irradiation, the heat generated by the laser pulse causes a thin layer of the Si surface to melt. Since the diffusivity of boron in the liquid phase (around $10^{-4}\,cm^2/s$) is about eight orders of magnitude higher than that in the solid state (around $10^{-12}\,cm^2/s$ at 1000°C) [18], the boron atoms start to diffuse instantaneously and become nearly uniformly distributed within the molten Si. Diffusion stops exactly upon reaching the liquid/solid interface, thus forming an abrupt junction [4,12]. Since the melt duration during LTP is typically in the tens of nanosecond regime, it is believed that diffusion of boron in the solid adjacent to the liquid/solid interface is negligible.

As shown in Fig. 12.3, the junction depth, χ_j determined at a background concentration of $1\times10^{18}\,cm^{-3}$, for the sample after laser annealing at $0.52\,J/cm^2$ is in the region of 300 Å and is shallower than that of reference samples using spike anneal by at least 280 Å. Furthermore, the boron concentration (see the fat portion of the SIMS profile) in this sample is as high as $3.4\times10^{20}\,atoms/cm^3$, a value that is greater than the equilibrium boron solid solubility (approximately $1.9\times10^{20}\,atoms/cm^3$ at 1100°C) in silicon [19]. This is manifested as an appreciable decrease in the sheet resistance after LTP. For example, the R_s of the $0.52\,J/cm^2$ laser annealed sample (around $200\,\Omega/sq$) is considerably lower than that of the spike annealed reference samples (R_s ranging from 294–308 Ω/sq), despite a junction depth difference of at least 280 Å. The above results strongly indicate that due to the near-zero thermal budget of the LTP, single-pulsed laser irradiation can produce abrupt, highly activated and ultrashallow p^+/n junctions for CMOS technologies.

12.2.2 Effect of Crystalline and Preamorphized Substrates

Figs. 12.4A and B show the SIMS profiles of boron in n-type Si (100) crystalline silicon and preamorphized silicon (PAI-Si) samples, respectively, subjected to single-pulse LTP at laser fluences of 0.50 and $0.60\,J/cm^2$. The boron was implanted at 0.5 keV with a dose of $1\times10^{15}\,cm^{-2}$. For the PAI-Si samples, they were preamorphized using Si^+ implantation at 10 keV with a dose of $2\times10^{15}\,cm^{-2}$ before the boron implantation. Similar to the results shown in Fig. 12.3, there is a formation of a boxlike dopant profile in the c-Si sample upon (shallow-melt) LTP at $0.60\,J/cm^2$. The formation of the abrupt junction follows the melting of the surface region of the c-Si sample upon laser irradiation. On the other hand, (nonmelt) LTP at $0.50\,J/cm^2$ does not induce any substantial melting in the c-Si sample [20,21] and leads to a diffusionless dopant profile that follows the as-implanted profile,

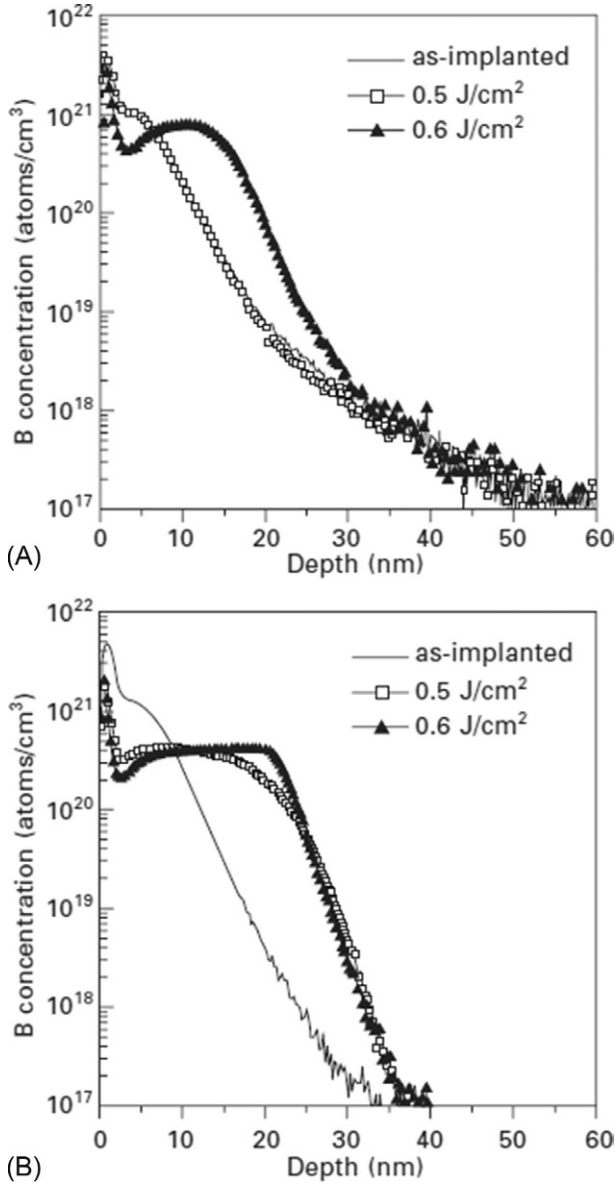


Fig. 12.4 SIMS profiles of boron in (A) crystalline and (B) preamorphized Si substrates subjected to single-pulse LTP at laser fluences of 0.50 and 0.60 J/cm^2.

as shown in Fig. 12.4A. This is due to the near-zero thermal budget of LTP that generates a negligible solid-phase boron diffusion.

In contrast to the case of the c-Si sample, similar boxlike profiles are formed with LTP at both 0.50 and 0.60 J/cm^2 in the PAI-Si sample. This is

possible due to the fact that the melting temperature of amorphous silicon (α-Si) is about 200°C lower than that of c-Si [3,4,6]. As a result, LTP melts the α-Si layer without melting the underlying c-Si substrate. Because the melting in the PAI-Si sample is defined by the Si^+ implantation generated α-Si layer, abrupt ultrashallow junctions of similar depth can be achieved in a wider range of laser fluences. This leads to an improved process window of about 20% laser fluence.

Fig. 12.5 shows the junction depth and junction abruptness of c-Si and α-Si for various laser fluences between 0.50 and 0.80 J/cm^2. The junction depths in the c-Si sample increase from 32.0 to about 35.0 nm when the laser fluence increases from 0.50 to 0.60 J/cm^2 (from nonmelt LTP to shallow-melt LTP). This is due to a melting shallower than 35.0 nm at 0.60 J/cm^2, leading to a junction depth defined by the unannealed dopant profile tail. Upon LTP at fluences greater than 0.60 J/cm^2, the junction depth in the c-Si sample shows a linear increase with increasing laser fluences, which is attributed to a linear relationship of the maximum melt depth in the c-Si sample with laser fluence, as shown in Fig. 12.6.

Fig. 12.6 shows that both extracted and simulated (by the simulation of laser interaction with materials (SILM)) [22] maximum melt depths indicate a threshold of melting of 0.52 J/cm^2 that defines the nonmelt regime

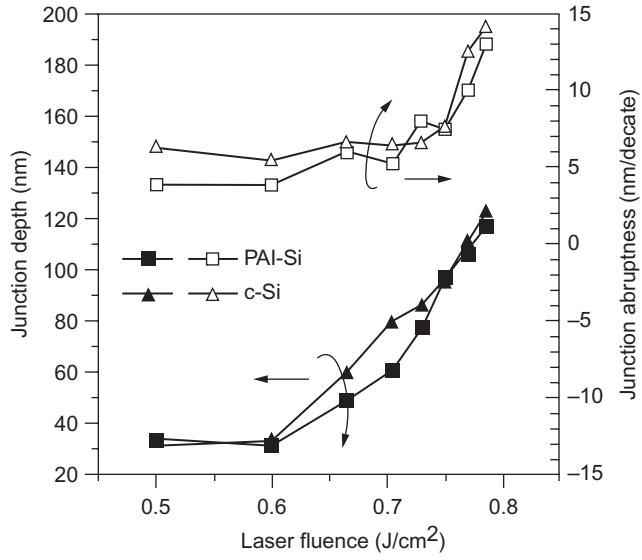


Fig. 12.5 Effect of laser fluence and PAI-Si on junction depth and junction abruptness of LTP formed p/n junctions.

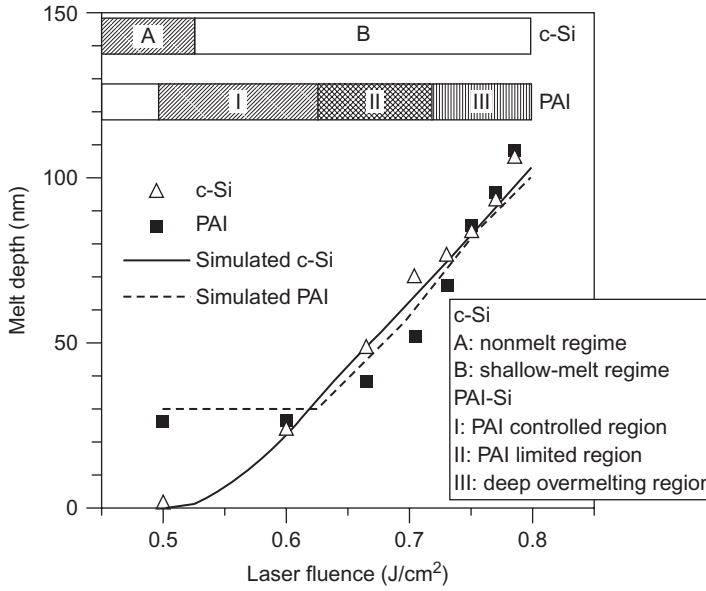


Fig. 12.6 Extracted maximum melt depth from SIMS profiles and SLIM simulated maximum melt depth as a function of laser fluence.

(Region A) and shallow-melt regime (Region B). The maximum melt depth follows a linear relationship upon laser irradiation at a fluence greater than the threshold of melting. Upon a deeper melting induced at higher fluences, the dopant atoms are redistributed to a deeper extent, leading to a junction depth seen in Fig. 12.5. The junction abruptness in the c-Si sample remains at approx. 6 nm/decade up to a laser fluence of 0.73 J/cm^2. SLIM indicates that laser irradiation at 0.75 J/cm^2 induces a deep melting of 85.0 nm and a melt duration of 12 ns at the full-width-half-maximum (FWHM). The short melt duration is insufficient to redistribute the boron atoms to the maximum melt depth achieved at 0.75 J/cm^2. This leads to the formation of a less abrupt junction, as depicted in Fig. 12.5.

The PAI-Si samples show a constant junction depth at 0.50 and 0.60 J/cm^2, in which the melting is controlled by the original PAI depth. Upon a deeper melting at higher laser fluences, the junction depth in the PAI-Si samples increases with increasing laser fluences. As shown in Fig. 12.6, melting of the entire original α-Si layer occurs in the PAI controlled region (Region I), leading to boxlike junction profiles defined by the original α-Si layer. Overmelting beyond the original α-Si layer, which occurs at a higher fluence, sees a c-Si substrate, namely in the PAI limited region (Region II) and the deep overmelting (Region III). Overmelting in the PAI limited

region melts slightly beyond the original α-Si layer, in which the lower melting temperature of the α-Si layer and high reflectivity of the melted Si surface limit further melting. Deep melting beyond the original α-Si layer surpasses the effects of the α-Si layer and causes a melting similar to the c-Si sample.

From Fig. 12.7, it is observed that the sheet resistances in both c-Si and PAI-Si samples decrease with increasing laser fluence, indicating an increase in the dopant activation [3]. The sheet resistance in both c-Si and PAI-Si samples reaches a minimum value of 150 Ω/sq for fluences greater than 0.73 J/cm^2. This implies that dopant activation has reached a maximum level upon deep melting of both c-Si and PAI-Si samples. It is important to note that nonmelt LA at 0.50 J/cm^2 has induced moderate activation corresponding to a moderate value of the sheet resistance.

Fig. 12.8 shows that the dopant activation in both c-Si and PAI-Si samples increases linearly with increasing laser fluences. Higher dopant activation in the PAI-Si sample upon LTP at 0.50 and 0.60 J/cm^2 is attributed to a deeper melting (both defined by the original α-Si layer) as compared with that in the c-Si sample. For laser fluences greater than 0.73 J/cm^2, the dopant activation in both c-Si and PAI-Si samples sees a maximum activation at about 75%. When compared with the dopant retention for laser fluences

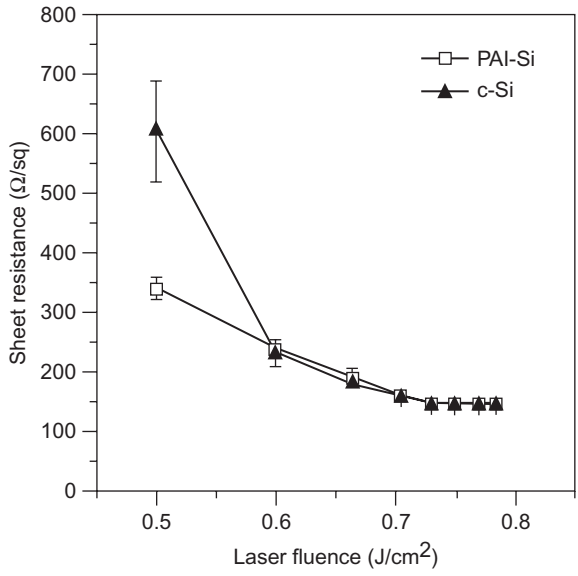


Fig. 12.7 Sheet resistance of crystalline and preamorphized Si substrate subjected to single-pulse LTP at various laser fluences.

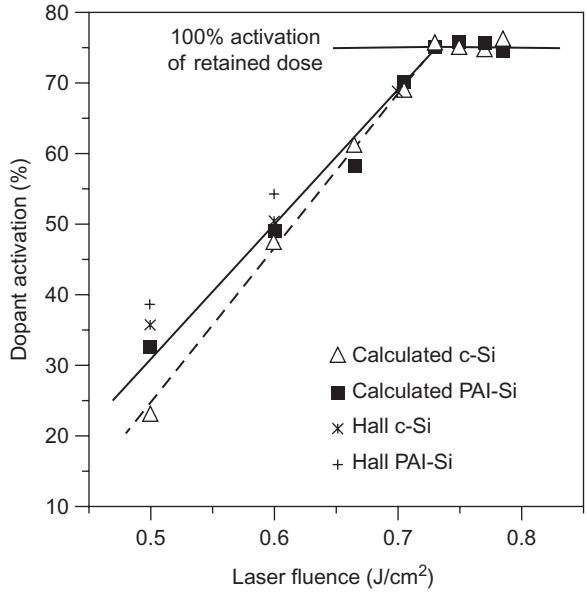


Fig. 12.8 Dopant activation as a function of laser fluence in crystalline and preamorphized Si substrates. Dopant activation obtained using Hall measurement is also included.

greater than $0.73\,J/cm^2$, the dopant activation corresponds to a 100% activation of the retained dopant in both samples [23].

12.2.3 Multiple-Pulse Laser Thermal Processing in Boron-Implanted Crystalline Si Substrate

Laser annealing to activate boron dopants can be performed using more than one laser pulse. Enhanced dopant activation is expected with an increasing number of laser pulses. However, the effectiveness of laser pulses may degrade after the first few pulses; this is discussed in this section.

Fig. 12.9 shows the SIMS profiles of a 0.5 keV, $1\times10^{15}\,cm^{-2}$ boron-implanted c-Si sample upon shallow-melt LA at $0.60\,J/cm^2$ and nonmelt LA at $0.50\,J/cm^2$, respectively, with various numbers of laser pulses. It is observed that subsequent laser irradiations do not significantly alter the junction depth and junction abruptness annealed by the initial laser irradiations [24], as shown in Figs. 12.9 and 12.10. Simulation results show that LTA at 0.60 and $0.50\,J/cm^2$ raises the surface temperature of the c-Si sample above 1000°C in less than a few tens of nanoseconds and eventually cools down to a room temperature at a time greater than 1 μs. This implies that the initial laser irradiation would not have any interaction with the subsequent laser

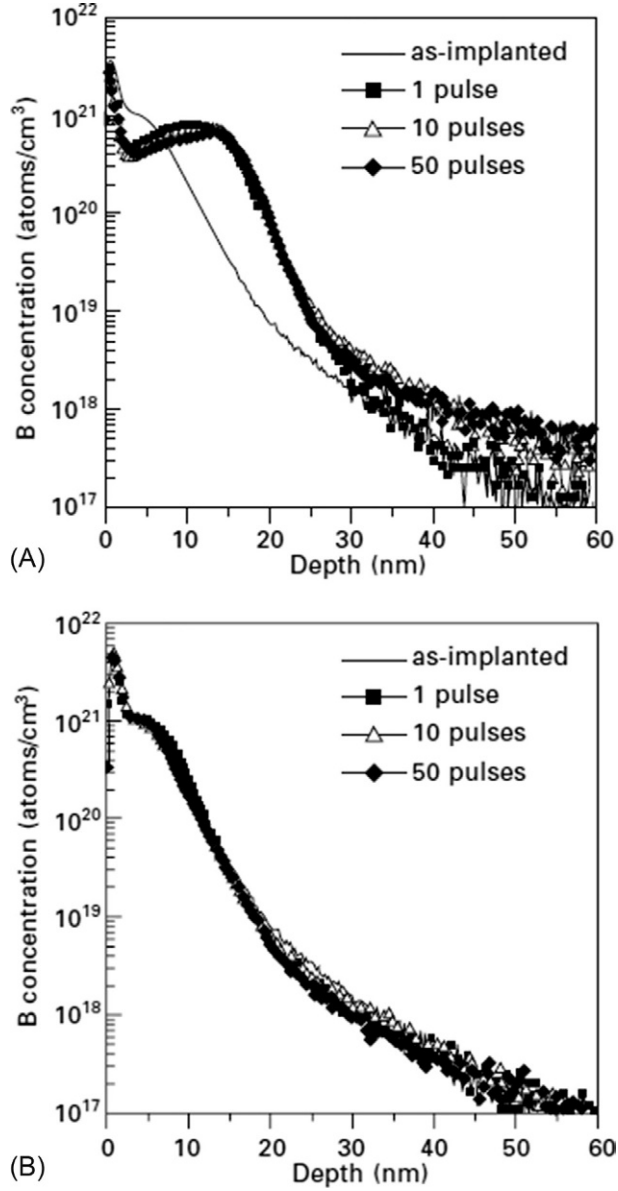


Fig. 12.9 SIMS profiles of boron in crystalline Si substrate subjected to (A) shallow-melt LTP at 0.60 J/cm^2 and (B) nonmelt LTP at 0.50 J/cm^2 with various numbers of laser pulses.

irradiations in a 1 Hz repetition rate. Thus, each of the laser irradiations can be considered as a separate and independent entity. Since each of the laser irradiations at 0.60 J/cm^2 induces a similar melt depth of 23.0 nm, the junction depth and junction abruptness remain unchanged upon multiple-pulse

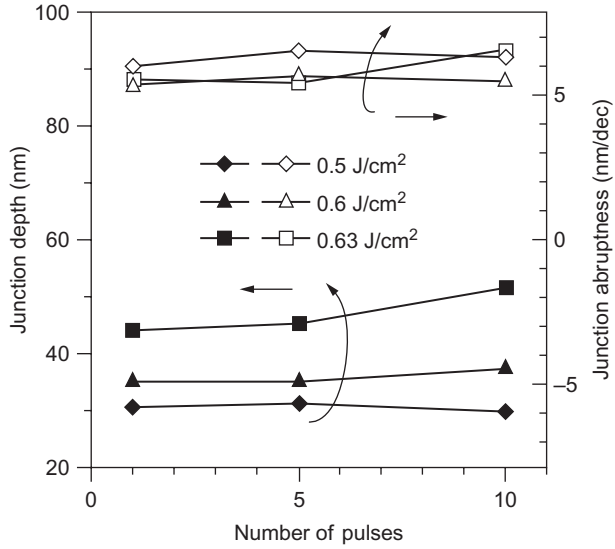


Fig. 12.10 Effect of number of laser pulses on junction depth and junction abruptness.

LTP. Nonmelt LA at $0.50\,J/cm^2$, on the other hand, causes no significant melting to the c-Si sample and induces a negligible diffusion of the as-implanted profile; therefore, the junction depth and junction abruptness also remain unchanged with increasing laser pulses.

12.2.4 Laser Thermal Processing in Boron Implanted Silicon-On-Insulator Substrate

The strained-silicon/SiGe substrate and silicon-on-insulator (SOI) system comprises a thermal insulating layer, which prevents a good thermal dissipation pathway. This gives rise to a highly nonequilibrium laser process and can vary significantly to that in normal bulk silicon substrate. We compare the formation of ultrashallow p^+/n junctions in bulk silicon and strained-Si/SiGe and SOI substrates using laser annealing in shallow-melt and nonmelt regimes.

Fig. 12.11 shows the SIMS profiles of boron in a preamorphized silicon and a SOI substrate, after single-pulse LTP at laser fluences of 0.20, 0.40, and $0.60\,J/cm^2$. In this experiment, boron was implanted at 0.5 or 1.0 keV with a dose of $5\times10^{14}\,cm^{-2}$ into n-type Si (100) and Si-on-insulator (SOI) substrates. The SOI wafer used has a topmost silicon (100) layer thickness of 182.0 nm and a buried silicon dioxide (BOX) layer thickness of 188.0 nm. The PAI samples were preamorphized using Si^+ implantation at 30 keV with a dose of $2\times10^{15}\,cm^{-2}$. It is worth noting that the laser fluences used

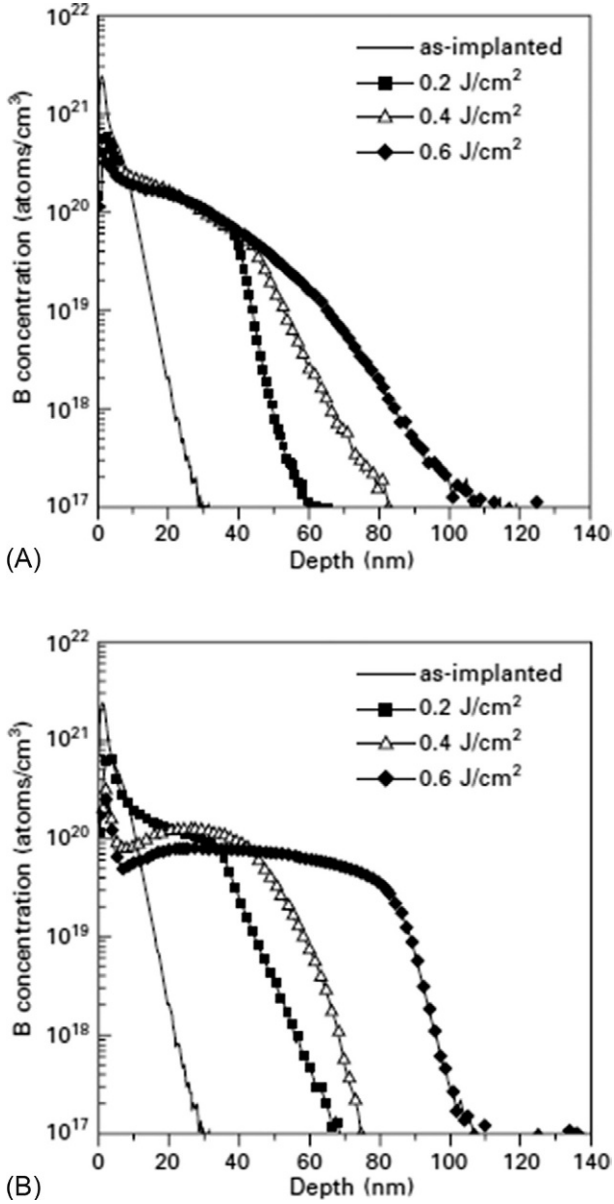


Fig. 12.11 SIMS profiles of boron in 30-keV Si^+ preamorphized (A) silicon and (B) SOI substrates subjected to single pulse LTP at fluence of 0.20, 0.40, and 0.60 J/cm^2.

are all above the threshold fluence for melting amorphous silicon. All the boron profiles in the SOI substrates have a deeper dopant distribution than that in the silicon substrate. In the case of 0.40 and 0.60 J/cm^2 laser fluences in the silicon substrate, due to a thick melted layer, boron could not

redistribute fast enough to form a step-like profile. On the other hand, step-like profiles are formed in the SOI substrate for the same fluences used for the silicon substrate.

The corresponding junction abruptness and junction depth are shown in Fig. 12.12. The profiles are at least 10.0 nm deeper for the SOI substrate, which suggests a deeper melt depth for the same laser fluence used. On the other hand, improved junction abruptness with increasing laser fluence in the SOI substrates further confirms a greater melting duration, in which the dopant is allowed to redistribute more uniformly. This indicates that the laser process has a strong dependence on the thermal conductivity of the substrate used [25].

The cross-sectional TEM (XTEM) micrograph of the silicon substrate after laser irradiation at 0.60 J/cm^2 is shown in Fig. 12.13A. The melt front has apparently stopped near the a/c interface. Since the laser fluence is unable to fully melt the PAI layer, the solidification process is mediated by explosive crystallization [6]. On the other hand, the XTEM image for the SOI substrate shows that the SOI layer is a perfect crystal after the laser irradiation at 0.60 J/cm^2, and no defect can be found even at the original a/c region. This indicates that the thermal insulating effect of the BOX layer causes the melt front to exceed the PAI layer, unlike in the case of normal silicon substrates. The laser-regrown layer from this overmelting does not contain any defects that were observed in the absence of overmelting [8,26].

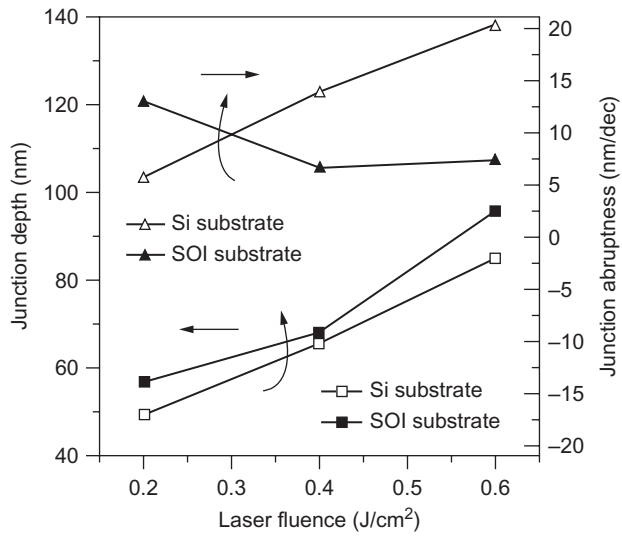


Fig. 12.12 Effect of substrate on the junction depth and junction abruptness.

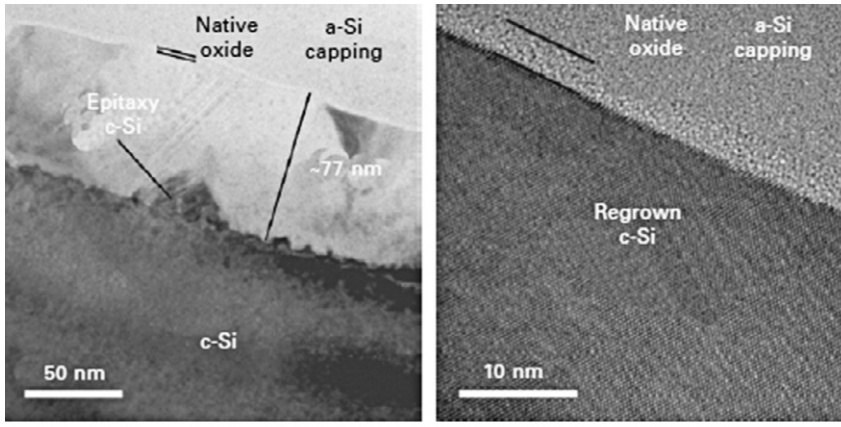


Fig. 12.13 Cross-sectional TEM micrograph of 30-keV Si^+ preamorphized (A) silicon and (B) SOI substrates subjected to single-pulse LA at 0.60 J/cm^2. The laser regrown layer in the SOI substrate is virtually defect free.

12.2.5 Laser Thermal Processing in Boron-Implanted SiGe Substrate

Fig. 12.14 shows the boron and the germanium profiles in bulk Si and strained-Si/SiGe substrates, respectively, subjected to single-pulse LTP at 0.60 J/cm^2 and multiple-pulse LTP at 0.40 J/cm^2. The strained-Si/SiGe substrate comprises a linearly graded SiGe layer 2 μm thick grown on p-type Si wafers. On top of the graded SiGe, 1 μm of uniform SiGe layer at 25% Ge content and 20.0 nm of strained Si layer were grown. In the case of the bulk Si substrate, the LTP at 0.60 J/cm^2 induces a shallow melting of 28.0 nm while 0.40 J/cm^2 induces no melting to the substrate. An abrupt boron profile at 0.60 J/cm^2 is contained in the melted region. The overlapping of the annealed profiles at 0.40 J/cm^2 with the implanted profile is an indication that the laser fluence is inadequate to melt the crystalline Si. On the other hand, all fluences, including the low-fluence LA of 0.40 J/cm^2, induce substantial melting in the strained-Si/SiGe substrate. The profiles are at least 100.0 nm deeper in the strained-Si/SiGe substrate than that in the bulk Si substrate. This indicates a substantial lowering of the threshold of melting in the strained-Si/SiGe due to a thermal confinement effect of the SiGe layer. A threshold of melting of 0.15 J/cm^2 is found for the strained-Si/SiGe substrate. A graded boron profile at a single-pulse LTP at 0.40 J/cm^2 results from a deep melted layer that boron could not redistribute fast enough to form a boxlike profile. The germanium step at the original

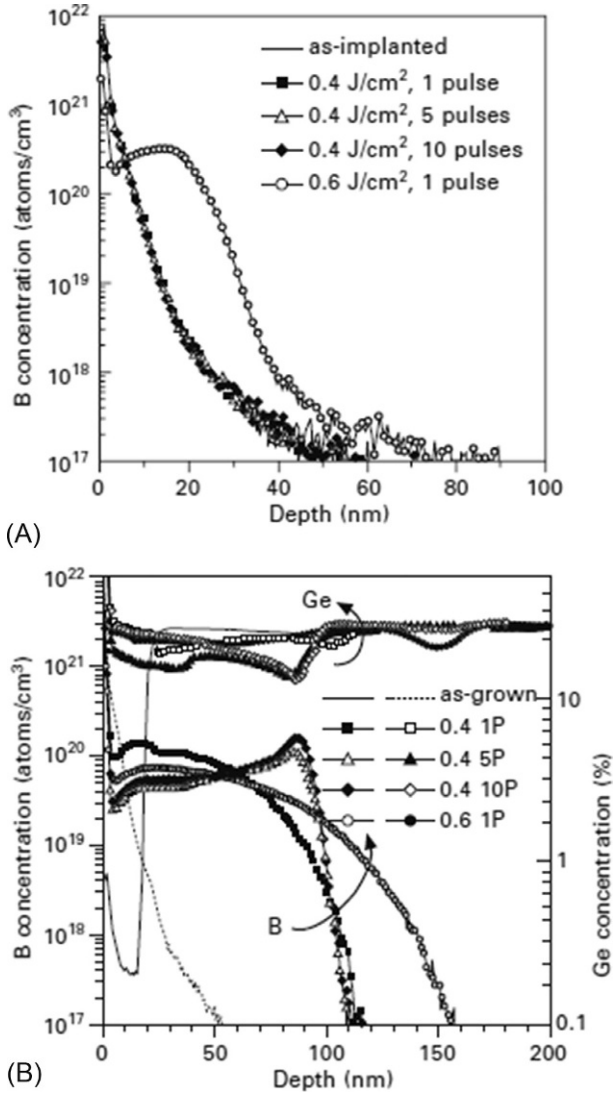


Fig. 12.14 SIMS profiles of boron in (A) silicon and (B) strained-Si/SiGe substrates subjected to single and multiple-pulse LA at 0.40 and 0.60 J/cm^2. Germanium profiles are also included in (B). *(Reused with permission from K.K. Ong, K.L. Pey, P.S. Lee, A.T.S. Wee, X.C. Wang, L.H. Wong, ECS Trans. 1(30) (2006) 1. Copyright 2006, The Electrochemical Society.)*

strained-Si/relaxed-SiGe interface in Fig. 12.14B suggests a possible melting of the relaxed SiGe layer prior to the strained-Si layer due to a lower melting temperature of SiGe than that of Si [27]. Boxlike profiles of boron and uniform germanium profiles are generated at 5- and 10-pulse LA at

$0.40\,J/cm^2$ due to a longer melting duration that allows a uniform distribution of boron and germanium atoms. As the thermal conductivity of the SiGe layer is very much less than Si [27], the SiGe layer in the strained-Si/SiGe substrate has an insulating effect that prevents heat dissipation. The calculated thermal energy transfer rate from the surface of the strained-Si to a depth beyond the graded-SiGe layer will decrease over 94% in the thermal energy transfer rate as compared to that of a bulk Si with the same substrate thickness. Similar to the SOI substrate, when applying LTP with pulse duration in nanoseconds to substrates such as the strained-Si/SiGe, one would expect a significant difference in the heating and cooling rates as compared to a silicon substrate.

Fig. 12.15A shows the SIMS profiles of boron and germanium in the strained-Si/SiGe substrate subjected to a shallow melt LA as low as $0.20\,J/cm^2$. The melting mechanism is similar to the case of $0.40\,J/cm^2$. This causes a great challenge in creating a shallow melting of the strained-Si without melting the SiGe layer that has a lower melting temperature than that of Si. Nonmelt LA seems to be the best alternative for the activation of junction [20,21]. Fig. 12.15B shows the boron and germanium profiles subjected to a nonmelt LTP at $0.10\,J/cm^2$. The complete overlapping of the boron and the germanium profiles with the as-implanted/as-grown profiles confirms no melting occurs during the LTP. No germanium out-diffusion, which would affect the performance of the strained-Si layer, is observed for the 23-ns laser pulse. A good activation in the nonmelt LTP is indicated by a low sheet resistance obtained. The Raman spectra of the strained-Si/ SiGe substrate shown in Fig. 12.16 indicate an absence of the Si-Si peak in the strained-Si layer at $0.20\,J/cm^2$. This indicates that the melting at $0.20\,J/cm^2$ has consumed the strained-Si and relaxed-SiGe layers, leading to a distribution of germanium into the original strained-Si layer. On the other hand, no degradation in the strain in the strained-Si layer was observed after the nonmelt LA at $0.10\,J/cm^2$ as revealed by the similar Raman spectra to that of the as-grown sample. Therefore nonmelt LA proves to be a promising alternative for annealing advanced semiconductor substrate with a thermally less conductive substrate.

12.2.6 Vacancy Engineering by Laser Irradiation in Boron-Implanted, Preamorphized Silicon Substrate

Laser-induced melting in silicon can be used to generate excess vacancies near the maximum melt depth before silicon substrate amorphization and subsequent boron implantation. By matching the preirradiated laser

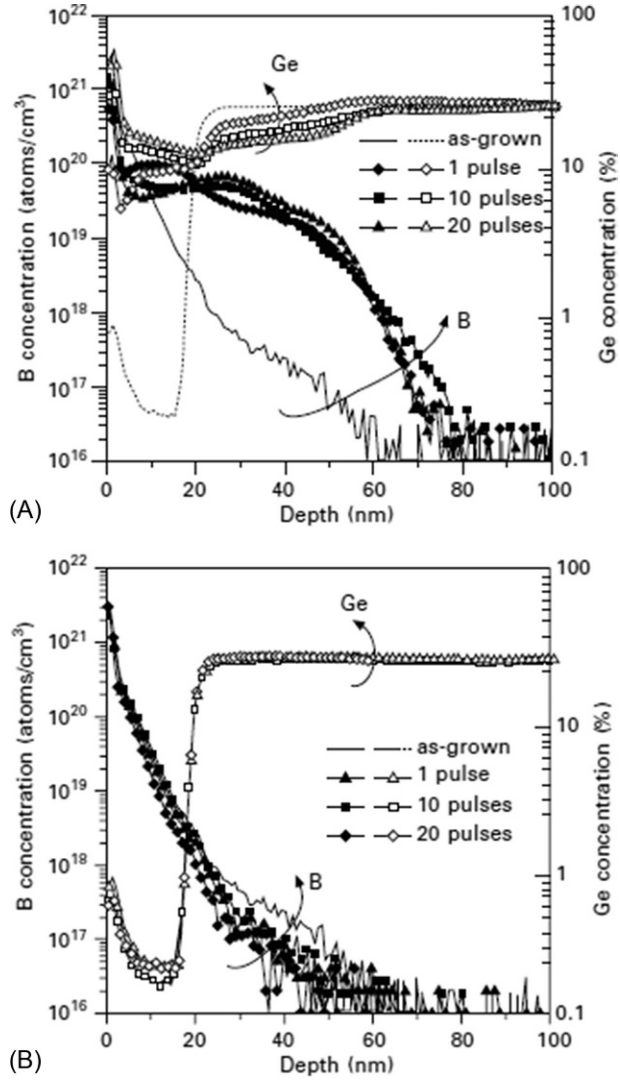


Fig. 12.15 SIMS profiles of boron and germanium in strained-Si/SiGe substrate subjected to (A) shallow-melt LA at 0.20 J/cm^2 and (B) nonmelt LA at 0.10 J/cm^2. *(Reused with permission from K.K. Ong, K.L. Pey, P.S. Lee, A.T.S. Wee, X.C. Wang, L.H. Wong, ECS Trans. 1(30) (2006) 1. Copyright 2006, The Electrochemical Society.)*

melt-depth with the implant amorphized depth, this approach can effectively reduce the silicon self-interstitials released from the end-of-range defect band, thus greatly suppressing boron transient enhanced diffusion (TED) and significantly removing end-of-range defects.

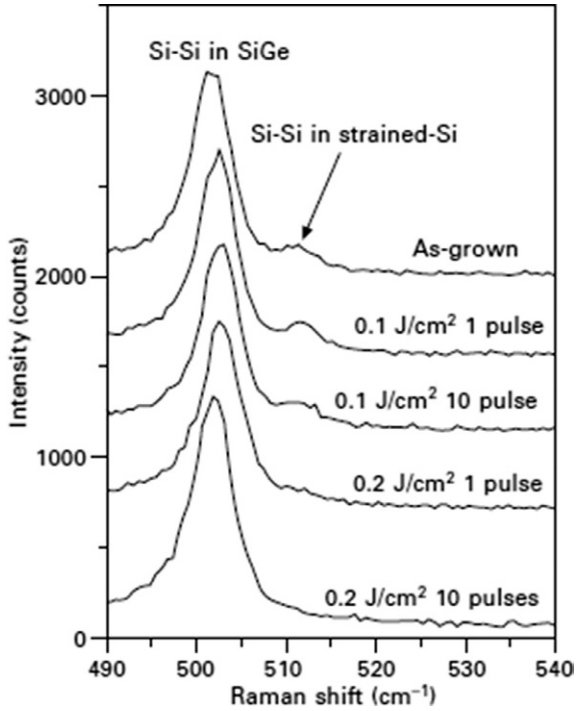


Fig. 12.16 Raman spectra of strained-Si/SiGe samples annealed at 0.2 J/cm^2 (shallow-melt LA) and 0.10 J/cm^2 (nonmelt LA). *(Reused with permission from K.K. Ong, K.L. Pey, P.S. Lee, A.T.S. Wee, X.C. Wang, L.H. Wong, ECS Trans. 1(30) (2006) 1. Copyright 2006, The Electrochemical Society.)*

Fig. 12.17A shows the SIMS profiles of boron in a crystalline silicon in comparison to those preamorphized by a 40 keV Si^+ implantation, with and without 0.72 J/cm^2 single-pulse laser preirradiation. After an RTA at 800°C for 60s, boron TED can be clearly observed in various cases. As expected, the boron profile in the crystalline substrate has the deepest diffusion depth, which can be mainly attributed to the channeling effect during the implantation. It is also evident that the samples with PAI have a shallower junction depth, with reference to the background concentration of 5×10^{18} atoms/cm^3. More importantly, the boron SIMS profile of the sample preirradiated with a laser prior to the 40 keV Si^+ PAI condition provides the shallowest boron distribution profile. The reduction in the diffusion depth is more than 30.0 nm (about 40%) compared to the identical PAI counterpart without undergoing the laser pulsing, implying that the boron TED has been suppressed.

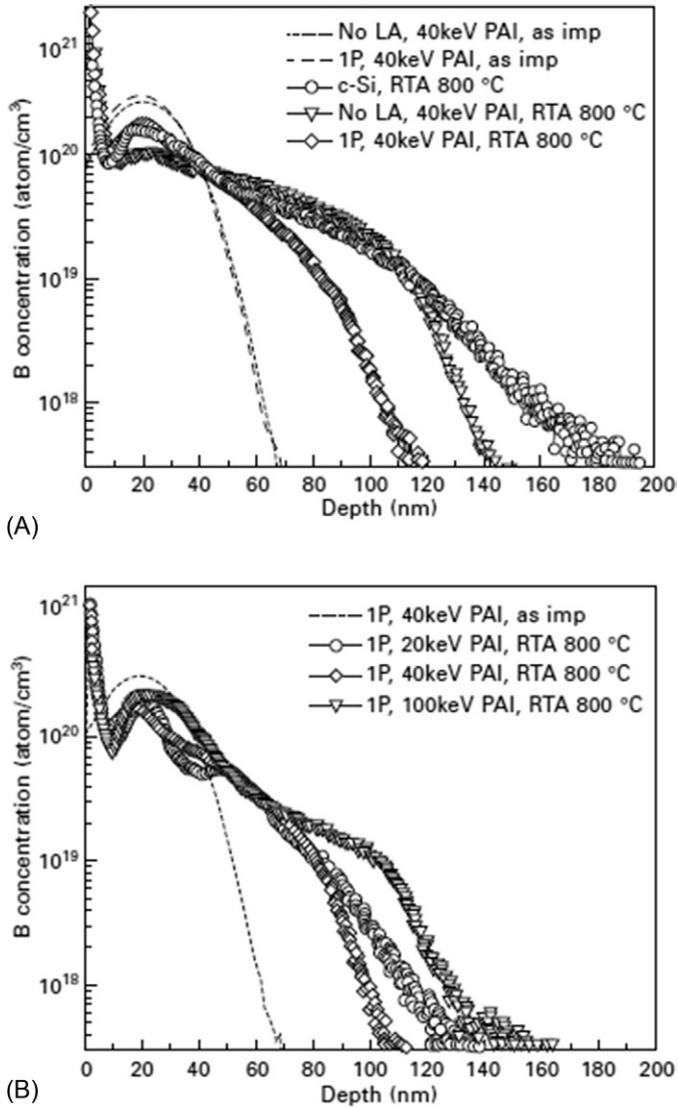


Fig. 12.17 (A) The SIMS profiles of boron in a c-Si and a PAI-Si sample subjected to a single-pulse laser preirradiation at 0.72 J/cm^2, subsequently followed by a RTP activation annealing of 800°C for 60s. (B) the SIMS profiles of boron in the PAI-Si (40 keV) sample, PAI-Si (20 and 100 keV) sample, subjected to a single-pulse laser preirradiation at 0.72 J/cm^2, subsequently followed by a RTP activation annealing of 800°C for 60s. The PAI-Si (40 keV) sample not preirradiated with laser is also included for comparison. *(Reused with permission from D.X.M. Tan, K.L. Pey, K.K. Ong, B. Colombeau, C.M. Ng, S.H. Yeong, A.T.S. Wee, C.J. Liu, X.C. Wang, Appl. Phys. Lett. 92 (2008) 203107. Copyright 2008, American Institute of Physics.)*

Fig. 12.17B shows the effect and interaction of PAI depth of about 40.0, 60.0, and 120.0 nm with the preimplant laser irradiation on the boron distribution upon RTA annealing. The annealed profiles demonstrate an unusual trend in the dopant diffusion length, which renders the 40 keV PAI sample as having the least dopant diffusion followed by the 20 keV and the 100 keV PAI boron profile. The 100 keV PAI gives the most diffused dopant profiles. Similar R_s results of 300 and 250 Ω/sq for the 20 and 40 keV PAI samples, respectively, have also been observed. But the R_s of the 100 keV samples increases to 550 Ω/sq. The variation in R_s can be indirectly inferred to the change in the dopant activation level, which is strongly related to the PAI conditions that affect the boron diffusion and activation in the laser preirradiated silicon substrates. Some R_s trend was also obtained when the samples were subjected to a 1000°C of RTA annealing.

For all three sets of results, the maximum melt depth of the samples is identical at about 60.0 nm for the same laser fluence of 0.72 J/cm^2, which was confirmed through the SLIM simulation [22]. Thus the vacancies formed by the laser preirradiation are located at a maximum melt-depth of 60.0 nm. Since a 20 keV Si^+ PAI energy will result in an amorphization depth of around 40.0 nm that is shallower than the maximum laser melt depth (around 60.0 nm), the Si interstitials introduced by the Si^+ PAI will reside at a displacement nearer the substrate surface compared to the location of the excess vacancies. During the RTA activation at 800°C, an EOR defect band forms around the a/c interface. The extended defects in the EOR region will then evolve through the Oswald ripening mechanism [28,29]. Since the vacancies are located at a deeper depth than the EOR defect band location, the recombination of the emitted self-interstitials from the EOR band with the laser-generated vacancies is less effective. Hence, the self-interstitials will tend to flow towards the silicon surface, leading to the formation of inactive boron-interstitial clusters (BICs) [29–31] as well as TED. In addition, boron trapping at a depth of ranging from 45.0 to 50.0 nm below the Si surface has been observed in Fig. 12.17B for the 20 keV PAI sample, which is attributed to the presence of the interstitial-rich EOR region.

The 40 keV Si^+ PAI has an effective amorphization depth that coincides with the maximum melt-depth induced by the laser fluence (around 60.0 nm). With the matching of two displacements, the initial supersaturation of interstitials is greatly reduced due to the recombination of the silicon interstitials with the melting laser-generated excess vacancies. The residual EOR extended defects can thus be reduced resulting in a shallow

junction profile as shown in Fig. 12.17B. It is expected that the flux of the silicon interstitials during thermal annealing is greatly decreased, reducing the interaction with the B atoms. This minimizes the boron interstitials pairing and BIC formation, thereby suppressing the corresponding boron TED and improving the dopant activation (lower R_s).

For the case of the 100 keV PAI sample, the amorphization depth (around 120.0 nm) is much deeper than the maximum melt-depth (around 60.0 nm) created by the laser preirradiation. Due to the amorphization of up to 120.0 nm, it is expected that no vacancies previously present at the maximum melt depth survive. Hence, it is similar to a case equivalent to a typical PAI implant without performing any laser preirradiation. TED will dominate and eventually the deep boron dopant profile is expected. Similarly, the supersaturation of the silicon interstitials from the EOR region toward the surface leads to signifcant BIC formation, which causes the junction to have a large R_s compared to the previous two cases.

Cross-sectional analysis of the preirradiated samples implanted with various Si^+ PAI conditions shows that the samples implanted with the PAI energy of 20 keV are observed to have a high density of residual EOR defects situated around the original a/c interface induced by the PAI, after thermal annealing (see Fig. 12.18). On the other hand, by matching the PAI depth with the prelaser melt-depth (with respect to the 40 keV PAI condition),

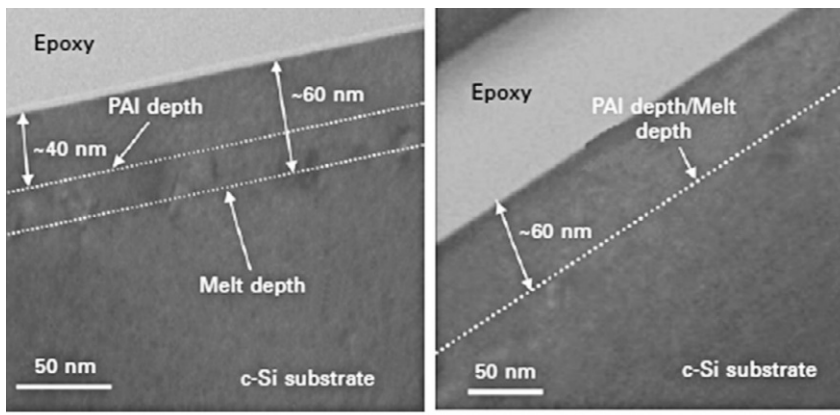


Fig. 12.18 Cross-sectional TEM micrographs for the samples that have undergone prelaser single-pulse irradiation of 0.72 J/cm^2 with Si^+ amorphization energies of (A) 20 keV and (B) 40 keV. *(Reused with permission from D.X.M. Tan, K.L. Pey, K.K. Ong, B. Colombeau, C.M. Ng, S.H. Yeong, A.T.S. Wee, C.J. Liu, X.C. Wang, Appl. Phys. Lett. 92 (2008) 203107. Copyright 2008, American Institute of Physics.)*

the XTEM results confirmed that silicon interstitials recombine with the laser-generated vacancies, which reduces the density of the extended defects at the EOR region, leading to a defect reduced region around 60.0 nm. The results demonstrate that the appropriate choices of the PAI energy to coincide the PAI depth with the corresponding laser fluence can effectively reduce dopant-defect interaction and improve junction characteristics.

12.3 LASER-INDUCED FORMATION OF SILICIDE

Device performance necessitates the scaling of device feature size and the tailoring of silicide contact formation becomes critical with a limiting thermal budget. The approach of LTP of silicides was first explored by Poate et al. [32], who demonstrated the formation of thin silicide layers by Q-switch Nd-YAG pulsed laser melting of Ni, Pd, or Pt film on Si. Laser-induced interaction between various types of metals such as Au, Pt, Pd, Ti, Co, Mo, Ni, and W with Si have since been reported [33–37]. These prior works established the fundamental understanding of the formation of metal-silicon compounds using laser irradiation. It was found that the formation of cellular structure in the solidifying phase was attributed to the supercooling and convection in the melt during the solidification process [36]. The possibility of amorphous phase formation found in the Pt-Si and Pd-Si has been correlated to the composition of the melt [33]. Another promising result has reported the formation of low resistivity (150–300 μΩcm) WSi_2 through pulsed laser irradiation in a vacuum environment while laser anneal in an N_2 atmosphere serves to accelerate the silicidation reaction during the laser annealing process [37].

Early experiments on silicide formation of the Ti/Si and Ni/Si system using a Q-switched ruby laser have found nonuniform elemental distribution and cellular structures in the samples [38]. It is possible to address this problem using continuous-wave (cw) laser or multiple-pulse laser irradiations [39,40] and limiting the sample thickness such that it is comparable to the diffusion distance during the melt lifetime [41]. Earlier works on Ni silicide formation via laser annealing focused on the formation of the $NiSi_2$ phase, which can easily form epitaxial films on Si substrates. Tung et al. reported epitaxial Ni and Co silicides formation on (100) and (111) Si through a LPE using the Q-switched ruby laser [42]. The interfacial instabilities and cellular structure can be suppressed by first carrying out furnace annealing to form polycrystalline $NiSi_2$ or $CoSi_2$ and subsequently melting the disilicide layers using laser irradiation.

Laser anneal silicide formation was predominantly performed under a high laser fluence (range of 0.70–1.50 J/cm^2) in many of the early works (during the 1980s). Owing to the energy deposited in the sample, the reaction of thin metal films on Si under such high fluences would usually result in Si-rich silicide phases. When formation of thin silicide layers is required for contact application, it is critical to tailor the laser energy such that it does not induce a very deep Si melt. The rate of solidification during the laser annealing process approaching 10^{10} K/s is far from equilibrium. Depending on the fluence, the melt might only last for tens of nanoseconds (similar to its laser pulse) before it resolidifies. Despite having a diffusion coefficient of element in liquid in the order of 10^{-4} cm^{-2}/s, melting in such short duration results in nonuniform elemental distribution in the molten film, especially when the thickness of the molten film is much thicker than the diffusion distance of the elements in the melt. During the solidification process of the molten layer, kinetics play an important role as a large undercooling can cause either nucleation or growth to take place.

The effect of laser fluences on different Ni silicide phase formation was demonstrated by Luo et al. in the late 1990s [43]. Lower fluence results in an amorphous overlayer in Ni silicide or germanosilicide whereas cell formation occurred after laser annealing at a high laser fluence due to constitutional supercooling (CSC). Morphology of the Ni germanosilicide formed on Ni/$Si_{0.76}Ge_{0.24}$ and Ni/$Si_{1-x-y}Ge_xC_y$ has been found to be stabilized with the suppression of agglomeration [43,44]. The study of laser annealing time has revealed an enhanced diffusion of the silicide layers based on PtSi formation induced by Nd:yAG pulsed laser annealing [45]. Laser irradiation using excimer pulsed laser of wavelength 308.0 nm within 0.20–1.80 J/cm^2 followed by thermal annealing have been used to prepare β-$FeSi_2$ semiconducting silicide [46]. Subsequently, laser annealing has attempted to eliminate the difficulty of Ti silicide transformation from C49 to C54 phase in a narrow structure [47]. The melt depth during excimer pulsed laser annealing can be controlled using amorphization of Si substrate, which enables the formation of stoichiometric titanium disilicide ($TiSi_2$) with defined silicide depth [48]. A desired process margin is possible following the melt depth as a function of laser energy at the amorphous Si/crystalline Si interface depth. Using single-pulsed laser annealing, it is possible to form nano-sized grains of C49 phase, which was found to lower the formation temperature of C54 $TiSi_2$ [49]. In a separate work, a C40 $TiSi_2$ template, formed after laser annealing, has been found to facilitate the C54 phase transformation at low temperature RTA without exhibiting any linewidth dependence [50].

Meanwhile, when a bilayer system consists of Ti-capped Co films on Si substrate was subjected to pulse laser irradiation, the high concentration of Ti was found to affect the crystallization of the Co silicide and resulted in an amorphous phase formation [51].

In the following sections, we illustrate the use of a 248.0 nm excimer pulse laser (with full width at half maximum of 23 ns) with fluence varying from nonmelt regime to beyond the melting threshold of the overlay metal films in forming Co and Ni silicides. A self-limiting melt phenomenon on substrates with a lower melting temperature than the overlay metal film will be illustrated. Emphasis is made on the structural correlation to the phase formation upon excimer pulse laser annealing with a viewpoint on the solidification mechanisms of the resultant silicide films.

12.3.1 Laser Annealing of TiN/Co on Si

Co silicidation formed using rapid thermal annealing is mainly used as Ohmic contacts in CMOS technology. Capping using TiN has been carried out to improve the quality of the $CoSi_2$ formed. Titanium nitride (TiN) capped cobalt (Co) film has been subjected to 248.0 nm excimer laser irradiation on preamorphized Si substrate (PAI) and resulted in unique growth mechanisms and microstructures of the resultant Co silicide [52]. At a low fluence laser pulse (0.20 J/cm^2), partial melting of the amorphous Si (a-Si) (T_m ~ 1420 K) and some Co (T_m ~ 1768 K) at the interface occurs without melting the TiN cap layer. This resulted in interdiffusion and intermixing of the Co and Si atoms in the liquid phase sandwiched between the nonmelted TiN/Co film stack and the partial nonmelted a-Si. At the instance of solidification, the contained hot melt of well-intermixed Co and Si may crystallize and propagate from the unreacted Co layer. The top unreacted polycrystalline Co layer could serve as nucleation sites for Co silicide to grow. Simultaneously, another silicide layer nucleates from the liquid/a-Si interface using the a-Si nuclei as the template. Eventually, the two propagating solid/liquid interfaces collide in the middle, often leaving an interfacial demarcation line at the position of the locus of the two colliding liquid/solid interfaces as illustrated in Ref. [52].

The structure and phase of the solidified layer is strongly affected by the solidification velocity [53], when considering only one liquid/solid interface propagating towards the top unreacted TiN/Co film stack during the solidification. The poor thermal conductivity of a-Si [54] limits the heat flow gradient for the heat transport at the liquid/a-Si interface, with an initial small interface velocity that allows ample time for recrystallization.

The growth of polycrystalline Co silicide enhances the rate of heat transfer from the liquid to the as-grown Co silicide due to its better thermal conductivity compared to that of a-Si. Crystallization takes place with limited grain growth occurring when velocity of the solidification front reaches some critical point.

When the laser energy is high enough ($0.70\,J/cm^2$) to melt the whole Co and PAI layer, the melt front propagates beyond the PAI layer. A concentration gradient of Co and Si atoms in the molten phase has led to a gradient of the freezing temperature of the liquid in front of the liquid/solid interface. When referred to the Co-Si phase diagram [55], the liquidus temperature of the more Si-rich Co binary system is higher than the Co-Si binary system which has the composition of Co:Si. Hence, the liquid in front of the initial liquid/solid interface would have been supercooling. The compositional gradient of liquidus molten phase and the supercooled at the initial liquid/solid interface have facilitated CSC which results in precipitated $CoSi_2$ formed between Si grains and cellular structures accompanied by the growth of defects being observed from the textured Co silicide in XTEM (Fig. 12.19).

As shown in Fig. 12.19B the dark contrast of defects that resembles stems and branches is attributed to twinning, which is generally known as "type B orientation." This happens due to the segregation of the Co solute atoms during CSC and later forms along the (111) direction that has the lowest interface energy. In addition, the growth of the highly textured Co silicide can be attributed to the epitaxial regrowth with Si substrate as a template.

12.3.2 Laser Annealing of Ni(Ti) on Si

Ni silicide formation on Si has been a key technology in CMOS devices due to the low resistivity NiSi formation, low processing temperature, and low silicon consumption. Owing to the oxidation issues, capping with Ti and alloying with Ti and other oxygen-scavenging elements are of interest. In conjunction with this, studies on laser annealing of Ni alloyed with 20 at% Ti have been carried out. COMSOL Multiphysics Modeling software has been adopted to predict the temperature generation in the sample during laser annealing [56]. Despite possible inaccuracies due to some simplification of procedures and limited thermophysical properties, it provides an overview of the generated temperature at the metal/substrate interface for different laser fluences. A correlation with experimental work has been carried out using Ni(Ti) (Ti ~ 20 at%) alloy film on Si substrate upon laser pulsed annealing using a 23 ns 248.0 nm KrF laser [57].

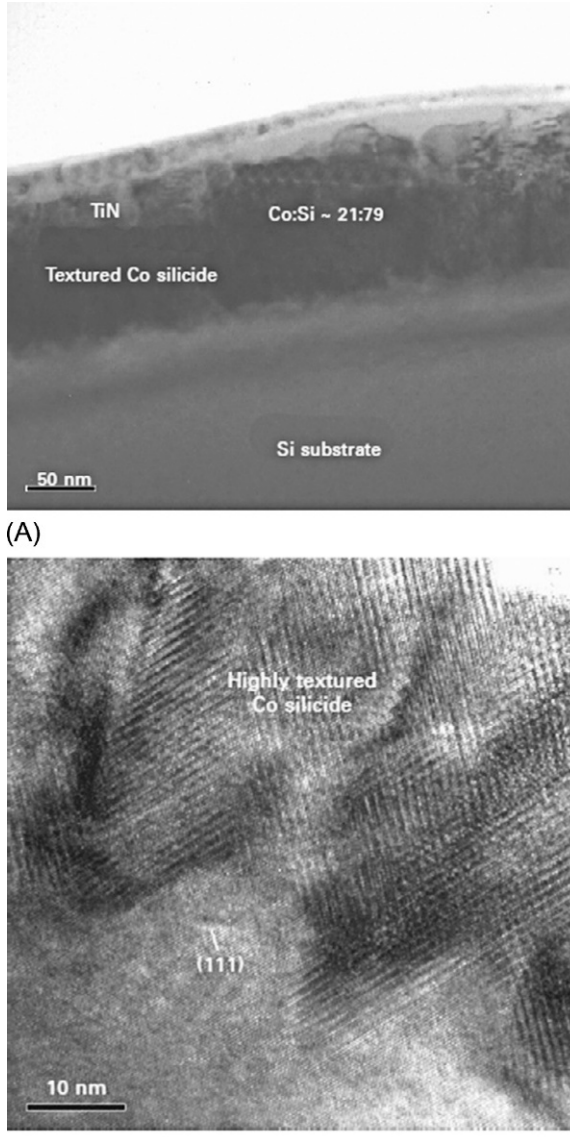
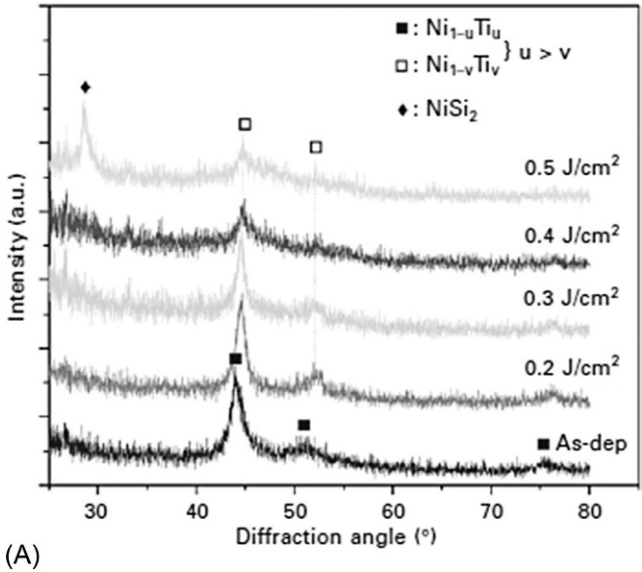


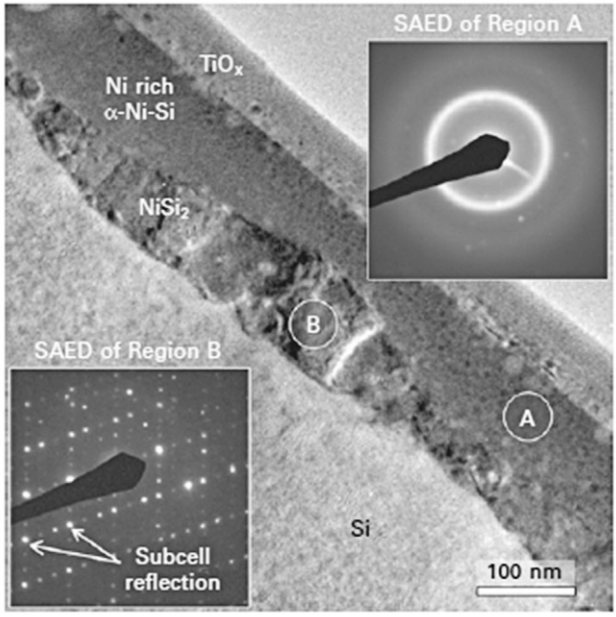
Fig. 12.19 (A) XTEM and (B) HRTEM images of the TiN/Co/Si system with PAI after single pulsed laser annealing at 0.70 J/cm^2. The highly textured Co silicide grows along the (111) direction of the silicon substrate in (B). *(Reused with permission from F.L. Chow, P.S. Lee, K.L. Pey, L.J. Tang, C.H. Tung, X.C. Wang, G.C. Lim, J. Appl. Phys. 99 (2006) 044902. Copyright 2006, American Institute of Physics.)*

Single-pulse laser annealing at $0.20\,J/cm^2$ results in a maximum interface temperature generated above 300°C (for 30 ns) according to COMSOL simulations. In this nonmelt regime, applying diffusion length estimation $\left(2\sqrt{Dt}\right)$, the Ni atoms with diffusion coefficient of $4.5\times 10^{-11}\,m^2/s$ in crystalline Si at 300°C will enable the atoms to travel for 1.8–3.5 nm, resulting in interdiffusion of the Ni-Ti-Si atoms and grain growth. The diffusion continues until the thermal energy is high enough to induce silicide formation. The presence of a temperature plateau in the simulated temperature profile indicates a complete melting of the metal film at $0.50\,J/cm^2$, signifying absorption of laser anneal energy by the latent heat of melting of the sample. Experimental work has found that single-pulse laser annealing results in the formation of $NiSi_2$ phase at $0.50\,J/cm^2$, below which no other crystalline silicide phase can be found (Fig. 12.20A). XTEM micrograph of the $0.50\,J/cm^2$ laser annealed sample is shown in Fig. 12.20B. The top layer TiO_x can be found due to the out-segregation of Ti atoms related to the high affinity of Ti to oxygen present in the annealing ambient or in the film (at 700°C, $\Delta G_{f\ Ni_3Ti} = -126.05$ kJ / mol; $\Delta G_{f\ TiSi_2} = -129.39$ kJ / mol; $\Delta G_{f\ TiO_2} = -815.93$ kJ / mol). Ti has a lower solid solubility in the $NiSi_2$ crystal than in the Ni lattice. It is believed that the majority of the Ti atoms were being pushed toward the surface during the rapid $NiSi_2$ nucleation and growth, resulting in oxygen gettering from the melt to form a thick TiO_x layer on the surface. This is facilitated by the large diffusion distance traveled by Ti atoms in a very short annealing time that can only be possible in a melt phase. Under such circumstances, the diffusion coefficient of the atoms can be of 5–8 orders in magnitude higher than that in a solid.

Estimation from COMSOL indicates that the maximum temperature of the sample reaches 1400°C at $0.50\,J/cm^2$, resulting in complete melting of Ni(Ti) film and part of the Si substrate forming an Si-rich region near the original Ni(Ti)/Si interface with Ni rich Ni-Si overlayer. From the Ni-Si phase diagram, the Si rich compound like $NiSi_2$ has a melting point of T_m of 933°C, whereas the Ni rich compound like Ni_2Si has T_m is around 1310°C. During the solidification process, the Si-rich inner layer is preferentially solidified as $NiSi_2$ owing to a similar crystal structure and lattice parameter with the Si substrate. Having a high congruent melting point has made the Ni_2Si nucleation from Ni-rich molten film became more difficult since the melt duration would be shorter than that experienced by the Si-rich layer, resulting in the formation of an amorphous Ni-rich overlayer in the sample (refer Fig. 12.20B). Furthermore, the nucleation of Ni_2Si from Ni-rich molten film may be retarded due to a difference in crystal structure between Ni_2Si (orthorhombic) and $NiSi_2$ (cubic).



(A)



(B)

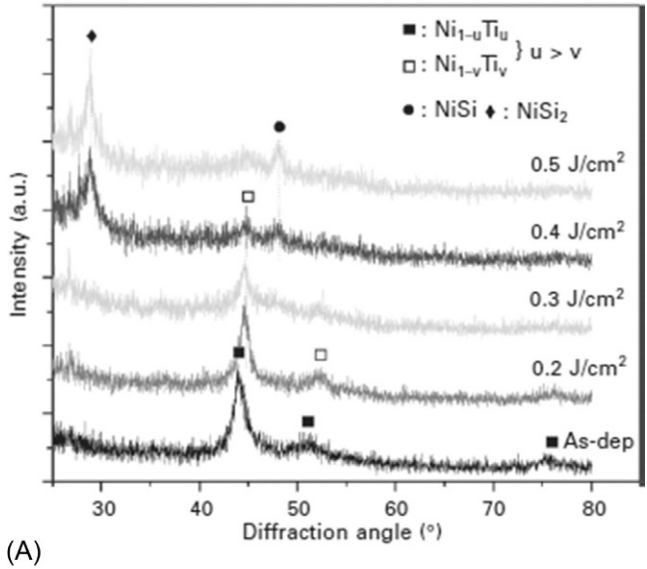
Fig. 12.20 (A) XRD spectra of as-deposited and annealed Ni_{1-x}(Ti)/Si samples after single pulse laser annealed at different laser fluences. (B) XTEM of sample after laser annealed at single pulse 0.50 J/cm^2. The SAED patterns of Region A and Region B are shown in the top and bottom insets, respectively. *(Reused with permission from Y. Setiawan, P.S. Lee, K.L. Pey, X.C. Wang, G.C. Lim, Appl. Phys. Lett. 88 (2006) 113108. Copyright 2006, American Institute of Physics.)*

When multiple pulse is applied, a five-pulsed laser anneal at $0.40\,J/cm^2$ resulted in the formation of $NiSi_2$ and a small amount of NiSi as shown in XRD spectra of Fig. 12.21A. The resultant structure is similar to the three-layer structure of the single pulse at $0.50\,J/cm^2$, except that the crystalline layer is slightly thicker and of higher coverage. The $NiSi_2$ phase formed at the interface was uniform without a formation of cellular structures, which has been plaguing laser annealed samples. This experiment shows that multiple-pulsed laser annealing has induced a better elemental mixing in the molten film, which reduced the localization compositional gradient and resulted in an absence of CSC. At 20-pulse laser annealing, the $0.30\,J/cm^2$ laser fluence is sufficient to form a polycrystalline NiSi phase without detectable $NiSi_2$ phase or amorphous in the sample as shown in Fig. 12.21B. Increasing the number of pulses has induced a better elemental redistribution inside the melt. The rapid solidification of melt results in a fine grain size of 12.2 nm in average for the 20-pulse annealing at $0.30\,J/cm^2$, which subsequently increases to 15.7 nm at $0.40\,J/cm^2$ at 20 pulses as a result of longer melt duration experienced by a hotter molten film induced at higher laser fluence. Subsequently, it was found that the 20-pulse annealing at $0.50\,J/cm^2$ leads to the nucleation of $NiSi_2$ grains at the interface until the melt front consumed more Si, making $NiSi_2$ formation more favorable at high laser fluences.

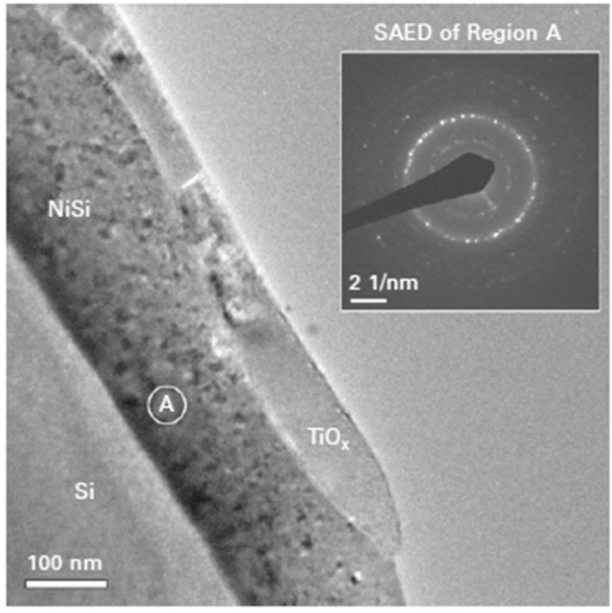
One of the factors causing the reaction enhancement during multiple-pulse laser anneal is the laser-induced surface roughening. This caused a reduction in the diffuse surface reflectance (from 46% in as-deposited sample down to about 31% after 20-pulsed laser annealing at $0.30\,J/cm^2$), which results in higher thermal energy in the sample. The amorphous overlayer on the sample usually has a lower thermal conductivity, a lower latent heat of melting, and a low melting point as compared to its crystalline counterpart, which generated a higher resultant temperature of the samples. In addition, formation of compounds like $NiSi_2$ during the preceding laser irradiation has a lower melting point, which leads to remelting of the existing compound, giving rise to deeper melting of the film. The prolonged melt duration allows the elements in the molten film to mix evenly to form the NiSi compound that was observed after 20-pulsed laser anneal at $0.30\,J/cm^2$.

12.3.3 Laser Annealing of Ni(Pt) on SiGe/Si Condensed Substrate

SiGe substrates have been widely adopted as a channel stressor, virtual substrates, or channel materials. Formation of Ni germanosilicide is required as contact material in SiGe devices. It has been shown that the critical issue



(A)



(B)

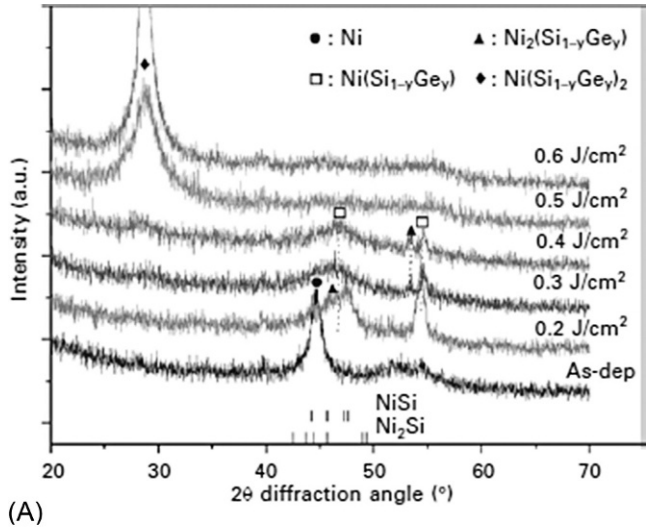
Fig. 12.21 (A) XRD spectra of as-deposited and annealed $Ni_{1-X}(Ti)_X/Si$ sample after five-pulsed laser annealing at different laser fluences. (B) XTEM of sample after laser annealed at 20 pulse 0.30 J/cm^2. The SAED pattern at location A is shown in the top inset. *(Part B is reused with permission from Y. Setiawan, P.S. Lee, K.L. Pey, X.C. Wang, G.C. Lim, F.L. Chow, J. Appl. Phys. 101 (2007) 034307. Copyright 2007, American Institute of Physics.)*

with Ni germanosilicide is the poorer morphological stability as compared to pure Ni silicide mainly due to Ge outsegregation and silicide agglomeration or islanding [58,59]. Pt alloying has been reported to play a role in improving the germanosilicide stability and reducing the oxygen contamination of the silicide film during rapid thermal processing [60]. Laser-induced melt-mediated Ni(Pt) germanosilicide formation on a $Si_{1-x}Ge_x$/Si substrate has been investigated [61,62]. It is known that pure Ge has a melting temperature lower than pure Si (938°C vs. 1414°C, respectively). In addition, due to the much poorer thermal conductivity of the $Si_{1-x}Ge_x$ alloy compared to pure-Si, the $Si_{1-x}Ge_x$ layer inhibits the conduction of heat and leads to a thermal confinement effect. This results in the generation of a higher temperature in the $Si_{1-x}Ge_x$/Si sample as compared to the Si-based sample during LA at the same laser fluence.

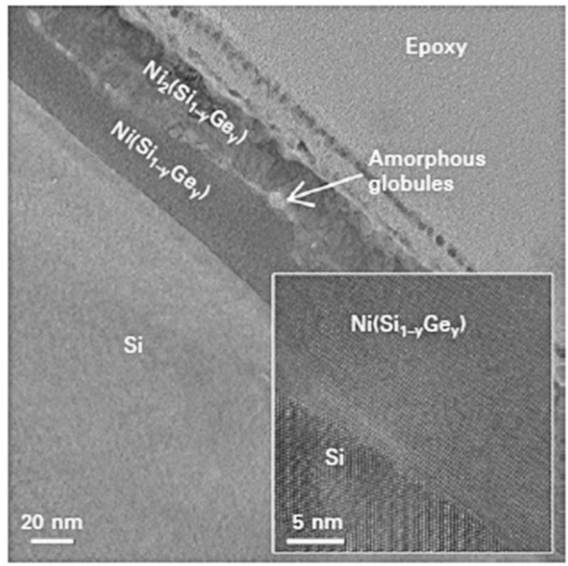
An experiment has been carried out using single-pulsed laser annealing at a different laser fluence of Ni film on graded SiGe substrate with a surface Ge concentration of 40%, which was fabricated through a series of oxidation and annealing steps (condensation process) [62]. As shown in the XRD spectra in Fig. 12.22A, a much lower reaction threshold was observed in the $Si_{1-x}Ge_x$ sample (at $0.20\,J/cm^2$) compared to pure Si substrates in which silicide does not usually form during single-pulsed laser anneal at fluence lower than $0.40\,J/cm^2$ [42]. The resultant films are multilayered structures with some amorphous globules interlayer and oxygen being incorporated on the surface layers as shown in Fig. 12.22B.

Multiple phase formation could easily occur during a single-pulsed LA process due to fast melting and solidification processes causing incomplete elemental mixing. A more uniform $Ni(Si_{1-y}Ge_y)$ formation can be achieved during LA at higher laser fluence (i.e., more than $0.3\,J/cm^2$) due to a slightly deeper and longer melting process. However, increasing the laser fluence to $0.5\,J/cm^2$ has resulted in the formation of $Ni(Si_{1-z}Ge_z)_2$ phase at an expense of $Ni(Si_{1-y}Ge_y)$ phase. Deeper melting is attributed to the formation of the Si-rich phase. It has been reported that continuous NiSi layer can be formed with multiple-pulsed laser annealing based on the enhancement of surface absorption and remelting of the phases formed [63].

It is noteworthy that it was found that upon alloying the Ni film with 10 at% Pt, it helps to significantly alleviate the problem of oxygen incorporation in the molten film [61]. The resultant silicide film formed has an atomically smooth epitaxial interface which can be seen in the XTEM micrograph of the sample after laser annealing for 20-pulsed at $0.40\,J/cm^2$ in Fig. 12.23A.



(A)



(B)

Fig. 12.22 (A) XRD spectra of Ni/SiGe after single pulsed laser annealing at different laser fluence. (B) XTEM micrograph of the Ni/$Si_{1-X}Ge_X$ sample after single pulsed laser annealing at 0.2 J/cm^2. The inset shows a HRTEM of the interface region. *(Reused with permission from Y. Setiawan, P.S. Lee, S. Balakumar, K.L. Pey, X.C. Wang, Electrochem. Solid State Lett. 11(9) (2008) H262–H265. Copyright 2008, The Electrochemical Society.)*

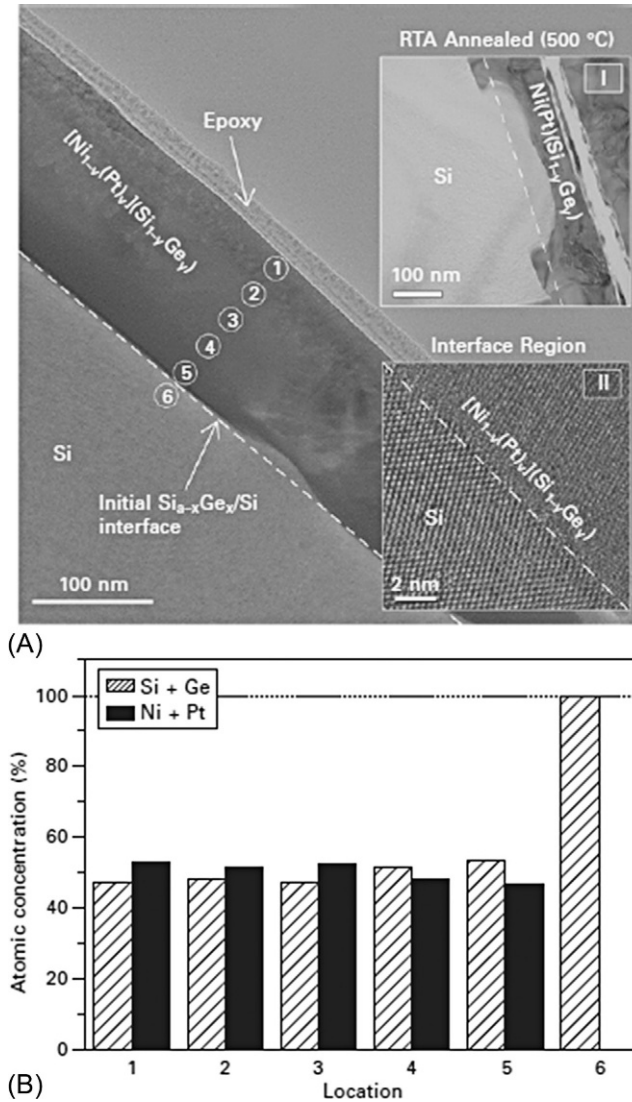


Fig. 12.23 (A) XTEM micrograph of Ni(Pt)/SiGe/Si sample after a 20-pulsed laser anneal at 0.40 J/cm^2. Inset I depicts the same sample after RTA annealing at 500°C for comparison. Inset II is the HRTEM micrograph of Ni(Pt)(SiGe)/Si interface of the laser annealed samples. (B) EDX elemental analysis of the Ni(Pt) germanosilicide film shown in (A). Locations 1–6 indicate the acquisition location starting from the surface to the Si substrate. *(Reused with permission from Y. Setiawan, P.S. Lee, K.L. Pey, X.C. Wang, G.C. Lim, B.L. Tan, Appl. Phys. Lett. 90 (2007) 073108. Copyright 2007, American Institute of Physics.)*

The EDX elemental analysis acquired from location 1–5 in Fig. 12.23A has been attained. As shown in Fig. 12.23B, no oxygen can be detected throughout the laser annealed Ni(Pt) germanosilicide layer. Although the diffusivity of an element increases significantly (up to 5–8 orders of magnitude higher) in molten form, Pt atoms that have a larger size than Ni were expected to be accumulated near the surface area. Owing to a low reactivity between Pt and oxygen, the presence of Pt atoms during the melting process resulted in a reduction of the oxygen diffusion into the molten Ni-Pt-Si-Ge layer which yielded a lesser oxygen contamination of the Ni(Pt) ($Si_{1-y}Ge_y$) layer. The creation of an epitaxial interface upon laser annealing is of great interest and requires further investigation.

12.4 CONCLUSIONS AND FUTURE TRENDS

The requirement of using low laser fluence becomes more stringent when performed on transistor structures. The XeCl (wavelength of 308.0 nm) pulsed excimer laser has been utilized to form $TiSi_2$ with 10 pulses at energy of 0.35 J/cm^2 on transistor structures. The study shows that heat generated by laser at the source drain region diffuses away efficiently, while trapping of heat in the gate region leads to deeper melting and therefore a thicker silicide layer [64]. On the other hand, Co silicided junction formed on shallow trench isolation (STI)-intensive structures has been realized using 248.0 nm excimer multiple-pulsed laser annealing at 0.30 J/cm^2 [65] and formation of laser induced Ni(Pt) silicided junction has been demonstrated [56]. Presence of different materials and structures in the transistors layout with different optical, thermal, and mechanical properties results in pattern effects. It might lead to nonuniform heating across the wafer causing die-to-die transistor performance variations. In some circumstances, the finite size of the laser beam during the laser anneal process induces a localized melting on the wafer and may cause a problem with wafer breaking [66]. Under both nonmelt and melt annealing procesess, remedies such as changing the laser wavelength, incident laser beam in a Brewster's angle [67], die layout modification [68], addition of reflective or absorptive capping, and modifying the laser annealing tool [66] have been proposed to tackle those problems. In a melt annealing process, efforts are focused on minimizing pattern damage under high energy annealing. The use of "phase switch" material in addition to the conventional laser absorber layer to create a self-limiting melting of a preamorphized junction has been reported by Shima et al. [69]. Baek et al. have studied the need to add a protective layer such as Al to

reflect some of the laser beam such that it does not induce too much damage to the TaN gate stack [70]. An addition of a thick layer of laser transparent material as a mechanical support to the sensitive parts of the transistors has also been investigated [71]. With all these efforts ongoing, pulsed laser annealing targeting the need for low thermal budget requirement during advanced MOS fabrication has become more attractive than ever.

REFERENCES

[1] E.C. Jones, E. Ishida, Shallow junction doping technologies for ULSI, Mater. Sci. Eng. R 24 (1998) 1.

[2] S. Shishiguchi, A. Mineji, T. Hayashi, S. Saito, Boron implanted shallow junction formation by high temperature/short time/high ramping-rate (400°C/sec) RTA, in: Tech. Dig. VLSI Technol. Symp., 1997, pp. 89.

[3] B. Yu, Y. Wang, H. Wang, Q. Xiang, C. Riccobene, S. Talwar, M. Lin, 70 nm MOSFET with ultra-shallow, abrupt, and super-doped S/D extension implemented by laser thermal process (LTP), in: Tech. Dig. Int. Electron Devices Meet, 1999, pp. 509.

[4] Y.F. Chong, K.L. Pey, A.T.S. Wee, A. See, L. Chan, Y.F. Lu, W.D. Song, L.H. Chua, Annealing of ultrashallow p^+/n junction by 248 nm excimer laser and rapid thermal processing with different preamorphization depths, Appl. Phys. Lett. 76 (2000) 3197.

[5] R.F. Wood, G.A. Geist, Modeling of nonequilibrium melting and solidification of laser-irradiated materials, Phys. Rev. B 34 (1986) 2606.

[6] M.O. Thompson, G.J. Galvin, J.W. Mayer, P.S. Peercy, J.M. Poate, D.C. Jacobson, A.G. Cullis, N.G. Chew, Melting temperature and explosive crystallization of amorphous silicon during pulsed laser irradiation, Phys. Rev. Lett. 52 (2360) (1984).

[7] R.F. Wood, C.W. White, R.T. Young, in: R.K. Willardson, A.C. Beer (Eds.), Semiconductors and Semimetals, vol. 23, Academic Press, Inc, Cambridge, MA, 1984.

[8] K.S. Jones, H. Banisaukas, J. Glassberg, E. Andideh, C. Jasper, A. Hoover, A. Agarwal, M. Rendon, Transient enhanced diffusion after laser thermal processing of ion implanted silicon, Appl. Phys. Lett. 75 (1999) 3659.

[9] Y.F. Chong, K.L. Pey, Y.F. Lu, A.T.S. Wee, T. Osipowicz, H.L. Seng, A. See, J.-Y. Dai, Liquid-phase epitaxial growth of amorphous silicon during laser annealing of ultrashallow p^+/n junctions, Appl. Phys. Lett. 77 (2000) 2994.

[10] Y.F. Chong, K.L. Pey, A.T.S. Wee, T. Osipowicz, A. See, L. Chan, Control of transient enhanced diffusion of boron after laser thermal processing of preamorphized silicon, J. Appl. Phys. 81 (2002) 4048.

[11] K. Goto, T. Yamamoto, T. Kubo, M. Kase, Y. Wang, T. Lin, S. Talwar, T. Sugii, Ultra-low contact resistance for deca-nm MOSFETs by laser annealing, in: Tech. Dig. Int. Electron Devices Meet, 1999, pp. 931.

[12] S. Talwar, Y. Wang, C. Gelatos, Laser thermal processing (LTP) for fabrication of ultra-shallow, hyper-abrupt, highly activated junctions for deca-nanometer MOS transistors, Proc. Electrochem. Soc. 2000–9 (2000) 95.

[13] H. Tsukamoto, P-n junctions formed by BF_2 ion implantation and laser annealing, Solid State Electron. 43 (1999) 487.

[14] S. Talwar, G. Verma, K. Weiner, C. Gelatos, Laser thermal processing for shallow junction and silicide formation", Proc. SPIE Conf. 3506 (1998) 74.

[15] M.J. Aziz, J.Y. Tsao, M.O. Thompson, P.S. Peercy, C.W. White, Solute trapping: comparison of theory with experiment, Phys. Rev. Lett. 56 (1986) 2489.

[16] J.M. Poate, J.W. Mayer, Laser Annealing of Semiconductors, Academic Press Inc., Cambridge, MA, 1982.

[17] B. Khaibullin, L.S. Smirnov, Pulsed annealing of semiconductors. Status report and unsolved problems (review), Sov. Phys. Semicond. 19 (1985) 353.
[18] Y. Makasi, M. Suzuki, A. Kitagawa, Transient phases of a-Si by rapid heating, J. Appl. Phys. 77 (1995) 1766.
[19] A. Armigliato, D. Nobili, P. Ostoja, M. Servidori, S. Solmi, Solubility and precipitation of boron in silicon and supersaturation resulting by thermal predeposition, in: H. Huff, E. Sirtl (Eds.), Semiconductor Silicon, 77–2, The Electrochemical Society, Princeton, NJ, 1977, pp. 638.
[20] S.B. Felch, D.F. Downey, E.A. Arevalo, S. Talwar, C. Gelatos, Y. Wang, Proc. Ion Imp. Technol. (2000) 167.
[21] S. Earles, M. Law, R. Brindos, K. Jones, S. Talwar, S. Corcoran, IEEE Trans. Electron Devices 49 (2002) 1118.
[22] R.K. Singh, J. Narayan, Mater. Sci. Eng. B3 (1989) 217.
[23] O.K. Kian, Pulsed laser annealing for the formation of ultra-shallow junctions for nanoscale metal-oxide-semiconductor technologies, PhD Thesis, Nanyang Technological University, 2008.
[24] S. Whelan, A. La Magna, V. Privitera, G. Mannino, M. Italia, C. Bongiorno, G. Fortunato, L. Mariucci, Phys. Rev. B 67 (2003). 075201.
[25] C. Park, S.D. Kim, Y. Wang, S. Talwar, J.C.S. Woo, in: Tech. Dig. VLSI Technol. Symp., vol. 69, 2001.
[26] Y.F. Chong, K.L. Pey, A.T.S. Wee, T. Osipowicz, L. Chan, A. See, J. Appl. Phys. 92 (2002) 1344.
[27] E. Kasper, Properties of Strained and Relaxed Silicon Germanium, INSPEC, 1995. p. 70.
[28] A. Claverie, B. Colombeau, G. Ben Assayag, C. Bonafos, F. Cristiano, M. Omri, B. de Mauduit, Mat. Sci. Semi. Proc. 269 (2000).
[29] B. Colombeau, A.J. Smith, N. Cowern, B.J. Pawlak, F. Cristiano, R. Duffy, A. Claverie, C.J. Ortiz, P. Pichler, E. Lampin, C. Zechner, Mat. Res. Soc. Symp. Proc. 810 (2004) C3.6.3.
[30] B.J. Pawlak, R. Surdeanu, B. Colombeau, A.J. Smith, N.E.B. Cowern, R. Lindsay, W. Vandervorst, B. Brijs, O. Richard, F. Cristiano, Appl. Phys. Lett. 84 (2004) 12.
[31] M. Cogoni, A. Mattoni, B. Uberuaga, A. Voter, L. Colombo, Appl. Phys. Lett. 87 (2005) 191912.
[32] J.M. Poate, H.J. Leanmy, T.T. Sheng, G.K. Celler, Appl. Phys. Lett. 33 (1978) 918.
[33] M.V. Allmen, S.S. Lau, M. Mäenpää, B.Y. Tsaur, Appl. Phys. Lett. 37 (1980) 84.
[34] M.V. Allmen, S.S. Lau, M. Mäenpää, B.Y. Tsaur, Appl. Phys. Lett. 36 (1980) 205.
[35] Y.F. Chong, K.L. Pey, A.T.S. Wee, M.O. Thompson, C.H. Tung, A. See, Appl. Phys. Lett. 81 (2002) 3786.
[36] G.J.V. Gurp, G.E.J. Eggermont, Y. Tamminga, W.T. Stacy, J.R.M. Gijsbers, Appl. Phys. Lett. 53 (1979) 273.
[37] S. Luby, E. Majkova, E. D'Anna, A. Luches, M. Martino, A. Tufano, G. Majni, Appl. Surf. Sci. 69 (1993) 345.
[38] G.G. Bentini, M. Servidori, C. Cohen, R. Nipoti, A.V. Drigo, J. Appl. Phys. 53 (1982) 1525.
[39] M.A. Harith, J.P. Zhang, P. Baeri, E. Rimini, G. Celotti, J. Appl. Phys. 57 (1985) 4560.
[40] T. Shibata, J.F. Gibbons, T.W. Sigmon, Appl. Phys. Lett. 36 (1980) 566.
[41] M.G. Grimaldi, P. Baeri, E. Rimini, G. Celotti, Appl. Phys. Lett. 43 (1983) 244.
[42] R.T. Tung, J.M. Gibson, D.C. Jacobson, J.M. Poate, Appl. Phys. Lett. 43 (1983) 476.
[43] J.-S. Luo, W.-T. Lin, C.Y. Chang, P.S. Shih, Nucl. Instrum. Methods Phys. Res. Sect. B 169 (2000) 124.
[44] J.-S. Luo, W.-T. Lin, C.Y. Chang, P.S. Shih, F.M. Pan, J. Vac. Sci. Technol. A18 (2000) 143.
[45] M.C. Li, X.-K. Chen, W. Cai, J.-H. Yin, J.-P. Yang, G. Wu, L.-C. Zhao, Mater. Chem. Phys. 72 (2001) 85.

[46] A. Datta, S. Kal, S. Basu, M. Nayak, A.K. Nath, J. Mater. Sci.: Mater. Electron. 10 (1999) 627.
[47] R.A. Roy, J.C. Cabral, C. Lavoie, Mater. Res. Soc. Symp. Proc. 35 (1999) 564.
[48] G. Verma, S. Talwar, J.C. Bravman, Appl. Phys. Lett. 78 (7) (2001) 925.
[49] Y.F. Chong, K.L. Pey, A.T.S. Wee, A. See, Z.X. Shen, C.-H. Tung, R. Gopalakrishnan, Y.F. Lu, J. Electron. Mater. 30 (2001) 1549.
[50] S.Y. Chen, Z.X. Shen, S.Y. Xu, C.K. Ong, A.K. See, L.H. Chan, J. Electrochem. Soc. 149 (2002) G609.
[51] F.L. Chow, K.L. Pey, P.S. Lee, C.H. Tung, X.W. Wang, G.C. Lim, Y.F. Chong, Electrochem. Solid State Lett. 7 (2004) G213.
[52] F.L. Chow, P.S. Lee, K.L. Pey, L.J. Tang, C.H. Tung, X.C. Wang, G.C. Lim, J. Appl. Phys. 99 (2006) 044902.
[53] P. Baeri, Thin Solid Films 241 (1994) 141.
[54] H. Wada, T. Kamijoh, Jpn. J. Appl. Phys. Part 2 35 (1996) L648.
[55] T.B. Massalski, Binary Alloy Phase Diagrams, American Society for Metals, Metal Park, OH, 1986.
[56] Y. Setiawan, Pulsed laser anneal silicide formation for advanced CMOS, PhD Thesis, Nanyang Technological University, 2008.
[57] Y. Setiawan, P.S. Lee, K.L. Pey, X.C. Wang, G.C. Lim, Appl. Phys. Lett. 88 (2006) 113108.
[58] T. Jarmar, J. Seger, F. Ericson, D. Mangelinck, U. Smith, S.-L. Zhang, J. Appl. Phys. 92 (2002) 7193.
[59] J. Hållstedt, M. Blomqvist, P.O.Å. Persson, L. Hultman, H.H. Radamson, J. Appl. Phys. 95 (2004) 2397.
[60] Md.A. Rahman, K.L. Pey, L.J. Jin, W.K. Choi, D.Z. Chi, D.A. Antoniadis, E.A. Fitzgerald, D.M. Issacson, Appl. Phys. Lett. 87 (2005) 182116.
[61] Y. Setiawan, P.S. Lee, K.L. Pey, X.C. Wang, G.C. Lim, B.L. Tan, Appl. Phys. Lett. 90 (2007) 073108.
[62] Y. Setiawan, P.S. Lee, S. Balakumar, K.L. Pey, X.C. Wang, Electrochem. Solid State Lett. 11 (9) (2008) H262–H265.
[63] Y. Setiawan, P.S. Lee, K.L. Pey, X.C. Wang, G.C. Lim, F.L. Chow, J. Appl. Phys. 101 (2007) 034307.
[64] G. Verma, S. Talwar, J.C. Bravman, IEEE Electron Devices Lett. 21 (10) (2000) 482.
[65] P.S. Lee, K.L. Pey, F.L. Chow, L.J. Tang, C.H. Tung, X.C. Wang, G.C. Lim, IEEE Electron Devices Lett. 27 (4) (2006) 237.
[66] J. Hebb, Patterns effects in thermal processing systems, in: Thermal Annealing Conference 2006 Workshop, Kyoto, Japan, 2006.
[67] M.O. Thompson, Submilisecond annealing—laser interactions and pattern effect mitigation, in: Rapid Thermal Annealing Conference 2006 Workshop, Kyoto, Japan, 2006.
[68] O. Gluschenkov, Pattern effects: tutorial on VLSI circuit impact, in: Rapid Thermal Annealing Conference 2006 Workshop, Kyoto, Japan, 2006.
[69] A. Shima, H. Ashihara, T. Mnie, Y. Goto, M. Horiuchi, Y. Wang, S. Talwar, A. Hiraiwa, in: International Electron Devices Meeting (IEEE, 2003), 2003, pp. 493.
[70] S. Baek, S. Heo, H. Choi, H. Hwang, IEEE Electron Devices Lett. 26 (2005) 157.
[71] V. Privitera, A.L. Magna, G. Fortunato, M. Camelleri, A. Magri, F. Simon, B.G. Svensson, Mater. Sci. Eng. B 92 (2004) 114–115.

This page intentionally left blank

CHAPTER 13

Laser-Induced Forward Transfer Techniques and Applications

M. Morales, D. Munoz-Martin, A. Marquez, S. Lauzurica, C. Molpeceres
Universidad Politécnica de Madrid, Madrid, Spain

13.1 INTRODUCTION

Many technological fields (from microelectronics to bioapplications) need printing with micron and submicron resolution of complex materials that must keep their properties after the transfer process. This process, ideally, must also be simple and fast enough to allow high throughput, low cost, and be industrially scalable.

Direct-write techniques are characterized by their ability to print free form patterns by the relative motion of its feature-defining tool over the surface or volume of a workpiece [1,2], in opposition to printing techniques that need preexisting patterns, such as lithographic masking, stamping, or molding [3]. Although the techniques that use preexisting patterns have a huge industrial impact due to their low cost in mass production, direct-write alternatives can offer a number of distinct advantages, such as reduced cost, start-up time, and resource footprint for device fabrication, allowing for rapid prototyping and easy process modifications and for small-volume device fabrication and component repair [4].

Laser-induced forward transfer (LIFT) is a noncontact direct-write technique that enables the deposition of small volumes of material (even <pL) into user-defined, high-resolution patterns with a wide range of structural and functional materials without the use of masks or molds [5,6]. LIFT has similar functionality to droplet-on-demand inkjet printing; however it does not suffer from nozzle clogging and material compatibility issues associated with the more prevalent nozzle-based techniques; this characteristic allows printing from solids to low viscosity fluids, including all intermediate viscosities and complex fluids.

Advances in Laser Materials Processing
https://doi.org/10.1016/B978-0-08-101252-9.00013-3
Copyright © 2018 Elsevier Ltd.
All rights reserved.

The first published process that can be related to LIFT was done by Braudy [7] in which a focused CW Argon laser beam (488 nm, 7 and 20 mW) was used to transfer different inks previously deposited onto a clear Mylar tape to print lines onto a substrate with and without air gap. At that point, the process was called laser writing (LW) or material laser recording and was used as a new deposition method for the direct writing of different dried inks to a substrate for the graphic industry [8–10]. These groups stopped working on this process and their work was forgotten until the late 1990s when it started to be cited again.

In 1986, Bohandy et al., using a pulsed excimer laser, were able to transfer copper (deposited on a fuse silica substrate) in a silicon substrate to print continuous lines. Bohandy et al. showed how the line thickness was increased when the laser pulse energy was increased [11,12]. This is considered in many works as the real origin of LIFT processes. Although in 1988 Bohandy presented a new work using a Nd:YAG laser at 532 nm, making the transfer of copper and silver films in air, where the LIFT terminology was used for the first time [13]. That work presents an experimental setup that is almost like the one that is still used now (with small differences depending on the LIFT approach followed, as will be discussed later in this chapter) and it was discovered that the optimum transfer, i.e. the smallest transfer, is obtained near the threshold of the process.

All the processes developed sought to avoid some of the limitations of the original process, mainly the transfer of delicate materials without damaging them (avoiding their degradation or loss of functionality) or improving the spatial resolution. The LIFT setup is mainly determined by the application.

Although LIFT has been considered from its invention a quite promising technique in different technological fields, their characteristic setup for transferring and the cost of the systems until only a few years ago, has prevented its industrial deployment. In the last years, this situation is changing and several companies like Orbotek, BASF, Poietis, Innofluence, etc., and reference institutes like Fraunhofer ILT are involved in real industrial integration of the technique, working not only in final applications, but also in a serious effort in machinery development for its integration in existing industrial lines.

The aim of this chapter is not to carry out an exhaustive review of all the publications of LIFT research (fundamental process studies or all their applications). Instead it gives an overview that shows the origin of the technique, its different implementations and variations, the physics that take

place in the transfer processes, and above all, the multiple applications that have been found in LIFT.

13.2 LIFT EXPERIMENTAL SETUP

LIFT is comprised of a complex laser–matter interaction mechanism, which involves energy conversion and phase transitions. There are many variations of the LIFT process [4] but most of them share a general setup and methodology. The main components in a LIFT process are:

- *Donor*: That is composed of several layers:
  - A substrate transparent to the laser. In near-infrared or visible laser wavelength, glass is the most common option, while in ultraviolet, quartz and fused silica are used. Other transparent materials, like flexible organic substrates, can also be used.
  - A thin film of the material to be transferred coats the transparent substrate. It is deposited using several simple methods, such as doctor blade, spin coating, or simply by surface tension in the case of some fluids. The thickness of this layer is a key parameter of the process, usually in the range of 0.1–100 μm.
  - An intermediate layer between the transparent substrate and the donor layer is sometimes placed to avoid the direct interaction of the laser with the material to be transferred.
- *Acceptor*: Substrate in which the donor is deposited. The wettability of this substrate (which is also affected by the surface finish or roughness) is important for the final shape of the transferred material. Usually the dot obtained in a single transference process is called voxel (volumetric pixel) and its volume and size determines the resolution of the process.
- *Gap*: Distance between the free surface of the donor film and the acceptor surface, which are kept parallel. This is also a key parameter of the LIFT processes, usually in the range of 0.1–1000 μm.
- *Laser*: Most studies have been done using short pulses (ns) or ultrashort pulses (ps or fs); although some LIFT variants use long pulses (from μs to cw). Shorter pulses are always desirable to reduce the thermal effects and to obtain smaller voxels [14]. The wavelength is chosen depending on the interaction material (intermediate layer or material to transfer) but UV is very common. Pulse energy and laser beam size are key parameters for the process; however, there are studies that show that laser fluence (which is proportional to pulse energy/spot area) is actually the key parameter [15].

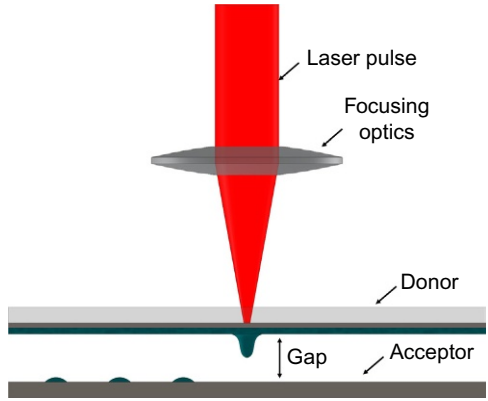


Fig. 13.1 Schematic of the standard LIFT setup.

A diagram of a typical LIFT setup is shown in Fig. 13.1.

The laser pulse interacts with the donor (usually this takes place very close to the interface but with some materials absorption can take place inside the donor) and the induced physical change, the exact nature depends on the LIFT variant and the donor material which will be explained later, pushes part of the material toward the acceptor substrate. There is a threshold fluence for the transfer, which is related to the physical mechanisms responsible for the material ejection, which will also be discussed later. Fluence values just above the transfer threshold give the smallest size voxels. As the fluence increases, new ejection regimes with different thresholds appear. For a successful, smooth, and high-resolution deposition, process parameters of LIFT need to be specifically controlled and optimized.

It is possible to scan the laser beam over the sample (usually with galvanometric mirror scanners) or move the donor and acceptor substrates to print complex patterns. Repetitive transfers over the same spot can thus be used to increase the transferred film thickness or to print 3D patterns [16,17]. This method is also suitable for printing multilayered structures by changing the donor film [18]. Compared to nozzle-based techniques like screen printing, inkjet printing, dispensing, aerojet printing, and e-jet printing, LIFT provides a noncontact, nozzle-free, direct-write, and mask-free method for transferring complex materials [19].

13.2.1 LIFT Characterization Techniques

The characterization of LIFT processes has been done by three main methods. One is the posttransfer morphological analysis study of the transferred

material on the acceptor substrate by optical microscopy, confocal microscopy, or scanning electron microscopy (SEM), etc. as a function of the process conditions including laser parameters, material properties, and gap distance. These studies give information about energy threshold for the transfer, three-dimensional profiles which are used to calculate the corresponding height, radius and volume, and spatial resolution among others, and are the basic tool for the process parameterization [15,20,26], see Fig. 13.2A–C.

Another method is the direct observation of the transfer process using time-resolved imaging techniques. These methods have been a crucial component for uncovering the nature of the LIFT mechanisms and identifying the complex phenomena responsible for the overall deposition behavior.

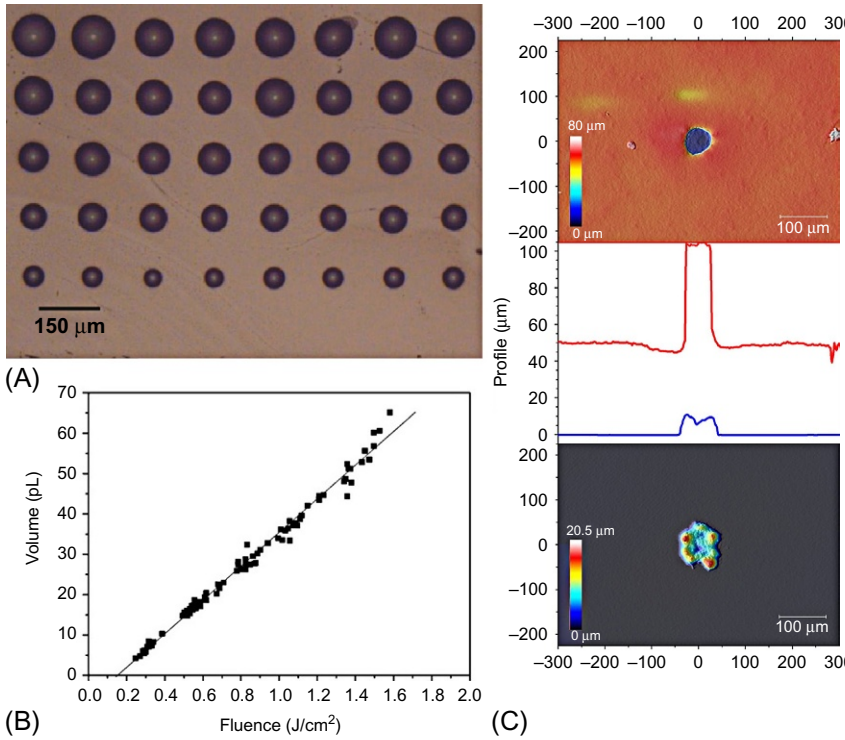


Fig. 13.2 (A) Microarray of droplets (mixture of water and glycerol (50%, v/v)) obtained at varying laser pulse energies [20]. (B) Plot of the droplets volume versus laser fluence [20]. (C) Example of confocal microscope images of donor film and correspondent transferred voxel from a 50 μm silver paste film. *Adapted from D. Munoz-Martin, C.F. Brasz, Y. Chen, M. Morales, C.B. Arnold, C. Molpeceres, Laser-induced forward transfer of high-viscosity silver pastes, Appl. Surf. Sci. 366 (2016) 389–396, https://doi.org/10.1016/j.apsusc.2016.01.029.*

These techniques can be applied to liquid or solid transfers, allowing the measurement of the droplet/pellet speed and acceleration during its flight and it can also show the impingement process when reaching the acceptor substrate. The pump-probe imaging technique is the most used in LIFT studies [21–24] but in the last years, more studies are using high-speed video [25].

In the pump-probe imaging technique, the temporal resolution of each frame is given by the pulse duration of the probe source (usually plasma flash lamps, fast diodes, or lasers with exposures of 10–30 ns). The laser and the probe are synchronized using a digital delay generator and controlled delays can be achieved. By changing the delay time, multiple events are recorded and a time sequence can be generated. Most imaging studies do not include the acceptor substrate to get a better illumination, but there are some that study the influence of the type of acceptor substrate and gap thickness between donor and acceptor [26–29]. Fig. 13.3A shows a standard configuration of the pump-probe imaging technique.

High-speed video studies are done using high-speed cameras (up to 100,000 fps) to record a video of the complete transference process of one unique event. The main advantage of this method is that it is possible to avoid the slight changes that can happen between different events. In this technique the laser, the camera, and the illumination unit (in this case pulse duration that is longer than the duration of the event) are synchronized to record the video. The temporal resolution of each frame is given by the frame rate of the camera [25]. Fig. 13.3B shows a standard configuration of the high-speed video technique.

The last method used to characterize the LIFT process is by actually measuring the properties of the transferred material; this is an indirect method and is usually complementary to the other methods and highly dependent on the specific application. In order to have a successful transfer process, it is fundamental to ensure that the material has not loss its functionality. For example, this can be the measurement of the electrical conductivity of a printed line, the solar cell efficiency after LIFT metallization, or the viability analysis of a living cell after the transfer, among others.

13.3 LIFT PHYSICAL PROCESSES

The LIFT physics is mainly controlled by the solid/fluid nature of the transferred donor. The laser interaction can produce a phase change in the donor material and its final rheological properties (from Newtonian fluids to solid films) will make the transfer process mainly a fluid motion problem

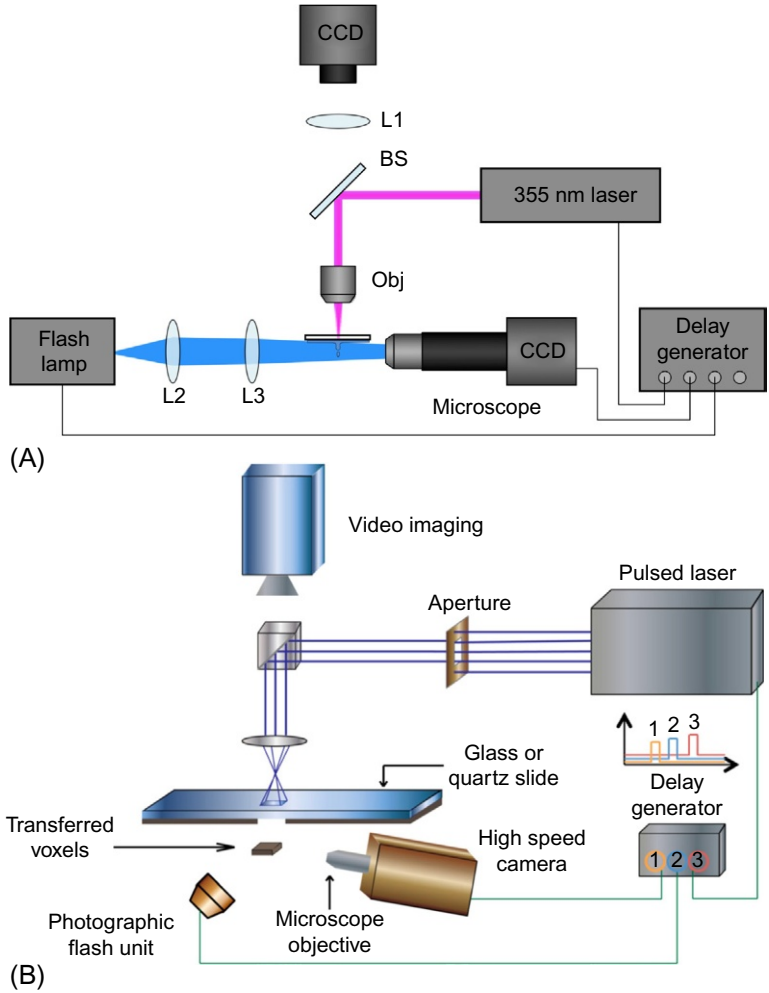


Fig. 13.3 (A) Schematic diagram of the system used to capture pump-probe images [30]. (B) Schematic diagram of the system used to capture high-speed video images [25].

or dominated by the mechanical breakdown of the material. In this section, a short overview of the main mechanisms that take place in these two regimes are presented.

13.3.1 Solid LIFT

In this regimen, the donor film is solid and the material is transferred in the solid phase. This is useful for applications that need the donor material to remain unchanged during the transfer.

The laser interacts directly with the solid donor film, heating it up without significant melting. Thermal stresses are induced inside the donor film [31] or a small volume of donor is ablated, generating a pressure in the interface [32]. In both cases, cracks are generated and propagated until the mechanical breakage of the donor film happens and a solid phase "pellet" is transferred, where the shape and size usually corresponds with the laser beam shape. There is a small parametric window to obtain these effects without melting the donor film. When using larger fluences a fluid LIFT process take place, which will be shown later. Fig. 13.4A shows a schematic of the solid LIFT.

The solid phase LIFT transfer is also the process behind the congruent transfer of high viscosity inks, referred to as laser decal transfer (LDT) [33]. In LDT there are no significant hydrodynamic effects happening in the bulk of the donor film that could change the "pellet." The "pellet" is usually ejected with such high speed that once it hits the acceptor it can be broken and disintegrated (sometimes this can happen even during the flight) and the shearing forces responsible for the breakdown are concentrated at the pellet perimeter and can modify the shape of the final deposited material. Therefore, the process must be done very close to the transfer threshold to have as little energy to spare as possible to reduce these undesirable effects. Fig. 13.4B shows the flight of the pellet and how some rotation is also presented. If the laser pulse energy is very close to the transference threshold it is possible to obtain small velocities in the pellet (around 1 m/s) to avoid any damage.

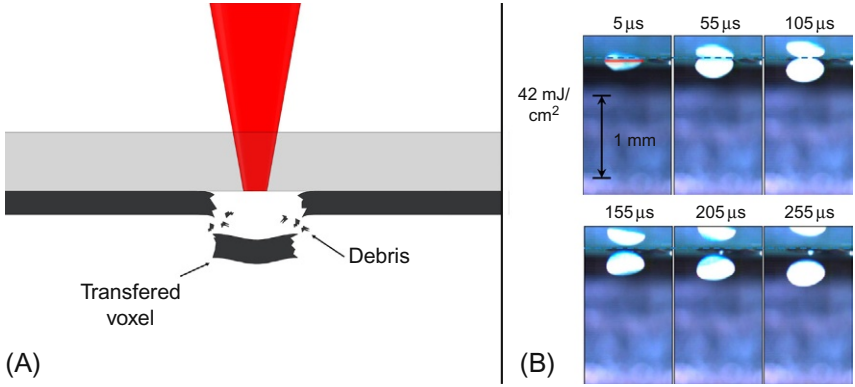


Fig. 13.4 (A) Schematic representation of solid phase LIFT. (B) Still frame images obtained from the high-speed video. Voxel transfer characteristic with high viscosity silver nanopastes. *Adapted from S.A. Mathews, R.C.Y. Auyeung, H. Kim, N.A. Charipar, A. Piqué, High-speed video study of laser-induced forward transfer of silver nano-suspensions, J. Appl. Phys. 114 (2013) 64910, https://doi.org/10.1063/1.4817494.*

In solid LIFT, as the "pellet" keeps the beam shape, it is possible to use light modulators for spatial beam shaping to modify the size and shape of the laser pulse and thus the ability to print congruent voxels with the desired shape [34]. Light modulation can be performed using digital micromirror devices (DMD) that are able to modulate the intensity of the incident laser beam in a binary fashion (on or off) on a per-pixel basis [35–37]; or by using a liquid-crystal spatial light modulator (SLM) that offers full grayscale intensity modulation and can generate intensity profiles, consisting of a low fluence interior surrounded by a high fluence perimeter [38]. This method allows the printing of complex shapes in a single transference step, as seen in Fig. 13.5.

13.3.2 Fluid LIFT Transfer

In this regime, the donor film can be solid or fluid but the transference is dominated by fluid motion. The laser is absorbed in the fluid and evaporates the local material generating a cavitation bubble with a pressure higher than the pressure of the surrounding fluid (Fig. 13.6). The bubble expands increasing its volume and reducing its pressure. The bubble growth is faster in the direction of the free surface where there is less fluid to move. Once the bubble pressure is lower than the surrounding pressure, expansion reverses until it collapses. The deceleration is greater at the tip near the free surface, the relatively negative pressures are stronger there and the fluid from the surroundings is pulled toward the tip. This liquid flows toward the tip leading to the formation of two jets, one flowing away from the bubble, the so-called primary jet, and another flowing into the bubble, the so-call

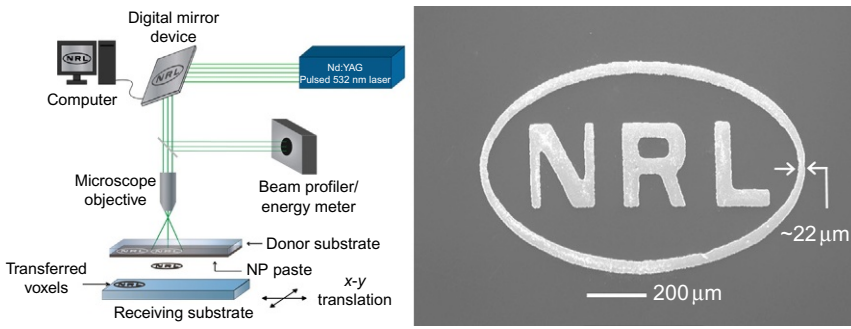


Fig. 13.5 (A) Schematic diagram and (B) results of LDT via DMD LIFT [39].

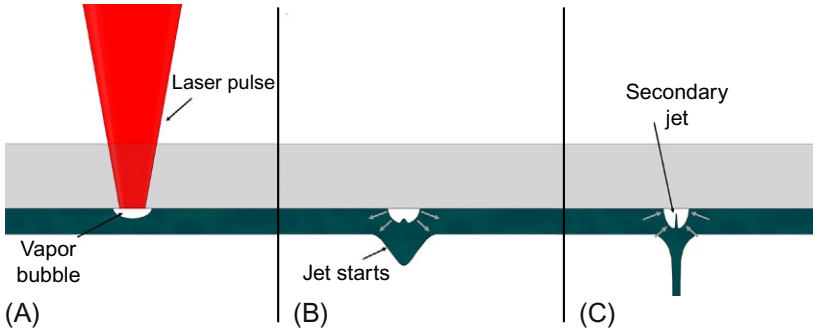


Fig. 13.6 Scheme of the bubble evolution and jet formation: (A) The laser is absorbed in the fluid generating a cavitation bubble; (B) the bubble expands and fluid from the surroundings is pulled toward the tip; (C) two jets are formed, one flowing away from the bubble (primary jet) and another flowing into the bubble (reentrant jet).

reentrant jet [40]. This kind of jet formation and development are discussed in several studies [24,41].

Different transfer regimes have been observed [24,42]. At low laser fluences, the bubble pressure forms a protrusion without enough energy and it recedes without transferring any fluid. At high fluences the vapor bubble pressure is high enough to overcome surface tension and multiple droplets are ejected at high speed and divergence. At intermediate fluences, the protrusion can overcome viscous forces and surface tension and a thin and stable jet of fluid is generated that continues propagating toward the acceptor substrate, with a jet velocity in the range of 10–250 m/s. The jet keeps expanding and thinning, and achieves a high aspect ratio before a pinching off due to Rayleigh-Plateau instability [22,24,30]. This detached column of fluid may further fragment into more droplets that, after impact, on the acceptor substrate can recombine into a single sessile droplet (Fig. 13.7).

For a given donor film and incident laser spot size, a minimum volume of ink is transferred at a threshold laser fluence. This threshold fluence and the associated transferred volume increase with laser spot size and donor film thickness. Beyond threshold, the deposited volume increases with fluence. Above a second threshold, the ejections become unstable and the material is no longer deposited within a single compact droplet [43,44]. The final deposited droplet depends on the inertial forces and surface tension and on wettability and viscosity [45,46]. With low impact velocities, the droplet spreads on the solid surface, while with higher velocities the droplet initiate splashing and satellite droplets are generated. The gap distance also plays a key role in the final transference process. If the gap distance is small

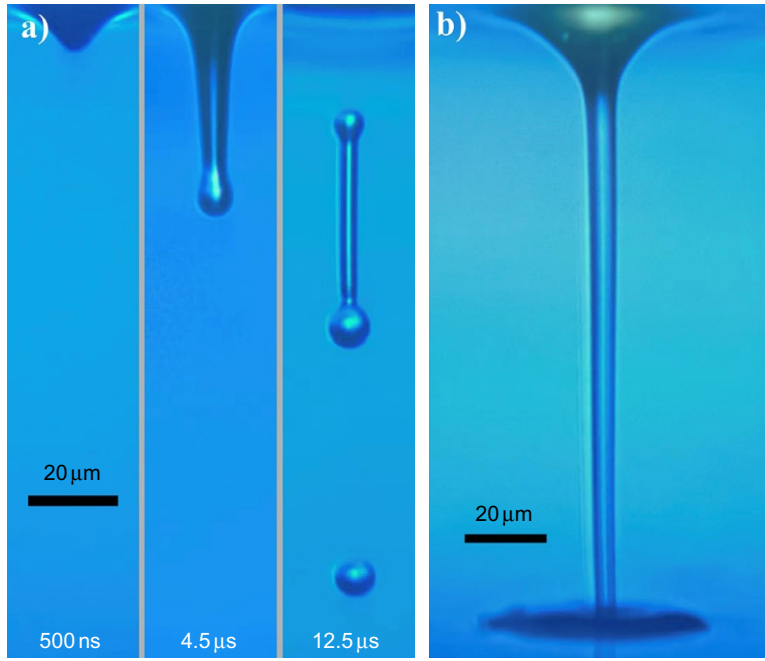


Fig. 13.7 Images of the jet evolution from a 5 µm donor film of NMP (A) jet pinch-off and break-up in several droplets using a 5.4 µJ laser pulse (B) jet impacts with an acceptor substrate (glass slide) with a 150 µm gap using a 7.7 µJ laser pulse. *Adapted from M.S. Brown, C.F. Brasz, Y. Ventikos, C.B. Arnold, Impulsively actuated jets from thin liquid films for high-resolution printing applications, J. Fluid Mech. 709 (2012) 341–370, https://doi.org/10.1017/jfm.2012.337.*

it is possible to get transference with the protruding jet before its recession. Even if the gap is small the bubble can contact the acceptor generating voxels with a larger diameter and a lower uniformity than those deposited through jet contact [47]. As it has been shown, the LIFT process is very sensitive to laser fluence and gap separation, and a well-defined voxel can be obtained only within a narrow fluence range and a small gap distance.

13.3.2.1 Ejection Mechanisms in Fluid LIFT of High Viscosity Fluids

In LIFT process of high viscosity pastes some of the regimes observed in LIFT of liquids can also be observed, mainly the low fluence and high fluence regimes (Fig. 13.8). But some new regimes can also be observed. At intermediate fluences, the flow and stretching of this protrusion of paste eventually leads to fragmentation into clusters of paste that are transferred to the acceptor substrate.

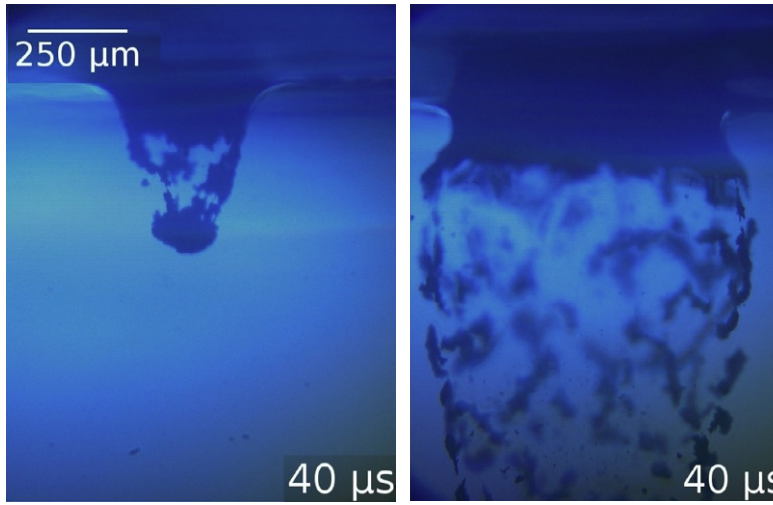


Fig. 13.8 Time-resolved images of LIFT of silver paste from a film of thickness 120 µm using laser fluences of approximately (A) cluster fragmentation (8.5 J/cm^2) and (B) explosive regime (23 J/cm^2) [26].

A different transfer mechanism occurs when the donor thickness is large enough relative to the gap. The protruding paste pillar reaches the acceptor while connected to the donor substrate. Once the pillar front impacts the acceptor substrate, confinement prevents the paste from fragmenting into pieces, stopping the expansion and stretching of the paste being transferred (Fig. 13.9). Eventually, the laser-induced vapor bubble collapses to an equilibrium shape, leaving a concave pillar taking the form of a liquid bridge wetting both the donor and acceptor. This pillar is stable due to the high viscosity and non-Newtonian character of the paste, inhibiting the spreading and thinning of the impacting pillar and effectively solidifying it. When the donor substrate is pulled off from the acceptor, the pillar breaks, leaving a single concrete-dot of paste on the acceptor substrate [26].

13.3.3 Ejection Mechanisms in Fluid LIFT of Solid Donor

The laser pulse duration has an important effect in the case of fluid LIFT from a solid donor. When a ns-pulsed laser is used, two ejections regimens are present [48]. For low fluence values, the physics involved in this process is like the standard fluid LIFT. The process starts with the laser melting the full thickness of the solid donor film. Some material is vaporized, generating a bubble. The pressure inside the bubble increases and deforms the

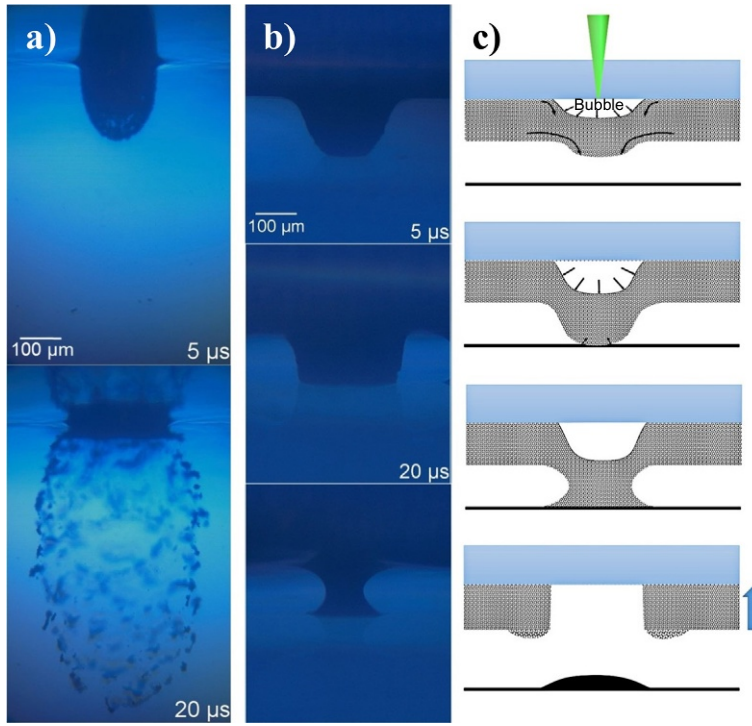


Fig. 13.9 LIFT of a 50 µm thick silver paste (A) without acceptor substrate the paste fragments in multiple pieces, (B) the 50 µm film is thick enough relative to the 50 µm gap distance so the pillar impacts the acceptor preventing it to break up, (C) scheme of the process of bridge formation and breakup. *Figure adapted from D. Munoz-Martin, C.F. Brasz, Y. Chen, M. Morales, C.B. Arnold, C. Molpeceres, Laser-induced forward transfer of high-viscosity silver pastes, Appl. Surf. Sci. 366 (2016) 389–396, https://doi.org/10.1016/j.apsusc.2016.01.029.*

fluid moving it toward the apex and forming a jet. The bubble pressure decreases and, if the conditions are right, a droplet or multiple droplets will be form. Basically, it is the same physics that is shown for viscous fluids, but in this case the laser is producing a local phase change from solid to liquid. For higher values of fluence, the pressure in the bubble is increased and an uncontrolled ejection takes place.

In the case of using a ps-pulsed laser, three ejections regimens are present [49]. Low fluence values, but larger than the threshold for the melting of the full thickness of donor film, lead to the ejection of a cap. Intermediate fluence values show jet formation from the apex of the cap. High fluences show spray ejection at high velocity (up to 700 m/s), as shown in Fig. 13.10.

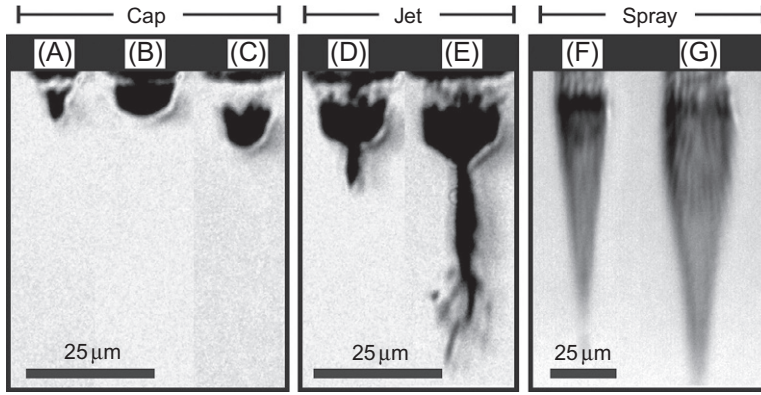


Fig. 13.10 Ejection of a 200 nm copper film, visualize 125 ns after the laser pulse. (A–C) Cap ejection regime at low fluences (314, 392, 480 mJ/cm^2); (D) and (E) jet ejection regime at intermediate fluences (660, 864 mJ/cm^2); (F) and (G) spray ejection regime at high fluences (1060, 1576 mJ/cm^2) [49].

The cap regimen is like the one observed with high viscosity pastes, although the thickness is completely different (less than a µm in solids and tens of µm in high viscosity pastes). The laser melts and vaporizes the donor film, the pressure in the bubble increases and the shape of the donor starts the jetting phase, but as it is being stretched, the wall gets thinner and the cap detaches from the rest of the material. The physics involved in the jet ejection regime is similar to the cap regime but the higher temperatures makes the fluid less viscous and through the tip escapes a jet (more violent as the energy is increased). The last regime is the usual spray ejection regimen in which the higher fluence vaporizes part of the material and generates a spray of small droplets.

13.4 VARIATIONS OF LIFT

In the standard LIFT the laser interacts with the donor material in order to generate the push that will transfer it, and this interaction can damage or modify the functionality of the donor. There are many variations of the LIFT process, each differing in how the laser is absorbed and converted into the mechanical energy required for material ejection in order to print a broader range of functional materials without modification.

13.4.1 Forward and Backward Transfer

Fig. 13.11A shows a scheme of the laser-induced backward transfer (LIBT) [50]. LIBT is similar to the forward process but the acceptor substrate must

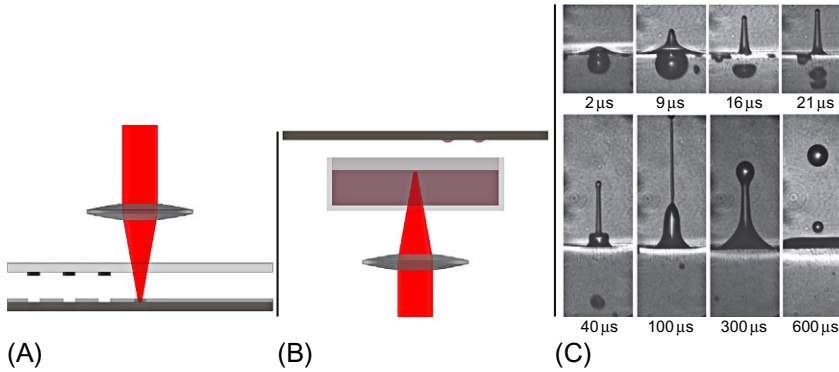


Fig. 13.11 Scheme of (A) LIBT and (B) film-free laser printing. (C) Time resolved images corresponding to a liquid ejection event generated with the film-free laser printing technique for a water and glycerol solution. *Adapted from A. Patrascioiu, J.M. Fernández-Pradas, J.L. Morenza, P. Serra, Film-free laser printing: jetting dynamics analyzed through time-resolved imaging, Appl. Surf. Sci. 302 (2014) 303–308, doi:10.1016/j.apsusc.2013.09.119.*

be transparent to the laser radiation. There are LIFT variants in which both options are possible.

13.4.2 Film-Free Laser Printing

There is a LIFT setup called film-free laser printing, in which the fluid is contained in a reservoir, transparent to the laser radiation (Fig. 13.11B). Ultrashort laser pulses (~fs) are focalized at some distance from the free surface of the fluid (that distance behaves as the film thickness) and due to nonlinear processes the bubble started there obtained similar results to the standard fluid LIFT [51,52,52a], as seen in Fig. 13.11C.

13.4.3 Indirect Interaction—LIFT

In the case of indirect transfer, it involves the application of an intermediary layer, which absorbs the laser radiation and shields the donor material from direct laser irradiation [44]. This prevents photolytic and pyrolytic damage to the transferred material and enables printing of many sensitive materials; it also allows the printing of laser-transparent fluids. The nature of this layer can also change the interaction ranging from pure thermal (the laser heats a metal film that vaporizes and produces a bubble in the material) to pure mechanical (the laser interacts with the intermediate layer, producing a blister that expands and pushes the material). Different layers and interactions have been proposed.

13.4.3.1 Absorbing Layer LIFT

The laser pulse energy is absorbed in the intermediate layer, heating up without ablation. The heat is then transferred to the fluid causing its local vaporization (Fig. 13.12A). The ejection dynamics is the same as the gas-actuated mechanism for the jet formation (same spatial and temporal evolution), despite using the intermediate layer. The first absorbing-layer materials demonstrated were thin metal or metal-oxide films [53–56].

13.4.3.2 Dynamic Release Layer LIFT (DRL-LIFT)

The laser pulse is fully absorbed in the intermediate layer, vaporizing it [57]. The generated pressure triggers the transfer of the donor to the receiver, leaving the donor unaffected. The intermediate layer is thus called dynamic release layer (DRL). The residual components of the DRL can contaminate the donor material and make this technique inadequate for some applications. This technique has been applied successfully to transfer metals, polymers, and biomaterials [15,58–60].

13.4.3.3 Blister-Actuated LIFT (BA-LIFT)

A thin polymer film can also be used as an absorbing layer to transfer inks free of damage [43,44]. This variant is called blister-actuated laser-induced forward transfer (BA-LIFT). BA-LIFT involves a rapidly expanding and sealed vapor, which deforms the polymer film and forms a blister (Fig. 13.12B).

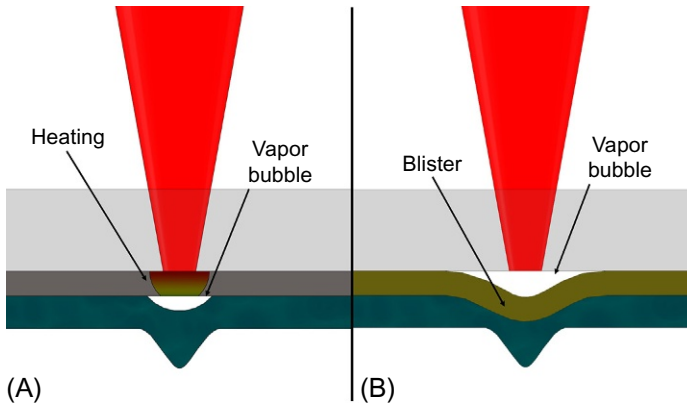


Fig. 13.12 Scheme of indirect interaction—LIFT: (A) The laser is absorbed in a metal layer that heats the fluid and generates a high pressure bubble (absorbing layer LIFT); (B) the laser is absorbed in a polymer film in the glass/polymer interface and the vapor generates a expanding blister that pushes the fluid (blister-actuated LIFT).

This blister drives the flow of the surround fluid. The trapped hot gases cool and are trapped inside the blister cavity. BA-LIFT thus allows transferring delicate inks without any contamination from the polymer layer. Fig. 13.13 shows time-resolved images of liquid ejection using BA-LIFT [30].

13.4.4 Matrix-Assisted Pulsed Laser Evaporation-Direct Write

The Matrix-Assisted Pulsed Laser Evaporation-Direct Write (MAPLE-DW) technique combines the interaction fundamentals of Matrix-Assisted Pulsed Laser Evaporation (MAPLE) with the LIFT application [61]. MAPLE is an alternative process to the standard Pulsed Laser deposition (PLD) technique [62], in which the material to be deposited is dissolved or mixed in particulate form into a solvent matrix material with a lower evaporation point. Then the laser pulse evaporates the matrix and releases the material with

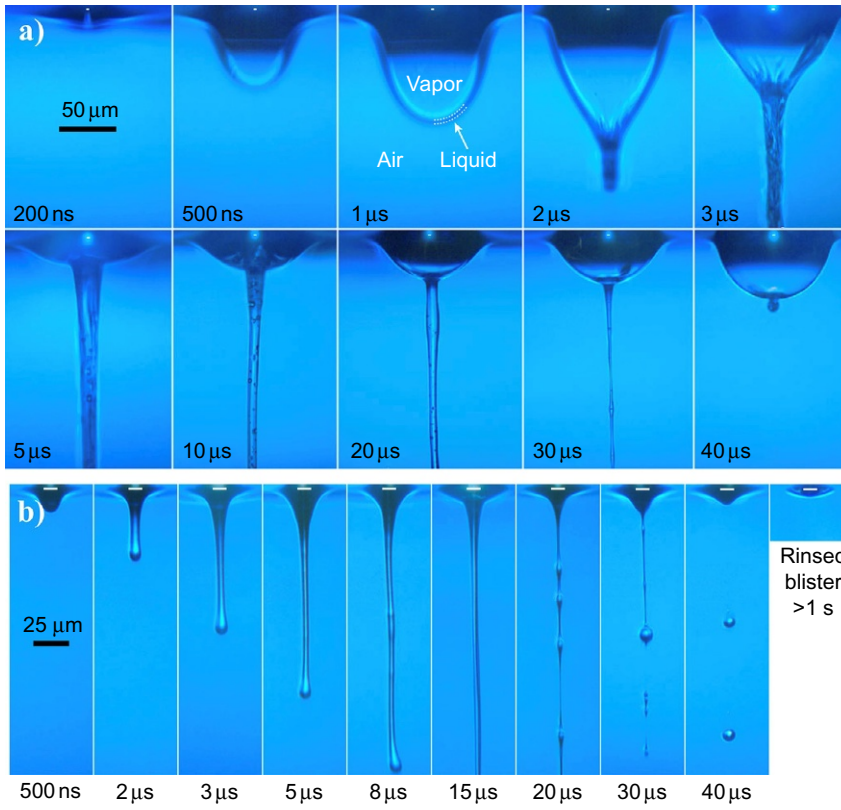


Fig. 13.13 Time-resolved images of liquid ejection into ambient air using (A) a 50-nm titanium absorbing layer and (B) a 7-µm polyimide absorbing layer [30].

enough energy to be deposited in the receiver substrate but without being damaged. This allows the deposition of complex molecules without damage.

In MAPLE-DW the mixture of material and solvent matrix is deposited on the donor substrate. The setup is similar to that of the standard LIFT, but the laser only evaporates the matrix (as in MAPLE) and propels small amounts of the material to the acceptor substrate. The main difference of MAPLE-DW with other LIFT variations is that it is a pyrolytic method only for the matrix material, and thus it is possible to avoid significant heating of the transferred material. MAPLE-DW has been used to successfully print a number of materials, such as metals [61], organics [63], and biomaterials [64].

13.4.5 Laser Molecular Implantation

Laser molecular implantation (LMI), other times referred to as laser-induced molecular implantation (LIMIT), is a variation of LIFT developed mainly for the selective implantation of fluorescent molecules into polymer films [65–67]. In this technique, the molecules are implanted in a thin polymer film that is applied to a glass substrate. The acceptor substrate, usually another polymer film, and the donor are kept in close contact. The laser pulse activates the dopant molecules and heats the polymer, which expands, increasing the contact between the films. The molecules are then transferred and implanted into the undopped film through a thermally activated diffusion process [68]. The temperatures reached are not sufficient to decompose the dopant or supporting polymer molecules so there is no explosive expansion-driven transfer.

As the donor and acceptor are both polymers they are interchangeable and backward-transfer is possible [69].

13.4.6 Long-Pulsed LIFT

Long-pulsed LIFT (LP-LIFT) is the definition of LIFT processes done using laser pulses in the order of μs or longer. LP-LIFT experimental setup is like the common LIFT configuration, but the donor and the acceptor are kept in close contact. The laser heats the donor, keeping it at a high temperature for a long time; the long pulse duration and the thermal expansion of the donor overcomes the small gap. The heated donor is annealed to the acceptor without melting and, when the two substrates are taken away, the heated donor is kept bounded to the acceptor [70]. The physics of this process is thus different to the one observed with ns laser pulses. In order to obtain the transference, two thresholds must be overcome: one is the usual fluence threshold and the other is a temporal threshold. Pulse durations of

at least 500 μs are needed, although this time depends on the material properties and thickness of the film. The first application of the LP-LIFT was the transfer of a 5 μm tungsten segment in the solid phase [70–72] without any melting and with good adherence. This thermal process is only suitable for solid materials that can be heated without damaging and in which the annealing process is possible.

13.4.7 BLAST LIFT

Ballistic Laser-Assisted Solid Transfer (BLAST) is a variation of the LIFT process for solid materials in which multiple, subthreshold energy femtosecond pulses are used to reduce the adhesion of the solid film to the transparent substrate until a solid block of material is ejected toward the acceptor substrate [32], as is shown in Fig. 13.14. The optimum fluence and number of pulses for solid pellet transfer depends mainly on the film thickness. As BLAST-LIFT works with very low fluences, it is possible to transfer more delicate or heat sensitive materials with it than with other LIFT variants. To obtain more repeatability shapes, BLAST LIFT has been performed with shaped laser pulses to weaken the contour before the transference, although this has little effect on optimum fluence and number of pulses.

13.5 APPLICATIONS OF LIFT

Direct writing techniques, like inkjet or LIFT, print in a serial process: in each spatial position or pixel, they transfer a controlled volume of material (voxel). Therefore, they are capable of printing complex and flexible designs

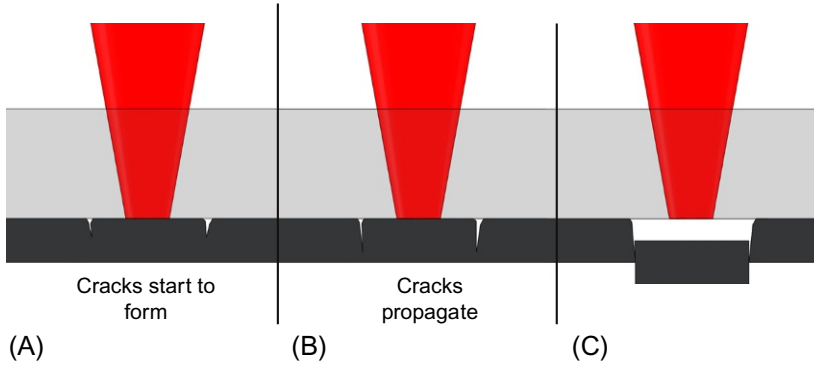


Fig. 13.14 Scheme of the BLAST-LIFT process: (A) Subthreshold energy femtosecond pulses generate cracks in the surface; (B) subsequent laser pulses propagate cracks through the donor film; (C) finally a solid block of material is ejected toward the acceptor substrate.

with the aid of a computer controlled system and without the need of any mask or stamp [73]. Due to its similarity with inkjet technique, the standard printing process seems to be the most straightaway application of LIFT. This was the first application proposed in the 1970s for the so-called LW process, in which a continuous argon laser was used for transferring inks and organic colorants from a carrier substrate [7,8]. Much more recently and using the standard LIFT configuration with a modulated CW laser, Hennig et al. [74] have implemented a LIFT machine for printing. Depending on the laser wavelength and the light absorption spectra of the ink, an absorption layer acting as a dynamic release layer is also needed. Combining a fast control software, a MHz-modulated high power laser, and a high speed polygon scanner it is possible to print at speeds larger than 1000 m/s with a resolution of 600 dpi, and using water-based, environmentally-friendly inexpensive inks.

However, the main advantage of using LIFT for printing is the possibility of printing a very wide range of materials, both inorganic and organic, solid or liquid [4,73,75], which makes LIFT a really flexible tool to be applied in very different fields. Three great groups of applications can thus be considered: First, those related with electronics, understood as the printing of the circuit itself and different active and passive elements such as diodes, transistors, sensors. Second, the use of LIFT as an additive manufacturing technique for microfabrication of 3D structures or surface functionalization. And finally, the third main area of application of LIFT is the printing of biomolecules or even living cells. In the next section, we will review some of the proposed LIFT applications.

13.5.1 LIFT for Electronics

The possibility of printing metals and other materials with high conductivity using LIFT have straightforward applications in the microelectronics industry. In the earliest works of LIFT, Bohandy et al. [11] proposed the use of LIFT for printing conductive copper lines. Those lines were transferred from a donor solid copper film using a line-focused beam, and they had a resistivity one order of magnitude larger than bulk copper. This basic LIFT configuration, with a solid donor layer, was used later to print Au lines [76], Au/sn pads [77], or 1-mm-long, 1-μm-wide Cu wires (Fig. 13.15) [78].

In later years, more studies have been done for printing metallic lines using inks or pastes with different rheology and particle sizes. Initially MAPLE-DW was used to print Ag silver lines [61] from micron-particle Ag powders dissolved in a polymeric carrier. Later, commercial inks or pastes

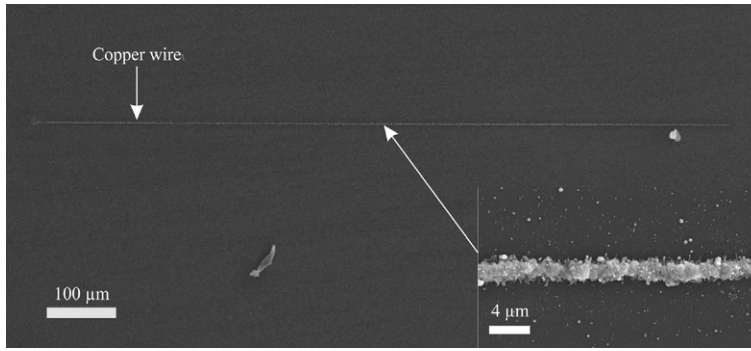


Fig. 13.15 SEM image of a continuous 1 mm long copper wire [78].

were used, easing the process. Depending on the viscosity of the fluid, two different approaches have been studied: On the one hand, donor layers consisting of high viscosity pastes more like solids to print well-defined shape voxels using LDT [16,79]. On the other hand, directly printing commercial low viscosity inks with metallic nanoparticles in a process more like LIFT printing of low viscosity fluids [20,80,81].

When it comes to printing whole circuits, LIFT has an additional advantage. As said before, LIFT is an additive laser direct writing technique, but the same experimental setup could be used for a subtractive laser process, such as micromachining the sample before printing the conductive materials. This two-step process was used by Piqué et al. [5] for printing planar embedded circuits in which the interconnections were printed using Ag particles bound with a polymer and dissolved into an organic carrier.

But the possible applications of LIFT in the electronics field is much wider than simply printing conductive lines. The capability of LIFT for printing a wide range of materials allows printing different active and passive elements of the circuit. In that sense, MAPLE-DW experiments show that it is possible to print capacitors, inductors, and resistors of complex oxides such as $BaTiO_3$, $SrTiO_3$, or $Y_3Fe_5O_{12}$ [61,76]. Organic polymers for different electronic devices such as light-emitting diodes (OLED) or thin-film transistors (OTFT) have been also printed using different variations of LDW techniques. Electroluminescent polymers have been printed using CW lasers and a pure thermal process, called LITI (laser-induced thermal imaging) [82,83], but also by standard LIFT with a donor material consisting of a multilayer structure [84,85].

In the case of polymers for OTFTs, different semiconductor materials such as copper phthalocyanine [86], diPhAc-3T [87], or P3HT [80,88] have

been printed directly from a single donor layer with low fluences. However, recent results show that printing OTFTs with LIFT demands more complex donor structures and, depending on the material to be printed, a dynamic release layer of triazene polymer is also needed [18,89,90].

Polymers printed by LIFT can also be used as passive devices in the circuit for chemical sensing. Tsouti et al. have fabricated a capacitive chemical sensor array with 256 sensing sites [91], printing on top of each microsensor different polymers (PHEMA, PAA, P4VP, PVP, PVC-co-PVA, PHS, and PMMA) as shown in Fig. 13.16. Depending on the material to be detected, a proper combination of polymers is needed. Di Pietrantonio et al. [92] have proposed a sensor for toxic compounds with printed chemoselective polymers. Those polymers have been printed using a two-step laser printing process: First the donor layer is deposited using MAPLE onto a substrate coated with a triazene layer, and second the sensor is printed using standard UV LIFT with the triazene layer acting as a dynamic release layer. Other materials printed for sensing applications are SnO_2 [93,94] or graphene oxide [95].

One particular electronic application of LIFT with very large industrial interest and possible future industrial implementation is the photovoltaic field. For example, LIFT has been proposed for creating high doped regions in the front [96] and back [97] of the solar cell. These highly doped regions, printed from phosphorous doped a-Si donor layers, reduce the series resistance of the cell. Moreover LIFT can be used to print metallic lines that act as fingers or busbars in the front metallization of the solar cell. Metallization plays a fundamental role in the fabrication of solar cells, since the deposition

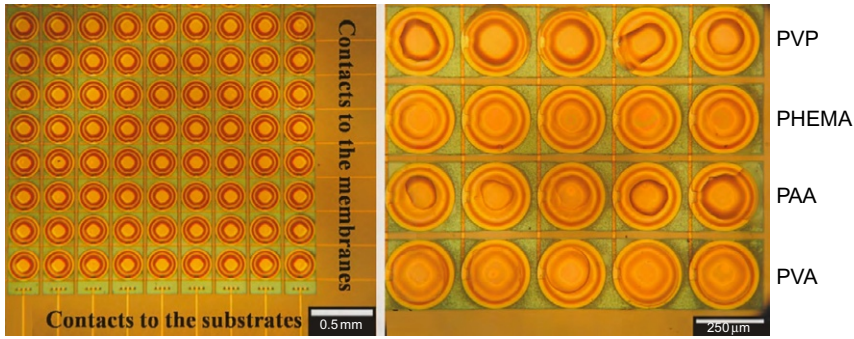


Fig. 13.16 Array of sensors printed using LIFT. *Adapted from V. Tsouti, C. Boutopoulos, D. Goustouridis, I. Zergioti, P. Normand, D. Tsoukalas, S. Chatzandroulis, A chemical sensor microarray realized by laser printing of polymers, Sens. Actuators B Chem. 150 (2010) 148–153, https://doi.org/10.1016/j.snb.2010.07.027.*

of fingers and buses using screen-printed silver pastes are one of the most expensive steps in the cell fabrication. The possibility of printing personalized free-form metallization patterns using direct writing techniques opens a wide field of applications in the building-integrated photovoltaic sector.

Two different processes have been proposed for printing metallic contacts. Röder et al. [98] proposed a two-step process in which a narrow nickel line (width below 10 μm) is first deposited by LIFT. This narrow finger is later thickened by nickel and copper plating, increasing the conductivity and reaching aspect ratios larger than 0.25. This technique has also been used by Wang et al. in a silicon solar cell based on all laser transferred contacts [99]. The front side metallization is made by LIFT of titanium, later thickened by electro-plating of silver up to a height of 2–3 μm. In the back of the cell, aluminum LIFT contacts were also printed before evaporating a continuous 1 μm Al layer, to create a highly doped region and thus ensuring the formation of a spatially controlled deep back surface field.

The second approximation to the metallization of solar cells is directly printing the fingers and the busbars of the cell in a single step, using Ag pastes as donor materials [100,101]. This approach is basically the same that is employed for printing metallic lines for other electronical applications but using the same commercial Ag pastes designed for standard screen printing. These lines have widths in the order of 100 μm and quite large aspect ratios, up to 0.6 (Fig. 13.17). However, the much higher viscosity and the micron size particulates of those silver paste strongly affects the physics involved in the printing process [26]. This direct metallization can also be made from solid donor materials as demonstrated by Zenou et al. [102]. LIFT metallization can thus be used to print free-form front grids without the need of any screen in a number of substrates, including c-Si wafers or flexible thin film CIGS [103]. Fig. 13.18 shows the possibilities of this technique, with fingers printed in a flexible substrate and an 18 cm^2 hexagonal pattern cell design.

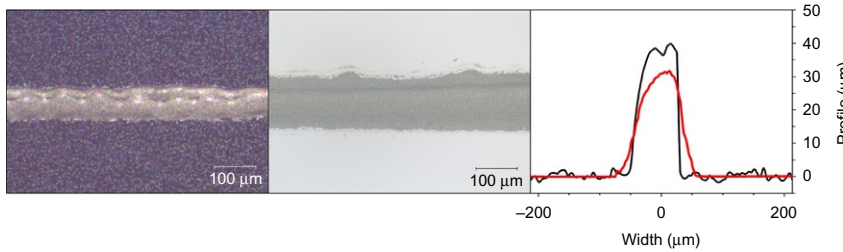


Fig. 13.17 Different lines printed using a commercial Ag paste for solar cell metallization [100].

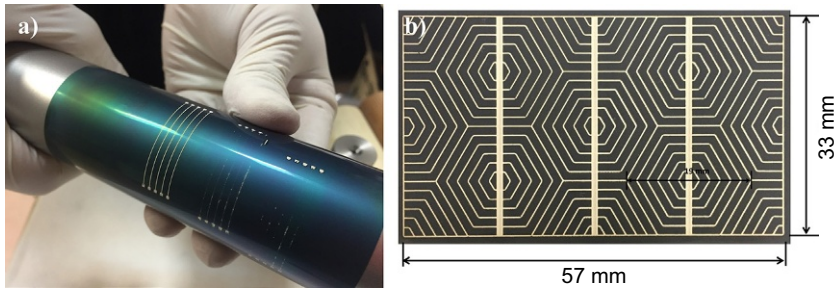


Fig. 13.18 (A) LIFT fingers printed in a flexible CIGS solar cell and (B) free-form metallization design on a c-Si solar cell [103].

Finally, LIFT can be employed together with other LDW techniques for laser processing of solar modules. Gilot et al. combine laser scribing and LIFT for first isolating the different cells in a thin-film module, and later LIFT depositing an isolating dielectric material to prevent undesired electrical contacting between two cells, and finally LIFT printing top metallic contacts for making the cells interconnection [104].

13.5.2 LIFT for Microfabrication

However, LIFT micromanufacturing is not limited only to 2D structures like those described above. Free-standing 3D structures can be produced by repeating the laser transfer process of single voxels in the same localization [73]. In this sense, it is worth mentioning the works made by Wang et al. [16] in which LDT has been applied to print vertical structures such as bridges, pyramids, or pillars (Fig. 13.19). The control of the beam can be improved by using spatial light modulators [34,35,38], which allows printing complex designs with a single laser shot, such as grids or letters (Fig. 13.20).

The aspect ratio of the pillars is limited by the adhesion between stacked voxels and the typical donor-acceptor gap distance, in the order of tens of μm, which is smaller than those characteristics of industrial 3D printing. These problems have been successfully overcome by Visser et al. [17], who have deposited metal pillars with diameters below 5 μm and lengths up to 2 mm and thus with extremely high aspect ratios, in the order of 200 (Fig. 13.21A). These pillars have been transferred using ps pulses and 200-nm-thick solid metal layers of gold and copper as donors, while maintaining standard gap distances between 20 and 50 μm. Again, the optimum experimental conditions for printing are quite limited by the laser fluence; only laser fluence well above transfer threshold produce drops deformed into disks are suitable for printing pillars.

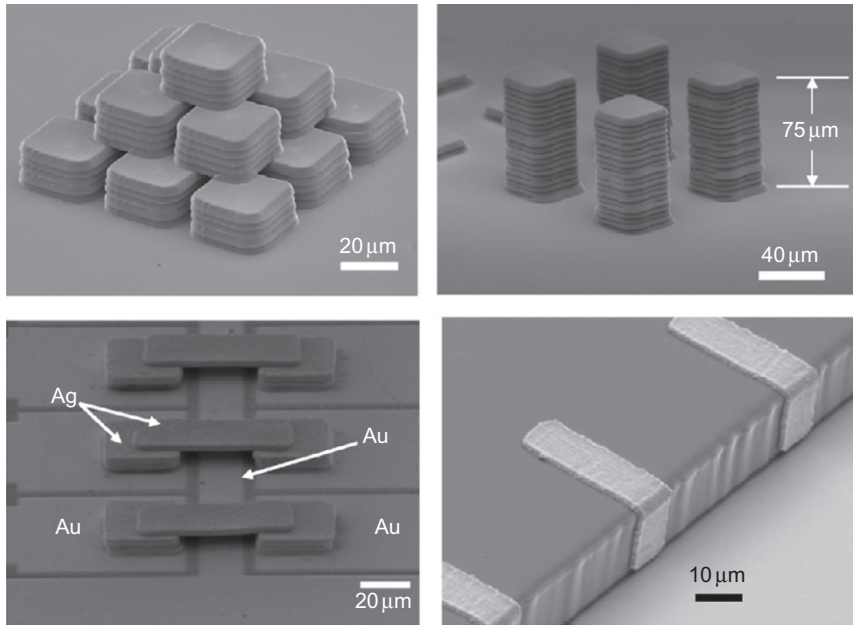


Fig. 13.19 SEM images of 3D structures printed using laser decal transfer [73].

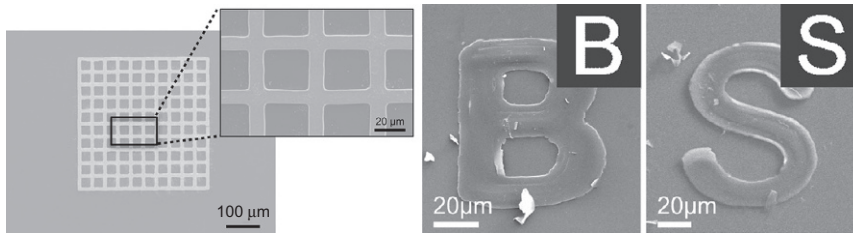
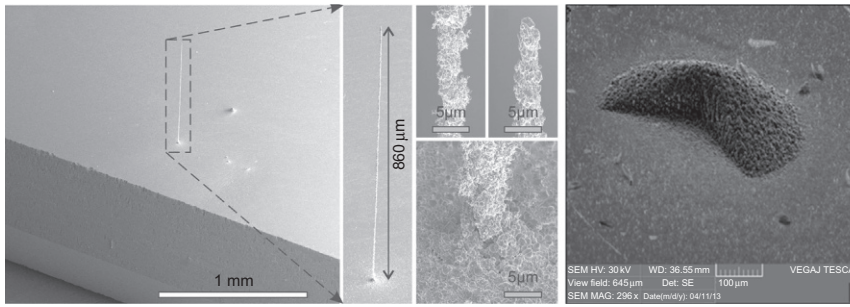


Fig. 13.20 Examples of structures printed using spatial light modulators: (A) grids [34] and (B) letters [35].

Moreover, it is possible to print even with large gap distances (more than 300 µm) and thicker metal donor layers (>300 nm) using subnanosecond laser pulses as shown by Zenou et al. [105,106]. In this case, the formation of a thermally self-induced nozzle in the surface of the donor layer allows the formation of a jet with high directionality. Pillars printed using this technique reach aspect ratios larger than 20 and, combined with a CAD software tool, it is possible to print complex 3D microstructures [105], as was shown in Fig. 13.16. LIFT can thus be used for surface modification, for example by printing periodic structures, creating plasmonic [107], or superhydrophobic structures [108].



(A) (B)

Fig. 13.21 3D structures printed using LIFT: (A) high aspect ratio copper pillar [17] and (B) cone like structure [105].

13.5.3 LIFT for Bioapplications

The ability of additive laser direct writing techniques to print microdroplets from a liquid suspension have a straightforward application in the biological field and a large research effort has been made in the last years [4,109]. There are two main lines of research developed around laser transfer of biological materials: one called laser pressure catapulting (LPC) and the other more related to the different LIFT processes described earlier.

LPC together with laser microdissection (LMD) is a well-established procedure widely used since its first report in 1996 under the name of laser capture microdissection (LCM) [110]. With this technology, a portion of tissue containing cells, proteins, DNA, RNA, or a mix of them, is cut with a laser and then transferred, using the aid of a laser, to a collector recipient. Typically, ultraviolet or near IR lasers are used for both the dissection and catapulting processes so the preparation of the substrate where the tissues or cells is crucial. More specifically IR based systems use a contact technique to isolate the previous cut tissue while a UV only system uses a laser pulse to catapult the tissue onto the collector or let it fall simply by gravity. Fig. 13.22 shows a scheme of the LCM process. UV radiation is known to cause photo-damage on cells, tissues, and DNA [111] so it is important to find a way to avoid or minimize the direct interaction of the laser with the tissue. Depending on the wavelength of the laser, a protective thin film can be added and cells and tissues are grown in this layer that aids in laser absorption. This layer can be made of ethylene vinyl acetate or polyethylene naphtholate for instance [112,113].

As said before this technique has been used as an important tool in the study of DNA, RNA, and protein analysis of isolated cells. A number of publications have been made using commercially available machines man-

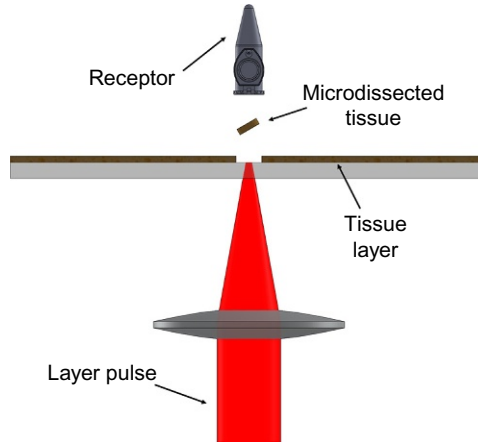


Fig. 13.22 Schematics of the laser capture microdissection (LCM).

ufactured by Leica (LMD6 and LMD7), ZEISS (PALM MicroBeam), or ThermoFisher (Arcturus XT) in the fields of DNA and RNA research [114,115], proteomics [116,117], plant research [118,119], and many others.

The techniques for laser transfer more related to LIFT are in an earlier stage of research in bio applications. The main difference between LCM and LIFT is that in LCM, the living material is grown and it is in the form of a "solid" tissue, while in LIFT, the biological material is immersed in a liquid matrix that sustains living conditions. The acceptor substrate can be, for example, a glass slide coated with a biocompatible layer, a scaffold, or even a live subject. Different variations of LIFT have been used to ensure high cell viability during and after the transfer process, such as DRL-LIFT with a thin metal layer with a thickness of just a few nanometers made of gold, titanium, silver or titanium oxide, BA-LIFT, or MAPLE-DW [109].

The main approach of LIFT in biological applications is to take advantage of the additive manufacturing capabilities of it. Studies made in 3D structures are more reliable than 2D ones because they are a more real approach [120]. Inkjet and extrusion are also alternatives for bioprinting and have found a wide range of applications in the field of regenerative medicine and toxicology studies [121]. In the case of inkjet, the main disadvantage is that the liquids used should have low viscosities and slow drying properties to avoid clogging the needles [122]. Extrusion process needs highly viscous liquids and cells are exposed to high pressures when they come out of the needle [121]. On LIFT based processes the transfer is completely contactless so no contamination or clogging of needles is present, and is also capable of handling a wide range of

viscosities and is the process with the highest cell viability of the three [123]. Another advantage of LIFT process is it is possible to watch in real time what are you transferring and thus allowing printing a single cell in a desired place [124]. The main disadvantages of LIFT in bioapplications is that substrate preparation can be time consuming and working in large areas can be complicated.

As mentioned before, one of the requirements for the cells to live, is for them be in a liquid environment that provides sufficient nutrients for them to live and reproduce. Dulbecco's Modified Eagle Medium (DMEM) and the Roswell Park Memorial Institute culture medium (RPMI) are two examples and two of the most used cell culture mediums. A culture medium can be printed directly but special care should be taken so the printed droplets do not dry off. Chen et al. [125] transferred normal bovine aortic endothelial cells directly from their culture medium to a Matrigel layer, which assures that transferred droplets do not dry and it is a relatively comfortable medium for the cells to survive and proliferate. Results in this experiment show near 100% viability, producing very little heat and shock damage. 3D patterning is also possible with this technique, but it is required to apply a new layer of Matrigel after the printing so cells can be printed on top.

Cells can also be resuspended in a different kind of matrix that is also able to sustain life and allow proliferation of cells. One example is hydrogels or bio inks that normally are natural or synthetic polymers able to crosslink and form a semi solid structure. The reason for using hydrogels is because the adequate use of them can allow the formation of 3D structures and at the same time keep the cells alive. An ideal matrix for printing hydrogels should have certain properties; biocompatibility, good biological interaction, and bio replication capacity are among the most important. If they are to be used for making 3D structures then the mechanical properties of the crosslinked gel are very important too, along with its capacity for degradation if implantation is planned. Hydrogels can be placed on both the donor and acceptor and can be crosslinked during the process or after. The ideal hydrogel should be able to support the cells, keep them alive, allow them to proliferate, have interconnection pores for nutrients to reach the cells, and be able to degrade while cells generate their own extracellular matrix (ECM). The most used natural hydrogels are collagen, gelatin, sodium alginate, fibrin, and hyaluronic acid. They can be used alone or mixed to improve the mechanical or biological properties of the gel. Except for sodium alginate, all the other hydrogels mentioned are part of the ECM, so they are an excellent option for printing and forming structures. However, these substances tend to be expensive, while sodium alginate is cheap, easy to crosslink, and its mechanical proper-

ties can be tailored easily, so sodium alginate is widely used among the field of bio printing. The main disadvantages are it does not have very good cell adhesion properties and the body cannot dissolve sodium alginate.

In the work by Gruene et al. [126], cell laden sodium alginate is prepared by first dissolving it in a saline solution, then mixing it with blood plasma, and lastly adding cells to the solution. This conglomerate is used for the donor, while the acceptor consists of the same hydrogel without cells and are crosslinked with a calcium chloride solution. Fig. 13.23 shows human adipose stem cells (ASCs) printed in 3D structures up to a height of 240 μm. Several observations were made of the printed stem cells. The first proliferation ability of the cells was assessed over 7 days, showing no significant difference when compared to nonprinted. Differentiation potential of 2D and 3D printed cells was measured and compared with control cells, with no negative effects. This work shows the capacity of laser printing to study cell-cell interactions or drug screening by generating tissue blueprints.

Gruene et al. used a mixture of fibrinogen and hyaluronic acid (HA) as a hydrogel for printing endothelial colony-forming cells (ECFCs) and ASCs into an acceptor slide with the same hydrogel but crosslinked with a

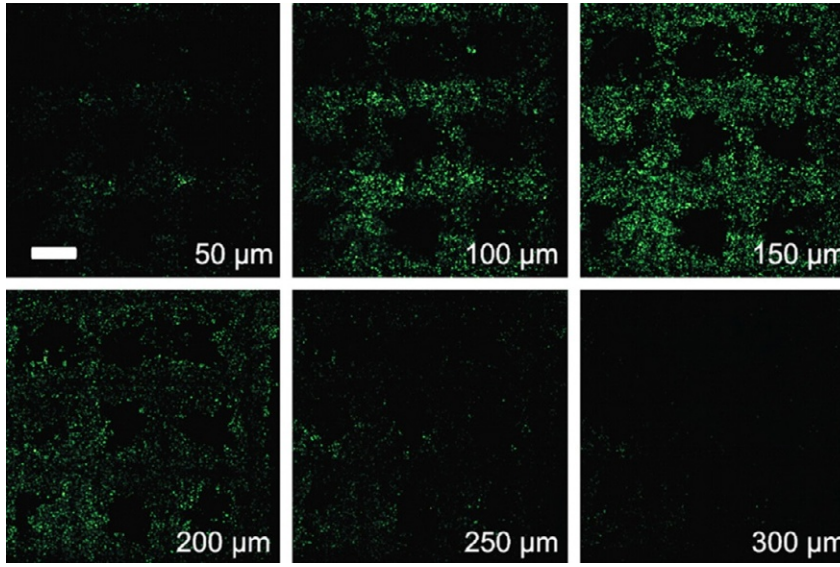


Fig. 13.23 Sectional view of the 3D ASCs graft taken at different heights by means of confocal laser scanner microscopy. Scale bar: 500 μm. *Adapted from M. Gruene, M. Pflaum, A. Deiwick, L. Koch, S. Schlie, C. Unger, M. Wilhelmi, A. Haverich, B.N. Chichkov, Adipogenic differentiation of laser-printed 3D tissue grafts consisting of human adipose-derived stem cells, Biofabrication 3 (2011) 15005, https://doi.org/10.1088/1758-5082/3/1/015005.*

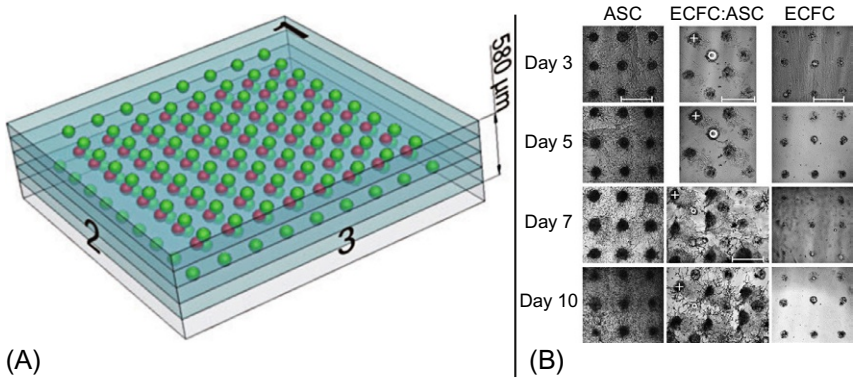


Fig. 13.24 (A) Schematic illustration of final 3D array of ASCs *(red spots)* and ECFCs *(green spots)* printed into a HA-fibrinogen matrix. (B) Visualization of cell-cell interactions by 3D cell arrays in mono and cocultures. Interactions of ASCs and ECFCs in comparison to separated arrays of ASCs and ECFCs cultivated for 10 days under VEGF-free conditions. A *circle* indicates the printed ECFC spot and a cross indicates the printed ASC spot. Scale bars = 800 mm. *VEGF*, vascular endothelial growth factor [127]. *(A) adapted form M. Gruene, M. Pflaum, C. Hess, S. Diamantouros, S. Schlie, A. Deiwick, L. Koch, M. Wilhelmi, S. Jockenhoevel, A. Haverich, B. Chichkov, Laser printing of three-dimensional multicellular arrays for studies of cell-cell and cell-environment interactions, Tissue Eng. Part C Methods 17 (2011) 973–982, https://doi.org/10.1089/ten.tec.2011.0185.*

thrombin solution [127]. Fig. 13.24A shows a 3D array of both types of cells. Survival rate, proliferation, and genotoxicity tests were made after printing the cells. Survival of the ASCs was 99.7% and of ECFCs 97.8%, with no differences in proliferation capacity or DNA damage after the printing process. Cell-cell interactions were studied during a period of 10 days. Fig. 13.24B shows how ASCs migrate to ECFCs and start to form vascular like structures.

Olfactory ensheathing cells (OECs) were printed by Othon et al. by taking a cell culture and mixing it with methyl cellulose [128]. Cells were printed in both a cell culture chamber and a Matrigel coated slide to form 3D structures. Cells were studied for 2 weeks, showing a successful capacity for survival and proliferation.

Printing of bigger structures was also accomplished by Xiong et al. [129], printing alginate circular and Y-shaped tubes. These structures were both printed with and without a cell laden hydrogel. Tubes had a diameter of 5 mm and a height of up to 11.5 mm for Y-shaped tubes. Cell viability after printing is of 63.8% and after 24 h of 68.2% for cylindrical tubes and of 68.1% after printing and 70.8% 24 h after. These viabilities are not the best but still acceptable for bio printing applications. The increase of viability after 24 h is due to the proliferation of cells. Fig. 13.25 shows printed cell laden tubes.

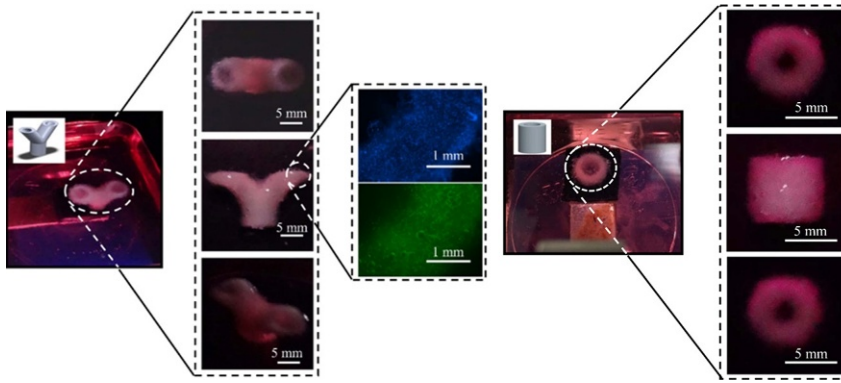


Fig. 13.25 Representative images of cellular tubes made with 2% alginate and 5×10^6 cells/mL; left: Y shaped form; right: cylinder form. *Adapted from R. Xiong, Z. Zhang, W. Chai, Y. Huang, D.B. Chrisey, Freeform drop-on-demand laser printing of 3D alginate and cellular constructs, Biofabrication 7 (2015) 45011, https://doi.org/10.1088/1758-5090/7/4/045011.*

Seeding scaffolds using laser bioprinting is also possible. Ovsianikov et al. seeded ovine endothelial cells (ECs) and ovine vascular smooth muscle-like cells (vSMCs) embedded in a sodium alginate hydrogel onto a poly(ethylene glycol) diacrylate (PEGda) scaffold made by two photon polymerization [130]. Fig. 13.26 shows the cell filled scaffold. Red areas correspond to ECs and red areas to vSMCs. With this technique, scaffolds can be made with a material with good mechanical properties beforehand, and then just seeded in a precise position with the aid of laser printing.

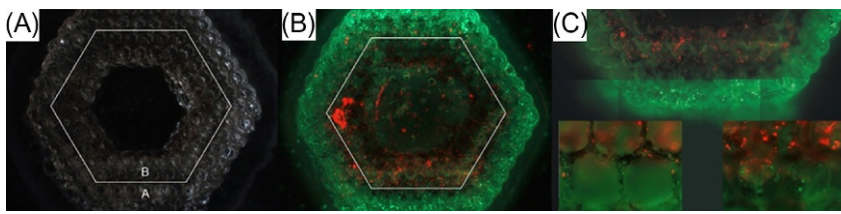


Fig. 13.26 Scaffold seeded with cells by means of laser-induced forward transfer (LIFT): (A) dark field image. The *white hexagon* indicates the border between the two scaffold areas seeded with vSMCs (A) and ECs (B), respectively; (B) fluorescence image indicating the location of different cell types after the LIFT procedure; (C) detailed image of the border area. The insets demonstrate that a sharp transition from vSMCs to EC-seeded regions is present along the entire thickness of the scaffold. *Adapted from A. Ovsianikov, M. Gruene, M. Pflaum, L. Koch, F. Maiorana, M. Wilhelmi, A. Haverich, B. Chichkov, Laser printing of cells into 3D scaffolds, Biofabrication 2 (2010) 14104, https://doi.org/10.1088/1758-5082/2/1/014104.*

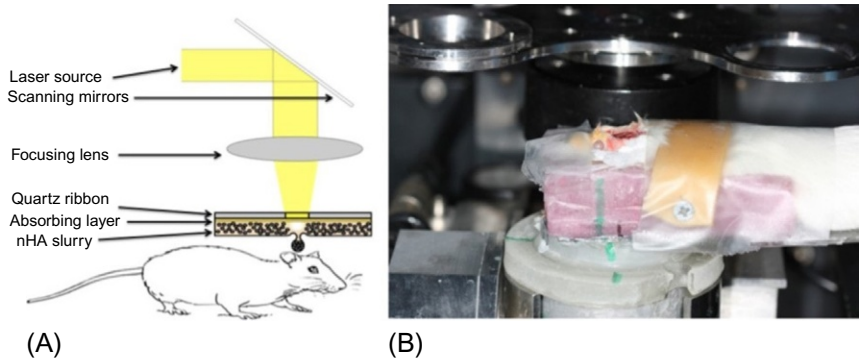


Fig. 13.27 (A) Schematic set up for in vivo laser printing; (B) specific holder for in vivo printing in mouse calvaria defects [131].

Printing cells directly to a living mouse was possible thanks to the development and adaptation of a high throughput machine for laser bio printing [131]. Nano-hydroxyapatite was deposited onto the mouse and produced a calvaria defect. Fig. 13.27 shows the setup of this process 29 of the 30 mice recovered after the procedure, without laser damage. This experiment proved that LIFT can be used for in-vivo bio printing and, in the future, for regenerative medicine applications.

Cells are not the only biomaterial that can be transferred; also, DNA, proteins and even drugs in drug delivery applications. Fernández-Pradas et al. showed a proof of concept for a way of manufacturing a biosensor working on the detection of DNA strands and proteins [132]; a solution containing a single strand cDNA of a human gene (MAPK3), a single strand cDNA of other human gene (ETS2), and a solution of human immunoglobulin. A series of droplets containing these solutions were printed into a poly-L-lysine coated glass to inspect later if all bioactivity of the molecules is still present. In all cases, the bioactivity of the biomolecule is still present and ready to be used for other purposes. Drug injection through a laser induced microjet was also demonstrated and it is another example of the capabilities of LIFT in the biological field [133].

13.6 CONCLUSIONS

In the past few years an increasing interest to use LIFT techniques for the direct writing of different materials has been observed. Although traditionally LIFT applications for electronics (including microelectronics, flexible

electronics, and photovoltaics) are still dominant, the LIFT transfer of biomaterials is gaining more and more interest due to its potential use in an important number of applications in biomedicine and biotechnology. Among them, applications in regenerative medicine are particularly attractive and this trend will probably continue in the future. However, what is particularly relevant about LIFT developments in the last few years, is the increasing activity in integration at the industrial level of this technique. As it has been shown, important efforts are in progress to find industrial solutions for metallization in PV industry with LIFT. In addition, an increasing number of start-ups and well-established companies are deeply involved in the development of machine concepts that use LIFT as the tool of choice for both 2D and 3D direct writing of materials. In conclusion, we are starting a new period for this technique which, undoubtedly, will reach a point of maturity that will allow its industrial integration in different strategic sectors.

ACKNOWLEDGMENTS

Work supported by EUROPEAN COMISSION APPOLO FP7-2013-NMP-ICT-FOF. 609355 and Spanish MINECO projects: SIMLASPV-MET (ENE2014-58454-R), HELLO (ENE2013-48629-C4-3-R), and CHENOC (ENE2016-78933-C4-4-R).

REFERENCES

[1] K.K.B. Hon, L. Li, I.M. Hutchings, Direct writing technology – advances and developments, CIRP Ann. Manuf. Technol. 57 (2008) 601–620, https://doi.org/10.1016/j.cirp.2008.09.006.
[2] D.B. Chrisey, The power of direct writing, Science 289 (2000) 879–881, https://doi.org/10.1126/science.289.5481.879.
[3] M.J. Madou, Fundamentals of Microfabrication: The Science of Miniaturization, CRC Press, Boca Raton, FL, 2002.
[4] C.B. Arnold, P. Serra, A. Piqué, Laser direct-write techniques for printing of complex materials, MRS Bull. 32 (2007) 23–32, https://doi.org/10.1557/mrs2007.11.
[5] A. Piqué, S.A. Mathews, B. Pratap, R.C.Y. Auyeung, B.J. Karns, S. Lakeou, Embedding electronic circuits by laser direct-write, Microelectron. Eng. 83 (2006) 2527–2533, https://doi.org/10.1016/j.mee.2006.06.004.
[6] K.D. Kyrkis, A.A. Andreadaki, G.D. Papazoglou, I. Zergioti, Direct transfer and microprinting of functional materials by laser-induced forward transfer, in: J. Perriere, E. Millon, E. Fogarassy (Eds.), Recent Advances in Laser Processing of Materials, Elsevier, Amsterdam, 2006, pp. 213–241.
[7] R.S. Braudy, Laser writing. Proc. IEEE 57 (1969) 1771–1772, https://doi.org/10.1109/proc.1969.7398.
[8] R.S. Braudy, Characteristics of organic colorants transferred by laser scanning, J. Appl. Phys. 45 (1974) 3512, https://doi.org/10.1063/1.1663811.
[9] D. Brisbane, Pattern Deposit By Laser, US Patent 3, 560.258, 1971.

[10] M.L. Levene, R.D. Scott, B.W. Siryj, Material transfer recording, Appl. Optics 9 (1970) 2260–2265, https://doi.org/10.1364/ao.9.002260.
[11] J. Bohandy, B.F. Kim, F.J. Adrian, Metal deposition from a supported metal film using an excimer laser, J. Appl. Phys. 60 (1986) 1538–1539, https://doi.org/10.1063/1.337287.
[12] F.J. Adrian, J. Bohandy, B.F. Kim, A.N. Jette, A study of the mechanism of metal deposition by the laser-induced forward transfer process, J. Vac. Sci. Technol. B: Microelectron. Process, Phenom. 5 (1987) 1490, https://doi.org/10.1116/1.583661.
[13] J. Bohandy, B.F. Kim, F.J. Adrian, A.N. Jette, Metal deposition at 532 nm using a laser transfer technique, J. Appl. Phys. 63 (1988) 1158, https://doi.org/10.1063/1.340023.
[14] D.P. Banks, C. Grivas, J.D. Mills, R.W. Eason, I. Zergioti, Nanodroplets deposited in microarrays by femtosecond Ti:sapphire laser-induced forward transfer, Appl. Phys. Lett. 89 (2006) 193107, https://doi.org/10.1063/1.2386921.
[15] M. Colina, M. Duocastella, J.M. Fernández-Pradas, P. Serra, J.L. Morenza, Laser-induced forward transfer of liquids: Study of the droplet ejection process, J. Appl. Phys. 99 (2006) 84909, https://doi.org/10.1063/1.2191569.
[16] J. Wang, R.C.Y. Auyeung, H. Kim, N.A. Charipar, A. Piqué, Three-dimensional printing of interconnects by laser direct-write of silver nanopastes, Adv. Mater. 22 (2010) 4462–4466, https://doi.org/10.1002/adma.201001729.
[17] C.W. Visser, R. Pohl, C. Sun, G.-W. Römer, B.H. Huis In't Veld, D. Lohse, Toward 3D printing of pure metals by laser-induced forward transfer, Adv. Mater. 27 (2015) 4087–4092, https://doi.org/10.1002/adma.201501058.
[18] C. Constantinescu, A.K. Diallo, L. Rapp, P. Cremillieu, R. Mazurczyk, F. Serein-Spirau, J.P. Lère-Porte, P. Delaporte, A.P. Alloncle, C. Videlot-Ackermann, Laser-induced forward transfer of multi-layered structures for OTFT applications, Appl. Surf. Sci. 336 (2015) 11–15, https://doi.org/10.1016/j.apsusc.2014.06.155.
[19] M. Nagel, Laser-induced forward transfer for the fabrication of devices, in: S.C. Singh, H.B. Zeng, C. Guo, W. Cai (Eds.), Nanomaterials: Processing and Characterization with Lasers, Wiley-VCH, Weinheim, 2012, pp. 255–316.
[20] P. Serra, M. Duocastella, J.M. Fernández-Pradas, J.L. Morenza, Liquids microprinting through laser-induced forward transfer, Appl. Surf. Sci. 255 (2009) 5342–5345, https://doi.org/10.1016/j.apsusc.2008.07.200.
[21] D. Young, R.C.Y. Auyeung, A. Piqué, D.B. Chrisey, D.D. Dlott, Time-resolved optical microscopy of a laser-based forward transfer process, Appl. Phys. Lett. 78 (2001) 3169, https://doi.org/10.1063/1.1372200.
[22] M.S. Brown, N.T. Kattamis, C.B. Arnold, Time-resolved study of polyimide absorption layers for blister-actuated laser-induced forward transfer, J. Appl. Phys. 107 (2010) 83103, https://doi.org/10.1063/1.3327432.
[23] D. Young, R.C.Y. Auyeung, A. Piqué, D.B. Chrisey, H. Denham, D.D. Dlott, Plume and jetting regimes in a laser based forward transfer process as observed by time-resolved optical microscopy, MRS Proc. 698 (2001), https://doi.org/10.1557/proc-698-q3.9.1.
[24] M. Duocastella, J.M. Fernández-Pradas, J.L. Morenza, P. Serra, Time-resolved imaging of the laser forward transfer of liquids, J. Appl. Phys. 106 (2009) 84907, https://doi.org/10.1063/1.3248304.
[25] S.A. Mathews, R.C.Y. Auyeung, H. Kim, N.A. Charipar, A. Piqué, High-speed video study of laser-induced forward transfer of silver nano-suspensions, J. Appl. Phys. 114 (2013) 64910, https://doi.org/10.1063/1.4817494.
[26] D. Munoz-Martin, C.F. Brasz, Y. Chen, M. Morales, C.B. Arnold, C. Molpeceres, Laser-induced forward transfer of high-viscosity silver pastes, Appl. Surf. Sci. 366 (2016) 389–396, https://doi.org/10.1016/j.apsusc.2016.01.029.

[27] C. Boutopoulos, A.P. Alloncle, I. Zergioti, P. Delaporte, A time-resolved shadowgraphic study of laser transfer of silver nanoparticle ink, Appl. Surf. Sci. 278 (2013) 71–76, https://doi.org/10.1016/j.apsusc.2012.12.002.
[28] M. Duocastella, A. Patrascioiu, V. Dinca, J.M. Fernández-Pradas, J.L. Morenza, P. Serra, Study of liquid deposition during laser printing of liquids, Appl. Surf. Sci. 257 (2011) 5255–5258, https://doi.org/10.1016/j.apsusc.2010.10.148.
[29] C. Unger, M. Gruene, L. Koch, J. Koch, B.N. Chichkov, Time-resolved imaging of hydrogel printing via laser-induced forward transfer, Appl. Phys. A 103 (2010) 271, https://doi.org/10.1007/s00339-010-6030-4.
[30] M.S. Brown, N.T. Kattamis, C.B. Arnold, Time-resolved dynamics of laser-induced micro-jets from thin liquid films, Microfluid. Nanofluid. 11 (2011) 199–207, https://doi.org/10.1007/s10404-011-0787-4.
[31] M.V. Shugaev, N.M. Bulgakova, Thermodynamic and stress analysis of laser-induced forward transfer of metals, Appl. Phys. A 101 (2010) 103, https://doi.org/10.1007/s00339-010-5767-0.
[32] D.P. Banks, C. Grivas, I. Zergioti, R.W. Eason, Ballistic laser-assisted solid transfer (BLAST) from a thin film precursor, Opt. Express 16 (2008) 3247–3249, https://doi.org/10.1364/OE.16.003249.
[33] A. Piqué, D.B. Chrisey, J.M. Fitz-Gerald, R.A. McGill, R.C.Y. Auyeung, H.D. Wu, S. Lakeou, V. Nguyen, R. Chung, M. Duignan, Direct writing of electronic and sensor materials using a laser transfer technique, J. Mater. Res. 15 (2000) 1872–1875, https://doi.org/10.1557/jmr.2000.0271.
[34] A. Piqué, H. Kim, R.C.Y. Auyeung, A.T. Smith, Laser forward transfer of functional materials for digital fabrication of microelectronics, J. Imaging Sci. Technol. 57 (2013) 1–8, https://doi.org/10.2352/j.imagingsci.technol.2013.57.4.040404.
[35] D.J. Heath, M. Feinaeugle, J.A. Grant-Jacob, B. Mills, R.W. Eason, Dynamic spatial pulse shaping via a digital micromirror device for patterned laser-induced forward transfer of solid polymer films, Opt. Mater. Express 5 (2015) 1129–1136, https://doi.org/10.1364/ome.5.001129.
[36] R.C.Y. Auyeung, H. Kim, N.A. Charipar, A.J. Birnbaum, S.A. Mathews, A. Piqué, Laser forward transfer based on a spatial light modulator, Appl. Phys. A 102 (2010) 21, https://doi.org/10.1007/s00339-010-6054-9.
[37] R.C.Y. Auyeung, H. Kim, S. Mathews, A. Piqué, Laser forward transfer using structured light, Opt. Express 23 (2015) 422–430, https://doi.org/10.1364/oe.23.000422.
[38] R. Pohl, M. Jansink, G.R.B.E. Röme, A.J. Huis In't Veld, Solid-phase laser-induced forward transfer of variable shapes using a liquid-crystal spatial light modulator, Appl. Phys. A 120 (2015) 427, https://doi.org/10.1007/s00339-015-9212-2.
[39] E. Breckenfeld, H. Kim, R.C.Y. Auyeung, A. Piqué, Laser-induced forward transfer of Ag nanopaste, J. Vis. Exp. (2016) e53728, https://doi.org/10.3791/53728.
[40] A. Patrascioiu, J.M. Fernández-Pradas, A. Palla-Papavlu, J.L. Morenza, P. Serra, Laser-generated liquid microjets: correlation between bubble dynamics and liquid ejection, Microfluid. Nanofluid. 16 (2014) 55–63, https://doi.org/10.1007/s10404-013-1218-5.
[41] M.S. Brown, C.F. Brasz, Y. Ventikos, C.B. Arnold, Impulsively actuated jets from thin liquid films for high-resolution printing applications, J. Fluid Mech. 709 (2012) 341–370, https://doi.org/10.1017/jfm.2012.337.
[42] M. Duocastella, J.M. Fernández-Pradas, P. Serra, J.L. Morenza, Jet formation in the laser forward transfer of liquids, Appl. Phys. A Mater. Sci. Process. 93 (2008) 453–456, https://doi.org/10.1007/s00339-008-4781-y.
[43] N.T. Kattamis, P.E. Purnick, R. Weiss, C.B. Arnold, Thick film laser induced forward transfer for deposition of thermally and mechanically sensitive materials, Appl. Phys. Lett. 91 (2007) 171120, https://doi.org/10.1063/1.2799877.

[44] N.T. Kattamis, N.D. McDaniel, S. Bernhard, C.B. Arnold, Laser direct write printing of sensitive and robust light emitting organic molecules, Appl. Phys. Lett. 94 (2009) 103306, https://doi.org/10.1063/1.3098375.
[45] M. Rein, Phenomena of liquid drop impact on solid and liquid surfaces, Fluid Dyn. Res. 12 (1993) 61–93, https://doi.org/10.1016/0169-5983(93)90106-K.
[46] D.B. van Dam, C. Le Clerc, Experimental study of the impact of an ink-jet printed droplet on a solid substrate, Phys. Fluids 16 (2004) 3403–3414, https://doi.org/10.1063/1.1773551.
[47] M. Duocastella, J.M. Fernández-Pradas, J.L. Morenza, P. Serra, Droplet printing through bubble contact in the laser forward transfer of liquids, Appl. Surf. Sci. 257 (2011) 2825–2829, https://doi.org/10.1016/j.apsusc.2010.10.070.
[48] R. Pohl, C.W. Visser, G.R.B.E. Römer, C. Sun, A.J. Huis In'T Veld, D. Lohse, Imaging of the ejection process of nanosecond laser-induced forward transfer of gold, J. Laser Micro Nanoeng. 10 (2015) 154–157, https://doi.org/10.2961/jlmn.2015.02.0008.
[49] R. Pohl, C.W. Visser, G.-W. Römer, D. Lohse, C. Sun, B.H. Huis In'T Veld, Ejection regimes in picosecond laser-induced forward transfer of metals, Phys. Rev. Appl. 3 (2015) 24001, https://doi.org/10.1103/physrevapplied.3.024001.
[50] P. Papakonstantinou, N. Vainos, C. Fotakis, Microfabrication by UV femtosecond laser ablation of Pt, Cr and indium oxide thin films, Appl. Surf. Sci. 151 (1999) 159–170, https://doi.org/10.1016/S0169-4332(99)00299-8.
[51] H. Desrus, B. Chassagne, F. Moizan, R. Devillard, S. Petit, R. Kling, S. Catros, Effective parameters for film-free femtosecond laser assisted bioprinting, Appl. Optics 55 (2016) 3879–3886, https://doi.org/10.1364/ao.55.003879.
[52] A. Patrascioiu, M. Duocastella, J.M. Fernández-Pradas, J.L. Morenza, P. Serra, Liquids microprinting through a novel film-free femtosecond laser based technique, Appl. Surf. Sci. 257 (2011) 5190–5194, https://doi.org/10.1016/j.apsusc.2010.11.093.
[52a] A. Patrascioiu, J.M. Fernández-Pradas, J.L. Morenza, P. Serra, Film-free laser printing: jetting dynamics analyzed through time-resolved imaging, Appl. Surf. Sci. 302 (2014) 303–308. https://doi.org/10.1016/j.apsusc.2013.09.119.
[53] J.M. Fernández-Pradas, M. Colina, P. Serra, J. Domínguez, J.L. Morenza, Laser-induced forward transfer of biomolecules, Thin Solid Films 453–454 (2004) 27–30, https://doi.org/10.1016/j.tsf.2003.11.154.
[54] M. Colina, P. Serra, J.M. Fernández-Pradas, L. Sevilla, J.L. Morenza, DNA deposition through laser induced forward transfer, Biosens. Bioelectron. 20 (2005) 1638–1642, https://doi.org/10.1016/j.bios.2004.08.047.
[55] B. Hopp, T. Smausz, N. Kresz, N. Barna, Z. Bor, L. Kolozsvári, D.B. Chrisey, A. Szabó, A. Nógrádi, Survival and proliferative ability of various living cell types after laser-induced forward transfer, Tissue Eng. 11 (2005) 1817–1823, https://doi.org/10.1089/ten.2005.11.1817.
[56] J.A. Barron, P. Wu, H.D. Ladouceur, B.R. Ringeisen, Biological laser printing: a novel technique for creating heterogeneous 3-dimensional cell patterns, Biomed. Microdevices 6 (2004) 139–147, https://doi.org/10.1023/b:bmmd.0000031751.67267.9f.
[57] W.A. Tolbert, I.Y.S. Lee, M.M. Doxtader, E.W. Ellis, D.D. Dlott, High-speed color imaging by laser ablation transfer with a dynamic release layer: fundamental mechanisms, J. Imaging Sci. Technol. 37 (1993) 411–422.
[58] L. Koch, S. Kuhn, H. Sorg, M. Gruene, S. Schlie, R. Gaebel, B. Polchow, K. Reimers, S. Stoelting, N. Ma, P.M. Vogt, G. Steinhoff, B. Chichkov, Laser printing of skin cells and human stem cells, Tissue Eng. Part C Methods 16 (2010) 847–854, https://doi.org/10.1089/ten.tec.2009.0397.
[59] T. Mito, T. Tsujita, H. Masuhara, N. Hayashi, K. Suzuki, Hollowing and transfer of polymethyl methacrylate film propelled by laser ablation of triazeno polymer film, Jpn. J. Appl. Phys. 40 (2001) L805–L806, https://doi.org/10.1143/jjap.40.l805.

[60] R. Fardel, M. Nagel, F. Nüesch, T. Lippert, A. Wokaun, Laser forward transfer using a sacrificial layer: Influence of the material properties, Appl. Surf. Sci. 254 (2007) 1322–1326, https://doi.org/10.1016/j.apsusc.2007.08.091.
[61] A. Piqué, D.B. Chrisey, R.C.Y. Auyeung, J. Fitz-Gerald, H.D. Wu, R.A. McGill, S. Lakeou, P.K. Wu, V. Nguyen, M. Duignan, A novel laser transfer process for direct writing of electronic and sensor materials, Appl. Phys. A: Mater. Sci. Process. 69 (1999) S279–S284, https://doi.org/10.1007/s003390051400.
[62] R.W. Eason, Pulsed Laser Deposition of Thin Films, John Wiley & Sons, Hoboken, NJ, 2007.
[63] R. Modi, H.D. Wu, R.C.Y. Auyeung, C.M. Gilmore, D.B. Chrisey, Direct writing of polymer thick film resistors using a novel laser transfer technique, J. Mater. Res. 16 (2001) 3214–3222, https://doi.org/10.1557/jmr.2001.0443.
[64] B.R. Ringeisen, D.B. Chrisey, A. Piqué, H.D. Young, R. Modi, M. Bucaro, J. Jones-Meehan, B.J. Spargo, Generation of mesoscopic patterns of viable *Escherichia coli* by ambient laser transfer, Biomaterials 23 (2002) 161–166, https://doi.org/10.1016/s0142-9612(01)00091-6.
[65] M. Goto, J. Hobley, T. Oishi, A. Kasahara, M. Tosa, K. Yoshihara, M. Kishimoto, H. Fukumura, Micro-patterning of multiple organic molecules by laser implantation, Appl. Phys. A 79 (2004) 157–160, https://doi.org/10.1007/s00339-003-2294-2.
[66] H. Fukumura, Y. Kohji, H. Masuhara, Laser implantation of fluorescent molecules into polymer films, Appl. Surf. Sci. 96–98 (1996) 569–571, https://doi.org/10.1016/0169-4332(95)00532-3.
[67] T. Okada, K. Hatanaka, J. Hobley, H. Fukumura, M. Kishimoto, Laser-induced molecular implantation at the focus of an objective lens: a comparative study among anthracene derivatives, in: Tech. Dig. CLEO/Pacific Rim 2001, 4th Pacific Rim Conf. Lasers Electro-Optics (Cat. No. 01TH8557), vol. 1, 2001, https://doi.org/10.1109/CLEOPR.2001.967724. pp. I–I.
[68] H. Fukumura, Laser molecular implantation into polymer solids induced by irradiation below ablation threshold, J. Photochem. Photobiol. A Chem. 106 (1997) 3–8, https://doi.org/10.1016/s1010-6030(97)00030-0.
[69] H. Fukumura, Y. Kohji, K. Nagasawa, H. Masuhara, Laser implantation of pyrene molecules into poly(methyl methacrylate) films, J. Am. Chem. Soc. 116 (1994) 10304–10305, https://doi.org/10.1021/ja00101a062.
[70] Z. Kántor, Z. Tóth, T. Szörényi, Metal pattern deposition by laser-induced forward transfer, Appl. Surf. Sci. 86 (1995) 196–201, https://doi.org/10.1016/0169-4332(94)00384-x.
[71] Z. Kántor, Z. Tóth, T. Szörényi, A.L. Tóth, Deposition of micrometer-sized tungsten patterns by laser transfer technique, Appl. Phys. Lett. 64 (1994) 3506, https://doi.org/10.1063/1.111255.
[72] Z. Kántor, T. Szörényi, Dynamics of long-pulse laser transfer of micrometer-sized metal patterns as followed by time-resolved measurements of reflectivity and transmittance, J. Appl. Phys. 78 (1995) 2775, https://doi.org/10.1063/1.360076.
[73] A. Piqué, R.C.Y. Auyeung, H. Kim, N.A. Charipar, S.A. Mathews, Laser 3D micro-manufacturing, J. Phys. D Appl. Phys. 49 (2016) 223001, https://doi.org/10.1088/0022-3727/49/22/223001.
[74] G. Hennig, T. Baldermann, C. Nussbaum, M. Rossier, A. Brockelt, L. Schuler, G. Hochstein, Lasersonic® LIFT process for large area digital printing, J. Laser Micro Nanoeng. 7 (2012) 299–305, https://doi.org/10.2961/jlmn.2012.03.0012.
[75] P. Serra, M. Duocastella, J.M. Fernández-Pradas, J.L. Morenza, The laser-induced forward transfer technique for microprinting, in: J.R. Lawrence, J. Pou, D.K.Y. Low, E. Toyserkani (Eds.), Advanced Laser Materials Processing, Woodhead Publishing, Oxford, 2010, pp. 367–393.

[76] D.B. Chrisey, A. Piqué, J. Fitz-Gerald, R.C.Y. Auyeung, R.A. McGill, H.D. Wu, M. Duignan, New approach to laser direct writing active and passive mesoscopic circuit elements, Appl. Surf. Sci. 154–155 (2000) 593–600, https://doi.org/10.1016/s0169-4332(99)00465-1.
[77] R. Bähnisch, W. Groß, A. Menschig, Single-shot, high repetition rate metallic pattern transfer, Microelectron. Eng. 50 (2000) 541–546, https://doi.org/10.1016/s0167-9317(99)00325-1.
[78] J.A. Grant-Jacob, B. Mills, M. Feinaeugle, C.L. Sones, G. Oosterhuis, M.B. Hoppenbrouwers, R.W. Eason, Micron-scale copper wires printed using femtosecond laser-induced forward transfer with automated donor replenishment, Opt. Mater. Express 3 (2013) 747–754, https://doi.org/10.1364/ome.3.000747.
[79] E. Breckenfeld, H. Kim, R.C.Y. Auyeung, N. Charipar, P. Serra, A. Piqué, Laser-induced forward transfer of silver nanopaste for microwave interconnects, Appl. Surf. Sci. 331 (2015) 254–261, https://doi.org/10.1016/j.apsusc.2015.01.079.
[80] I. Zergioti, Laser printing of organic electronics and sensors, J. Laser Micro Nanoeng. 8 (2013) 30–34, https://doi.org/10.2961/jlmn.2013.01.0007.
[81] L. Rapp, J. Ailuno, A.P. Alloncle, P. Delaporte, Pulsed-laser printing of silver nanoparticles ink: control of morphological properties, Opt. Express 19 (2011) 21563–21574, https://doi.org/10.1364/oe.19.021563.
[82] M.C. Suh, B.D. Chin, M.H. Kim, T.M. Kang, S.T. Lee, Enhanced luminance of blue light-emitting polymers by blending with hole-transporting materials, Adv. Mater. 15 (2003) 1254–1258, https://doi.org/10.1002/adma.200304721.
[83] S. Lamansky, T.R. Hoffend Jr., H. Le, V. Jones, M.B. Wolk, W.A. Tolbert, Laser induced thermal imaging of vacuum-coated OLED materials, Proc. SPIE 5937 (2005) 593702, https://doi.org/10.1117/12.627063.
[84] S.H. Ko, H. Pan, S.G. Ryu, N. Misra, C.P. Grigoropoulos, H.K. Park, Nanomaterial enabled laser transfer for organic light emitting material direct writing, Appl. Phys. Lett. 93 (2008) 151110, https://doi.org/10.1063/1.3001803.
[85] R. Fardel, M. Nagel, F. Nüesch, T. Lippert, A. Wokaun, Fabrication of organic light-emitting diode pixels by laser-assisted forward transfer, Appl. Phys. Lett. 91 (2007) 61103, https://doi.org/10.1063/1.2759475.
[86] L. Rapp, A.K. Diallo, A.P. Alloncle, C. Videlot-Ackermann, F. Fages, P. Delaporte, Pulsed-laser printing of organic thin-film transistors, Appl. Phys. Lett. 95 (2009) 171109, https://doi.org/10.1063/1.3255011.
[87] L. Rapp, F. Serein-Spirau, J.P. Lère-Porte, A.P. Alloncle, P. Delaporte, F. Fages, C. Videlot-Ackermann, Laser printing of air-stable high performing organic thin film transistors, Org. Electron. 13 (2012) 2035–2041, https://doi.org/10.1016/j.orgel.2012.06.020.
[88] M. Makrygianni, E. Verrelli, N. Boukos, S. Chatzandroulis, D. Tsoukalas, I. Zergioti, Laser printing and characterization of semiconducting polymers for organic electronics, Appl. Phys. A 110 (2012) 559–563, https://doi.org/10.1007/s00339-012-7134-9.
[89] L. Rapp, A.K. Diallo, S. Nénon, A.P. Alloncle, C. Videlot-Ackermann, F. Fages, M. Nagel, T. Lippert, P. Delaporte, Laser printing of a semiconducting oligomer as active layer in organic thin film transistors: impact of a protecting triazene layer, Thin Solid Films 520 (2012) 3043–3047, https://doi.org/10.1016/j.tsf.2011.10.159.
[90] M. Makrygianni, A. Ainsebaa, M. Nagel, S. Sanaur, Y.S. Raptis, I. Zergioti, D. Tsamakis, Laser printed organic semiconductor PQT-12 for bottom-gate organic thin-film transistors: fabrication and characterization, Appl. Surf. Sci. 390 (2016) 823–830, https://doi.org/10.1016/j.apsusc.2016.08.124.
[91] V. Tsouti, C. Boutopoulos, D. Goustouridis, I. Zergioti, P. Normand, D. Tsoukalas, S. Chatzandroulis, A chemical sensor microarray realized by laser printing of polymers, Sens. Actuators B Chem. 150 (2010) 148–153, https://doi.org/10.1016/j.snb.2010.07.027.

[92] F. Di Pietrantonio, M. Benetti, D. Cannatà, E. Verona, A. Palla-Papavlu, V. Dinca, M. Dinescu, T. Mattle, T. Lippert, Volatile toxic compound detection by surface acoustic wave sensor array coated with chemoselective polymers deposited by laser induced forward transfer: application to sarin, Sens. Actuators B Chem. 174 (2012) 158–167, https://doi.org/10.1016/j.snb.2012.07.106.
[93] A.P. Papavlu, T. Mattle, S. Temmel, U. Lehmann, A. Hintennach, A. Grisel, A. Wokaun, T. Lippert, Highly sensitive SnO_2 sensor via reactive laser-induced transfer, Sci. Rep. 6 (2016) 25144, https://doi.org/10.1038/srep25144.
[94] T. Mattle, A. Hintennach, T. Lippert, A. Wokaun, Laser induced forward transfer of SnO_2 for sensing applications using different precursors systems, Appl. Phys. A 110 (2012) 309, https://doi.org/10.1007/s00339-012-7472-7.
[95] S. Papazoglou, V. Tsouti, S. Chatzandroulis, I. Zergioti, Direct laser printing of graphene oxide for resistive chemosensors, Opt. Laser Technol. 82 (2016) 163–169, https://doi.org/10.1016/j.optlastec.2016.03.009.
[96] M. Colina, A. Morales-Vilches, C. Voz, I. Martin, P. Ortega, A. Orpella, G. Lopez, R. Alcubilla, Laser induced forward transfer for front contact improvement in silicon heterojunction solar cells, Appl. Surf. Sci. 336 (2015) 89–95, https://doi.org/10.1016/j.apsusc.2014.09.172.
[97] R. Ferré, R. Gogolin, J. Müller, N.-P. Harder, R. Brendel, Laser transfer doping for contacting n-type crystalline Si solar cells, Phys. Status Solidi 208 (2011) 1964–1966, https://doi.org/10.1002/pssa.201127046.
[98] T.C. Röder, E. Hoffmann, J.R. Kohler, J.H. Werner, 30 μm wide contacts on silicon cells by laser transfer. in: 35th IEEE Photovolt. Spec. Conf., 2010, pp. 3597, https://doi.org/10.1109/pvsc.2010.5614378.
[99] L. Wang, D.E. Carlson, M.C. Gupta, Silicon solar cells based on all-laser-transferred contacts, Progr. Photovolt. Res. Appl. 23 (2013) 61–68, https://doi.org/10.1002/pip.2395.
[100] M. Morales, Y. Chen, D. Munoz-Martin, S. Lauzurica, C. Molpeceres, High volume transfer of high viscosity silver pastes using laser direct-write processing for screen printing of c-Si cells, Proc. SPIE 9351 (2015) 93510B, https://doi.org/10.1117/12.2080092. 7 p.
[101] M.I. Sanchez-Aniorte, B. Mouhamadou, A.P. Alloncle, T. Sarnet, P. Delaporte, Laser-induced forward transfer for improving fine-line metallization in photovoltaic applications, Appl. Phys. A 122 (2016) 595, https://doi.org/10.1007/s00339-016-0113-9.
[102] M. Zenou, L. Baron, A. Sa'ar, Z. Kotler, Solar cell metallization by laser transfer of metal micro-droplets, Energy Procedia 67 (2015) 147–155, https://doi.org/10.1016/j.egypro.2015.03.298.
[103] Y. Chen, D. Munoz-Martin, M. Morales, C. Molpeceres, E. Sánchez-Cortezon, J. Murillo-Gutierrez, Laser induced forward transfer of high viscosity silver paste for new metallization methods in photovoltaic and flexible electronics industry, Phys. Procedia 83 (2016) 204–210, https://doi.org/10.1016/j.phpro.2016.08.010.
[104] J. Gilot, B. Emelin, Y. Galagan, R. Mandamparambil, R. Andriessen, Ultimate form freedom in thin film solar cells by postmanufacture laser-based processing, J. Photonics Energy 5 (2015) 57210, https://doi.org/10.1117/1.jpe.5.057210.
[105] M. Zenou, Z. Kotler, Printing of metallic 3D micro-objects by laser induced forward transfer, Opt. Express 24 (2016) 1431–1446, https://doi.org/10.1364/oe.24.001431.
[106] M. Zenou, A. Sa'ar, Z. Kotler, Laser jetting of femto-liter metal droplets for high resolution 3D printed structures, Sci. Rep. 5 (2015) 17265, https://doi.org/10.1038/srep17265.
[107] M.L. Tseng, C.M. Chang, B.H. Chen, Y.-W. Huang, C.H. Chu, K.S. Chung, Y.J. Liu, H.G. Tsai, N.-N. Chu, D.-W. Huang, H.-P. Chiang, D.P. Tsai, Fabrication of plasmonic devices using femtosecond laser-induced forward transfer technique, Nanotechnology 23 (2012) 444013, https://doi.org/10.1088/0957-4484/23/44/444013.

[108] H.-J. Li, W.-Z. Fan, H.-H. Pan, C.-W. Wang, J. Qian, Q.-Z. Zhao, Fabrication of "petal effect" surfaces by femtosecond laser-induced forward transfer, Chem. Phys. Lett. 667 (2017) 20–24, https://doi.org/10.1016/j.cplett.2016.11.026.
[109] N.R. Schiele, D.T. Corr, N.A. Raof, Y. Xie, D.B. Chrisey, Laser-based direct-write techniques for cell printing, Biofabrication 2 (2010) 32001, https://doi.org/10.1088/1758-5082/2/3/032001.
[110] M.R. Emmert-Buck, R.F. Bonner, P.D. Smith, R.F. Chuaqui, Z. Zhuang, S.R. Goldstein, R.A. Weiss, L.A. Liotta, Laser capture microdissection, Science 274 (1996), https://doi.org/10.1126/science.274.5289.998.
[111] T. Coohill, Uses and effects of ultraviolet radiation on cells and tissues, in: R.W. Waynant (Ed.), Lasers in Medicine, CRC Press, Boca Raton, FL, 2001, pp. 85–107. https://doi.org/10.1201/9781420040746.ch4.
[112] A. Vogel, V. Horneffer, K. Lorenz, N. Linz, G. Hüttmann, A. Gebert, Principles of laser microdissection and catapulting of histologic specimens and live cells, Methods Cell Biol. 82 (2007) 153–205, https://doi.org/10.1016/S0091-679X(06)82005-4.
[113] V. Espina, J.D. Wulfkuhle, V.S. Calvert, A. VanMeter, W. Zhou, G. Coukos, D.H. Geho, E.F. Petricoin, L.A. Liotta, Laser-capture microdissection, Nat. Protoc. 1 (2006) 586–603, https://doi.org/10.1038/nprot.2006.85.
[114] J. Barthelmann, J. Nietsch, M. Blessenohl, T. Laskay, G. van Zandbergen, J. Westermann, K. Kalies, The protective Th1 response in mice is induced in the T-cell zone only three weeks after infection with Leishmania major and not during early T-cell activation, Med. Microbiol. Immunol. 201 (2012) 25–35, https://doi.org/10.1007/s00430-011-0201-6.
[115] M.H. Alanne, E. Siljamäki, S. Peltonen, K. Väänänen, J.J. Windle, L.F. Parada, J.A. Määttä, J. Peltonen, Phenotypic characterization of transgenic mice harboring Nf1+/− or Nf1−/− osteoclasts in otherwise Nf1+/+ background, J. Cell. Biochem. 113 (2012) 2136–2146, https://doi.org/10.1002/jcb.24088.
[116] D.A.M. Mustafa, L.J. Dekker, C. Stingl, A. Kremer, M. Stoop, P.A.E.S. Smitt, J.M. Kros, T.M. Luider, A proteome comparison between physiological angiogenesis and angiogenesis in glioblastoma, Mol. Cell. Proteomics 11 (2012), https://doi.org/10.1074/mcp.M111.008466. M111.008466.
[117] R.B.H. Braakman, M.M.A. Tilanus-Linthorst, N.Q. Liu, C. Stingl, L.J.M. Dekker, T.M. Luider, J.W.M. Martens, J.A. Foekens, A. Umar, Optimized nLC-MS workflow for laser capture microdissected breast cancer tissue, J. Proteomics 75 (2012) 2844–2854, https://doi.org/10.1016/j.jprot.2012.01.022.
[118] J. Thiel, D. Riewe, T. Rutten, M. Melzer, S. Friedel, F. Bollenbeck, W. Weschke, H. Weber, Differentiation of endosperm transfer cells of barley: a comprehensive analysis at the micro-scale, Plant J. 71 (2012) 639–655, https://doi.org/10.1111/j.1365-313X.2012.05018.x.
[119] I. Damiani, F. Baldacci-Cresp, J. Hopkins, E. Andrio, S. Balzergue, P. Lecomte, A. Puppo, P. Abad, B. Favery, D. Hérouart, Plant genes involved in harbouring symbiotic rhizobia or pathogenic nematodes, New Phytol. 194 (2012) 511–522, https://doi.org/10.1111/j.1469-8137.2011.04046.x.
[120] D. Huh, G.A. Hamilton, D.E. Ingber, From 3D cell culture to organs-on-chips, Trends Cell Biol. 21 (2011) 745–754, https://doi.org/10.1016/j.tcb.2011.09.005.
[121] N.A. Sears, D.R. Seshadri, P.S. Dhavalikar, E. Cosgriff-Hernandez, A review of three-dimensional printing in tissue engineering, Tissue Eng. Part B Rev. 22 (2016) 298–310, https://doi.org/10.1089/ten.teb.2015.0464.
[122] H. Gudapati, M. Dey, I. Ozbolat, A comprehensive review on droplet-based bioprinting: past, present and future, Biomaterials 102 (2016) 20–42, https://doi.org/10.1016/j.biomaterials.2016.06.012.
[123] S.V. Murphy, A. Atala, 3D bioprinting of tissues and organs, Nat. Biotechnol. 32 (2014) 773–785, https://doi.org/10.1038/nbt.2958.

[124] N.R. Schiele, R.A. Koppes, D.T. Corr, K.S. Ellison, D.M. Thompson, L.A. Ligon, T.K.M. Lippert, Laser direct writing of combinatorial libraries of idealized cellular constructs: biomedical applications, Appl. Surf. Sci. 255 (2009) 5444–5447, https://doi.org/10.1016/j.apsusc.2008.10.054.
[125] C.Y. Chen, J.A. Barron, B.R. Ringeisen, Cell patterning without chemical surface modification: cell–cell interactions between printed bovine aortic endothelial cells (BAEC) on a homogeneous cell-adherent hydrogel, Appl. Surf. Sci. 252 (2006) 8641–8645, https://doi.org/10.1016/j.apsusc.2005.11.088.
[126] M. Gruene, M. Pflaum, A. Deiwick, L. Koch, S. Schlie, C. Unger, M. Wilhelmi, A. Haverich, B.N. Chichkov, Adipogenic differentiation of laser-printed 3D tissue grafts consisting of human adipose-derived stem cells, Biofabrication 3 (2011) 15005, https://doi.org/10.1088/1758-5082/3/1/015005.
[127] M. Gruene, M. Pflaum, C. Hess, S. Diamantouros, S. Schlie, A. Deiwick, L. Koch, M. Wilhelmi, S. Jockenhoevel, A. Haverich, B. Chichkov, Laser printing of three-dimensional multicellular arrays for studies of cell-cell and cell-environment interactions, Tissue Eng. Part C Methods 17 (2011) 973–982, https://doi.org/10.1089/ten.tec.2011.0185.
[128] C.M. Othon, X. Wu, J.J. Anders, B.R. Ringeisen, Single-cell printing to form three-dimensional lines of olfactory ensheathing cells, Biomed. Mater. 3 (2008) 34101, https://doi.org/10.1088/1748-6041/3/3/034101.
[129] R. Xiong, Z. Zhang, W. Chai, Y. Huang, D.B. Chrisey, Freeform drop-on-demand laser printing of 3D alginate and cellular constructs, Biofabrication 7 (2015) 45011, https://doi.org/10.1088/1758-5090/7/4/045011.
[130] A. Ovsianikov, M. Gruene, M. Pflaum, L. Koch, F. Maiorana, M. Wilhelmi, A. Haverich, B. Chichkov, Laser printing of cells into 3D scaffolds, Biofabrication 2 (2010) 14104, https://doi.org/10.1088/1758-5082/2/1/014104.
[131] V. Keriquel, F. Guillemot, I. Arnault, B. Guillotin, S. Miraux, J. Amédée, J.-C. Fricain, S. Catros, In vivo bioprinting for computer- and robotic-assisted medical intervention: preliminary study in mice, Biofabrication 2 (2010) 14101, https://doi.org/10.1088/1758-5082/2/1/014101.
[132] J.M. Fernández-Pradas, M. Duocastella, M. Colina, P. Serra, J.L. Morenza, Production of miniaturized biosensors through laser induced forward transfer, Proc. SPIE 6592 (2007) 65920R, https://doi.org/10.1117/12.722140.
[133] H. Jang, H. Yu, S. Lee, E. Hur, Y. Kim, S.-H. Lee, N. Kang, J.J. Yoh, Towards clinical use of a laser-induced microjet system aimed at reliable and safe drug delivery, J. Biomed. Opt. 19 (2014) 58001, https://doi.org/10.1117/1.JBO.19.5.058001.

This page intentionally left blank

CHAPTER 14

Production of Biomaterial Coatings by Laser-Assisted Processes

J. Lawrence*, J. Pou†, F. Lusquiños†, R. Comesaña†, M. Boutinguiza†
*University of Chester, Chester, United Kingdom
†University of Vigo, Vigo, Spain

14.1 INTRODUCTION

For centuries man has tried to find a solution to heal bone fractures, diseases, or joint replacement. But bone is a very complex composite material in which three levels of structure can be distinguished: (i) the nanostructure made up of noncollagenous organic proteins, and collagen nanofibers reinforced by crystals of hydroxyapatite (HA); (ii) the microstructure including lamellae, osteons, and Haversian systems; and (iii) the macrostructure including cancellous and cortical bone [1].

At the end of the 1950s, Sir John Charnley developed a total hip replacement device in which a metallic endoprosthesis was fixed to the host bone with polymethyl methacrylate (PMMA). The high success rates of this early fixation technique has led to the application of such devices in orthopedics as a routine operation. But the clinically significant loosening rates of cemented implants, especially in younger, active persons have encouraged the development of alternative techniques of implant fixation [2].

The last 50 years have seen a real revolution in materials science and applications, especially in the biomaterials field where ceramics have been used to improve the quality of life of humans. This revolution consists of the development of specially designed and fabricated ceramics for the repair and reconstruction of bone defects or traumatic diseases [3]. Calcium phosphate ceramics, especially hydroxyapatite (HA), are currently used as biomaterials for many applications in both dentistry and orthopedics, because they form a real bond with the surrounding bone tissue when implanted [4]. As a bulk, the hydroxyapatite is brittle and relatively weak, and thus cannot be used as implant devices to replace large bony defects or for load-bearing

Advances in Laser Materials Processing
https://doi.org/10.1016/B978-0-08-101252-9.00014-5
Copyright © 2018 Elsevier Ltd.
All rights reserved.

applications [3]. Therefore, HA is mainly applied in granular form in bone fillers or as coatings to improve fixation and osteointegration of cementless titanium-based implant devices [5].

For load-bearing purposes, titanium-based devices find their field of utilization but it is generally accepted, nowadays, that no chemical attachment of bone to a titanium surface will occur [6]. For this reason, much effort has been devoted in recent decades toward the application of HA as a coating on metallic substrates, in order to improve fixation and promote osteointegration of cementless titanium-based implant devices [7].

The first method developed for making a calcium phosphate coating on metallic implants was plasma spraying [8]. Due to the high deposition rate, the good biocompatibility of the coatings produced, and the possibility to coat large areas, this method is the most commonly used to apply HA as coatings. Nevertheless, there are some disadvantages as described in the literature [9,10]:

- Partial thermal decomposition of the hydroxyapatite material due to the very high temperature of the plasma, leading to the formation of other phases like tetracalcium phosphate, calcium oxide, and α-tertiary calcium phosphate [11].
- Very irregular morphology of the coating.
- Low adherence of the coating, even when it is thinner than the recommended 50 μm (so that grit blasting or metal powder sintering is necessary to roughen the substrate surface before coating it).
- Poor control of the coating thickness.
- Poor control of the physico-chemical properties, and, hence, of the biological stability of the coating.

Due to these drawbacks, other techniques have been the object of study in recent decades, such as electrophoretic deposition [12], magnetron sputtering deposition [13], ion-beam deposition [14], or the so-called biomimetic methods [15,16] but their results were not encouraging enough to attempt their implementation as industrial coating procedures for this kind of material.

14.2 THE LASER WAY TO PRODUCE COATINGS

There are three main methods based on laser technology that can be used to produce ceramic coatings on metallic substrates. First is laser chemical vapor deposition (LCVD). Briefly, this technique consists of the interaction of a laser beam with the coating precursor materials in the form of a gas mixture. Depending on the wavelength of the laser radiation and on the

precursor compounds, LCVD is governed by chemical reactions that are initiated by pyrolysis (photothermal or pyrolytic LCVD) or by photolysis (photochemical or photolytic LCVD) [17–19]. This technique has been successfully used to deposit structurally simple ceramics on metallic pieces such as silicon oxides [20–22], silicon nitrides [23], boron carbide [24], or cromium oxide [25]. Nevertheless, the complex structure of most calcium phosphates, especially hydroxyapatite, prevented the use of the LCVD techniques to produce such coatings on metallic prosthesis. The way to overcome this drawback using lasers as the energy source to assist the coating process is to use the precursor material in solid form. This led to the development of two different techniques: pulsed laser deposition (PLD), also known as laser ablation (La), and laser cladding. Both techniques have been used to produce bioceramic coatings on metallic substrates for biomedical applications. Therefore, the following sections of this chapter will be devoted to explaining the fundamentals of both techniques and their applications in the biomedical field.

14.3 PULSED LASER DEPOSITION OF BIOCERAMICS

14.3.1 Description of the Technique

Pulsed laser deposition is perhaps the simplest technique among all thin film deposition techniques. It consists of irradiating the surface of a target material with a sufficiently intense pulsed laser beam. The irradiated volume will be vaporized and the flux of material formed, and collected onto a substrate to grow a thin film. In fact, it is conceptually and experimentally simple. Fig. 14.1 shows a schematic diagram of a pulsed laser deposition apparatus. To avoid interaction with the ambient atmosphere, both target and substrate are placed into a vacuum chamber. The focused pulsed laser beam enters the chamber via a suitable window. Some devices are generally used to control the pressure, to insert a gas, to heat the substrate, or to control the substrate temperature.

When a sufficiently intense laser beam is focused on the surface of a target material, different phenomena take place, of either a pure thermal nature or an electronic nature, leading to the ejection of material from the target as a form of electrons, atomic species, diatomic species, and/or aggregates. The density and the excitation degree of these species on the target surface is very high, leading to the formation of a visible "plume" which expands in the direction perpendicular to the target. If a substrate is placed within the expansion trajectory of this plume, a fraction of the species will adhere to the substrate surface and start to form a film on it.

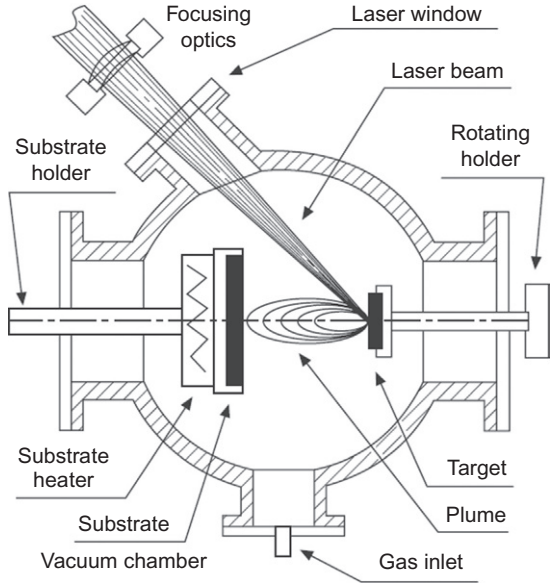


Fig. 14.1 Schematic diagram of a pulsed laser deposition apparatus.

This idea has been known practically from the early days of the first ruby laser in the 1960s. But it has been since the 1980s when it has been extensively used to produce thin films because of the superior properties of the high T_c superconducting (HTCS) thin films produced by the PLD technique. From the point of view of the target material, pulsed laser deposition is also known as laser ablation. This name stresses the intense material vaporization that takes place in the irradiated material and also leads to the formation of very interesting surface structuring.

It is outside the scope of this chapter to describe in detail all mechanisms involved in the PLD process but in a very simplified manner we can say that first the photons from the pulsed laser must be absorbed by the target material. This leads to collisional, thermal, electronic, exfoliational, hydrodynamic, and condensational processes. All these processes cause the sputtering of material from the target [26]. Moreover, particulates, also called droplets, are generated in some cases. Their sizes, chemistry, and microstructure depend upon the processing conditions and the material type. These processes are repeated thousands of times in a typical deposition run. Therefore, laser-irradiated surfaces become altered both physically and chemically. Morphological changes take the form of periodic structures. Cone formation, surface segregation, laser fluence dilution, and plume defection may also take place.

As mention earlier, during the PLD process an ablation plume is generated. This takes place within a time elapse of the few tens of nanoseconds duration of the laser pulses. This plume consists of a high pressure (~10–500 atm) bubble of hot plasma ($T = 10{,}000$ K) formed very close to the target surface [27]. The expansion of the plume has been modeled by fluid dynamics involving linear pressure gradients; however, interbeam collisions result in hydrodynamic effects such as Knudsen-layer formation, redeposition of material on the target, and shock fronts. Theoretical work by Metev and Meteva [28] suggested that the properties of PLD films are derived from the fact that the vapor has a high degree of supersaturation (10^5 J/mole), a high degree of ionization (~50%), and a high mean kinetic energy (~1000 eV). Experimental work carried out in the presence of ambient gases, demonstrated that a large number of gas phase collisions take place on the way from the target to the substrate that reduce both the ion fraction and the kinetic energy [29]. The nucleation and growth of the film on the substrate also involve many processes such as atomic deposition, reevaporation, cluster nucleation and growth, species diffusion within the surface, and cluster dissociation. Each of these processes may involve a different free energy change.

Among all processing parameters governing the film growth (such as density and energy of the condensing particles, their ionization degree and type, as well as the physicochemical properties of the substrate), the most important is substrate temperature. An exhaustive description of the PLD process, plasma formation, species transportation, film growth mechanisms, etc., can be found in a comprehensive book devoted entirely to this technique [30].

14.3.2 Production of Calcium Phosphates by PLD

The first papers on calcium phosphate thin films deposited by means of the PLD technique date back to 1992 [31,32]. Since then, many other groups have conducted extensive and intensive research for studying the influences of the processing parameters on the quality of the thin calcium phosphate films for medical applications [33–44].

In these and other works it has been demonstrated that the PLD technique presents some advantages to produce calcium phosphate coatings in comparison to the most used technique, plasma spraying:

- Adhesion of coatings to substrate is much higher without the necessity of a grit-blasting pretreatment of the implant surface [10].

- Coatings produced by PLD have a homogeneous composition and can be finely controlled by tuning the processing parameters [33].
- CaP coatings can be deposited on almost any type of surface, reproducing the texture of the underlying substrate [45].
- PLD can produce much thinner coatings than plasma spraying but assure a good osteointegration when inserted into a living bone [46].

As mentioned in the previous section, high fluences are needed and high energetic photons are preferable when performing the thin film growth by the PLD technique. Therefore, most of the work on pulsed laser deposition of calcium phosphates has been carried out using UV laser sources such as excimer or third-harmonic generation of a Nd:YAG. Only the early works were accomplished by using ruby laser [31,47,48]. The influence of different processing parameters on coating properties, such as chemical composition, morphology, or structure, has been studied.

Fig. 14.2 shows the surface morphology of a HA coating produced by the PLD technique using an ArF excimer laser. The appearance is quite smooth, and the surface topography of the titanium substrate can be clearly distinguished. A certain fine structure, noticeable in this figure, is present in the coating. Higher magnifications reveal that, in fact, the coating is formed by a network of superimposed fine polygonal HA crystallites varying in size from 100–500 nm, as can be observed in Fig. 14.3. Compare this homogeneous crack-free surface with the cracked surface of a CaP coating produced by plasma spraying full of splats (see Fig. 14.14B). The cross-section

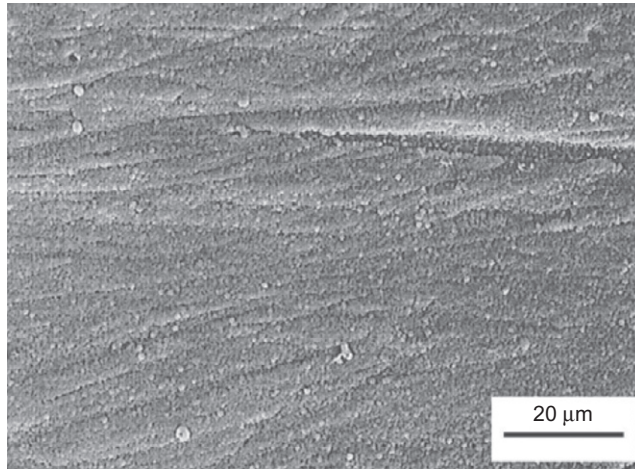


Fig. 14.2 Low magnification scanning electron micrograph of a PLD-HA coating surface. The surface topography of the titanium substrate can be easily distinguished [10].

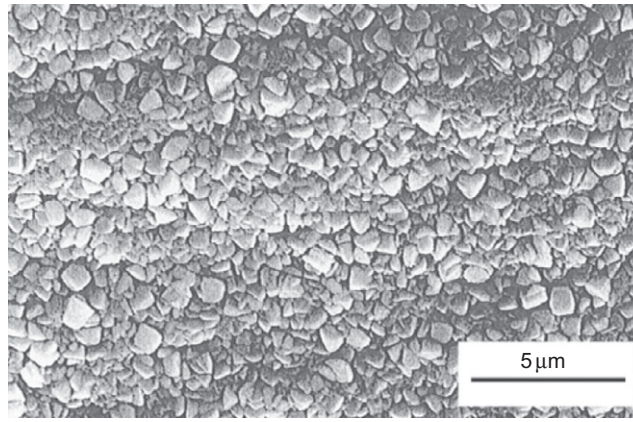


Fig. 14.3 Higher magnification of Fig. 14.2, revealing that the coating is formed by a network of polygonal-shaped HA crystallites [10].

of a PLD coating is shown in Fig. 14.4. The coating is dense and homogeneous, and no cracks can be detected along it. The acrylic resin used in the metallographic-like sample preparation is slightly separated from the surface of the coating, allowing the surface microstructure of the HA coating described in Figs. 14.2 and 14.3 to be seen. The detachment of the resin is due to its shrinkage, produced by the effect of the electron beam during the SEM observation.

X-ray diffraction (XRD) patterns of coatings produced at different ambient water pressures are shown in Fig. 14.5. The coatings produced at

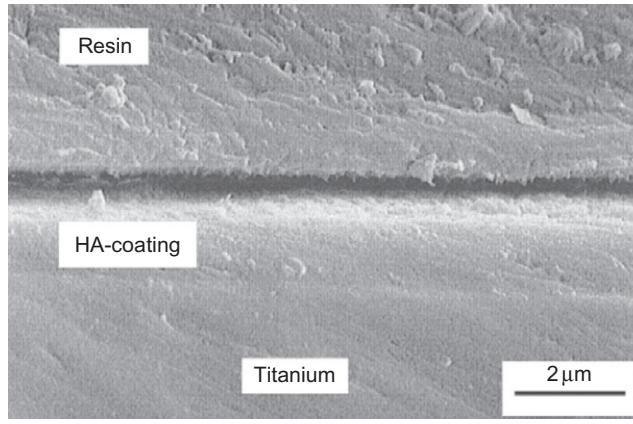


Fig. 14.4 Scanning electron micrograph of the cross-section of a PLD-HA coating, showing the good adherence between coating and substrate [10].

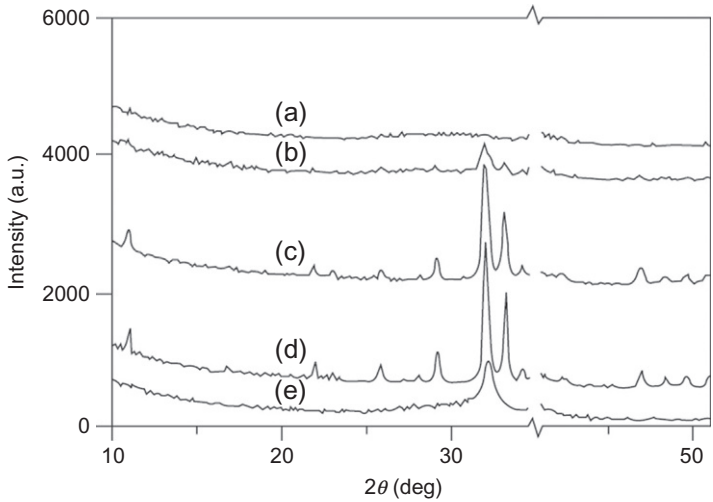


Fig. 14.5 Typical XRD patterns of calcium phosphate coatings produced by PLD at different deposition pressures of H_2O: (a) 0.80, (b) 0.60, (c) 0.45, (d) 0.30, and (e) 0.15 mbar [50].

0.15 mbar show a broad peak in the range where the main peaks of the apatitic structure are located. At 0.30 mbar, the structure of the apatite is completely defined, with the (2 1 1) and (1 1 2) reflections not resolved. When the pressure is increased, the coatings become less crystalline, with the reflections disappearing at 0.80 mbar. The refined unit-cell parameters of the crystalline coatings show that *a*-axis is shorter than that of stoichiometric HA and the *c*-axis longer. This distortion of the unit cell can be due to several factors: (i) ionic substitutions in the apatite lattice. The accommodation of the lattice to receive a substituting ion leads to the change in the unit-cell dimensions. (ii) Residual stresses in the coating. Because the coatings are very thin (0.83 μm), and are produced at relatively high temperatures (455°C), some residual stresses can exist due to the different thermal expansion coefficients of the substrate (titanium) and the apatite coating [51]. The shortening of the *a*-axis and the simultaneous lengthening of the *c*-axis is a typical effect of carbonate substitution for phosphate in the apatite lattice [52]. This point is corroborated by the Fourier Transform Infrared (FT-IR) spectra (see Fig. 14.6) which clearly show the carbonate bands at positions characteristic of substitution for phosphate: 873 cm^{-1} (ν_2 vibrational mode), and 1413 and 1454 cm^{-1} (ν_3 mode). The spectra of coatings obtained at higher temperatures appear more clearly defined than those produced at lower temperatures, indicating an increment in their crystallinity. Different vibrational modes of PO_4^{3-} and CO_3^{2-}, typical of carbonated apatites, can be appreciated.

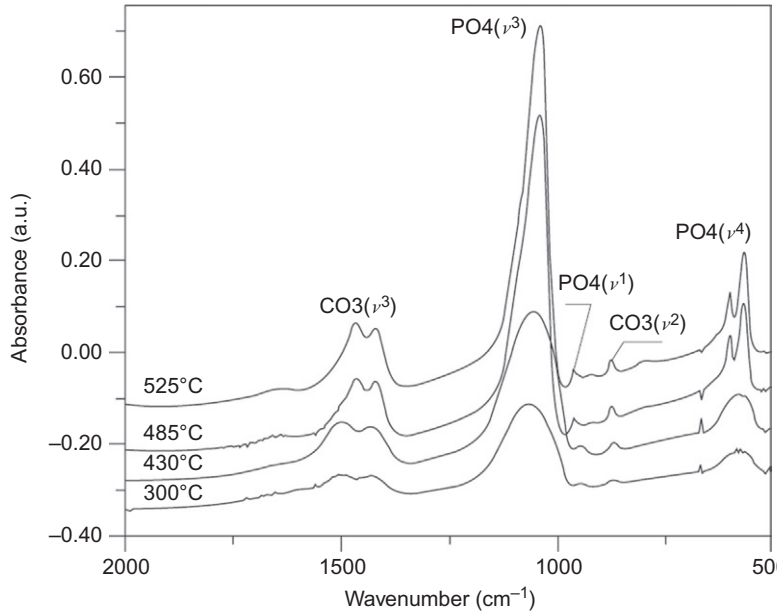


Fig. 14.6 FT-IR spectra of a series of coatings produced by the PLD method at 0.45 mbar of H_2O vapor at different substrate temperatures [53].

The calcium to phosphorous (Ca/P) ratio of the coatings is a parameter of major importance in this type of material because it is related to the good biocompatibility of the coatings when inserted in the real body. For the coatings produced by the PLD method the Ca/P ratio is dependent on both the substrate temperature and the water vapor pressure. The higher the temperature, the higher the Ca/P ratio, whereas higher pressures lead to lower Ca/P ratios.

Adhesion to the substrate is perhaps the key factor when considering the functional behavior of a coating in service. The results of the pull test applied to the coatings confirm the SEM observations shown in Fig. 14.4. For the PLD coatings, the tensile strength values obtained were higher than 58 MPa, being the fracture at the adhesive in all cases, without spallation of the coating [10]. This is a very good result, considering the fact that the titanium substrates were not grit-blasted, and therefore, the surface in contact with the adhesive was notably lower than the surfaces employed in the commercial plasma sprayed coatings.

Moreover, biological studies carried out in vitro using different types of cells such as fibroblast [54], rat bone marrow cells [55], or human fetal

osteoblast-like cell lines [56] demonstrated that thin calcium phosphate films produced by the PLD technique are noncytotoxic, the cells adhere perfectly to the CaP deposited film, proliferate adequately, and form an extracellular matrix which is the precursor of the real bone formation.

Assessment of the appropriateness of calcium phosphate coatings for biomedical devices such as bone substitution implants, has been carried out in different in vivo tests in dogs [57,58], rats [59], minipigs [60], and rabbits [46].

A comparative study of the biological stability and the osteoconductivity of hydroxyapatite coatings produced by ArF laser deposition and plasma spraying (PS) was conducted by Peraire et al. [46]. Three different implant groups were used: grit-blasted titanium rods coated with HA-PLD (2 mm thick), grit-blasted titanium rods coated with HA-PS (50 mm thick), and uncoated grit-blasted titanium. While the plasma-sprayed implants showed considerable instability and reduction in thickness after 24 weeks, but no statistical difference to the titanium group, the HA-PLD group showed a significantly higher amount of bone apposition (Scheffé test, $P < 0.05$) than the other two groups, without signs of degradation or dissolution. The histology study also confirmed these results (see Fig. 14.7): the surface

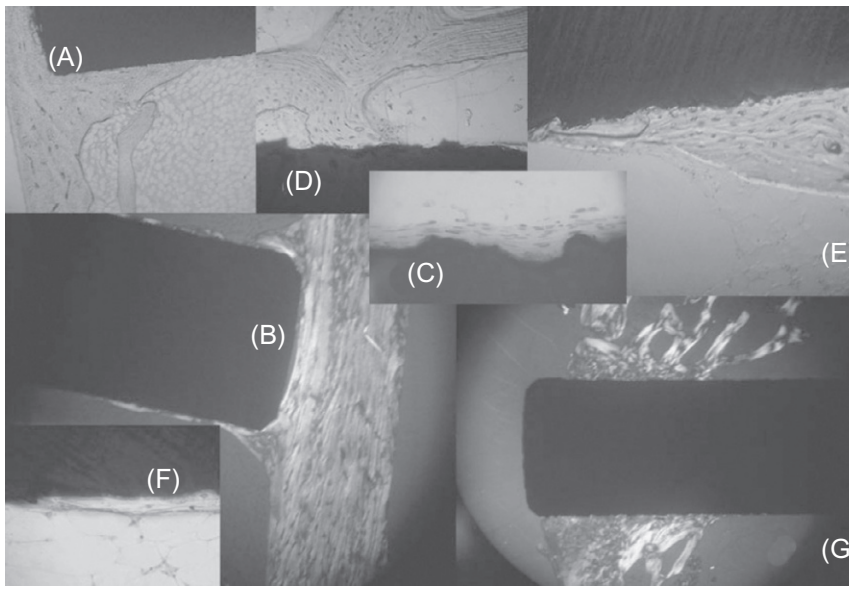


Fig. 14.7 Optical microscopy observation of a group of implants coated by HA via the PLD method: (A) cortical insertion area, (B) opposite endosteal area, (C) giant cell attached to central zone, (D–F) central zone, and (G) trabeculae growing from coating surface in central zone [46].

of the implants coated with a HA layer by PLD material presented good bone regeneration at both endosteal ends of the implant, the new bone was similar to the original cortical bone, and the presence of mature osteocytes was detected. Mineralized matrix in opposition to the PLD HA coated implant was observed in all examined areas (cortical insertion area, opposite endosteal area, and bone marrow) under polarized microscopy. The central area in contact with the bone marrow showed bone apposition areas interspersed in a very thin fibrous capsule, with large trabeculae growing from the coating surface (see Fig. 14.7). This is a demonstration that the ArF laser deposited coatings have been shown to produce osteoconduction in zones where the bone was previously absent, namely, in the bone marrow.

A comprehensive and thorough review of the production of calcium phosphates by means of the pulsed laser deposition technique, including modifications of the basic technique, was written by Prof. Betty León [61].

14.3.3 Production of Bioactive Glasses by PLD

Since the discovery in 1969 by Prof. Larry L. Hench of the ability of certain glass compositions to chemically bond to bone, an enormous amount of research work has been devoted to the field of so-called bioactive glasses. Because these materials are not strong enough to withstand the mechanical stresses inherent in load-bearing applications, several attempts have been made to use bioactive glasses in these types of applications. One solution has been the use of bioactive glass as a coating on a mechanically strong substrate.

Several techniques have been explored to apply a bioactive glass as a coating on a metallic substrate. Enameling, glazing, thermal spraying, rapid-immersion, sol-gel, electrophoretic deposition, or ion beam assisted deposition have been used to apply different types of bioactive coatings. Nevertheless, it is still a challenge to obtain a bioactive glass coating with high mechanical stability, showing a good bonding to the substrate, keeping the bioactivity after the deposition process, and being fast or economically feasible. Based on the very promising results obtained with calcium phosphates, several research groups used the PLD technique to deposit thin coatings of different types of bioactive glasses for biomedical purposes.

The first reported work is from D'Alessio and coworkers (Italy) who used a second-harmonic generation of a Nd:YAG laser ($\lambda = 532\,\text{nm}$) to deposit 45S5 Bioglass on a Ti6Al4V substrate [62,63]. Similar work was performed by Zhao and coworkers (China) but by using a KrF excimer

laser ($\lambda = 248$ nm) [64–66]. The group of Prof. Mihailescu (Romania) has used the same type of laser to produce coatings of silica based bioglass but with different composition [67–69]. Instead of using a bioglass in the SiO_2-Na_2O-CaO-P_2O_5 system they used glasses in the SiO_2-Na_2O-CaO-P_2O_5-K_2O-MgO system and had higher silica content (57%–61% instead of 45% of 45S5). The idea was to have a more stable coating while its bioactivity is slightly reduced. Generally speaking, all coatings perform well in terms of coating to substrate adhesion, bioactivity response when immersed in SBF even in the cell culture tests performed by the Romanian group. The main drawback is the presence of particulates or droplets on the surface of the coatings which may be a problem when implanted into bone if these particulates are released because they can cause an inflammatory response of the surrounding tissue.

The solution to this problem is the use of a shorter wavelength. The shorter the wavelength, the higher is the absorptivity of the material to the laser radiation. This means that the penetration depth will be shorter if we use a laser of a shorter wavelength, leading to a reduction of the droplet density on the surface of the deposited coatings. Lower absorptivity produces greater penetration depths, larger volume heating with a thicker layer of melted material, and the occurrence of a subsurface superheating effect once the evaporation begins, which leads to particle or droplet ejection [38]. This fact has been exploited by the group of Prof. González (Spain) to produce thin coatings of bioactive glasses with a droplet-free surface by using an ArF excimer laser ($\lambda = 193$ nm) [70–76]. They used bioglass in the SiO_2-Na_2O-CaO-P_2O_5-K_2O-mgO-B_2O_3 system with silica content between 42% and 59%. Among other studies devoted to exploring the influence of the different processing parameters on the coating quality, they performed a study of the aging and degradation of the film properties under different ambient conditions. They observed that bioactive glass films exposed to atmospheric humidity present important changes in structure and composition which may compromise their functionality when implanted [72]. But a unique work of this group is the deposition of a bioactive glass layer on the surface of a biomorphic SiC ceramic obtained from natural wood. As shown in Fig. 14.8, a layer of bioactive glass produced by PLD enhances the bioactivity of the biomorphic SiC. This is demonstrated by the CaP rich layer formed, even inside the natural cavities of the wood-like ceramic, after 72 h of immersion in simulated body fluid [73,77].

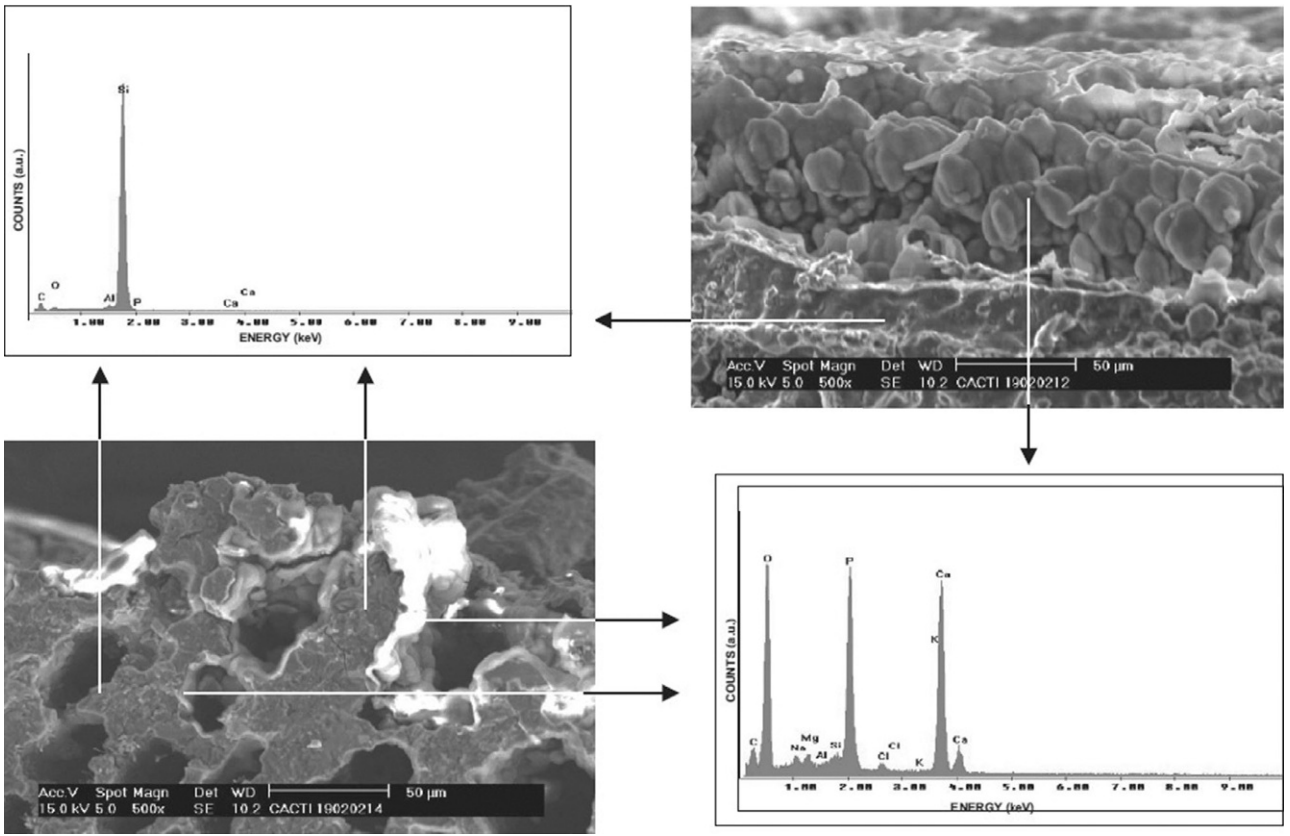


Fig. 14.8 Cross-section micrograph of a biomorphic SiC ceramic coated with bioactive glass by the PLD technique after immersion in simulated body fluid at 36.5°C for 72 h. The EDS analysis reveals the formation of a dense CaP rich layer over the surface and even within the cavities of the substrate material [73].

14.4 LASER CLADDING OF BIOCERAMICS

14.4.1 Description of the Technique

Laser surface cladding has become an alternative technique to conventional methods in order to produce large area coatings over metallic substrates [78]. Laser cladding utilizes a laser as an energy source to apply a layer of a desired material onto a substrate. The aim of this technique is to overlay one material with another to form a sound interfacial bond or weld without diluting the clad coating. In fact, dilution is generally considered to be contamination of the coating, degrading its mechanical or corrosion resistance properties [79]. In the metallurgical field this technique has demonstrated several advantages such as the following:

- Controlled shape of the clad within certain limits.
- Localized heating which reduces thermal distortion and the size of the heat-affected zone.
- Flexibility of the process.
- Controlled levels of dilution.
- Smooth surface finish, near isotropic mechanical properties, fine quench microstructures, and good fusion bonding.
- Minimum surface preparation required.

The coating material can be transferred to the substrate by two main approaches: either the material is preplaced (i.e., preplaced powder bed or a preplaced paste, or a coating obtained by another deposition technique) or the material is feed in real time (i.e., wire feeding or powder injection by a carrier gas) [79–84]. Among these alternatives, powder injection has been demonstrated to be the most flexible, robust, and effective way to provide the precursor material for the laser cladding process. In this technique, the energy provided by the laser is used to melt a thin layer of the substrate while the particles can be molten by the interaction with the laser beam and/or when arriving to the melting pool formed on the substrate. A relative movement between the substrate and the laser/powder jet allows forming a single clad track, while overlapping these tracks gives large area coverage [79]. To avoid the oxidation in the interaction zone, a shielding inert gas is applied. A rapid quenching takes place when the molten-pool goes away from the laser-irradiated area. Thus, the final result is a coating on the surface of the metallic substrate.

14.4.2 Production of Calcium Phosphate Coatings by Laser Cladding

14.4.2.1 Methods Using Preplaced Precursor Material

Cladding with preplaced precursor material is the simplest method provided the powder can be made to stick until the laser processes it. Fig. 14.9

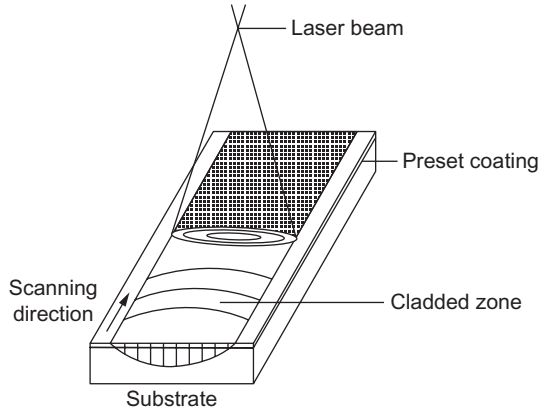


Fig. 14.9 Schematic representation of preplaced powder laser cladding technique [85].

shows a schematic representation of this simple technique. Moreover, the area under laser irradiation must be shrouded in inert gas. The first attempts to obtain calcium phosphate coatings by laser cladding using the preplaced powder technique were performed on stainless steel using a CO_2 laser as an energy source [86]. In their experiments, Zhang and coworkers used either pure hydroxyapatite ($Ca_{10}(PO_4)_6(OH)_2$) powders or mixtures of dicalcium phosphate dihydrate ($CaHPO_4{\cdot}2H_2O$, DCPD) and calcium carbonate ($CaCO_3$). In all the experiments, a bond layer was necessary to avoid coating delamination, assuring good bonding on the stainless steel substrate. Similar experiments were carried out by the group of J. Li but using a 2 kW Nd:YAG laser instead of a CO_2 laser [87]. In these experiments, no bond layer was used, resulting in the formation of a composite coating the main phases being hydroxyapatite and β-calcium pyrophosphate (β-DCP, $\beta\text{-}Ca_2P_2O_7$). The HA appears in granular form distributed among overlapped needle-like β-DCP.

Experiments on the most used titanium alloy (Ti6Al4V) using the powder preplaced laser cladding technique were also carried out. Deng and coworkers used a CO_2 laser to obtain a hybrid coating containing different calcium phosphate phases [85]. In their experiments, researchers included a small amount of yttria to induce the formation of bioactive phases. The same approach was followed by Zheng and coworkers but by using ceria instead of yttria as a bioactive enhancing factor [88,89].

The main drawback of the preplaced powder technique is the difficulties that arise with keeping the powder in place. Therefore, different strategies have been followed to solve this problem. Some researchers used an adhesive to stick the powder onto the substrate surface [90]. In these experiments three layers were applied consecutively on the Ti6Al4V substrate.

The composition of the preplaced powder was a mixture of DCPD, calcium carbonate, yttria, and titanium. In vivo tests performed on the dog femur showed that the three-layer coating was able to adapt to the stresses between the substrate and the new bone, helping osteointegration of the implant.

Another approach used to assure powder stability on the substrate surface, prior to the laser beam action, is to form a paste with the precursor powder and an adhesive agent [91–93]. Using an air spray gun, a calcium phosphate tribasic precursor powder was predeposited on the surface of a Ti6Al4V substrate [94–96]. The effect of a Nd:YAG laser beam on this suspension was the formation of a multiphase and multiscale coating ranging from meso- to nanoscale.

A different approach but still classified under the preplaced precursor material, is the laser treatment of calcium phosphate coatings applied by other methods. Therefore, laser surface treatment was used on electrophoretically deposited hydroxyapatite coatings on titanium substrate [97]. The results demonstrated that the laser treatment can eliminate delamination of weak interface of HA coatings by forming a strong Ti-HA composite layer at the interface as shown in Fig. 14.10.

More work has been done on the surface treatment of calcium phosphate coatings produced by a plasma spray. The main objectives were try

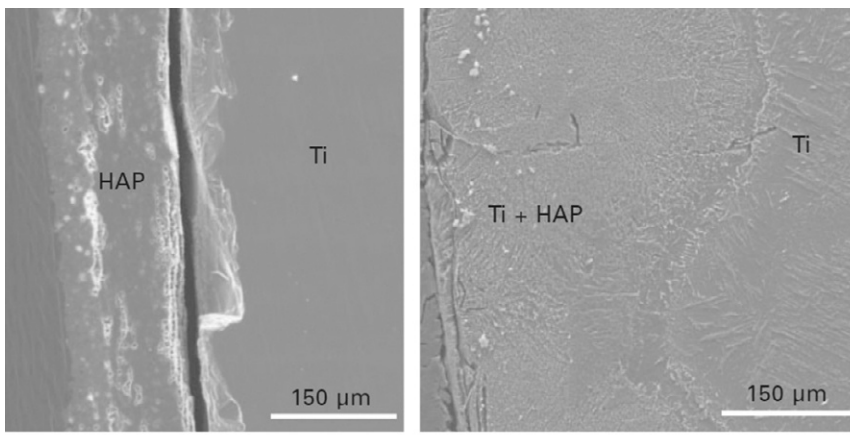


Fig. 14.10 SEM cross-sectional images of (A) electrophoretically deposited hydroxyapatite (HAP) coating on titanium substrate; (B) dual pass laser treated coating. Note that the laser treatment promoted the formation of a good bonding between the coating and the substrate. *Adapted from M. Roy, A. Bandyopadhyay, S. Bose, Laser surface modification of electrophoretically deposited hydroxyapatite coating on titanium. J. Am. Ceram. Soc. 91 (2008) 3517–3521.*

to seal the surface, repair the cracked coating, increase the plasma sprayed coating density, and improve the coating to substrate adhesion [98–100].

14.4.2.2 Coatings Obtained by Powder Injection

The objective pursued when starting to apply the laser surface cladding technique by powder injection to produce biocompatible coatings was to modify the surface of the titanium alloy substrate in such a way that the outer part of the coating acted as a biocompatible material but the inner part of it worked as the anchoring to the implant. The composition of the layers obtained by this technique basically depends on the laser power density, mass flow, and the relative speed of the substrate with regard to the laser beam. To achieve no dilution of the substrate material into the coating, the laser power density must be tuned to a moderate level (around 2000W/cm^2); therefore, the composition of the coating will be the only function on the precursor material. For example, using tricalcium phosphate powders (TCP, $Ca_3(PO_4)_2$), composite coatings of Ti-TCP were obtained on pure titanium substrates by means of a Nd:YAG laser working in coaxial configuration to the powder stream [101]. These composite coatings showed an increase of osteoblastic cell proliferation as compared to the bare titanium, demonstrating the good biocompatibility of the TCP coatings produced by laser cladding.

One of the main problems to solve when dealing with the production of calcium phosphate coatings on Ti6Al4V substrates is the fact that the melting point of the substrate is almost the same as the decomposition temperature of HA. Therefore, in order to have better control of the process, the off-axis powder feeding set up is preferred (see Fig. 14.11) [102].

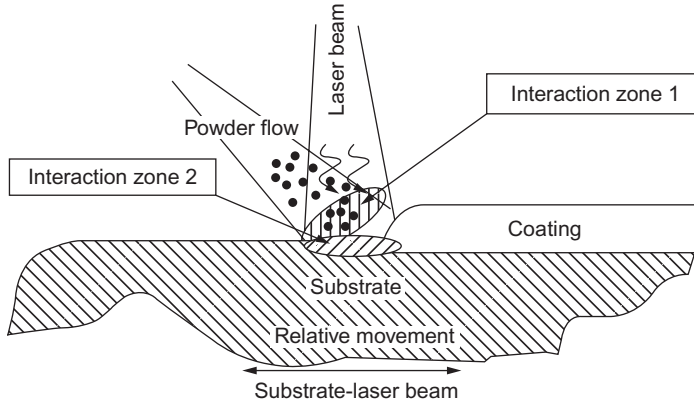


Fig. 14.11 Schematic representation of the off-axis powder injection laser cladding technique [102].

Fig. 14.12 shows the cross-section of a Ti6Al4V plate coated by the laser surface cladding technique overlapping several tracks [103]. As can be seen in this scanning electron micrograph, the dilution of the substrate in the coating is almost negligible. The four most representative zones of the coatings have been observed at a higher magnification and are also shown in this figure.

On the basis of the experimental XRD and EDX analyses and with the help of the knowledge about the high-temperature phases, all the phases present in the coating could be identified. The surface of the coating exhibits

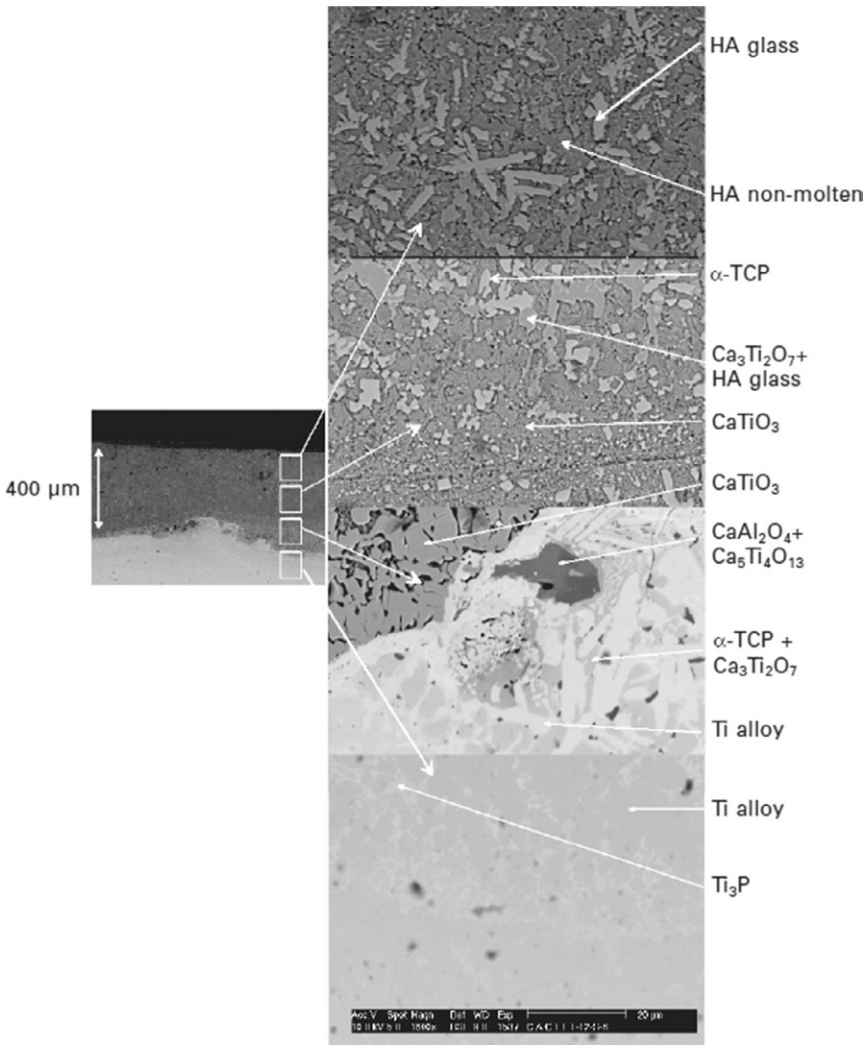


Fig. 14.12 SEM micrographs showing the general aspect of a cross section of an off-axis laser clad CaP coating and the four zones of interest at higher magnification [103].

the presence of zones that correspond to nonmolten HA and HA-glass (see the first enlarged zone of Fig. 14.12). Under the surface of the coating it is possible to distinguish three main phases:

α-TCP, a mixture of $Ca_3Ti_2O_7$ + HA glass and $CaTiO_3$. In the interface of the coating with the Ti-alloy substrate (third enlarged zone in Fig. 14.12), the presence of $CaTiO_3$, a mixture of $CaAl_2O_4 + Ca_5Ti_4O_{13}$, α-TCP + $Ca_3Ti_2O_7$ and the original titanium alloy can be noted. Finally, in the top surface of the alloy (last enlarged zone in Fig. 14.12) the presence of two main phases is revealed: Ti_3P and the original Ti-alloy.

During the formation of the calcium phosphate coatings by means of the off-axis powder feeding laser cladding technique, two interaction zones can be identified (see Fig. 14.11): an interaction zone between the precursor powder and the laser beam and a second interaction zone between the laser beam and the substrate. Despite the complexity of the coating production process, it is possible to suggest a model to explain the phenomena observed in the laser cladding process of HA onto Ti6Al4V.

In the laser cladding process the laser beam is focused onto the surface of the titanium alloy substrate. Due to the high energy density localized in the laser spot, the surface of the Ti6Al4V melts and forms a molten pool which is maintained during the laser irradiation. At the same time, the HA particles injected into the molten pool are partially melted by the interaction with the laser beam and also when they reach the hot molten pool. Then two liquids are formed: a liquid metal and a liquid mineral. Due to the different bonding nature (metallic and ionic) of these two liquids, they do not show mutual solubility. A schematic drawing of the situation created in the molten pool is depicted in Fig. 14.13 [102].

The top surface of the titanium alloy will melt to form a liquid metal. The molten volume and the depth of the melt depends on the laser power density, the speed of the X-Y table which moves the substrate, and the HA mass flow that shadows the alloy from the laser radiation.

The HA particles can be molten during flight through the beam, but if they arrive at the molten pool without being melted, they will decompose, leading to the liberation of water vapor, which will provoke the presence of large bubbles trapped in the coating when the solidification is completed. Another product of this decomposition is the liquid mineral which is formed by a mixture of CaO and P_2O_5. At the mineral/metal interface, the liquid mineral, the liquid metal, and HA particles can be in contact and the following reactions occur:

$$HA + TiO_2 \rightarrow CaTiO_3 + \alpha - TCP + H_2O(g)\uparrow \tag{14.1}$$

$$\alpha - TCP + TiO_2 \rightarrow CaTiO_3 + \alpha - Ca_2P_2O_7 \tag{14.2}$$

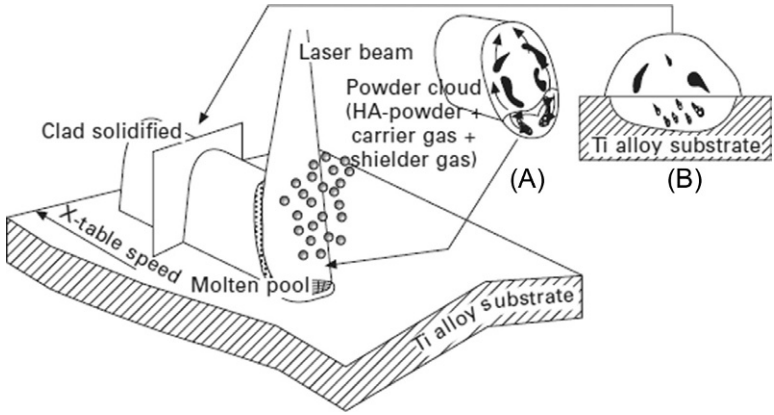


Fig. 14.13 Schematic drawing showing the formation of the coating (motion of the two liquids) and the final aspect [102].

$$\alpha - Ca_2P_2O_7 + Ti \rightarrow CaTiO_3 + CaO + P_2O_3\,(g)\uparrow \qquad (14.3)$$

$$2P_2O_{3\,(\text{from liquid mineral and the previous product})} + 3Ti \rightarrow 3TiO_2 + 4P \qquad (14.4)$$

The product TiO_2 (from Eq. 14.4) will react again with the HA and the P (from Eq. 14.4) dissolves immediately in the liquid metal to produce titanium phosphide or to form a solid solution in the Ti alloy. This TiO_2 could also react with V_2O_5 (from the oxidized original alloy), or with P_2O_5 (from the liquid mineral), or with P_2O_3 (product of the reaction above) to produce a mixture with a lower viscosity and allowing the faster diffusion of the liquid mineral. The presence of small bubbles in the interface can be attributed to the P_2O_3 that reacts quickly with the liquid metal. There are several compounds, from the HA decomposition in the molten pool, that can react with TiO_2 to produce another titanium-calcium-oxide compound.

There is an increasing amount of TiO_2 and a decreasing amount of P_2O_5 in the direction of the interface coating/substrate. Upon solidification, the phases precipitating first and most clearly are the binary phases with a high melting point, especially $CaTiO_3$, $Ca(PO_4)_2O$, α-$Ca(PO_4)_2$, and $Ca_9Al(PO_4)_7$.

XRD analysis using a thin-film detector revealed the presence of HA and α-TCP phases confirming the predictions given by the above reactions. The presence of the phases produced in the interface, in the surface or near surface, and below the interface is explained by the vigorous motion of the two liquids due to the buoyancy and surface tension forces mentioned above. The higher the power density, the more violent the motion of the molten pool and therefore the composition profiles will be attenuated.

The presence of calcium titanates and titanium phosphates in the region of the coating/substrate interface means that a good bonding—of chemical nature—of the coating to the substrate has been achieved (via this fusion between the CaP and the Ti alloy). The tensile strength of the coatings was measured by using the ASTM F1501 pull-test procedure. CaP coatings obtained by the laser cladding with lateral powder feeding, the average tensile strength value obtained was 37.9 MPa, which exceeds the 35 MPa threshold given by the standard. Finally, the presence of the HA-glass can be explained by the rapid quenching of the processing assisted by the laser.

The biocompatibility of any material to be inserted in the human body must be assessed by biologic testing including in vitro and in vivo testing. Attachment and proliferation of osteblast precursor cells are the main tests performed in vitro. In order to better understand the response of the osteoblast-like cells to the CaP coatings produced by side feeding laser cladding, it is important to take into account two factors: the topography of the coating surface and the chemical composition of those coatings. Fig. 14.14 shows the typical aspect of the surface of a CaP coating obtained by Nd:YAG laser cladding (Fig. 14.14A) and that of the CaP coatings produced by plasma spraying (Fig. 14.14B). As can be clearly seen, the coatings obtained by Nd:YAG laser cladding are smoother than those produced by PS. Quantitative roughness measurements of those surfaces gave *Ra* values of 7.7 μm for the coatings produced by the laser cladding technique while those obtained by PS gave a higher *Ra* value of 22.0 mm [104].

To evaluate the cell attachment and proliferation, three replicas from CaP coatings produced either by Nd:YAG laser cladding and by PS were compared at 3 and 6 h, and 6 and 18 days by SEM [49]. Proliferation was also measured by the alamar BlueTM assay. MG-63 osteoblastic cells seeded on the surface of the PS and Nd:YAG laser cladding coatings proliferated very well and presented a normal morphology. At early stages cells have adhered to the surface of both coating materials (see Fig. 14.15), showing either a fat morphology, making their nuclei visible, or a rounded morphology due to the events involved in cellular division. After 6 days of growing, cell layers were observed on both materials and after 18 days cell layers were thick. The CaP coatings obtained either by Nd:YAG laser cladding or by PS were susceptible to being colonized by the osteoblastic cells at a similar rate. There were no statistically significant differences in the proliferation of MG-63 cells on the Nd:YAG laser cladding coating when compared to the values exhibited by PS over an 18-day culture period.

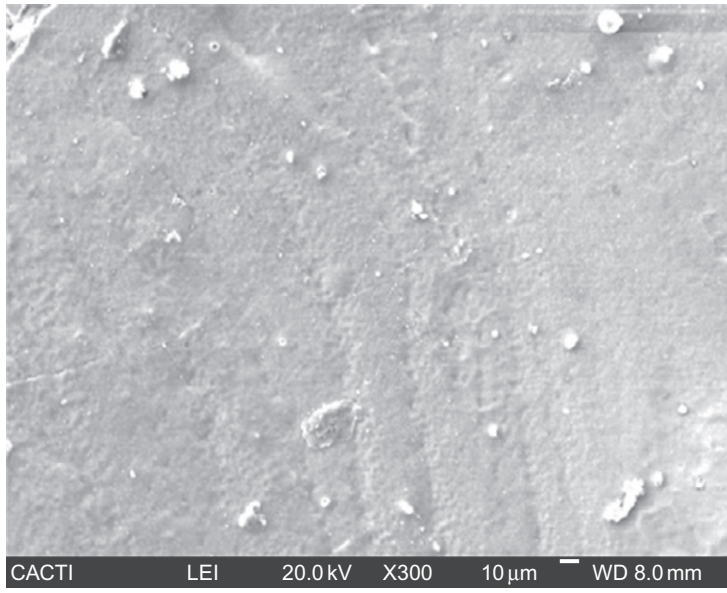


Fig. 14.14 SEM micrographs showing the surface topography of the coatings produced by the Nd:YAG laser cladding technique (A) and that of the coatings obtained by plasma spraying (B) [49].

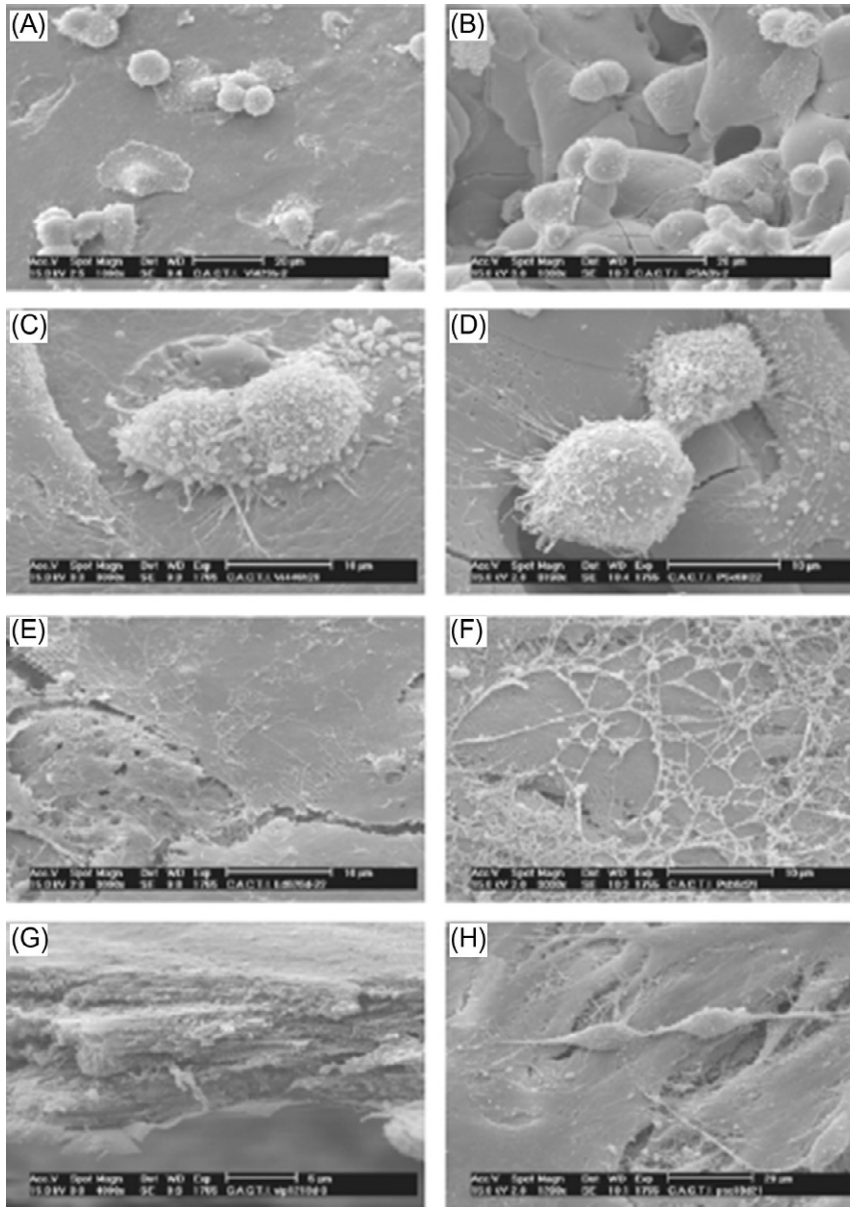


Fig. 14.15 SEM micrographs showing the cell morphology at 3 h (A) and (B), 6 h (C) and (D), 6 days (E) and (F), and at 18 days (G) and (H) after seeding of CaP coatings produced by Nd:YAG laser cladding (A), (C), (E), and (G) and CaP coatings produced by plasma spray (B), (D), (F), and (H) (De Carlos et al., 2006).

14.4.3 Production of Bioactive Glass Coatings by Laser Cladding

Glasses with certain composition in the SiO_2-Na_2O-CaO-P_2O_5 system are of great interest for medical applications due to their osteoconductive properties. In vivo and in vitro studies revealed that these bioactive glasses form a biologically active apatite layer in their surface that reacts with the host tissues and promotes a strong bonding at the interface. The bioactivity of these glasses is based on the existence of alkali and alkali earth cations (Na^+, Ca^+) in the silica network that disrupt its ordered structure and promote the formation of nonbridging silicon-oxygen groups (Si-O-NBO) [3].

Based on the fact that bioactive glasses resorb in the body, the coatings will not remain on the surface of the metallic implant permanently. Therefore, the main purpose of the bioglass coatings will be to improve the incorporation of the implants at the early stages of fixation by promoting bone ingrowth, thus allowing faster mechanical interlocking of the implant in the host bone. In this respect, the advantage of using the laser cladding technique for producing the coatings is the possibility to do it locally, exactly in the desired area of the implant surface. Just in the places where the implant design would benefit most from the introduction of bioactive glass.

Not much work has been devoted to producing bioactive glass coatings by the laser cladding method. The group of Prof. Yli-Urpo in Finland developed a method to coat titanium implants with bioactive glass by a kind of preplaced precursor material technique [105–107]. The method consists of a surface roughening by sand blasting and by bioactive glass powder blasting. Then the implant is dip-coated by immersion in a suspension of fine bioglass particles in ethanol. The implant is then removed from the solution and dried. The final step consists of scanning a low power CO_2 laser (just 6–8W) on the implant surface to melt the glass on the rough titanium surface. Obviously, the very low laser power density obtained on the implant surface is not enough to melt the implant outer layer; therefore the coating is just anchored due to the high surface roughness.

An alternative approach is to use the powder injection laser cladding technique to really form a metallurgical bond between the coating and the substrate. This method has been applied in our group to coat Ti6Al4V implants by a bioglass coating in the SiO_2-Na_2O_3-CaO-P_2O_5-K_2O system [108–111]. Matching the thermal expansion coefficient of substrate and coating is a key factor to assuring good coating stability. In this glass system, the thermal expansion coefficient is increased by the Na_2O, K_2O, and CaO content. Diverse empirical correlations allow estimation of its value as a function of the glass composition, and thus different compositions

can be tailored to match the metal alloy thermal expansion coefficient. Nevertheless, these changes on glass composition produced a significant reduction of glass bioactivity compared to that of the 45S5 bioactive glass (somehow the "gold standard" in bioactive glasses). Furthermore, bioactive glass viscosity-temperature dependence and the surface tension-temperature dependence are important properties in coating processes. The wettability over a metallic substrate is determined by the surface tension and viscosity of the bioactive glass, thus high viscosity-temperature variations can penalize coating wettability. Again, composition is a factor affecting the bioactive glass viscosity-temperature evolution; therefore, viscosity reductions can be achieved by modification of the glass component proportions. Using a Nd:YAG laser working at the fundamental mode ($\lambda = 1064$ nm) with laser power between 50 and 300 W, precursor powder mass flow values comprised between 10 and 30 mg/s, and substrate scanning speeds between 0.2 and 5.0 mm/s, sound coatings were obtained. Fig. 14.16 shows

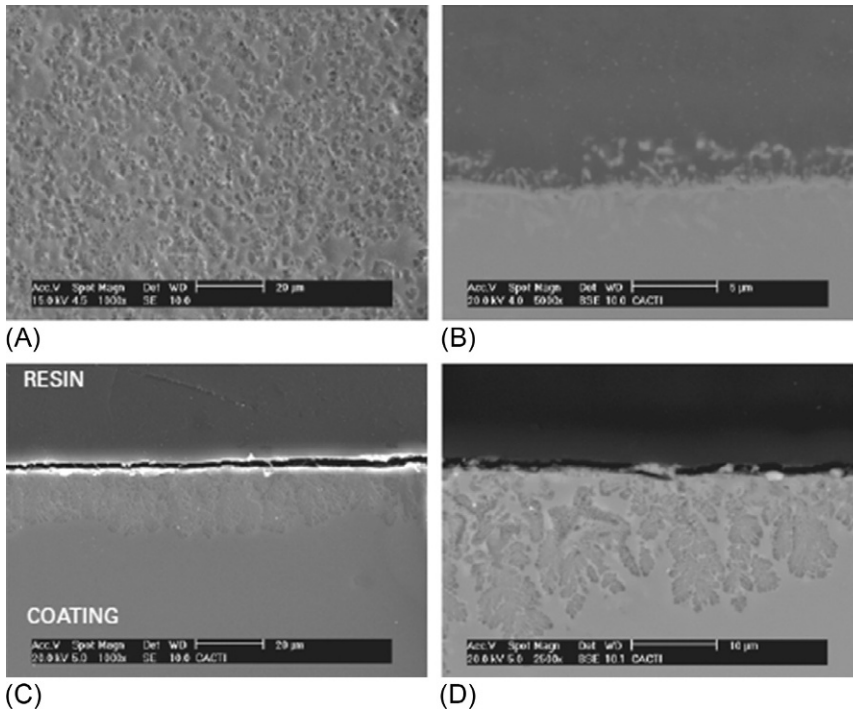


Fig. 14.16 SEM micrographs of a bioactive glass coating produced by the powder injection method on a Ti6Al4V substrate: (A) secondary electrons image of the surface; (B) backscattered electrons micrograph detail of the coating/substrate interface; (C) coating cross-section showing partial surface crystallization; (D) backscattered electrons micrograph detail of the partially crystallized outer layer of the coating [108].

the surface and cross-section aspect of a typical bioglass coating obtained by the powder injection laser cladding technique. The partial crystallization of the outer layer of the coating produces a slight reduction in bioactivity but increases coating stability as demonstrated in vitro [108].

14.5 CONCLUSIONS

Laser-assisted processes have been used to produce bioceramic coatings since the 1990s. As with other coating techniques, the most important bioceramics deposited are calcium phosphates and bioactive glasses. Due to the complex stoichiometry and structure of these bioceramics, the LCVD technique has not been used for this purpose. Instead, pulsed laser deposition and laser cladding (either by the preplaced precursor material or the powder injection techniques) have been used.

The PLD technique has demonstrated several advantages over the competing methods: (i) growth of thin films from precursor materials with high melting points, (ii) stoichiometric transfer of the target composition to the substrate, (iii) contamination absence, and (iv) substrate surface do not require a pretreatment by grit-blasting or to enhance coating adhesion. As to the negative points of PLD, this technique needs to be performed in a vacuum chamber to be able to control the ambient atmosphere and that the deposition rate is relatively low (at least if it is compared to the commercial technique for producing bioceramic coatings: plasma spraying).

An alternative to PLD is the laser cladding technique. Being a mature technique in the metallurgical field, it has recently been introduced in the biomaterials field. The results obtained by the few groups involved in this research are very promising. Notwithstanding, laser cladding is not as mature for an industrial scale-up to produce bioceramic coatings as the PLD technique is. In fact, commercial dental implants and orthopedic spine screws have been coated by PLD, demonstrating the uniformity of the coating thickness around the corners and sidewalls of implant devices.

REFERENCES

[1] J. Rho, Y. Kuhn-Spearing, L. Zioupos, Mechanical properties and the hierarchical structure of bone, Med. Eng. Phys. 20 (1998) 92–102.
[2] J. Charnley, Arthroplasty of the hip in a new operation, Lancet 1129 (277) (1961).
[3] L.L. Hench, J. Wilson (Eds.), An Introduction to Bioceramics, World Scientific, Singapore, 1993, p. 1.
[4] R.Z. LeGeros, Calcium phosphate materials in restorative dentistry: a review, Adv. Dent. Res. 2 (1988) 164–180.

[5] J.F. Kay, Calcium phosphate coatings for dental implants current status and future potential, Dent. Clin. N. Am. 36 (1992) 1–18.
[6] D.M. Brunette, Principles of cell behaviour on titanium surfaces and their application to implanted devices, in: D.M. Brunete, et al. (Eds.), Titanium in Medicine, Springer, Berlin, 2001, p. 485.
[7] M.J. Filiaggi, R.M. Pilliar, N.A. Coombs, Post-plasma-spraying heat treatment of the HA coating/Ti-6Al-4V implant system, J. Biomed. Mater. Res. 27 (1992) 191.
[8] K. De Groot, R. Geesink, C.P.A.T. Klein, Plasma sprayed coatings of hydroxyapatite, J. Biomed. Mater. Res. 21 (1987) 1735–1781.
[9] P. Cheang, K.A. Khor, Thermal spraying of hydroxyapatite (HA) coatings: effects on powder feedstock, J. Mater. Process. Technol. 48 (1995) 429–436.
[10] F.J. García-Sanz, M.B. Mayor, J.L. Arias, J. Pou, B. León, M. Pérez-Amor, Hydroxyapatite coatings: a comparative study between plasma-spray and pulsed laser deposition techniques, J. Mater. Sci. Mater. Med. 8 (1997) 861–865.
[11] C.P.A.T. Klein, J.G.C. Wolke, K. De Groot, Stability of calcium phosphate ceramics and plasma sprayed coatings, in: L.L. Hench, J. Wilson (Eds.), An Introduction to Bioceramics, World Scientific, Singapore, 1993, pp. 199–221.
[12] J.G.C. Wolke, K. Van Dijk, H.G. Schaeken, K. De Groot, J.A. Jansen, J. Biomed. Mater. Res. 28 (1994) 1477.
[13] T.S. Chen, W.R. Lacefield, Crystallization of ion beam deposited calcium phosphate coatings, J. Mater. Res. 9 (1994) 1284–1290.
[14] T. Hanawa, Y. Kamiura, S. Yamamoto, T. Kohgo, A. Amemiya, H. Ukai, K. Murakami, K. Asaoka, Early bone formation around calcium-ion-implanted titanium inserted into rat tibia, J. Biomed. Mater. Res. 36 (1997) 131–136.
[15] H.M. Kim, F. Mijaji, T. Kokubo, T. Nakamura, Preparation of bioactive Ti and its alloys via simple chemical surface treatment, J. Biomed. Mater. Res. 32 (1996) 409–417.
[16] H.B. Wen, J.R. De Wijn, Q. Liu, K. De Groot, F.Z. Cui, A simple method to prepare calcium phosphate coatings on Ti6Al4V, J. Mater. Sci. Mater. Med. 8 (1997) 765.
[17] D. Bauerle, Laser Processing and Chemistry, third ed., Springer-Verlag, Berlin, 2000.
[18] P. González, D. Fernández, J. Pou, E. García, J. Serra, B. León, M. Pérez-Amor, Photoinduced chemical vapour deposition of silicon oxide thin films, Thin Solid Films 218 (1992) 170–181.
[19] J. Mazumder, A. Kar, Theory and Application of Laser Chemical Vapor Deposition, Plenum Press, New York, 1995.
[20] J. Pou, S.J. Spencer, D. Fernández, P. González, E. García, B. León, S.R.J. Saunders, M. Pérez-Amor, The effect of coating density on the strain tolerance of corrosion resistant amorphous silica, Surf. Coat. Technol. 56 (1993) 267–272.
[21] J. Pou, P. González, E. García, D. Fernández, J. Serra, B. León, S.R.J. Saunders, M. Pérez-Amor, Ceramic coatings for high-temperature corrosion protection by laser-CVD processes, Appl. Surf. Sci. 79 (80) (1994) 338–343.
[22] T. Szörényi, P. González, M.D. Fernández, J. Pou, B. León, M. Pérez-Amor, Gas mixture dependency of the LCVD of SiO_2 films using an ArF laser, Appl. Surf. Sci. 46 (1990) 206–209.
[23] J. Serra, T. Szörenyi, D. Fernández, P. González, E. García, J. Pou, B. León, M. Pérez-Amor, Deposition of amorphous silicon nitride thin films by CO_2 laser induced CVD, J. Non-Cryst. Solids 187 (1995) 353–360.
[24] J.C. Oliveira, P. Paiva, M.N. Oliveira, O. Conde, Laser assisted CVD of boron carbide at atmospheric pressure, Appl. Surf. Sci. 138–139 (1999) 159–164.
[25] O. Conde, A.J. Silvestre, Laser-assisted deposition of thin films from photoexcited vapour phases, Appl. Phys. A 79 (2004) 489–497.
[26] R. Kelly, A. Miotello, Mechanisms of pulsed laser sputtering, in: D.B. Chrisey, G.H. Hubler (Eds.), Pulsed Laser Deposition of Thin Films, John Wiley & Sons, New York, 1994, p. 55.

[27] D.B. Geohegan, Diagnostics and characteristics of laser-produced plasmas, in: D.B. Chrisey, G.H. Hubler (Eds.), Pulsed Laser Deposition of Thin Films, John Wiley & Sons, New York, 1994, p. 115.
[28] S. Metev, K. Meteva, Nucleation and growth of laser-plasma deposited thin films, Appl. Surf. Sci. 43 (1989) 402.
[29] J.S. Horwitz, J.A. Sprague, Film nucleation and film growth in pulsed laser deposition of ceramics, in: D.B. Chrisey, G.H. Hubler (Eds.), Pulsed Laser Deposition of Thin Films, John Wiley & Sons, New York, 1994, p. 229.
[30] D.B. Chrisey, G.H. Hubler, Pulsed Laser Deposition of Thin Films, in: John Wiley & Sons, New York, 1994.
[31] P. Baeri, L. Torrisi, N. Marino, G. Foti, Ablation of hydroxyapatite by pulsed laser irradiation, Appl. Surf. Sci. 54 (1992) 210.
[32] C.M. Cotell, D.B. Chrisey, K.S. Grabowski, J.A. Sprague, C.R. Gosset, Pulsed laser deposition of hydroxylapatite thin films on Ti-6Al-4V, J. Appl. Biomater. 3 (1992) 87–93.
[33] J.L. Arias, F.J. García-Sanz, M.B. Mayor, S. Chiussi, J. Pou, B. León, M. Pérez-Amor, Physicochemical properties of calcium phosphate coatings produced by pulsed laser deposition at different water vapour pressures, Biomaterials 19 (1998) 883–888.
[34] J.L. Arias, M.B. Mayor, J. Pou, Y. Leng, B. León, M. Pérez-Amor, Micro-and nano-testing of calcium phosphate coatings produced by pulsed laser deposition, Biomaterials 24 (2003) 3403–3408.
[35] V.N. Bagratashvili, E.N. Antonov, E.N. Sobol, V.K. Popov, S.M. Howdle, Macroparticle distribution and chemical composition of laser deposited apatite coatings, Appl. Phys. Lett. 66 (1995) 2451.
[36] V. Cracium, I.W. Boyd, D. Cracium, P. Andreazza, J. Perriére, Vacuum ultraviolet annealing of hydroxyapatite films grown by pulsed laser deposition, J. Appl. Phys. 85 (1999) 8410–8414.
[37] J.M. Fernández-Pradas, G. Sardin, L. Cléries, P. Serra, C. Ferrater, J.L. Morenza, Deposition of hydroxyapatite thin films by excimer laser ablation, Thin Solid Films 317 (1998) 393.
[38] O. Guillot-Noël, R. Gómez-San Román, J. Perriére, J. Hermann, V. Craciun, C. Boulmer-Leborgne, P. Barboux, Growth of apatite films by laser ablation: reduction of the droplet areal density, J. Appl. Phys. 80 (1996) 1803–1808.
[39] S. Hontsu, M. Nakamori, H. Tabata, J. Ishii, T. Kawai, Pulsed laser deposition of bioceramics hydroxyapatite thin films on polymer materials, Jpn. J. Appl. Phys. 35 (1996) L1208–L1210.
[40] M. Jelínek, V. Olsan, L. Jastrabík, V. Studnicka, V. Hnatowicz, J. Kvítek, V. Havránek, T. Dostálová, I. Zergioti, A. Petrakis, E. Hontzopoulos, C. Fotakis, Effect of processing parameters on the properties of hydroxylapatite films, Thin Solid Films 257 (1995) 125–129.
[41] P. Serra, J. Palau, M. Varela, J. Esteve, J.L. Morenza, Characterization of hydroxyapatite laser ablation plumes by fast intensified CCD-imaging, J. Mater. Res. 10 (1995) 473.
[42] R.K. Singh, F. Qian, V. Nagabushnam, R. Damodaran, B.M. Moudgil, Excimer laser deposition of hydroxyapatite thin films, Biomaterials 15 (1994) 522.
[43] B.E. Tucker, G.H. Nancollas, C.M. Cotell, R.C.Y. Auyeung, M. Spector, Preconditioning and dual constant composition dissolution kinetics of pulsed laser deposited hydroxyapatite thin films on silicon substrates, Biomaterials 17 (1996) 631–637.
[44] C.K. Wang, J.H. Chern Lin, C.P. Ju, H.C. Ong, R.P.H. Chang, Structural characterization of pulsed laser-deposited hydroxyapatite film on titanium substrate, Biomaterials 18 (1997) 1331–1338.
[45] L. Clèries, E. Martínez, J.M. Fernández-Pradas, G. Sardin, J. Esteve, J.L. Morenza, Mechanical properties of calcium phosphate coatings deposited by laser ablation, Biomaterials 21 (2001) 967–971.

[46] C. Peraire, J.L. Arias, D. Bernal, J. Pou, B. León, A. Arañó, W. Roth, Biological stability and osteoconductivity in rabbit tibia of pulsed laser deposited hydroxylapatite coatings, J. Biomed. Mater. Res. 77A (2006) 370–379.
[47] L. Torrisi, Structural investigations on laser deposited hydroxyapatite films, Thin Solid Films 237 (1994) 12–15.
[48] L. Torrisi, R. Setola, Thermally assisted hydroxyapatite obtained by pulsed-laser deposition on titanium substrates, Thin Solid Films 227 (1993) 32–36.
[49] A. De Carlos, F. Lusquiños, J. Pou, B. León, M. Pérez-Amor, F.C.M. Driessens, K. Hing, S. Best, W. Bonfield, In vitro testing of Nd:YAG laser processed calcium phosphate coatings, J. Mater. Sci. Mater. Med. 17 (2006) 1153–1160.
[50] J.L. Arias, M.B. Mayor, F.J. García-Sanz, J. Pou, B. León, M. Pérez-Amor, J.C. Knowles, Structural analysis of calcium phosphate coatings produced by pulsed laser deposition at different water-vapour pressures, J. Mater. Sci. Mater. Med. 8 (1997) 873.
[51] J. Pou, P. González, E. García, D. Fernández, J. Serra, B. León, S.R.J. Saunders, M. Pérez-Amor, High-temperature corrosion-resistant ceramic coatings obtained by laser chemical vapour deposition, Vacuum 45 (1994) 1035.
[52] R.Z. LeGeros, O.R. Trautz, J.P. LeGeros, E. Klein, Carbonate substitution in the apatite structure, Bull. Soc. Chim. Fr. (1968) 1712–1718 (special issue).
[53] M.B. Mayor, J.L. Arias, S. Chiussi, F. García-Sanz, J. Pou, B.L. Fong, M. Pérez-Amor, Calcium phosphate coatings grown at different substrate temperatures by pulsed ArF-laser deposition, Thin Solid Films 317 (1998) 363–366.
[54] T.L. Parker, K.G. Parker, S.M. Howdle, E.N. Antonov, V.N. Bagratashvili, V.K. Popov, E. Sobol, C.J. Roberts, Biocompatibility of laser-deposited hydroxyapatite coatings: correlation of coating parameters with cell behaviour, Cell. Eng. 1 (1996) 91.
[55] L. Cléries, J.M. Fernández-Pradas, J.L. Morenza, Bone growth on and resorption of calcium phosphate coatings obtained by pulsed laser deposition, J. Biomed. Mater. Res. 49 (2000) 43–52.
[56] M. Seydlova, Z. Teuberova, T. Dostálová, B. Dvorankova, K. Smetana, M. Jelínek, T. Kocourek, W. Mróz, Biological properties of titanium implants covered with hydroxyapatite and zirconia layers by pulsed laser: *in vitro* study, J. Appl. Phys. 99 (014905) (2006) 1–6.
[57] C.M. Cotell, J.A. Conklin, R.C.Y. Auyeung, S.S. Wong, C.M. Klapperich, M. Spector, In vivo evaluation of pulsed laser deposited hydroxyapatite coating for prosthesis-bone bonding, Mater. Res. Soc. Symp. Proc. 414 (1996) 171–176.
[58] C. Peraire, A. Arañó, A. Arsuaga, A. Assenza, A. Borrell, A. Padrós, J.L. Arias, J. Pou, B. Leon, Final Report (EU CRAFT Project: BRE2.CT94.1533), 1997.
[59] E.N. Antonov, V.N. Bagratashvili, V.K. Popov, E.N. Sobol, S.M. Howdle, C. Joiner, K.G. Parker, T.L. Parker, A.A. Doktorov, V.B. Lkhanov, A.I. Volozhin, S.S. Alimpiev, S.M. Nikiforov, Biocompatibility of laser-deposited hydroxyapatite coatings on titanium and polymer implant materials, J. Biomed. Opt. 3 (1998) 423.
[60] T. Dostálová, L. Himmlová, M. Jelínek, C. Grivas, Laser-deposited hydroxyapatite films on dental implants – biological evaluation *in vivo*, Laser Phys. 8 (1998) 182.
[61] B. León, Pulsed laser deposition of thin calcium phosphate coatings, in: B. León, J.A. Jansen (Eds.), Thin Calcium Phosphate Coatings for Medical Implants, Springer, New York, 2009, pp. 101–156.
[62] L. D'Alessio, R. Teghil, M. Zaccagnino, I. Zaccardo, D. Ferro, V. Marotta, Pulsed laser ablation and deposition of bioactive glass as coating material for biomedical applications, Appl. Surf. Sci. 138–139 (1999) 527–532.
[63] L. D'Alessio, D. Ferro, V. Marotta, A. Santagata, R. Teghil, M. Zaccagnino, Laser ablation and deposition of Bioglass 45S5 thin films, Appl. Surf. Sci. 183 (2001) 10–17.
[64] Y. Zhao, M. Song, C. Chen, J. Liu, Effects of the substrate temperature on the bioglass films deposited by pulsed laser, Appl. Surf. Sci. 254 (2008) 6897–6901.
[65] Y. Zhao, M. Song, C. Chen, J. Liu, The role of the pressure in pulsed laser deposition of bioactive glass films, J. Non-Cryst. Solids 354 (2008) 4000–4004.

[66] Y. Zhao, M. Song, J. Liu, Characteristics of bioactive glass coatings obtained by pulsed laser deposition, Surf. Interface Anal. 40 (2008) 1463–1468.
[67] C. Berbecaru, H.V. Alexandru, A. Ianculescu, A. Popescu, G. Socol, F. Sima, I. Mihailescu, Bioglass thin films for biomimetic implants, Appl. Surf. Sci. 255 (2009) 5476–5479.
[68] L. Floroian, B. Savu, G. Stanciu, A.C. Popescu, F. Sima, I.N. Mihailescu, R. Mustata, L.E. Sima, S.M. Petrescu, D. Tanaskovic, D. Janackovic, Nanostructured bioglass thin films synthesized by pulsed laser deposition: CSLM, FTIR investigations and *in vitro* biotests, Appl. Surf. Sci. 255 (2008) 3056–3362.
[69] A.C. Popescu, F. Sima, L. Duta, C. Popescu, I.N. Mihailescu, D. Capitanu, R. Mustata, L.E. Sima, S.M. Petrescu, D. Janackovic, Biocompatible and bioactive nanostructured glass coatings synthesized by pulsed laser deposition: *in vitro* biological tests, Appl. Surf. Sci. 255 (2009) 5486–5490.
[70] J.P. Borrajo, P. González, S. Liste, J. Serra, S. Chiussi, B. León, M. Pérez-Amor, Pulsed laser deposition of bioactive glass films in ammonia and disilane atmospheres, Appl. Surf. Sci. 248 (2005) 369–375.
[71] J.P. Borrajo, P. González, S. Liste, J. Serra, S. Chiussi, B. León, M. Pérez-Amor, The role of the thickness and the substrate on the *in vitro* bioactivity of silica-based glass coatings, Mater. Sci. Eng. C 25 (2005) 187–193.
[72] P. González, J. Serra, S. Liste, S. Chiussi, B. León, M. Pérez-Amor, Ageing of pulsed-laser-deposited bioactive glass films, Vacuum 67 (2002) 647–651.
[73] P. González, J. Serra, S. Liste, S. Chiussi, B. León, M. Pérez-Amor, J. Martínez-Fernández, A.R. de Arellano-López, F.M. Varela-Feria, New biomorphic SiC ceramics coated with bioactive glass for biomedical applications, Biomaterials 24 (2003) 4827–4832.
[74] S. Liste, P. González, J. Serra, J.P. Borrajo, S. Chiussi, B. León, M. Pérez-Amor, J. García-López, F.J. Ferrer, Y. Morilla, M.A. Respaldiza, Study of the stoichiometry transfer in pulsed laser deposition of bioactive silica-based glasses, Thin Solid Films 453–454 (2004) 219–223.
[75] S. Liste, J. Serra, P. González, J.P. Borrajo, S. Chiussi, B. León, M. Pérez-Amor, The role of the reactive atmosphere in pulsed laser deposition of bioactive glass films, Thin Solid Films 453–454 (2004) 224–228.
[76] J. Serra, P. Gonzalez, S. Chiussi, B. Leon, M. Pérez-Amor, Processing of bioglass coatings by excimer laser ablation, Key Eng. Mater. 92–95 (2001) 635–638.
[77] A. De Carlos, J.P. Borrajo, J. Serra, P. González, B. León, Behaviour of MG-63 osteoblast-like cells on wood-based biomorphic SiC ceramics coated with bioactive glass, J. Mater. Sci. Mater. Med. 17 (2006) 523–529.
[78] E. Toyserkani, S. Corbin, A. Khajepour, Laser Cladding, CRC Press, Boca Raton, FL, 2004.
[79] W.M. Steen, Laser Materials Processing, Springer Verlag, London, 1993. p. 199.
[80] A. Gasser, Oberflächenbearbeitung mit CO_2 Lasern (Ph.D. Thesis), RWTH Aachen University, Germany, 1993.
[81] T.A. Jensen, Surface cladding, in: J.F. Ready, D.F. Farson (Eds.), LIA Handbook of Laser Materials Processing, Magnolia Publishing Inc., Orlando, USA, 2001, pp. 284–287.
[82] E. Lugscheider, H. Bolender, H. Krappitz, Laser cladding of paste bound hardfacing alloys, Surf. Eng. 7 (1991) 341–344.
[83] V.M. Weerasinghe, Laser Cladding of Flat Plates (Ph.D. Thesis), University of London, United Kingdom, 1984.
[84] V.M. Weerasinghe, W.M. Steen, Laser cladding with pneumatic powder delivery in Metbowzer, in: E. D (Ed.), Proceedings of 4th International Conference on Lasers in Materials Processing, ASM, Metals Park, OH, 1983, pp. 166–175.
[85] C. Deng, Y. Wang, Y. Zhang, J. Gao, *In situ* laser coating of calcium phosphate on Ti6Al4V surface for enhancing bioactivity, J. Iron Steel Res. Int. 14 (2007) 73–78.

[86] Y. Zhang, J. Gao, J. Tan, Z. Zou, Laser surface coating of a bioceramic composite layer, Surf. Coat. Technol. 58 (1993) 125–127.
[87] Y. Wang, Y. Li, H. Yu, J. Ding, X. Tang, J. Li, Y. Zhou, In *situ* fabrication of bioceramic composite coatings by laser cladding, Surf. Coat. Technol. 200 (2005) 2080–2084.
[88] M. Zheng, D. Fan, X. Li, W. LI, Q. Liu, J. Zhang, Microstructure and osteoblast response of gradient bioceramic coating on titanium alloy fabricated by laser cladding, Appl. Surf. Sci. 255 (2008) 426–428.
[89] W. Zhu, Q. Liu, H. Li, M. Zheng, A simulation model for the temperature field in bioceramic coating cladded by wide-band laser, Mater. Des. 28 (2007) 2577–2673.
[90] W. Zhu, Q. Liu, M. Zheng, X. Wang, Biocompatibility of a functionally graded bioceramic coating made by wide-band laser cladding, J. Biomed. Mater. Res. 87A (2008) 429–433.
[91] G.J. Cheng, D. Pirzada, M. Cai, A. Bandyopadhyay, Bioceramic coating of hydroxyapatite on titanium substrate with Nd:YAG laser, Mater. Sci. Eng. C 25 (2005) 541–547.
[92] D. Wang, C. Chen, J. Ma, T. Lei, Microstructure of yttric calcium phosphate bioceramic coatings synthesized by laser cladding, Appl. Surf. Sci. 253 (2007) 4016–4020.
[93] D. Wang, C. Chen, J. Ma, G. Zhang, *In situ* synthesis of hydroxyapatite coating by laser cladding, Colloids Surf. 66 (2008) 155–162.
[94] A. Kurella, N.B. Dahotre, Laser induced hierarchical calcium phosphate structures, Acta Biomater. 2 (2006) 677–683.
[95] A. Kurella, M.Z. Hu, N.B. Dahotre, Effect of microstructural evolution on wettability of laser coated calcium phosphate on titanium alloy, Mater. Sci. Eng. C 28 (2008) 1560–1564.
[96] S.R. Paital, N.B. Dahotre, Laser surface treatment for porous and textured Ca-P bio-ceramic coating on Ti-6Al-4V, Biomed. Mater. 2 (2007) 274–281.
[97] M. Roy, A. Bandyopadhyay, S. Bose, Laser surface modification of electrophoretically deposited hydroxyapatite coating on titanium, J. Am. Ceram. Soc. 91 (2008) 3517–3521.
[98] P. Cheang, K.A. Khor, L.L. Teoh, S.C. Tam, Pulsed laser treatment of plasma-sprayed hydroxyapatite coatings, Biomaterials 17 (1996) 1901–1904.
[99] S. Dyshlovenko, C. Pierlot, L. Pawlowski, R. Tomaszek, P. Chagnon, Experimental design of plasma spraying and laser treatment of hydroxyapatite coatings, Surf. Coat. Technol. 201 (2006) 2054–2060.
[100] K.A. Khor, A. Vreeling, Z.L. Dong, P. Cheang, Laser treatment of plasma sprayed HA coatings, Mater. Sci. Eng. A 266 (1999) 1–7.
[101] M. Roy, B.V. Krishna, A. Bandyopadhyay, S. Bose, Laser processing of bioactive tricalcium phosphate coating on titanium for load-bearing implants, Acta Biomater. 4 (2008) 324–333.
[102] F. Lusquiños, J. Pou, J.L. Arias, M. Boutinguiza, M. Pérez-Amor, B. León, F.C.M. Driessens, Production of calcium phosphate coatings on Ti6Al4V obtained by Nd:yttrium–aluminum–garnet laser cladding, J. Appl. Phys. 90 (2001) 4231–4236.
[103] F. Lusquiños, A. De Carlos, J. Pou, J.L. Arias, M. Boutinguiza, B. León, M. Pérez-Amor, F.C.M. Driessens, K. Hing, I. Gibson, S. Best, W. Bonfield, Calcium phosphate coatings obtained by Nd:YAG laser cladding: physicochemical and biologic properties, J. Biomed. Mater. Res. 64A (2003) 630–637.
[104] F. Lusquiños, J. Pou, M. Boutinguiza, F. Quintero, R. Soto, B. León, M. Pérez-Amor, Main characteristics of calcium phosphate coatings obtained by laser cladding, Appl. Surf. Sci. 247 (2005) 486–492.
[105] N. Moritz, E. Vedel, H. Ylänen, M. Jokinen, M. Hupa, A. Yli-Urpo, Creation of Bioactive Glass Coating on Titanium by Local Laser Irradiation; Part 1: Optimization of the Processing Parameters, Key Eng. Mater. 240–242 (2003) 221.
[106] N. Moritz, E. Vedel, H. Ylänen, M. Jokinen, M. Hupa, A. Yli-Urpo, Characterisation of bioactive glass coatings on titanium substrates produced using a CO_2 laser, J. Mater. Sci. Mater. Med. 15 (2004) 787–794.

[107] N. Moritz, S. Rossi, E. Vedel, T. Tirri, H. Yläneu, H. Aro, T. Närhi, Implants coated with bioactive glass by CO_2 laser, an *in vivo* study, J. Mater. Sci. Mater. Med. 15 (2004) 787–794.
[108] R. Comesaña, F. Quintero, F. Lusquiños, M.J. Pascual, M. Boutinguiza, A. Durán, J. Pou, Laser cladding of bioactive glass coatings, Acta Biomater. 6 (2010) 953–961.
[109] F. Lusquiños, R. Comesaña, F. Quintero, A. Riveiro, J. Pou, Bioceramic glass coatings produced by laser cladding technique, in: Proceedings of the Fourth International WLT-Conference on Laser in Manufacturing, LIM 2007, WLT, 2007, pp. 393–396.
[110] F. Lusquiños, R. Comesaña, F. Quintero, A. Riveiro, J. Pou, Production of bioactive glass coatings by Nd:YAG laser cladding, in: 21st European Conference on Biomaterials, ESB2007, 2007.
[111] J. Pou, F. Lusquiños, F. Quintero, A. Riveiro, R. Comesaña, M. Boutinguiza, B. León, M. Pérez-Amor, Laser processing and synthesis of ceramic biomaterials for osseointegrable applications, in: Proceedings of the Laser Materials Processing Conference ICALEO´2007, LIA, vol. 100, 2007, pp. 179–185.

CHAPTER 15

Thick Metallic Coatings Produced by Coaxial and Side Laser Cladding: Processing and Properties

J. Lawrence*, V. Ocelík†, J.T.M. De Hosson†
*University of Chester, Chester, United Kingdom
†University of Groningen, Groningen, The Netherlands

15.1 INTRODUCTION

Surface treatment by high power lasers embraces several different techniques utilizing the heat of a laser beam at the surface to modify the composition and microstructure and produce a wide range of metallurgical effects [1]. Laser cladding using a powder injection technique [2] comprises fusion of an alloy powder layer to a substrate with minimum melting of the substrate. Melting starts at the surface and the particles being heated and melted when passing the laser beam are trapped in the melt pool. This technique is used for the deposition of alloys on turbine blades, engine valves, valve seats, and drilling components. A wide variety of clad materials and substrates are reported in literature (an overview reference is made in [3]) for applications in automotive, aerospace, machinery, petrochemical, power generation, and shipbuilding industries.

There are two different ways of powder feeding: from the side or coaxially to the laser beam (see Fig. 15.1). When the powder stream is injected off-axis from the laser beam, substrate movement determines different local cladding conditions. For instance, a so-called "against hill" cladding condition takes place when the powder stream is applied from the side from which the substrate moves. In this case, the clad powder is trapped temporarily in a corner formed between the molten track and the fat substrate. This leads to higher powder efficiency than in the so-called "over hill" cladding set-up, when the powder is fed from the opposite side [4,5]. This set-up is preferably used when the so-called laser melt injection regime is

Advances in Laser Materials Processing
https://doi.org/10.1016/B978-0-08-101252-9.00015-7
Copyright © 2018 Elsevier Ltd.
All rights reserved.

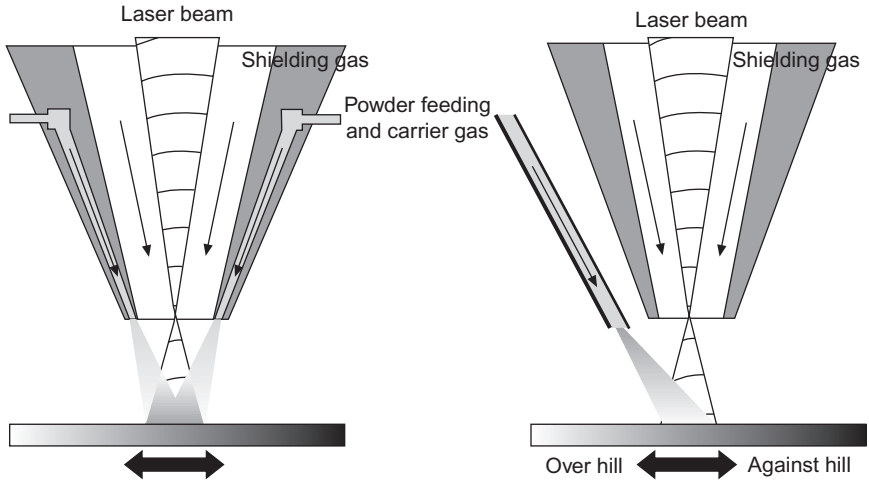


Fig. 15.1 The comparison of coaxial (left) and side (right) laser cladding set-up above the moving substrate.

required to inject ceramic particles into a tail of melt pool created by a laser beam with the aim to minimize the interaction time between the injected particles and the laser beam and to create a metal matrix composite layer at the surface of the treated piece [6–8].

When the powder stream is delivered coaxially with the laser beam, all directions of the substrate movement in a plane perpendicular to the laser beam are equivalent. The coaxial laser cladding process is thus independent of the cladding direction. Therefore, it is possible to produce equivalent tracks independently of the moving direction of the work piece. This advantage of coaxial laser cladding is employed in the formation of metallic parts from 3D designs by laser assisted direct manufacturing [9–11].

Many attempts to model the laser cladding process have been published so far [12–15] but the complete model description of the laser cladding process is rather complex, because numerous interactions (laser beam/powder stream, laser beam/substrate surface, powder stream/melt pool, powder stream/solid substrate, etc.) and physical phenomena (mass and heat transfer, fluid flow, phase transformations during rapid solidification, etc.) are present. Therefore, the experimental examination of the process parameter window and a search for a relationship between the laser clad track characteristics and the processing parameters is still necessary for the exploration of new coating/substrate combinations. In this chapter, we

will review the laser processing window parameters and relate them to the main single-track geometric features reducing the need for extensive and time-consuming experiments. Both the coaxial and side cladding set-ups will be examined for Ni- and Co-based alloys cladding on steel and cast iron substrates. It will be shown that for both cladding geometries, i.e. coaxial and side, processing maps can be constructed. Processing maps are extremely helpful in selecting the main processing parameters for coatings with required thickness. Moreover, for coaxial side cladding, results of model calculations of powder and substrate heating will be presented and the important role of the speed of powder particles inside the powder cloud will be shown. As an example, the cladding of thick Co and tool steel-based coatings on steel and cast iron substrates will be presented accompanied with a discussion of their microstructures, mechanical, and wear properties.

Although a wide variety of metallic alloy clad materials and substrates are reported in literature, only a few show results of laser cladding of tool steel powders on ordinary steel or cast iron substrates. Yellup [2] reported about laser deposited tool steel among other coatings with low dilution, high integrity, and fine structures. Mazumder et al. [16] also showed the possibility of building 3D parts from H13 tool steel using the so-called direct metal deposition technique, which is an advanced laser cladding technique with coaxial blowing powder. The repair of molds which have experienced severe damage during their service lifetime by local laser cladding of high speed steel with high molybdenum content was recently reported by Navas et al. [17]. Abrasive wear behavior of several laser clad tool steel coatings studied in the work by Wang et al. [18] showed that the laser track overlapping results in different properties inside a reheated zone in comparison with an area when material in the as clad condition exists. Here we will present a laser clad coating made from tool steel powder originally used to form parts via powder metallurgy processes. The material is commercially known as Vanadis23 (Udeholm) or MicroMelt23 (Carpenter Powder Products). It is a chromium-molybdenum-tungsten-vanadium alloyed high speed steel that shows high wear resistance, high compressive strength, good toughness, very good dimensional stability on heat treatment, and very good tempering resistance [19]. It will be demonstrated that the laser cladding of both these powders offers a wide processing window resulting in the formation of thick, microstructurally homogeneous, hard, crack and other defect-free coatings on ordinary steel substrates (Plates 15.1–15.23).

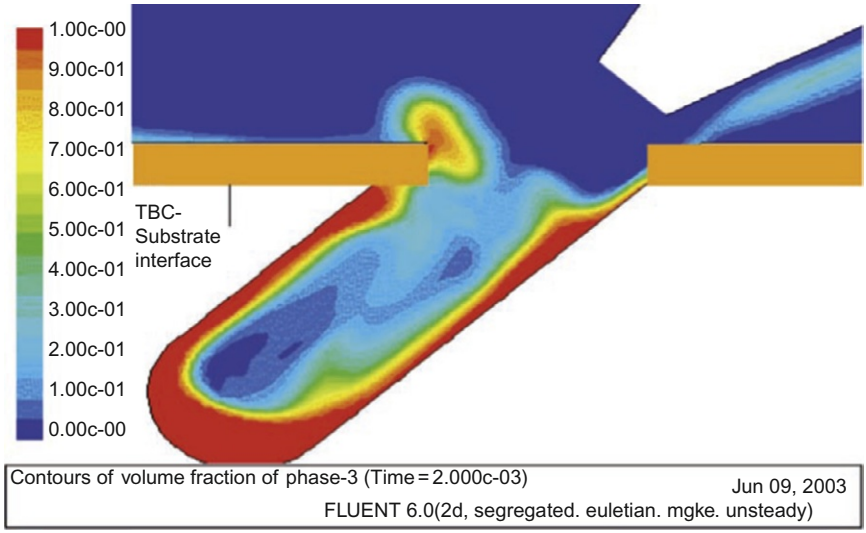


Plate 15.1 CFD modeling of angled laser drilling of thermal barrier coated Ni-alloy showing the melt flow characteristics, by the University of Manchester.

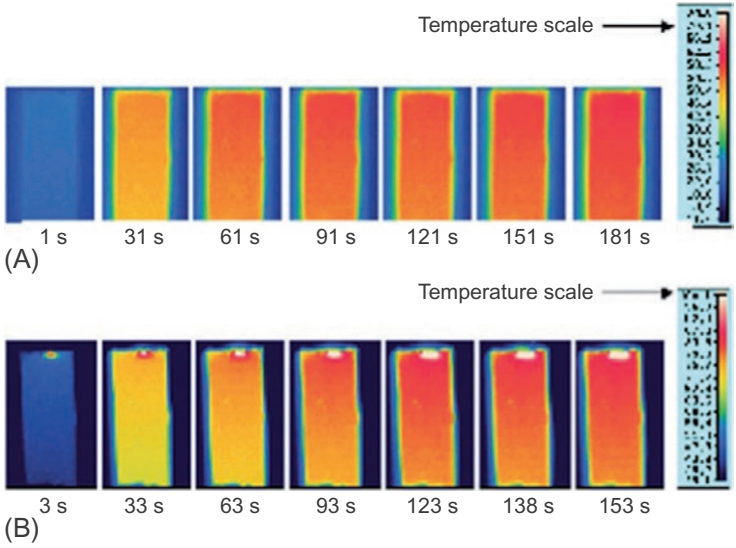


Plate 15.2 Typical thermal images of silicon specimens over time during irradiation with femtosecond laser pulses at spot size of (A) 0.3 mm and power of 210 mW and (B) 0.6 mm and power of 300 mW.

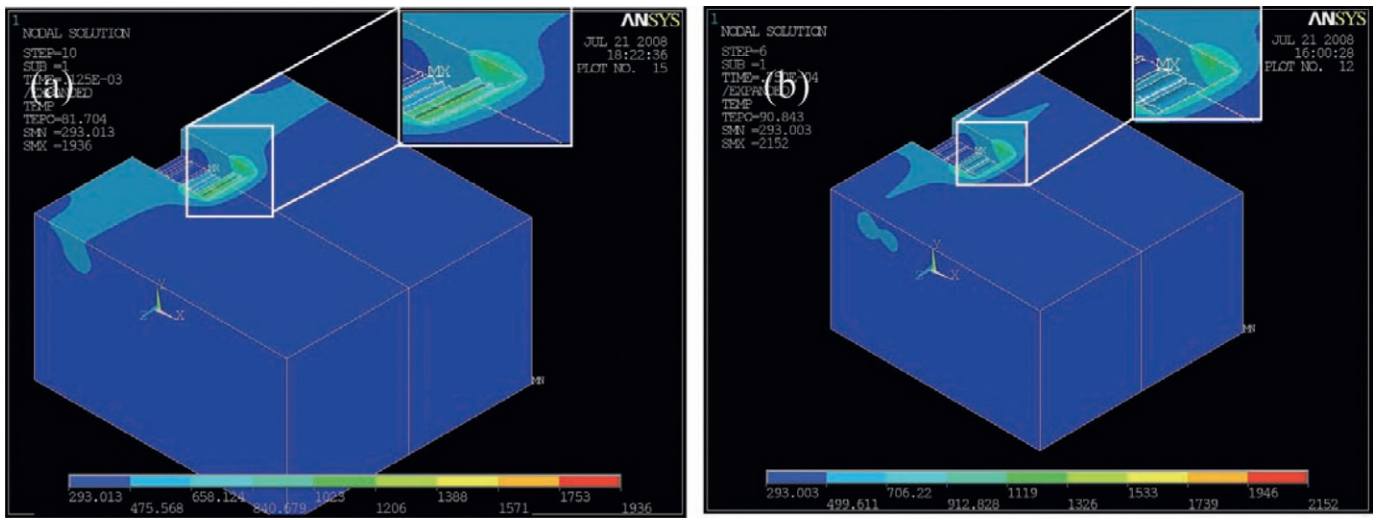


Plate 15.3 HAZ profile at (A) 400 mm/s and (B) 800 mm/s scanning speed.

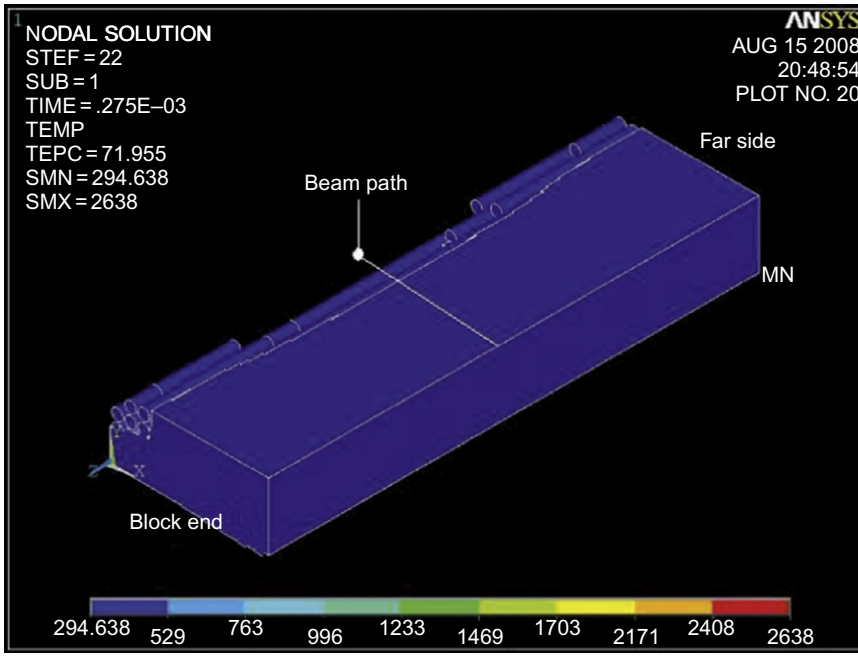


Plate 15.4 HAZ profile at 50 mm/s scanning speed after one track.

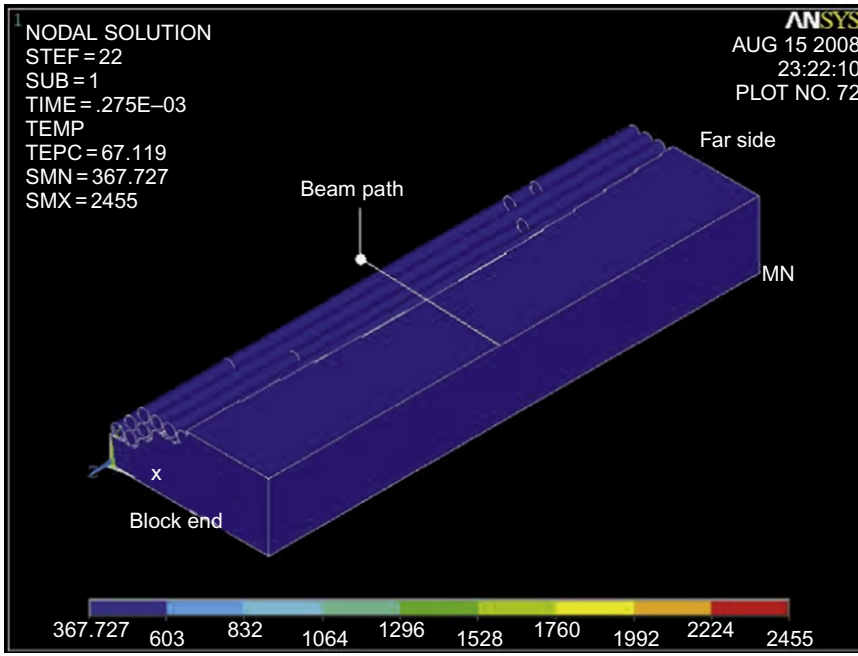


Plate 15.5 HAZ profile at 200 mm/s scanning speed after one track.

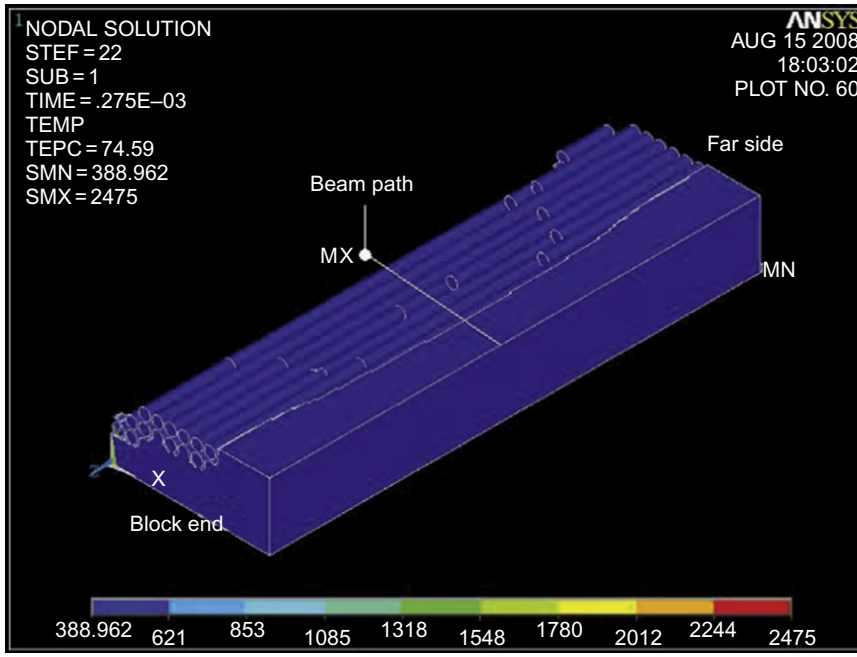


Plate 15.6 HAZ profile at 800 mm/s scanning speed after one track.

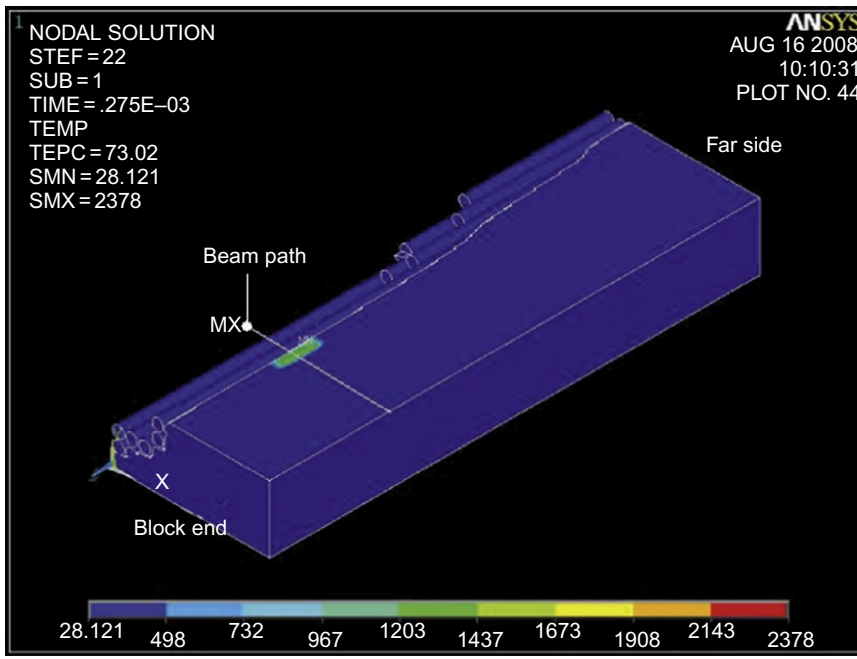


Plate 15.7 Predicted material removal at 75 mm distance in 2-ring processing.

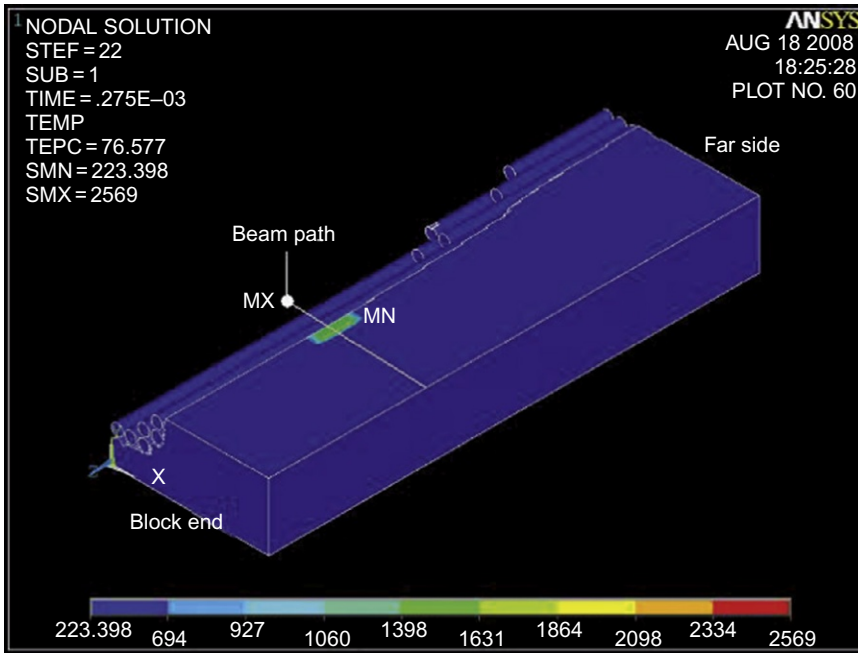


Plate 15.8 Predicted material removal at 100 mm distance in 2-ring processing.

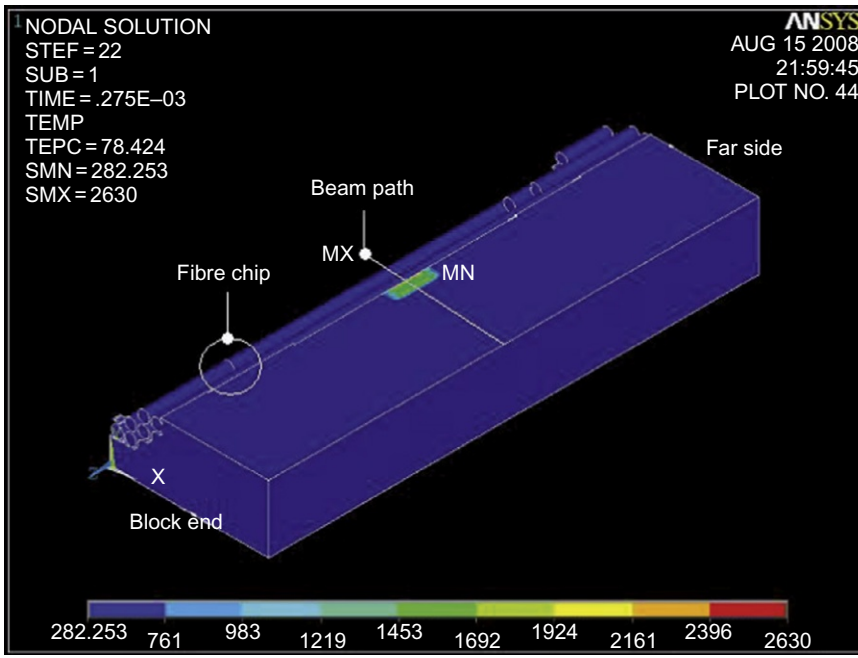


Plate 15.9 Predicted material removal at 150 mm distance in 2-ring processing.

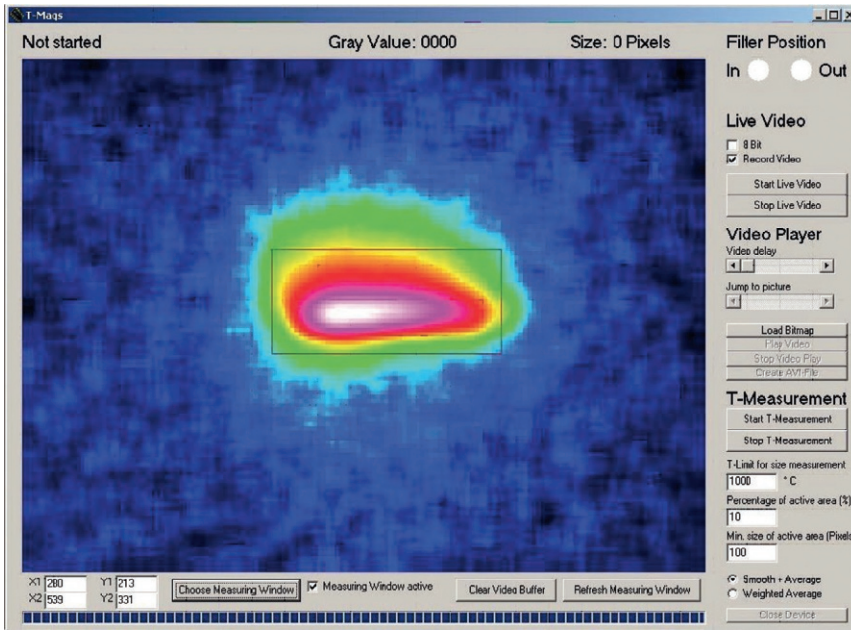


Plate 15.10 Screen shot of user interface, miscolored image, defining of measuring window, scanned laser beam, about 20 mm wide.

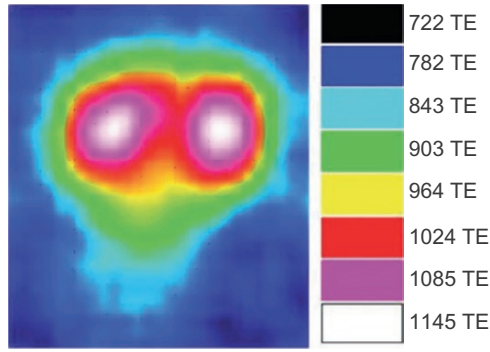


Plate 15.11 Thermographic image of simultaneous laser heat treatment of ball bearing screws, TE = temperature units, non-calibrated miscolored image.

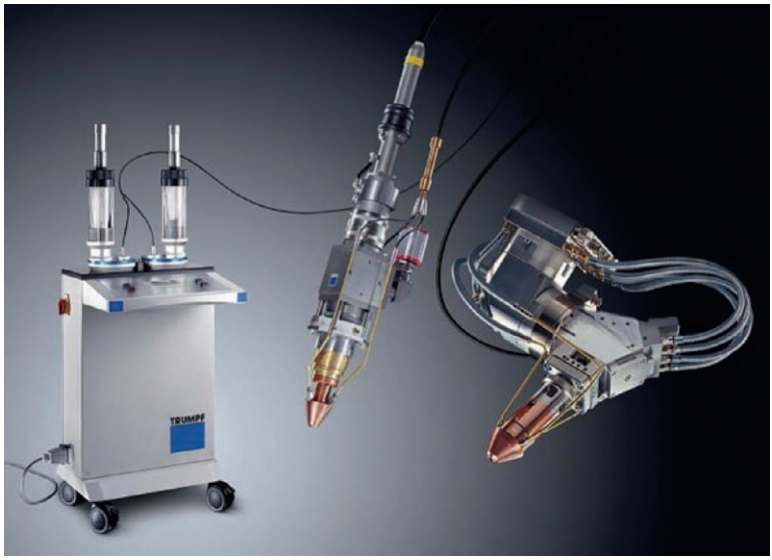


Plate 15.12 Trumpf deposition equipment, consisting of: powder feeder, focusing optics, and powder nozzle. *(Image courtesy of TRUMPF Laser- und Systemtechnik GmbH.)*

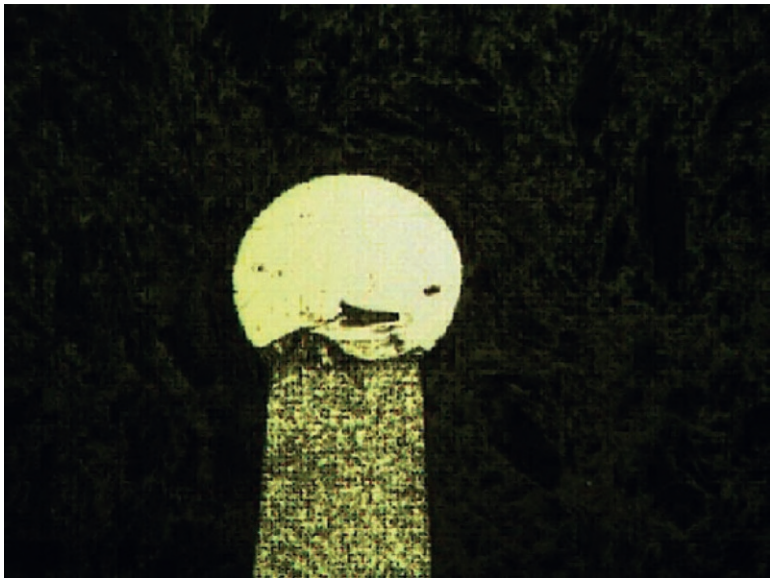


Plate 15.13 Inconel 718 deposited on the tip of a vane (0.015 mm wire feedstock).



Plate 15.14 A Huffman HC-205 Laser cladding system. *(Image courtesy of Huffman Corporation.)*

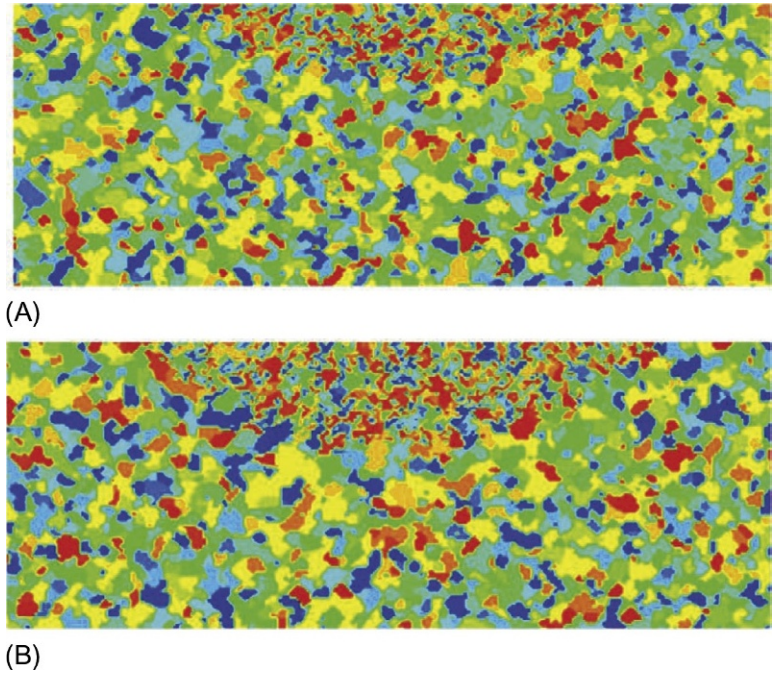


Plate 15.15 Monte Carlo modeled grain structure after recrystallization and grain growth during laser forming: (A) 400 W and 25 mm/s, and (B) 800 W and 50 mm/s [19a].

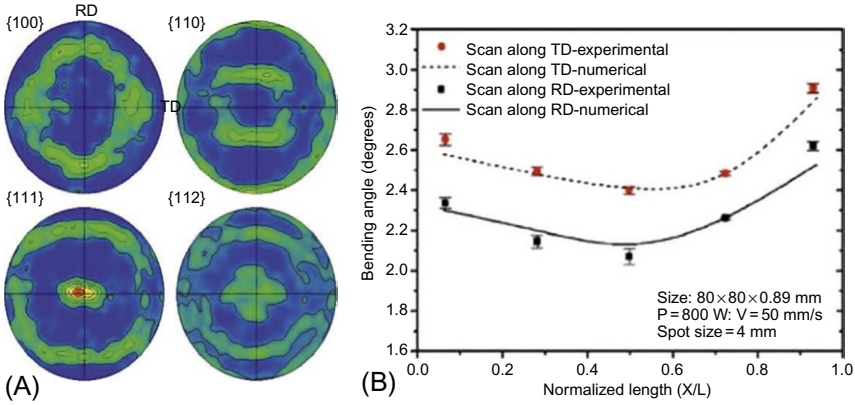


Plate 15.16 (A) {0 0 1}, {1 1 0}, {1 1 1}, and {1 1 2} pole figures of AISI 1010 cold-rolled steel sheet of 0.89 mm thickness; (B) numerical and experimental bending angles of 0.89 mm thick steel sheet with scanning along the RD and TD, respectively (Cheng and Yao, 2005).

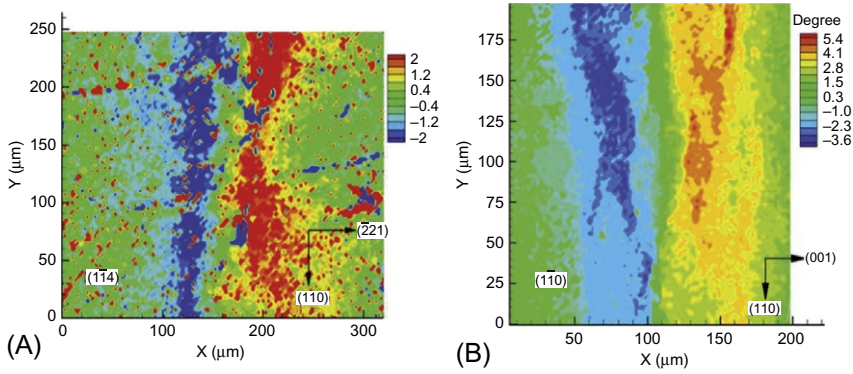


Plate 15.17 Lattice rotation contour map on sample surface. (A) $(1\,\bar{1}\,4)$ orientation [19b]; (B) (110) orientation [19c].

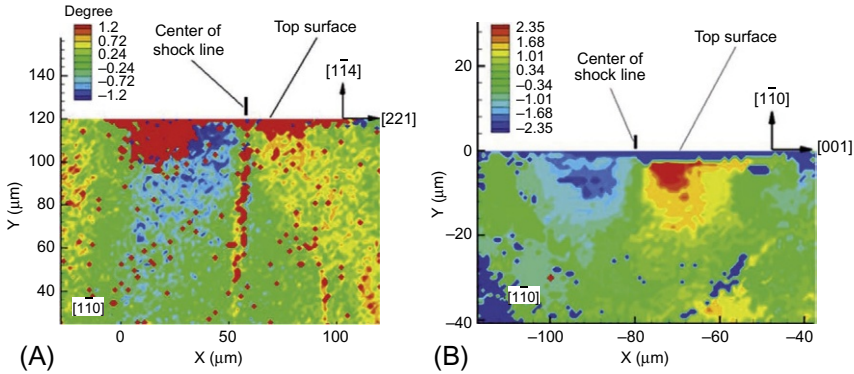


Plate 15.18 Lattice rotation contour map on the (1 1 0) cross-section. Positive rotation is counterclockwise about the *z*-axis; (A) $(1\,\bar{1}\,4)$ orientation (Wang et al., 2008a); (B) (1 1 0) orientation (Vukelic et al., 2008a).

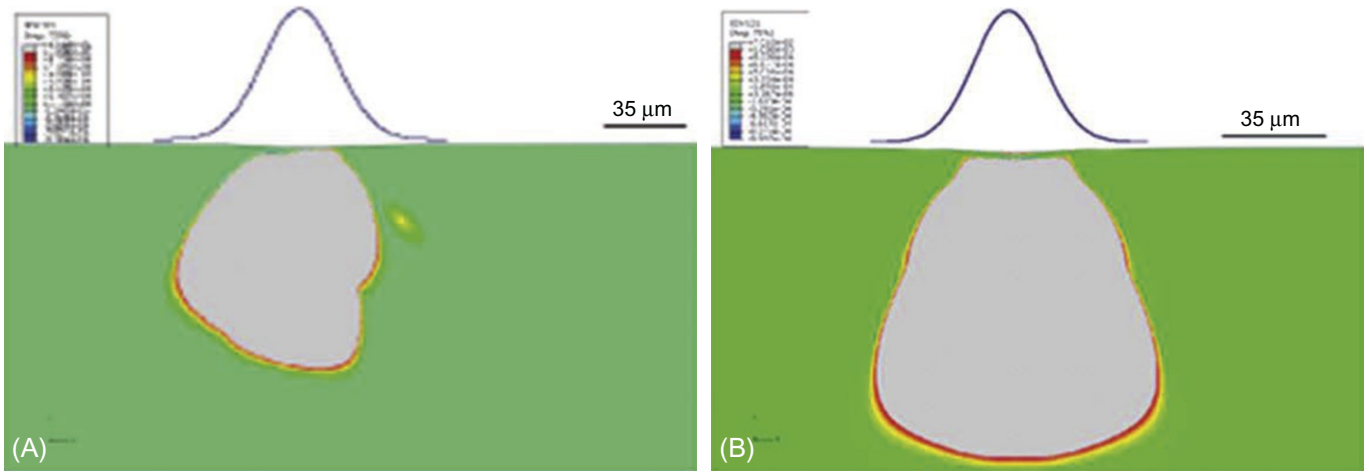


Plate 15.19 Total shear strain at the end of the loading step for (A) $(1\,\bar{1}\,4)$ orientation; (B) (1 1 0) orientation [19d].

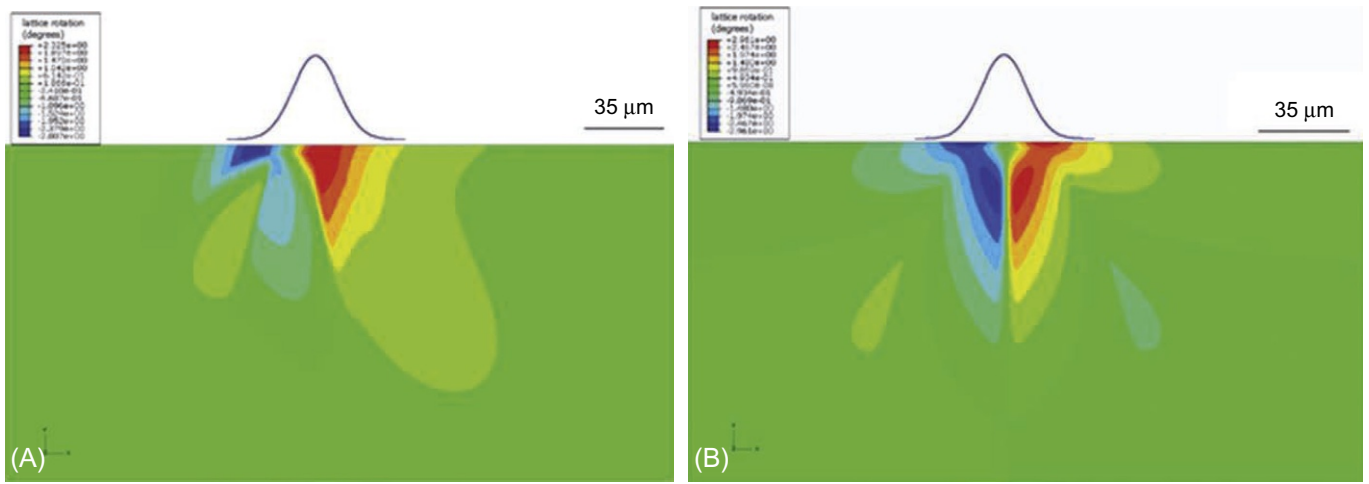


Plate 15.20 Lattice rotation contour map on the (1 1 0) cross-section by FEM. (A) ($1\,1\,\overline{4}$) orientation; (B) (1 1 0) orientation.

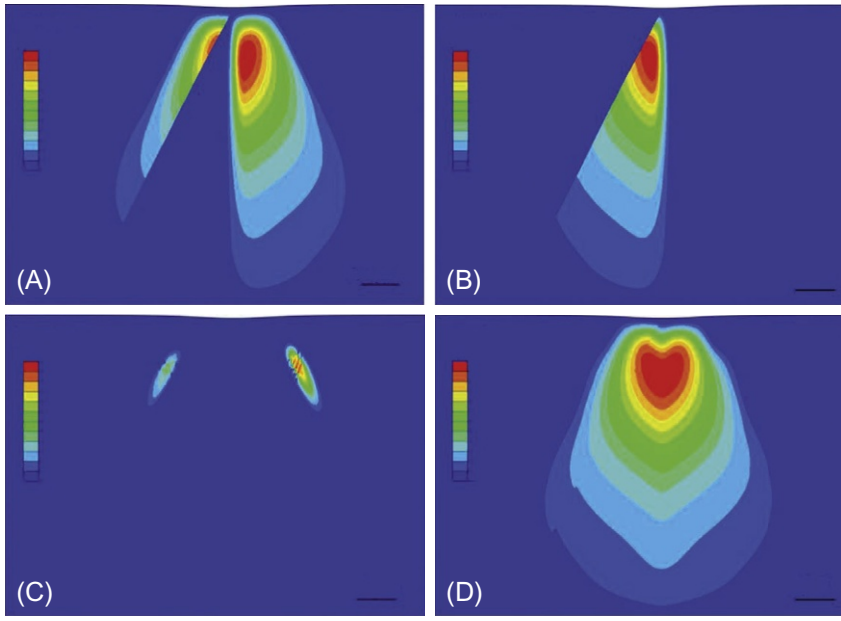


Plate 15.21 Numerical results—shear strain increments. (A) shear strain increment *iii*; (B) shear strain increment *i*; (C) shear strain increment *ii*; (D) total shear strain increment.

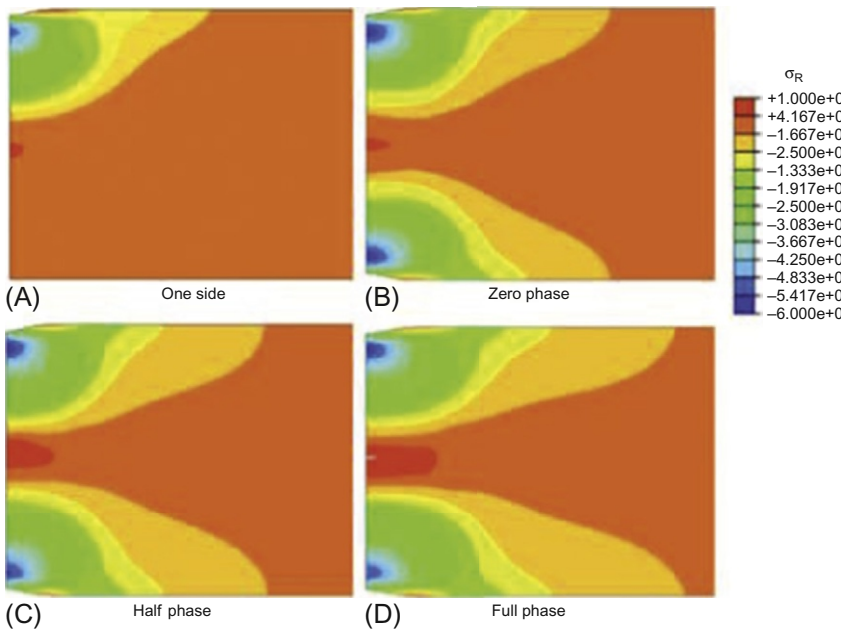


Plate 15.22 The residual stress distributions within the 100 μm thick plate by various irradiation methods. Laser intensity is 4.95 GW/cm^2, beam spot size is 12 μm, and pulse duration is 50 ns.

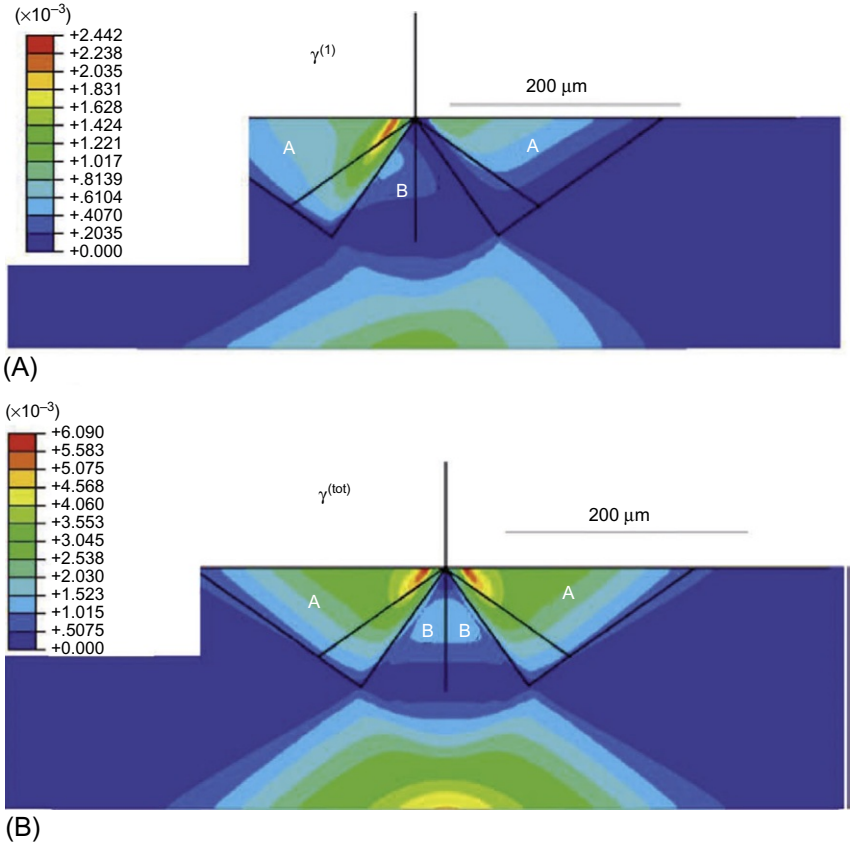


Plate 15.23 Shear strain contour in slip system: (A) slip system *i*; (B) total shear strain.

15.2 COAXIAL LASER CLADDING GEOMETRY AND THEORETICAL CALCULATIONS

Fig. 15.2 shows the real coaxial laser cladding geometry and the relevant geometric features of the coaxial laser process. The distance between the coaxial nozzle output and the cladding surface N_d is expected to be approximately 14 mm, due to the fixed shape of the powder cone escaping from the nozzle outlet (diameter of 9.5 mm under an angle of $\theta = 70$ degrees). In the coaxial set-up, the focal point of the laser beam is usually positioned near the nozzle output plane to secure the nozzle by minimizing the laser beam radius near it. The laser beam diverges from the focus point in angle $2\varphi = 13.7$ degrees. These two angles, together with the laser defocus distance, L_d, and the nozzle working distance, N_d, are the input variables

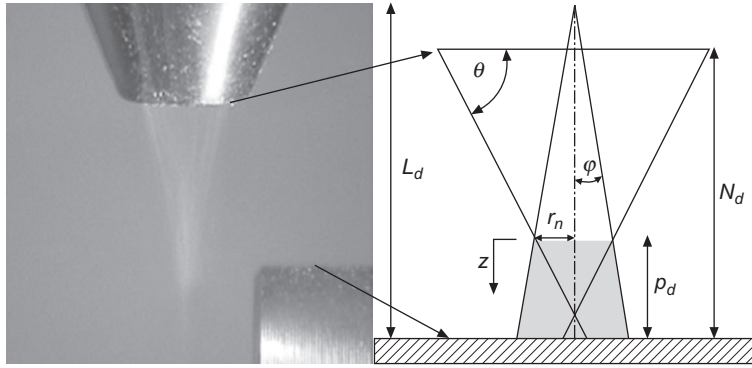


Fig. 15.2 Coaxial laser cladding geometry used in experiment and corresponding scheme for the calculation of the powder-laser beam interaction area.

required to calculate the distance, p_d, over which powder particles are interacting with the laser beam.

The laser power required to melt the substrate and powder, P_{ms} and P_{mp}, respectively, were calculated based on a model suggested by Jouvard et al. [13]. The basic assumptions are the following:

- The incident energy on the substrate contains two contributions: the laser energy coming from the transmitted beam and the heat energy coming from particles heated by the laser beam inside the interaction area. Only a fraction of particles, which contribute to the clad layer, is assumed to transmit the thermal energy to the substrate.
- The laser beam is attenuated inside an interaction area by the particle cloud according to Lambert-Beer's law [20]. A coordinate, z, is measured from the point where the interaction between the particle cloud and the laser beam starts (see Fig. 15.2).
- The spherical powder is homogeneously dispersed throughout the cross-section of the interaction area but its concentration decreases with z because of the increasing radius of the interaction area.
- The particle velocity inside the interaction zone is constant.
- Heat transfer at the surface of the substrate follows a one-dimensional, semi-infinite wall approximation.

Under these constraints, the laser power required to heat the substrate to the melting temperature P_{ms} can be written as

$$P_{ms} = \frac{\sqrt{\pi} k_s \left(T_{ms} - T_{is}\right)}{2\beta\sqrt{\alpha_s t_{int}}} \tag{15.1}$$

and the laser power required to heat the powder to the melting temperature P_{mp} is

$$P_{mp} = \frac{m_p C_p \left(T_{mp} - T_{ip}\right)}{\gamma} \tag{15.2}$$

using

$$\beta = \frac{A_s}{S_{int}} \exp\left(\frac{-\varepsilon F p_d}{\pi v_p \left(r_n^2 + r_n p_d \tan\ \phi\right)}\right) + \frac{3A_{pe}F}{4S_p S_{int} r_p \rho_p}\gamma \tag{15.3}$$

and

$$\gamma = \frac{S_p A_p}{\pi v_p} \int_0^{p_d} \frac{1}{\left(r_n + z \tan\ \phi\right)^2} \exp\left(\frac{-\varepsilon F z}{\pi v_p \left(r_n^2 + z r_n \tan\ \phi\right)}\right) dz \tag{15.4}$$

where T_{ms} is the substrate melting temperature, T_{is} is the substrate initial temperature, k_s is the substrate thermal conductivity, α_s is the substrate thermal diffusivity, t_{int} is the laser beam/substrate interaction time, m_p is the powder particle mass, C_p is the thermal heat capacity of powder material, T_{mp} is the particle melting temperature, T_{ip} is the particle initial temperature, A_s is the substrate absorption coefficient, A_p is the particle absorption coefficient, A_{pe} is the powder cladding efficiency coefficient, S_{int} is the laser beam/substrate interaction area size, ε is the powder extinction coefficient $\varepsilon = 3(1 - A_p)/2\rho_p r_p \rho_p$ is the powder material density, r_p is the radius of powder particle, v_p is the powder particle velocity, and S_p is the particle cross-section. In solving the integral in Eqs. (15.3), (15.4) numerically, one may calculate P_{ms} and P_{mp}. In our calculations, we suppose Sulzer-Metco 19E powder (Ni-based alloy) and low alloyed C45 steel substrate, using mainly the input parameters from Ion [3], Jouvard *et al.* [13], and Metco [21]. These calculations revealed the important role of the coaxial laser cladding parameter, namely the velocity of powder particles, v_p. This velocity is mainly determined by an amount of carrier gas used in the powder feeding system. The upper limit of this velocity can be estimated as the speed of the carrier gas escaping from the powder nozzle (0.25–1.5 m/s for our nozzle geometry).

Fig. 15.3 clearly shows the crucial role of the powder particle velocity in the processing zone. The laser power required to melt the substrate as well as the clad particles is plotted as a function of particle velocity in the case of cladding 60 μm size powder on steel substrate. The laser defocus distance, L_d,

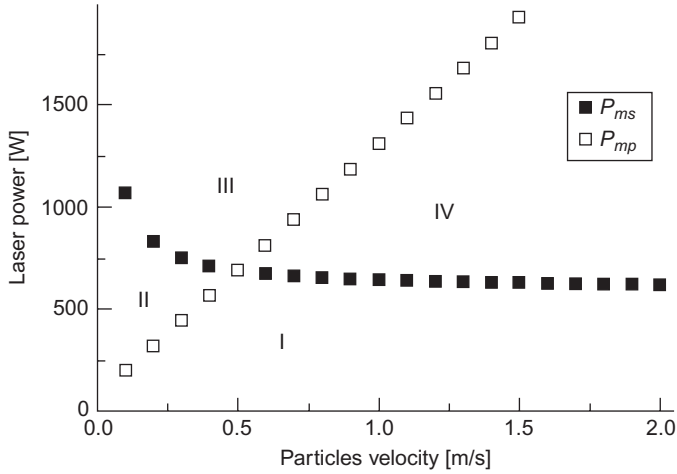


Fig. 15.3 Calculated laser power required to melt the substrate P_{ms} and the particle P_{mp} as a function of powder velocity for coaxial cladding of 19E Metco powder (80 µm size) on C45 steel substrate. Feeding rate $F = 141.7$ mg/s and laser beam scanning speed $S = 4.67$ mm/s.

was +15 mm, the nozzle working distance N_d was 14 mm, and the powder efficiency coefficient A_{pe} was set to 0.3 for this calculation, which represents a mean value observed in our cladding experiments. As Fig. 15.3 clearly demonstrates, the powder shielding effect influences P_{ms} only at low particle velocities. When the particle velocity is higher than 0.5 m/s, the P_{ms} change with v_p is not significant. On the other hand, the power required for heating the powder particle to the melting temperature P_{mp} increases linearly with particle velocity. The intersection of these two graphs forms four different areas for the coaxial cladding regime as indicated in Fig. 15.3. Inside area *I*, no cladding occurs. Inside area *II*, the clad track can be formed but the substrate is not melted and therefore a good metallurgical bond is not formed between the laser track and the substrate. Laser cladding is not successful in this area. Inside area *III*, the laser cladding process lies in an optimal zone. Area *IV* may be characterized as an area of low efficiency laser cladding. Solid powder particles reach the liquid surface with relatively high velocities, which leads to the solid-particle/liquid-surface interaction with a high repelling force [9].

The velocity of clad particles was not varied in our experiments. However, because of the relatively steep dependence of P_{mp} on particle velocity it is expected that an optimal particle speed can be found for a wide interval of powder sizes and properties.

Very often mixtures of various kinds of powders are used in coaxial cladding to form a final alloy composition directly after cladding. It is also possible to manufacture a composite coating with one sort of powder particles not completely melted. Recently, Matthews [22] has shown that the above calculation could be generalized for more powders fed coaxially as a mixture and the laser powers required for the melting of each of them could be calculated in this way.

15.3 EXPERIMENTAL EVALUATION OF COAXIAL AND SIDE CLADDING PROCESSES

The laser cladding operational window is usually defined in terms of laser beam power P, substrate scanning speed S, and powder feeding rate F, although several additional process parameters like laser beam spot size, laser beam energy distribution, amount and sort of shielding and carrier gas, size, speed, and feeding direction of powder particles, etc., also play a role. From a practical point of view, it is useful to introduce two new process parameters, i.e. the parameter P/S, which characterizes the amount of energy delivered per unit length of laser track, and the parameter F/S corresponding to the amount of new material delivered per unit length of laser track. Single laser tracks can usually be deposited for quite a broad operational range of the processing window. A complete clad layer is formed by successive deposition of single tracks side by side. However, if one wants to build up an optimal clad layer (well-bonded, thick, dense, and without pores and cracks) the single tracks should fulfill certain geometrical features, which can be achieved within a particular processing window.

To study the effects of the principal laser cladding parameters on the tracks we used the graded experiment [23,24]. This approach is based on a continuous change of one process parameter while the others are kept fixed. Single track experiments were performed at all combinations of five different levels of powder feeding rate F and five scanning speeds S realized through the rotation of the substrate bar under the coaxial laser head or through linear movement of the cladding head over the substrate plate for side cladding set-up. In each single track, the laser beam power P increased continuously from minimal to maximal value. In brief, 25 laser tracks were performed to explore the whole processing window for both cladding set-ups. Chemical compositions of materials used in our cladding experiments are summarized in Table 15.1.

Table 15.1 Chemical composition of clad powders and steel/cast iron substrates

Material	Form	Element (wt%)											
		Ni	**Cr**	**Si**	**B**	**Fe**	**Mn**	**Co**	**Mo**	**W**	**C**	**V**	**Cu**
Metco 19E	Powder	Bal.	16	4	4	4	–	2.4	2.4	2.4	0.5		
Eutroloy 16006	Powder	–	28.5	1.2	–	–	–	Bal	–	4.5	1.1		
Eutroloy 16012	Powder	1.0	29.5	1.2	–	1.0	–	Bal	–	8.5	1.6		
Micromelt 23	Powder	0.28	4.2	0.6	Bal	0.37	0.6	5.0	6.45	1.26	3.1	0.16	
C45 steel	Bar	–	0.20	0.2	–	Bal	0.06	–	0.05	–	0.46		
GG–B	Bar	0.3	2.0	Bal	0.7	3.4	0.5						
CGI	Plate	<0.1	2.5	Bal	0.3	0.45							

The computer-controlled laser cladding system consists of a Metco 9MP powder feeder, a coaxial or side cladding nozzle, a XYZ-Rotation CNC table, and the 2 kW continuous wave Rofin Sinar Nd:YAG laser. The laser beam with top-hat energy distribution characteristic (in focus) was focused above the substrate resulting in a laser beam spot size of 3.0 mm (coaxial cladding) and 3.6 mm (side cladding) in diameter. The computer control allows operating the laser power P during the laser cladding inside an interval of 200–1750 W via a linear change of laser lamps pumping power. Table 15.2 summarizes all the experimental details for all of the grade coaxial and side cladding experiments.

Because we study the laser cladding process using a laser power gradient experiment, the laser power gradient must be "reasonably small" to approach the steady state cladding regime. The linear change of laser power along a single laser track produces the laser power gradient of 6.9 W/mm in the case of the coaxial and 8.8 W/mm in the case of side cladding, respectively. The change of the laser power inside a processing area (beam size diameter) is then in both cases smaller than 35 W, which seems to be a reasonably small value, i.e., not departing too much from a steady state regime.

Fig. 15.4 shows a typical transversal cross-section of one laser track and defines the main geometrical quantities usually employed for a characterization of individual laser track: clad height H (mm), clad width W (mm), clad area above original surface A_c (mm^2), and molten substrate area A_m (mm^2). From these characteristics two other important quantities may be evaluated: dilution D and clad angle α. The dilution $D = A_m/(A_c + A_m)$ quantifies a relative amount of the substrate material that has been molten during the cladding process and mixed with an additional material. Although, for successful cladding some dilution between the coating and substrate is always required to ensure a good metallurgical bond; the fact that the high dilutions may degrade coating properties requires that it stays reasonably low. In practice the clad angle α is required to be large enough to avoid inter-run

Table 15.2 Variation of processing parameters in graded coaxial and side laser cladding experiments

Set-up	Powder	Substrate	Spot size [mm]	*P* range [W]	*S* range [mm/s]	*F* range [mg/s]	Track length [mm]
Coaxial	Metco 19E	C45 steel	3.0	200–1500	1.67–5.67	66.7–167	188
Side	Eutroloy 16006	GG-B	3.6	600–1750	2.0–6.67	33.3–100	130

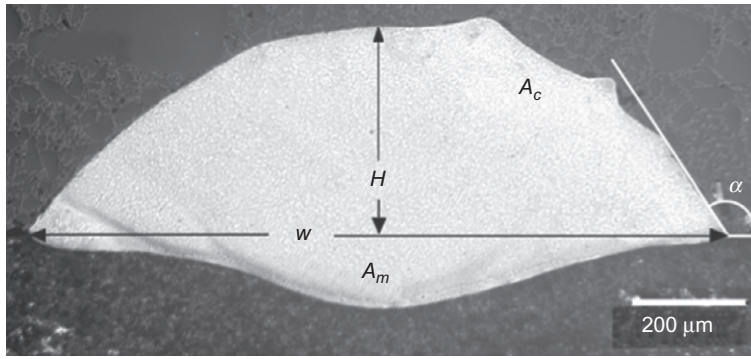


Fig. 15.4 A typical laser track transversal cross-section with main geometric characteristics: clad height *H*, clad width *W*, clad area A_c, molten area A_m, and clad angle α.

porosity [4] creation in the coating, while overlapping individual clad tracks. To avoid the systematic errors and considerable scatter of data an assumption is often made that the transversal cross-section of the laser track is a part of circle [25]. The clad angle α can be calculated from laser track width W and laser clad height H as: $\alpha = 180 - 2\arctan(2H/W)$ [26]. Experimental evaluation of the features of the laser clad track, like the shape of the molten zone and the dilution requires a cross-sectioning. For the recording of all geometrical features, the single laser tracks were cross-sectioned at regular intervals. The samples were mechanically polished and chemically etched for metallographic observations. A corresponding value of the energy of laser beam at each sectioned surface was assigned using a known value of linearly increased pumping power and a laser calibration curve [27], which relates the pumping power and the Nd:YAG laser beam output power.

15.4 STATISTICAL RELATIONS BETWEEN PROCESSING PARAMETERS AND LASER TRACK GEOMETRY

The laser cladding process is based on heat transfer among the laser beam, the substrate, and the powder, and mass transfer between the powder flow and the molten surface. Therefore, the investigation of the process can be performed based on so called combined parameters [28]. Two quantities are fundamental: the amount of powder provided per unit length of the laser track F/S and the total heat input per unit length of the laser track P/S. Fig. 15.5 brings the laser track cross-section map of coaxial cladding of Ni-based powder on C45 steel substrate varying P and F/S on vertical and horizontal axes, respectively. The similar map for side laser cladding of

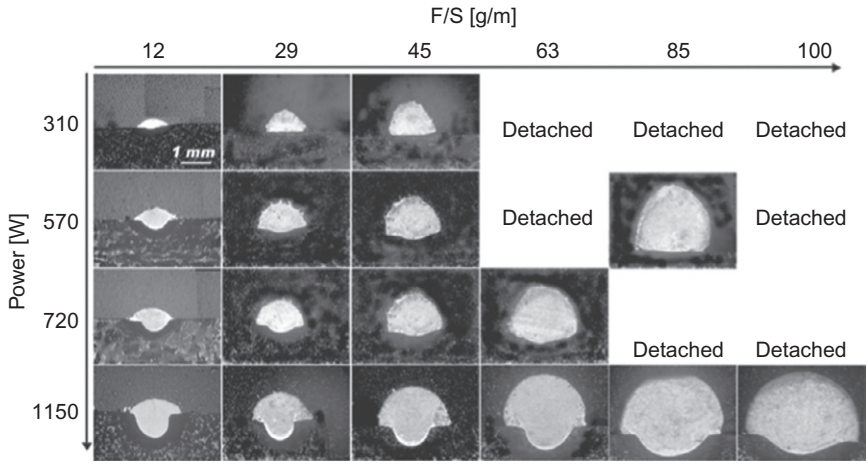


Fig. 15.5 Laser track transversal cross-section map for coaxial laser cladding of Ni-based powder on C45 steel substrate.

Co-based powder on cast iron substrate may be found elsewhere [29]. These maps clearly demonstrate some relevant aspects of the process parameters on the single clad track geometry.

First, the robustness of the process is observed, which produces the laser track within a very wide interval of laser cladding parameters. For instance, the clad area A_c is changed from $0.2\,\text{mm}^2$ for the most delicate laser track located at the left upper corner to more than $4\,\text{mm}^2$ for the largest one at the right lower corner in Fig. 15.5. Such an increase cannot simply be explained through the increase of in the amount of clad material delivered per unit length F/S, because this quantity increases only eight times. A substantial increase of powder-clad efficiency must be concluded. Observing the behavior of the clad height in Fig. 15.5 one may conclude that H mainly depends on the F/S parameter, while the laser power has a small impact on this quantity. On the other hand, the clad width is changed along both axis directions in Fig. 15.5. Cladding profiles above the diagonal from left/up to right/down corner of Fig. 15.5 are characterized by a small melting zone A_m and therefore also by a low value of dilution D. At higher values of F/S and low laser powers, no good bond is created and that leads to the detaching of the clad track from the substrate. In these cases, the attenuation of the heat input into the substrate, due to the powder shielding effect and high speed of the substrate, is so strong that the cladding process is realized under conditions described in area *II* in Fig. 15.3. Further detailed observation of

Fig. 15.5 leads to the conclusion that the depth of the substrate melt area is mainly determined by the laser power *P*.

In order to quantify the above-mentioned qualitative observations, the dependence of laser track characteristics on the main laser cladding parameters were statistically investigated for the both coaxial [30] and side cladding set-ups [29]. As an example of these studies Fig. 15.6 summarizes

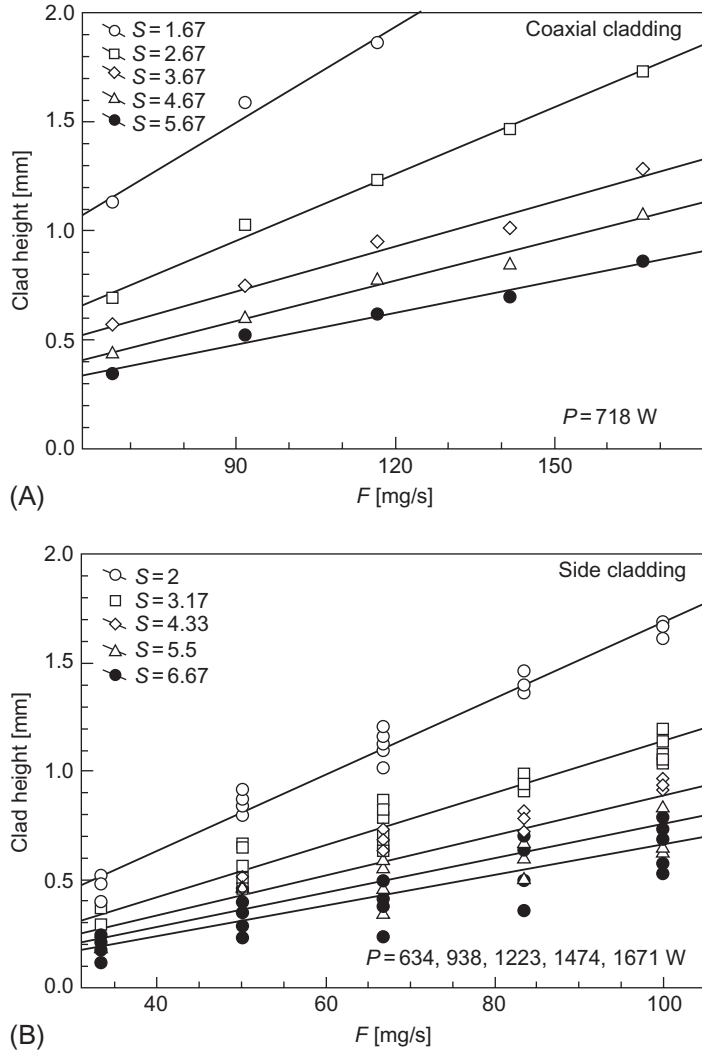


Fig. 15.6 Dependence of laser track height on feeding rate: (A) for one value of laser power *P* = 718 W during coaxial cladding; (B) for all inspecting values of laser power during side cladding.

the dependence of the laser track height H on the processing parameters. Fig. 15.6A shows almost a linear increase of the clad height with increasing feeding rate F for 5 different scanning speeds S (mm/s) just for one laser power $P = 718$W during coaxial cladding. Laser clad heights close to 2 mm can be easily achieved by choosing higher feeding rates and slower scanning speeds. Of course, some points with the highest values of F and the lowest values of S are missing in Fig. 15.6A because no metallurgical bond is formed due to the strong powder shielding effect, as mentioned earlier. A detailed statistical analysis revealed that the clad height H depends mainly on the feeding rate F and on the scanning speed S. The laser power does not play an important role. The same behavior was observed for side cladding set-up during laser cladding of Co- based powder [29]. Fig. 15.6B shows the dependence of laser clad height H on powder feeding rate F for different laser beam scanning speeds S and for all laser powers from 634 to 1671W. It may be concluded that similar linear dependences occur and that the laser power P may be considered as a "weak parameter" in influencing laser clad height. In the next step of our analysis we searched for a combined parameter derived (in this case) only from F and S on which H depends linearly. It was found that for both the coaxial and side cladding set-ups, clad height can be statistically described as a linear function of combined parameter F/S. Here we demonstrate this fact only for side cladding set-up in Fig. 15.7. The high value of the linear regression coefficient $R_s = 0.97$ in Fig. 15.7A confirms such a conclusion together with the normal probability plot of residuals for this statistical model shown in Fig. 15.7B. The value of linear regression coefficient for the same model applied on clad heights in coaxial cladding experiments was $R_c = 0.97$ with a similar character of residual plot as shown in Fig. 15.7B.

A similar statistical analysis was performed for all other parameters of laser track: track width W, clad area A_c, molten area A_m, clad angle a, dilution D, and powder efficiency P_e for both cladding set-ups. The combined parameter for each quantity was searched at first in a form close to the parameter already found for side laser cladding by Felde et al. [31]. When the correlation coefficient was smaller than 0.9 or the distribution of residuals did not show a Gaussian behavior, the other combined parameter was searched. Fig. 15.8 shows the statistical correlations between determined combined parameters and A_c—clad area (Fig. 15.8A) and W—clad width (Fig. 15.8B) in the case of coaxial and side cladding, respectively. These two examples are shown because of their highest and lowest value of correlation coefficients. The clad area A_c is controlled by the same $\sqrt{P} \cdot F / S$

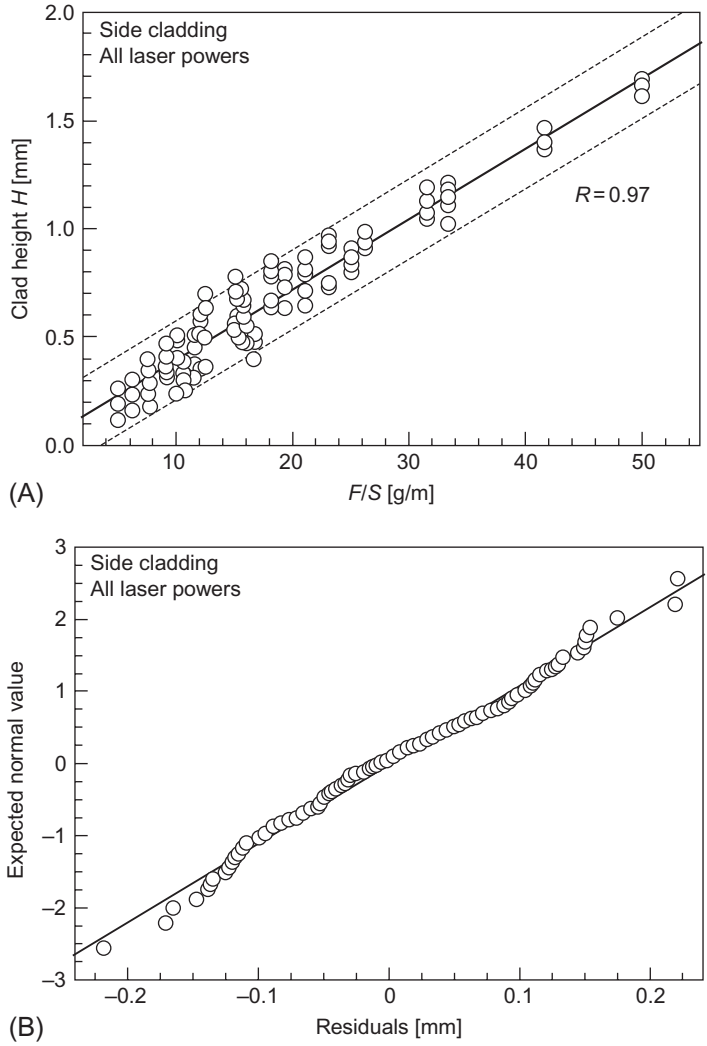


Fig. 15.7 (A) Dependence of clad height on value of combined parameter *F*/*S* and its linear fit with 95% confidence interval *(dashed lines)*; (B) normal probability plot of residuals for linear model presented in (A).

parameter with the relatively high correlation coefficient for both; coaxial ($R_c = 0.99$) and side ($R_s = 0.98$) cladding set-up. On the other hand, only a weak correlation coefficient $R_s = 0.90$ was found for $P / \sqrt{S}$ parameter, which controls the laser track width W during the side cladding. For the coaxial cladding set-up, the same parameter was detected as controlling one with a higher regression of $R_c = 0.95$.

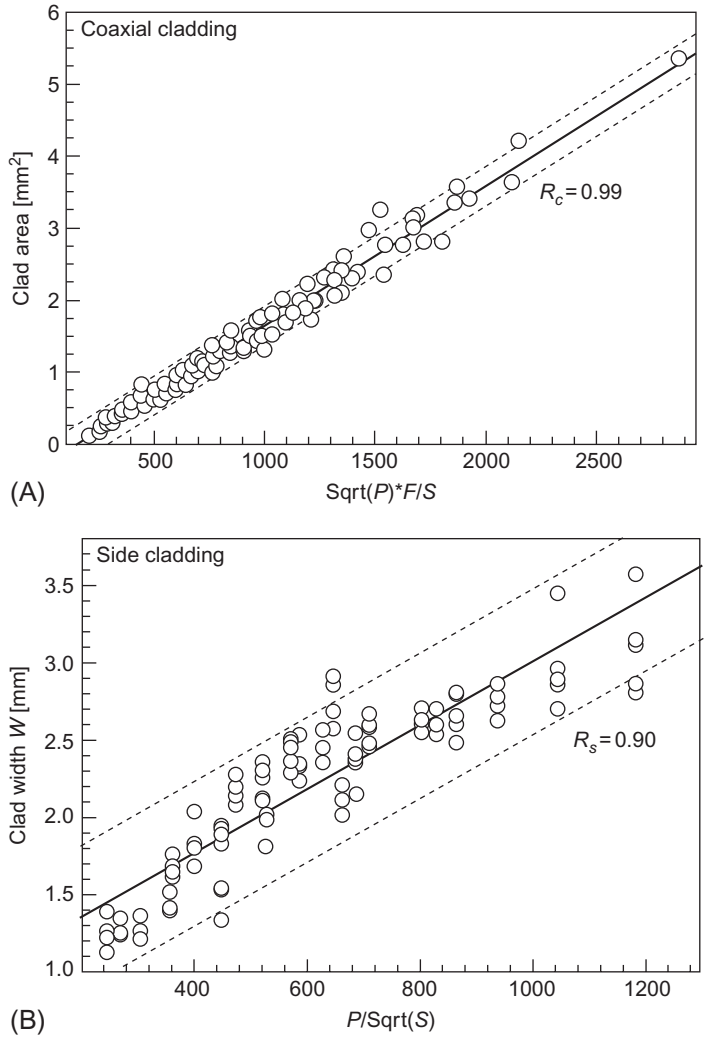


Fig. 15.8 (A) Dependence of clad area on value of combined parameter for coaxial cladding set-up and its linear fit with 95% confidence interval *(dashed lines)*; (B) Dependence of clad width on value of combined parameter for side cladding set-up and its linear fit with 95% confidence interval *(dashed lines)*.

The complete results of these statistical studies are summarized in Table 15.3, where the combined parameters with the highest regression coefficients are shown for all seven studied laser track quantities and for both the side and coaxial cladding set-ups. Combined parameters found for the coaxial cladding set-up by Felde et al. [31] are also noted for the sake of comparison.

Table 15.3 Combined laser cladding parameters that show linear correlations with geometrical characteristics of laser tracks for side and coaxial laser cladding set-up and their corresponding regression coefficients

	Side cladding		Coaxial cladding		Side cladding
Quantity	**Combined parameter**	R_s	**Combined parameter**	R_c	**Felde et al. [31]**
H	F/S	0.97	F/S	0.97	$\sqrt{P \cdot F / S^2}$
W	$P / \sqrt{S}$	0.90	$P / \sqrt{S}$	0.95	–
A_c	$\sqrt{P} \cdot F / S$	0.98	$\sqrt{P} \cdot F / S$	0.99	–
A_m	$P^2 / \sqrt{S}$	0.98	$P / \sqrt[3]{F \cdot S}$	0.95	–
α	$F / \sqrt{P \cdot S}$	0.94	S/F	0.90	S/F
D	$\ln\left(P / F \cdot \sqrt{S}\right)$	0.94			
	$\ln\left(P \cdot \sqrt{S / F}\right)$	0.90	$\sqrt{P \cdot S / F}$	0.92	$P\ S/F$
P_e	$\ln\left(P^2 / \sqrt{F}\right)$	0.94	$P\sqrt{F / S}$	0.91	–

Combined parameters found for coaxial cladding set-up by Felde et al. [31] are also noted.

It is interesting to note that the parameters found for laser clad height H, laser clad width W, and clad area A_c are the same for side and coaxial cladding. Although the regression coefficient for W during side cladding is relatively low ($R = 0.9$), we still prefer $P / \sqrt{S}$ as a combined parameter which controls laser track width because of its simplicity and consistency with the coaxial laser cladding case. The molten area A_m shows a little simpler parameter $P^2 / \sqrt{S}$ for side cladding in comparison with coaxial cladding. It depends only on two main laser cladding parameters with a correlation coefficient exhibiting an even higher value (0.98 against 0.95). However, the parameters for the rest of laser track characteristics, clad angle α, dilution D, and powder efficiency P_e, were found to be more complex in the side cladding process than in the coaxial one.

For a more in-depth discussion about the possible origin of these complex parameters, which control geometric shape, amount of molten material in substrate, dilution, and powder efficiency we refer to the work of de Oliveira et al. [30]. It appears that the basic laser track characteristics such as laser track height H, laser track width W, and clad area A_c are controlled by the same combined parameters for side cladding as for coaxial cladding and that the way in which the powder is delivered does not play an important role. A more complex situation is observed for the rest of the laser track characteristics because more physical phenomena are involved. It is interesting to note that for coaxial cladding, the highest value of powder efficiency was observed at about 50%, but for the side cladding set-up the maximal

value of this quantity approaches 90%. This is due to a better focusing of the powder stream to the molten area from the side and is also due to an easier collection of temporarily unused powder just in front of the laser melt pool.

In the application of the laser cladding process, the real coating is formed by an overlap of single laser tracks deposited side by side with a displacement, which minimizes the roughness caused by the "hills and valleys" profile formed by the individual laser tracks. In practice, a displacement of 2/3 of single laser track width between subsequent laser tracks is often used. Such an overlap creates a coating which is usually 20%–35% thicker than the height of a single laser track. The dilution is substantially reduced in comparison with single laser track dilution because during cladding with overlapping tracks, a substantial part of the laser beam energy is consumed in the remelting of the clad material at the side in the previous laser track [4].

In our thick coatings cladding experiments we always used a 33% overlapping of the laser tracks and we found that the dilution drops from its original value observed in the first laser track to a new "stable" value after three clad tracks. This new reduced value of dilution depends mainly on a used laser power and varies between 30% and 60% of the original value observed in the first laser track.

Based on these findings, it is possible to construct a so-called laser cladding processing map, which relates basic geometrical properties of cladding with their processing parameters for both the side and coaxial laser cladding process. Here we will only show such a map for side cladding of co-based powder on cast iron substrate but a similar map was constructed on the same principles for coaxial cladding of Ni-based alloy on steel substrate [30]. Fig. 15.9 represents such a map with S/F parameter on the horizontal axis and P parameter on the vertical axis. The points inside the map show all combinations of experimental parameters used in measurements and statistical analysis. Because of the linear statistical relation between H and F/S, the second horizontal axis (upper) may be drawn for H and the clad height may be directly deduced for each combination of experimental conditions. It should be noted here that this height H represents the height of individual laser track and not the final thickness of the coating, which is always slightly thicker depending on the overlap. The linear relation between A_c and the parameter $\sqrt{P} \cdot F / S$ allows parabolic-dashed isolines, which connect the experimental points with the similarly indicated values of clad areas A_c. To also incorporate the clad angle and the dilution into this laser cladding map a small modification of best combined parameters presented for these quantities in Table 15.3 must be made. For the

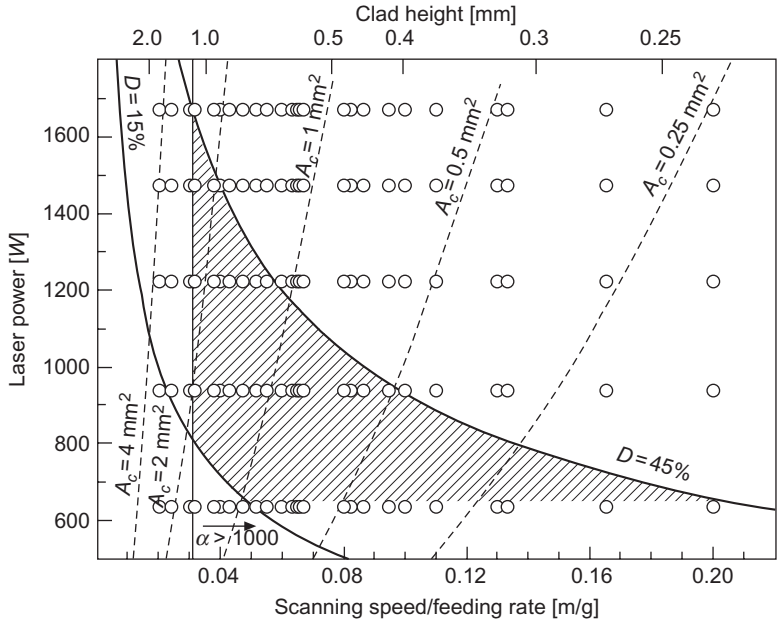


Fig. 15.9 Laser processing map for side laser cladding of Co-based alloy powder on gray cast iron substrate in *P* vs. *S/F* representation. Data points indicate values of processing parameters of analyzed laser track cross-sections. Vertical solid line corresponds to the condition for clad angle required for continuous coating. Two solid hyperbolic type lines mark out the area of acceptable dilution and crosshatched area shows the window, where an optimal clad layer can be formed. Dashed curves are isolines with denoted values of clad area A_c.

clad angle α the parameter S/F, which is preferred for coaxial and other side cladding set-up, is more appropriate to incorporate into Fig. 15.9. However, a relatively low correlation coefficient (only $R = 0.86$) was found for this parameter in the side cladding case. Therefore, the vertical line on the laser cladding processing map close to value $S/F = 0.03$ m/g marks only an approximate limit for $\alpha < 100°$ value [31] causing a so-called inter-run porosity. As the second parameter for dilution in Table 15.3 also contains the S/F parameter, two solid hyperbola-like curves are depicted with constant dilution $D = 15\%$ and 45% respectively. The area between these two lines represents the processing window of acceptable dilutions for laser clad coatings (~5%–25%). Together with the condition for clad angle and with respect to the experimentally explored area, the space of processing parameters for a successful formation of laser coating may be marked by the crosshatched area in Fig. 15.9.

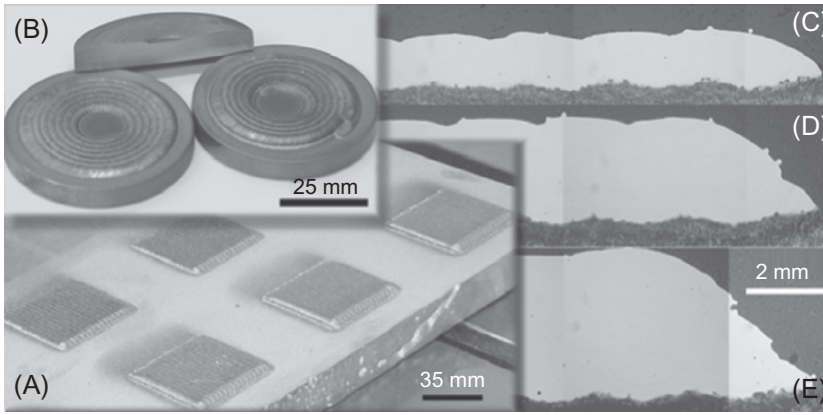


Fig. 15.10 Eutroloy 16006 (Co-based) coatings on CGI substrate created by the simple overlapping of subsequent (A) linear and (B) spiral laser tracks. As demonstrated on the perpendicular cross-sections the cladding of new layers may increase the coating thickness. (C) Single, (D) double, and (E) triple layers are shown with a thickness of 1, 2, and 3 mm, respectively.

This type of empirical laser cladding processing map may be used as a guide for the first "educated guess" and also for the subsequent "tuning" of optimal laser processing parameters during laser cladding of continuous coatings. Fig. 15.10 shows Eutroloy 16006 Co-based coating prepared by the side laser cladding process on compacted graphite iron substrates. The coating with a thickness of about 1 mm may be created in a single clad layer without any macro-pores and cracks (Fig. 15.10C). Laser cladding of a second and third layer allows the forming of thicker coatings, as Fig. 15.10D and E shows. However, when thicker coatings (>2 mm) were placed on a relatively stiff substrate (a 15 mm thick plate in Fig. 15.10A), cracking inside the coating or in the substrate (initiated from a side of coating/substrate interface) was sometimes observed. Fig. 15.10 also shows a possible geometrical variability during the overlapping of laser tracks. Squared coated areas were formed via overlapping of individual lineal laser tracks (Fig. 15.10A) and circular coatings result from a continuous spiral cladding (Fig. 15.10B).

15.5 MICROSTRUCTURAL CHARACTERISTICS AND PROPERTIES OF THICK METALLIC COATINGS

Geometry of the individual laser tracks and the final thickness of the coating are only two of the features that are important for functionality. The microstructure of the coatings as well as the heat affected zone in the substrate

are also important for functional properties of the laser clad coatings. These coatings usually exhibit excellent metallurgical bonding between clad of the layers and the substrate. Fine γ-Co dendrites surrounded by eutectic from γ-Co and hard carbides phases are characteristic for the microstructure of the laser clad co-based alloy coatings [32,33]. Near the coating/substrate interface the microstructure gradually changes, with a coarsening of eutectic and refining of dendrites. In the case of cast iron substrates, round non-dissolved residues of graphite flakes are dispersed in the microstructure. Inside the heat affected zone under the coating, a microstructure characteristic for nonmelted gray cast iron hardened by laser surface treatment [34] is observed. A sharp border line is present between the austenitized zone (AZ) and the non-transformed substrate material. In the upper part of AZ, where all cementite plates from originally pearlitic microstructures were successfully dissolved in austenite, lengthy martensite plates were formed. In the lower part of AZ, where remnant cementite plates still separate austenitic zones, only fine martensite is formed. This microstructure is formed because of high heating rates during the laser treatment of cast iron with a pearlitic matrix and due to the direct transformation of ferrite to austenite [35]. The presence of martensitic plates generates a relatively high hardness in this part of the heat affected zone.

Interesting microstructural and property features were observed on co-based coatings with higher content of tungsten [32]. The substantial fluctuations in hardness detected near laser track overlap areas were caused by two different reasons. The first drop is due to a different thermal history in overlap area where the tungsten forms larger W rich carbides with surrounded areas depleted of tungsten. Microstructural softening was detected in these areas with a local hardness value drop from 700 HV0.2 to about 620 HV0.2. The second, smaller drop in hardness is from a local increase of Fe content originated from iron substrate. The important role of internal interfaces created during the formation of co-based coatings by the overlapping of individual laser tracks could be directly observed by orientation imaging microscopy (OIM) [36] based on electron back scatter diffraction observations in a scanning electron microscope. Fig. 15.11 clearly demonstrates the complexity of the microstructure formed in overlapping areas of the Eutroloy 16012 coating created with a cladding speed of 15 mm/s and a 33% of overlapping factor. The upper part of Fig. 15.11 shows a transversal cross-section with five overlapped laser tracks and the lower part shows four different longitudinal cross-sections made through one track at different places marked by vertical lines in the upper image. It is natural to expect

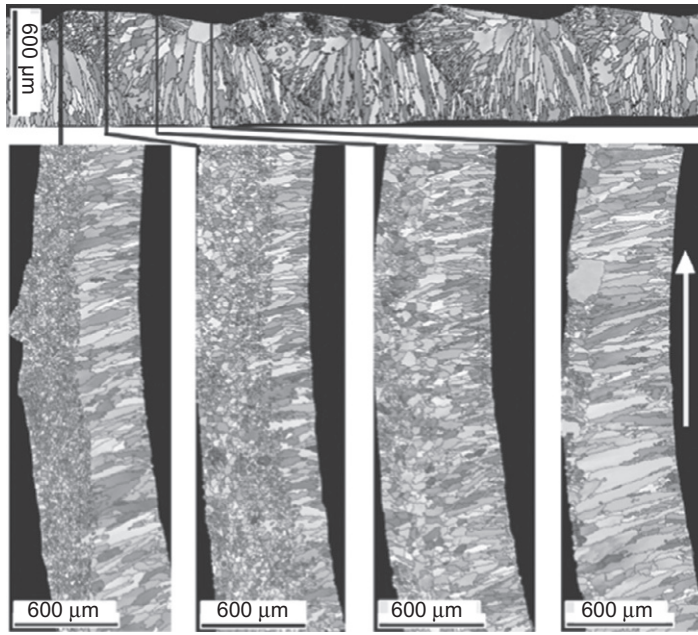


Fig. 15.11 Microstructure of Eutroloy 16012 coating studied by OIM. Inverse pole figures of Co grains on transversal (up) and different longitudinal (down) cross-sections in corresponding marked lines.

that these local microstructural features such as a sharp change in grain size or grain orientation might substantially influence the local properties of the coatings.

An open question still remains about how processing parameters (mainly laser beam scanning speed) may influence the formation of these sharp interfaces. The importance of laser beam scanning speed for the final microstructure of co-based coatings is evident from OIM observations performed on single laser tracks prepared with different laser beam scanning speeds. Fig. 15.12 shows the substantial differences in microstructures formed during the "slow" and "fast" cladding processes. The size, shape, and crystal orientation of individual Co grains are clearly visible in these observations. Laser track solidified at a slow scanning speed shows almost equiaxial grains on transversal cross-section (Fig. 15.12A), whilst the grains observed in the central part of the laser track prepared with high scanning speed are strongly elongated in the vertical direction (Fig. 15.12B). However, the longitudinal cross-sections made at the center of both laser tracks revealed that for both slow and fast scanning speeds, elongated grains are characteristic; but in the case of slow scanning speed, the axes of elongated grains are slanted more

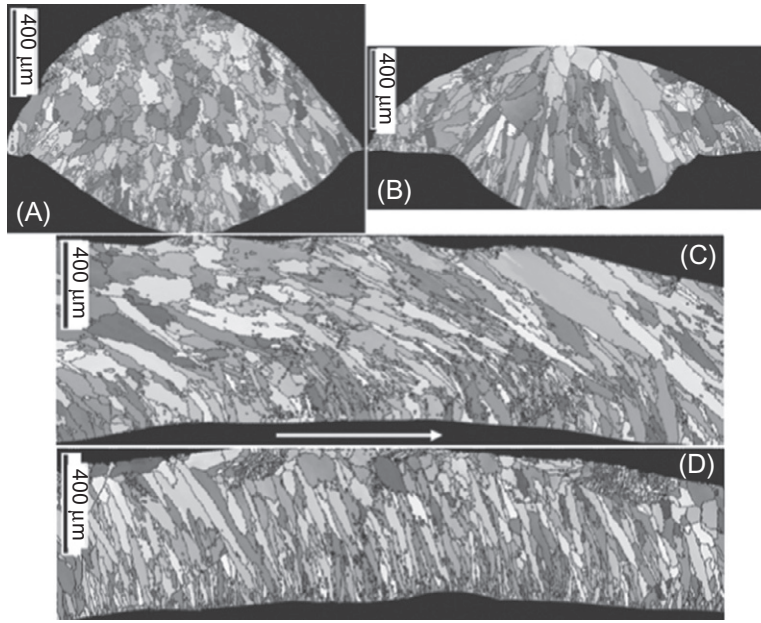


Fig. 15.12 OIM characterization of the size and orientation of Co grains at the transversal (A) and (B) and longitudinal (C) and (D) cross-section of single laser track made at 1 mm/s (A) and (C) and 15 mm/s (B) and (D) laser beam scanning speeds.

towards the cladding direction. This fact results in an observation for the transversal cross-section, where equiaxial grains with small dimensions are observed for slow cladding speed. The growth direction of co-based grains is clearly determined by the shape of solidification front [33]. This shape can be seen in Fig. 15.12C, as a series of small dots corresponding to the points with lower quality or non-indexable Kikuchi patterns originated from small inclusions or impurities segregated at the solid/liquid interface at the same time. From these observations one may conclude that laser cladding of thick metallic coatings could result in strongly textured and anisotropic microstructures and therefore structural observations not only in transversal but also in longitudinal cross-sections are required to reveal this anisotropy.

In the case of cladding, MicroMelt 23 tool steel coatings on different steel substrates for the above-mentioned microstructural anisotropy was not observed. The MicroMelt 23 powder used in laser cladding experiments shows a very stable behavior during feeding and laser cladding. It offers a relatively broad laser processing window in which it provides a regular single laser track shape and homogeneous pore-less coating after a 33% overlapping of consecutive laser tracks. Steel substrates with different

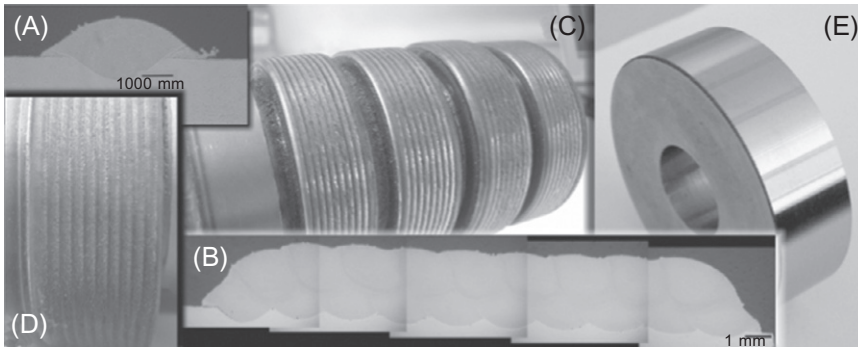
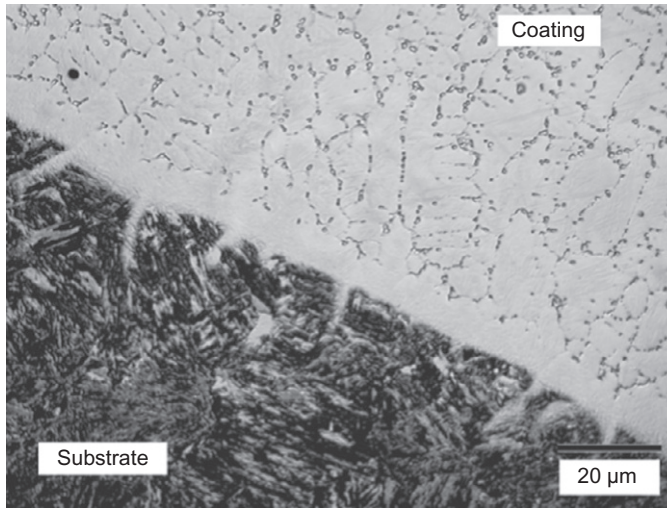
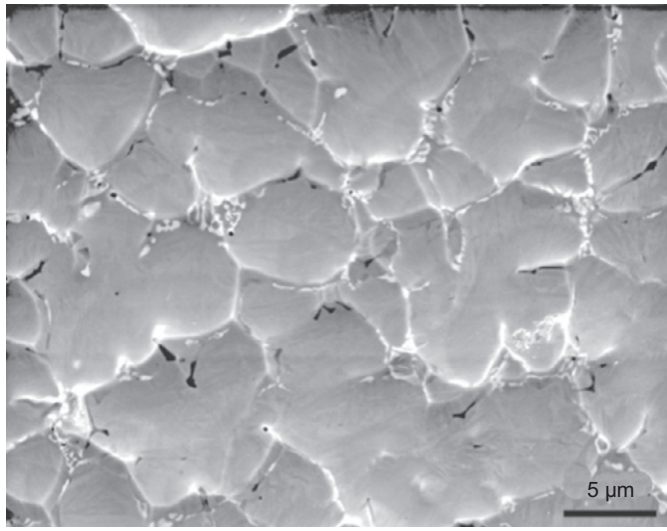


Fig. 15.13 Laser cladding of tool steel powder on steel substrates. (A) 1 mm height single laser track profile on transversal cut; (B) 3 mm thick coating prepared by 33% overlapping of individual laser tracks in two cladding layers; (C) and (D) 20 mm wide rings on 60 mm diameter bar coated by single and double layer laser cladding; (E) coated ring from bar on (C) after cutting, machining, and grinding.

compositions (C45, 100Cr6, and bearing steel) and geometries were tested. Fig. 15.13 shows the profile of an individual laser track (Fig. 15.13A) as well as a double layer coating (Fig. 15.13B). The individual laser track height of about 1 mm was achieved when a 1750W laser power, 5 mm/s scanning speed, and 150 mg/s powder feeding rate were used as main laser processing parameters during cladding on 60 mm for a diameter C45 steel bar. The 33% overlapping of such laser tracks provides 1.3–1.5 mm thickness of single clad layer and 2.4–3.0 mm thick double clad layer. A very low level of internal porosity is evident from microstructural observations on different layer cuts, but also from the surface smoothness after the machining, grinding, and finishing of the coating surface for final use (Fig. 15.13E). We faced some trouble with inter-run porosity between the very first laser tracks when relatively small substrates were used (8 mm in diameter bars) and when the laser power must be reduced due to the fast heating of the whole substrate piece. Fig. 15.14 shows the microstructure of the laser coating near the coating/substrate interface as well as details of the microstructure in the middle of the coating. The microstructure inside the laser track is very homogeneous with fine (5–15 μm) iron-based dendrites. Dendrite boundaries and interdendritic space is full of carbide precipitates and a hard eutectic interdendritic phase. This microstructure is homogeneously distributed through the whole coating, including inside and close to the laser track overlapping region, and the overall composition of the clad alloy measured by SEM-EDS is 4Cr-5W-3Mo-85Fe-3V (in wt%) that corresponds quite well with the composition of the original used powder (see Table 15.1). The interface between coating and substrate is relatively sharp (~10 μm) and it



(A)



(B)

Fig. 15.14 The microstructure of MicroMelt23 laser clad coating on C45 steel substrate. (A) Optical microscopy of the microstructure observed near coating/substrate interface (Nital etching); (B) SEM secondary electrons image of the coating microstructure.

consists of the thin iron-based layer formed by planar solidification [28] with local perturbations into the substrate microstructure.

The similarity between the X-ray diffraction spectra of the powder and the clad layer [37] suggests that the phase composition of the original alloy is conserved, i.e. also inside a clad layer, which means that the

change melt composition due to a dilution from the substrate does not influence the phase composition of the coating. However, less content of the austenitic iron phase after laser cladding is evident. Analysis of X-ray diffraction experiments and field emission gun electron microscopy observations using both secondary electron and back scatter electron detectors combined with EDS measurements leads to the conclusion that microstructural dendrites consist of martensite and retained austenite, while hard interdendritic Co_6W_6C and FeVSi phases were formed at the end of the solidification process [37].

Oriented image microscopy is also a powerful tool for phase analysis by scanning electron microscopy. We used it to quantify the amount of the martensite inside this coating and to visualize austenite and martensite grains orientations. Fig. 15.15 summarizes the results of OIM observations from one small place situated at the center of the cross-section from a single laser track. Unfortunately, a demanding surface polishing procedure [38] requiring precise ions polishing restricts more extensive OIM observations at different coating positions. Fig. 15.15A shows a SEM observation of the surface of mechanically polished tool steel coating followed by 120 min of polishing using 4.5 keV Ar^+ ions. The surface profile is characterized by a system of hills and valleys with a local roughness of $R_a = 41$ nm. Black areas on the image quality (IQ) map (Fig. 15.15B) indicate places where a highly tilted electron beam (75°) is shielded due to the local surface roughness and no indexable Kikuchi pattern is generated. OIM maps on Fig. 15.15C and D denote the areas, from which corresponding Kikuchi patterns were recognized as austenite and martensite, respectively. The same gray level on these maps belongs to the same grain of the corresponding phase, whereas the black area corresponds to the other phase. The conclusion concerning a presence of 45% of martensite in retained austenite may be drawn together with the validity of Kurdjumov-sachs orientation relationship between these two phases, as the distribution of misorientation angles between martensite and austenite grains plotted in Fig. 15.15E testifies.

Hardness, as an important characteristic for strength and wear performance, was measured to quantify the quality of the coatings. Fig. 15.16 characterizes the depth profile of Vicker's hardness measured by three close indents (see the insert in Fig. 15.16) through the cross-section of double layer tool steel laser coating on C45 steel substrate bar 60 mm in diameter. It may be concluded that in each clad layer, a characteristic decrease in hardness value exists, from the value of about 820 HV0.4 measured at the

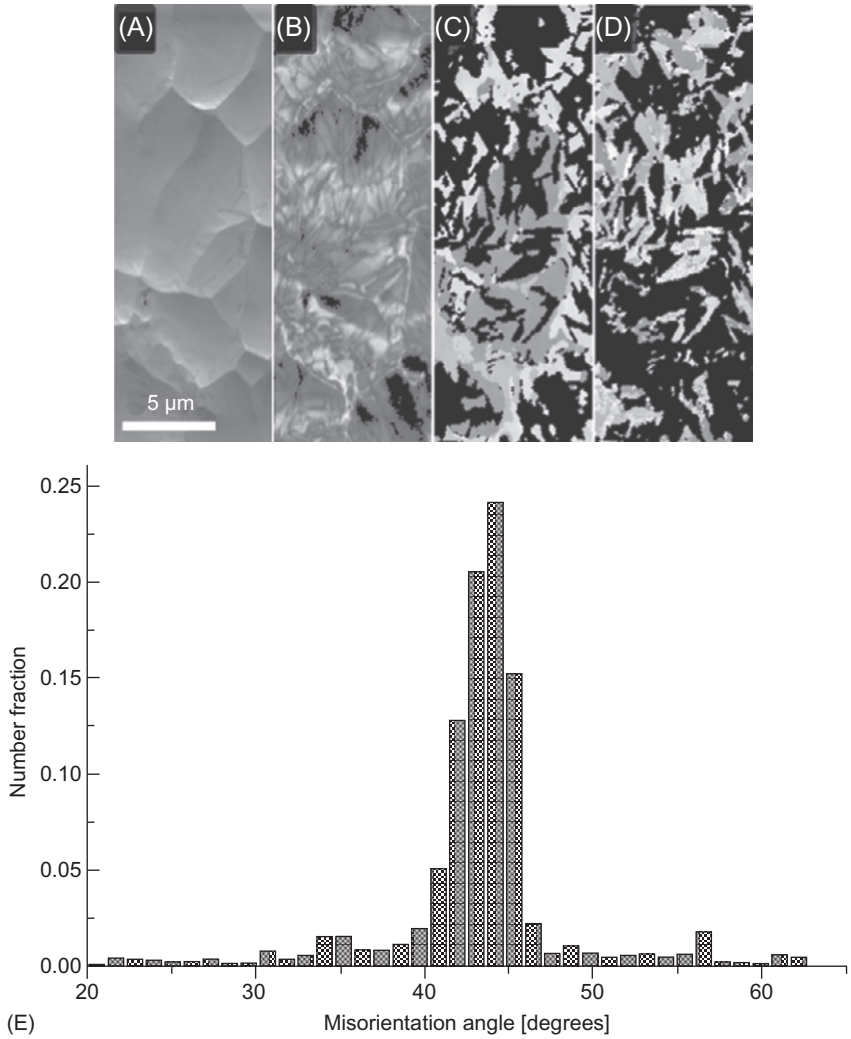


Fig. 15.15 OIM observations of tool steel coating microstructure. (A) SE image of the surface after precise ion polishing; (B) image quality image from the same place; (C) OIM image of austenite phase; (D) OIM image of martensite phase; (E) misorientation angle between martensite phase inside austenitic grains.

top of the layer to the value of about 730 HV0.4 measured at its bottom. Consequently, quite a sharp discontinuity in hardness value exists at the border of these two layers marked by the dashed line on the insert. Naturally, another sharp hardness change is detected at the coating/substrate interface (marked by a dashed line as well), because of a small hardening effect in heat affected zone (HAZ) of a massive C45 steel substrate.

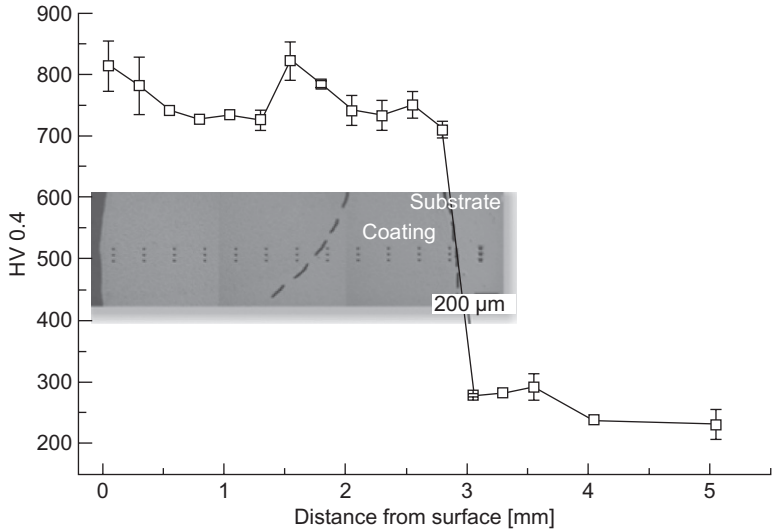


Fig. 15.16 Microhardness profile on transversal coating cross-section plotted as an average value measured from three indents at the same depth of 2.8 mm thick double layer coating. Dashed line denotes microstructural boundary between laser tracks made in the first and the second laser cladding layer and between the coating and substrate itself.

Another type of the hardness profile may be observed on the single-layer coating prepared on the relatively small (8.5 mm in diameter) bearing steel bar as Fig. 15.17 clearly indicates. In all four measured vertical directions (Fig. 15.17B), there is no substantial hardness decrease inside the coating, as was observed previously (Fig. 15.17). A substantial hardening effect in HAZ is also present, which moderates the hardness drop inside the substrate material. Due to a small angle between the cutting plane and the laser cladding direction, Fig. 15.17A maps a change of coating thickness within one revolution during laser the cladding process and it also scans the coating microstructure between two adjacent laser tracks. The graph insert in Fig. 15.17A shows clearly that a correlation exists between the coating thickness, which varies between 780 and 980 µm, and the coating hardness is measured at 200 µm depth.

The primary parameters controlling the size of the grains in austenite/ferrite transformations are the cooling rate and the amount of precipitates formed in the interdendritic spaces. When the melt is rapidly cooled, austenite does not have the time to transform into ferrite and due to the oversaturation of carbon, a diffusionless transformation takes place resulting in martensite. The resulting microstructure for high cooling rates is then

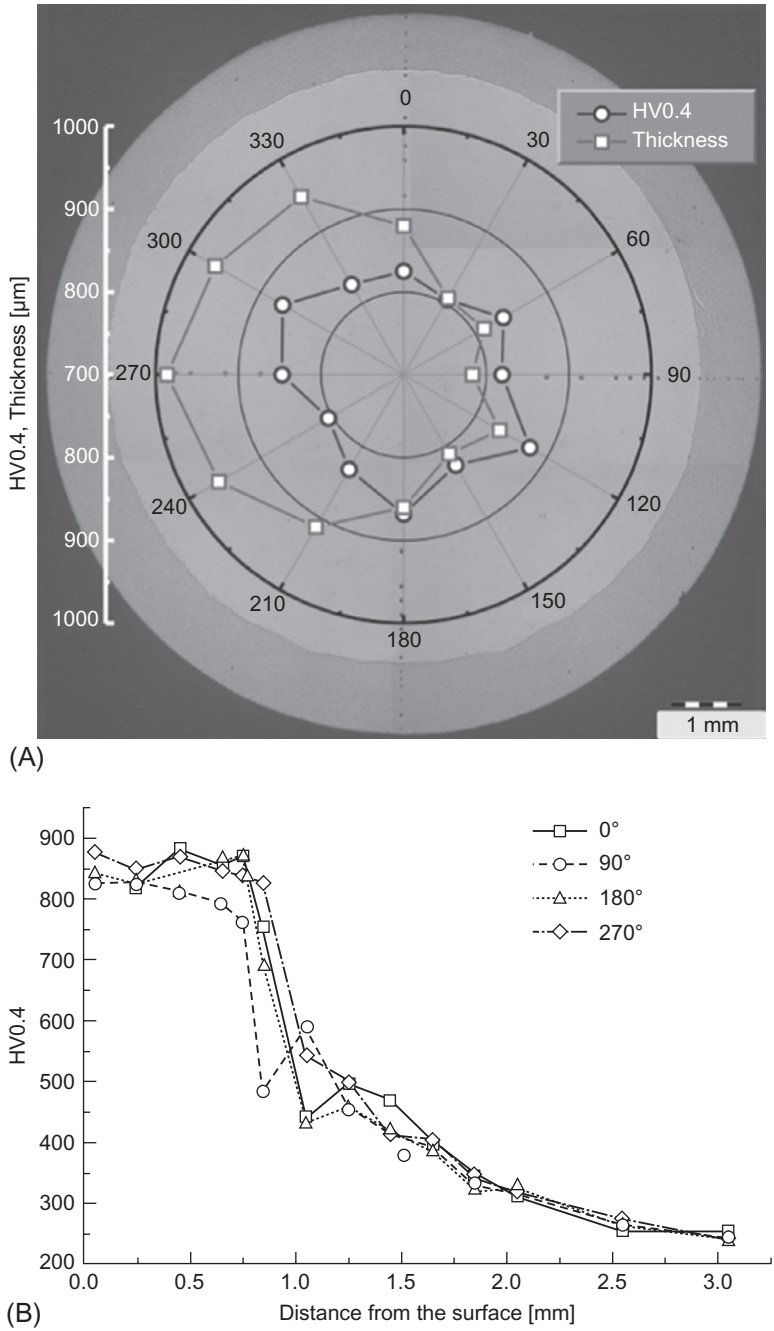


Fig. 15.17 (A) Optical micrograph of longitudinal cross-section of MicroMelt 23 coating on a 8.5 mm bearing steel bar. Insert shows the thickness and the microhardness (measured at depth of 200 mm from the surface) dependence of the coating on the rotation angle. (B) Microhardness profiles of MicroMelt 23 coating and substrate at four different angles.

composed of martensite, retained austenite, and carbides. Because of the high cooling rates in the laser cladding technique, the microstructure consists typically of fine grains, and supersaturated and non-equilibrium phases. However, different hardness profiles detected for coatings prepared at different laser cladding conditions indicates a different content of martensite inside the coating.

Usually, residual stresses detected inside the thick Co-based laser cladding coatings on both: macro [39] and micro [32] scale levels are strong tensile stresses, due to a substantial shrinkage after the solidification. On the other hand, the massive martensitic transformation in this tool steel material is associated with expansion and generation of compressive stress and together with a lower thermal expansion coefficient it results in minor tensile stresses or even in a compressive stress state [37]. This behavior seems to be crucial for the possibility to form the thick coating from this material without cracking, which is often observed when thick and hard coatings from other materials are prepared by laser cladding.

Moreover, the full potential of this tool steel coating with an interesting combination of high toughness, hardness, and wear resistance at elevated temperatures may be achieved, when appropriate thermal treatment recommended for powder metallurgy products [19] is applied on the final laser clad coating.

A few tests were performed to test these laser clad thick coatings. Four different MicroMelt 23 coatings were prepared by laser cladding on a C45 60 mm diameter bar for a rolling contact fatigue test performed at TNO Eindhoven. Thickness of the coatings after machining varied from 0.9 to 2.2 mm. All these coatings passed 10^7 revolutions at extremely high contact stress (2700 MPa) without any failure.

Fig. 15.18 summarizes the results of the wear test experiments when Eutroloy 16006 co-based coated cast iron pins slid on the surface of a cast iron disk coated with the same coating at different temperatures between the room temperature and 525°C [29]. After a certain run-in period in a sliding wear test the pin position registered in the experiment becomes almost linearly dependent on the sliding distance. Therefore, the wear rate can be estimated from the slope of the linear approximation of a very last portion of pin position and from the size of the circular contact area measured by SEM on each pin after tribotest. Fig. 15.18 shows the wear rate as a function of the test temperature together with the value of the mean friction coefficient after the run-in period. A more in-depth study of worn surfaces after the tests [40] reveals the key role of the oxide layer formed in

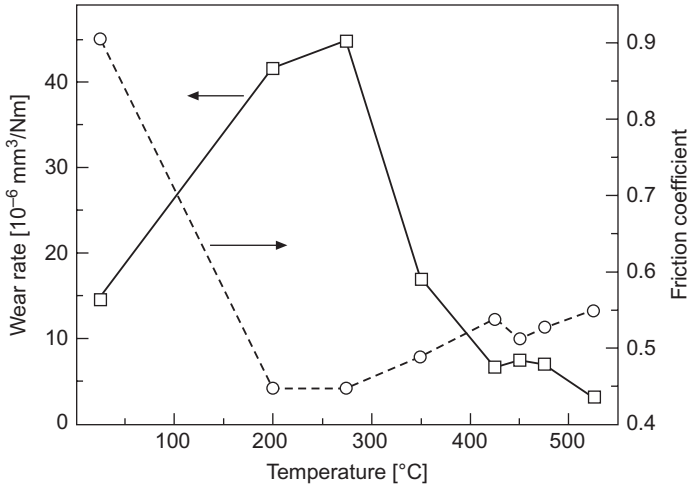


Fig. 15.18 Temperature dependence of wear rate and Cof of Co-base coating prepared by laser cladding.

the contact area. This oxide layer changes the character of sliding contact with increasing temperature and substantially increases wear resistance of co-based coating at elevated temperatures.

15.6 CONCLUSIONS

Influence of the laser processing parameters on final geometry of laser clad tracks was thoroughly investigated. It was shown that for both coaxial and side cladding set-ups the grade experiment in which the laser power is slowly and gradually changed during laser cladding while the other two main process parameters (scanning speed and powder feeding rate) are fixed, substantially reduces the amount of experimental work that is required for a proper study of the processing window. Moreover, from the observed statistical relations between main processing parameters and geometrical characteristics of a laser track, processing maps may be constructed. These maps confirm the robustness of laser cladding technology for Ni-, Co-, and Fe-based metallic coatings on different steel and cast iron substrates. Processing maps may serve as a guide for the first "educated guess" and also for subsequent "final tuning" of optimal laser processing parameters during laser cladding of continuous coatings.

In general, it may be concluded that the main advantage of the coaxial laser deposition lies in its directional independence originated from the rotational symmetry of the set-up. On the other hand, the side cladding

set-up provides a higher powder efficiency and larger processing window that may be achieved due to the possibility of the tuning of a feeding angle and position of a feeding nozzle. Therefore, side cladding may be preferred when a buildup of thick coating is required in one deposit layer just by the overlapping of single laser tracks and when the higher powder efficient process is required. Coaxial cladding dominates when a delicate cladding should be created or in the building of complicated 3D structures.

Formation of crack-free co-based and tool steel Fe-based thick coatings was demonstrated for both cladding geometries on different steel and cast iron substrates. It was confirmed that a substantial anisotropy present during fast solidification also introduces anisotropy in the final microstructure. Moreover, internal interfaces between the coating and substrate as well as between individual laser tracks or coating layers may cause a substantial source of discontinuities in microstructure and functional properties.

Morphology and the grow orientation of crystallographic grains in co-based coatings strongly depend on the speed of the laser cladding process. Crystallographic texture dependence on laser beam scanning speed was also observed. Low speed deposited laser tracks have shown a multiple fiber texture when observed in the transverse cross-section. In the case of fast deposition fiber texture, a processing of axis direction is present.

The microstructure of a laser deposited tool steel is fine grained and dendritic, with a presence of subdendritic martensite grains and retained austenite. The application of MicroMelt 23 powder for cladding of thick layers is very promising due to its high hardness, cracking resistance observed during the deposition experiments, and due to contact fatigue resistance at high contact stresses.

Co-based thick coating was deposited according to the invented processing map on cast iron substrate and tested in dry sliding behavior in the temperature range of automotive engine applications. The wear rate and friction coefficient behave in two different regimes depending on the temperature of the test. From room temperature to 275°C the coefficient decreases and wear rate increases. Above this temperature until 525°C the opposite behavior has been registered, i.e. friction coefficient starts to increase, whereas the wear rate decreases with temperature. The formation of a compact oxide layer on the metal-metal contact above 275°C is responsible for the decrease of friction coefficient and also for the decrease of wear rate.

ACKNOWLEDGMENTS

The work described in this chapter is part of the research program of IOP and M2i. Thanks is due to our collaborators over the years Uazir de Oliveira, Dave Matthews, and Marc de Boer for their stimulating discussions and experimental contribution described in this chapter.

REFERENCES

[1] W.M. Steen, Laser Material Processing, Springer-Verlag, London, 2003.
[2] J.M. Yellup, Laser cladding using the powder blowing technique, Surf. Coat. Technol. 71 (1995) 121–128.
[3] J.C. Ion, Laser Processing of Engineering Materials, Elsevier Butterworth-Heinemann, Oxford, 2005.
[4] W.M. Steen, V.M. Weerasinghe, P. Monson, SPIE 650 (1986) 226.
[5] R. Vilar, Laser cladding, J. Laser Appl. 11 (2) (1999) 64–79.
[6] A.B. Kloosterman, B.J. Kooi, J.T.M. De Hosson, Electron microscopy of reaction layers between SiC and Ti-6Al-4V after laser embedding, Acta Mater. 46 (1998) 6205–6217.
[7] Y.T. Pei, V. Ocelík, J.Th.M. De Hosson, SiCp/Ti6Al4V functionally graded materials produced by laser melt injection, Acta Mater. 50 (2002) 2035–2051.
[8] J.A. Vreeling, V. Ocelík, Y.T. Pei, D.T.L. Van Agterveld, J.Th.M. De Hosson, Laser melt injection in aluminum alloys: on the role of the oxide skin, Acta Mater. 48 (2000) 4225–4233.
[9] J.M. Lin, A simple model of powder catchment in coaxial laser cladding, Opt. Laser Technol. 31 (3) (1999) 233–238.
[10] I. Smurov, Laser cladding and laser assisted direct manufacturing, Surf. Coat. Technol. 202 (2008) 4496–4502.
[11] A. Yakovlev, Bertrand Ph, I. Smurov, Development of 3D functionally graded models by laser-assisted coaxial powder injection, laser-assisted micro and nano-technologies, in: V.P. Veiko (Ed.), Proceedings of SPIE, Bellingham, WA, 2004, p. 220.
[12] A.F.A. Hoadley, M. Rappaz, A thermal model of laser cladding by powder deposition, Metall. Trans. B 23 (1992) 631–642.
[13] J.-M. Jouvard, D.F. Grevey, F. Lemoine, A.B. Vannes, Continuous wave Nd:YAG laser cladding modelling: a physical study of track creation during low power processing, J. Laser Appl. 9 (1997) 43–50.
[14] S. Kumar, S. Roy, Development of a theoretical process map for laser cladding using two-dimensional conduction heat transfer model, Comput. Mater. Sci. 41 (2008) 457–466.
[15] M. Picasso, C.F. Marsden, J.D. Wagniere, A. Frenk, M. Rappaz, A simple but realistic model for laser cladding, Metall. Mater. Trans. B 25 (1994) 281–291.
[16] J. Mazumder, A. Schifferer, J. Choi, Direct materials deposition: designed macro and microstructure, Mater. Res. Innov. 3 (1999) 118–131.
[17] C. Navas, A. Conde, B.J. Fernández, F. Zubiri, J. De Damborenea, Laser coatings to improve wear resistance of mould steel, Surf. Coat. Technol. 194 (2005) 136–142.
[18] S.-H. Wang, J.-Y. Chen, L. Xue, A study of abrasive wear behaviour of laser-clad tool steel coatings, Surf. Coat. Technol. 200 (2006) 3446–3458.
[19] Vanadis, Vanadis 23—Super clean. High performance powder metallurgical cold work tool steel. http://www.uddeholm.com/files/vanadis_23-english.pdf, 2007.
[19a] Y. Fan, Z. Yang, P. Cheng, K. Egland, Y. Lawrence Yao, Numerical and experimental investigation of microstructure evolution and mechanical behavior of steel in laser forming, in: Proceedings of the 23rd International Congress on Applications of Lasers and Electro-Optics, 2004.

[19b] Y. Wang, J.W. Kysar, Y.L. Yao, Analytical solution of anisotropic plastic deformation induced by micro-scale laser shock peening, Mech. Mater. 40 (3) (2008a) 100–114.
[19c] S. Vukelić, Y. Wang, J.W. Kysar, Y.L. Yao, Comparative study of symmetric and asymmetric deformation of Al single crystal under micro scale shock peening, J. Mech. Mater. Struct. 4 (2008a) 89–105.
[19d] S. Vukelić, Y. Wang, J.W. Kysar, Y.L. Yao, Dynamic material response of aluminum single crystal under micro scale laser shock peening, J. Manuf. Sci. Eng. 131 (3) (2008b) 031015-1-013015-10.
[20] D.W. Smith, Powder characterization, Encycl. Mater. Sci. Eng. 5 (1986) 3859.
[21] Metco, Metco 19E Self-fluxing Nickel-Chromium Alloy Powder, 2000. Technical Bulletin #10-042, Sulzer Metco.
[22] D.T.A. Matthews, Surface Engineering: Amorphous Alloys and Nanocrystallinity, (Ph.D. Thesis), University of Groningen, 2008.
[23] P.A. Carvalho, N. Braz, M.M. Pontinha, M.G.S. Ferreira, W.M. Steen, R. Vilar, K.G. Watkins, Automated workstation for variable composition laser cladding—its use for rapid alloy scanning, Surf. Coat. Technol. 72 (1995) 62–70.
[24] R. Vilar, P. Carvalho, R. Colaço, Variable powder feed rate laser cladding applied to combinatorial materials design, in: S. Sudarshan, M. Jeandin, J.J. Stiglich (Eds.), Surface Modification Technologies XVIII, SM International/IOM Communications Ltd, Materials Park, Ohio/UK, 2006, pp. 265–270.
[25] R. Colaço, L. Costa, R. Guerra, R. Vilar, A simple correlation between the geometry of laser cladding tracks and the process parameters, in: J. Mazumder, O. Conde, R. Villar, W. Steen (Eds.), Laser Processing: Surface Treatment and Film Deposition, NATO ASI Series E: Applied Sciences, vol. 307, Kluwer Academic Publishers, 1996, pp. 421–429.
[26] H.-J. Bartsch, Handbook of Mathematical Formulas, Academic Press, New York, 1974.
[27] V. Ocelík, U. de Oliveira, A.H. Pieren, J.Th.M. De Hosson, Thick coating by coaxial laser cladding, in: T.S. Sudarshan, S.V. Joshi, G. Totten (Eds.), Proceedings of the International Conference on Advances in Surface Treatment: Research & Applications, ARCI, Hyderabad, India, 2004, pp. 191–198.
[28] E. Toyserkani, A. Khajepour, S. Corbin, Laser Cladding, CRC Press, London, 2005.
[29] V. Ocelík, U. de Oliveira, M. De Boer, J.Th.M. De Hosson, Thick Co-based coating on cast iron by side laser cladding: analysis of processing conditions and coating properties, Surf. Coat. Technol. 201 (2007) 5875–5883.
[30] U. de Oliveira, V. Ocelík, J.Th.M. De Hosson, Analysis of coaxial laser cladding processing conditions, Surf. Coat. Technol. 197 (2005) 127–136.
[31] I. Felde, T. Reti, K. Zoltan, L. Costa, R. Colaço, R. Vilar, B. Verö, A simple technique to estimate the processing window for laser clad coatings, in: Proceedings from the 1st International Surface Engineering Congress and the 13th IFHTSE Congress, 7–10 October 2002, Columbus, Ohio, ASM International, 2003, pp. 237–242.
[32] U. de Oliveira, V. Ocelík, J.Th.M. De Hosson, Microstresses and microstructure in thick cobalt-based laser deposited coatings, Surf. Coat. Technol. 201 (2007) 6363–6371.
[33] A. Frenk, W. Kurz, High speed laser cladding: solidification conditions and microstructure of a cobalt-based alloy, Mater. Sci. Eng. A173 (1993) 339–342.
[34] V. Ocelík, P.N. Tang, M.C. De Boer, U.O.B. de Oliveira, J.Th.M. De Hosson, Laser surface treatment of grey cast iron for automotive applications, in: J.T.M. de Hosson, C.A. Brebbia, S.-I. Nishida (Eds.), Computer Methods and Experimental Measurements for Surface Effects and Contact Mechanics VII, WIT Press, Southampton, 2005, pp. 221–230.
[35] N. Zárubová, V. Kraus, J. Čermák, Mechanisms of phase transformations during laser treatment of grey cast iron, J. Mater. Sci. 27 (1992) 3487–3496.

[36] D.J. Dingley, The development of automated diffraction in scanning and transmission electron microscopy, in: A.J. Schwartz, M. Kumar, B.L. Adams (Eds.), Electron Backscatter Diffraction in Materials Science, Kluwer Academic/Plenum Publishers, New York, 2000, pp. 1–16.
[37] V. Ocelík, U. de Oliveira, M. De Boer, J.Th.M. De Hosson, Thick tool steel coatings with laser clad, in: J.T.M. De Hosson, C.A. Brebbia, S.-I. Nishida (Eds.), Computer Methods and Experimental Measurements for Surface Effects and Contact Mechanics VIII, WIT Press, Southampton, 2007, pp. 13–22.
[38] V. Ocelík, J.A. Vreeling, J.Th.M. De Hosson, EBSP study of reaction zone in SiC/Al metal matrix composite prepared by laser melt injection, J. Mater. Sci. 36 (20) (2001) 4845–4850.
[39] U. de Oliveira, V. Ocelík, J.Th.M. De Hosson, Residual stress analysis in Co-based laser clad layers by lab X-rays and synchrotron diffraction techniques, Surf. Coat. Technol. 201 (2006) 533–542.
[40] U.O.B. de Oliveira, Laser treatment of alloys: processing, microstructure and structural properties, (Ph.D. Thesis), University of Groningen, 2007.

This page intentionally left blank

CHAPTER 16

Laser Consolidation—A Rapid Manufacturing Process for Making Net-Shape Functional Components

L. Xue
National Research Council of Canada, London, ON, Canada

16.1 INTRODUCTION

Free-form fabrication based on the laser cladding process is an emerging computer-aided manufacturing technology that uses a laser beam to melt injected powder (or wire) to form a solid, functional component layer by layer. This one-step computer-aided manufacturing process does not require any molds or dies, and therefore provides the flexibility to quickly change the design of the components. As a result, the lead-time to produce functional parts could be reduced significantly. As opposed to the conventional machining process, this new technology builds complete parts or features on a base component (or an existing component) by adding rather than removing material. The parts built using the technology are metallurgically sound, free of porosity or cracks. Various papers have been published by different institutions using laser cladding based free-form fabrication technology on several alloys and steels [1–7]. Although the technology has a great potential for many industrial applications, concerns about the surface finish and dimensional accuracy have been raised [8].

The National Research Council of Canada at its London Facility (NRC-London) has developed a laser consolidation process that turns the laser cladding based free-form fabrication technology into a new elevation for producing net-shape functional components that are difficult or even impossible to produce using conventional manufacturing technologies. Research work has been conducted on laser consolidation of various industrials materials (such as Ni-alloys, Co-alloy, Ti-alloy, Al-alloy, stainless

Advances in Laser Materials Processing
https://doi.org/10.1016/B978-0-08-101252-9.00016-9
Crown Copyright © 2018. Published by Elsevier Ltd. All rights reserved.

steels, and tool steels [9–14].) and its potential for various industrial applications [15–21]. In this chapter, an overview on NRC-London's work on laser consolidation research is presented. The observation of the unique microstructure along with functional properties of laser-consolidated materials is discussed. In addition, some examples of laser consolidation process for making net-shape functional components for various potential industrial applications are presented.

16.2 PROCESS DESCRIPTION

The laser consolidation process requires a substrate (new base or existing component) onto which a part is built (Fig. 16.1). A focused laser beam was irradiated onto the substrate to create a molten pool, while metallic powder was simultaneously injected through a nozzle into the pool. A computer numerical control (CNC) motion system (3–5 axes) was used to control the relative movement between the laser beam and the substrate. The laser beam and the powder feed nozzle followed a pre-designed laser path based on a computer aided design (CAD) model, creating a bead of molten material on the substrate, which solidified rapidly to form the first layer. The second layer was deposited on top of the first layer. By repeating this process, a solid thin wall structure was built up. When the laser path is designed properly to guide the laser beam movement, a complex shaped part can be built directly from a CAD model without any mold or die.

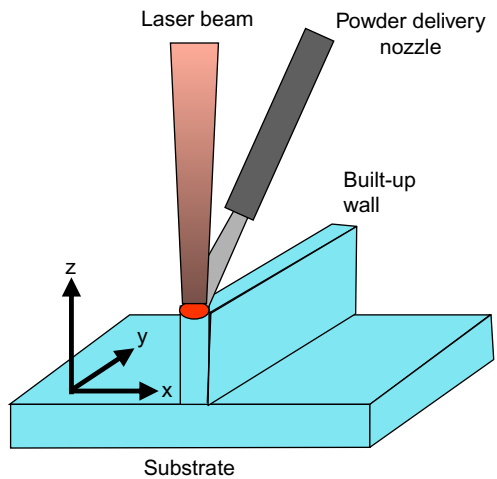


Fig. 16.1 An illustration of laser consolidation process.

A Lasag Nd:YAG laser coupled to a fiber-optic processing head was used for the laser consolidation work presented in this chapter. The laser was operated in a pulse mode with an average power ranging from 20 to 300 W. A Sultz-Metco 9MP powder feeder was used to simultaneously deliver metallic powder into the melt pool through a nozzle with the powder feed rate ranging from 1 to 30 g/min. All laser consolidation work was conducted at room temperature in a glove box, in which the oxygen content was maintained below 50 ppm during the process.

The microstructures of the laser-consolidated (LC) samples were examined metallurgically with an optical microscope as well as a Hitachi S-3500N Scanning Electron Microscope (SEM) equipped with an X-ray energy dispersive spectroscopy (EDS). A Philips X'Pert X-ray diffraction (XRD) system was used to identify the phases of the LC samples. A 100 kN Instron Mechanical Testing System was used to evaluate the tensile and fatigue properties of the LC samples. Flat tensile and fatigue specimens were machined from LC thin wall coupons (about 0.8–1 mm in thickness). The specimen surfaces in the gauge length area were manually polished down to 600 grit. All tensile and fatigue tests were performed at room temperature as per the respective ASTM standards. The microhardness of LC materials was measured with a Buehler Micromet II Microhardness Tester. A Falex ISC-200PC Pin-on-Disk System was employed to evaluate wear resistance of some LC materials as per ASTM Standard G99-95a. The amount of sample wear was determined by using a Dektak Surface Profiler to measure the cross-sectional depth profile of the wear scar. For each specimen, six to eight measurements were made in equal space along the whole wear scar and the average value of the wear loss area was then multiplied by the circumference of the wear scar to determine the wear volume loss of the sample. The amount of pin wear was determined by measuring the diameter of the circular wear scar on the ball to calculate the volume loss.

16.3 MICROSTRUCTURE AND MECHANICAL PROPERTIES OF LASER-CONSOLIDATED (LC) MATERIALS

16.3.1 Stainless and Tool Steels

16.3.1.1 Stainless Steel—316L

Low carbon austenite 316L stainless steel (S.S.) is widely used for various corrosion resistant applications. The 316L S.S. powder used for laser consolidation contains 0.024% C, 16.4% Cr, 10.4% Ni, 2.23% Mo, 1.42% Mn, and 0.45% Si. The LC 316L S.S. consisted of fine cellular dendritic

microstructure resulting from the rapid solidification inherent to the laser consolidation process (Fig. 16.2). The cellular grain growth occurred in random orientations. The XRD analysis showed that the LC 316L S.S. had exactly the same γ phase as the powder used: face-centered cubic structure with a lattice parameter of about 3.59 Å (Fig. 16.3). In addition, both the XRD results and optical microscopic observation revealed no preferred orientation observed in the LC 316L S.S.

The tensile properties of LC 316L S.S. along horizontal and vertical directions were almost the same due to no preferred microstructure

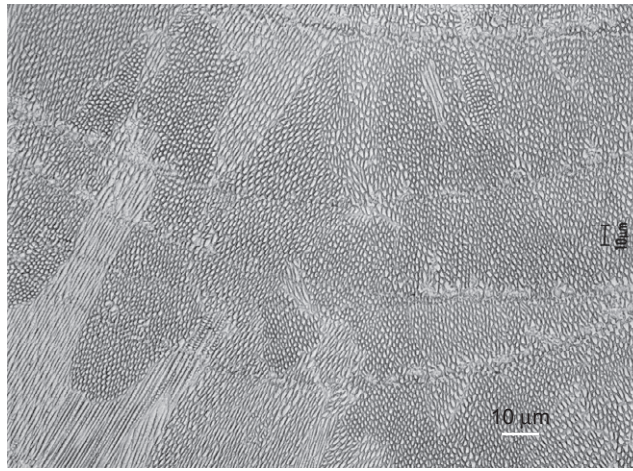


Fig. 16.2 Optical microstructure of LC 316L stainless steel (×500).

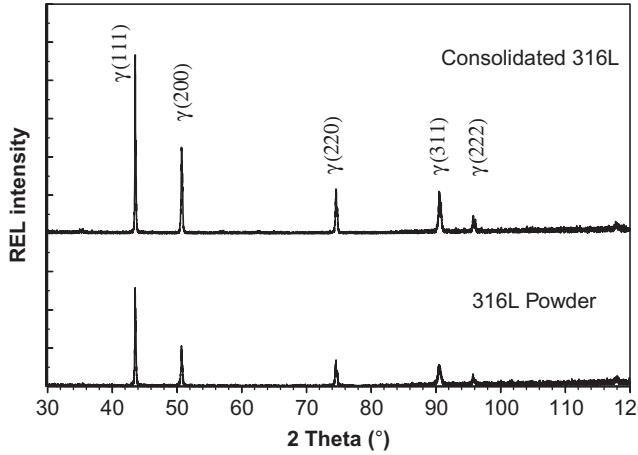


Fig. 16.3 Comparison of XRD pattern of LC 316L stainless steel with powder form.

Table 16.1 Tensile properties of LC 316L stainless steel

Conditions		$\sigma_{0.2}$ (MPa)	σ_{UTS} (MPa)	δ (%)
As-consolidated 316L	Horizontal	344	560.	35
	Vertical	328	540	43
Cast 316L (CF-3M) [22]		262	552	55
Hot finished & annealed 316L bar [23]		170	480	40
Cold finished & annealed 316L bar [23]		310	620	30

orientation (Table 16.1). Along the horizontal and vertical directions, the average yield strength of LC 316L S.S. was 344 and 328 MPa, while the tensile strength was 560 and 540 MPa, respectively. The elongation of the LC sample was 35% along the horizontal direction and 43% along the vertical direction. The LC 316L S.S. demonstrated higher yield strength as compared to the cast or the wrought material [22,23], while the tensile strength and elongation were comparable.

16.3.1.2 Tool Steel—H13

H13 is a hot work tool steel that has good resistance to thermal fatigue, erosion and wear, and is widely used for making molds and dies. The H13 powder used for laser consolidation contains 0.42% C, 5.04% Cr, 1.33% Mo, 1.06% V, and 0.88% Si. LC H13 samples were metallurgically sound and free of cracks or porosity. LC H13 tool steel showed a directionally solidified dendritic microstructure with layered features: very fine columnar dendrites (around 1–2 μm in dendritic arm spacing) aligned along the vertical direction (Fig. 16.4A). Cellular features were observed along the transverse cross-section (Fig. 16.4B).

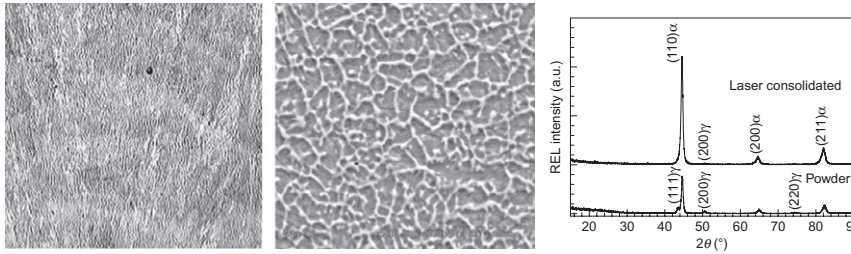


Fig. 16.4 Microstructure and phase of LC H13 steel: (A) optical micrograph along vertical cross-section (×200); (B) SEM photo along horizontal cross-section (×3000); (C) XRD patterns.

The XRD results indicated that the LC H13 steel consisted of a majority of α (martensite) plus a trace amount of γ phase (Fig. 16.4C), which was very similar to the H13 powder used for the consolidation except for the reduced amount of γ phase. Further XRD analysis indicated that the carbides extracted from the LC H13 material were of MC, M_7C_3, and possible M_3C types.

The LC H13 tool steel showed excellent tensile properties (Table 16.2). The average yield and tensile strengths of the as-consolidated H13 along the vertical direction were about 1288 and 2064 MPa, respectively, while the elongation was about 6% and the elastic modulus was about 216 GPa. Along the horizontal direction, the LC H13 showed significantly higher yield strength (1564 MPa) than along the vertical direction, while the tensile strength, elastic modulus, and elongation of LC H13 were comparable for both directions. It should be noted that the tensile properties of the LC H13 material had relatively small scatter. For example, along the vertical direction, the standard deviations of the yield strength and tensile strength were about 54 and 51 MPa, respectively, while the standard deviations of the elastic modulus and elongation were 4 GPa and 2.2%, respectively, which indicated that the laser consolidated H13 material at a reasonably good consistency.

Compared to the conventional cast or wrought material, the LC H13 tool steel demonstrated excellent tensile properties. From the Refs. [24–26], the yield and tensile strengths of the annealed cast or wrought H13 were about 370–510 and 670 MPa, respectively, while the yield and tensile strengths of the wrought H13 in hardened condition were in the range of 1290–1570 and 1500–1960 MPa, respectively. The tensile and yield strengths of the as-consolidated H13 were substantially higher than the annealed cast or wrought H13, and comparable to the hardened wrought H13. The elastic modulus of the as-consolidated H13 was about the same as the wrought material. However, the elongation of the as-consolidated H13 material was about 5%–6%, which was lower than the hardened wrought H13. A post heat treatment might be used to improve the elongation of the LC H13 material if required.

The LC H13 showed very good wear resistance. The pin-on-disk wear test results indicated that, under the given test conditions (3.175 mm diameter Cr steel ball of Rc.63; 250 g test load; total 4000 m sliding distance), as-consolidated H13 specimens showed significantly improved wear resistance as compared to hardened wrought H13 specimens. For example, the average volume loss of the as-consolidated H13 specimens was about

Table 16.2 Tensile properties of LC H13 tool steel

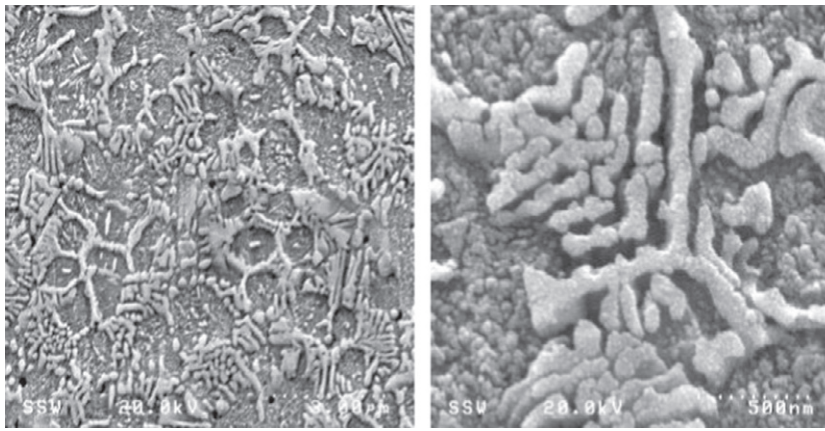
Material conditions		$\sigma_{0.2}$ (MPa)	σ_{UTS} (MPa)	E (GPa)	δ (%)
As-consolidated	Vertical	1288 ± 54	2064 ± 51	216 ± 4	6.0 ± 2.2
	Horizontal	1564 ± 24	2033 ± 38	214 ± 2	5.0 ± 2.8
Cast (annealed) [24]		370	670	–	Lower than wrought H13
Wrought (annealed) [25]		510	676	210	28
Wrought (1010°C/oil quench +605°C tempering) [26]		1290	1495	–	15
Wrought (1010°C oil quench +527°C tempering) [26]		1570	1960	–	13

0.14 mm^3, which was only about 1/3 of the volume loss of the hardened H13 tempered at 482°C (0.4 mm^3) and about one order of magnitude less as compared to the annealed wrought H13 material (1.45 mm^3). In addition, the average wear volume loss of Cr steel balls tested against the LC H13 specimens (0.21 mm^3) was also significantly less (only 1/3 to 1/4) than that of the balls tested against the hardened or annealed wrought H13 specimens (0.56–0.88 mm^3).

16.3.1.3 Tool Steel—CPM-9V

CPM-9V is a vanadium-carbide type of tool steel developed by Crucible Research for powder metallurgy applications. The CPM-9V powder contains 1.8% C, 9.26% V, 5.35% Cr, 1.24% Mo, and 0.91% Si. Compared to conventional tool steels, CPM-9V exhibits excellent wear resistance [27].

The LC CPM-9V had a very fine microstructure, which was very hard to identify under an optical microscope. A high resolution SEM photo (Fig. 16.5A) showed that as-consolidated CPM-9V had a two-phase microstructure: a light, very fine, and snowflake-like phase precipitated on the dark matrix. The thickness of the light snowflake-like phase was only about 100 nm (Fig. 16.5B). EDS analysis indicated that the light phase contained a higher percentage of vanadium (about 12%–14%) and chromium (about 6%–6.6%) as compared to the dark matrix (about 9% V and 5.7% Cr). The XRD analysis revealed that the light phase was $(V,Cr)_8C_7$ type carbides, while the dark portion was a α phase.



(A) (B)

Fig. 16.5 Microstructure of LC CPM-9V by high resolution SEM: (A) ×6500; (B) ×40,000.

As-consolidated CPM-9V material showed good tensile properties (Table 16.3). Along the vertical direction, the as-consolidated CPM-9V had an average yield strength of 821 MPa and a tensile strength of 1315 MPa. The elastic modulus of the consolidated CPM-9V was about 234 GPa. Unfortunately, all specimens failed outside of the gauge length and therefore, the accurate elongation data was not available. But based on the measured data within the gauge length, the average elongation of the as-consolidated CPM-9V would be 2.6% or higher. It should be noted that all tensile test data were very consistent and the scatter ranges were small, which again indicated that the laser consolidation process had good reproducibility.

LC CPM-9V also showed excellent wear resistance (Fig. 16.6). Pin-on-disk wear test revealed that, under the given test conditions (WC ball of 6.375 mm diameter; 500 g test load; total sliding distance of 8000 m), LC

Table 16.3 Tensile properties of LC CPM-9V tool steel

	Vertical direction (As-consolidated)			
Sample No.	σ_{UTS} **(MPa)**	$\sigma_{0.2}$ **(MPa)**	δ **(%)**	E **(GPa)**
#1	1358.9	883.8	2.3	229.6
#2	1295.0	787.0	2.8	230.6
#3	1303.8	835.9	2.2	244.5
#4	1303.8	778.1	3.1	232.7
Average	1315 ± 29	821 ± 49	2.6	234 ± 7

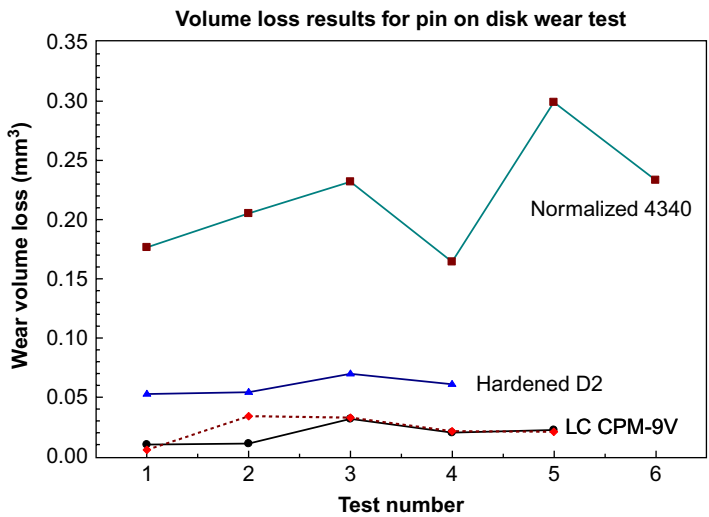


Fig. 16.6 Pin-on-disk wear test results (disk volume loss).

CPM-9V specimens (Rc.50–55) showed significantly better wear resistance as compared to the hardened D2 (Rc.64–65) and normalised 4340 (Rc.35–36) steels. The average volume loss of the LC CPM-9V specimens was about 0.0211 mm^3, which was only about 1/3 of the volume loss of D2 specimens (0.0595 mm^3) and about one order of magnitude lower as compared to the 4340 specimens (0.2185 mm^3). In addition, the wear loss of WC balls tested against the LC CPM-9V material was also significantly lower than that of the same balls tested against the D2 and 4340 steel. The average wear volume loss of the WC balls against the LC CPM-9V was about 0.01855 mm^3, which was only about a half or one third of the ball volume loss against the D2 and 4340 steel (0.0417 and 0.0538 mm^3), respectively. It is interesting to note that although the hardness of the LC CPM-9V material was only around Rc.50–55, its wear resistance was clearly superior to the hardened D2 steel with a hardness of around Rc.64–65, which was consistent with the observation of the powder metallurgy (P/M) CPM-9V material [25]. The excellent wear resistance of the LC CPM-9V may be attributed to the precipitation of $(V,Cr)_8C_7$ carbides due to the high vanadium contents in the alloy.

16.3.2 Ni-Based Alloys

16.3.2.1 IN-625 Alloy

IN-625 is a nickel-based solution hardening superalloy and the powder used for laser consolidation contains 0.03% C, 22% Cr, 9% Mo, 3.7% Ta, and Nb. Laser consolidation produced metallurgically sound IN-625 samples, free of cracks or porosity. The LC IN-625 material showed directionally solidified microstructure due to rapid solidification inherent to the process. The cross-sectional view along the vertical direction (build-up direction) reveals that columnar grains growing almost parallel to the build direction in the LC IN-625 (Fig. 16.7A), while the horizontal cross section showed that the LC IN-625 consisted of fine cells of around 2–3 μm in diameter (Fig. 16.7B). The XRD results revealed that the LC IN-625 had the same γ phase as the IN-625 powder: a face-centered cubic structure with a lattice parameter of 3.59 Å. The XRD results also revealed that the directional solidification of LC IN-625 material was along the (1 0 0) crystallographic plane, which was the typical dendritic growth direction of face-centered cubic structure materials.

The LC IN-625 material exhibited very good mechanical properties (Table 16.4). Along the horizontal direction (perpendicular to the build direction), the yield strength and tensile strength of the LC IN-625 material were 518 and 797 MPa, respectively, while the elongation was about

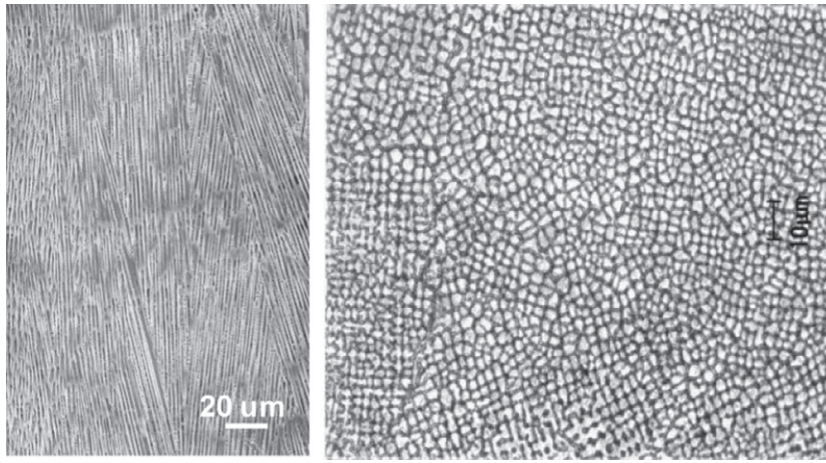


Fig. 16.7 Microstructure of LC IN-625 alloy: (A) vertical cross-sectional view (×250); (B) horizontal cross-sectional view (×500).

Table 16.4 Tensile properties of LC IN-625 alloy

Conditions		$\sigma_{0.2}$ (MPa)	σ_{UTS} (MPa)	δ (%)
LC IN-625 (as-consolidated)	Horizontal	518 ± 9	797 ± 8	31 ± 2
	Vertical	477 ± 10	744 ± 20	48 ± 1
Cast IN-625 [28]		350	710	48
Wrought IN-625 [29]		490	855	50

31%. When testing along the vertical direction (parallel to the build direction), both the yield and the tensile strengths were slightly lower at 477 and 744 MPa, respectively, while the percentage elongation increased significantly to 48%. The anisotropic behavior of the tensile properties of the LC IN-625 alloy may be attributed to its directionally solidified microstructure. The yield strength and the tensile strength of the LC IN-625 along both directions were significantly higher than the cast material and comparable to the wrought IN-625, although the elongation along the horizontal direction was slightly lower [28,29].

16.3.2.2 Waspaloy

Waspaloy (60Ni-19Cr-4Mo-3Ti-1.3Al) is a proprietary nickel-based, age-hardenable superalloy with excellent high temperature strength and good corrosion resistance, notably to oxidation at a service temperature

up to 650 C (1200°F) for critical rotating applications, and up to 870°C (1600°F) for other less demanding applications. The alloy's high-temperature strength is derived from its solid solution strengthening elements of molybdenum, cobalt, and chromium, and its age-hardening elements, aluminum and titanium. Its strength and stability ranges are higher than those typically available for IN-718. Waspaloy is used for gas turbine engine components that require considerable strength and corrosion resistance at high operating temperatures, including compressor and rotor discs, shafts, spacers, seals, rings and casings, and other miscellaneous engine hardware, aircraft assemblies and missile systems [30]. Waspaloy is typically manufactured from wrought and cast materials.

The optical micrograph of the as-consolidated Waspaloy along the vertical cross-section is displayed in Fig. 16.8A. The LC Waspaloy shows a directionally solidified microstructure: very fine columnar dendrites growing almost parallel to the build-up direction (vertical). A high-resolution SEM photo reveals that no γ' precipitation can be observed in as-consolidated Waspaloy (Fig. 16.8B). It also reveals that very fine carbides (white particles) are distributed uniformly at the inter-dendritic and intra-dendritic regions.

For wrought Waspaloy, a standard heat treatment procedure was used to control the precipitation of γ' particles. It includes solution treatment (1079°C for 4 h/air-cooling) followed by double aging treatments (843°C for 4 h/air-cooling; 760°C for 16 h/air-cooling). This procedure can also be used for treating LC Waspaloy. After the heat treatment, dendrites in the LC Waspaloy completely disappeared and all grains were re-crystallized. The LC Waspaloy shows very long grains along a vertical direction (Fig. 16.9A), while a transverse direction (Fig. 16.9B) shows somewhat nonuniform

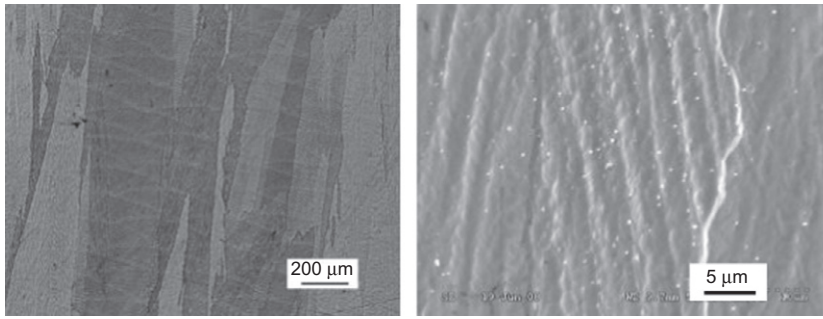


Fig. 16.8 Microstructure of as-consolidated Waspaloy: (A) optical microscope photo (×50); (B) SEM photo (×3000).

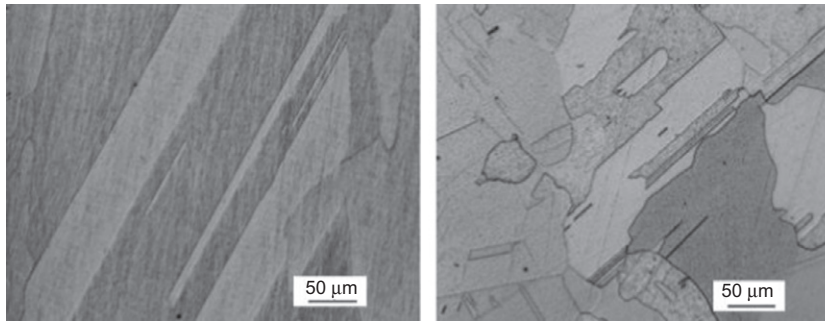


Fig. 16.9 Microstructure of heat-treated LC Waspaloy: (A) vertical cross-section; (B) transverse cross-section (×200).

equiaxed grains with microstructural features (such as twins) similar to heat-treated wrought Waspaloy. However, it is interesting to note that the grain size in the LC Waspaloy is substantially larger than that in the wrought Waspaloy. After the heat treatment, carbide precipitation was observed along the grain boundary as well as inside the grain in the LC Waspaloy.

Precipitation of γ' particles is the primary strengthening mechanism for the Waspaloy superalloy. The as-consolidated Waspaloy does not have γ'-precipitates. After the standard heat treatment, γ'-particles precipitate in the LC Waspaloy matrix, as indicated by the significant increase in its hardness (from HV 276 increased to HV 369). X-ray diffraction (XRD) method has revealed that the as-consolidated Waspaloy has single γ-phase but its strongest peak is $\gamma(200)$, which indicates that the LC Waspaloy has a preferred orientation along (100) plane. It is interesting to note that the directionally solidified microstructure is quite stable even at elevated temperatures. After exposure to the temperature above 760°C for more than 20 h (1032°C/4 h + 843°C/4 h + 760°C/16 h), the $\gamma(200)$ in the heat-treated (HT) LC Waspaloy is still the highest peak in the XRD pattern and the preferred orientation can still be observed by an optical microscope.

The as-consolidated Waspaloy shows reasonably good tensile properties (Table 16.5). The average yield and ultimate tensile strengths of the as-consolidated Waspaloy are about 508 and 797 MPa, respectively, while the elongation is about 40%. It should be noted that the tensile properties of the as-consolidated Waspaloy show reasonably small scatter. The standard deviations of yield strength and ultimate tensile strength are only about 19 MPa, while the standard deviations of the elongation are about 4%, which indicates that the laser consolidated Waspaloy has good consistency. After standard heat

Table 16.5 Tensile properties of LC Waspaloy

Material	$\sigma_{0.2}$ (MPa)	σ_{UTS} (MPa)	δ (%)
LC Waspaloy (as-consolidated)	508 ± 19	797 ± 19	40 ± 4
LC Waspaloy (HT)	769 ± 54	1226 ± 73	27 ± 3
Waspaloy Bar (HT) [31]	795	1280	25
Waspaloy Bar, Forgings, Rings (HT) [32]	758	>1103	15

treatment: solution treatment (1079°C for 4 h/air-cooling) followed by double aging treatments (843°C for 4 h/air-cooling; 760°C for 16 h/air-cooling), the tensile and yield strengths of LC Waspaloy significantly increase to 769 and 1126 MPa, respectively, while its elongation reduces to 27%.

Table 16.5 also compares the tensile properties of LC Waspaloy with wrought Waspaloy [31,32]. As expected, due to the difference in their microstructures, the as-consolidated Waspaloy has relatively low tensile and yield strengths but much better elongation as compared to heat-treated wrought Waspaloy. After heat treatment, the tensile properties (both strength and elongation) of the LC Waspaloy are fully comparable to the heat-treated wrought Waspaloy.

16.3.2.3 IN-718 Alloy

IN-718 is a precipitation-hardenable nickel-chromium superalloy containing significant amounts of iron, niobium, and molybdenum, along with a lesser amount of aluminum and titanium. It combines good corrosion resistance and high strength with outstanding weldability, including resistance to post-weld cracking. The alloy has excellent creep-rupture strength at temperature up to 700°C (1300°F). IN-718 has been widely used as a structural material for a variety of components in gas turbines, rocket motors, spacecraft, nuclear reactors, pumps, and tooling [33].

Similar to LC Waspaloy, the as-consolidated IN-718 also shows a directionally solidified microstructure due to the rapid solidification inherent to the LC process (Fig. 16.10). The cross-sectional view shows that as-consolidated IN-718 has columnar dendritic grains growing almost parallel to the build-up direction (Fig. 16.10A), while the horizontal cross section shows fine cell structure (Fig. 16.10B).

The standard heat treatment procedure used for wrought IN-718 was also applied for the LC IN-718 specimens: (1) solution treatment at 980°C for 1 h followed by air cooling; (2) aging at 720°C for 8 h followed by air cooling, and (3) aging at 620°C for 8 h followed by air cooling. Fig. 16.11A and B shows optical microscopic photos of heat-treated LC

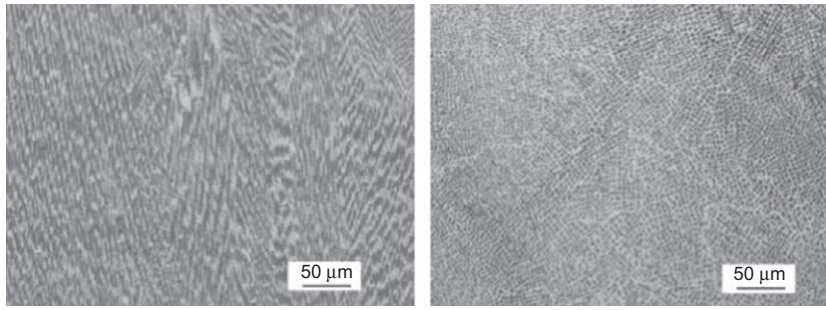


Fig. 16.10 Optical microstructure of as-consolidated IN-718: (A) vertical direction; (B) transverse direction (×100).

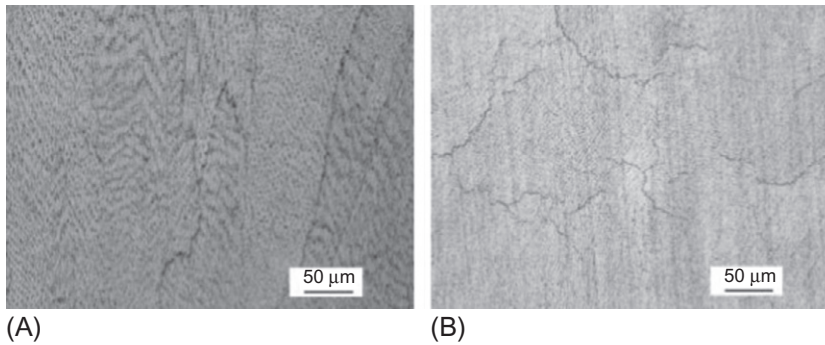


Fig. 16.11 Microstructure of heat-treated LC IN-718: (A) vertical direction; (B) transverse direction (×200).

IN-718 along the vertical and horizontal directions, respectively. Similar to the observation of LC Waspaloy, after the heat treatment, the original columnar dendrites in LC IN-718 disappeared. However, it is interesting to note that complete re-crystallization was observed in heat-treated LC Waspaloy, while some kinds of dendritic features can still be observed under the optical microscope in heat-treated LC IN-718. High resolution SEM observation further reveals that those features can be attributed to carbide particles existing in the prior inter-dendritic regions and no dendritic structures remained after the heat treatment.

For as-consolidated IN-718, no γ' particles can be observed. After the standard heat treatment, γ'-particles precipitate in the LC IN-718 matrix, as indicated by the significant increase in its hardness (from HV 257 increased to HV 445). However, we have not observed γ' particles under SEM with the current reagent.

The X-ray diffraction reveals that the as-consolidated IN-718 has the same γ phase as the IN-718 powder: a face-centered cubic structure. However, the as-consolidated IN-718 material shows a preferred orientation along the (1 0 0) crystallographic plane. The (1 0 0) plane is the typical dendritic growth direction of face-centered cubic structure materials. It is interesting to note that, after heat treatment, the preferred orientation along (1 0 0) still remained, although its original dendrites disappeared.

The laser consolidation process successfully produced metallurgically sound IN-718 samples, free of cracks or porosity. The as-consolidated IN-718 alloy shows reasonably good tensile properties (Table 16.6). Without γ′ precipitation, the as-consolidated IN-718 demonstrates good ductility (about 39% in elongation) but relatively less yield and tensile strengths (about 432 and 802 MPa, respectively).

LC IN-718 was heat treated as per the standard procedure used for wrought IN-718 alloy (solution treatment at 980°C for 1 h followed by air cooling; aging at 720°C for 8 h followed by air cooling, and aging at 620°C for 8 h followed by air cooling). After the heat treatment, the yield and tensile strengths of the LC IN-718 are increased to about 1085 and 1238 MPa, respectively, while the elongation is reduced to about 21%. The heat-treated LC IN-718 alloy demonstrates that its yield strength, tensile strength, and elongation are comparable to the various types of heat-treated wrought IN-718 material [33,34]. The microhardness of LC IN-718 is about HV 257 and HV 445 for as-consolidated and heat-treated conditions, respectively, while the hardness of heat-treated wrought IN-718 is about HV 420 [35].

16.3.2.4 IN-738 Alloy

IN-738 is a nickel-based γ′-precipitation hardening superalloy. The powder we used contains 16.1% Cr, 8.34% Co, 3.27% Al, 3.38% Ti, and other alloying elements. The alloy has excellent creep strength and hot corrosion resistance and has been used for manufacturing gas turbine airfoils in hot section [36]. Similar to other laser-consolidated nickel-base superalloys, the LC IN-738 also showed a directionally solidified microstructure: very fine

Table 16.6 Tensile properties of LC IN-718 alloy

Material	$\sigma_{0.2}$ (MPa)	σ_{UTS} (MPa)	δ (%)
LC IN-718 (as-consolidated)	432 ± 5	802 ± 21	39 ± 5
LC IN-718 (HT)	1085 ± 19	1238 ± 12	21 ± 2
Wrought IN-718 (HT) [33]	1036	1240	12
IN-718 Sheet (HT) [34]	1050	1280	22

columnar γ dendrites growing almost parallel to the building direction. XRD analysis revealed that the preferred orientation was along the (1 0 0) crystallographic plane. Precipitation of γ′ particles is the primary strengthening mechanism for the IN-738 superalloy. The as-consolidated IN-738 material did not show γ′-precipitates, while precipitated carbides were distributed uniformly along the interdendritic regions. After a standard heat treatment cycle (1120°C × 2 h/air cooling + 845°C × 24 h/air cooling), a significant amount of γ′-particles precipitated in the LC IN-738 matrix (Fig. 16.12A). Compared to the cast IN-738 (Fig. 16.12B), the heat-treated LC IN-738 showed the similar but finer bimodal γ′ distribution: coarse particles in near cuboidal shape plus fine particles.

The LC IN-738 material showed very good tensile properties (Table 16.7). Along the vertical direction, the tensile and the yield strength of the as-consolidated IN-738 was about 1202 and 869 MPa, respectively, while the elongation was about 18%. However, along the horizontal direction, the as-consolidated IN-738 showed comparable yield strength but relatively lower tensile strength and elongation as compared to the vertical direction. After the standard heat treatment, the tensile strength of the LC IN-738 along the vertical direction slightly increased to about 1269 MPa, while its yield strength and elongation remained almost the same. As compared to the heat treated cast IN-738 [37], the heat-treated LC IN-738 along the vertical direction showed 15% higher tensile strength and 240% higher elongation, although its yield strength was slightly reduced by about 5%.

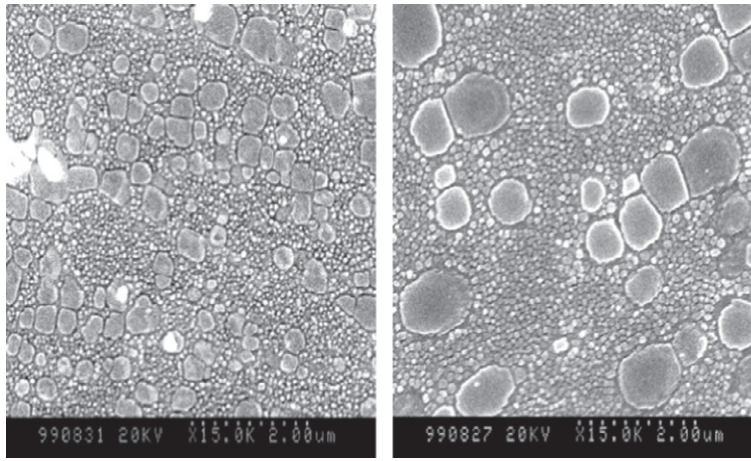


Fig. 16.12 SEM observation of γ′ precipitates in cast and LC IN-738 (×15,000).

Table 16.7 Tensile properties of LC IN-738 alloy

Material	Condition	σ_{UTS} (MPa)	$\sigma_{0.2}$ (MPa)	δ (%)
LC IN-738	Vertical direction (as-consolidated)	1202 ± 23	869 ± 5	18 ± 2
	Vertical direction (heat-treated)	1269 ± 35	869 ± 19	17 ± 2
	Horizontal direction (as-consolidated)	1084 ± 23	880 ± 14	6.7 ± 1.7
Cast IN-738 [37]	Heat-treated	1100	915	5

Table 16.8 Stress rupture life of LC IN-738 tested at 1010°C (1850°F) and 55 MPa (8 ksi)

Sample No.	LC IN-738	LC IN-738/Cast IN-738	Cast IN-738 Baseline
#1	515 h	123 h	206 h
#2	236 h	175 h	116 h
#3	485 h	128 h	187 h
#4	455 h	–	–
Average	423 h	142 h	170 h

The LC IN-738 material showed excellent stress rupture life (Table 16.8). Under the test condition (1010°C and 55 MPa), the average stress rupture life of LC IN-738 material was about 423 h, which was more than double the life of the cast IN-738 baseline (170 h). The excellent stress rupture life of the LC IN-738 may be attributed to its directionally solidified microstructure, uniform γ′ particle precipitation, and fine and uniform carbide distribution.

16.3.3 Ti-Base Alloy

Ti-6Al-4V is an (α + β) titanium alloy that contains α stabilizer element Al and β stabilizer element V. The typical as-cast Ti-6Al-4V microstructure consists of transformed β containing acicular α as well as α at prior-β grain boundaries, while the annealed wrought Ti-6Al-4V bar typically consists of equiaxed α grain plus intergranular β [38]. The microstructure of the LC Ti-6Al-4V along the vertical cross-section is shown in Fig. 16.13. The LC Ti-6Al-4V showed somewhat equiaxed grains (Fig. 16.13A) with acicular phase inside (Fig. 16.13B). A high-resolution SEM photo reveals that grain boundary was hard to distinguish and no secondary phase can be observed along it (Fig. 16.13C).

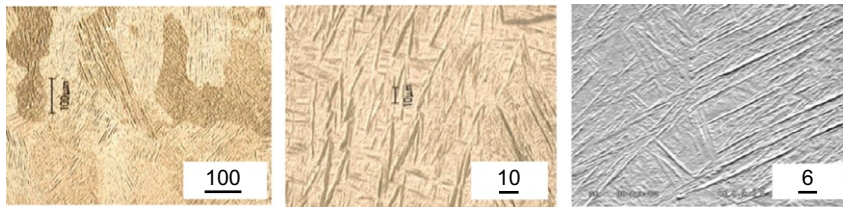


Fig. 16.13 Microstructure of LC Ti-6Al-4V: (A) optical micrograph (×100); (B) optical micrograph (×1000); (C) SEM micrograph (×1500).

XRD results revealed that that wrought Ti-6Al-4V had majority of α phase plus small amount of β phase evidenced by the existence of β(200) peak. It is interesting to note that the LC Ti-6Al-4V and Ti-6Al-4V powder only had single α-phase microstructure with α(101) as the strongest diffraction peak without any β peaks, which was consistent with the optical microscope and SEM observations. The lack of β phase in LC Ti-6Al-4V and powder Ti-6Al-4V may also be attributed to the high cooling rate inherent to the process. Based on the optical microscope, SEM and XRD results, the LC Ti-6Al-4V microstructure consisted of somewhat equiaxed α grains (transformed from β) with acicular features inside.

The as-consolidated Ti-6Al-4V demonstrated excellent tensile properties (Table 16.9). The yield and tensile strengths of thin-wall (about 0.8 mm thick) LC Ti-6Al-4V were about 1062 and 1157 MPa, respectively, while its elongation was about 6.2%. The tensile and yield strengths of the as-consolidated thin-wall Ti-6Al-4V were substantially higher than the

Table 16.9 Tensile properties of LC Ti-6Al-4V alloy

Materials	$\sigma_{0.2}$ (MPa)	σ_{UTS} (MPa)	E (GPa)	δ (%)
As-consolidated Ti-6Al-4V (thick-wall specimens)	899	979	121	11.4
As-consolidated Ti-6Al-4V (thin-wall specimens)	1062	1157	116	6.2
Cast Ti-6Al-4V (As-cast or annealed) [39]	890	1035	–	10
Wrought Ti-6Al-4V (annealed bar) [40]	825	895	110	10
Wrought Ti-6Al-4V (solution treated and aged bar) [40]	965	1035	110	8
Wrought Ti-6Al-4V (solution heat treated + aged) [41]	1103	1172	–	10

as-cast/annealed cast Ti-6Al-4V and annealed wrought Ti-6Al-4V [40,41], and comparable to the wrought Ti-6Al-4V in solution treated plus aged condition [40,41]. The elastic modulus of the thin-wall LC Ti-6Al-4V (116 GPa) was comparable to the wrought material (110 GPa), although the elongation of the LC material (6.2%) was lower than the cast or wrought Ti-6Al-4V (8%–10%). In other side, the as-consolidated thick-wall (about 1.5 mm thick) Ti-6Al-4V material was found to have slightly lower tensile and yield strengths but a higher elongation than the thin-wall LC material. The average yield and tensile strengths of this material in the as-consolidated condition were 899 and 979 MPa, respectively, while the average elongation was around 11.4%. It should be noted that the tensile properties of as-consolidated thick-wall Ti-6Al-4V were very comparable with the as-cast (or annealed) cast Ti-6Al-4V and annealed wrought Ti-6Al-4V material.

The LC Ti-6Al-4V also showed excellent bond strength to the wrought and laser-clad Ti-6Al-4V substrate. Under tensile testing at room temperature, the as-consolidated Ti-6Al-4V had an average bond strength of more than 1048 MPa to wrought Ti-6Al-4V substrate and more than 1072 MPa to laser-clad Ti-6Al-4V substrate. It is interesting to note that all bond test specimens failed in the LC Ti-6Al-4V tube due to the stress concentration effect instead of at the bond area, which indicated that the actual tensile strength at the bond area was higher than the data obtained.

The as-consolidated Ti-6Al-4V also demonstrated excellent high-cycle fatigue properties (Fig. 16.14). The plot also showed reference data for cast, cast plus HIP and annealed wrought Ti-6Al-4V [42] for comparison purposes. The endurance limit of the thin-wall (about 0.8 mm thick) LC Ti-6Al-4V specimens was around 400 MPa, which was at the high end of the scatter band of cast Ti-6Al-4V material. The endurance limit of the thick-wall (about 1.5 mm thick) LC Ti-6Al-4V material was in excess of 500 MPa, which was well at the high end of the scatter band of annealed wrought Ti-6Al-4V material. These preliminary results were very promising and demonstrated that the adjustment of LC processing parameters can significantly improve the fatigue properties of LC Ti-6Al-4V.

16.3.4 Co-Base Alloy

Stellite 6 is a Co-base wear resistant alloy containing 1% C, 27% Cr, 4.7% W, and 0.9% Si. The Co-Cr-W system alloy retains its hardness at elevated temperatures and is especially effective for wear applications at high temperatures or in a corrosive environment, and are widely used as a wear-,

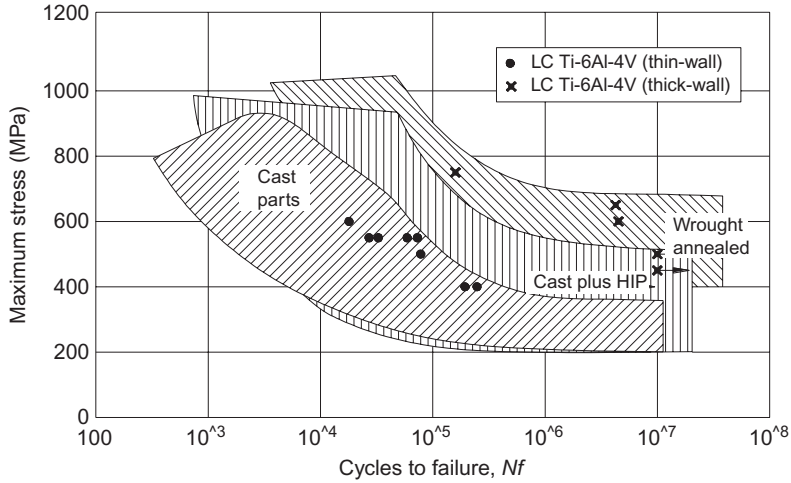


Fig. 16.14 Fatigue data of LC Ti-6Al-4V compared with cast and wrought/annealed Ti-6Al-4V ($R = +0.1$).

corrosion-, and heat-resistant material [43]. The LC Stellite 6 material showed a directionally solidified microstructure: very fine columnar dendrites growing almost parallel to the build vertical direction (Fig. 16.15). The details of the dendrite structure along the vertical cross-section were revealed by a high resolution SEM micrograph (Fig. 16.15C). The dark regions were dendrite arms, while the interdendritic regions appeared white.

The average primary and secondary dendrite arm spacing (DAS) was measured to be around 3.3 and 1.2 μm, respectively. X-ray energy-dispersive spectroscopy (EDS) results showed that the chromium was enriched in the interdendritic regions (about 33%–34%) as compared to about only 25%–26% in the dendrite region. Due to the limitation of the EDS, the carbon contents could not be determined. Based on the EDS results, it may be reasonable to deduce that chromium carbides were formed at the

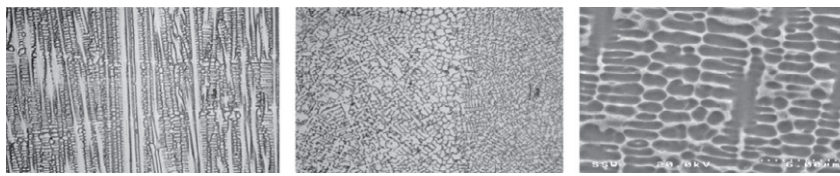


Fig. 16.15 Microstructure of LC Stellite 6 material: (A) optical photo along vertical cross-section (×1000); (B) optical photo along horizontal cross-section (×1000); (C) high magnification SEM photo along vertical direction (×3300).

interdendritic regions in the LC Stellite 6. XRD results revealed that LC Stellite 6 material had the same phase as the Stellite 6 powder used for laser consolidation: cubic α phase. Preferred orientation along (1 0 0) plane was observed in the LC material, which was consistent with the optical microscope observation (Fig. 16.15A). The carbides could not be detected by XRD technique due to their relatively small quantity.

Compared to the conventional casting or powder metallurgy material, Stellite 6 produced using laser consolidation demonstrated significantly better mechanical properties: harder, stronger, and even more ductile (Table 16.10). The tensile strength of LC Stellite 6 was about 1245 MPa in the vertical direction and 1362 MPa in the horizontal direction, which were about 50% higher than that of the cast or powder metallurgy Stellite 6 (about 793–896 MPa) [44]. The yield strength of conventional cast and powder metallurgy Stellite 6 was about 541–662 MPa, while laser consolidation increased the yield strength to 751 MPa (vertical direction) and 1023 MPa (horizontal direction), representing an increase of 15%–90%. The LC Stellite 6 material was also 25%–55% harder than conventional Stellite 6. The average hardness of the LC Stellite 6 was about Rc.58–59, while only about Rc.37–46 was exhibited by the same material produced by the casting or powder metallurgy method. The elongation of LC Stellite 6 material was about 3.1%–3.2%, which was similar to that obtained by investment casting (3%), but much better than that produced by sand casting (1%–2%) or the powder metallurgy method (<1%).

The excellent mechanical properties of the LC Stellite 6 were attributed to its refined microstructure produced by the rapid solidification inherent to

Table 16.10 Tensile properties of LC Stellite 6 alloy

Processing Method	Condition	σ_{UTS} (MPa)	$\sigma_{0.2}$ (MPa)	δ (%)	HRc
LC Stellite 6	As-consolidated (vertical)	1245 ± 55	751 ± 16	3.1 ± 0.1	58
	As-consolidated (horizontal)	1362 ± 30	1023 ± 15	3.2 ± 0.4	59
Sand casting [44]	Stress-relieved	834	541	1–2	46
Investment casting [44]	As-cast	793	662	3	37
Powder metallurgy [44]	–	896	-	<1	40

the laser consolidation process. It is well recognized that dendrite arm spacing (DAS) significantly affects the mechanical properties of cast alloys [45]. Generally speaking, an increase in the solidification rate reduces the DAS and results in increased mechanical properties [45]. The cooling rate during the conventional casting process is in the range of 10^{-3}–1 K/s, which results in a characteristic DAS of 50–500 μm. The characteristic DAS in the LC Stellite 6 material is only about 1.2–3.3 μm, which represents a cooling rate of 10^{3}–10^{6} K/s [46]. The fine DAS in the LC Stellite 6 directly contributes to its exceptional mechanical properties as compared to the conventional casting or powder metallurgy Stellite 6 material with a much coarser dendritic microstructure.

16.3.5 Al-Base Alloy

Al-Si alloys are one of the most important aluminum alloy systems, which possess medium strength, good flow characteristics, low melting point, and narrow freeze range. Al 4047 is one type of Al-Si alloy and the powder used in this study contains 11.41% Si and 0.17% Fe. LC Al 4047 material showed a rapidly solidified microstructure with layered features: very fine columnar dendrites layer (almost parallel to the vertical build direction) growing on a layer of very fine equiaxed grains (Fig. 16.16). The layered features may be attributed to the laser consolidation process itself. During the laser consolidation, the surface of the previously deposited layer would be remelted together with the injected powder and then re-solidified to form a new layer. Due to the high temperature gradient existed at the interface between the liquid layer and the previously deposited layer, a lot of nuclei formed on the most preferred seed sites and the previously deposited layer and grew into a layer of fine equiaxed grains. Then these grains further grew

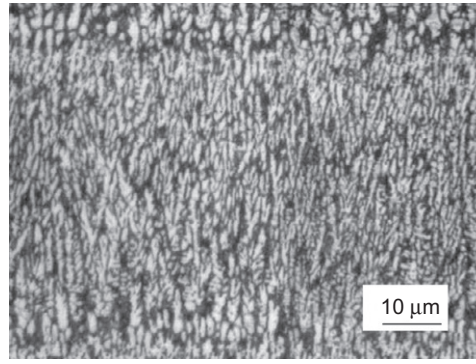


Fig. 16.16 Layer features observed in LC Al 4047 along vertical build-up direction (×1000).

Table 16.11 Tensile properties of LC Al 4047 alloy

Material	$\sigma_{0.2}$ (MPa)	σ_{UTS} (MPa)	δ (%)	E (GPa)
LC Al 4047 (as-consolidated)	139 ± 12	317 ± 12	8.7 ± 2.1	74 ± 6
Al 4047 sheet (tempered) [47]	184	197	3	–
Cast Al 413 (as-cast) [48]	145	300	2.5	–
Cast Al 443 (sand casting) [48]	55	130	8	71
Cast Al 443 (die-casting) [48]	110	230	9	71

along the direction of the maximum temperature gradient (parallel to the build-up direction) to form the columnar dendritic structure. Based on the high resolution SEM examination, LC Al 4047 material showed an average secondary dendrite arm spacing (DAS) of around 1–2 μm. Very fine cellular features were also observed along the transverse cross-section.

The as-consolidated Al 4047 alloy showed very good tensile properties (Table 16.11). The average yield and tensile strengths of the as-consolidated Al 4047 were about 139 and 317 MPa, respectively, while the elongation was about 8.7% and the elastic modulus was about 74 GPa. All tensile test readings had small scatter, which indicated that the laser consolidation process had good reproducibility. As compared to tempered Al 4047 sheet material [47], as-consolidated Al 4047 showed about a 70% higher tensile strength and about 3 times improved elongation, although its yield strength was about 24% lower.

Al 443 and Al 413 are two very important industrial cast Al-Si alloys. Al 443 contains 5.3% Si and is mainly used for sand castings and permanent mold castings. Al 413 is very similar to cast Al 4047 alloy, containing similar Si (11%–13%) but higher Fe (2%). Al 413 is used to make various thin-walled and intricately designed castings. As-consolidated Al 4047 showed tensile and yield strengths very similar to as-cast Al 413 [48], but with substantially improved elongation (8.7% vs. 2.5%). Compared to both sand cast and die cast Al 443 alloy [48], as-consolidated Al 4047 showed much better yield and tensile strengths and comparable elongation. The elastic modulus of LC Al 4047 (74 GPa) was about the same as cast Al 443 (71 GPa). Unfortunately, elastic modulus of cast Al 413 cannot be found in literatures for comparison.

16.4 CASE STUDIES OF VARIOUS INDUSTRIAL APPLICATIONS

16.4.1 Airfoils With Embedded Cooling Channels

NRC-London worked with GE Global Research to explore the potential application of the laser consolidation of Ti-6Al-4V alloy to produce

advanced gas turbine airfoil that contains complex geometric features that may be very difficult or even impossible to manufacture using other conventional manufacturing methods [17].

To test the capability of the laser consolidation process, an airfoil with embedded cooling channels was designed. It had a double-walled shape with seven bridges connecting two walls to provide structural integrity. The wall thickness of the inner and outer walls of the airfoil was about 0.762 mm, while the gap between the two walls was approximately 0.635 mm. The overall length of the airfoil was 33.02 mm and its overall width was around 10.16 mm. The height of the airfoil was set to 25.4 mm. The airfoil design contained many complex internal features such as sharp corners and relatively narrow gaps that extended throughout the body of the airfoil. These features would be very difficult if not impossible to produce using conventional manufacturing methods. The airfoil design provided a good technical challenge for laser consolidation process.

Using optimized processing methodology and laser path planning strategy, laser consolidation successfully built the net-shaped Ti-6Al-4V airfoils of about 25.4 mm in height as per the design (Fig. 16.17). The airfoil with embedded cooling channels was in the "as-consolidated" surface condition without further operation except grinding of the top surface. The laser

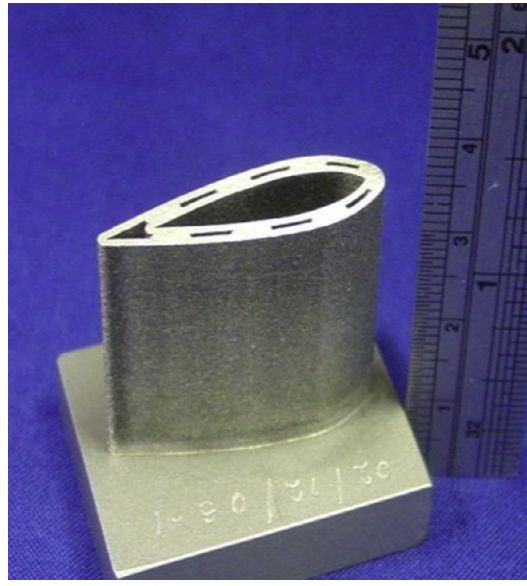


Fig. 16.17 Demonstration piece of the complex LC Ti-6Al-4V airfoil.

consolidation process demonstrated the unique manufacturing capability to produce functional net-shape components. The combination of the innovative design with the unique capability of the LC process can lead to the creation of components with highly complex geometry not possible with conventional means.

16.4.2 Net-Shape Functional Sonar Shells

The folded shell projector (FSP) is a compact flextensional sound source being developed by the Defense Research & Development Canada (DRDC) for low frequency sonar applications. The FSP radiates sound from a thin-walled cylindrical shell driven by a piezoelectric or magnetostrictive motor. The shell has superimposed corrugations (Fig. 16.16A), which creates a significant challenge for the existing manufacturing technology. In collaboration with DRDC, NRC-London investigated laser consolidation of IN-625 and Ti-6Al-4V alloys for manufacturing net-shape functional FSP shells for refining the FSP design as well as for field testing [18].

16.4.2.1 LC IN-625 FSP Shells

A CAD drawing of a FSP shell and an as-consolidated IN-625 FSP shell of the design after removing the loose powder are shown in Fig. 16.18A and B. The shell is about 130 mm in height and around 80 mm in diameter. It is evident that the as-consolidated shell showed very good surface finish. A magnified cross-sectional view (Fig. 16.18C) reveals that the laser consolidation process successfully manufactured the complex thin wall structure with excellent uniformity. It also showed that, as per the CAD design requirement, the laser consolidation process managed to generate

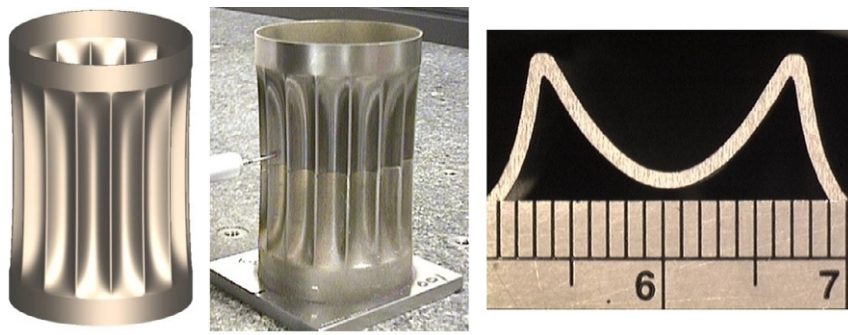


Fig. 16.18 IN-625 FSP shell: (A) CAD drawing; (B) LC IN-625 shell; (C) magnified cross-sectional view of crests on the half shell.

a sharp corner inside each crest, which was very difficult to form using conventional manufacturing methods.

In order to ensure the quality of the LC IN-625 shells, strict NDT inspections were performed on the LC shells by using ultrasonic, dye penetrant, X-ray, and magnetic methods. The NDT inspection results revealed that the LC IN-625 shells were metallurgically sound, without porosity, cracks, or other detectable defects. The functional testing performed by the DRDC on the folded shell projectors assembled with LC IN-625 shells demonstrated that the resonance frequency of the sonar devices matched excellently with the design prediction from the DRDC's finite element model.

16.4.2.2 LC Ti-6Al-4V FSP Shells

A Ti-6Al-4V version of the FSP was designed by the DRDC and manufactured by NRC-London. The shell is about 130 mm in height and around 55 mm in diameter. The surface uniformity of the LC Ti-6Al-4V shell was further improved and the line in the middle of the original LC IN-625 shell was eliminated (Fig. 16.19). Visual inspection and acoustic testing revealed that all shells were metallurgically sound, without any cracks or visible



Fig. 16.19 LC Ti-6Al-4V FSP shell.

defects. The dimensions of external fold profiles of Ti-6Al-4V FSP shells were inspected using a Brown & Sharpe Coordinate Measuring Machine (CMM) at 7 elevations [18]. The CMM probing path was created using Unigraphics to guide the measurement. The measurement results revealed that the LC Ti-6Al-4V FSP shell had an average deviation of 0.098 mm as compared with the CAD model with a minimum deviation of −0.282 mm and a maximum deviation of 0.177 mm. The diameter and wall thickness of the upper and lower flanges were measured using a micrometer with a ball end. The diameters of upper and bottom flanges were 54.501 and 54.606 mm, respectively, while the CAD model required 54.60 mm. The roundness was about 0.030 and 0.044 mm for upper and bottom flanges, respectively. The CAD model specified a wall thickness of 0.80 mm, while the measurement showed that the upper and bottom flanges had the same wall thickness of 0.864 mm. It is evident that the LC Ti-6Al-4V shell demonstrated excellent dimensional accuracy.

Fig. 16.20 illuminates a completed LC Ti-6Al-4V FSP assembly, while Fig. 16.21 shows its field testing results. It has been proven that the welded LC Ti-6Al-4V FSP met its design goals of resonant frequency, source level, and insensitivity to depth. The LC Ti-6Al-4V FSP was calibrated at depths of 15, 25, and 35 m, showing identical resonant frequency of 1500 Hz.

In collaboration with the DRDC, the laser consolidation process has been successfully utilized to manufacture seven Ti-6Al-4V and ten IN-625 complex FSP shells of four different designs and, at this moment, it is the



Fig. 16.20 Assembled LC Ti-6Al-4V FSP with welded Ti end caps.

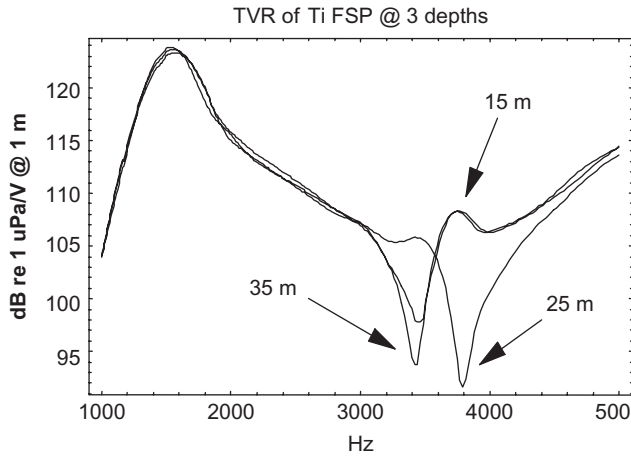


Fig. 16.21 Field testing results of LC Ti-6Al-4V FSP with welded Ti end caps.

only proven manufacturing technology to make functional net-shape FSP shells for field testing.

16.4.3 Structural Components for ARMS

Through the Advanced Robotic Mechatronics System (ARMS) project in collaboration with MD Robotics and Canadian Space Agency, NRC-London investigated laser consolidation as a rapid functional prototyping method for making Ti-6Al-4V structural components for the system [19]. One goal of the ARMS project was to develop a multifunctional structure capable of providing high structural stiffness, with dedicated features to support electronic driver/control cards and the data/power bus while allowing the dissipation of the heat generated by the electronic drivers. The laser consolidation process was successfully used to build functional demonstration pieces for the various designs as well as the final test-pieces of the multifunctional boom. Fig. 16.22 shows a Ti-6Al-4V boom built using the laser consolidation process. The boom had four ribs forming a slot to hold an electronic card. The LC Ti-6Al-4V boom was used in a as-consolidated surface finish, except for the contact surfaces that were machined for assembling.

Conventional design of a space robot manipulator generally consists of separate booms and joint housings that are connected to each other through a flanged interface, which substantially increases the weight and complexity. One-piece integrated boom/housing design is preferable to reduce the weight and complexity, and for increasing the interface stiffness of a

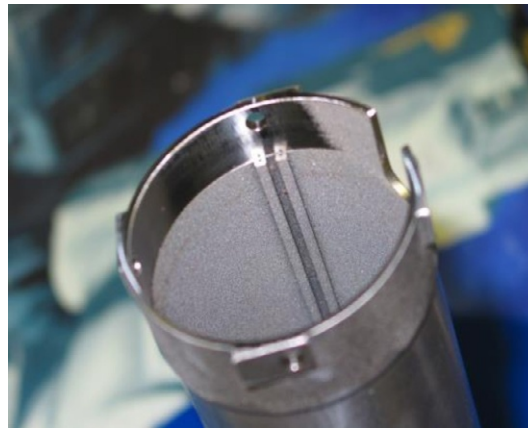


Fig. 16.22 LC Ti-6Al-4V boom with a slot to hold electronic card, after final machining.

typical robotic arm. However, it is extremely difficult or even impossible to make the one-piece integrated boom/housing using conventional manufacturing processes. The LC process is a free-form fabrication process that allows the building of net-shaped functional features on existing components. Therefore, it offers the unique capability to build multifunctional boom on pre-built housing to realize the innovative design for one-piece integrated boom/housing. Fig. 16.23 shows an integrated boom/housing manufactured using laser consolidation of Ti-6Al-4V alloy. The integrated LC Ti-6Al-4V boom/housing showed a as-consolidated surface finish, except for the contact surfaces that were initially machined for next stage final machining and assembling.



Fig. 16.23 LC Ti-6Al-4V integrated boom/housing, after initial machining.

The laser consolidation process successfully built multifunctional boom, housings #1 with interface, and housing #2 with integrated boom. The ARMS prototype robotic joint was assembled by MD Robotics using the LC Ti-6Al-4V structural components along with the other mechanical and electronic components. Fig. 16.24A and B shows a close view of the assembled joint, while Fig. 16.24C shows the ARMS with required payload during laboratory testing. The real-time testing results demonstrated that the laser-consolidated components performed very well and all design requirements such as low weight and high strength were achieved.

16.4.4 Functional Net-Shape Components for Potential Rocket Engine Applications

Design and manufacturing of rocket engines requires the manufacturing of various small quantity but complex shaped components. The laser consolidation process provides a unique capability to manufacture these small quantity functional components to shorten the manufacturing cycle and to reduce (or even eliminate) tooling cost. NRC-London worked with Pratt and Whitney Rocketdyne (PWR) to explore the laser consolidation process for manufacturing functional net-shape components as well as tooling for potential rocket engine applications [20].

16.4.4.1 LC IN-625 Demonstration Pieces

An IN-625 part was initially designed to demonstrate the capability of the laser consolidation process (Fig. 16.25A). It consists of 5 portions: (1) cylinder #1 (3 mm thick), (2) cylinder #2 (2 mm thick), (3) a conical top on a short cylinder (0.81 mm thick), (4) a circular fin (2 mm thick), and (5) a

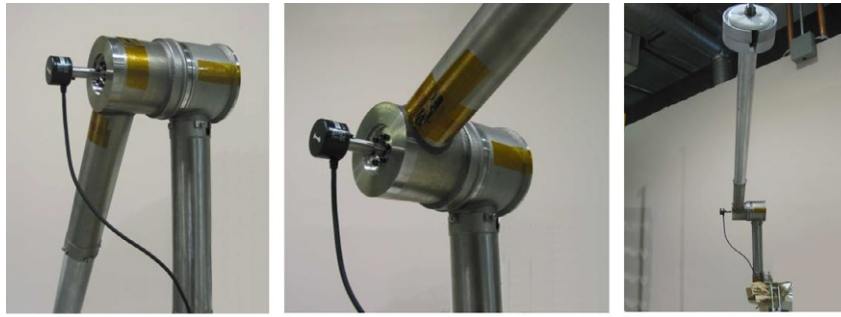


Fig. 16.24 Assembled ARMS with LC Ti-6Al-4V structural components: (A) and (B) close views; (C) testing with payload.

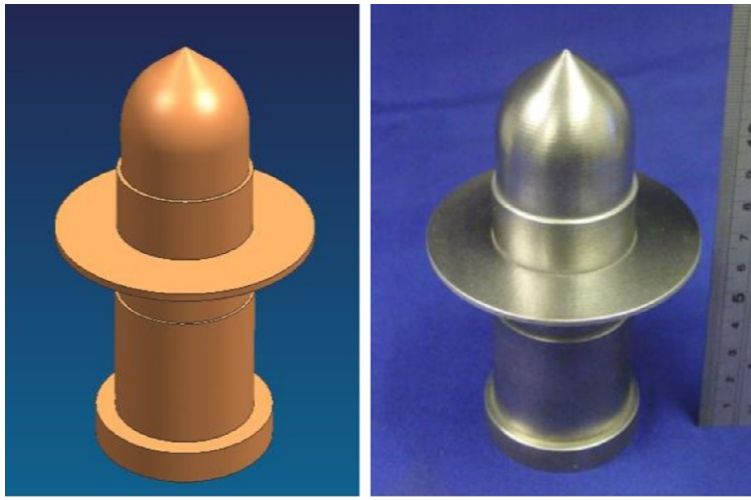


Fig. 16.25 IN-625 demonstration piece with conical top: (A) CAD drawing; (B) LC part.

substrate disk (50 mm in diameter and 9.4 mm thick). Laser consolidation of IN-625 was performed with a 5-axis motion system to build the demonstration piece on a 1020 steel substrate. A hole with a diameter of 8 mm was predrilled in the middle of the substrate to allow the release of the loose powder inside the part after laser consolidation. The steel substrate formed the part of the final demonstration piece. Fig. 16.25B shows the as-consolidated IN-625 demonstration piece after the removal of the loose powder. It is evident that the as-consolidated part showed very good surface finish.

The cross-sectional view of the part (Fig. 16.26A) reveals that, as per the CAD design requirement, the laser consolidation process managed to build

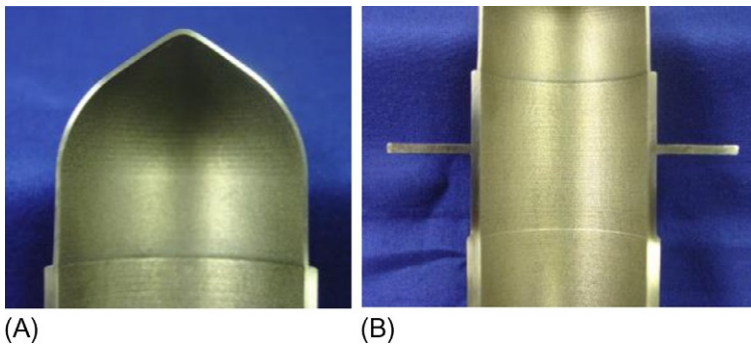


Fig. 16.26 Cross-section of LC IN-625 demonstration piece: (A) conical top; (B) middle section.

the LC IN-625 conical top with a very uniform wall thickness and the tip was sealed very well. Fig. 16.26B shows that all four sections of the LC IN-625 piece demonstrated uniform wall thickness. Detailed examination of the cross-section further revealed that all four portions of the LC IN-625 demonstration piece were metallurgically sound, without cracking or porosity. The bonding between sections and to substrate plate was excellent.

Dimensions measurement revealed that the internal diameter of the LC IN-625 part was 38.15 mm, which was only 0.05 mm larger than the design. The thickness of the conical top was 0.81 mm, exactly the same as the design. The thickness of the cylinder was about 0.15 mm thicker than the design, which may be attributed to the deviation in arranging existing multi-pass to fit the required thickness and can be improved in the future.

16.4.4.2 LC Ti-6Al-4V Spherical Hollow Ball

One of the demonstration pieces is a spherical hollow ball made of Ti-6Al-4V. The ball requires an outside diameter of 51.501 mm with a deviation of ±0.254 mm and a wall thickness of about 0.7 mm. The ball needs to be fully sealed without any unfinished pores or leaks. The Ti-6Al-4V hollow ball is usually manufactured by forming two halves of the ball separately through machining, forming, or other appropriated methods and then welding them together, which involves many manufacturing steps. For high end users, the thickness uniformity of the ball, especially at the weld area is always a big concern.

As a rapid manufacturing process, the laser consolidation process provides the possibility to build the spherical hollow ball directly. However, there is no reference available regarding other similar processes to build a spherical hollow ball directly from the Ti-6Al-4V powder. Laser consolidation was investigated to build the entire functional net-shape spherical hollow ball from the Ti-6Al-4V powder in one step to demonstrate its processing capability. A 5-axis motion system was used for this work. A special laser consolidation procedure was developed to build the ball from a Ti-6Al-4V substrate and to close it at the top. After laser consolidation, the ball was machined off from the substrate.

Fig. 16.27A shows a top view of the as-consolidated ball after removing the loose powder. It is evident that the as-consolidated Ti-6Al-4V ball showed reasonably good surface finish. Especially, since it revealed that the laser consolidation process successfully closed the hollow ball without any defects. Fig. 16.27B shows a bottom view of the ball, which reveals that a small portion of the substrate formed the part of the final ball after being cut off from the substrate.

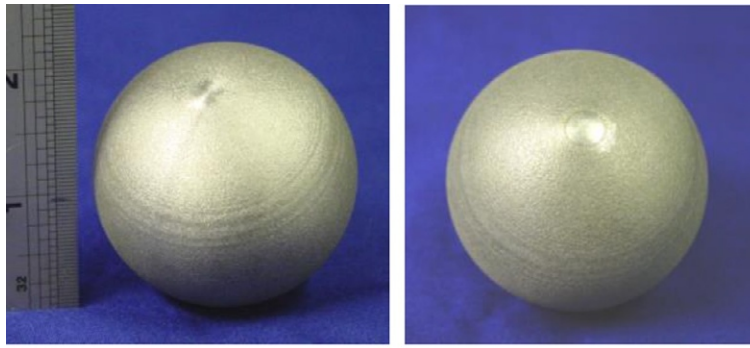


Fig. 16.27 LC Ti-6Al-4V hollow ball: (A) top view; (B) bottom view.

The outside diameters of the LC Ti-6Al-4V ball were measured using a Mitutoyo Precision Height Gauge, 45° apart along both polar and equatorial orbits, and data is listed in Table 16.12. The measurements were compared with the nominal diameter from the CAD model of the ball and the deviation was calculated for each measurement. Based on the CAD data, the outside diameter of the ball should be 51.501 mm. The measurement of the LC Ti-6Al-4V ball along polar orbit showed the maximum diameter of 51.575 mm and the minimum diameter of 51.397 mm. Along equatorial orbit, all the measurements were the same (51.575 mm in diameter), which demonstrated excellent uniformity of the ball.

It is obvious that the LC Ti-6Al-4V ball showed excellent dimensional accuracy. The deviation of the outside diameter of the LC Ti-6Al-5V ball was in the range of +0.074 and −0.104 mm, which was significantly less than the required deviation of ±0.254 mm. If you disregard the (★) data

Table 16.12 Measurement of outsider diameters of LC Ti-6Al-4V ball (mm)

Angle	Measurement	CAD	Deviation
Measured in polar orbit			
0°	51.575	51.501	+0.074
+45°	51.486	51.501	−0.015
+90°	51.397★	51.501	−0.104★
−45°	51.473	51.501	−0.028
Measured in equatorial orbit			
0°	51.575	51.501	0.074
+45°	51.575	51.501	0.074
+90°	51.575	51.501	0.074
−45°	51.575	51.501	0.074

that was affected by the cut-off process, the deviation will be even smaller (+0.074 mm and −0.028 mm).

16.4.5 LC IN-718 Impeller

Laser consolidation is a material addition process that can directly build functional features on an existing component to form integrated structure without the need of welding or brazing. For example, laser consolidation can be used to build net-shape functional components on a pre-machined substrate [21]. An impeller shape (Fig. 16.28) was selected to demonstrate the capability of the laser consolidation process using the 5-axis motion system. The impeller has a diameter of about 77 mm and a height of about 26 mm. There are nine long blades and nine short blades uniformly distributed.

A profiled substrate was pre-machined using a CNC lathe (Fig. 16.29) and was mounted on a 5-axis motion system using a simply designed fixture. Laser consolidation of IN-718 alloy was performed to build blades on the pre-machined base using the 5-axis motion system. Laser consolidation can be performed to complete building up a blade and then another one. However, the completed blade(s) will interfere with the laser beam and powder flow when building the other blades. To avoid the interference issue, laser consolidation was conducted to build one layer at a time for each blade.

Due to the impeller shape, large tilt-rotation movement is required for building each blade. Initial investigation indicated that the 5-axis motion system originally used for the project has serious dimensional accuracy and repeatability issues. The position error between two consecutive

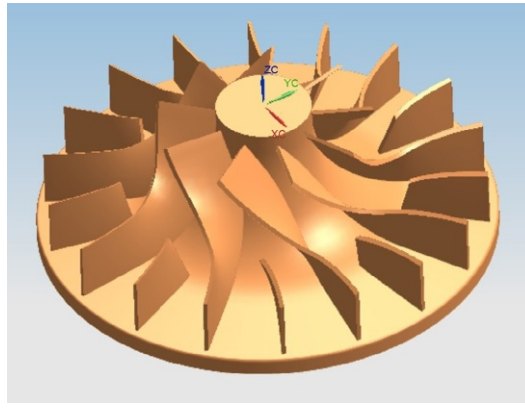


Fig. 16.28 A CAD model of an impeller to be manufactured using laser consolidation process.

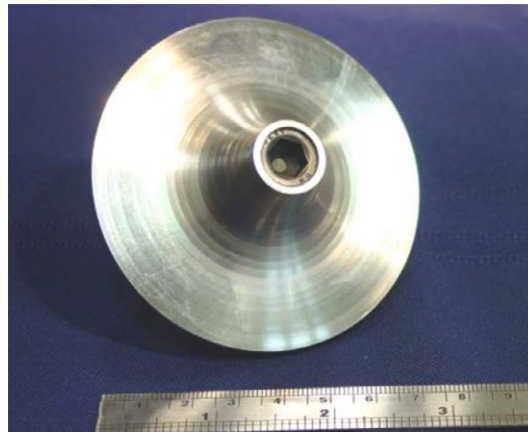


Fig. 16.29 A profiled substrate was pre-machined using a CNC lathe.

90° tilt movement can be as large as 0.025″ (0.635 mm) and even a lot more during the process. Due to the motion system problem, the laser-consolidated blades were melted down or double walls were formed during the laser consolidation process.

After changing to another 5-axis CNC motion system, laser consolidation was successfully conducted to build blades on the pre-machined substrate to form an integrated impeller. Fig. 16.30 shows an IN-718 impeller (left) with its blades directly built up on a pre-machine substrate using the LC process. The surface finish of the as-consolidated IN-718 blades is about 1.6 μm along the horizontal direction and about 2.94 μm along the vertical



Fig. 16.30 IN-718 impellers with laser-consolidated blades built on pre-machined substrate (the left one with as-consolidated surface and the right one after sand blasting).

direction. After sand blasting, laser-consolidated blades and pre-machined substrate show consistent surface finish (Fig. 16.30, right side).

It is evident that this novel process produces high quality, fairly complex shapes directly from a CAD model with good surface finishes in as-consolidated condition or after sand blasting. The bond between the LC features and the existing component is metallurgically sound, without crack and porosity. Compared to the conventional welding process, the heat input from the LC process to the substrate is minimal, resulting in a very small heat affected zone (several tens of micrometers). By using the LC process, more unique features can be added to the gas turbine components to provide additional functionality, and to reduce manufacturing time and cost.

16.4.6 Cold Spray Nozzles

Cold spray (or gas-dynamic spray) is a relatively new coating technology that addresses many of the limitations of conventional thermal spray processes. It is a solid-state coating process, in which small solid particles are accelerated to velocities between 300 and 1200 m/s by a supersonic or sub-supersonic jet flow, and are subsequently deposited onto a surface by impinging upon a substrate [49,50]. Coating formation in the cold spray process is mainly due to the high kinetic energy of the solid-state particles, in contrast to conventional thermal spray processes, in which coating formation depends on both thermal and kinetic energies. Because of relatively low operation temperature, cold spray is ideally suitable for depositing oxygen-sensitive materials, temperature-sensitive materials, and/or phase-sensitive materials. Cold-spray coatings generally have low oxide content and low thermal stress and retain the microstructure (e.g., nano-phase or amorphous structure) of the feed powder material. Thus, it provides a promising technique for many applications unachievable with existing practices.

In cold spray, the supersonic or sub-supersonic jet flow is generated through a converging-diverging de Laval type nozzle. Particles are usually injected axially into the gas flow at the inlet of the nozzle (upstream of the nozzle throat) [51,52]. There are many potential applications for cold spray coatings, for example, wear resistant, corrosion resistant, high thermal/electrical conduction, thermal barrier, thermal sink, etc. In some applications, cold spray offers unique advantages over other techniques but the uniformity of coating thickness is an important consideration.

Currently, the most commonly used cold spray nozzle has a round shape in the cross section. Round nozzles are easy for manufacturing, but the thickness of a single-track coating is not uniform. The cross-section of such

a single-track deposit is usually triangular (Fig. 16.31). Another type of commonly used cold spray nozzle has a rectangular cross section. Although the thickness uniformity of a single-track coating deposited using such nozzles is better than using round-shaped nozzles, it is still not satisfactory for certain demanding applications requiring uniform thin coatings.

To improve the cross-section thickness uniformity of single-track cold spray coatings, the following new nozzle design concepts were proposed: the cross-section shapes along the divergent section and at the nozzle exit, be designed to have a generally dumbbell shape such that solid particles within the nozzle are more uniformly distributed. There can be many designs for the nozzle cross-section shapes/dimensions based on such concepts. In this investigation, three shapes have been examined which are shown in Fig. 16.32 with the anticipated cross-section shape of single-track coating.

Although the novel nozzle design offers unique advantages to improve the coating uniformity, it creates a challenge for the existing manufacturing technology to make them. After considerable evaluation of alternative

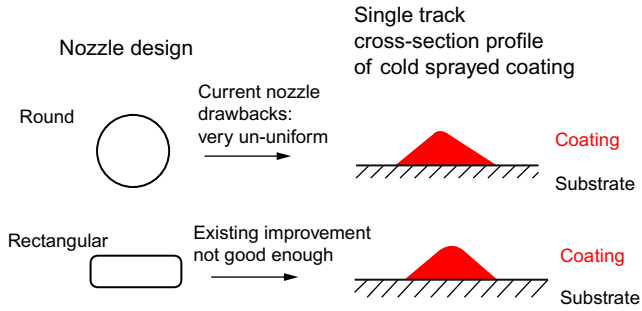


Fig. 16.31 Typical thickness profiles of a cross section of a single track cold spray coating produced using round-shaped and rectangular-shaped nozzles.

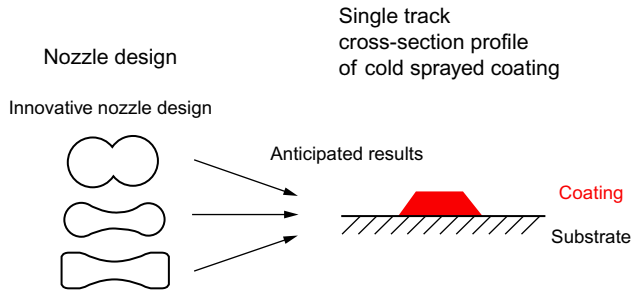


Fig. 16.32 Proposed nozzle cross section shapes for uniform thickness.

manufacturing technologies, laser consolidation was selected as the most promising method for making these functional cold spray nozzles. Laser consolidation of IN-625 was successfully used to build cold spray nozzles with newly designed shapes. Fig. 16.33 shows laser-consolidated cold spray nozzles with three different cross-sectional shapes, and three completed laser-consolidated nozzles with a length from 175 to 193 mm.

Cold spray experiments were performed using the newly designed nozzles. Two different sets of deposition conditions were used: (a) a single-track one-layer Al coating deposited on Zn-coated steel plate, and (b) a single-track multi-layer Al-4047 coating deposited on a Al-6061 plate. Fig. 16.34 compares the cross-section profiles of single-track coating deposited using a conventional round nozzle, a rectangular nozzle, and the newly developed laser-consolidated nozzle #3. The coating sprayed using the nozzle has a much better uniformity in thickness than the coating sprayed using the round nozzle. Although the rectangular nozzle produced more uniform coating thickness than using the round nozzle, it is still not as uniform as the coating sprayed using the newly developed nozzle.

Fig. 16.35 shows the cross-section profiles of single-track two-layer coating cold-sprayed using the conventional round nozzle and the new laser-consolidated nozzle #3. The thickness uniformity of the two-layer coating sprayed using the round nozzle is worse than that of the one-layer coating sprayed by the same nozzle. On the other hand, the two-layer coating sprayed using the LC nozzle #3 shows excellent thickness uniformity. The laser-consolidated new nozzles in combination with our previously developed downstream powder feeding cold spray system with symmetrically located multi-powder injectors [53] have

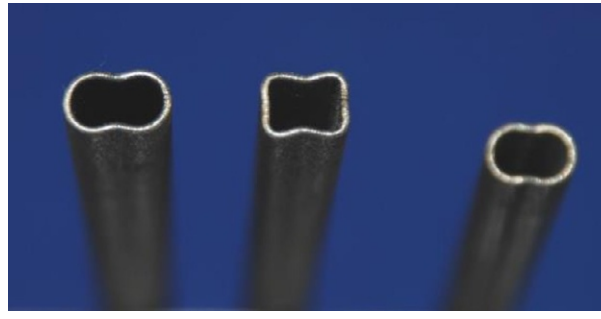


Fig. 16.33 Laser-consolidated IN-625 cold spray nozzles with different cross sectional shapes (#1, #2, and #3).

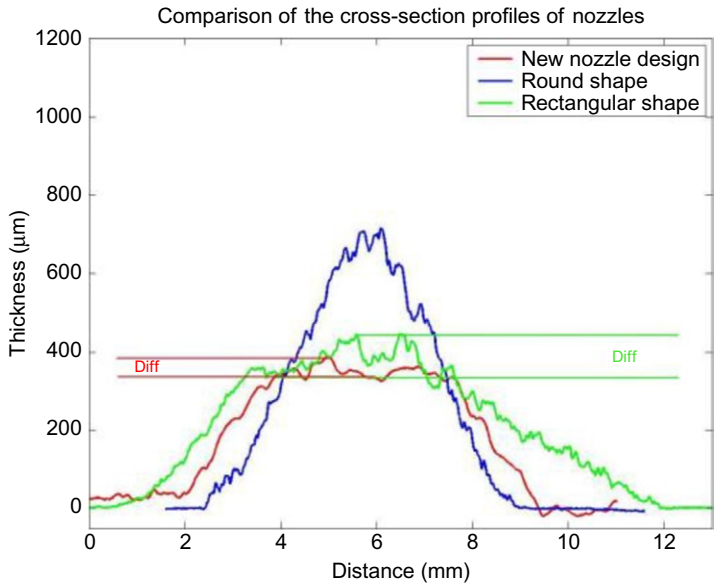


Fig. 16.34 Comparison of cross-section thickness profiles of single-track coating deposited using different nozzle cross-section shapes: round nozzle, rectangular nozzle, and LC nozzle #3.

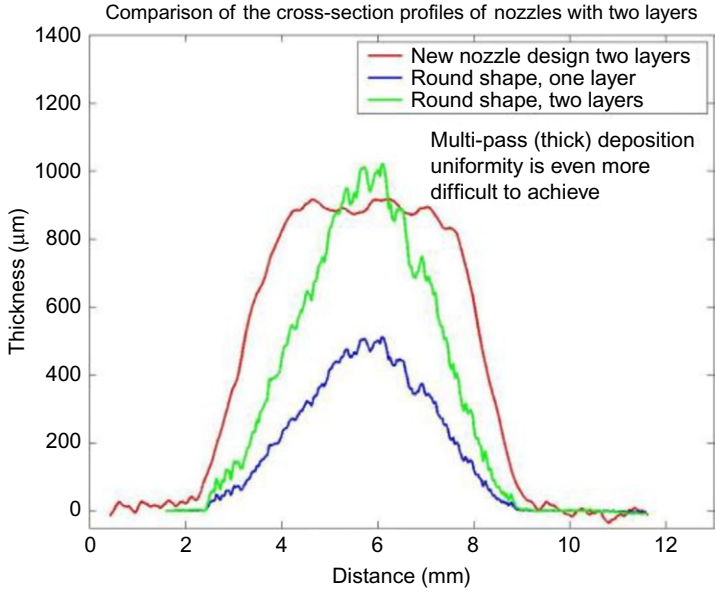


Fig. 16.35 Cross-section profiles of one-layer and two-layer coatings sprayed by round nozzle, and two-layer coating sprayed by innovative LC nozzle #3.

demonstrated great potential to produce cold spray coatings with excellent uniform thickness and provides the possibility for additive manufacturing by using cold spray technology.

16.5 FUTURE TREND OF THE TECHNOLOGY

As demonstrated in the previous sections of this chapter, laser consolidation process provides the unique capability to produce net-shape functional components directly from CAD models without molds or dies, which enables the rapid manufacturing of small quantity metallic components with short delivery time and reduced production cost. However, this technology is still emerging and much more developmental work is needed.

It is expected that more industrial materials will be investigated using the laser consolidation process. A comprehensive database of laser consolidated materials, its microstructure, mechanical, and other properties will be generated through collaboration among research organizations, universities, and industries. The processing capability of the technology will be further improved to build more complex net-shape functional components that cannot be produced currently. The processing speed will be substantially improved to meet industrial needs for production. The adoption of advanced sensing, control capability, and software development will further improve the robustness of the process in the production environment.

With the increased interest from various industries, it is expected that more industrial applications will be developed, especially in the fields of aerospace, defence, medical devices, and tooling. In combination with innovative design, the laser consolidation process along with the 5-axis CNC motion system provides unique capability to produce complex components with delicate details that are very difficult or even impossible to make using conventional manufacturing processes. In combination with other manufacturing technologies, laser consolidation can build integrated delicate features on components manufactured using conventional low cost methods. Compared to the traditional welding process, the heat input induced by the laser consolidation process to the substrate is minimal. Therefore, laser consolidation process also provides the possibility to build unique features on thin-walled components to provide additional functionality, and reduce manufacturing time and cost. In addition, since laser consolidation does not require any molds or dies, it provides the possibility to design and manufacture components directly through the internet to combine the real strength of virtual manufacturing and rapid manufacturing. It also provides the flexibility to change the design quickly to make functional components

to meet various industrial demands to produce customized components with significantly reduced lead-time. It is expected that this computer aided manufacturing (CAM) technology will make a huge impact on manufacturing in a wide range of industries in the near future.

ACKNOWLEDGMENTS

The author would like to thank Yangsheng Li, Andre Theriault, Jianyin Chen, Shaodong Wang, Sheng-hui Wang, Jimmy Jiang, Glen Campbell, Allan Gillett, Gary Wabersich, Nelson Santos, Brian Gibson, Jon Fenner, and Mike Meinert for their numerous contributions in process development, sample preparation, and characterization. Thanks are also due to many collaborators for their valuable contributions during various projects.

REFERENCES

[1] O. Milewski, G.K. Lewis, D.J. Thoma, J.I. Keel, R.B. Nemec, R.A. Reinert, Directed light fabrication of a solid metal hemisphere using 5-axis powder deposition, J. Mater. Process. Technol. 75 (1998) 165–172.
[2] D.M. Keicher, W.D. Miller, J.E. Smugeresky, J.A. Romero, Laser engineering Net shaping (LENS™): beyond rapid prototyping to direct fabrication, in: Proceedings of the TMS Annual Meeting 1998, 1998, pp. 369–377.
[3] M.A. McLean, G.J. Shannon, W.M. Steen, Laser generating metallic components, Proc. SPIE 3092 (1997) 753–756.
[4] D.J. Thoma, C. Charbon, G.K. Lewis, R.B. Nemec, Directed light fabrication of iron-based materials, Mater. Res. Soc. Symp. Proc. 397 (1996) 341–346.
[5] D.J. Thoma, G.K. Lewis, R.B. Nemec, Solidification behavior during directed light fabrication, in: Proceedings of the 2nd International Conference on Beam Processing of Advanced Materials, 1995, pp. 247–253.
[6] F. Klocke, H. Wirtz, W. Meiners, Direct manufacturing of metal prototypes and prototype tools, in: Proceedings of Solid Freeform Fabrication Symposium, 1996, pp. 141–148.
[7] G.A. Whitlow, G.J. Bruck, Laser beam casting of metal powder into near net shape products, in: Power Beam Processing: Electron, Laser, Plasma-Arc: Proceedings of the International Power Beam Conference, 1988, pp. 207–210.
[8] Sandia National Laboratories, Creating a complex metal part in a day is goal of commercial consortium, News Release on Sandia National Laboratories, http://www.sandia.gov/media/lens.htm, December 4, 1997.
[9] L. Xue, M.U. Islam, Free-form laser consolidation for producing metallurgically sound and functional components, J. Laser Appl. 12 (4) (2000) 160–165.
[10] L. Xue, J.-Y. Chen, M.U. Islam, Functional properties of laser consolidated wear resistant Stellite 6 alloy, in: D.E. Alman, J.W. Newkirk (Eds.), Powder Metallurgy Alloys and Particulate Materials for Industrial Applications, TMS, 2000, pp. 65–74.
[11] L. Xue, J.-Y. Chen, M.U. Islam, J. Pritchard, D. Manente, S. Rush, Laser consolidation of IN-738 alloy for repairing cast IN-738 gas turbine blades, in: Proceedings of 20th ASM Heat Treating Society Conference, St.-Louis, Missouri, USA, October 8–12, 2000, pp. 1063–1107.
[12] L. Xue, J.-Y. Chen, A. Theriault, Laser consolidation of Ti-6Al-4V alloy for the manufacturing of net-shape functional components, in: Proceedings of 21st International Congress on Applications of Lasers and Electro-Optics (ICALEO 2002), Scottsdale, USA, 2002, pp. 169–178.

[13] L. Xue, J.-Y. Chen, A. Theriault, Laser consolidation of Al 4047 alloy, in: Proceedings of 24th International Congress on Applications of Lasers and Electro-Optics (ICALEO 2005), Miami, USA, 2005, pp. 344–351.
[14] L. Xue, J. Chen, S.-H. Wang, Y. Li, Laser consolidation of Waspaloy and IN-718 alloys for making net-shape functional parts for gas turbine applications, in: Proceedings of 27th International Congress on Applications of Laser & Electro-Optics (ICALEO 2008), Temecula, CA, USA, 2008, pp. 255–263.
[15] L. Xue, A. Theriault, S.-H. Wang, J.-Y. Chen, Laser consolidation of functional shell structure, in: Proceedings of the 5th International Workshop on Advanced Manufacturing Technologies (AMT 2005), London, Ontario, Canada, 2008, pp. 231–236.
[16] L. Xue, A. Theriault, J.-Y. Chen, M.U. Islam, A. Wieczorek, G. Draper, Laser consolidation of CPM-9V tool steel for manufacturing rotary cutting dies, in: Proceedings of 10th International Symposium on Processing and Fabrication of Advanced Materials, 2001 ASM Materials Solution Conference and Exposition, Indianapolis, Indiana, USA, 2002, pp. 361–376.
[17] L. Xue, A. Theriault, M.U. Islam, M. Jones, H.P. Wang, Laser consolidation of Ti-6Al-4V alloy to build functional net-shape airfoils with embedded cooling channels, in: Proceedings of the 23rd International Congress on Applications of Lasers and Electro-Optics (ICALEO 2004), San Francisco, California, USA, 2004.
[18] L. Xue, C. Purcell, Laser consolidation of net-shape shells for flextensional sonar projectors, in: Proceedings of the 25th International Congress on Applications of Lasers and Electro-Optics (ICALEO 2006), Scottsdale, Arizona, USA, 2006, pp. 686–694.
[19] L. Xue, A. Theriault, B. Rubinger, D. Parry, F. Ranjbaran, M. Doyon, Investigation of laser consolidation process for manufacturing structural components for advanced robotic mechatronics system, in: Proceedings of 22nd International Congress on Applications of Lasers and Electro-Optics (ICALEO 2003, Jacksonville, Florida, USA), 2003, pp. 134–143.
[20] L. Xue, Y. Li, T. Van Daam, C. Bampton, Investigation of laser consolidation for manufacturing functional net-shape components for potential rocket engine applications, in: Proceedings of the 26th International Congress on Applications of Lasers and Electro-Optics (ICALEO 2007), Orlando, Florida, USA, 2007, pp. 161–169.
[21] L. Xue, Y. Li, S. Wang, Direct manufacturing of net-shape functional components/test-pieces for aerospace, automotive and other applications, J. Laser Appl. 23 (4) (2011) 042004.
[22] E.A. Schoefer, Properties of cast stainless steels, ASM Handbook Committee, ninth ed., Metals Handbook: Properties and Selection: Stainless Steels, Tool Materials and Special-Purpose Metals, vol. 3, American Society for Metals, Ohio, 1980, p. 113.
[23] ASM Committee on Wrought Stainless Steels, Wrought stainless steels, ASM Handbook Committee, ninth ed., Metals Handbook: Properties and Selection: Stainless Steels, Tool Materials and Special-Purpose Metals, vol. 3, American Society for Metals, Ohio, 1980, p. 21.
[24] Micronalloys, Information provided through an e-mail, 2002.
[25] http://www.moldsteel.com.
[26] T.V. Philip, T.J. McCaffrey, Ultrahigh-strength steels, ASM International Handbook Committee, 10th ed., Metals Handbook: Properties and Selection: Irons, Steels, and High-Performance Alloys, vol. 1, ASM International, Ohio, 1990, p. 442.
[27] K.E. Pinnow, W. Stasko, P/M tool steel, ASM International Handbook Committee, 10th ed., Metals Handbook: Properties and Selection: Irons, Steels, and High-Performance Alloys, vol. 1, ASM International, Ohio, 1990, pp. 786–789.
[28] G.L. Erickson, Polycrystalline cast superalloys, ASM International Handbook Committee, 10th ed., Metals Handbook: Properties and Selection: Irons, Steels, and High-Performance Alloys, vol. 1, ASM International, Ohio, 1990, p. 984.

[29] F.R. Morral, Wrought superalloys, ninth ed., Metals Handbook: Properties and Selection: Stainless Steels, Tool Materials and Special-Purpose Metals, vol. 3, American Society for Metals, Ohio, 1980, p. 219.
[30] Waspaloy, www.specialmetals.com.
[31] F.R. Morral, Wrought superalloys, ninth ed., Properties and Selection: Stainless Steels, Tool Materials and Special-Purpose Metals, vol. 3, American Society for Metals, Ohio, 1980, p. 221.
[32] SAE Aerospace, Aerospace Material Specification (AMS) 5707K: Nickel Alloy, Corrosion and Heat-resistant, Bars, Forgings, and Rings (58Ni-19.5Cr-13.5Co-4.3Mo-3.0Ti-1.4Al-0.05Zr-0.006B), January 2007.
[33] W.L. Mankins, S. Lamb, Nickel and nickel alloys, in: J.R. Davis, et al. (Eds.), ASM Handbook: Properties and Selection: Nonferrous Alloys and Special-Purpose Materials, vol. 2, ASM International, Ohio, 1990, pp. 438.
[34] F.R. Morral, Wrought superalloys, ninth ed., Metals Handbook: Properties and Selection: Stainless Steels, Tool Materials and Special-purpose Metals, vol. 3, American Society for Metals, Ohio, 1980, p. 219.
[35] S. Azadian, Aspects of Precipitation in the Alloy Inconel 718 (Doctoral thesis), Lulea University of Technology, Lulea, Sweden, 2004, p. 15.
[36] ASM Committee on Cast Corrosion-Resisting and Heat-Resisting Alloys, Heat-resistant casting, ASM Handbook Committee, ninth ed., Metals Handbook: Properties and Selection: Stainless Steels, Tool Materials and Special-Purpose Metals, vol. 3, American Society for Metals, Ohio, 1980, p. 278.
[37] ASM Handbook Committee, Properties of superalloys, ASM Handbook Committee, ninth ed., Metals Handbook: Properties and Selection: Stainless Steels, Tool Materials and Special-Purpose Metals, vol. 3, American Society for Metals, Ohio, 1980, pp. 244–245.
[38] R.R. Boyer, Titanium and titanium alloys, in: ASM Handbook Committee (Ed.), ASM Handbook, vol. 9, Metallography and Microstructures, ASM International, Ohio, 1985, pp. 458–475.
[39] J.R. Newman, Titanium castings, in: ASM Handbook Committee (Ed.), Metals Handbook, ninth ed., vol. 3, Properties and Selection: Stainless Steels, Tool Materials and Special-Purpose Metals, American Society for Metals, Ohio, 1980, p. 409.
[40] ASM Committee on Titanium and Titanium Alloys, Properties of titanium and titanium alloys, ASM Handbook Committee, ninth ed., Metals Handbook: Properties and Selection: Stainless Steels, Tool Materials and Special-Purpose Metals, vol. 3, American Society for Metals, Ohio, 1980, pp. 388–389.
[41] J.R. Davis, ASM Specialty Handbook: Heat-Resistant Materials, ASM International, Ohio, 1997, pp. 347–360.
[42] D. Eylon, J.R. Newman, J.K. Thorne, Titanium and titanium alloy castings, ASM Handbook Committee, ASM Handbook: Properties and Selection: Nonferrous Alloys and Special-Purpose Materials, vol. 2, ASM International, Ohio, 1990, p. 642.
[43] P. Crook, Cobalt and cobalt alloys, ASM Handbook Committee, ASM Handbook: Properties and Selection: Nonferrous Alloys and Special-Purpose Materials, vol. 2, ASM International, Ohio, 1990, pp. 446–454.
[44] Data supplied by Deloro Stellite Inc., June 1999.
[45] M.C. Flemings, Solidification Processing, McGraw-Hill Book Company, New York, 1974, pp. 342–343.
[46] D. Apelian, Solidification mechanics and mechanism, Encyclopedia of Materials Science and Engineering, vol. 6, Pergamon Press, New York, 1986, pp. 4525–4529.
[47] Eagle Alloys Group, Mechanical testing data for Al 4047 sample material, 2005.
[48] A.L. Kearney, Properties of cast aluminum alloys, ASM Handbook Committee, ASM Handbook: Properties and Selection: Nonferrous Alloys and Special-Purpose Materials, vol. 2, ASM International, Ohio, 1990, pp. 171–173.

[49] A.P. Alkhimov, A.N. Papyrin, V.F. Kosarev, N.I. Nesterovich, M.M. Shushpanov, Gas-dynamic spraying method for applying a coating, US Patent 5,302,414, April 12, 1994.
[50] R.C. Dykhuizen, M.F. Smith, Gas dynamic principles of cold spray, J. Therm. Spray Technol. 7 (2) (1998) 205–212.
[51] T. Schmidt, F. Gartner, H. Assadi, H. Kreye, Development of a generalized parameter window for cold spray deposition, Acta Mater. 54 (2006) 729–742.
[52] T. Stoltenhoff, H. Kreye, H.J. Richter, An analysis of the cold spray process and its coatings, J. Therm. Spray Technol. 11 (4) (2002) 542–550.
[53] L. Xue, S. Wang, J. Jiang, Cold gas dynamic spray apparatus, system and method, US Patent 9,168,546B2, October 27, 2015.

This page intentionally left blank

CHAPTER 17

Laser-Based Additive Manufacturing Processes

H. Sahasrabudhe*, S. Bose†, A. Bandyopadhyay†
*LENS Applications Engineer, Optomec Inc., Albuquerque, NM, United States
†Washington State University, Pullman, WA, United States

17.1 INTRODUCTION

Additive manufacturing, three-dimensional printing (3DP), solid freeform fabrication (SFF), layered manufacturing (LM), and rapid prototyping (RP) are collectively technologies that are can manufacture or fabricate a component additively. The simplest way to visualize any additive manufacturing technique is to think of the opposite of subtractive manufacturing processes such as milling. In additive manufacturing, a part is formed by layer-wise deposition of the materials in a three-dimensional pattern. The material is progressively "added" and a part is formed, thus the processes are collectively termed as "additive manufacturing." Additive manufacturing can be thought of as a sophisticated way of using a more conventional manufacturing technique. The basic way in which a material is processed in the additive manufacturing technique is not new, but the way in which it is processed over time is by following a predetermined blueprint from a CAD file. For instance, we can consider the very basic fused deposition modeling (FDM) technique of additive manufacturing. FDM technology uses the extrusion of a polymeric wire into a filament at an elevated temperature to create a thin filament. These thin filaments are then laid down on a platen, where they gradually cool down and solidify into hard shapes. The deposition process is in a three-dimensional pattern. The process, in its very basic form, is an extrusion process. However, the novelty that converts this process into additive manufacturing or 3DP is the way the extrusion products are utilized. Table 17.1 shows some comparisons between conventional or traditional manufacturing and additive manufacturing [1].

Additive manufacturing techniques have created opportunities for using newer designs and materials that were earlier thought to be cumbersome to

Advances in Laser Materials Processing
https://doi.org/10.1016/B978-0-08-101252-9.00017-0
Copyright © 2018 Elsevier Ltd.
All rights reserved.

Table 17.1 Comparison of conventional versus additive manufacturing [1]

Aspect	Conventional manufacturing	Additive manufacturing
Process	Casting, forging, extrusion, etc.	Utilization of the conventional processes in a novel way. For example, Extrusion in FDM, Microcasting in LENS
Equipment setup	Specific for each material and process. Each design needs a new setup or new process controls	Versatile for many materials. However, for each new material, the technique has to be carefully optimized and tested multiple times
Reproducibility	Highly reproducible. Processes like casting are sometimes carried out in batches of thousands. Room for human/operator error or variation is less	Fairly reproducible as long as the process is optimized and the operators are skilled. Human factor is crucial in many processes
Production volume	Efficient for high number production, large batches that reduce the overall tooling time, and other associated costs. Entire operation is optimized to reduce per part cost	Best suited for low-volume specialized manufacturing. Cost of an individual part may be high but processes are not typically used to produce volumes as high as conventional methods
Throughput	Increasing throughput means increasing the number of batches, which requires high initial costs but reduced per part costs	Increasing throughput means buying more machines and running them simultaneously
Secondary machining	Always required	Not always necessary as some processes can produce parts with excellent surface finishes
Heat treatment	Required many times for improving properties. For example, heat treatment of steel such as the tempering process	Usually not required. Heat treatment is sometimes done to reduce residual stresses and improve ductility of part
Multimaterial system	Not possible. Processes like welding are needed	Some techniques are capable of multimaterial manufacturing with different materials in the same component as per requirement

Table 17.1 Comparison of conventional versus additive manufacturing [1]—cont'd

Aspect	Conventional manufacturing	Additive manufacturing
Initial setup cost	Usually high, but costs reduce as number of parts increase, which is always the case	Initial machine costs are high
Raw material/ feed cost	High but efficient for high-volume production	Depends on the material. Steel powders could cost anywhere from $10 to $20 per pound whereas Ti6Al4V alloy would cost as much as 15–20 times more
Defining characteristic	Single design, high initial cost, high production volume, low part cost	Design specific, high initial cost, low specialty production irrespective of the per part cost

work with, or that the conventional manufacturing techniques simply were unable to process with certainty. For this reason, additive manufacturing has been getting a lot of attention. In this chapter, we will discuss the laser energy-based additive manufacturing techniques and focus on the material processing capabilities of metallic and metal-ceramic composite materials via these techniques. We will also consider some real-life applications of these laser-based additive manufacturing techniques.

17.2 TECHNIQUES

There are several additive manufacturing processes that are becoming popular for a variety of different applications and that are capable of processing a variety of different materials. These processes are fundamentally different, even for the same class of materials, and the choice of the process depends on the design of the part as well as the required properties. As an example, the selection between a powder bed fusion (PBF) process such as electron beam melting or a directed energy deposition method such as laser direct metal deposition (DMD) for the processing of titanium is as involved as the selection between extrusion and casting for making an Al 6061 alloy component. For the unexperienced user, the words "3D printing" often give an impression that the process can do almost anything with a material.

To organize the different available processes in a better way, the ASTM committee has put forward a standard for additive manufacturing technologies based on their fundamental way of fusing the material [2]. Fig. 17.1 describes the different classes of additive manufacturing techniques as

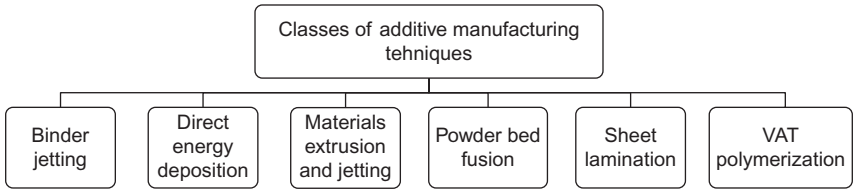


Fig. 17.1 Classification of additive manufacturing techniques.

categorized by the ASTM standard. Out of these six classes of techniques, only the direct energy deposition (DED) and PBF categories utilize a laser energy source for fusion of the material. Hence, only these two processes will be discussed here.

17.2.1 Direct Energy Deposition Techniques of Additive Manufacturing

In the DED techniques, there is a simultaneous introduction of the material and the energy source during operation. This energy source is used to directly melt the material at the site of deposition. The material can be fed in the form of powder or as a filament. Upon interaction with the energy source, the material melts almost instantly, creating a melt pool that then solidifies rapidly as the energy source moves away from the site. When this one-point deposition has to be scaled up for a continuous additive process, there has to be a continuous feed of the material. Also, the process has to be set up in a controlled *X*, *Y* axes table to create two-dimensional patterns using the melt, or deposit a thin line of the molten material that begins to rapidly solidify. If the *X*, *Y* stage can be programmed to move along a raster pattern, the material deposition will follow the same pattern. This in turn will create or deposit a layer. If a *Z* axis is included, either carrying the *X*, *Y* stage down or moving the deposition assembly up (as in most cases), another raster scanning pattern can now be deposited on the previously deposited layer. Thus, the process can deposit several layers that control the cross section of the actual part. Upon the deposition of several such layers, a complete part can be realized. This forms the most fundamental basis of the entire family of DED additive manufacturing techniques. The processes are further classified as those that are either used for creating two-dimensional geometries such as surface modification or coatings and cladding and processes that can be used for making three-dimensional structures. Since we are focused on the utilization of laser energy as the energy source for additive manufacturing, DED processes that utilize plasma energy and an electron beam (such as electron beam direct melting or EBDM) will not be discussed here.

17.2.1.1 Laser-Based Direct Energy Deposition Techniques for Two-Dimensional Geometry

The two main processes that have been used for two-dimensional part depositions are laser melt injection and laser cladding. Both processes use a laser for melting the incoming material, which is either a powder or a filament. The initial form of these processes is a two-step process in which a thin layer of powder is preplaced and compacted on the surface. A high-power laser is then scanned on this preplaced powder layer, causing it to melt. This phenomenon is shown in Fig. 17.2[3]. As the computerized motion control developed, the process gradually evolved into a single-step process in which the powder is injected into the surface while a simultaneous exposure to the laser radiation at the same point causes it to melt and solidify.

In 1981, Ayers et al., demonstrated that ceramic particles can be "blown" and injected into a surface, melting at the site of injection using laser energy [4]. The result of this is a layer of solidified ceramic particles, embedded in the remelted metallic surface. Such a process can also be carried out by using the feedstock in the form of a wire instead of powder. The earliest of such processes utilized localized shielding of the molten area or the melt pool to reduce the deleterious effect of oxygen from the environment.

17.2.1.2 Laser-Based Direct Energy Deposition Techniques for Three-Dimensional Geometry

The basis of the DED techniques for fabricating three-dimensional geometries is the same as described in the previous section. All these technologies have computer numeric controlled X and Y axes that carry out a raster

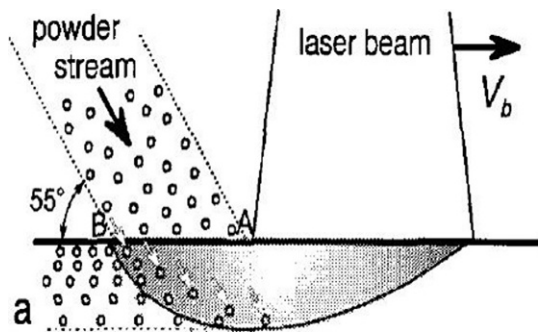


Fig. 17.2 Sketch of laser melt injection process. Courtesy of WIT Press from V. Ocelík, S. Nijman, R. van Ingen, U. Oliveira, J.T.M. De Hosson, Laser melt injection of hard ceramic particles into Al and Ti alloys processing, microstructure and mechanical behaviour, WIT Trans. Eng. Sci. 39 (2003).

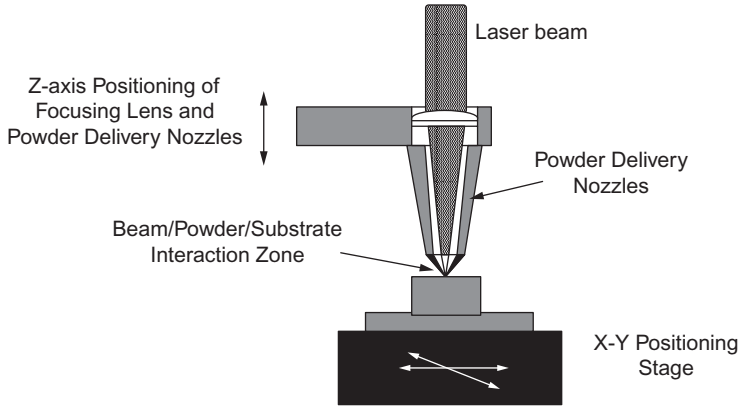


Fig. 17.3 Schematic representation of the LENS™ technology. From B.V. Krishna, S. Bose, A. Bandyopadhyay, Low stiffness porous Ti structures forload-bearing implants, Acta Biomater. 3 (6) (2007) 997–1006.

scanning motion and a setup that delivers the laser and the materials. The laser beam is mounted along the Z axis, so as to be able to deposit raster scans over a previously deposited layer. Such technologies are provided by numerous companies and can process a variety of different metal and ceramic materials. A popular technology of this category is Laser Engineered Net Shaping (LENS), developed by the Sandia National Laboratories. Fig. 17.3 shows the principle of operation of the LENS technology.

The LENS technology employs a glove box configuration to avoid oxygen. The XYZ axes and the main deposition assembly are enclosed in a glovebox and pressurized with an inert gas such as argon. There are numerous other additive manufacturing setups that are known by different names such as laser powder forming, laser DMD and DMD.

17.2.1.3 Laser Hybrid Manufacturing

To meet the demands of manufacturing operations, and to make laser-based DED additive manufacturing more viable for day-to-day manufacturing practices, the hybrid manufacturing approach is utilized. Hybrid manufacturing technologies use the earlier discussed laser deposition technology. However, they also offer machining capability in the same setup. These machines typically create a localized inert environment using argon, but glovebox configurations are also available. Hybrid manufacturing of materials is exciting to those who would like to take advantage of the laser-based deposition techniques and reduce a separate machining step. Companies such as Optomec Inc. and Hybrid Manufacturing Technologies (HMT) offer hybrid manufacturing solutions by integrating a machining platform with

an additive deposition system, effectively forming a hybrid manufacturing platform. Hybrid manufacturing is a relatively new addition to the nearly 20-year-old metal additive manufacturing world.

17.2.1.4 Laser-Assisted Repair

Repair of damaged components and the addition of valuable functional features are some of the unique possibilities of the laser-based DED additive manufacturing techniques. The setup of the additive manufacturing equipment does not necessarily change for carrying out a repair or a feature addition process. For successful repair, it is always necessary to know the precise location of the damaged region. Most repair operations carried out today utilize the same material as that in the existing components. However, due to the different manufacturing techniques—conventional manufacturing for the component and laser-based DED techniques for the repair—the microstructure of the component and the repair deposit differ significantly. For this reason, it is often necessary to employ a heat-treatment process for microstructural homogeneity. When the laser-based DED techniques are utilized for the addition of functional areas or features, many times the deposited material may not be the same as the component material. In this case, a good understanding of the metallurgical interaction of the different materials is required. Many materials cannot be combined for such operations. Others need a special way of deposition or can only be deposited to a limited extent. Such evaluations are critical for the success of the added features.

Technologies such as LENS have been utilized for critical repair of many high-value components. Simpler laser cladding operations have been used for improving the performance of existing components. Some of these examples are discussed later in this chapter in Section 17.5.

17.2.2 Powder Bed Fusion Methods for Additive Manufacturing

PBF additive manufacturing technology was both one of the very first and one of the most successful additive manufacturing technologies. Selective laser sintering (SLS) technology was invented in the mid-1980s at the University of Texas at Austin. Commercially, SLS was the first PBF technology [6,7]. At the Fraunhofer Institute ILT in Germany, the selective laser melting (SLM) technology was invented, which resulted in the emergence of two companies: SLM Solutions GmbH and Realizer GmbH. Also, two more similar PBF additive manufacturing technologies are available that utilize a laser energy source and powder bed [8]. These are laser cusing, commercialized by CONCEPTLASER, and direct metal laser sintering (DMLS) by

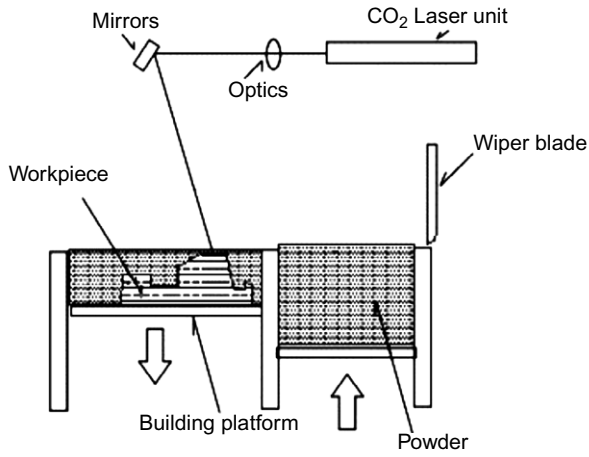


Fig. 17.4 Basic principle of laser based powder bed fusion process/direct metal laser sintering process. From M.W. Khaing, J.Y.H. Fuh, L. Lu, Direct metal laser sintering for rapid tooling: processing and characterization of EOS parts, J. Mater. Process. Technol. 113 (1) (2001) 269–272.

EOS. In the PBF additive manufacturing industry, the electron beam melting method is also very popular. Arcam offers commercial additive manufacturing equipment utilizing electron beam melting instead of laser energy [9]. All of the above technologies—SLS, SLM, laser cusing and DMLS—are similar in terms of the fundamental principle of operation. Hence, a generalized process description is discussed below that encompasses all these commercially available PBF additive manufacturing technologies.

17.2.2.1 The Powder Bed Fusion Process

As the name suggests, the process utilizes a bed of metal or alloy powder that can be spread into thin layers followed by precise sintering using a sharply focused energy source, either laser energy or an electron beam. Fig. 17.4 shows a representation of the PBF additive manufacturing process[10].

17.3 MATERIALS PROCESSED USING LASER-BASED ADDITIVE MANUFACTURING TECHNIQUES

In manufacturing and research and development, there may be hundreds of different materials that have been reported. For the sake of simplicity, the materials used in laser-based additive manufacturing are categorized in the most basic way: metals, ceramics, and polymers (materials such as ceramic- reinforced metal matrix composites fall under metals). In each of

these categories, first materials used in laser-based DED methods are discussed, followed by materials used in laser-based PBF methods.

All the powder bed systems either contain a reservoir bed of powder or a continuous-feeding hopper of powder. This powder is then spread, layered, or rolled into the build area using a precise roller or blade. Once this thin layer of powder is spread, the focused laser or electron beam scans the layer and selectively only melts and fuses areas according to the cross-sectional pattern determined by a CAD or slicing software. Once this scanning, melting, and fusion are achieved, another thin layer of powder is spread on this previously fused layer followed by another fusion laser scan in the predetermined cross-sectional design. By doing so, two goals are achieved: the particles of the powder fuse between each other in the same layer and the particles of the layer undergoing fusion also fuse with the layer below it that was previously fused. This leads to a continuous-LM process. As the part begins to take shape, it is lowered into the build area to accommodate the incoming layer of powder by the roller or blade. Many of the PBF setups utilize heating of the build chamber during the process. Such preheating is ideal for reducing thermal gradients and the subsequent microstructural gradients that can arise from the laser energy source [11]. Unlike the DED additive manufacturing processes discussed earlier in this chapter, the PBF process does not always completely melt the powder particles. Fusion can be achieved by only melting the exterior surfaces of the powder particles, which when partially molten will adhere to neighboring particles and will fuse upon subsequent cooling. The metal PBF additive manufacturing processes are carried out in an inert environment. The most typical environment is argon inert gas for metallic materials; sometime nitrogen can also be used for metallic materials that are nonreactive towards nitrogen. It is understood that if the PBF process utilizes an electron beam as the energy source, a high vacuum environment is a necessity.

17.3.1 A Brief Comparison of Laser-Based DED and PBF Additive Manufacturing Methods

The powder and filament based DED method and the PBF method are the two most successful and widely used laser-based additive manufacturing technologies. As mentioned earlier in the chapter, although the two technologies are for 3DP of parts, the capabilities of the two are vastly different. The selection of the method for processing is highly dependent upon the requirement of the final component. Considering the vitality of this,

we have discussed a few important factors that drive the selection of the laser-based additive manufacturing processes.

17.3.1.1 Material Requirement

Laser-based DED techniques are flexible in terms of the materials that can be processed if the materials are metallic, ceramic, or a ceramic-reinforced metal composite. To date, there has been no demonstration of a laser DED method for processing a polymeric material. Since the DED techniques can use a variety of different lasers and laser energies, a wide variety of low melting point alloys such as bronzes, common steels, titanium alloys, nickel alloys, and cobalt alloys can be processed as well as high temperature ceramics using refractory methods [discussed later in Sections 17.3 and 17.4]. There is also a unique laser-powered DED technique that uses a proprietary diamond powder for cladding components with diamond-like carbon [12]. It should be noted that, due to the deleterious effects of thermal shock on the structural integrity of the deposits, limitations exist in terms of component size, shape, and complexity when fabricating components from ceramic materials and refractory alloys using the laser-based DED additive methods.

For the PBF additive manufacturing technology, the most successful materials have been pure metallic materials and polymeric materials. Laser-based (or even electron-beam based) PBF additive manufacturing of ceramic materials is difficult. Therefore binder-jetting additive manufacturing technology is typically used for ceramic materials. A wide variety of metallic materials has been developed and proven successful using the PBF techniques.

The properties of the feedstock material are also important in both the DED and PBF additive manufacturing methods. The DED methods usually require powders that are in the larger range, mostly above 30–45 μm and smaller than 150–200 μm in diameter for spherical particles. Many times, nonspherical particles and slightly larger or smaller particles can also be used if a satisfactory flowability of the powder is achieved. This flowability is usually a standard set by the specific machine manufacturer. For the PBF additive methods, finer, spherical powder particles with a narrow powder size distribution of 20–30 μm are desired because the roller or the blade must be successful in spreading, or layering a thin layer of powder.

17.3.1.2 Part Size, Shape, and Surface Finish

These are some of the most important factors that affect the selection of an additive manufacturing process. Laser-based DED processes are capable of processing large and heavier components. More specifically, commercially

available technology such as the LENS technology can process parts that measure 5′×5′×6′. In contrast, the powder bed machines are suitable for parts smaller in size—typically a 1′×1′×1′ envelope. However, the PBF methods can produce parts of complex geometry and intricate structure with overhangs and extremely well-controlled dimensional tolerances. In the case of the DED additive methods, structures that have very large angles against gravity cannot be formed. The maximum achievable overhang angle varies from machine to machine and from manufacturer to manufacturer. Yet the DED technique cannot match the structural complexity and the intricacy that the PBF additive methods can demonstrate. The main reason for this is that in the PBF methods, the part is buried or formed in the bed of powder and is built downwards. Due to this, the initially fused layers and the surrounding bed of powder can act as a support structure for the overhanging features. Such a convenience is not available for the DED methods since they are essentially building-up methods. The DED additive methods are capable of processing more than one material in the same part since the powder is directly fed into the laser energy source and the mixing occurs in situ, or during the deposition process. Thus, for a multimaterial additive manufacturing application, a laser-based DED method can be beneficial; whereas for a single material requiring complex part fabrication, a PBF method is more suitable. A DED method is suitable for operations such as cladding and coating as well as for high value repairs and for the addition of functional areas and features whereas a PBF method is not capable of such tasks. As an example, a lased-powered DED method can repair the damaged areas of gas turbine blades whereas the PBF method can be utilized for the fabrication of a complete new blade! A related example is discussed later in Section 17.5.

Since the powder bed methods use a finer laser and finer material feedstock powder, the surface roughness is low while the surface finish is high compared to the DED additive methods. On most occasions, the parts fabricated using the PBF additive methods do not require any machining or finishing operation. This is, however, not the case for the DED additive methods. The DED additive methods produce parts with relatively high surface roughness and a finishing operation is often required.

17.3.1.3 Time and Efficiency

The DED additive manufacturing methods have an advantage over the PBF additive manufacturing methods in terms of processing time. The DED methods are tunable; they can be used at lower powers and slower speds for careful

repair of components or at higher powers and faster speeds for fabricating large components. The PBF methods are slower as compared to the DED methods simply due to the operation of the roller or the blade, followed by a second step of using the laser or the electron beam for selective fusion. However, the overall powder utilization is high in the PBF additive methods and the unused powder can always be reused. In the case of the DED methods, powder utilization efficiency is lower and the reutilization of the unused powder is dependent on several factors. When processing in inert environments, the powders can be reused, but typically the unused powders may not be reusable at all.

After considering the above factors, it can be concluded that there is no laser-based (or any other energy source) additive manufacturing technology that is a cure-all. The selection of the technology is dependent on these contributing factors, and is highly specific to each application.

17.4 MATERIALS USED IN LASER-BASED ADDITIVE MANUFACTURING TECHNIQUES

A wide variety of materials has been demonstrated for use in additive manufacturing with the earlier discussed DED and PBF techniques. The discussion will be divided into the most basic categories as metallic, ceramic, and polymeric materials. In each section, the materials are first discussed with their applicability to the laser-based DED techniques and then with the laser-based PBF techniques.

17.4.1 Metallic Materials Used in Laser-Based Additive Manufacturing

The precursor of the three-dimensional laser-based DED processes was the simpler two-dimensional processes of laser cladding. In 1996, a cobalt-based alloy (stellite) was successfully laser cladded onto a steel substrate. This was a single-step process involving the simultaneous injection, melting, and rapid solidification of fine stellite alloy particles in the steel surface [13]. Co-based alloys, being more wear and corrosion resistant than stainless steels, were popular materials for laser cladding of components used in such harsh environments. Due to this, much earlier research in laser cladding and associated technologies involved Co alloys. Stainless steel 316 was laser clad with a stellite alloy using a carbon dioxide laser and inert gas shielding using argon gas [14,15]. This laser clad coating of stellite on the stainless steel (SS) 316 substrate showed hardness that was up to 11.3 GPa at an optimized laser cladding power of 450W. Presence of carbide phases as well as HCP

Co was detected using XRD and TEM techniques during these studies. For similar applications, laser-clad stellite coatings on martensitic stainless steel showed a hardness of approximately 1000 HV [16]. These demonstrations did not show the feasibility of Co-based alloys for three-dimensional part manufacturing but were rather for surface modification applications. DED and PBF methods have shown promise in fabricating components using Co-based materials. In 2008, LENS, a laser-based DED technique, was successfully used for the processing of three-dimensional components using medical grade CoCrMo alloys [17]. This LENS processing was done at a laser power of 285 W, less than that seen earlier in the case of laser cladding. Upon processing, the researchers found the presence of carbide phases along with coarse columnar dendritic and finer equiaxed dendritic phases. These CoCrMo alloy structures showed a hardness of 40 HRC. Similarly, Espana et al. utilized the LENS process for the fabrication of CoCrMo alloy structures. These structures were designed with up to 70% porosity while their stiffness was tailored so as to match that of the human bone [18]. Hazelhurst et al. demonstrated SLM fabrication of CoCrMo alloy stems for biomedical applications. These stem components were structurally graded, being up to 40% lighter and more than 60% more flexible than traditionally manufactured stem components [19]. Monroy et al. conducted studies to understand the pore formation in SLM-processed CoCrMo parts and fabricated parts with a minimum possible porosity of 0.9% and an average porosity of 5.77% [20]. Takaichi et al. also used the SLM technique to process Co-Cr alloys and concluded that to obtain dense builds using the SLM technique, an energy density of more than 400 J mm^{-3} was needed, as opposed to energy density less than 150 J mm^{-3} [21]. The SLM processing also led to the evolution of a unique microstructure with fine cellular dendrites formed between elongated grains and parallel to the build direction. Owing to this unique microstructure, the yield strength, the ultimate tensile strength, and the elongation were higher as compared to the as-cast alloy.

Fe-based metallic materials are the most widely used metallic materials in the world. Hence, there is a great deal of interest in manufacturing Fe-based materials such as steels, tool steels, and stainless steels additively. In 1996, the reports of LENS-based processing of Inconel and SS316 indicate that the properties of the laser-processed materials are comparable to the traditionally processed materials [22]. In 1997, laser DMD was used to deposit H13 tool steel [23]. In 2001, Hofmeister reported the findings of LENS processing of SS316 and H13 tool steel and found that the molten range during LENS processing was between 0.5 and 1.5 mm, and the

resultant cooling rates ranged from 200 to 6000 K/s [24]. The microstructure was more dependent upon the changes in the Z build direction than the laser power or the scan speed; this was directly due to the changes in the conduction pattern during processing. The basic LENS process was characterized, and process efficiencies were measured using H13 and copper as the base material [25]. The laser transfer efficiency, or ratio of the energy absorbed by the workpiece to the energy generated by the source, was 30%–50%. The powder utilization efficiency was approximately 14%. SAE4140 steel was successfully processed using the DED LENS technology [26]. The surface roughness of the LENS 4140 steel deposit was estimated to be between 300 and 900 μinches. Discontinuities in the form of porosity or voids were notable in the LENS process samples. Such defects were termed as "lack of fusion" defects. However, there were no shrinkage cavities, cracks, or macrosegregation observed. The morphology of the deposits was columnar with cellular-cellular dendritic microstructural features. DMD of SS316 and H13 has also been demonstrated using a coaxial nozzle [27]. In addition to these, other important Fe-based materials were also processed using laser-based DED additive manufacturing techniques. Most notable of these include, SS420 [28], ASI431 martensitic steel [29], and Fe-based bulk metallic glasses [30–32]. Given the importance of such DED techniques for steels, several studies have proposed models for these processes [33,34].

The PBF techniques have also been successful in fabricating complex three-dimensional parts using Fe-based metallic materials. In 2000, Niu et al., successfully processed gas atomized powders of M2 high-speed tool steel by SLS. The researchers varied the laser power from 2.5 to 100 W and found that denser structures resulted at higher powers of laser scanning, while keeping the scan speed and line spacing constant [35]. In 2004, Kruth et al., demonstrated the SLM processing of Fe powder mixture of Fe, Ni, Cu, and Fe_3P. These SLM processed parts had surface roughness of 10–30 μR_a. The researchers achieved a bending strength of 630 MPa with a part density of 91% [36]. The density of SS316 primitive cubic structures was reported by Morgan et al. [37]. These cubic primitive structures were fabricated using the direct metal laser resintering technique, which is a variant of the general SLS technology. The porosity was measured in these samples using the Xylene impregnation method. It was observed that increasing the scanning speed reduced the density, and vice versa. Similarly, fine structured filter elements were fabricated using the SLM technique from steel and Inconel alloys, and these structures contained complex, interconnected three-dimensional porosities [38]. Tsopanos et al., investigated the dependence

of the processing parameters on the materials properties in SLM SS316L microlattice structures [39]. The authors fabricated an open cellular BCC microlattice structure that was a 20-mm^3 block and unit cell size of 2.5 mm. Laser scanning at 80W led to a porous microstructure in the struts of the lattice structure. This microlattice structure was also 50% weaker compared to the SS316 bulk values. The authors proposed an exposure time of 500 µs and laser power of 140W to meet the required strength-to-weight ratio. Effects of the processing parameters on the tensile properties of SS304 were also investigated by Guan et al., where researchers found that the properties of SS304 at the most ideal processing parameters exceeded the properties of wrought SS304 [40]. One of the advantages of additive manufacturing processes is the ability to generate controlled porosity and gradient porosity. This was demonstrated by SLM of SS316 [41] as well as by Yan et al., by creating lightweight structures [42] as shown below in Fig. 17.5.

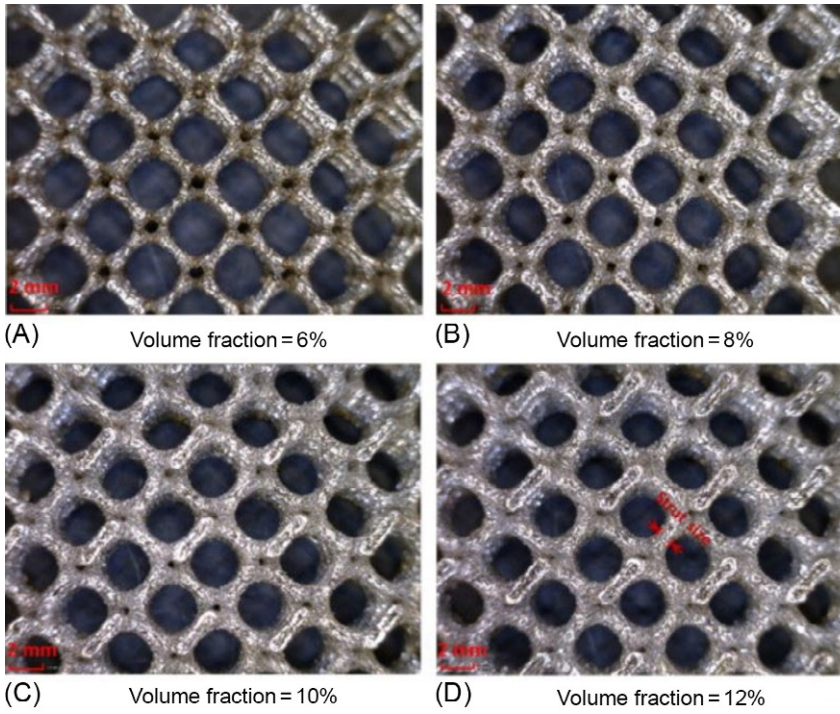


Fig. 17.5 Lightweight structures of stainless steel created using selective laser melting. From C. Yan, H. Liang, A. Hussein, P. Young, D. Raymont, Advanced lightweight 316L stainless steel cellular lattice structures fabricated via selective laser melting, Mater. Des. 55 (2014) 533–541.

Apart from Fe- and Co-based metallic materials, additive manufacturing of Ti- and Ni-based materials are of extreme engineering interest, often finding applications in specialized systems and assemblies. In 2000, laser additive manufacturing of the α,β Ti-6Al-4V alloy was demonstrated [43]. In these experiments, the additive manufacturing process of the Ti-6Al-4V alloy was investigated using a Nd:YAG laser and a CO_2 laser. The microstructure that evolved after processing showed a strong dependence on the laser type. With the Nd:YAG laser, grains grew at an acute angle, whereas with the CO_2 laser, the grains grew perpendicular. In both the cases, the microstructure was of the Widmanstatten type, the differences being in the size and distribution of the phases formed with respect to the laser used. The grains were finer with the Nd:YAG laser as compared to the CO_2 laser. These columnar morphologies, consisting of a fine or coarse Widmanstatten microstructure, are almost always found in laser-based direct energy processed titanium-based materials. Another study focused on the capabilities of the laser additive fabrication or direct laser fabrication (DLF) capabilities for Ti-based materials. In the study by Wu et al., overhanging structures with an angle of up to 30 degrees were successful. It was also found that at a lower power setting of 180W, extensive interconnected porosity was visible whereas at higher powers of 264–390W, the structures were almost completely dense [44]. As discussed with the capabilities using steels, porous structures of these materials are also of importance. Additive manufacturing offers a way to fabricate such structures. LENS, a DED technique, was used for processing such porous titanium alloy structures [5]. Using partial melting of the metallic powder, researchers formed structures that were up to 70% porous as shown in Fig. 17.6. Using the same LENS technology,

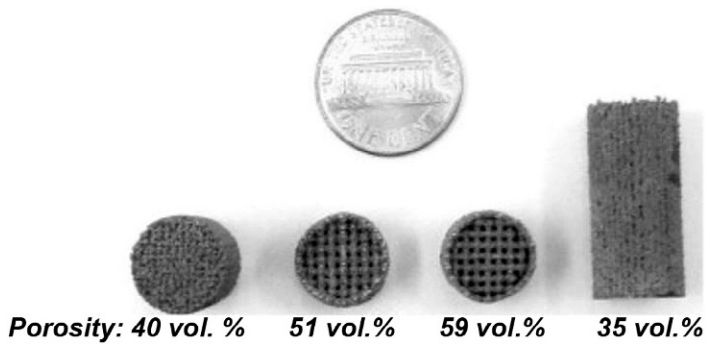


Fig. 17.6 Porous, low stiffness titanium structures fabricated using LENS additive technology. From B.V. Krishna, S. Bose, A. Bandyopadhyay, Low stiffness porous Ti structures forload-bearing implants, Acta Biomater. 3 (6) (2007) 997–1006.

structures of the NiTi-shaped memory alloy were also fabricated [45]. In addition to these, there were numerous studies conducted with laser-based DED technologies for predicting the microstructure, modeling the microstructural evolution, and providing predictive processing tools for titanium- based materials [46–49]. PBF technology has also been successful for processing Ti-based materials. In 1999, the SLS technology was utilized to process titanium-based material for biomedical applications [50]. The densities achieved in this study were about 80% with hot isostatic processing (HIP), increasing their densities. Interestingly, the components had a gradient microstructure with a generalized Widmanstaten microstructure. The interiors showed a coarse structure whereas the outer areas showed longer lamellar grains. Santos et al. also conducted similar studies with SLM [51]. A bone model fabricated using SLS is shown in Fig. 17.7.

It has been shown that selective laser melted titanium parts can reach densities of up to 95%. It was also mentioned that using secondary heat treatment and hot isostatic pressing improved the mechanical properties of the material. Hot isostatic pressing also improved the density of the parts to above 99%. The figure below shows the selective laser melted implant model of titanium in comparison to the actual bone model. Low volume RP of 40 titanium parts measuring 3 mm in height and 20 mm in diameter was accomplished in 7 h of processing time. These were also

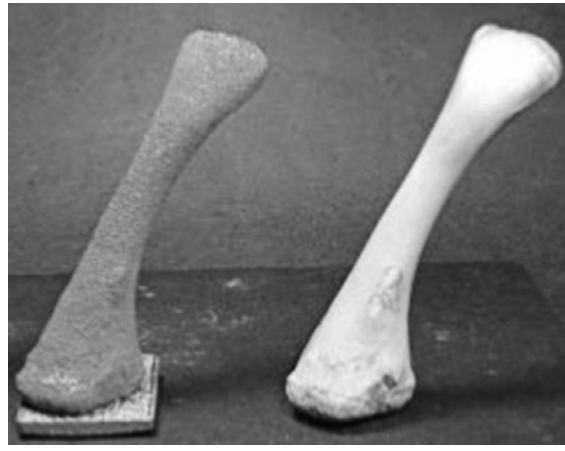


Fig. 17.7 A bone model fabricated using selective laser sintering method. From E. Santos, F. Abe, Y. Kitamura, K. Osakada, M. Shiomi, Mechanical properties of pure titanium models processed by selective laser melting, in: Proceedings of the Solid Free Form Fabrication Symposium, 2002, pp. 180–186.

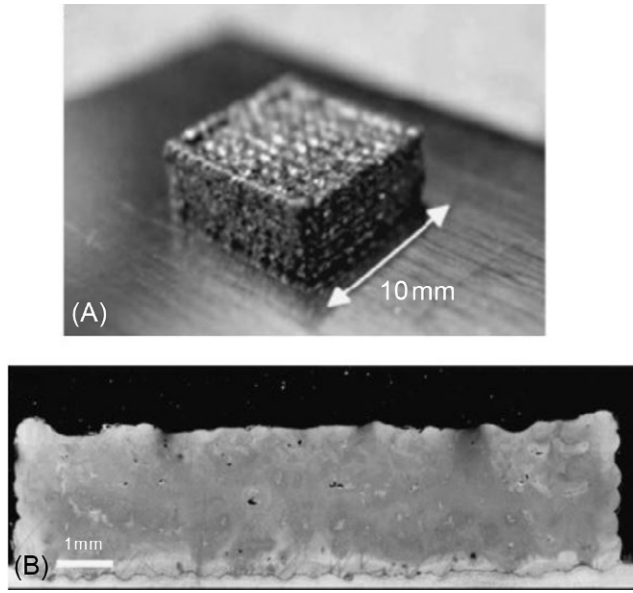


Fig. 17.8 Waspaloy structures fabricated using the selective laser sintering method. (A) Specimen fabricated using optimized laser processing parameter and (B) cross-section SEM image of the specimen showing about 0.3% porosity. From K.A. Mumtaz, P. Erasenthiran, N. Hopkinson, High density selective laser melting of Waspaloy, J. Mater. Process. Technol. 195 (1) (2008) 77–87.

investigated primarily for biomedical implant application [52]. An in-depth microstructural characterization of Ti-6Al-4V alloy was performed [Thijs et al., 2010]. Microscopy revealed the presence of the martensitic phase or the α' phase. Such a martensitic Ti phase has also been found in various instances of direct energy based additive processing of the alloy [53,54]. Overall the microstructure showed elongated grains that were several hundred microns in length. Similarly, Waspaloy was also processed with porosity as low as 0.3% [55]. This study also investigated the microstructure of the high density Waspaloy structures and revealed a fine dendritic microstructure. An example of this additively manufactured structure is shown in Fig. 17.8.

DLF, a variant of the DED technique, was utilized to process Ni-Cr alloy powder [56]. The researchers used the verticality of contours as a measure to evaluate the build quality at different powers. They observed that at rising powers, the verticality was affected or collapsed, and thus the build quality was inferior. Even at processing at such higher powers, no cracking was found in these laser-processed samples. Metallographic examination of these deposits showed a dark and white banded microstructure. The image in Fig. 17.9 shows the banded microstructural observations of the laser processed nickel specimens.

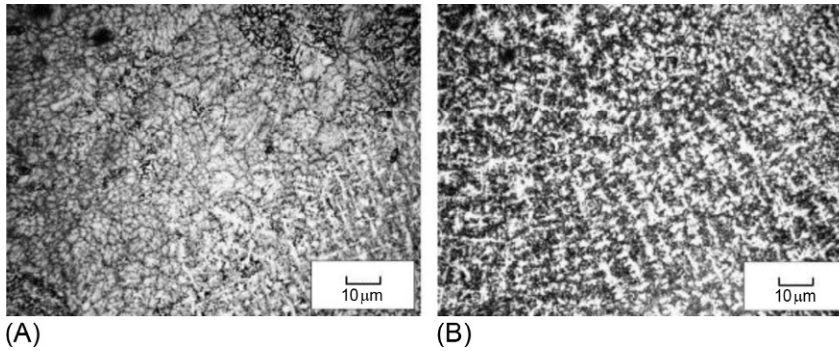


Fig. 17.9 Microstructure of Inconel-625 alloy fabricated using laser based direct energy deposition technique, showing dendrites are much smaller in light zone than in dark zone. (A) Dendrites in light zone and (B) Dendrites in dark zone. From L. Peng, T. Yang, L. Sheng, L. Dongsheng, Q. Hu, X. Weihao, Z. Xiaoyan, Direct laser fabrication of nickel alloy samples, Int. J. Mach. Tools Manuf. 45 (11) (2005) 1288–1294.

Inconel alloys, especially IN718 and IN625, are of immense engineering importance, especially in the aerospace, oil and gas, and tribological applications. IN718 was laser fabricated using the DED additive techniques. Research by Blackwell et al. revealed that tensile rods fabricated using laser techniques were present in a solution-treated condition [57]. The microstructure was a fine-grained cast microstructure as shown in Fig. 17.10. There was even indication of the "laser scans" or "laser marks" from successive processing in layers. Similar investigations were also carried out by Zhao et al. in 2010 [58].

17.4.2 Laser-Based Additive Manufacturing of Metal-Ceramic Composite Materials

Besides the interest in the additive manufacturing of pure metallic materials such as steels, Inconels, stellites, and Ti-6Al-4V alloys, additive manufacturing of metal-ceramic composites is also being investigated. Metal-ceramic composites are expected to have properties better than their metallic counterparts. Such composite materials are not always desired in a complete three-dimensional part form but can also be utilized as simple coatings and cladding. Such surface modifications can significantly improve the life and performance of the component. However, this does not undermine the importance of having three-dimensional components fabricated from such novel metal-ceramic composite materials. Tables 17.2 and 17.3 highlight some of the most popular metal-ceramic composites, categorized according to DED and PBF additive manufacturing techniques, along with some noteworthy points about the particular material system in discussion.

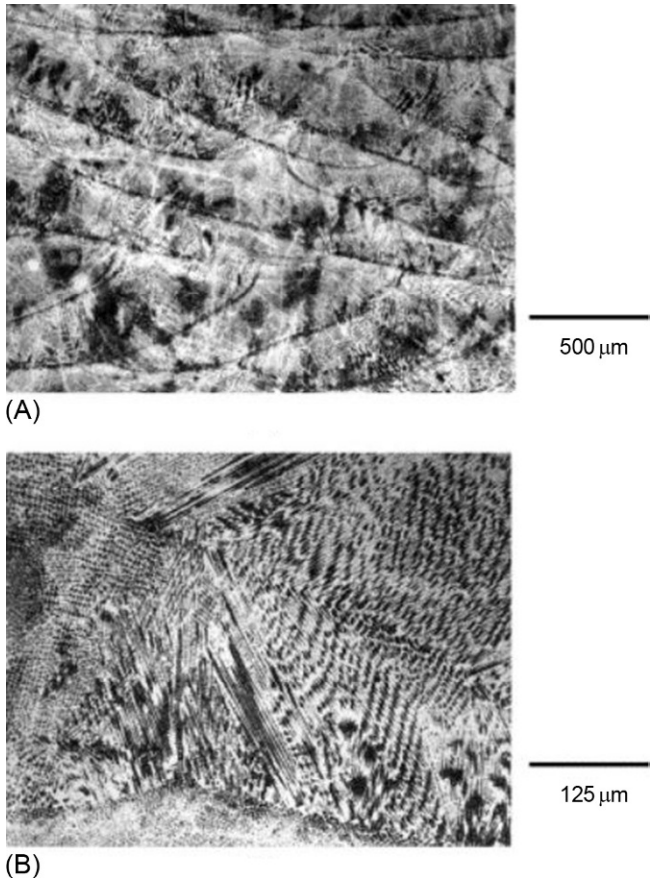


Fig. 17.10 Direct laser processed IN 718 alloy. (A) As-deposited IN718 showing evidence of individual passes and (B) detail of dendritic structure within a single pass. From P.L. Blackwell, The mechanical and microstructural characteristics of laser-deposited IN718, J. Mater. Process. Technol. 170 (1) (2005) 240–246.

17.5 APPLICATIONS

From studying the different types of metals and metal-ceramic composites that the laser-based DED and PBF additive manufacturing techniques are capable of processing, one can estimate the scope of the applications of these processes and the materials in engineering environments. There is an increasing amount of interest in these additive manufacturing techniques in the fields of aerospace, biomedical devices, the oil and gas industry, and critical repair industry. This section highlights a few selected examples of the laser-based additive manufacturing techniques.

Table 17.2 Metal-ceramic composite materials processed using laser-based direct energy deposition techniques

Laser based direct energy deposition techniques

Material class	Specific composite system	Technique	Source
Fe-based	SS316L-Silicon carbide	Direct laser	[59]
	SS316-Cr_2C_3	Direct laser	[60]
	SS316L-YSZ	LENS direct laser	[61]
	Fe-TiC	Direct laser	[62]
Co-based	Stellite-SiC	CO_2 laser cladding	[63]
	Co-WC	Direct laser/Laser clad	[64–66]
	CoCrMo-Ti6Al4V compositionally graded structures	Direct laser LENS	[67]
	Co-TiC	Laser clad	[68]
	CoCrMo-Calcium phosphate	Direct laser LENS	[69]
Ni and Ti based	Ti6Al4V-BN	Laser Clad, Laser Melt Injection	[70,71]
	Ti-B_4C	Laser Melt Injection	[72]
	Ti6Al4V-TiB	Direct Laser	[73]
	Ti-TiC	Direct Laser LENS	[74]
	Ni-TiC	Laser clad, direct laser	[75,76]
	Ti-Calcium phosphate	Direct laser LENS	[77]
	Ti-Titanium nitride-Silicon nitride	In situ LENS	[53]

Table 17.3 Metal-ceramic composite materials processed using laser-based powder bed fusion techniques

Laser-based powder bed fusion additive manufacturing techniques

Material class	Specific composite system	Technique	Source
Fe-based	SS316-Hydroxyapatite	Selective laser melting	[78]
	Fe-SiC	Direct metal laser sintering	[79]
	Fe-Graphite	Direct selective laser sintering	[80]
Ni- and Ti-based	Ti-Titanium boride	Selective laser melting	[81]
	TiAl-TiC in situ	Selective laser melting	[82]

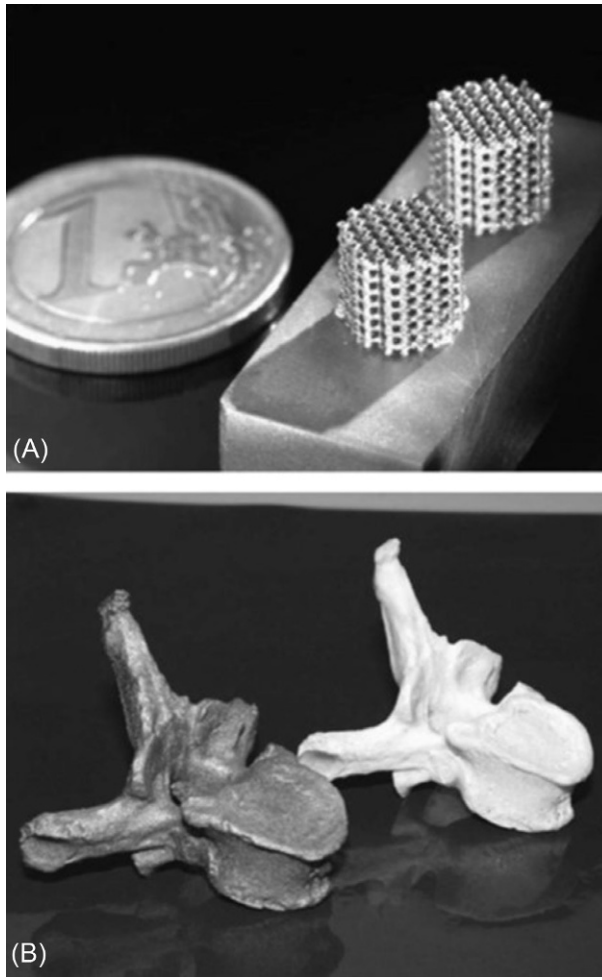


Fig. 17.11 Examples of DLF-fabricated Ti–6Al–4V parts, cylinders with cubic pore pattern (A), production time approx. 3 h, human vertebra (B) with original (right) and Ti–6Al–4V analog (left), production time approx. 12 h. From D.A. Hollander, M. Von Walter, T. Wirtz, R. Sellei, B. Schmidt-Rohlfing, O. Paar, H.J. Erli, Structural, mechanical and in vitro characterization of individually structured Ti-6Al-4V produced by direct laser forming, Biomaterials 27 (7) (2006) 955–963.

Fig. 17.11 shows an example of the 1:1 replica of a human vertebrae that was fabricated using the SLS technology [52]. This example emphasizes the part forming capability of the PBF process, and the usefulness of the PBF technology for making biomedical implant devices. Another example of a similar application was presented by Shishkovsky et al. [83]. Fig. 17.12A shows a porous NiTi alloy implant that was fabricated using the SLS/SLM technology.

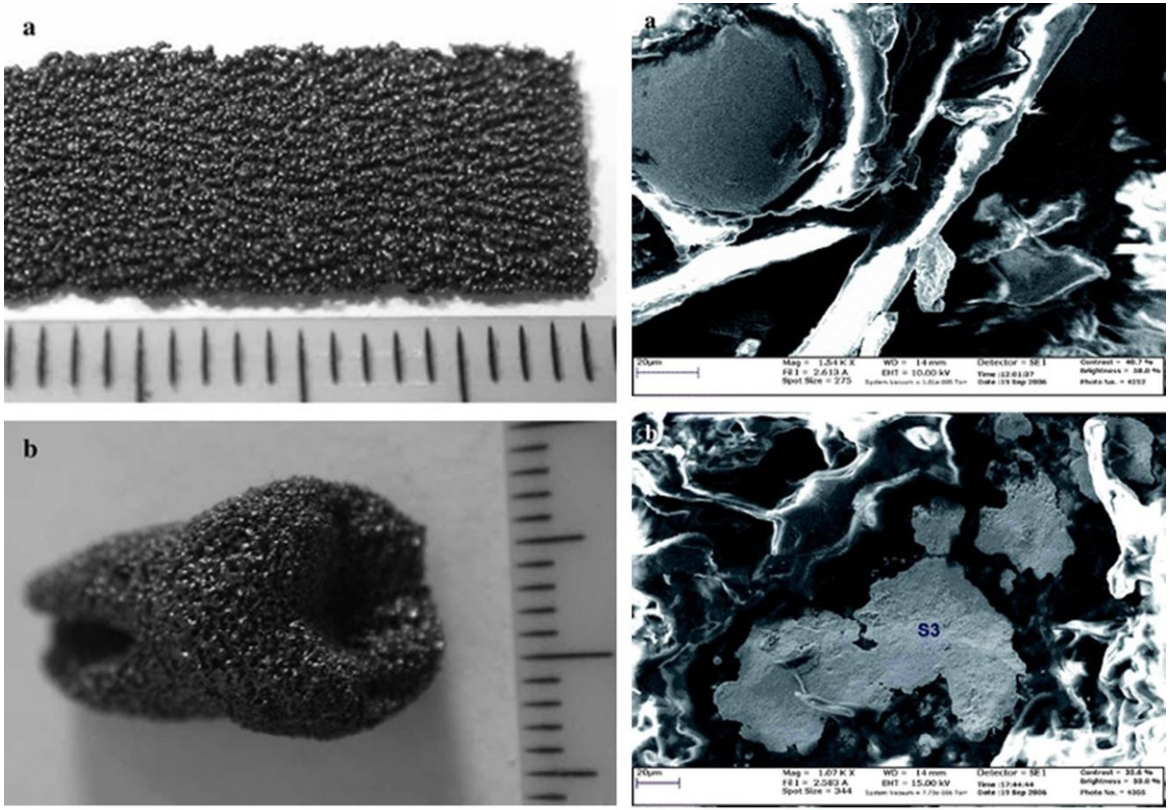


Fig. 17.12 Porous implants fabricated using the SLS/DLF process. (A) Top: Fabricated monolayer of nitinol; (A) Bottom: 3D part tooth of nitinol with the distance between consecutive markers on the scale being 1mm; (B) Top: Titanium implant microstructure after 3 months of biointegration and (B) Bottom: Nitinol implant microstructure after 3 months of biointegration. From I.V. Shishkovsky, L.T. Volova, M.V. Kuznetsov, Y.G. Morozov, I.P. Parkin, Porous biocompatible implants and tissue scaffolds synthesized by selective laser sintering from Ti and NiTi, J. Mater. Chem. 18 (12) (2008) 1309–1317.

For the process of osseo-integration or the ingrowth of new bone tissue in the otherwise bio-inert metallic implant, a porous surface is desirable. The images in Fig. 17.12B show the ingrowth of bone marrow cells when implanted in white laboratory rats for a period of 3 months. Such a complex and novel structure was possible due to the inherent advantages of the PBF technology.

The laser-based DED technologies have also been used for similar biomedical applications. A better bone attachment, reduction of surface degradation, and enhancement of the life of the implant have been reported for LENS-processed biomedical metallic materials [1,67,69,84–86]. In many of these demonstrations, not only is the additive LENS processing a novel aspect but many novel material systems have also been investigated and found beneficial for such crucial applications. Therefore these examples demonstrate that DED techniques are novel for fabricating structures and are also an excellent tool for research into material systems. A combination of two additive manufacturing technologies has also proved to be vital for fabricating patient specific implants [87]. As seen in Fig. 17.13, a polymer FDM system [not laser-based] was utilized to make a precise replica of a person's fractured skull. After finding the right design for an implant to fit in this lost (fractured) area, the actual implant was manufactured from a biomedical grade Ti alloy using the LENS technology. This example highlights a very important aspect of all laser-based additive manufacturing technologies—the ability to form a precise design and need-specific component.

From the numerous examples in Sections 17.3 and 17.4 and earlier in this section, powder bed and DED technologies are useful for mak-

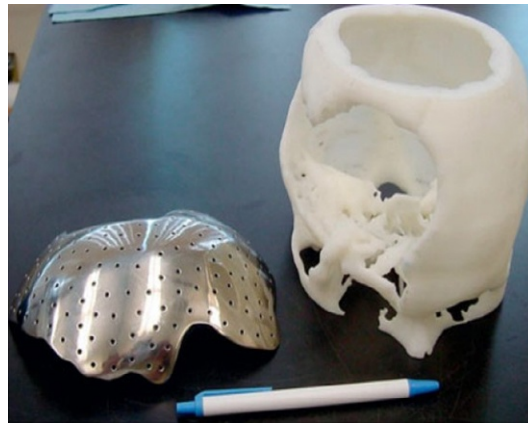


Fig. 17.13 A combination of FDM and DED LENS technology used to fabricate a patient-specific craniomaxillofacial implant from a biomedical Ti alloy. From A. Bandyopadhyay, S. Bose, S. Das, 3D printing of biomaterials, MRS Bull. 40 (02) (2015) 108–115.



T700 stage 1 blisk after LENS leading edge repair



Blisk after finishing

Fig. 17.14 Blisk repair on engine components of T700 engine using LENS technology and stellite alloy. From http://www.optomec.com/wp-content/uploads/2014/04/Optomec_LENS_Blisk_Repair_Datasheet.pdf.

ing three-dimensional structures. However, the DED technology, owing to the way it operates, is useful for the repair of vital components. Many such demonstrations have been done for high-value repair of components. Materials such as Inconel, Ti6Al4V, and AM355 steel have been routinely used in such applications [88–90]. Fig. 17.14 shows the repaired tip of a T700 land-based jet engine blisk using a stellite alloy. These repaired components were subjected to metallographic examination, a 60,000-cycle spin

test, and a 50,000-cycle fatigue test as well as erosion tests. The repaired components withstood these tests and were deemed worthy of service in the T700 engines.

17.6 SUMMARY AND FUTURE TRENDS

From the earlier sections, we understand that there are two main categories of additive manufacturing that utilize laser energy: DED and PBF. Using the DED and PBF techniques, it is possible to process a variety of different materials such as metals, ceramics, metal-ceramic composites, and polymers. Using the laser-based DED and the PBF techniques and the different materials' classes, one can achieve exceptional material properties that can enhance, elevate, and lengthen the life of a working component or design. However, there are limitations to both the DED and the PBF techniques and thus we have understood that there is no additive manufacturing technique available today that can be termed a "can do it all" method for additive manufacturing. It is necessary that the right technique and the right tool are chosen along with the right material for the success of additive manufacturing and for the successful exploitation of the material properties after processing.

Currently, the interest in applying additive manufacturing technologies in production is mainly for creating nearly the same designs and using the same materials. And this is well understood since a particular design and material are chosen after a thorough suitability assessment, and most often these designs and the materials have proven most suitable. However, this creates an obstacle for the adaptation of additive manufacturing. It often happens that while undertaking a feasibility study, or a basic study to understand the process and material performance for the particular component, the design is nonnegotiable. The thought process is, "The additive manufacturing tool must do what we want it to do." Although this is reasonable, modifiying or even simplifying the design can render the component more "additively manufacturable." This holds true for all additive manufacturing tools, not just for the DED and PBF techniques that are discussed in this chapter. This does not mean that the component needs severe modifications or that the design must change drastically. It only means that for the additive manufacturing technology chosen, the design must be optimized. When consideration is given for an existing component to be processed via the additive route, it must be understood that the present design was chosen at some point because it suited the conventional manufacturing process or that it was optimized for the conventional manufacturing process such as

forging or casting. And thus, it may not be the best optimized design for an additive process such as LENS or SLS. The following examples show the importance of optimized designs for additive manufacturing processes. As discussed by Vayre et al., the part is a right angle metal bracket. The part on the left shows a design that can be fabricated by subtractive CNC machining and the part on the right shows a geometry that is earlier for the additive manufacturing process [91] (Fig. 17.15).

Recently, Hallgreen et al., have also discussed the redesigning of structures to make them more feasible for additive manufacturing [92]. In addition, several advantages such as usage of lesser material and weight savings could be achieved. Fig. 17.16 shows the design of a beam that could be used

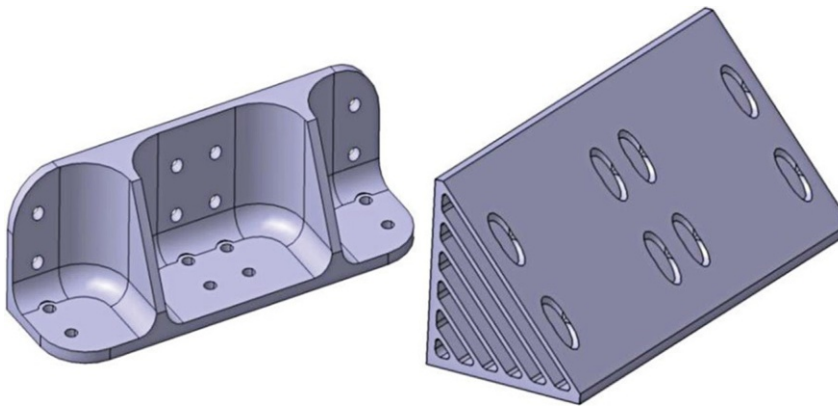


Fig. 17.15 Design optimization for suitability with additive manufacturing technique. From B. Vayre, F. Vignat, F. Villeneuve, Designing for additive manufacturing, Procedia CIRP 3 (2012) 632–637.

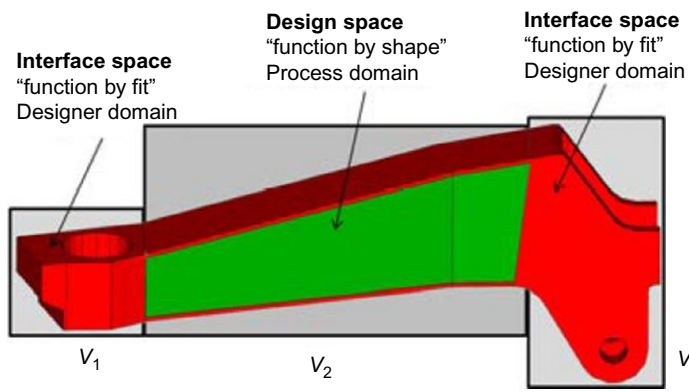


Fig. 17.16 Design for traditional manufacturing [92].

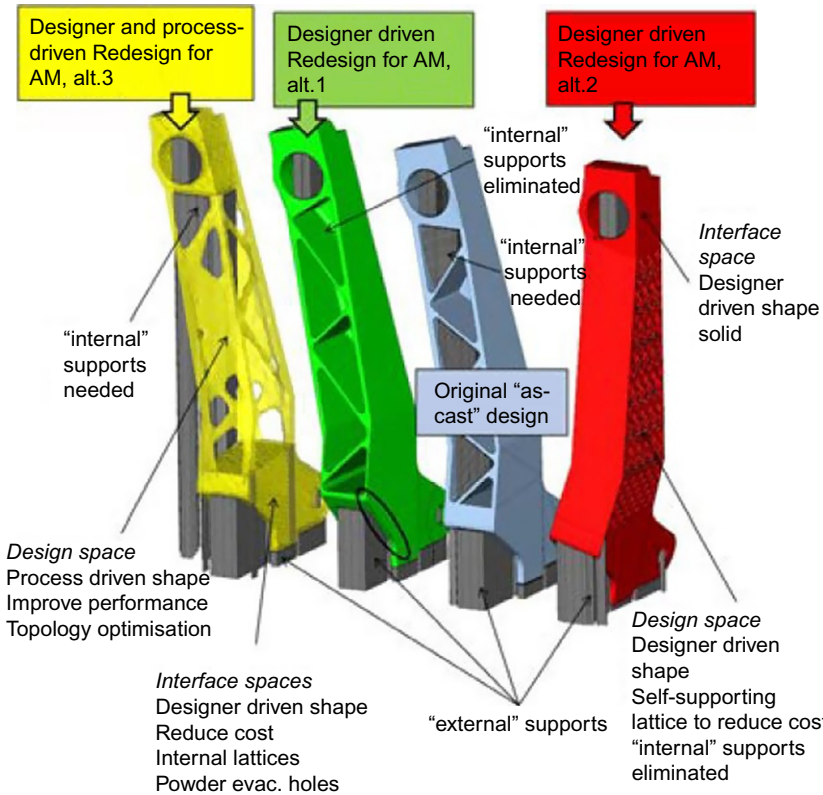


Fig. 17.17 Redesign options for additive manufacturing [92].

for traditional manufacturing. Fig. 17.17 shows the possible redesigns along with the advantages of each of the redesigns.

The second consideration for the future of additive manufacturing is the materials used in the process. Currently, the processes are marketed and optimized to process the same materials that are in use. But with time, more and more research into the material capabilities of additive manufacturing is being conducted. This does not mean that the current materials are to be completely abandoned or that there will a paradigm shift in the material for an application. From seeing the examples in Section 17.2, we can conclude that there are a lot of novel materials that can outperform the current materials. These systems are based on the current materials and only have a slight modification in some cases, but the ramifications in terms of properties and performance is significant. As an example, a certain transmission component that undergoes rapid, preferential wear is currently cast, machined

and case-hardened using steel. If this component's most susceptible area is laser DED modified using a steel matrix silicon carbide composite, there may be a substantial improvement in the life of the part. Or if a certain gear component is being repaired using the laser DED technique with the same material, there may be a possibility of repairing it with a better material.

If such design considerations are applied, the advantages of additive manufacturing can be exploited to the fullest. Altering designs, considering multimaterial structures, and sparingly using a more novel material will eventually lead to optimized systems that use each material and components more economically. This can subsequently lead to better performance or simply longer life of the designs. In conclusion, the future of additive manufacturing is not simply in making parts and components as they are and with the materials that are currently being used, but instead lies in developing more efficient and optimized structures with a combination of "as-performance-demands" materials.

The importance of additive manufacturing techniques in fabricating specialized and customized components cannot be overlooked. As seen from the example of fabricating a human skull/forehead replacement using LENS, additive manufacturing is capable of highly specific and customized part fabrication. Conventional manufacturing may also be capable of such customized applications; however, additive manufacturing will simply be more precise and faster.

REFERENCES

[1] H. Sahasrabudhe, Characterization of Ti and Co based biomaterials processed via laser based additive manufacturing (Ph.D. Thesis), Washington State University, 2016.

[2] ASTM Standard F2792-12a, Standard Terminology for Additive Manufacturing Technologies, ASTM International, West Conshohocken, PA, 2012. https://doi.org/10.1520/F2792-12A. www.astm.org.

[3] V. Ocelík, S. Nijman, R. van Ingen, U. Oliveira, J.T.M. De Hosson, Laser melt injection of hard ceramic particles into Al and Ti alloys processing, microstructure and mechanical behaviour, WIT Trans. Eng. Sci. 39 (2003).

[4] J.D. Ayers, R.J. Schaefer, W.P. Robey, A laser processing technique for improving the wear resistance of metals, JOM 33 (8) (1981) 19–23.

[5] B.V. Krishna, S. Bose, A. Bandyopadhyay, Low stiffness porous Ti structures for load-bearing implants, Acta Biomater. 3 (6) (2007) 997–1006.

[6] J.J. Beaman, C.R. Deckard, Selective laser sintering with assisted powder handling, U.S. Patent 4,938,816, issued July 3, 1990.

[7] C.R. Deckard, Method for producing parts by selective sintering, U.S. Patent 5,639,070, issued June 17, 1997.

[8] J.J. Beaman, Materials—Metals, in: Rapid Prototyping in Europe and Japan 102, JTEC/WTEC Panel Report 53, 1997.

[9] G.A. Whitlow, G.J. Bruck, J.E. Smith, Energy beam casting of metal articles, U.S. Patent 4,927,992, issued May 22, 1990.

[10] M.W. Khaing, J.Y.H. Fuh, L. Lu, Direct metal laser sintering for rapid tooling: processing and characterization of EOS parts, J. Mater. Process. Technol. 113 (1) (2001) 269–272.
[11] M. Agarwala, D. Bourell, J. Beaman, H. Marcus, J. Barlow, Direct selective laser sintering of metals, Rapid Prototyp. J. 1 (1) (1995) 26–36.
[12] http://www.dlc-cladding.com/.
[13] A. Frenk, M. Vandyoussefi, J.D. Wagniere, W. Kurz, A. Zryd, Analysis of the laser-cladding process for stellite on steel, Metall. Mater. Trans. B 28 (3) (1997) 501–508.
[14] J.D.M. Van Otterloo, J.T.M. De Hosson, Microstructural features and mechanical properties of a cobalt-based laser coating, Acta Mater. 45 (3) (1997) 1225–1236.
[15] J.D.M. Van Otterloo, J.T.M. De Hosson, Microstructure and abrasive wear of cobalt-based laser coatings, Scr. Mater. 36 (2) (1997) 239–245.
[16] R. Jendrzejewski, A. Conde, J. De Damborenea, G. Sliwinski, Characterisation of the laser-clad stellite layers for protective coatings, Mater. Des. 23 (1) (2002) 83–88.
[17] G.D. Janaki Ram, C.K. Esplin, B.E. Sticker, Microstructure and wear properties of LENS deposited medical grade CoCrMo, J. Mater. Sci. Mater. Med. 19 (2008) 2105–2111.
[18] F.A. España, V. Krishna Balla, S. Bose, A. Bandyopadhyay, Design and fabrication of CoCrMo alloy based novel structures for load bearing implants using laser engineered net shaping, Mater. Sci. Eng. C 30 (1) (2010) 50–57.
[19] K.B. Hazlehurst, C.J. Wang, M. Stanford, An investigation into the flexural characteristics of functionally graded cobalt chrome femoral stems manufactured using selective laser melting, Mater. Des. 60 (2014) 177–183.
[20] K. Monroy, J. Delgado, J. Ciurana, Study of the pore formation on CoCrMo alloys by selective laser melting manufacturing process, Procedia Eng. 63 (2013) 361–369.
[21] A. Takaichi, T. Nakamoto, N. Joko, N. Nomura, Y. Tsutsumi, S. Migita, Y. Igarashi, Microstructures and mechanical properties of Co-29Cr-6Mo alloy fabricated by selective laser melting process for dental applications, J. Mech. Behav. Biomed. Mater. 21 (2013) 67–76.
[22] M.L. Griffith, D.M. Keicher, C.L. Atwood, J.A. Romero, J.E. Smugeresky, L.D. Harwell, D.L. Greene, Free form fabrication of metallic components using laser engineered net shaping (LENS), in: Proceedings of the Solid Freeform Fabrication Symposium, University of Texas at Austin, Austin, TX, 1996, pp. 125–131.
[23] J. Mazumder, J. Choi, K. Nagarathnam, J. Koch, D. Hetzner, The direct metal deposition of H13 tool steel for 3-D components, JOM 49 (5) (1997) 55–60.
[24] W. Hofmeister, M. Griffith, Solidification in direct metal deposition by LENS processing, JOM 53 (9) (2001) 30–34.
[25] R.R. Unocic, J.N. DuPont, Process efficiency measurements in the laser engineered net shaping process, Metall. Mater. Trans. B 35 (1) (2004) 143–152.
[26] R.S. Amano, P.K. Rohatgi, Laser engineered net shaping process for SAE 4140 low alloy steel, Mater. Sci. Eng. A 528 (22) (2011) 6680–6693.
[27] A.J. Pinkerton, L. Lin, Multiple-layer laser deposition of steel components using gas- and water-atomised powders: the differences and the mechanisms leading to them, Appl. Surf. Sci. 247 (1) (2005) 175–181.
[28] G.A. Ravi, X.J. Hao, N. Wain, X. Wu, M.M. Attallah, Direct laser fabrication of three dimensional components using SC420 stainless steel, Mater. Des. 47 (2013) 731–736.
[29] I. Hemmati, V. Ocelík, J. Th, M. De Hosson, The effect of cladding speed on phase constitution and properties of AISI 431 stainless steel laser deposited coatings, Surf. Coat. Technol. 205 (21) (2011) 5235–5239.
[30] V.K. Balla, A. Bandyopadhyay, Laser processing of Fe-based bulk amorphous alloy, Surf. Coat. Technol. 205 (7) (2010) 2661–2667.
[31] H. Sahasrabudhe, S.A. Dittrick, A. Bandyopadhyay, Laser processing of Fe-based bulk amorphous alloy coatings on titanium, Metall. Mater. Trans. A 44 (11) (2013) 4914–4926.

[32] H. Sahasrabudhe, A. Bandyopadhyay, Laser processing of Fe based bulk amorphous alloy coating on zirconium, Surf. Coat. Technol. 240 (2014) 286–292.
[33] W. Liang, S. Felicelli, Analysis of thermal phenomena in LENS™ deposition, Mater. Sci. Eng. A 435 (2006) 625–631.
[34] L. Wang, S. Felicelli, Y. Gooroochurn, P.T. Wang, M.F. Horstemeyer, Optimization of the LENS® process for steady molten pool size, Mater. Sci. Eng. A 474 (1) (2008) 148–156.
[35] H.J. Niu, I.T.H. Chang, Selective laser sintering of gas atomized M2 high speed steel powder, J. Mater. Sci. 35 (1) (2000) 31–38.
[36] J.-P. Kruth, L. Froyen, J. Van Vaerenbergh, P. Mercelis, M. Rombouts, B. Lauwers, Selective laser melting of iron-based powder, J. Mater. Process. Technol. 149 (1) (2004) 616–622.
[37] R. Morgan, C.J. Sutcliffe, W. O'neill, Density analysis of direct metal laser re-melted 316L stainless steel cubic primitives, J. Mater. Sci. 39 (4) (2004) 1195–1205.
[38] I. Yadroitsev, I. Shishkovsky, P. Bertrand, I. Smurov, Manufacturing of fine-structured 3D porous filter elements by selective laser melting, Appl. Surf. Sci. 255 (10) (2009) 5523–5527.
[39] S. Tsopanos, R.A.W. Mines, S. McKown, Y. Shen, W.J. Cantwell, W. Brooks, C.J. Sutcliffe, The influence of processing parameters on the mechanical properties of selectively laser melted stainless steel microlattice structures, J. Manuf. Sci. Eng. 132 (4) (2010) 041011.
[40] K. Guan, Z. Wang, M. Gao, X. Li, X. Zeng, Effects of processing parameters on tensile properties of selective laser melted 304 stainless steel, Mater. Des. 50 (2013) 581–586.
[41] R. Li, J. Liu, Y. Shi, D. Mingzhang, Z. Xie, 316L stainless steel with gradient porosity fabricated by selective laser melting, J. Mater. Eng. Perform. 19 (5) (2010) 666–671.
[42] C. Yan, H. Liang, A. Hussein, P. Young, D. Raymont, Advanced lightweight 316L stainless steel cellular lattice structures fabricated via selective laser melting, Mater. Des. 55 (2014) 533–541.
[43] P.A. Kobryn, S.L. Semiatin, The laser additive manufacture of Ti-6Al-4V, JOM 53 (9) (2001) 40–42.
[44] X.H. Wu, J. Mei, Near net shape manufacturing of components using direct laser fabrication technology, J. Mater. Process. Technol. 135 (2) (2003) 266–270.
[45] B.V. Krishna, S. Bose, A. Bandyopadhyay, Laser processing of net-shape NiTi shape memory alloy, Metall. Mater. Trans. A 38 (5) (2007) 1096–1103.
[46] S.M. Kelly, S.L. Kampe, Microstructural evolution in laser-deposited multilayer Ti-6Al-4V builds. Part I. Microstructural characterization, Metall. Mater. Trans. A 35 (6) (2004) 1861–1867.
[47] S.M. Kelly, S.L. Kampe, Microstructural evolution in laser-deposited multilayer Ti-6Al-4V builds. Part II. Thermal modeling, Metall. Mater. Trans. A 35 (6) (2004) 1869–1879.
[48] J. Kummailil, C. Sammarco, D. Skinner, C.A. Brown, K. Rong, Effect of select LENS™ processing parameters on the deposition of Ti-6Al-4V, J. Manuf. Process. 7 (1) (2005) 42–50.
[49] S. Bontha, N.W. Klingbeil, P.A. Kobryn, H.L. Fraser, Thermal process maps for predicting solidification microstructure in laser fabrication of thin-wall structures, J. Mater. Process. Technol. 178 (1) (2006) 135–142.
[50] S. Das, M. Wohlert, J.J. Beaman, D.L. Bourell, Processing of titanium net shapes by SLS/HIP, Mater. Des. 2 (1999) 115–121.
[51] E. Santos, F. Abe, Y. Kitamura, K. Osakada, M. Shiomi, Mechanical properties of pure titanium models processed by selective laser melting, in: Proceedings of the Solid Freeform Fabrication Symposium, 2002, pp. 180–186.
[52] D.A. Hollander, M. Von Walter, T. Wirtz, R. Sellei, B. Schmidt-Rohlfing, O. Paar, H.J. Erli, Structural, mechanical and in vitro characterization of individually structured Ti-6Al-4V produced by direct laser forming, Biomaterials 27 (7) (2006) 955–963.

[53] Y. Zhang, H. Sahasrabudhe, A. Bandyopadhyay, Additive manufacturing of Ti-Si-N ceramic coatings on titanium, Appl. Surf. Sci. 346 (2015) 428–437.
[54] H. Sahasrabudhe, J. Soderlind, A. Bandyopadhyay, Laser processing of in situ TiN/Ti composite coating on titanium, J. Mech. Behav. Biomed. Mater. 53 (2016) 239–249.
[55] K.A. Mumtaz, P. Erasenthiran, N. Hopkinson, High density selective laser melting of Waspaloy, J. Mater. Process. Technol. 195 (1) (2008) 77–87.
[56] L. Peng, T. Yang, L. Sheng, L. Dongsheng, Q. Hu, X. Weihao, Z. Xiaoyan, Direct laser fabrication of nickel alloy samples, Int. J. Mach. Tools Manuf. 45 (11) (2005) 1288–1294.
[57] P.L. Blackwell, The mechanical and microstructural characteristics of laser-deposited IN718, J. Mater. Process. Technol. 170 (1) (2005) 240–246.
[58] X. Zhao, J. Chen, X. Lin, W. Huang, Study on microstructure and mechanical properties of laser rapid forming Inconel 718, Mater. Sci. Eng. A 478 (1) (2008) 119–124.
[59] J.D. Majumdar, A. Kumar, L. Li, Direct laser cladding of SiC dispersed AISI 316L stainless steel, Tribol. Int. 42 (5) (2009) 750–753.
[60] J.C. Betts, The direct laser deposition of AISI316 stainless steel and Cr3C2 powder, J. Mater. Process. Technol. 209 (11) (2009) 5229–5238.
[61] V.K. Balla, P.P. Bandyopadhyay, S. Bose, A. Bandyopadhyay, Compositionally graded yttria-stabilized zirconia coating on stainless steel using laser engineered net shaping (LENS™), Scr. Mater. 57 (9) (2007) 861–864.
[62] A. Emamian, S.F. Corbin, A. Khajepour, Tribology characteristics of in situ laser deposition of Fe-TiC, Surf. Coat. Technol. 206 (22) (2012) 4495–4501.
[63] G. Abbas, D.R.F. West, Laser surface cladding of stellite and stellite-SiC composite deposits for enhanced hardness and wear, Wear 143 (2) (1991) 353–363.
[64] Y. Xiong, J.E. Smugeresky, L. Ajdelsztajn, J.M. Schoenung, Fabrication of WC-Co cermets by laser engineered net shaping, Mater. Sci. Eng. A 493 (1) (2008) 261–266.
[65] M. Zhong, W. Liu, K. Yao, J.C. Goussain, C. Mayer, A. Becker, Microstructural evolution in high power laser cladding of Stellite 6+WC layers, Surf. Coat. Technol. 157 (2) (2002) 128–137.
[66] G. Xu, M. Kutsuna, Z. Liu, L. Sun, Characteristic behaviours of clad layer by a multi-layer laser cladding with powder mixture of Stellite-6 and tungsten carbide, Surf. Coat. Technol. 201 (6) (2006) 3385–3392.
[67] S. Dittrick, V.K. Balla, N.M. Davies, S. Bose, A. Bandyopadhyay, In vitro wear rate and Co ion release of compositionally and structurally graded CoCrMo-Ti6Al4V structures, Mater. Sci. Eng. C 31 (4) (2011) 809–814.
[68] H. Yan, J. Zhang, P. Zhang, Z. Yu, C. Li, P. Xu, L. Yunlong, Laser cladding of Co-based alloy/TiC/CaF2 self-lubricating composite coatings on copper for continuous casting mold, Surf. Coat. Technol. 232 (2013) 362–369.
[69] T. Gualtieri, H. Sahasrabudhe, S. Bose, A. Bandyopadhyay, Laser processing of tricalicum phosphate reinforced cobalt-chrome alloy coatings, Ceram. Trans. 251 (2014) 85–94.
[70] P.A. Molian, L. Hualun, Laser cladding of Ti-6Al-4V with BN for improved wear performance, Wear 130 (2) (1989) 337–352.
[71] J.S. Selvan, K. Subramanian, A.K. Nath, H. Kumar, C. Ramachandra, S.P. Ravindranathan, Laser boronising of Ti-6Al-4V as a result of laser alloying with pre-placed BN, Mater. Sci. Eng. A 260 (1) (1999) 178–187.
[72] A. Mehlmann, S.F. Dirnfeld, I. Minkoff, Laser-melt injection of B_4C on titanium, Surf. Coat. Technol. 42 (3) (1990) 275–281.
[73] F. Wang, J. Mei, W. Xinhua, Direct laser fabrication of Ti6Al4V/TiB, J. Mater. Process. Technol. 195 (1) (2008) 321–326.
[74] W. Liu, J.N. DuPont, Fabrication of functionally graded TiC/Ti composites by laser engineered net shaping, Scr. Mater. 48 (9) (2003) 1337–1342.

[75] S. Yang, N. Chen, W. Liu, M. Zhong, Z. Wang, H. Kokawa, Fabrication of nickel composite coatings reinforced with TiC particles by laser cladding, Surf. Coat. Technol. 183 (2) (2004) 254–260.
[76] Y. Li, P. Bai, Y. Wang, J. Hu, Z. Guo, Effect of TiC content on Ni/TiC composites by direct laser fabrication, Mater. Des. 30 (4) (2009) 1409–1412.
[77] A. Bandyopadhyay, S. Dittrick, T. Gualtieri, J. Wu, S. Bose, Calcium phosphate-titanium composites for articulating surfaces of load-bearing implants, J. Mech. Behav. Biomed. Mater. 57 (2016) 280–288.
[78] L. Hao, S. Dadbakhsh, O. Seaman, M. Felstead, Selective laser melting of a stainless steel and hydroxyapatite composite for load-bearing implant development, J. Mater. Process. Technol. 209 (17) (2009) 5793–5801.
[79] C.S. Ramesh, C.K. Srinivas, Friction and wear behavior of laser-sintered iron-silicon carbide composites, J. Mater. Process. Technol. 209 (14) (2009) 5429–5436.
[80] K. Murali, A.N. Chatterjee, P. Saha, R. Palai, S. Kumar, S.K. Roy, P.K. Mishra, A. Roy Choudhury, Direct selective laser sintering of iron-graphite powder mixture, J. Mater. Process. Technol. 136 (1) (2003) 179–185.
[81] H. Attar, M. Bönisch, M. Calin, L.-C. Zhang, S. Scudino, J. Eckert, Selective laser melting of in situ titanium-titanium boride composites: processing, microstructure and mechanical properties, Acta Mater. 76 (2014) 13–22.
[82] D. Gu, Z. Wang, Y. Shen, Q. Li, Y. Li, In situ TiC particle reinforced Ti-Al matrix composites: powder preparation by mechanical alloying and selective laser melting behavior, Appl. Surf. Sci. 255 (22) (2009) 9230–9240.
[83] I.V. Shishkovsky, L.T. Volova, M.V. Kuznetsov, Y.G. Morozov, I.P. Parkin, Porous biocompatible implants and tissue scaffolds synthesized by selective laser sintering from Ti and NiTi, J. Mater. Chem. 18 (12) (2008) 1309–1317.
[84] A. Bandyopadhyay, S. Tarafder, V. Krishna Balla, S. Bose, Laser processed tantalum for implants, Ceram. Trans. 237 (2012) 123–129.
[85] S. Dittrick, V. Krishna Balla, S. Bose, A. Bandyopadhyay, Wear performance of laser processed tantalum coatings, Mater. Sci. Eng. C 31 (8) (2011) 1832–1835.
[86] M. Das, K. Bhattacharya, S.A. Dittrick, C. Mandal, V.K. Balla, T.S. Sampath Kumar, A. Bandyopadhyay, I. Manna, In situ synthesized TiB-TiN reinforced Ti6Al4V alloy composite coatings: microstructure, tribological and in vitro biocompatibility, J. Mech. Behav. Biomed. Mater. 29 (2014) 259–271.
[87] A. Bandyopadhyay, S. Bose, S. Das, 3D printing of biomaterials, MRS Bull. 40 (02) (2015) 108–115.
[88] D.D. Gill, J.E. Smugeresky, C.J. Atwood, Laser Engineered Net Shaping™ (LENS®) for the Repair and Modification of NWC Metal Components, Sandia Report, 2006.
[89] http://www.lortek.es/files/fab-aditiva/efesto-ik4-lortek-27th-november-2013.pdf.
[90] http://www.optomec.com/wp-content/uploads/2014/04/Optomec_LENS_Blisk_Repair_Datasheet.pdf.
[91] B. Vayre, F. Vignat, F. Villeneuve, Designing for additive manufacturing, Procedia CIRP 3 (2012) 632–637.
[92] S. Hällgren, L. Pejryd, J. Ekengren, (Re) Design for Additive Manufacturing, Procedia CIRP 50 (2016) 246–251.

This page intentionally left blank

CHAPTER 18

Direct Infrared Laser Machining of Semiconductors for Electronics Applications

I. Mingareev*, L. Shah†, M. Richardson†, M. Ramme‡
*Florida Institute of Technology, Melbourne, FL, United States
†University of Central Florida, Orlando, FL, United States
‡TRUMPF North America, Farmington, CT, United States

18.1 INTRODUCTION

The modern electronics industry relies heavily on the technological maturity, performance, and cost efficiency of semiconductor wafer processing methods, most notably silicon and gallium arsenide. The development of novel electronic devices is increasingly focused on higher performance, ultracompact dimensions, and more integrated functionality [1–4]. Defect-free high-speed processing of thin wafers [5], reliable bonding of dissimilar materials [6], and a combination of electronics with microfluidic and photonic circuitry [7,8] are among the most wanted fabrication capabilities of the electronics research and development community. The economic competitiveness of the industry mandates the reduction of processing steps in the production workflow, the introduction of multi-purpose fabrication tools, and the use of low-cost materials with minimum environmental impacts.

At this point, laser applications in the electronics industry have become commonplace [9]. Over the last three decades, the laser processing of semiconductor wafers has been a very active and important research area. This research involved the use of both continuous-wave (CW) and pulsed laser sources, various processing regimes for wafer singulation and drilling, surface functionalization, laser-induced doping, deposition of thin films, and annealing. The following four major electronics manufacturing segments have shown to benefit most from the use of laser technologies.

- *Semiconductor front-end applications*. Integrated circuit (IC) technology relies on laser processes for photomask writing using ultraviolet (UV) laser sources [10]. In addition, laser-based metrology methods

Advances in Laser Materials Processing
https://doi.org/10.1016/B978-0-08-101252-9.00018-2
Copyright © 2018 Elsevier Ltd.
All rights reserved.

are actively utilized for the inspection of photomasks and wafer characterization.

- *Semiconductor back-end applications*. Laser-based dicing [11] is a very important application in the present-day electronics manufacturing workflow, offering fast, material-efficient, and gentle processing of wafers. New processing regimes using short and ultrashort pulse lasers were the subject of intense research, enabling crack-free processing of thin wafers with a low thermal impact on materials. In addition, lasers are widely used for marking purposes, trimming of IC components, edge isolation in photovoltaics (PV) [12], texturization, and localized wafer doping.
- *Advanced packaging applications*. Numerous laser-based processing applications were established in electronics packaging technologies [13,14], e.g., for the drilling of IC microvias and high-density interconnections, embedded passive trimming, microvias processing of dielectrics such as ceramics and polymers, welding, and soldering.
- *Flat panel display applications*. Many established and emerging laser processing methodologies are used for glass/sapphire substrate cutting, TFT display annealing, patterning, and marking [15].

Laser materials processing is based on the deposition of a well-defined amount of optical energy into the material with high spatial selectivity. Therefore the choice of the laser source is dependent on the application and the material. For semiconductor laser processing, the perfect processing system would provide infinitesimally small spot sizes resulting in microvias best spatial resolution possible in 3D, strong interaction on the target nearly independent of the target material, and produce no collateral change to the surrounding material. Given that these ideal conditions are unattainable, different solutions have emerged primarily influenced by the dynamics of laser absorption. From the perspective of the laser-material interaction, the primary consideration is if the absorption of light is a linear or nonlinear process. Nonlinear absorption mediate processing generally requires relatively expensive ultrashort pulse laser systems. However, nonlinear absorption uniquely enables 3D bulk processing whereas linear absorption is generally restricted to surface processing [16].

Over the years the electronics industry adopted various laser sources starting with CO_2 lasers and directly diode-pumped solid-state (DPSS) lasers operating in the wide range of wavelengths from IR to UV, to high-power

continuous-wave and pulsed fiber laser sources. Diode lasers currently provide unrivaled electrical-to-optical efficiency, compact/robust packaging, and relatively low cost. Furthermore, the spatial brightness of such systems continues to improve rapidly with commercially available multikilowatt fiber coupled diode systems offering comparable brightness to CO_2 and multimode fiber lasers. These advances in diodes have also made it possible to improve the performance of solid-state laser systems, in particular scaling average power. Of course, higher laser powers place higher demands on optics and beam handling systems as well as positioning equipment.

Infrared lasers with photon energies smaller than the energy band gap of commonly used semiconductors such as Si and GaAs enable an interesting new processing regime with many potential applications in the wafer and back-end manufacturing and packaging [17–19] fields. In this processing regime, semiconductors are semi-transparent, and 3D modifications become potentially feasible. While a few applications have already been demonstrated, such as "stealth dicing" [20] using lasers emitting at near-band-edge wavelengths, recent progress in the development of high-energy mid-infrared lasers, as well as novel energy deposition and material processing methodologies, can significantly widen the scope of practical applications.

This chapter describes recent advances in the development of numerical models and experimental methods for 2D and 3D processing of semiconductors with high spatial resolution. A summary of the main physical phenomena involved in laser-matter interactions is provided, such as absorption of light and ionization of matter, followed by energy transfer and structural changes in the material. Specifically, the use of infrared lasers for semiconductor processing is discussed. Two important cases of semiconductors irradiated with nanosecond and femtosecond infrared laser pulses are reviewed. Applications of ultrashort pulse lasers in surface texturing utilizing the effect of self-organized surface ripple formation, back-surface modifications, and metallization layer structuring and removal are presented.

18.2 MAIN PRINCIPLES OF LASER-MATTER INTERACTIONS

18.2.1 Absorption of Light and Ionization of Matter

In general, optical energy is transferred to material through photon-electron interactions, such as the photoelectric effect or the inverse Bremsstrahlung. In order to effectively absorb light, a sufficient density of electrons or other quasifree charge carriers needs to be present in the material. However, the

interaction of such charge carriers with the electric field of the incident laser light is strongly dependent on material properties. While charge carriers are readily available as a free-electron gas in metals, in dielectrics and semiconductors the electrons are initially bound to the lattice atoms. In that case absorption of light is only possible if material can be adequately ionized, such as through impact ionization, field ionization, multiphoton ionization, or avalanche ionization processes. In order to quantify the degree of material ionization, critical electron density N_c can be introduced that corresponds to the case of 100% reflective material, that is, the laser-induced plasma cannot accept any further optical energy. Moreover, laser-induced plasma can act as a shield and restrict propagation of laser light deeper into material, thus limiting materials processing to surfaces (2D) only.

For most dielectric materials, the photon energy $E = \hbar\omega$ in the infrared wavelength range is small compared to the material band gap E_g. However several electrons with energies $\hbar\omega < E_g$ can be absorbed in a multiphoton ionization process in order to raise bound electrons to the conduction band. This nonlinear absorption effect is possible due to the large electromagnetic field intensities inherent to the interaction of short (nanoseconds and shorter) laser pulses with matter. At even larger irradiation intensities, field ionization occurs as a consequence of the energy band deformations allowing bound electrons to tunnel into the conduction band. Impact ionization is another important ionization mechanism that is essential for the interaction of ultrashort laser pulses, mainly with nonmetallic materials. It is based on a generation of electron-hole pairs excited by high-kinetic-energy electrons interacting with bound electrons in the valence band. At large intensities, if sufficient densities of optically excited "seed" electrons are available in the materials, avalanche ionization becomes the major process of charge carrier generation.

Since nonlinear absorption processes are initiated at much higher laser intensities compared to linear absorption, the optical energy can be effectively deposited in spatially confined regions of the material (Fig. 18.1) by tailoring spatial, temporal, and spectral irradiation conditions. For example, by tightly focusing ultrashort laser pulses with durations of tens of picoseconds and shorter, with photon energies $\hbar\omega < E_g$, micro- and nanometer-scale 3D-modifications can be induced in the volume of transparent materials.

It should be noted that absorption of light in dielectrics and semiconductors can be considerably enhanced if defect states are present in the material, for example, due to crystal mismatches and other structural

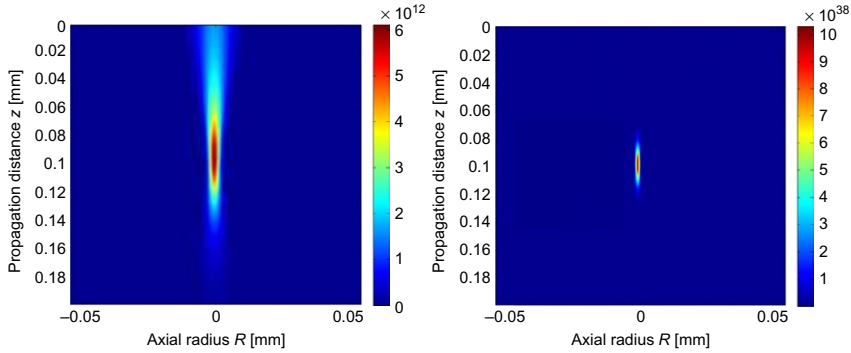


Fig. 18.1 Simulated electron density distributions produced in the volume of a 200-μm thick dielectric material by linear (left) and nonlinear (right) absorption processes. The incident laser radiation is focused in the center and propagates from top to bottom.

inhomogeneities, dopants and compositional defects, or preexisting laser-induced damage sites. For example, absorption increases by applying multiple laser pulses at the same spot in the material, leading effectively to a reduced threshold laser fluence needed to induce material changes.

18.2.2 Energy Transfer Phenomena and Structural Modifications

Once material is photo-ionized, a process of charge carrier redistribution begins. Especially at large irradiation intensities, a nonequilibrium electron distribution is quickly generated following ionization, and high-energy electrons are immediately involved in ballistic transport processes as well as electron-electron collisions. After a few tens of femtoseconds, a thermal equilibrium of the electron system is established followed by the initiation of the heat transfer processes from electrons to phonons. Depending on material, this process is accomplished within a few picoseconds. The electron system and lattice thermalize to a common temperature, marking the onset of thermal diffusion processes by phonons and subsequent material structure modifications, such as melting, evaporation, and other ablation phenomena.

During phonon thermalization, the material undergoes several stages of thermal and nonthermal transformations and various thermodynamic phase transitions, such as formation of plasma and electron emission, melting, vaporization, subsurface heating, boiling, and resolidification. At large irradiation intensities, the formation of plasma plumes occurs accompanied by a generation of shockwaves. If the lattice temperature reaches the melting

point of the material, the heterogeneous melting process is initiated, usually starting at lower melting threshold sites such as surfaces or internal defects. A melt front expands and/or propagates deeper into the material at speeds limited ultimately by the speed of sound, meaning that the material can be potentially heated even to larger than the melting point temperatures giving rise to transient thermodynamic nonequilibrium conditions, such as superheated fluids, phase explosions, etc. At certain irradiation conditions, materials can be subject to the so-called nonthermal melting, occurring when bound electrons are transformed to antibonding states reducing the screening effect of the ionic potential. As a consequence, ions start repelling each other, and when the resulting atomic displacements exceed the lattice constant by 10%–20%, nonthermal melting occurs.

Laser-melted material can emit particles such as clusters, molecules, ions, atoms, and electrons, which carry away heat when leaving the material surface. This vaporization process can significantly contribute to material ablation for irradiation with CW laser light, and nanosecond or longer laser pulses. However, vaporization alone is not considered the major material removal process using ultrashort laser pulses, due to the transient nature and short lifetime of melting and based on the experimental analysis of shockwave expansion. Other ablation mechanisms include the boiling of the molten material phase and consequently melt expulsions, and ablation due to rapid phase changes caused by large transient thermal gradients.

Thermal diffusion of the laser-irradiated region, roughly defined by the laser spot size and the absorption depth in material, leads to resolidification of the material. For surface irradiation, a crater or a groove will be produced, depending on the irradiation method. Consequently, irradiation with shorter pulse durations results in smaller heat-affected zones (HAZ) and more confined modified areas. Even if no significant amount of material was removed, the resolidified material structure may not be the same as before irradiation. Structural changes such as density modification, that is local rarefication or densification, crystal structure transitions (monocrystalline to polycrystalline), or the generation of voids in the bulk of materials can occur.

18.2.3 Heat Accumulation Effects

Application of multiple laser pulses onto the same material spot can considerably alter the material response to irradiation. If the pulse-to-pulse time intervals are smaller than the typical thermal energy dissipation time for single-pulse events, the material can be subject to a significant local heat buildup with temperatures potentially reaching several thousand Kelvin [21].

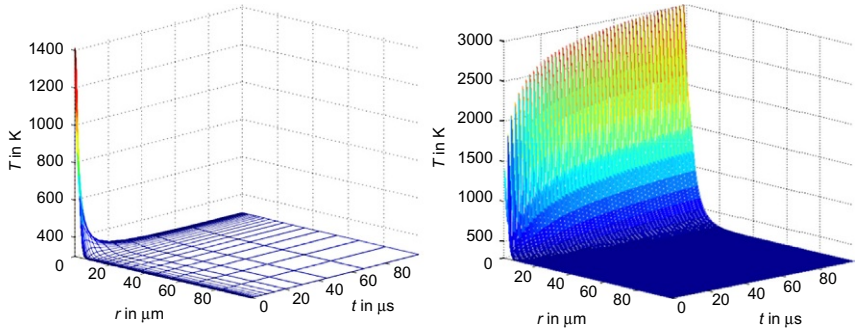


Fig. 18.2 Simulated heat diffusion following single-pulse irradiation (left), and irradiation with 50 pulses at the repetition rate 500 kHz and the same pulse energy (right).

This effect can lead to the formation of continuously modified tracks and confined volumes in the bulk of transparent materials. It can also significantly increase the ablation rate of material surfaces while still maintaining a fairly small HAZ (Fig. 18.2).

Heat accumulation is especially useful to the fabrication of optical wave-guiding features in dielectrics due to more homogeneous and smoothly shaped modifications, and resulting larger refractive index gradients.

The interaction of multiple pulses requires further optimization of dose per pulse and the temporal/spatial overlap of subsequent pulses. In the case of dissimilar materials, for example low-k dielectric coatings on Si, the optimal overlap can be very different from the substrate itself. Improper processing can lead to delamination and/or fracturing of the coating. The most important observables in this process are the ablation rate relative to the amount of melt/recast material. Given that the melt/recast will correspond to the HAZ, this determines the minimum street width for IC devices. Furthermore, melt or recast material may need to be removed in a separate process, which will significantly reduce the productivity/cost ratio of the laser process as a whole.

18.2.4 Principles of Laser Process Development and Optimization

Successful process development relies on proper identification and variation of process parameters responsible for functionality and performance of the application. In general, three major groups of process parameters (Table 18.1) can be identified: material properties, irradiation source capabilities, and the processing method adopted.

Table 18.1 Summary of process parameters

Material properties	Irradiation source properties	Processing method parameters
• Absorptivity	• Wavelength	• Focusing conditions
• Density	• Average power/pulse energy	• Scanning strategy
• Physical structure	• Repetition rate	• Translation speed
• Thermal conductivity	• Pulse duration	• Energy dose/fluence
• Chemical composition	• Pulse shape	• Spatial beam distribution
• Thermodynamic parameters	• Beam quality	• Irradiation duty cycle

Materials' optical properties determine the prevailing type of optical absorption. Physical properties, such as its crystalline or amorphous structure, initial surface roughness, density, and thermodynamic conditions, determine the material's response to irradiation. Chemical composition is essential for assessment of potential physical and compositional transformations.

Laser source characteristics such as the emission wavelength, power, and pulse duration determine the probable interaction regime and the range of energy densities while also providing a notion of achievable process efficiency. The optimal selection of processing methods and conditions (the choice of focusing conditions, scanning strategy, and other experimental approaches adopted to tailor the deposition of optical energy), however, is the major task of process development in laser materials processing.

In addition, it should be noted that a thorough knowledge of the fundamental physical phenomena involved in laser-matter interaction is a prerequisite to any successful process development. For many application areas, especially those relying on the interaction of ultra-high-intensity lasers with nonlinear media, this knowledge base is still very limited, requiring both extensive modeling efforts and parametric experimental studies. In particular, process optimization involves model- and experiment-based tailoring of spectral, spatial, and temporal deposition of optical energy in materials.

18.2.5 Irradiation of Semiconductors With IR Laser Pulses

The interaction of infrared laser pulses with semiconductors is of special interest, especially considering the possibility of 3D in-volume processing of semiconductor wafers, similar to the processing of dielectric materials that are transparent in the visible range. Compared to dielectrics, the semi-

conductors' energy band structure exhibits both thermally excited quasifree electrons in the conduction band much like metals, and a considerably large band gap between the valence and the conduction bands similar to dielectrics (for silicon: $E_g \approx 1.12\,\text{eV}$ at room temperature, compared to approx. 9 eV for fused silica).

When irradiated with photon energies below the band gap, for example in the visible or UV spectral region, the absorption in semiconductors is primarily linear and material modification is only possible at the surface, or within the optical penetration depth. While near-infrared laser radiation, for example at $\lambda = 1064\,\text{nm}$, can potentially reach several 100s μm into Si, true 3D-spatially selective material processing in this regime is not possible. Three primary absorption mechanisms can be identified for laser-semiconductor interaction utilizing high-intensity laser radiation with photon energies $\hbar\omega > E_g$ (e.g., at a wavelength in the visible and UV spectral ranges). Here, semiconductors are subject to intrinsic absorption, which involves interband electronic transitions. Free carrier absorption involves intraband transitions of photo-excited electrons with subsequent energy transfer to the lattice. Finally, defect- and impurity-induced absorption essentially resulting in a reduction in the energy band gap is the third major absorption mechanism. Nonlinear absorption processes do not play an important role in this excitation regime, since material is modified at much lower energy densities compared to excitation conditions needed for nonlinear absorption effects to become dominant. Therefore, due to the plasma shielding effect, primarily surface modifications occur.

However, optical excitation at photon energies above the band gap is a promising experimental approach that requires a thorough assessment of absorption and energy transfer mechanisms in semiconductors in order to determine optimal process conditions and a balance between linear and nonlinear interaction phenomena. In general, for photon energies $\hbar\omega < E_g$ and undoped and defect-free semiconductors, intrinsic or free carrier absorption is negligible. On the other hand, thermally excited and impurity- and defect-based charge carriers are always present in real semiconductor materials. Therefore, depending on irradiation conditions and initial electron densities in the material, nonlinear effects such as multiphoton absorption may become important interaction mechanisms, potentially enabling localized energy deposition in 3D. In particular, electron avalanche ionization may become prominent. However this nonlinear effect requires a sufficient density of "seed" electrons generated by other, lower-threshold linear and nonlinear absorption mechanisms.

In the following, 2D and 3D processing of semiconductors was studied utilizing analytical and numerical models, as well as experimentally, for two different irradiation regimes involving infrared pulsed laser light with ultrashort ($t_p \approx 100$ fs) and nanosecond ($t_p \approx 7 \ldots 100$ ns) pulse durations.

18.3 INFRARED ULTRASHORT PULSE LASER PROCESSING

In order to study the various absorption effects and laser induced modification phenomena in semiconductors, differently doped Si wafers were irradiated with 100 fs laser pulses at three different wavelengths. Irradiation at $\lambda = 0.8$ μm corresponds to the linear absorption regime, while excitation at 1.3 and 2.4 μm corresponds to photon energies smaller than the semiconductor energy band gap, and therefore possibly the nonlinear absorption regime. Specifically, two photons at 1.3 μm and three photons at 2.4 μm would be necessary to advance an electron from the valence band to the conduction band considering multiphoton ionization as the dominant mechanism.

18.3.1 Study of Absorption and Beam Propagation

In the first series of experiments, ablation/modification thresholds were determined for single-pulse excitation using variously doped Si wafers, including n- and p-doped, as well as undoped (intrinsic) wafers. The purpose of this study was to determine the effect of doping- or impurity-based charge carrier densities on light absorption and material modification processes. Fig. 18.3 shows the schematic of the irradiation setup, and the results of threshold pulse energy determination.

The diameters of surface craters produced at varying pulse energies were determined, and the threshold determination method by Liu [22] was adopted. The results show that the modification thresholds were within the same order of magnitude for all three wavelengths, although the theoretically assumed absorption regime changed from linear to multiphoton absorption. With the increasing number of photons needed to ionize valence electrons, the modification thresholds were expected to increase significantly. Based on experimental results, however, it can be concluded that multiphoton absorption was not significantly affecting the ionization scheme, since only a marginal increase in pulse energy was detected for irradiation at the wavelength 2.4 μm. A similar result was observed in experiments on intrinsic and doped GaAs wafers.

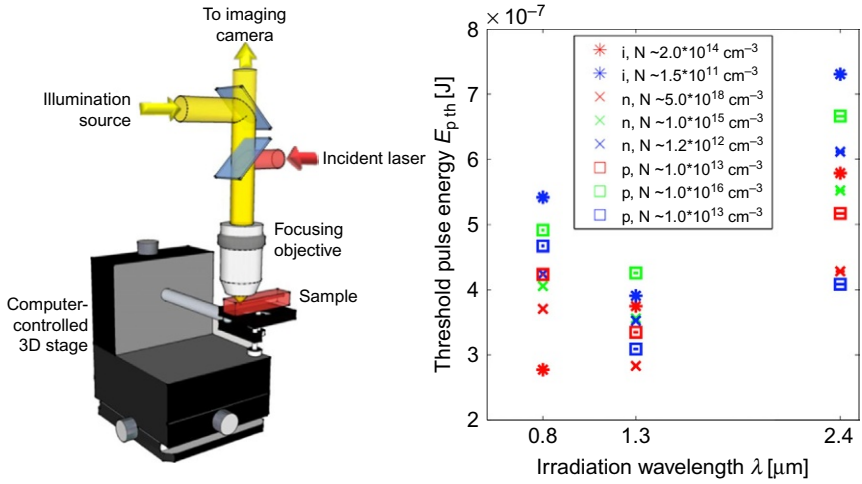


Fig. 18.3 Irradiation setup (left), and modification threshold pulse energies determined for variously doped Si wafers irradiated with ultrashort laser pulses at the wavelengths 0.8, 1.3, and 2.4 μm (right).

Numerical simulations of beam propagation and absorption in semiconductors were performed using a custom model based on a split-step algorithm, and using a complex beam parameter to account for irradiation with high-numerical-aperture optics. In addition, the model accounts for the effect of initial dopant concentration, self-focusing, plasma shielding effects, and carrier recombination, producing spatially and temporally resolved electron densities in the semiconductor bulk as a result.

Based on a simulation performed for propagation and the interaction of a single 100 fs laser pulse with differently doped Si wafers using emission wavelength $\lambda = 2.4\,\mu m$ (Fig. 18.4), it can be concluded that the adopted pulse energy is the primary factor that influences the laser-induced electron generation rate, and only an insignificant effect of dopant concentration was observed. However, at very high dopant concentrations exceeding approx. $10^{19}\,cm^{-3}$, the dopants can effectively contribute to the ionization processes.

The same numerical model was adopted to estimate the possibility of focusing ultrashort laser pulses in the bulk of semiconductors for 3D processing. In particular, it is essential to avoid intense generation of electrons at the surface of the materials and to prevent plasma shielding. Ideally only a relatively confined volume at or around the focal spot of laser radiation should be subject to intense light absorption in order to enable full 3D processing capability. Calculations of the electron density distribution along the

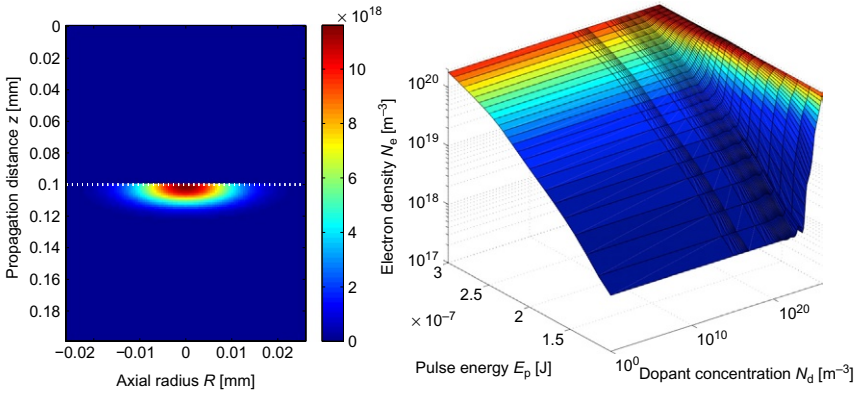


Fig. 18.4 Left: Example of calculated energy density and beam propagation in 2D for n-doped Si with dopant concentration $N_D = 10^{14}\,cm^{-3}$. Right: Calculated electron density for a range of dopant concentrations and a range of pulse energies.

optical propagation path, and the temporal evolution of the electron density were performed. For calculation, a single $\lambda = 2.0\,\mu m$ laser pulse with pulse duration 100 fs and pulse energy 1 μJ was focused using a NA = 0.5 focusing optic in 100-μm depth (Fig. 18.5).

The simulations show that the electron density quickly rises to the critical electron density level within a few-micron layer at the substrate surface, and effectively prevents further light propagation into the bulk. Most of the incident optical energy is reflected, and only a negligible portion of energy

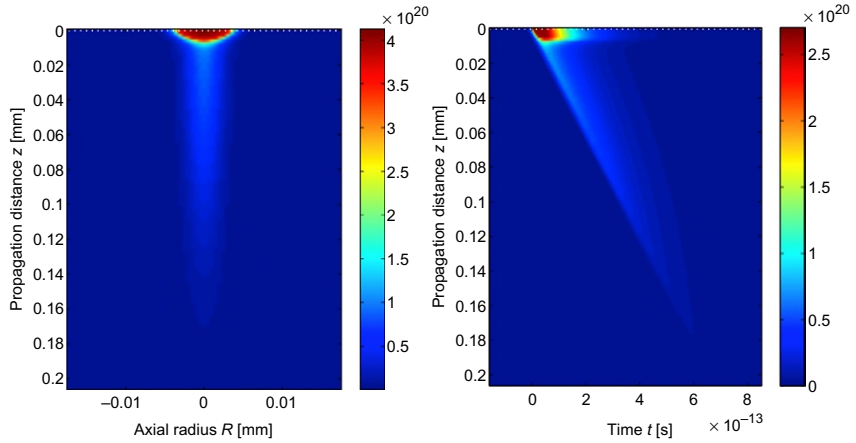


Fig. 18.5 Left: Simulated electron density distribution in 2D for ultrashort infrared pulse focused in 100-μm depth. Right: Calculated electron density evolution at axial radius position $R = 0$.

is transmitted and focused in the bulk. While the incident pulse energy could be potentially reduced to avoid the generation of critical electron densities at the surface and to increase transmission to the focal volume, it is estimated that the energy density in the bulk will not reach modification threshold levels. Therefore, no 3D modifications are possible according to this model and with the process conditions adopted. Further simulation efforts will be needed to estimate the possibility of bulk modifications in different processing regimes, such as using longer laser pulses and alternative energy deposition approaches.

18.3.2 Applications in Semiconductor Surface Functionalization

Laser texturing of active semiconductor areas exposed to light in photovoltaic modules is a time- and cost-efficient experimental approach that can significantly increase light harvesting efficiency of solar cells. The method is based on the generation of microscale surface roughness leading to lower reflectivity and therefore enhanced absorption of semiconductor substrates. Textured surfaces can be achieved by various scanning and interference-based irradiation processes using CW and pulsed laser sources. In addition, self-organized periodic structures, also known as surface ripples, can be induced.

The first ripple structures were observed shortly after the invention of the laser in 1965, when the formation of periodic structures was reported on semiconductors using visible pulsed laser light. Further studies were carried out on ripple formation in various materials including metals and dielectrics, and ripples were reported for irradiation with picosecond and longer pulses. The spatial periodicity of these "classical" ripples, or low-spatial-frequency LIPSS (LSFL), was approx. equal to the wavelength, and the direction was perpendicular to the polarization of utilized laser light (Fig. 18.6). In order to explain this effect, Sipe et al. [24] suggested an interaction mechanism of linear polarized light with microscopic surface features leading to periodically modulated light absorption in the thin surface material layer.

With the advent of ultrafast laser sources with sufficient pulse energies, new types of ripples were reported. Submicron surface structures with considerably smaller periodicity than the wavelength were demonstrated. These ripples are referred to as the high-spatial-frequency LIPSS (HSFL), and their origin is not yet well understood. According to a model by Jia et al., the formation of HSFL results from the interference of the second

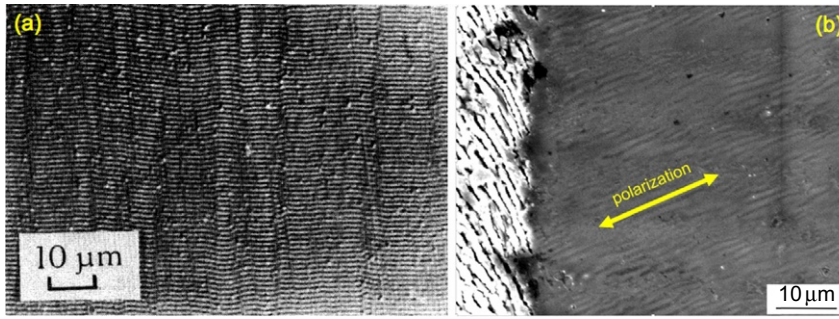


Fig. 18.6 Examples of various laser-induced ripple structures: (A) "Classical" low-spatial-frequency ripples [23], (B) low-spatial-frequency ripples generated with ultrashort laser pulses and "parallel" ripples.

harmonic generation (SHG) light generated at the material interface, and the periodicity is $\lambda/2n$, where n represents the material's refractive index. Reif et al. developed an alternative model that considers interaction of the incident laser light with surface plasmons and resonance effects affecting the optical absorption.

In addition, several other types of ripples were reported, including ultrafast laser-induced periodic structures that are parallel to the polarization of the incident light and featuring periodicity of approx. λ. These P-LSFL structures are often generated on roughened surfaces and at lower fluences compared to other types of ripples. The dependence of surface feature parameters on the laser irradiation conditions, especially the fluence levels, the wavelength, and the effective energy dosage, is still a matter of intense research, as no clear understanding of the underlying physical phenomena exists to date.

The fabrication of laser-induced periodical surface structures (LIPSS) was studied on semiconductor surfaces using ultrashort laser pulses with pulse duration $t_p = 100$ fs at the wavelengths 400, 800, and 2 µm. Infrared laser light was produced by an optical parametric amplifier, and the 400-nm emission was produced utilizing SHG from a Ti:Sapphire amplified femtosecond laser system. A $10\times/\mathrm{NA} = 0.25$ microscope objective was used to focus laser light onto the substrate surfaces. The beam was scanned across the surface at varying speeds, and with a varying degree of spatial overlap between adjacent laser pulses.

Wavelength dependence was studied by irradiating Si and GaAs wafers, and both low- and high-spatial frequency LIPSS were observed, with surface microgrooves oriented perpendicular to the polarization of laser

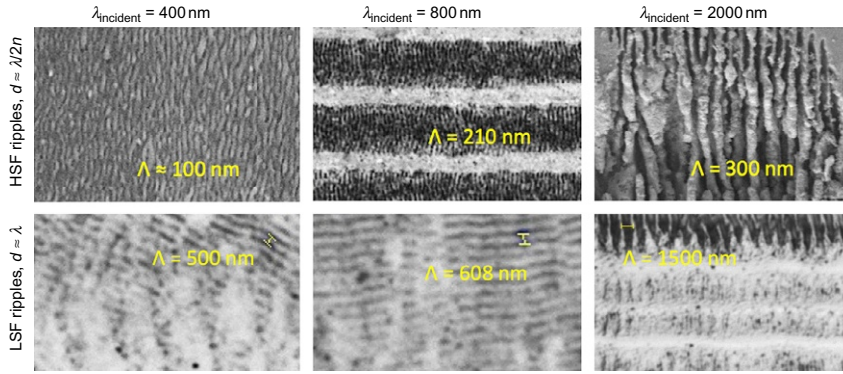


Fig. 18.7 Results of experimental studies on wavelength dependency of ripple spacing.

light (Fig. 18.7). For HSFL the deviation of the measured groove-to-groove spacing from the $\lambda/2n$ trend was considerable, and the microstructures appeared at the accumulated fluence levels above $2\,J/cm^2$. For LSFL the surface feature periodicity was smaller than the wavelength for irradiation at 800 and 2 μm, but slightly larger when irradiated at 400 nm.

Polarization dependence was studied by producing multiple overlapping modification tracks in GaAs with varying direction of the incident electromagnetic field (Fig. 18.8). The overlap between the tracks was approx. 30%, while individual tracks were written at the speed $v = 0.25$ mm/s parallel

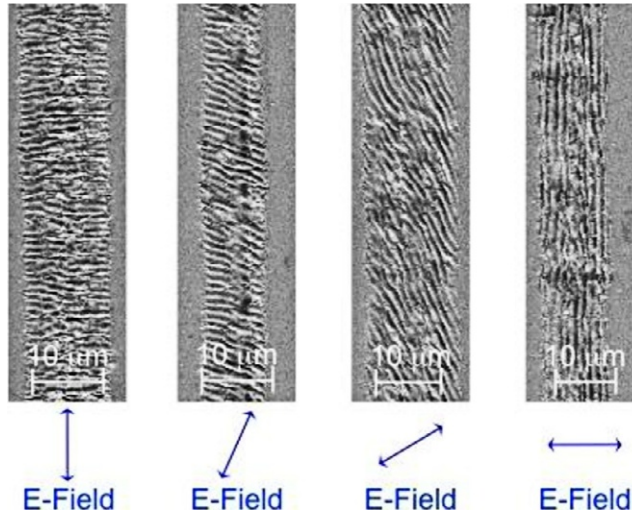


Fig. 18.8 Polarization dependence of LSFL orientation in GaAs irradiated at the wavelength 2 μm.

to the track direction. The results show that the direction of ripple microstructures was consistently perpendicular to the polarization direction, and the resulting ripple structure developed spatial coherency both within the tracks and between adjacent tracks. This "stitching effect" allows for the generation of very large periodically structured surfaces. Processing of Si and GaAs at the wavelengths 400 and 800 nm resulted in similar behavior, but the structures appeared at a significantly lower accumulated fluence of $0.3\,J/cm^2$, compared to $2\,J/cm^2$ for irradiation with 2 µm laser light.

An interesting new processing regime for ripple formation was observed in both materials irradiated with 2 µm light at low fluences (Fig. 18.9). These ripples are oriented parallel to polarization, and referred to as "parallel" ripples, or P-LIPSS here. The periodicity of the features was approx. $\Lambda = 450$ nm for both materials under investigation. The microstructures in GaAs appeared when processing at a translation speed of $v = 0.5$ mm/s and pulse energies $E_p = 136$ nJ. For Si, translation speed was $v = 0.25$ mm/s, and the pulse energy was $E_p = 129$ nJ. In both materials the irradiation fluence levels were approx. one order of magnitude lower than the corresponding modification thresholds. An effectively larger energy dose needed to induce P-LIPSS in Si is attributed to the removal of the surface oxide layer.

The experiments revealed that the stitching effect could not be reproducibly demonstrated for P-LIPSS structures, which can be potentially explained by the very narrow process window for such modifications. Since nearly Gaussian beam distributions were adopted in the experiments, only areas of certain intensity range, such as in the central region of the

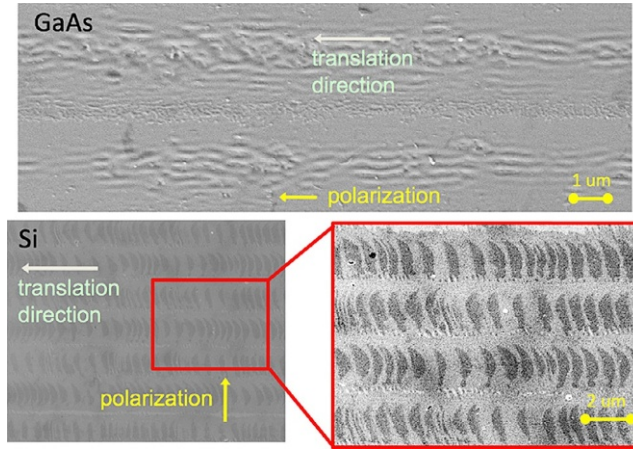


Fig. 18.9 New types of ripples observed in GaAs and Si irradiated at the wavelength 2 µm.

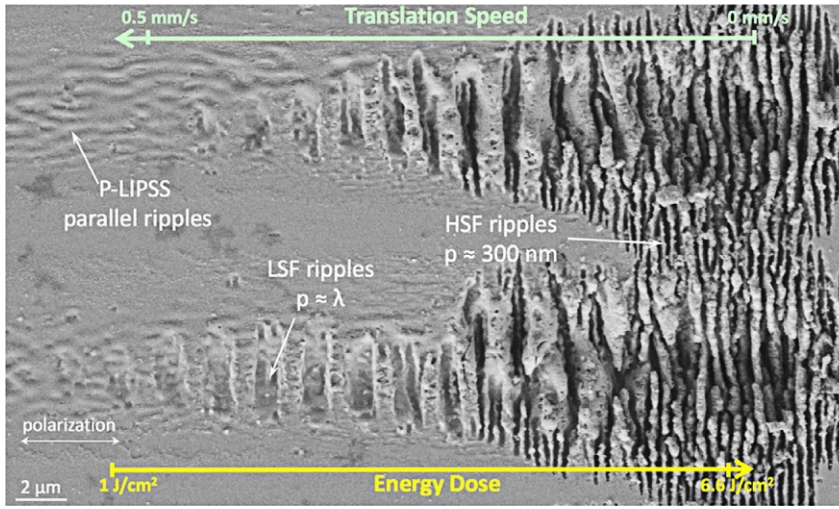


Fig. 18.10 Summary of ripple structures produced in GaAs at the wavelength 2 µm. All three types of LIPSS were detected.

beam intensity distribution within the $2w_0 = 26\,\mu m$ spot, were subject to the formation of P-LIPSS. Consequently, laser fluence levels in the track-overlapping region were outside the optimal range of process conditions.

The formation of all three types of LIPSS—low-spatial-frequency ripples (LSFL), high-spatial-frequency ripples (HSFL), and parallel ripples (P-LIPSS)—was demonstrated in a single irradiation process at the wavelength 2 µm by continuously varying the energy dose (Fig. 18.10). The translation speed was decreased from 0.5 mm/s to 0 mm/s (from left to right). The corresponding change in laser fluence was from $1\,J/cm^2$ to approx. $6.6\,J/cm^2$. Two such modifications were produced in an overlapping manner to demonstrate the stitching effect. The surface morphology changed gradually from P-LIPSS on the left, to LSFL in the center, to HSFL on the right. A small transition zone can be recognized between the different ripple microstructures.

18.4 INFRARED NANOSECOND PULSE LASER PROCESSING

The processing of semiconductors with infrared nanosecond pulses is a promising experimental approach that can be applied to both 2D and 3D wafer processing. Compared to ultrashort pulses, infrared nanosecond pulses with even larger pulse energies can be transmitted through the silicon wafer

without damaging the surface due to the generally lower intensities inherent in longer pulse durations. Although processing with nanosecond pulses potentially results in a larger HAZ compared to ultrashort pulses, the energy deposition can be tailored to reduce excessive thermal load on wafer material, and enable a number of applications useful in the electronics industry. Several experimental and modeling studies were performed to investigate this new processing regime utilizing our self-developed thulium-doped fiber laser operating at the wavelength $\lambda = 2\,\mu m$.

The laser source was based on the master-oscillator-power-amplifier (MOPA) principle, and could be operated both in nanosecond pulsed (pulse durations $t_p = 7 \ldots 100\,ns$) and continuous-wave (CW) mode. The maximum peak power was in excess of 40 kW, and up to 400 µJ of pulse energy was available for 7 ns pulses at 1 kHz repetition rate. The laser radiation was focused using an aspheric lens with the focal length $f = 7.5\,mm$. The strong refraction of semiconductor materials (refractive indices $n_{Si} = 3.45$, and $n_{GaAs} = 3.36$ at $\lambda = 2\,\mu m$) was taken into account, when positioning the wafers on a 3D translation stage (Fig. 18.11).

18.4.1 Front and Back Surface Processing of Semiconductor Wafers

In order to study the interaction of infrared nanosecond pulses with intrinsic semiconductors such as double-side polished Si and GaAs, first the modification thresholds were determined using the Liu method. It should be noted that irradiation of sample surfaces with single pulses did not result

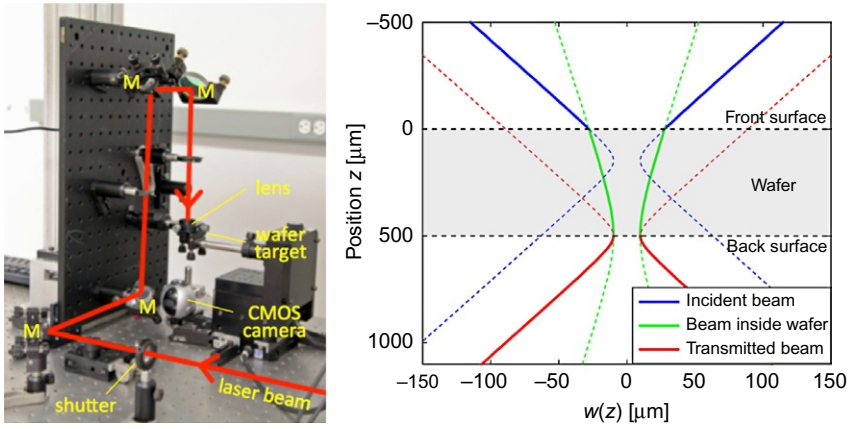


Fig. 18.11 Schematics of the irradiation setup (left), and diagram showing beam propagation through wafer (right).

in the consistent formation of craters, since considerable differences in the crater diameters were observed. Therefore, experiments were based on the detection of the cumulative effect of 20 pulses and then single-pulse threshold values were calculated. The results of surface modification thresholds are summarized in Table 18.2.

Since semiconductors are transparent at the wavelength 2 μm, a series of experiments was performed to clarify whether the transmitted energy is sufficient to induce modifications at the back surface of wafers. The experiments were also done to validate that the back surface of uncoated Si and GaAs wafers could be modified with high spatial selectivity and independently, without damaging the front surface. The influence of process parameters on the resulting surface morphology change was a matter of research by varying the pulse duration, the pulse energy, and the focusing conditions. Considering refraction of the materials, laser radiation was focused at the calculated positions corresponding to the largest fluence level being on the back surface.

Irradiation at fixed positions did not result in the consistent formation of modification craters on the back surface. However, trenches could be produced when translating the samples in the plane orthogonal to the laser propagation direction (Fig. 18.12). An analysis of the depth and morphology of trenches was performed, and the effective upper limit of energy density resulting in back surface modifications was calculated. The modification thresholds were $F_{thr} < 3.2\,J/cm^2$ for GaAs, and $F_{thr} < 17.2\,J/cm^2$ for Si. For these calculations, the Fresnel reflections from both wafer surfaces were taken into account, and the effectively transmitted energy to the back surface was determined using the ray tracing diagram in Fig. 18.11 (right) while disregarding absorption in the bulk of semiconductors entirely.

It should be noted that the unexpectedly high modification threshold for Si was obtained at a larger offset in z-direction (along the beam propagation direction) than predicted by the ray tracing model, with the

Table 18.2 Surface modification thresholds determined for irradiation with infrared nanosecond pulses

Material	Pulse duration [ns]	Front surface threshold fluence [J/cm^2]
Si	7	2.86
	100	3.22
GaAs	7	2.30
	100	3.38

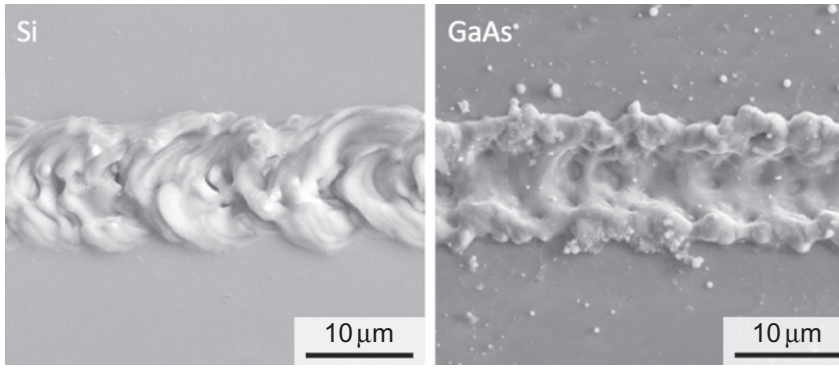


Fig. 18.12 Modification trenches obtained at the back surfaces of Si and GaAs wafers irradiated with $t_p = 7$ ns pulses at the wavelength $\lambda = 2$ µm.

calculated focal position being more than 50 µm beyond the back surface of a 500 µm thick wafer. Occasionally, irregular modifications were found even at lower fluence levels. For example, microscopic scratches and multiple microcraters could be found along the modification path of the laser. With repetitive irradiation, these micromodifications could lead to the formation of a well-defined modification trench. It should be therefore assumed that such initiation effects could play an important role in back surface processing. In general, however, only a rough estimation can be given for the back-surface modification threshold in Si (Fig. 18.13).

An assessment of various absorption phenomena, energy transfer pathways, and the energy budget was performed for infrared nanosecond laser pulse processing of semiconductors similar to ultrashort pulses. For simplification, a first-principle model of laser-induced heating of semiconductors with nanosecond pulses can be adopted. This model allows the estimation of the material temperature change ΔT following the irradiation at the fluence F, assuming the optical energy was added to the material uniformly within the "heating depth" L_H:

$$\Delta T = \frac{F(1-R)}{\rho c L_H}, \tag{18.1}$$

where c is the specific heat, ρ is the density, and R is the reflectivity. For the heating depth the following estimation can be provided:

$$L_H = \frac{1}{\alpha} + L_D + L_T. \tag{18.2}$$

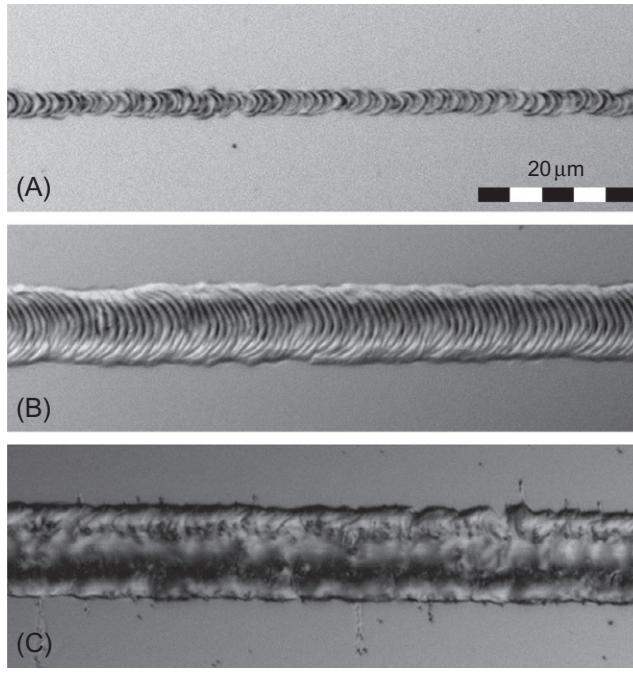


Fig. 18.13 Modification obtained at the back surface of Si wafer, when irradiated with 2 µm laser radiation at (A) $v = 1$ mm/s, $t_p = 7$ ns, $E_p = 194$ µJ, (B) $v = 1$ mm/s, $t_p = 100$ ns, $E_p = 194$ µJ, and (C) $v = 0.5$ mm/s, $t_p = 7$ ns, $E_p = 154$ µJ.

Herein, α is the total absorption coefficient, L_D is the carrier diffusion length, and L_T is the thermal diffusion length. The total absorption coefficient comprises the sum of various absorption contributions, for example resulting from the linear (single-photon), nonlinear (multiphoton), and free-carrier (intrinsic) absorption. For example, in order to increase the temperature of Si to the melting point, a total absorption coefficient on the order of $\alpha \sim 10^3 \ldots 10^4\,\mathrm{cm}^{-1}$ is needed. Considering multiphoton absorption, the major ionization mechanism in semiconductors irradiated at $\lambda = 2\,\mu\mathrm{m}$, and taking into account very small contributions from L_T and L_C (both being on the order of $<1\,\mu$m), the heating depth can be assumed to be the reciprocal of the multiphoton absorption coefficient, i.e., $L_H \approx \alpha_{MP}{}^{-1}$. Taking literature data for the two-photon absorption in Si, and three-photon absorption in GaAs at the wavelength 2 µm, the expected temperature rise originating from multiphoton absorption during a single pulse excitation process would be approx. 1 K. Therefore, it can be concluded that although the direct material heating contribution of the multiphoton absorption is small, it could potentially provide sufficient seed electron densities needed for avalanche ionization to engage.

The effect of nonlinear absorption was studied qualitatively using an open-aperture z-scan approach. Irradiation was performed using a $f = 25$ mm triplet lens, 100 ns pulses, and at a repetition rate of 10 kHz. Z-scan is a very powerful technique for the investigation of nonlinear optical properties of transparent materials. In this measurement approach, transmission through the wafer is measured as a function of the focal point position in the bulk, as well as of pulse energy. Experiments were performed in intrinsic 500-µm thick Si and 600-µm thick GaAs wafers (Fig. 18.14).

A transmission drop could be observed in both materials when the focused beam passed through the wafer. For Si, the transmission decrease was from 53.4% to approx. 41% at pulse energies $E_p \leq 25$ µJ, and the dependency of transmission change on the pulse energy was nonlinear. In contrast, the transmission level was nearly constant in GaAs, and decreased by only about 1%–2% as the focused beam passed through the wafer at pulse energies $E_p \leq 24.5$ µJ. At larger pulse energies, however, an abrupt decrease in transmission was detected in GaAs. Subsequent material analysis of irradiated areas showed that the material surface was damaged at these pulse energies.

Based on the experimental z-scan data, it can be concluded that two-photon absorption could play a significant role in the modification mechanism of Si. In case of GaAs, three-photon absorption was the only possible multiphoton absorption mechanism, which did not appear to contribute to the material modification significantly, however. Therefore, although multiphoton absorption is capable of providing seed electrons for subsequent avalanche ionization and therefore materials modification processes, possibly an alternative major absorption-enhancing mechanism must be assumed.

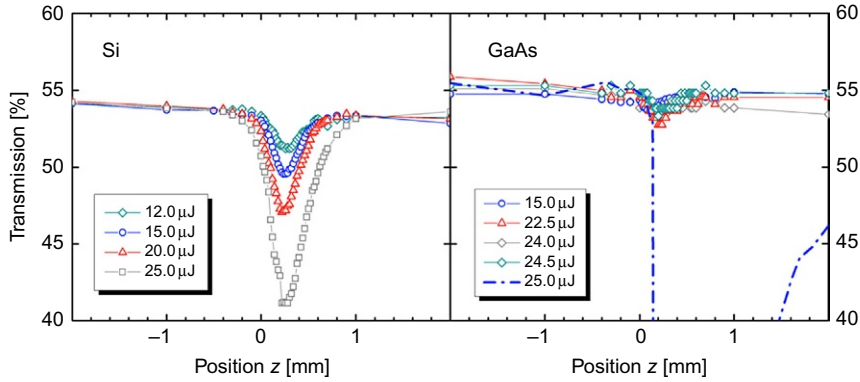


Fig. 18.14 Results of z-scan measurements in intrinsic Si and GaAs.

Iwata et al. [25] suggested a reasonable physical model for the alternative surface-enhanced absorption mechanism. According to this model, a very thin absorbing layer on the material surface can be assumed, which is not easily detectable by conventional techniques. Absorption enhancement could potentially result from micro- and nanoscopic surface imperfections caused either by sample preparation methods such as polishing, grinding, cutting, etc., or other structural and chemical irregularities, such as dangling bonds, native oxide layers, and lattice defects. Light can be more easily absorbed at such imperfections, and cumulative absorption phenomena will lead to greater material modification after each subsequent pulse. Results of experiments performed in this study confirm this model, as both isolated random microdamage zones were detected after single-pulse irradiation, and damage accumulation effects were observed.

In addition, it should be noted that many material properties of semiconductors are strongly dependent on the material temperature. Most important, the energy band gap of semiconductors decreases with the increasing temperature. According to the commonly used Varshni relation, the decrease in the energy band gap of GaAs would be significant, so that at a temperature of approx. 420°C the absorption regime would switch from three-photon to two-photon absorption.

18.4.2 Removal of Metal Coatings

The process knowledge of back surface modifications was successfully applied to space-selective removal of different metallization coatings from the back surface of Si wafers. Applications of this new experimental approach can have many benefits in the electronics industry, particularly because certain fabrication steps involving rotation and repositioning of wafers can be omitted while hybrid processes can be introduced. Precise control of energy deposition could result in the removal of the metal coating deposited by different approaches, while leaving the semiconductor substrate undamaged.

Four different material systems featuring multilayer metal coatings (ML 1–4) were utilized in the experiments (Table 18.3). The substrates used in ML 1 and ML 2 were intrinsic double-side polished Si wafers, and the substrates for ML 3 and ML 4 were 180-μm thick p-Si wafers featuring a random pyramid texture produced by wet etching. The base resistivity of p-doped Si was 4 Ω cm. The coatings were produced using sputter coating and plasma-enhanced vapor deposition (PECVD) techniques and commercial-grade equipment commonly used in the photovoltaics industry. In particular, coatings featuring material interfaces Ti/TiN and Ti/NiV are commonly used in many present-day and prospective PV module designs.

Table 18.3 Material composition of multilayer coated semiconductor samples

Notation	Substrate	Coating composition (bottom-top order)	Coating deposition method
ML 1	Intrinsic Si (1 mm)	Ni (100 nm)	Sputter coat
ML 2	Intrinsic Si (500 μm)	Ti (70 nm)	PECVD
ML 3	p-Si (180 μm)	SiO_2 (500 nm), TiN (100 nm), Ti (20 nm)	PECVD
ML 4	p-Si (180 μm)	SiO_2 (1500 nm), Ti (100 nm), NiV (200 nm), Ti (20 nm)	PECVD

It should be assumed that unlike in intrinsic Si substrates, an equilibrium charge carrier density could possibly influence linear absorption efficiency in p-doped Si. However previous research showed that the base resistivity levels are not significantly affected by dopant concentration. A series of experiments was performed to study the process of coating removal from the front surface. The goal of the experiments was to find out the minimum energy density resulting in coating removal, but to leave the substrate intact. Using the same $f = 7.5$ mm focusing optics as in back surface modification experiments, the effective accumulated laser fluence level needed to completely ablate the coating was found at $F_{thr} < 1.6\ J/cm^2$ for ML 3 and ML 4, and $F_{thr} < 1.2 J/cm^2$ for ML 1 and ML 2.

Surface resistance measurements were performed to quantify the coating removal efficiency using the four-terminal method with a Hewlett-Packard 3456A digital multimeter. Coatings were removed in a track along the full width of $10 \times 20\ mm^2$ substrates, and the resistance was measured between the two metallized areas remaining. For ML 3 and ML 4 the resistance was in the range $R = 76 \ldots 85\ k\Omega$, while for ML 1–2 the resistance was in excess of $R = 90\ k\Omega$. Fig. 18.15 shows examples of front surface metallization removal form substrates ML 3–4. The results reveal clearly defined modifications with the widths depending on irradiation conditions. The minimum modification width ranged from approx. 10 μm for ML 1–2 (flat surfaces) to approx. 15–20 μm for ML 3–4 (pyramid textured surfaces).

For coating removal form the back surfaces, focusing conditions and pulse energy levels were adjusted to account for light refraction in the wafers and Fresnel reflections from the surfaces. Examples of back surface coating processing are shown in Fig. 18.16. The results revealed less-consistent coating modifications, compared to the processing of front surfaces. At low laser fluences the processed areas still contained coating residues, especially at surface spots featuring large pyramid textures. With increasing laser fluence, the

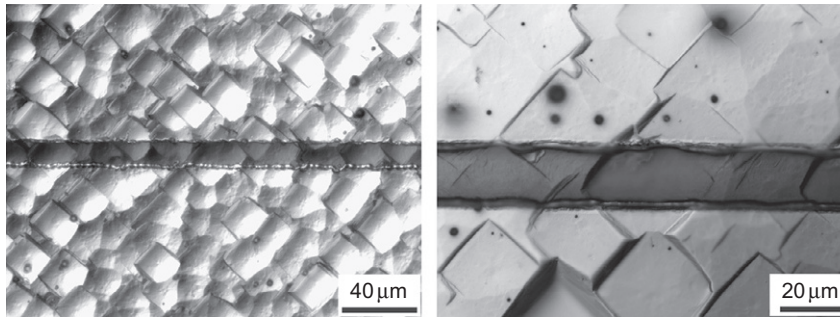


Fig. 18.15 Results of front surface removal of metallization layers at pulse energy $E_p < 8\,\mu J$. Left: Ti/NiV/Ti (ML 4), right: TiN/Ti (ML 3).

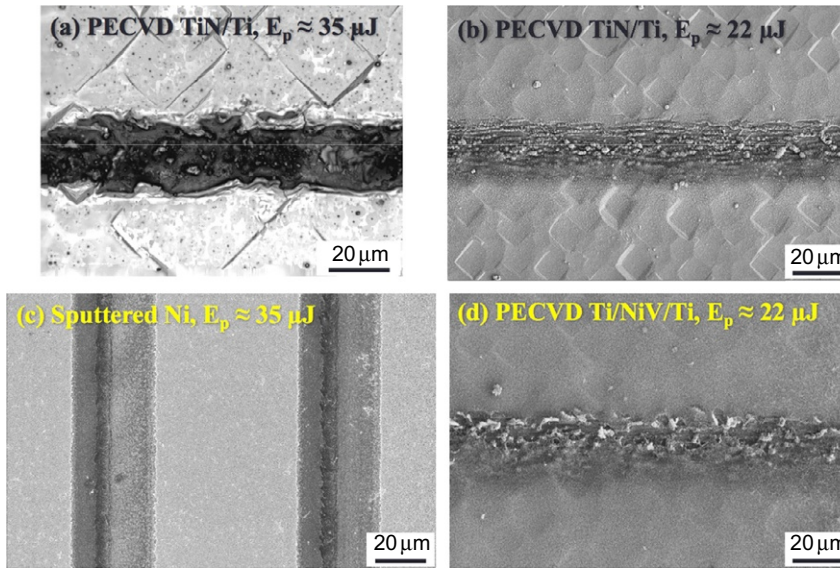


Fig. 18.16 Results of back surface removal of various metallization layers.

coatings were gradually removed. However, at even larger fluences substrate damage occurred before the coating could be completely removed.

Qualitative differences were observed for samples with different coating thicknesses. In ML 4, featuring coatings with the total thickness of 1.82 µm, consistent removal of the coating was not possible (Fig. 18.16D). In contrast, the processing of "simple" coatings in material systems ML 1–2 was consistent with well-defined modification boundaries.

The same experimental conditions were adopted to process large areas of coated back surfaces in multiple overlapping tracks (Fig. 18.17). The

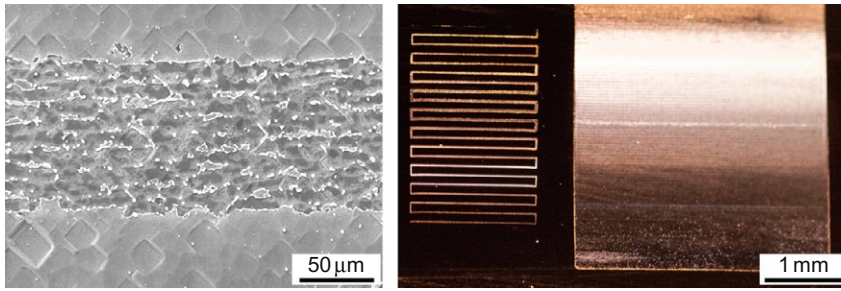


Fig. 18.17 Results of large-area removal of different metallization layers. Left: Sample ML 4 processed at $E_p \approx 32\,\mu J$. Right: Sample ML 2 processed at $E_p \approx 150\,\mu J$ and using a $f = 25\,mm$ triplet lens.

track overlap was varied to achieve coating removal with minimum residues left. Due to the pyramid textures present on substrates ML 3–4, a complete removal of metallization was not possible even at multiple irradiation along the same track or at high track overlaps of >90%. In contrast, large (multi-mm^2) areas of Ti-coating could be completely removed from the polished surfaces of ML 1–2 samples. Large area processing of ML 2 (Fig. 18.17, right) was performed using a $f = 25\,mm$ triplet lens in multiple tracks separated by 20 µm.

Resistance measurements between the laser-separated portions of metal coatings were performed using the four-terminal method to quantify the process efficiency and study the electrical properties of the ML 3 coating (Fig. 18.18, left). First, metal-coated substrates were precut to four samples

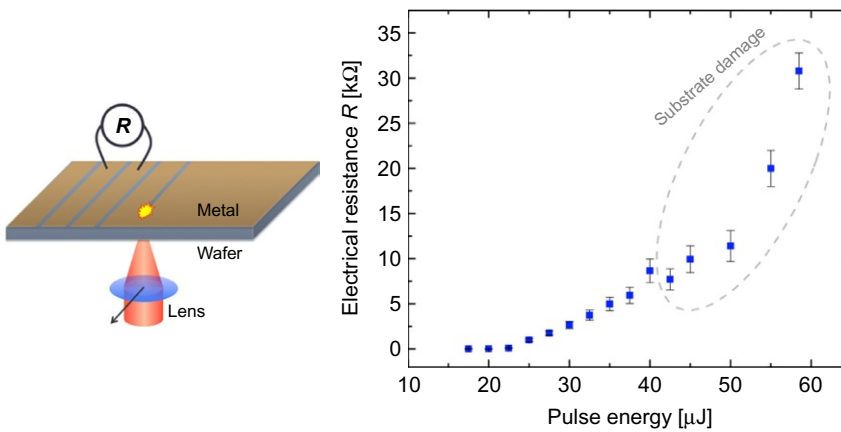


Fig. 18.18 Principle of electrical resistance measurement (left), and measurement results in dependency on the laser pulse energy (right).

with the dimensions $4 \times 25\,\text{mm}^2$. Then the coatings were irradiated using the back-surface modification method along the sample width in single tracks at translation speed $v = 1\,\text{mm/s}$, and under variations of pulse energy, leaving approx. 1 mm spacing between the tracks. Measurements were performed on four samples irradiated using the same process parameters, and resistance for each track was measured three times at different terminal positions.

The results of the measurements (Fig. 18.18, right) reveal that the resistance increased nearly linearly in the range of pulse energies $E_p \approx 22 \ldots 40\,\mu\text{J}$. However, at larger pulse energies, the measured values were inconsistent and the substrate appeared damaged. The largest value of electrical resistance obtained without inducing damage to the substrate was $R = 10\,\text{k}\Omega$, while values in excess of $R = 32\,\text{k}\Omega$ were obtained for partially damaged substrate.

In addition, resistance measurements were performed for a varying number of passes with approx. 25% overlap between the passes at constant pulse energy of $E_p = 28\,\mu\text{J}$ in ML3 samples. The results are summarized in Table 18.4.

Back surface processing of semiconductors could be potentially useful to a number of other applications in the electronics industry. Besides coating removal, or layer separation in general, space-selective modification of thin polycrystalline Si films buried under multimaterial semiconductor layers could be accomplished, as shown in previous research on laser-based resistance fine-tuning [26]. New material phases such as highly spatially confined Si/SiO_2 interfaces could be easily produced in 3D patterns [27]. Laser processing of multilayer systems could result in thickness-selective joining of different layers [28] and localized doping of semiconductors [29].

18.5 SUMMARY

Fundamentals and applications of infrared laser light to the processing of semiconductor wafers were presented. In particular, advancing laser direct machining methodologies utilizing nanosecond and femtosecond infrared laser pulses was the subject of intense research. For both of

Table 18.4 Electrical resistance of laser-processed coatings in dependence on the number of passes

Number of passes	1	2	4	12	50
Resistance [kΩ]	3.5	4.2	5.6	12.5	52.8

these laser-matter interaction regimes, predominant light absorption and energy transfer mechanisms were reviewed and modification thresholds were determined.

The feasibility of semiconductor bulk modification using the conventional direct machining approach similar to the processing of dielectrics was investigated. The surface modification thresholds for femtosecond laser-matter interaction were found to be independent of the excitation wavelength and therefore not significantly affected by multiphoton absorption processes. In addition, the dopant concentration of the irradiated samples could not conclusively be correlated to the modification threshold in experiments. A numerical model of the propagation and absorption process of ultrashort laser pulses was developed and revealed that a dependence of the modification threshold on the dopant concentration is unlikely. Furthermore, the results suggest that avalanche ionization may be the dominant absorption mechanism during femtosecond irradiation of semiconductors. Following the rapid rise in electron density in the vicinity of the surface, the incident optical energy is being reflected off the electron cloud, and therefore prohibited from propagation in bulk.

Applications of femtosecond laser pulses at various infrared wavelengths were studied by inducing periodic surface structures on surfaces of Si and GaAs. The reproducible generation of three types of LIPSS was studied as a function of energy dosage or accumulated energy. These structures include ripples with high and low spatial frequency (HSFL and LSFL, respectively) that are oriented perpendicular to the incident electric field. At very low laser fluences, surface ripple structures that are parallel to the polarization were detected and characterized.

A new processing regime of semiconductor wafers was studied by utilizing nanosecond pulsed laser radiation at the wavelength 2 μm. A self-built Tm-fiber laser system was adopted in experiments. Absorption of laser light was studied using the z-scan approach and analytical model approximations. Nonlinear material response was detected in Si, however, and possible contributions of different absorption mechanisms were estimated. It was found that although two-photon absorption is present for nanosecond laser-semiconductor interaction at the wavelength 2 μm, this absorption mechanism alone is not capable of inducing materials modifications. Secondary nonlinear processes like avalanche ionization require seed charge carriers to engage.

The transparency of Si and GaAs at 2 μm was utilized to study modification processes at the back surfaces of wafers. Modification thresholds were

determined, and the modification morphology was studied. In addition, the removal of different metallization layers from the back surface of Si wafers was studied. The removal efficiency was investigated by performing resistance measurements between the separated metal areas.

Continued research is necessary to fully understand the scope of laser-induced phenomena occurring during femtosecond and nanosecond laser irradiation of semiconductor materials. The results presented in this chapter present a good basis for further investigations.

REFERENCES

[1] T. Ohba, et al., Thinned wafer multi-stack 3DI technology, Microelectron. Eng. 87 (3) (2010) 485–490.
[2] C. Dunsky, Laser material processing in microelectronics manufacturing: status and near-term opportunities, Proc. SPIE 5713 (2005) 200.
[3] T. Saga, Advances in crystalline silicon solar cell technology for industrial mass production, NPG Asia Mater. 2 (3) (2010) 96–102.
[4] A. Goodrich, et al., A wafer-based monocrystalline silicon photovoltaics road map: utilizing known technology improvement opportunities for further reductions in manufacturing costs, Sol. Energy Mater. Sol. Cells 114 (2013) 110–135.
[5] J.M. Bovatsek, R.S. Patel, Highest-speed dicing of thin silicon wafers with nanosecond-pulse 355 nm q-switched laser source using line-focus fluence optimization technique, in: SPIE LASE, International Society for Optics and Photonics, 2010.
[6] K.F. Tamrin, Y. Nukman, S.S. Zakariyah, Laser lap joining of dissimilar materials: a review of factors affecting joint strength, Mater. Manuf. Process. 28 (8) (2013) 857–871.
[7] K.-W. Lee, et al., Three-dimensional hybrid integration technology of CMOS, MEMS, and photonics circuits for optoelectronic heterogeneous integrated systems, IEEE Trans. Electron Devices 58 (3) (2011) 748–757.
[8] R. Osellame, G. Cerullo, R. Ramponi (Eds.), Femtosecond Laser Micromachining: Photonic and Microfluidic Devices in Transparent Materials, vol. 123, Springer, Berlin, Heidelberg, 2012.
[9] P. Schaaf (Ed.), Laser Processing of Materials: Fundamentals, Applications and Developments, vol. 139, Springer, Berlin, Heidelberg, 2010.
[10] K. Venkatakrishnan, et al., Laser writing techniques for photomask fabrication using a femtosecond laser, Appl. Phys. A 74 (4) (2002) 493–496.
[11] V.R. Marinov, et al., Laser-assisted ultrathin die packaging: insights from a process study, Microelectron. Eng. 101 (2013) 23–30.
[12] D.E. Carlson, Laser processing of solar cells, in: Proc. SPIE Solar Energy + Technology, International Society for Optics and Photonics, 2012, pp. 847302–847302.
[13] V. Marinov, et al., Laser-enabled advanced packaging of ultrathin bare dice in flexible substrates, IEEE Trans. Compon. Packag. Manuf. Technol. 2 (4) (2012) 569–577.
[14] J.H. Lau, et al., Advanced MEMS Packaging, McGraw-Hill, New York, NY, 2010.
[15] J. Chen, Z. Wu, Laser cutting of ultra-thin glasses based on a nonlinear laser interaction effect, Proc. SPIE 8786 (2013) 87860E.
[16] D.W. Bäuerle, Laser Processing and Chemistry, Springer, Berlin, Heidelberg, 2013.
[17] P. Kadwani, et al., Q-switched thulium-doped photonic crystal fiber laser, Opt. Lett. 37 (10) (2012) 1664–1666.
[18] C. Gaida, et al., Amplification of nanosecond pulses to megawatt peak power levels in Tm^{3+}-doped photonic crystal fiber rod, Opt. Lett. 38 (5) (2013) 691–693.

[19] I. Mingareev, et al., Welding of polymers using a 2 μm thulium fiber laser, Opt. Laser Technol. 44 (7) (2012) 2095–2099.
[20] M. Kumagai, et al., Advanced dicing technology for semiconductor wafer-stealth dicing, in: IEEE International Symposium on Semiconductor Manufacturing, 2006. ISSM 2006. IEEE, 2006.
[21] R. Weber, et al., Heat accumulation during pulsed laser materials processing, Opt. Express 22 (9) (2014) 11312–11324.
[22] J.M. Liu, Simple technique for measurements of pulsed Gaussian-beam spot sizes, Opt. Lett. 7 (5) (1982) 196–198.
[23] J.F. Young, J.S. Preston, H.M. van Driel, J.E. Sipe, Laser-induced periodic surface structure. II. Experiments on Ge, Si, Al, and brass, Phys. Rev. B 27 (2) (1983) 1155.
[24] J.E. Sipe, J.F. Young, J.S. Preston, H.M. van Driel, Laser-induced periodic surface structure. I. Theory, Phys. Rev. B 27 (1983) 1141.
[25] H. Iwata, K. Asakawa, Accumulative damage of GaAs and InP surfaces induced by multiple-laser-pulse irradiation, Jpn. J. Appl. Phys. 47 (4) (2008) 2161–2167.
[26] E. Boulais, J. Fantoni, A. Chateauneuf, Y. Savaria, M. Meunier, Laser-induced resistance fine tuning of integrated polysilicon thin film resistors, IEEE Trans. Electron Devices 58 (2) (2011) 572–575.
[27] L. Rapp, B. Haberl, J.E. Bradby, E.G. Gamaly, J.S. Williams, A.V. Rode, Confined micro-explosion induced by ultrashort laser pulse at SiO_2/Si interface, Appl. Phys. A 114 (2014) 33–43.
[28] Z. Xu, K.H. Leong, P.G. Sanders, Laser surface alloying of silicon into aluminum casting alloys, J. Laser Appl. 12 (4) (2000) 160–170.
[29] M. Meseth, B.C. Kunert, L. Bitzer, F. Kunze, S. Meyer, F. Kiefer, M. Dehnen, H. Orthner, N. Petermann, M. Kummer, H. Wiggers, N.-P. Harder, N. Benson, R. Schmechel, Excimer laser doping using highly doped silicon nanoparticles, Phys. Status Solidi A 210 (11) (2013) 2456–2462.

CHAPTER 19

Laser Processing of Direct-Write Nano-Sized Materials

J. Lawrence*, O.F. Swenson†, V. Marinov†
*University of Chester, Chester, United Kingdom
†North Dakota State University, Fargo, ND, United States

19.1 INTRODUCTION

Printed electronics is a branch of electronics manufacturing and electronics material science that develops and applies organic and inorganic materials to create discrete components, systems, or entire devices by means of sequential and/or parallel material additive technologies such as screen printing, inkjet printing, or direct writing. In its "pure" form, a printed electronics device is realized by fabricating conductive traces as well as all required passive and active electronic components directly on the (usually) organic, flexible substrate. Today this is only possible for very simple electronic designs. Typically, a hybrid technology approach is employed in which most of the discrete electronic components are attached to the printed conductive traces on the flexible substrate using conventional packaging methods such as surface mount technology.

One of the pillars in the printed electronics technology is the capability of creating material structures with defined chemistry, geometry, and properties on the organic substrate. For most printed materials this is a two-step process that involves material deposition followed by an appropriate postdeposition treatment. The latter is the subject matter of this chapter. In Section 19.2, a brief overview of different parallel and sequential additive methods for creating patterned structures on organic substrates is presented. Emphasis is given to direct-write technologies and the need for laser sintering of the direct-write materials is established. The second part of this section deals with the synthesis and structure of typical direct-write materials, such as the nano-sized conductive inks. Section 19.3 discusses the fundamentals of the sintering process for nano-sized powders. A distinction is made between sintering processes for dry nanopowders and for nano-sized conductive inks. A two-phase sintering mechanism is suggested to explain

Advances in Laser Materials Processing
https://doi.org/10.1016/B978-0-08-101252-9.00019-4
Copyright © 2018 Elsevier Ltd.
All rights reserved.

some specifics of nano-sized ink sintering. Section 19.4 includes the results of laser sintering experiments. The results of successful laser sintering of silver nano-sized inks deposited with the maskless mesoscale material deposition (M^3D) direct-write technology are presented. The real-time dynamics of material properties during laser sintering are discussed. The property changes as a function of laser energy deposited per unit material volume are analyzed. The final sections offer some thoughts on future trends and applications of laser sintering in the area of microelectronics as well as a brief commentary on key books in the area.

19.2 DIRECT-WRITE DEPOSITION OF NANO-SIZED MATERIALS

19.2.1 Direct-Write Material Deposition Technology

Two different material additive techniques are commonly used to create patterned conductive traces on flexible substrates: parallel methods such as screen and stencil printing, microstamping, soft lithography, etc.; and sequential methods such as direct writing and inkjet printing. Screen and stencil printing are well established and inexpensive technologies for resolutions above 80–100 μm. Most of the features of a typical printed electronic device fall in the mesoscale range, such as between 1 and 100 μm. Using screen or stencil printing here is not feasible or cost-effective, whereas the thin-film, metallization/lithography-patterning techniques, applied in the nanoscale range, are prohibitively expensive. The so-called direct-write methods were designed to provide an inexpensive material deposition solution for the mesoscale range. The term "direct-write" describes a family of additive fabrication methods to create materials with controlled architecture and composition onto substrates in a sequential manner by moving the material deposition system or the substrate along a predefined path.

Direct-write methods offer broad and extremely important new capabilities, particularly in microelectronics and MEMS fabrication and packaging. Direct-write techniques enable the fabrication of a wide range of mesoscale components, from a variety of microelectronic components (interconnects with resistivity close to two times that of bulk silver, phosphor arrays for displays, coplanar resistors, capacitors, antennas, and yttrium iron garnet core inductors) [1], to semiconductors [2], power sources (microbatteries [3], fuel cells, solar cells [4]), sensor systems [5], and even various three-dimensional shapes [6]. Direct-write methods are particularly interesting for devices using a variety of different materials such as oxides, polymers, and metals

typically seen in electronics. Although direct-write methods were originally developed for electronics, recently direct-writing has been applied to a variety of other structures including optical waveguides with novel shapes such as unique curves and bends [7], and bioactive ceramic nanocomposites [8].

There are many different ways to direct-write or transfer patterned materials onto various types of substrates. A modified inkjet printing technology has been investigated at a fairly large scale for its suitability as a direct-write technique for electronics manufacturing [9]. M^3D uses atomization and aerodynamic focusing to deposit materials onto a substrate. The nano-sized ink is atomized into droplets of about 1 pm in diameter. The droplets enter a nitrogen gas stream and are transported to the deposition head where, after aerodynamic focusing, they are deposited onto the substrate. The process is noncontact, which allows deposition over curved surfaces and steps. This process is capable of writing features as small as 10 μm [10,11]. M^3D operates in two configurations depending on the type of atomizer, meaning pneumatic or ultrasonic. In the pneumatic configuration, a high-velocity gas stream shears a liquid into droplets. The same stream draws ink from a reservoir by means of the Bernoulli principle. The droplets are brought to the deposition head where the stream is focused prior to deposition by the sheath gas. In this configuration, the system can work with denser inks with viscosities of up to 1000 cP and particulate sizes of less than 0.5 μm. In the ultrasonic configuration, a piezoelectric transducer produces high-frequency pressure waves within the material that causes droplets to be ejected from the surface. In this configuration, the system works with low viscosity inks up to 30 cP and particle sizes of less than 50 nm. In matrix-assisted pulsed laser evaporation direct-write (MAPLE-DW) [3], the starting material is preprocessed prior to deposition. A thin layer of the material to be deposited, usually in a powder form, is bonded to a transparent backing creating the so-called ribbon. The material is then deposited from the ribbon to the substrate by a pulsed laser. The ribbon is fed continuously under the laser beam and the substrate is translated in the x–y plane in order to achieve the desired pattern. The laser pulses are overlapped in order to produce a continuous line. Resolution is mainly dependent on the size of the laser spot on the ribbon. The thickness of the deposition depends on the thickness of the material previously applied to the ribbon. Lines as narrow as 8 μm have been produced [12]. In the syringe-based nScrypt direct-write process [13], material is placed on a surface in a highly controlled manner. nScrypt systems use the patented Smart Pump technology allowing the dispensing of inks and pastes with viscosities in the range of 1 to 1 million

centipoises. A servo-controlled positive pressure pump with a precision of 0.1 psi (689 Pa) allows the writing of lines as small as 50 pm while offering dynamic dispense control, that is changing of the deposition parameters as material properties vary. Negative pressure is applied during valve closing in order to suck the material back inside the tip, allowing for clean stops and starts [14]. The dip-pen nanolithography [15] is based upon the transport of the deposited material from the tip of a conventional atomic force microscope to the surface of interest. Laser guidance of particles in hollow optical fibers uses radiation pressure of laser light focused in a hollow fiber to expel nanometer-sized particles through the fiber onto the substrate [16]. Another direct-write technology is direct-write thermal spraying developed by SUNY in Stony Brook's Center for Thermal Spray Research (CTSR). More details about these and other direct-write methods are available in Piqué and Chrisey [1].

A number of direct-write technologies such as inkjet printing and M^3D use nano-sized inks. Depositing the nano-sized material is just the first step in the process. To achieve their optimal properties these materials need to be heat-treated, or sintered. Sintering is a process in which the closely compacted particles (metallic or nonmetallic) are joined together without melting them in order to form a solid body. Sintering is a thermally activated process. Heat can be delivered in different ways; the most common method is heating the entire substrate with the deposited material in an oven. Unfortunately, the conventional oven sintering in many cases is incompatible with temperature-sensitive organic materials used in the flexible substrates. This is an area in which laser-assisted sintering can be a better option.

The method of sintering affects the material properties, often considerably, as illustrated by the following example [17]. Silver ink was deposited onto a PMMA substrate by means of the M^3D direct-write process, then heat-treated at 80°C to remove the solvents and other volatiles. Then the material was either oven-sintered at 120°C or scanned in situ with an Nd:YAG continuous wave laser with 50 mW laser power at 1 mm/s scanning speed. The measured bulk resistivity of the oven-sintered material was about 1.6 mΩ cm (1000 × bulk Ag) compared to the 16 μΩ cm (or 10 × bulk Ag) achieved in the laser-sintering process. The reason for this dramatic difference is, as the authors suggested, that the laser process, if properly controlled, can deliver significant heat in a very restricted in-depth area without damaging the underlying substrate material. Numerical modeling predicts that the surface temperature can reach more than 300°C on the surface

when the temperature just several tens of micrometers below is slightly higher than room temperature [11]. This allows for much higher sintering temperatures on the surface than those possible in the conventional oven processing, which eventually translates into better material properties.

19.2.2 Nano-Sized Printing Inks

Metallic nano-sized inks used in realizing conductive traces in printed electronics are colloidal systems, consisting of 2–100 nm nanoparticles encapsulated in a thin polymeric coating and dispersed in a liquid dispersion medium, usually a cosolvent system. Due to their high conductivity and thermal stability, gold and silver nanoparticles are the typical materials used in conductive printing inks [18]. A brief summary of the composition and material properties of some nano-sized conductive inks is available in [18].

During the synthesis of nano-sized inks, the nanoparticles have to be disagglomerated, suspended and remain in suspension, and achieve a practical concentration (about 50%–60% by weight). The synthesis is complicated by the fact that many direct-write processes need relatively low viscosities, usually less than 100 cP, and many of the nanoparticle materials to be dispersed have high specific gravity compared with the organic dispersion medium [19]. As with most colloids, stabilization is required to prevent dispersed phase (metal nanoparticles) from aggregating. Colloidal methods are used to break apart weakly bonded agglomerates, homogeneously disperse nanoparticles, and store the nano-sized inks without mass segregation. The potential usefulness of colloidal methods in developing reliable processing methods for advanced colloidal systems such as nano-sized printing materials cannot be overemphasized [20]. A number of basic interactions can be used to alter interparticle forces in the colloidal system. These include attractive Van der Waals forces, repulsive electrostatic forces, solvation (i.e., short range hydration or hydrophobic) forces and steric forces, in addition to attractive capillary (Laplace) forces [21]. The solvation and steric forces can be attractive or repulsive in nature. With the steric approach, for example, bifunctional macromolecules attach themselves to the particles. The macromolecular additives are usually completely soluble in the dispersing medium, but are designed with certain functional groups to bind them to the particles. The particles then repel one another once their separation distance is less than the radius of gyration of the macromolecule [22]. Virtually all nanoparticles need these surface dispersant coatings that permit dispersion in liquids and prevent oxidation or self-sintering. Uncoated silver will sinter to itself at room temperature, and uncoated copper will quickly

turn black. Uncoated aluminum and many other metals are pyrophoric. By varying the hydrophobic/hydrophilic nature of the surface coating, it is possible to encourage the material to disperse in a similar medium or to preferentially congregate on a second phase or at the substrate surface [19].

19.3 BACKGROUND OF NANO-SIZED MATERIALS SINTERING

19.3.1 Sintering of Dry Nanoparticle Materials

The sintering mechanism in the case of compacted dry metal powders is very well studied and widely published. Traditional sintering theories are based on the kinetics of mass transport motivated by differential surface curvature as described by the Gibbs-Kelvin model [20]. In general, the sintering mechanism involves two phenomena. The early densification stages are characterized by formation of necks between the solid particles brought in intimate contact during the compaction step. This is followed by a neck and grain growth and, as a result, reduction of the voids with a net result forming a solid with a low porosity and material properties close to those of the bulk material.

Compared to conventional, micrometer-sized particles, the sintering of nanoparticle compacted materials has its own specifics. Micromechanistic models for conventional powder densification are not applicable to nanocrystalline systems [23]. It is largely accepted in the research community that it may not be possible to explain the densification mechanism of compacted dry nanopowders with a single and all-inclusive model. Different mechanisms have been proposed to explain the densification and the change in material properties during different stages of sintering [24] but the common sintering models attribute a predominant mass transport path to a specific sintering stage [25]. One major difference is related to the sintering temperature. The onset of sintering is consistently reported to be significantly lower in nanoparticle materials compared to conventional materials [26]. For particles under 100 nm, Alymov et al. [26] developed an empirical relationship for the dependence of the sintering onset temperature, T_s, on the mean particle size, d:

$$\mathrm{Ln}\, T_s \propto 1/d \tag{19.1}$$

The ratio of sintering onset to melting temperature, which they calculated, is in good agreement with experimental data. Based on the nanocalorimetry studies of thin indium films, a simple expression was developed to relate melting point to nanoparticle size [27]:

$$T_m(r)156.6 - \left(\frac{220}{r}\right) \tag{19.2}$$

where $T_m(r)$ is the melting temperature in °C and r is the radius of the particle in nm. This equation reveals that significant melting point suppression happens when the nanoparticle radius approaches the sub-20 nm range. Similar results for other materials were reported by other researchers [28–30].

In more practical terms, there is one undisputed fact known to everyone working in this area: for a given material composition, the results of the sintering process strongly depend on the sintering temperature and sintering time. Also, when pressure is added to the sintering process of nanoparticle materials, densification improves considerably compared to conventional sintering [31]. The importance of these three parameters in the process of nanoparticle densification has been rigorously studied and modeled by Suryanarayanan and Sastry [32]. In the next section it will be shown that the behavior of nano-sized inks in sintering, especially the relationship between the three major process parameters and material properties, is quite different from dry nanopowders.

19.3.2 Sintering of Nano-Sized Inks

As discussed before, the direct-write process deposits nano-sized ink onto a substrate to create the required pattern. The composition of the as-deposited ink differs from that of the starting material. Most of the volatiles are removed during the deposition process or after the material has been deposited on the substrate, especially if the substrate has been routinely preheated. In most cases, the as-deposited ink can be considered a semi to almost completely dry substance with much higher metal content compared to the starting material. In our laboratory the nano-sized ink is routinely deposited on a polymer substrate heated to 75°C. The material spends some time on the heated platen until the entire pattern has been printed, then is removed from the deposition station and left at room temperature for a certain time before sintering. The same time/temperature profile was simulated in the thermogravimetric analysis (TGA) apparatus. The results shown in Fig. 19.1 indicate that most volatiles were removed from the deposited material by the time the material was transferred to the sintering equipment.

It is highly unlikely that all volatiles will be removed from the material during the presintering processing stages. Therefore, sintering should not be considered as a solid-state phenomenon; a gaseous phase may form in the

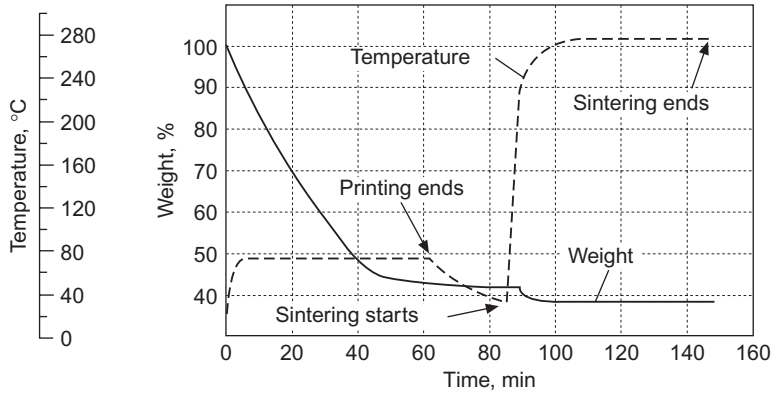


Fig. 19.1 TGA graph of unsintered nano-sized ink.

material as the remains of the solvents or absorbed moisture are removed or as organics undergo burnout. There is a good chance that this will happen in the very beginning of the sintering process as evident by the drop of the weight in Fig. 19.1 in the beginning of the sintering process at temperatures well below the maximum sintering temperature.

A series of simple experiments was performed to study the effect of sintering temperature, time, and pressure on the material properties of nano-sized inks. Lines of nano-sized silver ink printed on polyimide substrate were isostatically sintered in an oil bath within a heated compression chamber. The compression chamber was placed in a hot press preset to 220°C and subjected to various pressures up to 3200 psi (22 MPa). The electrical resistance of the sintered conductors was measured and used to evaluate the sintering results. The experimental data shown in Fig. 19.2

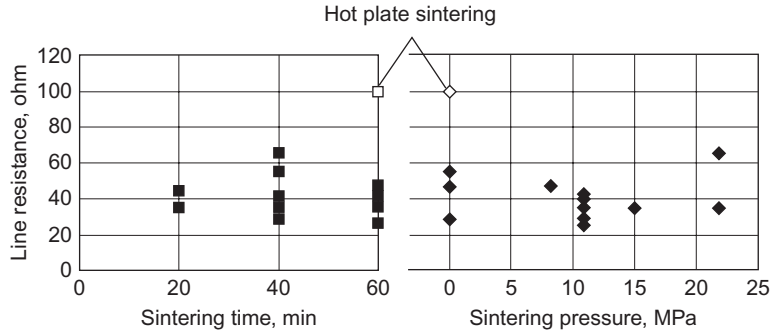


Fig. 19.2 Results from isostatic sintering experiments. A total of 36 samples of nano-sized silver ink were sintered at 220°C. The conductor lines were 16 mm long, 56 µm wide and 0.6 µm thick.

indicated that isostatic sintering provided better results than the conventional hot plate sintering, which is believed to be due to the more evenly and efficiently applied heat in sintering.

Perhaps the most surprising result from these experiments was that no obvious relationship was evident between the electrical resistance of sintered lines and the sintering time and sintering pressure. Later it will be shown that the effect of sintering temperature was also different from what one should expect. In the case of nano-sized silver ink, Sears et al. [33] reported that using only temperature as a variable in the process, solid-state sintering shows a linear relationship between temperature and porosity (volume fraction) within the normal sintering temperature range. If an inverse relationship is assumed between the sintered material density and electrical resistance, then it should be expected that the electrical resistance of sintered material will decrease gradually with the increase of sintering temperature, something that has been proven experimentally [34]. Such a gradual change in the electrical resistance was not evident in sintering nano-sized conductive inks. Instead, it has been observed that the resistance drops abruptly when a certain "threshold" value of the sintering temperature has been reached.

These observations are quite different from similar results for dry nanopowders. It will be difficult to interpret them with the theoretical developments applied to the process of sintering of dry nanopowders. A different mechanism is therefore required to explain the stages in sintering of nano-sized materials consisting of nanoparticles with protective coating.

A two-phase sintering mechanism is suggested (Fig. 19.3). Phase I is a very fast process characterized with thermal degradation of the dispersant coating surrounding the nanoparticles. At temperatures lower than the

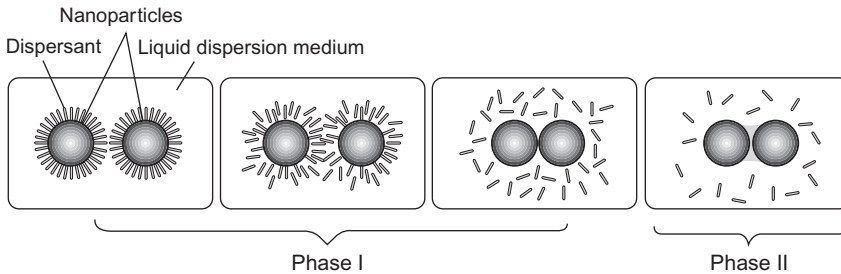


Fig. 19.3 Phases in sintering process of nano-sized particles dispersed in liquid. *(Adapted from Harima Co., NanoPaste: Programmable material for lead-edge circuit & connection (PowerPoint presentation), 2004.)*

temperature of thermal degradation the conductivity is very low. Even if the metal particles are closely packed (at this stage the material is almost dry), the coating serves as an insulator (Fig. 19.3A). Once the critical temperature is reached, the fast thermal degradation of the coating (Fig. 19.3B) results in a spontaneous aggregation of metal nanoparticles (Fig. 19.3C), accompanied by a dramatic and abrupt change in the electrical conductivity.

Phase II is a relatively slower material densification process. Since now the material consists mostly of aggregated dry metal nanoparticles, sintering should follow the densification mechanisms typical for conventional nanoparticle materials. The longer sintering times at this stage lead to partial coalescence of the nanoparticles with a corresponding gradual growth of particle aggregates (Fig. 19.3D), reduction in porosity, and increase in the electrical conductivity.

Additional experimental results and discussion will be presented in the next section to support the proposed sintering mechanisms. Very similar results were also reported by Allen et al. [35] who sintered silver nanoparticle inkjet-printed ink by using resistance heating. They demonstrated that the transition from a very low conductive to a highly conductive state occurred almost instantaneously, within two microseconds, after which the conductivity gradually increases. Their results are further discussed in the next section.

19.4 LASER SINTERING OF DIRECT-WRITE NANO-SIZED MATERIALS

19.4.1 Experimental Configuration

A continuous wave Nd:YAG (1064 nm) laser was used to irradiate silver nanoparticle ink deposited on polyimide substrates using M^3D. Dynamic in situ monitoring of the electrical resistance along 0.1 mm long lines was used to identify the laser energy required to initiate a resistance drop as well as that required to complete the transition. Direct-write lines on polyimide were also sintered by scanning the same laser along deposited lines.

For the dynamic resistance measurements, approximately 500 μm wide parallel electrodes were direct-write printed using the M^3D process on a polyimide substrate with less than a 100 μm gap between the electrodes. The electrodes were oven-sintered at 220°C for 60 min to make them conductive. The polyimide substrates were mounted on clean glass slides to maintain rigidity and an SMA coaxial RF cable connector jack was connected on the edge of the slide to the electrodes using silver-filled epoxy. A schematic

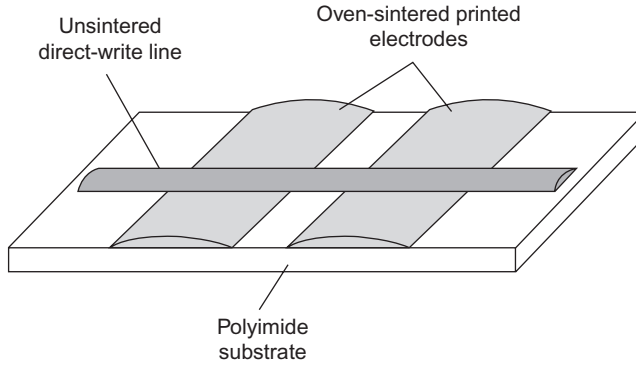


Fig. 19.4 Schematic of the substrate with oven-sintered direct-write electrodes and an unsintered line.

of the substrate is shown in Fig. 19.4. The unsintered line was direct-write deposited across the polyimide gap defined by the electrodes. The deposited nanoparticle inks, manufactured by Nano Size Ltd. (Migdal Ha'Emek, Israel), consisted of silver nanoparticles with an average size of 50 nm suspended in a mixture of solvents and up to 3 wt% dispersants. The direct-write printed electrodes had a gradual slope (about 6 degrees) at the gap.

For the laser scanning experiments, bulk resistivity measurements were made on direct-write lines deposited between one square millimeter screen-printed silver pads on polyimide. Fig. 19.5 shows a schematic of the screen-printed pads and direct-write lines deposited on a 125 μm thick polyimide (Kapton HN) substrate. The distance between pads was approximately 2.4 mm with an average pad thickness of 12 μm. Each experimental

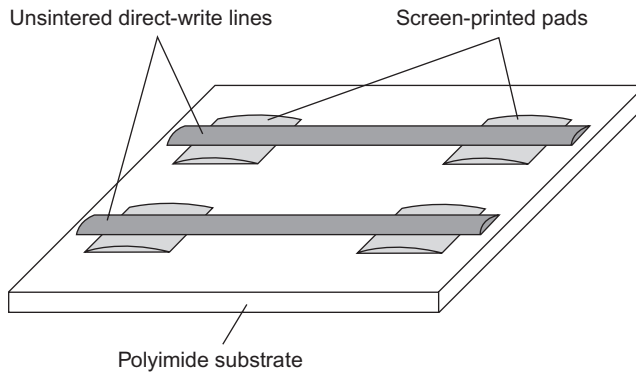


Fig. 19.5 Schematic diagram of the deposited line and screen-printed pads.

batch was designed by randomizing preset laser sintering parameters on the 60 lines residing on a single slide. For the first batch, the average sintered line-width was 58.1 μm with an average thickness of 0.64 μm. For the second batch it was 30.7 and 0.91 μm.

For the first batch, 150, 200, and 250 mW laser beams were scanned at 5 mm/s while 300, 400, and 500 mW laser beams were scanned at 10 mm/s to study the effects of scanning speed with a constant deposited laser energy per unit length. In the second batch, the scanning speed was kept at a constant 5 mm/s while the power level was varied among 125, 150, 175, 250, 500, and 750 mW. Ten randomized replications of each experimental setting were made.

A Quantronix Eagle 1064-nm CW Nd:YAG laser was used for sintering as depicted in Fig. 19.6. The output was polarized with a thin-film plate polarizer in order to attenuate the power using a half-wave plate followed by a second polarizer. A UNIBLITZ VS25 mechanical shutter was used to initiate the sintering process for dynamic resistance measurements and was placed before the Quantronix Qmark scanning head. The beam was stationary for the in situ measurements and was scanned along the sample for the scanned sintering measurements. The focused beam has a nearly Gaussian profile with a waist radius, determined at the $1/e$ intensity point, of 43 μm.

For the dynamic resistance measurements, a stationary sample was irradiated by the focused 0.5, 1.0, or 1.5W laser beam by opening the mechanical shutter for 100 ms. The power level on the sample increased as the shutter opened, a little less than 4 ms. The power output was constant after the shutter was completely opened until closing at 100 ms. The power level on the sample during the shutter opening was determined empirically by

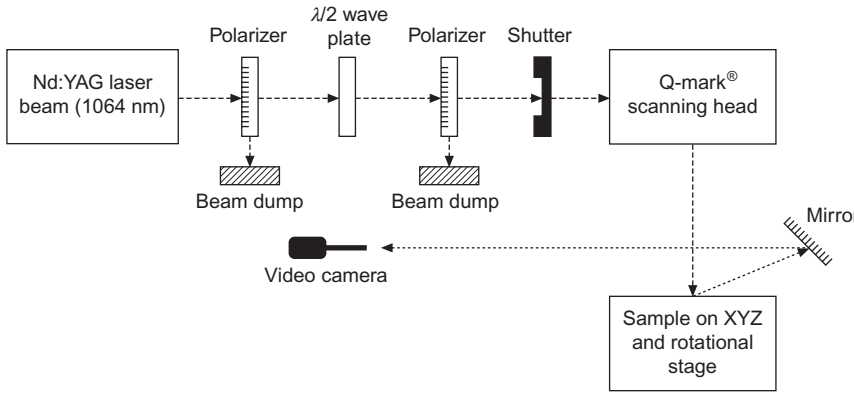


Fig. 19.6 Schematic diagram of the laser sintering system.

measuring the light scattered from a Spectralon cube placed at the sample position at the three power levels, 0.5, 1.0, and 1.5W. Each power level was replicated five times and averaged to determine the relative power level as a function of time.

Since the beam waist diameter (86 μm) was larger than the deposited line width, the power deposited on the line was calculated by integrating the area exposed. The correction term used was

$$P_{\text{line}}(a,b) = P_{\text{incident}} \times \text{erf}\left(\frac{a}{2w_o}\right) \times \text{erf}\left(\frac{b}{2w_o}\right) \tag{19.3}$$

where $P_{\text{line}}(a, b)$ was the power deposited within the line length a and line width b, P_{incident} is the incident power level, and w_o is the beam waist radius [36].

The resistances were measured using a Keithley 2010 multimeter and a four-channel Tektronix TDS-3034B oscilloscope as depicted in Fig. 19.7. A constant 100 μA current through the sample and parallel oscilloscope input was supplied from the multimeter. The 1-ms resolution oscilloscope data were used to calculate the in situ resistance while the multimeter data (slower) were used to validate the oscilloscope results.

For the laser scanning measurements, the dc resistances of the scanned lines were measured between the screen printed pads using the Keithley 2010 low-noise digital multimeter and the cross-sectional areas and lengths were measured to determine the bulk resistivities. Sintering on a hot plate was performed alongside one of the laser scanning batches as a point of reference for the bulk resistivity.

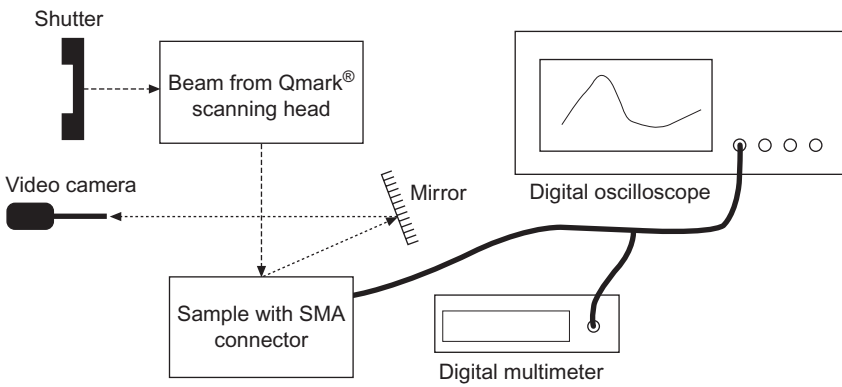


Fig. 19.7 Schematic of the in situ bulk resistivity measurement setup.

19.4.2 Experimental Results

Representative oscilloscope waveforms showing the bulk resistivity change with time along with the relative power on the sample during the shutter opening are shown in Fig. 19.8.

In Fig. 19.8, point (A) indicates the shutter opening and point (B) indicates the start of the resistivity drop calculated from the bulk-resistivity plot. The energy deposited from point (A) to point (B) is the energy required to initiate the resistivity transition. Point (C) indicates the end of the transition calculated from the bulk-resistivity data. The energy required from the shutter opening to this point was used to find the total energy needed to complete the resistivity transition. Point (D) marks the time when the shutter is completely open as calculated from the *Spectralon* cube scattering experiment. As seen from the plot, the resistance transition is completed before the shutter completely opens.

The power curve of Fig. 19.8 was integrated and corrected by Eq. (19.3) to calculate the deposited laser energy as a function of time starting from the shutter opening. This was used to analyze the bulk-resistivity as a function of deposited energy. Since the samples' physical dimensions varied, the energy deposited was normalized by dividing the deposited laser energy by the volume of the sintered material.

Fig. 19.9 shows the bulk resistivity change with respect to accumulated normalized energy. Accumulated normalized energy is the total deposited

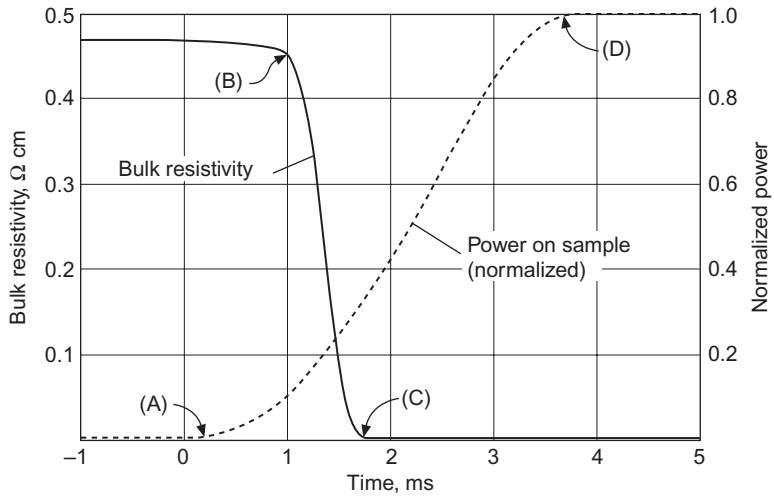


Fig. 19.8 Representative oscilloscope data processed to show the bulk resistivity change with time along with the normalized incident power.

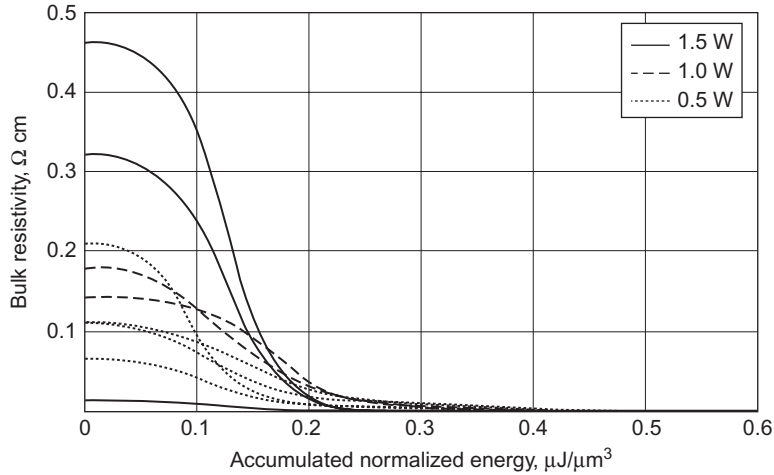


Fig. 19.9 Bulk resistivity change with the accumulated (normalized) energy showing the sintering initiation *(left shaded area)* and the sintering completion energy *(up to the right shaded area)*.

energy per unit volume, which increased with time as the laser beam continued irradiating the line. The resistivity transition initiation and completion energies are indicated by the shading in Fig. 19.9. The minimum energy absorbed by the sample to initiate the resistance change was approximately $0.05\,\mu J/\mu m^3$. The normalized deposited energy required to complete the resistance transition was about $0.34\,\mu J/\mu m^3$ regardless of the initial resistance. Only a small fraction of the total deposited energy ($37–150\,\mu J/\mu m^3$) was used towards sintering yet none of the lines were ablated or peeled off. The in situ experiment lines were about $100\,\mu m$ long yet the as-deposited resistivity varied significantly (see ordinate axis of Fig. 19.9). All the samples exhibited moderate bulk resistivities after sintering with a median of $10\,\mu\Omega\,cm$.

The deposited Ag nano-ink lines were observed to become reflective to visible radiation when irradiated with the laser beam for both the in situ and scanned experiments. Fig. 19.10 shows an image from a video of a deposited line becoming reflective for visible light as the laser beam scanned along it.

To investigate the reflectivity change, an 18-mm square pad was direct-write deposited on a fused silica slide at room temperature using nano-sized conductive ink producing a smooth surface by the overlapping lines. The slide was then heated to 75°C to correspond to the typical direct-write deposition onto a 75°C heated stage. The reflectance was

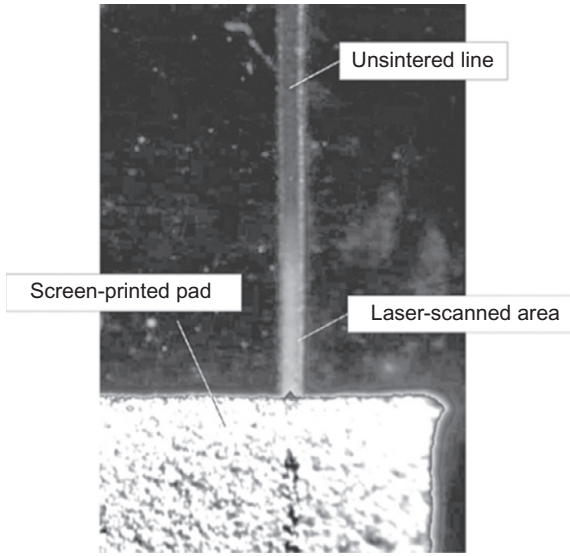


Fig. 19.10 Image from a recorded video showing increasing reflectivity of the scanned (sintered) line as compared to unsintered.

measured on a spectrophotometer before and after sintering the deposit for 1 h at 275°C and is displayed in Fig. 19.11. The transmission in both cases was negligible, indicating that the absorptance of the Nd:YAG laser wavelength at 1064 nm goes from approximately 55% to less than 3%. This indicates that the sintered line no longer absorbs significant laser radiation

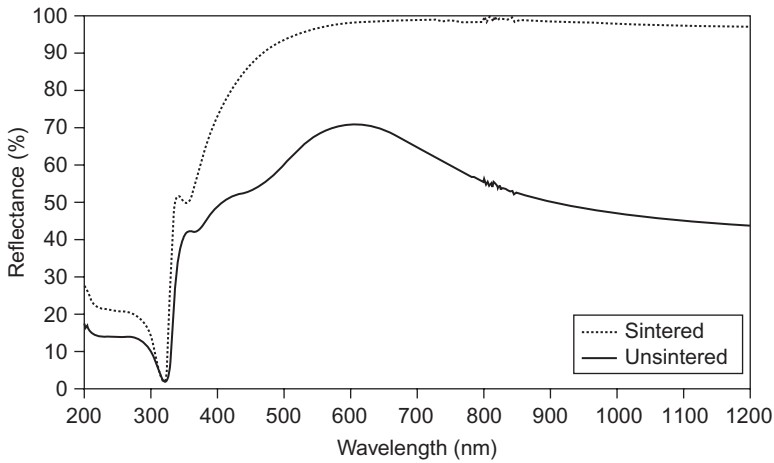


Fig. 19.11 Spectrophotometer reflectance of nano-sized ink direct-write deposited pad.

after the transition has occurred and explains why no further conductivity enhancement is observed in Fig. 19.9 although only a fraction of the deposited energy drove the transition to completion. From Fig. 19.8 we see that this transition is very fast, taking less than a millisecond. This rapid transition has been independently observed [35] using a totally different sintering technique, electrical current. They used a constant current across an inkjet-printed line and observed that the major transition in resistance occurs within two microseconds. The results of both these methods, laser heating and electrical current heating, support the argument that the rapid Phase I resistivity transition is due to the breakdown of the nanoparticle encapsulation coatings at a threshold temperature in the deposit.

The surface roughness was also observed to decrease with increasing irradiation power to a smooth surface as indicated in Fig. 19.12. In this sequence, four lines deposited at the same time with identical conditions were irradiated with powers of 0.5, 1.0, and 1.5W for 100 ms each as well

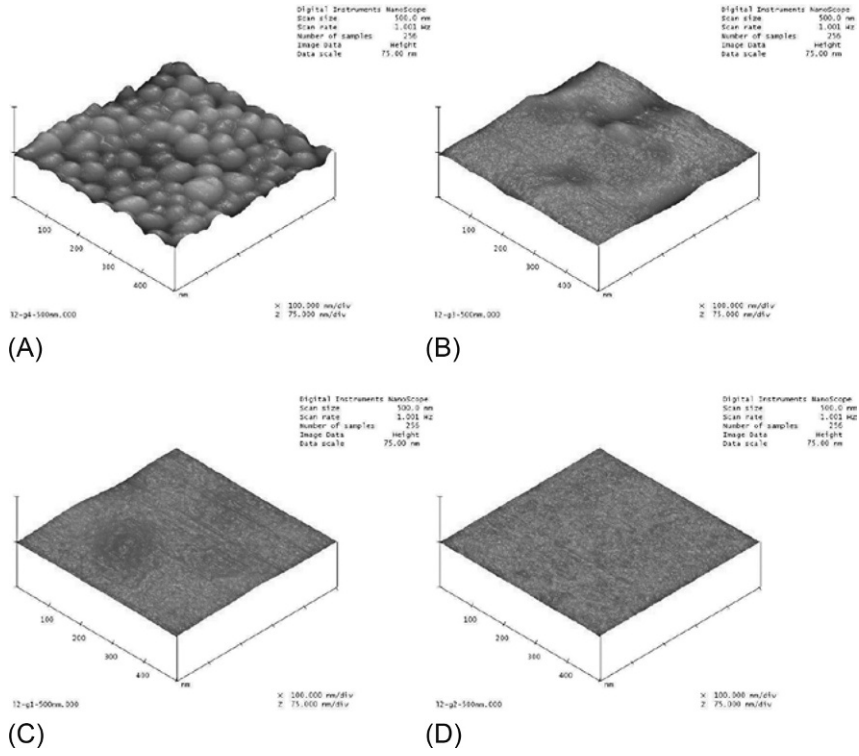


Fig. 19.12 AFM height scan (500 nm × 500 nm area) of conductive Ag nano-ink (A) unsintered, (B) 0.5 W, (C) 1.0 W and (D) 1.5 W laser irradiation for 100 ms.

as unsintered as in the results of Fig. 19.9. Atomic force microscope (AFM) scans were taken of the 12 irradiated spots plus four unsintered with representative lines presented in Fig. 19.12. Similar results were observed for all four samples for each of the four power levels. The unsintered lines, as represented in Fig. 19.12A are comparable to the AFM scan published by [37]. The surface roughness measured by the AFM for the samples is given in Table 19.1 for $2\,\mu m \times 2\,\mu m$ and $500\,nm \times 500\,nm$ areas. This decrease in surface roughness with increasing laser power supports the argument for a slower Phase II densification process. As discussed above, the reflectivity of the surface changed early in the irradiation so that the dynamics of the surface roughness decreasing with increasing power requires further study.

The bulk resistivity of the laser-scanned direct-deposited lines is plotted as a function of the normalized laser energy in Fig. 19.13. Since the samples' physical dimensions varied, the energy deposited was normalized by dividing the deposited laser energy by the volume of the sintered material. Four different regions are evident in Fig. 19.13, a region below $0.4\,\mu J/\mu m^3$ where no sintering was observed, a transitional region from 0.4 to $1.1\,\mu J/\mu m^3$, a sintering region ($1.2–1.8\,\mu J/\mu m^3$), and a region above $1.8\,\mu J/\mu m^3$ where the deposited material tends to peel off the substrate. Within the accuracy of the measurements, there is almost no variation in the bulk resistivity within the sintering region although it covers a significant normalized energy range. Within the sintering region, the laser scanning resulted in a lower bulk resistivity than the hot plate sintering. Yet the lowest bulk resistivity observed was five times higher than the theoretical bulk resistivity of pure silver ($1.6\,\mu\Omega\,cm$). The laser scanned bulk resistivity is comparable and lower than other sintering methods [38].

There were eight lines that peeled off the substrate at the highest laser energy setting. One randomly chosen peeled-off line was analyzed using a contact profiler, scanning electron microscope (SEM), and energy dispersive spectrometer (EDS). Fig. 19.14 shows both a contact profiler image and an SEM image of the peeled-off line.

Table 19.1 AFM roughness analysis for $2\,\mu m \times 2\,\mu m$ surface area of laser sintered conductive silver nano-sized ink

Laser power (W)	Average rms height (nm)
Unsintered	8.3
0.5	3.7
1.0	3.0
1.5	1.7

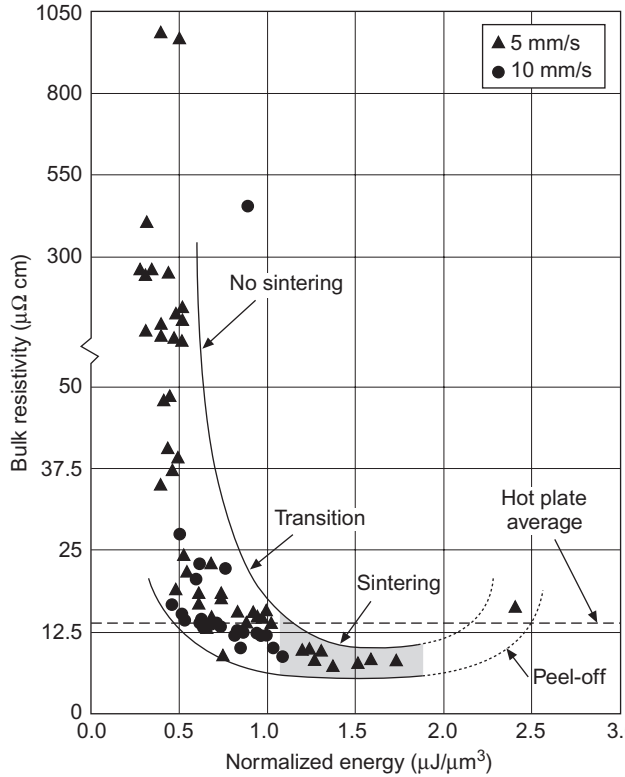


Fig. 19.13 Bulk resistivity of laser scanned lines as a function of normalized laser energy.

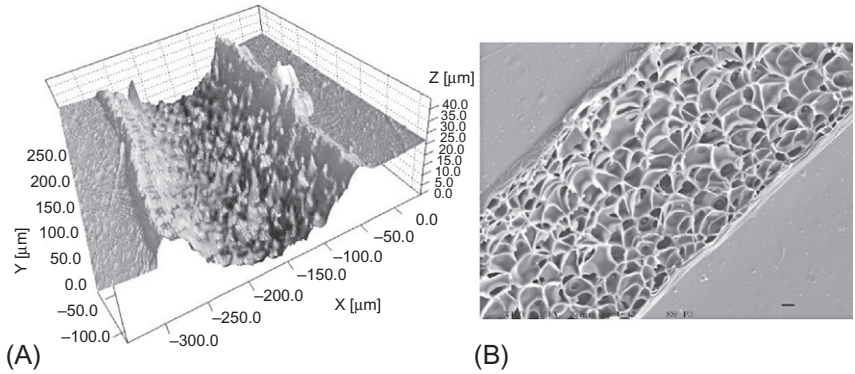


Fig. 19.14 Image of the peeled line from (A) contact-profiler and (B) SEM.

EDS analysis showed the presence of a trace of silver in the trench while significant amounts of silver were located on the edges. A probable explanation of the observation was that stress due to the mismatch in the coefficients of thermal expansion between the sintered silver and the polyimide substrate lifted the line from the substrate as the sintered line rapidly cooled. The "dimply" morphology (Fig. 19.14B) indicates bonding between the sintered silver and the polyimide.

19.5 FUTURE TRENDS

As we have shown, laser sintering of direct-write deposited silver nano-sized inks on polymeric substrates produces superior conductive traces to those produced by conventional oven heating. The discovery that a rapid Phase I transition, likely due to the breakdown of the organic materials encapsulating the nanoparticles, decreases the visible and near IR radiation absorptance of the conductor to negligible amounts suggests additional ultraviolet processing of nano-sized conductive inks to lower the bulk resistivity toward that of the pure metals. Further investigation of the roughness decreasing Phase II densification is also warranted.

An entire printed solution for more sophisticated printed electronic devices requires not only conductors but a much wider variety of materials, including metallic and nonmetallic formulations such as semiconductors, dielectrics, ferrites, resistors, and even superconductors. Both the material deposition technologies and the material formulation for many of these materials are here but their postprocessing, especially when done *in situ* and on a low-temperature substrate, seems to be one of the major obstacles hampering the widespread implementation and advance in the printed electronics. One possible approach is to construct multilayer hybrid direct-write material systems, defined here as material systems consisting of stacked layers with different metallurgy and different functions, deposited with inkjet printing or another direct-write method onto an organic substrate, and laser treated in situ. These types of materials and material deposition methods are fundamental in developing miniature all-printed electronics devices and laser sintering is seen as an enabling technology in this area.

One example of electronic devices that can benefit from the hybrid direct-write material systems is printed semiconductors. For decades there has been research on very thin transistors that can be deposited on flexible surfaces. These thin film transistors (TFTs) are a type of field effect transistors (FETs) commonly constructed by thin film depositions on glass or

organic substrates requiring low temperature processing [39]. Another more generic example is one in which the top layer is a material with a high sintering temperature. In this system the first layer from the organic substrate would be a wider heat dissipation metal layer that serves as a heat sink to uniformly dissipate the heat of sintering. Atop the heat sink is a dielectric layer added to electrically and thermally insulate the top layer. Suitable dielectric materials include ZnO and $Pb(Zr_{1/2}Ti_{1/2})O_3$ (PZT) ceramics. For the nano-sized PZT particles, it has been found that sintering can lead to effective densification at 600–800°C [40]. Another promising material is zinc oxide, which in nanoparticle form needs lower sintering temperatures, typically in the range of 330–730°C [41]. Zinc oxide is currently used in many electronics applications such as solar cells, touch panels, and flat-panel displays. A low-density thermal barrier layer could be added between the dielectric layer and the heat sink if the required heat for successfully sintering the dielectric layer is too high, which may be the case with the PZT ceramics. The material of choice for this layer would be SiO_2. The SiO_2 sol could be printed onto the heat sink. Ambient pressure drying could be then used to obtain a good aerogel layer [42,43].

19.6 SOURCES OF FURTHER INFORMATION AND ADVICE

The first systematic representation of direct-write methods was in the MRS symposium proceedings volume entitled *Materials Development for Direct Write Technologies*, which included papers from the MRS symposium held in San Francisco in April 2000 [44]. A significant part of the symposium papers was dedicated to the principles of various processing techniques, roughly grouped into four categories: droplet-based, laser-based, ion-and electron-beam techniques, and others, which included thermal spray and direct imprinting.

One of the most comprehensive texts and a logical continuation and extension of the research presented in the previous publication is entitled *Direct-write Technologies for Rapid Prototyping Applications*: *Sensors, Electronics, and Integrated Power Sources,* a chapter book, edited by Piqué and Chrisey [1]. The editors dedicated this book to the vision of Dr. Bill Warren, who led MICE while at DARPA. The book is organized in four parts and eighteen chapters contributed by 61 authors. It covers applications in electronics manufacturing, material systems for direct-write, a survey of direct-write methods, and a technology overview. A brief section in this book is dedicated to laser sintering of direct-write materials.

ACKNOWLEDGMENTS

This chapter is based on research sponsored by the Defense Microelectronics Activity (DMEA) under agreement H94003-07-2-0701. The United States government is authorized to reproduce and distribute reprints for government purposes, notwithstanding any copyright notation thereon.

REFERENCES

[1] A. Piqué, D.B. Chrisey (Eds.), Direct Write Technologies for Rapid Prototyping Applications, Academic Press, San Diego, 2002.
[2] H. Sirringhaus, T. Kawase, R.H. Friend, T. Shimoda, M. Inbasekaran, W. Wu, E.P. Woo, High-resolution inkjet printing of all-polymer transistor circuits, Science 290 (2000) 2123–2126.
[3] C.B. Arnold, R.C. Wartena, K.E. Swider-Lyons, A. Piqué, Fabrication of mesoscale energy storage systems by laser direct-write, MRS Proc. 758 (2002) LL3.6.1–LL3.6.12.
[4] N. Electronov, V.S. Serbezov, E. Dimitroff, N. Zlatanov, Production of solar cells from A_2B_6 compounds by MAPLE technology on polymer substrates, in: Proc. of SPIE Vol. #4637 Photon Processing in Microelectronics and Photonics, SPIE, 2002.
[5] Y.J. Lee, P.V. Brown, Tunable inverse opal hydrogel pH sensors, Adv. Mater. 15 (2003) 563–566.
[6] J.A. Lewis, G.M. Gratson, Direct writing in three dimensions, Mater. Today 7 (2004) 32–39.
[7] M.A. Mignatti, M.I. Campbell, R. Ruizpalacios, K.L. Wood, J.J. Beaman, Modeling and characterization of a novel, low-cost, direct-write waveguide, in: Solid Freeform Fabrication Proceedings, 2003, pp. 501–509.
[8] J.T.M. De Hosson, R. Popma, Sintering characteristics of nano-ceramic coatings, Defect Diffus. Forum 218–220 (2003) 51–66.
[9] P. Calvert, Inkjet printing for materials and devices, Chem. Mater. 13 (2001) 3299–3305.
[10] B. King, Maskless mesoscale materials deposition, Electron. Packag. Prod. 43 (2003) 18–20.
[11] M. Renn, Aerosol-based direct writing of interconnects, in: Proc. of 2nd Annual Digital Electronic Materials Deposition Conference, October 20–22, 2003, Scottsdale, Arizona, IMAPS, 2004.
[12] K. Vanheusden, P. Atanassova, J. Caruso, H. Denham, M. Hampden-Smith, K. Kunze, T. Kodas, A. Schult, A. Stump, Advanced materials systems for ultra-low-temperature, digital, direct write technologies, in: A. Piqué, D.B. Chrisey (Eds.), Direct Write Technologies for Rapid Prototyping Applications, Academic Press, San Diego, 2002.
[13] B. Li, P.A. Clark, K.H. Church, Robust direct-write dispensing tool and solutions for micro/meso-scale manufacturing and packaging, in: Proc. of 2007 ASME International Manufacturing Science and Engineering Conference, October 15–17, 2007, Atlanta, Georgia, ASME, 2007.
[14] K.H. Church, nScrypt-advanced syringe based digital printing, in: Proc. of 2nd Annual Digital Electronic Materials Deposition Conference, October 20–22, 2003, Scottsdale, Arizona, 2004.
[15] R.D. Piner, J. Zhu, F. Xu, S. Hong, C.A. Mirkin, Dip-pen nanolithography, Science 283 (1999) 661–663.
[16] F. Underdown, Laser guidance of particles in hollow optical fibers, Nano Technology Magazine, 2000, p. 6.
[17] K. Vanheusden, Electronic materials technology for the emerging low-cost printing industry, in: Proc. of 2nd Annual Digital Electronic Materials Deposition Conference, October 20–22, 2003, Scottsdale, Arizona, IMAPS, 2003.

[18] H.H. Lee, K.S. Chou, K.C. Huang, Inkjet printing of nano-sized silver colloids, Nanotechnology 16 (2005) 2436–2441.
[19] A. Rae, A. Skipor, M. Chason, "Warm" manufacturing, in: Proc. of 12 Annual SMTA Pan Pacific Symposium, January 30–February 1, 2007, Maui, Hawaii, SMTA, 2007, pp. 32–35.
[20] B.J. Kellett, F.F. Lange, Advanced processing concepts for increased ceramic reliability, in: J.G.P. Binner (Ed.), Advanced Ceramic Processing and Technology, vol. 1, William Andrew Publishing/Noyes, 1990, pp. 1–37.
[21] J.N. Israelachvili, Intermolecular and Surface Forces, Academic Press, London, 1985.
[22] J.N. Israelachvili, R.K. Tandon, L.R. White, Measurement of forces between two mica surfaces in aqueous polyethylene oxide solution, J. Colloid Interface Sci. 78 (1980) 430–443.
[23] M.G. McKimpson, Densification maps for nano-sized powders, Mater. Manuf. Process. 11 (1996) 935–949.
[24] M. Mayo, Processing of nanocrystalline ceramics from ultrafine particles, Int. Mater. Rev. 41 (1996) 85–115.
[25] J.R. Groza, Nanocrystalline powder consolidation methods, in: C.C. Koch (Ed.), Nanostructured Materials: Processing Properties and Potential Applications, second ed., William Andrew/Noyes Publishing, 2007, pp. 173–234.
[26] M.I. Alymov, E.I. Maltina, Y.N. Stepanov, Model of initial stage of ultrafine metal powder sintering, Nanostruct. Mater. 4 (1992) 737–742.
[27] L.N. Allen, Nanocalorimetry Studies of materials: melting point depression and magic nanostructures, in: NNUN Abstracts 2002/Materials, Physics, Processes & Characterization, 2002, p. 40.
[28] P. Buffat, J.P. Borel, Size effect on the melting temperature of gold particles, Phys. Rev. A 13 (1976) 2287–2298.
[29] S.L. Lai, J.Y. Guo, V. Petrova, G. Ramanath, L.H. Allen, Size-dependent melting properties of small tin particles: nanocalorimetric measurements, Phys. Rev. Lett. 77 (1996) 99–102.
[30] C.R.M. Wronski, The size dependence of the melting point of small particles of tin, Br. J. Appl. Phys. 18 (1967) 1731–1737.
[31] D.M. Owen, A.H. Chokshi, An evaluation of the densification characteristics of nanocrystalline materials, Nanostruct. Mater. 2 (1993) 181–187.
[32] I.R. Suryanarayanan, S.M.L. Sastry, Consolidation of nanoparticles—development of a micromechanistic model, Acta Mater. 47 (1999) 3079–3098.
[33] J. Sears, M. Carter, J. Colvin, Characterization of conductive inks deposited with maskless mesoscale material deposition, in: Proc. of TMS 2006 Annual Meeting, Mar. 12–16, 2006, San Antonio, TMS, 2006.
[34] S. Angappan, L. John Berchmans, C.O. Augustin, Sintering behaviour of $MgAl_2O_4$—a prospective anode material, Mater. Lett. 58 (2004) 2283–2289.
[35] M.L. Allen, M. Aronniemi, T. Mattila, A. Alastalo, K. Ojanpera, M. Suhonen, H. Seppa, Electrical sintering of nanoparticle structures, Nanotechnology 19 (2008) 1–4.
[36] R.L. McCally, Measurement of Gaussian beam parameters, Appl. Opt. 23 (1984) 2227.
[37] Harima Co, NanoPaste: Programmable material for lead-edge circuit & connection, (PowerPoint presentation), 2004.
[38] E. Kinzel, H. Sigmarsson, X. Xianfan, W. Chappell, Selective laser sintering of microwave components, in: Proc. of 2005 European Microwave Conference, vol. 1, 2005, p. 4.
[39] IDTechEx Ltd, Field Effect Transistor (Glossary of Printed Electronic Terms), 2008, http://www.idtechex.com/printedelectronicsworld/glossary (accessed 20.07.08).
[40] Z. Wang, W. Zhu, C. Zhao, O.K. Tan, Dense PZT thick films derived from sol-gel based nanocomposite process, Mater. Sci. Eng. B 99 (2003) 56–62.
[41] A.P. Hynes, R.H. Doremus, R.W. Siegel, Sintering and characterization of nanophase zinc oxide, J. Am. Ceram. Soc. 85 (2002) 1979–1987.

[42] G.S. Kim, S.H. Hyun, Synthesis and characterization of silica aerogel films for inter-metal dielectrics via ambient drying, Thin Solid Films 460 (2004) 190–200.
[43] H.S. Yang, S.Y. Choi, S.H. Hyun, C.G. Park, Ambient-dried SiO_2 aerogel thin films and their dielectric application, Thin Solid Films 348 (1999) 69–73.
[44] D.B. Chrisey, D. Gamota, H. Helvajian, D.P. Taylor (Eds.), Materials Development for Direct Write Technologies, MRS Proceedings, vol. 624, Materials Research Society, Pittsburgh, PA, 2000.

CHAPTER 20

Micro- and Nano-Parts Generated by Laser-Based Solid Freeform Fabrication

J. Lawrence*, A. Ostendorf†, A. Neumeister‡, S. Dudziak‡, S. Passinger§, J. Stampfl¶

*University of Chester, Chester, United Kingdom
†Ruhr University, Bochum, Germany
‡Laser Center, Hannover, Germany
§Leuze electronic GmbH & CoKG, Owen, Germany
¶TU Wien, Vienna, Austria

20.1 INTRODUCTION

Laser-based solid freeform fabrication (SFF) of three-dimensional micro- and nanoparts is a multidisciplinary field, involving intimate knowledge of mechanical and optical engineering, material science, and more (computer science, chemistry, fluid dynamics, etc.). In contrast to most laser-assisted processes operating in a material *removal* manner (e.g., drilling, cutting, structuring), laser-based SFF in general involves the generation of physical, three-dimensional objects by the *addition* of material in a layer-based production fashion. The layer-by-layer fabrication principle does not require the use of any special molds or tools, instead relying on three-dimensional model data as generated with computer-aided design (CAD) software or three-dimensional scanning systems like computer tomography (CT). Prior to fabrication, the model data is virtually sliced in (mostly constant) increments along the axis of the building direction, subsequently defined as the z-direction (Fig. 20.1).

Each virtual slice will correspond to a physical layer of the solid part and is assigned with a set of parameters required for production. Depending on the applied SFF method, three-dimensional physical objects are created by sintering, polymerization, blanking of metal sheets, or otherwise, from the bottom layer to their top. In the last decades, SFF has proven to be a respectable basis for the design, development, and manufacturing of products and consumer goods from various industries in the field of telecommunications, the automotive industry, information technologies, and aeronautics.

Advances in Laser Materials Processing
https://doi.org/10.1016/B978-0-08-101252-9.00020-0
Copyright © 2018 Elsevier Ltd.
All rights reserved.

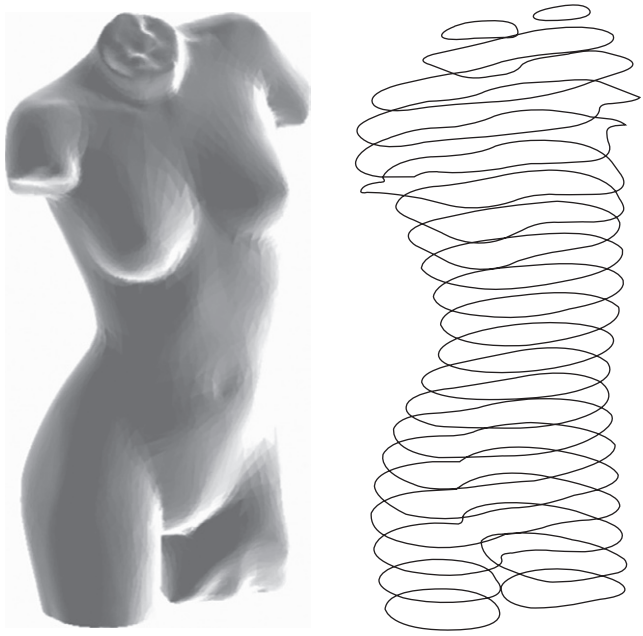


Fig. 20.1 The slicing procedure in additive manufacturing. The CAD files are virtually sliced at increments along the *z*-axis.

SFF may be used as a design tool during product development, an engineering field well known as rapid prototyping (RP). The generated objects, being mainly polymer parts, assist during the product development cycle by allowing a more significant visual and haptic study of a proposed design than CAD software visualization may ever provide. The broad industrial use of additive fabrication started in 1987, when the US company 3D Systems released the first commercially available machine based on the stereolithography (SL) principle (SL may be based on the Greek terms *stereos* (hard, spatial), as well as *graphein* (writing)). Three-dimensional parts are generated by the light-induced curing of a liquid polymer (also called a resin) that directly transfers into solid fragments after local illumination with a focused laser beam. In the majority of the available SL systems, ultraviolet (UV) light sources (in particular lasers) are used to induce free radical or cationic polymerization of individual layers. For the industrial fabrication of large-scale parts, the laser beam is deflected by two galvanometric mirrors and is subsequently focused into a polymer-filled processing chamber, where the curing (or photoforming) takes place in a constant working plane, which is the charging level of the liquid polymer inside

the chamber (typically matched with the focal plane of the laser beam). In general, the layer fabrication during SL is technically realized by using a positioning stage that moves stepwise inside the resin-filled chamber. A deposition system ensures a homogenous lamination of previously cured layers with liquid polymer before the next illumination cycle (Fig. 20.2). Ready-built three-dimensional parts are removed from the chamber after the final layer is built and cleaned.

Alternative SFF methods are starting to be investigated. Another industrially relevant method is selective laser sintering (SLS), a process developed at the University of Texas in 1988. It uses a laser system to selectively sinter or melt metallic and nonmetallic powders. Three-dimensional parts are grown in a similar "step and repeat" manner compared to SL. Several other SFFs do exist and are described in detail in the available literature [1–3].

Besides the most traditional SFF application, the RP, new approaches in freeform fabrication aim toward the fabrication of applicable parts for end-user purposes, widely termed as rapid manufacturing (RM). Still, contrary positions can be found about the meaning and definition of RM in the literature. Wohlers [4], for instance, defines RM as a *direct production method for finished goods using additive manufacturing*. In the case that "finished goods" includes tools and consumer products, Wohlers [4] is in accordance with Gebhardt [1], who uses an identical definition of RM, and further groups RM in direct tooling and direct manufacturing for the fabrication of tools and consumer goods, respectively. Various applications display the enormous potential of RM [4,5]. However, the broad industrial acceptance of RM has still not happened, and in most cases, engineers refer to conventional machining techniques to form complex parts.

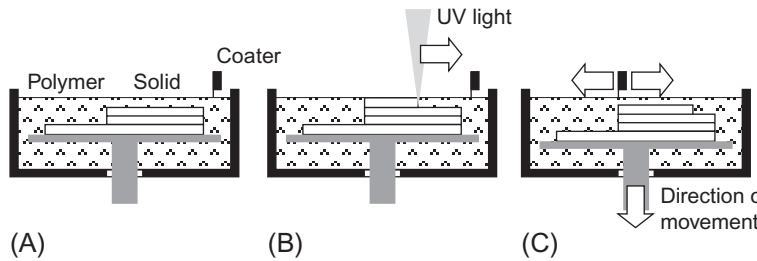


Fig. 20.2 The basic principle of conventional stereo lithography (SL), (A) starting of cycle, (B) illumination of layer, (C) movement of platform and re-coating (illustration applicable for both scanning and integral approach, see Section 20.2.1).

Another situation occurs when reflecting on the field of micro system engineering and components with spatial resolutions in the meso- and microscale regime. SFF is highly capable and in most cases, the only production method that can meet both the geometrical complexity and the resolution. Generally, the method of micro SFF operation might be oriented to one in macroscale processing, but the intended increase of the process resolution in SFF is strongly dependent on a couple of factors, partly determined by the optical equipment and setup as well as the mechanical and thermal stability of the machine platform (manufacturing side of view), and, of course, the material to be processed (material side of view). Within the last few years, several groups have done extensive research on transferring freeform fabrication to micro production. Within this chapter, the authors present the history and state-of-the art research on micro SFF using polymers (Section 20.2) and metals (Section 20.3)

20.2 MANUFACTURING BASED ON PHOTOPOLYMERIZATION

Additive fabrication using photopolymerization, including projection and scanning micro stereolithography (MSL, refer to Section 20.2.1), as well as two-photon laser lithography (TPP, refer to Section 20.2.2) can achieve the highest process resolution of all SFF processes. Both MSL and TPP are capable of producing high-precision three-dimensional elements that might be applied in various technical applications. Well-arranged technical papers and books on MSL concepts and processes are available [6,7]. Still, the TPP is an exceptional SFF approach, consequently being described in a separate section within this chapter, although the basic principle of both the MSL and TPP techniques are identical: the nature of both processes is based on the light-induced linking of (liquid) monomers into a solid, cross-linked polymer (chain of monomer units) by selectively generating free radicals in the area where the photon absorption occurs (Fig. 20.3), thus initiating the polymerization sequence.

Continuative details on photopolymerization and the light–matter interaction are broadly available in the literature [5,7]. While MSL is based on the direct absorption of optical radiation using UV light sources and lasers, which normally forces the user to work at the surface, the TPP is founded on the principle of two-photon absorption (2PA), a nonlinear effect during the absorption of the optical radiation which only takes place at high optical intensities obtained in the focal region of a femtosecond

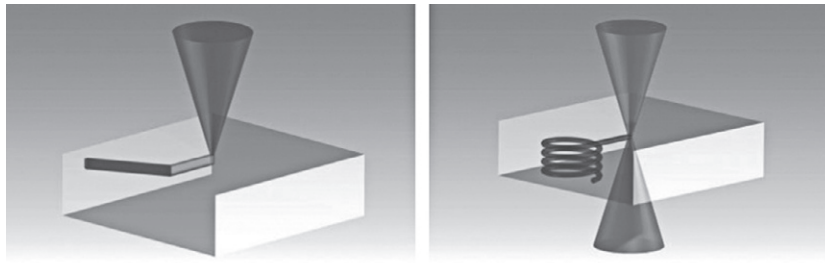


Fig. 20.3 Principle of light induced polymerization using a single-photon process (A), refer to Section 20.2.1 or a two-photon process (B), refer to Section 20.2.2.

(10^{-15} s) laser beam. This technique allows moving the focused laser beam three-dimensionally through the liquid matrix, as this material is transparent for nonfocused radiation. Although the technical realization of TPP processes has drastically emerged in recent years, the technological effort is still not trivial. Because laser beam sources that provide pulse durations in the femtosecond regime are required to start the TPP, the work is mainly done at lab scale. However, the industrial implementation and commercialization of the TPP principle is in progress and the first commercial system has recently been reported [8]. Parts of the MSL techniques that are described later in this chapter are already available for industrial part production. On the other hand, there is still a lack of sustainable machine concepts that offer reliable micro manufacturing capability on the large scale.

20.2.1 MSL

MSL, in general, is oriented at its macroscale counterpart, (except Ref. [9]) by photocuring a liquid monomer at the surface in a stepwise layer-by-layer fashion. MSL provides much better feature resolution than conventional SL, but the part size is often limited to a few mm. After first being reported by two groups in Japan [10,11], various MSL systems have been developed based on different design and operational principles, but all aiming at the fabrication of complex, three-dimensional parts with a much better process resolution than conventional SL may provide [12–18; and others]. Not all apply a laser beam as the illumination source, but in order to be complete, a brief description may serve the reader as an overview of the reported operational principles and diversity of technical approaches in MSL (Fig. 20.4). Some results obtained with laser-based MSL will be discussed later in this section.

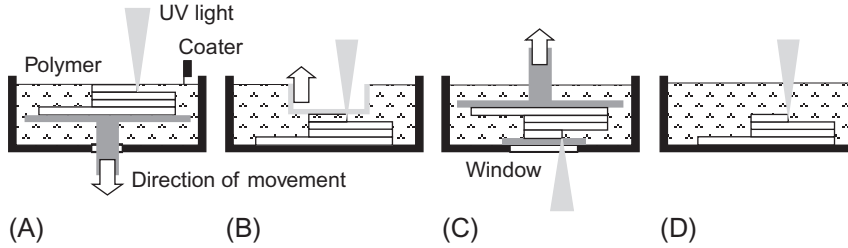


Fig. 20.4 Overview of reported MSL operation principles from left to right, (A) free surface method, illumination from the top ([12–19]; and others); (B) and (C) constrained/fixed surface, illumination from the bottom or top [10,11,20]; (D) super IH process, enabling under-surface fabrication with a single-photon process (1PP) [9,21], also: TPP (refer to Section 20.2.2).

The nature of all MSL techniques being described in this section is based on the excitation of the resin with UV or visible radiation provided by a laser or other types of light sources. As most of the resins are optimized for the UV range, the photon energy is absorbed in the single-stage process, resulting in a linear dependence between free radical generation and exposure energy (single-photon absorption). In the majority of the published literature, the polymerization rate is proportional to the number of free radicals, thus the polymerization is initialized at the surface of the resin volume. The only exception is the technology described by Ikuta et al. [9] and Maruo and Ikuta [21], where adapted conditions allow the polymerization only in the focal region, consequently enabling "undersurface" curing.

Fig. 20.4A shows the most conventional approach in MSL, as it is strongly oriented to the common stereolithography principle, where the processing region of the liquid resin is in direct contact with the gaseous medium surrounding it (free surface method). Here, different techniques are reported regarding the illumination procedure, both the scanning (vector-by-vector) and the projection (integral) method. During scanning, the relative movement between the focused laser spot and the resin is managed by using a galvanometric scanning device for precise positioning of the focal spot [16–19]. Another innovative method for MSL is the integral approach, where the geometrical layer information may be transferred in only one entire irradiation step by using a liquid crystal display [22,23], a digital micromirror device (DMD, Texas Instruments) [24] and/or an electro-optical mask [13] as a dynamically operating pattern mask applicable in the UV range. The geometrical information of each individual layer shape is imaged on the surface of the liquid polymer at high magnification. This enables a much faster method of operation than scanning MSL may

allow, because each layer is produced in one step. However, on the other hand, the working field is limited to a few mm in present systems and thus only one or a few parts can be produced per cycle. Additionally, the dynamically operating mask is a cost-intensive apparatus that might raise the overall machine part compared to a scanning MSL system. Fig. 20.5 illustrates results that have been produced with projection MSL.

The main challenge for both the scanning and integral approach is the layer preparation (Fig. 20.2C) in the case of the free surface method. After the illumination sequence, a layer of nonilluminated liquid needs to be deposited on previously cured features in order to be prepared for the next layer fabrication sequence. Since the typical layer thickness is less than 25 µm in MSL (compared to ~100 µm in conventional SL), the way the layer is actually produced is one of the main technological innovations in an MSL machine and consequently not reported in detail.

Analogue to the macro scale SL, specially adapted resin deposition systems may be used, but also a method named "deep-dip" (Fig. 20.6), where no coating mechanism is applied but the building platform is deeply immersed in the processing chamber and then moved backward into the intended position [15,26]. However, all the proposed deposition

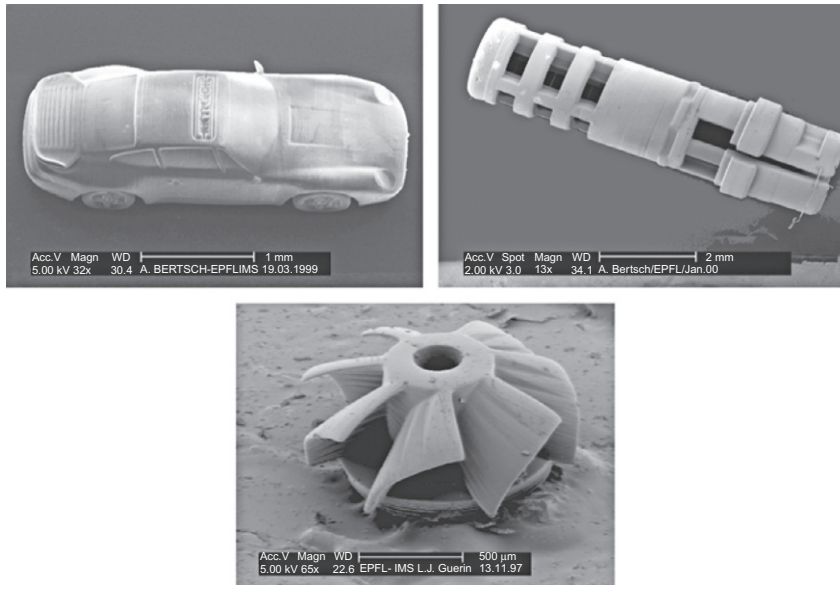


Fig. 20.5 Example results produced with projection MSL showing a car and a test component (top, [25]) and a micro turbine wheel (bottom, [12]).

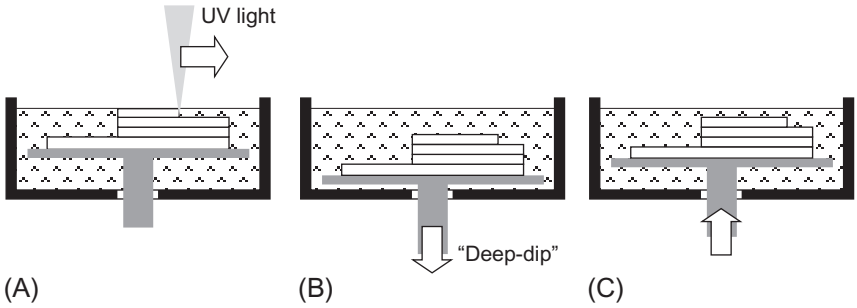


Fig. 20.6 Working principle of the "deep-dip" deposition method, described by Monneret et al. [15] and Tan and Gibson [26].

methods do not prevent waiting until the deposited layer of new monomer has settled under the influence of gravity and formed a planar surface. Especially in MSL, the instance of layer preparation is not a trivial one and, depending on the programmed layer thickness and the viscosity of the applied monomer, can take up to several minutes, consequently delaying the fabrication process. If three-dimensional parts consist of several tens of layers, which is often the case in MSL, the overall settling time is significantly high, thus monomers with a low viscosity are often intended in MSL.

Another situation occurs in the case of the fixed/constrained surface method (Fig. 20.4B and C). The resin is not in contact with a gaseous medium, but its level will be constrained by a solid part, forcing the resin to always form a layer with constant thickness. The most practicable way is to directly use a UV transparent entrance window for illumination purposes [10,11,20]. In that way, uniform layers can be formed. However, a high risk of process failure exists due to a strong adherence of cured features at the entrance window. In the first published MSL paper, Takagi and Nakajima [11] reported an optical setup that consisted of a continuous wave HeCd laser operating at 325 nm with 10 mW output power. For focusing purposes a condenser lens was applied that could be precisely moved below the entrance window in both x-and y-directions (Fig. 20.4C). The entrance window of the chamber has been coated with a PFA resin to minimize the adhesion of polymerized features. Results of their work are shown in Fig. 20.7.

In other contributions using the constrained method (Fig. 20.4B), a xenon lamp has been applied as a light source and subsequently focused in the reaction chamber that has been mounted on a translation stage to allow the relative movement between the liquid and the focal spot in the

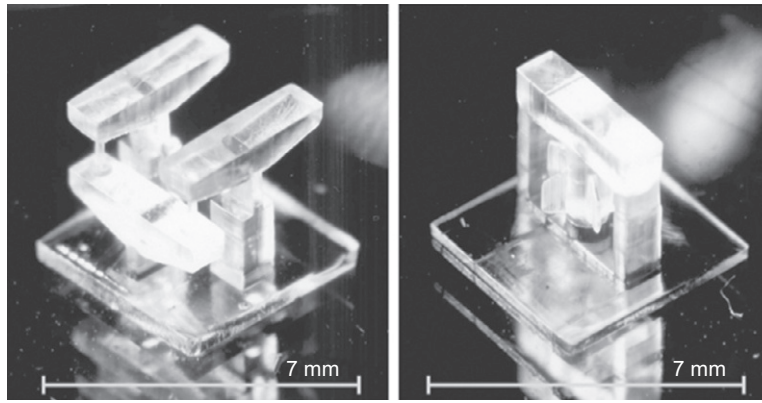


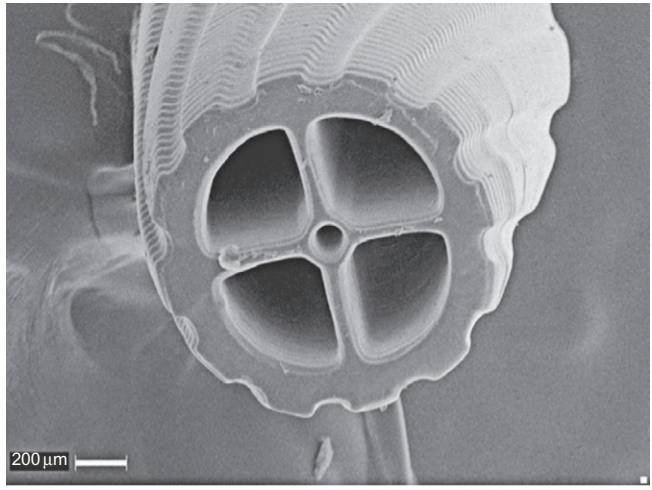
Fig. 20.7 Images of some of the earliest results [11] made with micro stereo lithography, a seesaw (left image) and a turbine (right image).

horizontal plane [10,20]. In order to enable positioning in the vertical direction, the focusing optic was mounted on a precision stage movable in the z-direction. Ikuta et al. [9] and Maruo and Ikuta [21] further presented a completely new approach in laser scanning MSL that was no longer restricted to working at the surface of the liquid polymer (undersurface manufacturing). Since the polymerization is nonlinear depending on the exposure (although the initiation reaction is linear to the exposure), polymerization only occurred in the focal region. As described, the incorporation of oxygen molecules in the liquid resin inhibited the curing reaction in the low energy region, since oxygen molecules scavenge the generated radicals. In that way, submicron three-dimensional writing was enabled by only using a single-photon process. This approach allowed passing the deposition or recoating process because the solid object is created inside the reaction chamber. One of the main disadvantages of this process is the relatively slow processing speed, which is usually in the order of mm/s (20–50 μm/s), compared to more than 100 mm/s in other developed scanning MSL apparatuses. Further, the structures that have been reported do not exceed an overall part size of 100 μm in all three directions, making it challenging for use in engineering applications such as MEMS or micro fluidic applications.

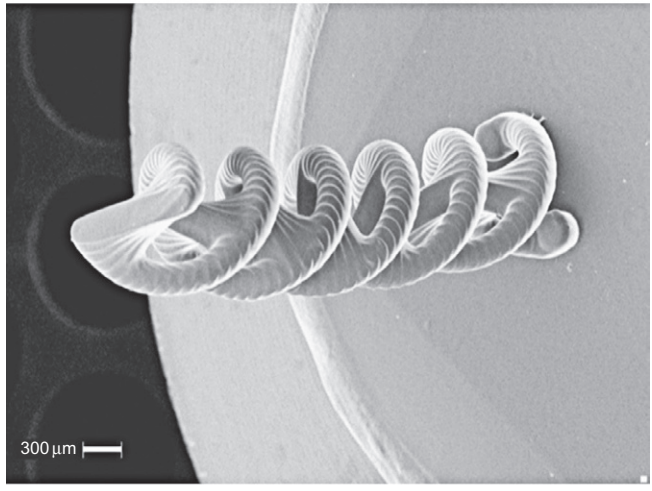
Some further results that have been produced with laser-based MSL will be presented next.

Farsari et al. [13] have used a 351-nm argon-ion laser and a special light modulator to build three dimensional components with a feature resolution of 5 μm.

The SEM images displayed in Fig. 20.8 show two components that have been built with the reported setup. The micro gear depicted in Fig. 20.8A is made up of 50 layers, each with a thickness of 50 µm. It consists of a hollow cylindrical bearing that is attached to the outer truncated cone by four spokes. The freestanding double helix shown in Fig. 20.8B consists of 105 layers, each with a thickness of 50 µm.



(A)



(B)

Fig. 20.8 SEM image of a micro gear and a double helix [13].

Neumeister et al. [16] have used a custom-made MSL apparatus (Fig. 20.9) that is equipped with a mode-locked frequency-tripled solid state Nd:YAG oscillator operating at $\lambda = 355\,\text{nm}$. Pulse trains with $\tau = 10\,\text{pi-}$ cosecond (ps) pulse duration are provided at a quasi-cw repetition rate of 100 MHz with a maximum output power of $P_L = 20\,\text{mW}$.

The fabrication of movable micro mechanical arrangements has been presented, by supporting parts to be movable with structures during processing (Fig. 20.10, images on the top left and right). After removal of the

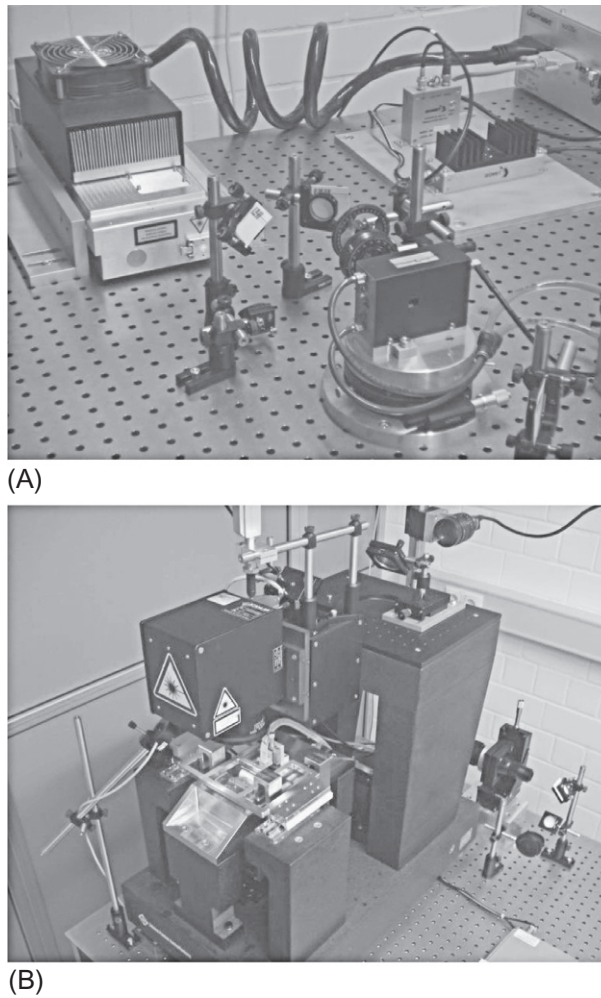


Fig. 20.9 Laser-based vector-by-vector MSL apparatus [16]. Optical setup with laser source and accusto-optical modulator (A), hard stone frame with galvanometric scanner and polymer processing chamber (B).

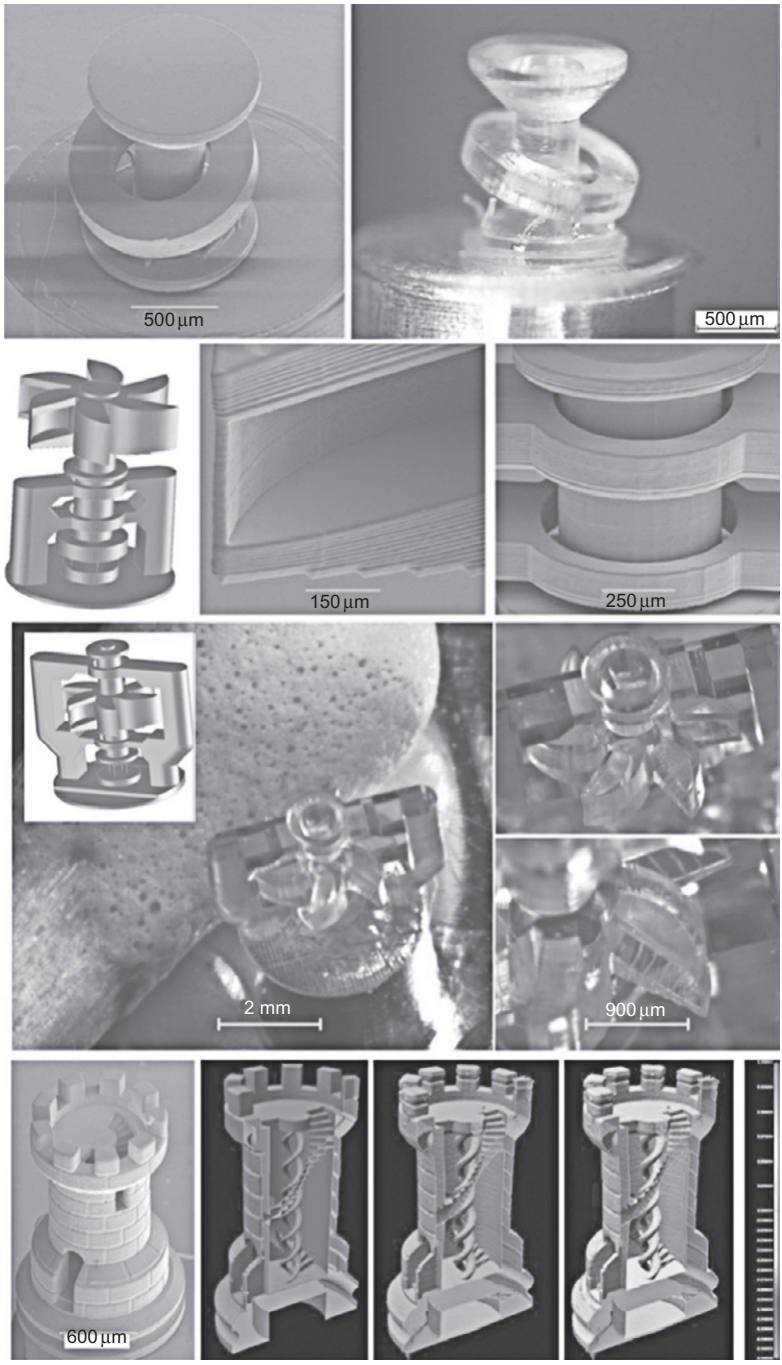


Fig. 20.10 Example geometries fabricated with laser-based vector-byvector MSL (freely movable micro mechanical arrangements), SEM image of a chess figure and virtual cross-sections made with micro computer tomography (mCT). The layer thickness in all structures was 10 mm.

fabricated three-dimensional model from the processing chamber, the support structures could be broken and the previously fixed parts (a ring as proof of principle and a wheel) were freely movable. The material was from the Ormocer class, a hybrid polymer with organic and inorganic parts.

In order to receive spatial information about the fabrication tolerance, a micro computer tomography (μCT) system has been used to analyze components having a highly complex internal geometry [27,28]. Beside the SEM image of the fabricated chess figure, three cross-sections show the input STL model, the fabricated structure, and a target performance comparison. Resulting from the μCT experiments, the achieved spatial precision was within 10–30 μm (Fig. 20.10, bottom).

SFF facilitates the fabrication of cellular structures and scaffolding materials for tissue engineering purposes (Fig. 20.11). The aim of currently ongoing research [29] is to fabricate cellular solids using SFF and in parallel study their mechanical behavior by computational simulation and experimental mechanical tests. The results from the numerical and experimental assessment will deliver feedback for improving the performance of artificial cellular solids.

20.2.2 TPP

TPP is based on 2PA, a nonlinear radiation-matter interaction relying on the excitation of an atom or molecule. TPP enables the fabrication of similar micron-sized parts compared to the Super IH process, but with an even better process resolution below 100 nm and a higher fabrication speed. While the absorption of the optical radiation during the Super IH process is described as linear dependent of the exposure, the excitation during TPP is a nonlinear one. In TPP, the atom or molecule is transferred from a lower state to an excited state of the same parity in a single step, which in contrast to a single photon process cannot be described as a dipole transition. The 2PA theory was first developed by Göppert-Mayer [30] in 1931, and experimentally realized in 1961 [31]. The long period of 30 years until 2PA was observed for the first time is reasonable considering the fact that a high intensity is needed for 2PA, which can only be achieved using a laser, which was first developed in 1960.

In contrast to 1PP, the 2PP process is initiated by wavelengths larger than 450 nm and very intense light fields. The polymer and initiators used for this are mostly transparent for the applied wavelength and show a high absorption cross-section at half the wavelength used. This makes it possible to focus the laser inside the polymer and induce a nonlinear polymerization

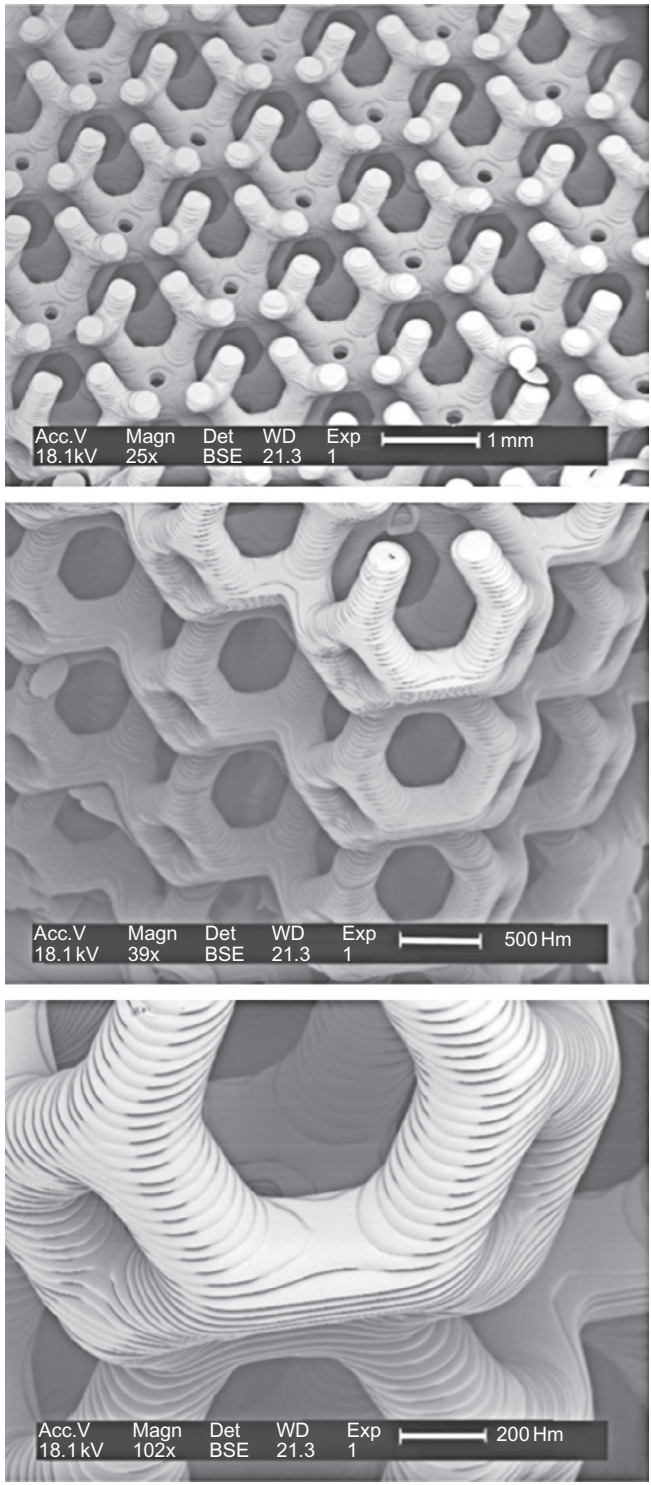


Fig. 20.11 Cellular structures made of Ormocer fabricated with a layer thickness of 50 mm [29].

process. 2PP initiation depends on the intensity of the light used because it is a nonlinear effect. Due to this, polymerization only takes place at the focal volume, which makes three-dimensional writing possible. Furthermore, the nonlinearity of the effect provides the possibility of reducing the size of the polymerized volume below the diffraction limit, as illustrated in Fig. 20.12. 2PP was demonstrated for the first time in 1997 [32] and since then it has found a wide range of applications in science. Some structure examples are shown in Fig. 20.13.

2PP has two main advantages compared to the UV-polymerization processes. Obviously, the three-dimensionality of 2PP, compared to a two-dimensional lithographic processes that only allows a quasi three-dimensional structuring by stacking layer-by-layer (except the Super IH process [9,21]), is the first great advantage. The second is the achievable resolution below the diffraction limit, which is not possible using a linear process. 2PP has two threshold values, one for starting the polymerization and one for the destruction of the polymer. In theory, by applying the correct intensity, it is possible to achieve infinitesimally small polymerized volumes (volume pixel (voxel)) limited only by the polymer properties. In reality the stability of the laser system and the setup limit the resolution. At present, about

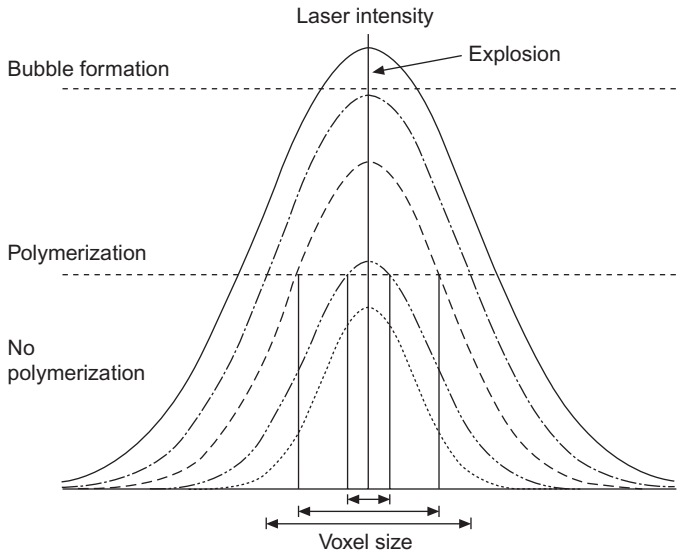


Fig. 20.12 Dependence of the polymerized volume on the laser intensity in 2PP, with the polymerization threshold and the threshold for polymer destruction. A reduction of laser intensity causes a smaller polymerization volume.

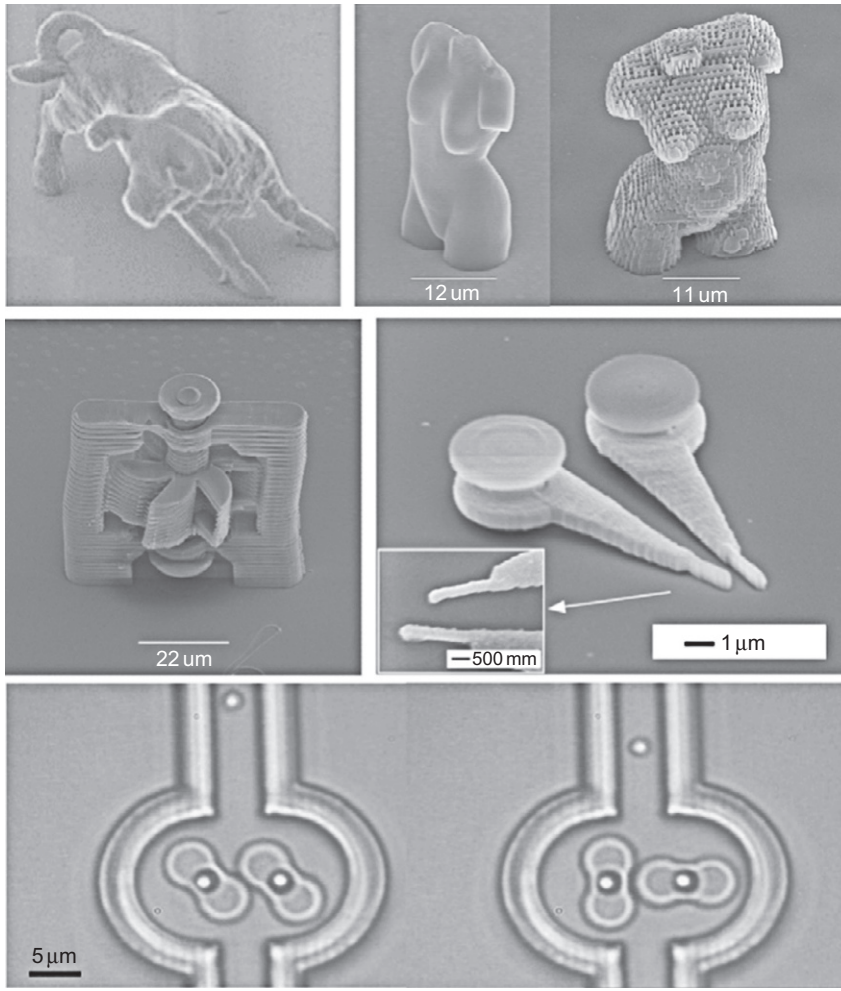


Fig. 20.13 Three-dimensional "Nanoart" (a microbull (left top) [33] and a Microvenus [34] (top right) as solid model and in the shape of a photonic crystal, a micro gearwheel [35] (middle left), a pair of nanotweezers [36] (middle right), and a lobed micropump [37] (bottom).

23 nm laterally is achieved [38] and three-dimensional structures with sub 100 nm features can be fabricated [39] as shown in Fig. 20.14.

In a few laboratories in the world, custom-made laboratory systems for 2PP have been available. The drawback of these systems is the very slow structuring speed of about 100 µm/s or less. Also, all these setups have been laboratory systems assembled by the research institution itself, and not appropriate for use in an industrial environment. These systems are also far from commercialization. To overcome these drawbacks and to bring 2PP

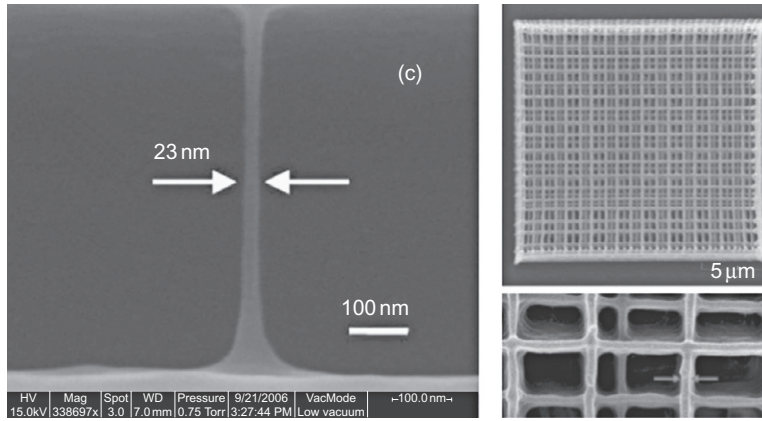


Fig. 20.14 A 23 nm rod [38] (left) and (right) a photonic crystal fabricated by 2PP with a resolution of about 69 nm [39].

into industrial applications, a commercial setup has been developed. All 2PP systems (both the laboratory and the commercial setup) are based on the same principal design, which is shown in Fig. 20.15. A 2PP setup consists of a femtosecond-laser source (typically a femtosecond oscillator); a fast shutter system (typically an acousto-optical modulator (AOM) from which the first diffraction order is used); a power adjustment that is usually realized by a $\lambda/2$ waveplate in combination with a polarization depending beamsplitter; an optional *XY*-galvoscanner for fast beam displacement; a focusing optic (in most cases a $100\times$ immersion oil microscope objective with a high numerical aperture); an *XYZ*-stage for the sample movement and placement; and a camera, viewing along the laser beam path for online process observation.

This kind of laboratory setup and the working principle of the components are well described in Serbin et al. [34]. This kind of self-built laboratory setup is commonly used in laboratories doing research on 2PP. They are suitable for scientific research on 2PP, but not for applications requiring large-scale structuring (i.e., industrial applications or industrial-related research). With 2PP laboratory systems, there are in general two structuring possibilities. One is by moving the laser beam with an *XY*-galvoscanner. This has the advantage of high dynamic movement and very precise structuring. But for high resolution structuring, a high-magnification immersion oil objective is necessary, which typically has a viewing field of smaller than $30\times30\,\mu m^2$. So the working field for structuring using a galvoscanner is limited to this size. Furthermore, the sample placement and *z*-positioning still have to be done using a translation stage. The other possibility for high

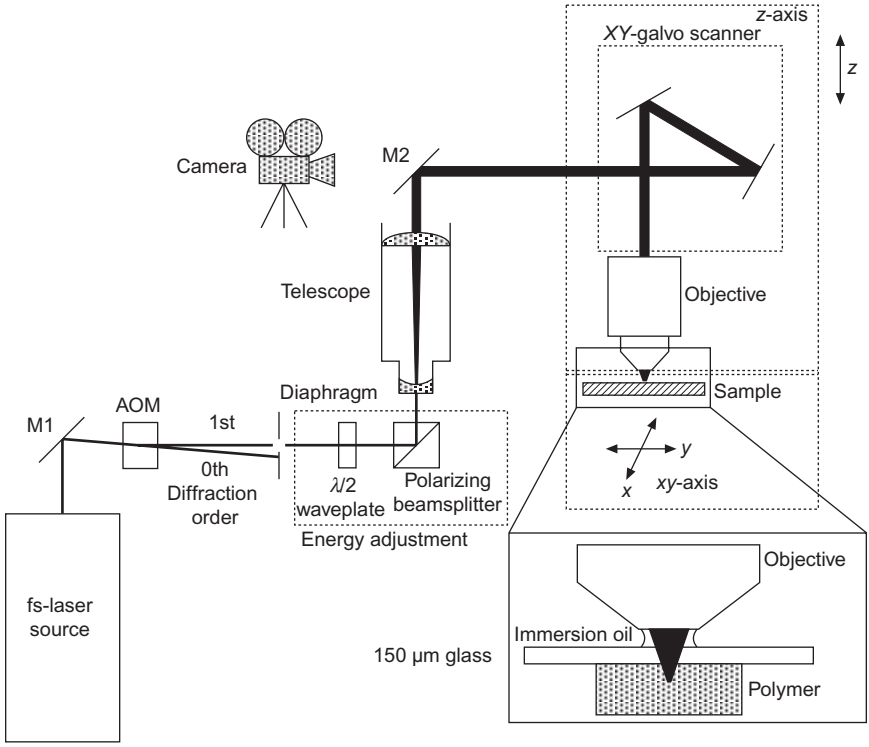
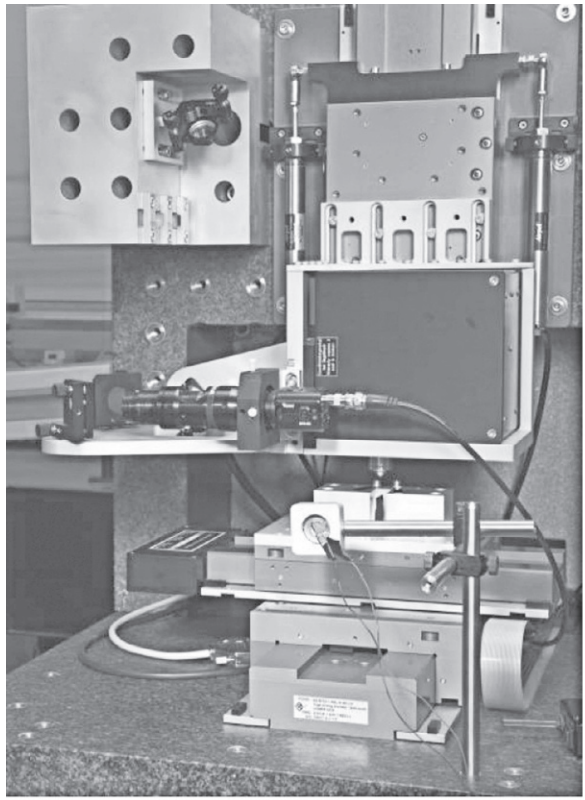


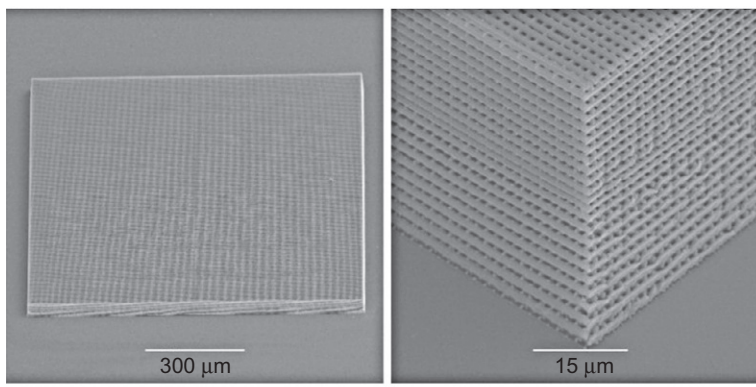
Fig. 20.15 Principal setup for a 2PP system with the fs-laser source, the AOM working as shutter system, the energy adjustment, a beam expander, the camera for online observation, the XY-galvoscanner, the focusing objective, and the sample on the positioning system.

resolution structuring is the use of a piezo-positioning system placed on top of an *XY*-translation stage. These systems provide nanometer-precise positioning of the sample, but are available only with a maximum travel range of $800 \times 800 \times 200\,\mu m^3$. The dynamics of the piezo systems are worse than a galvoscanner, but provide a larger travel range.

Nevertheless, both systems only provide structuring possibilities in very small areas, and need an additional *XYZ*-positioning system for larger travel distances and sample positioning. These kinds of systems are limited to structure sizes smaller than a millimeter. For structures with a resolution smaller than 1 µm, a typical writing speed of 100 µm/s or less is achieved, which is very slow. In order to overcome these drawbacks, the first commercial system for 2PP worldwide has been designed [8]. This system provides a structuring area of $10 \times 15\,cm^2$ with a resolution of sub 100 nm. Very stable and reproducible results are obtained for a resolution of 300 nm (Fig. 20.16).



(A)



(B)

Fig. 20.16 (A) Detail image of the M^3D system for 2PP, (B) SEM images of a face centred cubic photonic woodpile crystal with a period of 2 mm and a ridge width of about 300 nm fabricated with a structuring speed of 30 mm/s. Fabrication time of this structure was 20 min.

Besides the large structuring area, a 2PP fabrication speed of 30 mm/s could be demonstrated for the first time, which is about 300 times higher than other publications present [40]. This unique high-speed structuring opens up the possibility of large-scale three-dimensional structuring with resolutions down to 100 μm. With this high speed and large-scale structuring capability, new possibilities in various fields of applications open up (large-scale wave guiding, microfluidic, biomedicine). Also this decreased fabrication time makes the 2PP fabrication interesting for industrial applications because low-cost high-resolution three-dimensional parts become available.

20.3 MATERIALS FOR MICRO STEREOLITHOGRAPHY AND TWO-PHOTON LASER LITHOGRAPHY

Materials in classical stereolithography are currently suffering from two drawbacks. On one hand, cross-linked photopolymers have low toughness compared to most engineering polymers (e.g., thermoplastic materials such as polypropylene or ABS). On the other hand, the long-term properties of the utilized photopolymers are not sufficient. Photopolymers tend to yellow over time and, due to the tendency to take up water in a humid atmosphere, their mechanical properties degrade over longer periods of time. Although a controlled degradation can be beneficial in the case of applications requiring biodegradable polymers (e.g., tissue engineering), in most RP-applications long-term stable materials are preferred.

The currently targeted main markets for SL-materials lie in the fields of RP and rapid manufacturing, where the focus is on the structural properties of the utilized polymers. There are only a few applications that tap the potential of the functional properties (optical, electrical, biofunctional properties) of photopolymers. If MSL is to succeed, the above-mentioned issues have to be tackled. This section aims to present strategies to overcome material-related problems in lithography-based SFF techniques.

20.3.1 Highly Filled Photopolymers

Regarding the lack of toughness, micro- and nano-sized structures have a distinct advantage. According to the formula

$$\sigma_{fs} = \frac{K_{IC}}{\sqrt{a}} \cdot C$$

the failure strength, σ_{fs}, of a brittle material is determined by the fracture toughness, K_{IC}, of the material and the maximum length, a, of defects inside the material. C is a geometry-dependent constant. The maximum

crack length cannot exceed the part size, which means that micro- and nano-sized parts are inherently stronger than their macro-counterparts. Due to this fact, even very brittle materials like ceramics are an appealing choice as an MSL material. Ceramics offer an additional advantage since they do not suffer from long-term degradation. By using ceramic-filled photopolymers, MSL is capable of fabricating ceramic parts. If the amount of ceramic filler is higher than 42 vol%, the photopolymer can be burned off (debinding) and after further densification of the residual powder (sintering) a fully dense ceramic part can be obtained. Since the photopolymer only serves as an intermediate binder, problems with degradation and yellowing of the polymer are no issue any more. Due to the high stiffness, good corrosion resistance, and interesting optical properties, ceramics are usable in a wide variety of applications in biomedicine and optoelectronics. Since the thermal postprocessing includes a sintering step, care has to be taken to avoid excess shrinkage and warpage of the parts.

In combination with MSL, the challenge is to develop highly filled (45–55 vol% ceramics) resins exhibiting a low viscosity (2–10 Pas). Alumina [41], zirconia [42], and silica [43] have been successfully structured using SL. Problems arise when light-absorbing ceramics like silicon carbide have to be structured. In such cases indirect routes via a sacrificial SFF-mold have to be used [44]. Ceramic example parts (alumina) made by MSL are shown in Fig. 20.17.

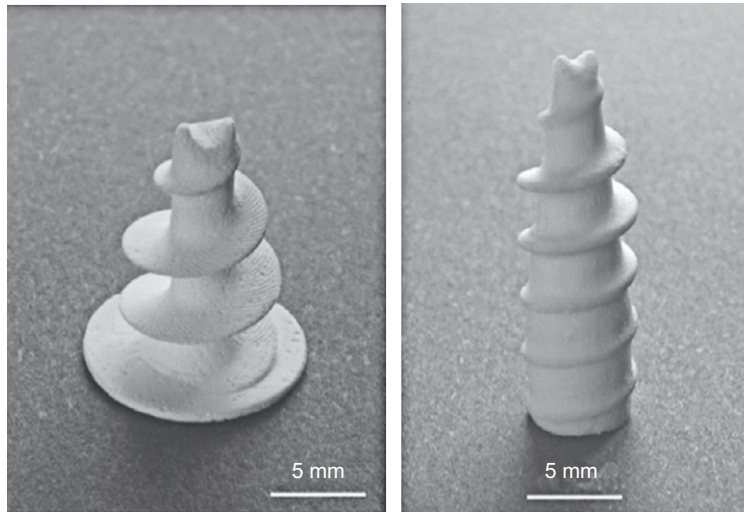


Fig. 20.17 Unsintered (left) and sintered (right) alumina parts made by micro stereo lithography.

20.3.2 Biofunctional Photopolymers

Due to its achievable precision and feature resolution, MSL offers a high potential for fabricating parts that can be used for applications in biomedicine. The possibilities offered by SFF are attractive, especially for the fabrication of tissue engineering scaffolds. In the context of photopolymerization, problems arise due to the fact that many commercially available monomers and initiators are toxic or an irritant. By choosing the appropriate reactive diluents, cross-linkers, and initiators, this problem can be minimized and photopolymers with good biocompatibility could be developed [45–47].

A further challenge is the development of biodegradable photopolymers. Currently used biodegradable SFF materials (e.g., polylactic acid used in fused deposition modeling) suffer from the fact that the degradation products change the pH-value of the local environment, with a potential risk of necrosis of the surrounding tissue. Photopolymers can be made degradable if the cross-linker (e.g., gelatin-acrylate [48]) contains enzymatically or hydrolytically cleavable bonds. If an acrylate-based photopolymer with gelatin as the cross-linker is used, the degradation products contain gelatin and polyacrylic acid (see Fig. 20.18). Currently there are concerns regarding the use of polyacrylic acid for clinical applications, requiring the development of completely new, nonacrylate-based photopolymers. A recently presented strategy [49] is the use of vinylesters instead of acrylates. The degradation products of a vinylester-based photopolymer contain nontoxic polyvinyl-alcohol instead of polyacrylic acid. Polyvinyl-alcohol causes no change in the pH and offers a clear benefit in comparison to currently used thermoplastic materials. Furthermore, the degradation kinetic can easily be tuned by choosing appropriate cross-linkers and varying the cross-link density. The above-mentioned photopolymers are compatible with SL, MSL, and 2PP, offering a new route for the fabrication of high-resolution scaffolds with defined biofunctional properties. Examples made by acrylate- and vinylester-based resins are shown in Fig. 20.19.

One of the main drawbacks of 2PP is the low write speed compared to currently used industrial SL-systems. On one hand, the write speed of 2PP-systems can be increased by using innovative lasers. On the other hand, new 2PP-initiators with improved two-photon cross-sections need to be utilized [50]. Owing to the currently limited productivity of 2PP-lithography, the ideal industrial application is one where the material volume, which has to be polymerized, is fairly small. An application that fulfills this requirement is the fabrication of optical waveguides [51], where 2PP is used to selectively change the refractive index of a material. Owing to total reflection inside the

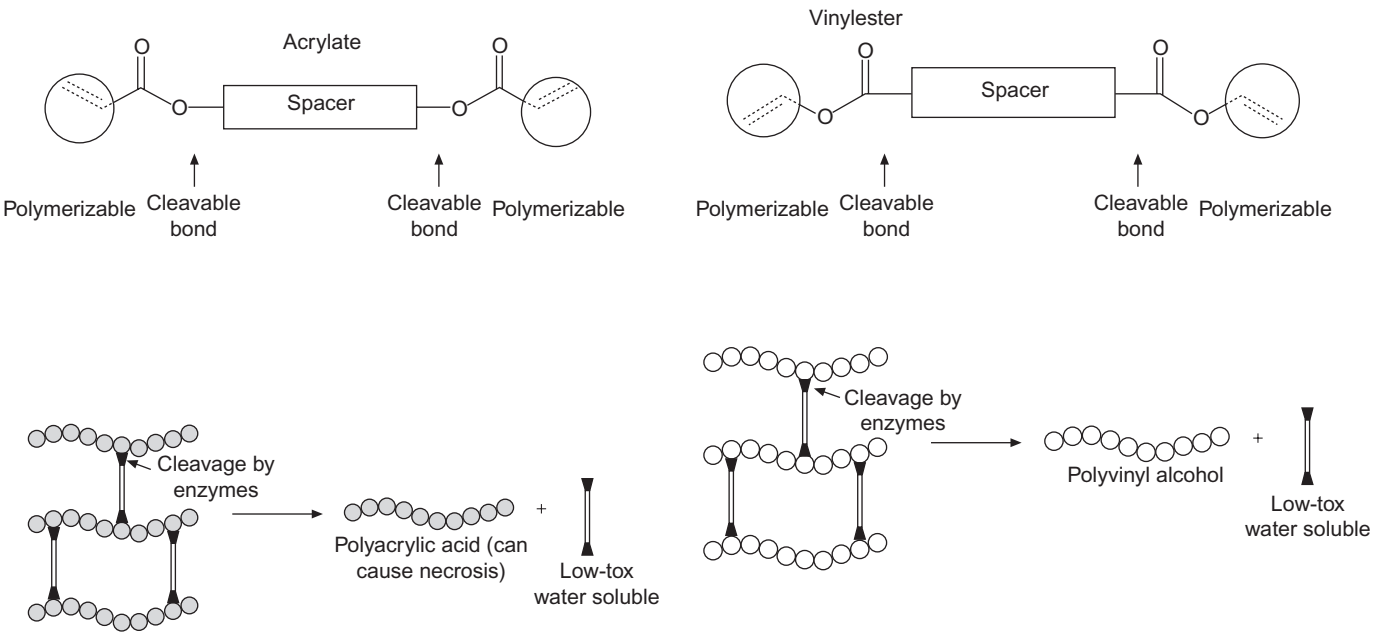


Fig. 20.18 Scheme for the bio-degradation of acrylate-based photopolymers (left) and vinylester-based polymers (right).

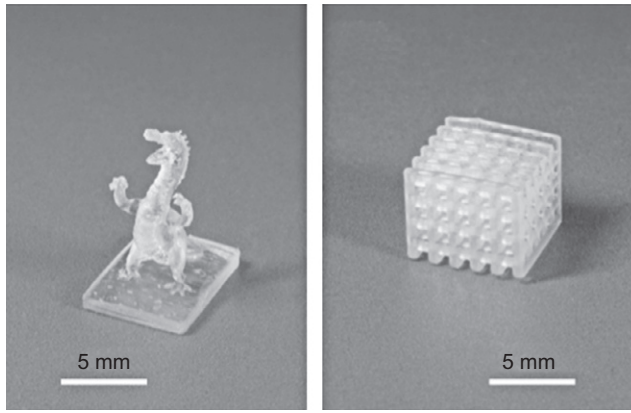


Fig. 20.19 MSL-parts made of acrylate (a) and vinylester (b).

polymerized regions, such a structure can serve as an optical waveguide. 2PP is the ideal fabrication method since the polymerization can take place inside a matrix material. By selectively steering the laser focus, three-dimensional waveguides can be written, even if optoelectronic components (light-emitting diodes, photodiodes, etc.), are embedded within the matrix material.

20.4 MANUFACTURING BASED ON SINTERING, MELTING, AND CLADDING

Laser-ased SFF processes for metallic work pieces in the micrometer scale are the focus of several research groups. Adapting laser sintering, laser melting, and laser cladding processes to achieve higher spatial resolutions and aspect ratios, several process names have come up that are similar or even identical but describe different manufacturing strategies. There are different names for related processes as well. For these reasons, a short overview concerning terms and definitions will be given first in this chapter before the processes are described in detail.

"*Laser sintering*" describes a process in which a powder material that is able to form a liquid phase is treated with laser radiation, leading to surface-fusing of the powder particles [52]. The liquefied material of adjacent particles forms cohesive melted mass areas due to the attempt to reduce the surface of the entire power material system. Cooled below melting point as a result of heat conduction, the particles are connected via the solidified melted mass areas, the so-called "sintering necks." Therefore

the powder material is not totally molten in this process. Variants of this process are selective, direct, and indirect laser sintering. On the one hand, SLS describes a powder bed-based method. Similar to the stereolithography technique, a layer of the builder material, in this case a metal powder, is deposited as a "powder bed" first. In order to form a three-dimensional part, selected areas of the powder bed corresponding to the 3D part's slices are treated with laser radiation. On the other hand, SLS is also used if the metal powder consists of an alloy, wherein at least one component is low fusion melting compared to the alloy partners or shows a much higher absorption of the used laser wavelength. Hence, only this component becomes selectively molten in the laser process, therefore forming the sintering necks between the unmolten particles or phases of particles in case the powder material is made from alloy bulk material.

Indirect laser sintering is a process that uses an additional binder phase. The metal powder particles are coated with a polymer binder first. In the laser process, it is only this binder that is molten. The solidified polymer connects the adjacent metal powder particles to each other. This polymer scaffold is removed in a baking process. Afterwards, the density of the porous metal powder component is increased via infiltration of a low fusion melting metal component. Processes in which at least one component forms a marginal melted material volume are also referred to as liquid phase sintering.

In contrast to this method, direct laser sintering is a process that allows the generation of close-to-production prototypes without the need for baking or densifying steps after the sintering process [3]. The used metal powders are uniphased; an alloy powder consists of atomized alloy melt instead of a mixture of the ratios of the alloy component powders.

Most of the laser sintering processes are so called two-step methods. This means that the powder material is first deposited in the work zone (commonly as a powder bed), followed by the application of laser power to the powder bed. Afterward, the powder bed is lowered by the thickness of one powder layer and a new layer of the powder bed is generated. The two steps are repeated until the workpiece has been fully generated. Laser sintering is not necessarily a two-step process but can be carried out as a single-step process as well. In this case, the powder material is fed simultaneously to the process zone while the laser power is applied. Powder feeding is realized using feeding systems in combination with coaxial or offaxial powder nozzles. In contrast to laser sintering, the characteristic trait of the laser melting processes is the complete melting of the powder material in order to achieve

workpiece densities close to the theoretical density of the material. The laser melting processes described in literature are two-step processes [52].

Laser cladding processes are, in contrast, mostly single-step processes. The definition of laser cladding itself by Toyserkani et al. [53] describes it as a coating process using laser radiation to generate a material connection between the substrate material and the coating material. The coating material is fully molten. Not only powders or wires are used but also pastes and foils, which are predeposited in the process zone. Single-step processes wherein the coating material is fully molten are known as laser forming as well. Summed up, the questions that need to be answered to characterize a laser-based micro SFF process using powder materials are:

- Is it a single-step or a two-step method?
- Is the material partially or fully molten?
- Is the material a uniphase material or does it consist of phases with different properties (melting temperature, wave length absorption)?

In the following sections, examples and detailed descriptions of laser-based SFF methods will be given.

20.4.1 Single-Step Methods

In single-step methods, the material of which the workpiece will consist is fed directly to the work zone while the laser process is running. The feeding can be realized using coaxial or offaxial nozzles. Using an offaxial nozzle, the mounting of the nozzle relative to the feed motion of the workpiece influences the geometry of the generated micro structure. In contrast, when using a well-adjusted coaxial nozzle, the process result does not depend on the feed direction. Fig. 20.20 shows sketches of process setups with a coaxial and an offaxial nozzle. While coaxial nozzles only allow the processing of powders, offaxial nozzles can be used to feed alternative materials, mostly wires. However, in micro processes this advantage is minor because powders are the preferred material as they offer the highest resolution options in the generation of 3D-micro parts.

Initial results of a research project concerning single-step micro laser sintering have been published by Matteazzi et al. [54]. In this process, the filler material is a nanophased iron-copper powder. The experimental setup for the micro sintering process consists of three device groups: the laser beam source and the optical system; the filler material transport and focusing; and all peripheral components. The beam source is a fiber laser, which combines the advantages of low optical degradation of the laser medium in long-term micro sintering processes, an excellent output power stability

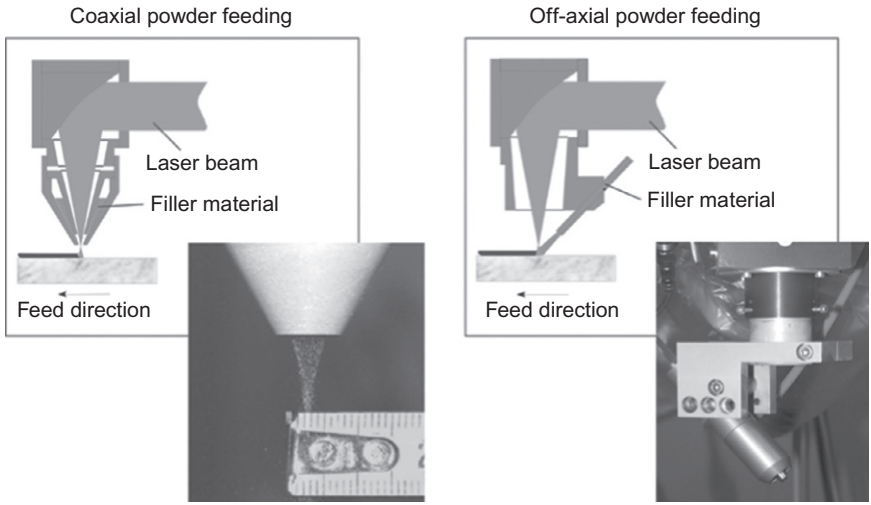


Fig. 20.20 Sketches of a process set-up with a coaxial and an off-axial nozzle.

and scalability, and the beam quality ($M^2 = 1.05$). To achieve both a small beam waist diameter and a sufficient distance to the process zone in order to allow the mounting of the powder nozzle, high-aperture laser objectives with diminished spherical aberration focus the beam in the work plane. Furthermore, a temperature control unit is installed, which enables the temperature measurement in the work zone and respectively the adaptation of the laser output power. The heat radiation emitted from the laser–material interaction zone is detected by a two-color quotient pyrometer and transformed into temperature information. The analogous signal is interpreted by the process control software TemCon, which allows real-time control operation, such as the adaptation of the laser power to achieve a preset temperature in the work zone.

Regarding the second device component group, a powder feeder was designed meeting the demands of minimum mass feeding of small powder particles. Owing to the increased surface ratio and therefore adhesion between powder particles and respectively the decreased floatability of small-particle powders, there is the danger of agglomeration forming and adhesion to feeder components. This would make a constant mass flow and particle speed at the spray hole impossible. To overcome these difficulties, a hybrid feeding technology has been developed, combining a mechanical feed principle with stimulation of feeder components via ultrasonics. Furthermore, coaxial nozzles showing different injection angles in order to modify the diameter of the powder focus and the focal

length (distance form spray hole to the work plane) have been developed. Within the peripheral component group, a heatable substrate holder and a shielding gas chamber account for an improvement of the micro sintering results. The substrate holder can be heated in a range from 50 to 400°C.

Sintering onto a heated substrate avoids chipping off gracile part areas and cracks within the sintered structures. Owing to the increased surface ratio in small powders, higher oxygen absorption is anticipated at elevated temperatures in the process. Therefore materials showing a high affinity for oxygen combined with a loss of certain properties have to be processed under a shielding gas atmosphere. A system of two combined protection chambers, an inner and an outer one, has been developed. The oxygen content at the process zone is measured during the process and can be kept below 30 ppm. Using this experimental setup, micro parts with a spatial resolution of 25 µm could be generated. The process temperature was adjusted to 1100°C, leading to a partial melting of the copper phase. This therefore induced liquid phase sintering but at the same time left a part of the particles unmolten, therefore keeping their original nanophased inner structure. An SEM image of a micro sintered punch and its cross section are shown in Fig. 20.21. Further experiments have been carried out regarding the adaptation of the process to a broader variety of materials, including single-phase metallic materials for micro cladding processes, such as 1.4404 steel powders. Moreover, an optical distance sensor has been added to the setup to control the built-up material volume. The TemCon software has been expanded to allow the adaptation of the preset temperature in critical regions of a micro workpiece, for example to enable the activation of the laser at a low output power combined with an adapted increase of power

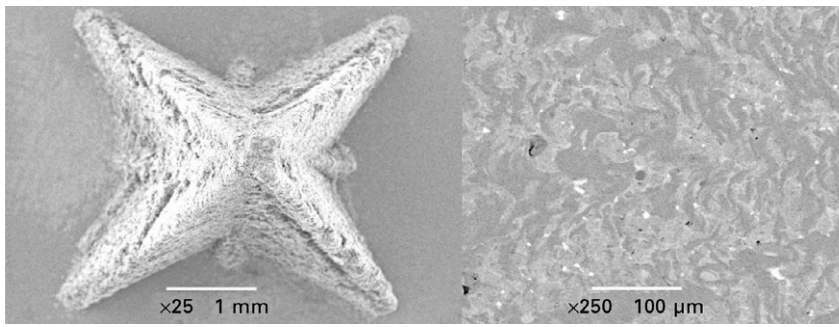


Fig. 20.21 Micro sintered punch (left) and cross-section of the punch showing iron and copper phases (right).

in a defined time frame. By doing so, imperfections at the beginning of a sintering/cladding track can be avoided.

Fig. 20.22 shows the latest results in single-step metal SFF. In the cladding process, micro structures with nearly theoretical density can be generated (no visible pores in the cross-section). Single cladding tracks show a minimum width of less than 30 µm. Details of the latest research results are described in Meier et al. [55] and Mewes [56].

Albert et al. published results on an experimental series concerning the setup of a hybrid micro machining process, consisting of a micro laser cladding process and an adjacent micro milling process to finish the micro cladded structures [57]. This process was designed to guarantee a constant quality of molded parts in plastics injection molding, since homogeneous heat dissipation is of vital importance. To achieve optimized heat dissipation in micro plastics injection molding tools, the aim is to apply highly thermal conductive layers to selective parts of the mold tool. Therefore, micro cladding of copper-steel powder mixtures, pure copper powders, and tool steel has been investigated. The experimental setup consists of an Yb:YAG laser source, combined with a coaxial powder nozzle mounted to a CNC handling system. The developed powder feeding system allows the processing of powders in a particle scale from 1 to 50 µm. Moreover, a prototype version of a pyrometer-based control circuit for the adaptation of the laser powder has been set up. Single cladding tracks with a width below 200 µm could be generated. Research on micro cladding has been carried out by Jambor et al. as well [58,59]. The experiments aim at structure sizes (track

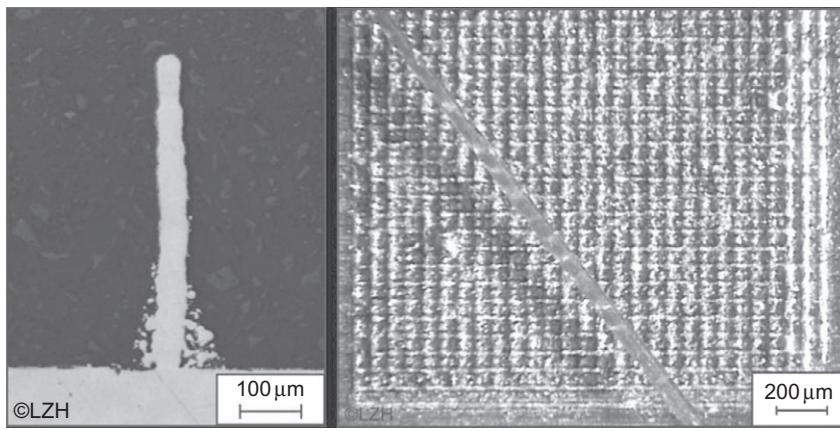


Fig. 20.22 Cross-section of a micro laser cladded wall structure (left) and single micro laser cladded tracks in comparison to a blond human hair.

width) between 20 and 100 µm realized via a powder injection through a coaxial nozzle. In the setup developed by Jambor, a shielding gas flow of argon and helium, respectively, prevents the material in the process zone from oxidization, keeping the content below 20 ppm.

The laser source is a single mode fiber laser with an output power range from 10 to 200 W. Using lenses of 200 mm focal length, the focus diameter in the work zone is of the order of 60 µm. As part of this research work, a powder feeding system including a coaxial nozzle has been developed as well. Both components were adapted to accommodate fine powders with particle diameters below 15 µm, realizing feed amounts of less than 0.2 g/min with gas flows smaller than 3 L/min. The diameter of the resulting powder focus is reported to strongly depend on the powder material, the quality of the coaxial nozzle, the gas volume used for transport of the particles, and the coaxial shielding gas stream. As reported by Becker et al. [60,61], the quality of the powder feeding limits the entire micro cladding process as inhomogenities in the powder stream lead to defects in the generated structures. The smallest powder focus diameter achieved by Jambor et al. was about 200 µm using a 316 L powder with particle sizes between 1 and 8 µm. The experimental setup contains a CCD camera allowing the observation of the powder focus in the inset. In experimental series with the mentioned filler material, single tracks with a width of 45 µm and a height of 10 µm could be generated. Overlapping the tracks, closed cladding surfaces can be achieved as well. Adapting the laser power to reduced heat dissipation in thin-walled structures, a bar made of a cobalt alloy with an aspect ratio of 10 (90 µm wide, 900 µm high) could be laser micro cladded. Summing up the presented research activities on single-step laser-based micro SFF processes, the generation of single tracks with a width smaller than 100 µm is possible. A variety of materials can be processed (see Section 20.3). The limiting factor of single-step processes so far is the powder feeding. Several feeding principles have been investigated by the named groups describing the investigation of feeding behavior of small powder particles as the main task in single-step processing. Powder feeding and focusing have been adapted to the demands of fine powders. Nevertheless, to fulfill serial production requirements, process stability still has to be improved. In order to increase the power efficiency and therefore to decrease the process costs, the powder focus diameter will have to be reduced further.

20.4.2 Two-Step Methods

Two-step laser sintering and melting is a well-established and commercialized method in RP and rapid tooling. The production technology and

machine systems are available for polymer materials as well as for metals and even mold sands [62–65]. While the smallest achievable width of single tracks in commercial applications is limited to orders of 150 µm, several research groups achieved an adaptation of the process technology to generate smaller workpieces with higher resolution. A higher resolution necessitates the use of powders with smaller particles. Due to the fact that the surface of all powder particles of a powder bed increases with decreasing diameter of the particles with the ratio $r1/r2$ (for $r2 < r1$), all surface size-dependent adhesive powers as well as hygroscopicity increase in the same order of magnitude, leading to a restricted flowability of the powders. The application of a powder bed using wiper techniques similar to those in commercial machine systems is therefore hardly possible. Powder agglomerates are formed at the wiping knife causing defects in the powder bed. To overcome these limitations, Matteazzi et al. [54] describe a powder storage and application system consisting of counter-rotating rollers (Fig. 20.23). From the reservoir, the powder is fed into the gap between two rollers, where it is compressed and laid onto the working plane as a precompacted powder layer [66].

Owing to the increased hygroscopicity, the process technique is integrated into a heatable vacuum chamber in order to dry the powders in storage and process and therefore to minimize the risk of powder agglomerates sticking to the rollers. Furthermore, the contamination of powders with oxygen, nitrogen, or hydrogen is reduced in the process. Using this experimental setup in combination with an Yb:YAG fiber laser, titanium and titanium alloys, iron-based alloys, silver, copper, gold, and tungsten-carbide-cobalt powders with $d_{50} < 20$ µm can be laser sintered and melted,

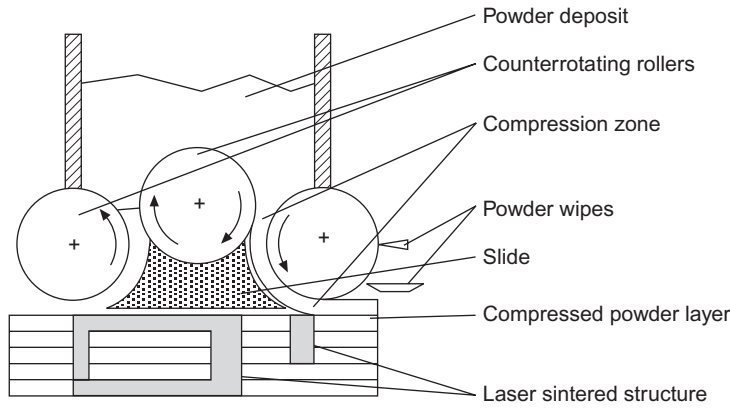


Fig. 20.23 Counterrotating roller mechanism for deposition of compressed powder layers.

respectively, to nearly 100% dense structures. In the latest experiments, the setup has been modified to allow the micro laser melting of nickel-titanium shape memory alloy powders. In order to preserve the one-way shape memory effect and therefore to keep impurities out of the process zone, the vacuum chamber was rebuilt to keep a high-vacuum atmosphere. An ultrasonic oscillator was added to the powder application system, allowing the powder bed preparation from NiTi powders <15 µm down to submicrometer range.

At Fraunhofer ILT, the selective laser melting (SLM) process has successfully been modified into a micro SLM process. An existing machine system built by Trumpf has been adapted to the requirements of a micro SFF process. There are two process chambers in the system, which can be argon-shielded and preheated to 500°C. In its original status, there is a 250W Nd:YAG laser system included that can be focused to a beam waist diameter of 200 µm. With this setup, structures with a minimum layer thicknesses of 30–100 µm, showing the smallest structure parts of 500 µm in width, could be generated, whereas these structures show nearly theoretical density and the expected mechanical properties. To allow the generation of micro parts, the intention was to reduce the melt pool volume. For that purpose, the laser and optics system has been rebuilt in order to decrease the beam waist diameter. At the same time, the original powder bed size and the achievable layer thickness of 30 µm should be retained to allow the generation of numerous or large workpieces showing micro structured areas at adequate buildup rates. To fulfill these boundary conditions, a fiber laser system was chosen. A beam expander was added to the optical system, enabling entry to the galvanoscanner unit at maximum aperture and therefore focusing the beam to the smallest possible beam waist of 70 µm using the original scanner and focusing optics setup. With an optimized scanning strategy, 100 µm wide titanium and stainless steel wall structures could be generated. The described adapted machine concept allows the generation of macro workpieces with micro structure details. An example is the generation of micro cooling units. Up to 70 cooling devices can be generated in the powder bed due to its retained size from the macro setup. The building time for a single workpiece is on the order of 10 min. The micro channels, respectively the separating plates (100 µm wide), are generated via the micro melting strategy. Fig. 20.24 shows laser micro melted parts.

Exner et al. [67,68] present a micro SFF process called laser micro sintering (LMS), which was developed as a modification of SLS in

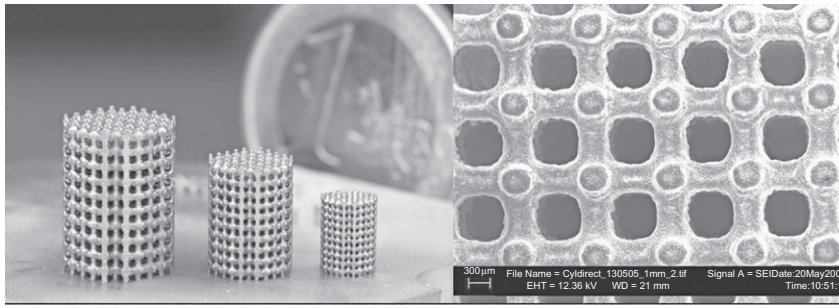


Fig. 20.24 Laser micro melted parts (left picture) and a detailed top view of the substructure.

2001/2002. The process varies from the described methods mainly in the laser source, as a q-switched laser system emitting 10–1000 ns pulses is used in the LMS process. Regenfuss et al. [69] present the following model for the q-switched micro sintering. The irradiated material is heated by the laser pulse. Exhausting vapor and possibly shielding gas form plasma. The plasma bulb expands rapidly, exerting pressure on the adjacent material, resulting in an overheated melt pool without boiling effects and a downward directed force onto the melt due to the increased pressure. The described mechanism is called the "condensing effect" of the laser pulse upon the powder layer. Expiration of the laser pulse and/or an exhaustive expansion of the plasma bulb cause a pressure breakdown, allowing spontaneous incidents of boiling in combination with rapid expulsion of solitary drops. Moreover, subsequent formations of slower jets can be observed which separate into droplets or collapse before solidification. As a result of the high cooling in the process zone, the molten material solidifies before spherical droplets are formed from the liquid material. Therefore, the so-called "balling effect" is inhibited in this process. The pulse frequency is varied between 5 and 100 kHz. Due to the reduced optical and thermal penetration depth, the applied powder layers may not exceed a certain thickness. Therefore, a ring rake system was developed, which allows the generation of powder layers in single-figure micrometer range. Fig. 20.23 shows an integrated micro turbine into a housing fabricated via the LMS process and its cross-section. The turbine is made of a stainless steel powder. The machine setup for the process is shown on the right of Fig. 20.25.

The structure resolution of this process is limited to 30 µm with a density of the sintered parts in order from 40% to 75%.

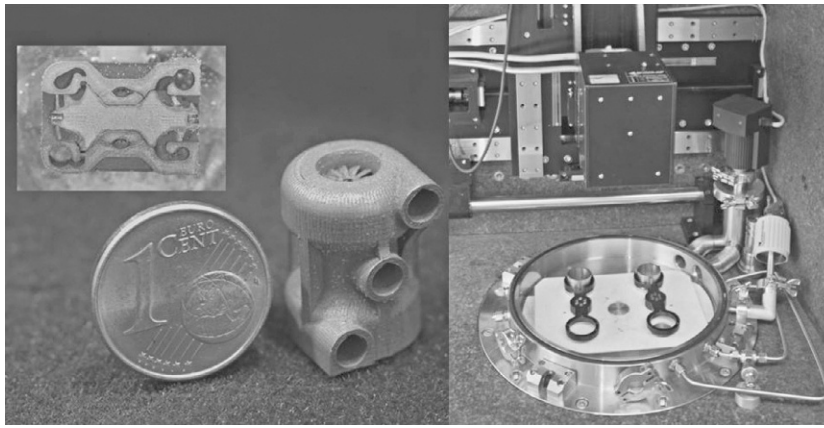


Fig. 20.25 Micro turbine made of stainless steel powder (A. Streek, Hochschule Mittweida), and the machine set-up for the "laser micro sintering" process.

20.5 MATERIALS FOR MICRO SINTERING, MELTING, AND CLADDING

In theory, all powder materials that form a liquid phase as a consequence of laser treatment can be processed in laser sintering, melting, and cladding. However, as described by Becker et al. [61], the feeding behavior of powders, especially the reproducibility and homogeneity of powder deposition, plays a major role regarding the process ability of powder materials regarding laser-based micro SFF processes. It is well known that the particle size of the powders is a limiting factor concerning the resulting part resolution. Therefore, the aim is to allow the processing of fine-grained powder fractions. The challenge in doing so is the fact that the flowability of powder materials, on which the powder feeding concepts for macro SFF processes are based, is strongly reduced for decreased powder particle sizes (see Section 20.3.2). For this reason, it is mainly the feeding technique that determines the suitability of a powder material for micro laser SFF processes. Fine-grained powder fractions can be produced via gas atomization or via milling techniques. In gas atomization, the so-called nanoval process [70] is used to produce small particle fractions of spherical powders in a narrow particle size distribution. Mechanomade powders are manufactured in a high-energy milling process. Powders of this production route are not spherical but show an irregular shape. Comparing gas atomization and the mechanomade production route, the milling process shows a higher rate of yield regarding particles of a medium size, $<20\,\mu m$, as the particle size can be influenced by variation of the milling time. Gas atomized powders

are usually subdivided into different particle size distributions via sieving, whereas the fraction of particles <25 µm often contains the smallest particles in submicrometer-range as well. Therefore, the advantage is that these powder fractions, containing a wide range of particle sizes (multimodal powders), can be compacted to form a highly dense powder bed (density up to 96%), as smaller particles fill the interspace of bigger ones. The maximum powder bed density of powders of a comparable particle size fraction generated by milling is usually lower due to the fact that no geometrically dense sphere package can be achieved but the irregular shaped particles cramp and form larger interspaces. However, the milling process offers the advantage that the material does not need to be transformed to its liquid phase to form powders, resulting in comparably low impurity contents, especially for materials showing an enhanced affinity for oxygen or nitrogen. Examples for a gas atomized powder and a milled powder are given in Fig. 20.26.

In both manufacturing routes, a broad variety of materials can be reworked to powdery material. Stainless steel and tool steel powders, such as from 1.4404, 1.2343, or 1.2709 materials, are available as small fraction sized gas atomized powders. Common alloys used in dental technology as well as pure noble metals, titanium, and titanium alloys can be processed, too. In addition to iron-based and titanium-based alloys, hard metals and so-called "cermets" can be pulverized in high-energy milling as well. The definite composition of powder materials for micro laser SFF processes is usually kept confident, as comparatively small variations in the composition can cause essential differences regarding laser process ability.

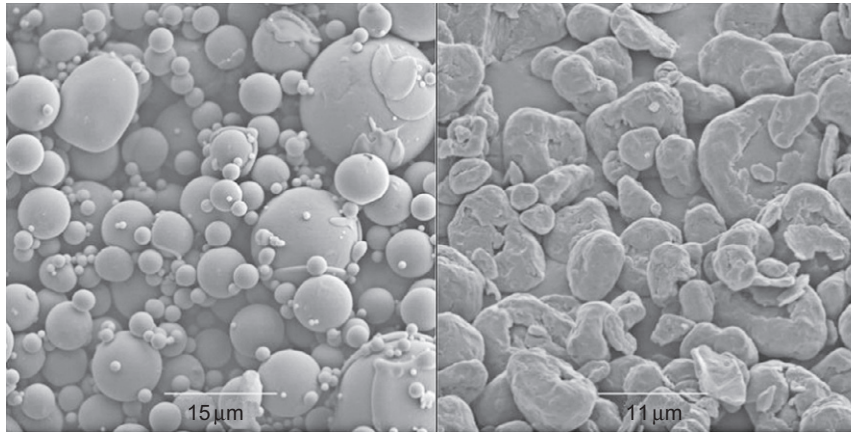


Fig. 20.26 Powder samples manufactured via gas atomization (left) and high-energy milling (right).

20.6 CONCLUSIONS

This present chapter gives an overview of the wide field of laser-based micro SFF using polymers as well as ceramic and metallic materials. Micro SFF is capable of fabricating high precision parts that cannot be produced by macroscale additive manufacturing or any other conventional machining technology. After being introduced a couple of years ago by different research groups, and mainly for demonstration purposes only, new advances in micro SFF now allow for the start of commercial business. Especially due to new and more reliable machine and process technology, but also due to the broader range of applicable materials, technical challenges may be solved using micro SFF. Applications can not only be found in classical sectors such as micromechnical or microfluidic, but also in the medical industry for implants.

The choice of the fabrication technology depends on the application and the desired part properties, regarding material properties and requested precision. Polymer-based components are still the more precise ones, while the metal-based show enhanced stability. Another innovative approach in micro SFF is the use of ceramic fillers inside light curable polymers, offering the manufacturing of highly dense ceramic parts via MSL.

REFERENCES

[1] A. Gebhardt, Generative Fertigungsverfahren, Hanser, Munich (Germany), 2007.
[2] P.F. Jacobs, Stereolithography and Other RP&M Technologies, RPA SME, ASME Press, Dearborn/ Michigan, New York/New York (USA), 1996.
[3] P.K. Venuvinod, W. Ma, Rapid Prototyping-Laser-Based and Other Technologies, Kluwer Academic Publisher, Boston/Dodrecht/London, 2004.
[4] T. Wohlers, Wohlers Report 2007, Wohlers Associates, Fort Collins/Colorado (USA), 2007.
[5] P.F. Jacobs, Rapid Prototyping and Manufacturing, Fundamentals of Stereolithography, CASA SME, Dearborn/Michigan (USA), 1992.
[6] A. Bertsch, S. Jiguet, P. Bernhard, P. Renaud, Microstereolithography: a review, in: Proc. of. Mat. Res. Soc. Sym., Boston/Massachusetts (USA), 2003, pp. 3–15.
[7] V.K. Varadan, X. Jian, V.V. Varadan, Microstereolithography and Other Fabrication Techniques for 3D MEMS, Wiley, Chichester (UK), 2001.
[8] A. Ostendorf, B. Chichkov, Two-photon polymerization: a new approach to micromachining, Photonics Spectra (2006) 72–80.
[9] K. Ikuta, S. Maruo, S. Kojima, New micro stereo lithography for freely movable 3D micro structure, Super-IH process with submicro resolution, in: Proc. of IEEE-MEMS, Heidelberg (Germany), 1998, pp. 290–295.
[10] K. Ikuta, K. Hirowatari, Real three dimensional micro fabrication using stereo lithography and metal molding, in: Proc. of IEEE-MEMS, Fort Lauderdale/Florida (USA), 1993, pp. 42–47.
[11] T. Takagi, N. Nakajima, Photoforming applied to fine machining, in: Proc. of Micro Machine and Human Science Symp., Nagoya (Japan), 1993, pp. 173–178.

[12] L. Beluze, A. Bertsch, P. Renaud, Microstereolithography: a new process to build complex 3D objects, in: Proc. of SPIE, Paris (France), 3680, 1999, pp. 808–817.
[13] M. Farsari, F. Claret-Tournier, S. Huang, C.R. Chatwin, D.M. Budgett, P.M. Birch, R.D.C. Young, J.D. Richardson, A novel high-accuracy microstereolithography method employing an adaptive electro-optic mask, J. Mater. Process. Technol. 107 (2000) 167–172.
[14] A.S. Limaye, D.W. Rosen, Process planning method for mask projection micro stereolithography, Rapid Prototyp. J. 13 (2) (2007) 76–84.
[15] S. Monneret, H. Le Gall, V. Badé, F. Devaux, A. Mosset, E. Lantz, Dynamic UV microstereolithography, Eur. Phys. J. AP 20 (2001) 213–218.
[16] A. Neumeister, R. Himmelhuber, T. Temme, U. Stute, Generation of micro mechanical systems using stereolithography, in: Proc. of SFF Sym., Austin/Texas (USA), 2006, pp. 12–24.
[17] X. Zhang, X.N. Jiang, C. Sun, Micro-stereolithography for MEMS, in: Proc. of ASME-MEMS, Anaheim/California (USA), 66, 1998, pp. 3–9.
[18] S. Zissi, A. Bertsch, S. Ballandras, S. Corbel, J.Y. Jezequel, C. Belin, D.J. Lougnot, J.C. Andre, Limites de la stéreolithographie pour des applications microtechniques, in: Proc. of Assises Européennes du Prototypage Rapide, Paris (France), 19, 1994 (French language).
[19] M. Schuster, C. Turecek, J. Stampfl, F. Varga, R. Liska, Biofunctional photopolymers for micro stereolithography', in: Proc. of LPM, Vienna (Austria), 2007.
[20] K. Ikuta, T. Ogata, M. Tsubio, S. Kojima, Development of mass productive micro stereo lithography (Mass-IH process), in: Proc. of IEEE-MEMS, San Diego/California (USA), 1996, pp. 301–306.
[21] S. Maruo, K. Ikuta, Three-dimensional microfabrication by use of single-photon-absorbed polymerization, Appl. Phys. Lett. 76 (19) (2000) 2656–2658.
[22] A. Bertsch, S. Zissi, J.Y. Jézéquel, S. Corbel, J.C. André, Nouveau procédé de microstereolithographie utilisant des filtrages dynamiques, in: Proc. of Assises Européennes du Prototypage Rapide, Paris (France), 12, 1995 (French language).
[23] V. Loubère, S. Monneret, S. Corbel, Microstereolithography using a liquid crystal display as dynamic mask generator, in: Proc. of Mechantronics, Kitakyushu (Japan), 1998, pp. 160–163.
[24] A. Bertsch, H. Lorenz, P. Renaud, 3D microfabrication by combining microstereolithographyand thick resist UV lithography, Sensors Actuat. 73 (1999) 14–23.
[25] A. Bertsch, B. Paul, C. Vogt, P. Renaud, Rapid prototyping of small size objects, Rapid Prototyp. J. 6 (4) (2000) 259–266.
[26] W. Tan, I. Gibson, Numerical study on the recoating process in microstereolithography, in: Proc. of SFF Sym., Austin/Texas (USA), 2005, pp. 50–59.
[27] A. Neumeister, R. Himmelhuber, C. Materlik, T. Temme, A. Ostendorf, Process accuracy during laser-based stereo lithography and production of Ormocer® micro systems with related mechanical properties', in: Proc. of VRAP, Leiria (Portugal), 2007, pp. 501–507.
[28] A. Neumeister, R. Himmelhuber, C. Materlik, T. Temme, F. Pape, Gatzen, A. Ostendorf, Properties of three-dimensional precision objects fabricated by using laser-based micro stereo lithography, J. Laser Micro/Nanoeng. 3 (2) (2008) 63–66.
[29] M.H. Luxner, J. Stampfl, H.E. Pettermann, Numerical simulations of 3D open cell structures—influence of structural irregularities on elasto-plasticity and deformation localization, Int. J. Solids Struct. 44 (2007) 2990–3003.
[30] M. Göppert-Mayer, Über Elementarakte mit zwei Quantensprüngen, Ann. Phys. 9 (1931) 273–294 (German language).
[31] W. Kaiser, C. Garret, Two-photon excitation in CaF_2: Eu^{2+}, Phys. Rev. Lett. 7 (1961) 229–231.

[32] S. Maruo, O. Nakamura, S. Kawata, Three dimensional microfabrication with two photon absorbed photopolymerization, Opt. Lett. 22 (1997) 2.
[33] S. Kawata, H.-B. Sun, T. Tianaka, K. Takada, Finer features for functional microdevices, Nature 412 (2001) 697–698.
[34] J. Serbin, A. Egbert, A. Ostendorf, B. Chichkov, R. Houbertz, G. Domann, J. Schulz, C. Cronauer, L. Frohlich, M. Popall, Femtosecond laser-induced two-photon polymerization of inorganic-organic hybrid materials for applications in photonics, Opt. Lett. 28 (2003) 301–303.
[35] S. Passinger, A. Ovsianikov, A. Ostendorf, B. Chichkov, Two-photon polymerisation: technique and system, Laser User 51 (2007) 44–45.
[36] S. Maruo, K. Ikuta, H. Korogi, Submicron manipulation tools driven by light in a liquid, Appl. Phys. Lett. 82 (2003) 133–135.
[37] S. Maruo, H. Inoue, Optically driven micropump produced by three-dimensional two-photon microfabrication, Appl. Phys. Lett. 89 (2006) 144101.
[38] D. Tan, Y. Li, F. Qi, H. Yang, Q. Gong, X. Gong, X. Duan, Reduction in feature size of two-photon polymerization using SCR500, Appl. Phys. Lett. 90 (2007).
[39] W. Haske, V. Chen, J. Hales, W. Dong, S. Barlow, Perry J. Marder, 65 nm feature sizes using visible wavelength 3-D multiphoton lithography, Opt. Express 15 (2007) 3426–3436.
[40] S. Passinger, Two-photon-polymerization and application to surface plasmon polaritions, PhD Thesis, University of Hanover, 2008, ISBN 978-3-86727-662-7.
[41] C. Hinczewski, S. Corbel, T. Chartier, Stereolithography for the fabrication of ceramic three-dimensional parts, Rapid Prototyp. J. 4 (3) (1998) 104–111.
[42] Y. Abouliatim, T. Chartier, C. Chaput, C. Delage, Fabrication of ceramics by stereolithography, RTe journal 4 (2007).
[43] C.E. Corcione, A. Greco, F. Montagna, A. Licciulli, A. Maffezzoli, Silica moulds built by stereolithography, J. Mater. Sci. 40 (18) (2005) 4899–4904.
[44] J. Homa, S. Zellhofer, J. Stampfl, Novel fabrication technique for ceramic filters, in: Proc. of ECERS, Berlin (Germany), 2007.
[45] B. Dhariwala, E. Hunt, T. Boland, Rapid prototyping of tissue-engineering constructs using photopolymerizable hydrogels and stereolithography, Tissue Eng. 10 (2004) 1316–1322.
[46] M. Schuster, C. Turecek, B. Kaiser, J. Stampfl, R. Liska, F. Varga, Evaluation of biocompatible photopolymers I: photoreactivity and mechanical properties of reactive diluents, J. Macromol. Sci. A Pure Appl. Chem. 44 (5) (2007) 547–557.
[47] M. Schuster, C. Turecek, A. Mateos, J. Stampfl, R. Liska, F. Varga, Evaluation of biocompatible photopolymers II: further reactive diluents, Monatsh. Chem. 138 (4) (2007) 261–268.
[48] M. Schuster, C. Turecek, F. Varga, H. Lichtenegger, J. Stampfl, R. Liska, 3D-shaping of biodegradable photopolymers for hard tissue replacement, Appl. Surf. Sci. 245 (2007) 1131–1134.
[49] R. Liska, M. Schuster, C. Heller, S. Baudis, N. Pucher, C. Turecek, V. Schmidt, H. Bergmeister, J. Stampfl, F. Varga, G. Weigel, New concepts of biocompatible and biodegradable photopolymers', in: Proc. of Medical Coatings and Adhesives, Berlin (Germany), 2008, pp. 117–127.
[50] C. Heller, N. Pucher, B. Seidl, L. Kuna, V. Satzinger, V. Schmidt, H. Lichtenegger, J. Stampfl, R. Liska, One- and two-photon activity of cross-conjugated photoinitiators with bathochromic shift, J. Polym. Sci. A Polym. Chem. 45 (2007) 3280–3291.
[51] R. Inführ, N. Pucher, C. Heller, H. Lichtenegger, R. Liska, V. Schmidt, L. Kuna, A. Haase, J. Stampfl, Functional polymers by two-photon 3D lithography, Appl. Surf. Sci. 254 (4) (2007) 836–840.
[52] A. Gebhardt, Rapid Prototyping, Hanser, Munich (Germany), 2003.

[53] E. Toyserkani, A. Khajepour, S. Corbin, Laser Cladding, CRC Press, Boca Raton/Florida (USA), 2004.
[54] P. Matteazzi, S. Czerner, H. Becker, P. Stippler, A. Ostendorf, Direct laser micro sintering using nanophased microscale powders, in: Proc. of Euro-u-Rapid, Leipzig (Germany), A1/4, 2005.
[55] O. Meier, H. Mewes, S. Czerner, S. Dudziak, Direct laser micro cladding with nano-phased powders, Proc. LANE 887–898 (2007).
[56] H. Mewes, Einstufiges Mikrolasersintern mit höchster Bauteilauflösung, Laser Mag. 2 (2008) 11–12 (German language).
[57] F. Albert, Laserauftragsschweißen für die Oberflächenvergütung von Mikrospritzguss-werkzeugen, Laser Mag. 1 (2008) 20.
[58] T. Jambor, K. Wissenbach, Micro-laser-cladding with high quality fibre lasers, in: Proc. of LIM, Munich (Germany, 2007, pp. 193–197.
[59] T. Jambor, K. Wissenbach, Micro-cladding with a fibre laser, Laser User 51 (2008) 38–40.
[60] H. Becker, S. Stippler, S. Czerner, A. Ostendorf, P. Matteazzi, Gradient components mady by micro sintering in combination with micro scale nano phased powders, in: Proc. of LPM, Williamsburg (USA), 2005, pp. 196–200.
[61] H. Becker, A. Ostendorf, P. Stippler, P. Matteazzi, Laser micro fabrication, in: Proc. of LIM, Munich (Germany), 2005, pp. 849–853.
[62] 3DSystems, 2008, http://www.3dsystems.com, 3D Systems Corporation.
[63] Concept, 2008, http://www.concept-laser.de, Concept Laser GmbH.
[64] EOS, 2008, http://www.eos.de, EOS GmbH.
[65] MCPHEK, 2008, http://www.mcp-group.de, MCP-HEK Tooling GmbH.
[66] GEPLZH, German Patent DE10053539, *Einrichtung zum Aufbringen eines pulverförmigen Materials auf eine Oberfläche,* Laser Zentrum Hannover e.V., Yb:YAG disc laser and role-based powder deposition for the micro-laser sintering, J. Mater. Process. Technol. 149 (1–3) (2007) 623–626.
[67] H. Exner, Lasermikrosintern—neuartiges Rapid Prototyping, Werkstofftech. SMM 8 (2007) 39–140 (German language).
[68] P. Regenfuss, A. Streek, L. Hartwig, S. Klötzer, T. Brabant, M. Horn, F. Ullmann, R. Ebert, H. Exner, Material depending mechanisms in laser micro sintering, Proc. LANE (2007) 403–418.
[69] P. Regenfuss, R. Ebert, H. Exner, Laser micro sintering, a versatile instrument for the generation of microparts, Laser Tech. J. 1 (2007) 26–31.
[70] Nanoval, 2008, http://www.nanoval.de/verfahren_de.htm.

FURTHER READING

[1] MBN, http://www.mbn.it/mechanomade.htm, 2008.

This page intentionally left blank

CHAPTER 21

Laser-Assisted Additive Fabrication of Micro-Sized Coatings

R.M. Mahamood[*,†], **E.T. Akinlabi**[*]
[*]University of Johannesburg, Auckland Park Kingsway Campus, Johannesburg, South Africa
[†]University of Ilorin, Ilorin, Nigeria

21.1 INTRODUCTION

LASER is an acronym that describes the process of a laser. The full meaning of LASER is Light Amplification by Simulated Emission of Radiation [1]. LASER is generated from a light source that is then amplified and controlled with the characteristic single wavelength that is known as monochromaticity, coherency (or same phase position), and low divergence (it spreads out in parallel lines) [1]. All these characteristics have made the intensity of the laser beam to be very high when compared to other light sources, thereby concentrating all the intensity of this beam of light at the needed point of interest. These important characteristics of LASER are responsible for their application in different areas of human endeavor. The use of LASER in engineering especially in material processing has been phenomenal. It has made a number of things possible that were not achievable in the past. An example of a technology that now use LASER effectively is additive manufacturing technology.

Additive manufacturing (AM) technology is an advanced manufacturing technology that has promised to revolutionize the manufacturing industry [2]. Additive manufacturing technology is a name that is used by the ASTM international F42 committee on additive manufacturing standard to describe the group of technologies that build three dimensional (3D) objects by adding materials layer by layer from computer aided design (CAD) model of the object [3]. There are seven classes of AM technologies, with some of them being used for making prototypes while some are used for the fabrication of functional parts. Some of these AM technologies are also used to improve the surface properties of components by using the

Advances in Laser Materials Processing
https://doi.org/10.1016/B978-0-08-101252-9.00021-2
Copyright © 2018 Elsevier Ltd.
All rights reserved.

technology to apply micro-sized coatings of materials such as polymers, metals, composites, or functionally graded materials. Some industries use AM technologies to apply thin film coatings on their products for improved properties; these industries include the energy industry, the electrical and electronics industries, automobile industries, aerospace industries, and the biomedical industry. This is mainly because most of the materials used in these industries are made of materials that need special surface properties which can only be achieved through surface modification, such as application of other materials through coatings.

Some of these industries rely on efficient technology for the coating of their functional parts. Biomedical industries for instance, use metallic materials for implants and for some devices that are used to temporarily hold implants in place during fractured bone surgery. The commonly used metals in this industry include titanium alloys, cobalt-chromium based alloys, and stainless steels. Although these materials could provide the needed strength and other properties that are important for their intended applications, the surface properties may be a limitation. The surface properties of these materials and the environment where they will be used could cause the release of toxic substances into the blood stream when these materials are corroded or because of wear debris. The release of such toxic metallic substances into the blood stream could cause skin inflammation to the patient and corrosion and wear of the implant could also result in the loss of the mechanical properties of the implant and lead to the eventual failure of the implant [4–7]. To prevent this and other problems, usually a micro-sized surface coating of other materials with the needed properties are applied to these implant materials which will help to improve the corrosion resistance, wear resistance, and aid in the biocompatibility of these materials. Some materials such as hydroxylapatite (HA) possess these properties but they lack other necessary properties such as strength and toughness that are important for the implant. It is this type of material that is coated on the metallic implant to prevent the associated problems that the metal could cause when it is not coated. Another important application where coatings are used is in the automobile industry. The combustion chamber is subjected to a very high temperature and high thermal stress which could result in the loss of important mechanical properties of the metallic material that is used in its construction. The metallic material is usually coated with high heat resistance materials which will prevent the transmission of the high thermal energy from the combustion chamber into the metallic material and will also help to retain the important properties of the combustion chamber material. Some of the

materials used as coating materials for the combustion chamber include the ceramic materials and refractory metals like nickel. An efficient manufacturing process is desired by the automobile and aerospace industries to achieve these and other types of coatings.

In this chapter, the different types of micro-size coatings and their areas of applications will be explained. The laser additive manufacturing technology is a very promising manufacturing process for applying micro-sized coatings on parts or components with materials such as metals, alloys, ceramics, and composite materials. The various types of laser assisted additive manufacturing processes that are used for the fabrication of micro-sized coatings on components will also be presented in this chapter. Two case studies are presented to demonstrate the capability of laser assisted additive manufacturing process for the fabrication of micro-sized metallic and composite coatings on titanium alloy substrate with improved mechanical and tribological properties. These case studies are analyzed and the influence of the laser assisted additive manufacturing process parameters on these properties are also presented in detail.

21.2 TYPES OF MICRO-SIZED COATINGS AND THEIR AREAS OF APPLICATIONS

The main purpose of applying micro-sized coating on the surface of parts or components is to modify the surface properties of the component and also to protect the surface from environmental attack, a harsh working environment, and protection against wear or to improve optical performance of the component. These micro-sized coatings help to extend the service life of these components by protecting them against all forms of damage that could damage the base material if not coated. There are different types of micro-sized coatings that are used for various applications. The type of application where the coating will be applied usually determines the type of coating that is applied. Another key important determining factor for selecting a type of coating for a particular application is the strength of the coating and the damage threshold that the coating should tolerate. There are four main types of coatings that are applied on components, they include polymer coatings, metallic coatings, ceramic coatings, and composite coatings. Metallic coatings are useful when high absorption property is required. Dielectric coatings are nonconductive or insulating coatings that are made of polymers and ceramics. The low absorption properties, high heat, and high wear resistance properties of ceramic coatings make these types

of coatings used in large number of applications where these properties are needed such as for high and low voltage applications. These types of coatings can also be applied to a limitless number of materials that enables the coatings to be used to solve most complex electrical problems and also used in optics for applications such as antireflective coatings in the energy industry. Micro-sized coatings with high mechanical strength and high wear resistance properties such as ceramic and composite coatings are used in applications like petrochemical, mechanical cutting tools, and biomedical applications. Optical, magnetic, and electrically active coatings are used in applications such as sensors, actuators, solar cells, and electroacoustic devices [8–10]. Some of the areas of application of micro-sized coatings are summarized in the diagram shown in Fig. 21.1.

21.3 LASER BASED ADDITIVE MANUFACTURING FOR MICRO-SIZED COATINGS

The use of micro-sized protective layer(s) of coatings on the substrate material is an efficient means of extending the service life of such material by reducing wear and premature failure of the component due to the impact of the mechanical properties of the coating material such as improved wear resistance, corrosion resistance, and high thermal resistance properties. A metallic coating may be applied on another metallic substrate where the property of the coating material is desired but the cost of such material may prohibit its use for the construction of such components. In another case, the coating material may not possess the required structural properties such as high strength and high toughness that are required for such application. These properties may not be available in the coating material while the metallic material that is used as the base material does not also have the needed surface property required for the intended application. Hence, there is need to apply micro-sized coating of a more expensive or metallic material with the required property for the protection of the base material. Metallic materials such as gold and platinum are coated on base metal of some high corrosion resistance applications. Other applications may require the use of ceramic or composite materials to be coated on the base material, especially in the thermal barrier application and wear resistance applications. Another important coating is the diamond-like carbon (DLC). DLC, an amorphous meta-stable carbon, is also used to coat the base materials because of its extraordinary properties. DLC has high wear resistant properties and is often used as coatings on cutting tools. DLC has high potential for heat

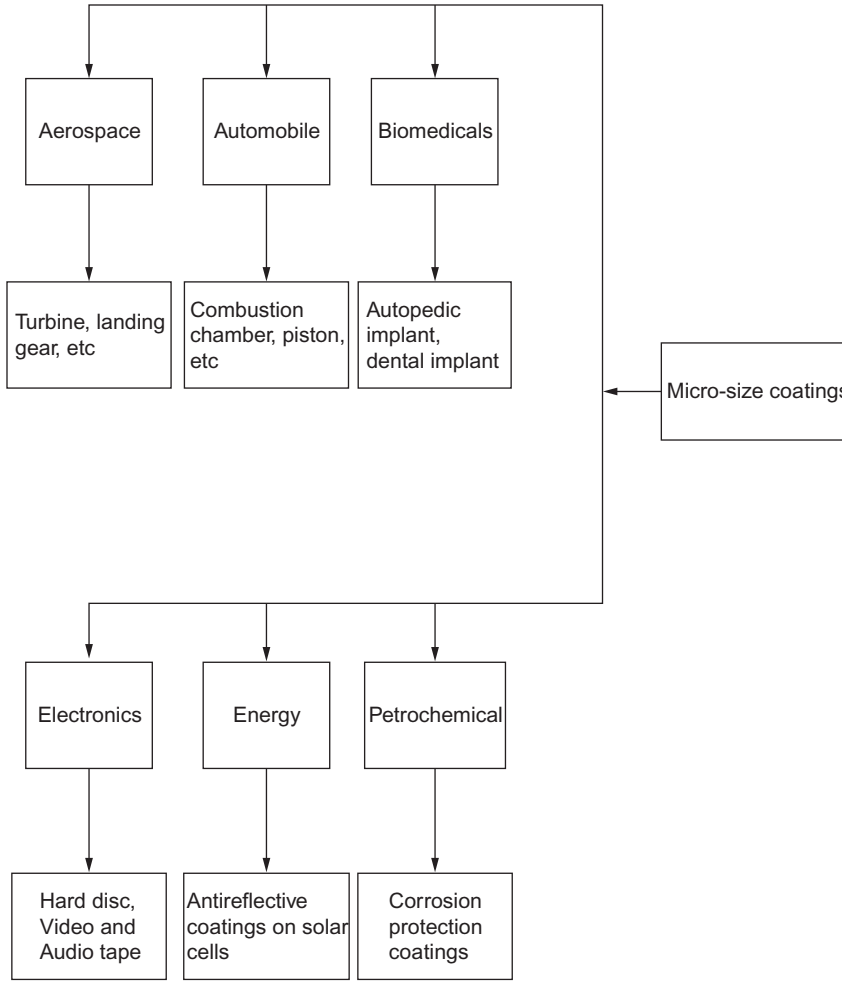


Fig. 21.1 Application areas of micro-size coatings.

dissipation which makes it useful in hybrid integrated circuits and computer disks. The excellent wear resistance, corrosion resistant, and biocompatibility makes the DLC favored in the biomedical industry [11–15]. DLC is also used in the automobile industry especially in the power train components and piston-bore assemblies. The tribological property of a coated-material depends on both the quality of the coating material and the fabrication process that is employed. There are different types of fabrication processes for applying the micro-sized coatings on materials that include the conventional processes, such as the chemical vapor deposition (CVD) and the physical

vapor deposition (PVD) processes which are complex and cumbersome [16,17]. One of the problems with these high temperature conventional coating processes is the lack of flexibility in the control of compositions and on-demand designs [18]. With laser-assisted additive manufacturing technologies, these coatings can be made on-demand and on site too.

Laser assisted additive manufacturing (LAM) process is a relatively new fabrication process for producing 3D components as well as for applying surface coating on components. The LAM process for fabrication of coatings has several advantages in surface modification of materials. The ability to accurately control the laser beam to only the needed area is one of the key advantages of using laser assisted additive manufacturing for fabrication of micro-sized coatings. The unique properties of laser beam such as high coherency, low divergence, and monochromaticity help their application in this type of coating process. The laser allows thin layers of coatings to be evenly distributed [19]. One of the challenges of producing micro-sized coatings using the conventional coating processes is that, they are prone to defects such as the formation of agglomerates which tends to stick to the surface that comes in physical contact with the surface being coated during the deposition process. The use of the laser-assisted additive manufacturing process to fabricate such micro-size coating can help to offset this challenge.

Laser sintering based additive manufacturing technique uses a laser beam to sinter powder material in a repeated scan profile to fabricate the necessary coating on the substrate material. The same process can be used to fabricate three dimensional (3D) parts directly from a computer aided design (CAD) model by adding materials layer by layer [20,21]. Directed energy deposition process is another class of laser assisted additive manufacturing process that can be used to fabricate micro-sized coatings that have been reported in research works. There are also several research works on the use of the laser assisted additive manufacturing process for the fabrication of micro-sized coatings. Some of these research works are reviewed in this section.

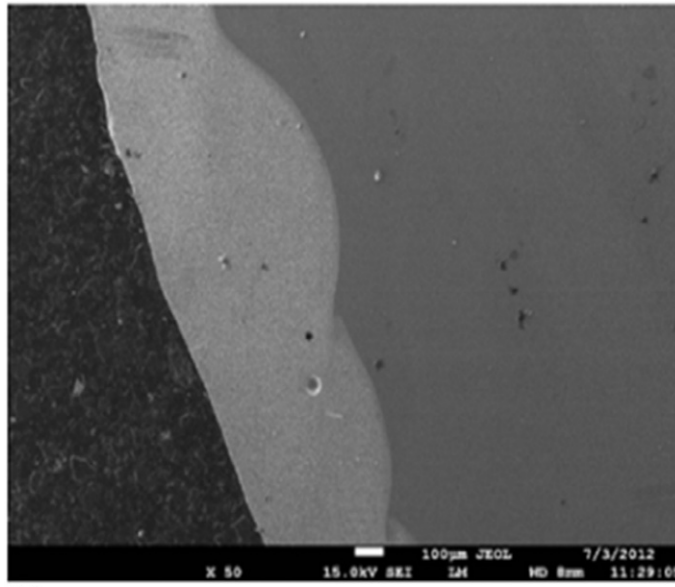
Baloyi et al. [22] conducted a study on the fabrication of micro-size coating of Ti6Al4V with zirconium and zirconia composite using laser additive manufacturing process. The aim is to improve the wear resistance and the corrosion resistance properties of the titanium alloy base material for biological application. The study was conducted using three different samples: sample prepared without binder, another samples with cold glue ($C_4H_6O_2$) binder, and the samples with polyvinyl alcohol (PVA) (C_2H_4O) binder. The Zirconium powder was premixed with each of the binders

which form zirconium + zirconia composite in situ during the laser metal deposition process. The coating was found to be evenly distributed. The binder was found to have influenced in the resulting microstructure, which was found to change the microstructural behavior when compared with the sample without any binder. The microstructure was seen to show less dendritic ZrC structure as a result of the addition of the binder when compared with the samples prepared without any binder. An improved hardness property was also observed in all the coated samples. The sample with the PVA binder has the least dendritic ZrC structure while the sample without binder has the highest quantity of dendritic ZrC structure. The sample with the PVA binder was also found to be crack free with good metallurgical integrity as a result of the less dendritic microstructure as shown in Fig. 21.2.

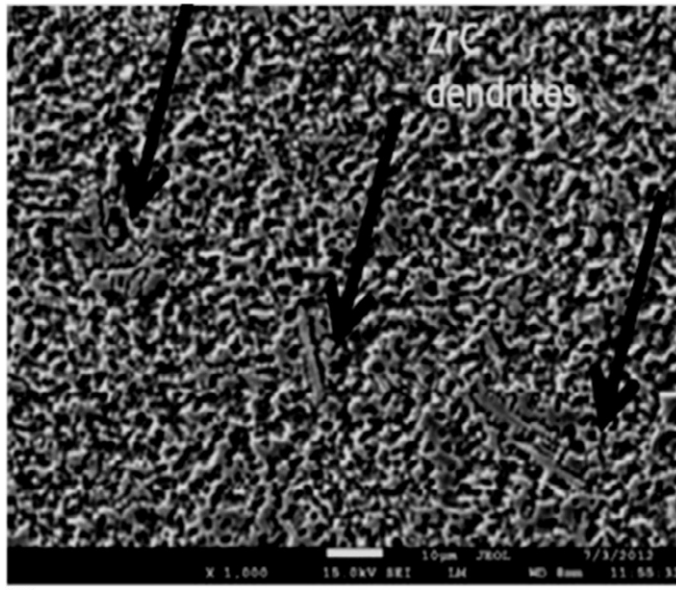
The sample with cold glue showed complex microstructures with different morphologies of dendritic ZrC structure and some cracks were observed in this sample. The sample without any binder has the least hardness value. The study concluded that the hardness property of Ti6Al4V substrate can be improved by coating it with Zr + PVA binder which is useful to prevent the toxicity of aluminum and vanadium ions, which could be released when the Ti6Al4V is used in corrosive environments (biological applications).

Zhang et al. [18] also investigated the use of Laser Engineered Net Shaping (LENS), a laser-assisted additive manufacturing process to fabricate micro-sized coating of Ti-Si-N in situ on commercially pure titanium (Cp-Ti). The powders of Cp-Ti and silicon powder were premixed and deposited on the titanium substrate using the LENS. Three samples were fabricated consisting of sample 1 with 100% Cp-Ti powder, sample 2 containing 90% Cp-Ti and 10% Si, and sample 3 consisting of 75% Cp-Ti and 25% Si. The influence of varying the percentage content of the Si on phase formation and on the hardness and wear resistance properties of the coatings produced were studied. The microstructure, the wear resistance, and the hardness properties were studied and compared. The result of the microstructural analysis showed that the microstructure of all the samples consisted of graded microstructures with in situ formed phases. The microstructures of the three samples are shown in Fig. 21.3. The variations in the microstructure and phase changes were found to affect the coating's hardness property and the wear resistance property.

The sample with the 90% Cp-Ti was found to have the highest hardness value while the sample with 75% Cp-Ti was found to have the least hardness value. The wear resistance behavior of the samples on the



(A)



(B)

Fig. 21.2 SEM microstructures for sample with PVA binder: (A) cross sectional view of the deposited layer; (B) higher magnification of (A) showing the presence of dendrites ZrC structure [22].

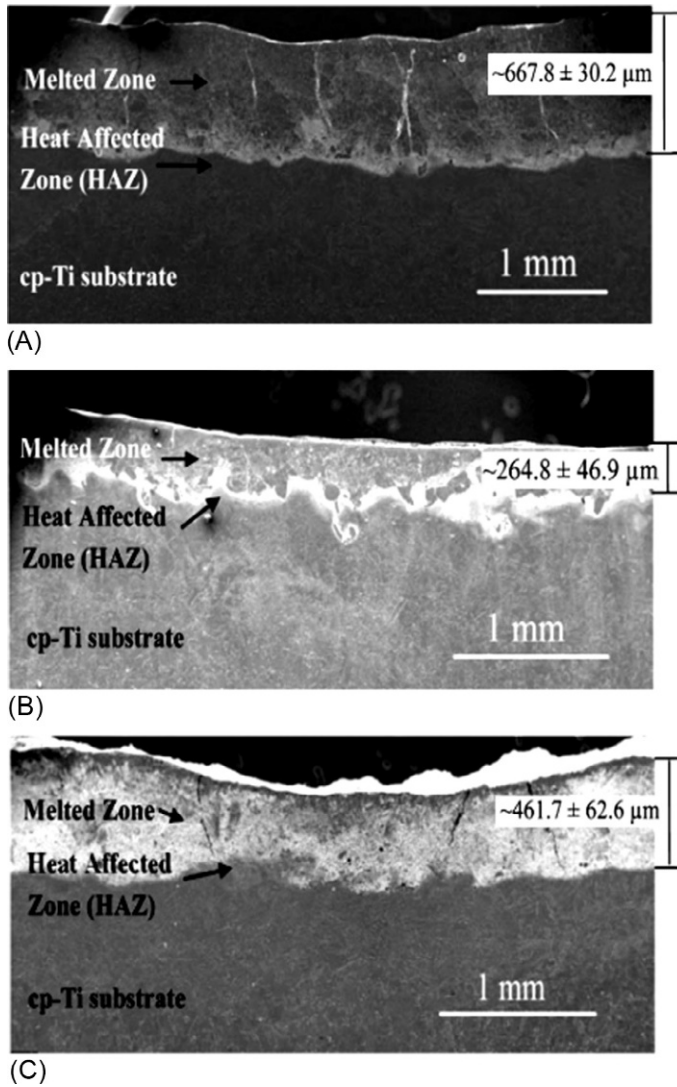


Fig. 21.3 SEM image of: (A) 0% Si coating on Cp-Ti; (B) SEM image of 10% Si coating on Cp-Ti; (C) SEM image of 25% Si coating on Cp-Ti [18].

other hand was found to be dependent on the percentage of Si content. The sample with the 25% Si showed the best wear resistance behavior. The sample with the 25% Si showed the least wear rate while the sample with the 0% Si showed the highest wear rate of all the three samples. However, the substrate has the poorest wear rate as the wear rates of all the samples were found to be lower than that of the substrate. It was

concluded that the addition of the Si helped to improve the tribological performance of the coatings produced.

Krzyzanowski et al. [23] investigated the cause of micro-cracking in micro-size bioactive glass coatings on the Ti6Al4V alloy using numerical and experimental methods. The condition that resulted in micro-cracking susceptibility of the coating using laser assisted additive manufacturing process was studied using the finite element analysis modeling. The thermal stress that developed as a result of the rapid cooling rate in the process was found to be responsible for the micro-cracking in the coatings. By preheating the substrate before the deposition process, cracking was decreased. The substrate preheating helped to reduce the cooling rate since the substrate usually acts like a heat sink. The micrograph of a sample produced on a substrate that was not preheated showing the micro-cracks is shown in Fig. 21.4.

A numerical model was developed to study the transient temperature distribution and the strain-stress fields during the cladding process. The maximum transient stress in the coating was found to be reduced as the number of layers is increased thereby reducing the cracking susceptibility as the number of the deposition layer is increased. The result of the numerical modeling was compared to the experimental data and it was found to be in close agreement with one another. The importance of the study conducted by Krzyzanowski et al. [23] was seen in the work

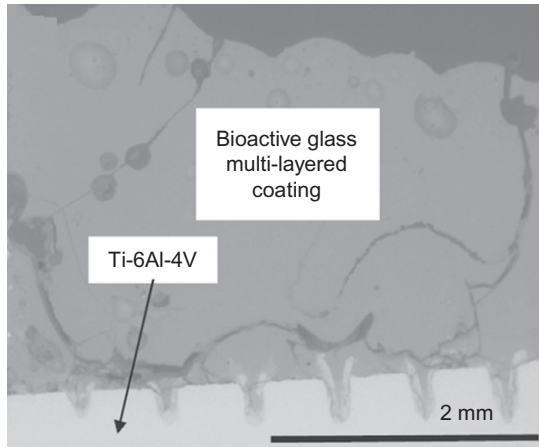


Fig. 21.4 SEM image showing cross section of bioactive glass multi layered coating on not preheated Ti6Al4V base plate (multiple tracks) at laser power 120 W [23].

of Ram and Stucker [24] who carried out the feasibility study on the use of LENS for the fabrication of micro-size coating of CoCrMo on titanium substrate for orthopedic implant application. The importance of preheating the substrate to reduce micro-cracks is seen in this study, as the authors experienced serious challenges in producing any sample without cracks. They were faced with cracks in single layer deposit and delamination occurred when the number of layers was increased. A portion of the deposit was crack free while other regions of the same sample experienced cracks. The cracking in the single layer of CoCrMo coating on the titanium substrate was attributed to the brittle intermetallic phases that were present in the coating and the residual stresses that were built up in the substrate with the porosity and other forms of defects serving as the stress risers. It was suggested that to fabricate a crack-free coating of the CoCrMo on the titanium substrate using the LENS, the substrates needed to be preheated.

Justin et al. [25] describes a method of fabricating micro-size coatings of hard and wear resistance material on porous medical implants using a laser metal deposition process in their patent. How to fabricate micro-sized coatings of biocompatible materials and functionally graded coatings with porous implants as the base material were explained in this patent. The porous material was selected as the base material to promote bone ingrowth which helps the implant to be held strongly in place on the bone of the patient. Balla et al. [26] also investigated the fabrication of functionally graded micro-sized coatings of yttria-stabilized zirconia using LENS. The study showed that compositionally gradient YSZ coatings with good metallurgical integrity can be fabricated using the LENS. It stated that the characteristic features of the coatings produced such as the segmentation cracks and the columnar grains as shown in Fig. 21.5 are desirable because they help to extend the life of thermal barrier coatings. The coating gradation was found to reduce the stress intensity at the interface, which has helped in the prevention of premature failure of the coating.

The high potential of laser-assisted additive manufacturing of micro-size coatings requires that more research work is needed in this area to position this technology ahead of the future industrial revolution which is expected to be based on additive manufacturing technology [25]. A case study of micro-size coatings of titanium alloy and titanium alloy composite on titanium alloy substrate is presented in the next section.

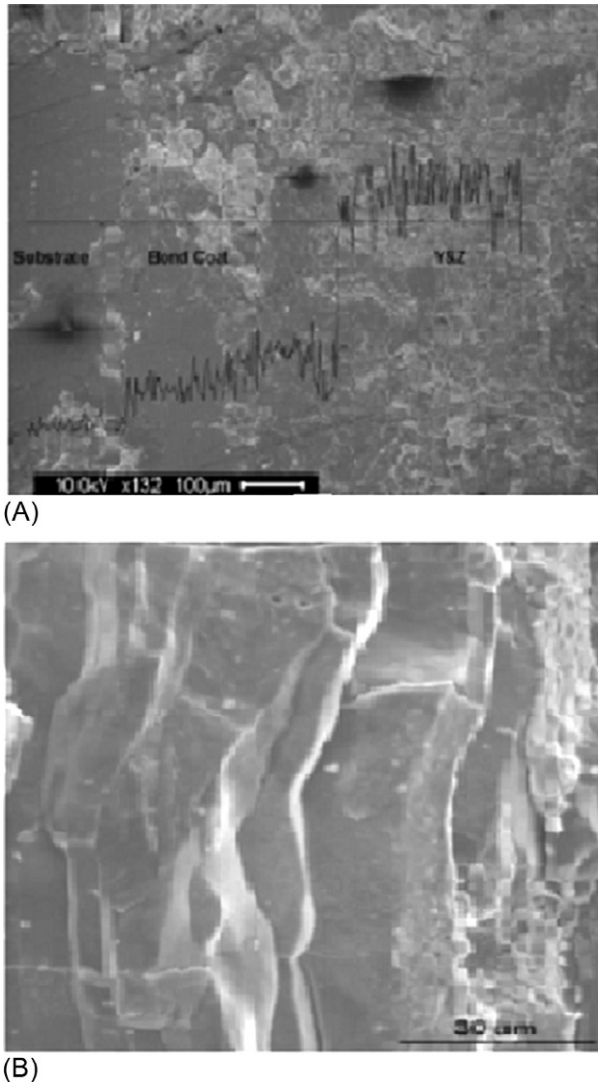


Fig. 21.5 (A) Typical microstructure of YSZ coating showing Zr distribution across the gradient coating; (B) fractured surface of the coating [26].

21.4 CASE STUDIES: FABRICATION OF TI6AL4V AND TIC/TI6AL4V COMPOSITE ON TI6AL4V SUBSTRATE USING LASER METAL DEPOSITION PROCESS

Laser metal deposition (LMD) process is a laser-assisted additive manufacturing that belongs to the directed energy deposition class of the additive

manufacturing process [3]. The LMD process is not only useful for the fabrication of 3D objects but can also be used to fabricate coatings on the surface of a part to improve the surface properties of the part. The additive manufacturing technology can also be used to repair a high valued part and to also correct defects in a manufactured part through the application of coatings in layers to fill such a void [26–29]. The LMD process is also an important manufacturing process that can be effectively used to process difficult to machine materials such as titanium and its alloys [30] because it is a tool-less manufacturing process.

Titanium alloy-Ti6Al4V is the most widely used titanium alloy that is used in industries because of its high strength to weight ratio and excellent corrosion resistance properties [31]. Despite these excellent properties, the wear behavior of this alloy is poor and needs surface modification if the material will be used in applications where it will be come in contact with or in rubbing action with other parts. The surface modification that can be performed on the titanium alloy can be in the form of micro-sized coatings of wear resistant materials such as ceramic or composite materials. The LMD process has also been proved to produce materials with improved properties and by adequately adjusting the processing parameters, the properties of the deposited material can be improved [32–37]. In this case study, the properties of micro-sized coatings of Ti6Al4V on Ti6Al4V and TiC/Ti6Al4V on Ti6Al4V are analyzed. The influence of processing parameters on the properties of the micro-sized coatings of Ti6Al4V on Ti6Al4V substrate using the LMD process is also investigated. The microstructures of the coatings were studied in relation to the evolved properties and performance of the coatings.

21.4.1 Experimental Method

The powders that were used for the coatings are the 99.6% pure Ti6Al4V powder and 99.5% pure TiC. The substrate is 99.6% pure Ti6Al4V with a thin plate 5 mm thick. The particle size range of the Ti6Al4V powder is between 120 and 350 μm while the particle size range of the TiC powder is below 60 μm. The Ti6Al4V alloy substrate was in annealed form and it was supplied by VSMPO-AVISMA Corporation, Russia. The TiC powder and the Ti6Al4V powder used in this case study were supplied by F.J. Brodmann and Co., L.L.C., Louisiana. The chemical composition of the Ti6Al4V powder, TiC powder, and the Ti6Al4V substrate are presented in Tables 21.1, 21.2, and 21.3, respectively. The particle size analysis is shown in Fig. 21.6A for the Ti6Al4V and Fig. 21.6B for the TiC powder.

Table 21.1 Chemical composition of Ti6Al4V substrate

Element	Al	V	Fe	C	N_2	H_2	O_2	Ti
W%	6.42	3.91	0.19	0.008	0.006	0.004	0.155	Balance

Table 21.2 Chemical composition of the TiC powder

Element	C	O_2	N_2	Fe	Al	Na	Ti
%	19.5	0.28	0.4	0.045	0.03	0.026	Balance

Table 21.3 Chemical composition of the Ti6Al4V powder

Element	Al	V	Fe	C	N_2	H_2	O_2	Ti
W%	6.20	3.90	0.18	0.008	0.005	0.005	0.150	Balance

Prior to the laser metal deposition process, the substrates were sand-blasted and washed with acetone to roughen the surface of the substrate and to remove dirt to help aid laser absorption. The LMD process was achieved using the experimental set-up that is available at the Center for Scientific and Industrial Research, National Laser Centre (CSIR-NLC) in Pretoria, South Africa. The experimental set-up consisted of a Kuka robot carrying Nd-YAG laser and coaxial powder nozzles in its end effector. The laser spot size of 2 mm was used throughout the experiment while the focal length of the laser was kept at 195 mm above the substrate. Two different experiments were conducted: the deposition of Ti6Al4V powder on the Ti6Al4V substrate and the deposition of TiC plus Ti6Al4V powder on the Ti6Al4V substrate. The pictorial diagram of the experimental set-up and the schematic diagram of the LMD process are shown in Figs. 21.7 and 21.8, respectively. The deposition process was achieved by focusing the Nd-YAG laser beam onto the substrate to create a melt pool by melting the surface of the substrate. A controlled quantity of powdered material was delivered into this melt pool, that melts and when solidified, forms a bead of metal. As the laser moves and the deposition process continues, a series of beads of metal are made and joined together to form a deposition track.

For the experiment, the Ti6Al4V powder was deposited onto the Ti6Al4V substrate, and each track was deposited using the processing parameters presented in Table 21.4. The second experiment where the TiC powder and the Ti6Al4V powder were deposited on the Ti6Al4V substrate, each of the powders were placed in separate uppers of the dual powder feeder used in the experiment. The two powders were deposited simultaneously onto the melt pool at 50W% TiC and 50W% of Ti6Al4V. The processing parameters in Table 21.5 were used to produce the samples.

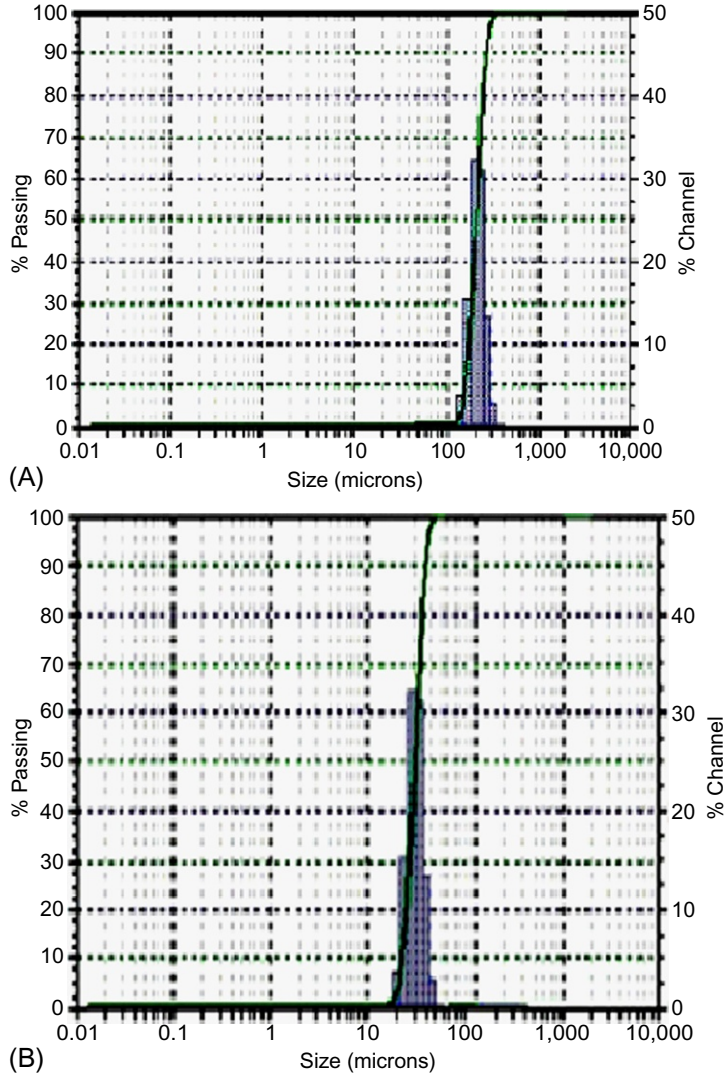


Fig. 21.6 Particle size analysis of: (A) Ti6Al4V powder; (B) TiC powder.

Four tracks were produced at each processing parameters at a 50% overlap percentage.

After the coating process, the coatings were cut across the deposition direction to reveal the cross section of the coatings. The cut samples were mounted with resin using a hot mounting process. The microstructural samples were prepared by following the standard of metallurgical sample preparation [38]. The samples were ground, polished, and etched using the Knoll reagent. The Kroll's reagent consists of 100 mL of water with 3 mL of

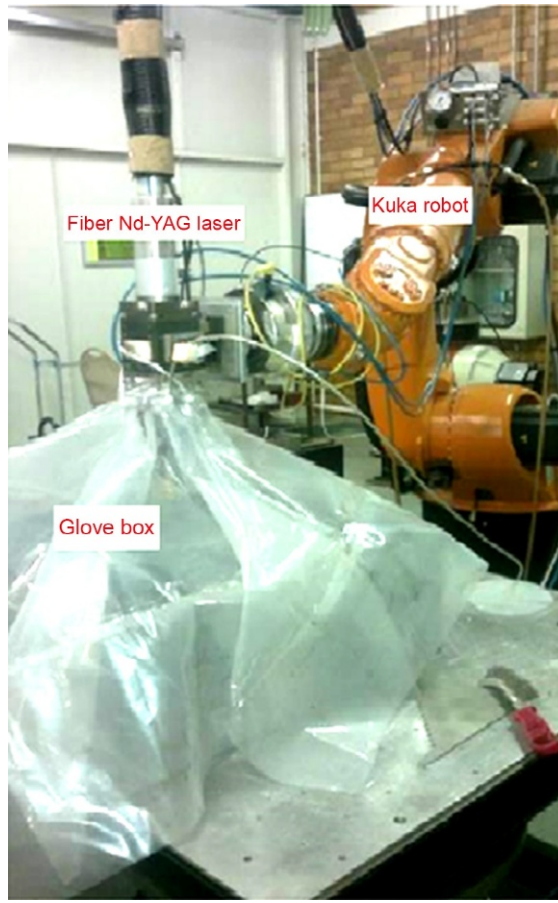


Fig. 21.7 Pictorial diagram of experimental set-up.

hydrofluoric acid and 2 mL of nitric acid. The cross-sections of the coatings were studied using optical microscopy by Olympus BX51M and a field emission scanning electron microscope (SEM) by TESCAN equipped with Oxford Energy Dispersion X-ray Spectrometer (EDS).

The Vicker's microhardness (Hv) measurements of the coatings were taken using a Metkon microhardness tester with a load of 500 g and at a dwelling time of 15 s. The distance between indentations was kept at 12 μm, according to the ASTM standard [39].

The wear test was performed on the sample with TiC/Ti6Al4V coatings on a Ti6Al4V substrate using a universal material tester (UMT 2CETR) tribotester. Dry sliding wear with ball-on-plate arrangement was performed using a Tungsten Carbide spherical ball as a counter body with a diameter of 10 mm, a load of 25 N, a stroke length of 2 mm, and a reciprocating frequency

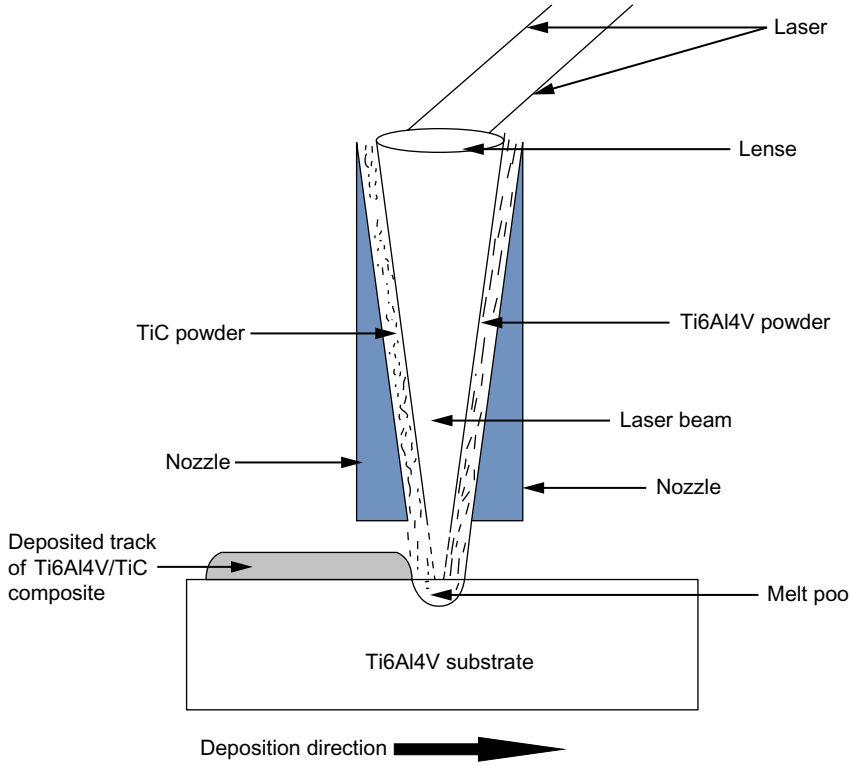


Fig. 21.8 Schematics of the LMD process [36].

Table 21.4 Processing parameter for Ti6Al4V powder on Ti6Al4V substrate

Sample designation	Laser power (kW)	Scanning speed (m/s)	Powder flow rate (g/min)	Gas flow rate (L/min)
A	1.6	0.05	2.88	4
B	2.0	0.05	2.88	4
C	2.4	0.05	2.88	4
D	2.8	0.05	2.88	4
E	3.2	0.05	2.88	4

Table 21.5 Processing parameter for Ti6Al4V powder on Ti6Al4V substrate

Sample designation	Laser power (kW)	Scanning speed (m/s)	Powder flow rate (g/min)	Gas flow rate (L/min)
A	3.2	0.15	2.88	2
B	3.2	0.25	2.88	2
C	3.2	0.35	2.88	2
D	3.2	0.45	2.88	2
E	3.2	0.55	2.88	2

of 20 Hz. The experiments were performed for 1200 s. The coefficient of friction was measured and recorded. The wear test was conducted according to the ASTM G133-05(2010) Standard [40]. The wear scars were studied using the optical microscope, SEM, and stylus surface analyzer (Jenoptik). The wear volumes were determined from the wear-track surface profile, using the stylus surface analyzer and the optical microscope. The wear volume loss was calculated using the formula proposed by Sharma et al. [41].

21.4.2 Results and Discussions for Experiments With Ti6Al4V Coatings on Ti6Al4V Substrate

The micrograph showing the microstructure of the Ti6Al4V substrate is shown in Fig. 21.9A while the morphology of the Ti6Al4V powder is shown in Fig. 21.9B. The Ti6Al4V powder is made up of a spherical gas atomized powder. The microstructure of the substrate is made up of beta phase (the dark colored parts) grain structures in the matrix of the alpha phase (the bright colored parts) that is typical of any Ti6Al4V as shown in Fig. 21.9A. The micrographs of the sample at a laser power of 1.6 W showing the coating thickness is shown in Fig. 21.10.

The maximum coating thickness of 227.74 μm was observed at a laser power of 1.6 kW as shown in Fig. 21.10A while the minimum coating thickness in the experiment was 158.25 μm and was observed at a laser power of 3.2 kW as shown in Fig. 21.10B. All the coatings were fully dense with no porosity observed. Fig. 21.11A shows the cross-section of the coating made at a laser power of 1.6 kW at high magnification showing the substrate-coating interface which is free from any form of discontinuity or defects. The laser fully melts the powder that ensures the sound metallurgical bonding that was observed in all the samples. The microstructure consists of columnar grain structures that grow epitaxially on the globular grains which were formed as a result of grain growth at the heat affected zone on the substrate. The columnar grain was observed to grow from the substrate towards the surface of the coating because of the directional solidification occurring in the process. The substrate is cooler and acts as a heat sink, making the solidification grow from the substrate to the top of the coating. The columnar grains were found to be reduced as the laser power was increased, which could be due to the larger melt pool created at a higher melt pool that resulted in a low rate of solidification. This causes more grain growth in the heat affected zone that reduces the quantity of globular grains formed, which are larger. Fig. 21.11B shows the micrograph of a sample produced at a laser power of 3.2 kW. It can be seen that the columnar grains are fewer and larger than that of Fig. 21.11A. More martensitic alpha grains are also

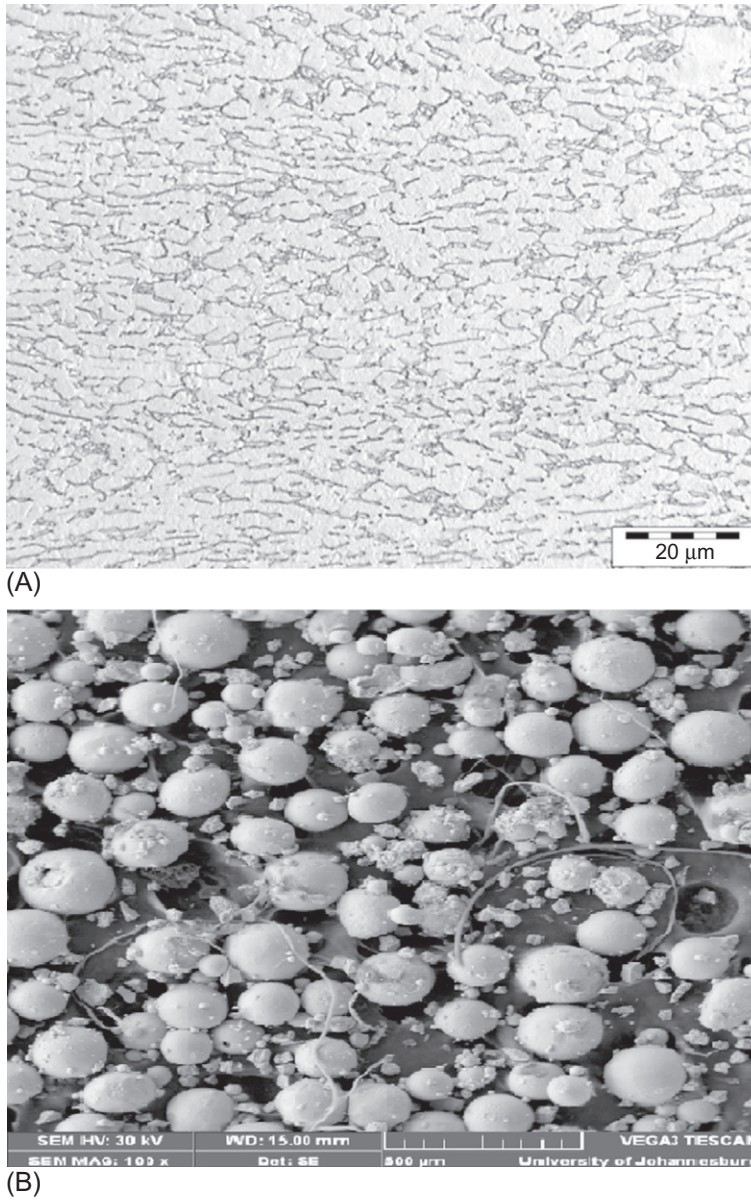


Fig. 21.9 Micrograph of the: (A) Ti6Al4V substrate; (B) Ti6Al4V powder.

observed in the sample at a low laser power as compared to the samples at a higher laser power, as shown in Fig. 21.12A and B, respectively. This could be a result of a smaller melt pool produced at a low laser power which solidifies rapidly, thereby promoting the formation of a non-equilibrium phase of martensitic alpha.

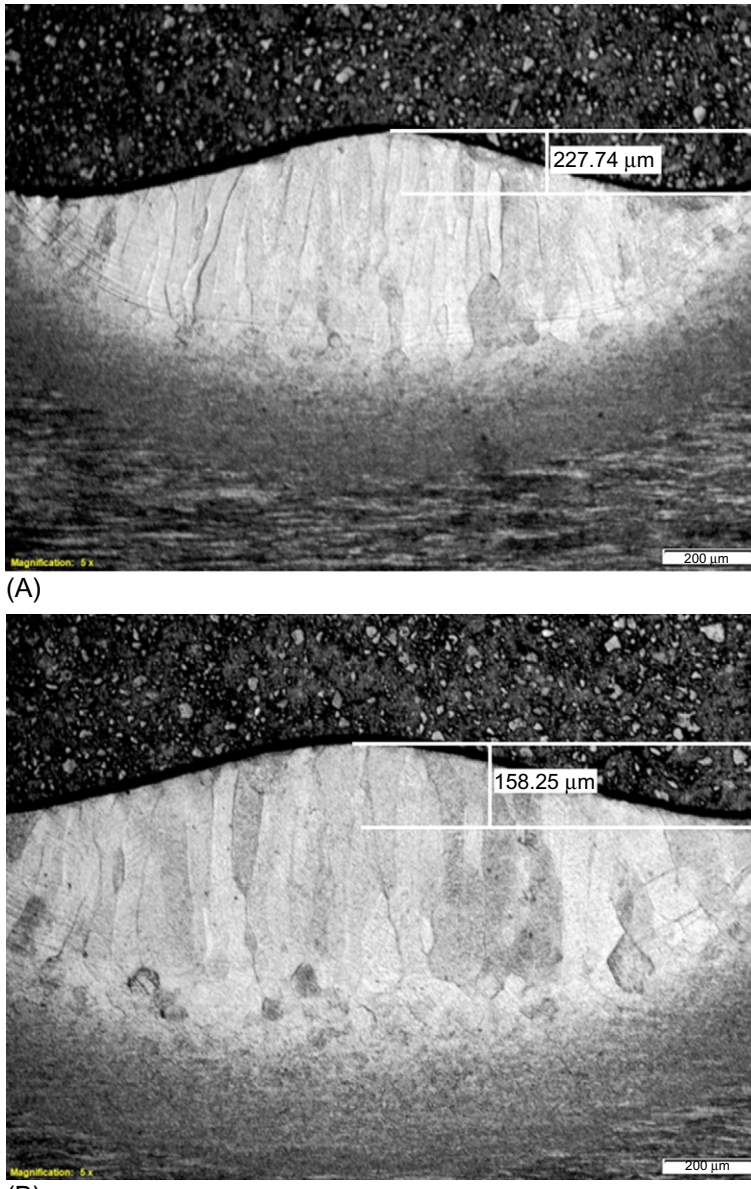
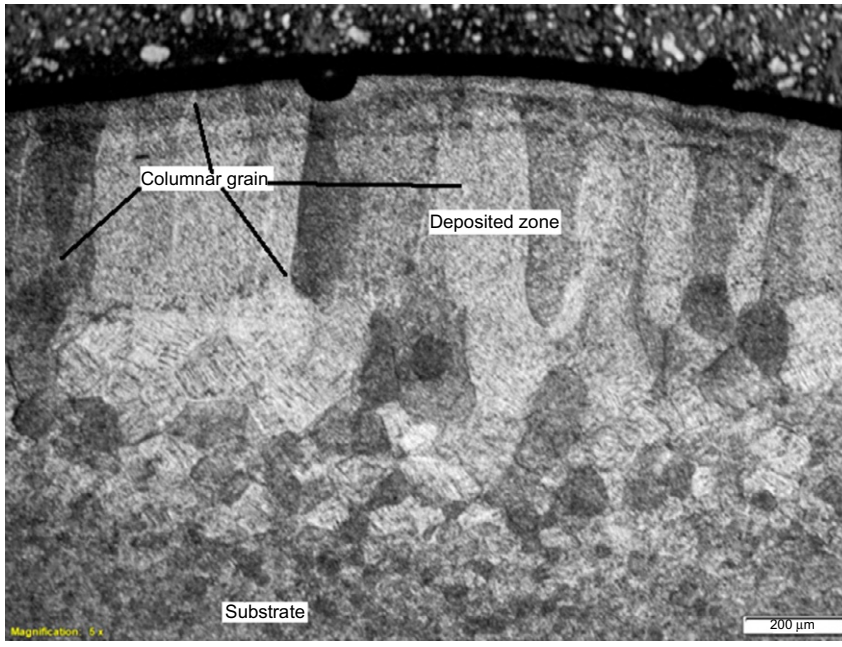
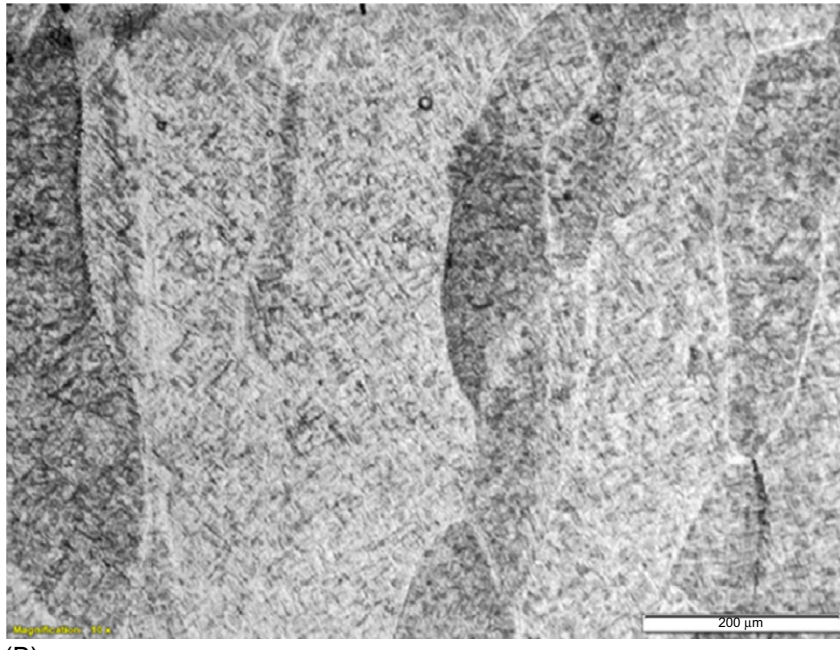


Fig. 21.10 Micrograph showing the coating thickness at a laser power of: (A) 1.6 kW; (B) 3.2 kW.

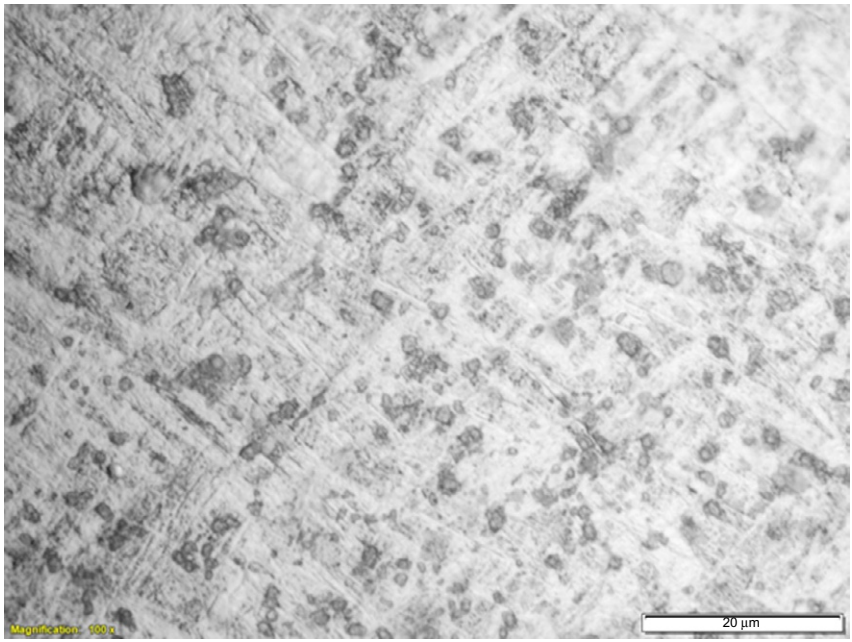


(A)

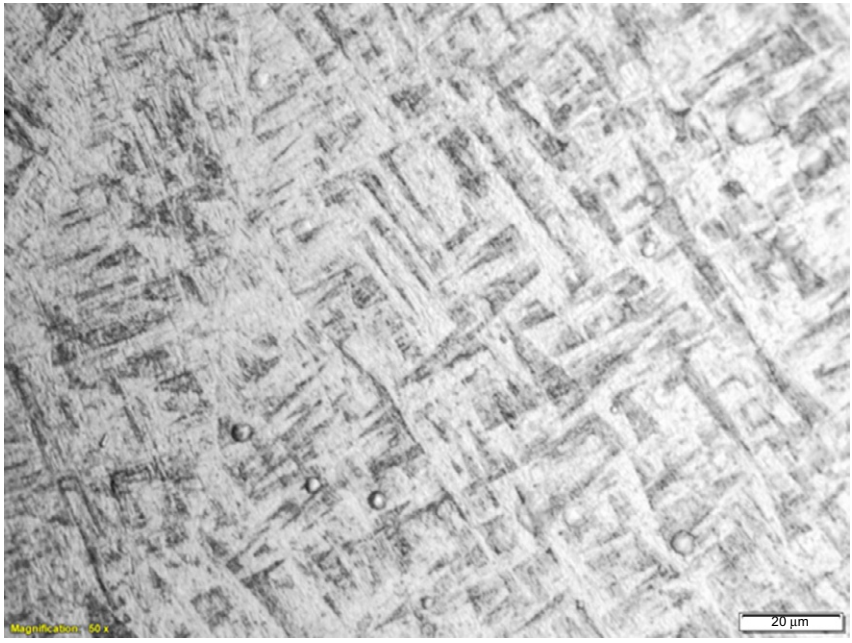


(B)

Fig. 21.11 Micrograph of the sample: (A) at a laser power of 1.6 kW showing the fusion zone between the substrate and the coated powder; (B) at 3.2 kW showing fewer columnar grains.



(A)



(B)

Fig. 21.12 Micrograph showing different quantities of martensitic alpha at: (A) 1.6 kW; (B) at 2.4 kW.

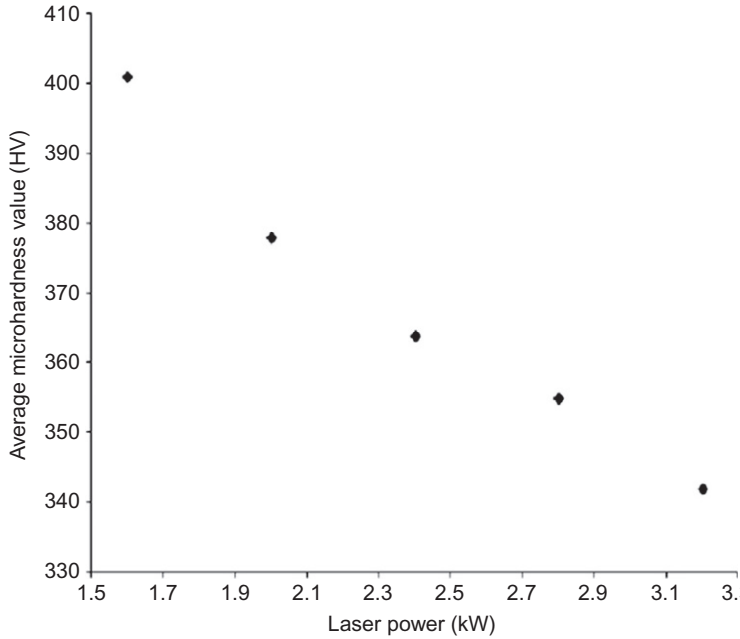
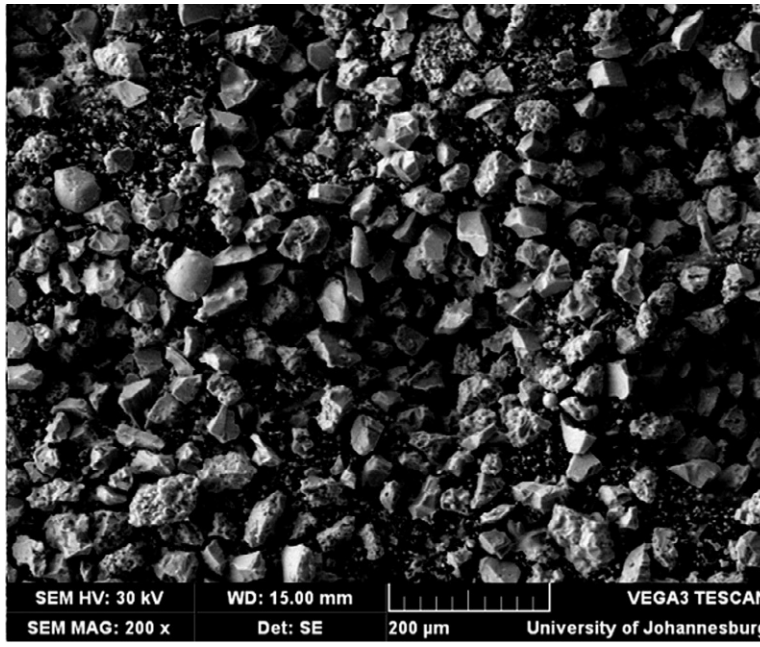


Fig. 21.13 The graph of microhardness versus laser power.

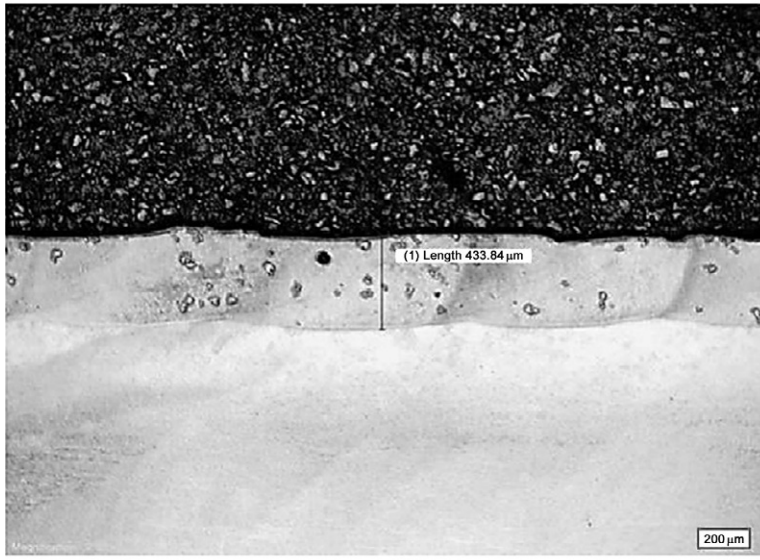
The microhardness results further proves the microstructural analysis results. The microhardness was found to reduce as the laser power was increased. The higher microhardness observed at a lower laser power could be due to the more martensitic alpha grains present, as seen in Fig. 21.12A. The substrate had the lowest microhardness value of about 300 Hv, while the sample at a laser power of 1.6 kW had a microhardness value of 401 Hv, and the sample at a laser power of 3.2 had a microhardness value of 342 Hv. The graph of the average microhardness against the laser power is shown in Fig. 21.13. This result showed that it is possible to use laser-assisted additive manufacturing technology for the fabrication of micro-sized coatings and with improved properties.

21.4.3 Results and Discussions for Experiments With Ti6Al4V Coatings on Ti6Al4V Substrate

The micrograph of the TiC powder is shown in Fig. 21.14A. The TiC powder is made of irregular shape particles; this is because it was produced through ball mill which is the characteristic of powder produced through this process. The minimum coating thickness in this experiment was 433.84 μm at a scanning speed of 0.35 m/s as shown in Fig. 21.14B, while the maximum coating thickness was 571.5 μm occurring at a scanning



(A)



(B)

Fig. 21.14 (A) Morphology of the TiC powder; (B) coating thickness of sample at scanning velocity of 0.35 m/s [36].

speed of 0.045 m/s. The microstructures of all the samples are characterized by unmelted carbide (UMC), dendritic TiC, and re-solidified (RSC) or secondary carbide as shown in Fig. 21.15. The quantities of each of these structures vary with the change in the scanning speed. The quantity of UMC increases with an increase in scanning speed. The quantities of dendritic TiC is reduced with an increase in scanning speed.

The reasons for these observations may be due to the proper melting of the TiC powder at a low scanning speed, which results in the formation of more dendritic TiC and less UMC. The laser material interaction time is high at a low scanning speed, hence the formation of the larger melt pool and resulting in more melting of the TiC powder. The microhardness graph shown in Fig. 21.16A revealed that the microhardness increased as the scanning speed was increased. The microstructural analysis supported this result because the unmelted TiC particles tended to increase the hardness of the coating as a result of the reinforcement role they played in the

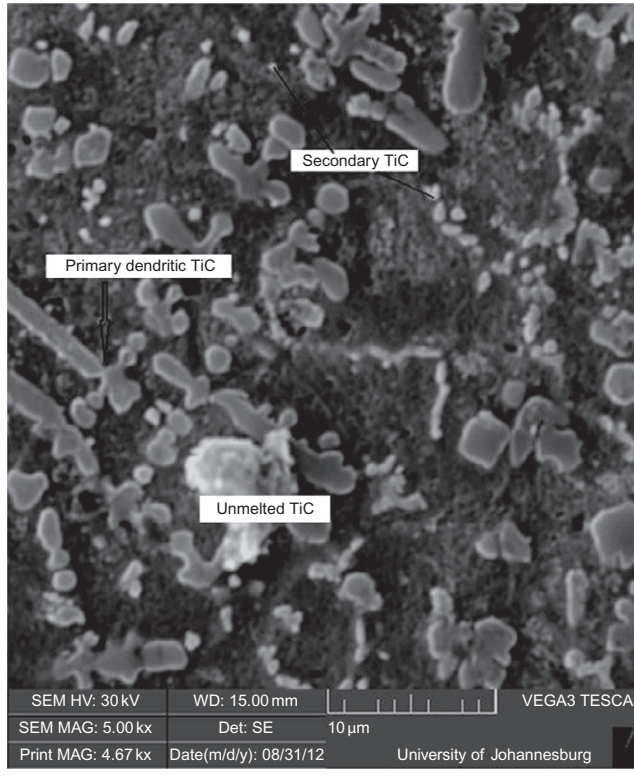


Fig. 21.15 Sample at scanning velocity of 0.055 m/s showing primary dendritic, unmelted carbide and secondary carbide [36].

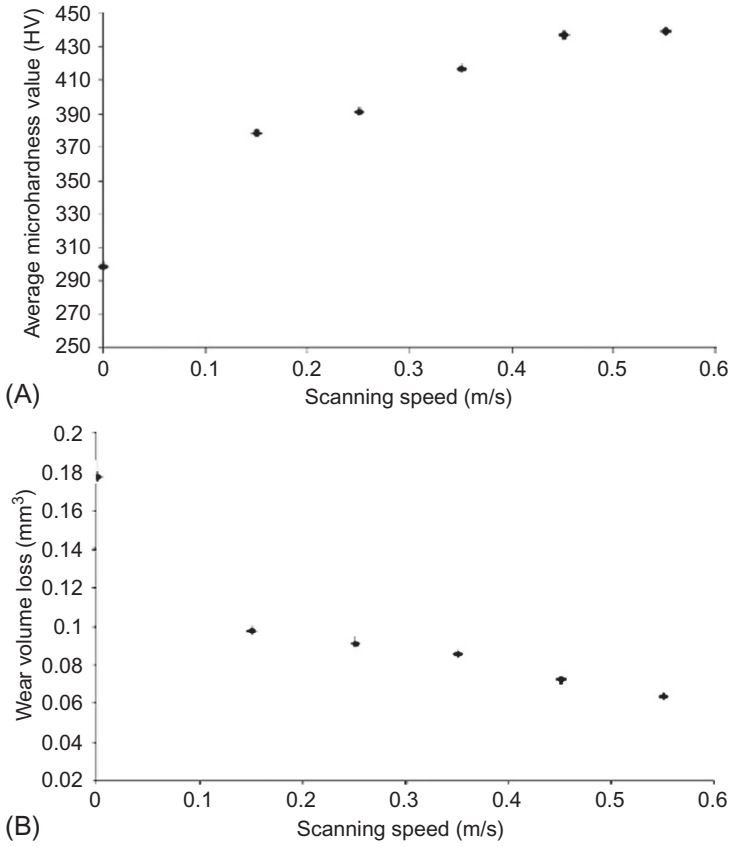


Fig. 21.16 Graph of: (A) Microhardness versus scanning speed; (B) wear volume loss versus scanning speed.

composite coating. The substrate was seen to have the lowest microhardness value; the large quantity of dendritic TiC occurring at low scanning speed was responsible for the higher hardness as compared to that of the substrate.

The wear results showed that as the scanning speed was increased, the wear resistance of the coating was increased, as shown in Fig. 21.16B. The substrate showed the highest wear volume loss due to the poor wear resistance behavior of the Ti6Al4V alloy. The coating of the TiC/Ti6Al4V composite on the Ti6Al4V substrate was seen to have improved the wear resistance behavior of the Ti6Al4V substrate. The reducing wear volume as the scanning speed was increased could be attributed to the higher quantity

of UMC seen in the microstructure, which helped as reinforcement in the matrix. The UMC would chip off during the sliding action and it would be ground into fine powder as the wear action progressed, which formed a powder lubricant that reduced the wear process.

21.5 SUMMARY

The use of the laser-assisted additive fabrication of micro-sized coatings was presented in this chapter. Different types of coatings and their areas of applications were reviewed. Some of the research works on the use of the laser-based additive manufacturing process for the production of micro-sized coatings in literature were reviewed. Two case studies on the use of the laser metal deposition process for fabrication of micro-sized coatings on titanium alloy using titanium alloy and titanium-titanium carbide composite were also presented. The properties of the coatings produced were analyzed and related to the processing parameters used in the study. The studies showed that the laser metal deposition process, a laser-assisted additive fabrication technology, can be used to produce coatings with better properties. Also, the properties of the coatings can be controlled by controlling the process parameters. This chapter has demonstrated the importance of the laser-assisted additive fabrication technology in the production of micro-sized coatings for improved properties and for the expansion of service life of components that are used in corrosive and wear producing environments.

ACKNOWLEDGMENTS

This work was supported by University of Johannesburg research council and the L'OREAL-UNESCO for Women in Science.

REFERENCES

[1] H. Haken, Laser Theory, Springer, Berlin, Heidelberg, 1983.
[2] R.M. Mahamood, E.T. Akinlabi, M. Shukla, S. Pityana, Evolutionary additive manufacturing: an overview, Opt. Lasers Eng. 27 (2014) 161–178.
[3] J. Scott, N. Gupta, C. Wember, S. Newsom, T. Wohlers, T. Caffrey, Additive Manufacturing: Status and Opportunities, Science and Technology Policy Institute, Available from: https://www.ida.org/stpi/occasionalpapers/papers/AM3D_33012_Final.pdf, 2012 (accessed 11.07.12).
[4] Y. Niki, H. Matsumoto, Y. Suda, T. Otans, K. Fujikawa, Y. Toyama, Metal ions induce bone-resorbing cytokine production thorough the redox pathway in synoviocytes and bone marrow macrophages, Biomaterials 24 (2003) 1447–1457.

[5] Y. Bi, R.R. Ran de Motter, A.A. Ragab, V.M. Goldberg, J.M. Anderson, E.M. Greenfield, Titanium particles stimulate bone resorption by inducing differentiation of marine osteoclasts, J. Biomed. Mater. Res. 83 (2001) 501–508.
[6] C. Wu, Y. Ramaswamy, D. Gale, W. Yang, K. Xiao, L. Zhang, Y. Yin, H. Zreiqat, Novel sphene coatings on Ti-6A1-4V for orthopedic implants using sol-gel method, Acta Biomater. 4 (2008) 569–576.
[7] M.L. Wang, L.J. Nesti, R. Tuli, J. Lazatin, K.G. Danielson, P.F. Sherkey, Titanium particles suppress expression of osteoblastic pheno-type in human mesenchymal stem cells, J. Orthop. Res. 20 (2002) 1175–1184.
[8] R.R. Willey, Practical Design and Production of Optical Thin Films, Willey Optical Consultants; CRC Press; Marcel Dekker Incorporated, Charlevoix, MI, 2002.
[9] Y.-K. Choi, Y.-K. Ha, H.Y. Jac-Eun, K. Kim, Improved transmittance in one-dimensional metallic photonic crystals, Phys. B Condens. Matter 338 (2003) 132–135.
[10] A. Alejo-Molina, J.J. Sanchez-Mondragon, D.A. May-Arrioja, D. Rpmero, J. Escobedo-Alatorre, A. Zamudio-Lara, Complex dispersion relation of dielectric photonic crystal with thin metallic layers, Microelectronic 40 (2009) 459–461.
[11] J.M. Lackner, C. Stottera, W. Waldhauser, R. Ebnera, W. Lenzb, M. Beutld, Pulsed laser deposition of diamond-like carbon coatings for industrial tribological applications, Surf. Coat. Technol. 174–175 (2003) 402–407.
[12] K. Honglertkongsakul, P.W. May, B. Paosawatyanyong, Electrical and optical properties of diamond-like carbon films deposited by pulsed laser ablation, Diam. Relat. Mater. 19 (2010) 999–1002.
[13] S.S. Yap, T.Y. Tou, Investigation of diamond-like carbon/silicon hetero junctions deposited by pulsed Nd:YAG laser, Vacuum 82 (2008) 1449–1451.
[14] H. Cho, S. Kim, H. Ki, Pulsed laser deposition of functionally gradient diamond-like carbon (DLC) films using a 355 nm picosecond laser, Acta Mater. 60 (18) (2012) 6237–6246.
[15] V.Yu. Fominski, S.N. Grigoriev, J.P. Celis, R.I. Romanov, V.B. Oshurko, Structure and mechanical properties of W-Se-C/diamond-like carbon and W-Se/diamond-like carbon bi-layer coatings prepared by pulsed laser deposition, Thin Solid Films 520 (21) (2012) 6476–6483.
[16] M.Z. Abdullah, M.A. Ahmad, A.N. Abdullah, M.H. Othman, P.H.A. Zainuddin, Metal release of multilayer coatings by physical vapour deposition (PVD), Procedia Eng. 148 (2016) 254–260.
[17] C. Piccirillo, C.J. Denis, R.C. Pullar, R. Binions, I.P. Parkin, J.A. Darr, P.M.L. Castro, Aerosol assisted chemical vapour deposition of hydroxyapatite-embedded titanium dioxide composite thin films, J. Photochem. Photobiol. A Chem. 332 (2017) 45–53.
[18] Y. Zhang, H. Sahasrabudhe, A. Bandyopadhyay, Additive manufacturing of Ti-Si-N ceramic coatings on titanium, Appl. Surf. Sci. 346 (2015) 428–437.
[19] Y. Wang, G. Li, C. Wang, Y. Xia, B. Sandip, C. Dong, Microstructure and properties of laser clad Zr-based alloy coatings on Ti substrates, Surf. Coat. Technol. 176 (2004) 284–289.
[20] R.M. Mahamood, M. Shukla, S. Pityana, Laser additive manufacturing in surface modification of metals. in: L. Santo, J.P. Davim (Eds.), Surface Engineering Techniques and Applications: Research Advancements, IGI Global, Pennsylvania, 2014, pp. 222–248, https://doi.org/10.4018/978-1-4666-5141-8.ch007.
[21] Y. Wang, G. Li, C. Wang, Y. Xia, B. Sandip, C. Dong, Microstructure and properties of laser clad Zr-based alloy coatings on Ti substrates, Surf. Coat. Technol. 176 (2004) 284–289.

[22] N.M. Baloyi, A.P.I. Popoola, S.L. Pityana, Laser coating of zirconium and ZrO_2 composites on Ti6Al4V for biomedical applications, S. Afr. J. Ind. Eng. 25 (1) (2014) 62–70.
[23] M. Krzyzanowski, S. Bajda, Y. Liu, A. Triantaphyllou, W.M. Rainforth, M. Glendenning, 3D analysis of thermal and stress evolution during laser cladding of bioactive glass coatings, J. Mech. Behav. Biomed. Mater. 59 (2016) 404–417.
[24] G.D. Ram, B.E. Stucker, A feasibility study of LENS® deposition of CoCrMo coating on a titanium substrate, J. Manuf. Sci. Eng. 130 (2) (2008). 024503-024503-5.
[25] R.M. Mahamood, E.T. Akinlabi, M. Shukla, S. Pityana, Evolutionary additive manufacturing: an overview, Opt. Lasers Eng. 27 (2014) 161–178.
[26] A. Pinkerton, L. Li, Multiple-layer cladding of stainless steel using a high-powered diode laser: an experimental investigation of the process characteristics and material properties, Thin Solid Films 453–454 (2004) 471–476.
[27] J. Song, Q. Deng, C. Chen, D. Hu, Y. Li, Rebuilding of metal components with laser cladding forming, Appl. Surf. Sci. 252 (22) (2006) 7934–7940.
[28] A.J. Pinkerton, W. Wang, L. Li, Component repair using laser direct metal deposition, Proc. IMechE B J. Eng. Manuf. 122 (2008) 827–836.
[29] B. Graf, A. Gumenyuk, M. Rethmeier, Laser metal deposition as repair technology for stainless steel and titanium alloys, Phys. Procedia 39 (2012) 376–381, https://doi.org/10.1016/j.phpro.2012.10.051.
[30] Z.M. Wang, E.O. Ezugwu, Titanium alloys and their machinability—a review, J. Mater. Process. Technol. 68 (1997) 262–270.
[31] K. Gupta, R.F. Laubscher, Sustainable machining of titanium alloys—a critical review, Proc. IMechE B J. Eng. Manuf. (2016), https://doi.org/10.1177/0954405416634278.
[32] R.M. Mahamood, E.T. Akinlabi, Effect of processing parameters on wear resistance property of laser material deposited titanium-alloy composite, J. Optoelectron. Adv. Mater. 17 (9-10) (2015) 1348–1360.
[33] R.M. Mahamood, E.T. Akinlabi, Effect of laser power and powder flow rate on the wear resistance behaviour of laser metal deposited TiC/Ti6Al4V composites, Mater. Today: Proc. 2 (4–5) (2015) 2679–2686.
[34] R.M. Mahamood, E.T. Akinlabi, M. Shukla, S. Pityana, Characterization of laser deposited Ti6A4V/TiC composite, Opt. Lasers Eng. 29 (3-4) (2014) 197–213.
[35] R.M. Mahamood, E.T. Akinlabi, S.A. Akinlabi, Laser power and scanning speed influence on the mechanical property of laser metal deposited titanium-alloy, Laser Manuf. Mater. Process. 2 (1) (2014) 43–55.
[36] R.M. Mahamood, E.T. Akinlabi, M. Shukla, S. Pityana, Scanning velocity influence on microstructure, microhardness and wear resistance performance on laser deposited Ti6Al4V/TiC composite, Mater. Des. 50 (2013) 656–666.
[37] R.M. Mahamood, E.T. Akinlabi, M. Shukla, S. Pityana, Characterizing the effect of laser power density on microstructure, microhardness and surface finish of laser deposited titanium alloy, J. Manuf. Sci. Eng. 135 (6) (2013), https://doi.org/10.1115/1.4025737.064502-064502-4.
[38] ASTM E3-11, Standard Guide for Preparation of Metallographic Specimens, vol. 03.01, ASTM International Book of Standards, 2011.
[39] ASTM E384-11e1, Standard Test Method for Knoop and Vickers Hardness of Materials, vol. 03.01, ASTM International Book of Standards, 2011.
[40] ASTM G133-05, Standard Test Method for Linearly Reciprocating Ball-on-Flat Sliding Wear, vol. 03.02, ASTM International Book of Standards, 2010.
[41] S. Sharma, S. Sangal, K. Mondal, On the optical microscopic method for the determination of ball-on-flat surface linearly reciprocating sliding wear volume, Wear 300 (1–2) (2013) 82–89.

FURTHER READING

[1] D.F. Justin, B.E. Stucker, D.J.R. Gabbita, D.W. Britt, Laser based metal deposition (LBMD) of antimicrobials to implant surfaces, US Patent 7,951,412, 2011.
[2] V.K. Balla, P.P. Bandyopadhyay, S. Bose, A. Bandyopadhyay, Compositionally graded yttria-stabilized zirconia coating on stainless steel using laser engineered net shaping (LENS™), Scr. Mater. 57 (9) (2007) 861–864.
[3] M.R. Mahamood, E.T. Akinlabi, Functionally Graded Materials, Springer Science Publisher, Switzerland, 2017.

CHAPTER 22

Multiphysics Modelling of Laser Solid Freeform Fabrication Techniques

J. Lawrence*, M. Alimardani†, C.P. Paul†, E. Toyserkani†, A. Khajepour†
*University of Chester, Chester, United Kingdom
†University of Waterloo, Waterloo, ON, Canada

22.1 INTRODUCTION

In today's highly competitive and fast-changing world, emerging advanced technologies have had an influential effect on the transition from mass production to flexible low-volume-production manufacturing strategies, in which complex structures capable of functioning in a multidisciplinary environment are prevalent. Laser solid freeform fabrication (LSFF) as a layered/additive manufacturing technique has shown tremendous potential for this new industrial environment. LSFF utilizes the advantageous features of additive manufacturing techniques and laser technology which itself has had tremendous impacts on many different fields of science and engineering within the last few decades.

In LSFF, a fully functional near-net three dimensional (3D) object can be fabricated directly from its CAD model by adding metallic materials into the design domain through sequential deposition tracks. Each track (clad) is created by rapid solidification of the additive materials and a thin layer of the surface of a moving substrate that are melted simultaneously employing a laser beam as a heat source. Additive nature as well as special attributes mainly resulting from unique laser beam characteristics has made LSFF a potential candidate in various applications such as rapid prototyping, coating, and parts repair especially for high-value tools. Small heat affected zone (HAZ), minimal dilution, direct deposition, and integration of CAD tools with the production process are some of the main features of LSFF that can eliminate many manufacturing steps compared to conventional methods, and also overcome the limitations of existing metal manufacturing technologies in terms

Advances in Laser Materials Processing
https://doi.org/10.1016/B978-0-08-101252-9.00022-4
Copyright © 2018 Elsevier Ltd.
All rights reserved.

of reduction of production time, enhancement of thermal controllability, and production of functionally graded parts (heterogeneous structures) [1–7].

A laser, a position device, and a material deposition system are the main equipment needed for the LSFF process. Additive material can be deposited into the process domain by different methods such as preplaced powder on the substrate, automatic powder injection, and wire feeding. Since utilizing LSFF in industry mainly requires deposition in complex path patterns, regardless of the technical advantages and disadvantages of different deposition methods, LSFF by powder injection has demonstrated to be more practical and efficient then the others. Fig. 22.1 shows a schematic arrangement of the LSFF process and its setup using powder injection for the material deposition.

Although the LSFF technique has shown many advantages, like other new techniques, LSFF also encounters several drawbacks, and consequently faces challenges in developing its full potential. The main drawbacks of LSFF mainly stem from the same sources as its advantages, the additive nature and the laser beam characteristics [8,9]. In LSFF, besides the layer-by-layer material deposition, the process domain undergoes a high cyclic heating and cooling regime. In addition, the heat source (i.e., laser beam), which is highly concentrated and moving across the fabrication domain, develops an uneven temperature distribution throughout the structure.

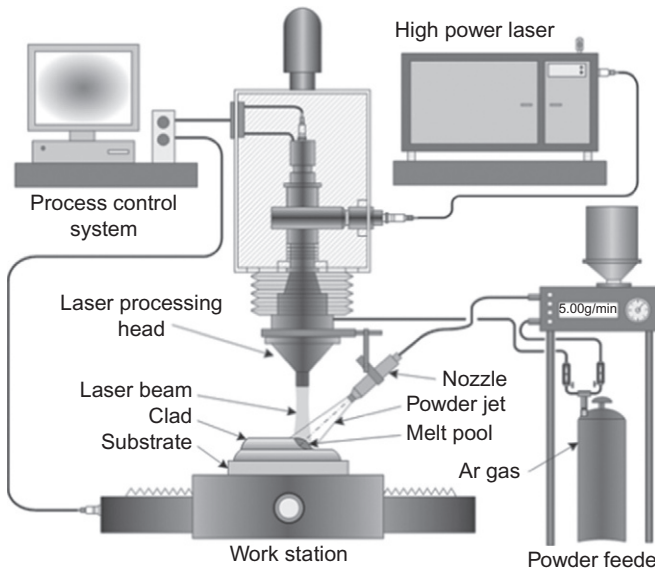


Fig. 22.1 Schematic arrangement of the LSFF setup.

This process characteristic makes LSFF vulnerable to thermal stresses, which are the primary source of potential delamination and crack formation.

On the other hand, LSFF, as a multidisciplinary technology, is governed by a large number of process parameters which are interrelated and highly sensitive to disturbances. These sensitive and interrelated parameters determine the circumstances of the involved physical phenomena such as heat conduction, melting, phase transformation, and solidification. Accordingly, final mechanical/metallurgical qualities of the fabricated parts using LSFF are highly dependent on the process parameters. Therefore, any disturbances or sudden changes of these parameters may compromise the geometrical accuracy and final structural qualities [10,11]. For instance, various interaction times, as a function of traverse speed, result in totally different outcomes in terms of the mechanical and metallurgical qualities.

In laser material processing, different interaction times and laser power intensities result in three different physical phenomena: vaporization, melting, and heating. Each of these three categories depends on the interaction time and laser power intensity, and produce different outcomes. LSFF, which is in the melting class, requires approximately an interaction time of 10^{-2} to 10^{-4} s, and a laser power intensity of 10^3 to 10^4 W/mm^2. In the same zone (melting class), by increasing the laser power intensities from 10^3 to 10^8 W/mm^2, and decreasing the interaction time from 10^{-3} to 10^{-8} s, simultaneously, the process condition would be appropriate for welding, alloying, and glazing, respectively [12,13]. Therefore, the sensitivity of LSFF to the process parameters and complexity of its involved physical phenomena make it difficult to produce consistent results that meet all desired mechanical and geometrical requirements, even under the same operating parameters. However, the limitations and drawbacks associated with this technique can be overcome efficiently by understanding the process and developing a comprehensive control plan to monitor and control the main process parameters [11,14]. In order to study the underlying phenomena from which the critical drawbacks of LSFF originate, it is first necessary to understand the relationships between the process parameters and their effects on the final build-up. Based on these relationships, it is then possible to control the process parameters and consequently counter external disturbances more efficiently during the fabrication process. Hence, developing a model of the process is exceptionally expedient to improve our understanding of this complex process and gain appropriate knowledge for the design of an efficient control plan.

This chapter describes the multiphysics numerical modelling of the LSFF process. For this purpose, an overview of physics of the process including

the LSFF governing equations and their associated boundary conditions is presented. After a brief discussion over recently developed numerical and analytical modelling approaches, a lumped model of the process is introduced to show a basic and simple modelling approach developed based on the ordinary differential equations (ODE). The remainder of this chapter is a case study devoted to a 3D multiphysics numerical approach developed to study the time-dependent temperature distributions, and thermal stress fields in respect to the geometrical formation of a build-up throughout the fabrication process.

22.2 PHYSICS OF LSFF

The LSFF process is one of the laser material processing techniques in which phase transformations from solid to liquid and liquid to solid occur. The physical domain of the LSFF process consists of a substrate, deposited material (i.e., clad), a powder stream, and a laser beam. The LSFF process is schematically shown in Fig. 22.2 in which h_c is the clad height, h_d is the depth of the melted substrate, and θj_{et} is the angle of the powder jet with respect to the substrate. To model the process, the laser beam specifications, material deposition, laser beam-powder interactions, and heat transfer throughout the process domain should be integrated in a dynamic fashion. All physical phenomena involved in the process can be assembled together

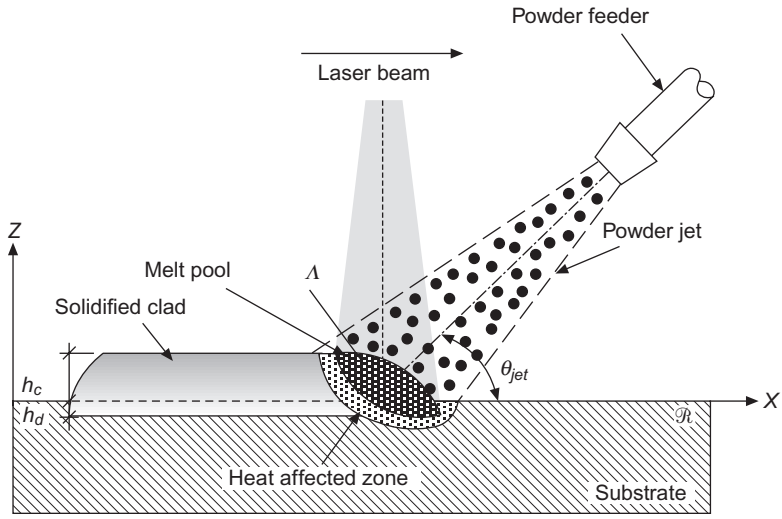


Fig. 22.2 Schematic of the deposition domain in the LSFF process with powder injection.

with a powder feeder based on their relationships through the process of governing equations. The following section addresses the governing equations of the process and their associated boundary conditions, as well as the significance of the process parameters in the modelling process.

22.2.1 Governing Equations

In LSFF, a main portion of the laser energy is directly absorbed by the substrate and forms a melt pool. The powder particles, which are simultaneously added to the process domain, absorb and carry some of the laser energy into the melt pool as well. Some part of the absorbed energy distributed throughout the process domain is then lost through convective and radiative losses. These physical phenomena in the process domain can mathematically be presented by continuity, momentum, and heat conduction equations as follows:

- Continuity equation:

$$\frac{\partial \rho}{\partial t} + \nabla \cdot (\rho \mathbf{U}) = 0 \tag{22.1}$$

- Momentum equations:

$$\frac{\partial (\rho u_x)}{\partial t} + \nabla \cdot (\rho \mathbf{U} u_x) = \nabla \cdot (\mu \nabla u_x) - \frac{\partial p}{\partial x} \tag{22.2}$$

$$\frac{\partial (\rho u_y)}{\partial t} + \nabla \cdot (\rho \mathbf{U} u_y) = \nabla \cdot (\mu \nabla u_y) - \frac{\partial p}{\partial y} \tag{22.3}$$

$$\frac{\partial (\rho u_z)}{\partial t} + \nabla \cdot (\rho \mathbf{U} u_z) = \nabla \cdot (\mu \nabla u_z) - \frac{\partial p}{\partial z} + \rho \mathbf{g} \tag{22.4}$$

- Heat conduction equation:

$$\nabla \cdot (k \nabla T) + Q = \frac{\partial (\rho c_p T)}{\partial t} + \mathbf{U} \cdot \nabla (\rho c_p T) \tag{22.5}$$

where ρ (kg/m^3) is density, t (s) is time, $\mathbf{U}$ (m/s) is the velocity vector, p (Pa) is the pressure, μ (kg/s · m) is viscosity, $\mathbf{g}$ (m/s^2) is the gravity field, k (W/m K) is thermal conductivity, c_p (J/kg K) is specific heat capacity, Q (W/m^3) is power generated per volume within the substrate, and u_x, u_y, u_z (m/s) are the liquid velocities in the x, y, and z directions, respectively. In addition to Eqs. (22.1)–(22.5), which are the main equations governing the LSFF process, the concentration equation and equations related to the evolution of free surface can also be considered along with the

main governing equations [13,15–18]. The concentration equation and the level set equation used for tracking the evolution of the free surface are respectively represented as follows:

$$\frac{\partial(\rho c)}{\partial t} + \nabla\cdot(\rho \mathbf{U} c) = \nabla\cdot(\rho D \nabla \mathbf{c}) + \nabla\cdot\left(\rho D \nabla(c_l - c)\right) - \nabla\cdot\left(\rho f_s (c_l - c_s)\mathbf{U}\right) \tag{22.6}$$

$$\frac{\partial \phi}{\partial t} + F|\nabla\phi| = 0 \tag{22.7}$$

where c is the solute concentration, f_s is the solid fraction, D is the mass diffusivity, $\varphi(x, y, t)$ is a distance function, and F is a speed function.

Another important physical phenomenon occurs in the LSFF process is the consequence of the nature of the temperature distribution, caused by the moving concentrated heat source across the process domain. The temperature gradients throughout the process domain cause thermal strains, which result in the deformation, and consequently, to thermal stresses. The thermal strain depends on the present temperature and the initial temperature, and is independent of stress. The total strain ε in a body can be represented as:

$$\varepsilon_{mn} = \varepsilon_{mn}^{M} + \varepsilon_{mn}^{T} \quad (m, n = 1, 2, 3) \tag{22.8}$$

where ε^M (m/m) and ε^T (m/m) are the strains contributed from the mechanical forces and temperature changes, respectively. As the stress is a linear function of strain, the constitutive equation for linear elastic materials is [19]:

$$\sigma_{ij} = D_{ijmn}\varepsilon_{mn} \quad (i, j, m, n = 1, 2, 3) \tag{22.9}$$

where σ_{ij} (Pa) is the elastic stress and D_{ijmn} (Pa) is the tensor of elastic coefficients with 81 components which are due to the symmetry of the stain and stress tensors. In general there are only 36 independent components.

As a small medium of the process domain goes under the high temperature regime, the HAZ and melt pool zone, the effects of the plastic strain, and phase transformation (i.e., volume change and transformation plasticity) should also be taken into account. Considering these effects, Eq. (22.8) can be written in its comprehensive form as:

$$\dot{\varepsilon}_{mn} = \dot{\varepsilon}_{mn}^{M} + \dot{\varepsilon}_{mn}^{T} + \dot{\varepsilon}_{mn}^{P} + \dot{\varepsilon}_{mn}^{T_p} + \dot{\varepsilon}_{mn}^{V} \quad (m, n = 1, 2, 3) \tag{22.10}$$

where ε^P (m/m) is the plastic strain, ε^{Tp} (m/m) is the contribution of the transformation plasticity effect, and ε^V (m/m) is the strain resulting from the

volumetric dilatation. Based on problem specifications, appropriate expressions for these strains are suggested in literature [20,21].

22.2.2 Boundary Conditions and Assumptions

To solve the equations governing the LSFF process, appropriate boundary and initial conditions are required for all points of an enclosed boundary during the process time, and particular conditions at one point in time (i.e., initial condition), respectively. For thermal strain and stress fields, it is also necessary to consider boundary conditions which prescribe the external forces and any displacement at the boundary surface. Furthermore, some of the process specifications such as the heat source (i.e., laser beam) and its moving effect need to be considered in the associated boundary conditions.

The second-order heat conduction Eq. (22.5) must be solved under the appropriate initial-essential and boundary conditions. The initial and essential conditions are:

$$T\left(x,y,z,0\right)=T_0 \tag{22.11}$$

$$T\left(x,y,z,\infty\right)=T_0 \tag{22.12}$$

where $T_0(K)$ is the ambient temperature. The convection and radiation boundary condition can be considered together as:

$$k\left(\nabla T\cdot\mathbf{n}\right)\Big|_{\Re}=\left[-h\left(T-T_0\right)-\varepsilon_R\sigma_R\left(T^4-T_0^4\right)\right]\Big|_{\Re}\quad \text{if } \Re\notin\Lambda \tag{22.13}$$

where $\mathbf{n}$ is the normal vector of the surface, ε_R is emissivity, h is the heat convection coefficient ($\mathrm{W/m^2K}$), σ_R is the Stefan-Boltzman constant ($5.67\times10^{-8}\mathrm{W/m^2K^4}$), $\mathscr{R}$ ($\mathrm{m^2}$) is the workpiece surface, and Λ ($\mathrm{m^2}$) is the area of the laser beam on the workpiece. $\mathscr{R}$ and Λ are shown in Fig. 22.2. The effect of the moving laser beam can also be considered as a surface heat source in the boundary conditions as follows:

$$k\left(\nabla T\cdot\mathbf{n}\right)\Big|_{\Re}=\left[\beta I\left(x,y,z,U,t\right)-h\left(T-T_0\right)-\varepsilon_R\sigma_R\left(T^4-T_0^4\right)\right]\Big|_{\Re}\quad \text{if } \Re\notin\Lambda \tag{22.14}$$

where β is the absorption factor, I ($\mathrm{W/m^2}$) is the laser energy distribution on the workpiece, and U (m/s) is the velocity in the x, y, and z directions, respectively. Initial conditions for stress and strain fields which prescribe the external forces and any displacement at the boundary surface at the beginning of the LSFF process are:

$$\varepsilon\left(x,y,z,0\right)\Big|_{T=T_0}=0\quad\text{and}\quad\sigma\left(x,y,z,0\right)\Big|_{T=T_0}=0 \tag{22.15}$$

Since the solute atoms throughout the solidification process disperse into the liquid phase as a result of rejection from the solidification front, the boundary condition can be defined as the gradient of the solute concentration on the liquid side [17]:

$$-D_l \frac{\partial c_l}{\partial n} = \left(1 - k_p\right) v_n c_l \tag{22.16}$$

where v_n (m/s) is the normal interface velocity. The boundary condition at the liquid-gas interface is:

$$c\,|_{\phi=0} = c_{pp} \tag{22.17}$$

where c_{pp} is the powder particle solute concentration. More details regarding the boundary conditions of free surfaces and forces applied at liquid-gas interfaces can be found in literature [16,17].

Since considering all phenomena realistically occurring during the LSFF process makes the problem highly complicated, some adjustments as well as assumptions for reducing the complexity of the problem must be considered. To name a few, many models were developed only for 2D domain. In some modelling approaches, the effect of the additive materials was ignored or considered in a decoupled fashion, while in some other approaches the additive materials were considered in the model with a predefined geometry. To simplify the mathematical formulation, the effects of heat losses through convection and radiation were partially/fully overlooked or considered together with a proper approximation. Because many physical phenomena are involved in this multifaceted process, a large number of diverse assumptions and adjustments can be listed. However, these assumptions are made in a way to keep any possible compromises to a minimum regarding the aspect of the process under investigation.

22.3 MULTIPHYSICS MODELLING OF LSFF PROCESSES

Solving complex differential equations as the bases of mathematical models of a process by means of numerical methods, which are well suited to computer implementation, has dramatically been alleviated with recent advances in high speed computers. Consequently, many fields of industry have been favorably circumstanced by modelling real-life problems. Once a model of a system is available, it is possible to carry out various analyses to gain a better understanding of the system. In addition, for a complex process, such derived models reduce the time and complexity involved in experimental methods. There are different modelling classifications; the main one groups

them in two classes: analytical models and numerical models. In this section, to show a basic and simple modelling approach to the LSFF process, a lumped model is introduced. A few numerical and analytical modelling approaches will be addressed, and finally the development of a 3D numerical model of the LSFF process for predicting transient geometrical, temperature, and thermal stress characteristics of the LSFF process as a function of process parameters and material properties is described in detail.

22.3.1 A Lumped Model of the LSFF Process

A lumped model of a complex process is a simplified version of the process mathematical model which comprises ODEs rather than partial differential equations. In this section, the development of a lumped model for laser material deposition by powder injection introduced by Toyserkani et al. [22] will briefly be described. To begin, the balance of energy in the process, which is imposed by different physical interactions and mechanisms, is shown in Fig. 22.3. In the figure, A_c (m^2) and r_l (m) denote the cross-section area of the deposited clad and the laser beam spot radius on the substrate, respectively.

The balance of energy shown in the figure can be expressed as:

$$Q_{cond} = Q_l - Q_{sr} - Q_L - (\eta - 1)Q_p - Q_{pr} - Q_{rad} - Q_{conv} \qquad (22.18)$$

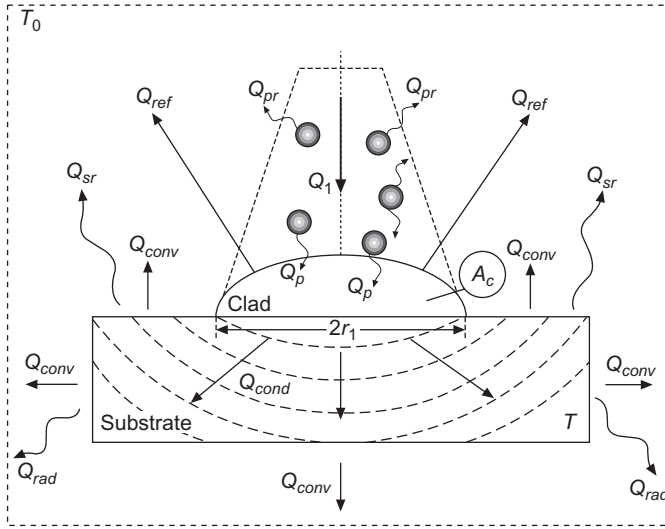


Fig. 22.3 Balance of energy in the LSFF process domain.

where Q_{cond} (J) is the total energy absorbed by the substrate, Q_l (J) is the energy imposed to the system by the laser, Q_{sr} (J) is the laser energy reflected from the surface of the substrate, Q_L (J) is the energy of latent heat, Q_p (J) is the laser energy absorbed by powder particles and added to the system, Q_{pr} (J) is the energy reflected from the powder particles, Q_{rad} (J) is the energy lost through radiation, and Q_{conv} (J) is the energy lost through convection.

Each term can be defined based on the process specifications. The energy added to the medium by the laser beam is presented by the following equation:

$$Q_l = A_l P_l \Delta t = \pi r_l^2 P_l \Delta t \tag{22.19}$$

where A_l (m^2) is the laser beam area on the substrate, P_l (W/m^2) is the average laser power density, and Δt (s) is the interaction time between the laser and any specific point on the substrate located on the deposition track. Considering the traverse speed u (m/s), the interaction time can be defined as:

$$\Delta t = \frac{2r_l}{u} \tag{22.20}$$

The portion of energy reflected from the substrate is presented by:

$$Q_{sr} = \left(1 - \beta_s\right)\left(Q_l - Q_p\right) \tag{22.21}$$

where β_s is the substrate absorbed coefficient. The energy of latent heat is also defined as:

$$Q_L = L_f \rho V \tag{22.22}$$

where L_f (J/kg) is the latent heat of fusion, ρ (kg/m^3) is the average density in the deposition zone, and V (m^3) is the volume of the melt pool. To define an expression for V, the clad cross-section can be considered as a portion of a cylinder with area of A_c as shown in Fig. 22.3. In this approach, the width of the clad and the melt pool length are assumed to be the same as the laser beam diameter on the substrate. Therefore, the cross-section of the clad is expressed as:

$$A_c = \frac{\dot{m}}{\rho_p u}\eta \tag{22.23}$$

where ρ_p (kg/m^3) is the powder particles density, $\dot{m}$ (kg/s) is the powder feed rate, and η is the powder catchment efficiency. In this approach, by ignoring the dilution, the volume of the melt pool can be defined as follows:

$$V = 2r_l A_c \tag{22.24}$$

The powder catchment efficiency is also assumed by the ratio of the laser beam and the powder stream areas on the substrate. At this stage to define an expression for the energy absorbed by the powder particles, a homogeneous distribution of the powder particles across the laser beam area on the substrate is assumed. By knowing the powder particles radius r_p (m), the number of particles entered in the laser beam area during the interaction time can be derived from the following equation:

$$n = \frac{3\dot{m}\Delta t}{4\pi\rho_p r_p^3} \tag{22.25}$$

Knowing the number of particles in the laser beam area, the attenuated area by the powder particle is defined as:

$$A_{atten} = n\pi r_p^2 = \frac{3\dot{m}\Delta t}{4\pi\rho_p r_p} \tag{22.26}$$

Using the equation obtained for A_{atten}, the laser energy absorbed by the particles is:

$$Q_p = \frac{A_{atten}}{A_l} Q_l = \frac{3\dot{m}\Delta t}{4\pi\rho_p r_p r_l^2} Q_l \tag{22.27}$$

Therefore, the reflected energy from the powder particles can be obtained as follows:

$$Q_{pr} = (1 - \beta_p) Q_p \tag{22.28}$$

where β_p is the absorbed coefficient of powder particles. The energy loss due to the radiation within the interaction time can be defined by:

$$Q_{rad} = A_l \varepsilon_R \sigma_R \left(T^4 - T_0^4\right) \Delta t \tag{22.29}$$

The energy loss due to the convection in this approach assumed for the laser beam area is presented as:

$$Q_{conv} = A_l h \left(T - T_0\right) \Delta t \tag{22.30}$$

where h (W/m^{2}K) is the heat convection coefficient. Finally, the energy absorbed by the substrate can be obtained using the following equation:

$$Q_{cond} = \rho c_p \int_{V_s} T\left(x, y, z, \Delta t\right) dV_s \tag{22.31}$$

where V_s (m^3) is the heat affected volume in the Cartesian coordinate system. Assembling all the expressions derived for the different energies

through Eq. (22.18), a lumped mathematical model for the laser material deposition is obtained.

22.3.2 Numerical and Analytical Modelling Approaches

In analytical models, most of the solution strategies are based on the mathematical formulation only employing differential equations. Since solving these differential equations for any complex or real-life problems is difficult or even in most cases impossible, significant simplifications involved in these types of modelling are prevalent, such as considering one-dimensional or steady-state models. In some less severe cases, the differential equations can be solved analytically by using numerical methods at the very end of the solution process. Although with the advent of high-speed computers, numerical methods are now established solution strategies for complex real-life problems, analytical methods for showing a specific point of view are still preferred. For LSFF, Steen [13] described different basic analytical modelling approaches.

For instantaneous stationary point source of energy Qpc_p assuming no heat exchanges through convection or radiation, the solution of the heat conduction equation, Eq. (22.5), is:

$$T = \frac{Q}{8(\pi\alpha t)^{2/3}} \exp\left\{-\left[(x-x')^2 + (y-y')^2 + (z-z')^2\right] / 4\alpha t\right\} \quad (22.32)$$

The effect of different heat sources can be added using superposition principle. Therefore, with the constant heat flow q supplied to the medium per unit time, the temperate at point (x, y, z) at any time is found by integrating Eq. (22.32) over a time span. The final result is:

$$T(x,y,z,t) = \frac{q}{4(\pi\alpha d_r)^{2/3}} \operatorname{erfc}\left[\frac{d_r}{(4\alpha t)^{1/2}}\right] \quad (22.33)$$

where d_r is $\left[(x-x')^2 + (y-y')^2 + (z-z')^2\right]^{1/2}$.

Using the solution for the continuous point source and integrating it over an area, it is possible to determine the temperature of a domain at any point during the heating process with a heat source of any different geometry. In addition to using the same method for the point source expressed by Eq. (22.33), the well-known Rosenthal solution for the moving heat source with a constant velocity along the x direction of a semi-infinite domain without radiation heat loss and melting is expressed as follows:

$$T(x,y,z,t) - T_0 = \frac{Q}{2\pi k} e^{-\nu x/2\alpha} \frac{e^{-\nu\left[\left(x^2+y^2+z^2\right)^{1/}\right]/2\alpha}}{\left(x^2+y^2+z^2\right)^{1/2}} \tag{22.34}$$

where ν (m/s) is the velocity of the moving heat source.

There are many numerical/analytical models developed more realistically within the framework of the LSFF governing equations. Several stationary and transient analytical and numerical thermal models have been developed in which various physical parameters related to the heat transfer phenomenon such as melt pool characteristics and geometry, interaction between melt pool and powder stream, thermal distribution throughout the process domain, and the effect of variations in the process parameters on the whole process were studied [16,22–25]. Among these studies, only a few have reported on the 2D and 3D modelling of the multilayer LSFF process [26–29]. A number of research groups have also conducted studies to integrate stress fields induced by a thermal gradient into modelling approaches as a major phenomenon which determine several mechanical-metallurgical qualities of the final part [21,30–32]. However, in these reported modelling approaches in addition to some simplifications and assumptions, the geometry of the deposited materials is defined in advance (i.e., a thin wall with a rectangular cross-section), or in a dynamic fashion, a new group of elements at each time step is activated to build up a thin wall with a rectangular cross-section. For more information related to the various modelling approaches in laser material processing, a list and brief review of the stationary and dynamic models developed by different research groups is provided by Toyserkani et al. [22].

22.4 NUMERICAL MULTIPHYSICS MODELLING—A CASE STUDY

In this section, different steps of a numerical approach for multiphysics modelling of the LSFF process by powder injection is described. In this approach, the shape of each deposited layer is predicted in a decoupled fashion, while the temperature distributions and the temporal thermal stress fields are dynamically determined using a coupled solution strategy [1,33].

The transient temperature distribution $T(x, y, z, t)$ throughout the domain of the LSFF process can be obtained from the 3D heat conduction equation along with its associated boundary conditions as explained in Section 22.2. In this approach, assuming linear elastic material, the thermal

stress fields are obtained using Eqs. (22.8) and (22.9). It should be noted that the heat conduction equation cannot properly represent the heat transfer mechanism in the melt pool zone which dominates by convection, resulting from Marangoni flows driven by surface tension gradients. For an accurate formulation, the melt pool and solid zones can be considered as separate regions and coupled through moving boundary conditions [34]. However, it is possible to formulate the heat transfer system of the melt pool as a part of the whole process domain, and it can also indirectly take other physical effects encompassed by other process governing equations into account by considering appropriate assumptions [35,36].

- For the laser beam energy distribution, a circular Gaussion TEM_{00} is considered. The beam profile for this case is defined as:

$$I(r) = \frac{2P_l}{\pi r_l^2} \exp\left[\frac{-2\left(r^2\right)}{r_l^2}\right] \tag{22.35}$$

  where r_l (m) is the laser beam radius, r (m) is the distance from the center of the laser beam, and P_l (W) is the laser average power. For a pulsed laser, laser power is $P_l = E \cdot f$, where E (J) is the energy per pulse and f (Hz) is the laser pulse frequency. The effect of the moving laser beam is taken into account by updating its position r on the surface of the substrate based on the relative velocity of the laser processing head and the substrate as follows:

$$r = \left[\left(x - \int_{t_0}^{t} u_x dt\right)^2 + \left(y - \int_{t_0}^{t} u_y dt\right)^2 + \left(z - \int_{t_0}^{t} u_z dt\right)^2\right]^{1/2} \tag{22.36}$$

  where u_x (m/s), u_y (m/s), and u_z (m/s) are the continuous velocities of the center of the laser beam in the x, y, and z directions, respectively. If the laser beam strikes a nonplanar surface, the circular beam is projected on the nonplanar surface accordingly.
- The effect of latent heat of fusion on the temperature distribution is considered by modifying the specific heat capacity [37]. Marangoni flow is also considered in the process formulation by modifying the thermal conductivity [36].
- The substrate absorbs a portion of the laser energy directly, and the powder particles also absorb and carry some of the laser energy into the melt pool. To simplify this mechanism, also called power attenuation, a method developed by Picasso et al. [38] is implemented. Based on this method, the total absorbed power by the substrate P_w can be defined as:

$$P_w = \beta_e P_l \tag{22.37}$$

where β_e is the effective absorption factor. Based on this method, an effective absorption factor is expressed as

$$\beta_e = \beta_w (1-\xi) + \eta_p \beta_p \xi + \eta_p \beta_p (1-\beta_w)(1-\xi)\xi \tag{22.38}$$

where ξ is the ratio of the attenuated power and the laser power, β_w is the substrate absorption factor, β_p is the powder absorption factor, and η_p is the powder efficiency which is the intersection areas of the powder stream and the laser beam on the substrate over the area of the powder stream.

- For a nonplanar surface, the effect of the angle of incidence of the laser beam is considered. To calculate this effect, an average angle is considered, regarding the intersection of the laser beam with a nonplanar surface.
- To reduce the computational time, a combined radiative and convective heat transfer coefficient (h_c) is considered in the mathematical model of the process [11]:

$$h_c = 24.1 \times 10^{-4} \varepsilon_R T^{1.61} \tag{22.39}$$

- Some specific parameters such as the absorption coefficient are considered to be temperature dependent. For other thermo-physical and optical properties, their averages relative to the process temperatures were calculated to consider their temperature dependency.
- For isotropic material, all the 81 components of D_{ijmn} defined in Eq. (22.9) turn to two independent entities.

Implementing the adjustments/assumptions listed above in the boundary conditions, Eqs. (22.13) and (22.14), and considering a moving laser beam on the surface of the substrate with a constant velocity positioned on the xy plane (i.e., $u_z = 0$), the final optimum boundary condition for thermal governing equation is derived as:

$$-K(\nabla T \cdot n)|_{\Re} = \frac{2}{\pi r_l^2} \beta_e P_l \exp\left[\frac{-2\left[(x-u_x t)^2 + (y-u_y t)^2\right]}{r_l^2}\right] - h_c (T - T_0) \quad \text{if} \quad \Re \in \Lambda \tag{22.40}$$

$$-K(\nabla T \cdot n)|_{\mathrm{R}} = -h_c (T - T_0) \qquad \text{if} \quad \Re \notin \Lambda \tag{22.41}$$

Furthermore, the stresses in terms of the strains represented by the thermoelastic constitutive equations, Eq. (22.9), can be given by [19]:

$$\sigma_{ij} = \frac{E}{(1+\nu)(1-2\nu)} \left[\nu\delta_{ij}\varepsilon_{kk} + (1-2\nu)\varepsilon_{ij} - (1+\nu)\alpha\Delta T\delta_{ij}\right] \quad (i,j,k=1,2,3) \tag{22.42}$$

where ν is Poisson's ratio, a (m/m K) is the coefficient of thermal expansion for isotropic materials, and δ is the Kronecker delta.

22.4.1 Modelling Architecture

To solve the LSFF mathematical model while considering the effect of additive material, a strategy is contrived by which the 3D geometry of each layer deposited either on the planar or nonplanar surfaces can be predicted throughout the deposition process. This strategy comprises two main steps:

Step 1 The coupled time-dependent temperature and strain-stress fields should be calculated throughout the LSFF domain by solving the governing equations under their defined boundary conditions. To incorporate the additive materials, the boundary of the moving melt pool on the substrate must be dynamically obtained over the fabrication time using the solution of the heat conduction equation. For this purpose, the process domain is sliced into n cross-sections in the x direction, as shown in Fig. 22.4A. Each cross-section is afterwards discretized in the yz plane as shown in Fig. 22.4B. From the solution of the heat conduction equation, each node is recognized by their positions (x, y, z) and their corresponding temperatures T_{xyz}. The temperatures on the nodes located on the boundaries of the slices are then assembled using their positions in the x, y, and z coordinates. Using this algorithm, the upper surface of the process domain with the melt pool boundary can be obtained for all time steps, as illustrated in Fig. 22.4C.

Step 2 Using the data obtained in the first step (locations and temperatures of the nodes on the surface of the substrate on which the laser beam

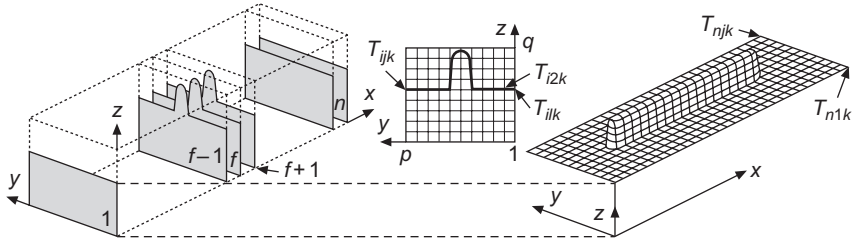


Fig. 22.4 Detection of the melt pool boundary on nonplanar surface.

runs), a thin layer of material with thickness of Δh (m) can be added to the nodes with temperatures higher than the melting temperature. Another required condition for these nodes is that they must be located on the intersection of the powder stream and the melt pool area. Putting this into mathematical language, the concept can be represented as follows:

$$h_{new}\big|_{\Omega} = h + \Delta h\big|_{\Omega} \quad \text{at } (x_h, y_h, z_h) \in A_{jet}^{melt} \tag{22.43}$$

$$A_{jet}^{melt} = \left\{ (x,y,z) \,|\, T_{(x,y,z)} \geq T_{melt} \bigcap (x,y,z) \in A_{jet} \right\} \tag{22.44}$$

where T_{melt} is the melting temperature of the substrate, and (x_h, y_h, z_h) are the coordinates of the nodes located on the intersection of the melt pool and powder stream. If this procedure continues throughout the deposition process of each layer, a clad with a realistic geometry will be created. This method is schematically illustrated in Fig. 22.5. The height Δh of the thin layer of material deposited at each time step into the LSFF domain, as shown in Fig. 22.5, can be calculated using the following mass conservation equation [22]:

$$\Delta h = \frac{\dot{m}\Delta t}{A_{jet}^{melt}\rho_p} \tag{22.45}$$

where Δt (s) is the time step, $\dot{m}$ (kg/s) is the powder feed rate, and p_p (kg/m^3) is the powder density.

After each layer's deposition, the process formulation should be updated for the next deposition regarding the new geometry of the process domain. It should be noted that the process for the thermal stress fields is being solved with the heat conduction equation simultaneously in a coupled fashion.

22.4.2 Solution Strategy of the Mathematical Model

For most practical problems involving irregular geometries and/or complicated boundary conditions and material properties, it is not generally possible to obtain analytical mathematical solutions. Such problems can be solved using numerical techniques. Since the mathematical model (i.e., the governing equations and their boundary conditions) of the LSFF process are complicated due to the complexity of the associated differential equations, the highly irregular 3D geometries of the deposited materials, interconnected operating parameters, and temperature dependent mechanical-material properties, and a moving heat source with a Gaussian distribution, finite element method (FEM) is employed to solve the mathematical model. For this purpose, COMSOL Multi-physics 3.2a (www.comsol.com) was used.

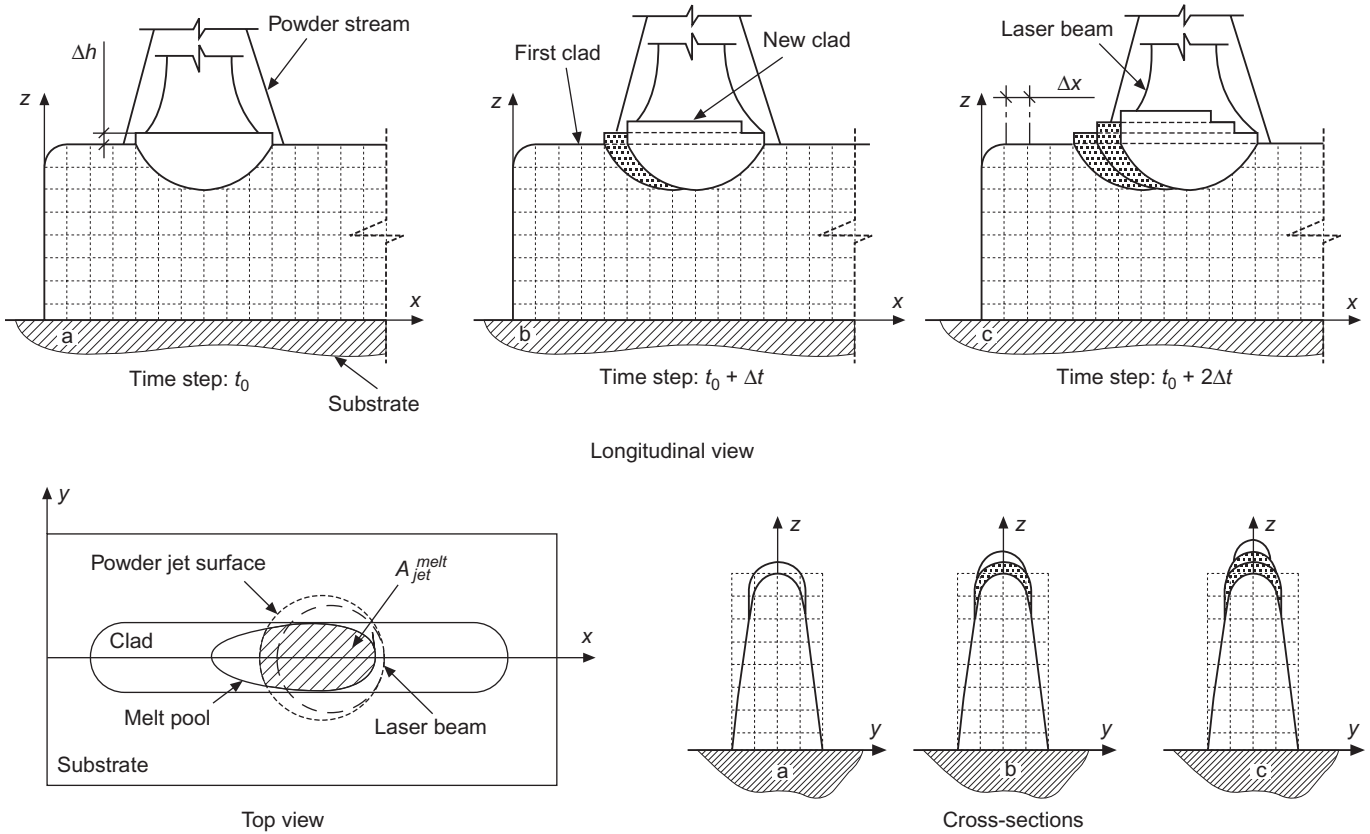


Fig. 22.5 Material deposition strategy in the LSFF process modelling.

To incorporate the additive material into the process domain, based on the method described in Section 22.4.1, a code was developed in MATLAB in which the required data of the heat conduction solutions are imported through the interface with COMSOL.

22.4.3 Case Study—Numerical Parameters

The proposed multiphysics numerical approach, described in the preceding sections, was used to model the LSFF process of a thin wall with four layers. The deposition process was simulated on a $25 \times 20 \times 5\,\text{mm}^3$ substrate. The material properties of AISI 304L steel were considered for both the substrate and powder particles. The absorption factor (β_w) of a flat surface, as a function of temperature [38], was used for the calculation of the absorption factor at any angle of inclination. Table 22.1 lists the process parameters and their values used for the simulation process.

Four-node tetrahedron elements were used to discretize the solid domain. To obtain the optimum number of elements in the model, a convergence test was conducted. This test was performed by increasing the number of elements in the FE model until the numerical solutions for the maximum temperature and thermal stress throughout the process domain and time converged to the particular values. In addition, all the required element quality checks of the FE model were automatically performed. Based on the results of the convergence test, the final discretized model for the first layer deposition has 82,025 elements and 484,076 degrees of freedom. Because the temperature distribution at the top surface of the model is of interest, a finer mesh was also used on the top surface instead of through the whole body of the model to prevent increasing the number of elements unreasonably.

The laser beam was programmed to scan a 15 mm straight line on the substrate with a starting point of (5, 0, 5) mm relative to the coordinate

Table 22.1 Process parameters

Process parameter	Value	Unit
$\dot{m}$—powder feed rate	2	g/min
P—laser power	300	W
r_{jet}—radius of the powder jet on the substrate	7.5^{e-4}	m
r_l—radius of the laser beam on the substrate	7.0^{e-4}	m
T_0—ambient temperature	298	K
T_m—melting temperature	1695	K
U—process speed	1.5	mm/s
ρ_p—powder density	7850	kg/m^3

system schematically shown in Fig. 22.5. To be consistent with the experimental process, as a finite time is required to turn off the laser and return it to its home position for the next layer deposition, a 20 s time span in which the laser is on and off for consecutive 10 s intervals was considered for the simulation process of the build-up of each layer. The temperature distribution and the stress/strain fields of the last time step of each simulation pass were also considered as the initial condition for the next simulation pass. To consider the effect of angle of incidence on the process, the effective absorption factor β_e, expressed by Eq. (22.38), was calculated for each layer. Therefore, the powder catchment efficiency η_p was required to be updated for each layer based on the geometrical specifications of each formed clad.

22.4.4 Experimental Procedure and Model Verification

To verify the numerical results, the same thin wall was also experimentally fabricated with the same operating parameters and conditions used in the numerical analysis. The experimental setup, schematically shown in Fig. 22.1, consisted of a four-axis CNC table, a LASAG FLS 1042 N Nd:YAG pulsed laser with a maximum power of 1000 W, and a 9MP-CL Sulzer Metco powder feeder. For temperature measurements around the melt pool, two XCIB high temperature inconel overbraided ceramic fiber insulated type K thermocouples with maximum temperature of 1250°C were used.

The laser intensity distribution was Gaussian TEM_{00}. The spot point of the laser beam was 5.08 mm under the focal point, with a diameter of 1.4 mm on the surface of the substrate. Argon gas with a flow rate of $2.3e^{-5}\,m^3/s$ was used to shroud the laser beam, and as a shield to protect the optical lenses. The same argon gas was also used as a conveying gas to carry powder to the deposition zone. The powder feed rate was adjusted to 2 g/min and remained within ±5% of this value throughout the experiment. The angle of the nozzle was set to 55 degrees with respect to horizontal. The powder used in the experiment was 98% pure on a metal basis. All other operating parameters are the same as those used in the numerical process and given in Table 22.1.

The numerical results were verified in terms of the temperature and stress-strain fields. The accuracy of the algorithm proposed for the material deposition was also checked with the appropriate experimental data. A comparison between the average heights of each layer obtained from the experimental and numerical results showed a maximum average relative error of 9.3%. This value represents the cumulative errors throughout the whole numerical analysis of the four-layer deposition. A geometrical comparison between the experimental and numerical results for only the fourth

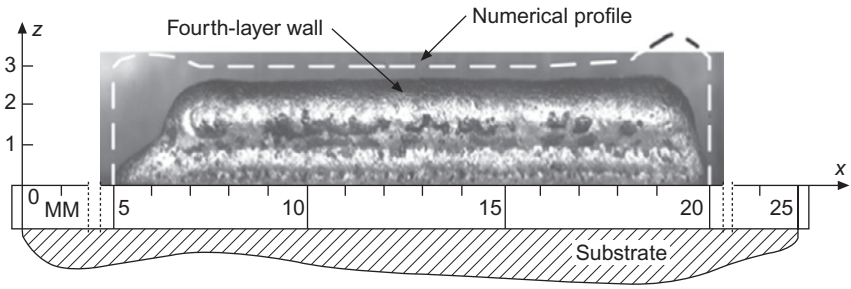


Fig. 22.6 Longitudinal views of the experimental and numerical fabrications of the thin wall.

layer is illustrated in Fig. 22.6. To verify the accuracy of the FE analysis in terms of the temperature distribution, the temperatures at two points in the substrate were dynamically measured during the fabrication process. The experimental results were compared with the same numerical results obtained from the simulation. The average relative errors for the first to fourth layers are 1.47%, 3.8%, 4.49%, and 5.51%, and 1.55%, 3.52%, 4.42%, and 5.29% for the first and second point, respectively. Fig. 22.7 shows the comparison between experimental and numerical temperature histories of the first point with a position of (17, 3, 3.5) mm in respect to the coordinate

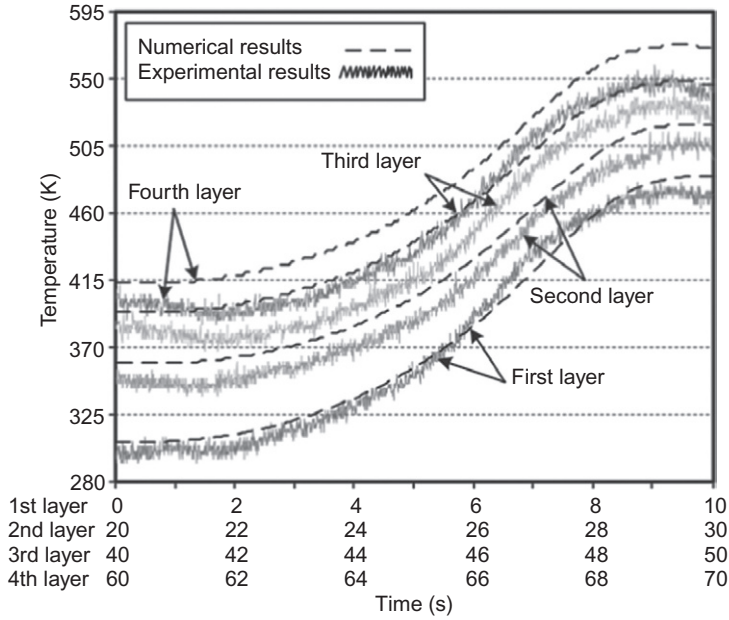


Fig. 22.7 Experimental and numerical temperature histories of the point (17, 3, 3.5) in the substrate [33].

system shown in Fig. 22.5. The model was also experimentally verified in terms of the distortion of the substrate caused by thermal stresses using two images taken of the substrate before and after the deposition process. The comparisons between the experimental and numerical results showed that the outputs of the model are generally in good agreement with the experimental results.

22.4.5 Temperature Distribution Throughout the Geometrical Formation in LSFF

Since the LSFF results strongly rely on the temperature distribution and its transformation throughout the fabrication process, studying this aspect of the process comprehensively is of crucial importance. The developed numerical model can predict the 3D geometry of the deposited material and its 3D relative temperature distribution at any time step during the simulation process. For instance, it is possible to obtain the time-dependent temperature and stress profiles of each desired point within the process domain throughout the build-up process as Fig. 22.8 shows the temperature profiles of four points along the deposition track on the plane $y = 0$. Using these data, it is possible to calculate the cooling/heating rate for any desired point across the process domain.

In addition to the temperature history of each point within the LSFF medium, temperature distribution throughout the process can provide more

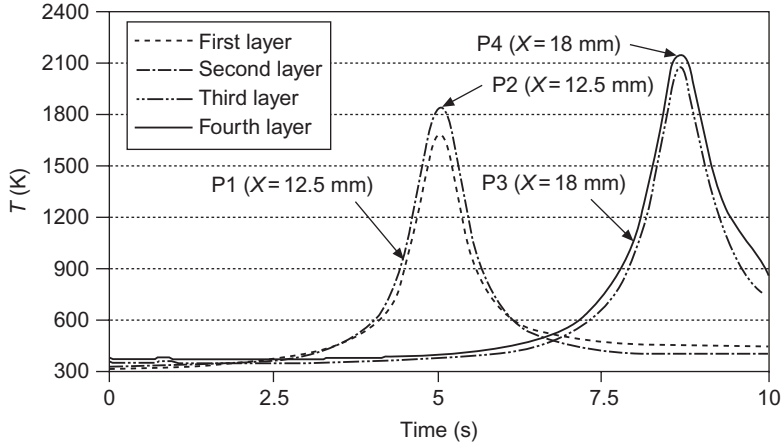


Fig. 22.8 Temperature profiles for the four points along the depositions of the first to fourth layer on the plane $y = 0$.

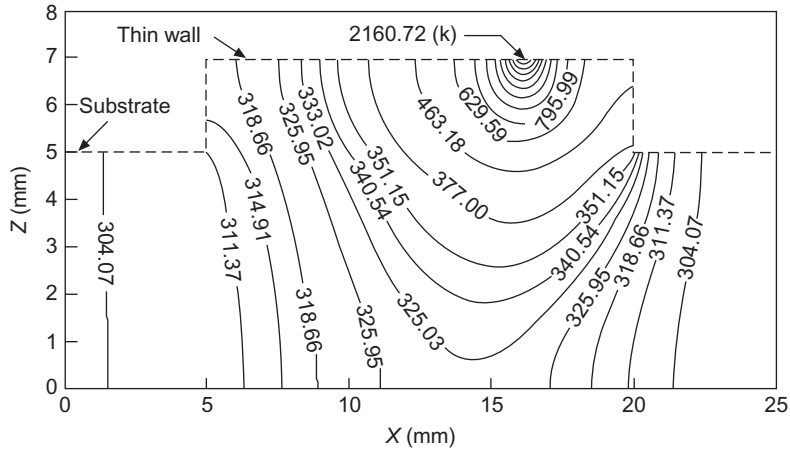


Fig. 22.9 Isothermal contours (K) on the plane $y=0$ before the fourth layer deposition at $t=7.5$ s [33].

information related to the melt pool, HAZ, and uniformity of temperature distributions as shown in Fig. 22.9 by isothermal contours. However, in order to comprehensively study the effects of the temperature fields on the qualities of the fabricated parts, in addition to the temperature distributions, their variations throughout the whole process provide another perspective regarding the trends of the temperature transformations throughout the fabrication process. Fig. 22.10 shows the maximum temperatures generated throughout the four-layer deposition process. As seen in Fig. 22.6, for the fourth layer, the numerical results of the geometry prediction show that more material was deposited at two end segments of the wall. The same geometrical patterns were observed for the second and third layers. Alimardani et al. [1] studied the correlation between the geometrical formation and the deposition track (X mm) maximum temperatures induced in the LSFF process. The reasoning was based on the variations of the nature of the heat losses from the first to the fourth layer. Due to geometrical changes, and consequently the nature of heat losses, the maximum temperatures for the first to the fourth layer increased throughout the build-up process as shown in Fig. 22.10. As more layers are deposited, the heat losses by convection/radiation relatively become more dominant than the heat losses by conduction. This behavior results in a higher temperature and a larger melt pool, which consequently results in a higher powder catchment. The same effect can also be observed between the middle and the end segments of the wall.

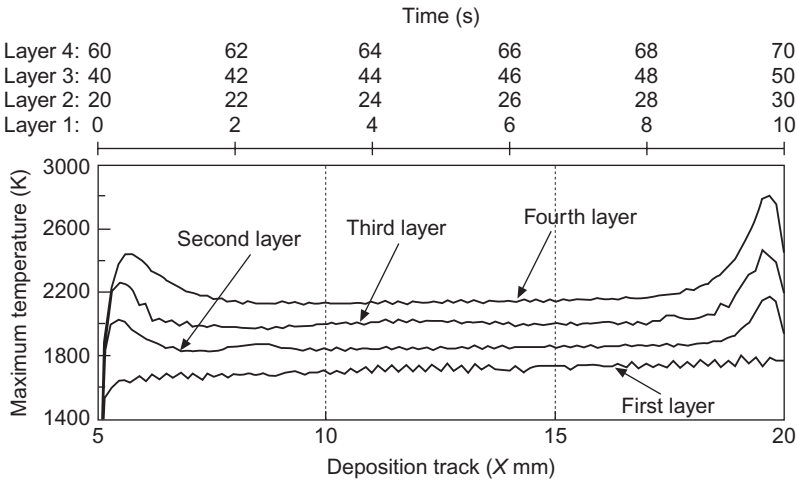


Fig. 22.10 Maximum temperatures (K) throughout the simulation of the four-layer wall [39].

22.4.6 Thermal Stress Fields Induced in the LSFF Process

Temperature distributions under a predefined set of the process parameters vary with the geometrical formation of a part throughout the fabrication process. With the same process parameters throughout the build-up process, the results in terms of the thermal stresses show that the changes in the thermal stresses are a function of the time-dependent geometry of the process domain and the temperature gradients. This is also implied by the governing equations. Corresponding to the temperature distribution and its transformation throughout the LSFF process, presented in Figs. 22.8–22.10, their counterparts for the thermal stresses can also be extracted from the numerical results. Contrary to the maximum temperatures evolution, the average maximum of thermal stresses exhibits different behavior and decreases from the first to the fourth layer depositions. This is due to the geometrical changes and the decrease in thermal gradients throughout the process (the substrate temperature within the build-up process increases). The average maximum thermal stresses of the second, third, and fourth layers compared to the first layer showed 20%, 22.5%, and 24% reductions, respectively. On the other hand, because of the sudden geometrical changes, although the average thermal stresses decrease during the successive layer depositions, the maximum stresses still occur at the end segments of layers 2–4.

Irregular formation at the two ends of the wall causes another stress concentration to take place at these two ends, in addition to the melt pool

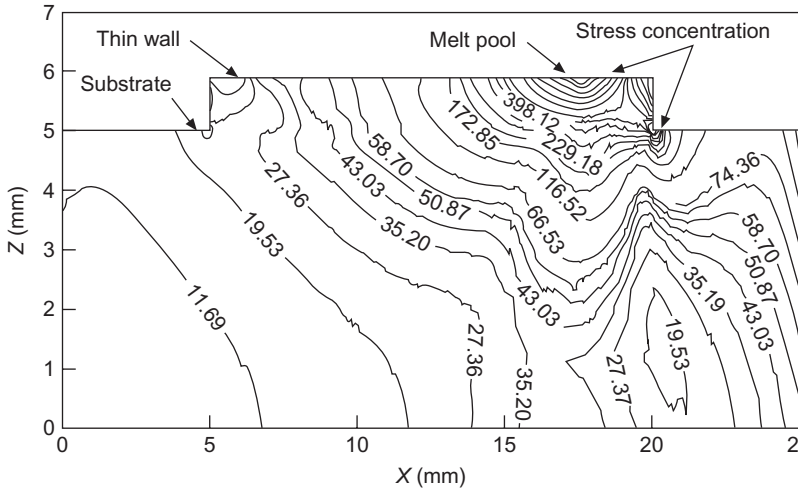


Fig. 22.11 Thermal stress field—Von Mises (MPa) at $t = 8.5$ s on the xz plane [39].

zone, as shown in Fig. 22.11. This indicates the zones that are inclined to potential delamination and crack formation.

A comprehensive and robust model can help to contrive methods to reduce the inconsistency in the process parameters, which were discussed in the last two sections, and in return enhance the results of the process. The modelling approach presented in this chapter had been used to study the effect of preheating and also clamping the substrate in order to manage the thermal stresses for reduction of the potential delamination and crack formation across the fabricated parts.

The numerical results related to the thermal stresses specifically at the melt pool and heat affected zones can improve considering the effects of all parts presented in Eq. (22.10) into the modelling algorithm.

22.5 CONCLUSIONS

In this chapter the underlying physics of the LSFF process along with the main process governing equations and their associated boundary conditions were briefly reviewed. The necessity of modelling this multifaceted process along with the major hurdles restricting the process from being modelled comprehensively was addressed. A lumped model was presented in which the process mathematical model is only defined based on the ODE equations. A multiphysics numerical modelling approach was described by which the geometry of the deposited material, temperature distributions,

and thermal stress fields throughout the fabrication process can be predicted. The experimental procedure for verification of the numerical results was another part that was followed by a discussion of the numerical and experimental results.

REFERENCES

[1] M. Alimardani, E. Toyserkani, J.P. Huissoon, Three-dimensional numerical approach for geometrical prediction of multilayer laser solid freeform fabrication process, J. Laser Appl. 19 (1) (2007) 14–25.

[2] L. Dubourg, D. Ursescu, F. Hlawka, A. Cornel, Laser cladding of MMC coatings on aluminum substrate: influence of composition and microstructure on mechanical properties, Wear 258 (11/12) (2005) 1745–1754.

[3] D. Hu, H. Mei, R. Kovacevic, Improving solid freeform fabrication by laser based additive manufacturing, Proc. Inst. Mech. Eng. B J. Eng. Manuf. 216 (9) (2002) 1253–1264.

[4] J.D. Kim, K.H. Kang, J.N. Kim, Nd:YAG laser cladding of marine propeller with hastelloy C-22, Appl. Phys. A Mater. Sci. Process. 79 (4/6) (2004) 1583–1585.

[5] C.P. Paul, P. Ganesh, S.K. Mishra, P. Bhargava, J. Negi, A.K. Nath, Investigating laser rapid manufacturing for Inconel-625 components, Opt. Laser Technol. 39 (4) (2007) 800–805.

[6] K. Samanta, B. Koc, Feature-based design and material blending for free-form heterogeneous object modelling, Comput. Aided Des. 37 (3) (2005) 287–305.

[7] M. Zhong, W. Liu, G. Ning, L. Yang, Y. Chen, Laser direct manufacturing of tungsten nickel collimation component, J. Mater. Process. Technol. 147 (2) (2004) 167–173.

[8] N.W. Klingbeil, J.L. Beuth, R.K. Chin, C.H. Amon, Residual stress-induced warping in direct metal solid freeform fabrication, Int. J. Mech. Sci. 44 (2) (2002) 57–77.

[9] W. Lee, J.M. Myoung, Y.H. Yoo, H. Shin, Effect of thermal misfit stress on crack deflection at planar interfaces in layered systems, J. Comput. Sci. Technol. 66 (2006) 435–443.

[10] H.Y. Chen, S.J. Huang, Adaptive fuzzy sliding-mode control for the Ti6A14V laser alloying process, Int. J. Manuf. Technol. Manag. 24 (2004) 667–674.

[11] D. Hu, R. Kovacevic, Sensing, modelling and control for laser-based additive manufacturing, Int. J. Mach. Tools Manuf. 43 (1) (2003) 51–60.

[12] J.F. Ready, LIA Handbook of Laser Material Processing, Laser Institute of America, Springer-Verlag Berlin Heidelberg, 2001, pp. 541–545.

[13] W.M. Steen, Laser Material Processing, third ed., Springer, New York, 2003.

[14] J. Liu, L. Li, In-time motion adjustment in laser cladding manufacturing process for improving dimensional accuracy and surface finish of the formed part, Opt. Laser Technol. 43 (2004) 477–483.

[15] J. Choi, L. Han, Y. Hua, Modelling and experiments of laser cladding with droplet injection, J. Heat Transf. 127 (2005) 978–986.

[16] L. Han, F.W. Liou, K.M. Phatak, Modelling of laser cladding with powder injection, Metall. Mater. Trans. A 35B (2004) 1139–1150.

[17] X. He, J. Mazumder, Transport phenomena during direct metal deposition, Appl. Phys. 101 (053113) (2007) 1–9.

[18] F.M. White, Heat Transfer, Addison-Wesley Publishing Company, Boston, MA, 1984.

[19] G.T. Mase, G.E. Mase, Continuum Mechanics for Engineers, second ed., CRC Press, Boca Raton, Florida, 1999.

[20] P. Ferro, H. Porzner, A. Tiziani, F. Bonollo, The influence of phase transformations on residual stresses induced by the welding process-3D and 2D numerical models, Model. Simul. Mater. Sci. Eng. 14 (2006) 117–136.

[21] S. Ghosh, J. Choi, Three-dimensional transient finite element analysis for residual stresses in the laser aided direct metal/material deposition process, J. Laser Appl. 17 (3) (2005) 144–158.
[22] E. Toyserkani, A. Khajepour, S.F. Corbin, Laser Cladding, CRC Press, Boca Raton, Florida, 2004.
[23] A. Fathi, E. Toyserkani, A. Khajepour, M. Durali, Prediction of melt pool depth and dilution in laser powder deposition, J. Phys. D. Appl. Phys. 39 (2006) 2613–2623.
[24] Y.L. Huang, J. Liu, N.H. Ma, J.G. Li, Three-dimensional analytical model on laser-powder interaction during laser cladding, J. Laser Appl. 18 (1) (2006) 42–46.
[25] A.J. Pinkerton, L. Li, Modelling the geometry of a moving laser melt pool and deposition track via energy and mass balances, J. Phys. D. Appl. Phys. 37 (2004) 1885–1895.
[26] L. Costa, R. Vilar, T. Reti, A.M. Deus, Rapid tooling by laser powder deposition: process simulation using finite element analysis, Acta Mater. 53 (2005) 3987–3999.
[27] L. Han, K.M. Phatak, F.W. Liou, Modelling of laser deposition and repair process, J. Laser Appl. 17 (2) (2005) 89–99.
[28] P. Peyre, P. Aubry, R. Fabbro, R. Neveu, A. Longuet, Analytical and numerical modelling of the direct metal deposition laser process, J. Phys. D. Appl. Phys. 41 (025403) (2008) 1–10.
[29] A. Vasinonta, J.L. Beuth, M.L. Grifith, A process map for consistent build condition in the solid freeform fabrication of thin-walled structures, J. Manuf. Sci. Eng. 123 (4) (2001) 615–622.
[30] R. Jendrzejewski, G. Sliwinski, Investigation of temperature and stress fields in laser cladding coating, Appl. Surf. Sci. 254 (4) (2007) 921–925.
[31] M.P. Mughal, H. Fawad, R.A. Mufti, M. Siddique, Deformation modelling in layered manufacturing of metallic parts using gas metal arc welding: effect of process parameters, Model. Simul. Mater. Sci. Eng. 13 (2005) 1187–1204.
[32] A.H. Nickel, D.M. Barnett, F.B. Prinz, Thermal stresses and deposition patterns in layered manufacturing, Mater. Sci. Eng. A 317 (2001) 59–64.
[33] M. Alimardani, E. Toyserkani, J.P. Huissoon, A 3D dynamic numerical approach for temperature and thermal stress distributions in multilayer laser solid freeform fabrication process, Opt. Lasers Eng. 45 (12) (2007) 1115–1130.
[34] A.P. Mackwood, R.C. Crafer, Thermal modelling of laser welding and related processes, Opt. Laser Technol. 37 (2005) 99–115.
[35] S. Kumar, S. Roy, C.P. Paul, A.K. Nath, Three-dimensional conduction heat transfer model for laser cladding process, Numer. Heat Transfer, Part B 53 (2008) 271–287.
[36] C. Lampa, A.F.H. Kaplan, J. Powell, C. Magnusson, Analytical thermodynamic model of laser welding, J. Phys. D. Appl. Phys. 30 (9) (1997) 1293–1299.
[37] S. Brown, H. Song, Finite element simulation of welding of large structures, J. Eng. Ind. Trans. ASME 114 (4) (1992) 441–451.
[38] M. Picasso, C.F. Marsden, J.D. Wagniere, A. Frend, M. Rappaz, A simple but realistic model for laser cladding, Metall. Mater. Trans. B 25B (2) (1994) 281–291.
[39] M. Alimardani, E. Toyserkani, J.P. Huissoon, C.P. Paul, On the delamination and crack formation in a thin wall fabricated using laser solid freeform fabrication process: an experimental-numerical investigation, Opt. Lasers Eng. 47 (11) (2009) 1160–1168.

This page intentionally left blank

CHAPTER 23

Process Control of Laser Materials Processing

J. Lawrence*, R.T. Deam†
*University of Chester, Chester, United Kingdom
†Swinburne University of Technology, Hawthorn, VIC, Australia

23.1 INTRODUCTION

One of the major advantages of laser processing is the possibility of processing at high speeds; that is above about 1 m/min. Laser processing also has a reputation for being high quality, which is mostly achieved through "open-loop" control. Open-loop laser materials processing technologies, such as welding, cutting, drilling, and cladding have developed into a widely-used technology in industrial production [1]. The processes are, however, inherently difficult to control and are currently limited to "nondemanding applications," which have a large process operating window. A new range of applications could emerge if highly reflective and highly heat-conductive materials could be processed. Nowadays, this is limited by the fact that relatively minor differences in the surface condition of the metal and the instability of the laser focus will cause dramatic effects on the absorbed laser energy. Here advanced and intelligent process control is the key to further applications. The monitoring and control of these processes is therefore an active area of research. Techniques such as optical and acoustic emission, and pyrometry and plasma charge sensing have been investigated and reported [2–8]. The control of arc welding systems has also been an active area of development [7,9–11]. While these have reported promising results, there are no reports discussing the broader question of the conditions under which control of these processes is practical. In order to provide a better understanding of the limitations of a closed-loop control, a series of experiments was conducted using a PID controller developed by LZH [12].

The complications of including phase changes in the study of the system response meant that only a laser heat treatment series of experiments was carried out. This not only makes interpretation of the results easier to understand, but also the modeling of the feedback process. The study therefore looks at the response solely due to the heat conduction within

Advances in Laser Materials Processing
https://doi.org/10.1016/B978-0-08-101252-9.00023-6
Copyright © 2018 Elsevier Ltd.
All rights reserved.

the solid material being treated; in this case of mild steel being heat treated along a narrow strip, the width of the heat-treated area is desired to be controlled within certain tolerances. The problem facing a production engineer is: How fast can the material be treated and the desired tolerances on the heat-treated area met?

The principle of the findings can be applied to other processes that involve the molten phase. However, it is not the purpose of this study to argue whether or not the molten pool has a shorter or longer response time than the response time due to heat conduction. If the molten pool has a response time that is shorter than the time response from the conduction in the solid, then the results of this study will give a good indication of the maximum processing speed, since the response of the system will be controlled by the longest time response. This is because the heat has to flow through the molten pool to be removed by heat conduction; or in electrical terms, the system is in series. If the molten pool has a much slower response time than the time response from the conduction in the solid, then the results of this study will overestimate the maximum controllable processing speed.

A good practical analogy to what is studied here is given by the following example. Suppose you want to paint a straight vertical line on a wall (freehand between predetermined marks). This line is to serve a decorative purpose. Therefore, there is a tolerance on the width variation that you will accept. On the other hand, decorating is not enjoyable to you, so you would like to finish the job as fast as possible. There is obviously a tradeoff between the speed that you can paint and the quality of the job. A slow and careful job looks brilliant, but may take too much time.

23.2 THEORY

The theory developed here will use the frequency domain properties of the diffusion equation to formulate how a control system would perform, given perfect instantaneous knowledge of the heated area formed by a laser being scanned over a workpiece. The arguments given will not follow a strict mathematical development. A quick summary of how we arrived at the results can be stated as:

The size of the heat-treated area depends on the heat flow from its edge. The heat-treated area will therefore shrink or grow as quickly as the information about the temperature distribution in the rest of the workpiece is adjusted to balance the heat flow. The properties of the heat diffusion equation mean that temperature information travels at a speed proportional to

the square root of the frequency. The temperature information must travel faster than the heat treatment process (the speed that the laser scans across the workpiece) to be useful to a control system. High frequency temperature information has to be used to "keep ahead" of the laser scan, thus imposing a low frequency limit on the control system. Unfortunately, in order to meet the quality requirements of the resultant heat treated area, the temperature information has to travel from a certain distance away from the heat source in order for the control system to "sense" changes in the heat flow, which introduces a phase delay to the control system. The phase delay cannot be too great (less than π), or the control system becomes unstable. Since the phase delay increases with frequency, this imposes an upper limit on the frequency that can be used by the control system. Thus, too high a frequency will lead to instability of the control system and too low a frequency will not allow the control system to "sense" changes ahead of the moving laser beam. These two constraints limit the maximum controllable laser processing speed.

23.2.1 Flow of Temperature Information

Control systems must use information to control a process. In this case, the information is transmitted by heat or temperature waves. The feedback system will use a control algorithm to try and keep the heated area within a quality specification, a set point, or desired temperature. The stability of control systems is usually analyzed in terms of the frequency response of the system as a whole. The physics of the system that is to be controlled dictates the fastest response of the feedback control that is possible. The analysis below is intended to find out what constraints are required for stable control of a fast-moving laser heat source.

The results of the analysis could be applied to controlling a weld pool size, if it were assumed that heat transport in the molten pool is much faster than in the solid. Thus, the heat flow in the solid will limit the response time of the system when a controlled procedure is used. The speed at which temperature information can travel in the solid is given by the group velocity.

23.2.2 Group Velocity

The heat diffusion equation at the surface of the workpiece is given by:

$$\rho C_p \left(\frac{\partial T}{\partial t} + \mathbf{U} \cdot \nabla T \right) - \nabla \cdot \left(\kappa \nabla T \right) = \dot{q}$$

where $\dot{q}$ is the laser power absorbed, and is what the control system will vary to control the heat input.

The equation for convective heat flow in the solid is given by:

$$\frac{\partial T}{\partial t} + \mathbf{U} \cdot \nabla T - v_{th} \cdot \nabla^2 T = 0$$

which for the purpose of this analysis can be written ignoring the convective term:

$$\frac{\partial T}{\partial t} - v_{th} \nabla^2 T = 0$$

The Fourier transform equation for time and space:

$$\left(i\omega + i\mathbf{U} \cdot \mathbf{k} - v_{th} \left| k^2 \right| \right) T = 0$$

and for the equation ignoring convection:

$$\left(i\omega - v_{th} \left| k^2 \right| \right) T = 0$$

The dispersion relation is derived by equating the expression inside the brackets to zero:

$$i\omega + i\mathbf{U} \cdot \mathbf{k} - v_{th} \left| k^2 \right| = 0$$

and for the case ignoring convection:

$$i\omega - v_{th} \left| k^2 \right| = 0$$

The group velocity is given by the expression:

$$C_g = \frac{\partial \omega}{\partial k}$$

Thus, the group velocity of "temperature" waves can be derived from the heat diffusion equation in the solid.

$$C_g = \sqrt{2v\omega} \left(1 + i \right) \tag{23.1}$$

where the real part is the speed of information transfer and the imaginary part is the damping of the amplitude or the loss of information signal strength. The convection term would be added (a vector add) to get the speed in relation to the moving source. In the direction of the laser movement, for information ahead of the laser spot, the group velocity must exceed the speed of the laser head, *U*.

The damping of the temperature waves will make the stable control of the treatment size or temperature more difficult (more prone to instability as the return signal to noise becomes smaller).

23.2.3 Typical Length Scale

This length scale will depend on the geometry of the heat source. It will be different for keyhole welding and conduction welding. For the heat treatment case discussed here, it will be the size of the laser spot.

The typical length scale is l. The time taken to travel this length is given by:

$$\tau = \frac{l}{c_g} \tag{23.2}$$

23.2.4 Quality

Information must arrive at the heat source before moving distance λ. This defines a time within which the temperature information must be given to the heat source:

$$\lambda > U\tau \tag{23.3}$$

Therefore,

$$\lambda > U\frac{l}{c_g} = U\frac{1}{\sqrt{2\nu\omega}\left(1+i\right)} \tag{23.4}$$

Thus, frequency must be higher than:

$$\omega > \frac{U^2 l^2}{2\nu\lambda^2} \tag{23.5}$$

for the information to arrive in time. This leads to the definition of a quality length scale, λ. The larger this value is, the lower the quality of the weld bead or treated area. It represents the tolerable length over which the treated area may lie outside the intended treatment temperature, size, or position. It would be expected that the quality length scale λ, would be a fraction of the typical length scale l. For example, the typical length scale in a heat treatment application would be the intended width or depth, so if a 20% variation in the width of the treated area was tolerable, then $\lambda = 0.2l$. Fig. 23.1 shows a schematic of the quality length for a laser heat-treated region. For the heat treatment case considered here, it is the maximum continuous length that the temperature is tolerated to be "out of specification."

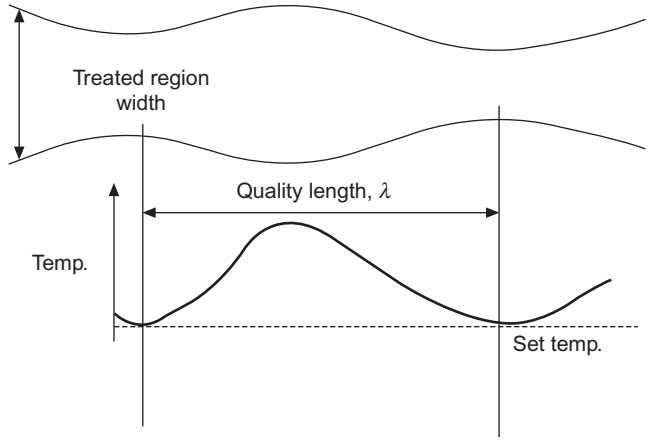


Fig. 23.1 Bead quality schematic.

The temperature overshoot and undershoot as well as the degree of thinning and thickening of the treated area will depend on the "challenge" that the control system must face. A small perturbation to the heat flow will result in a small variation in width along the quality length, whereas a large perturbation will result in a large change in width, which the control system will be able compensate for over the quality length.

23.2.5 Phase Shift

However, as the frequency increases, a growing phase shift is introduced. If this phase shift is too great, then the information will cause instability if used in a feedback loop to control the quality; this is shown in Eq. (23.6).

$$\omega < \frac{\pi}{\tau} \tag{23.6}$$

The phase shift must be less than 180 degrees (π radians).

23.2.6 Stable Operating Window

This leads to an upper and lower limit on the frequency component that can be used for feedback to control the heat source. Using Eqs. (23.5) and (23.6):

$$\frac{U^2 l^2}{2v\lambda^2} < \omega < \frac{\pi U}{\lambda} \tag{23.7}$$

Frequencies above the lower limit ensure that the information will arrive in time. Frequencies below the upper limit will not be out of phase.

23.2.7 Maximum Controllable Speed

Information between these frequency bounds can be used only if a stable control system is to be employed. This leads to a natural limit on the speed of laser processing:

$$U < \frac{2\nu\pi\lambda}{l^2} \tag{23.8}$$

Above this speed, there is no frequency window in which stable control is possible.

23.3 EXPERIMENTS

A series of experiments were designed to test the response of a controlled laser processing system to abrupt changes in thickness of a workpiece at different travel speeds.

The experiments were performed using a 2.5 kW Rofin Sinar laser and a 0.6 mm diameter step-index fiber terminated with 200 mm focal length collimating and focusing lenses positioned so that they formed a laser spot about 3.5 mm on the surface of the substrate. The surface temperature under the laser spot was measured using a Maurer two-color pyrometer capable of measuring temperatures between 500 and 1500°C and TemCon control software and hardware developed by LZH. The pyrometer was mounted vertically above the substrate and at 90° to the collimating lens via a bending cube.

The workpiece used was a 10 mm thick mild steel plate with 50 mm wide sections milled from one side so that its thickness varied discontinuously in steps (Fig. 23.2). The wall thickness of the milled sections was 2, 0.98, and 1.1 mm. The top surface of the sample, which was flat, was cleaned and grit blasted. The sample was mounted under the laser beam with the milled section in the opposite side from the laser beam. The control system

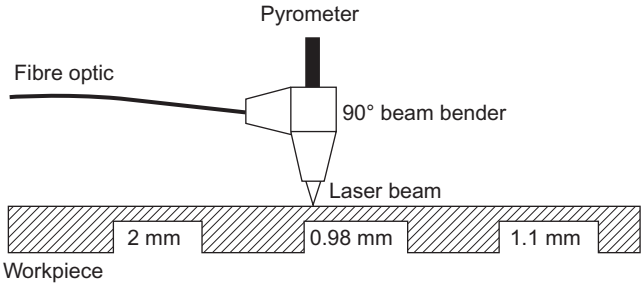


Fig. 23.2 Schematic of experimental layout.

was optimized to try and keep the temperature of the surface under the laser spot at 1200°C, in order to avoid any issues associated with the melt phase. The melting point of mild steel is 1538°C.

23.4 EXPERIMENTAL RESULTS

23.4.1 Initialization of Control Parameters

A series of experiments were carried out to optimize the control parameters for a 1 m/min travel speed on 10 mm thick mild steel. The system was set up to control the temperature under the laser beam spot to a set point of 1200°C. Table 23.1 summarizes the results of the PID tunning experiments. The system response was determined to be slightly underdamped. This can be seen in the control signal in Figs. 23.4–23.6.

Table 23.1 Control parameters used

Parameter	Value
Temperature set point	1200°C
Sample rate	1000 Hz
Smoothing	50 samples
P (proportional control constant)	0.0003
I (Integral control constant)	0.01

No differential control term was used.

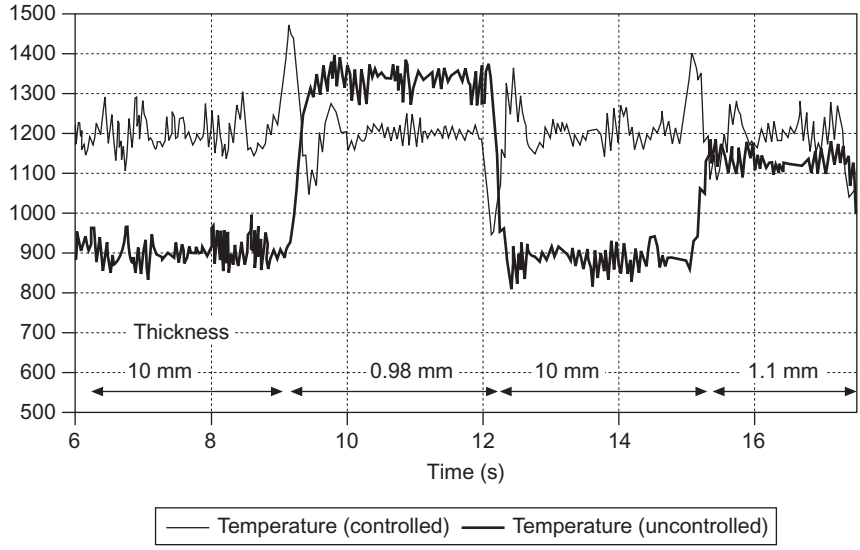


Fig. 23.3 Test comparisons at 1 m/min. Control set point 1200°C, and fixed power.

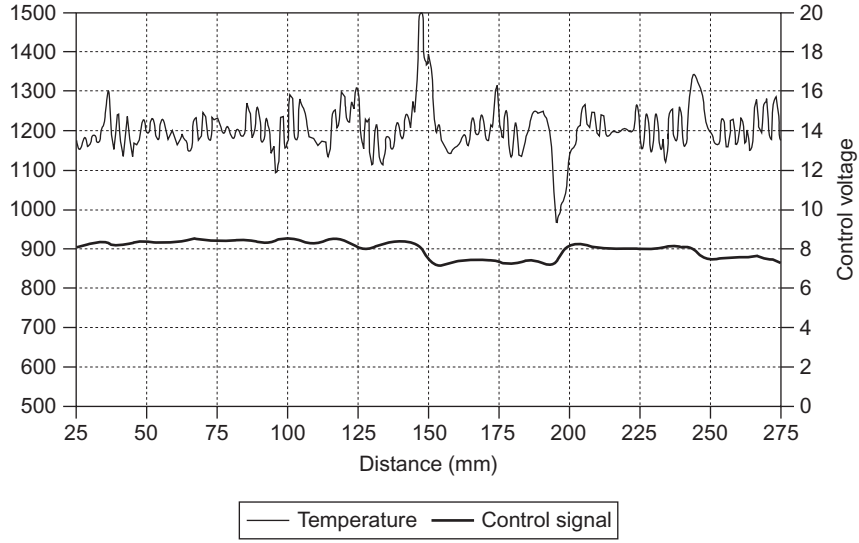


Fig. 23.4 Surface temperature and control signal: 2 m/min travel speed.

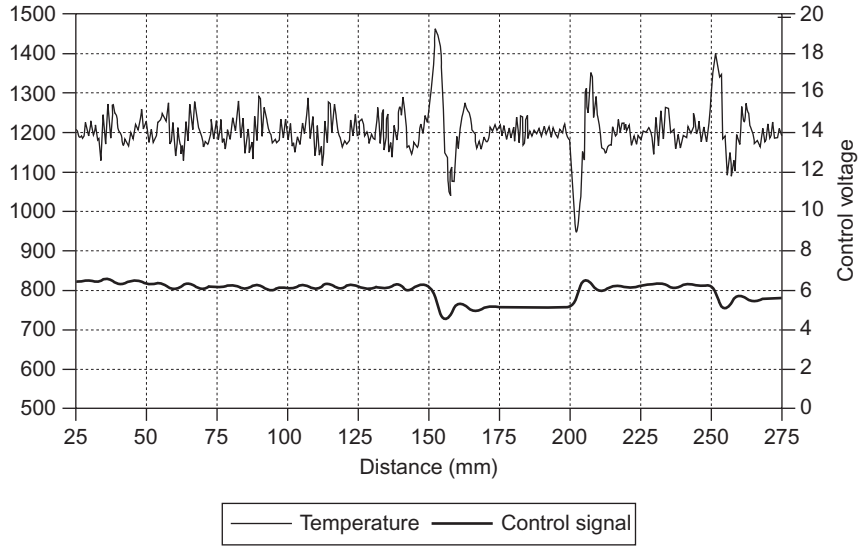


Fig. 23.5 Surface temperature and control signal: 1 m/min travel speed.

23.4.2 Measurements

The first set of experiments compared an uncontrolled run with a controlled run over the 10 mm plate with the 0.98 and 1.1 mm thick sections. Fig. 23.3 shows the results. The fixed power run shows a measured surface temperature

of about 900°C over the 10 mm thick sections, about 1350°C over the 0.98 mm thick section, and about 1150°C over the 1.1 mm thick section. The controlled run maintains about 1200°C (the set-point), except for overshoots and undershoots, which occur at the thickness transitions.

A series of runs was made at different travel speeds, with the control system activated. These were at 2, 1, 0.5, 0.25, and 0.125 m/min. The results are shown in Figs. 23.4–23.8.

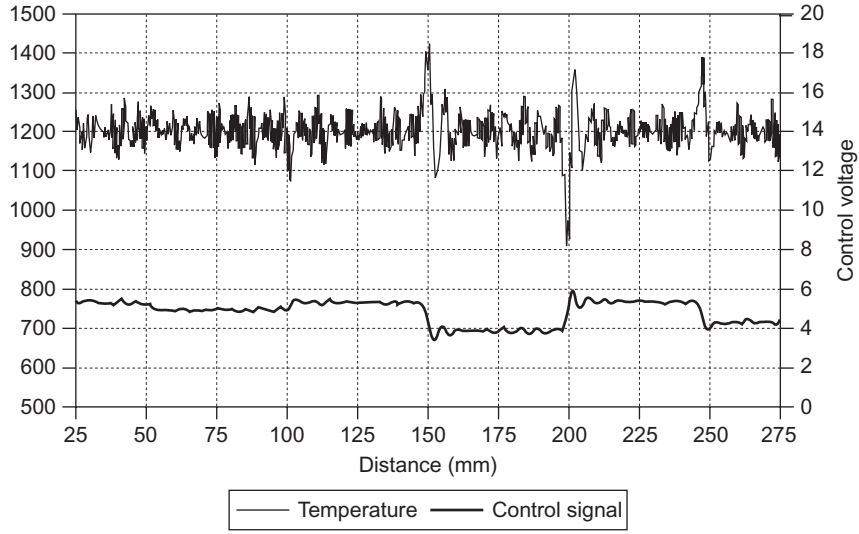


Fig. 23.6 Surface temperature and control signal: 0.5 m/min travel speed.

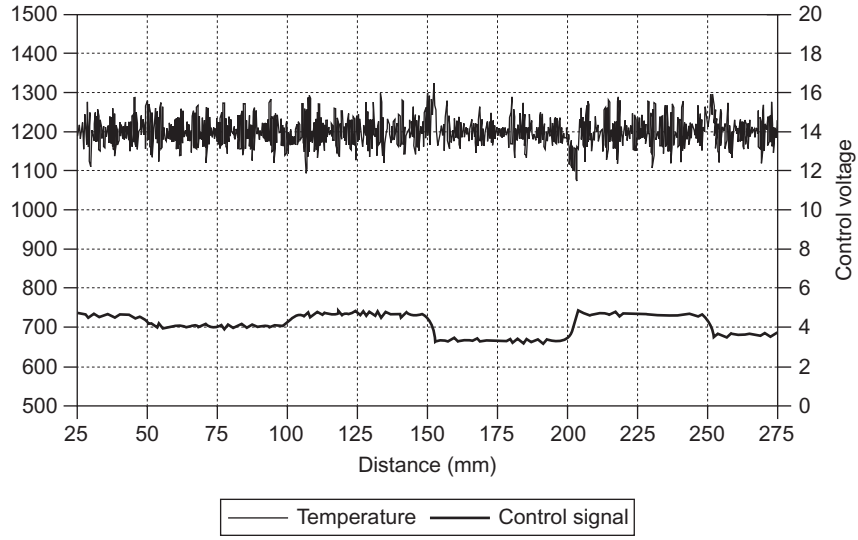


Fig. 23.7 Surface temperature and control signal: 0.25 m/min travel speed.

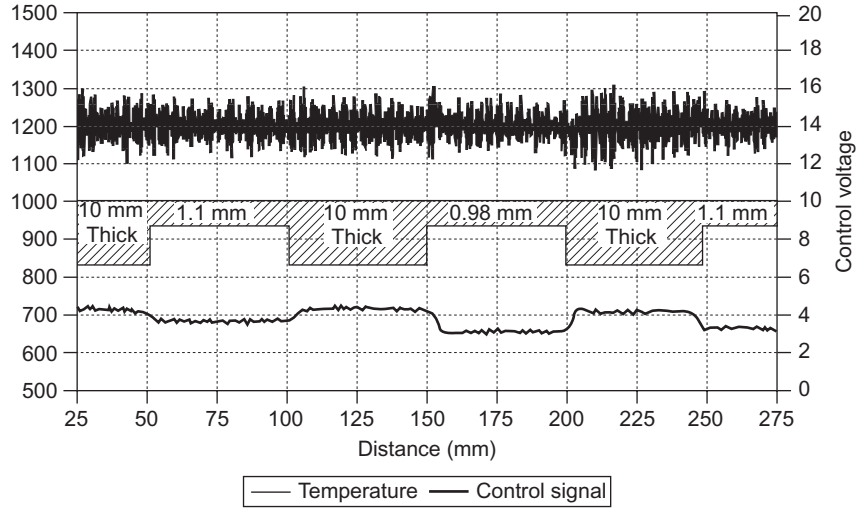


Fig. 23.8 Surface temperature and control signal: 0.125 m/min travel speed.

23.5 DISCUSSION

The size of the hot region (above 1200°C) will decrease as the travel speed increases. As the travel speed drops below about 0.5 m/min, the depth of the hot region begins to be affected by the 2 mm thick region. This is seen in the control signal in Figs. 23.6–23.8. The performance of the control system is good at travel speeds below 0.5 m/min. Figs. 23.4–23.6 show the overshoot and undershoot excursions (300°C at a travel speed of 2 m/min). The overall performance of the control system can be measured by recording the maximum deviation in the measured temperature from the set point of 1200°C over the thickness transitions which occurred at about 50, 100, 150, 200, and 250 mm along the plate. The full traces are shown in Figs. 23.4–23.8 and the maximum temperature deviations are shown in Table 23.2. However, the maximum deviations tell only part of the story. The length of the treated area that does not conform to the specified tolerance is also very important.

Table 23.2 Control performance vs. travel speed

Travel speed (m/min)	TD at 150 mm (°C)	TD at 200 mm (°C)	TD at 250 mm (°C)
0.125	99	−77	92
0.25	123	−127	101
0.5	224	−287	188
1	256	−257	198
2	300	−234	146

TD = temperature deviation

Although this is a very crude assessment of quality of the laser heat treatment process, it gives a numerical measure to what can be clearly seen in the traces. The thickness transition from 10 to 2 mm and back to 10 mm results in temperature deviations that are indistinguishable from the inherent noise. The inherent noise has a standard deviation from the set point of about 30°C and is most probably caused by the variation in the absorption of the laser beam by the workpiece. Developing a robust control system that will cope with this noise is part of the control engineer's challenge.

For thickness steps to 0.98 and 1.1 mm, clear overshoot and undershoot in the controlled temperature are seen. Below a travel speed of about 0.5 m/min, this control system can cope with the severe test of a sudden change in plate thickness. Such rapid changes in the heat sink configuration are not uncommon in engineering structures. Thick reinforcement webs often support a thin plate. Holes and slots are usually part of engineering structures and can act as powerful changes to the heat flow, if fast laser processing is carried out near them.

This suggests an alternative approach to the control problem. If more gentle changes in the heat sink could be designed into the structure, then higher quality laser processing could be achieved at higher speed. However, in practice, the system would still have to respond to unforeseen changes, such as step changes in the absorption due to uncontrolled changes in surface condition (i.e., rust and roughness).

23.5.1 Theory and Experiment

In the tests reported here, the system had to respond to a change in plate thickness, from very thick to about 1 mm. This means that the temperature information had to travel from the top of the plate (where the laser spot strikes the plate), to the back-face of the plate and back to the top again to be part of the control loop. The diameter of the spot was 3.5 mm. So that the leading edge of the spot would experience the changes in section thickness, before the trailing edge. The spot diameter will be taken as the typical length scale. Thus, knowing the thermal diffusivity of mild steel, Eq. (23.9) can be used to predict a minimum quality length for any particular travel speed:

$$\lambda = \frac{Ul^2}{2\pi\nu} \tag{23.9}$$

Using, $\nu = 5.2 \times 10^{-6}\,\mathrm{m^2/s}$, from Kaye and Laby [13] and $l = 3.5$ mm (diameter of the laser spot), the minimum predicted quality length is plotted against the travel speed shown in Fig. 23.9, together with the measured

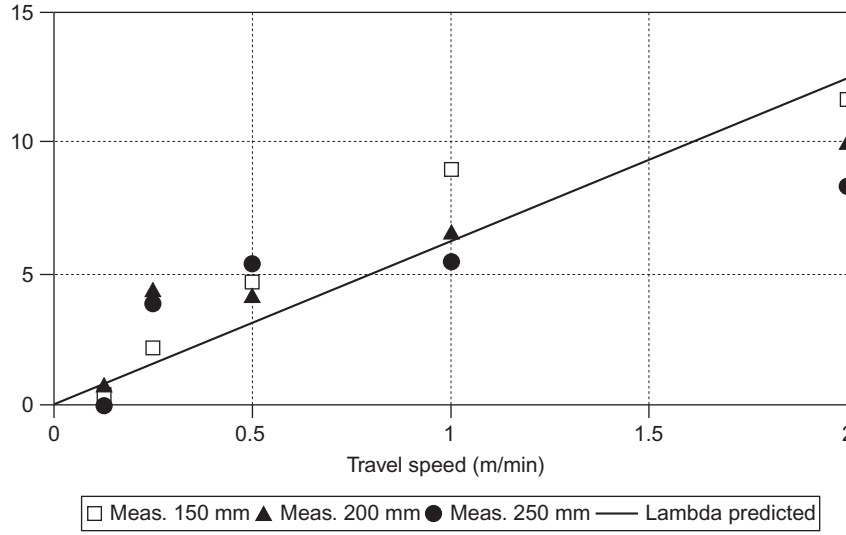


Fig. 23.9 Comparison of quality length at three thickness transitions.

quality length on the 10–0.98 mm transition (150 mm along the plate), the 0.98–10 mm transition (at 200 mm), and the 10–1.1 mm transition (at 250 mm along the plate). The measured quality length was taken as the width of the overshoot at each transition.

Agreement of the measured quality length and the predicted quality length is good. Note that the quality length tells the control engineer nothing about the size of the overshoot; just how far along the treated length it takes the control system to recover its set point. Thus, the production engineer may have the freedom to minimize the perturbations that the control system is subjected to, but Fig. 23.9 shows that demanding higher quality (smaller quality length) requires a lower travel speed. This reinforces what engineers know well: Higher quality takes more time.

23.6 CONCLUSIONS

A simple model of the performance of a control system for laser processing has been presented and compares well with an idealized experimental test. The model predicts that the maximum controllable travel speed depends on the quality required of the laser treated material. Higher quality requires a slower travel speed.

ACKNOWLEDGMENTS

This work was carried out at the Industrial Research Institute Swinburne, which is part of the Faculty of Engineering and Industrial Sciences, Swinburne University of Technology. Thanks to Mr. Brian Dempster for preparing the samples and Prof. Milan Brandt and Dr. Jim Harris for running the laser used in the experiments. The author also acknowledges the useful discussions and help given by colleagues many years ago in developing practical control systems for arc welding at Marchwood Engineering Laboratories (formerly part of the Central Electricity Generating Board near Southampton in England).

REFERENCES

[1] W.M. Steen, Laser Material Processing, Springer-Verlag, London, 1998.
[2] R.T. Deam, M. Brandt, J. Harris, Investigation of capillary waves excited by a Nd:YAG laser using pyrometry, J. Phys. D. Appl. Phys. 36 (2003) 10.
[3] W.W. Duley, Laser Welding, John Wiley and Sons, New York, 1998.
[4] B. Grunenwald, J. Shen, F. Dausinger, H. Hugel, Laser cladding with composite powders using pyrometric temperature control and beam combination, in: ISATA '93 International Symposium on Automotive Technology and Automation, Aachen, Germany, 1993.
[5] H. Haferkamp, M. Goede, K. Lindemann, Laser Hardening of CVD coated tool steel, in: 12th International Federation for Heat Treatment and Surface Engineering Congress, Melbourne, 2000.
[6] J. Norrish, Advanced Welding Processes, Institute of Physics, 1992.
[7] V.G. Prokoshev, D.V. Abramov, S.Y. Danilov, A.O. Kucherik, S.M. Arakelian, Diagnostics of the high temperature hydrodynamic phenomena for laser processing of the material, in: Laser Assisted Net Shape Engineering 3, Proceedings of the LANE 2001, 2001.
[8] E.T. Smith, E. Kannatey-Asibu, Visualization and acoustic monitoring of laser weld pool oscillatory behavior, in: ICALEO 1999, Laser Institute of America, 1999.
[9] R.T. Deam, Weldpool frequency: a new way to define a weld procedure, in: S.A. David, J.M. Vitek (Eds.), Recent Trends in Welding Science and Technology, ASM International, Gatlingburg, TN, 1989.
[10] S. Nagarajan, K.N. Groom, B.A. Chin, Infrared sensors for seam tracking in tungsten arc welding processes, in: S.A. David, J.M. Vitek (Eds.), Recent Trends in Welding Science and Technology, ASM International, Gatlingburg, TN, 1989.
[11] R.J. Salter, R.T. Deam, A practical frontface penetration control system, in: 2nd International Conference on Developments in Automatic and Robotic Welding, The Welding Institute, London, 1987.
[12] Laser Zentrum Hannover e.V., Web page. Laser Zentrum Hannover e.V., Hollerithallee 8, D-30419 Hannover, 2006.
[13] G.W.C. Kaye, T.H. Laby, Tables of Physical and Chemical Constants, Longman, London, 1986.

CHAPTER 24

Development of Laser Processing Technologies via Experimental Design

H. Sohrabpoor*, A. Issa†, A. Al Hamaoy‡, I.U. Ahad*, E. Chikarakara*, K. Bagga*, D. Brabazon*

*Dublin City University, Dublin Ireland
†Al Azhar University, Gaza, Palestine
‡Al-Nahrain University, Baghdad, Iraq

24.1 INTRODUCTION

24.1.1 Laser Processing

For many decades, the surface properties of materials have been enhanced by different coatings and surface modification techniques to meet component operational environments. This includes requirements for component life times when subjected to, for example, defined temperature, wearing, or fatigue conditions. In order to enhance the surface properties over conventional techniques, such as flame hardening and carburizing, advanced techniques such as electron, ion, plasma, and laser processing have been developed. Nowadays lasers with high energy density are commonly used in surface modification techniques.

Laser Surface Modification (LSM) can be defined as any laser material process that modifies one or more of the surface properties, with or without adding additional material. These processes are employed to modify or introduce certain desired physical and chemical properties of a material such as surface chemical composition or the surface morphology [1]. Such modifications have been applied for metals, polymers, and ceramics [2–7].

Scientists classify LSM either according to the modification type (hardening, glazing, texturing, shocking, etc.) or according to the processing temperature (heating, melting, or plasma). In this chapter, a review of methods for the experimental development of laser processing is presented. Specific examples are presented for Laser Cladding, Laser Surface Melting, and Laser Shock Peening.

Advances in Laser Materials Processing
https://doi.org/10.1016/B978-0-08-101252-9.00024-8
Copyright © 2018 Elsevier Ltd.
All rights reserved.

Laser surface heat treatment is a non-melting process, whereas in laser surface melting, the melting takes place in a thin layer which therefore solidifies rapidly forming a harder structure. During laser shock peening (LSP), surface compressive residual stress is imparted to the material via the shock waves from the laser processing. In laser cladding, the laser beam melts the metal surface while a second material is introduced to the surface. Examples of optimization of each of these types of laser processing techniques will be discussed later in this chapter. Before this, in the following sections, an introduction is given to the experimental design methods for laser process optimization.

24.1.2 Introduction to Laser Process Optimization

Ever since the advent and availability of lasers, their advancement has heavily relied on experimentally examining the effect of different process parameters on the material of interest. This has allowed an in-depth understanding of the lasers' effects and interactions with various materials.

The ultimate goal of studying the laser processing of materials is to optimize the process in terms of single or multiple objectives. *Optimization* in this context can be defined as mathematically or statistically modeling the laser process in order to obtain desired/best response based on the process parameters. Therefore, it requires identifying the process *input* (*control*) parameters and the process *output* (*response*) parameters. Optimization can be performed for single or multiple response parameters. These parameters can be either quantitative or qualitative depending on the research objectives. To this end, researchers rely on either experimental or simulation works or a combination of both to optimize laser processes.

Experiments are used extensively to optimize the process because of the high degree of complexity in thermal mathematical models, attempting to describe such processes and the multiple parameters and their possible interactions, governing the laser material interaction. Therefore, the fundamental physical simulations are often time consuming and cost intensive [8,9]. The exercise of *experimental modeling* of the laser processes is based on statistically studying the effects of varying the process input parameters on the process response parameters by conducting specifically planned experiments. This method is more commonly known as Design of Experiments (DoE). In the application of this method, prior understanding of the process allows the suggestion of the most appropriate process input parameters for investigation. The DoE usually starts with screening experiments aimed to identify if a suggested process input parameter has a significant effect on

the response or not. During this stage, varying one parameter at a time or a factorial design of experiments can be used for detecting the potential interactions between the parameters. Important conditions should be observed for the selection of an input parameter. The input parameter should be independent, controllable, and have a significant effect on the response. The choice of response parameter also relies on prior knowledge and experiences or on the objectives of the study. The main condition of selecting the response parameter is that it should be quantitatively or qualitatively measurable [10].

24.2 DESIGN OF EXPERIMENTS (DoE) METHODS

24.2.1 General Guidelines for Conducting DoE

Design of Experiments (DoE) is a systematic method for statistically modeling a process in order to get a mathematical/empirical relationship between the process parameters and the responses [11]. The process of coming up with a finalized DoE is an iterative one. It is comprised of several decisions, revisions, and simplifications. The experimenter must keep in mind that study conclusions or models of a process are not universal. They are, however, applicable for the investigated range of process conditions; such as process setup, parameters, study material, model type, etc. Therefore, the investigator should aim, when selecting the study objectives, to simplify these conditions as much as possible and select those that are controllable and repeatable. The investigator must spend a considerable amount of time and effort in planning for the intended DoE to ensure success. The seven stages involved in decision making, planning, and performing the DoE are as follows [12–16]:

1. Define the objectives of the experiment. To simplify the experiments and the analysis, this list should only involve precise questions that are to be addressed. An example of that would be to determine the correlation (if any) between laser beam power and cutting speed as parameters of a laser cutting process, and whether they influence the heat affected zone [17]. Furthermore, the objectives may need to be refined a number of times as the remaining planning steps are completed.
2. Identify all sources of variation, which are basically anything that, when changed, could influence the "observation" or "process response." Some variation sources have a major effect on the process response "treatment factors," often called "process parameters." For example, a laser drilling process parameter could be the laser beam depth of focus [18].

The process parameters and their levels from minimum to maximum should be selected. The levels of a process parameter should be laid out equally spaced for easy retrieval of the results and conclusions. Laser processes usually involve more than one process parameter. The experiments are called, in this case, a factorial design of experiment. This implies that the process responses are measured based on some combination of the levels of the various process parameters.

On the other hand, some variation sources have minor effects on the response that are called "nuisance factors." The effects of these factors are of no interest to the investigator. An example of these would be the glass sample thickness in the laser microchannel fabrication process [19]. Therefore, it is usually decided to fix the nuisance factors and perform the experiments at these fixed values. Alternatively, the nuisance factor is fixed and the experiments are performed and repeated for a second fixed value of the nuisance factor, and a third fixed value and so on, which is called "blocking." This could minimize the effect of these factors on the response. A noteworthy point about nuisance factors is that they are not always controllable. An example of a controllable nuisance factor could be the operator performing the experiments. Even if they are following strict procedure, in statistical terms, variability in the results may arise from changing the operator. An example of an uncontrollable nuisance factor could be variations in properties among batches of the study material. In laser processing, the surface finish of a material to be processed is a good example. If blocking is to be used in the latter case for minimizing the nuisance factors effects, enough material should be on hand for performing each block of experiments.

The third variation factor that can be considered in studying laser processes is the "study material." This is the workpiece treated by the combinations of laser process parameters to induce the measurable process responses. The main consideration with the selection of the material is that it should be representative of the process objectives to be concluded. This sets a limit on the scope of the study results and objectives, which may be revised.

Finally, the decision whether a variation factor is a process parameter or a nuisance factor is made by the investigator and depends on the process under study. It is important to note that during the decision making regarding the selection of parameters, that the more process parameters that are involved in the study may complicate the analysis without providing any added value or increasing the accuracy of the model.

3. At this stage the type of DoE design is selected. This means the way and combinations of process parameters that will be assigned to the selected samples for laser processing in order to obtain process responses. This influences the number of experiments needed to analyze the process and obtain an understanding of a model. The decision here includes whether the design will have the blocking factors or not. There are several types of DoE designs, such as the Factorial Design, the Fractional Factorial Design, Response Surface Methodology (RSM) like the Central Composite Design (CCD), and the Box-Behnken Design (BBD). You should read the previous studies [12–16] in order to gain knowledge of which DoE design suits most of your objectives. However, many investigators start their studies with a simple general Factorial Design. This is suitable if investigators have a few process parameters examined at a limited number of levels. At a later stage, when more knowledge about the process is acquired, a more focused investigation can be carried out. In this case, Fractional Factorial or RSM designs can be used at more parameter levels without increasing the number of experiments needed. For a given design, there is an important rule, which is to eliminate bias by randomizing the experimental runs. Experimental samples of the material should be taken and assigned randomly to each combination of the levels of the process parameters. This is required to ensure that the responses are not subject to or affected by uncontrollable sources such as the experimenter bias.
4. At this stage, decisions associated with the process response parameters need to be made. These may include: the units of the response parameters, the measurement methods and equipment, the measurement accuracy, precision and resolution, and the procedure for preparing a sample measurement. Process response parameters are usually suggested at an earlier stage. However, some difficulties may arise prohibiting/restricting the ability of data collection or measurement. This requires running a few pilot experiments to investigate some of the difficulties involved in the data collection. This may result in the need for modifying or rectifying the selection of the response parameters or the procedure of the data collection. The pilot experiments will also assist in coming up with a systematic/strict procedure to be followed by the experimenters throughout the DoE practice. This systematic procedure can take the form of a data collection sheet that shows the conditions and the sequence in which the responses are to be recorded. The study objectives may be revised at the end of this step to simplify the experimental procedures.

5. As explained in the previous steps, a pilot experiment may need to be performed. A few observations can be made without expecting any conclusions. The main idea is to practice the experimental procedures and to check for difficulties that may arise during an experiment or in data collection. Revisions and necessary changes of all previous decisions can be made after the examination of the results of the pilot experiment.
6. The process model type is selected, with the aim that it will best represent the extent of the relationship between the process parameters and the response parameters. The selected model should enable the investigator to mathematically define this relationship. The analysis techniques employed to derive a model are statistical in nature. These techniques will be applied to the collected data and will depend on the selected model type. The most commonly used model is the linear model. This model attempts to describe the process response parameter in terms of a linear combination of process parameters plus an error resulting from all minor sources of variations. A quadratic or curvilinear model is preferred in order to better fit and understand the relationship between the process input and output parameters and the results obtained.
7. Finally and before proceeding to perform the full set of experiments, some final revisions of the previous decisions can be performed that are necessary to simply increase the accuracy of the model. These revisions might be aimed to reduce the number of experiments or to narrow down the ranges of the selected parameters. Once the experimental design is ready, experiments and data collection may commence which provide the data for analysis and process model derivation.

24.2.2 Software Used for DoE

It should be noted that there are several available software packages designed to assist researchers throughout the DoE exercise including planning, analyzing, and optimizing the process. These include State-Ease Inc., Design-Expert [20], SAS Institute Inc., JMP [21], and Minitab [22]. These software packages provide a user-friendly interface equipped with 2D and 3D graphical representations of the results. Once a process model (mathematical or empirical) is derived, it can be used to draw an operational map of the process in terms of its parameters. It can also be employed to predict the responses for a given combination of process parameters within the investigated range by performing the simulations of the designed model. It is advisable that the model is validated by performing some validation experiments and checking the accuracy of the model predictions. After the

process model is obtained, further optimization can be performed by performing a new DoE with a more closely defined zone of investigation and range of process parameters. The aim of optimization studies is to find the values of the process parameters that produce the optimal process response. In practice, that means: output minimizing, maximizing, or producing a specific multi-modal optimization of process response.

24.2.3 Optimization Based on Mathematical Simulations

On the other hand, other researchers rely mainly on computerized thermal simulations to optimize laser processes, and conduct some experiments to iteratively-modify or validate their models' predictions. When the simulation model is ready and validated, it provides an inexpensive opportunity for optimizing the process [23,24]. *Simulation models* can be used to provide analytical and/or numerical solutions. The results of these simulations can be used to predict the effects of various forces and energy fields induced by the laser irradiation of the materials. These models are commonly known as Mathematical Models. These models generally treat a laser as a heat source. The laser effect on the material is modeled based on a single or a combination of different processes. The energy from the laser source is transferred to the workpiece by convection, direct radiation heat transfer, or conduction or combination of all of these processes. This allows simulation and prediction of heat generation and the progression of energy transfer in the material leading to subsequent heating, melting, and evaporation [11,23,24].

Despite the two main schools of optimization research, experiment, and simulation, many researchers find it very efficient and reliable to combine both types of studies. Therefore, the experimental studies are performed in order to directly understand process parameters effects allowing the control of process outcomes. The simulation models are used to support knowledge gain and give a deeper understanding of the physical behavior leading to the experimental results. These models also allow comparing and validating of the experimental findings. This type of comparative/augmented studies constitutes most of the reported studies on laser process optimization.

Response Surface Methodology (RSM) was also used in a study of laser microchannel fabrication process in the works of Issa [19], where a pulsed CO_2 laser (1.5 kW, 10.6 μm) was used to fabricate microchannels in soda-lime glass samples of a fixed 2 mm thickness. The microchannel dimensions, surface roughness, and morphologies were studied in terms of the laser processing input parameters (laser beam power, pulse repetition frequency, and scanning speed) using RSM. The collected results were

also used to study the effects of the process parameters on the material's volumetric and mass ablation rates. Results from the RSM model in this study were also compared to simulated results from a thermal mathematical model [19].

24.2.4 Experimental and Simulation Based Methods—A Brief Comparison

24.2.4.1 Advantages of Experimental Methods

- Little prior knowledge regarding laser physical interaction with the material is required.
- Quicker results for analysis.
- Model is highly relevant to results from the investigated regions of process parameters.
- Experimental results can be used directly to identify possible industrial applications.

24.2.4.2 Challenges With Experimental Methods

- Experimental model adequacy depends on the repeatability and reliability of the process setup, accuracy of process control, governance of experimental conditions, variability in batch-material properties, stability of laser source parameters, measurability of parameters, and accuracy of measurement methods.
- They are not always labor- and cost-effective.
- They do not provide deep insights to the physical phenomena underlying the process.
- They are only suitable for the investigated regions of process parameters.

24.2.4.3 Advantages With Simulation Methods

- Less human resource is required and material consumption is minimal.
- Provide more understanding of the process physical phenomena.
- Universality (not restricted to a specific range of input parameters), however, this universality is limited by the model assumption and boundary conditions.

24.2.4.4 Challenges With Simulation Methods

- Level of the details of processes and assumptions included in the model define the accuracy. Increasing the details and lowering the assumptions can make the model complicated. The adequacy of the simulation models depends on how comprehensively they account for many

process parameters (such as material properties, laser temporal mode, model assumptions, boundary conditions, material shape/thickness, ambient conditions, etc.).
- Availability of accurate values of material properties at high temperatures and short irradiation periods (materials generally behave non-linearly under these conditions), therefore, some material properties (such as thermal conductivity, evaporation temperatures, latent heats) may not be available under these conditions. This leads to assumptions which may not be very accurate.
- It is still challenging to model some processes that involve complex interactions between different materials such as welding and coating processes.
- Simulation modeling is also challenging for certain processes that involve complex underlying physical phenomena. For example, ultra-short laser pulses induce micro- and nano-scale modifications in the processed materials. The complexity arises due to changes occurring simultaneously in the physical and chemical properties of the processed materials.

24.2.5 General Experimental Setups

When it comes to conducting experiments with lasers, accuracy and precision are key factors. Therefore, the experimental conditions must be governed and maintained throughout the entire experiment. These conditions must be kept constant (if needed) in the future experiments. The experimental setup engineered in this way ensures the repeatability and reliability of results. Majority of the researchers working with laser processing rely on performing measurements of responses after the sample is processed. Many techniques and instruments can be used to fulfill this requirement based on the nature of measurements. These techniques include but are not limited to the Vernier scanner, profileometers, mechanical hardness measurement equipment, chemical analyzers, optical microscopy, SEM, and AFM [25–27]. Some published research work used in in situ or online setups to measure process responses in real-time. These responses can be the physical and chemical modifications in the processed material (such as transient temperature distributions, material phase transformations, optical properties, dimensions, and topography of structured zones) [24,28]. One major advantage in using in situ measurement setups is that they provide the ability to modify the process parameter in real-time to visualize the exact effect of input parameter variations on the obtained results.

24.3 MODELING AND OPTIMIZATION OF LASER PROCESSES WITH NONCONVENTIONAL APPROACHES

The correct selection of the process parameter values is vital in designing a successful manufacturing process. A well calculated decision on selecting the values for the processing parameters guarantees the good quality of the manufactured product and reduces the manufacturing expenditure, and increases the overall productivity of the manufacturing system. In order to design a model for the process parameters of a manufacturing process and perform optimization on that model, the complete understanding of the process is required. This understanding and thorough knowledge about the several processes involved in manufacturing can be obtained by experimental equations that are able to identify the practical restrictions, specification of machine capacities, development and implementation of an effective optimization criterion, and the understanding of mathematical and numerical optimization techniques [29].

Due to the high levels of the complexity involved in the laser surface modification techniques and multiple influences of the parameters on the process response, traditional methods of designing, manufacturing, and testing to control the process are generally inefficient and provide unsatisfactory results. The advanced modeling and optimization techniques have been developed and frequently used in various industrial sectors to control and optimize the manufacturing processes.

In order to design and develop these techniques, the relationship between the response of a process and input control factors should be explained objectively and numerically. This can be performed by the realization of the process through appropriate mathematical equations and optimization algorithms. The optimization techniques which have been found to be particularly useful for applications with laser based manufacturing processes are given below:

1. Response Surface Methodology (RSM)/Design of Experiments (DoE)
   Using RSM, the responses of a process can be optimized by understanding and calculating the quantitative influence of the control parameters. By introducing systematic variations in the input parameters, the response of the process is recorded and conclusions are drawn on the basis of the quantitative analysis of the results [30].
2. Artificial neural networks (ANN)
   ANNs are efficient systems in data modeling and are capable to represent complex input–output relationships [30].

3. Adaptive neuro-fuzzy inference system (ANFIS)
   For creating and testing connections between inputs and outputs of a system or process, ANFIS provides an opportunity to integrate both adaptive artificial neural networks and fuzzy logic to provide a feedback control system to obtain an accurate process response by adaptively changing the input control parameters [30]. The use of ANFIS provides adaptive control over the process, thus optimization can be performed automatically based on the feedback received from the process response.
4. Gray relational analysis (GRA)
   If a process involves multiple control inputs that provide influence and generate complex multiple responses and accurate information regarding the influence of control factors is unknown, the GRA can be used as an effective solution. In such cases, the multiple process response system is simplified by introducing a single gray, hazy, or fuzzy relational grade output response to provide a variety of possible solutions [30].
5. Technique for order preference by similarity to ideal solution (TOPSIS)
   The TOPSIS provides a rather simple but unique solution to model the relationship between input, control, and output response of a process or a system by selecting different criteria to reach a decision. The approach used in this method is based on iterations in criteria on the basis of compensation in the aggregation. The accuracy of results (poor or good) suggests which criteria is suited best for the process under consideration [30].
6. *Meta-Heuristic optimization*: Metaheuristics algorithms do not ensure a globally optimal solution but do provide a sufficient solution for immediate goals with limited and incomplete data availability. The solutions produced by such algorithms are generally dependent on the set of random variables generated during a stochastic process. In combinatorial optimization, by searching over a finite set of optimal solutions, metaheuristics can often discover decent solutions with less calculation tasks than other optimization algorithms, iterative methods, or simple heuristics. For example, imperialist competitive algorithm (ICA) is a meta-heuristic optimization method. The ICA algorithm consists of eight main steps (generating initial empires, assimilation, revolution, total power of an empire, imperialistic competition, elimination of powerless empires, and stopping condition) exchanging positions of the colony imperialists to detect the best solutions [30].

24.4 EXPERIMENTAL ANALYSIS OF LASER PROCESSING

24.4.1 Experimental Investigation of Laser Cladding

Sohrabpoor in 2016 presented an analysis of powder deposition factors for the laser cladding process, with ANFIS modeling and optimization [31]. In this work, an adaptive neuro-fuzzy inference system, ANFIS, was implemented to model the response of the deposition parameters based on the collected experimental data for the iron-based alloy powder deposition onto a mild steel substrate. It is concluded that for multi-response optimization problems of a manufacturing process where the outputs are well correlated to each other, the ANFIS-ICA method can be utilized. The structure of the ANFIS model for predicting outputs parameters is shown by Fig. 24.1.

Mondal et al. in 2014 used artificial neural network (ANN) for the prediction of the laser cladding procedure characteristics with the input date defined according to the Taguchi-based design condition [32]. In this work, nickel, chromium, and molybdenum mixture powder was used for laser cladding of AISI 1040 steel by a CO_2 laser. Input factors examined including laser power, scan speed, and powder feed rate to reach the maximum

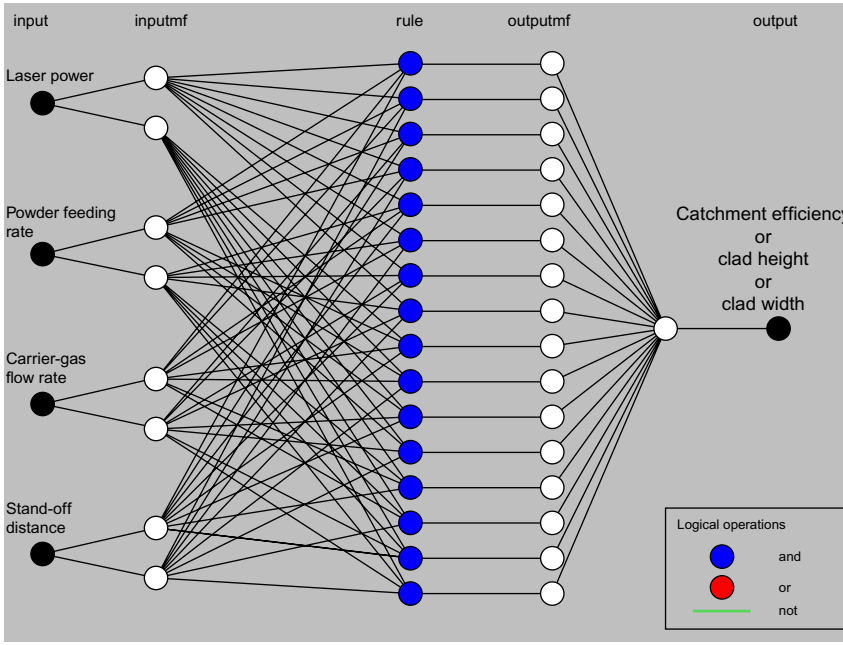


Fig. 24.1 Structure of developed ANFIS model for predicting of catchment efficiency, clad height, and clad width [31].

level of clad width and minimizing the clad depth. The correlation between the inputs and the outputs was implemented via the back-propagation method of ANN. It was found that the optimum condition of the cladding factors for multi-performance characteristics varied with the various combinations of weighting factors. The structure of 4-layered ANN model is shown in Fig. 24.2.

Guo et al. [33] in 2012 studied the effects of process parameters on the quality of a laser cladding layer of a Co-based alloy on 304 stainless steel with a high power diode laser (HPDL). To explore the optimum process parameters and reduce the times of procedure experiments in a practical engineering application, a back propagation (BP) neural network model was established. The calculation and predication results revealed an appropriate agreement with the experimental results. The research results have both a significant reference value and provide guidance in the selection of process parameters of a Co-based alloy cladding by HPDL. The structure of BP-NN model for laser cladding of a Co-based alloy is shown in Fig. 24.3. The results showed that the laser scanning speed has the most significant effect on the width, height, and depth of the laser cladding layer, and the powder feeding rate has the most major impact on the hardness of the laser cladding layer.

Marzban et al. [34] in 2014 investigated optimal process parameters to increase the laser cladding process performance. The design of the experiments was based on a L9 orthogonal array used to investigate the effects of input factors (laser power, scan speed, and powder feed rate) on output factors (clad height, width, and depth). Since three response factors were selected, in order to investigate the multi-response optimization of the process, the PCA was used in combination with TOPSIS.

The weight factors associated with the characteristics of the quality were determined by the PCA. The study found that by increasing the laser power during the processing, a positive effect on the clad width was achieved.

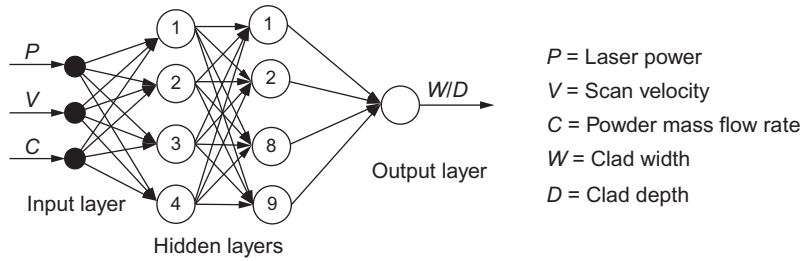


Fig. 24.2 Structure of 4-layered ANN model [32].

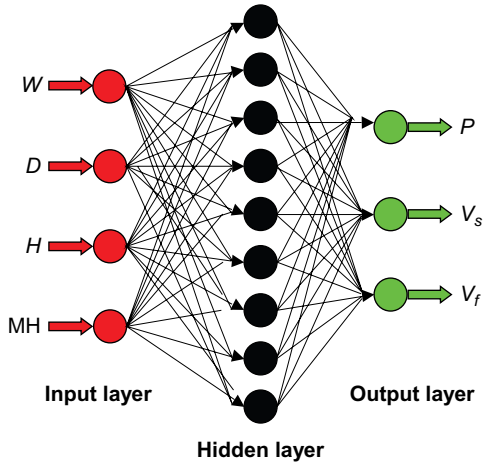


Fig. 24.3 Structure of BP-NN model for laser cladding a Co-based alloy by a HPDL [33].

Concurrently, a negative effect on the clad height and depth was also observed. Increasing scan speed was found to have a positive effect on the clad height, width, and depth. Fig. 24.4 shows the main effects of the input parameters on output response, implemented in Minitab 16 software.

Mondal et al [35] in 2013 used Taguchi and gray relational analysis in order to investigate optimal process parameters for the laser cladding of

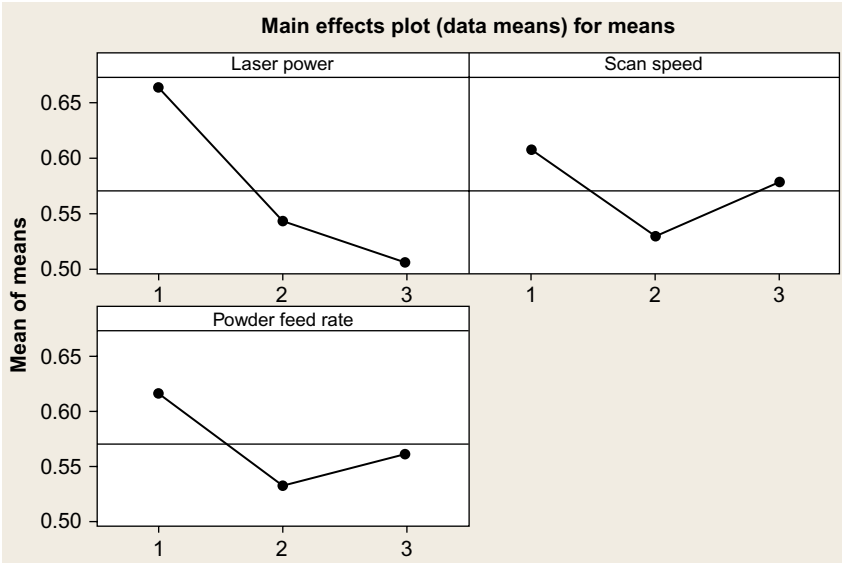


Fig. 24.4 Response of process factors to relative closeness of a particular alternative to ideal solution [34].

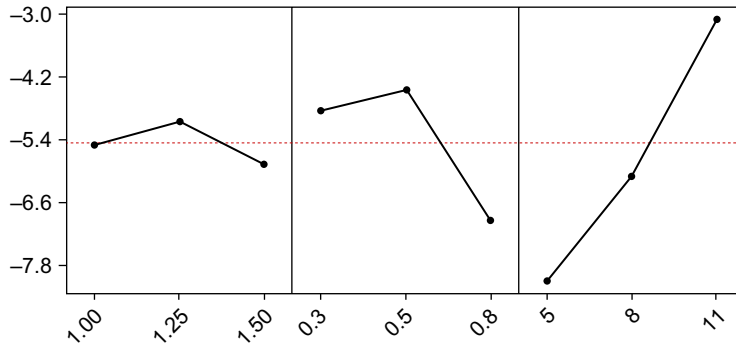


Fig. 24.5 Graph of gray relational grade [35].

AIS1040 steel plane surface. The impact of different laser deposition factors on the clad bead geometry was investigated. The laser power was selected as a source parameter and the scan speed and powder feed rate were selected as process condition parameters. The GRA was for the process modeling and optimization to examine the gray relation grade for each experiment. The best response of the laser cladding of AISI 1040 after optimization was obtained with the laser power of 1.25 kW, at a scanning speed of 0.8 m/min while keeping the powder feed rate at 11 g/min. Fig. 24.5 shows the gray relational grade. Also, it was concluded that for a complex multi response process such as laser cladding, the optimization problem can be converted in to a single objective optimization problem with GRA.

24.4.2 Experimental Investigation of Laser Surface Melting

During laser melting, a thin material surface layer melts and solidifies rapidly due to selfquenching. This results in the modification of the surface microstructure. For higher solidification rates, the melting should be limited to only the thin layer substrate. Therefore, this technique requires lower power densities at high transverse speeds [1].

In 2013 Sun et al. [36] produced highly dense samples with Ti6Al4V alloy powders using a selective laser melting (SLM) technique. The Taguchi method was used to optimize the selected parameters of LSM. These selected laser parameters were laser power, scanning speed, powder thickness, hatching space, and scanning strategy. The optimal parameters and a regression model was developed by design expert software and the analysis on the results obtained was performed using analyses of variance (ANOVA) methods and the signal-to-noise (S/N) ratios. The results indicated that

powder thickness provides major influence over density. The lowest powder thickness (0.02 mm) provides high density (~95%). Compared to the casting method, higher surface micro hardness was achieved by keeping the laser power at 80W.

Calignano [37] studied the manufacturability of overhanging structures using optimized support parts. The SLM technique was carried out for the Al and Ti alloys overhanging structures. Taguchi L_{36} design was used for the experimental study to identify the optimal design of the self-supporting overhanging structures. Several process parameters including hatching space, teeth height, and teeth base interval were optimized using the Taguchi method to obtain highly accurate geometry of the build material by reducing the deformations of the overhanging surfaces.

In 2015, Read et al. [38] investigated the influence of SLM on AlSi10Mg alloy porosity development. They correlated the statistical design of experimental approach with the energy density model to study the influence of laser power, scan speed, scan spacing, and island size using a Concept Laser M2 system on the SLM process. It was reported that for AlSi10Mg alloy, by keeping the critical energy density at about 60 J/m^3, minimum pore fraction can be achieved.

The surface modification of biomaterials is often desirable to improve the degree of biocompatibility of the implants [6]. The laser surface structuring of biomaterials has been reported extensively [7,25,26,39,40]. Chikarakara et al. [2] investigated the effect of a 1.5 kW CO_2 high speed laser on Ti-6Al-4V surface modification for biomedical implants application. During the laser processing, argon (being an inert) gas was used to minimize any unwanted chemical modifications induced on the workpiece surface. The processing parameters studied in this work were irradiance, pulse width, residence time, and sample pre-treatments. SEM was used to characterize surface topology, microstructure, and melt pool depth. From this study, a 3^2 factorial design is presented below to provide a detailed overview of the use of DoE in laser processing of materials.

The two parameters (irradiance and residence time) were selected to make a three-level factorial design of experiment to investigate laser surface processing of a Ti-6Al-4V alloy. A continuous wave (CW) mode laser was used to irradiate the workpiece at three levels of irradiance: 15.72, 20.43, and 26.72 kW/mm^2 and three levels of residence time: 1.08, 1.44, and 2.16 ms, see Table 24.1.

For surface laser processing, a laser beam with a 90 μm diameter was focused on the titanium alloy samples. In order to provide microstructural and

Table 24.1 Design of Experiments parameters for Ti-6Al-4V alloy laser surface processing [2]

ID	Irradiance (kW/mm^2)	Residence time (ms)
LSM 1	15.72	2.16
LSM 2	20.44	
LSM 3	26.72	
LSM 4	15.72	1.44
LSM 5	20.44	
LSM 6	26.72	
LSM 7	15.72	1.08
LSM 8	20.44	
LSM 9	26.72	

compositional homogeneity to the surface, the irradiation of the samples was carried out using a raster scan with a partial overlap of 30%. The pressure of the argon gas was kept at 200 kPa. Inert gas was used to prevent metal oxidation. To ensure uniform processing conditions and maximum absorbance during laser irradiation, the laser beam was kept perpendicular to the sample.

Fig. 24.6 highlights the modifications in the microstructure, roughness, and meltpool depth of the laser irradiated areas of the sample. It can be observed from the BSE images that increases in the irradiance of the laser on the sample surfaces results in modifications in the uniformity of the thickness of the irradiated area. The meltpool depth introduced in the laser processed surface can be modeled by the equation given in Table 24.2.

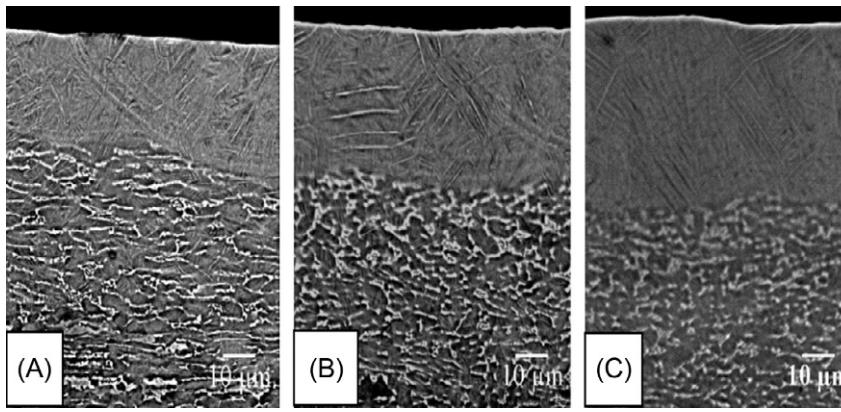


Fig. 24.6 Back scatter detector (BSE) surface morphology images of laser surface modified Ti-6Al-4V at a constant level of irradiance 26.72 kW/mm^2 and three levels of irradiance of residence time of: (A) 1.08; (B) 1.44; (C) 2.16 ms [2].

Table 24.2 Analysis for variance (ANOVA) table for meltpool depth—2FI model

Source	Sum of squares	Mean square	*F* value	*P*-value
Model	502.786	167.595	23.268	0.0023
A-Irradiance	135.375	135.375	18.795	0.0075
B-Residence time	366.601	366.601	50.898	0.0008
AB	0.81	0.81	0.112	0.7510
Residual	36.013	7.202		
Cor total	538.8			
R-squared	0.933	*Final equation obtained from the model:*		
Adj *R*-squared	0.893	*Meltpool depth* =		
Pred *R*-squared	0.879	−3.93448		
Adeq precision	14.047	+0.61818 × *Irradiance*		
		+11.26016 × *Residence time*		
		+0.15152 × *Irradiance* × *Residence time*		

The statistical findings from the ANOVA demonstrated that both input laser process parameters influence the meltpool depth of the irradiated surface. It was further observed that comparatively, the residence time effected more strongly on the meltpool depth of the processed material with respect to irradiance as the F-values obtained by ANOVA were 50.898 and 18.795, respectively.

By considering the interaction of both selected input factors, the statistical analysis showed low significance for influence on the meltpool depth. This result from the 2FI model was further confirmed by the coded factor model equation given below. The coded factors model equation was derived from the experimental design's low and high coded levels (−1 and 1).

$$\text{Meltpool depth } (\mu\text{m}) = 32.63 + 4.75A + 7.82B + 0.45AB$$

The predicted values of the meltpool depth from the model were plotted against the experimental values in Fig. 24.7. The model predicted the output response parameter (the meltpool depth) very close to the experimental values. The signal to noise ratio was also calculated to find the adequate precision of the model which was 14.047 in the study. The ratio higher than 4 confirms that the developed model can be used to optimize the process parameters for the desired output response.

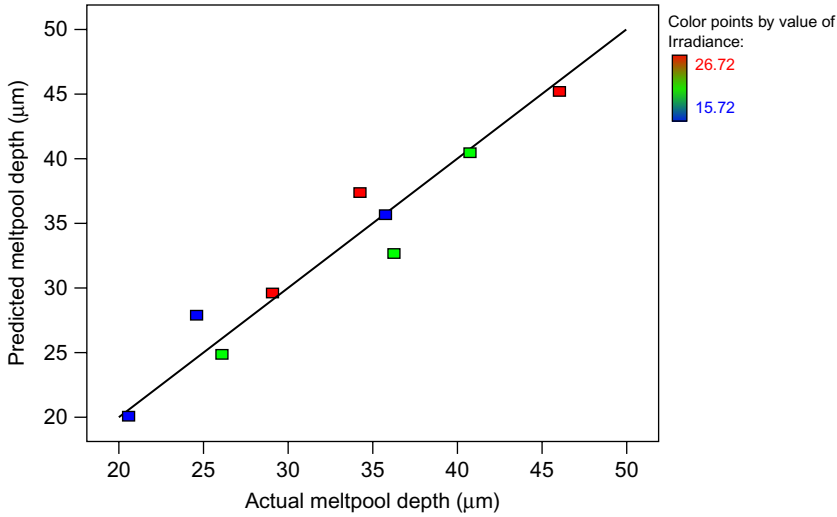


Fig. 24.7 A graph of the actual meltpool depth versus the predicted values [2].

24.4.3 Experimental Investigation of Laser Shock Peening

Laser Shock Peening (LSP) is an efficient surface treatment technique used to improve the fatigue performance of metals. In 2013, Sathyajith et al. [41] investigated the effect of laser shock peening without any coating on an aluminum alloy Al-6061-T6 with a 300 mJ infrared laser. It showed that micro hardness and surface compressive stress were significantly improved using laser shock peening technique without additional coatings. However trivial increase in surface roughness was also observed, as shown in Fig. 24.8.

Through this technique a pulsed laser was fired at the material surface, and the rapid expansion of the resultant formed plasma generated a high

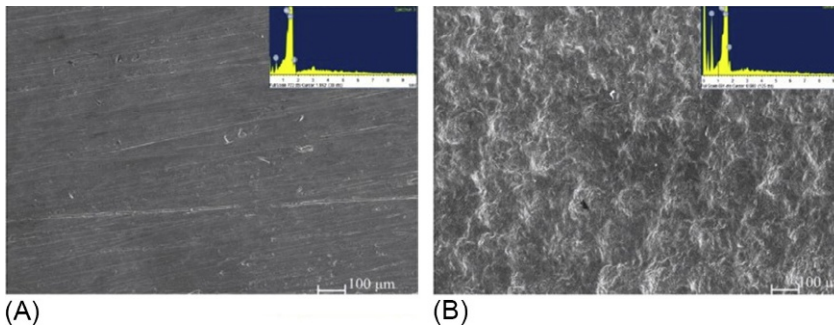


Fig. 24.8 Surface SEM micrograph: (A) pristine surface; (B) laser shock peened surface [41].

amplitude and short duration shock wave. The plasma by laser irradiation on the material was formed due to vaporization of an ablated layer placed on the surface of the material surface confined by water [42]. The shock wave generated stresses on the specimen surface, causing a compressive residual stress field which increased the surface hardness and fatigue life. From that we can understand that LSP is a mechanical process unlike other laser processing techniques based on the thermal processing of the materials [43].

Sibalija et al. [44] varied three Nd:YAG laser parameters in laser shock peening (LSP) to find the optimum parameters. The experiment was conducted on nickel-based superalloy Nimonic 263 sheets, and the selected LSP parameters for optimization included source voltage, focus position, and pulse duration. The group performed modeling and optimization using the advanced problem-independent method. The Taguchi quality loss function was used first to express the responses, then uncorrelated and synthesized into a single performance measure using the application of multivariate statistical analysis. Finally, the process model was built using an artificial neural network, and simulated annealing was utilized to find the optimal process parameters setting in a global continual space of solutions. The obtained global optimum for the process parameters provided improved micro hardness along with very fine grains and the overall surface roughness was reduced after LSP at these values. Therefore, it made the surface smoother with a clean microstructure, as well as an improved fatigue life.

24.5 CONCLUSION

Laser processing has a wide application range from micro/nano fabrication techniques to surface treatment, structuring, modification, and controlled surface plastic deformation. As the laser matter interaction is a complex phenomenon, the advancements in laser processing applications require accurate mathematical models to describe various processes occurred during the laser interaction with different materials. The models can be developed to predict the response of the laser processing for a specific application by establishing a relationship between the process input parameters (laser parameters and working conditions) and output response (resulting property of the processed material). A systematic approach is required to generate data that is required for the modeling and simulation of laser processing. Design of Experiments (DoE) has been extensively used to describe how the materials' properties can be controlled as a result of the control of processing conditions. In particular, the DoE approach has been successfully

used in laser processing to establish and validate the relationship between the laser process parameters, working conditions, and output responses. This allow definition of accuracy, repeatability, and reliability from the laser process, enabling the use of these techniques to be taken and employed more widely by industries that are adopting new laser based technologies more rapidly for both material modification and fabrication.

REFERENCES

[1] E. Kannatey-Asibu, Principles of Laser Materials Processing, vol. 4, John Wiley & Sons, Inc., Hoboken, NJ, 2009.

[2] E. Chikarakara, S. Naher, D. Brabazon, High speed laser surface modification of Ti-6Al-4V, Surf. Coat. Technol. 206 (14) (2012) 3223–3229.

[3] D. Karthik, S. Kalainathan, S. Swaroop, Surface modification of 17–4 PH stainless steel by laser peening without protective coating process, Surf. Coat. Technol. 278 (2015) 138–145.

[4] A. Riveiro, R. Soto, J. Del Val, R. Comesaña, M. Boutinguiza, F. Quintero, F. Lusquiños, J. Pou, Laser surface modification of ultra-high-molecular-weight polyethylene (UHMWPE) for biomedical applications, Appl. Surf. Sci. 302 (2014) 236–242.

[5] R.S. Faeda, H.S. Tavares, R. Sartori, A.C. Guastaldi, E. Marcantonio, Evaluation of titanium implants with surface modification by laser beam. Biomechanical study in rabbit tibias, Braz. Oral Res. 23 (2) (2009) 137–143.

[6] I. Ul Ahad, A. Bartnik, H. Fiedorowicz, J. Kostecki, B. Korczyc, T. Ciach, D. Brabazon, Surface modification of polymers for biocompatibility via exposure to extreme ultraviolet radiation, J. Biomed. Mater. Res. A 102 (9) (2014) 3298–3310.

[7] I.U. Ahad, B. Budner, H. Fiedorowicz, A. Bartnik, D. Brabazon, Nitrogen doping in biomaterials by extreme ultraviolet (EUV) surface modification for biocompatibility control, Eur. Cell. Mater. 26 (6) (2013) 145.

[8] A. Olabi, F. Alsinani, A. Alabdulkarim, Optimizing the CO_2 laser welding process for dissimilar materials, Opt. Lasers Eng. 51 (2013) 832–839.

[9] K. Huehnlein, K. Tschirpke, R. Hellmann, Optimization of laser cutting processes using design of experiments, Phys. Procedia 5 (2010) 243–252.

[10] S. Britten, A. Olowinsky, A. Gillner, Stress-minimized laser soldering of h-pattern multicrystalline silicon solar cells, Phys. Procedia 41 (2013) 153–163.

[11] A. Issa, D. Brabazon, M.S.J. Hashmi, 3D transient thermal modelling of laser microchannel fabrication in lime-soda glass, J. Mater. Process. Technol. 207 (1–3) (2008) 307–314.

[12] D. Montgomery, Design and Analysis of Experiments, John Wiley & Sons, Inc., Hoboken, NJ, 2008.

[13] R. Mason, R. Gunst, J. Hess, Statistical Design and Analysis of Experiments: with Applications to Engineering and Science, John Wiley & Sons, Inc., Hoboken, NJ, 2003.

[14] K. Hinkelmann, O. Kempthorne, Design and Analysis of Experiments, Special Designs and Applications, Wiley Publishing, Hoboken, NJ, 2012.

[15] D. Cox, N. Reid, The Theory of the Design of Experiments, Chapman & Hall/CRC Press, Boca Raton, FL, 2000.

[16] D. Angela, V. Daniel, Design and Analysis of Experiments, Springer-Verlag NY Inc., New York, 1999.

[17] K. Tamrin, Y. Nukman, I. Choudhury, Multiple-objective optimization in precision laser cutting of different thermoplastics, Opt. Lasers Eng. 57 (2015) 57–65.

[18] B. Adelmann, R. Hellmann, Rapid micro hole laser drilling in ceramic substrates using single mode fiber laser, J. Mater. Process. Technol. 221 (2015) 80–86.
[19] A. Issa, Computational Control of Laser Systems for Micro-Machining, Dublin City University, 2007.
[20] StatEase Inc., Available: http://www.statease.com/ (accessed 12.12.16).
[21] SAS Institute Inc., Available: http://www.jmp.com/en_us/home.html (accessed 15.12.16).
[22] Minitab., Available: http://www.minitab.com/en-us/ (accessed 15.12.16).
[23] S. Sihn, L. Childers, C. Walters, M. Forte, Computational and experimental study on laser heating of a Ni-based metal alloy, Int. J. Heat Mass Transf. 102 (2016) 1034.
[24] C. Fu, M. Sealy, Y. Guo, X. Wei, Finite element simulation and experimental validation of pulsed laser cutting of nitinol, J. Manuf. Process. 19 (2015) 81–86.
[25] I.U. Ahad, B. Butruk, M. Ayele, B. Budner, A. Bartnik, H. Fiedorowicz, T. Ciach, D. Brabazon, Extreme ultraviolet (EUV) surface modification of polytetrafluoroethylene (PTFE) for control of biocompatibility, Nucl. Instrum. Methods Phys. Res., Sect. B 364 (2014) 98–107.
[26] I. Ahad, H. Fiedorowicz, B. Budner, T.J. Kaldonski, M. Vazquez, A. Bartnik, D. Brabazon, Extreme ultraviolet surface modification of polyethylene terephthalate (PET) for surface structuring and wettability control, Acta Phys. Pol. A 129 (2) (2016) 241–243.
[27] M. Ahmed Obeidi, E. McCarthy, D. Brabazon, Methodology of laser processing for precise control of surface micro-topology, Surf. Coat. Technol. 307 (2016) 702–712.
[28] R. Schmitt, G. Mallmann, K. Winands, M. Pothen, Automated process initialization of laser surface structuring processes by inline process metrology, Phys. Procedia 41 (2013) 887–895.
[29] R. Rao, Advanced Modeling and Optimization of Manufacturing Processes: International Research and Development, Springer, 2010.
[30] T. Šibalija, V. Majstorović, Advanced Multiresponse Process Optimisation, Springer International Publishing, 2016.
[31] H. Sohrabpoor, Analysis of laser powder deposition parameters: ANFIS modeling and ICA optimization, Opt. J. Light Electron. Opt. 127 (8) (2016) 4031–4038.
[32] S. Mondal, A. Bandyopadhyay, P.K. Pal, Application of artificial neural network for the prediction of laser cladding process characteristics at Taguchi-based optimized condition, Int. J. Adv. Manuf. Technol. (2013) 2151–2158.
[33] S. Guo, Z. Chen, D. Cai, Q. Zhang, V. Kovalenko, J. Yao, Prediction of simulating and experiments for co-based alloy laser cladding by HPDL, Phys. Procedia 50 (2013) 375–382.
[34] J. Marzban, P. Ghaseminejad, M.H. Ahmadzadeh, R. Teimouri, Experimental investigation and statistical optimization of laser surface cladding parameters, Int. J. Adv. Manuf. Technol. 76 (5–8) (2014) 1163–1172.
[35] S. Mondal, C.P. Paul, L.M. Kukreja, A. Bandyopadhyay, P.K. Pal, Application of Taguchi-based gray relational analysis for evaluating the optimal laser cladding parameters for AISI1040 steel plane surface, Int. J. Adv. Manuf. Technol. 66 (1–4) (2013) 91–96.
[36] J. Sun, Y. Yang, D. Wang, Parametric optimization of selective laser melting for forming Ti6Al4V samples by Taguchi method, Opt. Laser Technol. 49 (2013) 118–124.
[37] F. Calignano, Design optimization of supports for overhanging structures in aluminum and titanium alloys by selective laser melting, Mater. Des. 64 (2014) 203–213.
[38] N. Read, W. Wang, K. Essa, M.M. Attallah, Selective laser melting of AlSi10Mg alloy: process optimisation and mechanical properties development, Mater. Des. 65 (2015) 417–424.
[39] H. Fiedorowicz, I. Ul Ahad, A. Bartnik, T. Fok, R. Jarocki, B. Korczyc, J. Kostecki, A. Szczurek, M. Szczurek, P. Wachulak, L. Wegrzynski, Laser plasma sources of soft X-rays and extreme ultraviolet (EUV) for application in science and technology, in: 2014 Int. Conf. Laser Opt., 2014, pp. 1.

[40] I.U. Ahad, B. Budner, B. Korczyc, H. Fiedorowicz, A. Bartnik, J. Kostecki, S. Burdyńska, D. Brabazon, Polycarbonate polymer surface modification by extreme ultraviolet (EUV) radiation, Acta Phys. Pol. A 125 (4) (2014) 924–928.
[41] S. Sathyajith, S. Kalainathan, S. Swaroop, Laser peening without coating on aluminum alloy Al-6061-T6 using low energy Nd:YAG laser, Opt. Laser Technol. 45 (1) (2013) 389–394.
[42] G. Tani, L. Orazi, A. Fortunato, A. Ascari, G. Campana, Warm Laser shock peening: new developments and process optimization, CIRP Ann. Manuf. Technol. 60 (1) (2011) 219–222.
[43] W. Braisted, R. Brockman, Finite element simulation of laser shock peening, Int. J. Fatigue 21 (7) (1999) 719–724.
[44] T.V. Sibalija, S.Z. Petronic, V.D. Majstorovic, A. Milosavljevic, Modelling and optimisation of laser shock peening using an integrated simulated annealing-based method, Int. J. Adv. Manuf. Technol. 73 (5–8) (2014) 1141–1158.

This page intentionally left blank

CHAPTER 25

Microstructural Characterization and Mechanical Reliability of Laser-Machined Structures

M. Mehrpouya*, H. Lavvafi†, A. Darafsheh‡
*Sapienza University of Rome, Rome, Italy
†Loyola University Medical Center, Maywood, IL, United States
‡Washington University School of Medicine, St. Louis, MO, United States

25.1 INTRODUCTION

The need for components and devices with micron-scale dimensions and with fine structures for applications in various fields, such as electronics, medical, biomedical, aviation, microelectromechanical systems (MEMS), energy, optics, and photonics has increased rapidly in recent years [1–3]. Although traditional machining tools are widely used as a major means of fabricating such microcomponents, there still remain significant issues in the predictability and productivity of the fabrication methods, especially for microcomponents with complex shapes [4]. For instance, the trend toward miniaturization of medical devices with high-precision production has introduced new challenges for manufacturing techniques [5,6]. Surface damage during the machining process using conventional techniques can affect the performance of the machined components, especially in some specific materials that are hard to machine [7]. In addition, some designs often include fine details that are difficult to achieve with rotary tool machining. Thus, there is great interest in the use of laser microfabrication techniques.

Lasers have made possible significant advancements in cutting, welding, and many other manufacturing processes [8–16]. The ability to machine fine details with high precision, accuracy, and speed on structures made of a metal, semiconductor, ceramic, and polymer via laser ablation has paved the way for the application of laser material processing in microelectronics and other industries [16–19]. The introduction of high-power lasers with ultrashort pulses has opened a new paradigm in the laser processing of materials,

Advances in Laser Materials Processing
https://doi.org/10.1016/B978-0-08-101252-9.00025-X
Copyright © 2018 Elsevier Ltd.
All rights reserved.

allowing the creation of very high-resolution features with very little mechanical or chemical damage to the medium [12,13].

Laser micromachining requires a large amount of energy. Depending on the material and the desired machining process, different types of lasers with various power sources are used. CO_2 and Nd:YAG lasers are the most common ones used in micromachining [15]. Improvements in the quality of the cutting, drilling, and micromachining of materials through the use of lasers have enabled us to produce finer details using laser-machining compared to more conventional engraving techniques. Lasers with short pulses in the picosecond (ps) and femtosecond (fs) range have become the popular choice for micromachining because of several advantages, such as high flexibility and very small induced heat affected zones (HAZs). Femtosecond lasers can provide high-quality micromachining with minimal thermal damage because the short pulse duration results in high peak power. As a result, the material is removed by vaporization instead of melting as it occurs in long-pulse (i.e., nanosecond) or continuous laser material processing. Nanosecond lasers usually provide higher energy with a relatively lower repetition rate, generating more thermal damage than picosecond and femtosecond lasers. [20–23].

Extensive research has been done on the effects of various process parameters on the productivity of laser machining processes. An area that deserves additional attention is the effect of laser processing on the structure and mechanical properties of the laser-affected materials. A highly energetic laser beam can cause multiple phase transformations in the substrate (i.e., evaporation, deposition, melting, and solidification) as well as solid-state phase transformations, which occur due to the fast cooling rate of molten materials. The selection of laser processing variables makes a major difference in the quality of the fabricated parts and their properties.

In this chapter, we review recent developments in laser micromachining processes, which involve the integration of various micromachining processes and laser sources for improving the quality of the machining process. This chapter also deals with the mechanical characterization and reliability of laser micromachined structures.

25.2 LASER MICROMACHINING AND ITS FEATURES

Various manufacturing and material processing operations, such as laser-assisted joining, forming, machining, and surface engineering, can be performed using high-power lasers due to their ability to produce localized intense heating. Lasers are widely employed for machining, using thermal

energy to break the chemical bonds in materials. A schematic representation of a typical laser machining process is illustrated in Fig. 25.1. When a laser beam with high energy density is focused on the surface of a material, the absorbed thermal energy can transform the work volume into a molten, vaporized, or chemically changed state. A flow of a high-pressure assist gas jet is then used to accelerate and remove the transformed material from the machining zone. The parameters governing this process depend on the material properties, such as thermal conductivity, reflectivity, specific and latent heats of melting, and evaporation [25–27].

Laser machining is applicable to a variety of materials. It is a flexible, repeatable, efficient, and controlled process. Lasers can be used to process a variety of alloys as well as traditional or novel materials, such as smart alloys. To achieve a high quality of machining and maintain the original properties of the base material, the laser operating parameters such as laser power and scan speed must be carefully chosen [28–32].

An important advantage of laser processing over conventional mechanical methods is that it works with minimal contact. For example, the fabrication of cooling holes in a thermal barrier-coated superalloy requires

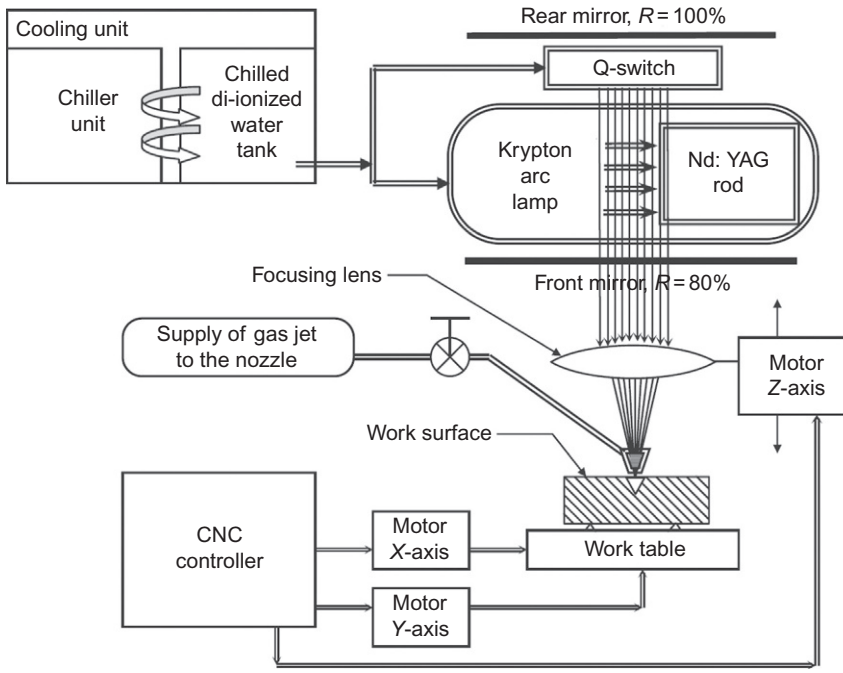


Fig. 25.1 Schematic illustration of an Nd:YAG laser machining system [24].

machining through an electrically nonconducting YSZ (yttria stabilized zirconia) layer, which is a challenging task using traditional methods such as electrodischarge and electrochemical machining. Laser machining, however, due to its noncontact nature, can be used to create such holes through melt ejection and vaporization as a result of focusing the laser beam on the surface of the material [33]. A summary of laser machining applications in several industries is tabulated in Table 25.1.

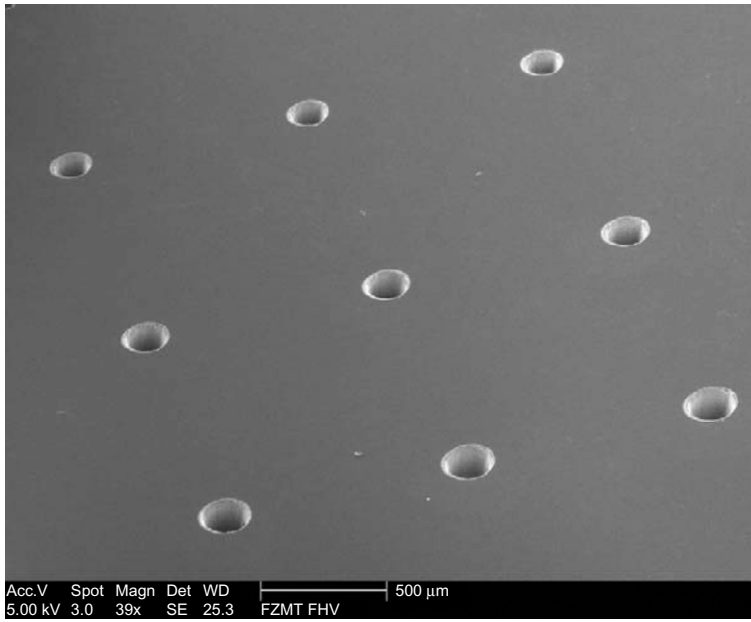
Laser micromachining has the ability to produce micron-scale structures through different methods such as direct writing, mask projection patterning, and patterning by interference of the laser beams [34,35]. The dynamics of the laser ablation process and the efficiency of laser machining depend on the optical and thermal properties of the material, such as reflectivity, absorption, and heat diffusion coefficients.

In several engineering applications, laser machining can replace the traditional mechanical material removal techniques because of its outstanding features, such as its flexibility and the fact that it is a thermal and noncontact process, as described in the following. Various material processing functions, such as welding, drilling, grooving, cutting, and heat treating can be performed by the same laser system integrated with a multiaxis positioning or robotic system. In this way, there is no need to transport the parts to specialized machines to perform each task. The ability to perform real-time monitoring of the laser processing allows online measurement of the key parameters of the sample. Hence, a high level of reproducibility can be achieved [36,37]. Due to its noncontact nature, the cutting force, tool wear, and machine vibration associated with typical mechanical methods can be eliminated in laser processing of materials because the energy transfer happens through irradiation of the material. Also, the rate of material removal is controlled by the laser processing parameters, such as laser power and processing and scanning speed, and is not affected by the maximum tool force, tool chatter, and built-up edge formation.

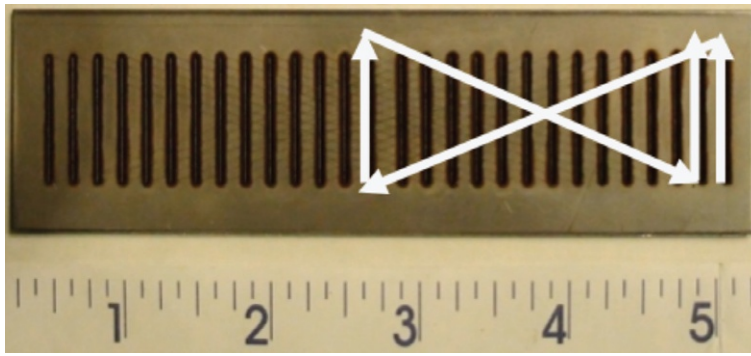
Fig. 25.2A shows an array of microholes drilled in a 3C–SiC wafer with a laser beam operating at a wavelength of 1040 nm with a pulse duration of 300 fs [38]. In that example, the laser beam moves along a circular path during the microlaser drilling process. Another example is shown in Fig. 25.2B for a single plate of heat exchange with microchannels used for waste heat recovery, in which the Nd:YAG nanosecond laser was used for machining while the laser beam was guided via an array of multiple mirrors inside the laser machine head. Arrows indicate the laser beam pattern that was used for micromachining [34,39].

Table 25.1 Some typical laser materials processing applications [1]

Heavy manufacturing	Light manufacturing	Electronics	Medical industry	General
Profile cutting in sheet and plate metals	Profile cutting in plastics and wood	High accuracy wire stripping	Flow orifices with <100 mm diameter	CVD diamond cutting
Seam and spot welding	Engraving	Via formation insulating material: Tab & MCM	Machining delicate or thermally sensitive materials	Ceramic and glass micromachining
Cladding and drilling	Drilling	Skiving of flexible circuits	Micromachining applications where edge quality and cleanliness are critical	Thin film patterning
		IC repair		Microlithography



(A)



(B)

Fig. 25.2 (A) Array of microholes in a 3C–SiC wafer with 400-µm thickness drilled with a solid-state laser with a pulse duration of 300 fs at a wavelength of 1040 nm [38]. (B) Laser carving of a stainless steel plate with dimension of 15 × 50 mm, applicable as a microchannel heat exchanger with a 400-µm channel width [34].

25.3 LASER SOURCES FOR LASER MACHINING

Lasers can produce monochromatic collimated light with small (submillimeter) spot sizes, high power, narrow bandwidth, and a precisely controlled wavelength. A laser requires three fundamental components: a lasing medium, a resonator cavity, and an energy source. The lasing medium can be a

solid (glass, crystal, fiber, powder), gas (atomic, ionic, molecular, excimeric), or liquid (organic dye). The resonator cavity is basically a pair of mirrors facing each other with the lasing medium between them. The energy source, or pump, provides the energy (usually through an optical or electrical excitation) required for exciting the molecules of the lasing medium to an upper-level energy state. These molecules would spontaneously emit incoherent and poorly collimated light under normal conditions. However, in a laser, the light emission of the lasing medium is reflected within the resonator cavity such that it passes through the lasing medium multiple times, generating stimulated emission of photons from the lasing medium on each pass. Because the stimulated emission is in phase with the stimulating light field, this amplification process produces coherent and monochromatic light. One of the mirrors in the cavity is partially transmitting, so a fraction of the light amplified in the cavity is extracted on each reflection, producing a useful beam [40,41].

Different types of lasers, such as CO_2, Nd:YAG, excimer, and femtosecond lasers are used for the machining processes of various types of materials. Characteristics of typical solid-state and gas lasers, operating in deep ultraviolet (UV) to mid-infrared (IR) wavelengths, used for microfabrication are tabulated in Table 25.2.

25.3.1 Nd:YAG Lasers

Nd:YAG lasers, with a wavelength of 1.064 μm in the near-IR region of the spectrum, are the most commonly used high-power solid state lasers. The lasing medium is a crystalline matrix of yttrium-aluminum-garnet (YAG, $Y_3Al_5O_{12}$) with neodymium ions (Nd^{3+}) dopants dispersed in it. A krypton and/or xenon flash lamp serves as the energy source to excite the lasing medium.

The Nd:YAG lasers, due to their good beam quality, are able to form a very small focused beam with associated small kerf widths that make them an excellent choice for microcutting materials. In the laser beam cutting (LBC) process, the laser beam is focused on the work material and is absorbed at the cutting front. The absorbed thermal energy heats the material, transforming the prospective kerf volume into a molten, vaporized, and/or chemically changed state that can be removed by a coaxial gas jet (see Fig. 25.3) [42–47]. In addition, the slag and the oxide scales formed on the surface due to laser cutting can be removed by acid pickling using an HNO_3 bath followed by electrolysis. A smooth surface can be achieved after electrochemical polishing.

Table 25.2 Laser types used in microfabrication application [35]

Type of laser	Laser material	Wave length	Pulse length	Frequency
Solid state laser	Nd:YAG (2nd harmonic)	532 nm	100–10 ns	50 Hz
	Nd:YAG (3rd harmonic)	355 nm		
	Nd:YAG (4th harmonic)	266 nm		
	Nd:YVO_4	1064 nm	2.8–7.9 ps	84 MHz to 77 GHz
	Nd:$GDVO_4$	1053 nm	37 ps	100 MHz
	Nd:BEL	1070 nm	2.9–7.5 ps	250 MHz to 20 GHz
	Nd:LSB	1062 nm	1.6–208 ps	177–240 MHz
	Nd:glass	1054 nm	7 ps	
	Nd:VAN	750–870 nm		
	Nd:YLF	1047–1053 nm	1.5–37 ps	76 MHz to 2.85 GHz
	Yb:YAG	1030 nm	340–730 fs	35–81 MHz
	Yb:glass	1025–1082 nm	58–61 fs	112 MHz
	Yb:GdCOB	1045 nm	90 fs	100 MHz
	Yb:KGW	1037 nm	176 fs	86 MHz
	Ti:sapphire	750–880 nm	6–150 fs	15 MHz to 2 GHz
	Cr:LiSAF	800–880 nm	12–220 s	82–200 MHz
	Cr:LiCAF	800–820 nm	20–170 fs	90–95 MHz
	Cr:SGaF	830–895 nm	14–100 fs	71–119 MHz
	Cr:LiSCaF	860 nm	90 fs	140 MHz
	Cr:Forsterite	1.21–1.29 μm	14–48 fs	81–100 MHz
	Cr:YAG	1.52 μm	44–120 fs	81 MHz to 1.2 GHz
	Fiber lasers	1.064 μm	100 ns	20–25 Hz
	Diode lasers	0.8 μm		
	Microchip lasers	1.064 μm	Less than 100 ps	100 kHz
Gas laser	ArF	193 nm	5–25 ns	1–1000 Hz
	KrF	248 nm	2–60 ns	1–500 Hz
	XeCl	308 nm	1–250 ns	1–500 Hz
	XeF	351 nm	0.3–35	1–1000 Hz
	CO_2 laser	10.6 μm	200 μs	5 Hz
	Copper vapor lasers	611–578 nm	30 ns	4–20 Hz

Machining of superalloys using Nd:YAG lasers with nanosecond pulses is a fairly well-established practice in the aviation industry. However, their relatively long pulses (typically several ns) lead to the diffusion of a significant amount of thermal energy into the surrounding material during the machining process [48]. As a result, collateral damage consisting of recast

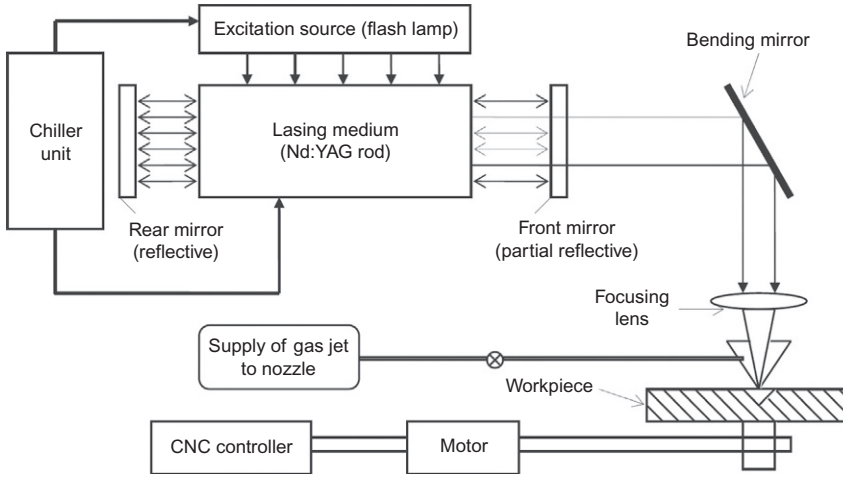


Fig. 25.3 Schematic diagram of an Nd:YAG laser beam cutting machine [42].

layer formation, melt debris, and microcracking often accompany nanosecond laser machining [33]. It should be noted that Nd:YAG fiber lasers are used in applications requiring low pulse repetition rate and high pulse energies (up to 100 J/pulse), such as hole piercing and deep keyhole welding applications [7,25].

25.3.2 Carbon Dioxide Lasers

CO_2 lasers, with an output wavelength of 10.6 μm in the far-infrared (FIR) region of the spectrum, are molecular lasers, a subgroup of gas lasers. The lasing medium is a combination of carbon dioxide, nitrogen, and helium gas molecules. The excitation of the carbon dioxide is achieved by increasing the vibrational energy of the molecule through an electric discharge.

CO_2 lasers are well established in industrial processes due to their low investment costs, high reliability, and suitability for processing almost all materials. The commercial CO_2 lasers exhibit the simultaneous achievement of short pulse duration, high peak power, and high beam quality. Consequently, pulse duration is typically in the order of ms down to μs, which results in a thermal material ablation process dominated by heat conduction [49,50]. Industrial uses for CO_2 lasers include laser machining, heat treatment, and welding [7,13,25]. Compact RF-excited wave guide CO_2 lasers are well suited for micromachining processing by controlling the wave guide loss in the laser resonator [35]. The actual pumping takes place by an AC or DC electrical discharge.

25.3.3 Excimer Lasers

Excimer (short for excited dimer) lasers with the output light in the UV to near-UV range are gas lasers in which the lasing medium is a compound of two identical species that exist only in an excited state. Commonly used excimer lasers are argon fluoride (ArF), krypton fluoride (KrF), xenon chloride (XeCl), and xenon fluoride (XeF), with the output wavelengths of 193, 248, 308, and 351 nm, respectively [51]. The compound lasing medium can be formed by inducing the noble gas (Kr, Ar, or Xe) into an excited state with an electron beam, an electrical discharge, or a combination of both. Excimer lasers can be used for machining solid polymers, removing metal films from polymer substrates and micromachining ceramics and semiconductors. They are also applicable for a laser treatment process [7].

Optimizing the productivity and quality of the components manufactured using lasers is of great importance. Both aspects are influenced by the selection of appropriate laser processing parameters, such as laser wavelength and power, cutting speed, and the assist gas parameter, which depend on the material structure, thickness, desired feature size, and economic considerations. [28,29,52]. Due to their shorter wavelength, UV lasers can be focused into a smaller spot compared to the IR lasers as the focused spot size is proportional to the wavelength. Since UV light is absorbed at a shallower depth in material, a fine control of the material removal can be achieved. However, the processing rate is slower because there is less material removal per pulse. UV lasers generally have a relatively short pulse length (<100 ns), which helps to attain a high power density on the target material. The minimal thermal effect results in a good edge quality. Short wavelengths with short pulse lead to a better edge quality. However, their capital and maintenance cost is much higher. UV lasers are best used when small feature sizes and good quality are more important than the cost [9].

IR lasers have relatively longer pulses (microseconds to milliseconds) and wavelengths compared to the UV lasers. Due to their long wavelength, the laser light absorption occurs far into the material. IR lasers are available in very high output powers up to tens of kilowatts and their cost is lower than the UV lasers.

25.3.4 Femtosecond Lasers

Most of the time, machining with a nanosecond laser generates considerable damage, such as recast layer, spatter, HAZs, and in the case of having a coated substrate, delamination of the ceramic coating [22,33,53]. Even pulses in the picosecond range may lead to an unacceptable distortion of medical devices

with fine and intricate geometries. Thus, in order to produce microcomponents free of distortion, the pulse duration has to be further reduced by several orders of magnitude down to the femtosecond domain [54,55]. Recent studies have shown that the abovementioned damages to the work material can be minimized by using femtosecond lasers because the very high peak intensities achieved as a result of short pulse duration lead to the material removal by vaporization, instead of melting as in long-pulse or continuous laser material processing.

Femtosecond lasers offer a new paradigm in machining quality with high spatial resolution, minimal thermal damage, and minimal heat diffusion into the machined area periphery, which leaves behind a small amount of molten material. This small HAZ contains a low level of thermal defects, common in ns-laser processing, such as cracking and chipping [20,56]. For example, laser-machined holes with a surface roughness of less than 2 μm and with no major collateral damage have been produced by femtosecond lasers [33,34]. One reason for the reduced damage is the decreased thermal penetration depth associated with shorter pulses, as schematically illustrated in Fig. 25.4 [58–60].

Due to minimal thermal and mechanical influences in femtosecond lasers, the major effect that limits the resolution of fabricated features using such lasers is the diffraction of light waves. Structures with diffraction-limited dimensions can be readily generated in the far field. The diffraction limit can be overcome using near field material processing techniques, such as by combining a femtosecond-pulse laser with a scanning near-field

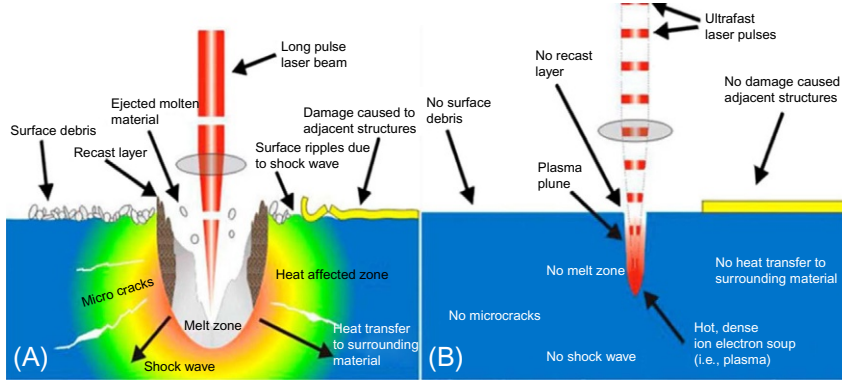


Fig. 25.4 Comparison of (A) nanosecond vs. (B) femtosecond laser ablation processes. Femtosecond lasers provide a smaller HAZ, more precise machining, and minimal collateral damage compared with their nanosecond laser counterparts [57].

optical microscope probe. In this way, the size of the generated structures is not limited by either the wavelength of laser light or thermal effects [61,62].

Sometimes there is a need to machine a variety of fine features in biomedical devices, such as in cardiovascular stents. One example is laser machining a NiTi (nitinol) cylinder with different wall thicknesses [63]. Fig. 25.5 exhibits a Nitinol stent machined by an ultrafast fiber laser. Clean, precise, straight cuts can be made in a single pass at 40 μJ pulse energy on target, 800 fs pulse duration, and 100 kHz repetition rate. The outer diameter of the tube is 3 mm with a 254-μm wall thickness [64–66].

It should be mentioned that femtosecond lasers require complicated optical devices and demanding maintenance. They also generate great scattering effects that deteriorate metal ablation [12,21,23].

25.4 METHODS OF MICROSTRUCTURE AND SURFACE EVALUATION

There are several methods practically used to evaluate the microstructure and surface characteristics of laser-machined components. These methods include but are not limited to optical microscopy (wide field and laser scanning confocal microscopy), scanning electron microcopy (SEM), transmission electron microscopy (TEM), and focused ion beam (FIB).

25.4.1 Optical Microscopy

Optical microscopy, which is a nondestructive and real-time imaging technique, is one of the most powerful and versatile investigation techniques in material sciences. The far-field spatial resolution of any standard lens-based

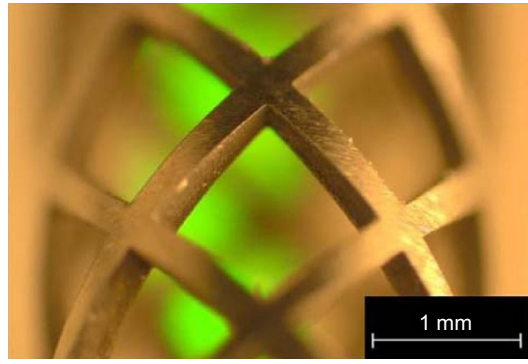


Fig. 25.5 Visible light microscope image of a nitinol stent machined with an ultrafast fiber laser [64].

optical microscope is limited by the wavelength of imaging light (λ) and by the numerical aperture (NA) of the lens system due to the diffraction of light waves. NA is defined by $NA = n \times \sin\theta$, in which n is the refractive index of the object-space medium and θ is the half-angle of the maximum cone of light that can enter (exit) the lens. For conventional white-light microscope systems, Abbe's diffraction-limit is $0.5\lambda/NA \sim 250$ nm. Confocal microscopes, benefiting from illumination and detection through pinholes, offer improvement in resolution as well as the ability to perform surface evaluation analysis. It should be noted that a variety of optical microscopy techniques based on near-field scanning probes and microscale lenses have been devised in recent years to overcome the diffraction limit. However, design complexity, slow acquisition time, and limited field of view have impeded their use to some extent [67–70].

Laser treatment will affect the surface properties of the materials. Usually when these effects are in the order of several microns, they can be readily characterized using conventional optical microscopy. Fig. 25.6A shows a cross-section of a 316LVM wire machined by using an Nd:YAG laser. The grained surface is restructured after thermal treatment as well as as-received material. Fig. 25.6B illustrates the microstructural change within the recast layer of a laser treated H13 tool steel, etched with 2% nital, in which regions of recast and HAZs are visible [34,71].

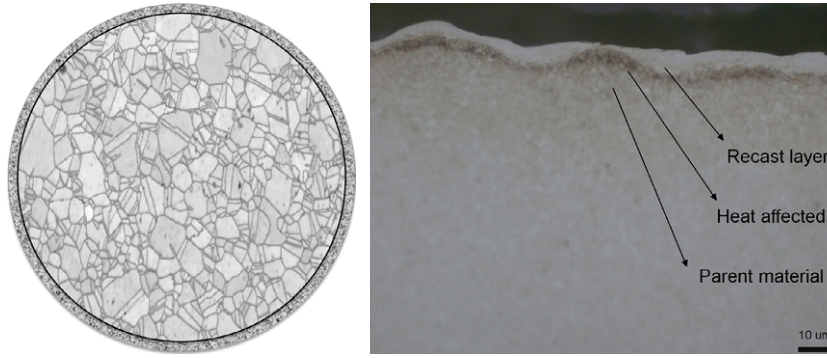


Fig. 25.6 (A) Schematic of the laser-machined wire representing the large central core and the outer skin of harder/softer material. Schematic also shows the typical grain structure in the core similar to that of as-received material. The surface grains are restructured by the laser treatment [34]. (B) Optical micrographs showing a microstructural change, such as dissolving carbides within recast layer, for H13 tool steel laser treated and etched with 2% nital showing regions of recast, HAZ, and parent metal [34].

25.4.2 SEM, TEM, and FIB

Scanning electron microscopy, transmission electron microscopy, and focused ion beam are the imaging techniques with nanometer and subnanometer scale resolution that are particularly used in the fields of semiconductor and materials science for site-specific analysis, deposition, and ablation of materials.

An SEM uses a focused beam of electrons to image the specimen in a vacuum chamber. A focused ion beam setup is similar to a scanning electron microscope setup; however, it uses a focused beam of ions. As an example of using FIB in order to investigate the nature of recast layer produced by the laser treating, FIB can be used to make a cross-section of the laser-treated specimens. In this approach, ion beam (Ga^+) assisted Pt deposition is used as a protection layer for subsequent milling for the cross-section. Fig. 25.7 shows the steps to make a cross-section of the laser-treated sample within the recast layer induced by an Nd:YAG laser [34].

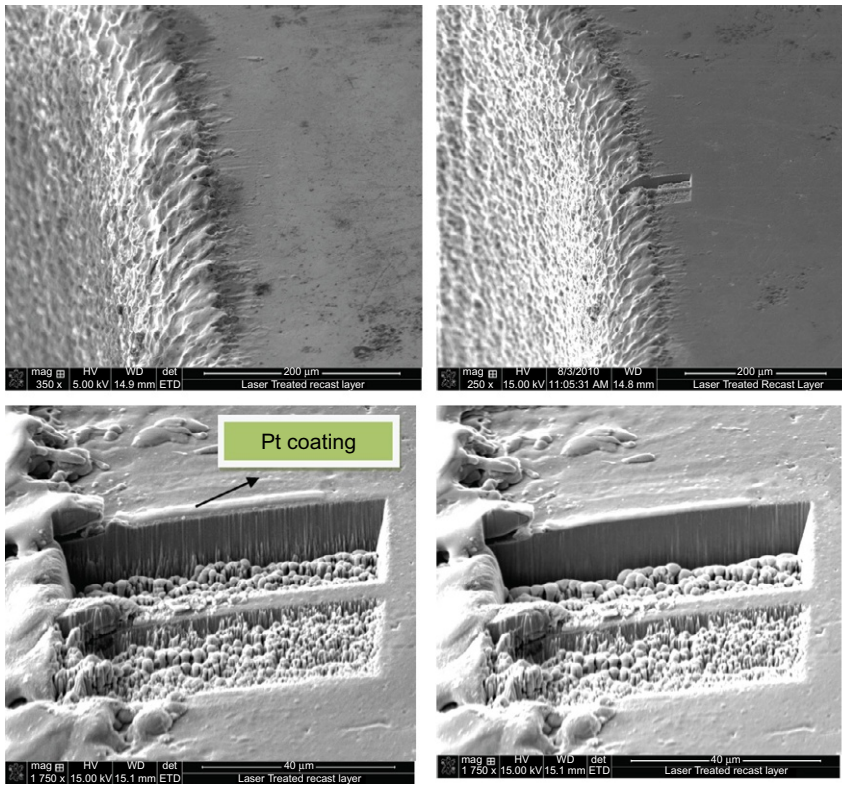


Fig. 25.7 Cross-sections showing the process of using FIB milling to study the HAZs and recast layer induced by laser treatment [34].

An example of using SEM has been presented in the following. The nitinol biliary stent can be successfully fabricated with a rounded shape and smooth edges in a precise dimension, clean surface morphology, no recast layer, and minimal HAZ produced by femtosecond laser micromachining. The SEM images of nitinol biliary stent by femtosecond laser with Type 5 path is shown in Fig. 25.8. The track of the laser beam can readily be observed in Fig. 25.8A using SEM. The surface morphology of the stent is still clean with no recast layer, and minimal HAZ is observed. The side view of the stent with Type 5 path is shown in Fig. 25.8B. As an aside, Fig. 25.8 indicates that the dimension precision of nitinol biliary stents can be significantly increased, with the structures becoming stronger and the manufacturing procedure shortened by the femtosecond laser as well [65].

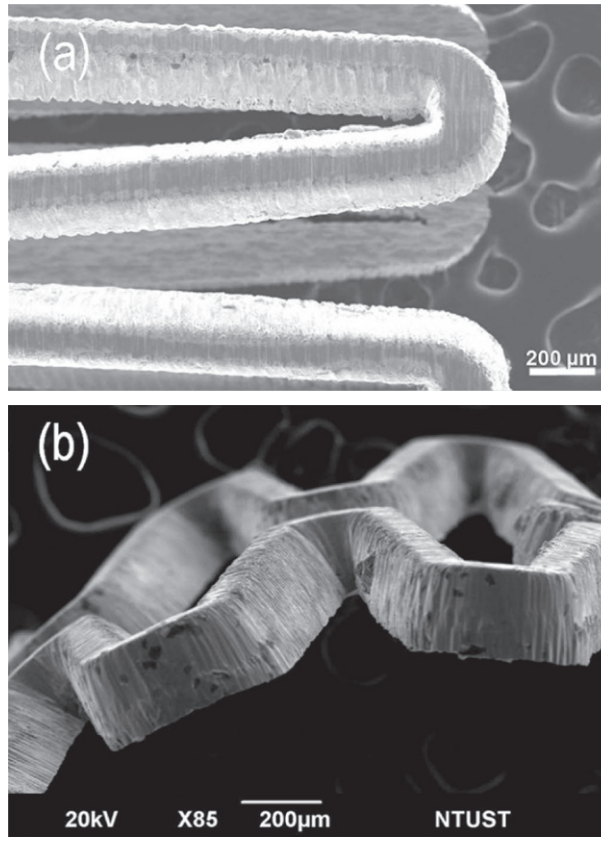


Fig. 25.8 SEM images of Nitinol biliary stent with Type 5 path: (A) top view (B) side view [65].

25.5 MECHANICAL CHARACTERISTICS AND LASER-INDUCED THERMAL EFFECTS

In the laser machining process, typically the laser beam is scanned over the target area creating the desired localized heating. During the laser-matter interaction, a very small layer of molten material is formed. The vapor plumes, formed by material vaporization, exercise an overpressure on the molten material. This results in the movement of the molten material toward the impact's edges. Fig. 25.9 demonstrates a schematic of laser processing by a fiber laser, which leads to melting a layer on the base material. The penetration depth in the melting region is schematically illustrated. One of the complications associated with laser processing is the creation of HAZs, which contain several types of undesirable effects such as distortion, surface cracking, embrittlement, decrease in weldability, and decrease in materials strength and corrosion resistance as well as reduced fatigue life. Sometimes the material properties in HAZs can be altered from the parent material, such as the creation of a resolidified material on the surface of the work material. In the subsequent sections we will discuss these issues in more detail.

25.5.1 Heat-Affected Zone

One of the difficulties in laser processing is the removal of the HAZs, such as resolidified material formed on the surface of the work material. The cooling rate in the resolidification zone significantly affects the microstructure of materials across the cross-section generated by the laser process. The laser parameters, including power and scanning speed, determine the

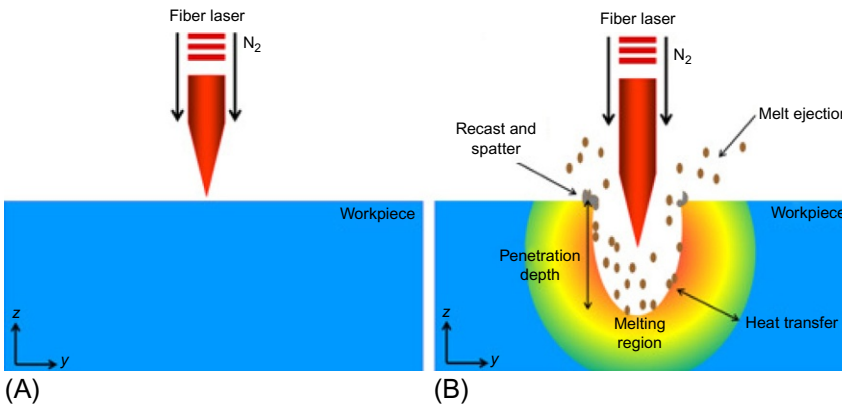


Fig. 25.9 The schematic of physical process in laser micromachining and drilling process with a static beam, (A) initial arrangement (B) after partial penetration [72].

microstructure of the materials after laser processing; it can be generally obtained from the adequate time-temperature transformation (TTT) diagrams [73]. In addition to resolidification and phase transformations, diffusion also plays an important role in defining the final metallurgical properties of laser-processed materials. The metallurgy of laser treated/machined material is highly dependent on local diffusion processes that in turn are driven by thermal and chemical gradients [73]. The function loss due to the HAZ can be minimized if a processing technique is designed to minimize the thickness of the HAZ, and the recast layers are removed after the process through various post-processing techniques. Ongoing studies have been carried out on various materials to reduce the HAZ with ultrafast lasers, such as femtosecond and picosecond lasers [74–76].

Thermal effects at the surface of the cutting kerf can lead to the alteration of the microstructure and/or mechanical properties of the laser-processed materials. It results in the formation of a distinct HAZ at the surface of the cutting edge that can be revealed by appropriate polishing and etching techniques. Hence, laser cutting parameters, such as laser power and scan speed, should be carefully chosen to minimize the heat-affected areas. Fig. 25.10 shows a typical HAZ in an Incoloy 800 HT superalloy sheet formed during laser cutting. Generally, the HAZ can be minimized by increasing the speed of the laser cutting process since higher cutting speeds reduce the heat transfer to the material [32,34,77,78].

The quality of the machining cannot be easily predicted due to the dynamic nature of the laser machining process. The cutting of ferrous alloys is an example illustrating the unpredictability of the laser cut quality. The

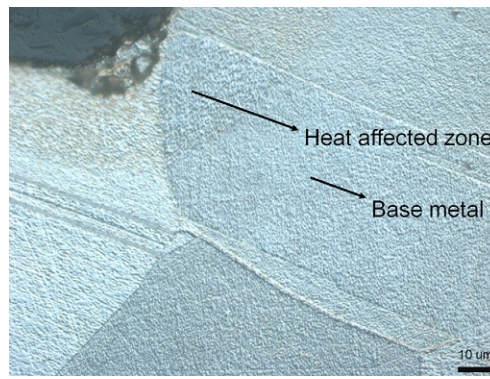


Fig. 25.10 Differential Interference Contrast micrograph showing the microstructural changes of a laser machined Incoloy 800 HT superalloy etched with marbles [34].

oxidation reactions with iron and other elements in the alloy add another source of heat, in addition to the laser beam itself, that causes the material removal to occur on two moving and often interacting fronts, the oxidation front and the laser beam front [52]. Striation (periodic lines appearing on the cut surface) affects the surface roughness, appearance, and geometrical precision of the products cut by laser and is an important quality factor in evaluating the laser cutting outcome [79]. Kerf width, surface roughness, and the size of the HAZ are often used to quantify laser cut quality. Fig. 25.11 illustrates the influence of the machining speed on the HAZ of XC42-steel sample. Fig. 25.11 shows that the heat-affected region decreased considerably with increasing the scan speed when the laser power remained constant ($P = 1000$W) [52].

Traditional laser manufacturing processes employ nanosecond and picosecond pulsed lasers to machine intricate designs of nitinol (NiTi) based cylindrical slugs. The significant drawback of the nanosecond and picosecond lasers is that they impart a significant amount of heat to the stent during machining. This leads to the creation of heat-affected areas including slag and recast, which should be removed with costly, labor-intensive post-processing steps such as electropolishing. Furthermore, these clean-up steps often involve the use of hazardous chemicals [63]. The fine features common in implantable and *ex vivo* medical devices require a manufacturing tool that can precisely machine micron-scale features without introducing significant heat to the rest of the workpiece. HAZs compromise device integrity, cause lower yields, and increase costly post-processing steps. Continuous wave lasers ablate through a thermodynamic process: localized heating of the target

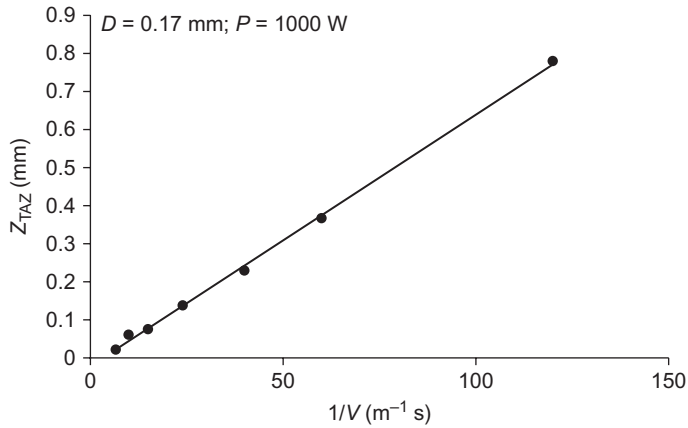


Fig. 25.11 Influence of machining speed on the HAZ [52].

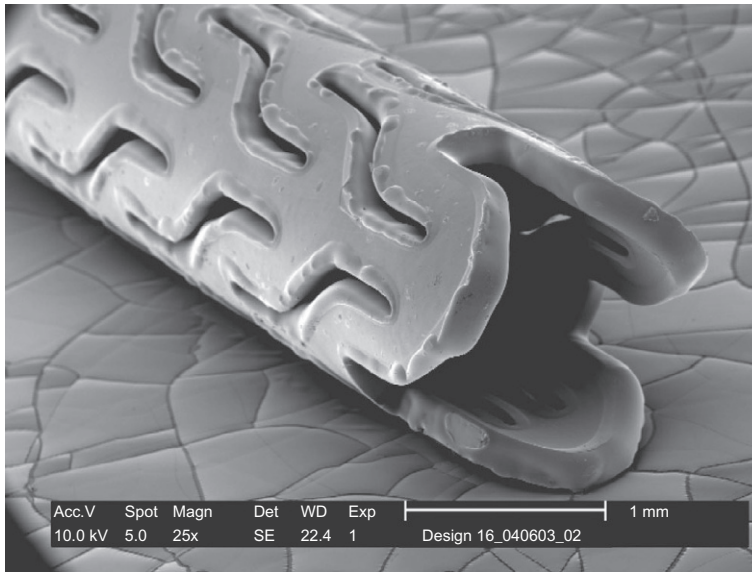
lattice followed by phase change or combustion [63]. The minimization of thermal effects is also a significant consideration in the laser processing of polymers and other temperature-sensitive materials. SEM images of stents micromachined by using a continuous-wave laser and a femtosecond laser are shown in Fig. 25.12A and B, respectively. Fig. 25.12A shows a stent machined by using a continuous-wave CO_2 laser in which indiscrete edges, melting, and other thermal effects suggestive of large HAZs are observed. When the stent is placed in the arteries, the melted features, burrs, cracks, and other defects induced during the laser micromachining may lead to the failure of the device due to the complicated cyclic fatigue loading [81]. Fig. 25.12B shows a stent with smooth and fine edges machined by using a femtosecond laser. It has been shown that materials processed using ultrashort pulse lasers show fewer thermal effects; for example, an absence of burrs was noted in microscale features processed using a femtosecond laser [61,80,82–84].

25.5.2 Hardness and Flexural Strength

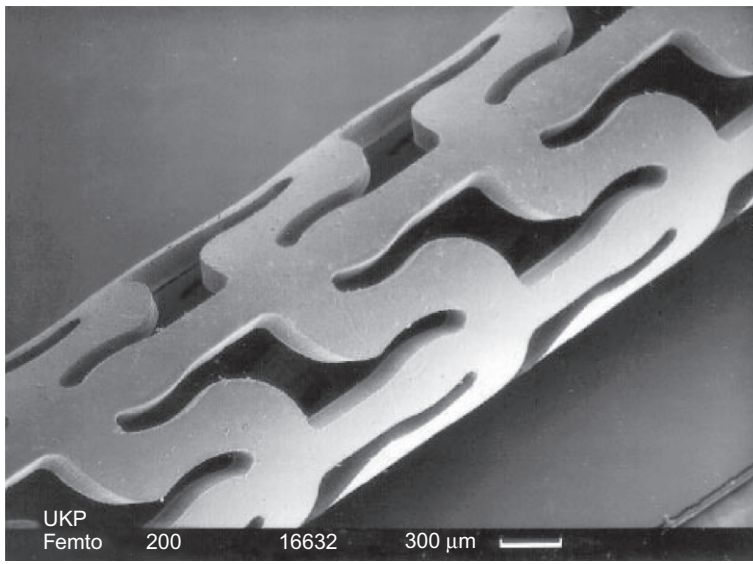
Studies of the mechanical properties of laser-machined materials have shown that the strength of such materials, characterized by the hardness and flexural strength, is affected by the thermal-affected zones and crack formation [85,86]. For example, it has been shown that the mean values of flexural strength of some laser-machined ceramics can be reduced to ~40% of that prior to laser machining [87]. Laser micromachining of silicon wafers has shown that the breaking limit after laser cutting will be reduced [88]. It has also been shown that the hardness of a titanium alloy sheet in HAZs is increased by ~10% after laser cutting [89].

The surface hardness is generally affected in some alloys subjected to laser treatment. For instance, surface microhardness of Nd:YAG laser-treated AISI 316LVM stainless steel was found to increase in the annealed wires, while the surface microhardness of Nd:YAG laser-treated hard wires decreased [48]. Since the laser primarily affects the surface properties of the materials, it does not measurably affect the smooth tension data or the tensile fracture surfaces, due to the relatively small affected cross-section. It is reported that the increased surface hardness of the laser-treated annealed stainless steel delays the crack initiation period, increasing a fatigue life in both low cycle fatigue (LCF) and high cycle fatigue (HCF) regimes [48].

Since the generation of a HAZ in laser micromachining is similar to the HAZ caused by other processes, such as laser welding, it is beneficial to point out some of the observations in hardness variation during



(A)



(B)

Fig. 25.12 (A) Poly(L-lactide) stent machined using a continuous-wave CO_2 laser. (B) Poly(L-lactide) stent machined using a femtosecond laser [61,80].

laser welding where the laser heat has altered the hardness of materials. Fig. 25.13 represents the hardness values of the cross-section of the welded steel CPW 800 sheets with a 2.5-mm thickness (150×300 mm). The hardness measurements are performed on the cross-section of the

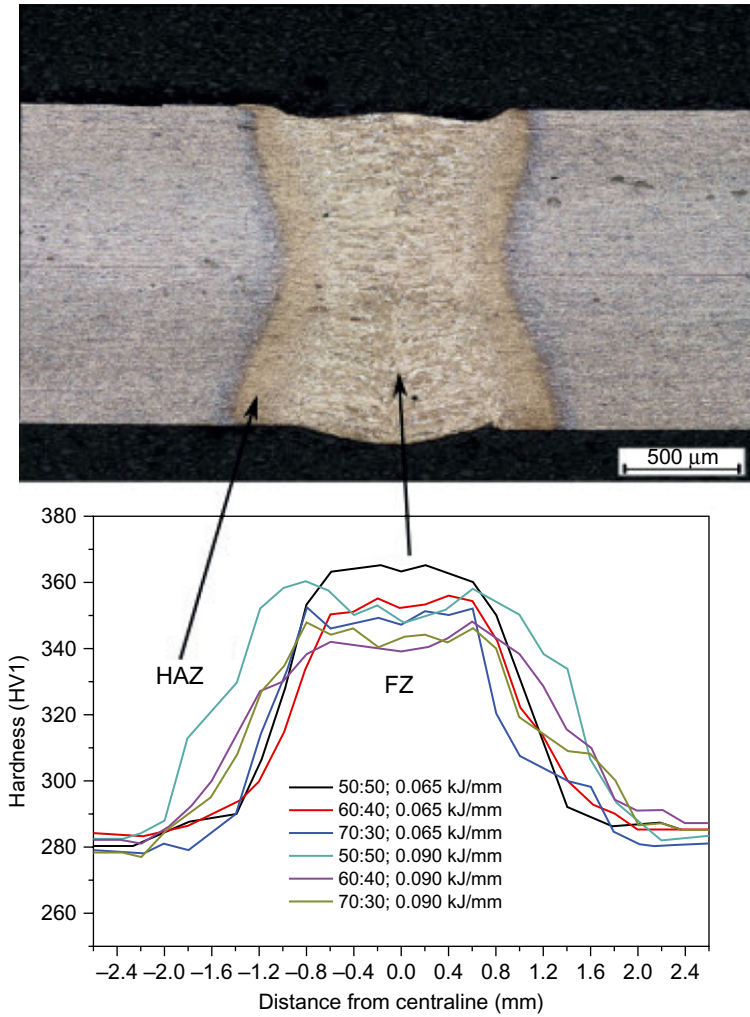


Fig. 25.13 Results of hardness measurements for various welding parameters [90].

weld in order to determine the quality of the welded joints. The highest hardness (i.e., 365 HV1) was found in the joint welded with a linear energy of 0.065 kJ/mm and a beam power distribution of 50:50. The lowest hardness (i.e., 340 HV1) was observed in the joint welded using a linear energy of 0.09 kJ/mm and a beam power distribution of 60:40. Increasing the linear energy of the weld decreased the hardness in relation to the same beam power distribution but with lower welding energy. It was concluded that the power distribution between the first and second beam affected the hardness of the welded joint [90–93].

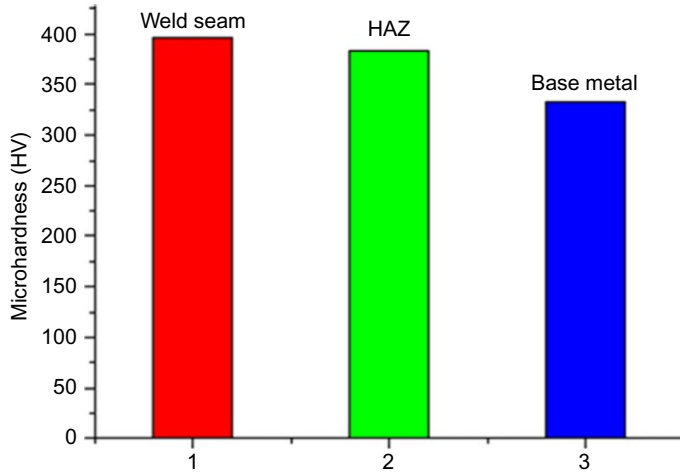


Fig. 25.14 Microhardness distribution from the welded seam to the base metal [94].

Fig. 25.14 shows the microhardness distribution of the transverse of a welded seam. It is shown that the highest hardness was found in the welded seam, at about an average of HV397. HV384 was the hardness of HAZ, and then sharply transitioned into the base metal, at a hardness of about HV333 [94].

25.5.3 Fatigue

Fatigue of materials, which is progressive and localized structural damage, refers to the gradual weakening of a material as a result of frequent loading and unloading [95]. In materials subjected to cyclic loading, when the loads are above a certain threshold, microscopic cracks begin to form at the stress concentrators. As a crack reaches a critical size, it will suddenly propagate and may cause catastrophic failure. Fatigue life is defined as the number of specified stress cycles that a specimen can tolerate before failure of a specified nature occurs.

As mentioned before, thermal damage and crack formation affect the strength of the machined components [89]. Surface roughness induced during laser machining with high power settings and/or lasers with longer pulse width (i.e., ns) results in more surface imperfections and consequently considerable loss in fatigue life. Conversely, low-energy finishing conditions with a low power setting and/or lasers with a shorter pulse width (i.e., fs and ps) introduce fewer damages to the laser-machined components. Fatigue specimens machined at different energies exhibit similar fatigue

failure mechanisms, which begin by initiating fatigue cracks at multiple locations within the surface defects in the recast layer or the HAZs [34,96]. It has been shown that under pull-push loading with a stress ratio of −1 and alternating stress with a magnitude of 0.6 UTS in the tool steel, fatigue cracks typically propagate into only a very small portion of the fracture surface before the overload fracture occurs due to fracture of the primary carbides and ductile microvoid fracture of the remaining matrix [96].

An example of fatigue studies of laser-machined wires is presented in the following where the fracture surfaces of the laser-treated 316LVM display several types of fracture surface features, depending on the number of cycles to failure (Nf). Fig. 25.15 is the SEM image of a 316LVM annealed wire machined with a femtosecond laser, fractured in flex bending fatigue after 4819 cycles. Fatigue fracture initiation is evident at the top and bottom of Fig. 25.15A. Fig. 25.15B shows a higher magnification view of fatigue striation-like features [34].

It should be mentioned that most machined materials entail stress-raising notches and other stress concentrators, such as persistent slip bands and grain interfaces that increase the nominal stress from cyclic loading. The specification and geometry of critical crack length is an important factor in controlling the fatigue behavior of the laser-machined materials where the

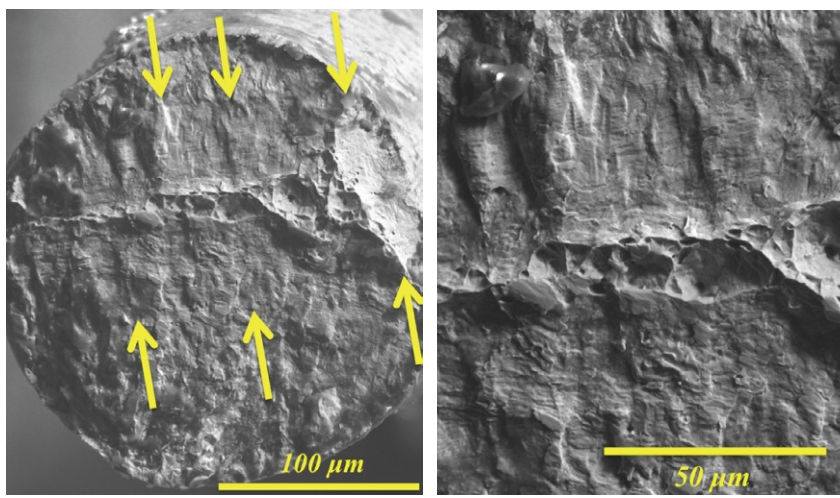


Fig. 25.15 (A) SEM image of 316LVM annealed machined with femtosecond laser, fractured in flex bending fatigue after 4819 cycles. Crack growth direction is top-to-bottom and bottom-to-top. (B) Higher magnification of (A) [34].

fatigue life is strongly dependent on the surface characteristics of a material. Sustained efforts have been made to derive fatigue computation methods applicable to different engineering applications [97,98].

25.5.4 Cracks

The laser-ablated materials are often removed from the workpiece by vaporization and/or melt ejection mechanisms during laser machining [99]. However, the melted part that is not removed from the workpiece is resolidified and forms a recast layer on the side walls and at the bottom of the cavity. The recast layer is usually brittle and acts as a nucleation site for cracking [89,99–102]. Process optimization and modeling studies are needed to reduce the recast layers produced during laser machining. Furthermore, cracks can be formed during laser processing due to other phenomena, such as phase transformation within the recast layer. If the laser causes the crystalline phase transformation, it can cause distortion as there is a mismatch in thermal properties of the resolidified layer (i.e., recast layer) and the parent materials. For example, in the recast layers of stainless steel, the microstructure is composed of a columnar structure of austenitic dendrites with minor phase of delta-ferrite in the interdendritic regions, grown epitaxial from the base material. The formation of such microstructural changes is due to rapid solidification as illustrated in Fig. 25.16 [99,103]. Energy-dispersive x-ray spectroscopy results showed that the most oxide layer found on the surface layer was produced when using oxygen as the assist gas, followed by that using argon and nitrogen [104].

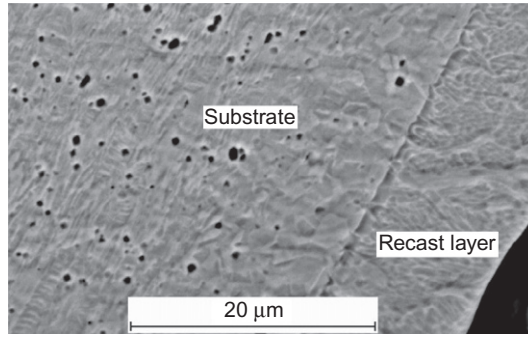


Fig. 25.16 Typical cross-section SEM image of laser-drilled type 305 stainless steel sheet showing the microstructure of the substrate and the recast layer when O_2 is used as the assist gas [99].

When the laser-machined components are designed to work in a liquid environment, it is important to make sure that the chemical and electrochemical corrosion properties of such components are appropriate based on the working environmental conditions.

Fig. 25.17 shows a cross-sectional SEM of a piece of laser-machined 316LVM by an Nd:YAG laser with nanosecond pulse and high power, which can cause multiple cracks within the recast layer. If such a piece is subjected to fatigue testing, these cracks can initiate the failure. Under scanning electron microscope inspection, the regions affected by laser micromachining revealed deep craters, higher surface roughness resulting from the melting, and solidification during the laser melting and cooling process. SEM exams of the surface affected by the laser show the presence of cracks, typical of thermally induced cracking within a recast layer as can be seen in Fig. 25.17. Microcracks are initiated at the surface of the recast layer and propagated toward the substrate. Fatigue cracks propagate into the brittle recast layer rapidly, but crack growth slows down once it gets to the tougher

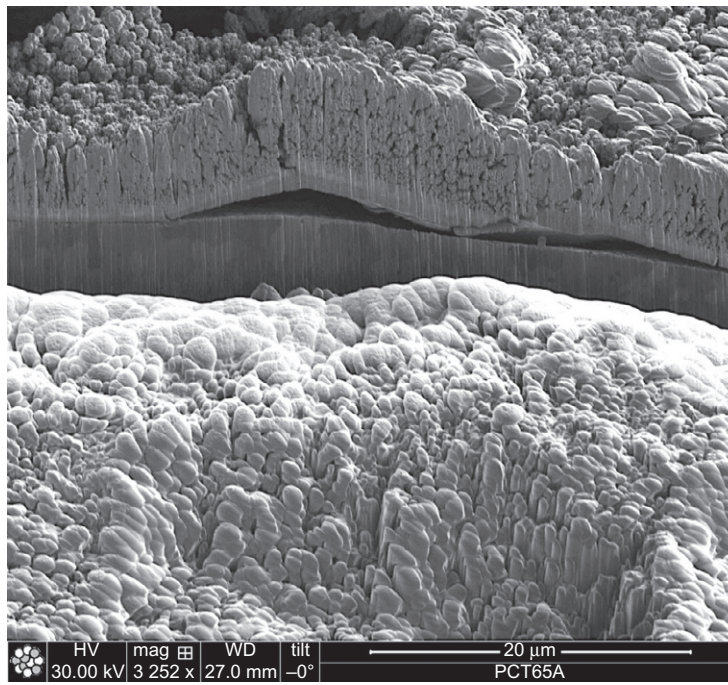


Fig. 25.17 Cross-section SEM micrograph of the laser-machined 316LVM by Nd:YAG laser. Grains of several micrometers (2.23 µm ± 0.34 µm) are observed by ion-induced secondary electron imaging [34].

parent alloy. Once sufficient cracks approach and get to the critical length, rapid fracture occurs in the remaining cross-section [48,96].

Crack formation can be minimized by using lasers with a shorter pulse width. Compared with nanosecond and continuous wave lasers, picosecond and femtosecond laser-machined materials suffer from fewer thermal effects, such as microcrack formation. An example of a hole-array and a pin-array machined on Ti-6Al-4V material by using the ps Lumera laser (RAPID) at 100 kHz, is demonstrated in Fig. 25.18. The microholes made through both percussion and trepanning drillings showed good circularity and sharp edge. No thermal damaged zones, resolidification layers, or microcracks were found on the drilled holes. The relative orientation between the holes/pins was in agreement with the design. Also, no microcracks or recast layers were observed on the sidewalls of the machined structure [21,105].

25.6 SUMMARY

Laser micromachining plays a key role in the manufacturing of small devices, which is especially important for medical device and implant applications such as cardiovascular stents, guide wires, and needles. Laser micromachining has been extensively researched and developed to overcome the challenges in manufacturing where the traditional machining does not work due to its limitations. One of the principle advantages of laser micromachining is its great potential to provide localized material effect for the manufacturing of miniature devices. However, the thermal effect of the laser machining process may reduce surface quality and accordingly the fatigue strength due to the generated HAZ, which deteriorates the

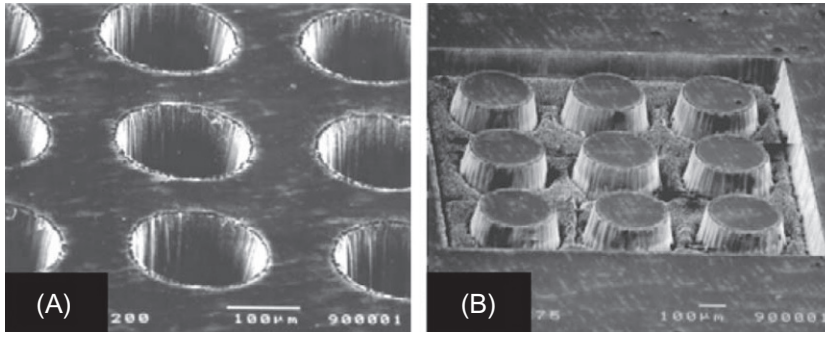


Fig. 25.18 (A) Array of holes with 175 μm diameter and 75 μm depth. (B) Array of pins with 250 μm diameter and 100 μm height [21].

performance of micromachined components. Applying various laser micromachining methods utilizing optimal parameters for each material can effectively control such barriers.

REFERENCES

[1] M.J. Madou, Fundamentals of Microfabrication and Nanotechnology, vol. II, CRC Press, Boca Raton, FL, 2011.
[2] S.Z. Chavoshi, X. Luo, Hybrid micro-machining processes: a review, Precis. Eng. 41 (2015) 1–23.
[3] M. Mehrpouya, H. Bidsorkhi, MEMS applications of NiTi based shape memory alloys: a review, Micro Nanosyst. 1 (8) (2016) 1–14.
[4] X. Luo, K. Cheng, D. Webb, F. Wardle, Design of ultraprecision machine tools with applications to manufacture of miniature and micro components, J. Mater. Process. Technol. 167 (2–3) (2005) 515–528.
[5] H. Lavvafi, J. Lewandowski, J. Lewandowski, Flex bending fatigue testing of wires, foils, and ribbons, Mater. Sci. Eng. A 601 (2014) 123–130.
[6] N. Muhammad, D. Whitehead, A. Boor, L. Li, Comparison of dry and wet fibre laser profile cutting of thin 316L stainless steel tubes for medical device applications, J. Mater. Process. Technol. 210 (15) (2010) 2261–2267.
[7] A.N. Samant, N.B. Dahotre, Laser machining of structural ceramics—a review, J. Eur. Ceram. Soc. 29 (6) (2009) 969–993.
[8] J.F. Ready, D.F. Farson, T. Feeley, LIA Handbook of Laser Materials Processing, Springer-Verlag, Berlin; Heidelberg, 2001.
[9] R.D. Schaeffer, Fundamentals of Laser Micromachining, CRC Press, Boca Raton, FL, 2012.
[10] J. Lawrence, J. Pou, D.K.Y. Low, E. Toyserkani, Advances in Laser Materials Processing: Technology, Research and Applications, Woodhead Publishing Limited, Cornwall, UK, 2010.
[11] J. Perriere, E. Millon, E. Fogarassy, Recent Advances in Laser Processing of Materials, Elsevier Ltd, Oxford, UK, 2006.
[12] D. Bäuerle, Laser Processing and Chemistry, Springer-Verlag, Berlin; Heidelberg, 2011.
[13] W.M. Steen, J. Mazumder, Laser Material Processing, Springer-Verlag, London, 2010.
[14] J. Krüger, W. Kautek, The femtosecond pulse laser: a new tool for micromachining, Laser Phys. 9 (1) (1999) 30–40.
[15] J. Ion, Laser Processing of Engineering Materials: Principles, Procedure and Industrial Application, Butterworth-Heinemann, Oxford, UK, 2005.
[16] P. Schaaf, Laser Processing of Materials: Fundamentals, Applications and Developments, Springer-Verlag, Berlin; Heidelberg, 2010.
[17] J. Dutta Majumdar, I. Manna, Laser material processing, Int. Mater. Rev. 56 (5-6) (2011) 341–388.
[18] T. Häfner, J. Heberle, M. Dobler, M. Schmidt, Influences on incubation in ps laser micromachining of steel alloys, J. Laser Appl. 28 (2) (2016) 022605.
[19] M. Olbrich, E. Punzel, P. Lickschat, S. Weißmantel, A. Horn, Investigation on the ablation of thin metal films with femtosecond to picosecond-pulsed laser radiation, Phys. Procedia 83 (2016) 93–103.
[20] K.C. Phillips, H.H. Gandhi, E. Mazur, S. Sundaram, Ultrafast laser processing of materials: a review, Adv. Opt. Photon. 7 (4) (2015) 684–712.
[21] W. Hu, Y.C. Shin, G.B. King, Micromachining of metals, alloys, and ceramics by picosecond laser ablation, J. Manuf. Sci. Eng. 132 (1) (2010) 011009.

[22] D.S. Correa, J.M. Almeida, G.F. Almeida, M.R. Cardoso, L. De Boni, C.R. Mendonça, Ultrafast laser pulses for structuring materials at micro/nano scale: from waveguides to superhydrophobic surfaces, Photonics 4 (1) (2017) 8.
[23] H. Lavvafi, D. Dudzinski, M. Young, J. Gbur, J.R. Lewandowski, J.J. Lewandowski, Parametric studies on femtosecond laser cutting of Ni-Ti shape memory alloy, in: Proc. MS&T 2012 Next Generation Biomaterials Symposium, 2012.
[24] A. Kuar, B. Doloi, B. Bhattacharyya, Modelling and analysis of pulsed Nd:YAG laser machining characteristics during micro-drilling of zirconia (ZrO 2), Int. J. Mach. Tools Manuf. 46 (12–13) (2006) 1301–1310.
[25] E. Chryssolouris, Laser Machining: Theory and Practice, Springer-Verlag, New York, NY, 1991.
[26] A.K. Dubey, V. Yadava, Experimental study of Nd:YAG laser beam machining—an overview, J. Mater. Process. Technol. 195 (1–3) (2008) 15–26.
[27] A. Riveiro, F. Quintero, F. Lusquiños, R. Comesaña, J. Pou, Influence of assist gas nature on the surfaces obtained by laser cutting of Al–Cu alloys, Surf. Coat. Technol. 205 (7) (2010) 1878–1885.
[28] A. Gisario, M. Mehrpouya, S. Venettacci, A. Mohammadzadeh, M. Barletta, LaserOrigami (LO) of three-dimensional (3D) components: experimental analysis and numerical modelling, J. Manuf. Process. 23 (2016) 242–248.
[29] A. Gisario, M. Mehrpouya, S. Venettacci, M. Barletta, Laser-assisted bending of Titanium Grade-2 sheets: experimental analysis and numerical simulation, Opt. Lasers Eng. 92 (2017) 110–119.
[30] A. Sharma, V. Yadava, Optimization of cut quality characteristics during Nd:YAG laser straight cutting of Ni-based superalloy thin sheet using grey relational analysis with entropy measurement, Mater. Manuf. Process. 26 (12) (2011) 1522–1529.
[31] A. Sharma, V. Yadava, Modelling and optimization of cut quality during pulsed Nd:YAG laser cutting of thin Al-alloy sheet for straight profile, Opt. Lasers Technol. 44 (1) (2012) 159–168.
[32] A. Sharma, V. Yadava, R. Rao, Optimization of kerf quality characteristics during Nd:YAG laser cutting of nickel based superalloy sheet for straight and curved cut profiles, Opt. Lasers Eng. 48 (9) (2010) 915–925.
[33] D.K. Das, T.M. Pollock, Femtosecond laser machining of cooling holes in thermal barrier coated CMSX4 superalloy, J. Mater. Process. Technol. 209 (15–16) (2009) 5661–5668.
[34] H. Lavvafi, Effects of laser machining on structure and fatigue of 316LVM biomedical wires, Ph.D. dissertation, Case Western Reserve University, 2013.
[35] S. Mishra, V. Yadava, Laser beam micromachining (LBMM)—a review, Opt. Lasers Eng. 73 (2015) 89–122.
[36] A. Pramanik, Developments in the non-traditional machining of particle reinforced metal matrix composites, Int. J. Mach. Tools Manuf. 86 (2014) 44–61.
[37] H. Booth, Recent applications of pulsed lasers in advanced materials processing, Thin Solid Films 453–454 (2004) 450–457.
[38] S. Zoppel, M. Farsari, R. Merz, J. Zehetner, G. Stangl, G.A. Reider, C. Fotakis, Laser micro machining of 3C–SiC single crystals, Microelectron. Eng. 83 (4–9) (2006) 1400–1402.
[39] M. Mehrpouya, S. Emamian, Recent advantages in laser fabrication of micro-channel heat exchangers, Mater. Werkst. 48 (2017) 205–209.
[40] J.C. Finlay, A. Darafsheh, Light sources, drugs, and dosimetry, in: B. Wong, J. Ilgner (Eds.), Biomedical Optics in Otorhinolaryngology: Head and Neck Surgery, Springer, New York, NY, 2016, pp. 311–336 (Chapter 19).
[41] B.E.A. Saleh, M.C. Teich, Fundamentals of Photonics, second ed., John Wiley & Sons, Hoboken, NJ, 2007.

[42] A.K. Dubey, V. Yadava, Multi-objective optimization of Nd: YAG laser cutting of nickel-based superalloy sheet using orthogonal array with principal component analysis, Opt. Lasers Eng. 46 (2) (2008) 124–132.
[43] J.D. Majumdar, I. Manna, Laser processing of materials, Sadhana 28 (3-4) (2003) 495–562.
[44] R. Rao, V. Yadava, Multi-objective optimization of Nd: YAG laser cutting of thin superalloy sheet using grey relational analysis with entropy measurement, Opt. Lasers Technol. 41 (8) (2009) 922–930.
[45] A.K. Dubey, V. Yadava, Optimization of kerf quality during pulsed laser cutting of aluminium alloy sheet, J. Mater. Process. Technol. 204 (1–3) (2008) 412–418.
[46] A.K. Pandey, A.K. Dubey, Simultaneous optimization of multiple quality characteristics in laser cutting of titanium alloy sheet, Opt. Lasers Technol. 44 (6) (2012) 1858–1865.
[47] C. Wang, X. Zeng, Study of laser carving three-dimensional structures on ceramics: quality controlling and mechanisms, Opt. Lasers Technol. 39 (7) (2007) 1400–1405.
[48] H. Lavvafi, M.E. Lewandowski, D. Schwam, J.J. Lewandowski, Effects of surface laser treatments on microstructure, tension, and fatigue behavior of AISI 316LVM biomedical wires, Mater. Sci. Eng. A 688 (14) (2017) 101–113.
[49] S. Gräf, G. Staupendahl, A. Krämer, F.A. Müller, High precision materials processing using a novel Q-switched CO_2 laser, Opt. Lasers Eng. 66 (2015) 152–157.
[50] A. Riveiro, F. Quintero, F. Lusquinos, R. Comesana, J. Pou, Parametric investigation of CO_2 laser cutting of 2024-T3 alloy, J. Mater. Process. Technol. 210 (9) (2010) 1138–1152.
[51] D. Basting, Excimer Laser Technology, Springer, Berlin, Heidelberg, 2005.
[52] N. Jebbari, M.M. Jebari, F. Saadallah, A. Tarrats-Saugnac, R. Bennaceur, J.P. Longuemard, Thermal affected zone obtained in machining steel XC42 by high-power continuous CO_2 laser, Opt. Lasers Technol. 40 (6) (2008) 864–873.
[53] R. Osellame, G. Cerullo, R. Ramponi, Femtosecond Laser Micromachining: Photonic and Microfluidic Devices in Transparent Materials, Springer, Berlin, Heidelberg, 2012.
[54] R. Mayerhofer, D. Mairhoermann, M. Mueller, Fiber lasers boost medical device production, Industr. Laser Solut. Manuf. 27 (3) (2012) 20.
[55] L. Cerami, E. Mazur, S. Nolte, C.B. Schaffer, Femtosecond laser micromachining, in: R. Thomson, C. Leburn, D. Reid (Eds.), Ultrafast Nonlinear Optics, Springer International Publishing, Cham, Switzerland, 2013, pp. 287–321.
[56] Q. Bian, X. Yu, B. Zhao, Z. Chang, S. Lei, Femtosecond laser ablation of indium tin-oxide narrow grooves for thin film solar cells, Opt. Lasers Technol. 45 (2013) 395–401.
[57] P. Bado, W. Clark, A. Said, Micromachining Handbook, Clark-MXR, Inc., Ann Arbor, MI, 2001.
[58] R.R. Gattass, E. Mazur, Femtosecond laser micromachining in transparent materials, Nat. Photonics 2 (4) (2008) 219–225.
[59] K.-H. Leitz, B. Redlingshöfer, Y. Reg, A. Otto, M. Schmidt, Metal ablation with short and ultrashort laser pulses, Phys. Procedia 12 (2011) 230–238.
[60] R. Viskup, High Energy and Short Pulse Lasers, InTech, Rijeka, Croatia, 2016.
[61] F. Korte, S. Nolte, B. Chichkov, T. Bauer, G. Kamlage, T. Wagner, C. Fallnich, H. Welling, Far-field and near-field material processing with. femtosecond laser pulses, Appl. Phys. A 69 (1) (1999) S7–S11.
[62] G.N. Makarov, Laser applications in nanotechnology: nanofabrication using laser ablation and laser nanolithography, Physics-Uspekhi 56 (7) (2013) 643–682.
[63] A.C. Tanous, Laser cutting takes the heat out of stent manufacturing, Industr. Laser Solut. Manuf. 25 (1) (2010) 20.
[64] M. Mielke, D. Gaudiosi, K. Kim, M. Greenberg, X. Gu, R. Cline, X. Peng, M. Slovick, N. Allen, M. Manning, M. Ferrel, N. Prachayaamorn, S. Sapers, Ultrafast fiber laser platform for advanced materials processing, J. Laser Micro/Nanoeng. 5 (1) (2010) 53–58.

[65] C.-H. Hung, F.-Y. Chang, Curve micromachining on the edges of nitinol biliary stent by ultrashort pulses laser, Opt. Lasers Technol. 90 (2017) 1–6.
[66] C.-H. Hung, F.-Y. Chang, T.-L. Chang, Y.-T. Chang, K.-W. Huang, P.-C. Liang, Micromachining NiTi tubes for use in medical devices by using a femtosecond laser, Opt. Lasers Eng. 66 (2015) 34–40.
[67] A. Darafsheh, Optical super-resolution and periodical focusing effects by dielectric microspheres, . Ph.D. dissertation, University of North Carolina at Charlotte, 2013.
[68] A. Darafsheh, Comment on 'Super-resolution microscopy by movable thin-films with embedded microspheres: Resolution analysis' [Ann. Phys. (Berlin) 527, 513 (2015)], Ann. Phys. (Berlin) 528 (11–12) (2016) 898–900.
[69] A. Darafsheh, C. Guardiola, A. Palovcak, J.C. Finlay, A. Cárabe, Optical super-resolution imaging by high-index microspheres embedded in elastomers, Opt. Lett. 40 (1) (2015) 5–8.
[70] A. Darafsheh, Influence of the background medium on imaging performance of microsphere-assisted super-resolution microscopy, Opt. Lett. 42 (4) (2017) 735–738.
[71] D. Araujo, F. Carpio, D. Mendez, A. Garcıa, M. Villar, R. Garcıa, D. Jimenez, L. Rubio, Microstructural study of CO_2 laser machined heat affected zone of 2024 aluminum alloy, Appl. Surf. Sci. 208–209 (2003) 210–217.
[72] N. Muhammad, B.D. Rogers, L. Li, Understanding the behaviour of pulsed laser dry and wet micromachining processes by multi-phase smoothed particle hydrodynamics (SPH) modelling, J. Phys. D. Appl. Phys. 46 (9) (2013) 095101.
[73] J. Dowden, The theory of laser materials processing: heat and mass transfer in modern technology, Springer, Dordrecht, The Netherlands, 2009.
[74] T. Kurita, T. Yamane, K. Ashida, S. Sasaki, Proposal for small heat-affected zone, high aspect ratio processing for metal, J. Mater. Process. Technol. 242 (2017) 228–234.
[75] T. Kurita, K. Komatsuzaki, M. Hattori, Advanced material processing with nano-and femto-second pulsed laser, Int. J. Mach. Tools Manuf. 48 (2) (2008) 220–227.
[76] D. Liu, J. Cheng, W. Perrie, A. Baum, P. Scully, M. Sharp, S. Edwardson, Z. Kuang, N. Semaltianos, P. French, G. Dearden, L. Li, K.G. Watkins, Femtosecond laser microstructuring of materials in the NIR and UV regime, in: Proc. 26th International Congress on Applications of Lasers and Electro-Optics (ICALEO'07), 2007, pp. 12–18.
[77] N.B. Dahotre, S. Harimkar, Laser fabrication and machining of materials, Springer, New York, NY, 2008.
[78] A. Grajcar, M. Różański, S. Stano, A. Kowalski, Microstructure characterization of laser-welded Nb-microalloyed silicon-aluminum TRIP steel, J. Mater. Eng. Perform. 23 (9) (2014) 3400–3406.
[79] L. Li, M. Sobih, P. Crouse, Striation-free laser cutting of mild steel sheets, CIRP Ann. Manuf. Technol. 56 (1) (2007) 193–196.
[80] N. Grabow, M. Schlun, K. Sternberg, N. Hakansson, S. Kramer, K.-P. Schmitz, Mechanical properties of laser cut poly (L-lactide) micro-specimens: implications for stent design, manufacture, and sterilization, J. Biomech. Eng. 127 (1) (2005) 25–31.
[81] P.R. Miller, R. Aggarwal, A. Doraiswamy, Y.J. Lin, Y.-S. Lee, R.J. Narayan, Laser micromachining for biomedical applications, JOM J. Miner. Met. Mater. Soc. 61 (9) (2009) 35–40.
[82] S.D. Gittard, R.J. Narayan, Laser direct writing of micro-and nano-scale medical devices, Expert Rev. Med. Devices 7 (3) (2010) 343–356.
[83] K. Sugioka, Y. Cheng, Ultrafast lasers—reliable tools for advanced materials processing, Light Sci. Appl. 3 (4) (2014) e149.
[84] C. Momma, U. Knop, S. Nolte, Laser cutting of slotted tube coronary stents, state of the art and future developments, Prog. Biomed. Res. 4 (1) (1999) 39–44.
[85] N. Muhammad, L. Li, Underwater femtosecond laser micromachining of thin nitinol tubes for medical coronary stent manufacture, Appl. Phys. A 107 (4) (2012) 849–861.

[86] M.F. Teixeira, V.A.V. Schmachtenberg, G. Tontini, G.D.L. Semione, W.L. Weingaertner, V. Drago, Laser composite surfacing of A681 steel with WC + Cr + Co for improved wear resistance, J. Mater. Res. Technol. 6 (1) (2017) 33–39.
[87] J. Zhang, T. Lee, X. Ai, W. Lau, Investigation of the surface integrity of laser-cut ceramic, J. Mater. Process. Technol. 57 (3-4) (1996) 304–310.
[88] S. Dauer, A. Ehlert, S. Büttgenbach, Rapid prototyping of micromechanical devices using a Q-switched Nd:YAG laser with optional frequency doubling, Sensors Actuators A Phys. 76 (1–3) (1999) 381–385.
[89] A.K. Dubey, V. Yadava, Laser beam machining—a review, Int. J. Mach. Tools Manuf. 48 (6) (2008) 609–628.
[90] M. Różański, M. Morawiec, A. Grajcar, S. Stano, Modified twin-spot laser welding of complex phase steel, Arch. Metall. Mater. 61 (4) (2016) 1999–2008.
[91] S. Stano, A. Grajcar, Z. Wilk, M. Różański, P. Matter, M. Morawiec, Microstructural aspects of twin-spot laser welding of dp-Hsla steel sheet joints, Arch. Metall. Mater. 61 (2) (2016) 731–740.
[92] Z. Xue, S. Hu, J. Shen, D. Zuo, E. Kannatey-Asibu Jr., Microstructure characterization and mechanical properties of laser-welded copper and aluminum lap joint, J. Laser Appl. 26 (1) (2014) 012002.
[93] H.N. Moosavy, M.-R. Aboutalebi, S.H. Seyedein, C. Mapelli, Microstructural, mechanical and weldability assessments of the dissimilar welds between γ′-and γ″-strengthened nickel-base superalloys, Mater. Charact. 82 (2013) 41–49.
[94] M. Pang, G. Yu, H.-H. Wang, C.-Y. Zheng, Microstructure study of laser welding cast nickel-based superalloy K418, J. Mater. Process. Technol. 207 (1–3) (2008) 271–275.
[95] R.I. Stephens, A. Fatemi, R.R. Stephens, H.O. Fuchs, Metal Fatigue in Engineering, John Wiley & Sons, Inc, New York, 2000.
[96] O.A. Zeid, On the effect of electrodischarge machining parameters on the fatigue life of AISI D6 tool steel, J. Mater. Process. Technol. 68 (1) (1997) 27–32.
[97] A. Medvedeva, J. Bergström, S. Gunnarsson, Inclusions, stress concentrations and surface condition in bending fatigue of an H13 tool steel, Steel Res. 79 (5) (2008) 376–381.
[98] J. Gbur, J. Lewandowski, Fatigue and fracture of wires and cables for biomedical applications, Int. Mater. Rev. 61 (4) (2006) 231–314.
[99] X. Wang, G. Ng, Z. Liu, L. Li, L. Bradley, EPMA microanalysis of recast layers produced during laser drilling of type 305 stainless steel, Thin Solid Films 453–454 (2004) 84–88.
[100] F. Yan, S. Liu, C. Hu, C. Wang, X. Hu, Liquation cracking behavior and control in the heat affected zone of GH909 alloy during Nd:YAG laser welding, J. Mater. Process. Technol. 244 (2017) 44–50.
[101] C. Karatas, O. Keles, I. Uslan, Y. Usta, Laser cutting of steel sheets: Influence of workpiece thickness and beam waist position on kerf size and stria formation, J. Mater. Process. Technol. 172 (1) (2006) 22–29.
[102] L. Shanjin, W. Yang, An investigation of pulsed laser cutting of titanium alloy sheet, Opt. Lasers Eng. 44 (10) (2006) 1067–1077.
[103] D. Jahns, T. Kaszemeikat, N. Mueller, D. Ashkenasi, R. Dietrich, H. Eichler, Laser trepanning of stainless steel, Phys. Procedia 41 (2013) 630–635.
[104] X. Wang, G. Ng, Z. Liu, L. Li, P. Skeldon, L. Bradley, Corrosion performance of recast layers produced during laser drilling of type 305 stainless steel, J. Corros. Sci. Eng. 6 (2003). Paper C123.
[105] B.T. Rao, R. Kaul, P. Tiwari, A. Nath, Inert gas cutting of titanium sheet with pulsed mode CO_2 laser, Opt. Lasers Eng. 43 (12) (2005) 1330–1348.

This page intentionally left blank

INDEX

Note: Page numbers followed by *f* indicate figures and *t* indicate tables.

A

Ablation geometry, 96–99
  laser beam and, 97*f*
  light-microscope, 104*f*
  polarization direction, 108
  qualitative evaluation, 113–115, 113–114*f*
  SEM, 104*f*
Absorption, 550–553, 563
Acousto-optical modulator (AOM), 611*f*
Adaptive neuro-fuzzy inference system (ANFIS), 717–718, 718*f*
Additive manufacturing (AM) technology, 635–636
  advantages, 520–521, 533–534
  applications
    human vertebrae replica fabrication, SLS/DLF technique, 528–530, 528*f*
    porous NiTi alloy implant fabrication, SLS/SLM technology, 528–530, 528*f*
    Ti-6Al-4V alloy, 528–530, 528*f*
  classification, 509–510, 510*f*
  considerations, 532–535
  vs. conventional manufacturing, 507, 508*t*
  design optimization, 532–533, 533*f*
  direct energy deposition
    hybrid manufacturing approach, 512–513
    laser-assisted repair, 513
    three-dimensional geometries, 511–512, 512*f*
    two-dimensional geometries, 511, 511*f*
  FDM technology, 507
  future trends, 532–535
  laser-based DED *vs.* PBF methods
    material requirements, 516
    part size, 516–517
    shape and surface finish, 516–517
    time and efficiency, 517–518
  materials, 514–515
  metal-ceramic composites
    DED techniques, 525, 527*t*
    PBF techniques, 525, 527*t*
  metallic materials
    bone model fabrication, SLS, 522–523, 523*f*
    Co-based alloys, 518–519
    CoCrMo alloys, 518–519
    Fe-based metallic materials, 519–521
    Inconel alloys, 525, 525*f*
    Nd:YAG laser and CO_2 laser, 522–523
    Ti-based materials, 522–523
  powder bed fusion methods, 513–514, 514*f*
  redesign options, 533–534, 534*f*
Additive multiple layer manufacturing, 35–36
Advanced packaging applications, 542
Advanced Robotic Mechatronics System (ARMS) project, 489
"Against hill" cladding condition, 413–414
Al-Cu alloy, 47*f*, 61*f*
Alloys, 54–55, 629
Aluminum (Al), 50–51, 54–55, 58, 185, 243
  bead-on-plate welds, 248–249, 249–250*f*
  fusion laser cutting, 45–48
  micro welding, 189–197
  Nd:YAG laser welding, 207–209
  penetration depths, 168, 168*f*
  technological properties and prices, 186*t*
  welded joints, 197–201
  welding metallurgy of, 186–187
  welding of, 187–188
Analyses of variance (ANOVA), 721–722, 724, 724*t*
Analytical models, 676
  hardness depth, comparison, 281*f*
  laser process, 268
  numerical and FEM analysis, 271–274
ANFIS. *See* Adaptive neuro-fuzzy inference system (ANFIS)
Arc-assisted laser welding process, 204–206
Arc welding, 203–204, 207–209
  power modulation, 218–219
  torch, 215

Artificial neural networks (ANN), 716, 718–719
Aspect ratio, 111–113, 112*f*
Assist gas jet, 55, 57
Atomic force microscope (AFM), 587–588, 715
Austenite-martensite transformation, 277, 280–281
Austenite-to-ferrite transformation, 274–275

B

Back propagation neural network (BP-NN) model, 719, 720*f*
Back scatter detector (BSE), 723, 723*f*
Balling effect, 626–627
Ballistic laser-assisted solid transfer (BLAST), 357, 357*f*
Beam/material interactions, 40–41
Beam mode
  CW CO_2 laser, 73
  pulsed Nd:YAG laser, 74
Beam propagation, 108–109, 550–553
Beam-shaping technique, 285
Bioactive glasses, 393*f*, 404–406
Bioceramics, 383–392, 394–406
Biofunctional photopolymers, 616–618
Biomaterial coatings
  laser cladding
    bioactive glass coatings, 404–406
    calcium phosphate coatings, 394–401
    technique description, 394
  LCVD, 382–383
  PLD
    bioactive glasses, 391–392
    calcium phosphates, 385–391
    technique description, 383–385
Blister-actuated LIFT (BA-LIFT), 354–355, 354–355*f*
Blocking, 710
Bone model fabrication, SLS, 522–523, 523*f*
Boron-implanted crystalline Si substrate, 309–311, 310*f*
Boron-interstitial clusters (BICs), 320
Box–Behnken design (BBD), 711
Bremmstrahlung process, 169–171
Brewster's angle, 334–335
Brown & Sharpe CMM, 487–488
Bulk resistivity measurement, 583–585*f*

C

Calcium phosphate
  ceramics, 381–382
  laser cladding
    off-axis powder feeding, 399
    powder injection, 397–401
    preplaced precursor material, 394–397
  thin films, 385–391
Calcium to phosphorous (Ca/P) ratio, 389
Carbon dioxide (CO_2) lasers, 5, 45, 69, 166–168, 167*f*, 178*f*, 205–211, 257, 263, 522–523, 739
  Al_2O_3 ceramic, 51–52
  cutting *vs.* fiber/disk laser, 23–24
  CW welding, 188
  fusion, 48
  HAZ, 47–48
  laser cladding, 395
  MAG hybrid welding, 216
  shielding gas composition, 217–218
  TIG hybrid welding, 218–219
Carbon fiber reinforced plastics (CFRPs), 121–124
  composite structures, cutting of, 124–132
  erosive laser processing, 147–148
  fabrication, 122–123
  HAZ, 122–123
  laser based ablation processes, 123, 145–147
  multipass-cutting, 139*f*
  process emissions, 147–149
  repair preparation for composites, 140–147
  thermoplastic composite, welding of, 124–132
Carbon fibers, 123, 142
Carbon/glass composite materials, 25–26
Central composite design (CCD), 285, 711
Ceramic matrix composites (CMM), 34–35
Ceramics
  fusion laser cutting, 48–49
  thermal cracking, 50
Cermets, 629
Chemical vapor deposition (CVD), 638–640

Cleaving temperatures, 74–75, 74*f*
Coaxial laser arc hybrid welding process, 205–206
Coaxial laser cladding process, 414
  experimental evaluation, 432–435
  powder-laser beam interaction area, 428–429, 429*f*
  processing parameters, 434*t*
Co-based alloys, 443*f*, 518–519
Co-based thick coating, 456
CoCrMo alloys, 518–519
Complementary metal-oxide-silicon (CMOS), 299, 303
Composites
  CFRPs, 121
  cutting structures, 124–132
  heat conductivity coefficients, 142*t*
  repair preparation, 140–141
    laser ablation, 145–147
    laser processing, 142–143
    laser sources used, 143–144
    surface treatments, 147
    system technology, 144–145
  thermal and optical properties, 143
  thermoplastic welding, 124–132
Computational fluid dynamics (CFD), 40–41, 416*f*
Computer aided design (CAD) model, 363, 462, 635–636
Condensing effect, 626–627
Confocal microscopy, 342–343
Continuity equation, 669
Continuous wave (CW), 322
  CO_2 lasers, 73, 207–209
  fiber laser, 26*f*
  laser hardening, 275–276, 278
  laser radiation, 111*f*
  laser welding, 153, 188
    laser-induced plume, 169–171
    Nd:YAG, 177*f*, 580
    welding results, 166–180
  mode laser, 722
Contour welding, 125–126
Control parameters, 700, 700*t*
Control systems, 695
Convection boundary condition, 671
Conventional hardening process. *See* Laser surface transformation hardening
Coordinate measuring machine (CMM), 487–488
Copper (Cu), 185
  EDX analysis, 196*f*
  micro welding, 189–197
  technological properties and prices, 186*t*
  welded joints, 197–201
  welding metallurgy of, 186–187
  welding of, 187–188
Copper–aluminum welded joints
  binary phase diagram, 187*f*, 197*f*
  dissimilar joints, 187–188
  dynamic fatigue test, 198–199*f*
  reliability, 197–198
  tensile strength, 199*f*
Co silicidation, 324
Coupled time-dependent temperature, 680
Crack-free co-based coatings, 456
Cracks, 754–756
  line-shaped laser cleaving, 82–83, 82*f*, 84–85*f*
  multiple laser beam, 83*f*
Critical angle, 99
Crystalline substrate effects, 304–309, 305*f*, 308*f*
Cutting-edge quality, 133
Cutting-on-the-fly method, 138
CW. *See* Continuous wave (CW)

D

Darken–Gurry ellipse, 186
Deep-penetration laser-beam welding, 235
Dektak Surface Profiler, 463
Design of experiments (DoE)
  experimental methods, 714–715
  experimental setups, 715
  guidelines, 709–712
  mathematical simulations, 713–714
  software packages, 712–713
Diamond-like carbon (DLC), 638–640
Diamond sawing, 90
Dielectric coatings, 637–638
Digital micromirror device (DMD), 347, 347*f*, 600–601
Diode lasers, 124–125, 207–209, 267*f*, 280, 542–543
  laser arc hybrid welding process, 207–209
  sol-gel surface deposition technique, 35*f*

Diode-pumped Nd:YAG laser, 52*f*, 207–209
Diode-pumped solid-state laser. *See* Fiber laser
Dip-pen nanolithography, 573–574
Direct energy deposition method
  additive manufacturing techniques
    hybrid manufacturing approach, 512–513
    laser-assisted repair, 513
    three-dimensional geometries, 511–512, 512*f*
    two-dimensional geometries, 511, 511*f*
  metal-ceramic composites, 525, 527*t*
Direct laser deposition, 35–36, 36*f*
Direct metal deposition technique, 415, 640
Direct production method, 597
Direct-write nano-sized materials
  deposited line and screen-printed pads, 581*f*
  dip-pen nanolithography, 573–574
  laser sintering, 574, 580–590
  material deposition system
    capabilities, 572–573
    parallel methods, 572
    sequential methods, 572
  M^3D direct-write process, 574–575
  mesoscale components, 572–573
  nano-sized materials sintering
    dry nanoparticle materials, 576–577
    nano-sized printing inks, 575–580
  nScrypt systems, 573–574
  spectrophotometer reflectance, 586*f*
Direct-write thermal spraying, 573–574
Disc lasers, 23–24, 40–41, 207–209
Dopant activation, 308–309, 309*f*
Dry metal powders, 576
Dulbecco's Modified Eagle Medium (DMEM), 366
Dynamic release layer LIFT (DRL-LIFT), 354, 354*f*

E

Electro-discharge machining (EDM), 27, 33
Electromagnetic radiation, 4
Electromagnetic weld-pool manipulation, 238–241, 239–240*f*
Electro-optical efficiency, 207–209
Endothelial colony-forming cells (ECFCs), 367–368, 368*f*
Energy dispersive X-ray spectrometry (EDS), 156, 588, 649–650, 754
Energy transfer
  absorption phenomena, 560
  structural modifications, phenomena and, 545–546
Enthalpy-based finite element model, 271
Eutroloy 16012 coating, 446*f*
Eutroloy 16006 Co-based coating, 444, 444*f*
Excimer lasers, 740
Excimer pulsed laser annealing technique, 299

F

Fatigue, 752–754
Fe-based metallic materials, 519–521
Femtosecond lasers, 34, 115–118, 545, 568, 732, 740–742
Fiber laser, 6, 18, 167*f*, 169, 173*f*, 207–211
  vs. CO_2 laser cutting, 23–24
Fillet weld joints, 193, 193*f*
Film-free laser printing, 353, 353*f*
Flat panel display applications, 542
Flexural strength, 749–752
Fluence. *See* Laser fluence
Fluid LIFT transfer
  bubble evolution, 348*f*
  high viscosity fluids, 349–350
  jet formation, 348*f*
  solid donor, 350–352
Focused ion beam (FIB), 744–745, 744*f*
Folded shell projector (FSP), 486–488
Fourier transform equation, 696
Fourier transform infrared (FT-IR), 387–388, 389*f*
4-layered ANN model, 719*f*
Fractional factorial design, 711
Free-form fabrication, 461
Functionally graded coatings, 645
Fused deposition modeling (FDM) technique, 507
Fusion laser cutting, 45–49
  cutting process improvement, 50–61
  difficult materials
    ceramics, 48–49
    metals, aluminum, and alloys, 45–48

metallurgical characteristics, 47–48
principles, 44–45

G

GaAs
ripple structures in, 557*f*
three-photon absorption in, 561
z-scan measurements, 562*f*
Gaussian mode intensity, 74
Glass fiber reinforced plastics (GFRP), 143, 143–144*f*
Gray relational analysis (GRA), 717, 720–721
Group velocity, 695–697

H

Hardness, 749–752, 751–752*f*
Heat accumulation effects, 546–547
Heat affected zone (HAZ), 47–48, 122–123, 132–133, 134*f*, 136, 546, 665–666, 686–687, 745
CFRPs, 122–123
CO_2 lasers, 47–48
influence of machining speed, 747–748, 748*f*
laser cladding, 417–419*f*
Heat conduction equation, 280–282, 669–670
Heat diffusion equation, 695
Heat radiation, 164–165, 166*f*
Heat sinks, 281–283, 282*f*
High-intensity laser beam, 44
Highly filled photopolymers, 614–615
High power diode laser (HPDL), 719, 720*f*
High-power fiber, 23–24, 41
High-pressure laser cutting, 59–61
High-repetition-rate femtosecond laser radiation, 115–118
High-speed video technique, 344, 345*f*
High-strength alloy steel (HLSA), 224–227
Hole-array, 756, 756*f*
Huffman HC-205 laser cladding system, 423*f*
Human vertebrae replica fabrication, SLS/DLF technique, 528–530, 528*f*
Hume–Rothery rules, 186
Hybrid laser welding process
arc welding, 30
coaxial laser arc, 205–206
drilling, 33, 34*f*
MAG, 216
TIG, 218–219
Hybrid wire/powder feeding direct laser deposition, 35–36, 36*f*
Hydroxylapatite (HA), 381–382, 396, 636–637
optical microscopy, 390*f*
polygonal-shaped crystallites, 387*f*
surface topography, 386–387, 386*f*

I

Imperialist competitive algorithm (ICA), 717
Inconel alloys, 525, 525*f*
Indirect interaction, LIFT
absorbing layer, 354
BA-LIFT, 354–355
DRL-LIFT, 354
Indirect laser sintering, 619
Industrial laser processing, 15
Industrial silicon dicing processes
laser-based scribe and break, 92
with laser radiation, 91–92
limitations, 93, 93*t*
mechanical dicing with diamond saws, 90
mechanical scribe and break, 91
scientific publications, 93, 94*t*
short pulse laser (*see* Laser dicing)
stealth dicing, 92
ultra-short pulsed laser radiation, 93, 94*t*
water jet hybrid dicing, 91
Infrared (IR)
lasers, 543, 740
nanosecond pulse laser processing, 557–567
pyrometers, 285
ultrashort pulse laser processing
absorption and beam propagation, 550–553
semiconductor surface functionalization, 553–557
In situ bulk resistivity measurement. *See* Bulk resistivity measurement
In-situ synchrotron X-ray diffraction analysis, 277

Integrated circuit (IC) technology, 541–542
Inverse Bremmstrahlung process, 169–171
Inverse laser surface heating problem, 269–270
In vivo laser printing, 370*f*
Ionization absorption, 543–545
Irradiation, 301*f*, 303, 548–550, 562
  multiple-pulse laser, 322
  semiconductors with IR laser pulses, 548–550
Isostatic sintering, 578*f*

J

Johnson–Mehl Avrami equation, 272

K

Knudsen-layer formation, 385
Koistinen–Marburger equation, 272
Kolmogorov equation, 272

L

Lambert–Beer's law, 429
Laplace transformation method, 277–278
Laser ablation (La), 145–147, 146*f*, 382–383. *See also* Pulsed laser deposition (PLD)
Laser annealing, 309
  Ni(Ti) on Si, 325–329
  SiGe substrates, 329–334
  silicide formation, 323
  TiN/Co on Si, 324–325
Laser arc hybrid welding process
  advantages and limitations, 209–210
  by CLOOS, 207*f*
  diode lasers, 207–209
  historical developments, 205–206
  industrial applications, 224–227
  laser beam, 204–205
  MIG/MAG, 210–211
  PAW hybrid welding, 213–214
  process parameters, 214
    angle of electrode, 216–217
    arc, laser beam relative positioning and, 215–216
    arc welding source, power modulation of, 218–219
    arc welding torch, laser beam relative positioning and, 215
    edge preparation, 220–221
    focal point position, 216
    joint configuration, 220–221
    joint gap, 220
    laser power, 214
    shielding gas composition, 217–218
    welding speed, 215
    wire feed rate, 219–220
  safety, 227–229
  schematic of, 204*f*
  seam appearances, 205*f*
  TIG hybrid welding, 211–213
  welding performance improvement, 221–224
Laser assisted additive manufacturing (LAM), 640
Laser-assisted arc-welding process, 204–205
Laser-assisted glass cleaving
  crack propagation, 81–85
  multiple laser system, 70–71, 71*f*
  numerical results and discussions, 74–81
  numerical simulation, 71–74
Laser-assisted in-situ keratomileusis (LASIK), 11–12, 11*f*
Laser-based dicing, 542
Laser-based SFF
  CAD software visualization, 596–597
  photopolymerization
    MSL, 599–607, 605–606*f*
    TPP, 607–614, 609–610*f*
  rapid prototyping, 596–597
  stereolithography (SL) principle, 596–597
  three-dimensional model data, 595–597
Laser based surface/material modification, 12
Laser beam, 164–165, 169, 413, 674
  ablation geometry, 97*f*
  energy distribution, 678
  energy loss, 675
  focal point position, 216
  high-intensity, 44
  high-power/low power, 12
  LSFF, 665–666
  offset effect, 191–193, 192–193*f*
  properties, 2*t*, 4–5
  relative positioning of, 215–216

Laser beam cutting (LBC) process, 737
Laser-beam welding, 236*f*
  ultrasound-assisted, 244–245
  weld pools
    alloying elements, 241–242
    approaches and methods, 238
    electromagnetic forces, 238–241
    gas feed, 242–243
    of metals, 235–238
    ultrasound method, 244
    vibration method, 243–244
Laser capture microdissection (LCM), 364, 365*f*
Laser chemical vapor deposition (LCVD), 382–383
Laser cladding, 413, 620, 718–721, 718–721*f*
  clad area, 440*f*
  clad height, 439*f*
  combined parameters, 435–436
  computer-controlled, 434
  HAZ profile, 417–419*f*
  manufacturing based on, 618–627
  materials for, 628–629
  processing map, 442–443
  single-step methods, 620–624
  tool steel powder, 448*f*
  two-step methods, 624–627
  wear rate, 455*f*
Laser consolidation (LC) process
  airfoil with embedded cooling channels, 484–486, 485*f*
  Al-base alloy, 483–484, 483*f*, 484*t*
  ARMS project, 489–491, 490–491*f*
  Co-base alloy, 480–483, 481*f*, 482*t*
  cold spray nozzles, 497–501, 498–500*f*
  future trends, 501–502
  IN-718 impeller, 495–497, 495–496*f*
  net-shape functional sonar shells
    IN-625 FSP shells, 486–487, 486*f*
    Ti-6Al-4V FSP shells, 487–489, 487–489*f*
  Ni-based alloys
    IN-625 alloy, 470–471, 471*t*, 471*f*
    IN-718 alloy, 474–476, 475*f*, 476*t*
    IN-738 alloy, 476–478, 477*f*, 478*t*
    Waspaloy, 471–474, 472–473*f*, 474*t*
  rocket engine applications
    IN-625 demonstration pieces, 491–493, 492*f*
    Ti-6Al-4V spherical hollow ball, 493–495, 494*t*, 494*f*
  stainless and tool steels
    CPM-9V tool steel, 468–470, 468–469*f*, 469*t*
    H13 tool steel, 465–468, 465*f*, 467*t*
    316L stainless steel, 463–465, 464*f*, 465*t*
    process description, 462–463, 462*f*
  Ti-6Al-4V alloy, 478–480, 479*t*, 479*f*, 481*f*
Laser-cut glass, 10*f*
Laser cutting
  aerodynamic interactions, 56*f*
  of brittle materials, 24–25
  composite and inhomogeneous materials, 25–26
  composite structures, 132–139
  fiber/disk laser *vs.* CO_2, 23–24
  in-process temperature monitoring, 140*f*
  striation-free and recast-free cutting, 28
  super-high speed remote cutting, 28–29
  thick-section materials, 27
  vapor pressure cutting, 28–29
  variable thickness materials, 27, 27*f*
Laser decal transfer (LDT), 346, 347*f*, 362
Laser dicing
  aspect ratio factors
    coaxial incidental continuous wave laser radiation, 110–115
    peak intensity, 105–106
    polarization direction, 108–109
    wavelength, 106–108
  high-repetition-rate femtosecond laser radiation, 115–118
  spatial beam shaping, 115–118
  surface phenomena, 103–104
Laser drilling, 32–33
  CFD modeling, 416*f*
  hybrid laser drilling, 33
  ultra-short pulse, 34
Laser Engineered Net Shaping (LENS), 511–512, 512*f*, 641
Laser fluence, 302–304, 302–303*f*, 306*f*, 343*f*, 348

Laser-induced backward transfer (LIBT), 352–353, 353*f*
Laser-induced forward transfer (LIFT), 9, 38
  additive manufacturing, 358
  applications, 357–370
  for bioapplications, 364–370
  BLAST, 357
  characterization techniques, 342–344
  c-Si solar cell, 362*f*
  direct-write techniques, 339
  for electronics, 358–362, 360*f*
  experimental setup, 341–344, 342*f*
  film-free laser printing, 353
  fluid LIFT transfer, 347–350
    high viscosity fluids, 349–350
    solid donor, 350–352
  forward and backward transfer, 352–353
  indirect interaction
    absorbing layer, 354
    BA-LIFT, 354–355
    DRL-LIFT, 354
  laser writing (LW), 340
  LMI, 356
  LP-LIFT, 356–357
  MAPLE-DW, 355–356
  for microfabrication, 362–363
  physical processes, 344–352
  seeding scaffolds, 369*f*
  solid LIFT, 345–347
  3D structures, 364*f*
  time-resolved images, 350*f*
  variations, 352–357
Laser-induced grooves, 117*f*
Laser-induced periodic surface structure (LIPPS), 12, 103–104
Laser-induced plasma, 216–217
Laser-induced plume, 170*f*, 174*f*
Laser-induced refractive index change (LIRIC), 11–12, 11*f*
Laser-induced thermal imaging (LITI), 359
Laser-irradiation, 159, 301*f*, 316–322, 725
Laser machining, 69, 85
  CFRPs, 121–124
    composite structures, cutting of, 124–132
    process emissions, 147–149
    repair preparation for composites, 140–147
    thermoplastic composite, welding of, 124–132
  cracks, 754–756, 754–755*f*
  fatigue, 752–754, 753*f*
  flexural strength, 749–752
  hardness, 749–752, 751–752*f*
  HAZ, 746–749, 747–748*f*
  laser sources
    carbon dioxide, 739
    excimer, 740
    femtosecond, 740–742, 741*f*
    Nd:YAG, 737–739, 739*f*
  micromachining, 732–734, 733*f*
  microstructure and surface evaluation
    FIB, 744–745, 744*f*
    HAZ, 745
    optical microscopy, 742–743, 743*f*
    SEM, 744–745, 745*f*
Laser material processing, 542, 667–669, 677
  advantages, 15
  economic impact, 7–8
Laser-matter interactions, 4*f*, 341
  energy transfer phenomena and structural modifications, 545–546
  heat accumulation effects, 546–547
  light and ionization absorption, 543–545
  process development and optimization, 547–548, 548*t*
  semiconductors irradiation, 548–550
Laser melting, 546
  injection regime, 413–414
  manufacturing based on, 618–627
  materials for, 628–629
  single-step methods, 620–624
  two-step methods, 624–627
Laser metal deposition (LMD) process, 646–661, 651*f*
Laser micro sintering (LMS), 626–627
Laser molecular implantation (LMI), 356
Laser-overlapping scanning, 290*f*
Laser pressure catapulting (LPC), 364
Laser-processed Si wafer, 116*f*
Laser processing
  applications, 735*t*
  DoE methods

experimental methods, 714–715
experimental setups, 715
guidelines, 709–712
mathematical simulations, 713–714
software packages, 712–713
experimental analysis
laser cladding, 718–721, 718–721*f*
laser surface melting, 721–724, 723*f*, 723–724*t*, 725*f*
LSP, 725–726, 725*f*
with nonconventional approaches, 716–717
optimization, 708–709
Laser shock peening (LSP), 708, 725–726, 725*f*
Laser sintering, 574, 580–590, 582*f*, 618–619
based additive manufacturing technique, 640
manufacturing based on, 618–627
single-step methods, 620–624
two-step methods, 619–620, 624–627
Laser solid freeform fabrication (LSFF)
boundary conditions and assumptions, 671–672
deposition domain, 668*f*
energy balance, 673*f*
governing equations, 669–671
material deposition strategy, 682*f*
multiphysics numerical modelling
experimental procedure, 684–686
lumped model, 673–676
mathematical model, 681–683
modelling architecture, 680–681
model verification, 684–686
numerical and analytical approaches, 676–677
process parameters, 683–684, 683*t*
temperature distribution, 686–687
thermal stress fields, 688–689, 689*f*
schematic arrangement, 666*f*
Laser spot welding defects
in A5083 alloy, 163*f*
monitoring and adaptive control, 164–166, 165*f*
solidification cracks, 163
suppression procedures, 159–163, 162*f*
Laser surface cladding, 382–383
bioceramics
bioactive glass coatings, 404–406
calcium phosphate coatings, 394–401
technique description, 394
powder injection, 404–406
preplaced powder, 395–396, 395*f*
Laser surface modification (LSM), 707
Laser surface transformation hardening
AISI 1045 steel, 287*f*
analytical modeling, 268–271
anisothermal model, 272–273
arbitrary geometry, 274
austenite kinetics, 271–272
background information, 264–268
beam shaping and scanning systems, 265–266
carbon diffusion, 264–265
definition, 257
experiment-based approach, 273
face centered cubic (FCC) crystal structure, 258
hardness values *vs.* depth, 272*f*
heat sink effects, 281–283
hypo-/hyper-eutectoid steels, 264–265
iron-carbon diagram, 259*f*
key way hardening, 266*f*
laser beam shaping, 285–291
martensite, 260–261*f*
materials for, 264
microhardness *vs.* distance, 276*f*
microstructures, 272
multilayer perceptron neural model, 273
numerical and FEM analysis, 271–274
online monitoring, 285–291
overlapping passes, 289*f*
overlapping ratio, 273
phase transformation behavior, 274–275
piston ring groove surface, 267*f*
regression model, 271
repetitive laser pulses, 275–278
residual stress distribution, 277*f*
temperature regions, 259*f*
thermal analysis, 264–265
time-temperature transformation diagrams, 262*f*
very low carbon steel thin sheets, 280–281
water-assisted, 283–285

Laser thermal processing (LTP), 299–300
advantages, 301
boron-implanted SiGe substrate, 314–316, 315*f*
boron implanted SOI substrate, 311–313, 312*f*
Laser track geometry, 432, 435–444, 435*f*
OIM characterization, 447*f*
side and coaxial laser cladding, 441*t*
Laser transmission welding (LTW), 123–124, 127*f*
absorbing characteristics, 125
for composites, 131–132
contour welding, 125–126
mask welding, 126
principles, 125*f*
quasisimultaneous welding (QS), 125–126
simultaneous welding, 126
stiffener panel example, 130–131, 131*f*
Laser-treated 316LVM, 753, 753*f*, 755–756, 755*f*
Laser welding, 4–5, 124–125, 203–204
conduction-mode, 204–205
defects, 153, 171–178
Al-alloys, 178
Zn-coated steel, 178
dissimilar materials, 31–32, 31*f*
hybridization, 203–204
hybrid laser arc welding, 30
joint gap, 220
net-shape welding, 32, 33*f*
porosity control, 32
spot-weld penetration, 154–156
thick-section materials, 30
ultra-thin-section materials, 30, 31*f*
weld quality, 221–224
Lasing medium, 736–737
LC CPM-9V tool steel
microstructure, 468, 468*f*
tensile properties, 469, 469*t*
wear resistance, 469–470, 469*f*
LC H13 tool steel, 465–468, 465*f*, 467*t*
LCVD. *See* Laser chemical vapor deposition (LCVD)
LDT. *See* Laser decal transfer (LDT)
Length scale, 697
LIFT. *See* Laser-induced forward transfer (LIFT)
Light absorption, 543–545
Light Amplification by Simulated Emission of Radiation (LASER), 207–209
adaptive control system, 165*f*
bead welding, 179–180, 179–180*f*
biomedical industries, 636–637
bioprinting, 369
case studies, 646–661
CFRP repair preparation, 142
characteristics, 635
cleaving (*see* Laser-assisted glass cleaving)
cutting efficiency, 50–51
deposited tool steel, 415, 456
energy, 669
fusion cutting (*see* Fusion laser cutting)
heat treatment, 421*f*
intensity distribution, 684
interaction, 344–345
lattice rotation contour map, 424*f*, 426*f*
from light source, 635
materials processing, 1
metallurgical effects, 413
microdissection, 364
in microfabrication, 737, 738*t*
micro-sized coatings, 637–645
micro welding, 189–197
MIG/MAG hybrid welding process, 205–206, 210–211, 221–224
Monte Carlo modeled grain structure, 423*f*
PAW hybrid welding, 213–214
and plume, interaction between, 174*f*
powder stream, 414
power, 214, 279*f*, 431*f*
preirradiation, 320
radiation, 91–92
scarfing process, 141–142
scribing of, 92
surface engineering, 34–35, 35*f*
in surface hardening, 263
surface micro-texturing, 37–38, 38*f*
systems, 41
thermal cracking, 52
TIG hybrid welding, 211–213
Trumpf deposition equipment, 422*f*

weld bead penetration, 166–169
welded joints, 189
Light industry
application space development
application trends, 9–13
driving forces, 8–9
source development and deployment, 13–16
laser, 1–7
materials processing, 7–8
previous reflections, 17–18
Light–matter interaction, 16
Line-shaped laser beam, 70*f*, 71–72, 75–77
LMD process. *See* Laser metal deposition (LMD) process
LMI. *See* Laser molecular implantation (LMI)
Long-pulsed LIFT (LP-LIFT), 356–357
Lorentz force, 238. *See also* Electromagnetic weld-pool manipulation
Low carbon austenite 316L stainless steel (S.S.)
optical microstructure, 463–464, 464*f*
tensile properties, 464–465, 465*t*
XRD analysis, 463–464, 464*f*
Low-spatial-frequency LIPSS (LSFL), 553
Low-temperature substrate, 590
LSFF. *See* Laser solid freeform fabrication (LSFF)
LTW. *See* Laser transmission welding (LTW)
Lumped model, 673–676

M

Mach shock disk (MSD), 56–58
Magnesium, Nd:YAG laser welding, 207–209
Magneto fluid dynamics, 238–240
Marangoni effects, 235–238, 236*f*, 241–243, 268, 677–678
MASERs, 3
Mask welding, 126
Master-oscillator-power-amplifier (MOPA) principle, 558
Mathematical model
laser material deposition, 675
LSFF, 680
solution strategy, 681–683
Mathematical simulations, 713–714
Matrix-assisted pulsed laser evaporation (MAPLE), 38
Matrix-assisted pulsed laser evaporation-direct write (MAPLE-DW), 355–356, 358–359, 573–574
Maurer two-color pyrometer, 699
Meta-Heuristic optimization, 717
Metal-based laser additive manufacturing, 9–10
Metal inert gas/metal active gas (MIG/MAG) welding, 207–209
Metallic nano-sized printing inks, 575–576
Metal matrix composites (MMC), 34–35
Metals
coatings, 563–567, 565*f*, 637–638
deep-penetration laser-beam welding, 235
fusion laser cutting, 45–48
Microelectromechanical systems (MEMS), 572–573, 731
Microhardness, 273, 279*f*
vs. distance, 276*f*
distribution of, 279*f*, 752, 752*f*
Micromechanistic models, 576
MicroMelt 23 tool steel coatings, 447–449, 449*f*, 456
Micro/nano fabrication, 36
direct-write micro-deposition, 38
laser surface micro-texturing, 37–38
nano-fabrication, 38–40
precision micro-cutting, 36–37
Micro sintering, 628–629
Micro-sized coatings, 637–638
application areas, 639*f*
CoCrMo, 644–645
gradation, 645
laser based additive manufacturing for, 638–645
porous material, 645
Ti6Al4V, 640–641, 644
types of, 637–638
Micro stereolithography (MSL), 599–607, 605–606*f*
challenges, 601
conventional and integral approach, 600–601
deep-dip deposition method, 601–602, 602*f*

Micro stereolithography (MSL) *(Continued)*
disadvantages, 602–603
fixed/constrained surface method, 602
materials for, 614–618
photopolymerization
challenges, 601
deep-dip deposition method, 601–602, 602*f*
fixed/constrained surface method, 600*f*, 602
illumination procedure, 600–601
reported operational principles, 599, 600*f*
Micro welding
Cu and Al, 189, 191*f*
laser beam offset effect, 191–193, 192–193*f*
process characterization, 190–191, 190*f*
thin interlayer filler materials, 193–197, 194–195*f*
Modified inkjet printing technology, 573–574
Momentum equation, 669
Mullite-alumina composite, 49*f*, 58–59, 60*f*
Multilayer LSFF process, 677
Multilayer perceptron neural model, 273
Multipass laser cutting, 133, 133*f*
Multiphysics numerical modelling
experimental procedure, 684–686
lumped model, 673–676
mathematical model, 681–683
modelling architecture, 680–681
model verification, 684–686
numerical and analytical approaches, 676–677
process parameters, 683–684, 683*t*
temperature distribution, 686–687
thermal stress fields, 688–689
Multiple laser beams
cleaving of, 76*f*
intensity profiles, 75*f*
line-shaped CO_2 laser beam, 70, 70*f*
pulsed laser beam, 70*f*
Multiple-pulse laser
annealing, 331
interactions, 5*f*
irradiations, 322
thermal processing, 309–311, 310*f*
Multiple spot laser brazing, 14*f*

N

Nano-fabrication
continuous wave laser ablation, 40*f*
field laser beam fabrication, 38–39
particle lenses, 39, 39*f*
Nanosecond lasers, 543, 732
vs. femtosecond, 741, 741*f*
Nano-sized ink direct-write deposited pad, 586*f*
Nano-sized materials sintering
dry nanoparticle materials, 576–577
nano-sized inks, 577–580
Nano-sized printing inks, 575–576
Nd:$Y_3Al_5O_{12}$ crystal, 207–209
Neodymium-doped yttrium aluminum garnet (Nd:YAG) laser, 5, 45, 50–51, 207–211, 386, 522–523, 733*f*, 737–739, 739*f*
absorption coefficient and temperature, 71, 71*f*
cladding technique, 401
diode-pumped, 52*f*
pulsed annealing, 323–324
PW laser welding, 153
Q-switch mode, 207–209
SEM micrographs, 402*f*
solid-state laser, 237–238
TIG hybrid welding, 215–216
Net-shape functional components
rocket engine applications
LC IN-625 demonstration pieces, 491–493, 492*f*
LC Ti-6Al-4V spherical hollow ball, 493–495, 494*t*, 494*f*
sonar shells
LC IN-625 FSP shells, 486–487, 486*f*
LC Ti-6Al-4V FSP shells, 487–489, 487–489*f*
Net-shape welding, 32, 33*f*
Ni-based alloys
IN-625 alloy, 470–471, 471*t*, 471*f*
IN-718 alloy, 474–476, 475*f*, 476*t*
IN-738 alloy, 476–478, 477*f*, 478*t*

laser consolidation process
LC IN-625 alloy, 470–471, 471*t*, 471*f*
LC IN-718 alloy, 474–476, 475*f*, 476*t*
LC IN-738 alloy, 476–478, 477*f*, 478*t*
Waspaloy, 471–474, 472–473*f*, 474*t*
Waspaloy, 471–474, 472–473*f*, 474*t*
Ni germanosilicide formation, 329–331
Ni silicide formation, 325
NiTi (nitinol) cylinder, 742, 742*f*, 748–749
Nitinol biliary stent, 745, 745*f*
Nonconventional approaches, 716–717
Non-Fourier effect, 270
Nonthermal melting, 545–546
Nuisance factors, 710
Numerical simulation
assumptions and boundary conditions, 72–73
beam mode
continuous-wave CO_2 laser, 73
pulsed Nd:YAG laser, 74
glass substrate, 72*f*
line-shaped laser, 71–72

O

Off-axis laser cutting, 59*f*
Off-axis powder feeding, 399
Off-axis powder injection laser cladding technique, 397, 397–398*f*
Olfactory ensheathing cells (OECs), 368
Open-loop laser materials process, 693
Optical Age, 2
Optical coherence tomography (OCT), 16
Optical 3D scanning, 138
Optical energy, 1–2, 17
Optical microscopy, 342–343, 742–743
Optimization, 708–709
Ordinary differential equations (ODEs), 667–668, 673
Organic light-emitting diodes (OLED), 359
Organic thin-film transistors (OTFT), 359–360
Orientation imaging microscopy (OIM), 445–446, 446*f*, 450
"Over hill" cladding condition, 413–414

P

2PA theory, 607
PCA, 719–720
Peak intensity, 99*t*, 102–106, 106*f*
Pearlite dissolution, 269*f*
Phase shift, 698
Phonon thermalization, 545–546
Photonic bandgap fibers, 14
Photonic crystal fibers, 14
Photopolymerization
micro stereolithography
challenges, 601
deep-dip deposition method, 601–602, 602*f*
fixed/constrained surface method, 600*f*, 602
illumination procedure, 600–601
reported operational principles, 599, 600*f*
two-photon laser lithography
advantages, 609–610
drawbacks, 610–611
fast shutter system, 610–611
femtosecond-laser source, 610–611
2PA theory, 607
polymer and initiators, 607–609
structuring possibilities, 611–612
Photopolymers
biofunctional, 616–618
highly filled, 614–615
Photo refractive keratectomy (PRK), 11–12
Physical vapor deposition (PVD), 638–640
Pico-second lasers, 34
Pilot experiments, 711–712
Pin-array, 756, 756*f*
Plasma arc welding (PAW), 207–209, 213–214
Plasma-enhanced vapor deposition (PECVD), 563
Plasmas
CO_2 laser welding, 170*f*
laser-induced, 117–118, 117*f*
shockwave emission, 4
Plasma spraying (PS), 382, 390–391, 396–397, 402*f*
PLD. *See* Pulsed laser deposition (PLD)
Plug efficiency. *See* Electro-optical efficiency
P/N junctions
laser-induced formation of, 300–322
LTP formed, 306*f*
Poiseuille–Hartmann flow, 238–240
Polarization, 555–556, 555*f*

Polyetheretherketone (PEEK), 121–123
Polyetherimide (PEI), 121–122
Polyetherketoneketone (PEKK), 121–123
Polymethyl methacrylate (PMMA), 381
Polyphenylene sulfide (PPS), 121–123
Poly(l-lactide) stent
  machined by using continuous-wave CO_2 laser, 748–749, 750*f*
  machined using a femtosecond laser, 749–751, 750*f*
Polyvinyl alcohol (PVA) binder
  samples with, 640–641
  SEM microstructures, 642*f*
Porosity, control, 32, 154, 163, 171–174
Porous NiTi alloy implant fabrication, SLS/SLM technology, 528–530, 528*f*
Powder bed fusion (PBF) methods, 513–514, 514*f*, 525, 527*t*
Powder catchment efficiency, 675
Powder injection laser cladding technique, 404–406
Power attenuation, 678–679
Prandtl–Meyer wave pattern, 56
Preamorphized (PAI) substrate effects, 304–309, 305*f*
  cross-sectional analysis, 321–322
  laser irradiation, 316–322
  sheet resistance, 308*f*
Precision micro-cutting, 36–37, 37*f*
Preplaced powder laser cladding technique, 395–396, 395*f*
Printed electronics, 571, 575, 590
Process control
  experiments
    control parameters, initialization of, 700, 700–702*f*, 700*t*
    control performance *vs.* travel speed, 703, 703*t*
    layout, 699–700, 699*f*
    measurements, 700–703*f*, 701–702
    quality length, 704–705, 705*f*
  theory, 694–699
    group velocity, 695–697
    length scale, 697
    maximum controllable speed, 699
    phase shift, 698
    quality, 697–698
    stable operating window, 698
    temperature information, 695
Process emissions, CFRPs, 147–149, 148*f*
Process modeling, 40–41
Process parameters, 709–710
Pulsed laser, 70*f*, 77, 77–80*f*
  annealing, 300
  Ni(Pt)/SiGe/Si sample, 333*f*
  Ni/SiGe, XRD spectra, 332*f*
Pulsed laser deposition (PLD), 355–356, 382–383
  bioactive glasses, 391–392
  calcium phosphates, 385–391
  high *Tc* superconducting (HTCS) thin films, 384
  schematic diagram, 384*f*
  technique description, 383–385
Pulsed Nd:YAG laser, 50, 70, 207–209
  beam mode, 74
  pulse length effect, 155*f*
  solidification cracks, 154–156
  spectroscopic measurement, 158*f*
  spot welding, 156–159, 157*f*
  type 316 austenitic stainless steel, 155*f*
  ultrafine particles, 158*f*
Pulsed wave (PW) laser welding, 153
Pulse energy, 99*t*, 102–103, 190*f*
Pulse peak power, 99, 99*t*
Pump-probe imaging technique, 344, 345*f*

Q

Q-switch CO_2 laser, 51
Q-switched ruby laser, 322
Q-switch Nd-YAG pulsed laser, 322
Quality length scale, 697
Quantronix Eagle 1064-nm CW Nd:YAG laser, 582
Quasi-CW Nd:YAG laser, 275–276
Quasisimultaneous welding (QS), 125–126, 127*f*, 130*f*

R

Radiation boundary condition, 671
Raman spectra, 318*f*
Raman spectroscopy, 132–133
Rapid functional prototyping method, 489
Rapid manufacturing (RM), 493, 597
Rapid prototyping (RP), 596–597
Rayleigh–Plateau instability, 348
Rayleigh scattering, 171

Recast-free laser cutting, 28, 29*f*
Recast layer, 743–745, 743*f*, 754
Remote cutting. *See* Multipass laser cutting
Remote sensing, 1
Resin transfer molding (RTM), 121
Resonator cavity, 736–737
Response surface methodology (RSM), 711, 713–714, 716
Rocket engine applications, LC process
  IN-625 demonstration pieces, 491–493, 492*f*
  Ti-6Al-4V spherical hollow ball, 493–495, 494*t*, 494*f*
Rosenthal's solution, 74–75
Roswell Park Memorial Institute culture medium (RPMI), 366

S

Scanning electron microscopy (SEM), 342–343, 450, 588, 744–745, 745*f*
Second harmonic generation (SHG), 553–554
Selective laser melting (SLM), 513–514, 518–519, 721–724
Selective laser sintering (SLS) technology, 513–514, 597
  bone model fabrication, 522–523, 523*f*
  Waspaloy structures, 523–524, 524*f*
Semiconductors
  back-end applications, 542
  front-end applications, 541–542
  irradiation, IR laser pulses, 548–550
  surface functionalization, 553–557
  wafers, front and back surface processing of, 558–563
Shadowgraph technique, 57–58
Shear strain, 425*f*, 428*f*
Shielding gas composition, 217–218
Short glass fiber reinforced thermoplastics, 123–124
Short pulse lasers, 144
Si^+ amorphization energies, 321*f*
Side cladding laser process, 432–435, 434*t*
Si drilling, 14
Silicide, laser-induced formation
  constitutional supercooling (CSC), 323–324
  laser annealing
    Ni(Ti), 325–329
    SiGe substrates, 329–334
    TiN/Co, 324–325
  LTP approach, 322
  Q-switch Nd-YAG pulsed laser, 322
  XRD spectra, 331
Silicon, 89
  dicing, ultra-fast laser radiation, 96–103
  electronic substrates, 90–93
  features, 89–90
  industrial dicing processes, 90–93
  p-polarization, 110*f*
  s-polarization, 110*f*
  wafer separation, 90
Silicon-on-insulator (SOI), 311
Simultaneous welding, 126
Single-pulsed laser
  annealing, 327
  irradiation, 303
Software packages, 712–713
Solid freeform fabrication (SFF). *See* Laser-based SFF
Solid phase LIFT transfer, 347
  LDT, 346
  schematic representation, 346*f*
  thermal stresses, 346
Spatial beam shaping, 115–118
Sputter coating, 563
Stainless and tool steels, LC process
  CPM-9V tool steel, 468–470, 468–469*f*, 469*t*
  H13 tool steel, 465–468, 465*f*, 467*t*
  316L stainless steel, 463–465, 464*f*, 465*t*
  process description, 462–463, 462*f*
State-of-the-art method, Cu-Al
  micro welding, 189–197
  welded joints, 197–201
  welding metallurgy of, 186–187
  welding of, 187–188
Stealth dicing, 92, 543
Steel-aluminum dissimilar joints, 249–254
Stefan–Boltzman constant, 671
Step-and-repeat cutting method, 138
Stereolithography (SL) principle, 596–597
Stitching effect, 555–556
Strained-silicon/SiGe substrate, 311
Strength-to-weight ratio, 121
Striation, 747–748

Striation-free laser cutting, 28, 29*f*
Super-high speed remote laser cutting, 28–29
Superposition principle, 676
Super-pulsed laser, 51
Surface acoustic waves, 291–292*f*
Surface processing, semiconductor wafers, 558–563
Surface roughness, 752–753
Surface temperature, 701–702, 701–703*f*

T

Technique for order preference by similarity to ideal solution (TOPSIS), 717
Tensile strength, 190–192, 190*f*, 192–193*f*, 199–200*f*
Thermal cleaving process, 69
Thermal conductivity, 281–282
Thermal cracking, 50
Thermal diffusivity, 704
Thermal expansion coefficient, 404–406
Thermal governing equation, 679
Thermal shock effects, 69
Thermogravimetric analysis (TGA), 577, 578*f*
Thermoplastic composites
  LTW, 124–132, 125*f*, 127*f*, 129–130*f*
  welding techniques, 124–125
Thermoplastic welding, 124–132
Thermoset plastics, 121–122
Thick metallic coatings
  hardness, 450–451
  laser clad co-based alloy coatings, 444–445
  microstructural characteristics, 444–445
  OIM, 445–446, 446*f*
Thin film coatings, 635–636
3D adipose stem cells (3D ASCs), 367, 367–368*f*
3D heat conduction equation, 677–678
3D Lagrangian type finite-element model, 286–287
3D numerical model, 672–673
Ti6Al4V alloy, 721–722, 723*t*, 723*f*
Ti-6Al-4V fiber laser cut, 23–24, 24*f*, 31–32
  hole-array, 756, 756*f*
  pin-array, 756, 756*f*
Ti-based materials, 522–523
Time-temperature transformation (TTT), 746–747
TiN/Co/Si system, 326*f*
TiO_2 nano particles, 40*f*
Titanium alloy-Ti6Al4V, 646–661
  chemical composition, 648*t*
  experimental method, 647–652
  experimental set-up, 650*f*
  micrograph of, 653–656*f*
  microhardness
    vs. laser power, 657*f*
    vs. scanning speed, 660*f*
  particle size analysis, 649*f*
  processing parameter for, 651*t*
  results, 652–661
  scanning velocity, 659*f*
  TiC powder, 658*f*
  Vicker's microhardness measurements, 650
  wear test, 650–652
  wear volume loss *vs.* scanning speed, 660*f*
Titanium disilicide ($TiSi_2$), 323–324
Titanium nitride (TiN), 324
Tool steel Fe-based thick coatings, 456
Transformation-induced plasticity (TRIP), 224–227
Transmission electron microscopy (TEM), 156
Tungsten inert gas (TIG) welding, 207–209, 211–213, 244
Two-photon laser lithography (TPP), 607–614, 609–610*f*
  advantages, 609–610
  drawbacks, 610–611
  fast shutter system, 610–611
  femtosecond-laser source, 610–611
  manufacturing, 607–614, 609–610*f*
  materials for, 614–618
  2PA theory, 607
  polymer and initiators, 607–609
  structuring possibilities, 611–612

U

Ultra-fast laser radiation
  ablation geometry, 96–99
  ablation model, validation of, 99–103
  beam diagnostics, 111*f*

hybrid ablation experiments, 111*f*
Ultra-fast laser sources, 553–554
Ultrashallow p^+/n junctions, 299
Ultra-short pulsed laser radiation, 93, 94*t*
Ultra-short pulse laser drilling, 34
Ultrasonic excitation, 246*f*, 248
laser beam welded dissimilar joints, 252*f*
steel-aluminum dissimilar joints, 249–254
weld surface, 252*f*
Ultrasonic welding, 187–188
Ultrasound-assisted laser-beam welding, 244–245
aluminum bead-on-plate welds, 248–249
experimental procedure, 246–248
Fe-Al phase diagram, 245*f*
molten mass, 245
motivation, 245
steel-aluminum dissimilar joints, 249–254
Ultraviolet (UV) lasers, 740

V

Vapor pressure laser cutting, 28–29
Vicker's hardness, 450–451
Volume absorption, 24–25

W

Water-assisted laser transformation hardening, 284*f*
beam profile *vs.* processing speed, 287*f*
conventional laser surface hardening process, 284–285
laser-overlapping scanning, 290*f*
Nd-YAG laser, 283
process setup and kinematics, 283*f*
spot technique, 288*f*
surface acoustic waves, 291–292*f*
thermal model, 286–287
3D Lagrangian type finite-element model, 286–287
2D scanner components, 287*f*
Water jet guide laser, 53
Water jet hybrid dicing, 91–92
Wavelength, 106–108, 107*f*
Weldability, 186
Welded joints, 186, 198
Welding defects, 154–156
Welding speed, 215
Weld penetration depth, 247*f*
Weld pools, laser-beam welding, 235
alloying elements, 241–242
approaches and methods, 238
electromagnetic forces, 238–241
gas feed, 242–243
of metals, 235–238
ultrasound method, 244
vibration method, 243–244
WHO-Fibers, 148–149
Wire feed rate, 219–220

X

X-ray diffraction (XRD), 156, 398–399, 449–450
calcium phosphate coatings, 388*f*
$MgAl_2O_4$ oxide particles, 156–159
PLD-HA coating, 387–388, 387*f*
X-ray transmission, 159, 161*f*, 171–174, 175*f*

Y

Ytterbium-doped yttrium aluminum garnet (Yb:YAG) laser, 207–209

Z

Zirconium powder, 640–641

This page intentionally left blank

Laser materials processing is a multidisciplinary field of science and engineering, with a wide range of applications in industry, research, and medicine. This new edition of *Advances in Laser Materials Processing* provides a revised, updated, and expanded overview of the area, covering fundamental theory, technology, and methods, traditional and emerging applications, and potential future directions.

The book begins with an overview of the technology and the main challenges of application in manufacturing. New and updated chapters focus on essential techniques and process, including cutting, welding, annealing, hardening, surface treatments, coating, and materials deposition. The final part of the book considers the mathematical modeling and control of laser processes. Throughout, chapters review the scientific theory underpinning applications, offer full appraisals of the processes described, and discuss potential future trends. With contributions from renowned researchers, this book provides comprehensive yet detailed coverage of the many topics that comprise the field of laser materials processing. It provides a reference source for scientists and engineers working in such areas as metals processing and microelectronics, as well as those conducting laser materials processing research in either academia or industry.

Key Features

- Provides a comprehensive practitioner guide and reference work explaining state-of-the-art laser processing technologies in manufacturing and other disciplines
- Explores challenges, potential, and future directions through the continuous development of new, application-specific lasers in materials processing
- Includes new chapters on laser hybrid welding, lasers for additive manufacturing, experimental design and much more

The Editor

Professor Jonathan Lawrence is Director of the Laser Engineering and Manufacturing Group at Coventry University, and Editor-in-Chief of *Lasers in Engineering and International Journal of Laser Science: Fundamental Theory and Analytical Methods.* His work has attracted over £5M in research funding and yielded six patents. He has published eight books and over 140 journal papers.

ISBN 978-0-08-101252-9

9 780081 012529

ELSEVIER

WP WOODHEAD PUBLISHING

An imprint of Elsevier

elsevier.com/books-and-journals